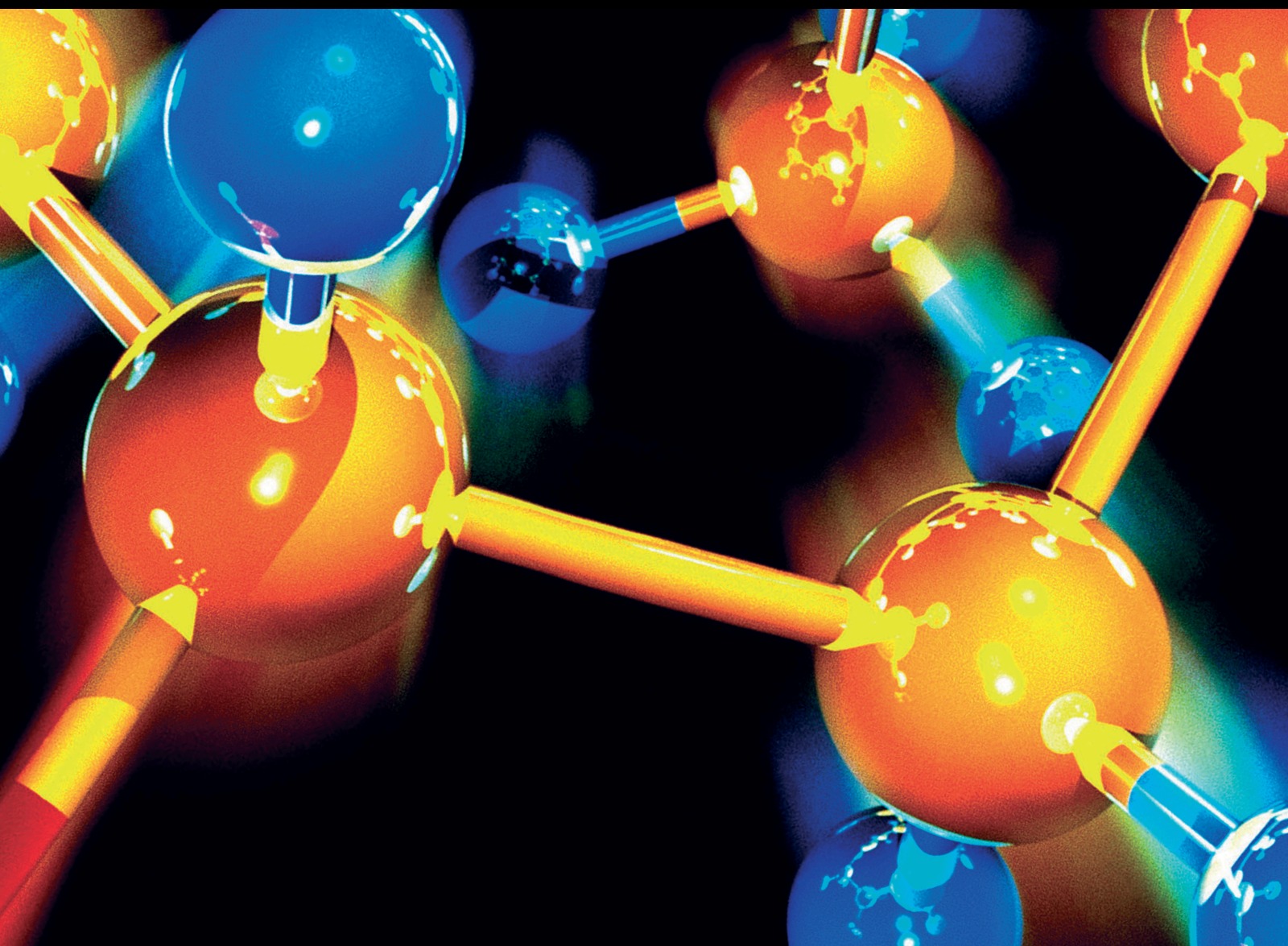


# Chemical Design and Environmental/ Energic Applications of Self- Assembled Nanocomposites and Nanostructures

Lead Guest Editor: Tifeng Jiao

Guest Editors: Bingbing Li and Peizhi Guo





---

**Chemical Design and Environmental/  
Energic Applications of Self-Assembled  
Nanocomposites and Nanostructures**

Journal of Chemistry

---

**Chemical Design and Environmental/  
Energic Applications of Self-Assembled  
Nanocomposites and Nanostructures**

Lead Guest Editor: Tifeng Jiao

Guest Editors: Bingbing Li and Peizhi Guo



---

Copyright © 2022 Hindawi Limited. All rights reserved.

This is a special issue published in "Journal of Chemistry." All articles are open access articles distributed under the Creative Commons Attribution License, which permits unrestricted use, distribution, and reproduction in any medium, provided the original work is properly cited.

# Chief Editor

Kaustubha Mohanty, India

## Editorial Board

Stefania Abbruzzetti, Italy  
Luqman C. Abdullah, Malaysia  
Dr Abhilash, India  
Amitava Adhikary, USA  
Daryoush Afzali, Iran  
Dr Mahmood Ahmed, Pakistan  
María D. Alba, Spain  
Juan D. Alché, Spain  
Mohammad A. Al-Ghouthi, Qatar  
Shafaqat Ali, Pakistan  
Mohd Sajid Ali, Saudi Arabia  
Gomaa A. M. Ali, Egypt  
Patricia E. Allegretti, Argentina  
Mohammednoor Altarawneh, Australia  
Marco Anni, Italy  
Alessandro Arcovito, Italy  
José L. Arias Mediano, Spain  
Hassan Arida, Saudi Arabia  
Umair Ashraf, Pakistan  
Iciar Astiasaran, Spain  
Narcis Avarvari, France  
Davut Avci, Turkey  
Mohamed Azaroual, France  
Hassan Azzazy, Egypt  
Renal Backov, France  
Suresh Kannan Balasingam, Norway  
Sukanta Bar, USA  
Florent Barbault, France  
Maurizio Barbieri, Italy  
James Barker, United Kingdom  
Davide Barreca, Italy  
Salvatore Barreca, Italy  
Jorge Barros-Velázquez, Spain  
Michele Benedetti, Italy  
Laurent Billon, France  
Marek Biziuk, Poland  
Jean-Luc Blin, France  
Tomislav Bolanca, Croatia  
Ankur Bordoloi, India  
Cato Brede, Norway  
Leonid Breydo, USA  
Wybren J. Buma, The Netherlands  
J. O. Caceres, Spain  
Claudio Cameselle, Spain

Joaquin Campos, Spain  
Dapeng Cao, China  
Stefano Caporali, Italy  
Zenilda Cardeal, Brazil  
Angela Cardinali, Italy  
Stefano Carli, Italy  
Maria F. Carvalho, Portugal  
Susana Casal, Portugal  
Thomas R. Caulfield, USA  
David E. Chavez, USA  
Riccardo Chelli, Italy  
Zhongfang Chen, Puerto Rico  
Zhen Cheng, USA  
Ester Chiessi, Italy  
Ann M. Chippindale, United Kingdom  
Vladislav Chrastny, Czech Republic  
Clara Cilindre, France  
Roberto Comparelli, Italy  
Filomena Conforti, Italy  
Christophe Coquelet, France  
Filomena Corbo, Italy  
Jose Corchado, Spain  
Maria N. D.S. Cordeiro, Portugal  
Claudia Crestini, Italy  
Gerald Culioli, France  
Manuela Curcio, Italy  
Shayessteh Dadfarnia, Iran  
Samuel B. Dampare, Ghana  
Umashankar Das, Canada  
Victor David, Romania  
Annalisa De Girolamo, Italy  
Antonio De Lucas-Consuegra, Spain  
Marccone A. L. de Oliveira, Brazil  
Paula G. De Pinho, Portugal  
Damião de Sousa, Brazil  
Francisco Javier Deive, Spain  
Albert Demonceau, Belgium  
Tianlong Deng, China  
Fatih Deniz, Turkey  
Stefano D'Errico, Italy  
Matthias D'hooghe, Belgium  
Claudio Di Iaconi, Italy  
Irene Dini, Italy  
Daniele Dondi, Italy

Yingchao Dong, China  
Dennis Douroumis, United Kingdom  
John Drexler, USA  
Qizhen Du, China  
Yuanyuan Duan, China  
Philippe Dugourd, France  
Frederic Dumur, France  
Grégory Durand, France  
Mehmet E. Duru, Turkey  
Takayuki Ebata, Japan  
Hani El-Nezami, Hong Kong  
Arturo Espinosa Ferao, Spain  
Carola Esposito Corcione, Italy  
Valdemar Esteves, Portugal  
Cristina Femoni, Italy  
Gang Feng, China  
Dieter Fenske, Germany  
Jorge F. Fernandez-Sanchez, Spain  
Alberto Figoli, Italy  
Elena Forte, Italy  
Sylvain Franger, France  
Emiliano Fratini, Italy  
Franco Frau, Italy  
Bartolo Gabriele, Italy  
Guillaume Galliero, France  
Andrea Gambaro, Italy  
Fernando Garay, Argentina  
Gonzalo Garcia, Spain  
Vijay Kumar Garlapati, India  
James W. Gauld, Canada  
Barbara Gawdzik, Poland  
Pier Luigi Gentili, Italy  
Beatrice Giannetta, Italy  
Dimosthenis L. Giokas, Greece  
Alejandro Giorgetti, Italy  
Alexandre Giuliani, France  
Elena Gomez, Spain  
Yves Grohens, France  
Katharina Grupp, Germany  
Tingyue Gu, USA  
Luis F. Guido, Portugal  
Maolin Guo, USA  
Wenshan Guo, Australia  
Leena Gupta, India  
Muhammad J. Habib, USA  
Jae Ryang Hahn, Republic of Korea  
Christopher G. Hamaker, USA

Ashanul Haque, Saudi Arabia  
Yusuke Hara, Japan  
Naoki Haraguchi, Japan  
Serkos A. Haroutounian, Greece  
Hongshan He, USA  
Nélio Henderson, Brazil  
Javier Hernandez-Borges, Spain  
Miguel Herrero, Spain  
Mark Hoffmann, USA  
Hanmin Huang, China  
Doina Humelnicu, Romania  
Charlotte Hurel, France  
Shahid Hussain, China  
Nenad Ignjatović, Serbia  
Ales Imramovsky, Czech Republic  
Muhammad Jahangir, Pakistan  
Philippe Jeandet, France  
Sipak Joyasawal, USA  
Sławomir M. Kaczmarek, Poland  
Ewa Kaczorek, Poland  
Hossein Kazemian, Canada  
Mostafa Khajeh, Iran  
Srećko I. Kirin, Croatia  
Anton Kokalj, Slovenia  
Sevgi Kolaylı, Turkey  
Takeshi Kondo, Japan  
Christos Kordulis, Greece  
Ioannis D. Kostas, Greece  
Yiannis Kourkoutas, Greece  
Henryk Kozłowski, Poland  
Yoshihiro Kudo, Japan  
Isabel Lara, Spain  
Bachir Latli, USA  
Jolanta N. Latosinska, Poland  
João Paulo Leal, Portugal  
Woojin Lee, Kazakhstan  
Yuan-Pern Lee, Taiwan  
Matthias Lein, New Zealand  
Landong Li, China  
Huabing Li, China  
Kokhwa Lim, Singapore  
Teik-Cheng Lim, Singapore  
Zhong-Wen Liu, China  
Xi Liu, China  
Jianqiang Liu, China  
Xinyong Liu, China  
Eulogio J. Llorent-Martínez, Spain

Pasquale Longo, Italy  
Pablo Lorenzo-Luis, Spain  
Zhang-Hui Lu, China  
Devanand Luthria, USA  
Konstantin V. Luzyanin, United Kingdom  
Mari Maeda-Yamamoto, Japan  
Isabel Mafra, Portugal  
Dimitris P. Makris, Greece  
Pedro M. Mancini, Argentina  
Marcelino Maneiro, Spain  
Giuseppe F. Mangiatordi, Italy  
Casimiro Mantell, Spain  
Ana B. Martin-Diana, Ireland  
Carlos A Martínez-Huitle, Brazil  
José M. G. Martinho, Portugal  
Andrea Mastinu, Italy  
Cesar Mateo, Spain  
Georgios Matthaiolampakis, USA  
Mehrab Mehrvar, Canada  
Saurabh Mehta, India  
Oinam Romesh Meitei, USA  
Saima Q. Memon, Pakistan  
Maurice Millet, France  
Angelo Minucci, Italy  
Liviu Mitu, Romania  
Hideto Miyabe, Japan  
Kaustubha Mohanty, India  
Ana Moldes, Spain  
Subrata Mondal, India  
José Morillo, Spain  
Giovanni Morrone, Italy  
Marta E. G. Mosquera, Spain  
Khaled Mostafa, Egypt  
Ahmed Mourran, Germany  
Markus Muschen, USA  
Benjamin Mwashote, USA  
Mallikarjuna N. Nadagouda, USA  
Lutfun Nahar, United Kingdom  
Mu. Naushad, Saudi Arabia  
Gabriel Navarrete-Vazquez, Mexico  
Jean-Marie Nedelec, France  
Orazio Nicolotti, Italy  
Nagatoshi Nishiwaki, Japan  
Tzortzis Nomikos, Greece  
Marjana Novic, Slovenia  
Beatriz P. P. Oliveira, Portugal  
Leonardo Palmisano, Italy

Mohamed Afzal Pasha, India  
Dario Pasini, Italy  
Angela Patti, Italy  
Massimiliano F. Peana, Italy  
Andrea Penoni, Italy  
Franc Perdih, Slovenia  
Jose A. Pereira, Portugal  
Pedro Avila Pérez, Mexico  
Maria Grazia Perrone, Italy  
Silvia Persichilli, Italy  
Thijs A. Peters, Norway  
Christophe Petit, France  
Marinos Pitsikalis, Greece  
Rita Rosa Plá, Argentina  
Fabio Polticelli, Italy  
Josefina Pons, Spain  
V. Prakash Reddy, USA  
María Quesada-Moreno, Germany  
Maurizio Quinto, Italy  
Franck Rabilloud, France  
Jamal Rafique, Brazil  
C.R. Raj, India  
Sanchayita Rajkhowa, India  
Teodorico C. Ramalho, Brazil  
Manzoor A. Rather, India  
Julia Revuelta, Spain  
Alberto Ritieni, Italy  
Muhammad Rizwan, Pakistan  
Manfredi Rizzo, Italy  
Maria P. Robalo, Portugal  
Maria Roca, Spain  
Nicolas Roche, France  
Samuel Lalthazuala Rokhum, India  
Roberto Romeo, Italy  
Antonio M. Romerosa-Nievas, Spain  
Ioannis G. Roussis, Greece  
Arpita Roy, India  
Deniz ŞAHİN, Turkey  
Nagaraju Sakkani, USA  
Diego Sampedro, Spain  
Shengmin Sang, USA  
Eloy S. Sanz-Pérez, Spain  
Vikram Sarpe, USA  
Adrian Saura-Sanmartin, Spain  
Stéphanie Sayen, France  
Ewa Schab-Balcerzak, Poland  
Hartwig Schulz, Germany

Gulaim A. Seisenbaeva, Sweden  
Serkan Selli, Turkey  
Murat Senturk, Turkey  
Beatrice Severino, Italy  
Sunil Shah shah, USA  
Ashutosh Sharma, USA  
Hideaki Shiota, Japan  
Cláudia G. Silva, Portugal  
Artur M. S. Silva, Portugal  
Ajaya Kumar Singh, India  
Vijay Siripuram, USA  
Ponnurengam Malliappan Sivakumar, Japan  
Tomás Sobrino, Spain  
Raquel G. Soengas, Spain  
Yujiang Song, China  
Olivier Soppera, France  
Ana Catarina Sousa, Portugal  
Radhey Srivastava, USA  
Vivek Srivastava, India  
Theocharis C. Stamatatos, Greece  
Athanasios Stavrakoudis, Greece  
Darren Sun, Singapore  
Kamal Swami, USA  
B.E. Kumara Swamy, India., India  
Elad Tako, USA  
Zhenwei Tang, China  
Shoufeng Tang, China  
Vijai Kumar Reddy Tangadanchu, USA  
Franco Tassi, Italy  
Alexander Tatarinov, Russia  
Lorena Tavano, Italy  
Tullia Tedeschi, Italy  
Vinod Kumar Tiwari, India  
Augusto C. Tome, Portugal  
Naoki Toyooka, Japan  
Andrea Trabocchi, Italy  
Philippe Trens, France  
Ekaterina Tsipis, Russia  
Andreas G. Tzakos, Greece  
Esteban P. Urriolabeitia, Spain  
Toyonobu Usuki, Japan  
Giuseppe Valacchi, Italy  
Patricia Valentao, Portugal  
Marco Viccaro, Italy  
Jaime Villaverde, Spain  
Marc Visseaux, France  
Balaga Viswanadham, India

Alessandro Volonterio, Italy  
Zoran Vujcic, Serbia  
Chun-Hua Wang, China  
Leiming Wang, China  
Carmen Wängler, Germany  
Yun Wei, China  
Wieslaw Wiczkowski, Poland  
Bryan M. Wong, USA  
Honghong Wu, China  
Frank Wuest, Canada  
Yang Xu, USA  
Yuangen Yang, USA  
Maria C. Yebra-Biurrún, Spain  
Mina Yoon, USA  
Tomokazu Yoshimura, Japan  
Sedat Yurdakal, Turkey  
Shin-ichi Yusa, Japan  
Claudio Zaccone, Italy  
Ronen Zangi, Spain  
John CG Zhao, USA  
Zhen Zhao, China  
Minghua Zhou, China  
Antonio Zizzi, Italy  
Mire Zloh, United Kingdom  
Grigoris Zoidis, Greece

# Contents

## **Chemical Design and Environmental/Energetic Applications of Self-Assembled Nanocomposites and Nanostructures**

Tifeng Jiao , Bingbing Li, and Peizhi Guo 

Editorial (1 page), Article ID 9759542, Volume 2022 (2022)

## **Hybrid Blood Purification Therapy Based on Camel Nanoantibody Immunoabsorbent on Patients with Chronic Renal Failure in Nephrology Department**

Tao Ma , Li Wang, and Xiuyong Li 

Research Article (8 pages), Article ID 8594814, Volume 2020 (2020)

## **The Diagnostic Value of Cystatin C and Mild Hypothermia Therapy Based on Immunturbidimetry Enhanced by Nanospheres in Asphyxia Neonate**

Xiaoping Dang, Xiaojian Hu , Yuancui Meng, Yan'e Yang, Lingfang Zheng, Qiong Zhang, Nan Dang, Jing Hao, Liang Zheng, and Feng Ni

Research Article (10 pages), Article ID 1549795, Volume 2020 (2020)

## **Synthesis of Bimetallic PdAg Nanoparticles and Their Electrocatalytic Activity toward Ethanol**

Fahui Gao, Yanru Yin, Zhengshuai Cao, Hongliang Li, and Peizhi Guo 

Research Article (9 pages), Article ID 1917380, Volume 2020 (2020)

## **Research Progress Review of Preparation and Applications of Fluorescent Hydrogels**

Weiwei Su, Ran Wang, Cheng Qian, Xuotong Li, Qi Tong, and Tifeng Jiao 

Review Article (17 pages), Article ID 8246429, Volume 2020 (2020)

## **Preventive Effect of Albumin Nano TPA Gene Plasmid Ultrasound Microbubble Carrier System on Thrombosis after Cardiac Valve Replacement**

Feng Qi, Linlin Zhao, Guohua Cai, Zhendong Sun, and Naishi Wu 

Research Article (8 pages), Article ID 9041821, Volume 2020 (2020)

## **Tennis Rehabilitation Training-Assisted Paclitaxel Nanoparticles in Treatment of Lung Tumor**

Di Hu  and YiMin Yang

Research Article (8 pages), Article ID 8823915, Volume 2020 (2020)

## **Chemical Compound Chemical Treatment in Animal Husbandry**

Xiaoling Tang  and Ting Peng

Research Article (8 pages), Article ID 4263124, Volume 2020 (2020)

## **Study on Preservation of Chilled Beef with Natural Essential Oil Nanocapsules**

Bin Xi , Yaqin Gao, Tianfen Guo, Weihong Li, Xiaoling Yang, and Tianqing Du

Research Article (9 pages), Article ID 8123254, Volume 2020 (2020)

## **Compatibility of Carbon Composite Biomaterials for Repairing Bone Tissue Injury in Wushu Training**

Jingfeng Ren 

Research Article (7 pages), Article ID 1247989, Volume 2020 (2020)

**Effect of Basketball Sports on Serum Superoxide Dismutase and Its Relationship with the Nanoparticle Drug Delivery System**

Jinzhong Wang and Zhenhua Guo 

Research Article (9 pages), Article ID 1623490, Volume 2020 (2020)

**Construction of Nursing Intervention Model and Clinical Empirical Study on Dopamine Beta Hydroxylase Gene Polymorphism in Children with ADHD**

Hongyi Zhao and Jiangyu Chen 

Research Article (9 pages), Article ID 9068736, Volume 2020 (2020)

**CPLD-Based Displacement Measurement System for Nanoscale Grating Ruler**

Jiyuan Sun and Chunlin Tian 

Research Article (8 pages), Article ID 5142892, Volume 2020 (2020)

**Carbon Nanomaterial Manufacturing System and Automatic Synthesis Equipment and Its Control Device and Control Methods**

Gaoxiang Lou  and Zongyan Cai

Research Article (7 pages), Article ID 3134679, Volume 2020 (2020)

**High Boron Silicon Nanotubes Combined with Tai Chi Exercise Rehabilitation Therapy in the Treatment of Knee Arthritis Patients**

Guang Ma 

Research Article (8 pages), Article ID 5452498, Volume 2020 (2020)

**Application of Nanosystems Synergized by Optics and Chemotherapy in the Treatment of Sports Rehabilitation Diseases**

Zhiwei Peng, Xianxiong Li , and Yu Zhang

Research Article (10 pages), Article ID 7124512, Volume 2020 (2020)

**Effects of Nanomaterials on the Body Composition of Patients with Dyslipidemia Based on Different Strength Sports Equipment**

Xiang Liu and Guoquan Ma 

Research Article (9 pages), Article ID 3649157, Volume 2020 (2020)

**Prevention and Control Technology for Harmful Toxic Gas Intrusion in High-Fire-Hazard-Risk Areas of Close-Distance Coal Seams**

Wei Wang  and Yuntao Liang

Research Article (12 pages), Article ID 9040825, Volume 2020 (2020)

**Industry Development of Derivative Functionalized Gold Nanomaterials and Their Application in Chemiluminescence Bioanalysis: Based on the Industrial Practice of China's Central Yunnan Urban Agglomeration**

Tengfei Ma and Hao Wu 

Research Article (9 pages), Article ID 5474506, Volume 2020 (2020)

# Contents

## **Muscle Injury in Bodybuilding Based on Mesoporous Multifunctional Nanomaterials for Sports Rehabilitation Training**

Changjun Zhao 

Research Article (9 pages), Article ID 1784036, Volume 2020 (2020)

## **Carbon Nanomaterials in the Treatment of Infectious Bone Defects and Wound Scars after Wushu Fractures**

Shenghui Wei, Lei Zou , Xu Hu, and Qiuming Li

Research Article (9 pages), Article ID 2094273, Volume 2020 (2020)

## **Planning Research on Application of Nanomaterial Technology in Disaster Prevention and Reconstruction**

Jun Shao, Huihui Yan , and Haosheng Xu

Research Article (9 pages), Article ID 7352816, Volume 2020 (2020)

## **Spectrochemical Technology in Nanomaterial Preparation and Art Appraisal Technology Research**

Xiao Tang 

Research Article (8 pages), Article ID 6938324, Volume 2020 (2020)

## **Nanometer Montmorillonite Modified Fly Ash Ecological Slope Protection Material and Its Preparation and Application**

Guochong Lou , Qinghui Zhong, and Jianguo Xie

Research Article (9 pages), Article ID 6953594, Volume 2020 (2020)

## **The Analysis of the Transformation Mechanism of cBN Crystals with the First-Principle Calculation**

Lichao Cai , Bin Xu , Meizhe Lv, and Xiaohong Fan

Research Article (6 pages), Article ID 8653032, Volume 2020 (2020)

## **Plane Animation Simulation of the Interaction between Carbon Nanomaterials and Cell Lysosomes**

Wen Liu , Feng Qiu, and Xi Zeng

Research Article (9 pages), Article ID 1980826, Volume 2020 (2020)

## **Comprehensive Evaluation of the Accelerated Aging Law of NEPE Propellants**

Yulong Liang, Mi Zhang, Hui Ren , and Qingjie Jiao

Research Article (7 pages), Article ID 8414505, Volume 2020 (2020)

## **Aggregation of Nanochemical Microcrystals in Urine Promotes the Formation of Urinary Calculi**

Yanting Lou , Wei He, and Zhengyao Song

Research Article (8 pages), Article ID 8516903, Volume 2020 (2020)

## **Effect of Football on Fatigue of Patients with Breast Cancer Treated with Nano-Chemotherapy**

Yu Zhang , Haonan Niu, and Zhiwei Peng

Research Article (7 pages), Article ID 7609803, Volume 2020 (2020)

### **Simulation of the Conductive Process of Nano ZnO Varistors Based on Animation Plane Form**

Xin Liu 

Research Article (9 pages), Article ID 9726173, Volume 2020 (2020)

### **Magnetic Nanomaterials in Chinese Medicine Chemical Composition Analysis and Drug Metabolism and Its Industry Prospect and Development Path Research**

Tengfei Ma and Peng Liu 

Research Article (8 pages), Article ID 1234269, Volume 2020 (2020)

### **Enzyme Producing Activity of Probiotics and Preparation of Compound Enzyme**

Ruokun Yi, Yanni Pan, Xingyao Long, Fang Tan , and Xin Zhao 

Research Article (8 pages), Article ID 9140281, Volume 2020 (2020)

### **Sunlight-Driven Synthesis of Silver Nanoparticles Using Pomelo Peel Extract and Antibacterial Testing**

Vinh Tien Nguyen 

Research Article (9 pages), Article ID 6407081, Volume 2020 (2020)

### **Microstructure and Corrosion Behavior of Laser-Cladding CeO<sub>2</sub>-Doped Ni-Based Composite Coatings on TC4**

Fangxia Ye , Wenxuan Shao, Xuchao Ye, Mingxia Liu, Yanxiang Xie, Peiying Bian, Xiaoyan Wang, Ling Liu, and Hong Wu

Research Article (10 pages), Article ID 8690428, Volume 2020 (2020)

### **Application and Effect of the Gymnastic Exercise Mode during Chemotherapy for Breast Cancer Patients**

Feifei Xie 

Research Article (9 pages), Article ID 6961018, Volume 2020 (2020)

### **Preparation and Photocatalytic Performances of WO<sub>3</sub>/TiO<sub>2</sub> Composite Nanofibers**

Xiuping Han , Binghua Yao , Keying Li, Wenjing Zhu, and Xuyuan Zhang

Research Article (12 pages), Article ID 2390486, Volume 2020 (2020)

### **Analysis of Cubic Boron Nitride Single Crystal Defects Growth under High Temperature and High Pressure**

Lichao Cai, Bin Xu, Meizhe Lv , Feng Jia, and Xingdong Yuan

Research Article (6 pages), Article ID 7853623, Volume 2020 (2020)

### **Efficient Optimization of *Gluconobacter oxydans* Based on Protein Scaffold-Trimeric CutA to Enhance the Chemical Structure Stability of Enzymes for the Direct Production of 2-Keto-L-gulonic Acid**

Lili Gao , Yuefeng Liu, Xiaoyu Zhang, and Hongsheng Zhang

Research Article (8 pages), Article ID 5429409, Volume 2020 (2020)

### **Microstructure and Texture Evolution of Aluminum in the Al-Nb/Ti/Ni Composite Fabricated by the ARB Process**

Nan Ye  and Xueping Ren 

Research Article (10 pages), Article ID 7584896, Volume 2020 (2020)

## Contents

---

**Facile Fabrication of SrTiO<sub>3</sub>@MoS<sub>2</sub> Composite Nanofibers for Excellent Photodetector Application**

Jinghong Li, Lun Zhang, Di Wang, Ran Wang, Xiujuan Liu, and Jingxin Zhou 

Research Article (7 pages), Article ID 4150439, Volume 2020 (2020)

## Editorial

# Chemical Design and Environmental/Energetic Applications of Self-Assembled Nanocomposites and Nanostructures

Tifeng Jiao <sup>1</sup>, Bingbing Li,<sup>2</sup> and Peizhi Guo <sup>3</sup>

<sup>1</sup>Hebei Key Laboratory of Applied Chemistry,  
Heavy Metal Deep-remediation in Water and Resource Reuse Key Lab of Hebei Province,  
School of Environmental and Chemical Engineering, Yanshan University, Qinhuangdao 066004, China

<sup>2</sup>Department of Chemistry and Biochemistry, Central Michigan University, Mount Pleasant, USA

<sup>3</sup>Institute of Materials for Energy and Environment, College of Materials Science and Engineering, Qingdao University, Qingdao, China

Correspondence should be addressed to Tifeng Jiao; [tfjiao@ysu.edu.cn](mailto:tfjiao@ysu.edu.cn)

Received 19 July 2021; Accepted 19 July 2021; Published 24 May 2022

Copyright © 2022 Tifeng Jiao et al. This is an open access article distributed under the Creative Commons Attribution License, which permits unrestricted use, distribution, and reproduction in any medium, provided the original work is properly cited.

Nowadays, the design and synthesis of self-assembled nanostructured composites have drawn much attention due to variable nanostructures and changeable properties. In view of various compositions in nanostructured composites, the application areas change from nano-biosensors, chemical reactions, and photocatalysts to organic semiconductors, etc. However, with wide and further investigation, more works seem to be explored for relative research and applications.

Herein, the aim of this special issue was to publish research/review papers targeting updated advances on the self-assembled nanomaterials with novel chemical reactions or important application properties. After the careful and rigorous review process of manuscripts, we have accepted 39 papers for publication in the present special issue. For example, Li and coworkers investigated the synthesis of SrTiO<sub>3</sub>@MoS<sub>2</sub> nanofibers by the electrospinning method, and the prepared composites showed good photoelectric properties with stable electrical conductivity and sensitivity for photodetectors. Nguyen studied the synthesis of silver nanoparticles with good antibacterial activities for potential food packaging applications. Han and coworkers built the WO<sub>3</sub>/TiO<sub>2</sub> composite nanofibers by the electrospinning strategy for enhanced model dye photocatalytic performance. Cai and coworkers considered the calculation of surface energy in the Li-N-B system using the density functional theory strategy. Gao and coworkers studied the catalytic activity toward ethanol electrooxidation of PdAg

NPs with synergistic effect. Specially, Su and coworkers presented the updated review on the preparation methods and applications of fluorescent gels, focused on utilizations in drug delivery and sensor fields. In summary, the present special issue demonstrates new insights to the readers into the updated information relative to Chemical Design and Environmental/Energetic Applications of Self-Assembled Nanocomposites and Nanostructures.

## Conflicts of Interest

The editors declare that they have no conflicts of interest regarding the publication of this special issue.

## Acknowledgments

The editors would like to thank all the authors, the reviewers, and the editorial team of the *Journal of Chemistry* for their valuable contribution and kind support in making this special issue possible.

Tifeng Jiao  
Bingbing Li  
Peizhi Guo

## Research Article

# Hybrid Blood Purification Therapy Based on Camel Nanoantibody Immunoabsorbent on Patients with Chronic Renal Failure in Nephrology Department

Tao Ma <sup>1</sup>, Li Wang,<sup>2</sup> and Xiuyong Li <sup>1</sup>

<sup>1</sup>Department of Blood Purification Center, Fuyang Second People's Hospital, Fuyang 236000, China

<sup>2</sup>Department of Nephrology, Shenzhen Longhua District People's Hospital, Shenzhen, China

Correspondence should be addressed to Xiuyong Li; [lxly8726@126.com](mailto:lxly8726@126.com)

Received 25 July 2020; Revised 27 October 2020; Accepted 11 November 2020; Published 17 December 2020

Academic Editor: Tifeng Jiao

Copyright © 2020 Tao Ma et al. This is an open access article distributed under the Creative Commons Attribution License, which permits unrestricted use, distribution, and reproduction in any medium, provided the original work is properly cited.

This paper proposes a study on the effect of hybrid blood purification therapy based on camel nanoantibody immunoabsorbent on chronic renal failure patients in nephrology department. In this paper, the hybrid blood purification therapy based on camel nanoantibody immunoabsorbent was applied to patients with chronic renal failure, and the curative effect of the patients was studied. In order to highlight the effect, a control group was set up for comparison. In this paper, the clearance effect of small molecule toxin, middle molecular toxin, and dialysis adequacy was analyzed. This study found that the average dialysis adequacy of the control group was 1.23% and that of the experimental group was 1.26%. The dialysis adequacy of the experimental group was significantly better than that of the control group. In addition, the clearance effect of small and medium molecular toxins in the experimental group was significantly better than that in the control group. It can be seen that the hybrid blood purification therapy based on camel nanoantibody immunoabsorbent is effective in the treatment of chronic renal failure patients in the department of nephrology. Therefore, it is of great value to apply camel nanoantibody in the clinical treatment of renal failure.

## 1. Introduction

Generally speaking, chronic renal failure refers to a variety of chronic kidney disease caused by the decline of glomerular filtration rate, resulting in toxic substances retention, electrolyte and acid base imbalance, endocrine disorders, and other clinical symptoms, and eventually develops into end-stage renal failure. The incidence rate of chronic renal failure has shown an upward trend in recent ten years. The treatment of this disease is maintenance treatment. The process is long and requires a lot of manpower and financial resources, whether it is a heavy burden to the country or to the family, or to the individual. Therefore, it is very important to study the treatment of chronic renal failure.

Scholars have found that there is a natural heavy chain antibody in camels. This antibody does not contain light chain. It is a single domain antibody obtained after cloning the variable region of heavy chain antibodies in camel. This

antibody is called nanoantibody and contains only one heavy chain variable region [1, 2]. Camel-derived nanoantibodies have many characteristics, such as small molecular weight, strong stability, good solubility, easy expression, weak immunogenicity, strong penetration, strong targeting, and simple humanization. Because of these characteristics, camel-derived nanoantibodies have achieved good application effect in the diagnosis and treatment of diseases. The application of camel-derived nanoantibodies can also reduce the cost [3, 4]. In this way, it will be of great significance to study the effect of camel-derived nanoantibodies in the treatment of renal failure patients, for the prevention and treatment of renal failure patients [5, 6].

Rabbit anti-camel antibodies can be detected by ELISA and western blotting, and their reactivity to all different camel IgG subclasses, which are purified from serum by differential affinity chromatography of protein-g and protein-a, is equal. Based on this, Shen used crude rabbit serum as raw material,

purified by protein a column affinity chromatography, and prepared a standard stock of rabbit anti-camel antibodies (1 mg/ml) to detect camelid immunoglobulin and its derivative nanobodies [7, 8]. On the other hand, rabbit anti-camel antibodies can also recognize nanobodies, and Shen provides an alternative method to detect the main body of these recombinant proteins [9, 10]. His research discusses the synthesis of nanobodies, which has certain reference significance for the research of this article, but his research lacks the research on the clinical application of nanobodies [11, 12]. In order to explore the possibility of transforming immunotoxins into clinical antibodies, Cooper humanized the nanoantibody sequence and further truncated the pe38 toxin from *Pseudomonas* exotoxin A (PE) to produce a more protease resistant form [3, 13]. Cooper successfully constructed the nanoantibody sequence-pe38 targeting CD7 molecule-modified immunotoxin and proved its potential in the treatment of CD7-positive malignant tumors, especially T-cell acute lymphoblastic leukemia [14, 15]. Cooper's research lacks experimental data, and its persuasiveness is weak [16, 17]. Ekart obtained high-titer anti-cd133 antibody from immunized camel, which provided basis for preparation of anti-cd133 nanoparticles [18, 19]. Ekart amplified the extracellular domain gene fragment of CD133 by PCR and connected it into pET28a plasmid to construct prokaryotic expression vector. The recombinant CD133 protein was induced to express by IPTG [20, 21]. In addition, he immunized one male Bactrian camel and two New Zealand rabbits with purified rcd133 antigen. The titer of polyclonal antibody and its specific binding to CD133 protein were detected by enzyme-linked immunosorbent assay (ELISA) and western blotting [22, 23]. Ekart's research confirmed that camel's high-titer anti-cd133 polyclonal antibody had higher specificity than rabbit's, which laid a good foundation for future experiments, but further exploration was needed in practical application [24].

Renal failure has always been a kind of disease that perplexes people's physical and mental health, and chronic renal failure is very serious to patients. With the development of science and technology, hybrid blood purification therapy based on camel nanoantibody immunoabsorbent has been applied in patients with chronic renal failure, but its efficacy needs further study. Therefore, this paper studies the effect of hybrid blood purification therapy based on camel nanoantibody immunoabsorbent on patients with chronic renal failure in nephrology department. In the research process, this paper analyzes the clearance effect of small molecular toxins, and dialysis adequacy. The results of this study show that the therapeutic effect of hybrid blood purification therapy based on camel nanoantibody immunoabsorbent is better than that of general blood purification therapy in all aspects. Therefore, it is of great value to apply camel nanoantibody in the clinical treatment of renal failure.

## 2. Materials and Methods

**2.1. Materials.** The main ingredients used in this paper are as follows: Sepharose CL-6B, DMSO, epichlorohydrin, 6-aminohexanoic acid, ethanolamine, N, N-dimethylformamide,

1-ethyl-(3-dimethylaminopropyl) carbodiimide, hydrochloric acid, acetone, N-hydroxysuccinimide, phenolphthalein, sodium thiosulfate, immunoglobulin (Ig), human serum albumin (HSA), glycine, and camel-derived nanoantibodies.

The main instruments used are as follows: enzyme-labeled instrument, UV-1201 visible spectrophotometer, SH-II circulating water vacuum pump, constant flow peristaltic pump BT00-100M, glass column, and G3 sand core funnel.

### 2.2. Experimental Methods

**2.2.1. General Information.** Forty-five patients with chronic renal failure in the Department of Nephrology from December 2018 to December 2019 in a hospital were selected. The age of these patients was 70 years old, and the youngest was 21 years old. The average age was 46 years old, including 28 male patients and 17 female patients. These patients had no symptoms of infection and excluded complications such as tumor, heart failure, pulmonary edema and liver disease.

**2.2.2. Experimental Design.** Blood purification is mainly based on the principle of semipermeable membrane, the blood and dialysate are introduced into the instrument at the same time for penetration, and the flow direction is opposite. The purpose of removing metabolites or toxic substances in the body is achieved through dispersion, transportation, and adsorption on both sides of the hemodialysis membrane. On the other hand, the residual water in the body can be removed by excessive filtration and osmosis, and the useful components such as acid carbonate can be supplemented to correct the interference of electrolyte, acid, and alkali.

In the experiment, we include 45 patients, randomly divided into two groups, the experimental group and the control group, including 23 patients in the experimental group and 22 patients in the control group. In the two groups of patients, from the age level, there is no significant difference between the two groups, which is not statistically significant. On the other hand, from the gender point of view, the patients between the two groups were not statistically significant, that is, there was no significant difference between the two groups in gender. In the experimental process, the experimental group was treated with hybrid blood purification therapy based on camel nanoantibody immunoabsorbent, while the control group was treated with conventional blood purification therapy. Other variables were controlled under the same conditions to maintain a single variable and ensure the reliability of the data.

**2.2.3. Observation Index.** Before and after blood purification treatment, we need to draw up some observation indexes to determine the experimental effect. Therefore, we chose arterial blood sampling, then separated the serum, and carried out routine detection in the laboratory of the hospital to determine the serum creatinine (SCR), urea nitrogen (BUN), blood phosphorus (P), and other indicators of the two groups of patients. On the other hand, we also need to

measure parathyroid hormone (PTH), which was completed by radioimmunoassay. In addition, we also need to calculate the clearance rate of each toxin and dialysis adequacy (kt/V):

$$\text{SRR} = \left[ \frac{(\text{CB} - \text{CA})}{\text{CB}} \right] \times 100\%. \quad (1)$$

In formula (1), CB and CA are blood concentrations before and after dialysis.

Then, the calculation formula of dialysis adequacy (kt/V) is as follows:

$$\left( \frac{\text{Kt}}{V} \right) = -\text{Ln}(R - 0.008t) + (4 - 3.5R) \times \left( \frac{\text{UF}}{W} \right). \quad (2)$$

In formula (2), Ln represents the natural logarithm, R represents the ratio of bun concentration after dialysis to that before dialysis, UF represents ultrafiltration volume, and W represents the weight of patients after dialysis.

**2.2.4. Data Processing.** In order to make the data more convincing, this paper carries out data processing. In the process of data processing, the data processing software is SPSS 20.0. On the other hand, the data in this paper were all tested by *F*-test and chi-square test. Among the data of each group,  $p < 0.05$  is the data with difference, that is, when the data of each group is  $p < 0.05$ , the data will have statistical significance.

### 3. Nanoantibody

**3.1. Structure of Nanoantibodies.** As we know, antibodies are immunoglobulins secreted by B lymphocytes or memory cells, which can specifically connect with the corresponding antigens and are an important part of the human immune system. Nanoparticles are the smallest known antigenic fragments. In general, the molecular weight of scFv is about 30 kd, while the molecular weight of nanoparticles is about 15 kd, which is equivalent to one-tenth of the normal antibody. On the other hand, there are sulfite bonds in the interior of the nanoparticles, and there are many hydrophilic residues on the surface. As we know, ordinary antibodies have six CDRs, while nanoantibodies only have three. However, although nanoantibodies have only three CDRs, they already have a complete antigen binding fragment. Not only that but also they have strong specificity and high affinity. We already know that nanoantibodies have three CDRs. How many CDRs does it have? It's four. The amino acid sequence of the skeleton region of the nanoantibody is relatively conservative. In this way, the amino acid sequence height of CDR can be changed, which is one of the determinants of the specificity of the nanoantibody.

#### 3.2. Characteristics of Nanoantibodies

**3.2.1. Small Molecule, Strong Structural Stability.** The nanoparticles are very small and have a molecular weight of one-tenth of the normal antibody. At room temperature, nanoantibodies are easier to store and use than other ordinary antibodies. Moreover, at 37°C for a week, the

nanoantibodies can maintain more than 80% of biological activity. On the other hand, the structure of the nanoantibody is very stable. Even if it is stored in the environment of 90°C for a long time, its nature can be restored, and its biological activity can be regained after the room temperature is restored.

**3.2.2. Good Solubility and Strong Tissue Penetration.** Hydrophobic residues and hydrophilic residues are related to the solubility of substances. In nanoantibodies, the hydrophobic residues become hydrophilic residues. In this way, the solubility of nanoantibodies is very good, which is better than that of general antibodies. On the one hand, nanoparticles have strong tissue penetration ability, can enter into dense tissue, play a role in it, and even effectively penetrate the blood-brain barrier.

**3.2.3. High Affinity.** Because of the structural specificity of nanoantibodies, nanoantibodies can reach the parts of the body that cannot be reached by normal antibodies. In this way, nanoantibodies can recognize specific epitope structures. In this way, both proteins and viruses in macromolecules, haptens, and peptides in small molecules can be recognized one by one with high affinity.

**3.2.4. Weak Immunogenicity to Human Body.** As we all know, the size and chemical structure of antibody molecules will affect immunogenicity, while the molecular weight of nanobodies is very small. Not only that but nanobodies have only one domain, so the immunogenicity of nanobodies will be weaker.

**3.2.5. Easy to Express, Purify, and Modify.** Nanobodies are not only small in molecular weight but also relatively simple in structure. Not only that but nanobodies are encoded by a single gene. In this way, it can be synthesized in microorganisms, and genetic engineering methods can be used to allow nanobodies to be expressed in large quantities in some microorganisms, thereby achieving large-scale production and obtaining more nanobodies, thereby reducing production costs.

### 4. Camel-Derived Nanoantibody

In order to maintain the normal function of heavy chain antibody, camel VHH gene has been selectively developed in many important functional sites. In the FR2 region of VH region of common antibodies, v37, g44, L45, and w47 interact with VL region, while in heavy chain antibody, these four amino acid residues are characteristic mutations, and the mutation sites are F (Y) 37, E44, R45, and g47. The changes of these four positions enhance the hydrophilicity of VHH, so it is not necessary to form a bilateral structure with VL to keep the structure stable. VHH camel gene and human VH gene are very similar, the similarity is as high as 80%–90%, and the structure is very similar. They contain three hypervariable regions (FVR) and four skeletal regions (FR). The difference

between VHH camel and human VH is small, but cannot be ignored. The CDR1 and CDR3 of VH were longer than VH. The CDR3 region of VHH gene is about 16–18 amino acids, while that of human and mouse VH gene is only 14 and 12 amino acids. At the same time, the VHH gene mutations of fr2v37, G44, L45, and w47 were significantly different.

**4.1. Preparation of Adsorbent.** The main synthetic steps of adsorbent are as follows:

(1) Epoxy activation

In this step, we first take Sepharose CL-6B of 5 mL, then wash it with double distilled water and drain it, and then replace the ethanol in agarose gel with double distilled water. After full cleaning, Sepharose CL-6B is then dried, and 2M NaOH is used to clean the gel, and then the liquid is drained. After this procedure is completed, we first put 5mL2MNaOH in the 50 mL cone bottle, then put the dried gel into the cone bottle, and shake it so that it can be mixed evenly. Then, 15 ml DMSO and 2.5 ml EPI were added. In addition, Sepharose CL-6B was placed in a 50 ml conical flask and immediately placed in a constant temperature shaker at 37°C. At the same time, timing was started. In this process, the reaction time was 12 min. After the reaction, Sepharose CL-6B was cleaned with 30% acetone, 70% acetone, and 100% acetone. After that, Sepharose CL-6B was cleaned with 70% acetone and 30% acetone. After that, Sepharose CL-6B was cleaned with a large amount of water.

(2) Coupling 6-aminocaproic acid

In this step, Sepharose CL-6B-EPI gel is first placed in the funnel of the G3 sand core and then washed with pH = 11 concentration of 0.1 M sodium carbonate/sodium bicarbonate buffer. After this step is completed, drain, and add 10 ml pH = 11, 0.1 M sodium carbonate/sodium bicarbonate buffer solution. Finally, 6-aminocaproic acid with final concentration of 0.34 M (about 250 times of epoxy density molar mass excess) was added, and the pH was adjusted with 2 m NaOH to make pH = 11, 37°C, and then the reaction was carried out at 170 rpm for 17 H.

(3) Ethanolamine blocks epoxy groups

We put the dried Sepharose CL-6B into a dry conical flask and then add 20 ml of 6% ethanolamine aqueous solution with pH = 10. The reaction was carried out at a temperature of 30°C and a rotation speed of 175 rpm for at least 4 hours. After the reaction is finished, according to the corresponding sequence, wash with large amount of double steam water, wash with 1M NaCl, wash with double steam water, and then measure the density of remaining epoxy group.

(4) NHS

In this step, we first use agarose gel to wash with double distilled water. This cleaning requires a lot of double distilled water. After this procedure is

finished, we use 1 M NaCl to wash and then use double distilled water to wash. After draining, we use DMF for flushing, which needs to be done twice. After these steps, we added 5 ml DMF into a dry conical flask and added ED-CHCl with final concentration of 0.2 m and NHS of 0.2 m, all of which were molar mass excess of 100 times epoxy density. After that, the reaction was carried out at a temperature of 30°C and a speed of 175 rpm for 6 h. After the reaction, it was cleaned with a large amount of DMF and stored in DMF at room temperature.

(5) Conjugation of nanoantibodies

In this step, we used ultrafiltration to change the solution into PBS buffer solution with pH 7.4 and concentration of 10 mm and then determined the protein concentration by BCA method. After that, the agarose gel was washed with a large amount of water, and Sepharose CL-6B was added to the PBS buffer to wash and dry. Then, the 3.4 mL nanoantibody solution was added into the 10 mL centrifuge, and 1mL Sepharose CL-6B gel was added to the centrifuge tube at a temperature of 30 degrees C for 175 rpm. The reaction time was 2H. After centrifugation, the supernatant was taken for determination, and the protein content in the supernatant was determined, and the supernatant was taken out for ultrafiltration preservation. After that, it was washed with 1m NaCl for twice, and then Sepharose CL-6B was centrifuged at 8000 rpm. After centrifugation, the supernatant was collected and ultrafiltered to recover the camel-derived nanoantibody. After that, the unreacted camel-derived nanoantibody in the supernatant was sucked away with a pipette gun. The remaining unreacted NHS was sealed with 6% ethanolamine solution of pH 8.0 and centrifuged at 30°C and 175 rpm for 4 h.

(6) Preservation

After the above steps are completed, we repeatedly clean Sepharose CL-6B-camel nanoantibody with double distilled water and then wash it with PBS solution after being dried. After cleaning for two times, then drain again. After that, put the prepared adsorbent in  $L \times$  PBS with pH 7.4, store it in a refrigerator at 4°C, and then add the final concentration of 0.2% according to the volume of PBS sodium azide was used as antibacterial agent.

## 5. Results and Discussion

**5.1. Analysis of Clearance Effect of Two Groups of Small Molecule Toxins.** After 6 months, the clearance effect of small molecule toxins in the two groups was analyzed and compared with that before the experiment [25, 26].

**5.1.1. Analysis of Clearance Effect of Blood SCR.** The clearance effect of blood SCR in the two groups before and after the experiment was analyzed, and the results are shown in Figure 1.

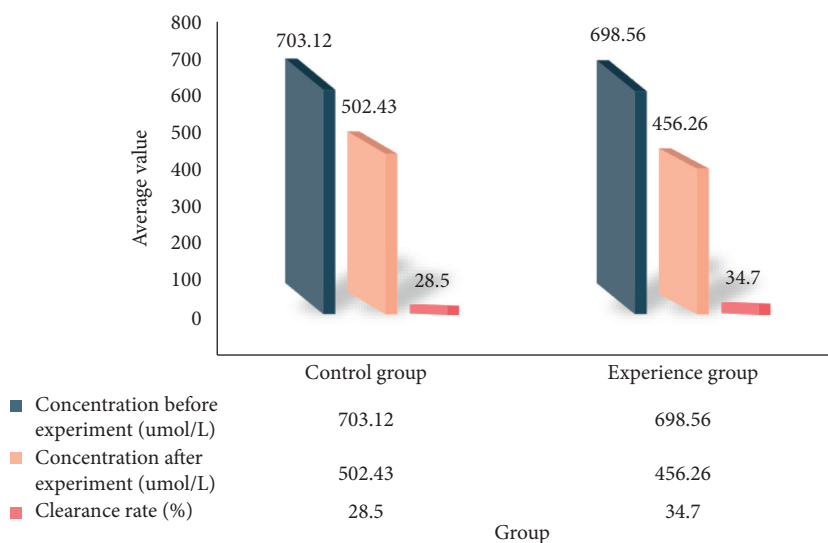


FIGURE 1: Analysis of SCR clearance effect in two groups.

Figure 1 shows the clearance effect of blood SCR between the two groups. In Figure 1, we can see that there is no significant difference between the two groups in blood SCR average concentration before the experiment. Among them, the average blood SCR concentration of the control group before the experiment is  $703.12 \mu\text{mol/L}$ , and the average SCR concentration of the experimental group is  $698.56 \mu\text{mol/L}$ , with no significant difference. After the experiment, the average value of blood SCR concentration in the control group was  $502.43 \mu\text{mol/L}$ , and the average value of blood SCR concentration in the experimental group was  $456.26 \mu\text{mol/L}$ . The average value of blood SCR concentration in the experimental group was significantly lower than that in the control group, and the data between the two groups had obvious differences. In addition, the average SCR clearance rate of the control group was 28.5% and that of the experimental group was 34.7%. The average SCR clearance rate of the experimental group was significantly higher than that of the control group [27]. Therefore, the clearance of SCR in the experimental group was better than that in the control group.

**5.1.2. Analysis of Clearance Effect of Blood P.** The clearance effect of blood  $p$  in the two groups before and after the experiment was analyzed, and the results are shown in Figure 2.

It can be seen from Figure 2 that, before the experiment, the average blood  $P$  concentration of the control group was  $2.43 \text{ mmol/L}$ , and the average blood  $P$  concentration of the experimental group was  $2.56 \text{ mmol/L}$ . Therefore, there was no significant difference between the two groups before the experiment. Then, after the experiment, the average blood  $P$  concentration in the control group was  $1.98 \text{ mmol/L}$ , and the average blood  $P$  concentration in the experimental group was  $1.82 \text{ mmol/L}$ . The average blood  $P$  concentration in the experimental group was lower than that in the control group. The blood  $p$  clearance rate was calculated. The average

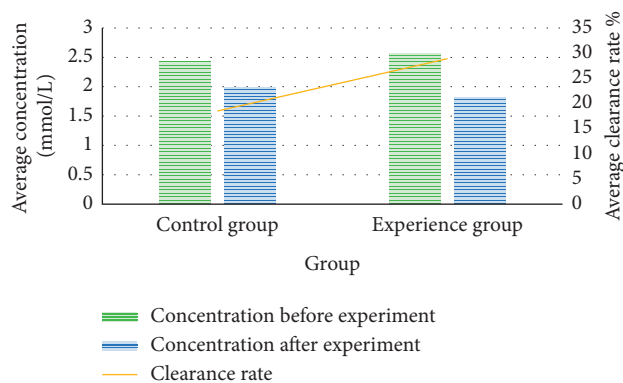


FIGURE 2: Analysis of clearance effect of  $P$ .

clearance rate of blood  $p$  in the control group was 18.5%, and the average clearance rate of blood  $p$  in the experimental group was 28.9%.

**5.2. Analysis of Clearance Effect of Intermediate Molecular Toxin (PTH) between the Two Groups.** The clearance effect of PTH between the two groups was analyzed. The results are shown in Table 1 and Figure 3.

It can be seen from Table 1 and Figure 3 that, before the experiment, there was no significant difference in blood PTH concentration between the two groups. The average blood PTH concentration of the control group was  $296.35 \text{ pg/ml}$  and that of the experimental group was  $295.35 \text{ pg/ml}$ . However, after different treatment methods, the average value of PTH concentration in the control group was  $248.56 \text{ pg/ml}$ , and the average value of PTH concentration in the experimental group was  $125.35 \text{ pg/ml}$ . The average value of PTH concentration in the experimental group was significantly lower than that in the control group. In addition, the PTH clearance rate of the experimental group was 57.6%, while that of the control group was only 16.1%. It can be seen that the treatment effect of the experimental group is better.

TABLE 1: Elimination effect of medium molecular toxin (PTH).

Group	Concentration before experiment (pg/ml)	Concentration after experiment (pg/ml)	Clearance rate (%)
Control group	296.35 ± 200.12	248.56 ± 100.12	16.1
Experience group	295.36 ± 231.35	125.23 ± 115.25	57.6

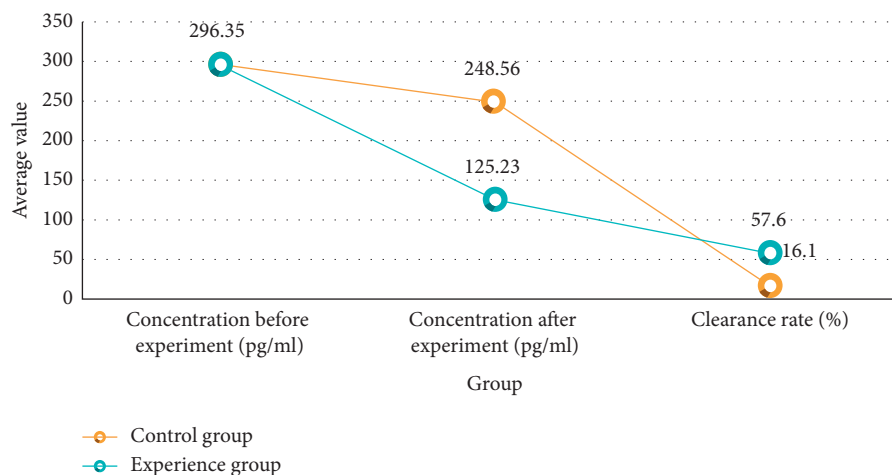


FIGURE 3: Analysis of the effect of removing middle molecular toxins.

TABLE 2: Analysis of blood bun concentration before and after the two groups.

Group	Concentration before experiment (mmol/L)	Concentration after experiment (mmol/L)
Control group	26.80 ± 11.19	10.74 ± 10.88
Experience group	27.30 ± 10.96	9.50 ± 12.50

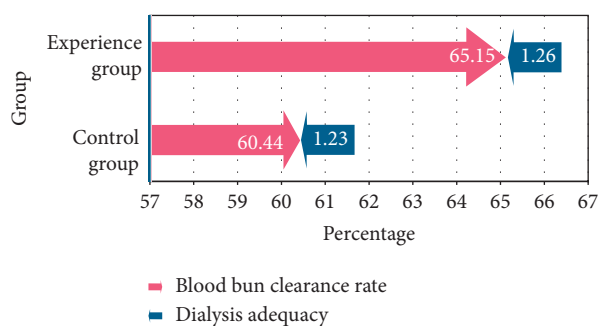


FIGURE 4: Comparison of blood bun clearance and dialysis adequacy between the two groups.

5.3. *Dialysis Adequacy (kt/V) Analysis between the Two Groups.* The blood bun concentration between the two groups was analyzed. The results are shown in Table 2.

It can be seen from Table 2 that, before the experiment, there was little difference in blood bun concentration between the two groups, but after the experiment, the blood bun concentration between the two groups changed, and the data between the two groups had difference.

The blood bun clearance rate and dialysis adequacy (kt/V) were compared between the two groups, and the results are shown in Figure 4.

It can be seen from Figure 4 that the average blood bun clearance rate of the control group was 60.44%, and that of

the experimental group was 65.15%. There was significant difference between the two groups. On the other hand, the average value of dialysis adequacy in the control group was 1.23%, and that in the experimental group was 1.26%. The dialysis adequacy of the experimental group was significantly better than that of the control group.

## 6. Conclusions

Due to the high cost of kidney transplantation, the difficulty in matching the kidney source and the high risk of surgery and the clinical treatment of patients with chronic renal failure is based on dialysis. Dialysis treatment can significantly improve the quality of life of patients and prolong survival time. With the development of science and technology, hybrid blood purification therapy based on camel-derived nanobody immunosorbent has emerged and has been proven effective through research. Many clinics have applied it to the treatment of patients with chronic renal failure in the Department of Nephrology, but its efficacy still needs to be explored in depth. For this reason, this article has conducted a study.

In the research process, this paper briefly introduces the preparation method of camel-derived nanoantibody immunoadsorbent and introduces the camel-derived nanoantibody to a certain extent. In the experiment, the control group was divided into two groups. The control group was treated with general blood purification therapy,

and the experimental group was treated with hybrid blood purification therapy based on camel-derived nanoantibody immunoadsorbent. Then, the clearance effect of small molecule toxin, middle molecular toxin, and so on was used in the experimental group. In addition to the effect and dialysis adequacy analysis, the treatment effect of the two groups was compared.

In this study, we found that the hybrid blood purification therapy based on camel nanoantibody immunoadsorbent has better effect than the general blood purification therapy in the clearance effect of small and medium molecular toxins. In addition, the dialysis adequacy is also significantly better than that of the general blood purification chemotherapy method. Moreover, the data between the two groups have obvious differences. Therefore, the hybrid blood purification therapy based on camel nanoantibody immunoadsorbent has a good effect in the treatment of patients with chronic renal failure in the Department of Nephrology.

### Data Availability

No data were used to support this study.

### Conflicts of Interest

The authors declare no conflicts of interest.

### Authors' Contributions

All authors have read and approved the final version of the manuscript.

### References

- [1] H. Muhammad, "Purification of polyclonal IgG specific for Camelid's antibodies and their recombinant nanobodies," *Central European Journal of Biology*, vol. 11, no. 1, pp. 1–9, 2016.
- [2] Y. Yu, J. Li, X. Zhu et al., "Humanized CD7 nanobody-based immunotoxins exhibit promising anti-T-cell acute lymphoblastic leukemia potential," *International Journal of Nanomedicine*, vol. 12, pp. 1969–1983, 2017.
- [3] D. Tsering and Q. Qian, "Electrolyte and acid-base disorders in chronic kidney disease and end-stage kidney failure," *Blood Purification*, vol. 43, no. 1–3, pp. 179–188, 2017.
- [4] N. A. Bazaev, V. M. Grinval'd, K. V. Pozhar, and B. M. Putrya, "Mathematical model of a biotechnical system for extrarenal blood purification using a portable Artificial kidney apparatus," *Biomedical Engineering*, vol. 49, no. 5, pp. 322–326, 2016.
- [5] A. Wiczorek, L. Matusiak, and J. C. Szepietowski, "Acquired perforating dermatosis associated with end-stage diabetic kidney failure in a hemodialysis patient," *Iranian Journal of Kidney Diseases*, vol. 10, no. 3, pp. 164–167, 2016.
- [6] K. Legrand, B. E. Stengel, W. Ngueyon Sime et al., "Perceived health and quality of life in patients with CKD, including those with kidney failure: findings from national surveys in France," *American Journal of Kidney Diseases*, vol. 75, no. 6, pp. 868–878, 2020.
- [7] J.-Q. Shen, L.-Y. Miao, and J.-F. Liu, "Fibroblast growth factor 23 resistance is probably involved in the mechanism of type 2 diabetes-induced nephropathy," *Journal of Diabetes and Its Complications*, vol. 30, no. 6, p. 1204, 2016.
- [8] B. Ellen, "Chronic kidney disease: exploring value-based healthcare as a potential viable solution," *Blood Purification*, vol. 47, no. 1–3, pp. 156–165, 2019.
- [9] H. F. Anja, "Perioperative hemodynamic instability and fluid overload are associated with increasing acute kidney injury severity and worse outcome after cardiac surgery," *Blood Purif*, vol. 43, no. 4, pp. 298–308, 2017.
- [10] A. Okuyucu, "The restorative effect of ascorbic acid on liver injury induced by asymmetric dimethylarginine," *Turkish Journal of Biology*, vol. 40, pp. 1–10, 2016.
- [11] B. S. Andrew, "Mineralocorticoid receptor antagonists in end-stage renal disease: efficacy and safety," *Blood Purification*, vol. 41, no. 1–3, pp. 166–170, 2016.
- [12] S. I. A. Hammour and K. Darwish, "Social problems resulting from chronic diseases (kidney failure and cancer): a survey study on the patients at Al-Bashear Hospital and Jordan Hospital," *Dirasat Human & Social Sciences*, vol. 45, no. 1, pp. 183–201, 2018.
- [13] D. S. Cooper, R. K. Basu, J. F. Price, S. L. Goldstein, and C. D. Krawczeski, "The kidney in critical cardiac disease," *World Journal for Pediatric and Congenital Heart Surgery*, vol. 7, no. 2, pp. 152–163, 2016.
- [14] N. Fabio, "Robust kidney perfusion mapping in pediatric chronic kidney disease using single-shot 3D-GRASE ASL with optimized retrospective motion correction," *Magnetic Resonance in Medicine*, vol. 81, no. 5, pp. 2972–2984, 2019.
- [15] J. Krauss and F. Botto, "Argentine consensus statement of cardiovascular risk evaluation in noncardiac surgery/brief version," *Revista Argentina De Cardiología*, vol. 84, no. 2, pp. 159–176, 2016.
- [16] R. Sajad, "Relationship between circadian rhythm of blood pressure and renal failure severity in patients with chronic renal failure," *Tehran University Medical Journal*, vol. 75, no. 10, pp. 738–744, 2018.
- [17] C. Y. Wang, "Cartilage MRI T2 relaxation time and perfusion changes of the knee in a 5/6 nephrectomy rat model of chronic kidney disease," *Osteoarthritis & Cartilage*, vol. 25, no. 6, pp. 976–985, 2016.
- [18] E. Robert, "Subendocardial viability ratio is impaired in highly proteinuric chronic kidney disease patients with low estimated glomerular filtration rate," *Therapeutic Apheresis & Dialysis*, vol. 20, no. 3, pp. 281–285, 2016.
- [19] O. V. Kamenskaia, A. S. Klinkova, and D. V. Khabarov, "Peripheral perfusion in CAD patients with various-stage chronic heart failure undergoing coronary artery bypass grafting," *Angiol Sosud Khir*, vol. 23, no. 1, pp. 67–73, 2017.
- [20] K. Satoshi, "Effects of chronic kidney disease on myocardial washout rate of thallium-201 in patients with normal myocardial perfusion on single photon emission computed tomography," *Annals of Nuclear Medicine*, vol. 31, no. 9, pp. 703–708, 2017.
- [21] K. Hirofumi, "Quantification of lung perfusion blood volume (lung PBV) by dual-energy CT in patients with chronic thromboembolic pulmonary hypertension (CTEPH) before and after balloon pulmonary angioplasty (BPA): preliminary results," *European Journal of Radiology*, vol. 85, no. 9, pp. 1607–1612, 2016.
- [22] W. H. Reinhart, "The optimum hematocrit," *Clinical Hemorheology and Microcirculation*, vol. 64, no. 4, pp. 1–11, 2016.
- [23] M. Aashish, B. K. Kobilka, and J. Steyaert, "Nanobodies to study G protein-coupled receptor structure and function,"

*Annual Review of Pharmacology & Toxicology*, vol. 57, no. 1, pp. 19–37, 2017.

- [24] M. J. Patel, “Cardiopulmonary exercise tests in patients with heart failure and chronic obstructive pulmonary disease,” *JACC: Heart Failure*, vol. 4, no. 4, pp. 262–264, 2016.
- [25] G. C. Zhang, J. Zhong, and Y. M. Yang, et al., Ternary BiVO<sub>4</sub>/NiS/Au nanocomposites with efficient charge separations for enhanced visible light photocatalytic performance,” *Chemical Engineering Journal*, vol. 375, Article ID 122093, 2019.
- [26] M. Feng, J. Gu, G. C. Zhang et al., “Homogeneous nickel bicarbonate nanocrystals as electrode materials for high-performance asymmetric supercapacitors,” *Journal of Solid State Chemistry*, vol. 282, Article ID 121084, 2020.
- [27] C. Jin, M. Feng, J. Zhong et al., “Insights into mechanism of size-controlled synthesis of CH<sub>3</sub>NH<sub>3</sub>PbBr<sub>3</sub> perovskite quantum dots and large nanoparticles with tunable optical properties,” *Organic Electronics*, vol. 82, Article ID 105712, 2020.

## Research Article

# The Diagnostic Value of Cystatin C and Mild Hypothermia Therapy Based on Immunoturbidimetry Enhanced by Nanospheres in Asphyxia Neonate

Xiaoping Dang,<sup>1</sup> Xiaojian Hu ,<sup>2</sup> Yuancui Meng,<sup>1</sup> Yan'e Yang,<sup>3</sup> Lingfang Zheng,<sup>1</sup> Qiong Zhang,<sup>4</sup> Nan Dang,<sup>5</sup> Jing Hao,<sup>6</sup> Liang Zheng,<sup>2</sup> and Feng Ni<sup>2</sup>

<sup>1</sup>Department of Neonatal, Second Affiliated Hospital of Xi'an Medical College, Xi'an 710038, China

<sup>2</sup>Department of Urology, Second Affiliated Hospital of Xi'an Medical College, Xi'an 710038, China

<sup>3</sup>Department of Pediatrics, Second Affiliated Hospital of Xi'an Medical College, Xi'an 710038, China

<sup>4</sup>Department of Nephrology, Second Affiliated Hospital of Xi'an Medical College, Xi'an 710038, China

<sup>5</sup>Department of Pharmacy, Second Affiliated Hospital of Xi'an Medical College, Xi'an 710038, China

<sup>6</sup>Department of Neonatology, Affiliated Hospital of Yan'an University, Yan'an, China

Correspondence should be addressed to Xiaojian Hu; 19084943@qq.com

Received 24 July 2020; Revised 27 October 2020; Accepted 15 November 2020; Published 12 December 2020

Academic Editor: Tifeng Jiao

Copyright © 2020 Xiaoping Dang et al. This is an open access article distributed under the Creative Commons Attribution License, which permits unrestricted use, distribution, and reproduction in any medium, provided the original work is properly cited.

In order to evaluate the early diagnosis value of CysC and the influence of mild hypothermia on the renal damage of asphyxia neonates, the serum cystatin C (CysC) levels of asphyxia neonates and normal neonates were measured by the nanomicrosphere-enhanced immunoturbidimetric method. The treatment was carried out, and the influence of mild hypothermia treatment on the renal damage of asphyxia neonates was analyzed. The results showed that the indicators of the asphyxia group were significantly higher than those of the control group, and the severe asphyxia group was significantly higher than that of the mild asphyxia group, which was statistically significant ( $p < 0.05$ ); the heart rate of patients in the mild hypothermia treatment group decreased gradually with the decrease in body temperature. And compared with the control group, there was a significant difference ( $p < 0.05$ ); after symptomatic treatment, the two groups of ALT, AST, BUN, and SCR were improved to varying degrees, and the difference was statistically significant compared with before treatment ( $p < 0.05$ ). Studies have shown that serum CysC level can be used as an indicator to detect glomerular filtration function and early asphyxia newborns, and it is sensitive and specific for early diagnosis of kidney damage. At the same time, it can be used to monitor clinical renal function and determine the status of asphyxia newborns.

## 1. Research Background

Neonatal asphyxia easily leads to multiple organ ischemia, hypoxia, and functional damage; therefore, early protection of renal function is of great significance [1]. According to a long-term follow-up study, if kidney damage occurs in the neonatal period, neonatal asphyxia is caused by various reasons before, during, and after birth [2]. It is one of the important causes of perinatal neonatal death and disability [3].

In China, the incidence of asphyxia is higher than 5%, and asphyxia death accounts for more than 30% of infant

death [4]. The main complications of asphyxia are dysfunction of brain, kidney, heart, and other organs, and kidney is one of the most vulnerable target organs [5, 6]. Neonatal asphyxia often occurs and is even life-threatening in severe cases. When asphyxia occurs, the endogenous creatinine clearance rate will decrease, nitric oxide in the kidney will increase, and the synthesis and expression of adhesion molecules between cells will increase, which can easily lead to impaired renal function [7]. Renal function usually includes glomerular filtration and reabsorption and secretion of renal tubules.

Glomerular filtration rate (GFR) is the most direct, objective, and sensitive indicator of glomerular filtration rate. It cannot be measured directly, but it can be measured by measuring the filter rate of a specific marker. For example, inulin removal and isotope labeling are external labels and the gold standard for evaluating glomerular filtration rate [8, 9]. However, this kind of special operation is complex, expensive, and invasive, which is difficult to promote in newborns. There are three forms of creatinine (CR): serum creatinine clearance rate, endogenous creatinine clearance rate, and blood creatinine glomerular filtration rate. These indexes are affected by many factors and are easily disturbed [10]. Although it is reabsorbed by the epithelial cells of the proximal convoluted tubules, it then decomposes in the cells, so the glomerular YSC does not return to the blood [11, 12]. From these characteristics, cystatin C is close to the ideal endogenous GFR marker reflecting the early damage of renal filtration barrier. The serum level is relatively stable and free from the interference of bilirubin, hemoglobin, cholesterol, age, gender, exercise, diet, inflammation, and other external factors [13]. It is more accurate and sensitive than SCR. Early diagnosis and treatment of renal damage are necessary to reduce mortality and improve the poor prognosis of renal damage.

## 2. Related Content

*2.1. Neonatal Asphyxia.* Various high-risk factors before, during, and after childbirth cause fetal distress, lead to anoxia and acidosis, and then damage the multiorgan function of the whole body. Immature renal function, poor glomerular filtration, poor reabsorption and excretion of renal tubules, asphyxia, and hypoxia stimulate arachidonic acid metabolism, increase the synthesis of thromboxane A<sub>2</sub>, make renal vessels contract, reduce renal blood flow, and reduce glomerular filtration rate [14, 15]. Severe hypoxia can cause renal cortex and medulla necrosis, nephron damage, abnormal cell energy metabolism, lactic acid accumulation, acidosis damage cell membrane pump function, and calcium influx. After asphyxia, proximal convoluted tubules and glomerular filtration membranes are sensitive to hypoxia and ischemia. The renal hemodynamics, renal blood flow velocity, and systolic blood flow velocity of asphyxiated neonates were monitored by color Doppler technique. The physiological characteristics of newborns and the pathophysiological changes after renal hypoxia can lead to acute renal failure, such as functional oliguria, anuria, hematuria, albuminuria, tubular urine, water, electrolyte, acid-base imbalance, etc. [16].

The incidence rate of neonatal is not low, but if the early intervention is reversible and the condition is aggravated, renal failure may occur, and life is seriously endangered. In addition, when neonatal renal function is damaged, the symptoms are not typical and early complications are difficult to distinguish. Therefore, early diagnosis is very important for the prevention and treatment of acute renal failure. Renal function includes glomerular filtration function, renal tubular reabsorption function, and secretion function [17]. Glomerular filtration rate is the most direct,

objective, and sensitive index to reflect glomerular filtration function. With the development of medicine and the improvement of renal function monitoring methods, more and more reports on renal function damage of newborn are presented. Neonatal asphyxia is one of the most common and important diseases endangering the health of newborn [18]. Metabolic or mixed acidosis caused by hypoxia and inhibition of central nervous system and respiratory circulation often develops into multiple organ damage, in which the incidence of renal damage is more than 50%. Therefore, the application of sensitive renal function detection method in the monitoring of renal damage after asphyxia is of positive significance in guiding clinical treatment and reducing the mortality and disability rate of asphyxiated newborns. In the past, serum creatinine and urea nitrogen were commonly used to monitor renal function, but the serum level of these markers was not stable, generally only increased when the glomerular filtration function lost more than 50%. Therefore, serum creatinine and urea nitrogen should not be used as indicators to detect mild or early glomerular filtration damage. There are also some low molecular weight proteins, such as microglobulin, and retinol binding protein. Microglobulin has been proved to reflect the change of glomerular filtration rate, but its level in blood circulation will be affected by infection, diet, liver disease, and other external factors, so as to change its production rate and limit its clinical application. The analysis of its gene sequence and promoter structure shows that cystatin C gene is a "housekeeping gene," which can be continuously transcribed and expressed in all tissues [19, 20]. All nucleated cells can secrete cystatin C.

*2.2. Early Diagnosis Index.* Routine urine examination often shows renal function damage: urine contains red blood cells, white blood cells, protein, renal tubular epithelial cells, and renal tubular type, which is the earliest and most common urinary system examination method with high sensitivity. Tongjianxia reported that it has clinical significance for asphyxiated newborns, but it is affected by collection time, placement time, urine chemical composition, and other factors, and the difficulty of urine collection for newborns is great, so its application value in neonatal asphyxia is limited. It is affected by protein intake, decomposition level, renal blood flow, and other factors. Only when the glomerular filtration rate drops to 1/3 of the normal value can the creatinine increase significantly [21, 22]. The creatinine level of the newborn represents the level of the pregnant woman, which is usually high. With the maturity of renal function, the clearance rate increased and SCR decreased. Therefore, detection is limited and can not predict early renal function damage. When renal function decreased, the increase of blood BUN and Cr was not directly related to the decrease of glomerular filtration rate, but in the form of antiparabola. That is, in asphyxia and hypoxia, glomerular filtration rate decreased and serum creatinine increased. Renal compensatory function is powerful; only when more than 75% of nephrons are destroyed and the glomerular filtration rate is reduced to less than 50%–60%, it can increase the blood

capsule and blood Cr, which has a more obvious reflection, and the sensitivity of the test is poor, so it is possible to miss the early pathological changes or slight renal damage of patients. Therefore, diagnosis may be delayed, which is not an indicator of early renal impairment. At present, the detection of urea nitrogen and creatinine is easy to carry out, and its practical value is still a routine item for the diagnosis of neonatal renal function in primary hospitals. Endogenous creatinine clearance rate (CCR) is a quantitative method which can reflect glomerular filtration function, roughly estimate effective renal units, and measure renal damage. When CCR is lower than 80%, blood BUN and SCR can still be in the normal range and CCR can reflect the impairment of glomerular function earlier. It is a suitable diagnostic method for the neonates with normal urine volume and azotemia. However, CCR is calculated based on the concentration of creatinine in the blood and urine. It still has the disadvantages of SCR. It is also influenced by many factors. For example, if you want to take a total urine volume of 4 or 24 hours, the retention sample may not be accurate and the measurement process is complex. In order to clear the plasma, the ML value of creatinine per minute must be calculated. It is difficult and limited for newborns. More than 99.9% of them enter the cytoplasm through the pinocytosis of renal proximal convoluted tubules and decompose into amino acids, so only a very small part of them are excreted from urine. Therefore, under normal circumstances, there is only a very small amount of microglobulin in human urine, so the microglobulin in urine is an indicator of kidney damage. In patients with acute and chronic renal failure, urinary  $\beta$  2-microglobulin increased significantly, 40 mg/L, which proved that such a high level of urinary  $\beta$  2-microglobulin could not be simply explained as the increase of glomerular filtration load, and renal tubules must also suffer serious damage. The increase of serum content can reflect the impairment of glomerular filtration function or the increase of filtration load. With the development of the disease and the increase of the age of the newborn, the improvement of the degree of hypoxic ischemia and the decrease of  $\beta$ 2-mg in serum are the sensitive indexes for the early recovery of renal tubular function.

It is of great clinical value to check the change of  $\beta$ 2-mg in blood and urine regularly for early detection of diabetic nephropathy. The detection of cystatin C (CysC) is an immunological method based on antigen antibody reaction. The sensitivity of enzyme-linked immunosorbent assay is high, and the accuracy of detection is not affected by bilirubin, hemoglobin, and other factors in the blood. Its accessory characteristics meet the requirements of ideal endogenous GFR markers: glomerular free filtration; no secretion or reabsorption of renal tubules; and no external space; it is stable in vivo, appears in plasma, and does not bind with protein; it is easy to detect in plasma and urine. More and more attention has been paid to the study of serum cystatin C. Fang Mingjun and QiuYuanyuan reported that the more severe the asphyxia, the higher the level of cystatin C. The serum concentration of premature infants was higher than that of term infants. In the two stages of preterm and full-term infants, it was not affected by inflammation,

bilirubin level, hemoglobin content, hemolytic factor, triacylglycerol, weight, and liver function change, and had nothing to do with gender, age, muscle volume, etc. The high concentration of sCysC in the early stage of life is related to the maturation of glomerular filtration function. With the gradual maturity of glomerular filtration function, the concentration tends to be constant. The formation of cystatin C in neonates is not affected by maternal factors or prerenal factors (i.e., dehydration). Its metabolism is only affected by glomerular filtration rate. It mainly exists in extracellular fluid, but there is almost no such substance in urine; that is, the level of cystatin C in urine is very low, so it is not necessary to evaluate renal function through cystatin clearance rate. So, the concentration of CysC in blood can be used as a sensitive index to reflect the early damage of glomerular filtration barrier and can better reflect the change of glomerular filtration rate, which is better than creatinine and urea nitrogen in the early stage of renal failure. We know that CysC is completely absorbed and metabolized in proximal renal tubules after glomerular filtration. The urine content of normal people is very small. Therefore, in theory, when the renal tubular reabsorption or/and metabolic function is damaged, the concentration of urinary CysC (uCysC) can be greatly increased. It is speculated that uCysC can reflect the function of proximal renal tubular. Some studies have shown that the increase of uCysC can not accurately reflect the damage of GFR, but it is very sensitive to reflect the damage of renal tubular function. Compared with the abovementioned traditional detection, sCysC is theoretically more sensitive than sCysC in reflecting GFR, especially in the case of a slight decrease in GFR, because of its unique molecular biological and biochemical characteristics. Compared with SCR, sCysC has higher diagnostic accuracy and sensitivity. SCR was not reported to be superior to sCysC. sCysC is superior to SCR in monitoring acute renal injury in critical children. sCysC is a simple and useful GFR marker, which is of great value for monitoring renal function in critically ill children.  $\beta$ 2-mg is also a marker of GFR, but it is affected by many factors such as inflammation and tumor. The incidence of renal function damage after neonatal asphyxia is in brain injury. The detection of blood BUN and SCR is of practical value in primary hospitals and is still the most commonly used indicator for diagnosis and monitoring. The prognosis of early diagnosis and treatment is good. It is difficult to find the early clinical symptoms of neonatal renal damage, so it is necessary to monitor renal function with a variety of sensitive indicators. In conclusion, CysC, as a new early indicator of renal function damage, has been evaluated as more sensitive or equivalent to SCR in many pediatric clinical research fields. Whether we can replace SCR as an indicator of renal function damage in clinical work remains to be further designed and scientifically studied to evaluate its clinical applicability.

*2.3. Immunoturbidimetry Enhanced by Nanospheres.* Polymer microsphere is a kind of composite material or polymer material whose diameter is between micrometer and

nanometer and whose shape is generally spherical. There are many preparation methods in the literature. At present, there are two main categories of polymers, including emulsion curing, single coacervation, and complex coacervation. The other is polymerization with monomer as raw material. According to the properties of microspheres, they can be divided into magnetic microspheres, fluorescent microspheres, and so on. According to the different surface functional groups, it can be divided into carboxylation, amination, sulfonation polymer microspheres, and so on. With the introduction of various functional groups into monodisperse polymer microspheres, their applications are more and more extensive. At present, it is mainly used in biomedical, analytical chemistry, colloid, in vivo drug analysis, and chromatographic separation. It shows a good application prospect in the field of high and new technology. At present, polymer microspheres have been commercialized in Europe, the United States, Japan, and other regions. Styrene is often used as the raw material monomer for the preparation of polymer microspheres because of its low price, easy access to raw materials, and easy polymerization. In order to detect and diagnose diseases, latex enhanced immunoturbidimetry (letia) is often used. By measuring the change of a value before and after the reaction, the concentration of antibody (antigen) in the sample can be calculated. Letia has been widely used in clinical, involving tumor, rheumatism, liver function, renal function, and other fields. Emulsion polymerization is the most commonly used method to prepare microspheres. The surface of PS microspheres is phenyl with strong hydrophobicity and low reactivity. It is not easy to react with antibodies, antigens, and other proteins. The antibody or antigen is physically adsorbed on the surface of the microspheres through the hydrophobic interaction between the hydrophobic part and phenyl. The physical adsorption is nonspecific and unstable. The adsorption of antibody on the surface of the microspheres will decrease with the prolongation of the reagent storage time. At the same time, when the microsphere adsorption containing solution contacts with other protein antibodies, the adsorbed antibodies are exchanged with the protein solution, so that the microsphere loses detection activity. Therefore, the stability and sensitivity of diagnostic reagents are affected. If carboxy or amino groups react strongly to introduce microspheres to immobilize antibody and microspheres through chemical bonding reaction, the firmness of antibody binding and microspheres can be enhanced to a large extent, and the phenomenon of antibody shedding and protein exchange can be avoided. The common methods of introducing active groups are copolymerization of different monomers and chemical modification of microsphere surface. Immunoassay is a method to detect various substances (drugs, proteins, microorganisms, etc.) by the specific binding reaction of antibody antigens.

At present, detection reagents are commonly used in clinical latex enhanced immunoassay, including  $\beta$  2-microglobulin detection reagent ( $\beta$  2-m), C protein detection reagent, pulmonary embolism detection reagent, glycosylated hemoglobin detection reagent, etc., which can be,

respectively, used in the detection and diagnosis of renal function, rheumatism, blood lipid thrombosis, diabetes, etc. The carriers commonly used in immunoassay include test tubes, microspheres, magnetic particles, nanospheres, and other materials. Because the molecular structure of polymer microspheres can be designed, more and more scientists are engaged in this field. In order to achieve the required specific properties and functions, the size and uniformity of microspheres can be controlled purposefully in the design and preparation process. The whole process is divided into growth period, constant speed period, and deceleration period. In the reaction process, the amount of initiator and emulsifier will affect the size and distribution of microspheres. In order to stabilize emulsion polymerization, the amount of emulsifier and initiator dosage should be appropriately prepared to obtain emulsion with uniform particle size. At the same time, in order to prevent the particles from polycondensation, it is beneficial to the stability of emulsion polymerization to reduce the reaction temperature and the stirring speed under the premise of ensuring the polymerization effect. In order to improve the probability of obtaining free radicals, lipophilic initiator is often used to initiate polymerization, which is a kind of "bulk polymerization" of single drop of small body liquid. Initiator and other factors affect the preparation of suspension polymer microspheres. With the increase of the initial dose, the particle size increases and the polymerization time shortens. The adsorption rate of stabilizer is relatively low, which can accelerate the agglomeration process and easily produce larger beads. If the amount of dispersant is too high and the viscosity of the system is too high, the amount of nucleation will be increased. The growth of polymer microspheres was affected by the inhibition of nuclear polymerization. The immobilized enzyme is practical and convenient for industrialization. The polymer microsphere with carboxyl functional group on the characteristic surface used in the test is to repair the surface of antigen monodisperse microsphere with immune cell substance of  $-NH_2$  under mild conditions, then increase the antibody, use the principle and fixed antigen antibody to make the microsphere agglomerate, and then use the spectrophotometer to determine whether agglomerate is to determine the number of immune cells. The principle of virus removal is similar to the purification and separation of biomacromolecules. In short, the nanomicrosphere-enhanced immunoturbidimetric method has the advantages of high throughput, easy automation, being simple and fast, no radioactive contamination, and suitability for the detection of large quantities of specimens. It is of great help to the diagnosis and treatment of newborns and improving the survival rate of newborns.

### 3. Experimental Setup

**3.1. Research Object.** The subjects of the study were 50 asphyxiated neonates with term asphyxia in our hospital. The gestational age was 30–45 weeks, and the birth weight was 2.5–3.0 kg. According to the diagnosis and grading criteria of neonatal asphyxia in the fourth edition of *Practical*

*Neonatology*, they were divided into mild and severe near asphyxia groups: 10 scores as Apgar score of 0–3 in severe asphyxia group and 10 scores as Apgar score of 4–7 in mild asphyxia group. In the control group, 10 full-term healthy newborns were selected as the control group. There was no significant difference in sex, gestational age, birth weight, and age among the three groups.

**3.2. Specimen Collection.** On the first day, the third day, and the seventh day of asphyxia, 5 ml of peripheral venous blood was taken from the patients of mild asphyxia group and severe asphyxia group, respectively, and serum was separated. In the control group, 5 ml of peripheral venous blood was taken on the second day of birth. The levels of CysC, BUN, Cr, and  $\beta$ 2-mg were determined by ELISA.

**3.3. Experimental Plan.** Detection of cystatin C in serum: cystatin C is detected using an immunoassay. Absorption of reactive solutions at specific wavelengths has been measured. There is a positive correlation between turbidity and serum cystatin concentration.

Particle enhanced immunoturbidimetry (PET) principle: the diameter of particle, which is covalently bound by carbodiimide reaction, and the size of ciggintex particle, which is bound with antigen, are used to precipitate PEG-6000 and turbidity, which are calculated by the turbidimetry method of 360 nautical miles, while a series of standards are the same. Operation: take serum or standard series and put into the reaction cup, add 10 gl distilled water Shen sampling needle, add 2309l reaction buffer, mix well, add cysteine protease inhibitor C immune particle suspension and distilled water Shen reagent needle, and measure the absorbance in 240s. Subtract the blank reading from the standard tube absorbance and make a picture. Subtract the blank reading from the sample tube absorbance and check the concentration of cystatin C from the standard curve.

Determination of serum creatinine: automatic biochemical instrument was used. Urea test: use urea test kit to test.

Determination of  $\beta$ 2-mg: the content of  $\beta$ 2-mg in serum samples of three groups of patients was detected by automatic biochemical instrument.

Glomerular filtration rate (EGFR):  $EGFR = k * height (CM) / SCR (mg/D1)$ , where  $k$  is a constant, indicating the output of urine creatinine per unit lean body weight, 0.45 for term infants and 0.33 for low birth weight infants, which can accurately estimate glomerular filtration rate.

Statistical processing: SPSS17.0 statistical software package was used for statistical analysis. Before statistical comparison of continuous data, normal test and Levene test were used. The measurement data were expressed by means of mean and standard deviation, and the group  $t$ -test was used for comparison between groups. The counting data is expressed in percentage, and the comparison between groups is performed by chi square test or Fisher exact probability method. Pearson correlation analysis was used to analyze the correlation between serum CysC and  $\beta$ 2-mg and renal function indexes. The difference was statistically

significant ( $p = 0.05$ ). In order to evaluate the feasibility of joint detection, sensitivity, specificity, positive predictive value, negative predictive value, positive likelihood ratio, and negative likelihood ratio need to be calculated, respectively.

## 4. Experimental Results

### 4.1. Cystatin C Comparison

**4.1.1. Laboratory Indicators.** According to the statistical analysis of data, as shown in Figure 1 and Table 1, CysC,  $\beta$ 2-mg, SCR, and BUN in the asphyxia group were significantly higher than those in the control group, and those in the severe asphyxia group were significantly higher than those in the mild asphyxia group ( $p < 0.05$ ). The levels of serum SCR, BUN,  $\beta$ 2-mg, and CysC in asphyxia group decreased gradually. The indexes of the first day of life in the mild asphyxia group were higher than those in the control group, the difference was statistically significant ( $p < 0.05$ ), but there was no statistical difference between the indexes of the third day and the seventh day of life in the mild asphyxia group and the control group. The indexes of the first day and the third day in the severe asphyxia group were higher than those in the control group and the mild asphyxia group ( $p < 0.05$ ).

**4.1.2. Diagnostic Value.** According to the statistical analysis of data, as shown in Figure 2 and Table 2, EGFR was used as the evaluation standard of renal function damage in asphyxia group. Compared with the levels of CysC,  $\beta$ 2-mg, SCR, and BUN on the first day after admission, the sensitivity and specificity of serum CysC were the highest. The difference was statistically significant ( $p < 0.05$ ). There was no significant difference between the two groups ( $p < 0.05$ ).

### 4.2. Mild Hypothermia Treatment

**4.2.1. Changes in Vital Signs.** According to the statistical analysis of data, as shown in Figure 3 and Table 3, the heart rate of patients in the mild hypothermia treatment group gradually decreased with the decrease of body temperature, and the central heart rate in the course of mild hypothermia treatment was significantly different from that before and in the control group ( $p < 0.05$ ). After mild hypothermia treatment, heart rate recovered with body temperature. After 12 hours of mild hypothermia treatment, the heart rate of children in the mild hypothermia treatment group recovered completely, and there was no significant difference between the two groups. Mild hypothermia was used to treat no arrhythmia and severe bradycardia. There was no statistical difference between the treatment group and the control group. There was no significant difference in blood pressure between the two groups before and after treatment. There was no significant change in blood pressure in the mild hypothermia group. After mild hypothermia treatment, blood pressure slightly decreased with the rise of body

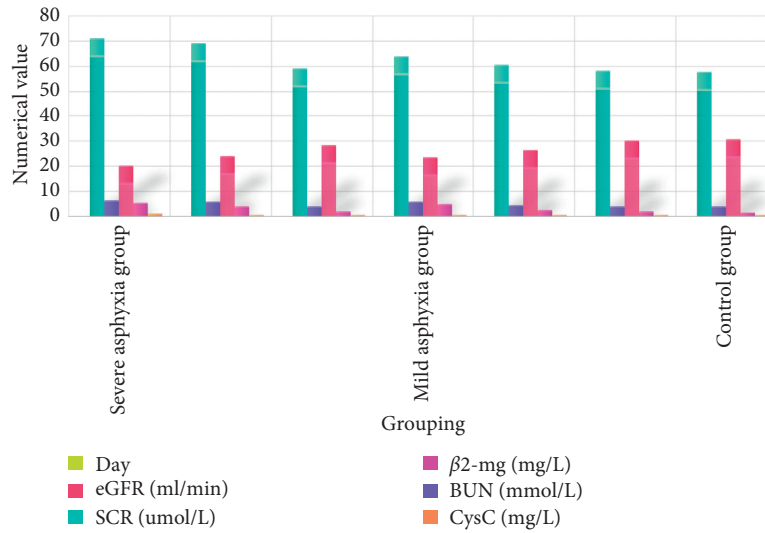


FIGURE 1: Laboratory indicators.

TABLE 1: Laboratory indicators.

Grouping		SCR ( $\mu\text{mol/L}$ )	BUN (mmol/L)	eGFR (ml/min)	$\beta 2\text{-mg}$ (mg/L)	CysC (mg/L)
Severe asphyxia group	Day 1	$72.0 \pm 7.32$	$7.13 \pm 0.66$	$21.11 \pm 4.02$	$6.08 \pm 0.77$	$1.54 \pm 0.25$
	Day 3	$69.7 \pm 6.88$	$6.48 \pm 0.51$	$24.64 \pm 3.04$	$4.82 \pm 0.66$	$1.42 \pm 0.32$
	Day 7	$59.73 \pm 6.15$	$4.72 \pm 0.49$	$29.22 \pm 3.43$	$2.58 \pm 0.77$	$1.18 \pm 0.28$
Mild asphyxia group	Day 1	$64.38 \pm 4.43$	$6.46 \pm 0.86$	$24.23 \pm 3.32$	$5.53 \pm 0.03$	$1.39 \pm 0.20$
	Day 3	$61.23 \pm 3.32$	$5.03 \pm 0.72$	$27.12 \pm 2.88$	$3.14 \pm 1.02$	$1.22 \pm 0.15$
	Day 7	$59.08 \pm 3.02$	$4.69 \pm 0.69$	$30.88 \pm 3.01$	$2.59 \pm 0.09$	$1.11 \pm 0.09$
Control group		$58.43 \pm 2.47$	$4.51 \pm 0.87$	$31.68 \pm 4.77$	$2.44 \pm 0.77$	$1.08 \pm 0.21$

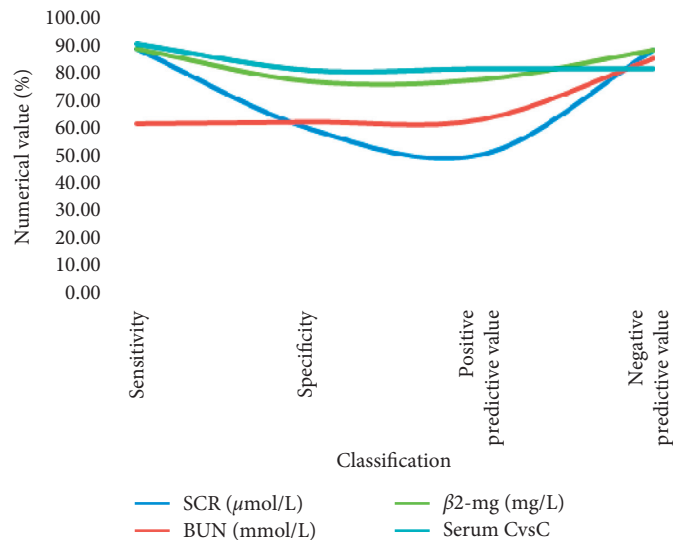


FIGURE 2: Diagnostic value.

TABLE 2: Diagnostic value.

Index	Sensitivity (%)	Specificity (%)	Positive predictive value (%)	Negative predictive value (%)
SCR ( $\mu\text{mol/L}$ )	88.47	59.49	50.00	88.09
BUN (mmol/L)	61.20	61.82	62.75	84.96
$\beta 2\text{-mg}$ (mg/L)	88.47	76.78	77.46	88.09
Serum CysC	90.07	80.66	81.25	81.25

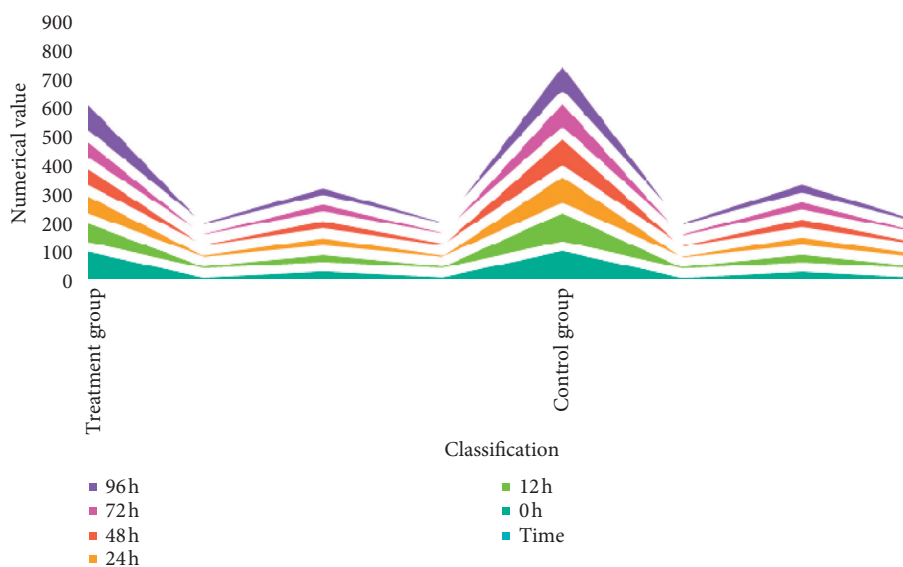


FIGURE 3: Changes in vital signs.

TABLE 3: Changes in vital signs.

Time	Treatment group				Control group			
	Heart rate	Breathing	Systolic pressure	Diastolic pressure	Heart rate	Breathing	Systolic pressure	Diastolic pressure
0	131 ± 8	38 ± 7	59 ± 10	39 ± 7	130 ± 9	37 ± 9	58 ± 9	37 ± 7
12	101 ± 8	39 ± 7	58 ± 5	38 ± 3	132 ± 9	38 ± 8	60 ± 6	38 ± 7
24	97 ± 13	38 ± 8	57 ± 5	38 ± 5	127 ± 7	36 ± 10	59 ± 7	42 ± 5
48	96 ± 8	35 ± 12	57 ± 11	39 ± 6	131 ± 11	36 ± 9	60 ± 8	38 ± 8
72	97 ± 5	37 ± 10	58 ± 5	37 ± 8	127 ± 10	39 ± 4	60 ± 5	37 ± 4
96	136 ± 10	39 ± 4	56 ± 6	36 ± 3	131 ± 8	39 ± 6	61 ± 6	38 ± 5

temperature, but there was no significant difference with the control group and mild hypothermia treatment process.

**4.2.2. Hepatorenal Function.** According to the statistical analysis of data, as shown in Figure 4 and Table 4, ALT, AST, BUN, and SCR in the two groups were increased in different degrees before treatment. After symptomatic treatment, ALT, AST, BUN, and SCR of the two groups were improved in different degrees, which was statistically significant compared with that before treatment ( $p < 0.05$ ). There was no significant difference between the two groups before and after treatment.

## 5. Analysis and Discussion

**5.1. Analysis of Experimental Results.** The results showed that the levels of serum  $\beta 2$ -mg and CysC were positively correlated, but negatively correlated with SCR, BUN, and GFR. The decrease of glomerular filtration rate and the impairment of renal function can be explained from the following aspects: the change of renal artery hemodynamics: some scholars have observed the change of renal artery hemodynamics in nearly asphyxiated newborns through Doppler ultrasound and found that the decrease of diastolic blood supply may be the main cause of renal injury and

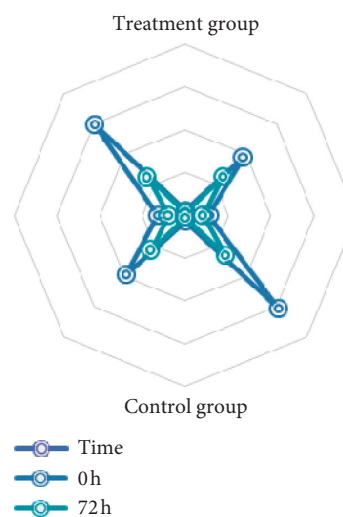


FIGURE 4: Hepatorenal function.

dysfunction after asphyxia. The systolic and diastolic phase of blood supply decreased, and the renal blood flow decreased. Blood flow mainly passes through the medulla of the kidney, resulting in short circuit of blood flow in the kidney and decrease of glomerular filtration rate. The important role of vasoactive substances in the occurrence and development

TABLE 4: Hepatorenal function.

Time (h)	Treatment group				Control group			
	BUN	Cr	ALT	AST	BUN	Cr	ALT	AST
0	5.44 ± 1.43	95.40 ± 39.87	27.70 ± 15.02	154.15 ± 94.70	6.58 ± 3.00	98.34 ± 46.64	31.65 ± 16.58	149.70 ± 93.06
72	3.01 ± 2.02	63.30 ± 25.58	20.57 ± 10.67	66.37 ± 23.59	3.07 ± 1.44	57.59 ± 24.60	19.59 ± 6.15	62.63 ± 19.24

of multiple organ injury asphyxia: some scholars released clips, causing ischemia and reinjecting renal blood flow into renal cortex, and the glomerular filtration rate is still not increased, so it can be seen that simple renal blood perfusion decreased. All of these explain the phenomenon of glomerular filtration rate decrease. The activity of renin-angiotensin system increased significantly, resulting in vasospasm. The content of renin in the outer layer of renal cortex was the highest, so the renal cortex ischemia was the most serious. At the same time, the imbalance of prostaglandin system and balance can also lead to renal ischemia and decreased glomerular filtration rate. In addition, the increase of endothelin during asphyxia can reduce the glomerular ultrafiltration coefficient (KF) and glomerular filtration rate through the contraction of mesangial cells. Asphyxia and hypoxia can damage renal tissue, especially proximal renal tubular cells, leading to changes in cytoskeleton, cell polarity, and renal tubular blockage. However, the renal tubules were damaged after the reabsorption of sodium and chlorine decreased, and the tubules with increased concentration of sodium and chlorine reached the dense point and then made the entering artery contract, and the resistance increased. A vicious circle is formed, that is, the so-called tube ball feedback mechanism. The detection of serum cystatin C is helpful to understand the severity of neonatal asphyxia. Glomerular filtration has the following advantages: cystatin C is not easy to pass through the fetal mucus barrier. Foreign scholars have studied the serum cystatin C and creatinine levels of healthy pregnant women and newborns and found that there is a significant difference between the serum cystatin C levels of mothers and newborns, and there is no linear correlation between the two, so they think most of the cystatin C of newborns comes from themselves. Because of the lobulation of the new kidney, the small glomerulus, the small filtering area of the membrane, and the short tubules of the new kidney, especially the proximal tubules, are only 1/10 of those of the adult.

The metabolic pathway of creatinine in newborns is relatively complex. In addition to filtering the renal ice, the renal tubules also discharge part of the renal ice out of the body. The excretion of urea nitrogen in the kidney and the concentration in the blood are significantly affected by the water content and urine volume of the human body. In preterm infants, increased renal reabsorption of creatinine affects serum creatinine concentration, whereas cystatin C does not. Once filtered, they are usually absorbed and broken down by epithelial cells near the convoluted tubules. Cystatin C is suitable for monitoring renal function due to its physical and chemical properties. Neonatal jaundice and hemolysis will affect the determination of creatinine levels through bilirubin, hemoglobin, and other factors. In

addition, the serum cystatin C concentration is very stable and can be maintained at room temperature for two days. The biological characteristics of cystatin C also make it a marker of glomerular filtration. Generally, we use the determination of material clearance rate as the most convenient method to evaluate the ability of kidney to control the concentration of extracellular fluid. Inulin and its isotopic labeled complex limit its routine clinical application, so some endogenous markers such as creatinine, urea, and uridine are often used to determine or selectively directly determine the plasma concentration (or their interaction). The latter are urea nitrogen, creatinine, and microglobulin. However, exogenous and endogenous markers are not stable in the blood; some of them are affected by other pathological changes, muscle mass, and diet.

Cystatin C is a direct gene product in recent years, which is a small molecule protein. Its synthesis is not affected by muscle mass and acute inflammatory response. Its tissue formation rate is quite stable; almost all of them are filtered by glomeruli, absorbed, decomposed, and metabolized in proximal convoluted tubules. It has many advantages in the evaluation of glomerular filtration function and has been paid more and more attention. It can also inhibit papain, fig protease, and cathepsins H and L. Therefore, the physiological function of cystatin C may be to regulate the activity of caspase. The mutation of caspase inhibitor C gene will lead to the rupture of cerebral artery and caspase inhibitor C (HCCAA) in hereditary amyloidosis. This is a clinical disease directly related to caspase inhibitor C, because caspase inhibitor C can be specifically expressed in almost all cell tissues. The rate of formation of caspase inhibitor C in the body is quite stable. In pediatric patients, neonatal jaundice and hemolysis will be interfered by bilirubin, hemoglobin, and other factors, which will affect the determination of creatinine level in the blood.

**5.2. Discussion.** The most common complication of neonatal asphyxia is dysfunction of brain, kidney, heart, and other organs, and kidney is one of the most vulnerable target organs. The incidence of severe asphyxia was high, because the blood flow of human kidney is very large, accounting for about 20% of cardiac output. The renal blood flow of newborn is small, accounting for only about 8%~12% of cardiac output in one week. After asphyxia, it is emphasized that the body's blood redistribution, the excessive accumulation of nitric oxide (no) in the local kidney, and the enhanced synthesis and the expression of intercellular adhesion molecules will damage the renal tissue; because the renal medulla is short, the transport of sodium, chlorine, and urinary hormones is weak, the permeability gradient of skin

and renal medulla is low, and the response of distal nephron to diuretic hormones is low. Prostaglandin interferes with the concentration mechanism. It affects the concentration function of kidney, especially in the case of insufficient blood perfusion and hypoxia. Therefore, when neonatal asphyxia occurs, renal blood vessels contract and blood perfusion decreases.

At the same time, the serum BUN and Cr are affected by many factors, such as blood volume, protein intake, and so on. Mild hypothermia can reduce energy metabolism, inhibit brain cell apoptosis, reduce the release of excitatory amino acids at the end of axon, inhibit nitric oxide synthetase, and significantly improve prognosis. When the body temperature drops, the blood viscosity may rise, the curve of oxygen dissociation may shift to the left, the utilization of oxygen by tissues may be reduced, causing metabolic acidosis, bradycardia, arrhythmia, the decrease of cellular immune function, the increase of infection risk, the prolongation of coagulation time, the abnormality of platelet function, and the slight drop of blood potassium, chorea, etc. The core body temperature causes water to build up in the respiratory tract and medium, which can lead to slow breathing. If the temperature is too low, the breathing stops, but a slight malaise and shortness of breath can affect breathing. Excessive cooling can cause brain damage by the following actions: polymorphonuclear leukocytes attach to the walls of blood vessels to exacerbate cerebral ischemia. Negative reactions released by the vaccine. Small blood vessels can cause a technological breakdown and increase the expression of some genes after ischemia.

Effects of hypothermia on IEO expression: IEQ is a group of genes that express rapidly and transiently after cerebral ischemia. Transient hemicerebral ischemia can induce a large amount of immediate early gene expression. Mild hypothermia promoted the late stage of gene expression, which was the result of rapid activation of cytoplasmic response elements after ischemia injury. The direct induction of early genes is a process of activation and repair of stress signals. In the early stage, the induction accelerating gene of mild hypothermia for the treatment of cerebral ischemia reflects the rapid recovery of signal transduction function to normal cells, so as to improve the repair ability of neurons. The effect of low temperature on HSP gene expression: HSP is a group of stress-induced protein HSP genes in biological cells after activation of some environmental factors and stress stimulation. At present, many kinds of heat shock proteins have been found, among which the most conservative and important is the Hsp70 family. Hsp70 family mainly includes HSP68, 72, 73, HSC (heat shock homology) 70, and hsp78. Among them, HSP70 and HSP72 are the most studied in depth in ischemic injury. HSP72 protein expression is a useful marker of stress response after cerebral ischemia. Mild hypothermia is safe and feasible for newborns. Although the current clinical trials show that mild hypothermia has no obvious side effects in a short period of time, it is undeniable that mild hypothermia can affect the whole body organ system. Understanding the pathophysiological changes of mild hypothermia is of great significance for the safe implementation of mild

hypothermia treatment. In clinical treatment, we should pay attention to the side effects of any treatment measures. The side effects of perinatal asphyxia and hypothermia are obviously overlapped, which brings some difficulties to clinical observation. We should be more careful. Hypothermia has a certain impact on all organs and systems of the whole body: during the treatment of hypothermia, the change and rewarming of cardiovascular system were observed, and the increase of mean arterial pressure was found. It causes the increase of vascular resistance, high viscosity and blood concentration, thrombocytopenia, and coagulation abnormality. In addition, due to the influence of platelet function, prothrombin, and partial thrombin time, the bleeding time is prolonged, which can cause circulatory failure and DIC. Hypothermia can lead to immunosuppression, inhibit leukocyte migration and phagocytosis, and easily increase septicemia, especially pneumonia. The level of antidiuretic hormone decreased. Low temperature can increase metabolic rate, increase oxygen consumption, shift oxygen separation curve to the left, decrease drug metabolism, hypoglycemia, metabolic acid, and low potassium, increase catecholamine, and stimulate glycogen release to cause hyperglycemia, etc. Cortisol increased, TSH increased, and antidiuretic hormone decreased. In the process of rewarming, as a result of vasodilation and decreased blood flow to the heart and the decrease of effective circulation blood volume and blood pressure, it leads to hypovolemic shock. When reheating, the intracranial pressure will suddenly rise. Low temperature rebound causes high temperature. When rewarming, the release of glycogen suddenly decreased, resulting in hypoglycemia, etc.

## 6. Conclusion

Serum CysC level was positively correlated with SCR and BUN and negatively correlated with GFR. The sensitivity and specificity of serum CysC in the diagnosis of renal function damage were higher than other indicators, which could be used as early indicators for monitoring renal damage in asphyxiated neonates. Combined with the biological and physicochemical characteristics of cystatin C, we believe that cystatin C is an ideal endogenous marker to reflect the early renal function damage in neonates. Mild hypothermia treatment has better therapeutic effect.

## Data Availability

No data were used to support this study.

## Conflicts of Interest

The authors declare that there are no conflicts of interest in this paper.

## References

- [1] H. Kletkiewicz, A. Nowakowska, A. Siejka et al., "Deferoxamine prevents cerebral glutathione and vitamin E depletions in asphyxiated neonatal rats: role of body temperature,"

- International Journal of Hyperthermia*, vol. 32, no. 2, pp. 211–220, 2016.
- [2] M.-H. Gagnon and P. Wintermark, “Effect of persistent pulmonary hypertension on brain oxygenation in asphyxiated term newborns treated with hypothermia,” *The Journal of Maternal-Fetal & Neonatal Medicine*, vol. 29, no. 13, pp. 2049–2055, 2016.
  - [3] A. A. Balushi, S. B. Vargas, J. Maluorni et al., “Hypotension and brain injury in asphyxiated newborns treated with hypothermia,” *American Journal of Perinatology*, vol. 35, no. 01, pp. 031–038, 2018.
  - [4] A. Yazdani, Z. Khoja, A. Johnstone, L. Dale, E. Rampakakis, and P. Wintermark, “Sildenafil improves brain injury recovery following term neonatal hypoxia-ischemia in male rat pups,” *Developmental Neuroscience*, vol. 38, no. 4, pp. 251–263, 2016.
  - [5] I. Oloyede and P. Udo, “An audit of some health facilities and equipment for neonatal resuscitation in south-south Nigeria,” *Nigerian Journal of Paediatrics*, vol. 43, no. 3, p. 197, 2016.
  - [6] L. Renter Valdovinos and I. Oulego Erroz, “Ecografía a pie de cama en el niño crítico,” *Anales de Pediatría*, vol. 85, no. 3, pp. 117–118, 2016.
  - [7] T. Niranjani, A. Thangaraj, B. Vishnu et al., “Phase changing material for therapeutic hypothermia in neonates with hypoxic ischemic encephalopathy—a multi-centric study,” *Indian Pediatrics*, vol. 55, no. 3, pp. 201–205, 2018.
  - [8] D. E. Clay, A. C. Linke, D. J. Cameron et al., “Evaluating affordable cranial ultrasonography in east african neonatal intensive care units,” *Ultrasound in Medicine & Biology*, vol. 43, no. 1, pp. 119–128, 2017.
  - [9] C. Jin, M. Feng, J. Zhong et al., “Insights into mechanism of size controlled synthesis of CH<sub>3</sub>NH<sub>3</sub>PbBr<sub>3</sub> perovskite quantum dots and large nanoparticles with tunable optical properties,” *Organic Electronics*, vol. 82, Article ID 105172, 2020.
  - [10] D. K. Mandal, P. Kumar, U. S. Prasad, S. Datta, I. Dawn, and S. Sarkar, “Etiological factors & clinical courses of birth asphyxia in rural and urban population of Kishanganj district,” *Bangladesh Journal of Medical Science*, vol. 16, no. 4, pp. 554–556, 2017.
  - [11] L. Vega, H. Boix, D. Albert, I. Delgado, and F. Castillo, “El intervalo QT corregido durante la hipotermia terapéutica en la encefalopatía hipóxico-isquémica,” *Anales de Pediatría*, vol. 85, no. 6, pp. 312–317, 2016.
  - [12] Y. J. Xu, L. M. Ran, S. S. Zhai et al., “Evaluation of the efficacy of atosiban in pregnant women with threatened preterm labor associated with assisted reproductive technology,” *European Review for Medical and Pharmacological Sciences*, vol. 20, no. 9, p. 1881, 2016.
  - [13] T. Yasmin, S. Akther, S. Sultana, and M. B. Amin, “Assessment of cranial sonographic findings of hypoxic ischemic brain injury in perinatal asphyxia,” *Journal of Medicine*, vol. 17, no. 1, p. 12, 2016.
  - [14] J. Mori, C. Tanikawa, Y. Funauchi, P. H. Y. Lo, Y. Nakamura, and K. Matsuda, “Cystatin C as a p53-inducible apoptotic mediator that regulates cathepsin L activity,” *Cancer Science*, vol. 107, no. 3, pp. 298–306, 2016.
  - [15] M. Schanz, D. Pannes, J. Dippon, C. Wasser, M. D. Alscher, and M. Kimmel, “The influence of thyroid function, inflammation, and obesity on risk prediction of acute kidney injury by cystatin C in the emergency department,” *Kidney and Blood Pressure Research*, vol. 41, no. 5, pp. 604–613, 2016.
  - [16] K. K. Lee, H. C. Tseng, Y. M. Hwu et al., “Expression of cystatin C in the female reproductive tract and its effect on human sperm capacitation,” *Reproductive Biology and Endocrinology*, vol. 16, no. 1, p. 8, 2018.
  - [17] M. Bi, Z. Huang, P. Li, C. Cheng, and W. Chen, “The association between elevated cystatin C levels with myocardial infarction: a meta-analysis,” *International Journal of Clinical and Experimental Medicine*, vol. 8, no. 11, pp. 20540–20547, 2016.
  - [18] J. Zhao, W. Deng, Y. Zhang et al., “Association between serum cystatin C and diabetic foot ulceration in patients with type 2 diabetes: a cross-sectional study,” *Journal of Diabetes Research*, vol. 2016, no. 6, pp. 1–7, Article ID 8029340, 2016.
  - [19] A.-S. Bargnoux, L. Piéroni, J.-P. Cristol et al., “Multicenter evaluation of cystatin C measurement after assay standardization,” *Clinical Chemistry*, vol. 63, no. 4, pp. 833–841, 2017.
  - [20] S. Lemoine, M. Panaye, C. Pelletier et al., “Cystatin C-creatinine based glomerular filtration rate equation in obese chronic kidney disease patients: impact of deindexation and gender,” *American Journal of Nephrology*, vol. 44, no. 1, pp. 63–70, 2016.
  - [21] S.-K. Yang, J. Liu, X.-M. Zhang et al., “Diagnostic accuracy of serum cystatin C for the evaluation of renal dysfunction in diabetic patients: a meta-analysis,” *Therapeutic Apheresis and Dialysis*, vol. 20, no. 6, pp. 579–587, 2016.
  - [22] A. Barbati, B. Cappuccini, M. C. Aisa et al., “Increased urinary cystatin-C levels correlate with reduced renal volumes in neonates with intrauterine growth restriction,” *Neonatology*, vol. 109, no. 2, pp. 154–160, 2016.

## Research Article

# Synthesis of Bimetallic PdAg Nanoparticles and Their Electrocatalytic Activity toward Ethanol

Fahui Gao, Yanru Yin, Zhengshuai Cao, Hongliang Li, and Peizhi Guo 

*Institute of Materials for Energy and Environment, State Key Laboratory of Bio-fiber and Eco-textile, College of Materials Science and Engineering, Qingdao University, Qingdao 266071, China*

Correspondence should be addressed to Peizhi Guo; [pzguo@qdu.edu.cn](mailto:pzguo@qdu.edu.cn)

Received 29 July 2020; Revised 2 October 2020; Accepted 25 November 2020; Published 7 December 2020

Academic Editor: Jo o Paulo Leal

Copyright © 2020 Fahui Gao et al. This is an open access article distributed under the Creative Commons Attribution License, which permits unrestricted use, distribution, and reproduction in any medium, provided the original work is properly cited.

Palladium-based bimetallic nanoparticles (NPs) have been studied as important electrocatalysts for energy conversion due to their high electrocatalytic performance and the less usage of the noble metal. Herein, well-dispersed PdAg NPs with uniform size were prepared via oil bath accompanied with the hydrothermal method. The variation of the Ag content in PdAg NPs changed the lattice constant of the face-centered cubic alloy nanostructures continuously. The Pd/Ag molar ratio in the PdAg alloy NPs affected their size and catalytic activity toward ethanol electrooxidation. Experimental data showed that PdAg NPs with less Ag content exhibited better electrocatalytic activity and durability than pure Pd NPs owing to both the small size and the synergistic effect. PdAg-acac-4 with the Pd/Ag molar ratio of 4:1 in the start system possessed the highest catalytic current density of 2246 mA/mg for the electrooxidation of ethanol. The differences in the morphology and electrocatalytic activity of the as-made PdAg NPs have been discussed and analyzed.

## 1. Introduction

Direct ethanol fuel cells (DEFCs), with many outstanding virtues, such as low toxicity, renewable capability, and low environmental pollutant emission, have been extensively studied as an ideal alternative for the energy source [1–10]. At present, the application of DEFCs in the commercial level is still limited on account of their low catalytic activity and high price of catalysts, as well as poor stability.

Platinum nanoparticles (NPs) are key electrocatalysts in commercial installations and industrial processes against conventional fossil fuels [11–13]. However, the commercialization of DEFCs based on platinum catalysts is seriously impeded by its high cost, limited natural reserves, and weak ability to resist the poisoning by the intermediate carbon monoxide (CO) produced in the ethanol oxidation reaction (EOR) [14–16]. Therefore, it is urgently needed to explore new, active, inexpensive, and stable catalysts. Nowadays, palladium (Pd) has attracted great interest as electrocatalysts owing to its good performance but relatively low cost [1–4, 6, 7, 17–26]. However, poor stability and limited active sites of Pd have seriously hindered its wider application. To

improve these, structural physical features of Pd electrocatalysts including the size, shape, and composition of catalysts have been developed. A large amount of Pd nanostructured catalysts, such as cubes [27], nanoplates [28], nanowires [29], nanoflowers [30], and tetrahedra [31], have been explored and synthesized which showed high electrocatalytic activity.

Compared to single-metal nanoparticles, bimetallic alloy nanoparticles can generally exhibit better performance owing to their unique structural features, which have received extensive attention in recent years [32, 33]. Moreover, the addition of another metal reduces the loading of the palladium metal, thus decreasing the cost of the catalyst [34–38]. Various metals, such as Ni [39, 40], Fe [41, 42], Cu [43–47], Pb [48, 49], and Ag [50–52], have been used in combination with Pd to increase the electrocatalytic activity of Pd-based bimetallic or multimetallic nanocatalysts. For example, Liu et al. reported the synthesis of a Pd-Ag free-standing nanowire rich in grain boundary with both high activity and stability toward the oxygen reduction reaction (ORR) via a facile modified polyol method [51]. Peng et al. prepared a hollow raspberry-like PdAg alloy nanosphere,

which possessed high electrocatalytic activity for ethanol oxidation in alkaline media [52]. We found that ultrathin PdPb nanowires can display excellent electrocatalytic activity due to the electron transfer between Pd and Pb, lowering the d-band center and weakening the adsorption of toxic intermediates. However, the development of high-performance electrocatalysts still needs more efforts, especially for bimetallic or multimetallic nanostructures.

Herein, we report the synthesis of well-dispersed PdAg alloy nanoparticles (NPs) with uniform size via a two-step method. The formation and the composition of the PdAg alloy NPs varied with the content of silver nitrate in the start synthesis systems. The electrocatalytic performance of the catalysts related to the content of Ag in the NPs and the highest catalytic current density of the PdAg alloy can reach as high as 2246 mA/mg obtained from the start synthesis system with the molar ratio of Pd to Ag of 4:1. Both the particle size and the structural nature of the PdAg NPs play important roles for the electrocatalysis of ethanol.

## 2. Experimental Section

**2.1. Materials and Reagents.** All chemicals including palladium (II) acetylacetonate, silver nitrate ( $\text{AgNO}_3$ ), ethylene glycol (EG), polyvinylpyrrolidone (PVP) (molar weight = 58,000), ethanol, and acetone were analytically pure and purchased from Sinopharm Chemical Reagents. Double distilled water was used in the experiments, and ultrapure water (18.2 M $\Omega$  cm) was used throughout electrochemical measurements.

**2.2. Synthesis of PdAg NP Catalysts.** In a typical synthesis, 105 mg PVP was added to a bottle (30 mL) containing 8 mL double distilled water and stirred in an oil bath at 80°C for 20 minutes. Meanwhile, 61.3 mg palladium acetylacetonate was stirred evenly in 3 mL double distilled water. The suspension of palladium acetylacetonate and PVP solution were mixed and stirred evenly, and then, the mixture was stirred in an oil bath at 90°C for 2 hours. A certain amount of  $\text{AgNO}_3$  was dissolved in 5 mL EG and mixed with the above solution; after stirred in an oil bath at 110°C for 2 hours, the mixture was transferred into a Teflon-lined stainless-steel autoclave and kept in an oven at 180°C for 10 h. After cooling down to room temperature, the products were collected by centrifugation with the addition of acetone and washed with the mixture of distilled water and ethanol several times, and then PdAg NPs were obtained after drying at 60°C for 10 h.

Four products were prepared from the start systems with the  $\text{AgNO}_3$  content of 34 mg/17 mg/8.5 mg/6.8 mg, named as PdAg-acac-1/PdAg-acac-2/PdAg-acac-4/PdAg-acac-5, respectively.

**2.3. Characterization.** The crystallographic information and composition were investigated using a Rigaku Ultima IV X-ray diffractometer (XRD, Cu  $K\alpha$  radiation  $\lambda = 0.15418$  nm). The morphology and structure of the samples were examined by a JEOL JSM-7800F scanning electron microscope (SEM) and a JEOL JEM-2100 Plus

transmission electron microscope (TEM). High-angle annular dark-field scanning transmission electron microscopy (HAADF-STEM) coupled with energy-dispersive X-ray (EDX) elemental mappings were measured with a JEOL JEM-2100F transmission electron microscope at an accelerating voltage of 200 kV.

**2.4. Electrochemical Measurements.** Electrochemical measurements were conducted on a CHI660E workstation at room temperature, and the measurements of cyclic voltammetry (CV) and chronoamperometric tests were carried out with a standard three-electrode system. The details were shown in our recent reports [53].

## 3. Results and Discussion

Both Pd and Ag crystals have a face-centered cubic (FCC) structure. The difference in the diameters of atoms of Pd and Ag is very small; thereafter, PdAg bimetallic alloy can be easily formed and was usually reported in the literature studies recently [50]. As shown in Figure 1, the three distinct diffraction peaks of the as-made samples in the XRD patterns located between pure Pd and Ag standard patterns appeared at 38.6°, 45.3°, and 67.2°, responding to the (111), (200), and (220) crystalline planes of PdAg alloy nanoparticles, respectively. It was obvious that all the diffraction peaks of PdAg-acac-1, PdAg-acac-2, PdAg-acac-4, and PdAg-acac-5 showed a negative shift to the standard peak of pure Ag compared with that of pure Pd (JCPDS No. 46-1043), which proved the formation of the PdAg alloy [51, 52]. Moreover, the more the content of Ag, the more the negative shift of the strongest diffraction peaks at 38.6°, which indicates the addition of Ag causes the lattice expansion in the PdAg alloy compared with pure Pd. Using a Rietveld refinement, the lattice constants are about 4.02 Å, 3.99 Å, 3.95 Å, and 3.92 Å for PdAg-acac-1, PdAg-acac-2, PdAg-acac-4, and PdAg-acac-5, respectively. These indicated the gradual increase of crystal cell size with the continuous increase of the Ag content in the PdAg bimetallic nanostructures.

Figure 2 shows the SEM images of PdAg-acac-1, PdAg-acac-2, PdAg-acac-4, and PdAg-acac-5. It can be seen that each PdAg alloy is well dispersed with a narrow size distribution. All the samples are granular with the size order of PdAg-acac-1 > PdAg-acac-2 > PdAg-acac-5 > PdAg-acac-4, and the particle size of PdAg-acac-4 is significantly smaller than any of the others. The composition of elements Pd and Ag of alloy NPs was identified by SEM-EDS (Table 1), and the atomic ratios of Pd/Ag are about 0.8:1, 1.9:1, 3.4:1, and 4.2:1 for PdAg-acac-1, PdAg-acac-2, PdAg-acac-4, and PdAg-acac-5, respectively. These results are a little different from those in the start systems, more likely related to the insoluble nature of palladium acetylacetonate in ethylene glycol.

Figure 3 shows the TEM and HRTEM images of all the four PdAg NP samples. All the four types of particles have a clear boundary. Obviously, the sizes of PdAg-acac-1, PdAg-acac-2, PdAg-acac-4, and PdAg-acac-5 NPs were about

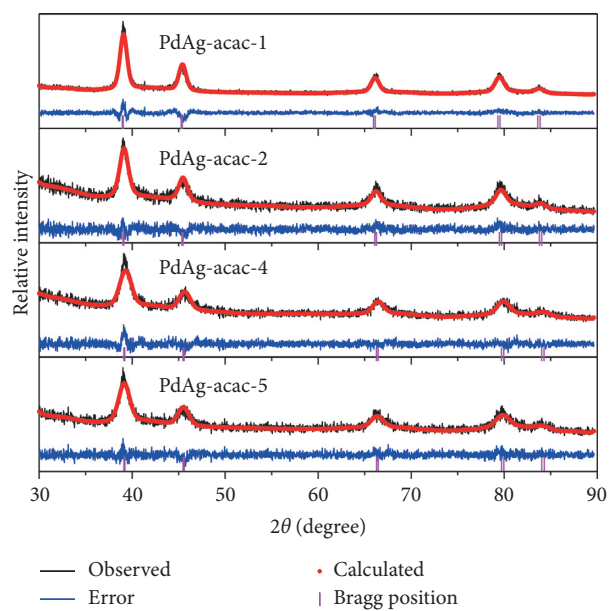


FIGURE 1: XRD patterns and Rietveld refinement results of PdAg-acac-1, PdAg-acac-2, PdAg-acac-4, and PdAg-acac-5.

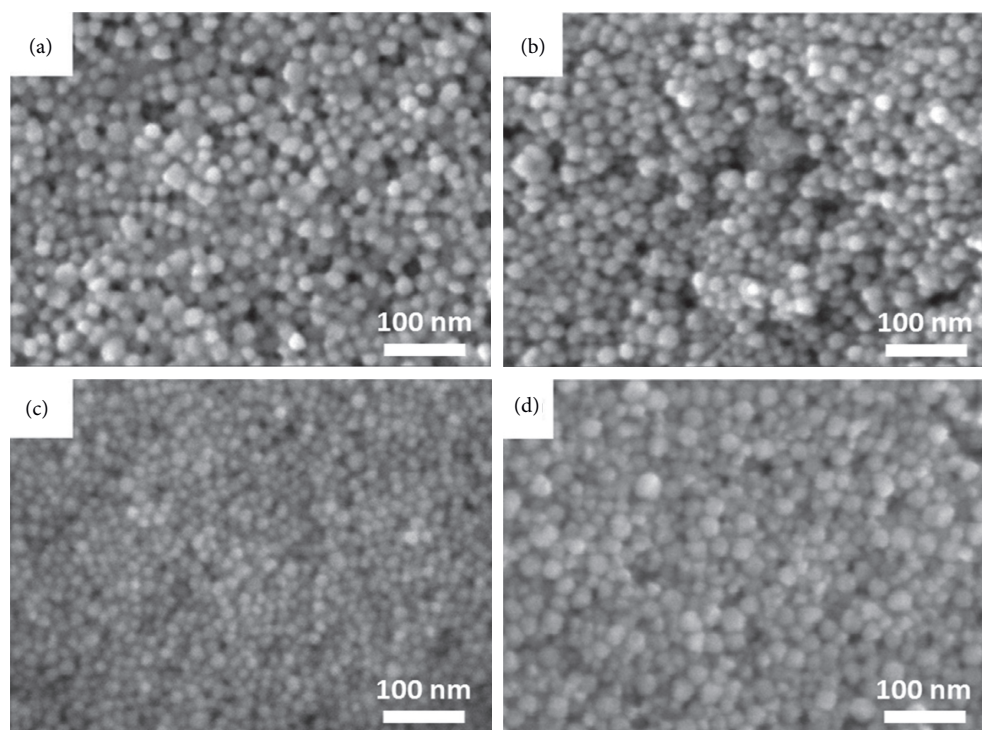


FIGURE 2: SEM images of PdAg-acac-1 (a), PdAg-acac-2 (b), PdAg-acac-4 (c), and PdAg-acac-5 (d).

TABLE 1: The atomic ratio of PdAg-acac-1, PdAg-acac-2, PdAg-acac-4, and PdAg-acac-5.

The atomic fraction	PdAg-acac-1	PdAg-acac-2	PdAg-acac-4	PdAg-acac-5
Pd (%)	44.33	65.38	76.84	80.20
Ag (%)	55.67	34.62	23.16	19.80

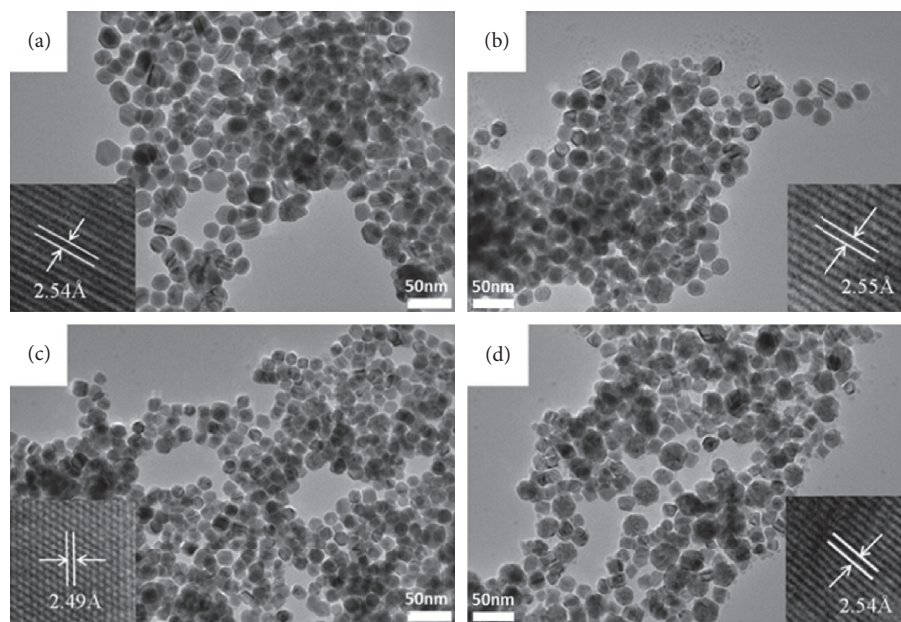


FIGURE 3: TEM and HRTEM images of PdAg-acac-1 (a), PdAg-acac-2 (b), PdAg-acac-4 (c), and PdAg-acac-5 (d).

$25 \pm 5$  nm,  $20 \pm 4$  nm,  $15 \pm 3$  nm, and  $18 \pm 4$  nm, respectively. The size of PdAg-acac-4 particles was the smallest, which was consistent with the SEM results. Clearly, pure Pd NPs obtained from the same conditions are rather irregular with a broad size range (Figure S1). As shown in the insets of Figure 3, the crystal lattice spacings were around 2.54 Å, 2.55 Å, 2.49 Å, and 2.54 Å corresponding to the (111) crystal plane of PdAg-acac-1, PdAg-acac-2, PdAg-acac-4, and PdAg-acac-5, respectively. Compared to the pure palladium NPs (Figure S1), the crystal plane spacing of the alloy samples is expanded, which is in agreement with the XRD results. To better understand the element distributions of Pd and Ag in the alloy, Figure 4 shows the HAADF-STEM images of singular PdAg-acac-4 NP. These images denote that elements Pd and Ag were evenly distributed in the sample. Ag atoms seem to be located in the center, leading to more Pd atoms than Ag atoms on the surface of single NP.

Electrochemical measurements were carried out to evaluate the catalytic activity of PdAg bimetallic NPs. Figure 5 shows typical CV curves of the PdAg NP-modified glass carbon electrodes (GCEs) in aqueous solutions containing 0.5 M  $\text{H}_2\text{SO}_4$ , 1 M KOH, and 1 M KOH/1 M  $\text{C}_2\text{H}_5\text{OH}$  at the same scan rate of 50 mV/s. It can be observed from Figure 5(a) that the typical peak around  $-0.23 \sim 0.1$  V is attributed to hydrogen adsorption/desorption on the surface of catalysts. In addition, the characteristic peak and corresponding integral area of PdAg-acac-1 and PdAg-acac-2 are significantly smaller than those of the other two samples, which indicates that more silver atoms might exist on the surface of palladium that reduce active sites on the surface of the catalysts. And then, the reduction of catalytic sites lowers the amount of hydrogen atoms adsorbed, which is further manifested as a decrease in the integral area of the characteristic peak. Furthermore, the featured peak of samples with a certain negative shift around 0.4 V is ascribed to the

reduction of Pd oxide, which reveals the enhanced adsorption capacity of the catalyst to oxygen, compared with pure palladium.

Figure 5(b) shows the CV curves of all the PdAg NPs in aqueous 1 M KOH solution. It is clear that the obvious peak appearing around  $-0.28$  V is the reduction peak of Pd oxide, and PdAg-acac-1 shows the most positive peak potential. Moreover, PdAg-acac-4 showed the most negative shift among the four samples, indicating that PdAg-acac-4 had a more active surface consistent with the sequence of the activity of these PdAg NPs in Figure 5(c).

The electrocatalytic activity of PdAg NPs was evaluated by electrooxidation of ethanol on the PdAg NP-modified GCEs, as shown in Figure 5(c). The catalytic peak current densities of PdAg-acac-1, PdAg-acac-2, PdAg-acac-4, and PdAg-acac-5 were about 782, 1406, 2246, and 1838 mA/mg, respectively. The electrochemical active surface areas (ECSAs) of the four samples can be calculated by the reduction region of Pd oxide based on the formula  $\text{ECSA} = Q / (0.424 \times \text{Pd}_m)$ , where  $Q$  stands for the corresponding electrical quantity of the integral of the peak from the reduction of Pd oxide [54]. After calculation, the ECSAs of PdAg-acac-1, PdAg-acac-2, PdAg-acac-4, and PdAg-acac-5 were around 112.4, 259.6, 486.3, and 395.2  $\text{cm}^2/\text{mg}$ , which were consistent with the order of electrochemical activity. It was clear that PdAg-acac-4 has the highest electrocatalytic activity, which can be closely related to the smallest particle size. On the one hand, the small decrease in the size of PdAg-acac-4 with other samples may not fully explain the drastic increase in the ECSAs. On the other hand, the increase of the Pd content in PdAg-acac-4 indicated more Pd atoms on the surface, as shown in Figure 4. In the meantime, the crystal cell enlarged with the Ag content increased, and the corresponding Pd-Pd bond elongated, leading to the downward shift of the d-band center. This may reduce the adsorption

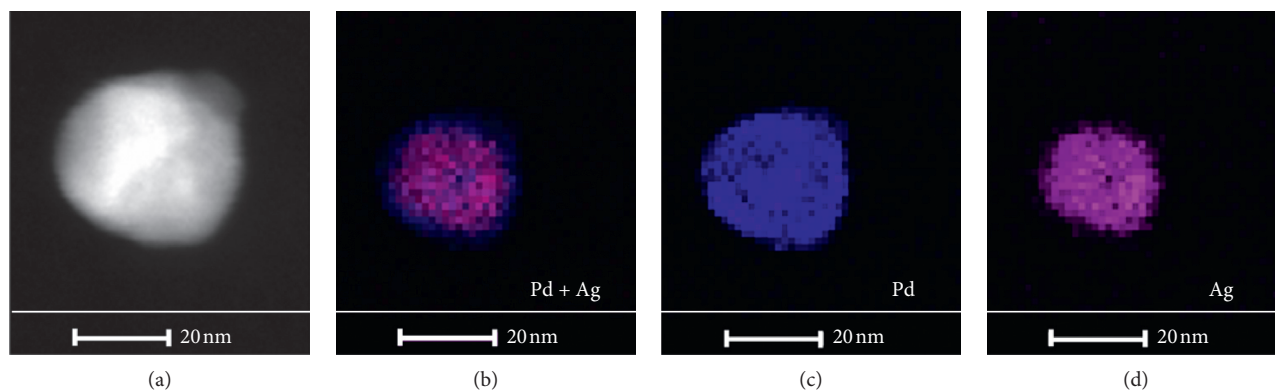


FIGURE 4: (a) STEM image of PdAg-acac-4 single nanoparticle and EDX element distribution maps of Ag + Pd (b), Pd (c), and Ag (d) in singular nanoparticle.

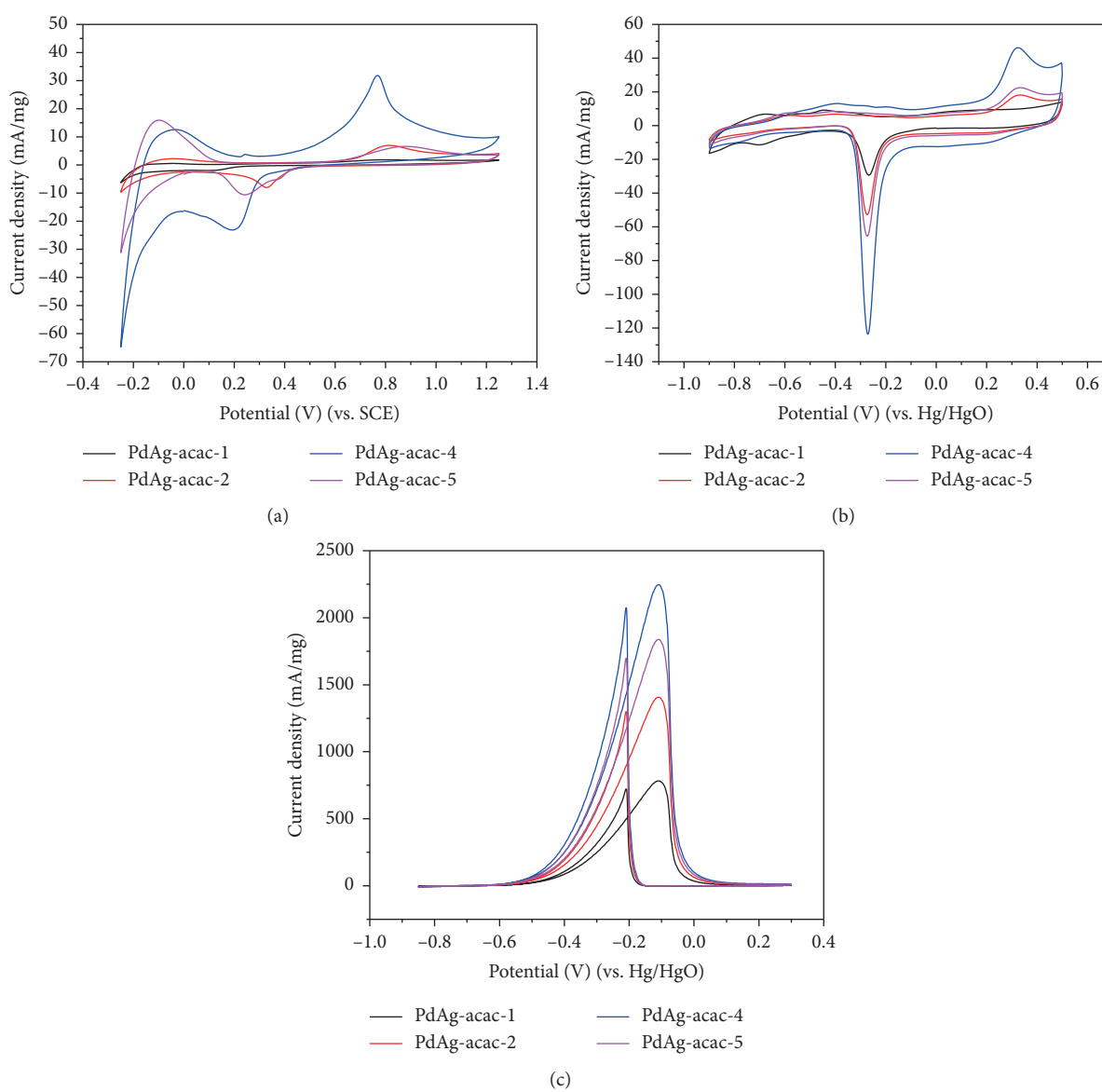


FIGURE 5: CV curves of the GCEs modified by PdAg-acac-1, PdAg-acac-2, PdAg-acac-4, and PdAg-acac-5 in aqueous solutions containing 0.5 M  $\text{H}_2\text{SO}_4$  (a), 1 M KOH (b), and 1 M KOH/1 M  $\text{C}_2\text{H}_5\text{OH}$  (c) at a scan rate of 50 mV/s.

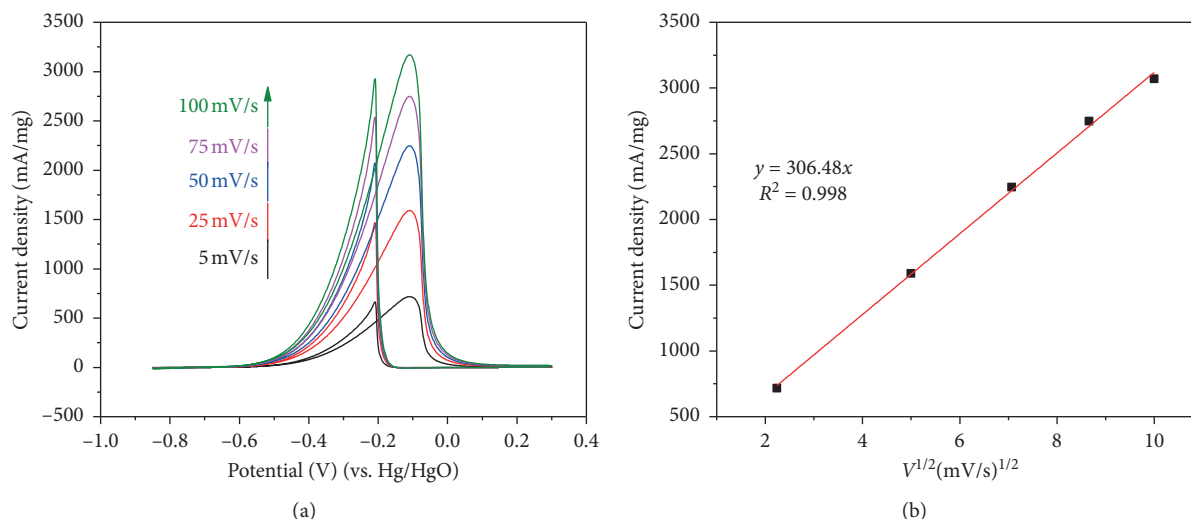


FIGURE 6: (a) CV curves of PdAg-acac-4 NP-modified GCEs at different scan rates. (b) Corresponding plot of the forward peak current versus the square root of the scan rate.

ability of the alloy NPs to toxic carbon-containing intermediates. Electrochemical data showed that the content of Ag in PdAg NPs has an optimal value for the electrocatalysis of ethanol. Meantime, pure Pd NPs show a catalytic current of about 1263 mA/mg (Figure S2). So, the highest activity of PdAg-acac-4 should be ascribed to the smallest size, the largest ECSA, and synergetic effect between Pd and Ag among all the alloy NPs.

Figure 6(a) shows the CV curves of the PdAg-acac-4-modified GCE for electrooxidation of ethanol at different scanning rates. Obviously, with the scan rate increased continuously, the peak current density of PdAg-acac-4 enhanced accordingly with the peak potential unchanged. As shown in Figure 6(b), it is evident that a linear relationship of the current density with the square root of the scan rate ( $V^{1/2}$ ) is obtained, indicating that the dynamics of the catalytic process of ethanol oxidation occurring on the surface of PdAg-acac-4 NPs is controlled by the diffusion process.

The variations of the peak current density with electrocatalytic cycles of all the PdAg NPs for ethanol oxidation are shown in Figure 7. It is clear that the peak current density of these samples reached the corresponding maximum value within 50 circles of CV measurement, which may be caused by the adsorption of organic residues and the existence of silver atoms on the surface of palladium atoms. This was in accord with those pure NPs with different surface chemistry [55]. And then, the current densities of the four samples were apparently attenuated after 100 cycles. It was obvious that the activity of PdAg-acac-4 was maintained better than any of the others not only after 100 cycles but also after reaching 300 cycles. Although it was faster for PdAg-acac-5 to reach its peak catalytic current density, the cyclic stability was poor, and the activity loss after reaching 300 cycles was large. These phenomena showed that the electrocatalytic performance of the PdAg NPs was increased initially with the gradual increase of the Ag content followed by a decrease in the activity with the Ag content continuously increased.

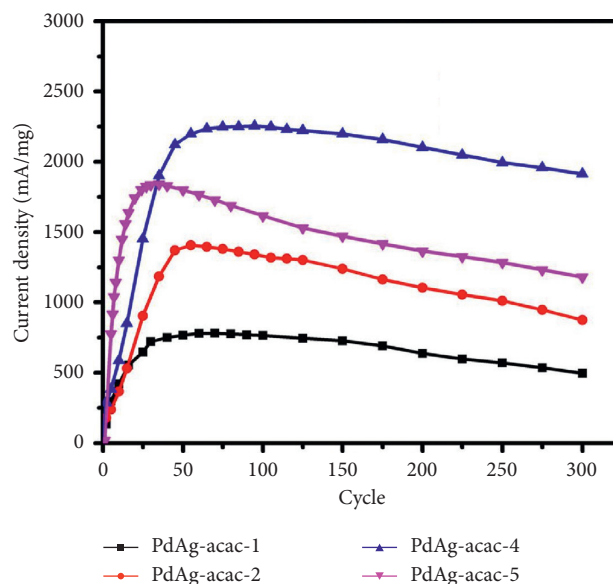


FIGURE 7: The variation of current density along with the cycle number for ethanol oxidation of the modified GCEs in 1 M KOH/ 1 M  $C_2H_5OH$  solutions at a scan rate of 50 mV/s.

#### 4. Conclusion

A series of well-dispersed PdAg NPs with uniform size and abundant active sites were synthesized via a two-step method. The size of PdAg NPs first decreased with the increase of the Ag content and then increased slightly. However, the lattice constant gradually enlarged with the Ag content within the experimental conditions. Electrochemical measurements showed that the catalytic current density of PdAg-acac-4 with moderate Ag content could reach as high as 2246 mA/mg, the highest among all the alloy PdAg NPs. The enhanced catalytic activity of PdAg-acac-4 can be attributed to both the small size effect and the synergistic effect

in bimetallic electrocatalysis, which will be helpful in the design of bimetallic catalysts with higher performance in the future.

### Data Availability

The data used to support the findings of this study are included within the article.

### Conflicts of Interest

The authors declare that they have no conflicts of interest.

### Authors' Contributions

Fahui Gao and Yanru Yin contributed equally.

### Acknowledgments

This work was supported by the National Natural Science Foundation of China (Grant no. 21773133), the World-Class Discipline Program of Shandong Province, and the Taishan Scholar's Advantageous and Distinctive Discipline Program of Shandong Province.

### Supplementary Materials

Figure S1: SEM, TEM, and HRTEM images of pure Pd nanoparticles. Figure S2: CV curve of GCEs modified by pure Pd nanoparticles in aqueous solution containing 1 M KOH/1 M C<sub>2</sub>H<sub>5</sub>OH at a scan rate of 50 mV/s. (*Supplementary Materials*)

### References

- [1] M. Choun and J. Lee, "Electro-oxidation of mixed reactants of ethanol and formate on Pd/C in alkaline fuel cells," *Journal of Energy Chemistry*, vol. 25, no. 4, pp. 683–690, 2016.
- [2] J. Yang, Y. Xie, R. Wang et al., "Synergistic effect of tungsten carbide and palladium on graphene for promoted ethanol electrooxidation," *ACS Applied Materials & Interfaces*, vol. 5, no. 14, pp. 6571–6579, 2013.
- [3] E. Hasheminejad, R. Ojani, and J. B. Raoof, "A rapid synthesis of high surface area PdRu nanosponges: composition-dependent electrocatalytic activity for formic acid oxidation," *Journal of Energy Chemistry*, vol. 26, no. 4, pp. 703–711, 2017.
- [4] R. Jana, U. Subbarao, and S. C. Peter, "Ultrafast synthesis of flower-like ordered Pd<sub>3</sub>Pb nanocrystals with superior electrocatalytic activities towards oxidation of formic acid and ethanol," *Journal of Power Sources*, vol. 301, pp. 160–169, 2016.
- [5] J. Yin, L. Zhang, T. Jiao et al., "Highly efficient catalytic performances of nitro compounds and morin via self-assembled MXene-Pd nanocomposites synthesized through self-reduction strategy," *Nanomaterials*, vol. 9, no. 7, p. 1009, 2019.
- [6] A. S. Douk, H. Saravani, and M. Noroozifar, "Novel fabrication of PdCu nanostructures decorated on graphene as excellent electrocatalyst toward ethanol oxidation," *International Journal of Hydrogen Energy*, vol. 42, pp. 15149–15159, 2017.
- [7] W. Du, K. E. Mackenzie, D. F. Milano, N. A. Deskins, D. Su, and X. Teng, "Palladium-tin alloyed catalysts for the ethanol oxidation reaction in an alkaline medium," *ACS Catalysis*, vol. 2, no. 2, pp. 287–297, 2012.
- [8] R. M. Altarawneh and P. G. Pickup, "Pt and PtRu catalyst bilayers increase efficiencies for ethanol oxidation in proton exchange membrane electrolysis and fuel cells," *Journal of Power Sources*, vol. 366, pp. 27–32, 2017.
- [9] J. Sánchez-Monreal, P. A. García-Salaberri, and M. Vera, "A genetically optimized kinetic model for ethanol electro-oxidation on Pt-based binary catalysts used in direct ethanol fuel cells," *Journal of Power Sources*, vol. 363, pp. 341–355, 2017.
- [10] M. Lv, X. She, Q. Li et al., "Synthesis of magnetic MnFe<sub>2</sub>O<sub>4</sub>/polyaniline composite microspheres and their electrocatalytic activity for oxygen reduction reaction," *Science of Advanced Materials*, vol. 7, no. 9, pp. 1686–1693, 2015.
- [11] F. Colmati, G. Tremiliosi-Filho, E. R. Gonzalez, A. Berná, E. Herrero, and J. M. Feliu, "The role of the steps in the cleavage of the C-C bond during ethanol oxidation on platinum electrodes," *Physical Chemistry Chemical Physics*, vol. 11, no. 40, pp. 9114–9123, 2009.
- [12] M. Sung and J. Kim, "Oxygen evolution reaction on Pt sphere and Ir-modified Pt sphere electrodes with porous structures," *International Journal of Hydrogen Energy*, vol. 43, no. 4, pp. 2130–2138, 2018.
- [13] Y. Shen, B. Gong, K. Xiao, and L. Wang, "In situ assembly of ultrathin PtRh nanowires to graphene nanosheets as highly efficient electrocatalysts for the oxidation of ethanol," *ACS Applied Materials & Interfaces*, vol. 9, no. 4, pp. 3535–3543, 2017.
- [14] R. Wang, Q. Liu, T. Jiao et al., "Facile preparation and enhanced catalytic properties of self-assembled Pd nanoparticle-loaded nanocomposite films synthesized via the electrospun approach," *ACS Omega*, vol. 4, no. 5, pp. 8480–8486, 2019.
- [15] K. A. Abu-Safieh, A. S. Abu-Surrah, H. D. Tappa et al., "Novel palladium(II) and platinum(II) complexes with a fluoropiperazinyl based ligand exhibiting high cytotoxicity and anticancer activity in vitro," *Journal of Chemistry*, vol. 2016, Article ID 7508724, 7 pages, 2016.
- [16] S. Xiong, J. Lan, S. Yin et al., "Enhancing the electrochromic properties of polyaniline via coordinate bond tethering the polyaniline with gold colloids," *Solar Energy Materials and Solar Cells*, vol. 177, pp. 134–141, 2018.
- [17] C. Li, M. Iqbal, B. Jiang et al., "Pore-tuning to boost the electrocatalytic activity of polymeric micelle-templated mesoporous Pd nanoparticles," *Chemical Science*, vol. 10, no. 14, pp. 4054–4061, 2019.
- [18] C. X. Guo, L. Y. Zhang, J. Miao, J. Zhang, and C. M. Li, "DNA-functionalized graphene to guide growth of highly active Pd nanocrystals as efficient electrocatalyst for direct formic acid fuel cells," *Advanced Energy Materials*, vol. 3, no. 2, pp. 167–171, 2013.
- [19] Z. Zhang, L. Xin, K. Sun, and W. Li, "Pd-Ni electrocatalysts for efficient ethanol oxidation reaction in alkaline electrolyte," *International Journal of Hydrogen Energy*, vol. 36, no. 20, pp. 12686–12697, 2011.
- [20] Y.-Y. Feng, Z.-H. Liu, W.-Q. Kong, Q.-Y. Yin, and L.-X. Du, "Promotion of palladium catalysis by silver for ethanol electro-oxidation in alkaline electrolyte," *International Journal of Hydrogen Energy*, vol. 39, no. 6, pp. 2497–2504, 2014.
- [21] B. Zou, X. S. Chen, J. J. Xia, and C. S. Zhou, "Alkaline ionic liquid modified Pd/C catalyst as an efficient catalyst for oxidation of 5-hydroxymethylfurfural," *Journal of Chemistry*, vol. 2018, Article ID 2018743, 9 pages, 2018.
- [22] A.-L. Wang, H. Xu, J.-X. Feng, L.-X. Ding, Y.-X. Tong, and G.-R. Li, "Design of Pd/PANI/Pd sandwich-structured nanotube array catalysts with special shape effects and synergistic effects for

- ethanol electrooxidation," *Journal of the American Chemical Society*, vol. 135, no. 29, pp. 10703–10709, 2013.
- [23] H. Mao, T. Huang, and A. Yu, "Surface palladium rich  $\text{Cu}_x\text{Pd}_y$ /carbon catalysts for methanol and ethanol oxidation in alkaline media," *Electrochimica Acta*, vol. 174, pp. 1–7, 2015.
- [24] Y. Wang, Y. Zhao, J. Yin, M. Liu, Q. Dong, and Y. Su, "Synthesis and electrocatalytic alcohol oxidation performance of Pd-Co bimetallic nanoparticles supported on graphene," *International Journal of Hydrogen Energy*, vol. 39, no. 3, pp. 1325–1335, 2014.
- [25] J. Zhang, M. Huang, H. Ma, F. Tian, W. Pan, and S. Chen, "High catalytic activity of nanostructured Pd thin films electrochemically deposited on polycrystalline Pt and Au substrates towards electro-oxidation of methanol," *Electrochemistry Communications*, vol. 9, no. 6, pp. 1298–1304, 2007.
- [26] H. Huang, Y. Wei, B. Shen et al., "Synthesis of multiple-twinned Pd nanoparticles anchored on graphitic carbon nanosheets for use as highly-active multifunctional electrocatalyst in formic acid and methanol oxidation reactions," *Advanced Materials Interfaces*, vol. 7, no. 11, Article ID 2000142, 2020.
- [27] Y. J. Xiong, B. Wiley, J. Y. Chen, Z. Y. Li, Y. D. Yin, and Y. N. Xia, "Corrosion-based synthesis of single-crystal Pd nanoboxes and nanocages and their surface plasmon properties," *Angewandte Chemie*, vol. 117, pp. 8217–8131, 2005.
- [28] K. A. Homan, M. Souza, R. Truby et al., "Silver nanoplate contrast agents for in vivo molecular photoacoustic imaging," *ACS Nano*, vol. 6, no. 1, pp. 641–650, 2012.
- [29] Y.-F. He, J.-T. Feng, Y.-Y. Du, and D.-Q. Li, "Controllable synthesis and acetylene hydrogenation performance of supported Pd nanowire and cuboctahedron catalysts," *ACS Catalysis*, vol. 2, no. 8, pp. 1703–1710, 2012.
- [30] M. S. Ahmed and S. Jeon, "Synthesis and electrocatalytic activity evaluation of nanoflower shaped Ni-Pd on alcohol oxidation reaction," *Journal of The Electrochemical Society*, vol. 161, no. 12, pp. F1300–F1306, 2014.
- [31] A.-X. Yin, X.-Q. Min, Y.-W. Zhang, and C.-H. Yan, "Shape-selective synthesis and facet-dependent enhanced electrocatalytic activity and durability of monodisperse sub-10 nm Pt-Pd tetrahedrons and cubes," *Journal of the American Chemical Society*, vol. 133, no. 11, pp. 3816–3819, 2011.
- [32] H. Zhao, W. Qi, X. Zhou, H. Wu, and Y. Li, "Composition-controlled synthesis of platinum and palladium nanoalloys as highly active electrocatalysts for methanol oxidation," *Chinese Journal of Catalysis*, vol. 39, no. 2, pp. 342–349, 2018.
- [33] M. Yang, X. Lao, J. Sun et al., "Assembly of bimetallic PdAg nanosheets and their enhanced electrocatalytic activity toward ethanol oxidation," *Langmuir*, vol. 36, no. 37, pp. 11094–11101, 2020.
- [34] C. Qiu, J. Zhang, and H. Ma, "Fabrication of monometallic (Co, Pd, Pt, Au) and bimetallic (Pt/Au, Au/Pt) thin films with hierarchical architectures as electrocatalysts," *Solid State Sciences*, vol. 12, no. 5, pp. 822–828, 2010.
- [35] K. Zhang, D. Bin, B. Yang, C. Wang, F. Ren, and Y. Du, "Ru-assisted synthesis of Pd/Ru nanodendrites with high activity for ethanol electrooxidation," *Nanoscale*, vol. 7, no. 29, pp. 12445–12451, 2015.
- [36] X. Yuan, Y. Zhang, M. Cao et al., " $\text{Bi}(\text{OH})_3/\text{PdBi}$  composite nanochains as highly active and durable electrocatalysts for ethanol oxidation," *Nano Letters*, vol. 19, no. 7, pp. 4752–4759, 2019.
- [37] G. Sheng, J. Chen, H. Ye et al., "Hollow PdCo alloy nanospheres with mesoporous shells as high-performance catalysts for methanol oxidation," *Journal of Colloid and Interface Science*, vol. 522, pp. 264–271, 2018.
- [38] F. Gao, Y. Zhang, F. Ren, Y. Shiraishi, and Y. Du, "Universal surfactant-free strategy for self-standing 3D tremella-like Pd-M (M=Ag, Pb, and Au) nanosheets for superior alcohols electrocatalysis," *Advanced Functional Materials*, vol. 30, no. 16, Article ID 2000255, 2020.
- [39] L. Feng, H. Chong, P. Li et al., "Pd-Ni alloy nanoparticles as effective catalysts for miyaura-heck coupling reactions," *The Journal of Physical Chemistry C*, vol. 119, no. 21, pp. 11511–11515, 2015.
- [40] M. Wang, W. Zhang, J. Wang et al., "PdNi hollow nanoparticles for improved electrocatalytic oxygen reduction in alkaline environments," *ACS Applied Materials & Interfaces*, vol. 5, no. 23, pp. 12708–12715, 2013.
- [41] Y. S. Kang, D. Choi, J. Cho et al., "Highly active and durable ordered intermetallic PdFe electrocatalyst for formic acid electrooxidation reaction," *ACS Applied Energy Materials*, vol. 3, no. 5, pp. 4226–4237, 2020.
- [42] W. Wang, R. Wang, S. Ji, H. Feng, H. Wang, and Z. Lei, "Pt overgrowth on carbon supported PdFe seeds in the preparation of core-shell electrocatalysts for the oxygen reduction reaction," *Journal of Power Sources*, vol. 195, no. 11, pp. 3498–3503, 2010.
- [43] D. Sengupta, J. Saha, G. De, and B. Basu, "Pd/Cu bimetallic nanoparticles embedded in macroporous ion-exchange resins: an excellent heterogeneous catalyst for the Sonogashira reaction," *Journal of Materials Chemistry A*, vol. 2, no. 11, pp. 3986–3992, 2014.
- [44] C. Hu, H. Cheng, Y. Zhao et al., "Newly-designed complex ternary Pt/PdCu nanoboxes anchored on three-dimensional graphene framework for highly efficient ethanol oxidation," *Advanced Materials*, vol. 24, no. 40, pp. 5493–5498, 2012.
- [45] K. Jiang, P. Wang, S. Guo et al., "Ordered PdCu-based nanoparticles as bifunctional oxygen-reduction and ethanol-oxidation electrocatalysts," *Angewandte Chemie International Edition*, vol. 55, no. 31, pp. 9030–9035, 2016.
- [46] C. Xu, Y. Zhang, L. Wang et al., "Nanotubular mesoporous PdCu bimetallic electrocatalysts toward oxygen reduction reaction," *Chemistry of Materials*, vol. 21, no. 14, pp. 3110–3116, 2009.
- [47] J. Xue, G. Han, W. Ye et al., "Structural regulation of PdCu<sub>2</sub> nanoparticles and their electrocatalytic performance for ethanol oxidation," *ACS Applied Materials & Interfaces*, vol. 8, no. 50, pp. 34497–34505, 2016.
- [48] C. Tang, N. Zhang, Y. Ji et al., "Fully tensile strained Pd<sub>3</sub>Pb/Pd tetragonal nanosheets enhance oxygen reduction catalysis," *Nano Letters*, vol. 19, no. 2, pp. 1336–1342, 2019.
- [49] N. Ma, S. Wang, X. Liu et al., "PdPb bimetallic nanowires as electrocatalysts for enhanced ethanol electrooxidation," *Science China Materials*, vol. 63, no. 10, pp. 2040–2049, 2020.
- [50] F. Gao, Y. Zhang, P. Song et al., "Self-template construction of sub-24 nm Pd Ag hollow nanodendrites as highly efficient electrocatalysts for ethylene glycol oxidation," *Journal of Power Sources*, vol. 418, pp. 186–192, 2019.
- [51] X.-J. Liu, X. Yin, Y.-D. Sun et al., "Interlaced Pd-Ag nanowires rich in grain boundary defects for boosting oxygen reduction electrocatalysis," *Nanoscale*, vol. 12, no. 9, pp. 5368–5373, 2020.
- [52] C. Peng, Y. Hu, M. Liu, and Y. Zheng, "Hollow raspberry-like PdAg alloy nanospheres: high electrocatalytic activity for ethanol oxidation in alkaline media," *Journal of Power Sources*, vol. 278, pp. 69–75, 2015.
- [53] P. Guo, Z. Wei, W. Ye et al., "Preparation and characterization of nanostructured Pd with high electrocatalytic activity,"

*Colloids and Surfaces A: Physicochemical and Engineering Aspects*, vol. 395, pp. 75–81, 2012.

- [54] Y. Gong, X. Liu, Y. Gong et al., “Synthesis of defect-rich palladium-tin alloy nanochain networks for formic acid oxidation,” *Journal of Colloid and Interface Science*, vol. 530, pp. 189–195, 2018.
- [55] Y. Yin, N. Ma, J. Xue et al., “Insights into the role of poly(vinylpyrrolidone) in the synthesis of palladium nanoparticles and their electrocatalytic properties,” *Langmuir*, vol. 35, no. 3, pp. 787–795, 2019.

## Review Article

# Research Progress Review of Preparation and Applications of Fluorescent Hydrogels

Weiwei Su,<sup>1</sup> Ran Wang,<sup>1</sup> Cheng Qian,<sup>2,3</sup> Xuotong Li,<sup>3</sup> Qi Tong,<sup>1</sup> and Tifeng Jiao<sup>1</sup> 

<sup>1</sup>Hebei Key Laboratory of Applied Chemistry,

Heavy Metal Deep-Remediation in Water and Resource Reuse Key Lab of Hebei Province,

School of Environmental and Chemical Engineering, Yanshan University, Qinhuangdao 066004, China

<sup>2</sup>School of Electrical Engineering, Yanshan University, Qinhuangdao 066004, China

<sup>3</sup>National Engineering Research Center for Equipment and Technology of Cold Strip Rolling, Qinhuangdao 066004, China

Correspondence should be addressed to Tifeng Jiao; [tfjiao@ysu.edu.cn](mailto:tfjiao@ysu.edu.cn)

Received 16 July 2020; Revised 21 October 2020; Accepted 11 November 2020; Published 29 November 2020

Academic Editor: Jo o Paulo Leal

Copyright © 2020 Weiwei Su et al. This is an open access article distributed under the Creative Commons Attribution License, which permits unrestricted use, distribution, and reproduction in any medium, provided the original work is properly cited.

The fluorescent gel with good flexibility and biocompatibility has attracted more and more attention due to its excellent optical properties. In this paper, the research progresses in preparation methods and applications of fluorescent gels are reviewed. In addition, the preparation methods of self-assembly and polymerization of fluorescent gel are also introduced. In this paper, it should be noted that some outstanding research about the fluorescent gels used in sensors, bio-imaging probes, drug delivery, and other application fields is summarized. This work provides useful reference information for further exploration and study of fluorescent hydrogels.

## 1. Introduction

In recent years, the development of hydrogels has attracted the attention of researchers. Hydrogel is a polymer with a three-dimensional network structure swollen by water [1]. Hydrogels can be classified into two types according to their sources: synthetic and natural hydrogels. Natural hydrogels have higher water absorption capacity, and their hydrophilic structures enable them to contain large amounts of water in their three-dimensional network. In addition, natural hydrogels show good flexibility, biocompatibility, and long service life [2]. Moreover, due to its similar structure to extracellular matrix, natural hydrogel can also be used in tissue engineering fields such as drug delivery and cell transfer. Synthetic hydrogel is rich in raw materials and has a long service life. Compared with natural hydrogels, synthetic hydrogels have better mechanical strength and stability and wider adjustable range of structure and performance, which make them play an important role in biomedical, biosensing, and tissue engineering fields.

Fluorescence is a common phenomenon, which has been studied in detail all over the world. In 1970, Galley et al. independently found that the spectral properties of aromatic fluorophores embedded in different rigid and highly viscous media did not conform to the classical rules [3]. The fluorescence spectrum shows different color fluorescence, which also depends on the excitation wavelength; different excitation leads to different color states. The distribution of excited states and the different dielectric relaxation rate in a certain environment promote the different emission of fluorescence.

Fluorescent hydrogel is a kind of polymer gel, which has attracted the attention of scientists because of its special luminescent properties [4–8]. Fluorescent gel can be regarded as the combination of light and gel, which possesses excellent properties of hydrogel. Adjusting the chromophore and the environment of the excited state can change the state of the fluorescent hydrogel and the change of its emission spectrum, making it have great significance in the fields of biosensor, fluorescence probe, imaging tracking, and cancer treatment. This review mainly introduces the

preparation methods, types, and properties of fluorescent hydrogels, as well as their application in related fields, and looks forward to their application research and development prospects.

## 2. Preparation Method

With the expansion of the application field of hydrogels, people have more requirements for their performance. In order to improve the comprehensive performance of fluorescent hydrogels and better meet the requirements of different application fields, researchers have developed different preparation methods. The water-soluble or hydrophilic polymers can form hydrogels through certain chemical or physical crosslinking. The fluorescent hydrogels can be prepared by self-assembly, polymerization, crosslinking, and other methods. Among them, self-assembly belongs to physical crosslinking and it is a method to prepare hydrogels based on weak interaction forces. Polymerization is a kind of chemical crosslinking, because chemical reaction occurs, which causes the intermolecular covalent bond to act to form hydrogel. From these two parts, the preparation method of fluorescent hydrogel is briefly described below.

**2.1. Physical Crosslinking.** Physical crosslinking is the formation of hydrogels through physical forces such as electrostatic interaction, ion interaction, hydrogen bonding, and chain winding. At present, self-assembly is the most common physical crosslinking method, and self-assembly plays an important role in various technical fields [9, 10]. Self-assembly is a process in which small structural units are spontaneously arranged to form an ordered structure without human intervention, which exists in natural and unnatural systems. These structural units consist of molecules, nano- and micromaterials, or larger materials. Based on the interaction of noncovalent bonds (such as hydrogen bond, van der Waals force, electrostatic interactions, and  $\pi$ - $\pi$  interactions), they also spontaneously organize into a series of regular structures. The following is a brief description of the preparation of hydrogels from these different weak interaction forces.

**2.1.1. Electrostatic Interaction.** The fluorescent hydrogel can be prepared by electrostatic interaction. For example, Xia et al. [11] reported a self-assembled peptide based printable fluorescent hydrogel, which has the ability to grow the beta folded fiber through self-assembly [12–14]. Here, the sequence of the ion complementary peptide is selected as the self-assembly motif, and the N-terminal of the peptide is capped by the powerful ligand 2,2-bipyridine (Bpy), for metal ion chelation (Figure 1(a)). According to the investigation, the metal ion  $\text{Eu}^{3+}$  has excellent fluorescence performance, so it is selected as the metal ion center here. The self-assembled motif contains lysine (K) of the side chain protonated amino group and glutamic acid (E) with carboxylic acid on the side chain. The electrostatic interaction between positive and negative ions, coupled with the hydrophobic interaction between phenylalanine (F) residues

and the  $\pi$  stacking effect, can be self-assembled into a fibrous hydrogel structure under neutral pH (Figure 1(b)). Bpy-KFEFKFEF with the combination of metal ions  $\text{Eu}^{3+}$ ,  $\text{Eu}^{3+}\text{Eu}^{3+}$ ,  $\text{Eu}^{3+}$  and Bpy". Please check and confirm the correct usage." and Bpy, and the hydrogel has photoluminescence properties (Figures 1(c) and 1(d)).

**2.1.2. Hydrogen Bonding.** In solution systems, intramolecular and intermolecular hydrogen bonding can also act as a physical crosslinking point. Chu et al. [15] selected two nonaromatic functional amino acids, serine (S/Ser) and aspartic acid (D/Asp), and used them as side chains of amino acids (Figure 2(a)). Their unique structure can generate extended hydrogen bond networks during self-assembly. There are different side chains of amino acids, and the pH value of self-assembly is also different, which is pH dependent. The hydroxyl containing tetraphenylethene-serine acid (TPE-Ser) with the lowest molecular weight will self-assemble into supramolecular hydrogels under physiological pH conditions. Tetraphenylethene-aspartic acid (TPE-Asp) side chains with carboxyl groups will undergo self-assembly and hydrogelling process under weak acidic conditions (Figure 2(b)). Because TPE has strong hydrophobicity, the rotation of phenyl group is limited and the molecules of benzene ring cannot rotate in aqueous medium, which makes the space limited luminescence, so the gel shows enhanced fluorescence intensity. Yan et al. [16] reported a reversible multi-sensitive quantum dot gel formed by hyperbranched polyamidoamine (PAA) on the surface of functional fluorescent semiconductor quantum dots (QDs). Furthermore, the formed QDs gel showed stronger fluorescence than the corresponding solution.

**2.1.3. Other Weak Interaction Forces.** There are many reports about the physical crosslinking of hydrogels [17]. In addition to electrostatic interaction and hydrogen bonding, weak interactions also exist in the gels, such as the  $\pi$ - $\pi$  stacking and hydrophobic interactions. For example, Ji et al. [18] have successfully synthesized luminescent supramolecular crosslinked polymer gel based on benzo-21-crown-7 (B21C7)/dialkyl ammonium salt host-guest interaction with TPE. Because TPE has the effect of aggregation induced emission (AIE), the luminescence intensity of hydrogel will also increase with the increase of concentration. Zhang et al. [19] also applied the crosslinking method. A supramolecular polymer gel with AIE effect was prepared by the combination of host-guest interaction and TPE. Subject-guest interaction is also a weak interaction, including  $\pi$ - $\pi$  stacking and hydrophobic interaction. In addition, non-coordination action is also a kind of weak interaction force. Bhowmik et al. [20] proposed a new design strategy of rare Earth luminescent materials based on self-assembly, prepared a supramolecular gel doped with lanthanide complexes, and sensitized the gel by doping pyrene into the gel in a non-coordinated manner. Lanthanide ions are part of the gel matrix and participate in the self-assembly process. At the same time, hydrogel as a matrix of lanthanide enhances the luminescence potential.

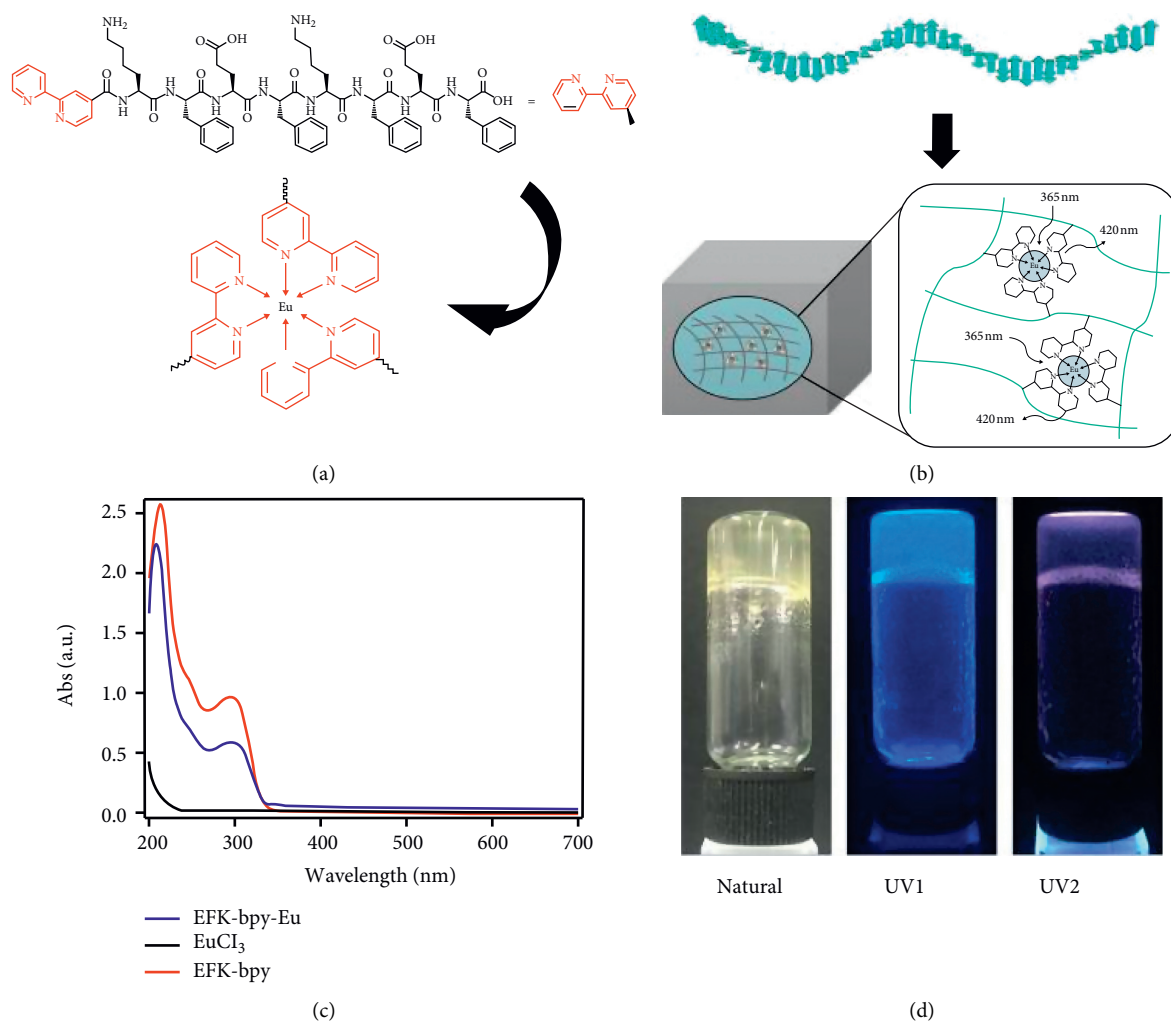


FIGURE 1: Schematic diagram and related fluorescence diagram of self-assembled peptide. (a) The molecular structure of EFK-Bpy peptide and the structure of EFK-Bpy-Eu peptide. (b) Schematic diagram of co-assembled hydrogel and energy transfer process. (c) UV-Vis absorption spectra of EFK-Bpy hydrogel (4 mM), EuCl<sub>3</sub> (1.3 mM), and EFK-Bpy-Eu hydrogel (1.3 mM). (d) Optical images of EFK-Bpy-Eu hydrogels irradiated by natural light (left), ultraviolet 1 (330–390 nm) and ultraviolet 2 (220–280 nm) (reprinted from [11]).

**2.2. Chemical Crosslinking.** Chemical crosslinking refers to the connection of polymer chains through chemical reaction. Generally speaking, when external force is applied, the fluidity of crosslinked gel will decrease. In addition, the swelling property will decrease, and the chemical resistance and solvent resistance will increase [21]. Chemical hydrogels are three-dimensional network polymers formed by chemical bonds and crosslinking, which are irreversible. Among them, different crosslinking agents also have different effects on the formation of hydrogels. By changing the concentration and properties of the crosslinking agent, the external environment at the time of crosslinking, such as temperature, can precisely adjust the mechanical properties in the linear and strain strengthened state [22]. Polymerization is one of the chemical crosslinking methods and plays an important role in the preparation of hydrogels. It is a common form in the formation of fluorescent hydrogels, including free radical polymerization, precipitation

polymerization, emulsion polymerization, and in situ polymerization.

**2.2.1. Emulsion Polymerization.** Emulsion polymerization usually refers to the polymerization reaction initiated by heat, light, radiation, and initiator in the microemulsion system with the polymerizable monomer as the dispersed phase and water or other media as the continuous phase. In 2010, Shibata et al. [23] prepared injectable hydrogel beads by polymerization. They first synthesized the fluorescent monomer GF consisting of glucose recognition sites, fluorescent sites, spacers, and polymerization sites. Subsequently, the fluorescent monomer GF was polymerized with acrylamide monomer and crosslinking agent, and then the fluorescent polyacrylamide hydrogel beads with injectable size were prepared (Figure 3). Because of the good hydrophilicity and biocompatibility of acrylamide, the use of

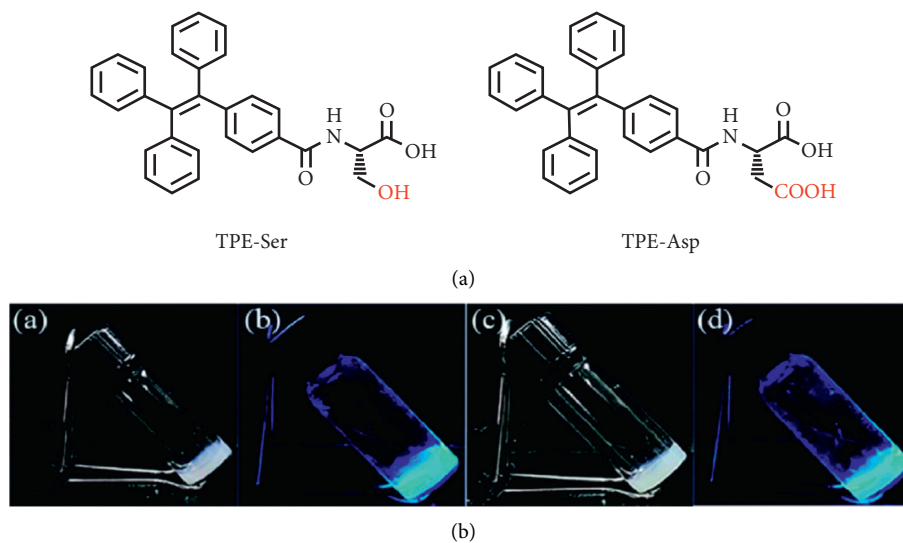


FIGURE 2: The structural formula of TPE-Ser and TPE-ASP and the optical picture after self-assembly. (a) The structural formula of TPE-Ser and TPE-ASP, (b) TPE-Ser (2% w/v, pH = 7.1) and TPE-Asp (2% w/v, pH = 6.0) self-assembling optical images of hydrogels. Among them, the first two were TPE-Ser gels, and the other two were TPE-Asp gels. (A) (C) are ordinary light, and (B) (D) are ultraviolet light (reprinted from [15]).

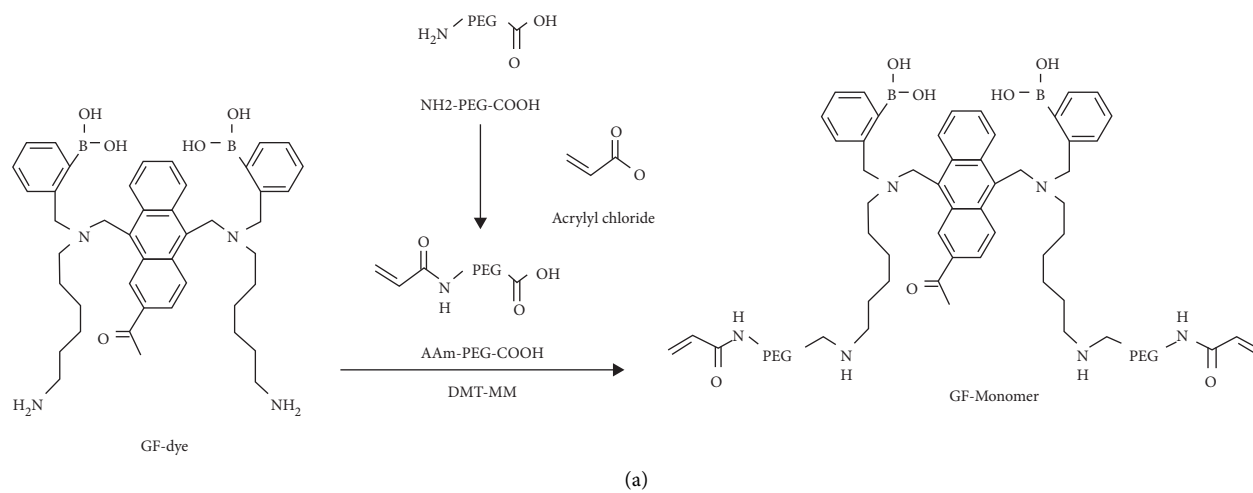


FIGURE 3: Continued.

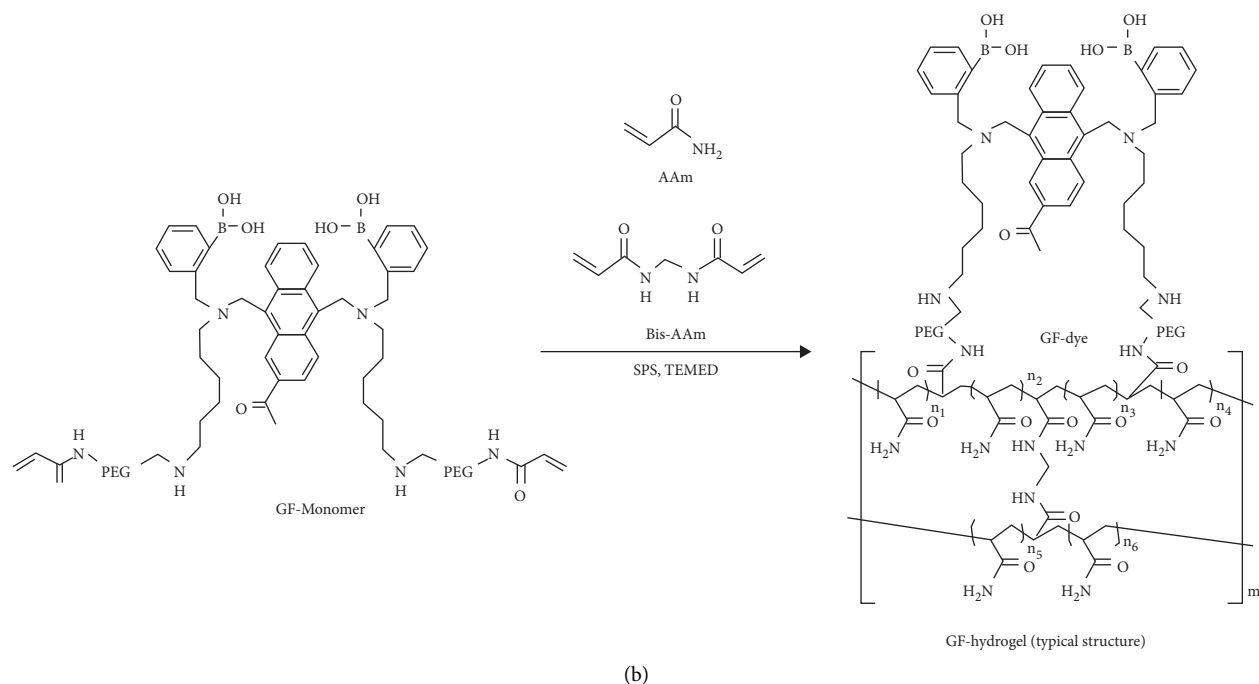


FIGURE 3: Synthesis of fluorescent monomer (GF-monomer) and hydrogel (GF-hydrogel). (a) Preparation of GF monomer. (b) Preparation of GF hydrogel (reprinted from [23]).

acrylamide as a polymerization site can greatly promote the polymerization process.

In addition, numerous studies have been conducted on fluorescent hydrogels, which have been used to synthesize various functional fluorescent gels. Nishiyama et al. [24] synthesized polyacrylic acid (PAAc) gel particles containing DNA by emulsion polymerization, and certain chemical reagents were added to assist in the polymerization process, for example, initiator potassium persulfate, crosslinking agent *n*, *n*-methylene bisacrylamide, etc. Then, PAAc gel particles containing DNA were immersed in bromo-ethane (EtBr) solution to prepare PAAc gel particles with DNA-EtBr complex. The fluorescence intensity of PAAc gel particles embedded in DNA-EtBr complex showed high sensitivity and was found to decrease exponentially with pH. Therefore, it can be used in the development of optical micro pH sensor.

**2.2.2. Free Radical Polymerization.** Free radical polymerization can be finished by a water-soluble molecule which contains a double bond. The crosslinker is usually a molecule containing at least two polymerizable double bonds, which can generate free radicals during the reaction and then conduct polymerization.

Chen et al. [25] have prepared an easily synthesized thermal responsive organic hydrogel and used covalent bonded 10-phenophthiazine (PTH) to achieve controlled free radical polymerization. Various monomers (acrylate, methacrylate, acrylamide, vinyl ester, and vinyl amide) were polymerized by reversible addition-fragmentation chain transfer polymerization (RAFT) and atom transfer radical polymerization (ATRP). The study reported that the “high

and low” temperature of the fluorescent hydrogel, the “switch” of the light, and the “in and out” of the catalyst could switch the real-time controlled radical polymerization reaction. The “and” gating of controlled radical polymerization is realized, which provides a valuable idea for the design of logic control.

**2.2.3. Precipitation Polymerization.** Precipitation polymerization is a process in which the resulting polymer does not dissolve in monomers but is precipitated continuously as the reaction progresses. The monomer and initiator can be dissolved in the reaction medium, and the polymer is insoluble in the reaction medium during the reaction. Wang et al. [26] prepared a hybrid nano-hydrogel, which was prepared by precipitation polymerization of polyethylene glycol (PEG) macromonomer, chitosan, and graphite carbon dots (CDs) in aqueous medium in one pot without surfactant. Chitosan chain and CDs are crosslinking agents in aqueous solution, so that hydroxyl and amino groups on the repeating unit of chitosan chain, hydroxyl and carboxyl groups on CDs surface, and the ether oxygen on the PEG macromolecule monomer can form hydrogen bond association or complexation. Then, PEG and other macromolecules were used as monomers for one-pot precipitation polymerization. When these PEG macromonomers are polymerized and crosslinked, chitosan chains will be physically entangled in the formed nonlinear PEG chain network, and CDs will be fixed in situ in the polymerized gel network, where the fixation of CDs is due to hydrogen bonding. When these aqueous dispersions of hybrid nanogels are exposed to ultraviolet rays (365 nm), they will obviously emit green-blue light. Due to the embedding of

CDs, the hybrid nano-fluorescent hydrogel also retains the characteristics of CDs and has pH responsiveness and high-efficiency synergistic response, which makes it have great potential in medical diagnosis and treatment in vivo.

**2.2.4. In Situ Polymerization.** In situ polymerization is developed from nanocomposites and is a method to disperse nanoparticles and polymerize them in situ under certain conditions. Zhu et al. [27] synthesized the thermal sensitive poly (N-isopropylacrylamide)/Au nanocomposite fluorescent hydrogels (PNIPAM/Au) by in situ gamma irradiation assisted polymerization, which initiated the polymerization in situ by inducing the reduction of aqueous chloroauric acid ( $\text{HAuCl}_4 \cdot \text{H}_2\text{O}$ ). These studies keep emerging, providing a broader space for the development of fluorescent gel in the future.

**2.2.5. Other Chemical Crosslinking Methods.** All fluorescent gels prepared by chemical reaction belong to chemical crosslinking method. In addition to the above chemical crosslinking methods, there are other crosslinking methods such as graft copolymerization and complexation crosslinking. For example, Kawa and Takahagi [28] made terbium (III) nuclear dendrimer copolymers with n-isopropylacrylamide and prepared a transparent hydrogel which can produce green fluorescence. Ma et al. [29] reported a method of using glutaraldehyde crosslinked bovine serum albumin (BSA) (or human serum albumin (HSA)) to form a new luminescent biological hydrogel (Figure 4(a)). Glutaraldehyde (GA) has low cost, dry reactivity, and good chemical stability compared with the same kind of aldehydes, so it is widely used as a good crosslinking agent [30]. The crosslinking of glutaraldehyde and BSA mainly occurs on the  $\alpha$ -amino group of lysine [31]. In this study, a high concentration of BSA solution was used to generate a large number of 3D networks during the intermolecular crosslinking process, thus forming a gel phase, and the gel showed strong green and red autofluorescence in the larger excitation wavelength range (Figure 4(b)). The results of UV-Vis and fluorescence spectra indicate that three kinds of fluorescent compounds may form in BSA hydrogels with GA as crosslinking agent. The luminescence of this gel is speculated, which may be attributed to four aspects: firstly, secondary amines and ethylenediamines in the molecule are believed to contribute to the fluorescence mechanism. Second is electronic transition, such as  $\pi$ - $\pi^*$  transition of C=C bond. Third is synergism of several amino acids close to each other. Lastly, the charge around the fluorophore in BSA hydrogel is another potential factor affecting fluorescence. In short, a new fluorescent gel was prepared by crosslinking method, and the mechanism of its luminescence could be further studied and discussed. In addition to GA, genipin is commonly used as crosslinking agent. As a water-soluble bifunctional crosslinking agent, genipin is highly respected in the preparation of crosslinked fluorescent gel. For example, Muzzarelli [32] used genipin to rapidly crosslink with chitosan (usually with protein or amine) to produce blue

fluorescent hydrogels, which play a great role in biomedicine and pharmaceutical auxiliaries.

In addition, the most common forms of alginate are its gel and polyvalent metal ions, but in practical application, gels without any polyvalent metal ions are welcome [33]. Recently, Kasak et al. [34] have prepared polyvalent non-metal alginate fluorescent hydrogels by dynamic complexing method. Crosslinking occurs through the dynamic complexation of 5-oxo-2, 3-dihydro-5H-[1, 3]-thiazolo[3, 2-a]pyridine-3, 7-dicarboxylic acid (TPDCA), carboxylic acid groups in alginate cages and sodium ions (Figure 5). First, different substances, TPDCA and CDs, were synthesized under different external conditions and then crosslinked. The gelation ability and stability of the gels were verified by the gel and inverted tests of stainless steel balls for 16 hours. Among them, molecular fluorophore TPDCA is the key component to initiate gelation, and the existence of fluorophore provides them with bright luminescence.

### 3. Types and Properties of Luminescence

At present, hydrogels can be divided into two types: self-luminescence and non-self-luminescence. Self-luminescence can emit strong fluorescence without other substances.

**3.1. Self-Luminescent Hydrogel.** Although different covalent bonding and physical embedding methods have been developed to immobilize the fluorophores, their application has been greatly limited due to the complexity of the synthesis route, the potential leakage and photobleaching of the fluorophores, the impact of fluorescent markers on the degradation mode and their application. Unlike non-self-photoluminescence hydrogels, self-luminous hydrogels do not require additional phosphors or fluorophores to label them. In recent years, researchers have immersed many painstaking efforts in the field of unconventional luminescent gel. According to the investigation, a few polymers only contain auxiliary chromophores or unconventional chromophores, such as carbonyl, ester, and amide, which can emit strong fluorescence. At the same time, a small number of clusters can also achieve fluorescence emission and avoid the traditional luminescence defects, that is, aggregation induced quenching (ACQ) effect. On the contrary, it will cause aggregation induced emission (AIE) effect, when the aggregation degree is larger, and the fluorescence is significantly enhanced.

**3.1.1. Cluster Luminescence.** Cluster luminescence is most common in metal nanoclusters, such as gold nanoclusters, silver nanoclusters, etc. In the gel field, it is not common to include metal nanoclusters, and most of them are based on polymer and small molecule clusters. Based on the completely non conjugated structure of saturated C-C, C-O, or C-N bonds, the clusters show bright fluorescence, which is called cluster luminescence [35–38]. In general, with the increase of cluster size, the fluorescence increases. For example, Sugár et al. [39] simulated dimyristoylphosphatidylcholine/distearoylphosphatidylcholine (DMPC/DSPC) lipid bilayer by using Ising model and

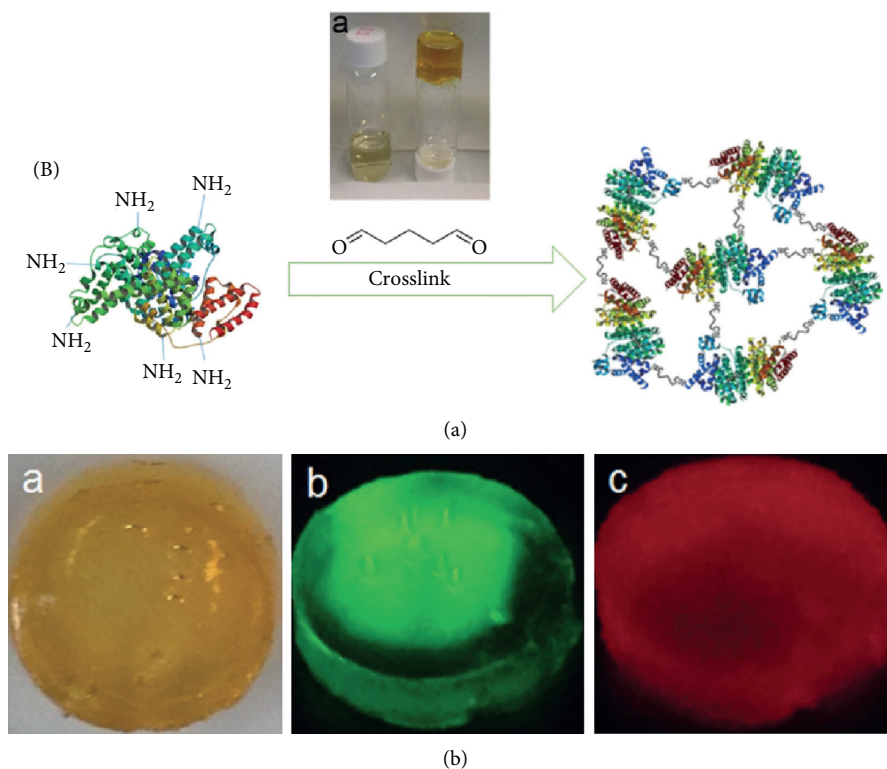


FIGURE 4: Schematic diagram and macroscopic photoperiod of crosslinked BSA hydrogels. (a) Schematic diagram of crosslinked BSA hydrogels. Among them, the right sample bottle contains BSA hydrogel after crosslinking with GA, while the left sample bottle contains 20% BSA solution as a comparison. (b) Macroscopic picture of GA crosslinked BSA hydrogel under normal white light, 470 nm and 595 nm (reprinted from [29]).

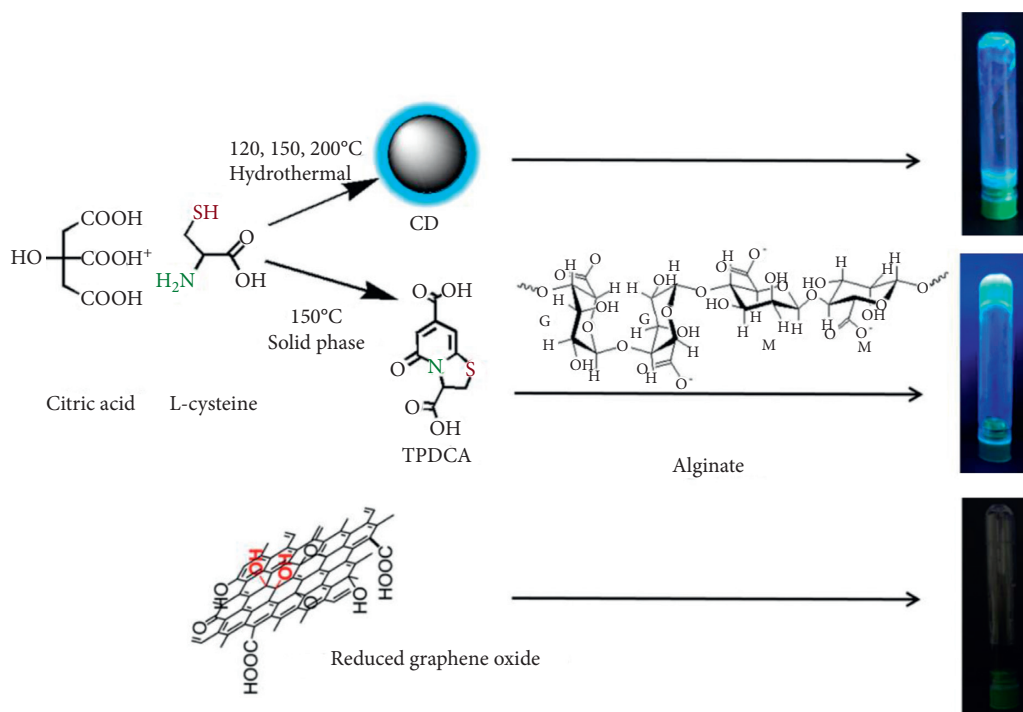


FIGURE 5: Schematic diagram of synthesis of crosslinked alginate fluorescent hydrogels. Among them, the picture on the right was shot under the excitation of ultraviolet lamp (reprinted from [34]).

Monte Carlo method, and it can be found that there was a strong positive correlation between the permeation threshold temperature of gel cluster and FRAP threshold temperature.

### 3.1.2. Unconventional Chromophore Luminescence.

Conventional fluorescent polymers are composed of conjugated main chains or  $\pi$  electron systems, which form enough conjugation by covalent bonding, thus producing bright fluorescence. However, their defects, such as poor photostability and high cytotoxicity, limit their application [40]. Due to these limitations, researchers have discovered and designed a series of unconventional luminescent hydrogels. Xu et al. [41] reported the autofluorescence of carbonyl hydrogels. Even without any specific functional groups, polyacrylamide (PAM) gels are autofluorescent. In this work, polymers with carbonyl groups were synthesized from different monomers, and very similar fluorescence could be observed in the gel. Meanwhile, the fluorescence lifetime of the dried PAM gel was measured. The average life expectancy was 1.28 ns, similar to that of the traditional fluorophore containing large conjugated structure. In this work, the factors affecting the fluorescence intensity were studied, and it was found that the fluorescence properties were related to the gel structure. In addition, the water content in the gel also affects the luminous intensity. With the decrease of water content, fluorescence increases gradually. Like traditional fluorescent gel, adding some specific metal ions can quench fluorescence.

3.2. *Non-Self-Luminous Hydrogel.* Non-self-luminous hydrogel does not have fluorescence emission itself and needs other light emitting materials to achieve fluorescence emission. In general, the organic fluorescent substances, quantum dots, and metal complexes are usually labeled by physical or chemical methods, and then the non-self-luminous hydrogels emit fluorescent quantities.

### 3.2.1. Multiresponse Supramolecular Luminescent Hydrogel.

Compared with single response fluorescent gel, multi-response supramolecular luminescent hydrogel can respond to many factors and improve the utilization and sensitivity of fluorescent gel. Therefore, the multi-stimulus responsive fluorescent gel has become the focus of current research [42]. The synthesis of supramolecular luminescent hydrogels by rotaxane with typical mechanical interlocking structure has become a research hotspot. At present, rotaxane usually prepares supramolecular gels with multiple stimulus responses by self-assembly in solution [43]. Sun et al. [44] prepared the first rotaxane with fluorescent functional group based on BODIPY and aromatics. Then, using the rotational alkane as gelation factor, by means of the  $\pi$ - $\pi$  interaction between the phenylene parts of the adjacent column aromatic ring of the rotaxane, noncovalent action such as  $\pi$ - $\pi$  interaction between BODIPY and imidazolium parts, the 3D crosslinking network is finally self-assembled (Figure 6). Among them, BODIPY is its fluorescent chromophore. By

heating-cooling, vibrating-standing at temperature, and adding different anions, the gel can realize reversible gel-solution transformation. At the same time, it also has stimulation response to different pH values. After being exposed to hydrochloric acid (HCl) gas, the fluorescence intensity of the thin film gel is significantly reduced by 50%, and at the same time, under ultraviolet light, the fluorescence color changes from yellow to purple-red.

Ma research group of Tianjin University [45] reported a fluorescent hydrogel composed of lanthanide and nucleoside. Here, nucleosides, the main component of nucleic acids, act as ligands and successfully chelate with lanthanide elements to form complexes in water. Then, it can self-assemble into fluorescent gel with characteristic luminescence of lanthanide series elements, and the prepared fluorescent hydrogel showed fluorescent photochromic characteristics in response to external stimuli such as pH value and temperature. Intelligent stimuli responsive hydrogels may undergo reversible deformations when triggering various external stimuli. Cheng and colleagues [46] proposed a double-layer hydrogel actuator with fluorescent coumarin groups. Under the stimulation of pH or temperature, the double-layer hydrogel shows reversible deformation behavior, and the whole hydrogel has bright fluorescence due to the introduction of coumarin units. In conclusion, the research progress of multi-response supramolecular luminescent hydrogels has always been a hot topic.

3.2.2. *White Luminescent Hydrogel.* White light emitting (WLE) hydrogel has attracted considerable attention in the manufacture of intelligent molecular machines, equipment, luminescent lamps, and materials [47].

Xia et al. [11] reported a fluorescent hydrogel based on peptide motif and transition metal ion assembly. The introduction of metal ions to immobilize them on the hydrogel network at specific locations can prevent the aggregation and self-quenching of chromophores. In addition, white light emission is realized by using three different metal ions (Figure 7). Because the emission spectra of  $\text{Eu}^{3+}$ ,  $\text{Ru}^{2+}$ , and  $\text{Ir}^{2+}$  are complementary in the visible range,  $\text{Eu}^{3+}$ ,  $\text{Ru}^{2+}$ , and  $\text{Ir}^{2+}$  are selected here to form fluorescent metal complexes with EFK-Bpy. The emission spectra of EFK-Bpy-Eu, EFK-Bpy-Ir, and EFK-Bpy-Ru hydrogel excited by 365 nm can cover the whole visible range. Therefore, white light emission can be easily realized by adjusting the proportion of the three components.

Lanthanide has always been popular in the field of luminescence because of its good luminescent properties, even though it is expensive. Recently, Xue et al. [48] reported a pure white emissive hydrogel composed of luciferin and carbon dots with high quantum yield. By adjusting the stoichiometry of lanthanide complexes, fluorescein and carbon dots, a pure white emitting hydrogel can be obtained. The absolute yield of WLE hydrogel was up to 18.00% by computation.

### 3.2.3. Reversible Fluorescent Chromotropic Hydrogel.

More and more attention has been paid to the development of advanced sensors and luminescent materials, which are

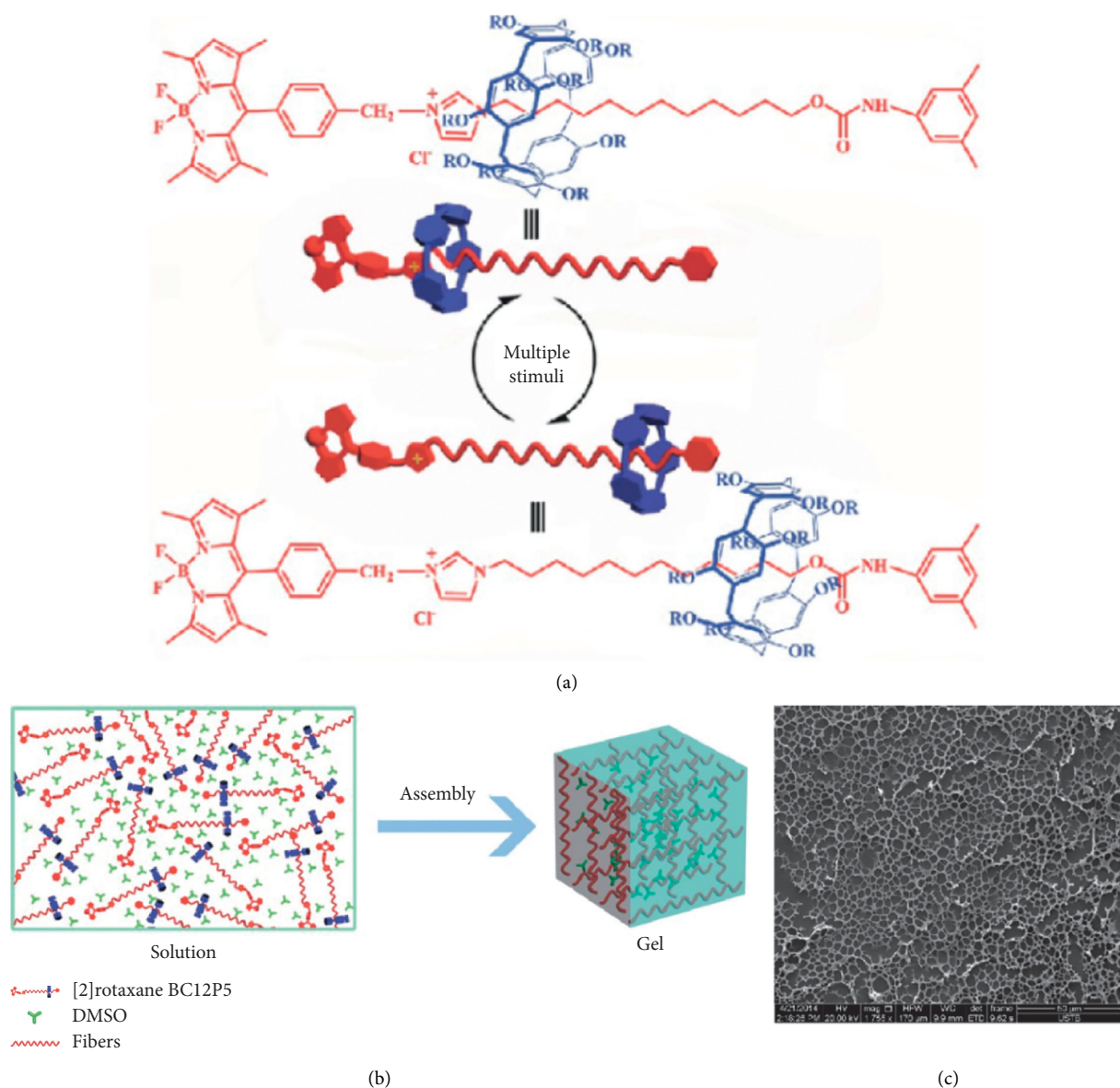


FIGURE 6: Schematic diagram and gel SEM diagram of the wheel molecule and gel structure. (a) The structure of rotaxane and the schematic diagram of its structural transformation under various stimuli. (b) Schematic diagram of self-assembly of BC12P5 in supramolecular gels. (c) SEM images of rotaxane-based supramolecular gels formed in DMSO (reprinted from [44]).

dynamically changing in response to external stimuli [49, 50]. Reversible fluorescent chromotropic hydrogel is also used as a kind of fluorescent gel. Yang et al. reported a work based on polymer hydrogel containing lanthanide elements and prepared reversible fluorescent color-changing gel by using lanthanide-mannose compound in gel matrix [51]. Among them, mannose, as a ligand, coordinated with lanthanide ions ( $\text{Eu}^{3+}$  and  $\text{Tb}^{3+}$ ) in aqueous solution, sensitized rare Earth ions to emit light, and first formed lanthanide mannose (Ln-Man) complex. Subsequently, gelatin network was introduced into the system to prepare the rare Earth hydrogel successfully (Figure 8). The prepared fluorescent gel has fluorescence discoloration function for  $\text{Fe}^{2+}$ , and the recovery rate of fluorescent discoloration is 63.2% after three cycles of “ON/OFF.” Despite the decrease of

fluorescence intensity, the “ON/OFF” switchable emission is reversible in response to  $\text{Fe}^{2+}$  and edetic acid (EDTA) due to the dynamic coordination between lanthanide and mannose. Because of its good biocompatibility, the gel can be used as a 3D cell culture medium and still has a reversible “ON/OFF” fluorescence characteristic in the matrix.

**3.2.4. Color Matching Intrinsic Luminescence Metal-Organic Frameworks (MOF) Gel.** In recent years, metal-organic framework has been a new material which attracts much attention. As for the tintable intrinsic luminescent MOF gel, it has been developed as early as 2018. Chen group of Nankai University [50] reported for the first time a series of coloring luminescent lanthanide MOF gel materials. Lanthanide metal ions and organic ligands with unevenly

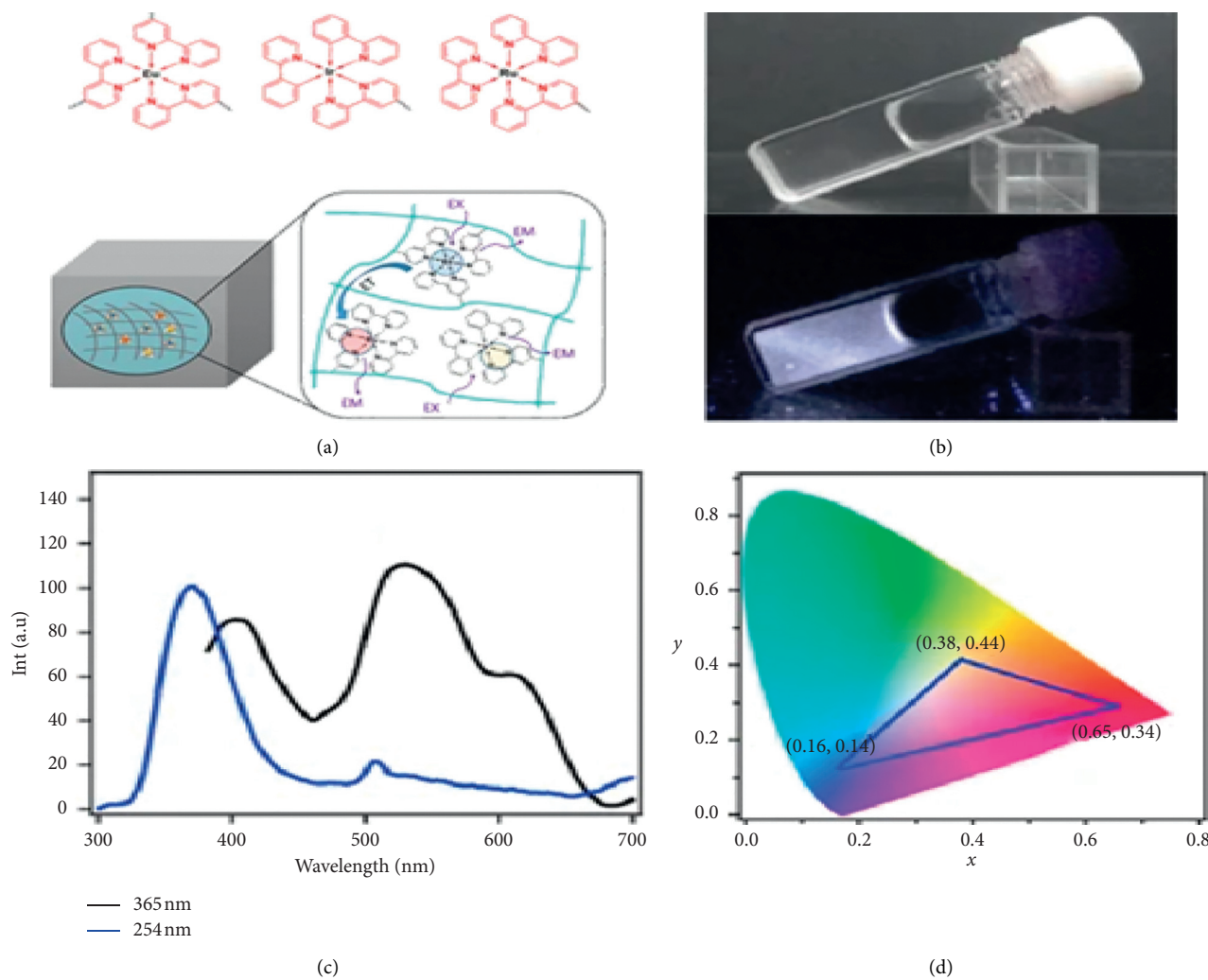
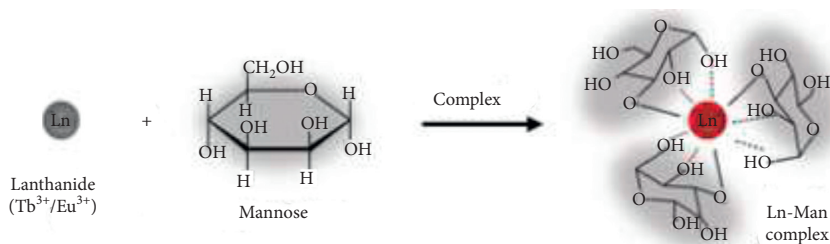


FIGURE 7: White light emission mechanism. (a) The schematic diagram of the hydrogel was co-assembled. (b) Photo of WLFH (12 mm) illuminated by natural light (top) and UV 1 (bottom). (c) Emission spectrum of WLFH ( $\lambda_{ex} = 365$  nm,  $\lambda_{ex} = 254$  nm). (d) Color chart of EFK-Bpy-Eu, EFK-Bpy-Ir, and EFK-Bpy-Ru hydrogel (reprinted from [11]).



(a)

FIGURE 8: Continued.

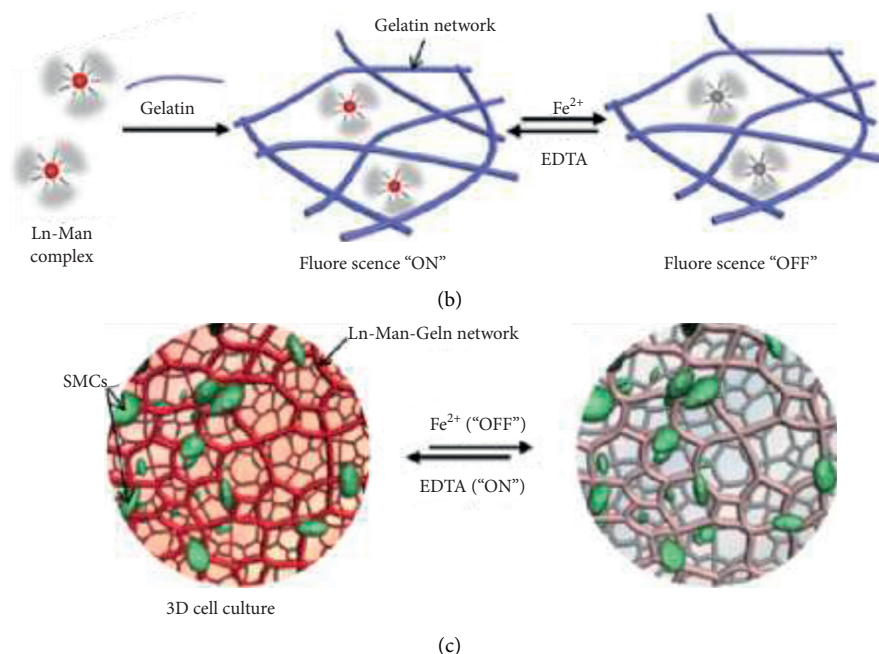


FIGURE 8: Gel formation and its application as a substrate for 3D cell culture. (a) The formation of lanthanide mannose (Ln-Man) complex. (b) The formation of lanthanum mannose gelatin (Ln-Man-Geln) hydrogel and the fluorescence “ON/OFF” on Fe<sup>2+</sup>/EDTA. (c) Ln-Man-Geln hydrogel as a schematic diagram of 3D cell culture medium (reprinted from [51]).

distributed carboxyl groups were selected. Nanobelts were formed through the high valence and biased carboxyl distribution of Ln<sup>3+</sup> ions, boric acid groups were introduced to improve anisotropic growth through steric hindrance and hydrogen bonding, and then these nanobelts were wound together and gelled to form MOF gel (Figure 9(c)). Among them, the addition of boron in the side chain of Isophthalic acid (ISP) changed the ligand's entropy, hydrogen bond, and steric hindrance, which played an important role in the formation of MOF gel. Monometallic MOF shows red, green, and blue fluorescence. Therefore, mixed metal MOF gel was prepared by adjusting the type and/or proportion of Ln<sup>3+</sup> ions; single wavelength excitation can make it obtain full-color luminescence (Figure 9(a)). As an excellent chemical/physical hybrid gel with excellent optical properties, it will have great potential in the field of target detection and biosensing.

#### 4. Study on the Application of Fluorescent Hydrogel

Luminescent materials have attracted considerable attention due to their wide potential applications, especially hydrogels. Based on the noncovalent interaction of gel factor, soft materials, which have highly swelling, degradable, and adjustable rheological properties, are more convenient for synthesis and preparation methods, responsive to external stimuli, and have unique physical properties and self-repairing properties. The special properties of these unique structures make them have great potential in sensors, fluorescence imaging, molecular devices, and biological therapy.

**4.1. Sensors.** Fluorescence-based sensors have been routinely used in biology, physiology, pharmacology, and environmental science. Because of their physiological compatibility, fluorescent gel sensors have attracted wide attention in medicine. Diabetes is a very common chronic disease at present, which is accompanied by various complications, and it is particularly necessary to detect and observe it in real time.

Park and Park [52] reported a glucose sensor with fluorescence and size changing dual response, which was fabricated by microfluidics. Poly(acrylamide) (PAAm) hydrogel forms PAAc hydrogel under the treatment of sodium hydroxide and tetramethylethylenediamine (TEMED). Finally, gelatin was modified to combine fluorescent CDs, glucose oxidase (GOx), horseradish peroxidase (HRP), and gel droplets. The reaction of GOx and HRP with glucose will produce gluconic acid and -OH radicals, which will lead to fluorescence quenching and size reduction of CDs, respectively. Moreover, the glucose sensor shows good sensitivity (linear range is about 30 mM; detection limit is 0.052 mM). Because of its good biocompatibility, it has no other side effects on organisms, so it is of great significance to use it as a long-term glucose test.

Lanthanide-based sensors have unique spectral properties such as long fluorescence lifetime and large Stokes shift. Therefore, many people love to use it to make fluorescent gel for sensor [53]. Weng et al. [54] reported fluorescence hydrogels based on Eu-Iminodiacetate (Eu-IDA dynamic) coordination, which can be dynamically broken and bonded under pH, temperature, metal ions, ultrasonic treatment, and various force stimuli and can switch light device and sol-gel

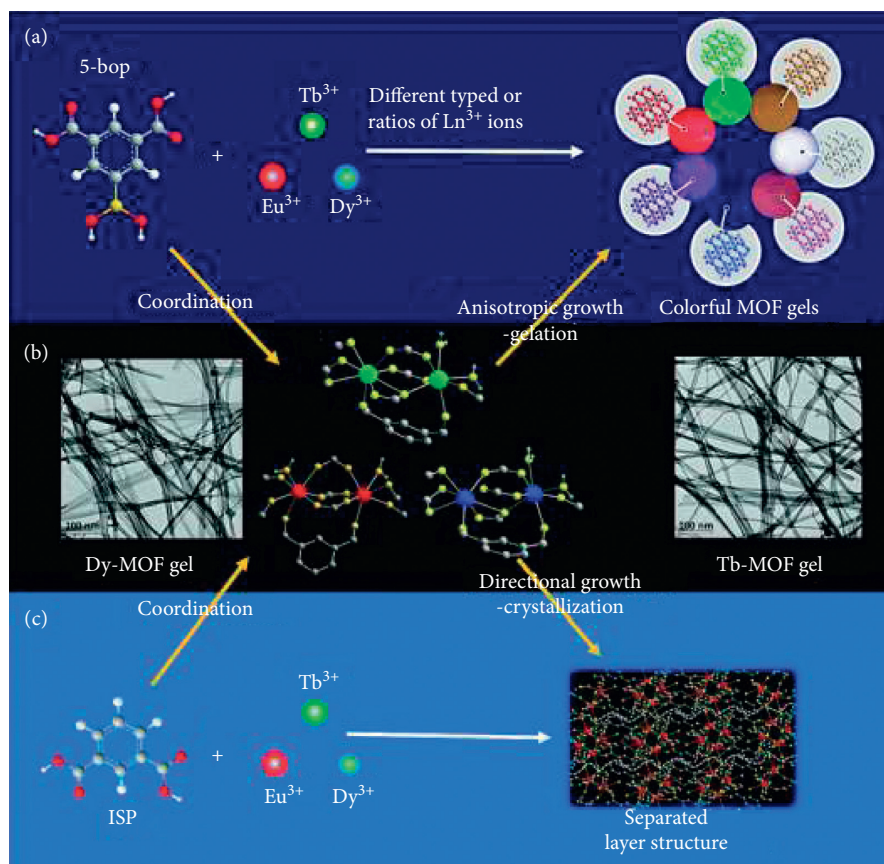


FIGURE 9: Formation and photoluminescence of chemical/physical hybrid gel with intrinsic fluorescence emission. (a) Choosing different types and proportions of  $\text{Ln}^{3+}$  ions to form MOF gel with different colors. (b) Formation of Dy-MOF and Tb-MOF. (c) Formation of MOF gel (reprinted from [50]).

transition easily. Intelligent optical materials can respond to a variety of stimuli, which provides a new method for the development of multi-responsive biosensors.

**4.2. Biological Imaging Probe.** Prior to this, Mehwish et al. [55] summarized the supramolecular fluorescent hydrogels used as biological imaging probes in detail. This includes the research of preparation methods, excellent fluorescence properties, prospective applications in biological imaging, and opportunities and challenges in the future and makes a detailed classification and description of the imaging mechanism of different types of fluorescent probes. The team points out that the supramolecular gel fluorescent probes are highly specific and have excellent stability and sensitivity. At the same time, molecules are assembled by noncovalent bonds, such as hydrogen bonds and hydrophobic interactions, which makes the imaging method more physiological and have good biocompatibility. Therefore, fluorescent gel has a larger market in the application field of biological imaging probes.

Subsequently, Xu et al. [56] reported a fluorescent hydrogel probe for monosaccharide detection. The anthracene fluorescence probe based on boric acid was functionalized with acrylamide unit to incorporate into the hydrogel system for monosaccharide detection (Figure 10). The fluorescence probe

showed a strong fluorescence opening response after being exposed to fructose. According to the fluorescence response, the sensitivity of the probe was improved 10 times by adding D-fructose, and it showed excellent monosaccharide detection ability. Recently, the application of hydrogel fluorescent probes has not been reduced and is still in active research and development [57–59].

**4.3. Drug Delivery.** Using appropriate drug delivery system can ensure higher bioavailability of drugs, and it can exert its efficacy for a long time. Fluorescent gel with good biocompatibility and biodegradability and no toxic and side effects has become a suitable material [60, 61]. The sulfhydryl-disulfide bond is easily broken in the cell, resulting in the destruction of the nanomaterials 3D network, and further accurately releasing the drug. Therefore, in the redox drug delivery system, the disulfide bond has been the most commonly used functional group to prepare nanogels to achieve controlled release of drugs in cancer cells [62]. At the same time, the design of nanogels with redox response and aggregation induced emission luminescence (AIEgen) function can achieve accurate and traceable delivery of drugs.

Ma et al. [63] reported a multifunctional nanogel project with redox reaction and AIEgen characteristics.

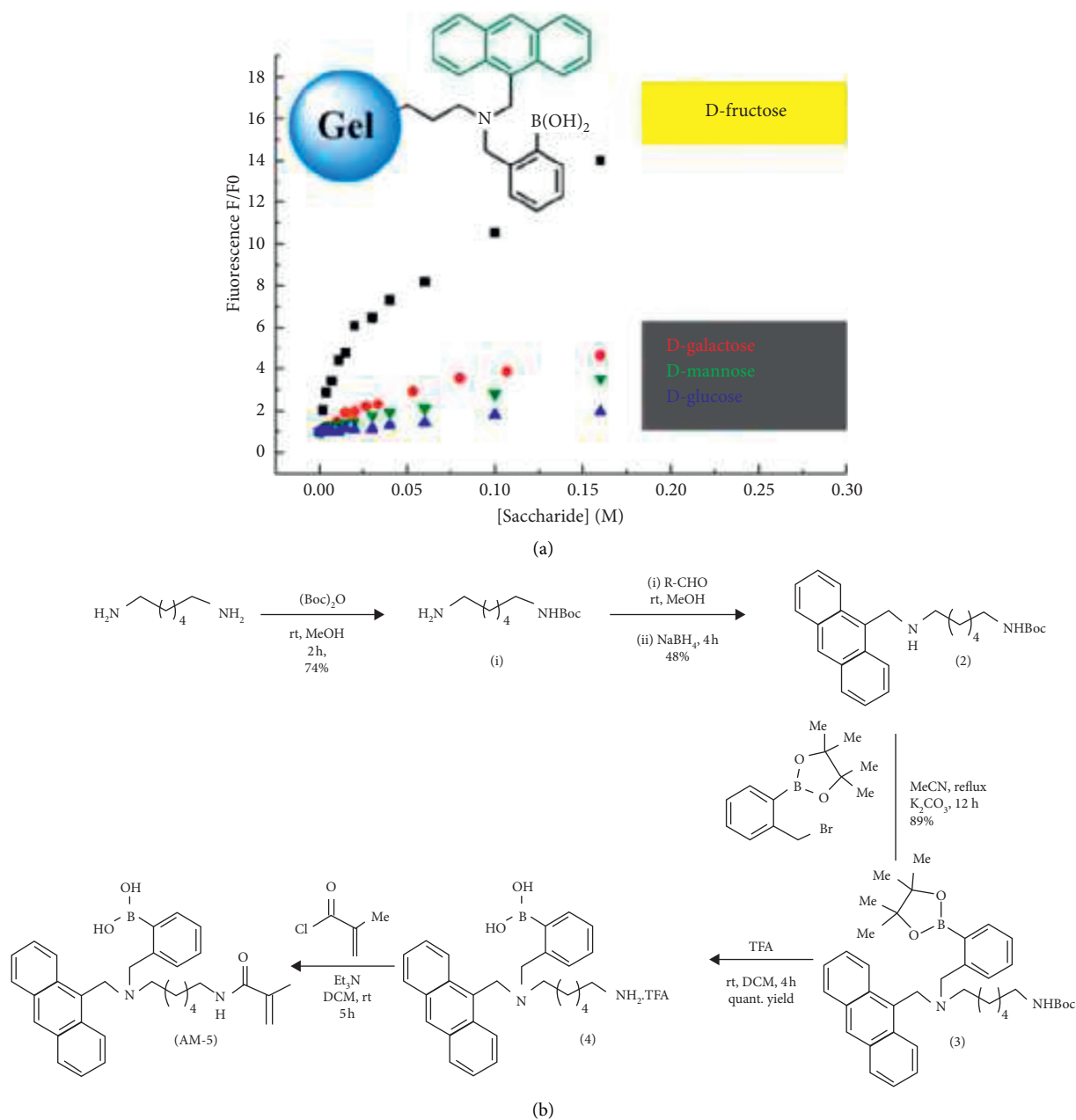


FIGURE 10: The detection of monosaccharide and the route of gel probe synthesis. (a) Schematic diagram of monosaccharide detection based on fluorescence. (b) Synthesis of boric acid fluorescent probes (reprinted from [56]).

All-transretinoic acid (ATRA), with a disulfide bond as a linking agent and a group of aggregation induced luminescence (TPENH<sub>2</sub>) grafted with hyaluronic acid (HA), forms a fluorescent gel HA-ss-ATRA/TPENH<sub>2</sub>HNP's delivery carrier: ATRA as the hydrophobic core of multifunctional hyaluronic acid nanomaterials (HNPs), HA as a hydrophilic agent, using disulfide bond as redox sensitive bonds between HA and ATRA, and preparing HA-ss-ATRA two affinity conjugates, which can control the release of drugs according to the intracellular environment (Figure 11). Finally, HA-ss-ATRA, dichloroethane (EDC), and N-hydroxysuccinimide (NHS) were co-dissolved in formamide to modify AIE fluorescence

group. With the successful preparation of HNPs with unique AIE characteristics, adriamycin loaded on them is selectively absorbed by cancer cells, and real-time imaging in dynamic environment is realized.

**4.4. Other Applications.** Fluorescent gel has excellent water content and unique luminescent properties. It can be used as a sensor and effectively adsorb heavy metals and other environmental pollutants [64, 65].

At present, fluorescence hydrogels are used to encrypt and protect data information so as to realize the possibility of multi-stage data security. Zhang research group of

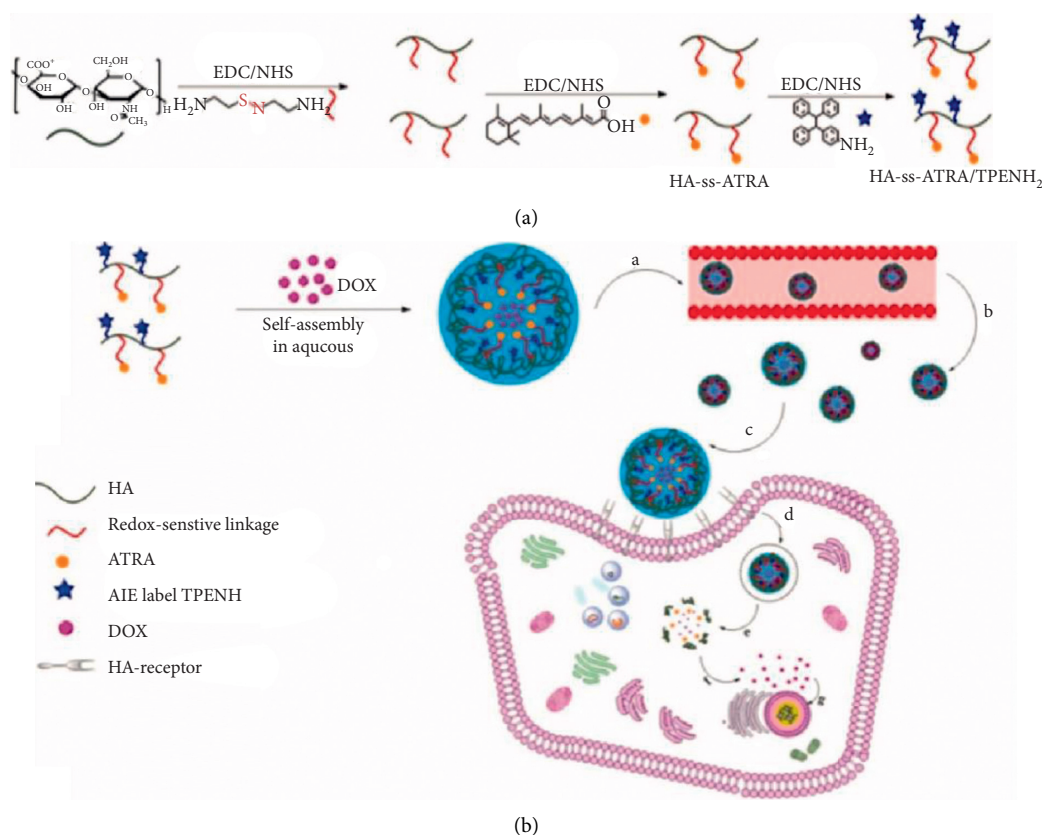


FIGURE 11: Formation process and mechanism of multifunctional hyaluronic acid nanogel (HA-ss-ATRA/TPENH<sub>2</sub> HNP). (a) Synthesis of HA-ss-ATRA/TPENH<sub>2</sub> conjugate. (b) HA-ss-ATRA/TPENH<sub>2</sub> HNP is formed and used for drug delivery (reprinted from [63]).

Ningbo Institute of Materials [66] showed a 3D based anti-counterfeit platform based on fluorescent hydrogel, shape memory, and self-repair feature and made full use of the data inside the 3D structure to encrypt. At the same time, the research group [67] reported a safe information storage method, which can store information on fluorescent hydrogel based on controllable ion imprinting. When the 2D information of fluorescence quenching and the 3D information of activation are exposed to ultraviolet rays and put into water, it can be decrypted in layers and dimensions. Fluorescent gel can also be used to manufacture special materials [68]. Due to its excellent self-healing function, fluorescent hydrogels can also be used as medical excipients in biomedicine [69, 70]. In a word, the function of fluorescent hydrogel is reflected in many aspects, and there will be more room for further application in the future [71–77].

## 5. Conclusion

The hydrophilic functional groups attached to the polymer backbone make the gel have high water absorbency and unique 3D network. The fluorescent hydrogels with good biocompatibility and luminescence properties show good application prospects in biomedicine. At present, the fluorescent hydrogels have been widely used in sensors, biological imaging probes, and so on. In this review, three

different preparation methods are introduced, which are used to construct fluorescent hydrogels with excellent properties. However, the fluorescent hydrogels also have some defects. For example, the gel prepared by noncovalent interaction has poor mechanical stability due to the weak interaction between the gels. Therefore, based on the good prospect of fluorescent hydrogel, accelerating the perfection of fluorescent gel defects and preparing better fluorescent hydrogels are particularly important.

## Data Availability

The data used to support the findings of this study are included within the article.

## Conflicts of Interest

The authors declare no conflicts of interest.

## Acknowledgments

The authors greatly appreciate the financial support of the National Natural Science Foundation of China (Nos. 21872119 and 22072127), the Talent Engineering Training Funding Project of Hebei Province (No. A201905004), and the Research Program of the College Science and Technology of Hebei Province (No. ZD2018091).

## References

- [1] E. M. Ahmed, "Hydrogel: preparation, characterization, and applications: a review," *Journal of Advanced Research*, vol. 6, no. 2, pp. 105–121, 2015.
- [2] E. Caló and V. V. Khutoryanskiy, "Biomedical applications of hydrogels: a review of patents and commercial products," *European Polymer Journal*, vol. 65, pp. 252–267, 2015.
- [3] A. P. Demchenko, "The red-edge effects: 30 years of exploration," *Luminescence*, vol. 17, no. 1, pp. 19–42, 2002.
- [4] A. Griffith, T. J. Bandy, M. Light, and E. Stulz, "Fluorescent hydrogel formation from carboxyphenyl-terpyridine," *Chemical Communications*, vol. 49, no. 7, pp. 731–733, 2013.
- [5] A. Khabibullin, M. Alizadehgiashi, N. Khuu, E. Prince, M. Tebbe, and E. Kumacheva, "Injectable shear-thinning fluorescent hydrogel formed by cellulose nanocrystals and graphene quantum dots," *Langmuir*, vol. 33, no. 43, pp. 12344–12350, 2017.
- [6] T. H. Kim, J. Seo, S. J. Lee, S. S. Lee, J. Kim, and J. H. Jung, "Strongly fluorescent hydrogel as a blue-emitting nanomaterial: an approach toward understanding fluorescence–structure relationship," *Chemistry of Materials*, vol. 19, no. 24, pp. 5815–5817, 2007.
- [7] J. T. Suri, D. B. Cordes, F. E. Cappuccio, R. A. Wessling, and B. Singaram, "Continuous glucose sensing with a fluorescent thin-film hydrogel," *Angewandte Chemie-International Edition*, vol. 42, no. 17, pp. 5857–5859, 2003.
- [8] B. Tan, H. Zhao, L. Du, X. Gan, and X. Quan, "A versatile fluorescent biosensor based on target-responsive graphene oxide hydrogel for antibiotic detection," *Biosensors and Bioelectronics*, vol. 83, pp. 267–273, 2016.
- [9] K. Ariga, J. P. Hill, M. V. Lee, A. Vinu, R. Charvet, and S. Acharya, "Challenges and breakthroughs in recent research on self-assembly," *Science and Technology of Advanced Materials*, vol. 9, no. 1, Article ID 014109, 2008.
- [10] G. M. Whitesides and B. Grzybowski, "Self-assembly at all scales," *Science*, vol. 295, no. 5564, pp. 2418–2421, 2002.
- [11] Y. Xia, B. Xue, M. Qin, Y. Cao, Y. Li, and W. Wang, "Printable fluorescent hydrogels based on self-assembling peptides," *Scientific Reports*, vol. 7, Article ID 9691, 2017.
- [12] G. von Maltzahn, S. Vauthey, S. Santoso, and S. Zhang, "Positively charged surfactant-like peptides self-assemble into nanostructures," *Langmuir*, vol. 19, no. 10, pp. 4332–4337, 2003.
- [13] X. Zhao and S. Zhang, "Molecular designer self-assembling peptides," *Chemical Society Reviews*, vol. 35, no. 11, pp. 1105–1110, 2006.
- [14] R. V. Ulijn and A. M. Smith, "Designing peptide based nanomaterials," *Chemical Society Reviews*, vol. 37, no. 4, pp. 664–675, 2008.
- [15] N. T. Chu, R. D. Chakravarthy, N. C. Shih et al., "Fluorescent supramolecular hydrogels self-assembled from tetraphenylethene (TPE)/single amino acid conjugates," *RSC Advances*, vol. 8, no. 37, pp. 20922–20927, 2018.
- [16] J. J. Yan, H. Wang, Q. H. Zhou, and Y. Z. You, "Reversible and multisensitive quantum dot gels," *Macromolecules*, vol. 44, no. 11, pp. 4306–4312, 2011.
- [17] T. Y. Cheng, M. H. Chen, W. H. Chang, M. Y. Huang, and T. W. Wang, "Neural stem cells encapsulated in a functionalized self-assembling peptide hydrogel for brain tissue engineering," *Biomaterials*, vol. 34, no. 8, pp. 2005–2016, 2013.
- [18] X. F. Ji, P. Wang, H. Wang, and F. H. Huang, "A fluorescent supramolecular crosslinked polymer gel formed by crown ether based host-guest interactions and aggregation induced emission," *Chinese Journal of Polymer Science*, vol. 33, no. 6, pp. 890–898, 2015.
- [19] C. W. Zhang, B. Ou, S. T. Jiang et al., "Cross-linked AIE supramolecular polymer gels with multiple stimuli-responsive behaviours constructed by hierarchical self-assembly," *Polymer Chemistry*, vol. 9, no. 15, pp. 2021–2030, 2018.
- [20] S. Bhowmik, S. Banerjee, and U. Maitra, "A self-assembled, luminescent europium cholate hydrogel: a novel approach towards lanthanide sensitization," *Chemical Communications*, vol. 46, no. 45, pp. 8642–8644, 2010.
- [21] T. Katashima, U. i. Chung, and T. Sakai, "Mechanical properties of doubly crosslinked gels," *Polymer Journal*, vol. 51, no. 9, pp. 851–859, 2019.
- [22] D. C. Schoenmakers, A. E. Rowan, and P. H. J. Kouwer, "Crosslinking of fibrous hydrogels," *Nature Communications*, vol. 9, Article ID 2172, 2018.
- [23] H. Shibata, Y. J. Heo, T. Okitsu, Y. Matsunaga, T. Kawanishi, and S. Takeuchi, "Injectable hydrogel microbeads for fluorescence-based in vivo continuous glucose monitoring," *Proceedings of the National Academy of Sciences*, vol. 107, no. 42, pp. 17894–17898, 2010.
- [24] T. Nishiyama, Y. Kagami, T. Yamauchi, and N. Tsubokawa, "Preparation of stimulus-sensitive gel particles with a DNA-dye complex and their pH sensitivity," *Polymer Journal*, vol. 44, no. 5, pp. 396–400, 2012.
- [25] M. Chen, S. Deng, Y. Gu, J. Lin, M. J. MacLeod, and J. A. Johnson, "Logic-controlled radical polymerization with heat and light: multiple-stimuli switching of polymer chain growth via a recyclable, thermally responsive gel photoredox catalyst," *Journal of the American Chemical Society*, vol. 139, no. 6, pp. 2257–2266, 2017.
- [26] H. Wang, J. Di, Y. Sun et al., "Biocompatible PEG-chitosan@carbon dots hybrid nanogels for two-photon fluorescence imaging, near-infrared light/pH dual-responsive drug carrier, and synergistic therapy," *Advanced Functional Materials*, vol. 25, no. 34, pp. 5537–5547, 2015.
- [27] C. H. Zhu, Z. B. Hai, C. H. Cui, H. H. Li, J. F. Chen, and S. H. Yu, "In situ controlled synthesis of thermosensitive poly(N-isopropylacrylamide)/Au nanocomposite hydrogels by gamma radiation for catalytic application," *Small*, vol. 8, no. 6, pp. 930–936, 2012.
- [28] M. Kawa and T. Takahagi, "Improved antenna effect of terbium(III)-cored dendrimer complex and green-luminescent hydrogel by radical copolymerization," *Chemistry of Materials*, vol. 16, no. 11, pp. 2282–2286, 2004.
- [29] X. Ma, X. Sun, D. Hargrove et al., "A biocompatible and biodegradable protein hydrogel with green and red autofluorescence: preparation, characterization and in vivo biodegradation tracking and modeling," *Scientific Reports*, vol. 6, Article ID 19370, 2016.
- [30] M. E. Nimni, D. Cheung, B. Strates, M. Kodama, and K. Sheikh, "Chemically modified collagen: a natural biomaterial for tissue replacement," *Journal of Biomedical Materials Research*, vol. 21, no. 6, pp. 741–771, 1987.
- [31] A. J. Habeeb and R. Hiramoto, "Reaction of proteins with glutaraldehyde," *Archives of Biochemistry and Biophysics*, vol. 126, no. 1, pp. 16–26, 1968.
- [32] R. A. A. Muzzarelli, "Genipin-crosslinked chitosan hydrogels as biomedical and pharmaceutical aids," *Carbohydrate Polymers*, vol. 77, no. 1, pp. 1–9, 2009.
- [33] M. M. Pérez-Madrugal, J. Torras, J. Casanovas, M. Häring, C. Alemán, and D. D. Díaz, "Paradigm shift for preparing versatile  $M^{2+}$ -free gels from unmodified sodium alginate," *Biomacromolecules*, vol. 18, no. 9, pp. 2967–2979, 2017.

- [34] P. Kasak, M. Danko, S. Zavahir et al., "Identification of molecular fluorophore as a component of carbon dots able to induce gelation in a fluorescent multivalent-metal-ion-free alginate hydrogel," *Scientific Reports*, vol. 9, Article ID 15080, 2019.
- [35] X. Zhou, W. Luo, H. Nie et al., "Oligo(maleic anhydride)s: a platform for unveiling the mechanism of clusteroluminescence of non-aromatic polymers," *Journal of Materials Chemistry C*, vol. 5, no. 19, pp. 4775–4779, 2017.
- [36] E. Zhao, J. W. Y. Lam, L. Meng et al., "Poly[(maleic anhydride)-alt-(vinyl acetate)]: a pure oxygenic nonconjugated macromolecule with strong light emission and solvatochromic effect," *Macromolecules*, vol. 48, no. 1, pp. 64–71, 2015.
- [37] H. Zhang, Z. Zhao, P. R. McGonigal et al., "Clusterization-triggered emission: uncommon luminescence from common materials," *Materials Today*, vol. 32, pp. 275–292, 2020.
- [38] R. Hu, N. L. C. Leung, and B. Z. Tang, "AIE macromolecules: syntheses, structures and functionalities," *Chemical Society Reviews*, vol. 43, no. 13, pp. 4494–4562, 2014.
- [39] I. P. Sugár, E. Michonova-Alexova, and P. Lee-Gau Chong, "Geometrical properties of gel and fluid clusters in DMPC/DSPC bilayers: Monte Carlo simulation approach using a two-state model," *Biophysical Journal*, vol. 81, no. 5, pp. 2425–2441, 2001.
- [40] X. Guan, D. Zhang, T. Jia et al., "Unprecedented strong photoluminescences induced from both aggregation and polymerization of novel nonconjugated  $\beta$ -cyclodextrin dimer," *Industrial & Engineering Chemistry Research*, vol. 56, no. 14, pp. 3913–3919, 2017.
- [41] H.-X. Xu, Y. Tan, D. Wang et al., "Autofluorescence of hydrogels without a fluorophore," *Soft Matter*, vol. 15, no. 17, pp. 3588–3594, 2019.
- [42] S. Wei, W. Lu, X. Le et al., "Bioinspired synergistic fluorescence-color-switchable polymeric hydrogel actuators," *Angewandte Chemie International Edition*, vol. 58, no. 45, pp. 16243–16251, 2019.
- [43] Y. Liu, H. Wang, P. Liang, and H. Y. Zhang, "Water-soluble supramolecular fullerene assembly mediated by metal-lobridged $\beta$ -cyclodextrins," *Angewandte Chemie International Edition*, vol. 43, no. 20, pp. 2690–2694, 2004.
- [44] N. Sun, X. Xiao, W. Li, and J. Jiang, "Multistimuli sensitive behavior of novel bodipy-involved pillar 5 arene-based fluorescent 2 rotaxane and its supramolecular gel," *Advanced Science*, vol. 2, no. 9, Article ID 1500082, 2015.
- [45] Q. Ma, M. Zhang, X. Xu et al., "Multiresponsive supramolecular luminescent hydrogels based on a nucleoside/lanthanide complex," *ACS Applied Materials & Interfaces*, vol. 11, no. 50, pp. 47404–47412, 2019.
- [46] Y. Cheng, K. Ren, D. Yang, and J. Wei, "Bilayer-type fluorescence hydrogels with intelligent response serve as temperature/pH driven soft actuators," *Sensors and Actuators B: Chemical*, vol. 255, pp. 3117–3126, 2018.
- [47] Z. Wang, B. Chen, A. S. Susha et al., "All-copper nanocluster based down-conversion white light-emitting devices," *Advanced Science*, vol. 3, no. 11, Article ID 1600182, 2016.
- [48] J. Xue, X. Xu, Y. Zhu, and D. Yang, "Lanthanide based white-light-emitting hydrogel mediated by fluorescein and carbon dots with high quantum yield and multi-stimuli responsiveness," *Journal of Materials Chemistry C*, vol. 8, no. 10, pp. 3380–3385, 2020.
- [49] S. Zhu, S. Tang, J. Zhang, and B. Yang, "Control the size and surface chemistry of graphene for the rising fluorescent materials," *Chemical Communications*, vol. 48, no. 38, pp. 4527–4539, 2012.
- [50] F. Chen, Y. M. Wang, W. Guo, and X. B. Yin, "Color-tunable lanthanide metal-organic framework gels," *Chemical Science*, vol. 10, no. 6, pp. 1644–1650, 2019.
- [51] K. Meng, C. Yao, Q. Ma et al., "A reversibly responsive fluorochromic hydrogel based on lanthanide-mannose complex," *Advanced Science*, vol. 6, no. 10, Article ID 1802112, 2019.
- [52] H. I. Park and S. Y. Park, "Smart fluorescent hydrogel glucose biosensing microdroplets with dual-mode fluorescence quenching and size reduction," *ACS Applied Materials & Interfaces*, vol. 10, no. 36, pp. 30172–30179, 2018.
- [53] K. Ai, B. Zhang, and L. Lu, "Europium-based fluorescence nanoparticle sensor for rapid and ultrasensitive detection of an anthrax biomarker," *Angewandte Chemie International Edition*, vol. 48, no. 2, pp. 304–308, 2009.
- [54] G. Weng, S. Thanneeru, and J. He, "Dynamic coordination of Eu-iminodiacetate to control fluorochromic response of polymer hydrogels to multistimuli," *Advanced Materials*, vol. 30, no. 11, Article ID 1870073, 2018.
- [55] N. Mehresh, X. Dou, Y. Zhao, and C. L. Feng, "Supramolecular fluorescent hydrogelators as bio-imaging probes," *Materials Horizons*, vol. 6, no. 1, pp. 14–44, 2019.
- [56] S. Xu, A. C. Sedgwick, S. A. Elfeky et al., "A boronic acid-based fluorescent hydrogel for monosaccharide detection," *Frontiers of Chemical Science and Engineering*, vol. 14, no. 1, pp. 112–116, 2020.
- [57] H. Niu, X. Li, H. Li et al., "Thermosensitive, fast gelling, photoluminescent, highly flexible, and degradable hydrogels for stem cell delivery," *Acta Biomaterialia*, vol. 83, pp. 96–108, 2019.
- [58] S. H. Park, J. Y. Seo, J. Y. Park et al., "An injectable, click-crosslinked, cytomodulin-modified hyaluronic acid hydrogel for cartilage tissue engineering," *NPG Asia Materials*, vol. 11, 2019.
- [59] Y. Wang, Y. Xue, J. Wang et al., "A composite hydrogel with high mechanical strength, fluorescence, and degradable behavior for bone tissue engineering," *Polymers*, vol. 11, no. 7, Article ID 1112, 2019.
- [60] A. P. Singh, A. Biswas, A. Shukla, and P. Maiti, "Targeted therapy in chronic diseases using nanomaterial-based drug delivery vehicles," *Signal Transduction and Targeted Therapy*, vol. 4, no. 33, 2019.
- [61] J. Li and D. J. Mooney, "Designing hydrogels for controlled drug delivery," *Nature Reviews Materials*, vol. 1, Article ID 16071, 2016.
- [62] S. P. H. Moghaddam, J. Saikia, M. Yazdimamaghani, and H. Ghandehari, "Redox-responsive polysulfide-based biodegradable organosilica nanoparticles for delivery of bioactive agents," *ACS Applied Materials & Interfaces*, vol. 9, no. 25, pp. 21133–21146, 2017.
- [63] Y. Ma, H. Zhou, F. Hu, Z. Pei, Y. Xu, and Q. Shuai, "Multifunctional nanogel engineering with redox-responsive and AIEgen features for the targeted delivery of doxorubicin hydrochloride with enhanced antitumor efficiency and real-time intracellular imaging," *Artificial Cells, Nanomedicine, and Biotechnology*, vol. 46, no. 3, pp. S900–S910, 2018.
- [64] X. Guo, D. Xu, H. Yuan et al., "A novel fluorescent nanocellulosic hydrogel based on carbon dots for efficient adsorption and sensitive sensing in heavy metals," *Journal of Materials Chemistry A*, vol. 7, no. 47, pp. 27081–27088, 2019.
- [65] H. Ehtesabi, S. Roshani, Z. Bagheri, and M. Yaghoobi-Avini, "Carbon dots-sodium alginate hydrogel: a novel tetracycline

- fluorescent sensor and adsorber,” *Journal of Environmental Chemical Engineering*, vol. 7, no. 5, Article ID 103419, 2019.
- [66] Y. Zhang, X. Le, Y. Jian, W. Lu, J. Zhang, and T. Chen, “3D fluorescent hydrogel origami for multistage data security protection,” *Advanced Functional Materials*, vol. 29, no. 46, Article ID 1905514, 2019.
- [67] X. X. Le, W. Lu, J. He, M. J. Serpe, J. W. Zhang, and T. Chen, “Ionoprinting controlled information storage of fluorescent hydrogel for hierarchical and multi-dimensional decryption,” *Science China Materials*, vol. 62, no. 6, pp. 831–839, 2019.
- [68] D. Staneva, I. Grabchev, and P. Bosch, “Fluorescent hydrogel-textile composite material synthesized by photopolymerization,” *International Journal of Polymeric Materials and Polymeric Biomaterials*, vol. 64, no. 16, pp. 838–847, 2015.
- [69] B. Li, Y. Zhang, B. Yan et al., “A self-healing supramolecular hydrogel with temperature-responsive fluorescence based on an AIE luminogen,” *Rsc Advances*, vol. 10, no. 12, pp. 7118–7124, 2020.
- [70] W. Yang, X. Wu, F. Liu, Y. Dou, Z. Hu, and W. Hao, “A fluorescent, self-healing and pH sensitive hydrogel rapidly fabricated from HPAMAM and oxidized alginate with injectability,” *RSC Advances*, vol. 6, no. 41, pp. 34254–34260, 2016.
- [71] C. Qian, R. Wang, M. Li et al., “Facile preparation of self-assembled black phosphorus-based composite LB films as new chemical gas sensors,” *Colloids and Surfaces A: Physicochemical and Engineering Aspects*, vol. 608, Article ID 125616, 2021.
- [72] J. Bai, R. Wang, M. Ju, J. Zhou, L. Zhang, and T. Jiao, “Facile preparation and high performance of wearable strain sensors based on ionically cross-linked composite hydrogels,” *Science China Materials*, 2020.
- [73] M. Cao, Y. Shen, Z. Yan et al., “Extraction-like removal of organic dyes from polluted water by the graphene oxide/PNIPAM composite system,” *Chemical Engineering Journal*, vol. 405, Article ID 126647, 2021.
- [74] L. Ge, M. Zhang, R. Wang et al., “Fabrication of CS/GA/RGO/Pd composite hydrogels for highly efficient catalytic reduction of organic pollutants,” *RSC Advances*, vol. 10, no. 26, pp. 15091–15097, 2020.
- [75] R. Su, H. Wang, Y. Sun, and P. Guo, “Structural regulation of porous MnO<sub>2</sub> nanosheets and their electrocapacitive behavior in aqueous electrolytes,” *Colloids and Surfaces A: Physicochemical and Engineering Aspects*, vol. 609, Article ID 125579, 2021.
- [76] C. Qian, J. Yin, J. Zhao et al., “Facile preparation and highly efficient photodegradation performances of self-assembled artemia eggshell-ZnO nanocomposites for wastewater treatment,” *Colloids and Surfaces A: Physicochemical and Engineering Aspects*, vol. 12, 2020.
- [77] M. Liu, G. Ouyang, D. Niu, and Y. Sang, “Supramolecular gelatons: towards the design of molecular gels,” *Organic Chemistry Frontiers*, vol. 5, no. 19, pp. 2885–2900, 2018.

## Research Article

# Preventive Effect of Albumin Nano tPA Gene Plasmid Ultrasound Microbubble Carrier System on Thrombosis after Cardiac Valve Replacement

Feng Qi,<sup>1</sup> Linlin Zhao,<sup>2</sup> Guohua Cai,<sup>1</sup> Zhendong Sun,<sup>1</sup> and Naishi Wu <sup>1</sup>

<sup>1</sup>Department of Cardiac Surgery, Second Affiliated Hospital of Harbin Medical University, Harbin 150086, China

<sup>2</sup>Department of Cardiac Surgery, Liaoning Provincial People's Hospital, Shenyang 110016, China

Correspondence should be addressed to Naishi Wu; [wsh68@126.com](mailto:wsh68@126.com)

Received 25 July 2020; Revised 6 October 2020; Accepted 5 November 2020; Published 21 November 2020

Academic Editor: Tifeng Jiao

Copyright © 2020 Feng Qi et al. This is an open access article distributed under the Creative Commons Attribution License, which permits unrestricted use, distribution, and reproduction in any medium, provided the original work is properly cited.

After cardiac valve replacement, most patients will have different degrees of thrombosis, different parts of the thrombus, and even more frequent occurrence of postoperative thrombosis; therefore, the prevention of postoperative thrombosis is particularly important. The purpose of this study was to investigate the preventive effect of albumin nano tPA gene plasmid ultrasound microbubble carrier system on thrombosis, especially in cardiac valve. The experimental control method was used. Firstly, 11 dogs meeting the experimental requirements were selected. Secondly, the data of albumin nanoparticles and microbubbles were analyzed. The average size of albumin particles was 132.0 nm, the average size of microbubbles was  $3.1 \pm 1.6 \mu\text{m}$ , and the zeta potential was  $13.70 \pm 1.95 \text{ MV}$ . The concentration of microbubbles was  $4.2 \pm 1.3 \times 10^6/\text{ml}$ . Finally, 11 dogs were divided into two groups. The experimental group was treated with albumin nanoparticles ultrasound microbubble, and the others were the control group. It was found that the levels of tPA and D-dimer in the experimental group were significantly increased and maintained at a high level at 1 week after operation, and the prothrombin time was detected and the international normalized ratio was calculated at the same time. No significant changes were found in the experimental group.

## 1. Introduction

Valvular heart disease is a kind of serious heart disease, which could lead to heart failure, dyspnea, and edema; valve replacement should be carried out in time. Congenital heart valve disease has life-threatening consequences, which requires early valve replacement. In addition, after cardiac valve replacement, hemorheology changes abnormally and produces emboli, which leads to the possibility of cerebral embolism, reaching 50%. Albumin nanoparticles were initially used only as diagnostic reagents. Now, albumin nanoparticles are a relatively mature drug delivery system, and related drugs and diagnostic agents have been put on the market [1, 2]. Albumin nanoparticles can be administered through a variety of ways, such as intravenous injection, intramuscular injection, oral administration, and intra-arterial injection [3, 4]. Tissue-type plasminogen activator

(tPA) is a tissue plasminogen activator that selectively activates plasmin [5, 6]. However, the way in which plasminogen activator gene can be effectively transferred into terminal cells has not been solved. Therefore, whether the plasma tissue-type activator can be effectively expressed for a long time and play a local anticoagulant effect is still a key problem to be solved [7, 8]. Oschatz pointed out in the study that clinical transcatheter heart valve thrombosis is more common than previously thought, which is characterized by imaging abnormalities, gradient increase, and N-terminal pro brain natriuretic peptide level, which mostly occurs after balloon dilated transcatheter aortic valve replacement and valve replacement [9, 10]. To test this idea, he studied 87 patients [11, 12]. Among the 87 patients, 46 (53%) had mitral valve replacement, 27 (31%) had aortic valve replacement, and 14 (16%) had double valve replacement. The research of Oschatz is accidental and its reliability is not high [13, 14]. In

order to explain the influence of element measurement on bubble size distribution, Sauter's average diameter, and volume mass transfer coefficient as performance indicators of pressure dissolved microbubble generator, Dasi studied the influence of swirl chamber, crushing plate, and other elements on the performance of pressurized dissolved microbubble generator [15, 16]. In the process of the experiment, Dasi used a crushing disk and B-type cyclone chamber to improve the efficiency of the pressurized dissolved microbubble generator. At the same time, the experimental results were quantitatively summarized [17, 18]. Dasi's research results show that in terms of influencing bubble size, the crushing disk has the best efficiency, and its contribution rate to D50 and Sauter's average diameter is 27.84% and 45.16%, respectively. In other cases, the influence of swirl chamber on mass transfer coefficient is better than that in other cases [19, 20]. Dasi's research has great reference value, but the economy of its research method needs to be improved [21, 22]. In order to prepare ultrasound microbubbles carrying herpes simplex virus thymidine kinase (HSV-TK) gene and target HepG2 cells, Carlyle observed its targeting ability in vitro and its inhibitory effect on proliferation of HepG2 cells. Carlyle accumulated ultrasound microbubbles carrying HSV-TK on the surface of HepG2 cells and detected proliferating cell nuclear antigen (PCNA) and thiazolyl blue (MTT) [23, 24]. He found that the proliferation ability of targeted microbubbles was significantly decreased, and the apoptosis was significantly increased. The cell invasion test of Carlyle showed that the gene targeted microbubbles group ( $22.18 \pm 2.01$ ) was significantly less than that of the control group and the non-targeted microbubbles group, which had a good inhibitory effect on the proliferation and invasion of HepG2 cells [25]. Therefore, gene targeted microbubbles have a good inhibitory effect on HepG2 cells. Ultrasound targeted microbubble destruction (UTMD) is a noninvasive microRNA delivery method. Carlyle's research method is relatively advanced, but its practicability still needs to be further verified. Based on the analysis of the basic state and characteristics of albumin nanoparticles and ultrasound microbubble system, 11 dogs were selected and divided into two groups. In the experimental group, albumin nanoparticles ultrasound microbubble carrier was used to treat the thrombus after cardiac valve replacement preventive effect.

## 2. Materials and Methods

### 2.1. Relevant Materials

- (1) Eleven healthy domestic dogs weighing 28–36 kg were male. They were divided into control group ( $n = 5$ ) and treated with cardiac valve replacement and nonanticoagulant therapy. In the experimental group, 6 rats underwent cardiac valve replacement and targeted gene therapy.
- (2) The reagents used included plasmid pSec Tag 2B, competent cells *E. coli* JM109, hamster ovary cells, dh5a competent bacteria, RNAiso Plus, PrimeScript,

RT Master Mix (perfect real time), SYBR Premix Ex Taq™ II (TLI RNaseH Plus). HindIII, KpnI, BamHI, and XhoI, and E.Z.N.A. Endo-Free Plasmid Maxi Kit. Human umbilical vein endothelial cell line EA.hy926 Cells. DMEM/F12 basic medium, dipalmitoylphosphatidylcholine (DSPC). Methods: Vent DNA polymerase and T4 DNA ligase, fetal serum, 0.25% Trypsin-EDTA, and Opti-MEM, respectively. Sheep anti-human tPA polyclonal antibody, rabbit anti-sheep polyclonal antibody, and AssayMax human tissue-type plasma activator ELISA kit. Bovine serum albumin (BSA), tPA ELISA kit, and halo-carbon-218 were used.

- (3) The related instruments include rotary evaporator, rotary evaporator, vacuum drying oven, one hundred thousandth electronic balance, ultrasonic cleaner, ultrasonic gene transfection system, laser particle size detection, and zeta potential analyzer, probe diameter  $0.8 \text{ cm}^2$ , probe area, probe frequency 3 MHz, energy range 0–6 w/cm, built-in working cycle pulse setting and digital timer, optical microscope, ultrasonic vibrometer, CO<sub>2</sub> incubator, ultra clean table, precision pH meter, fluorescence microscope, desktop high-speed low-temperature centrifuge, circulating water vacuum pump, and multifunctional enzyme marker.

## 3. Methods

After operation, a thromboembolism model was established in dogs to replace heart valves and plasma activator gene (TPA) encapsulated in nanoparticles. Albumin nanoparticles were prepared and transported by albumin ultrasound microbubble channel. The effects of albumin nanoparticles on thrombosis and local vascular smooth muscle cell proliferation were observed. The plasmids with high expression of tPA gene were prepared, and plasma nanoparticles carrying tPA were prepared from albumin. Albumin was used to prepare glycosidic acid ultrasound microbubble channel and combined with tPA-loaded plasma nanoparticles to form targeted diagnostic ultrasound microbubble vector. After mechanical tricuspid valve replacement in dogs, targeted ultrasound diagnosis was performed to observe the preventive effect of postoperative thrombosis. The expression of tPA antigen in heart tissue was detected by immunohistochemistry, and the content of tPA and D-dimer in blood was detected by ELISA. At the end of the experiment, local thrombosis was observed in each group. It should be noted that the heart valve should be taken as the center, about 1 cm of coronary artery and vein bridge should be taken, and the heart valve tissue from the anterior wall of the heart should be taken for routine, immunohistochemistry, and in situ hybridization. Immunohistochemistry was used to detect the expression of tPA in myocardium. The first antibody was sheep anti-human tPA polyclonal antibody (dilution 1/100). The expression of proliferating cell nuclear antigen (PCNA) was detected by LSAB method. Anti-PCNA mouse monoclonal antibody (diluted 1/400) was performed according to the kit. Human

lung cancer was positive for PCNA and PBS was used as negative control instead of antibody. A PDGF-B mRNA oligonucleotide detector was designed. The sequence was position 91 5-gat CGC ACC AAT GCC AAC ttctg GTG TGG CCG CCC TGC GTG gag GTG cag-3141. The effectiveness and specificity of digoxin were detected by dot blot hybridization. The concentration of digoxin (1.5 ng/UL) was determined. The expression of PDGF-B mRNA was detected by conventional in situ hybridization. Then, the internal thickness and area of coronary artery were measured by pathological image analyzer, and the ratio of corneal thickness was calculated accurately. The formula was as follows: lumen stenosis rate = (1 - existing lumen area/area below the elastic membrane) × 100%. The number of PCNA positive cells in 200 coronary artery cells was measured as the number of in situ hybridization positive cells. After statistical calculation, the internal area is  $0.25 \text{ cm}^2 \times 4$  (i.e.,  $1 \text{ cm}^2$ ), which is lower than the high-power field (×400) of the microscope.

**3.1. Construction and Expression of Gene Plasmid.** In this experiment, three pairs of primers were designed according to three EST sequences and tPA gene sequences to amplify the three fragments of tPA from three EST cloning plasmids. Three EST clones were cultured on LB containing ampicillin and chloramphenicol. Three EST clone plasmids were extracted and three tPA amplified fragments were used as PCR vectors. The enhancement products were recovered and identified in sequence analysis. HindIII and XhoI, HindIII and KpnI, KpnI and BamHI, and BamHI and XhoI were digested by pSec Tag 2B and three tPA—tPA-1, tPA-2, and tPA-3, respectively. The products were cleaned with Qiagen PCR product purification kit. Meanwhile, T4 DNA ligase was used. The decontamination products were transformed into *E. coli* JM109 cells by 14°C overnight. The resistant colonies were screened from LB tablets containing ampicillin. The recombinant plasmids were detected by PCR, and the recombinant plasmids were extracted and identified. The recombinant plasmid was transfected into CHO cells by calcium phosphate coprecipitation method. The expression of tPA was detected by indirect immunofluorescence.

The primers for tPA gene and three EST sequences are as follows: t-PA-1F: 5'-CCCaagcttATGGATGCAATGAAGA-GAGGG-3', t-PA-1R: 5'-GGggtaccACGGTAGGCT-GACCCATTC-3', t-PA-2F: 5'-GGggtaccCACAGCCTCACCGAGTCG-3', t-PA-2R: 5'-CGggtaccAGCAG-GAGCTGATGAGTATGCC-3', t-PA-3F: 5'-CGggtaccTCTCTGCCGCCACTGCT'-3', t-PA-3R: 5'-CCctcgagGCGGTCGCATGTTGTCAC-3'.

The primer sequence of the primer sequence is t-PA-1F: 5'-CCC aag ctt ATG GAT GCA ATG AAG AGA GGG-3', t-PA-1R: 5'- GGg gta ccA CGG TAG GCT GACCCA TTC-3', t-PA-2F: 5'-GGg gta ccC ACA GCCTCA CCG AGT CG-3', t-PA-2R: 5'-CGg gat ccAGCA GGA GCT GAT GAG TAT GCC-3', t-PA-3F: 5'-CGg gat ccT CTC TGC CGC CCA CTG CT'-3', t-PA-3R: 5'-CCc tcg agG CGG TCG CAT GTT GTCAC-3'. The lowercase sequences were HindIII, KpnI, BamHI, and XhoI.

Three fragments were amplified and sequenced. The plasmid pSec Tag 2B and three fragments t-pa-t, PA-2, and t-pa-3 were digested and purified with hind3 and xho3, hind3 and kpn854444, kpn3 and bamh2, and bamh3 and xho854444. T4dna lithium was extracted overnight under 14°C ligase. The ligation products were transformed into *E. coli* JM109 cells, and anti-ampicillin colonies were collected, and recombinant plasma was extracted and cultured for identification. The recombinant plasmid was transfected into plasma of Chinese hamster ovary cells by calcium phosphate coprecipitation method. The expression of tPA antigen was detected by immunofluorescence.

**3.2. Preparation of Ultrasound Microbubbles.** First, a sterile 10 ml bovine serum albumin liquid (5% (g/M)) was prepared, in which 10% sucrose was prepared and placed in a 50 ml covered plastic centrifuge tube. Oxygen and charcoal gas were used to corrode the liquid (flow rate: 6 ml/min), about 10 min, ultrasonic treatment was carried out for 1 minute in turn (condition: 180 W, stable frequency: 20 kHz), and the prepared micropores were stored at 4°C for future use. The morphology, size, and number of microvessels were observed under microscope. The size and surface zeta potential of the microvessels were measured by Zetasizer 3000 analyzer.

Secondly, on the one hand, the albumin nanoparticles (containing 1 mg plasmid) were added into 5 ml albumin microbubbles and 10 ml of 50% glutaraldehyde solution and then incubated at 4°C for 2 hours for interconnection (the final concentration of glutaraldehyde solution was 0.1%). On the other hand, during the preparation of nanoparticles, the supernatant was collected after centrifugation, and the amount of plasmid remaining in the nanoparticles was detected. The encapsulation ratio shall be calculated according to the ratio of total amount to balance. The amount of plasmids carrying albumin nanoparticles ultrasound microbubble complex was calculated.

With normal serum, centrifugation, stratification, centrifugation speed of 200 r/min, for 1 minute, suspension foam was obtained to obtain nano microbubbles containing targeted ultrasound contrast factor (carrier) gene  $0.88 \times 10^9 \sim 1.8 \times 10^9$ /ml microbubbles were found in 10 ml targeted contrast medium, and the gene plasmid content was 2 mg. It is then stored at 4 degrees Celsius for later use.

Finally, Zetasizer 3000 was fully used to determine the size and zeta potential of albumin nanoparticles. Albumin nanoparticles need gel retardation test and encapsulation efficiency test. The prepared albumin nanoparticles (containing 2 mg plasmid) were added into 10 ml albumin microbubbles, added 50% glutaraldehyde solution 10 ml, and incubated for 2 h at 4 degrees Celsius. After cross-linking, centrifugation (rotating speed 200 r/min, 1 minute), suspension foam was obtained, and then the carrier was obtained. The microbubble concentration was adjusted to  $(0.8-1.8) \times 10^9$  cells/ml.

**3.3. Targeted Ultrasound Therapy of TPA Gene-Loaded Albumin Nanobubbles.** The distribution of albumin nanoparticles in vivo mainly depends on its size and surface

properties. Nanoparticles have a solid particle skeleton. Only nanoparticles with a diameter less than 100 nm can pass through the hepatic sinusoidal endothelial cell window and accumulate in the liver without entering the human body. Nanoparticles modified with hydrophilic groups in the range of 100–200 nm can avoid phagocytosis of reticuloendothelial system and become a long circulating system. To obtain colloidal system with good physical and chemical properties is a prerequisite for the use of protein nanoparticles as drug carriers and surfactants. Therefore, the preparation process has an important impact on the in vivo activity and targeting of albumin nanoparticles after intravenous injection. After tricuspid valve replacement in the experimental group, the heart rate of chest wall surface was detected by two-dimensional ultrasound. *Imaging.* After intravenous injection of 10 ml albumin nanovesicles containing tPA gene, cardiac imaging was significantly improved. The chest wall was directly connected to the right ventricular tube of the anterior wall of the heart for 30 minutes. The chest wall was examined by two-dimensional ultrasound to observe the description of the heart. The ultrasonic frequency was 1 MHz and the intensity was 1.5 w/cm<sup>2</sup>. In the control group, the tricuspid valves were replaced by conventional cardiopulmonary bypass (CPB), and then they were intravenously injected with 10 ml normal saline and irradiated with ultrasound (as before). Intravenous injection of tPA 10 ml gene (containing tPA 2 mg) of nano albumin microvascular can significantly improve the development of related organs. Postoperative antibiotics were used to prevent traumatic infection. There was no anticoagulant therapy in each group. Before and after the operation (four weeks), the content of D-dimer and tPA were detected by ELISA. A dephosphorylase is used to remove the phosphorus group at the fifth end of DNA. Dephosphorylation of 5-limb vectors can reduce the occurrence of self-cyclization of vectors, thus reducing the production of false positive clones.

In order to improve the therapeutic potential of UTMD, microbubble gene vectors should have sufficient capacity to concentrate DNA and/or specific cell or tissue selectivity. Therefore, after 70–80% digestion of EA.Y926 cells the day before the experiment, 5000 wells were divided into 96 vertical plates and cultured overnight at 70–80% fusion rate. Albumin nanoparticles with plasmid content of 0.05 UG, 0.1 mg, 1 mg, and 10 UG were added into each axis, which was composed of 0.5 UG/ml plasmid, 1 UG/ml, 10 UG/ml, and 100 UG/ml, and added into the conventional culture medium, and incubated at room temperature for 20 hours. Then, add 10 u1CCK-8 solution to each well. The plates were incubated in incubator for 4 hours. The absorbance at 450 nm was determined by enzyme-linked immunosorbent assay, and the number of units was calculated according to the standard curve.

#### 4. Results and Discussion

On the one hand, with the development of molecular biology, tissue-type plasminogen activator (tPA) has been used as a target for gene therapy in thrombosis-related diseases, so as to achieve the purpose of anticoagulation. This not only

avoids the systemic bleeding complications caused by drug thrombolysis, but also plays a role in the local long term to prevent thrombosis. Intravenous tissue plasminogen activator (tPA) was first introduced as a safe and effective thrombolytic agent, and then new thrombolytic agents, anticoagulants, and antiplatelet drugs were introduced. These drugs were considered as potential safety drugs with more favorable interactions. In addition to chemical thrombolysis, other techniques, including transcranial ultrasound thrombolysis and microbubble cavitation, have been introduced.

##### 4.1. Analysis of Albumin Nanoparticles and Microbubbles.

The average diameter of nanoparticles is 132.0 nm and the average surface area of zeta is +31.88~+40.03 mv. The average entrapment efficiency was 73.97%. Gel retardation analysis and DNase I protection experiments showed that nanoparticles had protective effect on DNA plasma. The ultrasonic microsphere was round and vesicular, with uniform size and good dispersion, and the diameter was 2–5 μm. The albumin microbubbles containing 10% sucrose were stored at 4°C for 30 days with the same morphology and good thermal stability (40°C for 30 minutes). After interaction with albumin nanoparticles, the above properties did not change significantly. The particle size and zeta potential are shown in Table 1.

Under the microscope, the cationic microbubble suspension was observed. The microbubbles were spherical in shape, and the size distribution was uneven. There was no obvious fusion and rupture. It is not difficult to see from Table 1 that the average size of microbubbles is  $3.1 \pm 1.6 \mu\text{m}$  and zeta potential is  $13.70 \pm 1.95 \text{ MV}$ . The microbubble concentration was  $(4.2 \pm 1.3) \times 10/\text{ml}$ . The particle size was  $218.1 \pm 1.1 \text{ nm}$  and zeta potential was  $-15.30 \pm 0.91 \text{ MV}$ . The average size of nanoparticles ultrasound microbubble complex was  $4.5 \pm 1.8 \mu\text{m}$ . The zeta potential was  $2.79 \pm 1.40 \text{ MV}$ . The concentration was  $(3.0 \pm 1.3) \times 10/\text{ml}$ .

The results of particle size, morphology, and entrapment efficiency of tPA-loaded albumin nanoparticles are shown in Figure 1.

According to Figure 1 and SEM results, albumin nanoparticles are spherical, uniform in size, and well dispersed. The particle size analysis of Zetasizer 3000 showed that the average particle size was 132.0 nm, the maximum particle size was 153.1 nm, and the minimum particle size was 48.9 nm. The average multiple scattering index is 0.34. The average surface area of zeta was  $31.32 \pm 41.42 \text{ MV}$ . The blocking rate of the sample was detected by UV spectrophotometer, and the total DNA content of plasmid was determined. The results showed that the average absorption efficiency was 73.58%, which met the experimental requirements.

##### 4.2. Survival Rate of Albumin Nanoparticle Ultrasound Microbubble Complex.

In vitro and in vivo ultrasound imaging experiments show that complex of albumin nanoparticle microbubbles has a significant impact on ultrasound imaging, indicating that the microbubbles still

TABLE 1: Particle size and zeta potential.

	Particle size	Zeta potential
Plasmid albumin nanoparticles	$218.1 \pm 1.1$ nm	$-15.30 \pm 0.91$ mV
Cationic microbubbles	$3.1 \pm 1.6$ nm	$13.70 \pm 1.95$ mV
Albumin nanoparticles ultrasound microbubble complex	$4.5 \pm 1.8$ nm	$2.7 \pm 1.40$ mV

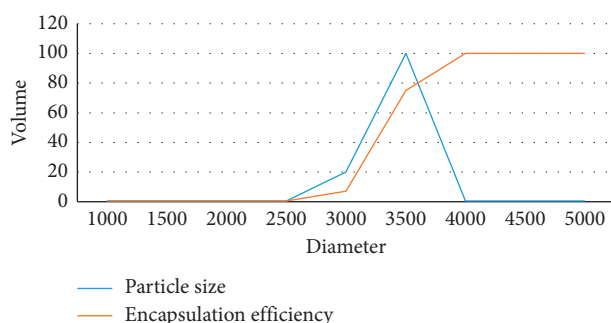


FIGURE 1: Analysis of particle size of Zetasizer 3000 instrument.

have good acoustic performance even after inhalation of nanoparticles. We treated the complex of albumin nanoparticle ultrasound microbubbles with endothelial cells EA.hy926. Albumin nanoparticles were detected in the acute toxic cells of ultrasound microbubble complex for 20 hours. The cell survival rate of albumin nanoparticles ultrasound microbubble complex is shown in Figure 2.

According to the data in Figure 2, for most concentration groups, there was no obvious cytotoxicity effect; only slight decrease of cell activity was observed in the highest concentration group, and the average cell activity was between 80%–120% compared with the control group.

**4.3. Comparison of tPA Content before and after Operation.** Thrombolysis or microthrombosis in situ may be the cause of poor clinical improvement after recanalization in acute ischemic stroke. Therefore, the thickness and area of heart valve are one of the important factors. The comparison of intimal thickness and area between the 5 normal dogs in the control group who underwent cardiac valve replacement and nonanticoagulant therapy alone and the 6 dogs in the control group receiving targeted gene transfer therapy at the same time with cardiac valve replacement is shown in Figure 3.

It can be seen from Figure 3 that the average thickness of the heart valve in the control group is 67.22 nm, and the average thickness of the six ordinary dogs in the experimental group is 17.14 nm. In the comparison of area size, the average thickness of the control group is 24.95 mm, and the

data of the experimental group is 21.13 mm. The detection results of blood D-dimer and tPA before and 4 weeks after targeted gene transfer in experimental group and control group are shown in Table 2.

It can be seen from Table 2 that the D-dimer and tPA content of the control group before operation were  $78.36 \pm 6.12$  and  $0.19 \pm 0.08$ , respectively, and the two values after operation were  $80.50 \pm 3.35$  and  $0.18 \pm 0.03$ , respectively. At the same time, the levels of D-dimer and tPA were  $79.22 \pm 4.56$ ,  $0.17 \pm 0.05$ ,  $856.78 \pm 100.20$ , and  $0.67 \pm 0.11$  in the control group before and after the operation. The two indexes of fibrinolytic activity in the experimental group were significantly higher than those before the gene transfer, the control group before and after the operation. There was no significant difference in the ratio. The changes of tPA and D-dimer in venous blood of experimental group at different periods after operation are shown in Figure 4.

It can be seen from Figure 4 that the average value of tPA in the experimental group before operation is 0.19, and it changes to 0.50 one week after operation. At this time, D-dimer also changes from 89.56 to 835.28. In the following weeks, the content of tPA increased steadily until the eighth week, and then slightly decreased to 0.79 at the 12th week after operation, but the tPA content was still very high, and the change trend of D-dimer was roughly the same as that of tPA. In the experimental group, the two indexes were significantly increased and maintained at a high level 1 week after operation until the end of the experimental observation at 12 weeks after operation. Prothrombin time was detected and the international normalized ratio was calculated, and no significant change was found.

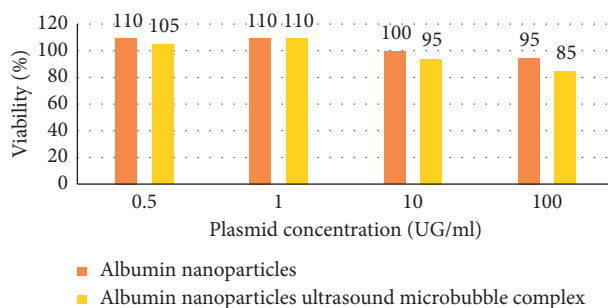


FIGURE 2: Cell viability of nanoparticles and nanoparticle ultrasound microbubble complexes.

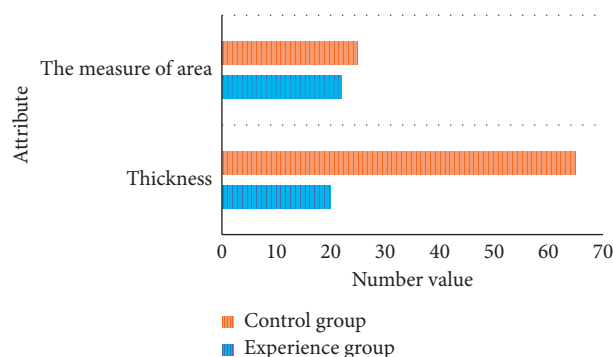


FIGURE 3: Results of cardiac valve morphology measurement in each group.

TABLE 2: D-dimer before and 4 weeks after targeted tPA gene transfer and tPA content ( $\mu\text{g/L}$ ,  $X \pm s$ ).

Grouping		D-dimer	TPA content
Control group	Preoperative	$78.36 \pm 6.12$	$0.19 \pm 0.08$
	After operation	$80.50 \pm 3.35$	$0.18 \pm 0.03$
Experience group	Preoperative	$79.22 \pm 4.56$	$0.17 \pm 0.05$
	After operation	$856.78 \pm 100.20$	$0.67 \pm 0.11$

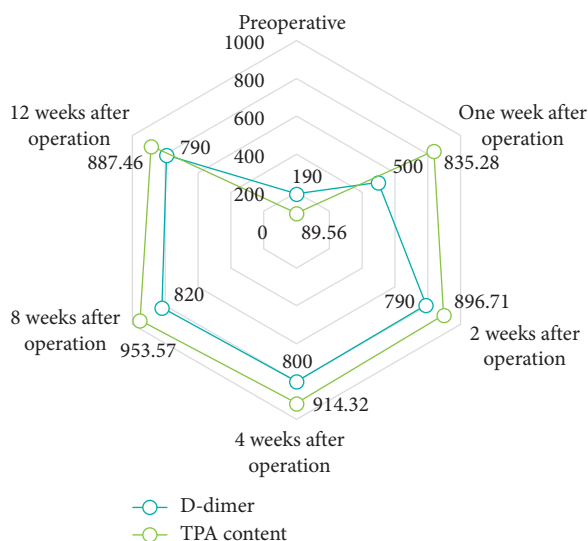


FIGURE 4: Changes of tPA and D-dimer in venous blood after valve replacement in control group ( $x \pm s$ ,  $\mu\text{g/ml}$ ).

## 5. Conclusions

Most methods of gene transfer into human body are to inject the target gene into target tissue directly. For cardiovascular diseases, direct injection of myocardial or plasmid DNA or adenovector into cardiac catheters is carried out. In view of the application of ultrasound contrast agent, microbubbles have been confirmed to have the function of directional delivery while enhancing ultrasound imaging by using microbubbles. It can target gene or drug delivery to achieve the purpose of treatment of diseases and can create a safe and effective drug ultrasound-mediated targeted delivery system. At present, there are many studies on albumin as liquid membrane microbubbles, which are nontoxic and easy to prepare. The disadvantage is its poor stability. In this experiment, 10% sucrose was selected as glycoprotein, which not only avoided the above conditions, but also had good microbubble stability. Because the inert gas fluorocarbon is the most commonly used gas in the preparation of ultrasound microbubbles, in this experiment, we used the physical inhalation (one-step method) to prepare albumin nanoparticles loaded with tPA gene. The particle size was about 132.0 nm, the particle size was relatively uniform, the dispersion was good, and the entrapment efficiency was 73.58%. Gel electrophoresis analysis showed that it had a good protective effect on DNA enzyme. The slight damage of ultrasound on microbubbles may be reversible damage and permeability of target cell membrane caused by ultrasound or mechanical factors, resulting in the rupture of microbubbles with diameter of 7 mm and the expansion of endothelial cell space. The target gene reaches tissue cells

through the gap between microbubble rupture and endothelial cells. In this study, tPA gene expression plasmid was constructed, and the appropriate vector was selected to transfer tPA into the body cells to obtain effective and sustained tPA production, so as to achieve the purpose of long-term anticoagulation and prevention of thrombosis. Using three EST cloning plasmids as matrix, three tPA fragments were amplified and cloned into pSec Tag 2B plasmid to prepare recombinant pSec Tag 2B tPA. In the experimental group, although the normal endothelial cells attached to the surface of the biological valve, the degree of valve leaf degeneration has been slowed down, but the incidence of valve thrombosis is still high due to the incomplete and partial shedding of endothelium and no anticoagulant treatment after operation. The results showed that the targeted release and gene expression of albumin nanoparticles loaded with gene plasmids could be enhanced by ultrasound destruction of microbubbles. This method is a simple and effective new technology for targeted gene transfer. With the development of molecular biology and ultrasound medicine technology, it will provide a new way to study the prevention of human diseases.

### Data Availability

The data used to support the findings of this study are included within the article.

### Disclosure

Feng Qi and Linlin Zhao are considered as the co-first authors.

### Conflicts of Interest

The authors declare no conflicts of interest regarding the publication of this paper.

### Authors' Contributions

Feng Qi and Linlin Zhao contributed equally to this work.

### References

- [1] S. C. Hofferberth, M. Y. Saeed, L. Tomholt et al., "A geometrically adaptable heart valve replacement," *Science Translational Medicine*, vol. 12, no. 531, 2020.
- [2] J. Jose, D. S. Sulimov, M. El-Mawardy et al., "Clinical bio-prosthetic heart valve thrombosis after transcatheter aortic valve replacement," *JACC: Cardiovascular Interventions*, vol. 10, no. 7, pp. 686–697, 2017.
- [3] D. Wojciechowska, A. R. Liberski, P. Wilczek et al., "The optimal shape of an aortic heart valve replacement-on the road to the consensus," *Qscience Connect*, vol. 2017, no. 3, p. 1, 2017.
- [4] H. Togun, M. Ahmed, L. Rabee, and F. Adel, "Evaluation study of heart valve replacement for patients aged from 10 to 80 years at Al-nasiriyah heart center/Iraq," *Journal of Engineering and Applied Sciences*, vol. 14, no. 4, pp. 1339–1348, 2019.
- [5] O. Seddon, R. Ashrafi, J. Duggan et al., "Seroprevalence of Q fever in patients undergoing heart valve replacement surgery," *The Journal of Heart Valve Disease*, vol. 25, no. 3, pp. 375–379, 2016.
- [6] A. Araújo-Filho, M. Cerqueira-Neto, L. Cacao, G. Oliveira, T. Cerqueira, and V. Santana-Filho, "Effect of prophylactic non-invasive mechanical ventilation on functional capacity after heart valve replacement: a clinical trial," *Clinics*, vol. 72, no. 10, pp. 618–623, 2017.
- [7] D.-J. Kim, H.-S. Kim, M. K. Oh, E.-Y. Kim, and J.-G. Shin, "Cost-effectiveness of genotype-guided warfarin dosing in the patients with mechanical heart valve replacement under fee-for-service system," *Clinical Therapeutics*, vol. 39, no. 8, p. e9, 2017.
- [8] E. T. Mehmet and D. Mehmet, "The effectiveness of heart valve replacement surgery in a non-referral regional hospital: the analysis of outcomes after isolated and complex valve replacement," *The Heart Surgery Forum*, vol. 22, no. 5, pp. E343–E351, 2019.
- [9] S. Oschatz, S. Kohse, V. Senz, T. Eickner, K.-P. Schmitz, and N. Grabow, "Accelerated in vitro-calcification of potential urethane based heart valve replacement materials," *Current Directions in Biomedical Engineering*, vol. 4, no. 1, pp. 221–224, 2018.
- [10] S. Ghazanfari, A. Driessen-Mol, S. P. Hoerstrup, F. P. T. Baaijens, and C. V. C. Bouten, "Collagen matrix remodeling in stented pulmonary arteries after transapical heart valve replacement," *Cells Tissues Organs*, vol. 201, no. 3, p. 159, 2016.
- [11] X. L. Yang, D. Wang, G. Y. Zhang et al., "Comparison of the myocardial protective effect of sevoflurane versus propofol in patients undergoing heart valve replacement surgery with cardiopulmonary bypass," *BMC Anesthesiology*, vol. 17, no. 1, p. 37, 2017.
- [12] Y. Lu, J. Wang, R. Huang et al., "Microbubble-mediated sonothrombolysis improves outcome after thrombotic microembolism-induced acute ischemic stroke," *Stroke*, vol. 47, no. 5, pp. 1344–1353, 2016.
- [13] N. Ding, "Sleep apnea increase the perioperative risks of heart valve replacement surgery," *Chest*, vol. 149, no. 4, p. A575, 2016.
- [14] L. P. Dasi, J. Grande-Allen, K. Kunzelman, and E. Kuhl, "The pursuit of engineering the ideal heart valve replacement or repair: a special issue of the annals of biomedical engineering," *Annals of Biomedical Engineering*, vol. 45, no. 2, pp. 307–309, 2017.
- [15] W. Xiaowei, G. Yannik, P. Jathushan et al., "Thrombus-targeted theranostic microbubbles: a new technology towards concurrent rapid ultrasound diagnosis and bleeding-free fibrinolytic treatment of thrombosis," *Theranostics*, vol. 6, no. 5, pp. 726–738, 2016.
- [16] B. Mead, N. Kim, K. Negron et al., "Intersections of neuro-modulation, focused ultrasound, and gene delivery with brain-penetrating nanoparticles," *The Journal of the Acoustical Society of America*, vol. 142, no. 4, p. 2669, 2017.
- [17] J. A. Kopechek, A. R. Carson, C. F. Mctiernan et al., "Cardiac gene expression knockdown using small inhibitory RNA-loaded microbubbles and ultrasound," *PLoS One*, vol. 11, no. 7, Article ID e0159751, 2016.
- [18] A. Goyal, F. Yu, M. G. Tenwalde, X. Chen, F. Villanueva, and J. Pacella, "Low dose TPA improves reperfusion efficacy of microvascular obstruction using ultrasound with microbubbles," *Journal of the American College of Cardiology*, vol. 67, no. 13, p. 160, 2016.

- [19] H. Asadi, D. Williams, and J. Thornton, "Changing management of acute ischaemic stroke: the new treatments and emerging role of endovascular therapy," *Current Treatment Options in Neurology*, vol. 18, no. 5, pp. 1–19, 2016.
- [20] L. Carlyle, D. D. Wang, A. Taylor et al., "NO two systoles the same: personalizing transcatheter heart valve selection for transcatheter aortic valve replacement," *Journal of the American College of Cardiology*, vol. 67, no. 13, p. 327, 2016.
- [21] Y. Ji, Z. Han, L. Shao, and Y. Zhao, "Evaluation of in vivo antitumor effects of low-frequency ultrasound-mediated miRNA-133a microbubble delivery in breast cancer," *Cancer Medicine*, vol. 5, no. 9, pp. 2534–2543, 2016.
- [22] W. Gao, L. Qiao, Y. Gao et al., "Effect of microbubble-enhanced ultrasound on percutaneous ethanol ablation of rat walker-256 tumour," *European Radiology*, vol. 26, no. 9, pp. 3017–3025, 2016.
- [23] J. Wang, P. Li, R. Tian et al., "A novel microbubble capable of ultrasound-triggered release of drug-loaded nanoparticles," *Journal of Biomedical Nanotechnology*, vol. 12, no. 3, pp. 516–524, 2016.
- [24] Y. Wang, X. Li, L. Liu, B. Liu, F. Wang, and C. Chen, "Tissue targeting and ultrasound-targeted microbubble destruction delivery of plasmid DNA and transfection in vitro," *Cellular and Molecular Bioengineering*, vol. 13, no. 1, pp. 99–112, 2020.
- [25] B. Chertok, R. Langer, and D. G. Anderson, "Spatial control of gene expression by nanocarriers using heparin masking and ultrasound-targeted microbubble destruction," *ACS Nano*, vol. 10, no. 8, p. 7267, 2016.

## Research Article

# Tennis Rehabilitation Training-Assisted Paclitaxel Nanoparticles in Treatment of Lung Tumor

Di Hu <sup>1</sup> and YiMin Yang<sup>2</sup>

<sup>1</sup>School of Sports Institute, Wuhan Business University, Wuhan 430056, Hubei, China

<sup>2</sup>School of International Tennis Academy, Wuhan Sports University, Wuhan 430079, Hubei, China

Correspondence should be addressed to Di Hu; [ddpp916@163.com](mailto:ddpp916@163.com)

Received 18 September 2020; Revised 23 October 2020; Accepted 26 October 2020; Published 20 November 2020

Academic Editor: Tifeng Jiao

Copyright © 2020 Di Hu and YiMin Yang. This is an open access article distributed under the Creative Commons Attribution License, which permits unrestricted use, distribution, and reproduction in any medium, provided the original work is properly cited.

Paclitaxel nanoparticles are a compound with unique anticancer effects. Its mechanism of action is to prevent tumor rupture by stabilizing tumor proteins, while preventing cell division, leading to cell death, thereby inhibiting the spread of lung tumors. This article aims to study the treatment of lung tumors with paclitaxel nanoparticles assisted by tennis rehabilitation training. In this paper, paclitaxel nanoparticles were prepared by a solvent displacement method, and their particle size and morphology were measured. The TA2 series of experimental rats were selected to establish animal lung tumor models, and they were randomly divided into 5 groups: local injection of saline, porphyrin, and low-, medium-, and high-dose paclitaxel nanoparticles for treatment. The experimental results in this paper show that the average particle size of the paclitaxel nanoparticles prepared in the experiment is about 153,54 nm. Each treatment group inhibited tumor development to varying degrees. Among them, the inhibitory volume rate of paclitaxel nanoparticles in the middle- and high-dose groups was significantly higher than that in the paclitaxel treatment group, indicating that paclitaxel nanoparticles can release drugs slowly.

## 1. Introduction

From the 1970s to the 1980s, Granqvist, Buhrman, and others first proposed the term nanoparticle in the United States and conducted in-depth theoretical research. The term “nanoparticle” is closely related to modern science. But it has a long history in real life. In nanoscience, a particle is defined as an independent unit that can describe the properties of matter. There are many studies on nanoparticles in the scientific community today. This is because nanoparticles have many possible applications in the fields of medicine, physics, optics, and electronics. Many countries and institutions, including my country and the National Institute of Nanotechnology in the United States, have provided a lot of government funds to concentrate on studying different types of nanoparticles through experiments, theories, and computer simulations.

Tumors in society are now one of the main factors affecting human health. As the main application of nanoparticles as a drug container, it is very important for people

to fully understand the interaction between nanoparticles and biofilms. In the past ten years, due to the wide application of nanoparticles in drug delivery, therapy, and bio-imaging, their interaction with cell membranes has attracted more and more attention, but their safety issues have also attracted much attention. Understanding the basic principles of the interaction between nanoparticles and cell membranes is important for improving the evaluation of nanoparticles and their potential toxicity.

Noveletto et al.'s new methods of sports rehabilitation include serious games because they include (in a motivating way) the three basic elements of rehabilitation: reinforcement, repetition, and task-oriented training. His research aims to evaluate the therapeutic effects of biomedical SG and scoring system for lower limb exercise rehabilitation of patients with hemiplegic stroke. He was inspired by the classic video game Pong, whose goal is to not only to control a tennis racket but also to use muscle power. However, there are too many uncontrollable factors in tennis rackets, which

will make muscle training not so smooth [1]. The purpose of this study by Yu et al. is to explore the synergistic antitumor effect and mechanism of paclitaxel nanoparticles (PTX-NPs) combined with radiotherapy (RT) on human cervical cancer. Using methoxy poly(ethylene glycol)-poly to prepare PTX-NP by solid-phase dispersion method and combining with RT can effectively treat cervical cancer. The *in vivo* antitumor activity of PTX-NP combined with RT was evaluated using nude mice carrying Hela cell xenograft tumors. The results were evaluated using microfluorine 18-deoxyglucose PET/computed tomography and immunohistochemistry. However, due to the unstable factors of mixed chemicals, the result data will be inaccurate [2]. Rozario et al. have developed a novel method to track lung tumor movement during radiotherapy in real time. The goal is to gradually increase the target radiation dose while reducing the dose to sensitive structures, thereby increasing local control without increasing toxicity. This method uses the analog and digital reconstructed radiographs as a reference to analyze the megavolt image of the eye diagram of the beam for radiotherapy treatment, but the technology of tracking motion is too complicated and not so easy to implement [3].

The innovation of this article lies in the application of nanotechnology in photodynamic tumor therapy, which can improve the stability of photosensitizers, volume targeting, the depth of action of photodynamic therapy, and simple oxygen production in various ways. Based on nanoparticles, photodynamic therapy can also be combined with other therapies. The application of nanotechnology to photodynamic therapy can improve the effect of tumor treatment, reduce adverse effects, and expand the scope. This is a new technology with great development potential.

## 2. Tennis Rehabilitation Training-Assisted Nanoparticle Method

**2.1. Liquid Chromatography.** The absorption efficiency of paclitaxel nanoparticles was determined by high-performance liquid chromatography. Accurately weigh about 2 mg of nanoparticles, dissolve them in 5 mL of acetonitrile, add distilled water to make the volume 10 mL, stir, and filter thoroughly. As a sample solution, the point external standard method was used for the determination, and the external standard was paclitaxel. The HPLC experimental conditions were C18 column reversed phase; mobile phase was acetonitrile-water (volume ratio 40:40); flow rate was 1.2 mL/min; and detection wavelength was 234 nm [4].

### 2.2. Nanoparticle Preparation Method

**2.2.1. Solvent Replacement Method.** The displacement of the thermodynamically stable dispersion system formed by the miscible liquid is called the solvent displacement method and is used for the manufacturing magnetic nanoparticles. By changing the ratio of alcohol, oil, and water in the reaction system, the morphology and particle diameter of the reaction system can be changed. In the reaction system, hydrophilic groups and hydrophobic groups can not only

dissolve and disperse nanoparticles but also prevent the accumulation of nanoparticles. This paper studies the ultrathin silica particles produced by the hydrolysis of tetraethyltetracycline by the microcoating method and shows that the dependent particle size of the compound is determined by the linear water-oxygen ratio and the concentration of ammonium hydroxide. The nanoparticles prepared by the microalgae method have good morphology and small particle size [5]. However, due to the complexity of the reaction system, the introduction of organic solvents, the control of the reaction time, etc., the processing after the experiment becomes complicated.

**2.2.2. Hydrothermal Synthesis Method.** The hydrothermal method is a synthetic method that uses substances in an aqueous solution to undergo chemical reactions under high temperature and pressure. It has developed rapidly, among which American researchers used hydrothermal synthesis to make the crystal framework, which laid a good foundation for the rapid development of hydrothermal synthesis [6]. The other one used water, ethyl orthosilicate, triethanolamine, and tetraethylammonium hydroxide as raw materials and synthesized a new type of intermediate silicate hydrothermal composition in a certain proportion and method. It is mainly used in catalytic reactions.

The heat of solution method makes up for some of the shortcomings of the hydrothermal method. Its production principle is similar to that of the hydrothermal method. It changes the water solvent into a solvent. For example, the hydrothermal method is not suitable for easily hydrolyzed compounds, which also expands the field of material production [7].

**2.2.3. Precipitation Method.** The method of depositing inorganic substances on the nanocore particles and forming a shell layer on the surface of the inorganic substances after hydrolysis is called the precipitation method. During the reaction, in order to deposit inorganic materials on the surface of the nanoparticles, the coupling coefficient needs to be increased. In this paper, bipolar nonionic polymer is used as the coupling agent, and ethyl silicate is used to make polyvinylpyrrolidone adsorb on the surface of nanoparticles. After adding ethyl orthosilicate to the solution for hydrolysis, the nanoparticles with silica shell on the surface are taken to prepare composite nanomaterials [8].

**2.2.4. Sol-Gel Method.** In the sol-gel method, the raw materials are first dispersed in a solvent. If a reactive monomer is generated by the hydrolysis reaction, the reactive monomer will polymerize to form a salt, forming a macroscopically restricted network structure. Finally, the target material is prepared by drying and heat treatment. The sol-gel method is a widely used method. The preparation conditions are mild, and the reaction process control is simple. The main chemical reactions are hydrolysis and concentration. However, the gel-sol method has developed

rapidly due to its long-term reaction and perishable substances.

**2.3. Motion Flow Evaluation Algorithm for Sports Rehabilitation Training.** To analyze the athlete's movement information, it is necessary to record the three-dimensional coordinate values of the connection points received from Kinect in real time. The infrared camera of the motion detector can reach a maximum rate of 30 frames per second. At this rate, the system will record a maximum of 450 image frames within the specified training time range, that is, the spatial coordinate values of maximum 450 connection points. The three-dimensional point set created in this way is used as a set of training data. If the standard energy is input, in order to achieve the distance between the two point sets, it can be used as an evaluation criterion for an appropriate driving route [9]. This paper uses Hausdorff distance algorithm and time dynamic distortion algorithm to match the joint space coordinate set and template coordinate set and combines the efficiency and error of the two algorithms to calculate the final motion similarity value. This method is combined with the action H-D similarity evaluation method, and two ranging algorithms are combined. The specific rules are as follows:

$$G = [\alpha G_{\text{HD}} + (1 - \alpha)G_{\text{DTW}}]. \quad (1)$$

Among them,  $D_{\text{HD}}$  and  $G_{\text{DTW}}$  are the similarities between the training action flow calculated by the Hausdorff distance measurement algorithm and the time distortion dynamic algorithm. In this article, it is represented from level 1 to level 5;  $\alpha$  represents the confidence level of the Hausdorff distance measurement algorithm in the evaluation result. On the contrary, the confidence of the evaluation result of the latent time distortion algorithm is represented by  $1 - \alpha$ .  $G$  is the final equivalent score of the training action process and the standard action process, which is the result of rounding the trust of the two algorithms [10].

Rehabilitation training conforms to the characteristics of periodic training. This article introduces a method of evaluating the similarity between periods of approximate periodic signals for the traditional Chinese massage technique to evaluate the similarity of the changes in the action angle waveform.

The matching problem of two time series can be solved according to the inconsistency of the period, and the two similar periodic signal sequences are as follows:

$$\begin{aligned} T_i &= \{s_i, s_{i+1}, \dots, s_{t_i+n_i-1}\}, \\ T_j &= \{s_j, s_{j+1}, \dots, s_{t_j+n_j-1}\}. \end{aligned} \quad (2)$$

The sequence length is represented by  $n_i$  and  $n_j$ , respectively. According to the basic principle of linear interpolation, the  $T_j$  sequence is compressed to the same as the  $T_i$  sequence, and this new sequence is marked as  $\{T'_j\}$ . The waveform error is

$$e_{i,j} = \frac{\sum_{k=1}^{n_i} |P_{i,k} - P_{j,k}|}{n_i}. \quad (3)$$

Then,  $\{T_j\}$  the average waveform error for other subsequences is

$$\bar{e}_i = \frac{1}{m-2} \sum_{k=1}^{m-1} e_{i,k}. \quad (4)$$

Among them,

$$\bar{s} = \frac{1}{m-1} \sum_{k=1}^{m-1} \left( \max_{1 \leq k \leq m-1} \{T_k\} - \min_{1 \leq k \leq m-1} \{T_k\} \right). \quad (5)$$

The above formula represents the average value of the maximum change in subsequence information. The similarity of  $S$  waves shows that, for the average error of consecutive periodic signal sequences, if the error is smaller, the two shapes are more similar, and the greater the error, the lower the similarity [11].

### 3. Paclitaxel Nanoparticles Treatment of Lung Tumor Experiment

#### 3.1. Preparation of Paclitaxel Nanoparticles

##### 3.1.1. Experimental Steps

Step 1: dissolve hydrophobic anticancer drug molecules in a good solvent to make hydrophobic anticancer drug molecules, prepare a hydrophobic anticancer drug molecule solution according to the volume ratio of good solvent to poor solvent (0.5–5): 100. The anticancer molecule solution was added to a poor solvent at a temperature of 20–30°C, magnetically stirred for 1–120 minutes, and then frozen to obtain a preliminary nanoparticle suspension for milking [12].

Step 2: add an aqueous solution of amphibian thiazine with a concentration of 1–10 mg/mL to the nanoparticle presuspension with a volume ratio of 1/100. After ultrasonic dispersion for 1–120 minutes, you can take the nanometer containing anticancer drugs. Particles and nanoparticles containing anticancer drugs may be dispersed in the water phase.

**3.1.2. Experimental Preparation.** The composition of medical polycaprolactone adopts vacuum distillation to perfect the monomer caprolactone. Under the protection of nitrogen, the catalyst F68 was added to the polymerization tube in proportion, and octane was added for proportionality. Evacuate and fill with high-purity nitrogen, replace it three times, and then seal the pipeline under vacuum [13]. After mixing the reagents uniformly in a 140 watt oil bath, they are transported to a constant temperature kiln at 140°C for 48 hours and then discharged for cleaning.

Accurately weigh polycaprolactone paclitaxel powder and dissolve it in acetone solution. After the stirring state (120 r/min) is completely dissolved, slowly inject the acetone-paclitaxel-polycaprolactone solution into the polyvinyl

alcohol aqueous solution, emulsify it with a stirrer to form an oil-water emulsion, and stir in the absorber under normal pressure. Until the organic solvent is completely removed, it is centrifuged at 23000 r/min for 30 minutes, washed and centrifuged three times, then precipitated with distilled water to remove free paclitaxel and polyvinyl alcohol, and finally stored in the frozen state. Collect all hypertexts at the same time during centrifugation and washing to detect the contents of free packages [14].

### 3.2. Preparation Experiment of Lung Tumor Cells

**3.2.1. Cell Recovery.** Before resuscitating the cells, use a sterilized ultraclean UV lamp stand for 30 minutes and wipe with 75% ethanol. Then, quickly remove the previously frozen lung cancer cells from the nitrogen tank and transfer them to the water pipe in the tank at 37°C. Stir gently to thaw the frozen solution quickly. First spray 75% alcohol into the cooling chamber and then move it to the aseptic workbench for operation. Before adding the appropriate amount of medium, put the frozen cells in a centrifuge tube, centrifuge at 1000 rpm, remove the hypertext, add fresh medium with a small size, add evenly, and resuspend the cells. Transfer the suspended cell liquid to a Petri dish containing 3 ml of fresh medium, and place it in a 37°C stable temperature incubator with 5% carbon for cell culture [15].

**3.2.2. Cell Passage.** Lung tumor cells are attached cells, so cell culture is carried out in the usual way. The cell density reached 80% of the lower surface of the dermatophyte and considered to be able to pass down. The workbench after sterilization should be sterilized by ultraviolet radiation 30 minutes in advance, and a tube used on the workbench should be wiped with 75% ethanol. Gently push the surface with a pistol, then drip the old medium, and then rinse the cell surface with 1 ml of PBS. Repeat the same function three times [16]. After washing with PBS, add 1 ml of coagulation to stop the cloth and make the cloth completely contact the cells. After stopping the drug for 2 minutes, transfer to an inverted microscope to observe cell inhibition. When the cells become round and the cell spacing increases, discard tryptophan, add 2 ml of fresh medium to stop the digestion, slowly and repeatedly press to wash the cells attached to the crop plate, then transfer the cell fluid to a 10 ml centrifuge tube, and centrifuge at 1000 rpm. After centrifugation, remove the hypertext, add an appropriate amount of fresh medium, press the cells carefully with a pipette about 7 times until the cell fluid is evenly dispersed, and then place the cell fluid in a new Petri dish to continue cultivation for future use [17].

**3.3. Experiments of Paclitaxel Nanoparticles in the Treatment of Lung Tumors.** Fifty lung tumor mice were randomly divided into 5 groups: blank control group, paclitaxel positive control group, and low-, medium-, and high-dose paclitaxel nanoparticle groups, with 10 mice in each group. The positive control group was treated with purpurin on the 8th and 11th

days. On the 14th and 17th days after tumor vaccine inoculation, the paclitaxel nanoparticle group was given only on the 8th day after inoculation (low-dose group 30 mg/kg, 60 mg/kg in the medium-dose group, and 90 mg/kg in the high-dose group (local injection); blank control group: no intervention was done. Starting from day 0, the volume is measured every two days. Flow cytometry measures cell cycle changes [18].

Main content: pathological observation and evaluation of the weight, size, and cell flow of experimental mice before and after treatment on the therapeutic effect of experimental mice with lung cancer were performed.

## 4. Analysis of Paclitaxel Nanoparticles in the Treatment of Lung Tumors

### 4.1. Paclitaxel Nanoparticle Analysis

**4.1.1. In Vitro Characterization Analysis.** In vitro characterization of paclitaxel nanoparticles measured an average particle size of 234.53 nm and a distribution coefficient of 0.136, as shown in Figure 1. The particles were observed by transmission electron microscope as spherical objects of uniform size, and the diameter size was consistent with the particle size detection results. Experimentally, the drug content of paclitaxel nanoparticles was 19.58%, and the embedding rate was 93.25% [19].

**4.1.2. In Vitro Release Analysis.** The in vitro release curve of the particles shows that paclitaxel nanoparticles can continuously release the drug within 30 days, as shown in Figure 2. After testing and calculation, the release rate of the drug in the burst release period is 80%, and the release rate after 30 days is 90%. The release curve of the cumulative release rate versus time shows that the cumulative release curve is close to a straight line, which is basically in line with the constant rate of drug release (level 0 release) kinetics. Paclitaxel nanoparticles can maintain a longer validity period due to the protective effect of the polycaprolactone carrier in the body, can continue to release the drug, and have a significant slow-release effect [20].

**4.1.3. Analysis of Inhibition of Lung Tumor Growth.** The experiment observed the inhibitory effect of paclitaxel polycaprolactone/F68 blended drug-loaded nanoparticles and paclitaxel injection on the tumor growth of TA2 mouse breast cancer lung metastasis model. From the comparison of tumor growth inhibition rate, it can be seen that the paclitaxel polycaprolactone/F68 blended drug-loaded nanoparticle administration group has a significant effect compared with the blank control group at two doses equivalent to the total paclitaxel amount of 60 and 90 mg/kg. The antitumor effect of the dose group equivalent to 30 mg/kg of paclitaxel is close to that of the paclitaxel positive control group (the total amount of paclitaxel is 5 mg/kg  $\times$  4) [21]. With the increase in the dose of paclitaxel, the antitumor effect of the paclitaxel polycaprolactone/F68 blended drug-loaded nanoparticle administration group also increased. When the total amount of paclitaxel is 90 mg/kg, the antitumor effect of ester/F68 blended drug-loaded

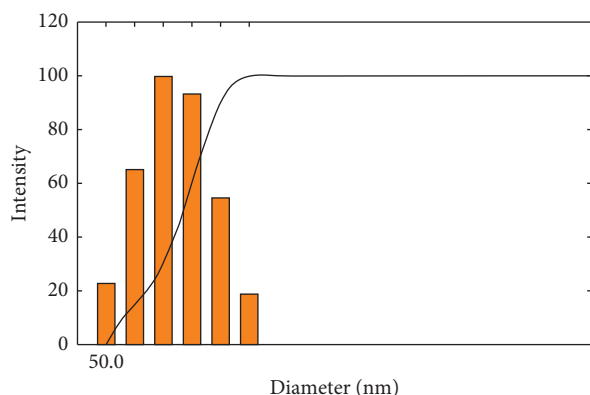


FIGURE 1: Size distribution of nanoparticles.

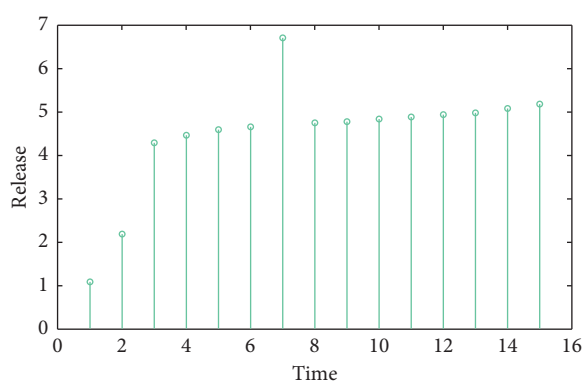


FIGURE 2: In vitro release of paclitaxel nanoparticles.

nanoparticles was significantly higher than that of the paclitaxel injection group. This indicates that the antitumor effect of paclitaxel drug-loaded nanoparticles is dose-dependent [22]. From the observation results of the growth inhibition effect of each administration group on the TA2 mouse breast cancer lung metastasis model, it can be seen that the tumor growth of the mice in the high-dose paclitaxel polycaprolactone/F68 nanoparticle administration group was significantly inhibited, as shown in Figure 3. In the experimental animal group, the tumors of 3 mice disappeared completely.

**4.2. Analysis of Paclitaxel Nanoparticles in the Treatment of Lung Tumors.** The in vitro activity of PTX and HA preparations was evaluated by the MTT method. The IC50 value calculated by the OD value measured by the MTT method is an important indicator for evaluating the cytotoxicity of drugs or preparations [23]. The smaller the IC50 value, the greater the killing power of the drug on tumor cells.

Table 1 shows the IC50 values of paclitaxel and HA preparations on lung tumor MCF-7 and lung tumor HepG2 cells. It can be seen that the IC50 values of the two cancer cells are relatively small, indicating that the IC50 values for both tumor cells are relatively large. This result indicates that it has greater cytotoxicity to both tumor cells, and the cytostatic effect gradually increases with the extension of the culture time [24]. It can be seen from the table that the IC50 value that acts on lung tumor cells is

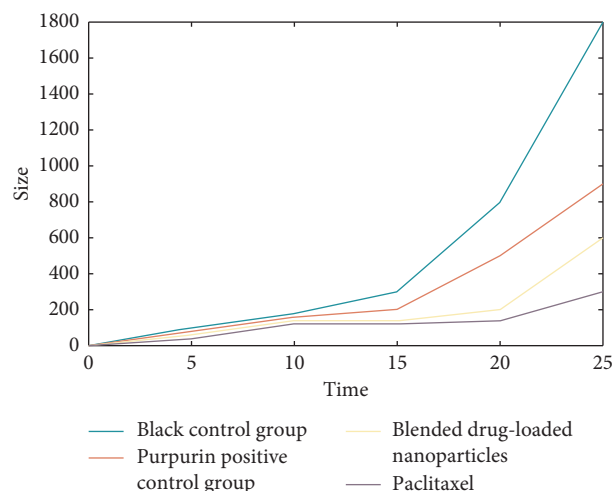


FIGURE 3: Line chart of lung tumor volume change.

TABLE 1: IC50 values of lung tumor cells.

Drug	Time (h)	IC50 ( $\mu\text{g/ml}$ )	
		HepG2	MCF-7
PTX	24	1.22	0.8
	48	0.84	0.77
	72	0.77	0.33
HA	24	1.85	1.49
	48	1.03	0.5
	72	0.93	0.33

smaller than that of lung tumor cells. The drug acts on different tumor cells. The preparation group has a better choice for MCF-7 lung tumor cells with high HA receptor expression. It can be seen from the table that the IC50 value that acts on lung tumor cells is smaller than that of lung tumor cells. The drug acts on different tumor cells, the preparation group has better selectivity and higher cytotoxicity for MCF-7 lung tumor cells with high HA receptor expression. With the extension of the culture time, the inhibitory effect of the preparation HA group on HepG2 cells was similar to that of the PTX group, while the inhibitory effect on lung tumor MCF-7 cells was stronger than that of the PTX group. The results show that the preparation HA can well inhibit the growth of tumor cells and has a significant effect on tumor cells with high expression of CD44 receptor.

The positive control is a drug group containing the same concentration of free paclitaxel, and the negative control is a blank medium without anticancer drugs. The survival rate of the cells in the negative control group is calculated as 100%. The killing effects of nanoparticles and positive control on lung tumor cells are shown in Figure 4, respectively. The results showed that the killing effect of nanoparticles on lung tumor cells was significantly higher than that of the positive control. The concentration of the added drug was 0.001, 0.01, 0.1, 1, and 10  $\mu\text{M}$  in terms of the concentration of paclitaxel. The median survival concentration is lower than that of free paclitaxel [25].

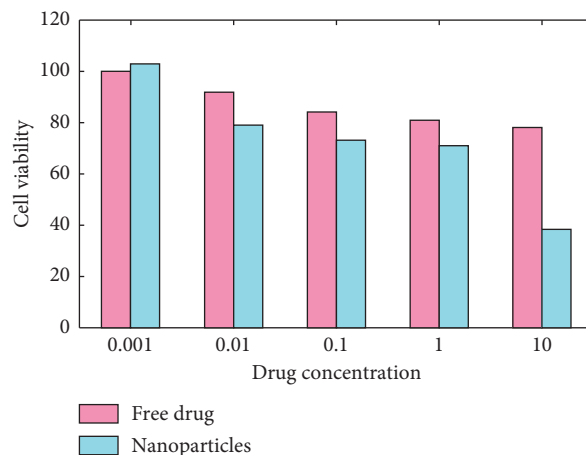


FIGURE 4: The killing of lung tumor cells by drugs.

It can be seen from the above results that the particle morphology of the nanoparticles provided in this article are relatively uniform and easy to control. The results of the cytotoxicity test showed that for HT29 cells and CT26 cells, the half-survival concentration of the nanoparticles in this article was lower than the free paclitaxel drug, which indicated that the nanoparticles had a highly effective killing effect on HT29 cells and CT26 cells. Therefore, the nanoparticles containing anticancer drugs provided in this article can enter tumor cells more efficiently and kill them, and the effect is better than that of free drugs [26].

#### 4.3. Analysis of Motion Flow in Tennis Rehabilitation Training.

The upper limb dyskinesia of patients is mainly reflected in the limited range of motion when completing related actions. According to the evaluation method mentioned above to determine the degree of rehabilitation, this article divides the evaluation results of the motion flow similarity of each group of training actions into five levels. Due to individual differences, the range of joint motion given in the article is based on the percentage of the maximum joint motion of the patient's healthy limb. Table 2 shows the five-level classification table of shoulder joint-abduction movements [27].

The somatosensory rehabilitation training system designed in this paper captures and calculates the real-time angle and angular velocity of the corresponding joints while capturing the three-dimensional motion coordinates of the human joint points [28]. As above, this article chooses the maximum joint angle value that the patient can achieve in a set of training process as the patient's joint range of motion and calculates the waveform similarity of the template action and the training action joint angle waveform. The calculation result is used as the scoring result of the completion of the training action. This set of experiments selects the joint angle information corresponding to the five sets of training data in Table 2. Taking the fifth set of experimental data as an example, draw a comparison chart of the training action shoulder joint angle curve and the fifth-level template joint angle curve in MATLAB, as shown in Figure 5.

TABLE 2: Five-level classification of abduction movements.

Training action	Action level	Determination		Rating
		Joint range of motion	Scope of this article	
Shoulder abduction	Insufficient	0%~50%	0°~70°	Level 1
		50%~65%	70°~85°	Level 2
		65%~75%	85°~125°	Level 3
	Full	75%~90%	125°~145°	Level 4
		90%~100%	145°~160°	Level 5

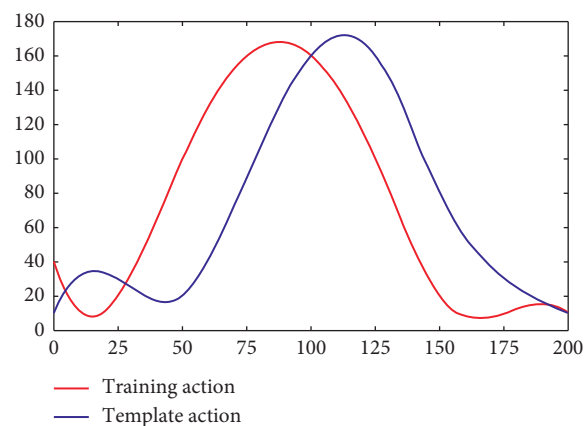


FIGURE 5: Comparison of joint angles.

From the data analysis in the figure, it can be concluded that the maximum angular velocity of the two trainings is the same, and the overall upward or downward trend is the same. The maximum angular velocity is 170. It can be seen from the training movement and the fourth-level template movement trajectory. The degree of coincidence is the highest; that is, the training rating is judged to be the fourth

level. This is the same as the result obtained by applying the fusion algorithm; that is, it is feasible to apply two distance measure fusion algorithms to determine the similarity of the motion flow [29].

**4.4. Analysis of the Treatment of Lung Tumors by Sports Rehabilitation Training.** Sports rehabilitation training played a role both during and after the tumor treatment. The results of the study showed that, during the treatment of breast cancer survivors, the experimental group achieved significant improvements in function, mental health, and main complaints and after the treatment in oxygen demand, changes in cardiopulmonary function, self-esteem, depression, and anxiety. There were significant differences among breast cancer survivors in the experimental group.

In patients with peripheral blood stem cell transplantation, exercise rehabilitation guidance has played a positive and beneficial role in certain aspects, such as improving physical fitness (such as non-fatty matter), improving muscle strength and function, improving symptoms (such as pain and diarrhea), shortening hospital stay, and improving mental health and emotional conditions. Sports rehabilitation guidance has also shown many advantages in the treatment of patients with mixed solid tumors, such as physical fitness, aerobic metabolism, bone salt deposition, shoulder mobility, pain, fatigue, completion rate of training programs, and own survival quality and emotional state. Kirshbaum reported that the role of aerobic exercise in breast cancer patients receiving adjuvant therapy was significantly higher than its role after the end of treatment [30].

Sports rehabilitation training can reduce tumor recurrence and prolong overall survival. This article explores the correlation between exercise intervention and survival in a group of female patients with invasive lung tumors. The study followed up 4,000 breast cancer survivors aged 22–77. The longest follow-up time among the participants was 5 years. Women who participated in more exercise had lower breast cancer mortality and all-cause mortality (38% to 48%). Even if the known prognostic factors are adjusted, such as age, family history, disease stage, hormone therapy, treatment method, energy intake, and BMI, its advantages are still significant. Analyzing the correlation of 2000 women's exercise, cancer recurrence, and total mortality in women with early breast cancer through data analysis, it is found that moderate-intensity exercise can reduce mortality, but high-intensity exercise does not.

## 5. Conclusions

The standard matching algorithm discussed in this article has certain practical value for the classification and recognition of actions, but it should be noted that the execution of the algorithm has a long delay; that is, the execution speed of the matching algorithm needs to be improved. In the following research, we will find the optimization strategy of the fusion algorithm and realize the possibility of merging with the distributed computer and other parallel computing methods to reduce the total load time of the system platform.

The application of the nanoparticle carrier technology studied in this paper in the treatment of tumors by PDT not only makes up for the current deficiency of PDT tumor treatment but also adds many new features of PDT, further improving the effectiveness of PDT, reducing adverse effects, and expanding the scope of application of PDT. The adverse effects have expanded the scope of application of PDT. This basic research has fully demonstrated the great potential of nanotechnology in PDT tumor treatment, but how to transform this technology from laboratory research to industrial production is a big problem. Nanoparticle carriers have been used for improvement many times. But how to transform this technology from laboratory research to industrial production is a big problem. Nanoparticle carriers have been used many times to improve the functions of various organs in the human body. Its long-term impact remains to be seen. Its long-term effects remain to be seen.

In this paper, Camel was used as a template to design and screen new high-performance paclitaxel nanoparticles with anticancer activity. Based on this, we will do the following work on peptide carriers: (1) develop targeted anticancer drugs through receptor-mediated targeting molecules and chimera 18-Camel; (2) coordinate anticancer drugs by combining targeted drugs and anticancer drugs with siRNA carrying tumor suppressor genes and antirejection genes; (3) to study the anticancer effect in mice, the synergistic anticancer effect in vivo as a gene carrier, the distribution of paclitaxel in mice, and the evaluation of toxicity.

## Data Availability

No data were used to support this study.

## Conflicts of Interest

The authors declare that they have no conflicts of interest regarding the publication of the research article.

## References

- [1] F. Noveletto, F. L. F. Soares, S. C. Domenech, M. d. S. Hounsell, and P. B. Filho, "Biomedical serious game system for lower limb motor rehabilitation of hemiparetic stroke patients," *IEEE Transactions on Neural Systems and Rehabilitation Engineering*, vol. 28, no. 6, pp. 1481–1487, 2020.
- [2] Y. Yu, S. Xu, H. You et al., "In vivo synergistic anti-tumor effect of paclitaxel nanoparticles combined with radiotherapy on human cervical carcinoma," *Drug Delivery*, vol. 24, no. 1, pp. 75–82, 2017.
- [3] T. Rozario, T. D. Chiu, M. Chen et al., "A novel markerless lung tumor-tracking method using treatment MV beam imaging," *Applied Sciences*, vol. 8, no. 12, p. 2525, 2018.
- [4] S. Radu-Tiberiu and B. Alin Marius, "Improving the quality of life through participation in physical activity- the tennis camp pilot study," *Timisoara Physical Education and Rehabilitation Journal*, vol. 10, no. 19, pp. 159–164, 2017.
- [5] P.-C. Leung, "Rehabilitation training in artificially heated environment," *Journal of Exercise Rehabilitation*, vol. 13, no. 5, pp. 546–549, 2017.
- [6] C. M. Custodio and E. M. Wisotzky, "Is cancer rehabilitation fellowship training necessary for graduating physiatrists who

- wish to enter the field of cancer rehabilitation?" *PM & R the Journal of Injury Function & Rehabilitation*, vol. 9, no. 9, p. S429, 2017.
- [7] N. Geoffroy, C. Michel, M. Bernard, and P. Jacques, "Os acromiale in professional tennis players," *Orthopaedic Journal of Sports Medicine*, vol. 6, no. 5, Article ID 232596711877372, 2018.
- [8] N. Li, H. Cai, L. Jiang et al., "Enzyme-sensitive and amphiphilic PEGylated dendrimer-paclitaxel prodrug-based nanoparticles for enhanced stability and anticancer efficacy," *ACS Applied Materials & Interfaces*, vol. 9, no. 8, pp. 6865–6877, 2017.
- [9] T. Hu, C. Qian, Y. Xuan et al., "Radionuclide I-131 labeled albumin-paclitaxel nanoparticles for synergistic combined chemo-radioisotope therapy of cancer," *Theranostics*, vol. 7, no. 3, pp. 614–623, 2017.
- [10] S. Tiwari, A. B. Tirosh, and A. Rubinstein, "Increasing the affinity of cationized polyacrylamide-paclitaxel nanoparticles towards colon cancer cells by a surface recognition peptide," *International Journal of Pharmaceutics*, vol. 531, no. 1, pp. 281–291, 2017.
- [11] F. Xie, W.-F. Ding, Z.-J.-L. Liu et al., "In vivo antitumor effect of endostatin-loaded chitosan nanoparticles combined with paclitaxel on Lewis lung carcinoma," *Drug Delivery*, vol. 24, no. 1, pp. 1410–1418, 2017.
- [12] L. N. Turino, M. R. Ruggiero, R. Stefania, J. C. Cutrin, S. Aime, and S. Geninatti Crich, "Ferritin decorated PLGA/paclitaxel loaded nanoparticles endowed with an enhanced toxicity toward MCF-7 breast tumor cells," *Bioconjugate Chemistry*, vol. 28, no. 4, pp. 1283–1290, 2017.
- [13] V. Elena, B. Chiara, C. Alessia et al., "Albumin and hyaluronic acid-coated superparamagnetic iron oxide nanoparticles loaded with paclitaxel for biomedical applications," *Molecules*, vol. 22, no. 7, p. 1030, 2017.
- [14] T. Wang, Y. Liu, and C. Wu, "Effect of paclitaxel-mesoporous silica nanoparticles with a core-shell structure on the human lung cancer cell line A549," *Nanoscale Research Letters*, vol. 12, no. 1, p. 66, 2017.
- [15] T. M. Celik, Y. Çiğdem, U. Sedat et al., "Development and characterization of paclitaxel-loaded PLGA nanoparticles and evaluation of cytotoxicity on MCF-7 cell line by MTT assay," *Proceedings*, vol. 1, no. 10, p. 1030, 2017.
- [16] F. Madani, B. Esnaashari, B. Mujokoro, F. Dorkoosh, M. Khosravani, and M. Adabi, "Investigation of effective parameters on size of paclitaxel loaded PLGA nanoparticles," *Advanced Pharmaceutical Bulletin*, vol. 8, no. 1, pp. 77–84, 2018.
- [17] K. J. Surendra, T. Suchi, J. Ruchi, and J. Nilesh, "Formulation and evaluation of protein bound paclitaxel nanoparticles for injectable suspension," *Journal of Drug Delivery and Therapeutics*, vol. 10, no. 3, pp. 51–57, 2020.
- [18] J. Li, Y. Gu, Z. Wei et al., "Molecular mechanism for selective cytotoxicity towards cancer cells of diselenide-containing paclitaxel nanoparticles," *International Journal of Biological Sciences*, vol. 15, no. 8, pp. 1755–1770, 2019.
- [19] N. Yu, J. Li, Z. Yuan, D. Dan, L. Xiaolin, and X. Huae, "Superior antitumor effect of self-assembly supramolecular paclitaxel nanoparticles," *RSC Advances*, vol. 10, no. 22, pp. 12999–13005, 2020.
- [20] Z. Min, L. Xin, L. Yuanyuan et al., "Ascorbyl palmitate-incorporated paclitaxel-loaded composite nanoparticles for synergistic anti-tumoral therapy," *Drug Delivery*, vol. 24, no. 1, pp. 1230–1242, 2017.
- [21] J. Mo, L. Wang, X. Huang et al., "Multifunctional nanoparticles for co-delivery of paclitaxel and carboplatin against ovarian cancer by inactivating the JMJD3-HER2 axis," *Nanoscale*, vol. 9, no. 35, p. 13142, 2017.
- [22] L. F. Wei, "Comparison between corticosteroid and lidocaine injection in the treatment of tennis elbow: a randomized, double-blinded, controlled trial," *American Journal of Physical Medicine & Rehabilitation*, vol. 97, no. 9, p. 1, 2018.
- [23] P. C. Chao, T. C. Yeh, C. L. Huang et al., "Successful treatment of bipolar disorder by resection of lung tumor: a case report," *Indian Journal of Psychiatry*, vol. 60, no. 3, pp. 369–370, 2018.
- [24] H. Mamdani, S. Ahmed, S. Armstrong, M. Tony, and I. J. Shadia, "Blood-based tumor biomarkers in lung cancer for detection and treatment," *Translational Lung Cancer Research*, vol. 6, no. 6, pp. 648–660, 2017.
- [25] S.-W. Kim, Y. K. Lee, J. H. Hong et al., "Cancer treatment: mutual destruction of deep lung tumor tissues by nanodrug-conjugated stealth mesenchymal stem cells (adv. Sci. 5/2018)," *Advanced Science*, vol. 5, no. 5, p. 1870030, 2018.
- [26] X. Zhu, L.-Z. Zhu, and R.-J. Yang, "Role of inferior phrenic artery in the interventional treatment of lung metastases tumor: a report of 11 cases," *Journal of Cancer Research and Therapeutics*, vol. 14, no. 1, p. 61, 2018.
- [27] J. Miyamoto, T. Nakagawa, and H. Hirayama, "Metastatic brain tumor from lung adenocarcinoma presenting a unique radiographic pattern during afatinib treatment: a case report," *No Shink Geka Neurological Surgery*, vol. 46, no. 3, p. 213, 2018.
- [28] M. Jiang, N. Zhou, D. Liu et al., "P3.03-018 tumor cavitation in lung metastases in patients with solid tumor treated with apatinib," *Journal of Thoracic Oncology*, vol. 12, no. 11, p. S2280, 2017.
- [29] Y. Peng, Y. Wang, and X. Z. Hao, "Utility of multiple increased lung cancer tumor markers in treatment of patients with advanced lung adenocarcinoma," *Zhongguo Fei Ai Za Zhi/Chinese Journal of Lung Cancer*, vol. 20, no. 10, pp. 690–694, 2017.
- [30] M. Nagasaka, M. Crosby, N. Thummala, and A. J. SukariAbrams, "P2.07-040 pre-treatment tumor volume in non-small cell lung cancer (NSCLC) as a predictor of response to PD-1 inhibitors," *Journal of Thoracic Oncology*, vol. 12, no. 11, p. S2431, 2017.

## Research Article

# Chemical Compound Chemical Treatment in Animal Husbandry

Xiaoling Tang <sup>1</sup> and Ting Peng<sup>2</sup>

<sup>1</sup>Hunan Vocational College of Environmental Biological Technology, Hengyang 421005, Hunan, China

<sup>2</sup>Department of Chemistry, Zhejiang Xianju High School, Taizhou 317300, Zhejiang, China

Correspondence should be addressed to Xiaoling Tang; [tangxiaoling@hnebp.edu.cn](mailto:tangxiaoling@hnebp.edu.cn)

Received 6 August 2020; Revised 9 September 2020; Accepted 21 September 2020; Published 20 November 2020

Academic Editor: Tifeng Jiao

Copyright © 2020 Xiaoling Tang and Ting Peng. This is an open access article distributed under the Creative Commons Attribution License, which permits unrestricted use, distribution, and reproduction in any medium, provided the original work is properly cited.

The acidulant is widely used in the production of animal husbandry, and its use is affected by many factors, including environmental factors, dosage, diet composition, and animal's own factors, so only the correct use of the acidulant can bring good results in animal production and financial income. This article takes acidifier as an example to study the application of compound chemical treatment in livestock farms. In this paper, the effect of using acidulant in the first 1 to 3 weeks after early weaning of piglets is obvious through this experimental study. The effect gradually decreases after 3 weeks and basically has no effect after 4 weeks. Experimental studies have found that the combination of organic acids, antibiotics, and high copper is the most effective. These three have different functions and have complementary or additive effects. Under harsh feeding conditions, especially when the environmental sanitation and environmental conditions are relatively poor, the effect of acidulants is better than good feeding conditions. Experimental data show that fulvic acid depletes milk's somatic cells in a short period of time and then quickly activates immune function, which is indicated by the increase in lymphocytes in the blood. When a large number of somatic cells migrate to the breast, the somatic cells in milk will also increase, thereby improving the immunity mediated by human cells. The experimental results show that the BFA formula added 1% to the cattle feed. After the research control of this experiment, the milk output increased by 9–17%, and the quality milk output increased by 19.12%, so the use of acidulant increased feed compensation and reduces gastrointestinal diseases and the reproduction of microorganisms in the rumen of dairy cows.

## 1. Introduction

Acidifier is organic or inorganic acid material, and it can be added to animal feed or drinking water alone or mixed, to inhibit the growth and reproduction of some harmful microorganisms, reduce the oxidative odor of feed, and can improve metabolism and certain human functions. In recent years, acidifiers have been widely used in the production of livestock feed and play an important role in improving the production efficiency of livestock. However, the environmental factors, dosage, dietary composition, animal type, age, weight, physiological stage, and other factors are greatly affected, so understanding the correct use and precautions of acidifiers requires careful study.

Biochemical fulvic acid is simulated natural humic acid production environment. According to specific biological oxidation reaction, organic medium was inoculated with

various microbial strains to rapidly form BFA preparation, which is another environment-friendly biochemical product of the local Luyuan Animal Husbandry Company [1, 2]. Its effective components in fulvic acid, DNA, are a kind of multivalent phenol-type polycondensate with nitrogen compounds, and aromatic compounds, containing phenol hydroxyl, hydroxyl, hydroxyl of alcohol, alcohol, acid, enol base, sulfonic acid, amino, free Ti hydrogen, half Ti base, and Ti base, such as oxygen- and carbon-based functional groups, have the high cation exchange capacity, integration capability, buffering capacity, south catalysis, and adsorption capability and can be directly involved in the tissue of redox process, greatly improving the activity of enzymes in the body; biochemical fulvic acid has been used in the development of animal husbandry, aquaculture, agriculture, and medicine. New concepts were introduced in the field of nutrition and immunology [3, 4].

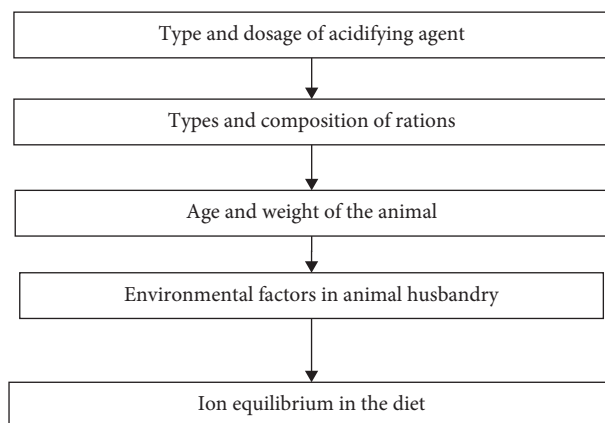


FIGURE 1: Flow charts affecting acidification effects.

Korsten et al. added 1.6% calcium formate in the feed to reduce the pH value of the feed by 0.6 and added 1% calcium formate and 0.5% propionic acid to reduce the pH value of the feed by 0.7 [5]. Flores et al. added 1.5% citric acid and 1.6% fumaric acid to the diet of piglets and reduced the dietary pH from 6.32 to 4.82 and 4.73 and the gastric contents from 4.33 to 3.86 and 3.87, respectively [6]. It can be seen that acidifying agents can reduce the pH of stomach contents to some extent. Each enzyme has an appropriate pH environment, and the appropriate pH for pepsin is 2.2–3.6. The activity of pepsin decreased significantly when pH was higher than 3.7 and was inactivated when pH was higher than 6.0.

## 2. Research on Acidifier

### 2.1. Classification of Acidizing Agents

**2.1.1. Inorganic Acidifier.** Inorganic acidifiers usually include  $\text{H}_3\text{PO}_4$ ,  $\text{HCl}$ , and  $\text{H}_2\text{SO}_4$ , have strong sour taste and large output, and are easy to promote and use. Tests show that  $\text{H}_2\text{SO}_4$  is essentially disabled. Due to different electrolysis conditions,  $\text{HCl}$  in use will affect the dietary effect.  $\text{H}_3\text{PO}_4$  has the function of acidification, supplementing the mineral elements of phosphorus, and has a high cost performance, so it can be widely used in actual production. In short, inorganic acids acidify better than organic acids and have a price advantage. The disadvantage of inorganic acid is that it is difficult to grasp the reasonable amount of addition. Therefore, if the concentration is low, it will be invalid. If the concentration is high, it will damage the processing machine [7, 8].

**2.1.2. Organic Acidifier.** Common organic acidifying agents include formic acid, acetic acid, propionic acid, butyric acid, sorbic acid, fumaric acid, malic acid, tartaric acid, and citric acid [9]. Organic acidifiers are corrosive and expensive, but because of their taste, they often function in the body's tricarboxylic acid cycle, which promotes the growth and development of new animals, so feed companies give them priority.

**2.1.3. Compound Acidifier.** The use of organic or inorganic acidifiers alone has many advantages and disadvantages, and different reaction principles enable them to coordinate and complement each other. Artificial blending of two single acidifiers as complex acidifiers can provide rapid pH control, excellent buffering capacity, and higher cost performance, while reducing damage to equipment and machinery [10]. Further optimization of the mixing ratio to form mixed acidifiers is a general trend, and the appearance and application of odorous acidifiers in lactating cows is the best evidence. The mixed acidifying agent usually presents as powder. The additive amount is 1.0–1.5 kg/feed [11].

Many acidifiers use white carbon black as the carrier and adsorb inorganic or organic acids. Silica itself has no nutritional value. The acidifier produced by a local research company is a compound organic acid obtained by direct enzymolysis of feed raw materials and fermentation. Its carrier is the raw material of fermentation feed and has high nutritional value, which is a breakthrough in the preparation of acidifier [12].

**2.2. Factors Affecting Acidification Effect.** In recent decades, many countries have imposed strict restrictions on the addition of antibiotics because the contamination of animal products with chemical residues of antibiotics is a serious threat to human health [13]. Acidifiers are becoming more and more popular as highly efficient, pollution-free, residue-free, and environmentally friendly feed additives, which can promote growth and inhibit the growth and reproduction of pathogenic microorganisms [14]. Because different acidifiers often have a synergistic effect on each other, a proportional mixing of different acidifiers can be more effective in preventing disease. Most complex acidifiers are based primarily on organic acids and are mixed with other organic acids. The use of compound acidification agents can increase the acidification effect of diet, significantly reduce the pH value of piglets' stomachs, and help to maintain the most suitable acidic environment in the digestive tract [15]. Most tests show that the combined acidifier is superior to the single acidifier.

**2.2.1. Type and Dosage of Acidizing Agent.** There are many types of acidifiers, which have different molecular weights, solubility, dissociation constant, and energy value and have different effects. Insufficient dose cannot achieve the required acidification effect, and too much dose will affect the normal performance of animal production capacity.

**2.2.2. Types and Composition of Meals.** Different dietary types have different acidification effects.

**2.2.3. Age and Weight of the Animal.** Animal age and weight should be taken into account when adding acidifiers to feed. For example, after birth, the gastric acid secretion of piglets is insufficient, and digestive function is gradually improved with age and weight gain, gastric acid secretion is gradually increased, and acidification effect is decreased.

**2.2.4. Environmental Factors for Raising Livestock.** Hygiene, feed density, temperature, humidity, and various fence pressures also influence the effect of the acidifier.

**2.2.5. Ion Balance in Diet.** Adding inorganic or organic acidizing agents to the diet of animals often disrupts the ion balance of diet and leads to metabolic acidosis in animals [16].

Compound acidifier is composed of several specific proportions of single acidifier. According to the different composition, it can be divided into two categories: total acid compound acidifier and acid compound acidifier. All-acid compound acidifiers consist mainly of one acid and synergistic compound acidifier one or more other acids [17, 18]. Currently, the most common acidifiers for all acid compounds are phosphoric acid and lactic acid. Phosphoric acid consists mainly of phosphoric acid and is mixed with other inorganic and organic acids. The lactic acid system consists mainly of lactic acid and is mixed with other inorganic and organic acids. Organic acid and organic acid salt form a composite acidulant through chemical coordination, which is the development trend of composite acidulant. Figure 1 shows a flow chart that affects the acidification effect.

### 2.3. On the Role of Acidifier

**2.3.1. Action Mechanism of Acidifier.** There are many kinds of acidizing agents used in fodder, and there are mainly three kinds in feed production, namely, inorganic acidifying agent, organic acidifying agent, and compound acidifying agent. The inorganic acids commonly used in production mainly include phosphoric acid, which is relatively cheap. The main organic acids are citric acid, fumaric acid, lactic acid, propionic acid, malic acid, sorbic acid, formic acid, and acetic acid. The compound acidifier can be divided into two kinds: the whole acid compound acidifier and the salt compound acidifier. The most common type of all-acid compound acidifier is phosphoric acid and lactic acid. The complex acidifier is a new generation of complex acid which

is complexed by scientific proportion of organic acid and inorganic acid. It has strong acidity, low dose, fast action, and better effect than single acidifier. It is the tendency of feed acidifier application that the drug is safer and more effective. The action mechanism of acidifier is mainly reflected in the following aspects [19, 20]:

(1) *Reduce the pH Value of Feed, Reduce the pH Value in the Stomach, and Improve the Activity of Digestive Enzymes.* Adding acidifying agents to animal feed lowers the pH of the stomach, activates pepsin, and speeds up protein breakdown. Protein decomposition also stimulates the secretion of more trypsin in the duodenum, leading to complete protein degradation and absorption [21]. The gastric acid secretion of early weaning piglets is insufficient, the diet pH of piglets is between 5.8 and 6.5, and the gastric pH of piglets depends on PEPase, which is usually higher than the appropriate activity range. Absorption of organic acids in pig feed can increase the growth potential of piglets [22]. According to the experimental results in the literature, adding 1.6%~2.1% fumaric acid in the feed can increase the average daily weight gain of piglets by 9%, feed intake by 5.2%, and feed utilization rate by 4.4%. The effect of adding hydrochloric acid and sulfuric acid into the diet of weaned piglets was studied in the experiment. The results showed that the intake quantity of weaned piglets decreased sharply, and the daily weight gain and the feed utilization rate decreased seriously.

(2) *Slow Down the Rate of Gastric Emptying.* The stimulating factors that promote the speed of digestive tract and gastric emptying are the volume and pH value of gastric contents [23]. After acidic chyme enters the small intestine, it stimulates the mucosa of the small intestine, making it secrete gastric inhibitory hormone, reflexivity inhibits gastric peristalsis, slows gastric emptying, and allows more time for protein digestion in the stomach [24].

(3) *Improve Gastrointestinal Microflora.* The suitable pH value for the growth of common pathogenic microorganisms in the gastrointestinal tract is neutral base. For example, the suitable pH value of *Escherichia coli* is 6.2~8.2, *Streptococcus* 6.1~7.5, and *Staphylococcus* 6.7~7.6, and lactic acid bacteria and other beneficial bacteria are suitable for growth and proliferation in an acidic environment [25]. Therefore, acidifying agents can inhibit the proliferation of harmful microorganisms and promote the proliferation of beneficial bacteria by reducing the pH value of the gastrointestinal tract. The metabolite of lactic acid bacteria (lactic acid) can block the binding of *E. coli* to its receptor in the intestine and inhibit the growth of *E. coli*. The main cause of diarrhea in weaned piglets is the increase in pH value in the gastrointestinal tract due to insufficient gastric acid secretion, which provides a suitable environment for the mass reproduction of *E. coli*. Within 2 days after weaning of piglets, *Lactobacillus* in ileum almost drops to zero, the pH value in ileum increases, and the mass reproduction of *E. coli* leads to diarrhea in piglets. The frequency of diarrhea can be significantly reduced by adding acidification agent into piglets'

feed. Foreign studies have shown that organic acids entering the intestinal tract can change the intestinal morphology, such as weaned piglet's small intestinal crypt depth becoming shallow and increasing villi height.

(4) *Promote the Absorption of Minerals and Vitamins.* Some major and trace elements in the alkaline environment are easy to form insoluble salt and very difficult to absorb. Acidifier can not only reduce the pH value of gastrointestinal contents but also form complex which can be easily absorbed and utilized with some mineral elements. Many scholars have proved that the addition effect of high copper and acidifying agent has an additive effect; that is, fumaric acid, citric acid or phosphoric acid, and copper form a complex with high biological potency, which promotes the absorption and retention of copper and reduces the oxidation catalytic activity of copper at the same time.

Some organic acids, such as fumaric acid, have anti-oxidant effects, and citric acid is an antioxidant booster. When fumaric acid was added to premix and kept for 6 months, the stability of vitamin A and vitamin C was improved compared with that without fumaric acid. The acidic environment of the small intestine also facilitates the absorption of vitamins A and D.

(5) *Directly Participating in Energy Metabolism in the Body.* As an energy source, some organic acids are important intermediates in the process of energy conversion and can be directly involved in metabolism. For example, the triclosate cycle reaction is initiated by the condensation of acetyl and oxaloacetate to citric acid; fumaric acid is also an intermediate product of the triclosate cycle; and lactic acid is also involved in metabolism in the body and is one of the end products of glycolysis. It release energy, so organic acid can be used as energy source.

### 2.3.2. Action Mechanism of Composite Acidifier

(1) *Adjust the Balance of Microbial Flora in the Digestive Tract.* For the growth of the most harmful bacteria in the gastrointestinal tract, the optimum acidity and alkalinity are neutral slants. *E. coli*, for example, has a suitable pH of 6–8, while beneficial bacteria such as *Lactobacillus* are adapted to grow and reproduce in acidic environments. When acidifying agents enter the digestive tract of livestock and poultry, lowering the pH value can promote the growth and reproduction of beneficial bacteria (such as *Lactobacillus*) and change the living environment of harmful bacteria (such as *E. coli* and *Salmonella*) and can control or kill *Staphylococcus*, *Bacillus*, and other harmful bacteria.

(2) *Reduce the pH Value of Digestive Tract and Enhance the Activity of Digestive Enzymes.* Studies have shown that normal digestive physiology can be maintained only when the pH of the animal gastrointestinal tract is stable in a reasonable range. If the pH value is too high, pepsinogen activation will be severely impaired. Pepsin is inactivated at pH above 6. In the early stages of weaning, the digestive and immune systems of

TABLE 1: Application experimental data of BFA on fat pigs.

	Daily gain	Feed efficiency
Pig feed	21%–26%	9%–14%
Extensive conditions	33%–56%	22%–36%

piglets are immature. During the period between breastfeeding and feed feeding, the production of acid in the esophagus and gastrointestinal tract of piglets is insufficient, making it difficult for the stomach of adult pigs to become acidic (pH 2.0–3.5). The addition of acidifying agent can reduce the pH value of stomach of young animals, provide a reasonable environment for digestion of animals, activate pepsin to maintain high activity, help to soften feed and decompose nutrients, help to cause disease, and prevent microbial digestive tract. The external environment enters the animal body and stimulates the duodenum to secrete more trypsin, which leads to the complete protein absorption and the improvement in feed utilization. Citric acid in the feed is very effective: it is directly involved in the body's metabolism and promotes the absorption of nutrients. Some trace elements in weak or alkaline environment tend to form insoluble acids and difficult to absorb in livestock and poultry. When the acidifier is added to the feed, the trace element salt is easily decomposed and the complex with the acidifier is easily formed and then absorbed. Many scholars have demonstrated that the effects of adding high copper and acidifying agents have additive effects, such as increasing copper's oxidative catalytic activity, stress resistance, and animal immunity. Some studies have found that piglet feed has the highest nitrogen content of solid nitrogen fertilizer. The fertilizer is a neutral nitrogen fertilizer, has relatively stable physical and chemical properties and low hygroscopicity, and is easily soluble in water. When fertilized in soil, fertilizers are less efficient because they must be converted into bicarbonate and absorbed in large quantities into crops.

2.4. *Mechanism of BFA.* The biochemical fulvic acid (BFA) is an active substance that simulates the natural humic acid formation environment and is fermented by organic materials such as crop straws. Due to its small molecular weight, it is easy to absorb and use in animals and has functions such as regulating physiological functions, nutritional management, disease prevention, and livestock treatment and is widely used in livestock and veterinary clinics.

2.4.1. *To Promote Growth, Can Be Used as a Growth Accelerator.* One is that nucleic acids, amino acids, vitamins, inositol, polysaccharides, and other substances found in biochemical fulvic acid can directly participate in human metabolism, which is an excellent nutrient and growth hormone in livestock and poultry. Second, nutrients are completely transformed into small molecular nutrients to promote the absorption of metabolites and improve productivity; thirdly, biochemical fulvic acid contains a quinone group, which is involved in the REDOX reaction of human body, maintains a strong metabolism, and promotes cell division and growth. Fourthly, biochemical fulvic acid ACTS on the vegetative

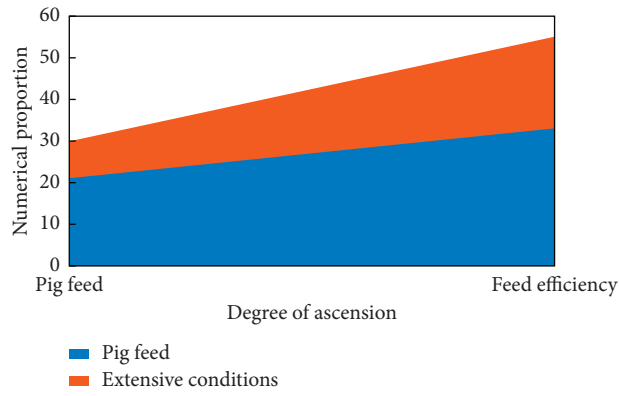


FIGURE 2: Application experimental data of BFA on fat pigs.

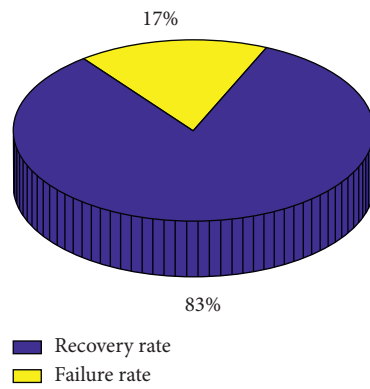


FIGURE 3: Data on cure rates.

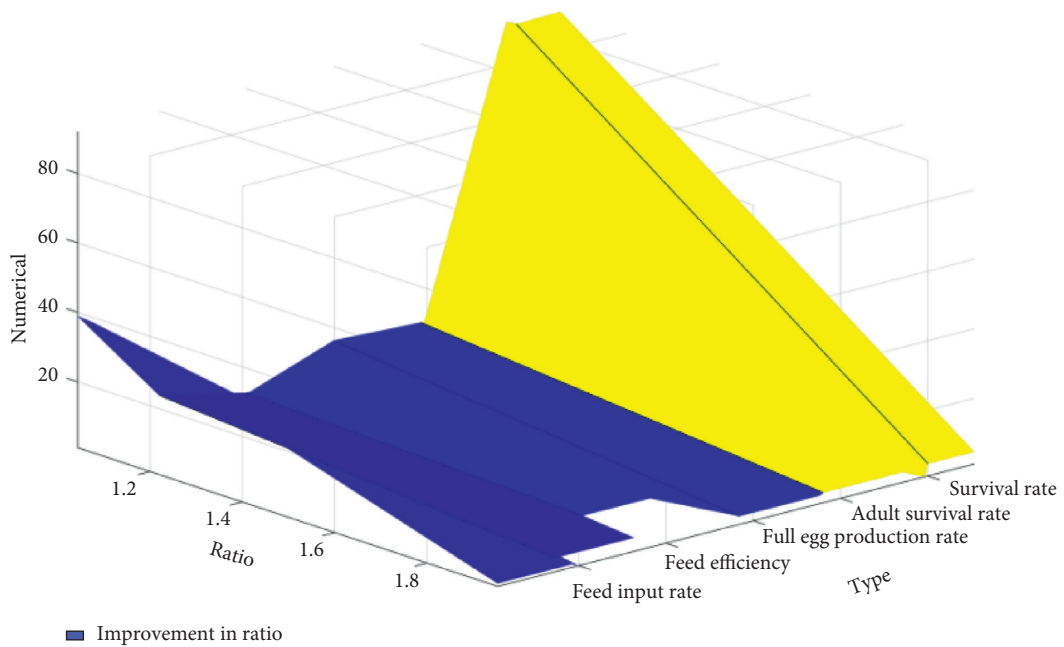


FIGURE 4: Specific data of BFA preparation added in feed.

TABLE 2: Blood analysis specific data.

	Numerical
Neutrophils	7.21%–21.34%
Lymphocyte	14.3–14.65%
Newcastle disease antibody	16.18–33.23%

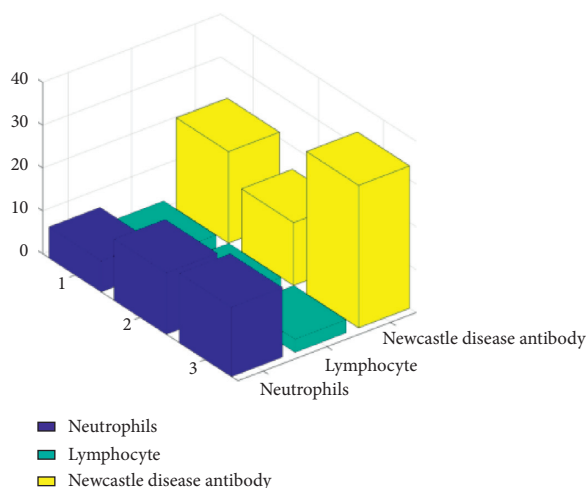


FIGURE 5: Blood analysis specific data.

nervous system inhibits sympathetic excitation and slows down the heartbeat. Increased intestinal activity increases the content of digestive juices, reduces body temperature and consumption, and keeps livestock and poultry quiet, thereby improving feed use. Fifthly, biochemical fulvic acid is produced by fermentation of various common microbial strains, which contain various active enzymes, which can effectively promote the digestion and metabolism of livestock and poultry and reduce feed remuneration.

**2.4.2. To Prevent and Treat Diseases and Enhance Immune Function.** First of all, biochemical fulvic acid can cause human body to produce interferon, activate reticuloendothelium system, enhance nonspecific immunity, and has a strong resistance to pathogenic microorganisms; second, biochemical fulvic acid can activate monocyte system to increase cell number, phagocytic ability, and phagocytic activity and has an infectious stimulation effect on thymus, which can improve antistress ability and viral bacterial disease; third, its strong adsorption ability can effectively absorb feed and digestive tract and metabolic process and adsorb a variety of toxic and harmful substances; fourth, biochemical fulvic acid is an organic acid preparation, which can effectively regulate the pH value of the digestive tract.

### 3. Experimental Study on Acidifier

**3.1. Selection of Experimental Materials.** The addition of organic acids to a simple corn and soybean meal diet significantly improved piglets' daily weight gain, but the acidification effect of

adding a complex diet containing dairy products remains unclear. Minerals and high protein diets have strong acid binding abilities. Compared with grain feed, it has a lower pH required for digestion. A diet high in calcium carbonate (59 g/kg DM) almost completely prevents bell-shaped acidification in the stomach. Diets with high CP (>30%) did not increase piglets' daily weight gain, whereas diets with low CP (18%) did.

**3.2. Selection of Experimental Acidifier.** In this study, the effect of acidifying agent was obvious in the first 1~3 weeks after early weaning of piglets, gradually decreased after 3 weeks, and basically had no effect after 4 weeks. Therefore, choosing an acidulant should be based on the age and weight of the animal.

**3.3. Experimental Environment Setting.** The results show that the combined use of organic acids and antimicrobials is usually better than the single use. In addition, the combination of organic acids, antibiotics, and high copper has the best effect. The three have different functions and have complementary or additive effects. The effect of acidifier is better than that of acidifier in the condition of poor environment.

## 4. Application of Compound Chemical Treatment in Animal Husbandry

### 4.1. Application of Compound Chemical Treatment in Raising Pigs and Cows

- (1) The application of BFA preparation in porcine breeding. According to the experiments of Supervisor Gu Zilin and others in many pig farms, adding 0.6–1.2% pig feed can increase daily weight gain by 21%–26% and feed utilization rate by 9%–14%; under the extensive condition, the daily gain was increased by 33%–56%, the feed utilization rate was increased by 22%–36%, and the feed meat ratio was 3.45 : 1–3.2 : 1.0.12 kg less material consumption per kg weight gain than the control group. BFA has the functions of preventing gastroenteritis, piglet diarrhea, and white myopathy. Long-term application of BFA in breeder pigs can improve the lactation rate and pregnancy rate of sows and improve semen level. The experimental data of application of BFA in fattened pigs are shown in Table 1 and Figure 2.
- (2) Adding 1% of BFA into the feed of dairy cows can increase the milk yield of dairy cows by 9–17% and the special milk yield by 19.12%. It increases price of feed, lowers digestive tract disease, promotes the cows in the rumen microbial growth, accelerates the speed of rumen microbial protein synthesis, increases animal body by feed protein and protein nitrogen utilization, prevents metabolic disease, reduces postpartum reproductive system disease, prolongs peak milk production, and maintains high ability of cattle of sexual reproduction rate and high yields. Prevention and treatment of dairy

cow mastitis has special effects, among which the effective rate of acute mastitis is 100%, the cure rate is 83%, the recessive mastitis can be controlled below 13%, the clinical mastitis can be reduced by 1.8–2.1 percentage points, and the alcohol-positive milk can be prevented. Fulvic acid can cause dairy cow milk somatic cells to decrease for a short time, and then the immune function is activated very quickly; the performance is increased lymphocytes in the blood because the somatic cells move to the breast in large quantities, so the somatic cells in milk also increase, thus improving the cellular immunity of the body. Among them, the highly functional phagocytes also remove the causes of mastitis so that mastitis can be cured. Combined with antibiotics, mastitis has a better effect without any toxic and side effects and has antistress so that the milk yield is relatively stable and the cure rate is shown in Figure 3.

#### 4.2. Application of Compound Chemical Treatment in Raising Chickens

- (1) Adding 1.3% BFA preparation into chicken feed can increase the growth rate and improve the uniformity of chicken and improve the specific and nonspecific immunity of chicks. The survival rate is as high as 97%–99.2%. The survival rate of laying hens was 97%–100% when 1.5% BFA was added into the feed. In addition, the egg production period is advanced by 4–6 days, and the egg production peak (egg production rate is above 90%) can be extended by more than two months. The egg production rate increased by 12.3%, the feed utilization rate increased by 13.58%, and the feed input decreased by 4.61%. Compared with the control group, the strength and thickness of the eggshell increased by 10.7%–15.8% and 5.9%–11.2%, respectively. The thickness of the sponge layer of the eggshell also increased significantly, and the soft-broken egg rate decreased by 41.6%. 2% BFA preparation was added into the feed of broiler chickens, and it was confirmed that the feed utilization rate was increased by 8.1% and 0.192 kg of feed was saved per kg of weight gain. The meat ratio of 7-week-old broiler is 2.2–2.26:1. Group dosing decreased by 26%, reduced drug retention, and improved meat quality. The specific data of ADDING BFA in feed are shown in Figure 4.
- (2) Blood analysis showed that the antibody values of neutrophils, lymphocytes, and Newcastle disease increased by 7.21–21.34%, 14.3–14.65%, and 16.18–33.23%, respectively. The maintenance time of antibody peak increased by 3–7 days. For infectious bronchitis, laryngotracheitis, pullorosis, coccidiosis, and Salmonellosis, it has good prevention and control effect. Specific data of blood analysis are shown in Table 2 and Figure 5.

## 5. Conclusions

- (1) Biochemical fulvic acid (BFA) is not only a mixed nutritional product of microbial metabolites but also an antibiotic-based drug. Its application performance is basically stable, and the effect is even more stable than antibiotic. With the growing demand for green, pollution-free meat, eggs, and milk, the country has set strict quality standards for staple foods entering the market, causing serious problems for the feed industry. There is an urgent need to “people-oriented” and produce new pollution-free green products. So far, some feed producers have unilaterally pursued feed “effects” against the perverse psychology of some farmers. In the production of feed, regardless of the state of health of the consumer, large amounts of antibiotics must be added, and only the growth and production of livestock and poultry is sought. In order to achieve the purpose of production, many feed producers add chemical elements that have toxic and side effects to humans and animals, high residues of chemical elements, adrenaline, and diazepam. Prolonged use of antibiotics in feed not only destroys the normal microbial system of the gastrointestinal tract but also accumulates residual drugs and strains in animals, increasing drug resistance and increasing drug use. The increase and effectiveness of drugs decrease year by year. In recent years, some probiotics, oligosaccharides, enzyme preparations, and saponins have emerged, but due to poor stability or inconsistent efficacy, they cannot completely replace antibiotics. With the advent of BFA, a new green feed additive has been provided for harmless livestock and poultry breeding as well as alternative feed, thus opening up a wide range of potential applications in animal husbandry.
- (2) Due to the various functional groups and active factors contained in biochemical fulvic acid, it exhibits various unique physical and chemical properties and can perform various physiological functions after entering the bodies of plants and animals. By inhibiting or activating this enzyme, it acts on the metabolism of animals and plants, reflects a significant stimulating effect, and plays a therapeutic role by regulating endocrine hormones and improving the immune function of the human body. Due to its easy bioabsorption and strong biological activity, biochemical fulvic acid has many uses and application effects in animal husbandry, veterinary medicine, and food, but it is the best dose for special animals. As further studies have not yet been undertaken, studies in determining yield are of great development value.
- (3) The research results of this paper show that adding 1% of BFA into cow feed can increase the milk yield of primary milk by 9–17% and the milk yield by 19.12%. Biochemical fulvic acid is a kind of green physiological active substance, which is obtained by fermenting special microorganisms with straw and

other organic matter. Through the research results, it is found that it has the function of promoting the growth of animals and plants and enhancing immunity and has been widely used in ruminants, monogastric animals, and aquatic animals in recent years.

## Data Availability

No data were used to support the findings of the study.

## Conflicts of Interest

The authors declare that there are no conflicts of interest regarding this submission.

## Acknowledgments

This study was supported by the pillar Project of Hunan Vocational College of Environmental Biological Technology.

## References

- [1] L. Ayed, N. Asses, N. Chammem, and M. Hamdi, "Improvement of green table olive processing wastewater decolorization by *Geotrichum candidum*," *Desalination and Water Treatment*, vol. 57, no. 37, pp. 17322–17332, 2015.
- [2] Z. Liu, X. Li, F. Hu, and P. Zhan, "Oxidation performance of FeO/Na<sub>2</sub>S<sub>2</sub>O<sub>8</sub> process for the treatment of landfill leachate biochemical effluent as well as activator characterization," *Desalination and Water Treatment*, vol. 107, pp. 109–117, 2018.
- [3] B. Elzen and B. Bos, "The RIO approach: design and anchoring of sustainable animal husbandry systems," *Technological Forecasting and Social Change*, vol. 145, pp. 141–152, 2019.
- [4] A. Eicker, E. Forootan, A. Springer, J. Kusche, and L. Longuevergne, "Does GRACE see the terrestrial water cycle 'intensifying'?" *Journal of Geophysical Research: Atmospheres*, vol. 121, no. 2, pp. 733–745, 2016.
- [5] H. Korsten, A. C. J. Z. V. D. Made, W. M. V. Weerden et al., "Characterization of heterogeneous prostate tumors in targeted pten knockout mice," *PLoS One*, vol. 11, no. 1, Article ID e0147500, 2016.
- [6] A. L. Flores, K. Risley, J. Zanoni et al., "Factors of success for transitioning from a scientific role to a supervisory leadership role in a federal public health agency, 2016," *Public Health Reports*, vol. 134, no. 5, pp. 466–471, 2019.
- [7] M. K. Gecer, M. Akin, M. Gundogdu, S. P. Eyduran, S. Ercisli, and E. Eyduran, "Organic acids, sugars, phenolic compounds, and some horticultural characteristics of black and white mulberry accessions from Eastern Anatolia," *Canadian Journal of Plant Science*, vol. 96, no. 1, pp. 27–33, 2016.
- [8] H. Zheng, Q. Zhang, J. Quan, Q. Zheng, and W. Xi, "Determination of sugars, organic acids, aroma components, and carotenoids in grapefruit pulps," *Food Chemistry*, vol. 205, pp. 112–121, 2016.
- [9] T. S. Anirudhan, F. Shainy, and J. Christa, "Synthesis and characterization of polyacrylic acid-grafted-carboxylic graphene/titanium nanotube composite for the effective removal of enrofloxacin from aqueous solutions: adsorption and photocatalytic degradation studies," *Journal of Hazardous Materials*, vol. 324, pp. 117–130, 2016.
- [10] B. Qin, G. Dou, Y. Wang, H. Xin, L. Ma, and D. Wang, "A superabsorbent hydrogel-ascorbic acid composite inhibitor for the suppression of coal oxidation," *Fuel*, vol. 190, pp. 129–135, 2017.
- [11] D. Li, Y. Jiang, S. Lv et al., "Preparation of plasticized poly (lactic acid) and its influence on the properties of composite materials," *PLoS One*, vol. 13, no. 3, Article ID e0193520, 2018.
- [12] L. Zhu, Y. Li, C. A. Carrera, Y.-C. Chen, M. Li, and A. Fok, "Calibration of a lactic-acid model for simulating biofilm-induced degradation of the dentin-composite interface," *Dental Materials*, vol. 33, no. 11, pp. 1315–1323, 2017.
- [13] V. G. Goffman, V. V. Sleptsov, N. N. Kovyneva, N. V. Gorshkov, O. S. Telegina, and A. V. Gorokhovskiy, "Effect of nanosized potassium polytitanate on the properties of proton-conducting composite based on phosphotungstic acid and polyvinyl alcohol," *Theoretical and Experimental Chemistry*, vol. 52, no. 5, pp. 1–5, 2016.
- [14] H. Zhang, J. Zhu, X. Cheng et al., "Effect of modified vermiculite on the interface of a capric acid-expanded vermiculite composite phase change material with phase transition kinetics," *Journal of Wuhan University of Technology-Materials Science Edition*, vol. 34, no. 2, pp. 345–352, 2019.
- [15] X. Zhang and Y. Xu, "The fabrication of polypyrrole/D-tartaric acid composite used as electrode in supercapacitors," *Materials Letters*, vol. 190, pp. 240–243, 2017.
- [16] F. Lynda, B. Tanushree, N. Powe, and A. Sebastian, "Acid balance, dietary acid load, and bone effects—a controversial subject," *Nutrients*, vol. 10, no. 4, p. 517, 2018.
- [17] J.-H. Lee, H. H. Kim, Y. H. Cho, T.-S. Koo, and G. W. Lee, "Development and evaluation of raloxifene-hydrochloride-loaded supersaturatable SMEDDS containing an acidifier," *Pharmaceutics*, vol. 10, no. 3, p. 78, 2018.
- [18] A. Septembre-Malaterre, F. Remize, and P. Poucheret, "Fruits and vegetables, as a source of nutritional compounds and phytochemicals: changes in bioactive compounds during lactic fermentation," *Food Research International*, vol. 104, pp. 86–99, 2018.
- [19] H. E. E. Malik, R. H. H. Hafzalla, O. H. A. Ali et al., "Effect of probiotics and acidifiers on carcass yield, internal organs, cuts and meat to bone ratio of broiler chicken," *Journal of Agriculture and Veterinary Sciences*, vol. 9, no. 12, pp. 18–23, 2016.
- [20] J. Wang, J. Yuan, K. W. Kim, and F. Xiao, "Chemical, thermal and rheological characteristics of composite polymerized asphalts," *Fuel*, vol. 227, pp. 289–299, 2018.
- [21] Y. Zhang, X. Rui, J. Wei et al., "Wet-chemical processing of phosphorus composite nanosheets for high-rate and high-capacity lithium-ion batteries," *Advanced Energy Materials*, vol. 6, no. 10, Article ID 1502409, 2016.
- [22] M. Niu, W. Xu, S. Zhu et al., "Synthesis of nanoporous CuO/TiO<sub>2</sub>/Pd-NiO composite catalysts by chemical dealloying and their performance for methanol and ethanol electro-oxidation," *Journal of Power Sources*, vol. 362, pp. 10–19, 2017.
- [23] O. Budnik, A. Budnik, K. Berladir, V. Sviderskiy, and P. Rudenko, "Structural conformation of polytetrafluoroethylene composite matrix," *Chemistry & Chemical Technology*, vol. 10, no. 2, pp. 241–246, 2016.
- [24] Y. Liang, H. Ding, and Q. Xue, "Characterization of brucite/TiO<sub>2</sub> composite particle material prepared by mechanochemical method," *Surface Review and Letters*, vol. 25, no. 4, p. 1132, 2018.
- [25] M. Zatoń, J. Rozière, and D. Jones, "Mitigation of fuel cell PFSA membrane chemical degradation using composite cerium oxide-PFSA nanofibres," *Journal of Materials Chemistry A*, vol. 5, no. 11, pp. 5390–5401, 2017.

## Research Article

# Study on Preservation of Chilled Beef with Natural Essential Oil Nanocapsules

Bin Xi <sup>1,2</sup>, Yaqin Gao,<sup>1,2</sup> Tianfen Guo,<sup>1,2</sup> Weihong Li,<sup>1,2</sup> Xiaoling Yang,<sup>1,2</sup> and Tianqing Du<sup>1,2</sup>

<sup>1</sup>Lanzhou Institute of Husbandry and Pharmaceutical Sciences, Chinese Academy of Agricultural Sciences, Lanzhou 730050, Gansu, China

<sup>2</sup>Quality Safety Risk Assessment of Animal Products, Ministry of Agriculture, Lanzhou 730050, Gansu, China

Correspondence should be addressed to Bin Xi; [xibin@caas.cn](mailto:xibin@caas.cn)

Received 7 August 2020; Revised 21 September 2020; Accepted 14 October 2020; Published 20 November 2020

Academic Editor: Tifeng Jiao

Copyright © 2020 Bin Xi et al. This is an open access article distributed under the Creative Commons Attribution License, which permits unrestricted use, distribution, and reproduction in any medium, provided the original work is properly cited.

Beef is rich in amino acids and vitamin B6, carnitine, potassium, protein, and other nutrients. It can improve the body's ability to resist disease and is especially suitable for growth, development, and postoperation and postrehabilitation care. Under such circumstances, the demand for beef consumption in various countries continues to grow steadily. At present, domestic beef prices continue to rise, and beef supply is insufficient. In addition, fresh beef is easy to be infected with microorganisms in the process of cold storage, which makes fresh beef deteriorated. Therefore, it is very important to add preservatives to prolong the shelf life of chilled beef. In this paper, the preservation of chilled beef with nanocapsules made of natural essential oil from plant extracts was studied. In this study, cumin, *Zanthoxylum*, ginger, cinnamon, clove, and thyme were selected to study the effect of six kinds of essential oils on beef preservation through comparative experiments. On the basis of such research data, the six kinds of essential oils were compounded, respectively, and different nanoessential oil capsules were applied to the fresh-keeping of chilled beef to make different kinds of nanoessential oil capsules. Through the experiment, the compound essential oil with better preservation effect was obtained. And through the comparison, cinnamon essential oil has obvious antibacterial activity, while ginger essential oil has the worst antibacterial effect. The pH value of beef can be changed and the degradation rate of protein in beef will be slowed down by applying appropriate amount of decomposed plant essential oil to beef samples. Through the above experimental results, we applied the compound essential oil to the preservation of cold and fresh beef at nanometer level and found that the effect was significant, which was worthy of application in major beef products processing plants.

## 1. Introduction

Meat and meat products play an important role in people's life. With the gradual improvement of people's living standards, food safety has gradually become the focus of attention. Especially in recent years, the problem of food safety has become increasingly prominent. Not only do people have higher and higher requirements for the preservation technology of meat and meat products, but also China is a country with a large population in the world and the largest meat production and consumption market in the world. Therefore, researchers attach great importance to the research on the preservation technology of meat, chicken,

and meat products. In our daily life, the common raw meat is cold fresh meat, normal temperature meat, and frozen meat. We call frozen meat when the storage temperature is lower than  $-23^{\circ}\text{C}$  and the internal temperature of meat is lower than  $-15^{\circ}\text{C}$  [1]. Normal temperature meat refers to the normal temperature meat directly slaughtered. The definition of cold fresh meat [2] refers to the fresh meat which is slaughtered in strict accordance with the national quarantine standards and finally matures after a refrigeration process of about  $4^{\circ}\text{C}$ . During the storage of chilled meat, due to the role of active enzymes in meat, protein is decomposed into peptide chain and small molecule amino acid molecules [3]. The shelf life of hot meat is shorter than that of cold meat

because it is easier to be contaminated by bacteria. Although the growth of microorganisms in frozen meat is inhibited, frozen meat still has the characteristics of poor sensory quality and nutrient loss after thawing. Therefore, cold and fresh meat with its excellent quality gradually occupies an important proportion in the market. Cold fresh meat is favored by consumers because of its delicious quality and attractive appearance. Because cold meat is inevitably processed by bacterial contamination, although cold meat has been kept in a low-temperature state, for most chilly bacteria, it is still growing and reproducing, so it is particularly important to extend the cooling of meat. The preservation time replaces adding preservatives..

Beef and its products have the advantages of high protein content and rich amino acids, which are loved by consumers at home and abroad. Beef is an important source of protein in daily diet, which can provide rich amino acids for human daily metabolism. In addition, the peptide produced by bovine belt can promote metabolism and maintain health in human metabolism. At the same time, beef is rich in iron, tin, zinc, copper, manganese, and other trace elements. These trace elements play an important role in human metabolism and the formation of antioxidant enzymes. The fatty acids and fat-soluble vitamins contained in beef are also necessary for human daily diet. In 2018, China's beef production reached 6.89 million tons, ranking the third in the world, accounting for 10% of the world's total. In recent years, in the production and sales of domestic fresh meat, the proportion of cold fresh meat is gradually increasing [4]. Therefore, extending the shelf life of chilled meat is of great significance to the development of chilled meat. Fresh beef is easy to be polluted and deteriorated by microorganisms during cold storage. Oxidation and microbial contamination are the main reasons for the deterioration of frozen beef.

On the one hand, chemical preservatives can inhibit the growth and reproduction of microorganisms; on the other hand, they can prolong the deterioration of food or inhibit biological metabolism, which is called chemical preservatives [5]. Chemical synthetic preservatives are favored by consumers because of their low price. However, some chemical preservatives are harmful to human body. For example, nitrite, as a kind of chemical preservative, can not only inhibit the growth of microorganisms, but also make food more colorful. However, the long-term consumption of nitrite will affect the normal function of red blood cells, resulting in the difficulty of oxygen transport. In addition, nitrite [6] is a chemical preservative and its use is limited. It is nontoxic in use. In case of excessive use or under certain conditions into nitrosamines, nitrosamines have the risk of cancer. At present, the main chemical preservatives used in China are organic acids and their salts, such as sorbic acid and its potassium salt, dehydroacetic acid and its sodium salt, and benzoic acid and its sodium salt. Although chemical preservatives are widely used, traditional chemical preservatives may be replaced by natural, nontoxic, and safe natural preservatives with the prominent safety problems of food additives. In recent 20 years, natural preservatives extracted from plants, animals, and microorganisms have been widely used in practice and recognized by consumers.

At present, natural preservatives are mainly studied in China. Most of these natural preservatives are extracted from plants or microorganisms, with good antibacterial effect, practicality, and high safety. Natural preservatives come from animals, microorganisms, and plants in nature.

The main components of cinnamon essential oil [7] are cinnamaldehyde, cinnamyl ester, salicylaldehyde, etc. In recent years, cinnamon essential oil has been widely used in preservation research because of its broad-spectrum antibacterial and excellent antioxidant properties. Thyme essential oil is extracted from the stems and leaves of thyme. Thyme is characterized by a strong aroma when it blooms. Thyme can inhibit bacteria and scavenge free radicals. Thyme essential oil not only has a strong inhibitory effect on common bacteria in life, but also eliminates free radicals in food and prevents food from being oxidized [8]. Ginger is an important life spice, which is widely used in clinical treatment of traditional Chinese medicine [9]. As a kind of medicinal plant and spice, clove has been found to be a natural food preservative in recent years. At present, many reports have confirmed that clove volatile oil has good antibacterial and antioxidant properties and is a natural antioxidant and antibacterial agent. Clove essential oil has strong special flavor and is volatile, insoluble in water, and sensitive to light, oxygen, and temperature. These factors greatly restrict the application of clove essential oil in food preservation. In order to improve its stability in food processing and cover up its bad flavor, microencapsulation of core materials can effectively solve this problem. Cumin is a kind of spice, mainly used for meat seasoning, but it also can be used in the processing and production of various foods. It is a natural source of medicine and food. The results showed that the bacteria treated with natural essential oil had some abnormal phenomena, such as cell shrinkage, local deformation, cell wall and membrane rupture, and cell system loss. The main components of *Zanthoxylum bungeanum* are flavonoids, volatile oil, alkaloids, and so on. These substances are very common in plants and have inhibitory effects on spoilage bacteria and pathogenic bacteria in food. *Zanthoxylum bungeanum* will become one of the important sources of natural food preservatives.

Due to the different types and concentrations of preservatives, the antibacterial activity of preservatives will also change greatly. Therefore, it is not possible to inhibit the growth of all microorganisms by one preservative alone. In order to obtain better preservatives, several kinds of preservatives are commonly used to combine and play the synergistic antibacterial and antioxidant effects of different preservatives. The combination of different preservatives can not only obtain better preservation effect, but also reduce the amount of preservatives under the same preservation effect. Compound natural preservatives are safer, more broad-spectrum antibacterial and can prevent antibiotic resistance. In this paper, based on the study of different essential oils on the preservation of chilled beef, the essential oils were compounded to obtain the composite essential oil nanocapsules with better preservation effect.

## 2. Preservation Effect of Different Essential Oils on Chilled Beef

**2.1. Extraction of Plant Essential Oil.** The traditional extraction methods of plant essential oil [10] include solvent extraction, absorption, and pressing. The extraction of plant essential oil mainly depends on the hydrophobicity or mild degree of target molecules, and the extraction rate of most essential oils is less than 5%. Therefore, there are many innovative nonthermal extraction methods, such as ultrasound, high voltage, and pulsed electric field assisted extraction, to overcome the above constraints. Water distillation was used in this experiment. The raw material from the factory is crushed by a small motor and passed through 60 mesh. The ratio of plant material and distilled water is 1 : 100, and the distilled water is soaked at 100°C for 1 hour. The distillate is condensed by the condensate and collected. Anhydrous sodium carbonate was used as desiccant for dehydration and drying. The essential oil was collected and stored at 4°C away from light.

The cumin oil, *Zanthoxylum* essential oil, cinnamon essential oil, clove essential oil, ginger essential oil, and thyme essential oil were diluted with 0.5% Twain 100 solution to make cumin essential oil, *Zanthoxylum* essential oil, cinnamon essential oil, clove essential oil, ginger essential oil, and thyme essential oil at concentrations of 0.1%, 0.2%, 0.3%, 0.4%, 0.5%, 0.6%, 0.7%, 0.8%, 0.9%, 0.9%, 0.9%, 0.9%, 0.8%, and 0.9%, respectively. After the treatment solution is prepared, put them into the refrigerator at 4°C in the dark environment.

**2.2. Configuration of Culture Medium.** Take 10 g as the basic unit, put the sample beef, pure salt, peptone, and agar powder into 1000 ml distilled water, respectively, according to the ratio of 1 : 1 : 2 : (2-3), heat them, and stir all mixture for sterilization.

**2.3. Preparation of Bacterial Suspension.** Activated strain: sterilize the test tube with appropriate amount of culture medium, and then place it until it solidifies to form an inclined plane. Then the strain was transplanted to the slope of the medium under aseptic conditions. Finally, the treated medium was put into the biochemical incubator for one night.

Preparation of bacterial suspension: the bacteria cultured on the slope of the strain were extracted into 0.1 L liquid medium and cultured for 24 h to produce bacterial suspension. Then, the concentration of colony count can be calculated by plate counting method, which is about 106–108 CFU/g.

**2.4. Determination of Bacteriostatic Zone.** Firstly, a filter paper with a diameter of 0.1 cm was prepared, and 1 ml of bacterial suspension was absorbed with the prepared filter paper and added into the culture dish obtained by 2.3. Then, the filter paper with the prepared essential oil was put into the culture dish. After the above operation, put the culture

dish into the incubator maintained at normal temperature. After 24 hours, the diameter of inhibition zone was measured.

**2.5. Determination Method of MIC.** Take 2 ml of the prepared bacterial suspension and add it to the sterilized clean plate, mix it with nutrient agar in the culture dish, and finally add appropriate amount of preservative solution to mix it evenly. In this experiment, two parallel tests were performed with each concentration inverted for one day. The minimum inhibitory concentration (MIC) is the concentration of preservative when there is no colony in the dish. The results showed that the antibacterial effect was inversely proportional to MIC.

**2.6. Orthogonal Experiment.** As shown in Table 1, the minimum inhibitory concentrations of six essential oils against *Pseudomonas fluorescens* were obtained, and the optimal compound concentration of essential oils was further studied by orthogonal experiment.

**2.7. Study on the Preservation Effect of Compound Preservative on Chilled Beef.** Choose compound preservative: take about 50 g fresh beef and apply 0.1% Tween 100 evenly on fresh beef. The above operation was carried out once and twice in total. When the surface of beef is dried, the dried beef is weighed on the weighing table, and the water absorption rate can be calculated as 7.0%. According to the calculated water absorption and the results obtained in Section 2.6, 1, 2, 3, 4, 5, and 6 in the orthogonal experiment were prepared in 1, 2, 4, 8, and 16 times of each formula, respectively, and then stored for 24 h. Then TVB-N was used as the evaluation index of storage and preservation effect to select a more suitable proportion scheme for subsequent experiments. 0.1% Tween 100 was used as control, and a blank group was set up without coating treatment.

For sample treatment, take fresh beef and put it into refrigerator at 4°C to make chilled beef. The knife, plastic chopping board, plastic tray, and preservative film were sterilized and disinfected. Then take out the prepared cold and fresh beef, on the treated table, the beef is processed into small pieces of about 50 g, and then put them on the treated plastic tray, and they are randomly divided into three groups: blank group, experimental group, and control group. Evenly spread the compound preservative solution determined in 2.7 on 50 g beef pieces and repeat the above operation again after 10 minutes. Then the control group was treated with 0.1% Tween 100, and the blank group was placed without any treatment. After all the steps, put the processed beef sample into the aseptic room, dry both sides of the beef sample, and then wrap it with plastic film and put it in the refrigerator at 4°C. At 0 d, 4 d, 8 d, 12 d, and 16 d after treatment, 3 samples were taken from each treatment group for index determination.

Determination of cooking loss was improved according to Rezaeinia et al. [11]. Take appropriate amount of meat pieces  $x_0$ , put them into the cooking bag and seal them, and

TABLE 1: Orthogonal experiment table of six essential oils.

Experiment number	Factor					
	Cumin essential oil concentration	Concentration of <i>Zanthoxylum bungeanum</i> essential oil	Concentration of refined cinnamon oil	Concentration of clove essential oil	Thyme essential oil concentration	Ginger essential oil concentration
1	1	1	1	1	1	1
2	1	2	2	2	2	2
3	1	3	3	3	3	3
4	1	1	1	1	1	3
5	1	2	2	2	1	3
6	1	3	3	3	1	3
7	2	1	3	1	1	2
8	2	2	2	3	1	2
9	2	3	1	2	1	2

put them into water at 75°C. Observe the temperature of the meat pieces. When the central temperature of the meat pieces rises to 65°C, maintain this state and continue to cook. After 40 minutes, take them out, use filter paper to absorb the moisture on the surface of the meat pieces, and then place the meat pieces in the room to let them cool to the indoor temperature. Then the meat was weighed and the weight was recorded as  $X_1$  g.

Determination of centrifugal loss rate: weigh 0.01 kg sample, wipe the moisture on the surface of the sample, and put it into the centrifugal tube for weighing after grinding. After weighing, it was centrifuged. After centrifugation, take out the centrifuge tube to clean the water in it. Pay attention to the water on the surface of the centrifuge tube which should also be wiped dry. Finally, the sample and the centrifuge tube are put together for weighing. Centrifugal loss rate is the most intuitive index to measure the water holding capacity of meat, and it is also a very important index.

Determination of meat color [12] was performed according to Wang. After the meat is taken out of the refrigerator, the color difference meter is used to measure the meat on the surface at five different positions randomly, and the value of the color difference meter is recorded. Each piece was measured five times; then all the values were added and divided by 5.

Determination of TBA value was performed using spectrophotometry; refer to GB/t5009.81-2019.

Determination of shear force was performed as follows: take 5 cm, 50 g of meat, clean the connective tissue and fat on the surface of the meat, then put it into the cooking bag and seal it, and put it into the water at 75°C. Then take it out and place it in the indoor environment and let it cool to the indoor temperature. Then, a 1.05 cm diameter sampler was used to take cylindrical samples along the direction of muscle fibers. At least three cylindrical samples were taken from each meat sample. The force of meat samples was measured by tenderness meter. To ensure the accuracy of the results, each column sample should be measured at least 5 times.

MFI determination was improved according to Delgado's method. Take 0.01 kg meat sample, add 0.08 L MFI buffer ice bath homogenization and then centrifuge it, and then

remove the supernatant. The precipitate was homogenized with MFI buffer and then centrifuged, and the supernatant was removed. 0.05 L buffer suspension was used for precipitation, and 0.05 L buffer solution was used to help filter 300 mesh nylon. The protein concentration of myofibrillar extract was determined by double contraction urine method, and the white concentration was adjusted to 0.1 mg/ml. The absorbance was measured at 550 nm. Finally, the measured data is multiplied by 210.

Determination of lysosomal cathepsin activity: using the method provided in the kit, the meat sample was treated with PBS solution, and then the corresponding reagent was added according to the method provided. The absorbance and protein concentration were measured at 440 nm, and then the enzyme content ( $\mu$ /g) was calculated.

### 3. Preparation of Natural Nanoessential Oil Capsules

Technology is based on microencapsulation technology. Microcapsule technology is a kind of micropackaging technology, which uses polymer film to encapsulate microimages of gas, liquid, and solid [13]. The materials purchased by backpacks are called new material packaging, while polymers rich in new materials are called monetary talents. Generally speaking, the diameter of microcapsules is between 1 and 35  $\mu$ m, and nanocapsule technology can prepare nanomicrocapsules. Compared with traditional microcapsules, nanocapsules have good biocompatibility, targeting, and sustained release, which can effectively reduce the sensitivity of bioactive substances and improve the bioavailability of bioactive substances. The main advantages of nanocapsules in food are to slow down the volatilization rate of volatile compounds, delay the loss time of aromatic components in spices, and cover up the release of some undesirable flavor components. It can greatly prolong the effective time of bioactive substances, reduce the effective addition of bioactive substances, reduce the toxic and side effects of some active substances, effectively improve the stability of bioactive substances, and prevent sensitive substances from being damaged by light, oxygen, and temperature. In the food industry, as a new carrier of functional active substances, nanocapsules increase the

available range of these substances, especially for men. Soluble substances play a good role in compatibilization and improve its compatibilization effect, so that it can be better used by people.

The selection of microcapsule wall materials has always been the focus of research, and the application effect of microcapsules often depends on the selection of wall materials, because the wall materials will affect the controlled release of microcapsules and the permeability, solubility, fluidity, and other properties of microcapsules. Therefore, the selection and preparation of wall materials are the key technology in the field of micropackaging and also the premise of realizing the micropackaging technology. Generally speaking, the selection of wall materials of microcapsules should follow the following principles: the wall materials and core materials should keep chemical stability without chemical reaction, so that the wall materials have good mass transfer performance and stable extrusion resistance, and the whole microcapsule has certain solubility, permeability, and stability. If industrial development, large-scale production, and low-cost wall materials are involved, the research and development of low-cost wall materials can be realized, and the preparation process is a necessary condition. Traditional wall materials of microcapsules generally refer to natural polymer materials. They are nontoxic, biocompatible, film-forming, and cheap. They are the most commonly used wall materials for microcapsules. Generally speaking, as long as the materials have good film-forming properties and certain strength and toughness and can be coated around the new materials, they can be used as microcapsules of natural polymer materials, mainly including carbohydrates, proteins, and fats.

Chitosan [14] is a kind of high molecular polysaccharide, and its molecular structure is very similar to that of glycosaminoglycan. Chitosan has unique molecular structure and chemical properties. In nature, only chitosan is a kind of natural polymer material with positive charge and biodegradation. For example, crabs and shrimps are widely found in crustaceans of marine arthropods, such as insects, fungi, and algae, as well as in the cell walls of higher animals and plants. They are nontoxic, tasteless, and irritant. The degree of deacetylation of chitosan is more than 90%, which can be called medical grade chitosan.

Chitosan nanocapsules were prepared by ionic gel method. Chitosan was dissolved in 2% glacial acetic acid to prepare 6 mg/ml chitosan solution, which was stirred by magnetic force at 55°C for 1 h and filtered with 0.5  $\mu\text{m}$  microporous filter paper, and the pH of chitosan filtrate was adjusted to a proper value with 3 mol/L sodium hydroxide solution. After the completion of the above operation, 60 ml of the prepared chitosan solution was extracted, and an appropriate amount of Tween 70 was added into it, stirred at 55°C for 0.5 h, and then put into the room for cooling to the indoor temperature. Then the essential oil was added into the absolute ethanol to obtain the 60 mg/ml essential oil solution. Then the essential oil solution was added into the chitosan solution. The essential oil solution was stirred at room temperature for 0.5 h. Then, 2.0 mg/ml sodium polyphosphate solution was added into the chitosan essential oil

emulsion drop by drop. After stirring at room temperature for 1 h, the chitosan essential oil nanocapsule dispersion was obtained. After centrifugation at 13000 rpm for 0.5 h, nanoparticles were prepared as the capsules will float in distilled water and freeze-dry for analysis.

## 4. Results and Discussion

**4.1. Antibacterial Activity of Natural Essential Oil.** As shown in Figure 1, the antibacterial activity of the six essential oils on the two bacteria is relatively obvious, among which cinnamon oil has the strongest inhibitory effect on bacteria, and ginger essential oil has the worst antibacterial effect.

**4.2. MIC Determination of Six Essential Oils.** As shown in Figure 2, cinnamon essential oil has the best bacteriostatic effect, followed by ginger essential oil and thyme essential oil. When the concentration of cinnamon essential oil was 0.006%, there were colonies in the medium. However, when the concentration reached 0.06%, cinnamon essential oil could completely inhibit the growth of bacteria in the culture dish. The MIC of cinnamon essential oil is 0.06%. When the concentration of thymol essential oil is greater than 0.0012% and less than 0.065%, there is bacterial growth in Petri dishes. When the concentration reaches 0.126%, thyme essential oil will completely inhibit the growth of the flora. Therefore, the MIC value of cinnamon essential oil is 0.126%. When the concentration of ginger essential oil is less than 0.026%, bacteria grow in the culture dish. When the concentration is higher than 0.09%, ginger essential oil will completely inhibit the growth of bacteria, so the MIC value of cinnamon essential oil is 0.09%. The MIC value of *Zanthoxylum bungeanum* essential oil was 0.36%. The MIC value of clove essential oil is 0.06%.

**4.3. Orthogonal Test Results.** As shown in Table 2, the MIC values of six essential oils against a specific bacterium were taken as reference, and they were set to the highest concentration of each influencing element, and then orthogonal experiment was conducted. The factors affecting the bacteriostatic effect are cumin essential oil > *Zanthoxylum bungeanum* Maxim > cinnamon essential oil > ginger essential oil > thyme essential oil > clove essential oil. According to the experimental results, the best compound essential oil concentration can be calculated as follows: cumin essential oil 0.82%, *Zanthoxylum* 0.69%, cinnamon essential oil 0.45%, ginger essential oil 0.4%, and thyme essential oil 0.35%.

**4.4. Effect of Compound Preservative Solution on pH Value of Beef.** As shown in Figure 3, the pH value of fresh meat ranges from 5.7 to 6.3, the pH value of lower grade fresh meat is 6.3–6.5, and the pH value of processed meat is greater than 6.5. With the increase of storage time, the pH value of three groups of samples first shows a downward trend and then increases gradually. After anaerobic fermentation, the slaughtered fresh beef produces lactic acid

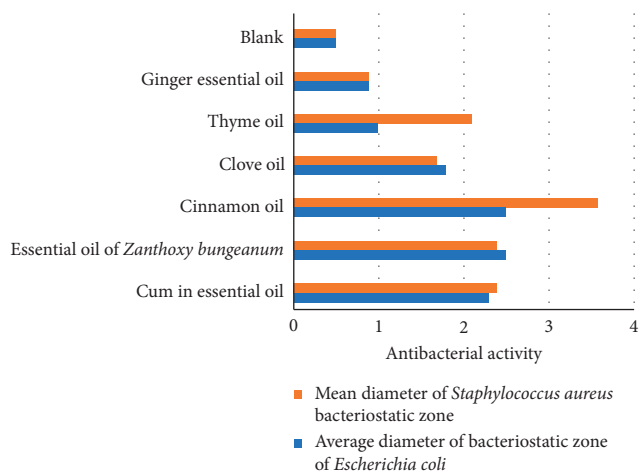


FIGURE 1: Determination of bacteriostatic zone of six essential oils against two kinds of bacteria.

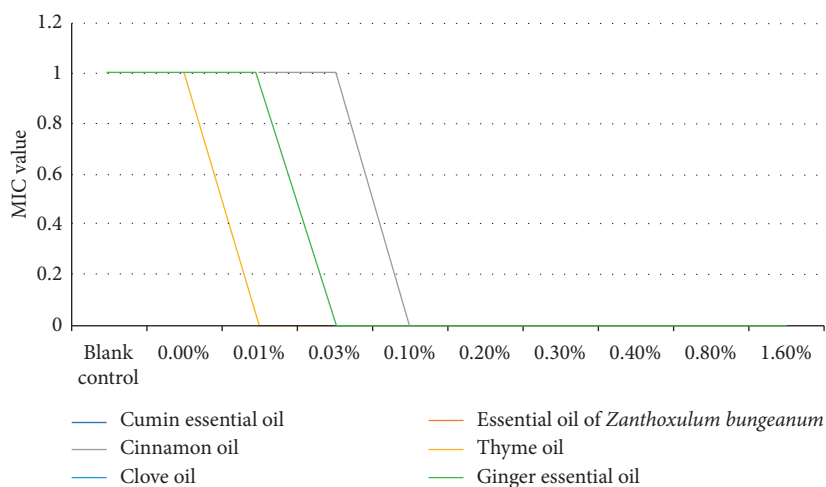


FIGURE 2: Minimum inhibitory concentration of six essential oils.

TABLE 2: Orthogonal experiment table.

Experiment number	Cumin essential oil	Essential oil of <i>Zanthoxylum bungeanum</i>	Cinnamon oil	Clove oil	Thyme oil	Ginger essential oil	Blank	Diameter of bacteriostatic zone 1 (cm)	Diameter of bacteriostatic zone 2 (cm)	Average diameter (cm)
1	1	1	1	1	1	1	1	1.2	1.4	1.3
2	1	2	2	2	2	2	2	1.2	1.2	1.2
3	1	3	3	3	3	3	3	1.5	1.55	1.53
4	2	2	1	2	2	3	3	1.5	1.45	1.47
5	2	2	2	3	3	3	1	1.8	1.5	1.65
6	2	2	3	3	1	2	2	1.5	1.3	1.4
7	3	3	3	1	3	3	2	1.8	1.9	1.85
8	3	3	3	2	1	3	3	1.6	1.6	1.6
9	3	3	3	3	2	2	1	1.8	1.6	1.7
K1	4.30	4.70	4.30							
K2	4.40	4.50	4.5							
K3	5.01	4.6	4.95							
K1	1.45	1.55	1.45							
K2	1.50	1.51	1.51							
K3	1.71	1.55	1.66							
R	0.29	0.07	0.25							

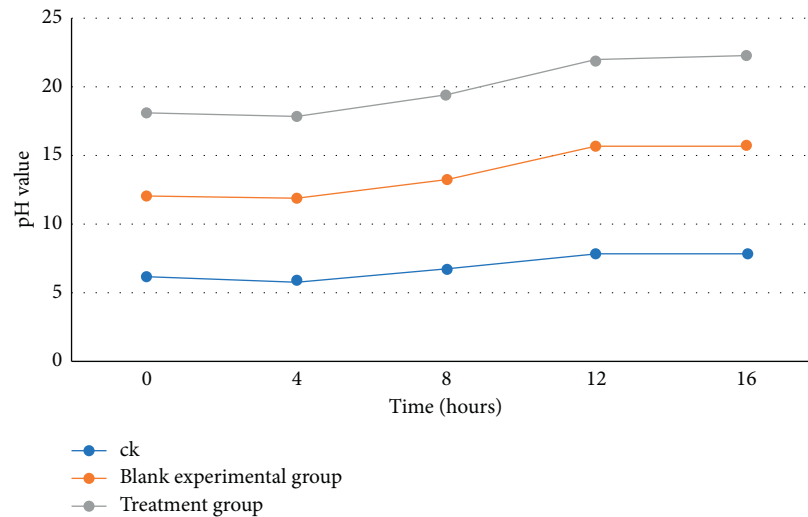


FIGURE 3: pH value of coated beef.

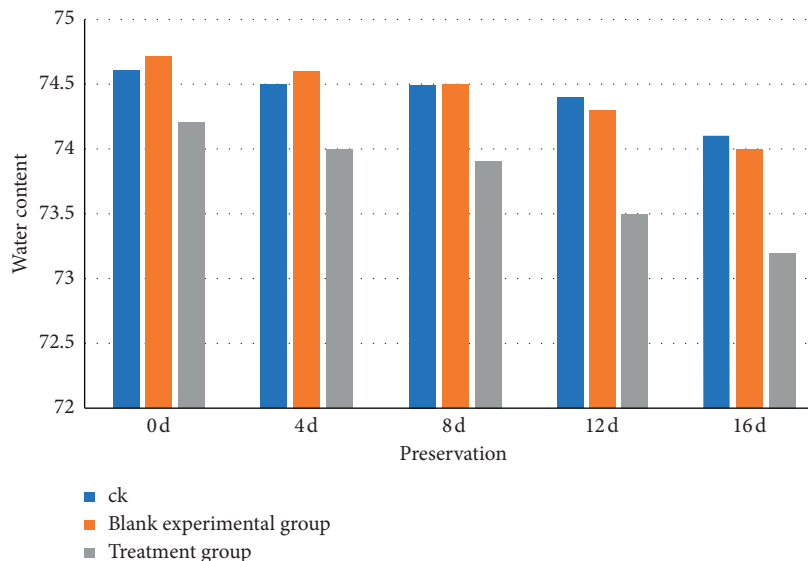


FIGURE 4: Changes of water content of beef after coating preservation treatment.

and phosphoric acid, which makes the pH value of meat decrease. In the process of meat ripening and storage, the endogenous proteases and microorganisms in meat can produce proteolytic enzymes, which can decompose muscle proteins into polypeptides and amino acids and generate basic groups. In this process, the pH value of meat increases. During storage, the pH values of blank group and control group were mostly the same, and the difference between them was not obvious. The pH value of blank group increased to 6.60, which did not conform to the pH value of subfresh meat, and the meat sample of blank group became deteriorated meat. The pH value of the control group increased to 6.60%, and the pH value of the treatment group became 5.89, which was 10.67% and 11.21% lower than that of the blank group and the control group, respectively. The pH value of the two groups was still within the range of the pH value of fresh meat. At the 19th hour, the pH value of the

treatment group changed to 6.21, and the pH value of the control group and the blank group was 7.82 and 7.67, respectively. According to the above experimental results, it can be concluded that the application of plant essential oil to beef samples can adjust the pH value of beef and slow down the protein degradation of beef muscle.

**4.5. Effect of Compound Preservative Solution on Water Content of Beef.** As shown in Figure 4, with the increase of storage time, the water content of the three groups of experimental meat samples decreased, but the difference between the control group and the blank group was small. The difference between the treatment group and the control group and the blank group began to become obvious on the 16th day. In conclusion, the water content of the control group and the blank group did not change significantly. The

water content of the blank group changed by 0.75% from the 0th day to the 16th day and decreased by 0.61% in the control group and 1.11% in the treatment group. Compared with the control group, the dosage of the control group decreased by 10.0%. This may be due to the osmotic effect. After the essential oil was applied to the beef sample, the concentration outside the cell was higher, and the concentration inside the cell was lower, which resulted in the osmotic effect. The water molecule changed from the low concentration part to the high concentration part, and the water molecule transferred from the inside of the cell to the outside of the cell. From the overall situation, the water content of the treatment group decreased the most, but the water content of the three groups of experimental meat samples changed little during the experiment. It can be concluded that the operation of applying plant essential oil to beef has little effect on the moisture content of beef.

## 5. Conclusion

In this article, the application of natural essential oil nanocapsules in cold fresh beef insurance is studied. Through a comparative study of six essential oils of cumin, pepper, cinnamon, thyme, clove, and ginger, a more practical nanopreservation is developed. In this study, chitosan was used as the core material to prepare chitosan natural nanoessential oil. The nanoessential oil capsule was applied to the preservation of chilled beef. It was found that nanocapsule could slow down lipid oxidation in beef and effectively inhibit the growth of microorganisms in beef. By comparing the antibacterial activity of six essential oils, it was found that cinnamon essential oil had the strongest inhibitory effect on bacteria, while ginger essential oil had the worst antibacterial effect. When the MIC concentration of ginger essential oil is higher than 0.09%, ginger essential oil can completely resist the growth of bacteria, so the MIC concentration of cinnamon oil should be set above 0.09%. The best concentration of six essential oils was tested by bacteriostatic effect and other factors: cumin essential oil 0.82%, *Zanthoxylum* content 0.69%, cinnamon essential oil 0.45%, ginger essential oil 0.4%, and thyme essential oil 0.35%. The pH value of fresh meat is 5.7–6.3, and that of other fresh meat is 6.3–6.5. After the experimental treatment, the pH value of the prepared meat is greater than 6.5, and the pH value of the three groups of samples shows a downward trend at first and then increases gradually. Proteases and microorganisms in cooked beef can produce proteolytic enzymes, and the storage time of degraded beef is very short, but plant essential oil can help reduce the degradation rate and prolong the storage time. Compared with the control group, the decrease of beef moisture in the treatment group was 10.51% more than that in the control group and 0.33% more than that in the blank group. Although the application of essential oil has little effect on inhibiting the water loss of beef, it still has a small effect. In this experiment, chitosan natural essential oil nanocapsules were prepared by nanoencapsulation of compound essential oil. This product was applied to the preservation of chilled beef, and the storage time was much better than before,

which provided a theoretical reference for the research of new natural preservatives for chilled beef.

## Data Availability

The data used in this article are available from the corresponding author upon request.

## Conflicts of Interest

The authors declare that there are no conflicts of interest.

## Acknowledgments

This work was supported by the Project of Agricultural Product Quality Safety Risk Assessment of China (No. GJFP202001503) and the Project of Special Funds for Basic Scientific Research Operating Expenses of Public Research Institutes at the Central Level (No. 1610322020019).

## References

- [1] M. Alagupalamuthirsolai, S. J. Ankegowda, M. Murugan, R. Sivaranjani, B. Rajkumar, and H. J. Akshitha, "Influence of light intensity on photosynthesis, capsule yield, essential oil and insect pest incidence of small cardamom (*Elettaria cardamomum* (L.) Maton)," *Journal of Essential Oil Bearing Plants*, vol. 22, no. 5, pp. 1172–1181, 2019.
- [2] N. Wang, X. T. Wang, Z. D. Wang, and W. Ding, "Effect of electron beam irradiation dose on the quality of vacuum-packaged chilled fresh beef," *Modern Food Ence and Technology*, vol. 31, no. 7, pp. 241–247, 2015.
- [3] E. Oberhofnerová, M. Pánek, and M. Bhm, "Effect of surface pretreatment with natural essential oils on the weathering performance of spruce wood," *Bioresources*, vol. 13, no. 3, pp. 7053–7070, 2018.
- [4] H. Gong, Z. Yang, M. Liu et al., "Time-dependent categorization of volatile aroma compound formation in stewed Chinese spicy beef using electron nose profile coupled with thermal desorption GC-MS detection," *Food Science and Human Wellness*, vol. 6, no. 3, pp. 137–146, 2017.
- [5] J. Mehrdad, G. Ahmad, A. K. Omid, and A. Shima, "Improving postharvest vase-life and quality of cut gerbera flowers using natural and chemical preservatives," *Journal of Central European Agriculture*, vol. 16, no. 2, pp. 199–211, 2015.
- [6] S. S. García, E. C. Hellen, A. Manuel, M. Gracia, and I. Silvia, "Evaluation of the antimicrobial activity and cytotoxicity of different components of natural origin present in essential oils," *Molecules*, vol. 23, no. 6, p. 1399, 2018.
- [7] M. Dmitruk, A. Sulborska, B. Żuraw, E. Stawiarz, and E. Weryszko-Chmielewska, "Sites of secretion of bioactive compounds in leaves of *Dracocephalum moldavica* L.: anatomical, histochemical, and essential oil study," *Brazilian Journal of Botany*, vol. 42, no. 4, pp. 701–715, 2019.
- [8] A. Bezysov, H. Dubova, and N. Rogova, "New methods of plant selection for food aroma recovery aided by oxidation processes," *Acta Universitatis Cibiniensis. Series E: Food Technology*, vol. 19, no. 2, pp. 15–26, 2015.
- [9] L. M. Xia, L. L. Cui, Y. L. Jiang et al., "Meta-analysis of clinical efficacy of traditional Chinese medicine in the treatment of aplastic anemia," *World Journal of Traditional Chinese Medicine*, vol. 3, no. 4, pp. 457–467, 2017.

- [10] Y. Yuan, M. F. Li, W. S. Chen et al., "Microencapsulation of shiitake (*Lentinula edodes*) essential oil by complex coacervation: formation, rheological property, oxidative stability and odour attenuation effect," *International Journal of Food Science & Technology*, vol. 53, no. 7, pp. 1681–1688, 2018.
- [11] H. Rezaeinia, B. Ghorani, B. Emadzadeh, and N. Tucker, "Electrohydrodynamic atomization of balangu (*Lallemantia royleana*) seed gum for the fast-release of *Mentha longifolia* L. essential oil: characterization of nano-capsules and modeling the kinetics of release," *Food Hydrocolloids*, vol. 93, pp. 374–385, 2019.
- [12] B. Grzesiak, B. Kołodziej, G. Anna, and H. Krukowski, "The effect of some natural essential oils against bovine mastitis caused by *Prototheca zopfii* isolates in vitro," *Mycopathologia*, vol. 183, no. 4, pp. 1–10, 2018.
- [13] M. Mahboubi, "Management of acute cough by *Zataria multiflora* boiss as an alternative treatment," *Journal of Integrative Medicine*, vol. 16, no. 1, pp. 20–25, 2018.
- [14] M. M. Elghandour, M. Z. Salem, R. Greiner, and A. Z. Salem, "Effects of natural blends of garlic and eucalypt essential oils on biogas production of four fibrous feeds at short-term of incubation in the ruminal anaerobic biosystem," *Journal of the Science of Food and Agriculture*, vol. 99, no. 2, pp. 967–968, 2019.

## Research Article

# Compatibility of Carbon Composite Biomaterials for Repairing Bone Tissue Injury in Wushu Training

Jingfeng Ren 

*Department of Sports, Henan University of Technology, Zhengzhou 450000, Henan, China*

Correspondence should be addressed to Jingfeng Ren; renjinfeng1986@haut.edu.cn

Received 12 August 2020; Revised 9 September 2020; Accepted 22 September 2020; Published 17 November 2020

Academic Editor: Tifeng Jiao

Copyright © 2020 Jingfeng Ren. This is an open access article distributed under the Creative Commons Attribution License, which permits unrestricted use, distribution, and reproduction in any medium, provided the original work is properly cited.

With the improvement of economic level, more and more people begin to pursue a healthy lifestyle, among which sports have become an important way of modern people's sports, but in the process of sports, there will inevitably be some injuries, especially in martial arts training, and bone is the most vulnerable part. Because of the special physiological characteristics of cartilage tissue, it is difficult to recover after injury. This problem has become the main health problem in real life, which greatly affects people's health and quality of life. At present, the technology of carbon composite biological nanomaterials is more and more mature, and the bioactive composite materials are composed of polymers and bioactive components, which have very good biocompatibility. In recent years, the bioactive composite materials have been applied to clinical practice and achieved very good results. Based on this, this paper considers linking the bioactive carbon composite biomaterials with the recovery of bone tissue damage, and according to the biocompatibility of bioactive composite materials, it is applied to the repair of bone tissue injury in clinical practice. In this paper, two kinds of carbon composite biomaterials, calcium carbonate composite and graphene composite, were synthesized by electrochemical method and photocatalytic reduction method. The crystal of calcium carbonate complex and graphene composite was extracted by changing the experimental time and the parameters of the solution in the experiment, and then the two carbon composite materials were analyzed as biomineralization complex biocompatibility, cell growth, and cell activity of the complex as a drug carrier for bone tissue injury. The experimental results show that the two kinds of carbon composite biomaterials can provide a very good interface for cell adhesion and spreading. This experiment proves that the artificial bone made of carbon composite biological nanomaterials has good biocompatibility, and the biocompatibility of carbon composite biological nanomaterials can be directly applied to clinical bone tissue repair surgery.

## 1. Introduction

Nanotechnology refers to the study of the characteristics of the laws of motion of electrons, atoms, and molecules and processes materials and materials in the range of 0.1 to 100 nanometers [1]. The size of nanomaterials is closely related to organisms. For example, the linearity of the RNA protein complex, which is one of the life elements, is between 15 and 20 nm, and the size of various viruses in organisms is also in the nanorange. Nanobiomedical materials are the intersection of nanomaterials and biomedical materials. Nanoparticles are combined with other materials to make various composite materials. With the deepening of research and the development of technology, nanomaterials have begun to penetrate into many disciplines, showing

great potential application value, and have obtained preliminary application in some fields [2]. In recent years, the theoretical and experimental research of biological nanomaterials has become the focus of attention, especially the biochemistry, biophysics, and biomechanics of nucleic acids and proteins, and their intelligent composites have become the frontier of interdisciplinary subjects of life science and materials science. Carbon nanomaterials are carbon materials with at least one dimension less than 100 nm on the dispersed phase scale. There are three types of carbon nanomaterials: carbon nanotubes, carbon nanofibers, and carbon nanospheres. Carbon element is one of the most closely related elements in nature, and in recent years, the research of carbon nanotechnology is more and more, a variety of carbon nanotransistors and

sensors emerge endlessly, and carbon nanotechnology is widely used in many fields [3, 4].

Bone defect mainly includes bone defect and defect repair. The bone defect is a common clinical disease and one of the prominent problems in orthopedic treatment. Bone tissue injury belongs to cartilaginous injury. Soft tissue contusion is the injury of muscle, ligament, and other tissues as well as peripheral nerves and blood vessels. These tissues are affected by different internal and external damage factors, leading to tissue damage and tissue physiological dysfunction [5]. Soft tissue injury is usually affected by the pressure of external mechanism. When it reaches certain strength, it will cause injury and produce symptoms. Generally, it can be divided into acute injury and chronic cumulative injury. When soft tissue becomes blunt or severely injured by violence, it may lead to local soft tissue contusion and laceration. Soft tissue injury is a common disease in human motion system. Due to acute injury and chronic cumulative injury, soft tissue injury can lead to different conditions and degrees of symptoms of neck, shoulder, back, and waist, legs, and limbs. In recent decades, it has been found that a large part of diseases originates from soft tissue muscles and ligaments, nerves, blood vessels, etc., which directly cause great damage [6]. Tissue repair refers to the repair and replacement of local tissues and cells caused by pathogenic factors. These pathogenic factors lead to injury and death through the regeneration of adjacent healthy cells and restore tissue integrity. Soft tissue injury repair technology begins with human anatomy and physiopathology. The physiological and pathological changes of soft tissue in the lesion site are observed and analyzed visually, the target is accurately located, and the lesion tissue is completely repaired by manual operation. The damaged tissue can return to its normal state and relieve the pain completely. There are three stages in the repair and repair process of soft tissue injury repair technology: local inflammatory reaction stage, cell proliferation and differentiation and granulation tissue formation stage, and tissue repair and shaping stage. The repair process after injury mainly depends on the fibroblasts in the loose connective tissue inside the tendon. These cells will proliferate and synthesize collagen. Due to excessive secretion, it also fills the tissue gap of tendon (internal ligament) and finally forms collagen fiber, which makes tendon and ligament degenerate and harden.

Bionics is science applied and realized in engineering. Bionics is a scientific method to construct technical systems by imitating the functions and behaviors of all systems in the biological world. It breaks the boundary between biology and machines and conveys various systems [7–9]. Our ancestors imitated the birds flying in the sky, invented the plane, imitated the animals in nature, and invented the car, radar, and so on. The development of modern civilization is inseparable from the science of bionics. In 2019, a Swiss researcher developed a kind of bionic artificial leg, which allows patients to contact naturally, and does not need the brain to control walking all the time. The purpose of bionics is to analyze biological processes and structures and their analysis for future design purposes. The idea of bionics is

based on natural evolution and coevolution. Human technology is optimized and coordinated with each other. It is undoubtedly a good opportunity to simulate the adaptive function of organisms to the environment. The research scope of bionics includes mechanical bionics, molecular bionics, energy bionics, and information technology control bionics. The bionics studied in this paper is carbon composite biological nanomaterials. It imitates the human learning process and creates a machine called “perceptron.” The machine can learn and change the weight of the connection between components through training, so as to realize pattern recognition. In addition, it also studies and simulates the control mechanisms in biological systems, such as dynamic balance, motion control, animal orientation and navigation, and bionics of man-machine systems [10].

Biocompatibility refers to the reaction characteristics of organisms to nonactive substances and usually refers to the compatibility between the substances and the main body. After implanting biomaterials into the human body, they will have an impact and effect on the specific biological tissue environment, the biological tissue will also have an impact and effect on the biomaterials, and the circulation between the two will continue until the balance is reached or the implants are removed [11]. Biocompatibility has always been a theme in the research of biomaterials. Biocompatibility mainly depends on the nature and use of the material. The properties of materials and products, including shape, size and surface roughness, residual toxic low molecular substances during polymerization or material preparation, pollution of material processing technology, degradation products of materials in vivo, etc., are all related to the properties of materials and substances. Short-term contact with the human body will produce toxicity, irritation, teratogenicity, and local inflammation to cells and the whole body. Long-term exposure may have mutagenic, teratogenic, and carcinogenic effects, and abnormal coagulation and hemolysis will be caused by blood contact. Therefore, biocompatibility is an important index to be considered and evaluated when considering the use of materials in the biomedical field. In this paper, it was confirmed that the activation of peripheral blood mononuclear cells by carbon composite biomaterials was small. Carbon composite biomaterial technology is helping to improve the immune compatibility, mechanical properties, and biocompatibility of cartilage. This work can solve the problem of biocompatibility between soft tissue repair and carbon composite biomaterials. It is suitable for clinical practice and has important research value and application value.

## 2. Electrochemical Synthesis of Calcium Carbide Complex

Calcium carbonate is an inorganic mineral widely existing in nature and an important component of bone tissue. Due to the diversity of calcium carbonate forms, crystal morphology is easy to control in the process of biomineralization [12]. Generally, the technology of calcium carbonate is to synthesize the chitosan calcium carbonate denuded shell structure by layered deposition method and immerse the

prepared chitosan membrane in calcium chloride solution to form chitosan and calcium carbonate film in the CO<sub>2</sub> atmosphere. However, the mechanical properties of the composites prepared by the above methods are not high and the preparation process is complex, which limits its application as scaffold materials. Therefore, in this part of the experiment, we use the electrochemical method, which is not only simple but also highly efficient. We control the number of reactants and electrochemical parameters to realize the carbon composite biological nanomaterials composite. Because of its good biocompatibility, nanotechnology provides a very good theoretical framework for cell culture and bone tissue repair.

**2.1. Main Reagents of Experimental.** The main reagents used in experiments and tests are listed in Table 1.

**2.2. Main Instruments of Experimental.** The main instruments of experimental and equipment used in experiments and tests are listed in Table 2.

**2.3. Preparation of Calcium Carbide Complex.** Hydroxyapatite is the main inorganic component of albumin in bone tissue. It has good biocompatibility and high bioactivity and can form a chemical bond with bone tissue. However, the brittleness and processing difficulty of hydroxyapatite restrict its industrial application. Polycaprolactone (PCL) is a biodegradable polyester material with good biocompatibility and physical and mechanical properties but lacks biological activity [13]. Natural bone is mainly composed of nano HA and collagen, which can be considered as a dual-phase composite material containing nanocrystals. Therefore, from the perspective of bionics, the combination of matrix and hydroxyapatite with organic polymer composites, especially the preparation of degradable polymers, can enhance the secondary performance, develop the advantages and avoid the disadvantages, and learn from each other to obtain the ideal bone repair materials.

In this experiment, nano calcium carbonate was modified by the wet method. The slurry with a solid content of 20% was prepared by adding 5 g nano calcium carbonate and anhydrous ethanol into a three-port flask. After ultrasonic vibration for 30 minutes, 10% silane coupling agent KH-570 (i.e., calcium carbonate mass) was added at 80°C, then mechanically stirred for 1.5 hours, and then filtered and washed. Finally, the modified nano calcium carbonate was prepared by vacuum drying, grinding, and sieving. Then, 0.100 g chitosan was added to the solution of 45 ml microcomputer controlled electronic universal testing machine, the pH value was adjusted to 3 as mixed acid, and then ultrasonic dispersion ultrasonic instrument was used for 2 h. Finally, a certain amount of licio 4 was added for ultrasonic dispersion for 2 h. An appropriate size of stainless steel iron was cut, washed in anhydrous ethanol or distilled water, and finally blow-dried with nitrogen for standby. A three-electrode, namely, Ag-AgCl electrode, Pt electrode, and stainless

TABLE 1: Main reagents of experimental.

Experimental reagent	Main functions
Nano calcium carbonate	Particle size is 40 nm–60 nm
Deionized distilled water	Made in laboratory
Anhydrous ethanol	Analytical pure
Coupling agent KH-570	Analytical pure
Methyl methacrylate (MMA)	Analytical pure, refining before use
Azodiisobutyronitrile (AIBN)	Analytical pure
Concentrated sulfuric acid	Analytical pure
Anhydrous calcium carbonate	Analytical pure
Ammonium carbonate	Analytical pure
Potassium permanganate	Analytical pure

steel iron sheet was prepared. The dry stainless steel shoe was used as the working electrode. The electrochemical material solution parameters, electrochemical voltage parameters, and time by cyclic voltammetry were adjusted, and finally, calcium carbonate complex was got.

Using the same preparation, separation, and purification methods mentioned above, the control experiment of extracting calcium carbonate complex crystal from pure water without adding licio 4 was carried out. Sodium carbonate solution and calcium chloride solution were mixed in equal volume to form calcium carbonate crystal through a chemical reaction. During the experiment, the reaction time of calcium carbonate crystal was changed. The reaction time was 2 hours, 6 hours, 12 hours, 1 day, 2 days, 4 days, and 7 days.

**2.4. Performance Representation.** Dissolution test: a certain amount of pure PMMA samples and nanocomposite materials with different calcium carbonate contents were put into a single port flask containing chloroform for 3D-4D to observe the dissolution rate, and scanning electron microscope observation and analysis: the cross-section of the composite was sprayed with gold, and the cross-section morphology was observed by scanning electron microscopy (SEM).

FT-IR analysis: after the sample and KBr powder were pressed, the composition changes were analyzed and studied.

Mechanical property test of composite materials: 100D electronic universal testing machine controlled by computer was used to test bending strength and tensile strength according to GB 1039–1992, and the impact strength test was conducted by JB 6 impact testing machine according to GB 1039–1992.

### 3. Study on Graphene Calcium Carbide Complex

Graphene is a kind of two-dimensional carbon nanomaterials. It is a hexagonal honeycomb lattice composed of carbon atoms of SP hybrid orbitals. Graphene has good solubility in nonpolar solvents, and it can also adsorb and desorb various atoms and molecules [14–16]. The PZ orbitals

TABLE 2: Main instruments used in the experiment.

Experimental apparatus	Supplier
Computer-controlled electronic universal testing machine (100D)	Jinan test Gold Group Co., Ltd.
Impact testing machine (JB6)	Wuzhong Material Testing Machine Factory
Scanning electron microscope	Japan Electronic Optics Corporation
FT-IR Fourier transform infrared spectrometer	Nicolet, USA
Kq118 ultrasonic cleaner	Kunshan Ultrasonic Instrument Co., Ltd.
JA2003N electronic analytical balance	Shanghai Precision Scientific Instrument Co., Ltd.
CO <sub>2</sub> incubator	Shimadzu, Japan
Ultra clean table	Suzhou Purification Scientific Instrument Factory
Vacuum dryer	Shanghai Yiheng Scientific Instrument Co., Ltd.
General purpose desktop centrifuge	German Sigma Company

perpendicular to the plane of each carbon atom form a large polyatomic bond throughout the carbon layer, which provides excellent electrical and optical properties. Graphene has good toughness and can be bent, but the graphite paper composed of graphene has a lot of holes, so the graphite paper is very fragile. However, after oxidation to get functional graphene, and then from the functionalized graphene to make graphite paper, it will be very solid and reliable. Compared with carbon nanotubes, graphene is more suitable for the study of biomaterials. The edge of graphene is longer, which is easier to be doped and chemically modified than carbon nanotubes. It is easier to accept functional groups and has better biocompatibility. In addition, the structure of graphene is very stable, and the carbon bond is only 1.42, so the force between atoms is very strong. At room temperature, even if the surrounding carbon atoms collide, the interference of electrons inside graphene is very small [17, 18]. The research and application of graphene at high temperatures makes graphene applied in many fields and has made a series of progress in chemistry, materials, biology, and semiconductor. So, it is necessary to study graphene. In terms of biology, graphene has been used to accelerate the osteogenic differentiation of human bone marrow mesenchymal stem cells, and the epitaxial graphene on silicon carbide is used to make biosensors. Graphene can also be used as a nerve interface electrode without changing or destroying the signal strength or scar tissue formation. Due to the flexibility [19], biocompatibility, and conductivity of the graphene electrode, the stability is much higher than that of the tungsten electrode or silicon electrode. Graphene oxide can effectively inhibit the growth of *E. coli* without harming human cells. However, the industrialization of graphene is still in the early stage, and some applications are not enough to reflect the "ideal" properties of graphene. However, many researchers around the world are exploring the application of "killer mace." In the future, graphene will face many challenges in the detection and certification work, so we still need to innovate in means and methods.

**3.1. Preparation of Graphene Composites.** The experimental instruments and reagents in this part of the experiment are shown in Tables 1 and 2.

Graphene nanocomposites were prepared by the photocatalytic reduction method. Graphene and tetra butyric acid were used as raw materials, and sodium dodecylbenzene

sulfonate and polyethylene glycol were used as surfactants. Ethanol, glacial acetic acid, deionized water, and ammonium nitrate were selected as solvents, and the volume ratio was 20:1:1:0.2. Graphite oxide was added to TiO<sub>2</sub> colloid obtained by hydrolysis of isopropyl titanium, and nano-graphite oxide dispersion was obtained by ultrasonic treatment. Finally, graphene nanocomposites were obtained by reducing graphite oxide under UV irradiation. Due to the strong conjugation between trimethylene and graphene, the derivatives of trimethylene can be easily grafted onto graphene. Without destroying the internal structure of graphene, the dispersion of graphene in organic solvents can be effectively improved. It provides the conditions for further functionalization and application of graphene. Firstly, the surface of polyethylene was treated with a cationic surfactant solution, filtered and dried to obtain the surface treated polyethylene powder. The surface-treated polyethylene powder was dispersed and stirred to obtain the mixture. The mixture was sprayed and dried at high temperatures to obtain polyethylene graphene mixture powder. Finally, the mixed powder was added to hydrazine hydrate solution, reduced, washed, and dried to obtain the stone graphene composites.

**3.2. High-Temperature Modification of Graphene Composites.** Modification of graphene oxide dispersion in water: graphite oxide prepared by the Hummers method was dispersed in water for ultrasonic treatment, and hydrazine hydrate was added at 100°C. The partially reduced graphite oxide was prepared, and then the partially reduced graphite oxide was treated with epoxy resin/hardener (4:1) acetone solution and stirred for several hours. After the reaction, the graphite oxide was dried to a suitable shape at 60°C and annealed in nitrogen at 250°C for 2 h to completely reduce the unreduced graphite oxide, so as to improve its conductivity. Finally, the electromagnetic shielding effect of graphene/epoxy resin composite is less than or equal to 21 dB, which basically meets the commercial application requirements of 20 dB [17].

Modification of graphene oxide by manganese dioxide: in this method, graphene was prepared by an improved Hummer method, and the mixture of graphene and manganese dioxide was prepared by Yanjing microwave method. The mixture of graphene and manganese dioxide was prepared by a redox reaction. Firstly, 100 ml and 1.65 mg/ml

graphene solution was prepared by ultrasonic wave for 1 h. 95 g potassium permanganate was added to the ultrasonic graphene solution and stirred for 10 min. Then, the stirred solution was heated in a microwave oven for 5 minutes, cooled to room temperature, washed with deionized water and absolute ethanol several times, and finally dried in a drying oven at 100°C for 12 hours. This method is a low cost, suitable for mass production, and has practical significance. The electrochemical test shows that the impedance curve of the mixture of graphene and manganese dioxide is a typical electrochemical characteristic curve. With the decrease of frequency, the impedance curve gradually becomes diffusion control. In addition, the capacitor formed by the electrode also has good electrochemical capacitance characteristics. The first charge-discharge ratio is 237 F/g, which is higher than that of graphene or nano manganese dioxide prepared by traditional methods.

Sodium borohydride was used to modify graphene: firstly, carboxyl and carbonyl groups around graphene were used together with sodium borohydride and then reacted with *p*-aminobenzene sulfonic acid in an ice bath for 2 h, and then the sulfonic group was grafted onto graphene oxide and then reduced with hydrazine at 100°C for 24 h. The solubility of layered graphene in water was 2 mg/ml.

## 4. Results Analysis

**4.1. Biocompatibility of CaCO<sub>3</sub> Composites.** In this experiment, in order to further study the biocompatibility of CaCO<sub>3</sub> composites, we tested MC3T3 cells in different time periods; the time selected is 2 hours, 6 hours, 12 hours, 1 day, 2 days, 4 days, and 7 days. The growth of cells was observed at different time periods. The control experiment used in this paper was the cell active cell and growth experiment on the blank stainless steel sheet. The experimental group was to observe the growth of cells on cnt-CaCO<sub>3</sub> composite material. The experimental results are shown in Figure 1.

As we all know, the MTT method can reflect the number of cells indirectly. With the prolongation of culture time, the cell activity of both groups was improved, but the cell activity of CaCO<sub>3</sub> composite material was significantly enhanced, which indicated that calcium carbonate nanocomposite could promote cell growth and proliferation. It can be seen from Figure 1 that the cell activity on stainless steel sheet and CaCO<sub>3</sub> composite material has little difference, less than 0.05, at two hours after the experiment. However, with the growth of time, after 12 hours, the growth of cells on the stainless steel sheet began to be significantly lower than that on the CaCO<sub>3</sub> composite. On the fourth day, the cell activity on the CaCO<sub>3</sub> composite was more than twice that of the blank stainless steel sheet. On the seventh day, the difference was more. The cell activity on the stainless steel sheet was only 0.3, but the activity on CaCO<sub>3</sub> composite was 0.8. The results show that carbon nanotubes prepared by this method are simple and effective nanocomposites, which can promote the growth and proliferation of cells.

Next, we analyze the growth trend of cell activity on CaCO<sub>3</sub> composite and stainless steel sheet.

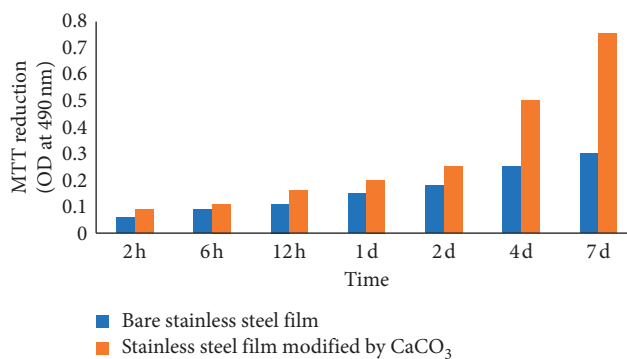


FIGURE 1: MTT comparison of cells on stainless steel sheet and CaCO<sub>3</sub> composite at different culture time periods.

The MTT growth trend of cells on stainless steel sheet and CaCO<sub>3</sub> composite materials during the experiment can be seen in Figure 2. It can be seen from Figure 2 that in the experiment on CaCO<sub>3</sub> composite, the cell activity has been increasing, the maximum value of cell activity is 1, the minimum value is 0, the cell growth rate is very fast, and the slope of the straight line is also increasing between the two adjacent times. On the seventh day of the experiment, the cell activity had reached 0.8, but our experiment only lasted for a week. It is believed that in the next two days, the cell activity can reach nearly 100%. On the contrary, the cell activity on the stainless steel sheet is also increasing, but the increasing rate is slower than that on the CaCO<sub>3</sub> composite. On the first day, the difference between the two is smaller, but with the increase of experimental time, the gap between the two is also growing. In particular, at the end of the experiment, the slope of cell activity on the stainless steel plate in the adjacent time was getting smaller. This result is consistent with our previous conjecture. Through the experimental comparison, we can see that the biocompatibility between cells and CaCO<sub>3</sub> composites is good, which can be widely used in clinical practice. It is this kind of bioactive inorganic material that forms graphene, which makes calcium carbonate composite have good biocompatibility and can be a potential bone repair material.

**4.2. Biocompatibility of Graphene Composites.** The biocompatibility of graphene composites is determined by its molecular structure. This is because the edge of the graphene molecular structure is longer, it is easier to doping and chemical modification than carbon nanotubes, and it is easier to accept functional groups, so it has better biocompatibility. We analyzed the biocompatibility of graphene composites and observed cell growth and cell activity on graphene composites.

0.1 mol/l H<sub>3</sub>PO<sub>4</sub> buffer (PBS, pH = 7.4) was used as the supporting electrolyte. CV was used in all electrochemical experiments. Ag-AgCl electrode was used as a reference electrode, platinum electrode as a counterelectrode, and God/AuNPs/chit/GNS/GC as a working electrode. Before the experiment, 8 ml PBS buffer was put into a small beaker and reduced with high purity nitrogen for 30 min. During

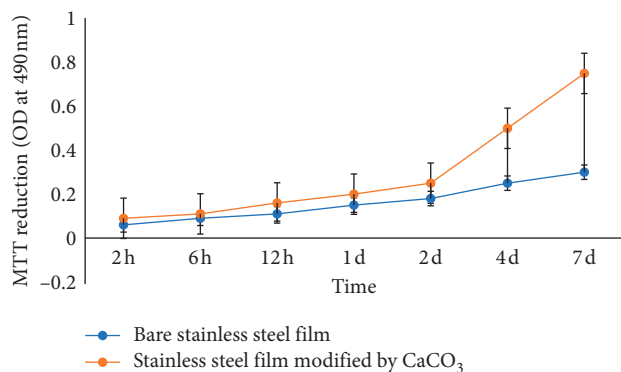


FIGURE 2: MTT growth trend of cells on stainless steel sheet and CaCO<sub>3</sub> composite at different culture time periods.

the experiment, the N<sub>2</sub> saturated atmosphere was maintained in the small beaker.

According to the change of cell activity on graphene shown in Figure 3, with the increase of time, the cell activity increases in Figure 3 are a network graph, and the scale of each net represents 0.2. From the graph, we can see an obvious change between the experiment for two hours and seven days. The cell activity changes from 0.2 to 0.8 directly, indicating that graphene has good biocompatibility.

The advantage of this experiment is that there is no special requirement for the template, catalyst, surfactant, and other special materials. Graphene has good biocompatibility, bioactivity, and diversity. We hope to apply it to cell adhesion, in vitro cell culture, tissue compatibility scaffold, nanobiosensor, and other medical fields.

It can be seen from Figure 4 that after the experiment, the proportion of total cell activity in carbon composite materials and stainless steel iron sheet is 4:1, which indicates that the growth rate of cells in carbon composite materials is faster, which is the same as the experimental hypothesis. Under the action of strong acid and oxidant, carboxyl groups and hydroxyl groups are introduced on the surface and both ends of carbon nanotubes. In the process of preparing carbon nanotubes calcium carbonate composites, the carboxyl groups on the wall of carbon nanotubes combine with calcium ions in CaCl<sub>2</sub>. Due to the presence of CO<sub>3</sub><sup>2-</sup>, calcium ions are easy to form calcium carbonate, which is mainly controlled by diffusion. With the development of electrochemical reaction, the acidity of the electrolyte increases with the release of H<sub>2</sub>. The surface of the working electrode is covered with more calcium ion carbon nanotubes, which weakens the repulsion force of the electric field to carbonate, indirectly promotes the diffusion of CO<sub>3</sub><sup>2-</sup> calcium ion, and accelerates the formation of calcium carbonate. This indicates that CO<sub>3</sub><sup>2-</sup> provides a good environment for cell growth and diffusion and promotes the further proliferation and differentiation of fine cells. The growth of cells on the surface of carbon nanotubes/calcium carbonate composite is obviously better than that of the blank stainless steel sheet, and this advantage is more obvious with the extension of culture time. This experiment shows that the composite has a good promotion effect on cell growth.

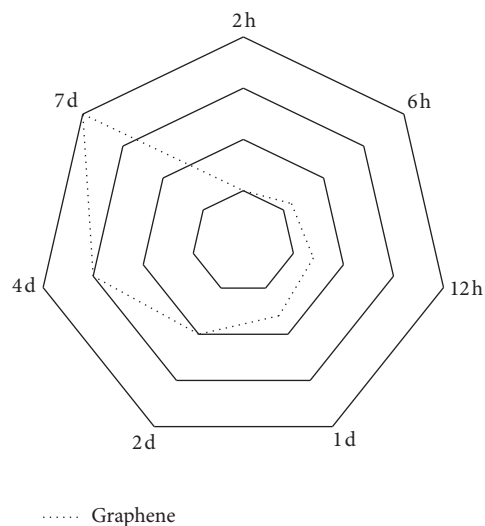


FIGURE 3: Changes of cell activity on graphene.

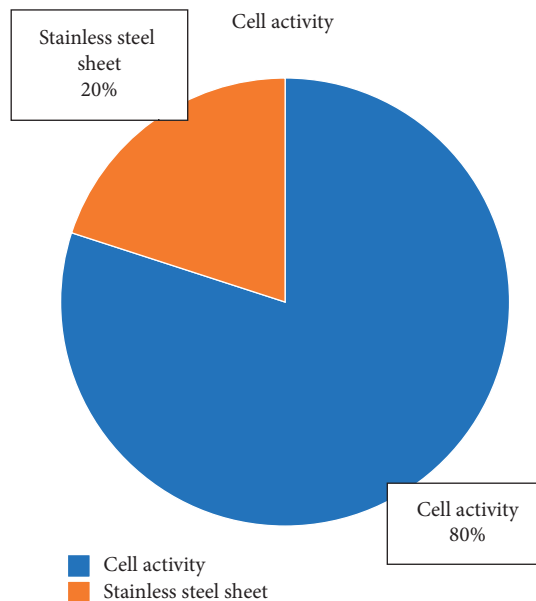


FIGURE 4: Proportion of total cell activity in carbon composites and stainless steel iron sheets.

## 5. Conclusions

In this paper, two carbon composite models, calcium carbonate composite and graphene composite, were established by using carbon composite as a template. The biocompatibility, cell growth, and cell activity of two kinds of carbon composites as a biomineralization complex as a drug carrier for bone tissue injury were studied. In this experiment, carbon composite materials were extracted by a one-step electrochemical method. The method is simple and fast and only needs to change the time and solution parameters. Under the effect of the electric field, positively charged chitosan moves to the cathode and forms calcium carbonate complex crystal on the stainless steel plate. The extraction of

graphene carbon composites by photocatalytic reduction method can be understood as the solubility of carbon composites in aqueous solution depends on the pH value of the solution. Nanocarbon composite scaffolds can promote the adhesion and proliferation of bone marrow mesenchymal stem cells, promote the secretion of osteoblasts in the extracellular matrix, and enhance the calcification of tissue-engineered bone. In microenvironment, it is more conducive to the economic growth and differentiation of bone marrow mesenchymal stem cells and promotes and accelerates the regeneration and repair of bone tissue injury. Bone tissue engineering is developing rapidly in the field of sports medicine supporting the quality of treatment. With the continuous development of composite material research and the continuous improvement of artificial bone material production technology, the structure, performance, and various biological activities of biomedical materials similar to human tissue can be obtained in future research centers, which brings new hope for the development of artificial bone repair materials for bone defect repair. The experiment in this paper also proved that the carbon composite biomaterial has very good biocompatibility in the repair of bone tissue injury, which can be applied to clinical practice.

### Data Availability

No data were used to support this study.

### Conflicts of Interest

The authors declare that they have no conflicts of interest.

### References

- [1] X. He, "Basic research on the compatibility of composite biomaterials in the repair of bone tissue injury," in *Proceedings of the Abstracts Compilation of the 11th National Sports Science Conference*, vol. 10, no. 4, pp. 97–110, Washington, DC, USA, November 2019.
- [2] M. Lu, H. Li, Y. Wang et al., "Research on mechanical properties and tissue compatibility of carbon fiber reinforced nano-hydroxyapatite/polyamide 66 composites," *China Tissue Engineering Research*, vol. 156, no. 78, pp. 727–757, 2015.
- [3] S. Wu, "Construction of chitin/carbon nanotube composite material and its application in biomedicine," *Chinese Journal of Tissue Engineering Research*, vol. 741, no. 4, pp. 9–19, 2017.
- [4] S. Zhang and B. Wang, "Synthetic biodegradable nerve catheter to repair injured peripheral nerve: good biocompatibility," *Chinese Journal of Tissue Engineering*, vol. 19, no. 25, pp. 4054–4058, 2015.
- [5] Y. Lou, Z. Pan, R. Wu et al., "Biocompatibility of  $\alpha$ -calcium sulfate hemihydrate composite functionalized multi-walled carbon nanotube bone repair materials," *Journal of Bioengineering*, vol. 124, no. 3, pp. 85–93, 2018.
- [6] W. Zhang, "Controllable construction and biocompatibility of biomimetic calcium carbonate nanocomposites," *Journal of Bioengineering*, vol. 45, no. 12, pp. 85–93, 2018.
- [7] Z. Ma, "Research hotspots of tissue engineering cartilage scaffold materials and repair of cartilage sports injuries," *China Tissue Engineering Research and Clinical Rehabilitation*, vol. 2, no. 22, pp. 185–193, 2018.
- [8] X. Dou, H. Cai, Q. Li et al., "Biomimetic synthesis and cell compatibility study of HA-PEC nanocomposite bone repair materials," *National Academic of Bio Composites*, vol. 45, no. 22, pp. 422–435, 2019.
- [9] T. Guo, T. Yang, J. Wu et al., "In vivo experiments to evaluate the biocompatibility of the new articular cartilage repair material polyvinyl alcohol/nanohydroxyapatite polyamide 66," *China Tissue Engineering Research*, vol. 12, no. 1, pp. 31–34, 2018.
- [10] M. Chen and F. Wu, "Artificial composite bone in repairing bone defects," *China Tissue Engineering Research*, vol. 11, no. 48, pp. 9797–9800, 2017.
- [11] X. Yang, X. Chen, and H. Wang, "Acceleration of osteogenic differentiation of PR osteoblastic cells by chitosan containing nanofibrous scaffolds," *Biomacromolecules*, vol. 10, no. 10, pp. 2772–2778, 2009.
- [12] R. Y. Zhang and P. X. Ma, "Synthetic nano-fibrillar extracellular matrices with predesigned microporous architectures," *Journal of Biomedical Materials Research*, vol. 52, no. 2, pp. 430–438, 2000.
- [13] H. Wang, Y. Li, Y. Zuo, J. Li, and S. Ma, "Biocompatibility and osteogenesis of biomimetic nano-hydroxyapatite/polyamide composite scaffolds for bone tissue engineering," *Biomaterials*, vol. 28, no. 12, pp. 3338–3348, 2007.
- [14] M. H. Ho, D. M. Wang, H. J. Hsieh et al., "Preparation and characterization of RGD-immobilized chitosan scaffolds," *Biomaterials*, vol. 26, no. 3, pp. 197–206, 2005.
- [15] J. Lee, Y. Choo, J. E. Choi et al., "Effect of immobilized cell-binding peptides on chitosan membranes for osteoblastic differentiation of mesenchymal stem cells," *Biotechnology and Applied Biochemistry*, vol. 52, no. 45, p. 69, 2009.
- [16] C. Y. Hsieh, S. P. Tsai, M. H. Ho et al., "Analysis of freeze-gel ion and cross-linking processes for preparing porous chitosan scaffolds," *Carbohydrate Polymers*, vol. 67, no. 1, pp. 124–132, 2004.
- [17] Q. Hu, B. Li, M. Wang, and J. Shen, "Preparation and characterization of biodegradable chitosan/hydroxyapatite nanocomposite rods via in situ hybridization: a potential material as internal fixation of bone fracture," *Biomaterials*, vol. 25, no. 5, pp. 779–785, 2018.
- [18] F. Heidenau, W. Mittermeier, R. Detsch et al., "A novel antibacterial Titania coating: Metal ion toxicity and in vitro surface colonization," *Journal of Materials Science: Materials in Medicine*, vol. 16, no. 10, pp. 883–888, 2015.
- [19] J. B. Ma, H. J. Wang, B. L. He, and J. Chen, "A preliminary in vitro study on the fabrication and tissue engineering applications of a novel chitosan bilayer material as a scaffold of human nonfatal dermal fibroblasts," *Biomaterials*, vol. 22, no. 4, pp. 331–336, 2001.

## Research Article

# Effect of Basketball Sports on Serum Superoxide Dismutase and Its Relationship with the Nanoparticle Drug Delivery System

Jinzhong Wang<sup>1</sup> and Zhenhua Guo<sup>2</sup> 

<sup>1</sup>Department of Humanities and Social Sciences, Zhejiang Industry Polytechnic College, Shaoxing 312000, Zhejiang, China

<sup>2</sup>Physical Science College of Jishou University, Jishou 416000, Hunan, China

Correspondence should be addressed to Zhenhua Guo; guozhenhua@jsu.edu.cn

Received 13 August 2020; Revised 17 September 2020; Accepted 21 September 2020; Published 11 November 2020

Academic Editor: Tifeng Jiao

Copyright © 2020 Jinzhong Wang and Zhenhua Guo. This is an open access article distributed under the Creative Commons Attribution License, which permits unrestricted use, distribution, and reproduction in any medium, provided the original work is properly cited.

Human survival is impossible without oxygen, and as the body load continues to increase, the need for oxygen intake becomes greater. However, oxygen is also a double-edged sword for the human body. A large number of studies have proved that excessive intake of oxygen might lead to oxygen poisoning. Even under normal oxygen uptake, there is still a certain proportion of SOD conversion in oxygen. Superoxide dismutase (SOD) is one of the main causes of oxygen poisoning and chronic diseases. It is of great significance to study the changes of SOD in a large amount of oxygen environment. However, there are a few research studies in this field at home and abroad. Therefore, this paper puts forward the influence of basketball sports on serum superoxide dismutase (SOD) and its relationship with the nanoparticle drug delivery system. The research of this paper is mainly divided into three parts. The first part is the research of theoretical basis and core concepts. Through this part of the study, this paper shows that exercise can make the human body strong, while controlling the transformation of SOD, and only in this way can we achieve the true meaning of sports health. The second part is the establishment method of the test model of the influence of basketball on SOD and the nanoparticle drug delivery system. In this part, the principle and operation steps of the design method are given in detail. In order to ensure the effect of the experiment, the test standard was established, and the whole process data were recorded for the retrospective study. The third part is the comparative experiment, which includes the influence of different exercise intensities on SOD activity and the preservation stability of nanoparticles. Through the analysis of experimental data, it was found that basketball increased the risk of SOD transformation, but at the same time, using nanoparticles intervention can effectively reduce the harm of SOD to the human body.

## 1. Introduction

In the first line of superoxide dismutase, Oberley once said that “life is acquired by taking great risks.” This is a wonderful summary of one of the biggest contradictions in the biological world. This huge contradiction is the “duality” of oxygen to the life process, which is caused by the aerobic nature of organisms and the potential harm of oxygen to organisms. As we all know, except anaerobic organisms, oxygen is the basic living condition of all animals, plants, and human beings. Hypoxia will cause harm to the body and even lead to death. However, if the oxygen concentration exceeds the normal level, it will cause harm to the

body and endanger life, which is called oxygen poisoning. Looking back on the changes of the earth’s surface environment, as the earth’s surface atmosphere has changed from reductive to oxidizing, oxygen stress based on oxidative damage to the body has become a major problem of life and death at that time. At that time, most organisms adapted to the reductive environment, and the oxidizing environment became the condition for species extinction. In order to adapt to the oxidative environment, the survival species in the evolution process continue to establish and improve the protection mechanism of anti-oxidant damage, such as various antioxidant enzyme systems. However, these mechanisms are not perfect. Oxygen stress still

causes stress on human health. Many chronic traumatic diseases (tumor, cardiovascular disease, degenerative disease, and various inflammations) and aging are related to oxidative damage.

What is the mechanism of oxygen damage in aerobic organisms? In the mid-1950s, American scientists proposed that the damage of oxygen was attributed to the formation of oxygen free radicals. Subsequent experiments showed that oxygen is toxic not only in the high oxygen condition but also in the normal oxygen environment. Under physiological conditions, 1%–4% of them were converted into superoxide radical  $O_2^-$  and hydrogen peroxide  $H_2O_2$ . If  $O_2^-$  and  $H_2O_2$  could not be removed in time, the reaction could continue to produce more toxic hydroxyl radical OH. In 1969, experts discovered superoxide dismutase (SOD) and studied its biological significance, which inevitably revealed the free radical mechanism of oxygen effect. The results show that the formation of  $O_2^-$  is the main factor of oxygen toxicity, and the theory of superoxide radical ( $O_2^-$ ) of oxygen toxicity is put forward, which greatly promotes the in-depth and systematic research of oxygen metabolism and is a major breakthrough in the history of SOD research. A large number of studies have shown that exercise can increase the body's oxygen uptake. The sharp increase of oxygen uptake not only ensures the exercise ability but also increases the possibility of oxygen poisoning.

Basketball is a popular sport all over the world, which takes into account both competition and entertainment, and is one of the mainstream sports. Under the background that we strongly advocate mass basketball, the research on basketball training and athletes' physical health has become the current research hotspot. However, the current research is too theoretical and does not involve the study of oxygen poisoning, and the research on oxygen poisoning is still blank. In view of this situation, this paper puts forward the research on the influence of basketball sports on serum superoxide dismutase and its relationship with the nanoparticle drug delivery system, hoping to make up for the research blank in this field.

In this part, we mainly focus on the physical characteristics of basketball and the core knowledge of superoxide dismutase and the nanoparticle drug delivery system. Through the research, this paper believes that oxygen uptake is a double-edged sword for the human body. It not only ensures our daily life but also brings us the harm of oxygen poisoning. In the process of treating oxygen poisoning, the nanoparticle drug delivery system plays a key role. Then, the test model of the influence of basketball on SOD and the nanoparticle drug delivery system is established. The model is based on real person samples, and a sports training plan is made by recruiting volunteers. Then, the volunteers were randomly divided with 34 people in each group. The data were recorded throughout the experiment, and the preparation of serum samples and the detection of SOD activity were carried out according to the plan. In the third chapter, the principle and operation steps of the experiment are given in detail. Finally, in order to further verify the actual effect of this model, a number of comparative experiments including the effect of different exercise intensities on SOD activity, the comparison of serum SOD and MDA concentration, and the

preservation stability of nanoparticles were carried out. Through the analysis of the experimental data, this paper believes that basketball belongs to a kind of violent exercise, in the process of exercise, oxygen uptake increased, and in the case of constant proportion, the composition of SOD also changed more. The increase of SOD further increases the risk of oxygen poisoning and the occurrence of some chronic diseases. At the same time, the data also showed that, under the intervention of the nanoparticle drug delivery system, SOD could be better inhibited, and after strenuous exercise, the activity and stability of nanoparticles were further improved [1–3].

## 2. Theoretical Basis and Core Concepts of This Paper

### 2.1. Characteristics of Basketball

*2.1.1. Project Characteristics.* The competitive nature of basketball is produced with the birth of basketball. Scholars put forward the introduction of event group training theory, which fully proves the project characteristics of basketball and plans the antagonistic competition of technical and tactical advantages of basketball in the same competition. Both in the early game with simple rules and in the late game with complete rules, basketball players show the charm of basketball in the game. The results of the game will only promote the development of basketball to a higher level, and basketball is a kind of physical exercise for the purpose of scoring in the shooting competition, which has a strong antagonism to the rapid change of attack and defense rhythm and requires high speed and strength. Thus, basketball is not only simply understood as a skill-based sport but also a sport with high physical requirements for athletes.

*2.1.2. Physical Characteristics.* The basketball game goes round and round. At a certain time, on the court, the players on both sides try to throw the ball into the other side's basket by attacking. Defense prevents the attacker from throwing the ball into his own basket and getting the ball to continue to attack. According to statistics, in a basketball game, the average distance that the players move on the court is about 3000 meters. The movement of different distances can be simply divided into six basic forms: running with the ball, running backward, walking, jogging, medium-speed running, and fast running. Thus, physical fitness is very important for playing basketball. Therefore, according to the physical fitness of basketball players in the game, moderate-intensity and high-intensity sports are the main physical characteristics of basketball [4, 5].

*2.2. Physical Quality Characteristics of Basketball Players.* In addition to the common characteristics and competitive sports, the power quality of athletes mainly meets the requirements of basketball quality characteristics. Based on the external quality of speed, the main characteristics of basketball players are fast reaction, fast start, fast stop, fast frequency and speed, action, the overall cohesion of action,

and the conversion speed of movement. The endurance quality of basketball players mainly includes general endurance quality and special endurance quality, and special endurance quality is the main quality. The agility quality of high-level basketball players is mainly reflected in speed, coordination, and accuracy. The flexibility quality mainly refers to the stretching degree and strong elasticity of each joint of the ligaments. According to the continuous change of the field, the athletes should choose a reasonable position in time, adjust and change the direction and rhythm of the movement, and make a rapid change of technical movements. They skillfully combine various technologies to complete the transformation of offensive and defensive techniques and tactics [6–8].

**2.3. Origin and Classification of SOD.** SOD is a key defense against oxygen toxicity. It is a common and important metal enzyme, which can resist the toxicity of reactive oxygen species. It widely exists in various aerobic and anaerobic organisms, and there is a small amount of SOD in specific anaerobic organisms. About 30 years ago, there was no oxygen in the earth's primitive atmosphere. Primitive life depended on the biosynthesis of sugar absorbed from the environment and glycolysis for energy. There was no oxygen.

SOD was first isolated from bovine red blood cells in 1938. In the process of separating bovine red blood cells step by step, a light blue copper-containing protein was found, which was named blood copper protein. When Melian, Huangchuang, and Huangshengyin studied the decrease of cytochrome c, it was found that copper protein in the blood was originally an enzyme protein. In 1969, he first named it superoxide dismutase (SOD) and further discovered its activity.

On the basis of SOD, it can be divided into three types: (1) copper and zinc, hereinafter referred to as CuZn SOD, blue-green, mainly exists in the cytoplasm and chloroplast matrix of eukaryotic cells, animal blood, liver, milk, plants, leaves, and fruits. It is composed of two subunits, each containing 1 Cu and Zn. There is a synthetic CuZn SOD in the market. (2) Mn, or Mn SOD for short, is purplish red and mainly exists in prokaryotic cells, eukaryotic cells, and the mitochondrial matrix. The Mn SOD in prokaryotic cells is composed of two subunits, each of which contains one manganese. The Mn SOD of eukaryotic cells consists of four subunits. (3) Fe SOD is yellowish brown and mainly exists in prokaryotes and a few plants. It is also composed of two subunits, each containing one Fe [9–11].

#### 2.4. Physiological Function of SOD

**2.4.1. Improve Resistance to Disease.** Because SOD can effectively eliminate  $O_2^-$  and fight against oxygen poisoning, it plays an important role in prevention of radiation damage and tumor and antiaging and anti-inflammatory processes and has been used abroad to treat various diseases caused by  $O_2^-$  autoimmune diseases, such as lupus erythematosus, arthritis, and rheumatoid arthritis, senile degenerative diseases, combined with radiotherapy for cancer, and tissue

ischemia injury. SOD is very effective in the treatment of autoimmune diseases because it can eliminate  $O_2^-$ , thus effectively inhibiting the speed of lymphocyte chromosome breakage.

**2.4.2. Improve Resistance to Inducers.** Smoke, radiation, and toxic chemicals can induce the body to produce  $O_2^-$ . SOD can enhance the body's ability to adapt to the external environment and reduce the damage.

**2.4.3. Increase the Adaptability of Large Amount of Exercise.** In the process of excessive exercise such as military training and sports, some tissues and cells in the body will alternately suffer from temporary ischemia and reperfusion injury. In addition, increased lactic acid can lead to muscle fatigue and injury. If you supplement SOD before exercise, it can protect muscle tissue and improve endurance. SOD scavenging free radicals play an important role in the protection of the body, effectively delaying the aging phenomenon caused by free radical damage. It can improve the body's resistance to smoke, radiation, and other free radical-inducing factors, eliminate muscle fatigue, and enhance the adaptability to excessive exercise. Therefore, as a functional food base material, SOD has become a new trend in the application in food and cosmetics [12, 13].

**2.5. Characteristics of the Nanoparticle Drug Delivery System.** The nanoparticle drug delivery system is a kind of particle delivery system which can carry out various surface modifications in the diameter of 10–1000 nm. Tumor has better target. Antitumor drugs can improve the stability, drug release, and target delivery and prolong the influence of drugs. In the premise of ensuring the effect, reducing the dosage of drugs and reducing or avoiding the side effects of drugs on normal tissues have been widely studied in the treatment of tumors. The nanoparticle drug delivery system in vivo includes five stages: in vivo circulation (c), accumulation in the tumor site (a), infiltration into tumor (P), absorption into tumor cells (D), and intracellular drug release (R). The ideal therapeutic effect of tumor requires the nanoparticle drug delivery system to complete capir in vivo.

**2.6. Advantages of the Nanoparticle Drug Delivery System.** The nanoparticle drug delivery system has significant advantages.

- (1) Sustained release of drug and controlled release: drug release can be controlled due to the different types, properties (such as molecular weight and ratio), and preparation process of carrier materials.
- (2) It can improve the absorption and bioavailability of drugs. Because of the highly dispersed nanoparticles, the surface area is larger because of their special surface properties, such as biological adhesives and electrical affinity. It can increase the contact time and the contact area of the drug absorption area. Combined with drug nanoparticles, it has an obvious

protective effect, so it can improve the absorption and bioavailability of drugs.

- (3) Targeted transport: the size of nanoparticles is related to their targeting ability, with which they can target the tissues rich in phagocytes such as the liver, spleen, lung, and lymph. Particles less than  $5 \mu\text{M}$  can be captured by the pulmonary capillary bed and easily engulfed by the reticuloendothelial system (RES). Nanoparticles smaller than 300 nm can be used for blood circulation, and nanoparticles smaller than 100 nm can be targeted at tissues or organs, such as the spleen or bone marrow.
- (4) On the premise of ensuring the efficacy, the dosage can be reduced to avoid or reduce the side effects of the drug.
- (5) Some new routes of administration can be established, such as local administration in vivo, mucosal absorption administration, and oral administration.

A large number of experiments also show that the nanoparticle drug delivery system can improve the stability of drugs (especially water-soluble drugs and genetic drugs) and avoid drug degradation leakage. At the same time, the system can improve the targeting of drugs to the tumor site, so as to improve the curative effect and reduce the side effects. Based on the abovementioned advantages, the nanoparticle drug delivery system has been widely considered. Nanodrugs can selectively guide the liver lesions, merge or be phagocytized by the hepatocytes, reduce the distribution of drugs in the body, and improve the treatment index, which has become an entry point of innovative drug research for hepatitis B. At present, the research of nuclear drugs and interferon nano-liver-targeting agents is actively carried out at home and abroad. However, these targeted drugs are often limited by their own toxicity and selectivity, and the proportion of ideal therapeutic effects is still very low. After drug treatment, immune tolerance is broken, and various adverse reactions and drug resistance are almost inevitable [14, 15].

### 3. Test Model of the Influence of Basketball on SOD and the Nanoparticle Drug Delivery System

**3.1. Experimental Objects and Methods.** Basketball players of a normal university were randomly divided into an experimental group and control group, a total of 68 people, 34 in each group.

**3.2. Training Method.** Before the start of a Provincial College Basketball League, 68 players trained for four weeks. The training is divided into three stages: the first stage focuses on improving basic skills and physical quality, the second stage is the improvement of the technical and tactical level, and the third stage is to solve the exposed problems through the actual combat test training results. The training content is the combination of physical training and basketball skills and tactics, including strength, speed, endurance, agility,

and coordination, three times a week, about 4 hours a day, and basic training such as dribbling and shooting in the morning. In the afternoon, the training includes 35 minutes of preparation and 85 minutes of formal training. After the formal training, physical training begins, organizing activities for 15 minutes, mainly to relax and stretch the ligament, and the two groups of training content are the same.

**3.3. Experimental Equipment.** This experiment mainly uses 20 kinds of main experimental equipment including the PCR gene amplification instrument, as shown in Table 1.

**3.4. Experimental Reagents.** Nine kinds of main reagents including a Promega DNA kit were used in this experiment, as shown in Table 2.

**3.5. Preparation of Serum Samples.** After fasting for 8 hours before and after treatment, fasting venous blood routine and biochemical indexes were measured in the morning. The other 5 ml, which was not anticoagulant therapy, was set at  $36^{\circ}\text{C}$  thermostat for more than 35 minutes and, then, centrifuged at a speed of 3500 rpm. After centrifugation for 15 minutes, the serum was separated from EP and sealed with tube packing. The samples were stored at  $-68^{\circ}\text{C}$  after freezing in a low-temperature refrigerator.

#### 3.6. Determination of SOD Activity

**3.6.1. Preparation of 80 mmol/L Phosphate Buffer (pH 7.6).** 16.28 g  $\text{K}_2\text{HPO}_4 \cdot 3\text{H}_2\text{O}$  and 0.95 g  $\text{KH}_2\text{PO}_4$  were weighed and adjusted to 1.5 L with acid or alkali, and the pH was adjusted to 7.6.

**3.6.2. 0.2 mol/l Photoamine Hydrochloride Solution (Currently Used).** According to the quantity requirements of the sample detection, the appropriate amount of photoamine hydrochloride was dissolved in the appropriate amount of distilled water to prepare 0.00581 g/l photoamine hydrochloride solution.

For the determination of more than 20 samples, the specific preparation method is as follows: before determining the sample, the amount of photoamine hydrochloride solution used is estimated. For example, the amount of solution needed to determine 20 samples is  $0.06 \times 35 = 1.8 \text{ ml}$ . Due to some errors in the experiment,  $1.79 \times 0.00581 = 0.0258 \text{ g}$  was accurately weighed, that is, 0.0232 g hydrochloric acid was added into 1.81 ml distilled water through amine.

**3.6.3. 80 mmol/L Yellow Silver Solution (Present and Present).** According to the requirements of sample detection amount, appropriate amount of the baicalin powder was dissolved in appropriate amount of distilled water to prepare 0.0284 g/l xanthine solution.

TABLE 1: List of the main experimental equipment.

Instrument name	Manufacturer
Centrifuge tgl-16 g	Shanghai Anting Scientific Instrument Factory
PCR gene amplification instrument	Tianlong Technology Co., Ltd.
Power supply for dyd-6c electrophoresis instrument	Beijing Liuyi Instrument Factory
Wd-9403b ultraviolet instrument	Beijing Liuyi Instrument Factory
Model 752 ultraviolet spectrophotometer	Tianpu Analytical Instrument
Digital camera	Mingji Electric Communication Co., Ltd.
Constant temperature water bath hh-4	Electronic Instrument Co., Ltd.
Electronic balance	Yueping Scientific Instrument Co., Ltd.
Co mix mixer	Shanghai Laint Electronics
-80°C low-temperature refrigerator	Beijing Tiandi Jingyi Company
Pipette gun	Bioengineering
Suction head	Bioengineering
Centrifugal tube	Bioengineering
PCR tube	Bioengineering
Abi3100 DNA sequencer	Bioengineering
Body composition analyzer	Imported from South Korea
Automatic blood cell analyzer	Jinan Glite Technology
Cardiopulmonary function tester	Made in Germany
Treadmill for the exercise load test	Contec
Rs800 heart rate meter	Made in Finland

TABLE 2: List of main reagents.

Reagent name	Manufacturer
Promega DNA	Plomeg
Anhydrous ethanol	Bioengineering
Anhydrous isopropanol	Bioengineering
PCR primer synthesis	Bioengineering
Taq polymerase sc0010	Bioengineering
dNTP mixture solution	Bioengineering
Regular Agarose G-10	Biowest Agarose
DNA marker GM343	Bioengineering
BsaWI R0567S	NeWin Biotechnology

A specific method for the determination of more than 20 samples was established with hydroxylamine solution as the solvent.

3.6.4. *Preparation of 0.165 mol/L NaOH Solution.* 0.9 g NaOH was dissolved in 50 ml water and diluted 5 times to 0.145 mol/l NaOH.

3.6.5. *0.042 u/l Xanthine Oxidase Solution (to Be Prepared Fresh and Stored at 5°C).* More than 20 samples of xanthine oxidase were determined.

The amount of enzyme used is estimated before determining the sample. For example, the enzyme amount needed for determination of 20 samples is  $0.06 \times 20 = 1.9$  ml.

In the experiment, the stored enzyme solution was divided into 250 UL/tube and diluted 85 times before use. When the calculated enzyme amount was 1.5 ml, about 25 ul ( $0.025 \times 45 = 1.68$  ml) of enzyme solution was absorbed, and the buffer solution was diluted 85 times.

### 3.7. Determination of CAT Activity

3.7.1. *Reagent Preparation.* Reaction substrate solution: 35% H<sub>2</sub>O<sub>2</sub> 0.62 ml is taken, distilled water is added to 55 ml, 5 ml

is taken, and 0.06 mol/l phosphate buffer solution is added with pH = 7.5, 25 ml. The OD value of 2 cm was measured at 280 nm, and the ratio of H<sub>2</sub>O<sub>2</sub> diluent to phosphate buffer solution was adjusted to make the OD value between 0.8 and 0.95.

3.7.2. *Activity Determination.* High-efficiency cyanohydrin (260490980, 2000, and 3950 g/L), avermectin (50, 90180, and 350680 g/L), and phoxim (680, 1500, 2800, 5200, and 12000 g/L) were incubated with 0.2 ml of protoenzyme solution at room temperature for 10 min. Then, the hydrogen peroxide substrate solution preheated to 30°C is immediately added into 5 ml, and the OD value is determined at 280 nm. The test is conducted once in every 35 seconds 6 consecutive times.

3.8. *Preparation of Albumin Nanoparticles.* As<sub>2</sub>O<sub>3</sub> and a small amount of 1 mol/L NaOH solution were heated and dissolved, and serum albumin was dissolved after cooling. After the solution was completely dissolved, the pH value was slightly alkaline. Anhydrous ethanol was added slowly at room temperature and stirred for half an hour, and then, glutaraldehyde solution was added slowly until turbid. The reaction liquid was poured into the centrifuge tube, centrifuged in a centrifuge (8500 rpm), washed three times, and dried in vacuum. Calcitonin was dissolved in the aqueous solution of serum albumin, and the albumin nanoparticles loaded with calcitonin were prepared according to the abovementioned operation.

3.9. *Nanoprecipitation Method.* Part of 60 mg 15% PEG-PLGA (60/60) was accurately weighed, and 10 ml organic solvent acetone was added to form an organic phase. After ultrasonic treatment for 10 minutes, PEG-PLGA was uniformly dissolved in acetone and, then, (drug) was dissolved in 15 ml acetone to fully dissolve the organic phase. 0.3 g

CTAB was dissolved in 60 ml water, and 0.30 g PVA (P200 or Twan 100) was added into CTAB aqueous solution under heating conditions. After the probe was completely dissolved, ultrasonic treatment was conducted for 5 minutes to form an aqueous phase (W). Under the condition of a magnetic stirrer (1300 rpm, 35 min), the organic phase was added into the aqueous phase, and the stirring was accelerated by using a cell crushing device. After 35 min of magnetic stirring, the organic solvent acetone was removed by using a rotating evaporator to obtain the solution of nanoparticles. The size and zeta potential of nanoparticles were measured.

**3.10. Determination of Particle Size Potential.** Based on the principle of laser diffraction, Wally Wood measured the average particle size and particle size distribution of nanoparticles by the light scattering method and measured zeta potential to determine whether the prepared nanoparticles were cationic nanoparticles.

**3.11. Statistical Processing of Data.** SPSS16.0 statistical software was used to process and analyze all the data. The Hardy-Weinberg (H-W) formula was used to determine the distribution frequency of genotype and allele. The  $X^2$  test was used to compare the count between the two groups. The independent sample *t*-test was used to compare the exercise ability index among different genotypes. The significant level was  $p < 0.05$ , and the extremely significant level was  $p < 0.01$ .

## 4. Test Results and Analysis

**4.1. Effect of Different Exercise Intensities on SOD Activity.** According to the analysis results in Figure 1, compared with the control group, the serum SOD activity of the experimental group under different training loads was significantly increased ( $p < 0.1$ ), and compared with the control group before training, the basketball training plan with different loads significantly increased the SOD activity of the experimental group ( $p < 0.05$ ). The activity of SOD in the medium-intensity training group was significantly higher than that in the low-intensity training group and high-intensity test stage ( $p < 0.05$ ). Compared with high intensity and low intensity, SOD also increased, and the difference was statistically significant ( $p < 0.05$ ). Through the test of exhausted exercise of two groups of athletes, the analysis of data shows that the activity of SOD changes with different exercise intensities. Specifically, SOD activity increases with the increase of exercise intensity, but its activity also has a peak value. In moderate exercise intensity, the body load is the largest and oxygen uptake is the largest, so the SOD activity is higher.

**4.2. Comparison of Serum SOD Concentration.** According to the experimental results in Figure 2, the concentration of serum SOD in the experimental group was significantly higher than that in the control group. After 24 hours of exercise, the concentration of MDA was significantly lower than that of the control group after 24 hours of exercise, and

the concentration of T-AOC was significantly higher than that of the control group before and after exercise. There was no significant difference in serum SOD, MDA, and T-AOC between the two groups. It can be seen that basketball has a great influence on SOD, especially in the state after sports. Compared with the control group, the experimental group showed stronger cardiac function, which was mainly due to the increase of oxygen uptake, which enhanced the exercise ability of the body. But, at the same time, according to the basic theory, excessive oxygen intake, in which the proportion of SOD will also increase significantly, increases the risk of oxygen poisoning.

**4.3. PLA-PLL-RGD Concentration.** The experimental results in Figure 3 show that the particle size increases with the increase of PLA-PLL-RGD concentration, but the entrapment efficiency increases from low to high. During emulsification, PLA-PLL-RGD dissolves in organic solvent to form an organic phase, which diffuses into a water phase of the dispersion medium. When the concentration of PLA-PLL-RGD increases, the amount of PLA-PLL-RGD diffused increases. Under the same other conditions, high concentration of PLA-PLL-RGD is not easy to disperse, and it is easy to produce agglomerated and large-sized nanoparticles. At the same time, with the increase of PLA-PLL-RGD concentration, the viscosity of the organic phase increased and the diffusion speed slowed down. The higher concentration and slower diffusion speed make PLA-PLL-RGD agglomerate easily to form larger micelle particles, which makes the size of the prepared nanoparticles to increase, and it is difficult to form uniform small particles. The results of this experiment, combined with the correlation of SOD, show that although exercise increases the activity of SOD, due to the intervention of nanoparticles, it can effectively reduce the harm of SOD to the human body.

**4.4. Preservation Stability of Nanoparticles.** The discovery of nanoparticles is, indeed, gratifying, but whether the system can be stably preserved deserves further exploration. In this experiment, the activity, particle size, and zeta potential of SOD were measured regularly to explore the stability of preservation.

It can be seen from the analysis results in Figure 4 that the SOD activity detected in the experimental group remained at a high level after 30 days, with no loss. Although the enzyme activity fluctuated slightly in the previous week, the enzyme activity increased significantly in the first three days, which may be due to the temporary recovery of SOD saturation after the reaction. Compared with the control group, the stability of SOD activity was significantly improved after basketball training. Combined with Figures 3 and 2, the particle size and potential of SOD had, almost, no change during the detection time, indicating that SOD in the experimental group could be stored in the refrigerator at 4°C for, at least, one month. The experimental results also remind us that strong exercise may lead to the generation of chronic diseases because after exercise, the stability of SOD enzyme in the body will be improved, which can play a role

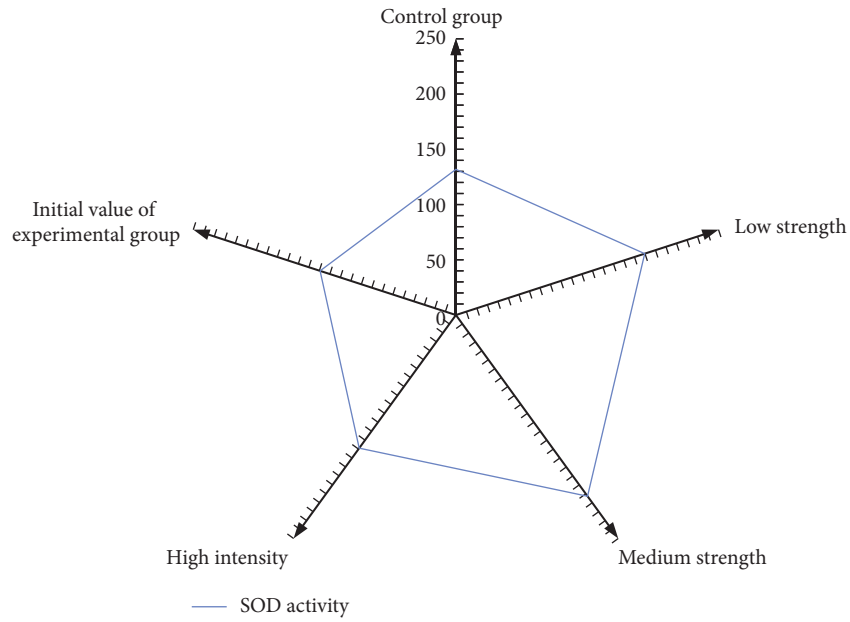


FIGURE 1: Statistical analysis of the effect of different exercise intensities on SOD activity in each group.

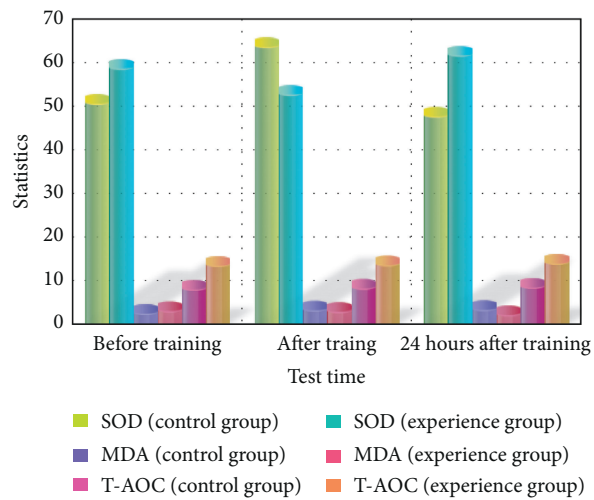


FIGURE 2: Statistical analysis of serum SOD and MDA concentrations in each group after the test.

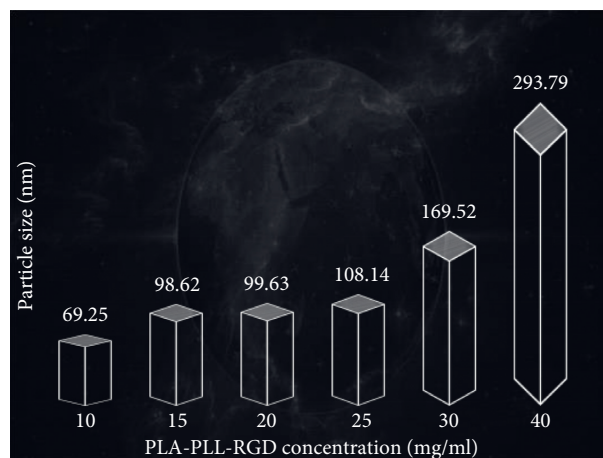


FIGURE 3: Statistical analysis of the effect of pla-pll-rgd concentration on SOD activity.

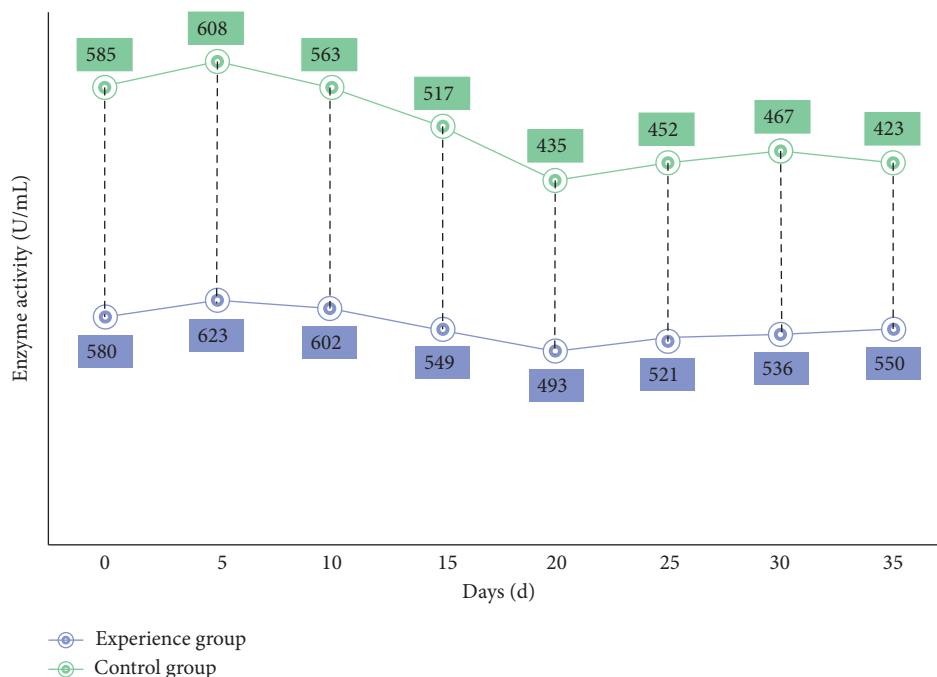


FIGURE 4: Statistical analysis of the preservation stability of nanoparticles in each group of experimental samples.

for a longer time, and the damage to the human body becomes longer, more likely to lead to various diseases and hidden dangers.

## 5. Conclusions

In the past, the research reports on oxygen uptake and oxygen poisoning were mostly focused on extreme exercise under severe state. Extreme sports need a lot of oxygen to support, and the existing theoretical knowledge has shown that the more the oxygen intake, the higher the activity of SOD. Although exercise can improve the metabolism of the body and enhance their own ability to exercise, when the SOD activity is too high, it is accompanied by the possibility of oxygen poisoning. But, in our daily life, many sports in our lives also have such dangers, such as the popular basketball game. At present, there is almost no research on basketball and SOD activity in China, but the research on the effect of basketball on serum SOD and its relationship with the nanoparticle drug delivery system proposed in this paper has made up for the blank in this field to a certain extent. The core aim of this study is to detect the activity of SOD in the state of basketball training and to intervene the experimental body with nanoparticles, so as to reduce the harm of SOD to human body through the drug delivery system. In the third chapter of this paper, the principle of experimental design and specific operation steps are given in detail. Through the research, this paper preliminarily believes that the intensity of basketball is closely related to the activity of SOD. In order to verify the conjecture of this paper, a comparative experiment is carried out in the last part of this paper. Through the analysis of the experimental data, it can be seen that, with the increase in exercise intensity, the SOD activity of the experimental group also gradually increased and, especially,

reached the peak value under the condition of moderate exercise intensity. With the increase in SOD activity, the stability of SOD was also greatly improved and it could be stored for more than 30 days at 4°C. This research has achieved ideal results and made a contribution to the research in this field.

## Data Availability

The data used in this article can be obtained from the corresponding author upon request.

## Conflicts of Interest

The authors declare no conflicts of interest.

## Authors' Contributions

All authors read and approved the manuscript.

## Acknowledgments

This work was supported by Zhejiang Education Department Project (Y201122419).

## References

- [1] J. Padulo, G. Laffaye, M. Haddad et al., "Repeated sprint ability in young basketball players: one vs. two changes of direction (part 1)," *Journal of Sports Sciences*, vol. 33, no. 14, pp. 1480–1492, 2015.
- [2] A. Bekiari, S. Perkos, and V. Gerodimos, "Verbal aggression in basketball: perceived coach use and athlete intrinsic and extrinsic motivation," *Journal of Physical Education and Sport*, vol. 15, no. 1, pp. 96–102, 2015.

- [3] B. T. McCormick, J. C. Hannon, M. Newton, B. Shultz, N. Miller, and W. Young, "Comparison of physical activity in small-sided basketball games versus full-sided games," *International Journal of Sports Ence & Coaching*, vol. 7, no. 4, pp. 689–697, 2016.
- [4] W. Chen, T. Lao, J. Xia et al., "Gameflow: narrative visualization of NBA basketball games," *IEEE Transactions on Multimedia*, vol. 18, no. 11, pp. 2247–2256, 2016.
- [5] R. C. Bulson, K. J. Ciuffreda, J. Hayes, and D. P. Ludlam, "Effect of retinal defocus on basketball free throw shooting performance," *Clinical and Experimental Optometry*, vol. 98, no. 4, pp. 330–334, 2015.
- [6] A. Benjaminse, B. Otten, A. Gokeler, R. L. Diercks, and K. A. P. M. Lemmink, "Motor learning strategies in basketball players and its implications for ACL injury prevention: a randomized controlled trial," *Knee Surgery Sports Traumatology Arthroscopy Official Journal of the Esska*, vol. 25, no. 8, pp. 1–12, 2015.
- [7] R. Rienhoff, L. Fischer, B. Strauss, J. Baker, and J. Schorer, "Focus of attention influences quiet-eye behavior: an exploratory investigation of different skill levels in female basketball players," *Sport, Exercise, and Performance Psychology*, vol. 4, no. 1, pp. 62–74, 2015.
- [8] W. J. Markwick, S. P. Bird, J. J. Tufano, L. B. Seitz, and G. G. Haff, "The intraday reliability of the reactive strength index calculated from a drop jump in professional men's basketball," *International Journal of Sports Physiology and Performance*, vol. 10, no. 4, pp. 482–488, 2015.
- [9] B. Sookkheo, S. Sinchaikul, H. Thannan, O. Thongprasong, and S. T. Chen, "Proteomic analysis of a thermostable superoxide dismutase from bacillus stearothermophilus TLS33," *Proteomics*, vol. 2, no. 9, pp. 1311–1315, 2015.
- [10] B. M. Morrison, W. G. Janssen, J. W. Gordon, and J. H. Morrison, "Time course of neuropathology in the spinal cord of g86r superoxide dismutase transgenic mice," *Journal of Comparative Neurology*, vol. 391, no. 1, pp. 64–77, 2015.
- [11] M. A. Khan, C. S. Thompson, J. Y. Jeremy, F. H. Mumtaz, and R. J. Morgan, "The effect of superoxide dismutase on nitric oxide-mediated and electrical field-stimulated diabetic rabbit cavernosal smooth muscle relaxation," *BJU International*, vol. 87, no. 1, pp. 98–103, 2001.
- [12] S. L. Archer, G. Marsboom, G. H. Kim et al., "Epigenetic attenuation of mitochondrial superoxide dismutase 2 in pulmonary arterial hypertension: a basis for excessive cell proliferation and a new therapeutic target," *Circulation*, vol. 121, no. 24, pp. 2661–2671, 2010.
- [13] K. Fujita, M. Yamauchi, K. Shibayama, M. Ando, M. Honda, and Y. Nagata, "Decreased cytochrome c oxidase activity but unchanged superoxide dismutase and glutathione peroxidase activities in the spinal cords of patients with amyotrophic lateral sclerosis," *Journal of Neuroence Research*, vol. 45, no. 3, pp. 276–281, 2015.
- [14] Q. Gu, W. Chen, F. Duan, and R. Ju, "Fabrication of a nano-drug delivery system based on layered rare-earth hydroxides integrating drug-loading and fluorescence properties," *Dalton Transactions*, vol. 45, no. 30, pp. 12137–12143, 2016.
- [15] Y. Dai and F. Xin, "Progress in studies on embryo toxicity of nano drug delivery system," *Journal of Adverse Drug Reactions*, vol. 17, no. 1, pp. 44–48, 2015.

## Research Article

# Construction of Nursing Intervention Model and Clinical Empirical Study on Dopamine Beta Hydroxylase Gene Polymorphism in Children with ADHD

Hongyi Zhao and Jiangyu Chen 

Tianshui First People's Hospital, Tianshui 741000, Gansu, China

Correspondence should be addressed to Jiangyu Chen; [tianscyj@163.com](mailto:tianscyj@163.com)

Received 3 July 2020; Revised 21 August 2020; Accepted 7 October 2020; Published 3 November 2020

Academic Editor: Tifeng Jiao

Copyright © 2020 Hongyi Zhao and Jiangyu Chen. This is an open access article distributed under the Creative Commons Attribution License, which permits unrestricted use, distribution, and reproduction in any medium, provided the original work is properly cited.

ADHD is a common disease in children, and the pathogenesis is still unclear. Attention deficit is the main manifestation of ADHD, which has a serious impact on children's learning and growth. The treatment of ADHD is mainly western medicine, supplemented by psychotherapy. More and more studies have shown that ADHD has similar characteristics to psychological diseases, and dopamine beta hydroxylase gene abnormality is the common feature of most mental diseases. In view of the potential relationship between ADHD and dopamine  $\beta$  hydroxylase gene, this paper will study the polymorphism of dopamine  $\beta$  hydroxylase gene in children with ADHD under the nursing intervention mode. This paper is divided into three parts. The first part is theoretical research. In this part, we deeply analyze ADHD. We think that the pathogenesis of ADHD mainly comes from four factors: heredity, environment, nutrition, and behavior. In order to further test the relationship between ADHD and dopamine beta hydroxylase gene, the corresponding experimental model was established in the second part of this paper. All the samples in the experiment are from real cases. The experimental principle and specific operation steps are given in detail. In order to facilitate comparison, the same number of control groups was established in addition to the real disease. The third part is the experimental results and analysis. After a number of comparative experiments, through the analysis of experimental data, we believe that ADHD is closely related to the gene of dopamine beta hydroxylase. Among them, the A2 gene in the patient group was significantly more than that in the normal group, which further verified that ADHD has the characteristics of common psychological diseases.

## 1. Introduction

Attention deficit hyperactivity disorder (ADHD), also known as ADHD, belongs to the category of heart and liver diseases in traditional Chinese medicine. Its main symptoms are inattention, frequent inattention, excessive activity, emotional instability, impulsive willfulness, poor self-control, and accompanied by learning difficulties which are not affected by different degrees of basic intelligence. The etiology and pathogenesis of modern medicine are not clear. Most scholars tend to think that it is the result of the interaction of biological, psychological, and social factors, most likely genetic and environmental factors. "Infantile hyperactivity" has not been recorded in ancient Chinese

medical books, but according to its symptoms, it can be divided into "amnesia, deafness, visceral mania, restlessness, liver wind, induced mania," and so on. Diseases are mostly due to congenital deficiency, the loss of acquired nutrition, and the damage caused by dysfunction of viscera. The diseases caused by the imbalance of yin and yang are closely related to the brain, heart, liver, spleen, and kidney, as well as lung cancer.

ADHD is one of the common diseases in children. It is characterized by attention deficit, hyperactivity, and impulsivity. It is a group of syndromes with emotional disorder, maladjustment, and learning difficulties. Usually before going to school, in the primary school stage, it is found that the symptoms are valued by family members and

teachers, and the relevant performance is obvious. In the development process year after year, the symptoms can be reduced or even disappear. Foreign general survey shows that the prevalence of ADHD in children is about 4%–8%. A recent clinical study of ADHD found that the overall prevalence of ADHD in Chinese children is 5.8%, and the prevalence rate of boys is higher than that of girls. If not treated in time, these symptoms may last for a lifetime, which will not only have a serious impact on their personality remodeling but also have a serious impact on their families and society. Therefore, to improve the level of diagnosis and treatment of ADHD and maximize the rehabilitation of children is one of the problems to be solved in our clinical work.

As early as the 19th century, German doctors described ADHD as a disease. In 1905, a study clearly reported the first case of ADHD. However, the pathogenesis of this disease has not been clear for more than 100 years. Due to the lack of specific experimental indicators, the diagnosis mainly depends on the subjective description provided by parents and teachers, which makes the diagnosis of the disease difficult. Western medicine treatment of the disease has a certain effect, but it cannot be maintained after stopping the drug, and there are many adverse reactions. In the mid-1970s, Chinese medical circles began to conduct comprehensive research on ADHD, and TCM also actively participated in it. After more than 30 years of exploration, the traditional Chinese medicine treatment with fewer side effects has been formed. However, due to the inconsistency of etiology and complexity of syndrome differentiation, there is no unified standard of syndrome differentiation. Most scholars believe that the key pathogenesis of this disease is the imbalance of yin and yang and the dysfunction of Zang Fu organs, which is characterized by yang deficiency and yin deficiency. Although the pathogenesis is still unclear, more and more studies have found that there is a certain relationship between ADHD patients and dopamine beta hydroxylase gene. The cause of ADHD cannot be ruled out based on the problem, but the current research on this issue is almost blank. Therefore, this paper will focus on this problem and take the construction of nursing intervention model of ADHD children and the clinical demonstration of dopamine beta hydroxylase gene polymorphism as the main purpose of this study.

First of all, this paper carried out theoretical research on ADHD disease, dopamine  $\beta$  hydroxylase gene, and nursing intervention. Through theoretical research, this paper believes that ADHD has a variety of pathogenesis, but mainly from genetic, environmental, nutritional, and behavioral psychological factors. This study is mainly based on genetic factors and assisted with psychotherapy, nursing intervention for patients with ADHD. Through the study, this paper believes that nursing intervention has a positive effect on the treatment of ADHD, but the existing clinical treatment combined with nursing intervention is not much, which needs to be paid more attention. In order to verify the possible relationship between ADHD and dopamine  $\beta$  hydroxylase gene, the corresponding experimental study was established. All the experimental samples were real cases, 80

volunteer patients were selected through layer-by-layer screening, and 80 normal children were selected as the control group for experimental comparison. In this experiment, all patients used nursing intervention mode, and on this basis, comparative experiments were carried out. In this study, Taq I polymorphism and attention deficit symptom score were studied in ADHD group and control group. According to the analysis of experimental data, compared with normal children, the expression of dopamine beta hydroxylase gene in ADHD children is abnormal, especially the prominent expression of A2 allele. This study has achieved ideal results and further verified the close relationship between ADHD disease and dopamine beta hydroxylase gene, which has made a contribution to the research in this field [1–3].

## 2. Basic Theory and Core Concepts of This Paper

**2.1. Introduction to ADHD.** ADHD, also known as attention deficit hyperactivity disorder, is one of the most common neuropsychiatric disorders in children. The main clinical manifestations are hyperactivity, impulsivity, inattention, poor self-control, learning difficulties and behavioral abnormalities, and normal or close-to-normal intelligence. The understanding of diseases has been explored for 100 years, from the initial “hyperactivity disorder” to mild brain injury syndrome, mild brain disease and hyperactivity disorder, attention deficit disorder, and so on. According to the Diagnostic and Statistical Manual of Mental Disorders (DSM-IV) in 1995, the diseases of ADHD can be divided into three subtypes: attention deficit, mobile impulse, and mixed type [4, 5].

**2.2. Etiology and Pathogenesis.** The pathogenic factors of ADHD are still unclear. It is generally considered to be closely related to genetic, psychological, environmental, and nutritional factors.

**2.2.1. Genetic Factors.** The incidence rate of ADHD in children is closely related to genetic factors. Studies have found that mothers of ADHD children develop unhealthy habits such as smoking and drinking during pregnancy. These behaviors have many adverse effects on the development of fetus, which may lead to ADHD in children. The rate of ADHD children with ADHD was higher than that of ADHD children in other families. The study shows that 15.3% of the 565 ADHD children have a family history of ADHD, including 15 twins with ADHD. Therefore, the occurrence of ADHD is related to genetic factors. It can be said that inheritance is the internal cause of the disease, and other causes, such as brain injury and environmental factors, are exogenous ADHD.

**2.2.2. Environmental Factors.** ADHD is considered to be a disease closely related to environmental factors. Environmental factors mainly include family and social psychological factors. Bad family environment is the basis of the

formation of ADHD. Parents, family members' words and deeds, and the surrounding environment have a great influence on the formation of a child's character. Environmental factors, such as family, divorce, doting on children, speaking very seriously, even economic poverty, housing, and alcohol, may lead to psychological disorders, inattention, being easy to move, and being impulsive.

**2.2.3. Nutritional Factors.** Studies have shown that artificial colors, additives, and preservatives are contained in foods such as sugars and beverages, cakes, and biscuits, which may cause and aggravate the symptoms of ADHD, such as inattention and behavioral impulse. Children eat too much food containing preservatives, artificial colors, and additives, which has a negative impact on children's growth and development, in addition to affecting children's brain thinking, resulting in ADHD.

**2.2.4. Behavioral Psychological Factors.** Children's behavioral and psychological problems are one of the factors causing ADHD, such as attention problems caused by playing video games for a long time. Some studies have investigated the impact of video games on ADHD. The results show that, regardless of the type of video games, children's inattention is directly proportional to the length of playing games. Children's over-watching of TV programs is also an important factor leading to ADHD. The US government conducts scientific research on the impact of television, mainly to observe the impact of television on ADHD. Researchers put experimental mice in front of the color TV that broadcast the program and conduct experiments for five hours a day. The researchers found that the behavior of this group of mice was active and normal reaction. After a period of abnormal behavior, the mice suddenly became stale and completely stopped. Thus, behavioral factors can also lead to ADHD [6, 7].

### 2.3. Treatment of ADHD by Western Medicine

#### 2.3.1. Drug Therapy

(1) *Central Nervous Stimulant.* Methylphenidate, a respiratory stimulant, can be used in the treatment of ADHD, many of which can directly stimulate the respiratory central system of the medulla oblongata. The most common adverse reactions were insomnia, dizziness, headache, nausea, fasting, palpitations, elevated blood pressure, increased heart rate, aggressive behavior of children and adolescents, growth inhibition, seizures, visual abnormalities, etc. In addition, respiratory central stimulants include dextran methyl ester, dextran amphetamine, and mixed amphetamines.

(2) *Non-Central Nervous Stimulants.* Paroxetine, a specific norepinephrine reuptake inhibitor, has been used more frequently at home and abroad than paroxetine hydrochloride, which has been used for 12 years. Its adverse reactions include loss of appetite, nausea, vomiting, fatigue, insomnia, emotional instability, dizziness, and increased

diastolic blood pressure and heart rate. Among the tricyclic antidepressants, imipramine, dicimab, and nortirine are effective in the treatment of ADHD, but their adverse reactions include sudden death of unknown cause.

Butylphenylacetone indirectly promotes the neurotransmission of dopamine and norepinephrine and has adverse reactions such as loss of appetite, insomnia, irritability, rash, nocturia, and increased convulsion, which slightly increases the risk of drug-induced convulsion. Monoamine oxidase inhibitors are effective in the treatment of ADHD, but they have limitations, which may lead to hypertensive crisis and serotonin syndrome.

SSRI and SNRI: Fluoxetine of SSRI and venlafaxine of SNRI are mainly used in combination with anti-ADHD drugs.

Modafinil is originally a drug for the treatment of narcolepsy, which can improve the awakening state of ADHD children and cause many adverse reactions, including insomnia, headache, and anorexia.

**2.3.2. Psychobehavioral Therapy.** In clinical treatment, it is found that parents' anxiety and other negative emotions will aggravate the condition of children. Therefore, psychological counseling is very necessary. A study through clinical observation of 50 children with ADHD found that psychological nursing combined with drug therapy is more effective than drug treatment alone. The comprehensive psychotherapy mode of sandbox therapy, sensory integration training, and parent training can effectively improve the symptoms of children with ADHD and relieve the parental rearing pressure.

**2.4. Nursing Intervention.** Nursing intervention: it is the result of diagnosis and treatment and nursing. It is the single behavior of nurses in the process of diagnosis and treatment. Nursing intervention is the formulation and implementation of nursing measures. The purpose of nursing intervention is to improve the health status and comfort of patients. Nursing intervention can change or control the various effects on the system adaptive stimulation, that is, to eliminate stimulation, enhance stimulation, reduce stimulus, or change stimulus, so that all the effects on individual adaptation are within the scope. Intervention can also focus on improving people's coping ability, expanding the scope of adaptation, so that all stimuli can act on the scope of adaptation, thereby promoting adaptation responses. Intervention scope: nurses may encounter diseases and can take nursing intervention. Intervention methods are as follows: clinical nursing technology, various inspection measures, drug intervention, health education, social psychological behavior intervention, and family intervention. The intervention measures include the establishment of rehabilitation environment, implementation of patients, family education, family rehabilitation nursing technical consultant, psychological support and consultation of patients, resuscitation of other members of patients, application and management of prescriptions, rehabilitation activities of other rehabilitation hospitals to strengthen teaching, maintenance of continuity

of rehabilitation activities, follow-up, etc. Omaha system divides nursing intervention into health education, guidance and consultation, treatment and procedure, and case management and monitoring. Nursing intervention is the change of nursing mode from single function nursing to holistic nursing, and it is a process of continuous and scientific development of nursing work. In the implementation, not only is the comprehensive quality constantly improved, but also the psychological, social, and professional skills and knowledge are constantly expanded, so as to better adapt to the changes of nursing concept and behavior [8–10].

**2.5. Dopamine Beta Hydroxylase Gene.** Dopamine beta hydroxylase gene ( $D\beta H$ ) is encoded by DBH and located on chromosome 9q34, adjacent to ABO blood group gene.  $D\beta H$  is one of the key enzymes in dopamine metabolism. It oxidizes dopamine to norepinephrine, which is the rate limiting enzyme in the synthesis of norepinephrine. In human body,  $D\beta H$  exists in dissolved state and membrane state, and the amount is almost equal. Circulating  $D\beta H$  exists in a dissolved state, derived from the membrane bound  $D\beta H$  stored in the vesicles, and released into the synaptic space when the vesicles leave the cell. Plasma  $D\beta H$  activity was relatively stable after 4–7 years and was not affected by diet, activity, external stimulation, circadian rhythm, and season. However, the level of individuals varies greatly.  $D\beta H$  exists as dimer and/or tetramer in chromaffin granule synaptic vesicles of adrenal medulla and dense nucleus of peripheral and central noradrenaline neurons. It is the only catecholamine synthase existing in synapses and vesicles. Generally speaking, the changes of norepinephrine level and  $D\beta H$  activity can be used as indicators of sympathetic nervous system function.  $D\beta H$  activity is used to indicate the long-term and continuous changes of sympathetic nervous system function.  $D\beta H$  activity is considered as a reliable indicator of sympathetic nervous system activity, which has been recognized by many scholars at home and abroad [11–13].

### 3. Experimental Methods and Steps

**3.1. Research Group.** All the students (5–15 years old) in a primary school were investigated. In this experiment, the children's behavior questionnaire (simplified version of teacher's questionnaire) and modern psychiatric diagnosis manual were used. A total of 80 children with ADHD were selected, including 60 males and 20 females. A total of 80 normal children (60 males and 20 females) were selected as control group.

**3.2. Diagnostic Methods of ADHD.** The Conners children's behavior questionnaire (simplified teacher questionnaire) was used, with 12 items, including 0-no, 1-yes, 2-some, 3-more, 4-severe, and total score  $\geq 10$ .

Using Conners children's behavior questionnaire, a total of 45 items were summarized as behavior problems, learning problems, psychosomatic disorders, anxiety, and hyperactivity index.

The diagnosis of ADHD is based on the diagnostic criteria of DSM-IV, which has 13 items and lasts for more than 7 months.

The diagnosis is made by a psychiatrist above the chief physician. The final diagnosis excludes schizophrenia, affective disorder, mental retardation, generalized developmental disorder, epilepsy, and other organic diseases.

**3.3. Experimental Reagent.** In this experiment, 11 kinds of main reagents including pyramine standard solution were used. The specific names and manufacturers are shown in Table 1.

**3.4. Experimental Apparatus.** This experiment mainly uses 9 kinds of main experimental instruments including low-pressure electrophoresis instrument. The name and manufacturer of the instruments are shown in Table 2.

#### 3.5. DNA Extraction from Blood

- (1) 250  $\mu\text{l}$  fresh venous blood (insufficient blood and buffered GA).
- (2) Add 25  $\mu\text{l}$  protease K solution and mix well.
- (3) After 250  $\mu\text{l}$  buffer GB is added, the mixture is inverted and placed at 68°C for 12 minutes. Then, the bacteria in the solution are clarified and centrifuged to remove the beads on the inner wall of the tube cover.
- (4) After adding 250  $\mu\text{l}$  absolute ethanol and stirring for 12 seconds, flocculation and sedimentation will occur, and the water droplets on the inner wall of the pipe cover will be removed by simple centrifugation.
- (5) Add the solution obtained in Step (4) and flocculation precipitation into the adsorbent column CB3 (put the adsorbent column into the collection tube), centrifuge at 11800 rpm for 25 seconds, and then put the adsorbent column CB3 into the collection pipe after pouring out the waste liquid.
- (6) 550  $\mu\text{l}$  buffer GD is added to the adsorbent column CB3 and centrifuged at 11,800 rpm for 25 seconds. After the waste liquid is poured, put the adsorbent column CB3 into the collection pipe.
- (7) 650  $\mu\text{l}$  bleach PW is added to the adsorbent column CB3 and centrifuged at 11,800 rpm for 25 seconds. After the waste liquid is poured, the adsorbent column CB3 is put into the collection tube.
- (8) Repeat Step (7).
- (9) The adsorbent column CB3 is put into the collecting tube and centrifuged at 11,800 rpm for 3 minutes. After the waste liquor is poured out, the adsorbent column CB3 is placed at room temperature for several minutes to completely dry the remaining bleaching solution in the adsorbent.

TABLE 1: List of main experimental reagents.

Name	Manufacturer
Diamine standard solution (20 nm)	Sigma, USA
Tyramine hydrochloride	Sigma, USA
Catalase	Shanghai Bioengineering Co., Ltd
Youjiangning	Sigma, USA
N-ethyl maleimide	Shanghai Dongfeng Biotechnology Co., Ltd
Ascorbic acid	Shanghai Bioengineering Co., Ltd
Partial sodium sulfite	Shanghai Bioengineering Co., Ltd
Sodium periodate solution	Produced by Guangdong Shantou Xilong chemical plant
Dowex-50w × 8 ( <i>H</i> <sup>+</sup> , 200–400 mesh)	Sigma, USA
Amine hydroxide	Tianjin Kemeo Reagent Development Center
Sodium acetate buffer	Sigma, USA

TABLE 2: List of main experimental instruments.

Name	Manufacturer
PCR thermal cyclers	LifePro Thermal Cycler
Electric constant temperature water bath box	Shanghai Xinmiao Medical Device Manufacturing Co., Ltd
UV projection reflectance analyzer	Yongjia Shangtang Teaching Instrument Factory
Low-pressure electrophoresis apparatus	Beijing Liuyi Instrument Factory
Vertical automatic electrothermal pressure steam sterilizer	Shanghai Shen'an Medical Device Factory
Electric blast drying oven	Beijing Yongguangming Medical Equipment Factory
Desktop centrifuge	Hunan Xiangyi Laboratory Instrument Company
Electronic balance	Guangdong Huruiming Instrument Co., Ltd
Gel imaging system	Shanghai Jiapeng Technology Co., Ltd

(10) The adsorbent column CB3 is placed in a clean centrifuge tube, and 100–250  $\mu\text{l}$  elution buffer TE is added in the middle of the membrane. The buffer solution is placed at room temperature for 3–6 minutes, centrifuged at 11800 rpm for 3 minutes, and collected into a centrifuge tube.

### 3.6. Determination of Plasma *D* $\beta$ H Activity

(i) Principle: *D*  $\beta$  H transforms tyramine into pyrazine, which is oxidized to bis by sodium iodate photo-benzaldehyde, and then the absorbance change is measured at 420 nm absorption peak with spectrophotometer, and 11  $\mu\text{mol}/\text{min}$  of diamine per minute generated per liter of blood (<35°C) represents the active unit of *D*  $\beta$  H (IU:  $\mu\text{mol}/\text{L}/\text{min}$ ) [14, 15].

(ii) The determination steps are as follows.

- (1) 62  $\mu\text{l}$  heparin anticoagulant plasma was diluted to 450  $\mu\text{l}$  with double distilled water.
- (2) The enzyme solution was added into a centrifuge tube containing 250  $\mu\text{l}$  1 m (pH 5.0) sodium acetate buffer.
- (3) The plasma inhibitor 0.2 m-ethylmaleimide 130  $\mu\text{l}$  was added.
- (4) 250  $\mu\text{l}$  insulation solution (containing 65  $\mu\text{l}$  of 0.5 m tyramine, catalase, 0.52 m sodium chloride, and 0.06 m youjiangning) was added.
- (5) 65  $\mu\text{l}$  ascorbic acid 0.3 m reducing agent was added (Vit C, fresh preparation).

(6) Another blank tube was taken and inactivated in boiling water bath for 6 minutes, and the remaining solution was the same as that of the detection tube.

(7) It was placed in 35°C water bath for 2 hours.

(8) 550 l of precipitated enzyme protein was added to each tube to terminate the reaction, centrifugation: 2600 rpm.

(9) The supernatant was transferred to the chromatographic column with 0.6–0.8 ml dowex-60w × 8 (*H* + 300–500). The wall and sediment were cleaned with 1 ml of double distilled water, and the rinsing solution was also sent to the column.

(10) Dilute 3 times with 5  $\mu\text{l}$  of double distilled water, and clean the centrifuge tube with cleaning solution

(11) Use 1  $\mu\text{l}$  4M ammonium hydroxide (NH<sub>4</sub>OH) solution to elute amine on the adsorption column

(12) 200  $\mu\text{l}$  of 2% sodium periodate solution was put in the eluent, let the amine change into p-light benzaldehyde, then 250  $\mu\text{l}$  10% sodium sulfite solution was added to reduce excess periodic acid, and the absorbance was determined at 450 nm with a UV spectrophotometer.

(13) The other was in the tube, and +30 nm diamine 1 ml, 5 m amine hydroxide 1  $\mu\text{l}$ , then 250  $\mu\text{l}$  3% sodium periodate solution, and 10% sodium bisulfite solution were added as standard.

(14) The preparation process of dowex-50w × 8 resin: take 20–60 g resin, soak for 3 hours,

remove the small particles on the upper part of the resin repeatedly, and keep the precipitation resin. Rinse with water for 2 hours. Then, soak the column in 0.6 N hydrochloric acid for 2.5 h, wash it with water until it is neutral, repeat twice, and finally put the column into neutral water with a loading capacity of 0.7–0.9 ml.

**3.7. Nursing Intervention Methods.** The two groups of children had the same clinical treatment plan. The control group was given routine treatment and nursing plan, namely, basic nursing guidance such as school entrance, health education of parents, drug treatment operation, and psychological intervention, while the experimental group was given comprehensive nursing in treatment.

- (1) Social support: parents are encouraged to communicate with the school head teacher regularly, tell the children the basic situation, let the teacher face the disease, and understand the disease, showing the abnormal situation of the school. Eliminate discrimination and misunderstanding, give correct education and key protection of children, refuse bullying other students, and children get more encouragement and help in school.
- (2) Behavior correction: compared with competitive sports children, the form of knowledge competition, and the diversion of their attention and play to their character and disease characteristics, gradually alleviate and correct their high mental symptoms. Use mild language to communicate with children and summarize and guide their bad behaviors. Children's hard language is strictly forbidden to be angry; encourage children's positive behavior, let them gradually realize that it is correct to do so, and continue to do so.
- (3) Environment shaping: The parents were told to change the children's environment, to give a more warm and harmonious family atmosphere, and the main color of the children's bedroom is warm. And arrange some plants and cultivate their good mood to encourage children to do the right thing. We do not need to ask children to study too much, let them relax, spend more time with children, carry out outdoor activities, and cultivate the feelings between parents and children, so as to gradually correct their psychological state.

**3.8. Statistical Method.** The genotypes of ADHD children and their parents can be obtained by separating 8% acrylamide gel, and the genotype of the family control group can be obtained by removing parental genotypes.

Spsv15 and sas7.0 were used for data management and statistical analysis. The data were input twice to check whether there were logical errors. Hardy Weinberg equilibrium analysis was performed using  $\chi^2$  test, and core family association analysis was performed by HHRR and ETDT methods to detect the association between polymorphism

and ADHD. Four table data or  $X$  table data  $\chi^2$  test were used in children and control group.

## 4. Experimental Results and Analysis

### 4.1. Gel Electrophoresis Experiments and Analysis of Plasma D Beta H Activity

**4.1.1. Results of Gel Electrophoresis Analysis.** Results: the results of gel electrophoresis are shown in Figure 1.

Results analysis: the results of gel running test showed that the separation effect of DNA was good, no breakage, the concentration was visible, and the sampling position was at the 16th in the first row. The next step of judgment and analysis can be carried out.

**4.1.2. Analysis of Plasma D  $\beta$  H Activity.** Results analysis: 80 people in ADHD group were  $(17.81 \pm 1.41) \mu\text{mol/L/min}$ , and those in control group were  $(17.83 \pm 1.72) \mu\text{mol/L/min}$ . There was no significant difference in D  $\beta$  H activity between the two groups ( $t = 2.52, P = 0.05$ ). There was no significant difference in D  $\beta$  H activity between the two groups ( $P > 0.05$ ). There was no significant difference in D  $\beta$  H activity between A2/A2, A2/A3, and A3/A3 genotypes in ADHD group ( $F = 1.669, P > 0.05$ ).

**4.2. Comparative Analysis of the Detection Rate of Anxiety Disorder.** 160 children in the two groups were investigated. 80 children in ADHD group were examined. 35 children with ADHD had anxiety disorder. 80 children in the control group were examined, including 6 with anxiety disorder.

According to the statistical analysis chart in Figure 2, the detection rate of anxiety emotional disorder in ADHD children was significantly higher than that in non-ADHD children. The difference of detection rate of anxiety emotional disorder between ADHD children and non-ADHD children was statistically significant ( $\chi^2 = 8.524, P < 0.05$ ). ADHD as a common mental illness in children, where the detection of anxiety-type emotional disorder has positive significance, can reflect the psychological state of children through data and provide help for the treatment effect through the research of psychological state.

**4.3. Comparison of Genotype and Allele Distribution.** The distribution of DBH I vs5 Taq I genotypes and alleles in 80 children with ADHD and 80 normal controls was studied by the statistical analysis chart in Figure 3. The experimental data showed that, compared with the two genotypes, the A2/A2 genotype in ADHD group was significantly increased, while the A1/A1 and A1/A2 genotypes were significantly decreased ( $P = 0.007$ ). By comparing the alleles of the two genotypes, A1 was significantly decreased and A2 was significantly increased in ADHD children; the difference was statistically significant ( $P = 0.001$ ). The or value of A1 was 0.53, which was a protective factor for ADHD, and the or value of A2 was 2.65, which was a risk factor of ADHD. This study confirmed that there are many gene risk factors in patients with ADHD, which has a potential relationship with

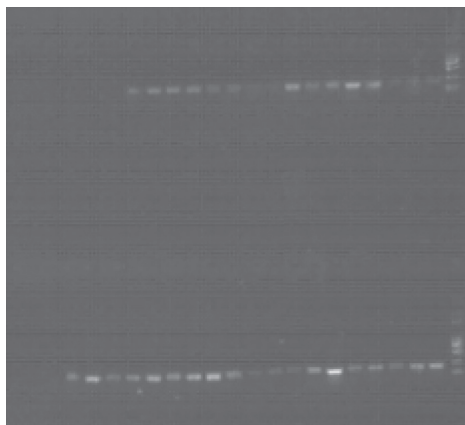


FIGURE 1: Results of gel electrophoresis.

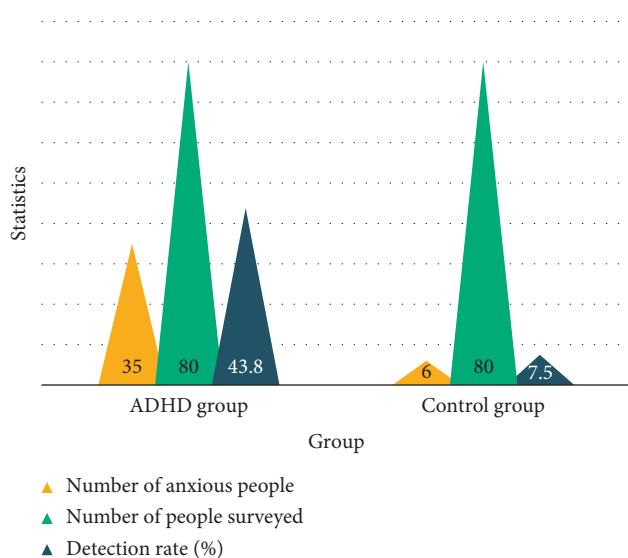


FIGURE 2: Analysis of the detection rate of anxiety disorder in ADHD children.

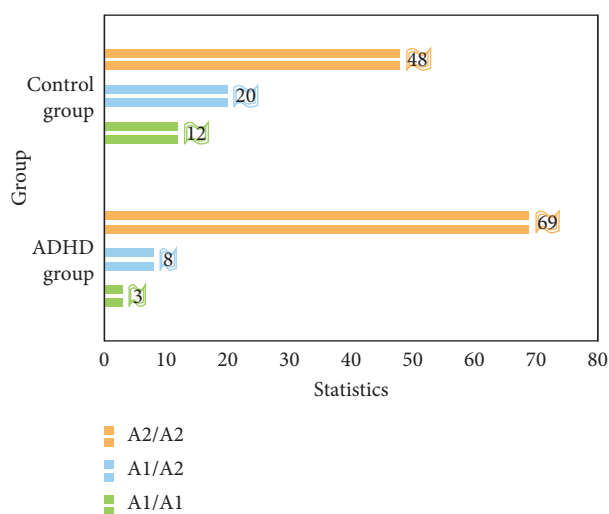


FIGURE 3: Comparative analysis of genotype and allele distribution between ADHD children and normal controls.

the pathogenesis of ADHD. Generally speaking, the more risk factors in the gene, the higher the probability of mental illness. This study also proved this point again.

**4.4. Comparison of Allele Frequency Distribution of  $D\beta H$  Gene *Taq I* Polymorphism.** According to the statistical analysis results in Figure 4, two alleles were found between the ADHD group and the control group. The allele frequency of A1 in ADHD group was slightly lower than that in the control group, and the allele frequency of A2 was slightly higher than that of the control group. There was no significant difference in allele frequency distribution of  $D\beta H$  gene *Taq I* polymorphism between the two groups ( $P > 0.05$ ). Although there was no significant difference in *Taq I* polymorphism between the two groups, the subdivided indexes still had comparative significance. It can be concluded that the A2 allele of ADHD patients also reflects the dynamic relationship between ADHD and  $D\beta H$  gene. This study further confirmed the  $D\beta H$  gene characteristics of ADHD as a mental disease and provided a new direction for the follow-up treatment.

**4.5. Comparative Analysis of Symptom Scores of Attention Deficit.** According to the statistical analysis in Figure 5,  $t = 12.262$ ,  $P < 0.01$ , the difference was highly statistically significant, indicating that ADHD group can significantly improve the symptoms of attention deficit, and the control group before and after treatment of attention deficit symptom score comparison  $t = 10.126$ ,  $P < 0.01$  has high statistical significance, indicating that the control group can significantly improve the symptoms of attention deficit. After treatment, the scores of attention deficit symptoms of the two groups were compared,  $t = 2.028$ ,  $P = 0.029 < 0.05$ , indicating that the effect of nursing intervention mode in the treatment of attention deficit in ADHD group was better than that in control group. This study is based on the nursing intervention module. Through the experimental analysis, it shows that the nursing intervention mode has a positive effect on the treatment of ADHD. For children who have been suffering from the disease, the treatment at all stages has an improvement effect.

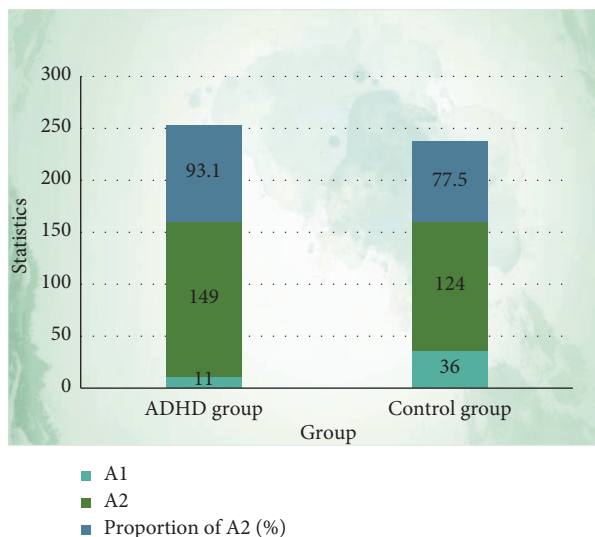


FIGURE 4: Comparison of allele frequency distribution of D  $\beta$  H gene Taq I polymorphism between ADHD group and control group.

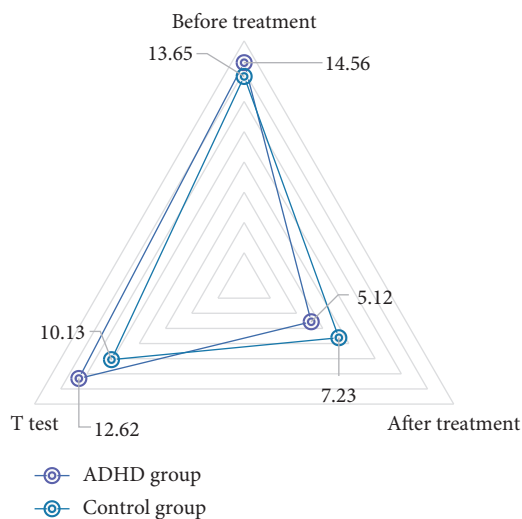


FIGURE 5: Analysis chart of ADHD group and control group.

## 5. Conclusions

ADHD is a typical mental disorder, which has the first place in children's mental illness. Due to the high incidence rate of ADHD, there will be a large number of patients every year. Because the pathogenesis is not clear, there is no authoritative diagnosis and treatment program. Therefore, the study of ADHD patients based on change has become particularly important, which has a good reference value for clinical treatment research. In this paper, based on the nursing intervention model of dopamine beta hydroxylase gene polymorphism, it is based on the genetic factors of ADHD as the main direction. This paper summarizes the theoretical basis of the main research on ADHD at present and makes an in-depth analysis of it and puts forward constructive suggestions for the prevention and treatment of ADHD. The corresponding experimental model was established by the method of comparative experiment. Through the

experimental model, a number of experiments including Taq I polymorphism and anxiety disorder were carried out. Analysis of experimental data shows that ADHD, as a mental disorder, has the common characteristics of common psychological diseases. In the pathogenesis, genetic factors may play an important role. The research results further verify the genetic theory. This experiment has achieved ideal results, made a contribution to the research in this field, and provided a new idea for the clinical treatment of ADHD.

## Data Availability

No data were used to support this study.

## Conflicts of Interest

The authors declare that there are no conflicts of interest regarding the publication of this paper.

## References

- [1] H. C. Lou, J. Andresen, B. Steinberg, T. McLaughlin, and L. Friberg, "The striatum in a putative cerebral network activated by verbal awareness in normals and in ADHD children," *European Journal of Neurology*, vol. 5, no. 1, pp. 67–74, 2015.
- [2] T. U. Hauser, V. G. Fiore, M. Moutoussis, and R. J. Dolan, "Computational psychiatry of ADHD: neural gain impairments across marrian levels of analysis," *Trends in Neurosciences*, vol. 39, no. 2, pp. 63–73, 2016.
- [3] C. Tye, K. A. Johnson, S. P. Kelly et al., "Response time variability under slow and fast-incentive conditions in children with ASD, ADHD and ASD + ADHD," *Journal of Child Psychology and Psychiatry*, vol. 57, no. 12, pp. 1414–1423, 2016.
- [4] A. T. Azadi, S. A. Marshall, J. A. Mautone et al., "Parent attendance and homework adherence predict response to a family-school intervention for children with ADHD," *Journal of Clinical Child & Adolescent Psychology*, vol. 44, no. 1, pp. 58–67, 2015.
- [5] A. Patterson and M. Equit, "Comorbidity of ADHD and incontinence in children," *European Child & Adolescent Psychiatry*, vol. 24, no. 2, pp. 127–140, 2015.
- [6] I. Verheul, W. Rietdijk, J. Block, I. Franken, H. Larsson, and R. Thurik, "The association between attention-deficit/hyperactivity (ADHD) symptoms and self-employment," *European Journal of Epidemiology*, vol. 31, no. 8, pp. 793–801, 2016.
- [7] J. H. Newcorn, V. Harpin, M. Huss et al., "Extended-release guanfacine hydrochloride in 6-17-year olds with ADHD: a randomised-withdrawal maintenance of efficacy study," *Journal of Child Psychology and Psychiatry*, vol. 57, no. 6, pp. 717–728, 2016.
- [8] Z. Ramos-Quiroga, "Nursing intervention of venous thrombosis after picc catheterization%picc nursing intervention after venous thrombosis," *Chinese Community Physician*, vol. 34, no. 4, pp. 134–135, 2018.
- [9] N. Klafke, C. Mahler, C. Von Hagens et al., "A complex nursing intervention of complementary and alternative medicine (cam) to increase quality of life in patients with breast and gynecologic cancer undergoing chemotherapy: study protocol for a partially randomized patient preference trial," *Trials*, vol. 16, no. 1, pp. 1–12, 2015.
- [10] C. He, X. Liang, and Y. Qu, "Effect observation of continuous nursing intervention for the patients with acute myocardial infarction after pci%. Observation of the effect of continuous care on patients with acute myocardial infarction and coronary intervention therapy," *China Medical Herald*, vol. 13, no. 1, pp. 159–162, 2016.
- [11] J. Long, G. Huang, B. Liang, W. Ling, X. Guo, and J. Jiang, "The dopamine beta-hydroxylase gene polymorphism rs1611114 is associated with schizophrenia in the Chinese Zhuang but not Chinese han population," *Molecular Genetics & Genomics*, vol. 291, no. 5, pp. 1–9, 2016.
- [12] J. Long, G. Huang, B. Liang et al., "The dopamine beta-hydroxylase gene polymorphism rs1611114 is associated with schizophrenia in the Chinese Zhuang but not Chinese han population," *Molecular Genetics and Genomics*, vol. 291, no. 5, pp. 1813–1821, 2016.
- [13] M. Su, M. Hashemi, S. Shahrabadi, M. Rezaei, and M. Taheri, "Lack of association between dopamine beta-hydroxylase (dbh) 19-bp insertion/deletion polymorphism and risk of schizophrenia," *Iranian Journal of Psychiatry*, vol. 11, no. 4, pp. 239–243, 2016.
- [14] W. G. Telford and R. A. Miller, "Detection of plasma membrane ca(2+)-atpase activity in mouse t lymphocytes by flow cytometry using fluo-3-loaded vesicles," *Cytometry*, vol. 24, no. 3, pp. 243–250, 2015.
- [15] W. Li, C. Wang, J. Lin, Qi. Wang, Y. Liu, and J. Chen, "Value of quantitative detection of plasma cell-free dna in the assessment of inflammatory bowel disease activity," *Chinese Journal of Digestion*, vol. 38, no. 6, pp. 382–385, 2018.

## Research Article

# CPLD-Based Displacement Measurement System for Nanoscale Grating Ruler

Jiyuan Sun<sup>1,2,3</sup> and Chunlin Tian<sup>1,4,5</sup> 

<sup>1</sup>College of Mechanical and Electrical Engineering, Changchun University of Science and Technology, Changchun 130022, Jilin, China

<sup>2</sup>College of Electrical and Information Engineering, Beihua University, Jilin 132021, Jilin, China

<sup>3</sup>Jilin Guangyu Technology Co., Ltd., Jilin 132021, Jilin, China

<sup>4</sup>Guangdong Guangji Hi Tech Co., Ltd., Foshan 528000, Guangdong, China

<sup>5</sup>Changchun University of Science and Technology, Chongqing Research Institute, Chongqing 401135, Chongqing, China

Correspondence should be addressed to Chunlin Tian; [tcl@cust.edu.cn](mailto:tcl@cust.edu.cn)

Received 21 July 2020; Revised 29 August 2020; Accepted 14 October 2020; Published 3 November 2020

Academic Editor: Tifeng Jiao

Copyright © 2020 Jiyuan Sun and Chunlin Tian. This is an open access article distributed under the Creative Commons Attribution License, which permits unrestricted use, distribution, and reproduction in any medium, provided the original work is properly cited.

With the continuous development of science and technology, industrial production has higher and higher requirements for precision. Many high-precision measurement technologies emerge as the times require, and nanoscale grating ruler displacement measurement technology is one of them. As a kind of precision sensor, nanoscale grating ruler has important application in displacement measurement system. CPLD has the advantages of high integration and fast programming speed, which is often used to control the displacement measurement system of nanoscale grating ruler. The purpose of this paper is to deeply explore the measurement effect and related application principle of nanoscale grating ruler displacement measurement system based on CPLD technology. A set of nanoscale grating ruler displacement measurement system is designed based on CPLD technology. The output signal of grating ruler is programmed by CPLD. The  $x$ -axis displacement of the experimental platform controlled by stepping motor is measured, and the measured data are recorded by carrying out analysis and research. The results show that compared with the traditional phase difference measurement system, the measurement accuracy of the system based on CPLD is improved by 24.7%, the robustness of the measurement system is improved by 18.6%, and the measurement speed is increased by 27.3%. Therefore, this kind of nanoscale measurement precision grating ruler displacement measurement control system based on CPLD has three characteristics: high measurement accuracy, strong anti-interference ability, and high measurement motion efficiency, which can effectively meet the requirements of grating ruler displacement measurement system for high-precision manufacturing technology.

## 1. Introduction

Manufacturing is already a major pillar industry of a country, and it is the most fundamental technological foundation on which a country depends for prosperity. At present, manufacturing engineering science and mechanical manufacturing engineering technology are rapidly developing towards the two directions of ultraprecision and miniaturization. Ultraprecision micromachining has developed into one of the important technical contents of advanced machinery manufacturing [1]. At present, the processing of superfine materials has gradually entered a

new field of nanotechnology. Grating measurement displacement technology with higher nanometer order and high resolution is already an indispensable important part in the processing of modern superfine materials, and it is also urgently needed. One of the three key technologies is studied and solved [2]. Compared with other linear and displacement measuring sensors, the grating ruler has a high technical comprehensive application advantage in improving the measurement digital display accuracy, resolution, reliability, technical requirements for the application environment, and prices. Therefore, the use of grating rulers has a very wide range of applications in

measuring digital displays, CNC machine tools, and measuring instruments [3].

Nanometer-scale grating interferometric measurement technology mainly uses interference diffraction-type gratings. The grating pitch is generally  $2\ \mu\text{m}$  or  $0.5\ \mu\text{m}$ . The diffraction width of the grating line is close to the diffraction wavelength of light, which can produce interference diffraction and short-wave interference luminescence. The phenomenon and so on forms fringes, and its principle for measuring light is also called the principle of optical interference diffraction [4]. In view of the shortcomings of the control accuracy of the traditional standard scale displacement measurement and management system, this paper proposes a CPLD-based two nanometer-scale displacement measurement control system for standard grating size, which is used in precision instrument industry production and testing equipment. In the scale mobile sensor, CPLD has many advantages such as high system integration, fast working speed, convenient programming, low price, and so on [5]. On the basis of optimizing and improving the key technology of the displacement measurement system of the nanoscale grating ruler, using CPLD to assist the development can not only improve the accuracy, integration, and reliability of the displacement measurement system, but also reduce the production cost of the displacement sensor of the nanoscale grating ruler.

In order to explore the measurement effect and related application principles of the CPLD-based nanoscale displacement measurement system, this paper consults a large number of related materials. Among them, Versino et al. introduced the existing displacement measurement system in China and emphasized that the existing relatively backward displacement measurement technology could not meet the industrial production requirements of high-precision requirements and analyzed the current research status and research of nanoscale grating rulers in China significance and put forward the technical guidance and research direction of nanoscale grating ruler [6]. Xu et al. gave a detailed introduction to the principles and applications of nanotechnology, carefully discussed the core theories of nanotechnology, pointed out that the emergence of nanotechnology is a huge industrial change, and affirmed the importance of nanotechnology, but also pointed out that nanotechnology. The shortcomings of technology and the points of attention in application are shown in [7]. Peipei et al. elaborated the development process and application field of CPLD in detail, discussed the working principle of CPLD, and summarized a set of CPLD programming control technology, and the experiment proved the feasibility of CPLD programming control technology [8]. Pinna et al. designed a CPLD-based scale displacement measurement system for nanoscale gratings, improved the design ideas, and made a detailed introduction to the working principle of this scale displacement measurement system. This design is still in the testing stage [9]. Through research, Wang et al. found that the CPLD-based nanoscale displacement measurement system has the characteristics of high measurement accuracy, convenient operation and practicality, high

system robustness, and high detection efficiency. It is a displacement measurement technology with broad application prospects [10].

## 2. Purpose

The purpose of this article is to explore the measurement effect and related application principles of the CPLD-based nanoscale displacement measurement system. On the basis of summing up the precious experience of previous people, this paper has made relevant improvements in research methods and design schemes. First of all, this article uses CPLD as the technical basis for the measurement of the zero-point displacement of various nanotechnical-grade solid grating sizes and provides the zero-point measurement temperature reference directly in the form of physical software during the design of the system software, using a solid with low hot spots and expansion temperature coefficient. Nanogratings are made directly from solid materials such as quartz or zero-point thermal expansion coefficient glass. Secondly, this article takes the multimeasurement grating system as the technical basis, adopts the principle of the new static grating error parameter corrector, and based on the research of the current measurement results, the multimeasurement grating system as the technical basis is based on the secondary. A new type of high-precision grating measurement sensor for measuring nanoparameter gratings of moiré fringe diffraction signals.

## 3. Working Principle of Grating Ruler

The basic principle of the design of the displacement signal measurement and processing system on the grating ruler is mainly to use the relative direction between the scale and the raster scanning image mask to move to form moiré fringes under the illumination of the incident light source [11]. The moiré fringes pass through multiple photoelectric. After the signal sensor is converted, it becomes an approximate sine and cosine wave photoelectric signal, which is the original raster scanning mask signal [12]. Then we use different pulse tube fine analysis methods to obtain different automatic counters and pulse metering signals for the measuring device and step distance [13]. The pulse count signal is generally considered to be a continuous two-path orthogonal pulse signal. The two pulse signals are, respectively, connected to the subsequent two-way reversible automatic counting control circuit, the calculated parameter value of the counter is multiplied by the value, and the step of the measuring device is the radial displacement of the measuring scale and its measured count value [14]. The maximum speed of the grating ruler movement measurement allowed signal movement cycle speed is generally determined by the measurement grating ruler input and output movement frequency and the input signal movement cycle frequency of the raster scan image signal. The calculation formula of the maximum displacement speed of the grating ruler measurement is shown in the following equation:

$$L = \sum_{j=1}^{V-N} \frac{D_f}{D} * \text{Info}(D_f). \quad (1)$$

Among them,  $L$  represents the maximum displacement speed of the grating ruler;  $D$  represents the output frequency.

Under the certain premise that the movement signal oscillation period of the measured signal of the grating is unchanged,  $v$  is proportional to its frequency at the maximum output of the grating ruler, and the step speed during measurement corresponds to its resolution. If we increase the current electronic measurement [15], the electronic subdivision multiple and frequency of the subdivision counting circuit will also increase its resolution (due to the reduction in step speed during measurement), because we are subject to the maximum response output frequency of the current electronic metering subdivision counting circuit and for subsequent. The maximum input response frequency of the electronic counting subdivision circuit is very limited. With the continuous increase of the electronic subdivision frequency multiples, the maximum output response frequency of the grating ruler will also decrease, so the maximum measurement speed may allow the measurement speed to decrease. Therefore, when the maximum allowable speed is measured, the maximum measuring speed step of grating ruler is directly proportional to the positive and negative proportion of the maximum grating speed. Therefore, the nanoscale ruler is used for high-speed movement measurement (the maximum speed when moving at the allowed speed is generally  $\geq 10$  m/s), the movement resolution is generally set to the order of nanometers ( $0.3 \sim 1 \mu\text{m}$ ), and if used for nanometer scales with low-speed movement measurement (movement speed is generally  $\leq 200$  mm/s), the resolution is likely to reach the order of micro-nano ( $1 \sim 30$  nm).

#### 4. Signal Switching Synthesis of Grating Ruler

The displacement measurement in the above cases is one of the advanced grid rulers (coarse grid ruler) suitable for low-resolution and high-speed measurement in the fast startup state, and the other is the ordinary nano or advanced standard grid ruler (fine grid ruler). When the positioning motion control process of the detection system changes from fast motion to medium motion to slow motion, when the axis of the detection system starts to move at high speed, the number of pulses is generated by the fast switching motion and the number of pulses of the nanoscale scientific ruler [16]. The coarse and fine optical rulers simultaneously measure the movement of the system axis and the displacement velocity at the beginning of the movement [17]. An important characteristic of a single fine grid ruler is that the maximum speed allows the system to move and the measurement speed is proportional to the maximum resolution. Therefore, the measurement speed  $v$  exceeds the maximum speed of the fine grid ruler during the measurement period 1-2 and the system deceleration movement [18]. During the measurement of the speed  $V_{\text{max}}$ , the system will decelerate. During the measurement period 3,

the other measurement indication signals on the coarse fiber scale are valid, and the other measurement indication signals on the fine grid ruler are valid and invalid [19]. When the  $V_{\text{max}}$  speed in period 3 is decelerated, the pulse signal of the displacement gauge and the roughness scale is used as the signal of the maximum displacement characteristic measurement degree [20]. In addition, since the displacement characteristic of acceleration enables speed movement, the maximum allowable measurement speed and the measurement moving speed ( $> 1$  m/s) at full scale can be obtained [21]. When a chemical system starts to move slowly and continuously at a certain time (in the v-type 1 nanometer chemical lattice ruler, the counter and pulse are switched quickly, and this process is actually at a certain moment) (the chemical lattice ruler counter is pulse edge, the moment when the zero point rises rapidly), a rapid movement clears the switching process between the precise grating ruler and the counter. The counting pulse calculation formula of the nanoscale grating ruler is shown in the following equation:

$$f = \int \int_{\Omega} (y^2 + M^2) p dM. \quad (2)$$

Among them,  $f$  represents the pulse number of the nanoscale grating ruler;  $M$  represents the grating ruler grid number.

#### 5. Design of Measurement System

In this paper, the CPLD2018 chip is mainly used to subdivide the direction output control signal circuit of a nano-quality conductor grating ruler [23]. According to the directional phase shift relationship between the two orthogonal direction encoding control signals, the two orthogonal inputs of the chip are encoded. The signal is converted into two control signals for output: one signal output is the four-bit triple frequency control signal after the object is subdivided, and the other signal output is the direction control signal when the object moves [24]. After the fine resolution, the signal with nano power level and grating size will be connected to the microcontroller; that is, the two cent pins of a CPLD2018 are connected to the cnp2 port of the automatic controller. The signal parameters are synchronously counted and automatically calculated and processed to obtain an actual displacement in the  $x$ - and  $y$ -directions. That is, when an  $x$ -direction two-axis edge-finding motor can drive the two-axis edge-finding device to move on an  $x$ -direction axis, if a touch contact encounters a passively detected object, the motor generates a control signal to output, the controller [25]. After detecting and receiving the signal input by the motor, a corresponding control action and data processing can be performed. This control system mainly adopts the photoelectric driven inductive workpiece edge finder, using the conductive motion characteristics of an object of a workpiece. When a trigger probe directly touches the object to the surface of a workpiece object, an inductive loop is formed on the circuit, which generates a contact output electrical signal. Using these basic characteristics of the automatic edge finder, it is fixed on the  $y$ -shaped axis, and

the wireless contact signal is obtained to insert the output trigger signal to the edge of the surface of the automatic workpiece object, forming the edge output trigger signal input of the automatic controller. In the structural design of the control system, the control management system realizes the transmission of control data packets and the reception of the control system commands to the transmitter through the serial bus communication. There is a half-port or full-duplex single-port serial data communication port inside the controller, so a serial data communication can also be conveniently carried out between a controller and two upper computers at the same time. Before the motor performs a serial communication, it must meet certain voltage conditions, because the parallel serial port voltage of the cold machine is higher than the rs220 voltage level and the parallel serial port tbl20 level of the single-chip computer, so they must be between them. There is a circuit connected to the serial converter above the voltage level. The automatic collection of the output data of the automatic displacement of a nanoscale microscale is to collect the signal data output by the displacement of a nanoscale microscale through the fine-grain resolution. Since a nanometer-size level is a physical period of the output signal of the grating size, it represents a displacement of  $4\ \mu\text{m}$ , and the cycle of each point of the output signal after fine resolution represents a displacement of  $2\ \mu\text{m}$ . After calculating the value of the counter in the controller, it is displacement data. The numerical calculation formula of the counter of the nanoscale grating ruler displacement measurement system is shown in the following equation:

$$N(c) = (S_k - T_k) * F_k * (N - c_k)k^N, \quad (3)$$

where  $N(c)$  represents the value of the grating counter, and  $N$  represents the calculation period coefficient of the grating.

## 6. Implementation of Measurement System Based on CPLD

The biggest feature of the nanoscale grating displacement measurement system designed in this paper is that except for some peripheral analog circuits, the digital circuits involved are all realized by CPLD. Each part of the circuit is designed and compiled in the CPLD development software MAX+PLUS II to generate programming files and then downloaded to the CPLD chip. The two same-frequency signals FR and FS output the phase difference signal phase through the CPLD phase detector. The phase signal is sent to the gate of the counter as the gate signal to control the counting time of the counter, and its function is equivalent to the gate circuit. The input pulse reference count signal is multiplied by the pulse frequency multiplier and used as a pulse counter. The counter pulse count signal pulse is input to CLK, and at the same time it is sent to the integrated control processing link for control conversion. Because the grating rule requires a total of 1200 pulse signals throughout, CPLD internally designs an 18-bit reversible counter; the lower 10 bits represent data, the highest bit is the status bit, and the display result is 1, indicating that the current

position of the grating ruler is in the negative direction of the initial zero point. If it is 0, it means that the current position of the nanoscale grating ruler is the square of the initial zero point. The three pairs of square wave signals output by 4006 after being shaped by  $90^\circ$  phase difference are A1 and B1, A2 and B2, A3 and B3, respectively. When the A-channel signal in CPLD has an upward edge, the B-channel signal is detected. If the B-channel signal is high, it indicates that the nanoscale grating ruler is moving in the positive direction, and the current counter increases by "1." If the signal of channel B is low, it means that the nanoscale grating ruler is moving in the negative direction, and the current counter is decremented by "1." Due to the high efficiency, signal-to-noise ratio, and other photoelectric signal characteristics of the photoelectric converter using clad two chips, it can only directly reach the optimal value required by the process performance design of the related device system under the appropriate operating timing conditions, and the output performance is stable reliable photoelectric signal; the process design of the driving integrated circuit has therefore become one of the key issues in the process design process. In this paper, the external pulse filter signal is shaped by 4006 trigger pulse filter and then sent to the cold for the feeder. The CPLD uses the CPLD to count and calculate the external pulse filter signal and store the pulse data in the internal pulse register. The single chip microcomputer reads the data quickly through a bus data interface, transforms the scaled function of the input data frequency, and sends it to the bus LCD line for precision display. The working parameters of the CPLD chip in the measurement system designed in this paper are shown in Table 1.

## 7. Verification Results and Related Discussions

*7.1. A Statistical Result of Displacement Measurement Speed and Accuracy of Nanoscale Grating Ruler.* Using CPLD-based displacement measurement system of nanoscale grating, the principle verification experiment was carried out on the displacement measurement system. The comparison results of the measurement data show that the displacement measurement system of the nanoscale grating and the displacement measurement system of the commercial laser interferometer can describe the movement of the moving stage. As the displacement of the moving stage increases, the displacement difference between the two measurement systems gradually increases. This is caused by the cosine error caused by the angle between the measuring direction of the nanoscale or laser interferometer and the moving direction of the moving table. Statistical analysis shows that the correlation coefficient of the measured data of the two displacement measurement systems is 0.8627, and the experiment verifies the correctness of the principle of the nanoscale displacement measurement system. The cosine error of the displacement measuring system of the nanoscale grating ruler based on CPLD is shown in Table 2.

Through the analysis of the displacement measurement system based on CPLD-based nanoscale ruler and the displacement measurement system of laser interferometer on the displacement measurement of the moving platform, the

TABLE 1: CPLD chip working parameters.

Model	Basic materials	Signal period	Frequency
Test deployment	Ceramics	0.25	-1000
Voltage	Aluminum alloy	0.33	-850
Electric current	Copper alloy	0.47	-1200
Power	Glass	0.59	-1130
Length	Steel belt	0.84	-1480

TABLE 2: Cosine error of displacement measurement system of nanoscale grating ruler.

Group	Collection speed	Coarse grating	Fine grating	Switch synthesis (%)
Operating cycle	165.7	55.34	338.7	19.5
Operating hours	215.3	62.88	426.1	36.7
Large range	185.6	71.25	297.4	65.3
Cosine error	203.8	81.61	358.2	75.1

measurement consistency experiment was carried out. The CPLD controls the grating ruler to make periodic reciprocating movements in the measurement direction, and at the same time the grating ruler and the laser interferometer displacement measuring system measure the displacement of the moving table at a frequency of 5 Hz. Using a laser interferometer or cosine interferometer to measure the linear displacement error in the system can be measured with a laser. Compared with the measurement data of the grating ruler and the laser interferometer displacement measurement system, the moving stage moves back and forth at intervals of (-5 mm, 10 mm), the absolute value of the difference between the measurement data (Dev) is less than 50 nm, and the measurement time is less than 0.3 s. The study found that compared with the traditional laser interferometer displacement measurement system, the measurement speed of the CPLD-based nanoscale grating displacement measurement system has increased by 27.3%. The specific data is shown in Figure 1.

As can be seen from Figure 1, compared to the traditional laser interferometer displacement measurement system, the measurement speed of the CPLD-based nanoscale grating displacement measurement system is increased by 27.3%.

The calculation result of the CPLD-based nanoscale displacement measurement system is calculated through the formula. The zero position  $L$  of the nanoscale displacement sensor is 85.3 mm, and the measured displacement value can be calculated. According to the four sets of measurement results measured at the same fixed position, the effective display digits are 0.005 mm, and the displacement resolution reaches 0.2 mm, which meets the precision requirements of the nanograting sensor. Therefore, the displacement measurement system based on the CPLD-based nanoscale grating ruler can effectively improve the displacement measurement accuracy of the sensor and improve the measurement accuracy by 24.7%. Other relevant data are shown in Figure 2.

It can be seen from Figure 2 that the CPLD-based displacement measurement system of the nanoscale grating ruler can effectively improve the displacement measurement

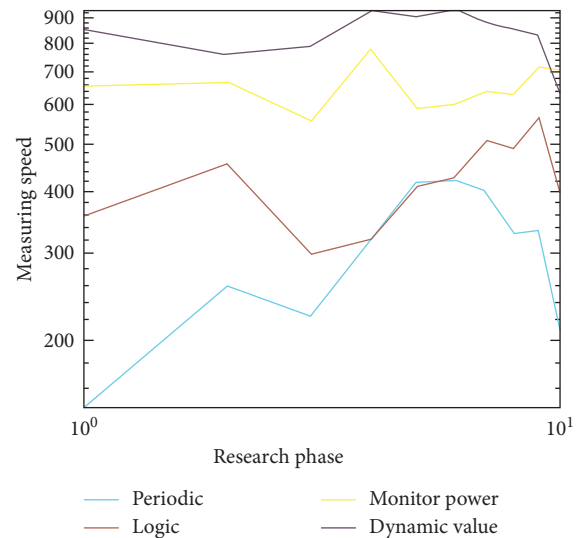


FIGURE 1: CPLD-based nanoscale grating ruler displacement measurement system increases measurement speed.

accuracy of the sensor, and the measurement accuracy is improved by 24.7%.

## 7.2. Statistical Results of Displacement Measurement Speed and Accuracy of Nanoscale Grating Ruler.

In order to check the measurement effect of the CPLD-based nanoscale displacement measurement system, a high-precision displacement measurement system based on CPLD is designed in this paper. The CPLD design produces a stable excitation pulse L1, which is used for displacement measurement directly with the induction pulse L2 in the CPLD. CPLD smoothens the displacement measurement data by counting data processing, eliminating random errors caused by the high-frequency crystal oscillator, and the corresponding displacement resolution reaches 0.05 mm. The research results show that the CPLD-based nanoscale displacement measurement system simplifies the design of the entire system compared to the traditional displacement measurement circuit implemented by discrete components,

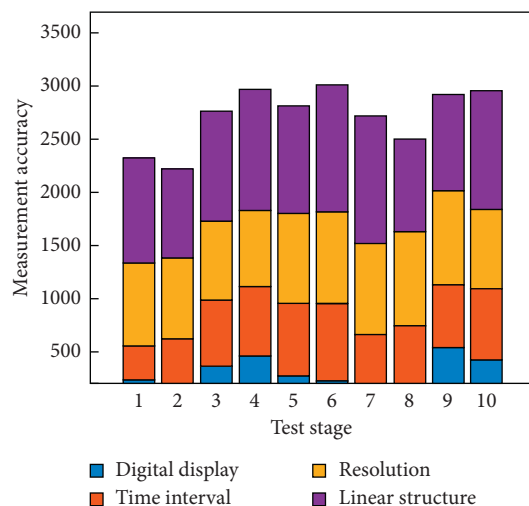


FIGURE 2: Effective improvement of the sensor's displacement measurement accuracy.

which can effectively improve the measurement accuracy of the system and the measurement system. Flexibility and stability improve the robustness of the measurement system by 18.6%. The specific data is shown in Figure 3.

It can be seen from Figure 3 that comparing the CPLD-based nanoscale displacement measurement system to the traditional displacement measurement circuit implemented by discrete components, the system robustness increased by 18.6%.

The experimental results show that from the data analysis of the small-scale microdisplacement model measurement simulation experiment system, it can be clearly seen that the deviation between the average value of the straight line and the simulated reference value of the small-displacement simulation measurement experiment system based on the precision nanometer of CPLD and the advanced rectangular grating scale is, respectively, between 108 and 261 nm, the average deviation of the straight line from the mixed value with the analog value is between 98 and 197 nm, the average value is much smaller than the measurement accuracy of the traditional capacitor displacement measurement sensor, and the average value measured by the system is credible. It can be clearly seen from the data analysis of the large-displacement motion measurement technology laboratory that the large-displacement motion measuring instrument based on maple's new nano-quality micro-grating ruler has the largest average value of the displacement measurement within a certain period of time for each large-displacement motion measurement of the system. The difference between the value and the minimum measured value distribution should not be less than 40 nm, the distribution is relatively concentrated, the variance is small, and the stability is relatively good. The two displacement measurement values are in the range of 9.62–10.37 nm and 19.5–22.3 nm, and the measurement values are reliable. The research found that the diffraction efficiency of the nanoscale grating ruler in the plane of the nanoscale grating ruler varies greatly. The rate of change of the diffraction efficiency of the nanoscale grating ruler is related to the grating density. The relevant data is shown in Figure 4.

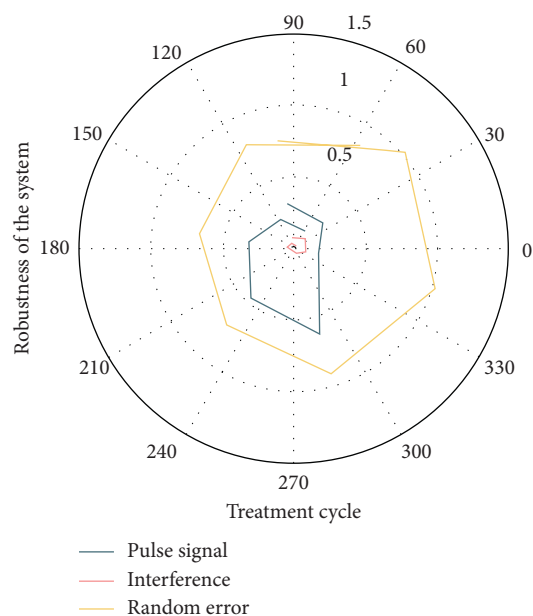


FIGURE 3: Improvement of the flexibility and stability of the measurement system.

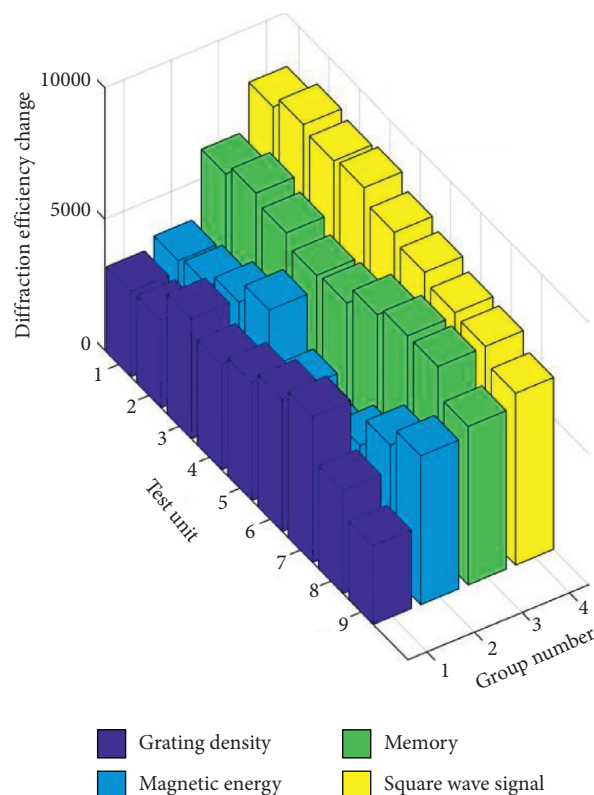


FIGURE 4: Rate of change of diffraction efficiency of nanoscale.

It can be seen from Figure 4 that the change rate of the diffraction efficiency of the nanoscale grating in the nanoscale grating ruler surface is 0.165% nm, and the change rate of the diffraction efficiency of the out-of-plane detection nanograting can reach 0.483% nm.

## 8. Conclusions

Nanoscale grating ruler has an important application as a precision sensor in displacement measurement systems. Traditional displacement measurement systems such as laser interferometric distance measurement system and acoustic wave distance measurement system have been unable to meet the ever-changing requirements of high-precision production technology. Appearing to fill the gap in this field, CPLD is a commonly used programming control system that can achieve high-precision control of instruments and equipment. Based on nanotechnology and CPLD, a new displacement measurement technology came into being. This is the CPLD-based displacement measurement of nanoscale grating rulers system. The research results show that the CPLD-based displacement motion measurement and control system with nanometer-scale precision grating size mainly has three characteristics: high measurement accuracy, strong anti-interference ability, and high measurement motion efficiency, which can effectively meet the requirements of high-precision manufacturing processes and scale displacement motion measurement system requirements.

## Data Availability

No data were used to support the study.

## Conflicts of Interest

The authors declare that they have no conflicts of interest regarding the publication of this study.

## Acknowledgments

This work was supported by the National Key Research and Development Project, Integrated Test Technology and Application for Large Aircraft Assembly Intelligent Equipment (no.2019YFB1707505), and Scientific and Technological Developing Scheme of Jilin Province, "Research on Laser Processing Technology and Equipment of Aviation Wire Harness Terminal" (no. 20200401139GX).

## References

- [1] Y. Lu, C. Wei, W. Jia et al., "Two-degree-freedom displacement measurement based on a short period grating in symmetric littrow configuration," *Optics Communications*, vol. 380, no. 6, pp. 382–386, 2016.
- [2] L.-J. Wang, M. Zhang, and Y. Zhu, "A displacement measurement system for ultra-precision heterodyne littrow grating interferometer," *Guangxue Jingmi Gongcheng/Optics and Precision Engineering*, vol. 25, no. 12, pp. 2975–2985, 2017.
- [3] Q. Lv, W. H. Li, Bayanheshig et al., "Interferometric precision displacement measurement system based on diffraction grating," *Chinese Optics*, vol. 10, no. 1, pp. 39–50, 2017.
- [4] Z. Zhang, M. Zhang, and Q. Zhao, "A simplified analysis for deformation behavior of buried pipelines considering disturbance effects of underground excavation in soft clays," *Arabian Journal of Geosciences*, vol. 8, no. 10, pp. 7771–7785, 2015.
- [5] Y. Shang, C.-F. Li, and X.-R. Fu, "Two generalized conforming quadrilateral mindlin-reissner plate elements based on the displacement function," *Finite Elements in Analysis and Design*, vol. 99, no. 7, pp. 24–38, 2015.
- [6] D. Versino, T. O. Mourad, and F. L. Addessio, "A global-local discontinuous galerkin finite element for finite-deformation analysis of multilayered shells," *Computer Methods in Applied Mechanics and Engineering*, vol. 283, no. 3, pp. 1401–1424, 2015.
- [7] Y. Xu, R. H. Chen, Q. WuCao, and X. Yu, "Synthesis and cyanide anion recognition of a new displacement fluorescence chemosensor based on two-branched aurone," *Fibers and Polymers*, vol. 17, no. 2, pp. 181–185, 2016.
- [8] W. Peipei, L. Xi, Q. Decheng et al., "Two-dimensional displacement measurement based on two parallel gratings," *Review of Scientific Instruments*, vol. 89, no. 6, pp. 65–105, 2018.
- [9] S. Pinna, S. Melo, F. Laghezza et al., "Photonics-based radar for sub-mm displacement sensing," *IEEE Journal of Selected Topics in Quantum Electronics*, vol. 23, no. 2, pp. 168–175, 2017.
- [10] J. Wang, M. Pierce, A. Donnellan, and J. Parker, "Web services for dynamic coloring of UAVSAR images," *Pure and Applied Geophysics*, vol. 172, no. 8, pp. 2325–2332, 2015.
- [11] Y. O. U. Wei-wei, M. A. O. Jian-liang, and Y. E. Hua, "Design of TFT-LCD display controller based on STM32 and CPLD," *Chinese Journal of Liquid Crystals & Displays*, vol. 30, no. 3, pp. 444–450, 2015.
- [12] T. J. Ma, W. Liu, and W. Liao, "A study of signal collecting & processing and display based on CPLD for multiple nuclear pulses," *Hedianxixue Yu Tance Jishu/Nuclear Electronics & Detection Technology*, vol. 38, no. 5, pp. 725–729, 2018.
- [13] H. Chen, Z. Du, and X. Liu, "A new method for observing the bifurcation of a nonlinear system based on CPLD," *Journal of Information Hiding and Multimedia Signal Processing*, vol. 8, no. 5, pp. 1141–1148, 2017.
- [14] P. Z. Wiczorek, "Lightweight TRNG based on multiphase timing of bistables," *IEEE Transactions on Circuits and Systems I: Regular Papers*, vol. 63, no. 7, pp. 1043–1054, 2016.
- [15] L. Hui, L. Xingqiao, and L. Jing, "CMAC-ADRC algorithm based on adaptive parameter identification for asynchronous motor speed control system," *Transactions of the Chinese Society for Agricultural Machinery*, vol. 46, no. 3, pp. 358–365, 2015.
- [16] L.-H. Wu, X.-Z. Zhang, X.-L. Pan, and M.-Y. Wu, "Design of an static reconfiguration based on FPGA system," *International Journal of Multimedia and Ubiquitous Engineering*, vol. 11, no. 2, pp. 99–106, 2016.
- [17] G. L. Jian, D. W. Ji, B. H. Wen, and F. W. Zhao, "Research on the neutral-point voltage balance for NPC three-level inverters under non-ideal grid conditions," *Energies*, vol. 11, no. 6, pp. 1331–1135, 2018.
- [18] S. Li, H. Wang, Y. Li, Q. Li, B. Zhang, and H. Zhu, "A new mini-grating absolute displacement measuring system for static and dynamic geomechanical model tests," *Measurement*, vol. 105, no. 5, pp. 25–33, 2017.
- [19] G. H. Yuan and N. I. Zheludev, "Detecting nanometric displacements with optical ruler metrology," *Science*, vol. 364, no. 6442, pp. 771–775, 2019.
- [20] J. Lu, X. H. Chen, and Q. F. Tang, "Variable coupling time grating sensor and effects of sensor-head attitudes on

- measuring errors,” *Guangxue Jingmi Gongcheng/Optics and Precision Engineering*, vol. 24, no. 9, pp. 2271–2282, 2016.
- [21] X. R. Xiao, M. X. Wang, H. Liang, Q. Gong, and L.-Y. Peng, “Proposal for measuring electron displacement induced by a short laser pulse,” *Physical Review Letters*, vol. 122, no. 5, pp. 1–6, 2019.
- [22] G. Zhu, C. Zhang, and M. Fu, “Development of alternating light field space-time coupling type displacement measuring system,” *Guangxue Jingmi Gongcheng/Optics and Precision Engineering*, vol. 25, no. 8, pp. 2011–2022, 2017.
- [23] K. Liu, M. Sun, Y. Wu, and T. Zhu, “Comparison of accuracy stability using a thermal compensator and grating ruler,” *Journal of the Brazilian Society of Mechanical Sciences and Engineering*, vol. 38, no. 8, pp. 2403–2411, 2016.
- [24] J. Yang and J. Zhang, “Automatic verification system for time grating angular displacement sensors,” *Zhongguo Jixie Gongcheng/China Mechanical Engineering*, vol. 26, no. 14, pp. 1932–1937, 2015.
- [25] S. Sun, S. C. Li, L. P. Li et al., “Design of a displacement monitoring system based on optical grating and numerical verification in geomechanical model test of water leakage of tunnel,” *Geotechnical & Geological Engineering*, vol. 36, no. 22, pp. 1–12, 2018.

## Research Article

# Carbon Nanomaterial Manufacturing System and Automatic Synthesis Equipment and Its Control Device and Control Methods

Gaoxiang Lou  and Zongyan Cai

*School of Construction Machinery, Chang'an University, Xi'an, Shannxi 710064, China*

Correspondence should be addressed to Gaoxiang Lou; 2015025007@chd.edu.cn

Received 6 August 2020; Revised 6 September 2020; Accepted 20 October 2020; Published 3 November 2020

Academic Editor: Tifeng Jiao

Copyright © 2020 Gaoxiang Lou and Zongyan Cai. This is an open access article distributed under the Creative Commons Attribution License, which permits unrestricted use, distribution, and reproduction in any medium, provided the original work is properly cited.

In recent years, people are committed to developing new technologies and technologies for energy storage and conversion, environmental detection, high-performance sensors and energy security, and other aspects of the increasingly prominent problems in the field of environmental and biosafety. The purpose of this paper is to explore the manufacturing system and automatic synthesis equipment of carbon nanomaterials, understand the control device and control method, and analyze the structure and morphology characteristics of three kinds of carbon nanomaterials produced by carbon nanomaterial manufacturing system by X-ray diffraction and infrared spectroscopy. The results show that the carbon nanomaterial manufacturing system and automatic synthesis system in this paper solve the problems of high cost, low efficiency, and small scale of the existing carbon nanomaterials manufacturing and achieve the precision control of automatic production, so that the productivity is increased by 20%–35%, and the cost is reduced by 15%–30%. Therefore, they are widely used in the fields of science and technology, environmental protection, and intelligent manufacturing broad prospects. Carbon nanotube manufacturing equipment and automatic synthesis equipment have great production advantages, which can greatly improve the quality and efficiency of carbon nanomaterials. UPY, GO, and UGO carbon nanomaterials produced by carbon nanotube manufacturing equipment are not easy to fall off from the materials. When the wavelength is 500 nm, the absorption frequency of the three materials is the largest. With the extension of the spectral wavelength, the absorption frequency of the three materials is reduced by 52%, 33%, and 34.7%, respectively.

## 1. Introduction

In recent years, due to the increasingly prominent problems in the field of energy security, environment, and biosecurity, people are committed to solving these severe challenges and research and development for energy storage and conversion, environmental detection, performance sensors, and other aspects. Because the size of the nanomaterial is within 100 nm, it has a high specific surface area and a special morphological structure, so it has unique physical and chemical properties. With the increasing demand for high-performance devices and efficient technologies, people are paying more and more attention to nanomaterials with advanced functions. Advances in nanotechnology and nanomaterials provide new directions for the design and

development of electronic devices, sensors, lithium-ion batteries, environmental testing, and other fields.

The research and development of carbon nanomaterial manufacturing systems have greatly promoted the synthesis of carbon nanomaterials and enhanced the application of carbon nanomaterials in the fields of science, technology, and environment. Fernandes modified the glassy carbon electrode with carbon nanocomposites in his research. Carbon nanocomposites show high stability and have a high current intensity and easy to distinguish REDOX peak [1]. Agata introduced research results related to transparent heating elements made of carbon nanomaterials and adopted an alternative method of vacuum deposition of transparent resistance layers and etching low resistance patterns, aiming to make carbon nanomaterials easy to

realize in large-scale applications [2]. In the experiment, Lee demonstrated the method of using a solution plasma system to produce low-dimensional carbon nanomaterials and its application in flexible conductive paper and compared and studied the effects of graphite rod diameter and ferritin molecular concentration on the production of carbon nanomaterials, and it is verified that carbon nanotubes can be synthesized in this way [3]. Izumi studied the carbon black material in arc black manufactured by chemical vapor deposition (ACB) and carbon nanocoil (CNC) through arc discharge and compared activated carbon (AC) with carbon nanomaterials of various specific capacitances. The reason for using carbon nanomaterials to maintain specific capacitance even at high scan rates is almost the same [4]. Zhang pointed out in his research that carbon nanomaterials have made great progress. Carbon nanomaterials are a better choice for manufacturing biosensors, where higher electron mobility, high chemical stability, electrochemical activity, and higher electric points can promote enzyme adsorption, biocompatibility, and piezoelectric properties, introduce the latest trends in carbon nanotube synthesis, analyze the performance of biosensors, and summarize future challenges and prospects [5]. In summary, the research and development of carbon nanomaterial manufacturing systems have a very broad application prospect.

Automated synthesis equipment is an advanced industrial technology that can greatly improve people's labor productivity. There are many types of research on automated synthesis equipment. In his research, Alur explored the performance advantages of automated synthesis equipment, gave automated synthesis equipment a specification and a set of candidate programs, and successfully found a candidate program that meets the specifications, indicating that automated synthesis equipment already has certain intelligence [6]. Khan pointed out in the article that automated synthesis equipment is a favorable choice for future quantum computing technology because they have multiple advantages over existing nonautomated equipment. You can easily combine classic binary functions by combining two bits into a quaternion value. Expressed as a quaternary function, it is widely used in the scientific field [7]. Osipov considered the problem of automatic synthesis equipment action programs in a constantly changing environment, studied the deductive and comprehensive capabilities of automated synthesis equipment cycles and self-replicating programs and proposed a method for synthesizing such action programs under various possible conditions [8]. Bazhenov introduced a new nuanced analysis of the chemical conversion that occurs during the synthesis of guanidine phosphate oligonucleotides (PGOs) by automated synthesis equipment, which gives the automated synthesis equipment better stability under deblocking conditions [9]. Satsangi confirmed in his research that the design of the reversible system of automated equipment is very different from the traditional system, explored evolutionary algorithms, and used enhanced quantum heuristic evolutionary algorithms to synthesize digital circuits and reference circuits of various automated synthesis equipment, and evolved with other algorithms, and existing search and optimization techniques

were compared for performance analysis [10]. It can be seen that the application fields of automated synthesis equipment are extensive, which is of great help to human production and life.

This article discusses the control device and control method of the carbon nanomaterial manufacturing system and automatic synthesis equipment in detail. The research results show that carbon nanotube manufacturing equipment and automated synthesis equipment have great production advantages, which can greatly improve the quality and efficiency of carbon nanomaterials. The carbon nanomaterial manufacturing system and automated synthesis system studied in this paper solve the existing carbon nanomaterials. The problems of high manufacturing cost, low efficiency, and small scale and the precision control of automated production have been achieved, which has increased productivity by 20%–35% and cost by 15%–30%. Therefore, they have potential in science and technology, environmental protection, and intelligence. Manufacturing and other fields have broad prospects. The innovation of this article is that by analyzing and comparing the three materials produced by the carbon nanomaterial manufacturing system, it is found that compared with the traditional production method, the carbon nanomaterial manufacturing system has certain stability and reliability and is a carbon nanomaterial application in the field of environmental protection, and scientific research provides new ideas.

## 2. Materials and Methods

This experiment studied the working principle of the carbon nanomaterial manufacturing system and automatic synthesis equipment, as well as the advantages and disadvantages of its control device and control equipment. The carbon nanomaterials produced by the carbon nanomaterial manufacturing system are divided into three types of samples: UPY, GO, and UGO, and were compared with the carbon nanomaterials produced by the traditional carbon nanomaterial manufacturing method to compare the advantages of the carbon nanomaterial manufacturing system. In addition, this study also introduces a set of the intelligent control system for high-throughput nanomaterial synthesis and mainly introduces the control device of automatic synthesis equipment and the control method of each reaction, equipped with an electromagnetic stirrer and electric heating module, which are independent of rotational speed, temperature control, and six bidirectional monomer feeding peristaltic pumps. The Cartesian robot is responsible for the reagent injection, accurate movement to the reaction, the reaction of stirring speed, temperature, and the amount of each reagent which is controlled by the computer and real-time detection [11]. Automated synthesis equipment can be used to synthesize high-throughput materials such as carbon nanomaterials by coprecipitation and hydrothermal methods [12].

The main chemical reagents and raw materials are as follows: sublimation sulfur, ethyl tetra silicate, acetyl trimethyl ammonium chloride, ethanolamine, 1-oleic acid, CAI alkane of ammonium nitrate, sucrose, hydrofluoric

acid, absolute ethanol, sulfurization carbon, multiwalled carbon nanotubes (diameter 20 to 50 nm), multiwalled carbon nanotubes (diameter 60–100 nm), ammonia, sodium hydroxide, piano black, nitric acid, potassium stannate, nitrate hexahydrate. Zinc nitrate hexahydrate, methanol, urea, N-methyl alkenone, 2-1 imidazole bis(II) fluorinated methylamine imide lithium, 1,2 dioxane, and 1,3 dioxolane and lithium nitrate.

The main experimental instruments and equipment are as follows: desktop X-ray diffractometer (Rigaku Corporation), field emission scanning electron microscope (Hitachi), field emission transmission electron microscope (US FEI Corporation), ASAP2020 automatic specific surface area and porosity analyzer (Micromeritic Corporation), TA449F3 thermogravimetric Analyzer (Netsch), Ultrasonic Cleaning Machine (Kunshan Ultrasonic Instrument Co., Ltd.), Glove Box (Mirounga (China) Co., Ltd.), High-Speed Refrigerated Centrifuge (Shanghai Tianshan Instrument Equipment Engineering Co., Ltd.), Electric Thermostat Oil bath pot (Zhengzhou Great Wall Industry and Trade Co., Ltd.), charge and discharge tester (Jinmao Electronics Co., Ltd.), etc. Other instruments and equipment used in this experiment are shown in Table 1.

### 3. Carbon Nanomaterial Chemical Property Test

After the manufacture of the carbon nanomaterial manufacturing system is completed, the carbon nanomaterials prepared by the system are tested. First, the elemental composition and structure of the material were analyzed by X-ray diffraction. The test voltage was 30 kV, the current was 15 mA, and the X-ray wavelength during the experiment was set to 0.15418 nm. Next, the surface morphology of the material sample is checked by scanning electron microscope (SEM), and the qualitative and semi-quantitative inspection of the sample is checked by X-ray energy dispersive spectroscopy (EDS) attached to it [13]. The preparation of the test sample was as follows: paste the sample on the sample stage using conductive glue (if the sample has poor conductivity, it needs to be sprayed with gold), and then put the sample into the sample chamber of the scanning electron microscope and evacuate it with a vacuum instrument. Observe the morphology of the sample and test its composition [14].

Carbon nanomaterials' specific surface area (BET) and pore size distribution test were as follows: the parameters such as the specific surface area, pore size, and pore size distribution of the sample are determined by nitrogen isothermal adsorption-desorption method. The first is the preparation of test samples: the test in the experiment requires 20–50 mg of powder sample. Then, we perform thermogravimetric analysis (TGA): the temperature is controlled by the instrument program throughout the process, and the relationship between the quality of the material that changes with time or temperature is measured. It is usually used to detect the composition and thermal stability of materials. In this experiment, TGA was used to detect the components of the sample and the corresponding

content of each component [15]. The experimental conditions are air or nitrogen, the flow rate is usually 40 SCCM, the test temperature is gradually increased from 30°C to 800°C, and the sample heating rate is kept at 10°C/min, not too fast. The preparation of test samples was as follows: prepare 5 ~ 10 mg powder samples.

### 4. Design of Automated Synthesis Equipment

This study discloses a set of automated synthesis equipment. The design of the equipment mainly includes three parts, namely, system flow, hardware design, and software design [16]. First, open the control software on the computer; you can set the number of various reagents to be added in each reaction position in the control interface. After setting the parameters, the host computer controls the Cartesian robot to move the filling head to the first reaction position to fill the reagent. First, the host computer controls six peristaltic pumps to inject the reagent into the first reaction position and sends it to the lower computer through the serial port: the temperature, heating time, speed (DC motor), and rotation time of the first reaction position. The lower computer receives the temperature, heating time, rotation speed (DC motor), and rotation time of the third reaction position to start temperature control and speed control [17]. Secondly, after the upper computer controls the peristaltic pump to fill the first reagent, it sends a positioning command to the lower computer. After the lower computer receives the positioning command, an IO port generates a trigger signal (low level) [18].

*4.1. Hardware Design.* SSR solid state relay is used to accurately control the heating power module of the heating mantle, 3144 Hall sensor speed measurement module, based on the L298 N dual H-bridge DC motor drive module to achieve speed control of the magnetic stirring motor, rectangular coordinate robot arm module, and STM32F103ZET6 main controller module [19]. Among them, the PT100 three-wire platinum thermal resistance bridge temperature measurement conversion module is used as the temperature acquisition application of the reaction position, and the measured voltage signal is sent to the main controller ADC port for temperature measurement application. Moreover, the 3144 hall sensor is used as the speed measurement application of the magnetic stirring motor, and the measured pulse signal is sent to the STM32F103ZET6 main controller to realize the speed measurement application. Based on the L298 N dual H-bridge DC motor drive module as the driving application of the magnetic stirring motor, the device uses a Hall sensor to detect the change of the magnetic field. The Hall sensor is based on the Hall effect. For the basis of its work, it is used as a Hall switch in electronic products, such as the flip phone to open the bright screen and close the interest screen [20]. Hall effect: connect the current  $I$  to the upper and lower ends of the semiconductor block, and then apply a uniform magnetic field with a magnetic field strength of  $B$  in the vertical direction of the semiconductor block. The Hall voltage  $U_H$

TABLE 1: Other instruments and equipment used in this experiment.

Name	Type	Source
Vacuum tube furnace	OTF-1200X	Hefei Keying Material Technology Co., Ltd.
Vacuum drying oven	DZF-6020	Shanghai Vichang Technology Co., Ltd.
Electric constant temperature blast drying oven	DHG-9070A	Shanghai Vichang Technology Co., Ltd.
Electronic balance	BT 25S	Sartorius Scientific Instruments Co., Ltd.
Ultrasonic cell crusher	JY92-11N	Ningbo Xianzhi Biotechnology Co., Ltd.
Circulating water type multipurpose vacuum pump	SHB-III	Zhengzhou Great Wall Science, Industry and Trade Co., Ltd.

will be generated in the direction perpendicular to the current and magnetic field. This effect is the Hall effect, and the relationship is

$$U_H = K \frac{(B * I)}{D}, \quad (1)$$

where  $K$  represents the Hall coefficient, the size of the Hall coefficient is related to the material of the semiconductor wafer, and  $D$  represents the thickness of the semiconductor wafer.

**4.2. Software Design.** The automated synthesis equipment used in this study uses the STM32F103ZET6 ARM chip with Cortex-M3 as the main control chip. The software design of the automatic synthesis equipment control system mainly includes the PT100 three-wire platinum thermosetting resistance bridge temperature measurement conversion module, which is used to measure the voltage signal of the reaction position temperature [21]. The three-wire PT100 platinum thermal resistance bridge temperature conversion module transmits the reaction voltage signal of the temperature measurement to the ADC port through the main controller to realize the temperature measurement program. The PWM output controls the SSR solid state relay to control the electric heating power. The setting procedure for controlling the electric heating temperature is based on 3144 Hall sensors measuring the pulse signal to the main controller, and the TIM implements the speed regulation program [22]. The PWM output controls the DC motor L298 N dual H-bridge driver module to control the application speed of the magnetic stirrer motor and receives the temperature, heating time, speed, rotation time, and step serial port configuration program parameters received from the PC through the serial port.

## 5. Automated Synthesis Equipment for Testing the Structure of Carbon Nanomaterial

In this study, the structure of carbon nanomaterials was tested by automatic synthesis equipment. In this study, the Fourier Transform Infrared Spectrometer (FTIR) in the automatic synthesis system was used for structural testing. The principle is that molecules can selectively absorb infrared rays of certain wavelengths, thereby causing vibrations and rotational energy levels in the molecules. It can also be used to determine the functional groups on the sample surface by measurement [23]. During the experiment, FTIR was used to test Go and characterize the related

groups on its surface. The specific test method is as follows: first, the completely dried sample is mixed with potassium tribromide at a determined ratio of three, firstly ground in an agate mortar for about 20 minutes, and then pressed by a tablet press under a pressure of 15 M·PA for 1 minute to obtain tablets with thickness and density that meet the requirements. Then, the tablet was put in a vacuum oven and dried at 60°C for 24 h, and then the sample was tested and identified. The wavenumber range of the test is from 400 cm to 500 cm. In the study of carbon nanomaterials, the research proves that the structural regularity of carbon nanomaterials and the number of carbon nanolayers can be analyzed by Raman spectroscopy [24]. The basic principle of the Raman spectroscopy used is as follows: when monochromatic light illuminates the sample, electrons are excited by absorbing the energy of photons. If the interaction between incident photons and electrons is inelastic scattering, the frequency of the scattered light will be greater or less than the frequency of the incident light, and the scattering process is Raman scattering [25]. The specific test conditions of Raman spectroscopy are as follows: the wavelength of Raman excitation light is 532 nm, and the test wave number is 500 cm–2500 cm.

## 6. Results and Discussion

**6.1. Performance Analysis of Carbon Nanomaterial Manufacturing System.** The research results show that when analyzing the chemical properties of the carbon nanomaterials produced by the carbon nanomaterial manufacturing system, it is found that during the process of program setting, different machine temperatures will have a certain impact on the production of carbon nanomaterials by the machine. The three materials produced by the equipment are labeled UPY, GO, and UGO. The conclusion is that the mass fraction of carbon nanomaterial residues at different temperatures is different. The specific data obtained by the study are shown in Table 2.

Transmission electron microscopy mainly uses high-energy electron beams for imaging, which are used to project accelerated and concentrated electron beams onto very thin samples. The basic principle of the transmission electron microscope is as follows: once the electrons collide with the atoms in the sample, the direction will change, resulting in a solid angle scattering on the plane, and the angle of the scattering angle is related to the density and thickness of the sample. Samples of different materials have a unique scattering angle, so observation with a transmission electron microscope can form different light and dark images on a

TABLE 2: Residual mass fraction of carbon nanomaterials at different temperatures.

Group	600°C	700°C	800°C
UPY	15.41	13.26	11.15
GO	57.83	54.44	51.89
UGO	38.99	34.06	31.24

plane, which is helpful to distinguish the composition and structural differences of the sample. In this study, the characteristics and the low-temperature adsorption and desorption ability of the three carbon nanomaterial intermediate layers were mainly analyzed using transmission electron microscopy. The specific results are shown in Figure 1.

It can be seen from the data in Figure 1 that at a temperature of 0.2°C, the intermediate layers (MPC) of the three materials UPY, GO, and UGO are not easily removed from the carbon nanomaterials, but as the temperature continues to increase, the probability of removing the intermediate layer of the material is increased by about 20%–60% than before. It can be seen that carbon nanomaterials have a certain low-temperature resistance, and the application scenarios are more extensive than ordinary materials, reflecting the advantages of carbon nanomanufacturing equipment. Studies have shown that when X-ray diffraction passes through different crystalline substances, X-rays will generate different degrees of scattering, indicating that different materials have different constituent elements and groups or different structures. The diffraction spectrum of carbon nanoparticles shows different characteristics in terms of number, position, the order of relative intensity, and even the shape of diffraction peaks. The XRD results can be used to study the structure of carbon nanomaterials and the atomic distribution in crystals. Because there are different atomic groups between different layers, the layer spacing of carbon nanomaterials is different. XRD is known to test carbon nanomaterials. After X-ray diffraction analysis, the elemental composition of carbon nanomaterials is shown in Figure 2.

It can be seen from the data in Figure 2 that carbon elements account for the vast majority of carbon nanomaterials, reaching 96.1%, and magnesium elements account for 2.1%. Studies have shown that a certain amount of magnesium elements in carbon nanomaterials can make the structure of carbon nanomaterials. It is more uniform and detailed. In addition, sodium element accounts for 1.1%, titanium element accounts for 0.4%, and phosphorus element accounts for 0.4%. It can be seen that the carbon nanomaterials manufactured by the carbon nanomaterial manufacturing system have certain advantages, reflecting the better performance of the carbon nanomaterial manufacturing system used in this study.

6.2. Control of Automated Synthesis Equipment and Comparison of Carbon Nanomaterial Structures. The control of the automatic equipment is mainly achieved through its function. The main function of the automatic synthesis

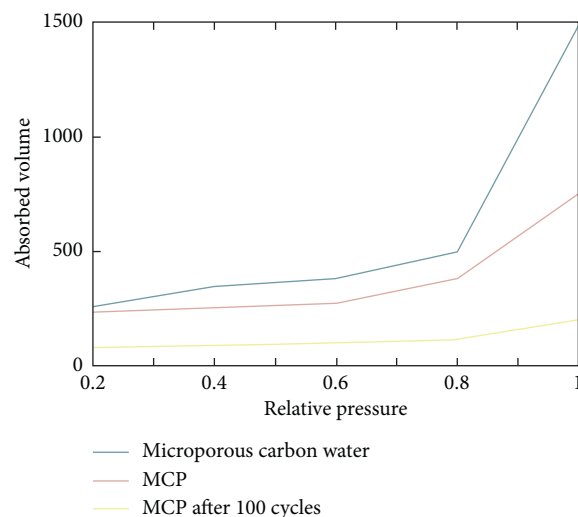


FIGURE 1: Low-temperature adsorption and desorption isotherm diagram of carbon nanomaterial intermediate layer.

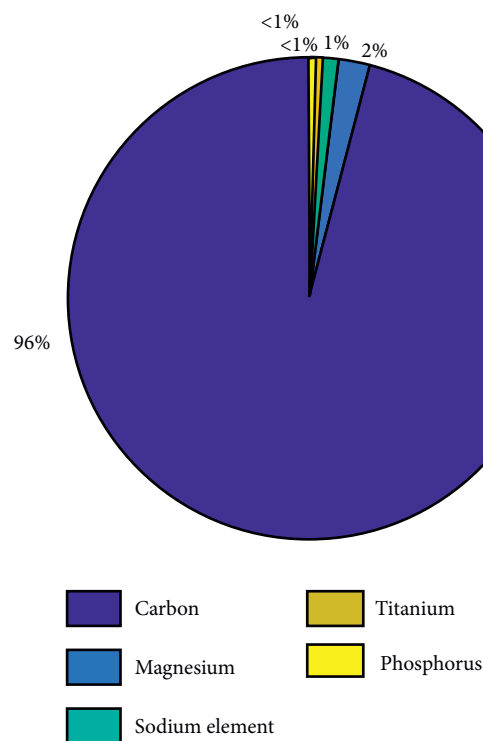


FIGURE 2: Elemental composition of carbon nanomaterials.

equipment is processed by the main controller through analog-to-digital conversion and then converted to temperature through the algorithm and then through the temperature setpoint, according to the heating temperature difference PWM signal, and then the heating power is changed to achieve temperature control. Then, the Hall sensor module is connected to collect the pulse signal of the STM32 TIM main control terminal. The TM edge set during the period rises to trigger the function, which is used to collect the time and the measured motor speed between the

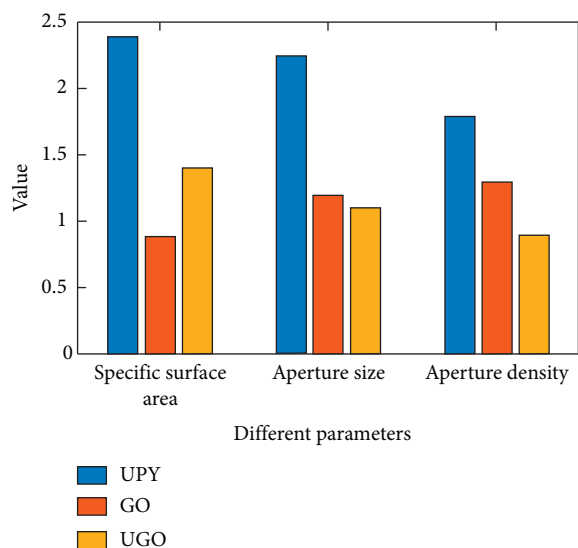


FIGURE 3: Comparison chart of specific surface area and pore size of three carbon nanomaterials.

two pulse signals. Then, the main controller which is the IO terminal interface of the low-level trigger signal was set to execute the rectangular coordinate robot module, allowing the machine to move smoothly up and down on the machine through the serial port. It should be noted that various parts of the entire system are assigned various tasks to simplify programming difficulty and improve programming efficiency. The biggest competitive advantage of this automated synthesis equipment is the fact that it has extremely high performance, is equipped with the mainstream cortex core, and has strong software support. In this study, the structure of three carbon nanomaterials was tested using automatic synthesis equipment. The specific results are shown in Figure 3.

As can be seen from the data in Figure 3, among the three carbon nanomaterials of UPY, GO, and UGO, UPY has the largest specific surface area, 17% and 25% larger than GO and UGO, respectively. Among the three materials, UGO has a pore size of 1.3 and pore density. The smallest is 0.9. Fourier Transform Infrared Spectroscopy (FTIR) can selectively absorb infrared light of certain wavelengths, thereby causing partial transitions of vibrational energy and rotational energy in the molecule. Studies have shown that the functional groups on the sample surface can be determined by measuring the interferogram and performing Fourier changes. FTIR can be used to characterize the groups on the surface of carbon nanomaterials. The specific test method is as follows: mix the completely dried sample with KBr in a certain ratio, grind it in an agate mortar for 20 min, and then compress it by a tablet press at a pressure of 15 M·Pa for 1 min to obtain a tablet. Put the tablet in a vacuum oven, dry at 60°C for 24 hours, and then perform testing and characterization analysis. The test wavenumber range is from 500 nm to 2500 nm. The specific data is shown in Figure 4.

From the data in Figure 4, it can be seen that the three types of carbon nanomaterials UPY, GO, and UGO produced using carbon nanofabrication equipment have the highest frequency of absorbed light when the spectral

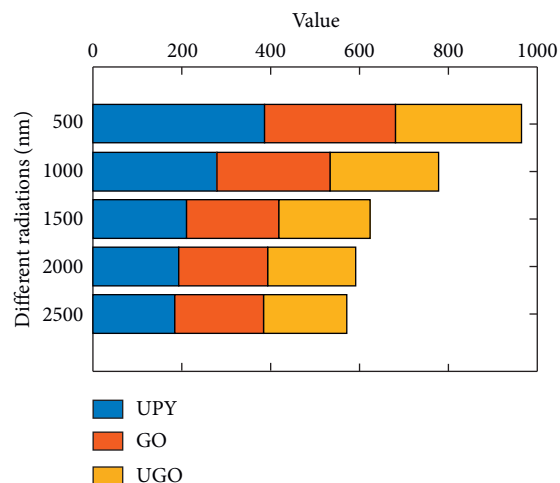


FIGURE 4: Infrared spectrum structure test chart of three carbon nanomaterials.

wavelength is 500 nm, which are 384, 296, and 285, respectively. The spectrum wavelength is continuously extended, and when the spectrum wavelength is prolonged by 4 times from the beginning, reaching 2500 nm, the frequencies of the three materials UPY, GO, and UGO are reduced by 52%, 33%, and 34.7%, respectively. This material is not easy to absorb infrared wavelengths and has the characteristics of being thick and not easy to reflect. In this way, the problems of low efficiency and high cost of carbon nanomaterial production are solved, the production efficiency is increased by 20%–35%, and the cost is reduced by 15%–30%.

## 7. Conclusions

The research results show that carbon nanotube manufacturing equipment and automated synthesis equipment have great production advantages and can greatly improve the quality and use efficiency of carbon nanomaterials. The three types of carbon nanomaterials produced by carbon nanotube manufacturing equipment, UPY, GO and UGO, are not easy to break. When the wavelength is 500 nm, the three materials have the highest frequency of absorbing light, and with the extension of the spectral wavelength, the frequency of absorbing light of the three materials decreases by 52%, 33%, and 34.7%, respectively. The carbon nanomaterial manufacturing system and automated synthesis system studied in this paper solve the problems of high manufacturing cost, low efficiency, and small scale of existing carbon nanomaterials and achieve precision control of automated production. It increases productivity by 20%–35%, and the cost is reduced by 15%–30%, so they have broad prospects in the fields of science and technology, environmental protection, and intelligent manufacturing.

## Data Availability

The data in this article is available.

## Conflicts of Interest

The authors declare that they have no conflicts of interest.

## Acknowledgments

This work was supported by the National Natural Science Foundation of China (Grant no. 51305042).

## References

- [1] D. M. Fernandes and C. Freire, "Carbon nanomaterial-phosphomolybdate composites for oxidative electrocatalysis," *Chemelectrochem*, vol. 2, no. 2, pp. 269–279, 2015.
- [2] S. D. Agata, G. Wroblewski, K. Kielbasinski et al., "Carbon nanomaterials dedicated to heating systems," *Circuit World*, vol. 41, no. 3, pp. 102–106, 2015.
- [3] B.-J. Lee and G.-H. Jeong, "Ferritin-mixed solution plasma system yielding low-dimensional carbon nanomaterials and their application to flexible conductive paper," *Current Applied Physics*, vol. 15, no. 11, pp. 1506–1511, 2015.
- [4] H. Izumi, Y. Okabe, Y. Suda, H. Takikawa, H. Tanoue, and H. Ue, "Manufacturing of electric double-layer capacitors using carbon nanocoils and evaluation of their specific capacitances at a high scan rate," *Electronics & Communications in Japan*, vol. 99, no. 5, pp. 3–10, 2016.
- [5] Y. Zhang, Z. Kang, X. Yan, and Q. Liao, "Zno nanostructures in enzyme biosensors," *Science China Materials*, vol. 58, no. 1, pp. 60–76, 2015.
- [6] R. Alur and S. Tripakis, "Automatic synthesis of distributed protocols," *Acm Sigact News*, vol. 48, no. 1, pp. 55–90, 2017.
- [7] M. H. A. Khan, H. Thapliyal, and E. Munoz-Coreas, "Automatic synthesis of quaternary quantum circuits," *The Journal of Supercomputing*, vol. 73, no. 5, pp. 1733–1759, 2017.
- [8] V. Y. Osipov, "Automatic synthesis of action programs for intelligent robots," *Programming and Computer Software*, vol. 42, no. 3, pp. 155–160, 2016.
- [9] M. A. Bazhenov, A. V. Shernyukov, M. S. Kupryushkin, and D. V. Pyshnyi, "Study of the staudinger reaction and reveal of key factors affecting the efficacy of automatic synthesis of phosphoryl guanidinic oligonucleotide analogs," *Russian Journal of Bioorganic Chemistry*, vol. 45, no. 6, pp. 699–708, 2019.
- [10] S. Satsangi, C. Patvardhan, and P. K. Kalra, "Automatic synthesis of reversible circuits," *International Journal of Computer Applications*, vol. 140, no. 11, pp. 31–36, 2016.
- [11] Z. Xiao-Jun, L. I. Yun-Gang, and Z. Jin-Ming, "Automatic synthesis and micro imaging study of a serotonin imaging agent," *Journal of Isotopes*, vol. 28, no. 1, pp. 1–6, 2015.
- [12] L. Lessard and S. Lall, "Convexity of decentralized controller synthesis," *IEEE Transactions on Automatic Control*, vol. 61, no. 10, pp. 3122–3127, 2016.
- [13] H. Saggion, "Automatic text simplification," *Synthesis Lectures on Human Language Technologies*, vol. 10, no. 1, pp. 1–137, 2017.
- [14] D. Zats, A. P. Iyer, G. Ananthanarayanan, R. Agarwal, R. H. Katz, and Ion Stoica, "Fastlane: making short flows shorter with agile drop notification," *Reliability Engineering & System Safety*, vol. 84, no. 1, pp. 19–32, 2016.
- [15] A. Janicki, F. Alegre, and N. Evans, "An assessment of automatic speaker verification vulnerabilities to replay spoofing attacks," *Security and Communication Networks*, vol. 9, no. 15, pp. 3030–3044, 2016.
- [16] M. Kimura, "Manufacturing technology using carbon fiber reinforced plastic," *Journal of the Japan Society for Precision Engineering*, vol. 81, no. 6, pp. 494–497, 2015.
- [17] N. A. Agudelo and L. D. Pérez, "Synthesis and characterization of polydimethylsiloxane end-modified polystyrene from poly (styrene-co-vinyltriethoxysilane) copolymers," *Materials Research*, vol. 19, no. 2, pp. 459–465, 2016.
- [18] L. J. D. Oliveira, M. Filgueira, S. C. Cabral, and M. Filgueira, "Study of the TiC coating on powder metallurgy diamonds tool's performance," *Materials Research*, vol. 18, no. 3, pp. 441–447, 2015.
- [19] L. Kojecky, I. Zelinka, and P. Saloun, "Evolutionary synthesis of automatic classification on astroinformatic big data," *Parallel Algorithms and Applications*, vol. 32, no. 5-6, pp. 429–447, 2017.
- [20] L. Thévenoux, P. Langlois, and M. Martel, "Automatic source-to-source error compensation of floating-point programs: code synthesis to optimize accuracy and time," *Journal of Software Maintenance & Evolution*, vol. 29, no. 7, pp. 1–24, 2017.
- [21] S. Lee, S. Han, I. Lee, J.-Y. Sim, H.-J. Park, and B. Kim, "Cost-efficient and automatic large volume data acquisition method for on-chip random process variation measurement," *JSTS: Journal of Semiconductor Technology and Science*, vol. 15, no. 2, pp. 184–193, 2015.
- [22] Y. Li, Q. Liu, R. Tong, and X. Cui, "Shared and service-oriented CNC machining system for intelligent manufacturing process," *Chinese Journal of Mechanical Engineering*, vol. 28, no. 6, pp. 1100–1108, 2015.
- [23] R. Geiger and J. Pahl, "Carbon composite manufacturing in automotive volume production," *Lightweight Design Worldwide*, vol. 10, no. 4, pp. 46–51, 2017.
- [24] P. Hu, "The strategy analysis for Chengdu's industrial carbon emission (manufacturing and environmental management)," *Journal of Information & Management*, vol. 31, no. 4, pp. 120–130, 2017.
- [25] N. Dugin, T. Zaboronkova, and E. Myasnikov, "Using carbon-based composite materials for manufacturing C-range antenna devices," *Latvian Journal of Physics and Technical Sciences*, vol. 53, no. 5, pp. 17–23, 2016.

## Research Article

# High Boron Silicon Nanotubes Combined with Tai Chi Exercise Rehabilitation Therapy in the Treatment of Knee Arthritis Patients

Guang Ma 

Department of Physical Education, Lvliang College, Lvliang, Shanxi 033001, China

Correspondence should be addressed to Guang Ma; 37017@llhc.edu.cn

Received 6 August 2020; Revised 17 September 2020; Accepted 12 October 2020; Published 31 October 2020

Academic Editor: Tifeng Jiao

Copyright © 2020 Guang Ma. This is an open access article distributed under the Creative Commons Attribution License, which permits unrestricted use, distribution, and reproduction in any medium, provided the original work is properly cited.

Tai Chi exercise is gentle, convenient, and easy to learn. It is more economical than traditional medical treatments, and it is regarded as the first choice for rehabilitation therapy by patients with knee arthritis. This article aims to study Tai Chi exercise rehabilitation therapy combined with high boron silicon nanotubes to treat knee arthritis patients. This article mainly introduces the treatment of knee arthritis patients with Tai Chi, which is reflected in the improvement of patients' walking ability and stability, and explores a three-dimensional motion model to provide better help for patients with knee joints. The article uses data mining methods to collect data on the gene expression of human knee joints and analyzes the causes of knee arthritis caused by its internal structure. The experimental results of this paper show that, under Taijiquan exercise rehabilitation treatment, the time needed by knee arthritis patients to get up and run is reduced by 14%, the standing time of one leg is significantly improved, the fall rate is reduced by 13%, and the body's static balance ability is improved.

## 1. Introduction

**1.1. Background and Significance.** Knee osteoarthritis is a chronic deformable arthritis that is most common for the elderly. When the knee arthritis is severe, the bones will disappear. As a result, the friction between the bones and bones increases, which makes the patient's walking, daily activities, and other obstacles worse. Tai Chi exercise is an effective treatment for knee arthritis proposed by the American Rheumatism Association. Tai Chi emphasizes flexibility and requires practitioners to keep in touch and repeat it all the time but not monotonously. According to a large number of studies, Tai Chi exercise can strengthen the body, mainly reducing the pain on the sick body, improving the flexibility of the body's joints, and helping the treatment of patients with knee arthritis; it can also purify the mind.

The importance of Tai Chi for practitioners has gradually evolved from the initial five strong bodies to longevity and has the health and other heart and lung functions of Tai Chi. The most special aspects of Tai Chi are the control of the balance mechanism and the treatment of knee arthritis. It has received more and more attention and learning from the elderly.

**1.2. Related Work.** The Tai Chi exercise proposed by Miller and Taylor-Piliae is beneficial to cognitive and physical functions and may affect the safe driving performance of the elderly. The main purpose of this research is to compare the cognitive processes and physical functions of elderly Tai Chi practitioners related to safe driving with standard reference values; the second purpose is to study the relationship between Tai Chi exercise habits, cognitive processes, and physical functions related to safe driving performance and explore potential predictive indicators of safe driving performance. However, this research is solely related to safe driving, which makes the research not very comprehensive [1]. Lee et al. studied the effect of extracorporeal shock wave therapy on pain and function in patients with degenerative knee arthritis. 20 patients with degenerative knee arthritis were divided into conservative physical therapy group and extracorporeal shock wave therapy group. Both groups received conventional conservative physical therapy. Then, extracorporeal shock wave therapy plus extracorporeal shock wave therapy was received. However, because there were not enough control groups during the study, the research results were not very accurate [2]. Janssen et al. proposed that rehabilitation after treatment of non-small cell

lung cancer (NSCLC) has a beneficial effect on exercise capacity, but there is limited insight into the impact on quality of life (QoL) and fatigue, and its purpose is to examine the treatment of NSCLC stages I to IIIa of adult patients and pulmonary rehabilitation (PR) results related to fatigue, QoL, and exercise capacity. However, due to the excessive number of cells, the conclusion is not very accurate [3].

**1.3. Main Content.** This paper combines the finite element model, the dynamics of the knee joint, and the movement data of Tai Chi and reveals the regularity of the change of the tension of the knee joint of Tai Chi. In order to understand the impact of knee-knocking movement on the internal structure of the knee joint, it will provide theoretical support for the practice of Tai Chi and physical rehabilitation training in the future.

According to the establishment of the Comprehensive Research Institute, this article randomly divides elderly patients with knee deformity arthrosis as a control group into three-month Tai Chi practice groups. The functional ability of the subjects who walked to the knee joint before and after intervention was tested. A motion capture system is designed to obtain the parameters of the rebound force of the test subject's feet and the ground, then calculate the stability force according to the formula, and finally compare the data with the actual data.

## 2. Treatment of Knee Arthritis

**2.1. Principal Component Analysis.** In this document, a five-part scale is used to rank the impact indicator  $n$  ( $n=8$ ). When the score is "5 points", this means that the indicator is needed; the score of "4 points" means that it is more needed; and the scores of "3 points" and "2 points" mean that it is not needed. When the score is "1 point", this means that the indicator is not needed at all. It is planned to use the principal component analysis method to calculate the weights and obtain the specific weight ratio [4].

The main component analysis, abbreviated as PCA, is an important method of multifactor statistical analysis. It collects the information propagated by a set of variables in some comprehensive indicators (principal component, PC) and reduces the dimension of the dataset, which simplifies the problem. The usual mathematical process is to linearly combine the initial index  $n$  into a new comprehensive index. The most commonly used method is to express the change of  $f_1$  (the first linear combination selected, that is, the first comprehensive indicator), that is, variable 1,  $F_1$ , contains more information. Therefore,  $F_1$  is the variable with the greatest variability among all linear combinations, because  $F_1$  is called the first principal component. However, the information of the initial  $P$  index is not enough to be represented by the first principal component  $F_1$ ; then the second linear combination  $F_2$  can be selected to represent it. In order to effectively reflect the initial information, the existing information of  $f_1$  does not need to appear in  $f_2$ , expressed in mathematical language as  $\text{Cov}(f_1, f_2) = 0$ ; then,

$f_2$  is called the second main component; the third, fourth, and first major components can be manufactured to scale. The first and the main components can be manufactured in proportion [5].

The mathematical model of principal component analysis can be derived from the following three formulas:

$$\begin{aligned} F_1 &= a_{11}X_1 + a_{21}X_2 + \cdots + a_{n1}X_n, \\ F_2 &= a_{12}X_1 + a_{22}X_2 + \cdots + a_{n2}X_n, \\ F_k &= a_{1m}X_1 + a_{2m}X_2 + \cdots + a_{pm}X_n, \end{aligned} \quad (1)$$

among which,  $t_{ij}$  is the coefficient of each component, expressed as

$$t_{ij} = \frac{f_{ij}}{\sqrt{\lambda_j}}, \quad j = 1, 2, L, m. \quad (2)$$

$a_i$  is the comprehensive importance in the principal component, expressed as

$$a_i = \sum_{j=1}^m \left( \frac{\lambda_j}{k} \right) t_{ij}, \quad k = \lambda_1 + \lambda_2 + l + \lambda_m. \quad (3)$$

Through normalization, the final index weight  $w_i$  is determined as

$$w_i = \frac{a_i}{\sum_{i=1}^n a_i}. \quad (4)$$

Finally, the comprehensive score model of principal component analysis is

$$Y = w_1X_1 + w_2X_2 + \cdots + w_nX_n. \quad (5)$$

Finally, an index weight value  $w$  was calculated for each dimension. From the index weights, the weight ratio of Tai Chi exercise to the treatment of knee arthritis is the largest [6].

**2.2. Data Mining Method.** In this article, we use data mining methods. First, we collected gene expression profile data related to human knee osteoarthritis, and then we selected gene expression profiles that meet the requirements [7]. Then, we used GEO2R to obtain different expressed genes. Next, the use of DAVID for the enrichment analysis of the expressed genes in GO-comment and KEGG pathways and the use of cell landscape for the integration of different integrated genes to participate in the interaction of different biological pathways are of great research significance for network visualization, analysis, and discussion.

We selected the project type as a series and restricted the species to humans to obtain the relevant qualified series. In order to expand the search scope, in addition to searching for keywords in the gene expression database, an additional search was also conducted in the PubMed library, containing additional filter conditions: (1) search contains grid term, osteoarthritis; (2) document language should be English [8].

Since the experimental object and experimental platform are selected from different datasets, the cell type, control group type, and data type selected by the experiment should

be further checked. The specific classification condition is defined as follows: the source of the abandoned sample is not joints or fibers, such as stem cells, excluding the normal control group without OA or with no record. Screening according to experimental methods, in addition to “RT-PCR expression profile”, we retained only high-performance analytical techniques (sequencing or “fine adjustment”). At the same time, we selected the data type as the gene expression profile, in addition to noncoding RNA, methylation, and other expression profiles: “noncoding pattern of RNA sequence”, “methylation pattern by array (genotype plate)”. Finally, the concept of meaningless records was abandoned, and the information of the data set was confirmed. The meaningless record concept confirms the information in the dataset [9].

**2.3. Quantitative Research Method of Knee Motion.** In order to evaluate the stability of the test object, it is necessary to calculate the value of the horizontal force required to break the balance of the test object. This evaluation method is based on the stable margin defined by Koozekanani et al. [10]. The stability margin refers to the distance where the COP is the smallest from the support surface. If the remaining amount is zero, then the human body will be in balance, and the remaining stable amount is proportional to its own physical ability. To make the stability margin zero, you only need to add a to the system, and then the formula is

$$C_d = \vec{d}_{cp} \times \vec{F}_r \quad (6)$$

$\vec{d}_{cp}$  refers to the smallest distance to COP from the supporting surface, and  $\vec{F}_r$  refers to the magnitude of the rebound force formed with the ground. In addition, if there is a virtual enough foot to compensate for the horizontal force the system bears, then the torque created by a single virtual horizontal force may destroy the stability of the human body. To make the virtual horizontal force sufficiently sensitive in the center, the lever arm ( $h_{CM}$ ) is selected as the distance of the center of gravity from the support surface. Therefore, the cause of unstable arthropods can be expressed as the following formula:

$$C_d = h_{CM} \times \vec{F}_D \quad (7)$$

We further derived

$$\vec{F}_D = -\frac{|\vec{F}_r|}{|h_{CM}|} \cdot \vec{d}_{cp} \quad (8)$$

The area surrounded by the ground projection positions of the three marked points of the foot (the first middle finger, the fifth middle finger, and the heel point) is defined as the supporting surface. Calculate the magnitude of the virtual horizontal force on both sides of the support surface, and use the minimum value to describe the stability characteristics of the test object. The minimum virtual force is the value of the force required for human body instability and is directly related to human body stability [11].

The direction of  $\vec{F}_D$  indicates the direction in which the subject is most likely to lose balance and is related to the vector indicating the average direction characteristic of the foot. The vector  $O_f$  of the average foot orientation coincides with the direction of the left foot and defines a positive direction that destabilizes the human body. The angle of this vector is counterclockwise. However, in this study, the amount of unstable force is mainly used to measure the body's ability, regardless of the direction of the force, to maintain a balance with the falling force [12]. The smaller the value of the instability is, the easier the personal stability is destroyed.

This method evaluates dynamic balance, and dynamic performance balancing elements vary according to the shape and size of the bearing surf, so the difficulty of balancing can be fully understood. At this point, using this model to properly evaluate the stability of patients with deformed knee arthritis will help to optimize the evaluation and optimize the effect of Taijiquan education on the entire knee arthritis intervention program [13].

### 3. Experiment of Tai Chi on Knee Joint

**3.1. Parameter Collection.** Before starting the experiment, calibrate the Weikang and Kistler 3D force platform and 3D calibration system in the experimental area. All people wear experimental clothing (ordinary cotton shorts, vests, cotton socks, and rubber shoes) prepared in the laboratory and use anthropometry to measure the basic characteristics of the human body such as weight and height. The requirements and basic ideas of the experiment are roughly clear. The subject will use 47 infrared reflections attached to the corresponding positions on the body surface to determine the head and torso. Before the formal exercise test, the upper and lower limbs are doubled and statistical data are collected as required [14]. In this study, Weikang cameras were used for sampling. The frequency is 80 Hz, and the sampling frequency of the Kistler 3D power platform is 980 Hz. Typical movement requires an individual to walk 12 meters at a comfortable body speed. The corridor contains two 3D power boards at the same height as the ground. Of course, All experimental subjects used in this article adopt a natural forward approach. When two force plates measure one foot of data and the two data are continuously in two data levels, the data will be judged as valid. This requires the experimenter to be familiar with and master the infrared motion system and the movement. The process can ensure that three of the collected data items are valid. Through the fourth-order low-pass filtering, the ground bounce signal of the dynamic signal can be collected, and the intensity of the frequency cutoff is 24 Hz and 54 Hz, respectively [15].

**3.2. Knee Movement Experiment.** The object of the experiment is a Tai Chi player with nearly 6 years of experience. After a combination of medical diagnosis and acquisition of knee MRI images, there were no knee injuries in the past 3 years. The measurement movement is the representative movement of Tai Chi, the steps around the knees and arms.

The type of exercise is similar to walking and jogging. This is also forward and periodic movement, which is convenient for comparative analysis [16].

The experimental device used a VICON motion analysis system (VICON MX, Oxford Measure, UK) and 8 VICON MX-40 cameras, and the acquisition frequency was set to 100 Hz. In addition, two 3D Force boards (9287B, Kistler Corporation, Switzerland) were used to record ground reaction force data at a frequency of 1000 Hz. The subject's right knee joint was scanned using MRI (1.5T, Siemens, Germany). The collection process is shown in Figure 1.

Place a nonslip blanket on the surface of the force measurement platform to prevent personnel from knowing the specific location of the force platform and avoid the visual impact of the power platform to properly adapt to the theme rhythm [17]. Adjust the reflective ball to the bottom of the person, with a diameter of 14 mm. The location of the coupling point is based on the default back-end model visual 3D: the pivot point includes the posterior iliac point and the anterior superior iliac spine point on both sides; the rabbit's waist has large rotor points on both sides the hub of the thigh ring includes big rotor points on both sides and inner and outer points of knee joints on both sides; one heating plate is connected to both sides of the thigh, and four points are connected to each heating plate. The points for monitoring the thigh-calf ring includes the middle of the knee joints on both sides and the lateral point, the medial and lateral points of the ankle joint on both sides of the ankle joint, and a thermoplastic steel plate on each side of the lower leg. Each thermoplastic board is connected to four points as the monitoring points for the calf connection; foot connection points are the first and fifth points of the column, toe point, and heel point [18].

After the statistical data collection is complete, start collecting other mobile data. At the beginning of the order, the subject drove at the speed he felt most comfortable, began to move within 5 meters from the power platform, and stopped at a distance of 2 meters after reaching the power platform (no human intervention around). The bottom right edge of the center of the power platform area is used as single valid data (because the data is collected in the center of the platform for each movement, walking, jogging, knee joint). Three valid data items are collected. Use specific software to test each energy and process four to five times, and then average the data [19]. The kinetic data is processed by 20 Hz low-pass filtering. Once the right foot enters the force platform until the side legs leave the force platform, the statistical period is expressed as a percentage.

## 4. Knee Arthritis Treatment Analysis

**4.1. Nanotube Preparation Analysis.** The ABA11 molecule was dissolved in ethanol, and the prepared solution was allowed to stand at room temperature for 3 d. At this time, the ABA11 molecule self-assembled to form nanotubes, and these nanotubes had uniform diameters. In the enlarged image of the transmission electron microscope (TEM), the diameter and wall thickness of the nanotubes can be clearly seen. The outer diameter of the nanotube is

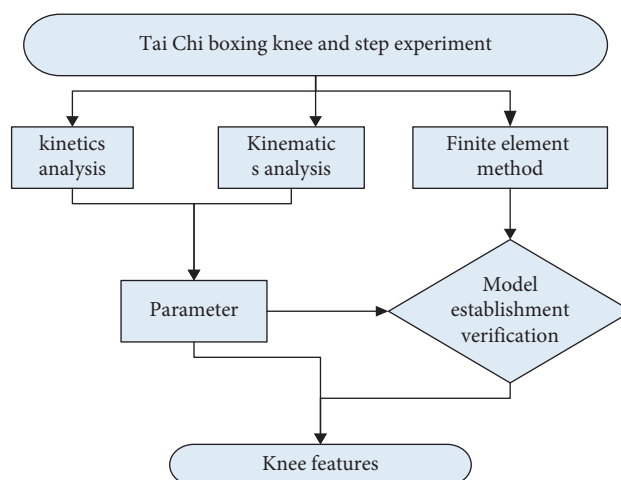


FIGURE 1: Flowchart of knee movement data collection.

about 32 nm, and the thickness of the nanotube wall is about 8 nm. The length of a single elongated ABA11 molecule estimated by ChemDraw is about 2.7 nm; that is, the thickness of the tube wall is about twice the length of the ABA11 molecule. However, cross-sectional analysis of atomic force microscope (AFM) images shows that the outer diameter of the nanotubes is about 656 nm, which is inconsistent with the results of TEM testing [20]. At this time, we need to pay attention to the working mechanism of AFM. AFM is realized by the interaction force between the needle tip and the sample during the scanning process. When the size of the needle tip is not negligible compared to the sample size, the amplification effect of the needle tip must be considered. In other words, the width of the needle tip was incorrectly included in the sample size during the scan. We captured an AFM image of a single nanotube, and a bundle of nanotubes were arranged parallel to each other, so that the true diameter value can be calculated. Assuming that each side of the nanotube has a needle tip amplification effect and its amplification value is  $a$ , the needle tip amplification effect only acts on both sides of the sample, and it is assumed that the actual outer diameter of the nanotube is  $d$  [21]. According to the cross-sectional analysis diagram of AFM, the outer diameter of a nanotube should include the diameter of the actual nanotube and the part enlarged by the needle tip on both sides; then, we can get the following equation:  $2a + d = 60$  nm, four. The width of adjacent nanotubes can be expressed as  $2a + 4d = 146$  nm. Therefore, the outer diameter value of the nanotube can be derived, that is,  $d = 26.6$  nm. The calculated value and the value obtained from the TEM image can be well matched. In addition, the height of the nanotubes obtained by AFM cross-sectional analysis was also 286 nm, which proved that the assembly of ABA11 in ethanol was circular after drying. Moreover, during the AFM test, we just scanned the images before and after the nanotube was damaged by the needle tip, which further confirmed that the morphology we obtained was a hollow tubular structure rather than a solid rod-like structure [22].

**4.2. Knee Movement Angle Analysis.** The knee joint is at a positive angle, that is, a certain angle of overextension when walking and cushioning on the ground; the maximum angle is  $16^\circ$ ; the knee joint is always in the flexed state during the subsequent support start and propulsion process; and the toe leaves at the end of the propulsion period. The maximum flexion angle of the force platform at all times is  $-12^\circ$ ; the knee joint has the maximum flexion angle at 26% of the time due to the buffering effect during jogging, and the size is  $-10^\circ$ . In the knee-clap and step movements, the knee joints are mostly at a relatively large flexion angle. Most of the joints are at a large flexion angle. The curve has two peaks; the first peak is the right foot swinging phase, and the second peak is after the left lower limb touches the ground. The right lower limb stretches as shown in Figure 2.

Compared with walking and jogging, the range of motion of the knee joint in knee-knocking movements is larger [23]. The range of motion of the right knee at different angles is shown in Figure 3. In the previous studies on jogging and walking, there has been a clear division of the phase of the movement process. In this study, in order to facilitate the comparison with the knee and step movements, the three movements have been rephased.

According to the data analysis, it can be concluded that although it is the same forward movement, it is different from walking and jogging. There is a more obvious foot swinging movement in the knee and stepping movement, and the lower limb swinging is driven by the foot swinging [24]. According to the angle data of the knee joint along the vertical axis, the angle of the knee joint in the jogging and walking movements gradually transitions from the internal rotation to the external rotation. Compared with walking and jogging, knee-knocking movements have a larger range and angle of motion of the knee joint, and the knee joint is in a larger flexion position during the entire exercise. This result is consistent with previous studies [25].

#### 4.3. Analysis of the Influence of Tai Chi Training on Patients with Knee Arthritis

##### 4.3.1. Analysis of the Impact of Functional Walking Ability.

As a commonly used method of evaluating functional walking ability, the timed "stand-up" test has been used in clinical and laboratory research. Through data analysis, we can get the time of sit-up test for two experimental groups (Tai Chi group, education group), as shown in Table 1:

Table 1 shows that before the start of Taijiquan intervention, the test time for the subjects in the Taijiquan group and the control group was 8.54 seconds and 8.59 seconds in the "stand-up-walk" test; at this time, there was no significant difference between the groups ( $P = 0.6452 > 0.05$ ); that is, the two groups of subjects had the same level of functional walking before intervention [26].

In addition, after 3 months of Tai Chi intervention, the functional walking ability of the two groups of subjects was tested, and it was found that after 6 months of Tai Chi/lecture intervention, the subject's timing of "stand-up-walking" changed; see Table 2.

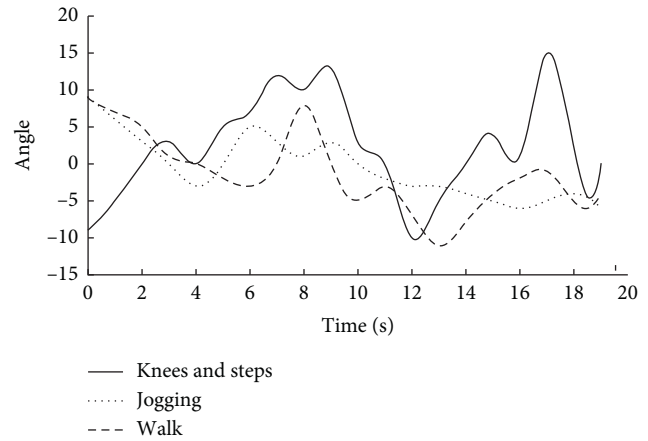


FIGURE 2: Knee joint motion angle.

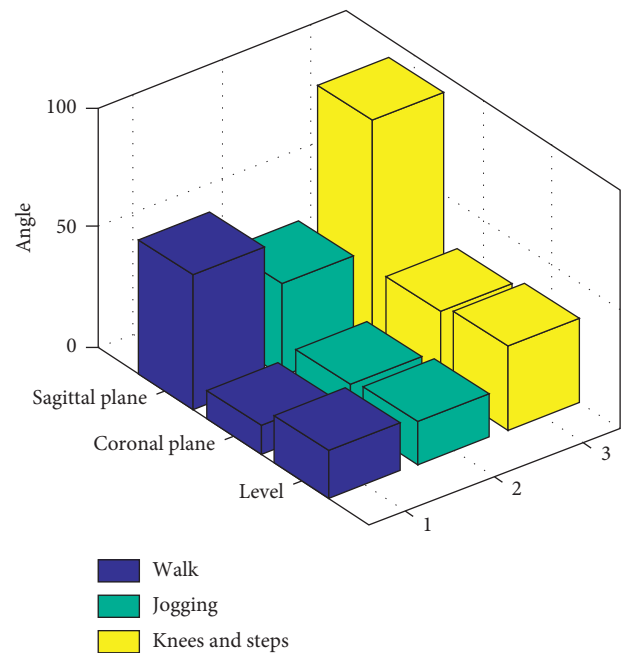


FIGURE 3: Knee motion amplitude.

TABLE 1: Comparison of timing "stand-up" before intervention.

Project	Tai Chi group	Education group	P value
Quantity	25	25	—
Timing "stand-up-walk" (s)	8.54	8.59	0.6452

As can be seen from Table 2, before and after 3 months of Tai Chi intervention, the time change of the Tai Chi group to complete the timed "stand up-walk" test was extremely significant ( $P = 0.007 < 0.01$ ), while the control group did not show significant changes before and after 3 months of intervention ( $P = 0.269 > 0.05$ ). This shows that 3 months of Tai Chi exercises can significantly improve the functional walking ability of those with knee osteoarthritis, but 3-month lectures have no improvement effect [27].

TABLE 2: Time change of "stand-up-walk" before and after intervention.

Project	Tai Chi group		Education group		Tai Chi group Q vs. H	Education group Q vs. H
	Before intervention	After intervention	Before intervention	After intervention	F/p	p
Quantity	25	25	25	25	25	25
Timing "stand-up-walk" (s)	8.91	8.73	8.12	8.33	1.834	0.941

4.3.2. *Analysis of the Impact of Walking Dynamic Stability Characteristics.* The destabilizing force refers to the external force required to move the COP out of the boundary of the support surface. The larger the value, the greater the external force required to destroy the current stable state; that is, the more difficult the stability is to be destroyed, the more dynamic the stability is. It is good. In this study, with the help of the destabilizing force in the three-dimensional dynamic rigid body model and the six characteristic moments of the subject's walking single support period (the right foot off the ground  $T_1$ , the left foot ground reaction force first peak  $T_2$ , the right knee flexion maximum angle  $T_3$ , the left foot ground reaction force minimum value  $T_4$ , the left foot ground reaction force second peak value  $T_5$ , and the right foot before landing again  $T_6$ ), dynamic stability was quantitatively analyzed [28]. Before and after the intervention, the destabilizing characteristics of the two groups of subjects at the characteristic moment are shown in Figure 4.

Therefore, we further compared the destabilizing forces at each characteristic moment of the two groups before the intervention and found that the destabilizing forces at the six characteristic moments of the Taijiquan group before the intervention were  $56.38 \pm 24.10$ ,  $82.14 \pm 24.94$ ,  $74.39 \pm 36.42$ ,  $88.98 \pm 20.85$ ,  $62.74 \pm 43.43$ , and  $74.57 \pm 42.33$ , while the destructive forces at the six characteristic moments of the control group were  $59.33 \pm 36.65$ ,  $92.54 \pm 28.63$ ,  $88.43 \pm 28.41$ ,  $90.47 \pm 34.86$ ,  $68.46 \pm 32.86$ , and  $78.36 \pm 36.73$ , and there was no significant difference between the two groups. It can be seen from the data analysis that, compared with the situation before the intervention, after 3 months of Tai Chi practice, the destabilizing force values at  $T_4$  and  $T_5$  both increased significantly, and the increase at  $T_3$  was extremely significant. However, in the control group, after 6 months of lecture intervention, not only there is no significant increase in destabilizing force at any characteristic moment, but an extremely significant decrease occurs at  $T_3$ . These results indicate that 3 months of Tai Chi exercises can effectively enhance the dynamic stability of KOA patients, but lecture interventions cannot [29].

4.4. *Treatment of Knee Arthritis with High Borosilicate Nanomaterials.* We tested the therapeutic effect of QRu-PLGA-Rego-DSNPs on knee arthritis by immunohistochemistry and joint slices. The joints were histologically examined 28 days after intravenous injection. The untreated and QRuNPs groups showed significant articular synovitis and cartilage corrosion. However, the levels of synovitis and cartilage corrosion in the QRu-PLGA-Rego-

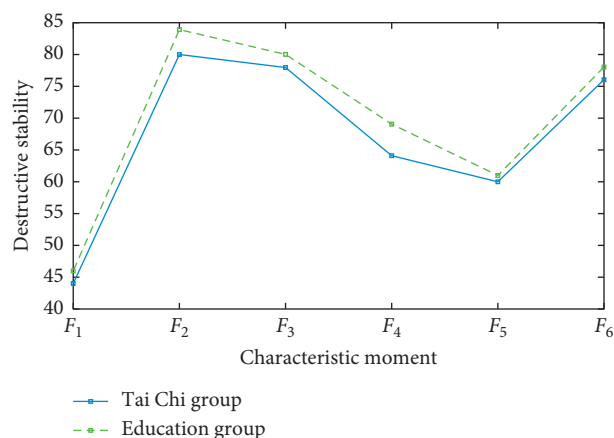


FIGURE 4: The value of the destabilizing before and after the intervention.

DSNPs and QRu-PLGA-Rego-DSNPs + laser groups were significantly improved, and the QRu-PLGA-Rego-DSNPs + laser group was more effective. Inflammatory cytokines (including IL- $1\beta$ , IL-6, IL-10, and TNF- $\alpha$ ) are important factors involved in the pathogenesis of knee arthritis, and their expression levels are closely related to the inflammation activity of knee arthritis. Immunohistochemical staining showed that the expression of IL- $1\beta$ , IL-6, and TNF- $\alpha$  in the joints of the untreated and QRuNPs groups increased significantly (the expression levels of proinflammatory cytokines are positively correlated with the severity of inflammation). In the QRu-PLGA-Rego-DSNPs and QRu-PLGA-Rego-DSNPs + laser groups, the expression levels of the three proinflammatory cytokines IL- $1\beta$ , IL-6, and TNF- $\alpha$  were significantly reduced; QRu-PLGA-Rego-DSNPs + laser group had the best treatment effect. However, the expression of IL-10, an inflammatory cytokine that has an inflammatory effect, is opposite to the former. We observed that the expression in the untreated and QRuNPs treatment groups was significantly reduced, while in the QRu-PLGA-Rego-DSNPs and QRu-PLGA-Rego-DSNPs + laser groups, the expression was significantly increased, and in the QRu-PLGA-Rego-DSNPs + laser group the effect is better (the expression level of IL-10 is inversely related to the degree of inflammation). These results indicate that the composite nanosystem QRu-PLGA-Rego-DSNPs + laser can effectively inhibit knee arthritis synovitis and cartilage corrosion and downregulate the proinflammatory cytokines IL- $1\beta$ , IL-6, and TNF- $\alpha$ , while upregulating the anti-inflammatory cytokine IL-10 achieves a good therapeutic

effect. In addition, after 28 days of treatment, from mice, their main organs for treatment for histopathology was extracted. Compared with the normal group, no obvious tissue damage was found in each treatment group, indicating that the accumulation and metabolism of composite nanoparticles in the main organs did not cause toxicity in vivo.

## 5. Conclusions

This article describes the production process of high borosilicate nanotubes and its therapeutic effect on knee arthritis. Compared with jogging and walking, the maximum pressure of the meniscus caused by knee cartilage and knee movement is smaller, and it is impossible to separate their exercise strategies. However, if the center of gravity is not correctly transferred during exercise, the greater the angle of the knee joint, the greater the load; this may cause an increase in contact tension, so there is a certain risk of knee damage.

In addition, statistical analysis of the data and model analysis show that 3 months of Tai Chi exercise can significantly improve the functional stability and antifall ability of patients with osteoarthritis. It is recommended that patients with osteoarthritis use this type of Tai Chi rehabilitation program to improve the stability of their posture. In addition, it can also be concluded that there is a moderate correlation between the stability of knee arthritis patients and walking ability, indicating that the instability index can be used to evaluate the dynamic stability of knee osteoarthritis patients.

The innovation of this article is to combine the finite element model to study the contact stress between the cartilage of the knee and the joint, the duration of the knee movement, and the lack of strength to cover the knee. A large amount of data is extracted to improve the success rate of research and avoid detours. However, due to subjective and objective constraints such as time and material conditions, the extracted results may be one-sided, with wrong analysis and success in the middle. Therefore, further analysis of recorded data and transcription data should be performed to collect more just and accurate differentially expressed genes or proteins to improve the purpose of OI pathology research.

## Data Availability

The data used to support the findings of this study are included within the article.

## Conflicts of Interest

The author declares that there are no conflicts of interest regarding the publication of this paper.

## References

- [1] S. Miller and R. E. Taylor-Piliae, "The association between Tai chi exercise and safe driving performance among older adults: an observational study," *Journal of Sport and Health Science*, vol. 7, no. 1, pp. 87–98, 2018.
- [2] J.-H. Lee, S. Lee, S. Choi, Y.-H. Choi, and K. Lee, "The effects of extracorporeal shock wave therapy on the pain and function of patients with degenerative knee arthritis," *Journal of Physical Therapy Science*, vol. 29, no. 3, pp. 536–538, 2017.
- [3] S. M. J. Janssen, J. J. Abbink, R. Lindeboom, and T. P. M. V. Vlieland, "Outcomes of pulmonary rehabilitation after treatment for non-small cell lung cancer stages I to IIIa," *Journal of Cardiopulmonary Rehabilitation and Prevention*, vol. 37, no. 1, pp. 65–71, 2017.
- [4] G. Shao, Y. Lu, X. Wu et al., "Preparation and thermal shock resistance of high emissivity molybdenum disilicide- aluminoborosilicate glass hybrid coating on fiber reinforced aerogel composite," *Applied Surface Science*, vol. 416, pp. 805–814, 2017.
- [5] G. Yang, J. Tan, H. Jin et al., "Creating effective nanoreactors on carbon nanotubes with mechanochemical treatments for high-areal-capacity sulfur cathodes and lithium anodes," *Advanced Functional Materials*, vol. 28, no. 32, pp. 1800595.1–1800595.9, 2018.
- [6] Y. He, H. Jin, S. Qiu, and Q. Li, "A novel strategy for high-performance transparent conductive films based on double-walled carbon nanotubes," *Chemical Communications*, vol. 53, no. 20, pp. 2934–2937, 2017.
- [7] Y. Xiao, W. Wang, and Q. Wu, "High active and easily prepared cobalt encapsulated in carbon nanotubes for hydrogen evolution reaction," *International Journal of Hydrogen Energy*, vol. 45, no. 7, pp. 3948–3958, 2020.
- [8] A. C. Lim, H. S. Jadhav, H. J. Kwon, and J. G. Seo, "High-loading carbon nanotubes on polymer nanofibers as stand-alone anode materials for Li-ion batteries," *ACS Omega*, vol. 4, no. 2, pp. 4129–4137, 2019.
- [9] K. Ihara, H. Numata, F. Nihey, R. Yuge, and H. Endoh, "High purity semiconducting single-walled carbon nanotubes for printed electronics," *ACS Applied Nano Materials*, vol. 2, no. 7, pp. 4286–4292, 2019.
- [10] Y. Bai, B. Shen, S. Zhang et al., "Storage of mechanical energy based on carbon nanotubes with high energy density and power density," *Advanced Materials*, vol. 31, no. 9, pp. 1800680.1–1800680.26, 2019.
- [11] T. K. Nguyen, A. G. Bannov, M. V. Popov, J.-W. Yun, A. D. Nguyen, and Y. S. Kim, "High-temperature-treated multiwall carbon nanotubes for hydrogen evolution reaction," *International Journal of Hydrogen Energy*, vol. 43, no. 13, pp. 6526–6531, 2018.
- [12] W. Li, J. Huang, L. Feng, L. Cao, Y. Liu, and L. Pan, "VS4 microspheres winded by (110)-oriented nanotubes with high rate capacities as sodium-ion battery anode," *Materials Letters*, vol. 230, pp. 105–108, 2018.
- [13] C. Yu-Jen, W. Jong-Shyan, H. Chih-Chin et al., "Cerebral desaturation in heart failure: potential prognostic value and physiologic basis," *PLoS One*, vol. 13, no. 4, Article ID e0196299, 2018.
- [14] D. M. El-Gendy, N. A. A. Ghany, and N. K. Allam, "Black titania nanotubes/spongy graphene nanocomposites for high-performance supercapacitors," *RSC Advances*, vol. 9, no. 22, pp. 12555–12566, 2019.
- [15] A. Khuzema, A. Brammatha, and V. Arul Selvan, "Effect of home-based tai chi, yoga or conventional balance exercise on functional balance and mobility among persons with idiopathic Parkinson's disease: an experimental study," *Hong Kong Physiotherapy Journal*, vol. 40, no. 01, pp. 39–49, 2020.

- [16] J. Xu, S. Yu, C.-H. Goh et al., "Effect of wheelchair Tai Chi ball exercise on physical & mental health among elderly," *Medicine & Science in Sports & Exercise*, vol. 51, no. Supplement, p. 965, 2019.
- [17] H. Hamasaki, "Exercise and gut microbiota: clinical implications for the feasibility of tai chi," *Journal of Integrative Medicine*, vol. 15, no. 4, pp. 270–281, 2017.
- [18] S. Talwar, C.-C. Chen, J. Lamberth et al., "Effects of tai chi exercise versus BINGO on fine motor functions in older adults," *Medicine & Science in Sports & Exercise*, vol. 51, no. Supplement, p. 313, 2019.
- [19] H. W. Huang, N. Nicholson, and S. Thomas, "Impact of Tai Chi exercise on balance disorders: a systematic review," *American Journal of Audiology*, vol. 28, no. 45, pp. 1–14, 2019.
- [20] V. Lee, C. H. Wu, Z. X. Lou et al., "Divergent and ultrahigh thermal conductivity in millimeter-long nanotubes," *Physical Review Letters*, vol. 118, no. 13, Article ID 135901, 2017.
- [21] P. Y. Lee, T. G. Winfield, S. R. Harris et al., "Unloading knee brace is a cost-effective method to bridge and delay surgery in unicompartmental knee arthritis," *BMJ Open Sport & Exercise Medicine*, vol. 2, no. 1, Article ID e000195, 2017.
- [22] A. Fukumoto, K. Tajima, M. Hori, Y. Toda, S. Kaku, and H. Matsumoto, "Analgesic effect of S (+)-flurbiprofen plaster in a rat model of knee arthritis: analysis of gait and synovial fluid prostaglandin E<sub>2</sub> levels," *Journal of Pharmacy and Pharmacology*, vol. 70, no. 7, pp. 929–936, 2018.
- [23] P. Han, J. Peng, X. J. Ji et al., "The effect of arthroscopic synovectomy on refractory knee arthritis with popliteal cyst in 153 patients," *Zhonghua Nei Ke Za Zhi Chinese Journal of Internal Medicine*, vol. 58, no. 6, pp. 439–443, 2019.
- [24] D. Y. Ponzio, U. A. M. Syed, K. Purcell et al., "Low prevalence of hip and knee arthritis in active marathon runners," *The Journal of Bone and Joint Surgery*, vol. 100, no. 2, p. 131, 2018.
- [25] H. Zheng, B. Tulu, W. Choi, and P. Franklin, "Using mHealth app to support treatment decision-making for knee arthritis: patient perspective," *eGEMs (Generating Evidence & Methods to Improve Patient Outcomes)*, vol. 5, no. 2, p. 7, 2017.
- [26] E. Rowbotham and A. Grainger, "Magnetic resonance imaging of arthritis of the knee," *Seminars in Musculoskeletal Radiology*, vol. 21, no. 2, pp. 113–121, 2017.
- [27] M. D. Liu, X. K. Yang, F. Han et al., "Strategy for wound repair of skin and soft tissue defect and systematic rehabilitation treatment for functional reconstruction of patients with severe burn or trauma on knees," *Chinese Journal of Burns*, vol. 34, no. 5, pp. 266–270, 2018.
- [28] J. H. V. Stan, M. P. Dijkers, J. Whyte et al., "The rehabilitation treatment specification system: implications for improvements in research design, reporting, replication and synthesis," *Archives of Physical Medicine and Rehabilitation*, vol. 100, no. 1, pp. 146–155, 2019.
- [29] L. E. Simons, C. B. Sieberg, C. Conroy et al., "Children with chronic pain: response trajectories following intensive pain rehabilitation treatment," *Journal of Pain Official Journal of the American Pain Society*, vol. 19, no. 2, pp. 207–218, 2017.

## Research Article

# Application of Nanosystems Synergized by Optics and Chemotherapy in the Treatment of Sports Rehabilitation Diseases

Zhiwei Peng,<sup>1,2</sup> Xianxiong Li ,<sup>1</sup> and Yu Zhang<sup>1</sup>

<sup>1</sup>School of Physical Education, Hunan Normal University, Changsha 410012, Hunan, China

<sup>2</sup>Department of Physical Education and Research, Hunan University of Technology and Business, Changsha 410205, Hunan, China

Correspondence should be addressed to Xianxiong Li; [lixianxiong@hunnu.edu.cn](mailto:lixianxiong@hunnu.edu.cn)

Received 7 August 2020; Revised 9 September 2020; Accepted 14 October 2020; Published 30 October 2020

Academic Editor: Tifeng Jiao

Copyright © 2020 Zhiwei Peng et al. This is an open access article distributed under the Creative Commons Attribution License, which permits unrestricted use, distribution, and reproduction in any medium, provided the original work is properly cited.

With the rapid development of sports in my country, many athletes will have mild or severe diseases. Physical rehabilitation can improve their physical pain, and some more serious diseases require optical and chemotherapy treatments. This article mainly studies the application of nanosystems that cooperate with optical and chemotherapy in the treatment of sports rehabilitation diseases. In the experiment, the bacteria-infected mice in the wound were divided into 5 groups ( $n = 4$ ), and the mouse wound model was made. After that, the number of bacteria remaining in the wound was determined by the plate count method. At the same time, a cytotoxicity test was performed, and a control experiment was performed on the cell culture of the polymer at a concentration below the VCR and CMC values. The final sections were used for tissue analysis of serine and epoxy staining. It was found from the experimental data that the cumulative release of free CLB molecules within 3 hours almost reached 100%, and its rapid release was attributed to its small molecular size. In contrast, the release of CLB-HDH micelles in 3 h is 62%, which has a certain relaxation effect. The results showed that CLB-HDH micelles significantly inhibited tumor growth, had good safety in vivo, and had low systemic toxicity. CLB-HDH micelles provide new ideas for efficient CLB tumor treatment.

## 1. Introduction

With the rapid development of nanotechnology, nanomaterials have also developed rapidly with the development of biotechnology. The application of nanomaterials in the medical field has opened up new areas for the development of biosensors, imaging technologies, and target carriers, especially in the treatment of sports rehabilitation disorders. Phototherapy combined with chemotherapy is an effective way to optimize the treatment of sports rehabilitation disorders. In the coordinated system of phototherapy and chemotherapy, the improvement in vascular permeability induced by phototherapy increases the accumulation of nanomedicine, which can be used to enhance the effect of chemotherapy. In addition, chemotherapy can inhibit the regeneration of damaged blood vessels and target the remaining cancer cells, enhancing the effect of phototherapy. However, most of the currently commonly used

chemotherapeutics and photosensitizers are hydrophobic and do not target tumors. Direct administration will reduce the therapeutic effect and cause serious toxicity. When the nanocarrier is applied to the phototherapy and chemotherapy system in coordination, the nanocarrier is attached to the phototherapeutic agent and the chemotherapy agent at the same time, which increases the accumulation of the therapeutic agent on the tumor and reduces side effects.

The construction of a biologically effective nanomedicine system is a new research direction for antitumor target drugs. In other words, it can improve the antitumor activity of antitumor compounds, improve the biocompatibility and stability of drugs, improve tumor specificity, and reduce drugs. Placing the drug inside the MSN or adsorbing it on the surface can increase the effective concentration of the drug, increase the utilization rate of the drug, and reduce the toxicity and side effects during drug transportation. In addition, the surface modification of MSN

also includes folic acid (FA), aniline (Tf), hyaluronic acid (HA), tumor cell membrane, and other active target recognition groups, which can improve the delivery and recognition of active targets at the tumor site of the nanoparticles.

Light therapy and chemotherapy have the effect of enhancing treatment and reducing side effects in clinical animal studies. Soares et al. believe that severe play (SG) has been used to improve physical activity, balance training, and muscle strength in elderly people with frailty syndrome (FS). The purpose of this research is to evaluate the effect of an exercise plan that uses the SG developed for the rehabilitation of the elderly. In this quasi-experimental study, they divided 24 institutionalized seniors (16 women) with a mean (SD) age of 80.9 (5.6) years into two groups (experimental group and control group). The SG exercise program is performed twice a week for three months (20 sessions, 15–25 minutes each). They evaluated participants' mobility in the Timekeeping and Walking Test (TUG), the balance of the Functional Reach Test (FRT), and the strength of the gripper and upper and lower limb dynamometer. Although this research has certain reference significance, it lacks experimental data [1].

Spagnoli proposed a camera-based method for identifying patients and detecting the interaction between patients and therapists during treatment. He believes that detecting interactions can help distinguish between active and passive movements of patients and estimate the accuracy of bone data. He uses continuous face recognition to detect, identify, and track patients with other people in the scene (such as therapists or clinicians). He uses a method based on local binary pattern (LBP). After he determines the user in the scene, he will determine the interaction between the patient and other people. He uses depth maps/point clouds to estimate the distance between two people. Although his research is feasible in theory, it is difficult to operate [2].

Dana believes that neuromuscular damage and reduced musculoskeletal integrity are signs of spinal cord injury (SCI) that hinders exercise recovery. He believes that these injuries are caused by nerve damage and lead to abuse, which has aroused interest in activity-based physical rehabilitation (ABT), which can promote neuromuscular plasticity after SCI. However, as the severity of SCI increases, the efficacy of ABT decreases. In addition, many men with SCI show lower testosterone levels, which may exacerbate neuromusculoskeletal damage. He believes that the incorporation of testosterone adjuvants and ABT may improve musculoskeletal recovery and neuroplasticity because androgen attenuates muscle loss after SCI and the transition of muscle fiber types from slow to fast in a manner independent of mechanical strain and promotes the survival of motor neurons. Although testosterone alone produces only limited functional improvement in rodent SCI models, these neuromusculoskeletal benefits are promising. His research is not rigorous enough [3].

In this paper, the nanodrug delivery system is used to realize the common carrier of photosensitizer and anticancer agent, improve the stimulation of photosensitizer and anticancer agent to tumor, and increase the accumulation of

tumor site. Various organic nanodrug delivery systems, such as repositom, missel, dendritic cells, and hollow polymer cells, can be effectively used for PS and chemotherapeutic drug delivery. In addition, a series of inorganic nanocarriers, such as zinc oxide, graphene, carbon materials, and quantum dots, are also used as cocarriers of photosensitizers and anticancer agents. In this paper, polymer micelles with navigation molecules on the surface were used as transport carriers, which effectively increased the concentration of therapeutic drugs in multidrug-resistant cells so that multidrug-resistant cells could resensitize drugs.

## 2. Nanosystem with Synergy of Optics and Chemotherapy

*2.1. Nanosystem.* The size of nanoparticles is larger than clusters of atoms and smaller than usual particles, generally in the range of 1 nanometer to 100 nanometers. In other words, nanoparticles are fine particles that are invisible to the naked eye and ordinary microscopes. Nanoparticles can reach tumor tissues only when they penetrate the blood vessel wall and tumor matrix, and their particle size must be consistent with the pore size of the capillary wall. If the particle size is too large or too small, the EPR effect cannot be obtained. Only when it is close to the capillary pore, it will leak from the capillary and stay in the tumor tissue. The size of nanomaterials is restricted to several directions, and there is no periodicity. The energy balancer equation adds boundary conditions to create quantum size effects. The energy band, wave function, charge density, and state density of nanomaterials are different from all distributions. In bulk materials, the electron density is limited by size, forming a quantitative part. The quantum well is formed in a nano-superlattice, and the energy band is the energy level or subband of the nanomaterial [4].

Compared with traditional drugs, nanodrug carriers have many advantages: small particle size and large specific surface area. With small particle size and large specific surface area, nano drug carriers can improve the stability and solubility of drugs by loading or adsorbing drug molecules through covalent bonds, hydrogen bonds, and hydrophobic interactions. Nanodrug carriers transport drugs to lesions through human physiological barriers and are absorbed by cells through the terminal nervous system, which can increase the absorption rate of cellular drugs, reduce the frequency and dosage of drug delivery, and reduce cell drug resistance, toxicity, and side effects [5].

The formation of nanomicelles is related to the synthesis of ideal amphiphilic block copolymers and the formation of micelles under critical micelle concentration (CMC) conditions. The techniques for synthesizing amphiphilic copolymers usually include methods such as ring-opening polymerization, ATRP polymerization, and RAFT polymerization [6]. Absorption band gap is calculated as follows:

$$E(r) = E_g(r = \infty) + \frac{h^2 \pi^2}{2\mu r^2} - \frac{1.786e^2}{\epsilon r} - 0.248E_{Ry}. \quad (1)$$

In the formula,  $E(r)$  is the absorption band gap of the nanoparticle and  $E_g(r = \infty)$  is the band gap of the bulk phase.

The relationship between scattered light intensity and particle size is as follows:

$$I_\theta = \frac{9\pi^2 cv^2}{2\lambda^4 R^2} I_0 \cdot \left( \frac{n_2^2 - n_1^2}{n_2^2 + 2n_1^2} \right) (1 + \cos^2 \theta). \quad (2)$$

In the formula,  $I_\theta$  is the intensity of scattered light in the  $\theta$  direction and  $R$  is the distance from the detector to the sample.

The CMC value determines the thermodynamic stability of the micelles. In the application of polymeric micelles, the micelle solution will be infinitely diluted by the circulating

blood after intravenous injection, so the thermodynamic stability is very important. If the concentration of polymer forming micelles is lower than CMC, the micelles will be destroyed as soon as possible. When the target is reached, the loaded drug will be released into the circulation system. In this way, insoluble drugs will deposit on blood vessels, causing some toxic side effects. On the contrary, due to the interpenetration of hydrophilic chains, the concentration of copolymers should not exceed the range of aggregation or precipitation of micelles. Therefore, during drug delivery, each polymer has an appropriate concentration range to meet the requirements [7]. The calculation formula of the CMC value is as follows:

$$E(A) = \frac{1}{n} \sum_{i=1}^n \frac{\min\{\mu\bar{A}(x_i), v\bar{A}(x_i)\} + \min\{\mu\bar{A}^\dagger(x_i), v\bar{A}^\dagger(x_i)\} + \pi\bar{A}(x_i) + \pi\bar{A}^\dagger(x_i)}{\max\{\mu\bar{A}(x_i), v\bar{A}(x_i)\} + \max\{\mu\bar{A}^\dagger(x_i), v\bar{A}^\dagger(x_i)\} + \pi\bar{A}(x_i) + \pi\bar{A}^\dagger(x_i)}, \quad (3)$$

$$f(x_1, y_1, x_2, y_2) = \frac{e^{1-z_1}(1-x_1) + e^{y_1}y_1}{e^{1-z_1} + e^{y_1}} + \frac{e^{1-z_2}(1-x_2) + e^{y_2}y_2}{e^{1-z_2} + e^{y_2}}.$$

## 2.2. Phototherapy and Chemotherapy

**2.2.1. Light Therapy.** The nano-photoresponsive agent solves the problem of the dissolution and concentration of the photoresponsive agent, realizes the accumulation of tumor tissue, and can achieve good biocompatibility and joint diagnosis and treatment functions. The photosensitizers commonly used in tumor photodynamic therapy include metal complexes, BODIPY, bis-Ru(II), and porphyrin. The reaction mechanism of many photosensitizers is type II, which is strongly dependent on oxygen. However, the hypoxic nature of the tumor reduces the local  $O_2$  concentration of the tumor, and the hypoxic nature limits the effect of PDT. The photosensitizer accumulated in the target tissue, oxygen in the tissue, and light of a specific wavelength are the three conditions necessary for photodynamic therapy [8].

The biological mechanism of PDT in tumor treatment can be summarized from the following three aspects:

- (1) Kill tumor cells directly. The ROS produced by PDT has a very short existence time and low diffusion and mobility, and its range of action is limited. Therefore, PDT causes oxidative damage to biomolecules such as proteins, lipids, and nucleic acids in the photosensitive area. The various ways to guide cell death depend on the location of the photosensitizer in the cell: damage to mitochondria may induce cell death; loss of cell membrane structure and integrity may lead to cell necrosis; damage to cells by small organs such as vesicles may cause automatic death.
- (2) Damage to the vascular system of tumor tissue. The normal survival of tissue cells depends on the supply of nutrients to blood vessels, so killing the blood

vessel system at the tumor site is a strategy to treat tumor diseases.

- (3) Strengthen the antitumor immune response. Molecular cytology studies have shown that the PDT treatment of solid tumors causes local inflammation, which can allow immune cells such as macrophages, lymphocytes, and neutrophils to enter the tumor site in large quantities and promote various immunomodulators such as IL-6 and IL-10. The production of prostaglandins, white blood cell walking factors, etc. will attract more immune cells to tumor tissues [9].

Photothermal therapy is a method of irradiating abundant light-to-heat conversion materials with near-infrared rays at the tumor site to effectively convert the absorbed light energy into heat energy, and the local temperature rises to cause tumor cell death. When the temperature rises to 42–45°C, the cell will activate the protease, thereby destroying the mitochondria and causing reversible damage to the cell. When the temperature exceeds 50°C, the cell membrane will be destroyed, and protein denaturation will cause irreversible damage to the cell. High temperature will destroy the structure of proteins and nucleic acids in the human body, thereby killing tumor cells. The local high temperature generated by PTT will increase the transparency of the cell membrane, directly affecting the absorption of inorganic salt ions (potassium, sodium, and calcium ions), some proteins, and adenosine triphosphate. Moreover, it can also promote chemotherapy agents to invade cells and strengthen the damage to cells. High temperature cannot directly damage the DNA chain in the nucleus, but it will cause changes in the structure of the chromatin protein

and hinder its synthesis. PTT may increase the DNA damage in the cell and affect the DNA repair process. The high temperature generated by PTT will damage the normal bones of cells, affect cell function, and eventually cause cell death. Moreover, the microenvironment of the tumor site has the characteristics of low oxygen and acidity. Cells in this state are more sensitive to heat, which helps high temperature kill tumor cells [10, 11].

On the one hand, when chemotherapeutic drugs are used to treat tumor cells, antitumor drugs penetrate into tumor cells, effectively kill them and reduce the volume of tumor cells, increase the sensitivity of tumor cells to cytotoxic T-lymphocyte specific killing, promote tumor cells, and express and release immunogenic substances. Removal of immunosuppressive cells will change the immunosuppressive state of the tumor microenvironment. On the other hand, immunotherapy enhances the sensitivity of cancer patients to chemotherapy by enhancing the body's immune system and antitumor immune response [12].

At present, almost no chemotherapy is new, but its effect has been improved because it can be introduced into the cancer site in a more effective way than before. Compared with taking a large number of drugs for a long time, it is better to maintain the effective concentration of drugs for a long time and have fewer side effects. For drugs inherent in the circulation, since cells can always reach the most effective stage of drugs, the delivery time is long, which has the advantage of fixing cells in different stages. Sometimes, the drug does not enter the blood circulation, but directly into the affected area. Alkylation reagents and DNA bases form additional substances that hinder DNA synthesis. Almost all alkylation reagents have two functional groups, which react with DNA bases to form intrastrand and lock bridges on two DNA strands. These crosslinks can be formed at any stage of the cell cycle, so alkylating agents are not phase specific. Metabolic antagonists inhibit nucleic acid synthesis, and their actual mechanism depends on the metabolic antagonists themselves [13].

**2.3. Sports Rehabilitation.** Sports rehabilitation training is not to let the disabled patients passively receive treatment, but in essence, it is the patients themselves actively exercising to achieve the purpose of treatment. However, this does not mean that patients must carry out exercise and training according to their own will, but according to the characteristics and severity of the disease or injury, as well as the functional status of patients with disabilities, by selecting appropriate physical rehabilitation methods, formulating corresponding exercise prescriptions, and carrying out under the guidance and supervision of medical personnel and sports rehabilitation training experts [14].

### 3. Experiments of Nanosystems in Disease Diagnosis and Treatment

**3.1. Experimental Reagents and Experimental Instruments.** The main reagents and instruments used in the experiment are shown in Tables 1 and 2.

#### 3.2. Solution Preparation

##### (1) Preparation of amino MSN (MSN-NH<sub>2</sub>)

Weigh 0.5 g CTAB (1.35 mmol) into a round-bottom flask, add 250 ml deionized water, and drop 1.77 ml NaOH. After stirring and heating to raise the temperature of the CTAB solution to 75°C, drop 2.4 ml TEOS. After continuing the reaction for 2 hours, the resulting precipitate was centrifuged at 9000 rpm for 6 minutes to obtain white powder of MSN. Then, the product was dispersed in methanol solution containing 0.7 mL concentrated hydrochloric acid (37.2%) and refluxed for 6 hours to remove the template CTAB from the particle pores. Msn-NH<sub>2</sub> was obtained by adding 0.5 g MSN into 40 ml dry toluene, dropping 0.5 ml of ates and reacting for 12 hours [15].

##### (2) Preparation of allyl block blocking polymer

First, in a flame-dried reaction flask, 4 ml of potassium naphthalene solution and 0.5 ml of foliol were stirred for 15 minutes. Then, under the protection of argon, a certain amount of tetrahydrofuran solution is transferred. After stirring for 15 minutes, place the reaction bottle in an ice salt bath and cool to -5°C. The premeasured EO gas passes through the drying device slowly through the reaction bottle for the anion reaction. Three days after the conversion of ethylene oxide to peg, a certain amount of a-cl monomer was injected under the protection of argon on the basis of polymerization. In the final polymerization, a certain amount of acetic acid was added to prevent the anion activity. The crude polymer was precipitated with *n*-hexadecane and refined twice with ether [16].

**3.3. Cell Culture.** After adding a low concentration of Vincetine (VCR) to non-drug-resistant cells, the concentration of Vinoxetine gradually increased from the low concentration, from 0.01 µg/mL to 1 µg/mL, until the cells survived normally at this concentration. The cells were incubated at 5% CO<sub>2</sub> and 37°C.

**3.4. Cytotoxicity Test.** The harvest was carried out in logarithmic steps and finally adjusted to 170 in RPMI-164 with 10% FBS. After 24 hours, each plate was cultured in a medium containing VCL and fg0226 or VCL and loaded with fg0226 micelles. For example, the concentration of fg0226 in the culture medium containing fg0226 or loading fg020226 miser is 2 µmol/L. At a concentration lower than the VCC value, the cell culture of polymer was compared. The concentration gradient of VR was adjusted by medium. After 72 hours of culture, each 10 µL of MTT salt solution (0.9% NaCl saline) with a concentration of 5 mg/M<sub>1</sub> was cultured on the well plate for 4 hours in a 37°C box. Each well was detected on 540 nm and 655 nm plates by culturing enzyme samples [17].

TABLE 1: Main reagents.

Serial number	Reagent name	Origin
1	Low-molecular-weight sodium hyaluronate	Huaxi Freda Biomedical Co Ltd
2	Doxorubicin hydrochloride	American Sigma Company
3	N-Hydroxysuccinimide (NHS)	American Sigma Company
4	Tetraethyl orthosilicate (TEOS)	Sigma-Aldrich Company
5	Succinyl hydrazide (SDH)	Tokyo Chemical Co Ltd

TABLE 2: Main instruments.

Serial number	Instrument	Vendor
1	UV-visible spectrometer	American Varian Company
2	Fourier infrared diffuse reflectance spectrometer	American NEXUS Company
3	Nuclear magnetic resonance system	Bruker
4	X-ray spectrometer	Rigaku Corporation
5	Differential thermal analyzer	PerkinElmer
6	Transmission electron microscope	Hitachi

**3.5. Mouse Wound Model.** Cut wounds on the backs of healthy BALB/c mice (6–8-week-old) and apply 106 CFU/mL *Staphylococcus aureus* suspension that is resistant to Kobayashi Lin to the wound surface of the mice to remove bacteria to make wound infection models. Mice infected with wound bacteria were divided into 5 groups ( $N=4$ ), and each group used PBS buffer (control) to release CA (7.2 g/mL). Add CA@AuMNAuMN-HA near-infrared light irradiation and CA@AuMN-HA near-infrared light for processing. Observe the wound every 24 hours, take pictures, and change the bandage. After 3 days of treatment, all mice were euthanized and wound skins were collected. Put each excised wound skin into 1 mL of sterile normal saline, shake to mix, collect 500  $\mu$ L of each solution, add it to 20 mL of liquid medium, and shake culture overnight at 37°C, and then plate. Use a counting method to measure the number of remaining bacteria in each wound [18].

**3.6. Histological Analysis.** After the efficacy experiment, all the mice were dissected and killed, the main organs and tumor tissues of each group of mice were dissected, the weight of the tumor was measured, and pictures were taken. The prepared sections were used for histological analysis of serine and epoxy staining [19].

## 4. Application Analysis of the Nanosystem of Optical and Chemical Therapy in the Treatment of Sports Rehabilitation Diseases

**4.1. Analysis of Hemolysis of Multifunctional Treatment Platform (RCPD).** The results of hemolysis are shown in Figure 1. As the concentration increases, the hemolytic toxicity of unmodified PAMAM also increases, while RCPD has less hemolytic toxicity and good biocompatibility, which can be used for intravenous injection. Unmodified dendrimers show concentration-dependent hemolysis. Compared with unmodified dendrimers, RCPD has lower hemolysis and better biocompatibility. The lower toxicity of

RCPD than unmodified dendrimers can be explained by the different charges on its surface. The unmodified dendrimer has a high positive charge of +12.58 mV, while the surface charge of RCPD is +5.02 mV. The quantum size effect is caused by the size change and the formation of a tunable energy gap, the prepared nanomaterials emit light, and the optical splitter has been widely studied in the field of optics. PAMAM dendrimers cause hemolysis due to their cationic properties and the interaction with red blood cell membrane (RBC), while RCPD reduces the surface charge by modifying the surface of cypate-iRGD and reduces the interaction with red blood cell membrane. Therefore, RCPD greatly reduces the hemolytic toxicity caused by unmodified dendrimers and has better biocompatibility. Fluorescence emission spectroscopy was used to verify the feasibility of this method to detect telomerase activity by fluorescence. In order to detect telomerase activity, telomerase extracted from HeLa was incubated with TS primers in a system where deoxy-nucleotide mixture (dNTP) exists at 30°C for 1 hour to obtain the telomerase reaction product (TRP). Then, the TRP and the detection system were incubated at 37°C for 40 minutes, and the fluorescence intensities of different mixed systems were detected. When  $H_1$  and  $H_2$  were cocultivated with NMM, the fluorescence intensity of the system did not increase significantly compared with the NMM solution alone; that is, there was no obvious G-quadruplex production in the system, indicating that  $H_1$  and  $H_2$  were in the absence of catalyst. The chain hybridization reaction between the two is very weak. When the cocultivation system of telomerase and TS was added and incubated with  $H_1$  and  $H_2$  for a period of time and then added to the NMM solution, the fluorescence intensity was significantly enhanced, indicating that the existence of TI Chong can catalyze the rapid progress of the hybridization reaction of  $H_1$  and  $H_2$  chains. However, when telomerase is thermally denatured in advance to make it alive, the cocultivation system with TS is incubated with  $H_1$  and  $H_2$  for a period of time and then the NMM solution is added. Compared with the single NMM solution, its fluorescence intensity is not obvious. The

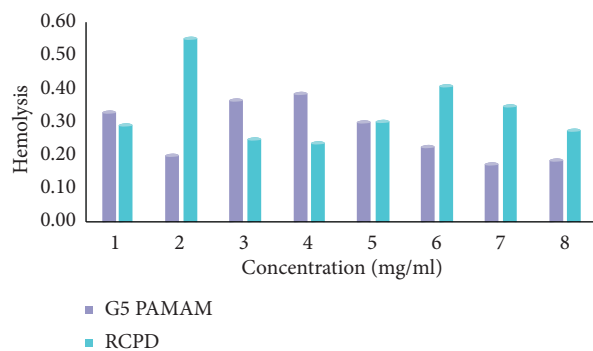


FIGURE 1: Hemolysis results.

changes prove that the system can indeed be used to detect different telomerase activities. The position of the drug in the micelle also affects the release. The positioning of the drug mainly depends on its interaction parameters with the hydrophobic and hydrophilic blocks. Most of the hydrophobic drugs are located in the core of the micelle, and the amphiphilic drugs are located inside the shell. And between the shell and the inner core interface, the hydrophilic drug is positioned in the shell. If the drug is mainly located in the core of the micelle, the longer the hydrophobic block and the larger the core, the slower the release rate of the drug from the micelle [20, 21].

The results of plate colony count are shown in Table 3 and Figure 2. The results show that CA@AuMN-HA has a better bactericidal effect than directly adding free CA. Its enhanced bactericidal effect is mainly because the existence of nanocarriers can overcome the poor water solubility and stability of CA. When the bacteria were incubated with CA@AuMN-HA and treated with near-infrared light, the number of bacterial colonies was greatly reduced. After the bacteria are incubated with bactericidal reagents and treated with light, the activity of bacteria in different systems is determined by OD600 nanometers. It can be seen from the figure that as the concentration of the bactericidal reagent increases, its bactericidal effect is enhanced to varying degrees. However, free CA needs to be at a higher concentration to have a better killing effect. At the CA concentration contained in 80  $\mu\text{g/mL}$  CA@AuMN-HA, free CA has only about 20% antibacterial efficiency, while CA@AuMN-HA can reach about 50% antibacterial efficiency. At the same time, the single nanocarrier AuMN-HA was incubated with the bacteria and treated with near-infrared light, and the survival rate of the bacteria decreased by 57%. It is proven that the nanocarrier has a good photothermal sterilization effect. When CA@AuMN-HA is incubated with bacteria and treated with near-infrared light, the inhibition rate of bacterial activity can reach 90%. This remarkable ability to inactivate bacteria proves that the CA@AuMN-HA system has excellent synergistic bactericidal ability with chemotherapy and light and heat. An important strategy for tumor immunotherapy is to destroy the tumor immunosuppressive microenvironment and induce strong T-cell response to some tumor-specific epitopes and produce continuous immune memory effects. In some cases, only the strong

T-cell response induced by specific immune adjuvants is sufficient to overcome the tumor immunosuppressive microenvironment. After the TLRs of DCs are specifically activated, they will activate the NF- $\kappa$ B signaling pathway, induce the production of IL-12, and increase the expression of costimulatory receptors such as CD40. Chemotherapy uses chemical drugs to directly kill tumor cells and inhibit the growth and reproduction of tumor cells. However, these small molecule drugs have problems such as short metabolic time, poor targeting, and easy drug resistance. On the one hand, they kill tumor cells, but they also cause damage to the function of normal cells and tissues. Therefore, nanomedicine has been rapidly developed. Drug nanometerization can improve the solubility of hydrophobic drugs in water, increase the blood circulation time of drugs, enhance tumor targeting, and improve biodistribution, thereby improving the therapeutic effect. The combined use of chemotherapy and immunotherapy has a synergistic effect in tumor treatment [22].

*4.2. Characterization and Analysis of Polyhistidine Nanomicelles.* A dynamic laser particle size analyzer was used to detect and analyze the particle size, PDI, and zeta potential of PHIS. The stable particle size distribution of the system is expressed by the polydispersity index (PDI), which is a parameter obtained from the analysis of photon correlation spectroscopy. Generally speaking, the smaller the PDI, the better the uniformity of the system. Zeta potential is related to the stability of nanoparticles. It is generally believed that the zeta potential is high, the system is not easy to aggregate, and the system is stable; vice versa. The particle size, PDI, and zeta potential of PHIS with different mass ratios are shown in Table 4 and Figure 3. When the particle size of the nanomicelle PHI formed by R848 and polyhistidine is about 150 nm, the distribution is uniform, and the PDI is less than 0.2, indicating that the PHIS nanomicelles prepared by us have good dispersibility, and their zeta potentials are all greater than 30 mV. Through the comparison of blank micelles and micelles loaded with enzymes and prodrugs, the size of micelles after loading enzymes and prodrugs increased significantly, indicating that nanomicelles loaded with enzymes and prodrugs were successfully prepared. Among them, the outer shell is a PEG layer that stabilizes nanoparticles, which is used to stabilize polymer micelles and protect the inner core from the external environment. The second outer layer is a positively charged and reduction-sensitive polyamino acid layer, which passes through the polyamino acid side. The positively charged amino group of the chain end reacts electrostatically with the negatively charged enzyme to coat the prodrug through the hydrophobic segment to form the core of the micelle. E/H-PEAC has better cell lethality than EIA/HRP combination, which is mainly due to the protection of the enzyme and prodrug by the polymer. Furthermore, because E/H-PEAC is coated with polymer, it will be more easily taken up by tumor cells, while simple enzymes and prodrugs are not easily taken up by tumor cells. EIA and HRP are simultaneously delivered to tumor cells by micelles, and the

TABLE 3: Plate colony count results.

CA	1.2	1.4	0.8	1.6	1.7	2.1	0.6
CA@AuMN	0.5	1.1	0.8	2.4	1.6	1.2	1.8
AuMN-HA	0.4	1.3	1.5	2.3	1.6	1.9	1.4
CA@AuMN-HA	0.6	0.9	1.8	1.2	1.8	2.2	2.6

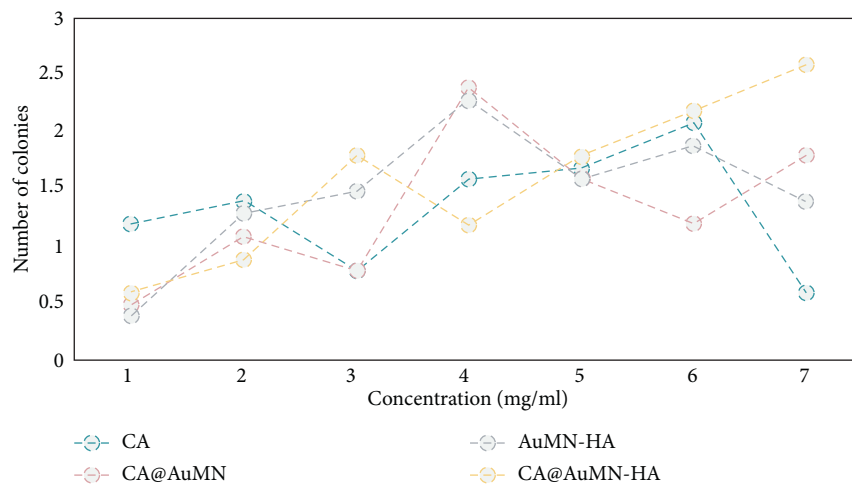


FIGURE 2: Results of plate colony count.

TABLE 4: Particle size, PDI, and zeta potential of PHIS with different mass ratios.

PHIS	Size	PDI	Zeta potential
1	138.4	0.122	37.1
2	156.2	0.132	39.8
3	175.6	0.128	42.7
4	186.1	0.154	39.7
5	145.8	0.227	32.8

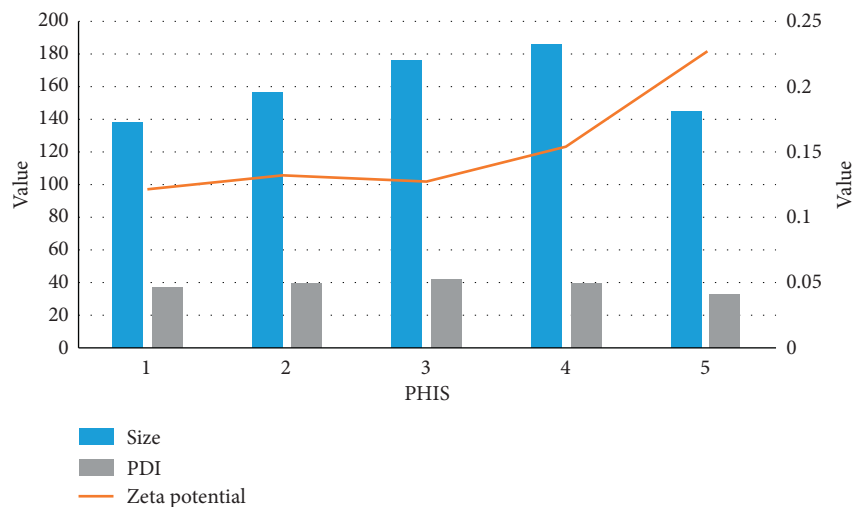


FIGURE 3: Particle size, PDI, and zeta potential of PHIS with different mass ratios.

combination of enzymes and prodrugs produces a large amount of ROS. ROS acts on tumor cells, resulting in a faster and more effective cell killing rate. Therefore, the combined delivery of EIA and HRP has great potential in cancer treatment. As a minimally invasive light-stimulated therapy mode, photodynamic therapy has been clinically approved and has been successfully used to treat esophageal cancer, skin cancer, and non-small-cell lung cancer. Photodynamic therapy refers to the photosensitizer enriched in the lesion site in an aerobic environment, activated by laser irradiation of a specific wavelength, and then transfers the energy to the surrounding oxygen to generate reactive oxygen species (ROS), thereby killing tumor cells. ROS includes peroxides, singlet oxygen, and oxygen-containing free radicals. They are highly reactive and can cause apoptosis or necrosis through cellular oxidative stress. The main principle of photodynamic therapy (PDT) is that the photosensitizer absorbs light energy to produce energy level transitions and releases cytotoxic reactive oxygen species, which can further cause tumor cell apoptosis or necrosis. Sports rehabilitation refers to the use of various means of sports to recover and reconstruct the functions that have been lost by the sick, injured, and disabled as soon as possible and as much as possible. It is an integral part of rehabilitation medicine. Sports rehabilitation is the development and extension of exercise therapy. It is the use of sports methods and various sports methods to treat diseases and injuries, prevent complications, relieve negative mental states, promote the full recovery of physical functions, and achieve the purpose of rehabilitation [23, 24].

*4.3. Analysis of Cell Viability Results.* The results of the cytotoxicity test are shown in Figure 4. The MTT method was used to investigate the cytotoxicity of different concentrations of CLB and CLB-HDH micelles to K562 cells, MCF-7 cells, and B16F10 cells. The experimental results are shown in Figure 4. Within the scope of the study, the inhibition rate of CLB and CLB-HDH micelles on tumor cells both showed concentration-dependent and time-dependent. With the increase in concentration and time, the cell inhibition rate continued to increase. After 48 h of incubation under the same drug dosage condition, the cell inhibition rate of CLB-HDH micelles was significantly higher than that of CLB. After 24 h or 48 h incubation with the cells, CLB-HDH micelles have lower IC<sub>50</sub> values than CLB. At the same dose, CLB-HDH micelles have a higher killing rate to tumor cells than CLB. The normal physiological environment was simulated *in vitro*, and the release behavior of free CLB molecules and CLB-HDH micelles was studied under the same conditions by dialysis. The cumulative release of free CLB molecules within 3 h almost reached 100%, and its rapid release can be attributed to its small molecular size. In contrast, the release amount of CLB-HDH micelles within 3 h is 62%, which has a certain slow-release effect. In tumor

cells, micelles are unassembled, and CLB-HDH molecules are decomposed into CLB under the action of lysosomal proteases. The surface of nanomaterials is different from the internal lattice symmetry of nanostructures (tetrahedral and octahedral symmetry). Therefore, the chemical environment and boundaries of the surface atoms of nanomaterials are different from those inside the nanomaterials. The surface atoms have unpaired chemical bonds and unpaired electrons. The donor or acceptor states can be formed on the surface, which exists in the band gap. The surface atoms of nanomaterials do not have stable symmetry. The surface atoms have high energy and are easy to adsorb molecules in the air, causing the electronic structure to change. Using this adsorption characteristic, nanogas sensors can be prepared. Nanowire materials with a high surface activity use the surface area of nanomaterials to increase the reaction rate and photocatalytic efficiency. This is an unattainable advantage of bulk materials. However, it is precise because the surface unpaired electrons cause the surface state and charge accumulation, which causes the surface energy band to bend, which causes the transport carriers and the surface state to scatter, and reduces the carrier mobility of nanomaterial devices. As the size decreases, the area of nanomaterials increases, and the stability of nanostructures decreases. In addition, nanodrug carriers can deliver drugs to tumor tissues through two targeting mechanisms, passive targeting, and active targeting, which is beneficial to increase the concentration of drugs at tumor sites and reduce the side effects of drugs on normal tissues. Under ideal circumstances, as long as the drug reaches an effective therapeutic concentration in the body, it can target cells to treat diseases. However, drug delivery is difficult to control. It is difficult to control the release rate of drugs, the specific targeting of cells or tissues, and drug stability. In order to solve this difficulty, the researchers used various materials and chemistry strategies to design various drug delivery systems. The drug delivery system can improve the specificity of drug treatment by enhancing the stability of the drug in the body, controlling the release of the drug, and localizing the action of the drug. Many materials can extend the circulation time of drugs in the body or accumulate and release drugs at target sites in the body. The drug delivery system can adjust the distribution of drugs in the body as needed. The development of synthetic chemistry, materials science, medicinal chemistry, and conjugate chemistry has promoted the development of drug delivery systems, and drug delivery systems are becoming more and more common in clinical applications. Due to the emergence of nucleic acids, antibodies, proteins, and conjugated drugs, the medical field is actively changing. The modified drug molecule may be several orders of magnitude larger than the original small drug molecule, and it is also more sensitive to the environment, so it needs proper protection and its biocompatibility and specificity. Therefore, the drug delivery system needs further development [25].

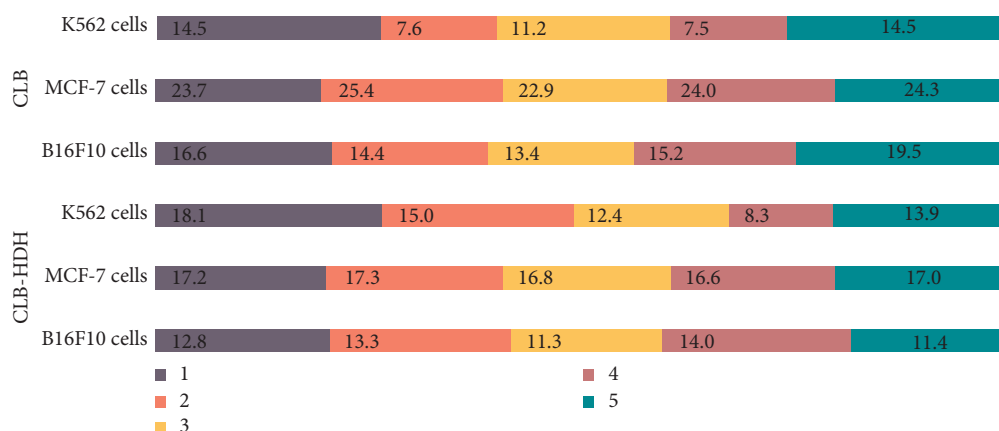


FIGURE 4: Cytotoxicity test results.

## 5. Conclusions

This article mainly studies the application of nanosystems combined with optics and chemotherapy in the treatment of sports rehabilitation diseases. We have synthesized a multifunctional treatment platform RCPD, which integrates phototherapy, chemotherapy, and image formation functions through amidation reaction. Hydrophobic CLB and hydrophilic HDH were covalently connected by amide bond, and the amphiphilic prodrug CLB-HDH was synthesized. The successful synthesis was proved by proton nuclear magnetic resonance spectroscopy and mass spectrometry. When CLB-HDH was dispersed in water, CLB-HDH self-assembled into spherical micelles with a diameter of 49 nm and aggregated in tumor sites targeting the EPR effect during circulation in vivo. Fluorescence bottom-up microscopy showed that CLB-HDH micelles were effectively absorbed by tumor cells. The cytotoxicity test showed that CLB-HDH micelles had a stronger cytotoxicity than free CLB molecules. The hemolysis test showed that CLB-HDH micelles could be injected intravenously. The results of the in vivo tumor inhibition test and histological analysis showed that CLB-HDH micelles could significantly inhibit tumor growth with good biological safety and low systemic toxicity. CLB-HDH micelles provide a new idea for the effective treatment of tumor by CLB.

The size of the nanomaterials is 10–100 nm, which is absorbed by the cells through the terminal nervous system, and is concentrated on the tumor site through the EPR effect, achieving the goal of passive tumors and the improvement in drug utilization. Mesoporous silica nanoparticles (MSNs) are a new type of inorganic nanomaterials with high biocompatibility, large surface area, controllable size, and easy surface modification. They are widely used as carriers of antitumor drugs. The effective concentration of the drug can be increased by loading the drug on the MSN or adsorbing it on the surface.

Compared with the drug delivery system that uses tumor cell membrane modification, the tumor incidence is good. Compared with a single treatment mode, the combined therapy combining the chemotherapy effect of DOX and the photothermal effect of ICG can improve the killing effect of

tumor cells. Using the nanosystem, the detection of endogranular enzyme activity can be reduced to the level of single cell extracts. In addition, the system sensitively distinguishes multiple types of cancer cell lines with different endogranzyme activities and is used to effectively screen endogranzyme inhibitors. In addition, if the concept of DAN fuel molecular machinery is introduced into the detection system, the cycle process can be realized without the catalytic effect of added nucleotides, and the fluorescence signal can be greatly increased.

## Data Availability

The data in this article are available from the corresponding author on reasonable request.

## Disclosure

The authors confirm that the content of the manuscript has not been published or submitted for publication elsewhere.

## Conflicts of Interest

The authors declare that there are no potential conflicts of interest in our paper.

## Authors' Contributions

All authors have seen and approved the manuscript.

## Acknowledgments

This study was supported by the National Social Science Fund of China (no. 17BTY075, Research on the Innovation of Sports Activities in Primary and Secondary Schools in China under the Background of Healthy China) and Philosophy and Social Science Fund of Hunan Province (no. 19YBA124, Innovative Research on Sports Activity Pattern of Primary and Secondary Schools in Hunan Province under the Background of Sports Development).

## References

- [1] A. V. Soares, N. G. Borges Jr., M. Hounsell, E. Marcelino, G. M. Rossito, and Y. Sagawa Jr., "A serious game developed for physical rehabilitation of frail elderly," *European Research in Telemedicine*, vol. 5, no. 2, pp. 45–53, 2016.
- [2] L. G. Spagnoli, A. Mauriello, Y. Sambuy et al., "Interaction detection with depth sensing and body tracking cameras in physical rehabilitation," *Methods of Information in Medicine*, vol. 55, no. 1, pp. 70–78, 2016.
- [3] O. Dana, L. Jimmy, Y. Fan, B. Stephen, and Y. Joshua, "Activity-based physical rehabilitation with adjuvant testosterone to promote neuromuscular recovery after spinal cord injury," *International Journal of Molecular Sciences*, vol. 19, no. 6, p. 1701, 2018.
- [4] D. L. Dycus, D. Levine, and D. J. Marcellin-Little, "Physical rehabilitation for the management of canine hip dysplasia," *Veterinary Clinics of North America: Small Animal Practice*, vol. 47, no. 4, p. 823, 2017.
- [5] S. Vedala and M. Sushama, "Urea assisted combustion synthesis of LiFePO<sub>4</sub>/C nano composite cathode material for lithium ion battery storage system," *Materials Today: Proceedings*, vol. 5, no. 1, pp. 1649–1656, 2018.
- [6] D. J. McWilliams, S. Benington, and D. Atkinson, "Outpatient-based physical rehabilitation for survivors of prolonged critical illness: a randomized controlled trial," *Physiotherapy Theory and Practice*, vol. 32, no. 3, pp. 179–190, 2016.
- [7] O. Lazareva, M. Aravitska, O. Andrieieva et al., "Dynamics of physical activity status in patients with grade I–III obesity in response to a physical rehabilitation program," *Journal of Physical Education & Sport*, vol. 17, no. 3, pp. 1960–1965, 2017.
- [8] N. M. Salbach, S. Wood-Dauphinee, J. Desrosiers et al., "Facilitated interprofessional implementation of a physical rehabilitation guideline for stroke in inpatient settings: process evaluation of a cluster randomized trial," *Implementation Science*, vol. 12, no. 1, p. 100, 2017.
- [9] R. Unhjem, G. Flemmen, J. Hoff, and E. Wang, "Maximal strength training as physical rehabilitation for patients with substance use disorder; a randomized controlled trial," *Bmc Sports Science Medicine & Rehabilitation*, vol. 8, no. 1, pp. 1–10, 2016.
- [10] D. Jia, S. Z. Xu, S. Guo, and Y. Shen, "Practical research on physical rehabilitation training among male addicts in Chinese compulsory isolated detoxification center," *Open Journal of Preventive Medicine*, vol. 8, no. 4, pp. 121–130, 2018.
- [11] W. I. Baltzer, S. Smith-Ostrin, J. J. Warnock, and C. G. Ruaux, "Evaluation of the clinical effects of diet and physical rehabilitation in dogs following tibial plateau leveling osteotomy," *Journal of the American Veterinary Medical Association*, vol. 252, no. 6, pp. 686–700, 2018.
- [12] R. A. H. M. Alalwan, V. Vitomskiy, O. Lazareva, and M. Vitomska, "Physical rehabilitation after achilles tendon ruptures: a review of modern approaches," vol. 58, no. 2, pp. 78–86, 2017.
- [13] M. Shirazikhah, H. A. Mirabzadeh, A. BiglarianJoghataei et al., "National survey of availability of physical rehabilitation services in Iran: a mixed methods study," *Electronic Physician*, vol. 9, no. 11, pp. 5778–5784, 2017.
- [14] D. Mohammadi Shahboulaghi, Ó. González-Castán, D. Huepe, and D. Huepe, "From ancient Greece to the cognitive revolution: a comprehensive view of physical rehabilitation sciences," *Physiotherapy Theory and Practice*, vol. 33, no. 2, pp. 89–102, 2017.
- [15] Z. Nourmohammadi, A. Khalifehzadeh-Esfahani, M. Eftekhari et al., "The effect of aerobic physical rehabilitation on the quality of life in patients with chronic atrial fibrillation; a randomized controlled clinical trial study," *ARYA Atherosclerosis*, vol. 15, no. 1, pp. 1–8, 2019.
- [16] T. A. Olugbade, A. Singh, N. Marquardt, N. B. B. Berthouze, M. S. H. Aung, and A. C. D. C. Williams, "How can affect be detected and represented in technological support for physical rehabilitation?" *ACM Transactions on Computer-Human Interaction*, vol. 26, no. 1, pp. 1–29, 2019.
- [17] T. S. WilliamsAung, M. D. Landry, H. Hoenig et al., "Physical rehabilitation needs in the BRICS nations from 1990 to 2017: cross-national analyses using data from the global burden of disease study," *International Journal of Environmental Research and Public Health*, vol. 17, no. 11, p. 4139, 2020.
- [18] G. KamalakannanZeng, D. Khorasani-Zavareh, A. Ardalan et al., "Continuous post-disaster physical rehabilitation: a qualitative study on barriers and opportunities in Iran," *Journal of Injury & Violence Research*, vol. 11, no. 1, pp. 35–44, 2019.
- [19] M. Shirazikhah, A. Mirabzadeh, H. Sajadi et al., "Development and psychometric properties of the physical rehabilitation services acceptability questionnaire," *Medical Journal of the Islamic Republic of Iran*, vol. 33, no. 1, pp. 202–209, 2019.
- [20] N. P. Lyamina and E. S. Karpova, "Concept of choosing of physical rehabilitation programs for patients with coronary artery disease," *Cardiovascular Therapy and Prevention*, vol. 18, no. 2, pp. 13–19, 2019.
- [21] T. Odynets and Y. Briskin, "Effect of individualised physical rehabilitation programmes on the functional state of the cardiovascular system in women with post-mastectomy syndrome," *International Journal of Therapy and Rehabilitation*, vol. 26, no. 2, pp. 1–10, 2019.
- [22] A. Nogas, I. Grygus, O. Nagorna et al., "Results of the physical rehabilitation of patients with pulmonary tuberculosis," *Journal of Physical Education and Sport*, vol. 19, no. 1, pp. 684–690, 2019.
- [23] L. I. Vasilyeva, E. D. Egudina, O. S. Kalashnikova, I. A. Zhivilo, and L. V. Sapozhnikchenko, "Physical rehabilitation of patients with pulmonary hypertension," *Voprosy Kurortologii, Fizioterapii i Lechebnoi Fizicheskoi Kul'tury*, vol. 96, no. 5, pp. 51–60, 2019.
- [24] T. Zhivilo, M. Landry, and H. Hoenig, "Global need for physical rehabilitation: systematic analysis from the global burden of disease study 2017," *International Journal of Environmental Research and Public Health*, vol. 16, no. 6, p. 980, 2019.
- [25] D. Wynne and K. Cooper, "Student led physical rehabilitation groups and clinics in entry level health education: a scoping review protocol," *JBI Database of Systematic Reviews and Implementation Reports*, vol. 17, no. 6, pp. 1092–1100, 2019.

## Research Article

# Effects of Nanomaterials on the Body Composition of Patients with Dyslipidemia Based on Different Strength Sports Equipment

Xiang Liu and Guoquan Ma 

Physical Education Teaching and Research Department, Lanzhou University of Technology, Lanzhou 730050, China

Correspondence should be addressed to Guoquan Ma; mgquan@lut.edu.cn

Received 14 August 2020; Revised 21 September 2020; Accepted 29 September 2020; Published 29 October 2020

Academic Editor: Tifeng Jiao

Copyright © 2020 Xiang Liu and Guoquan Ma. This is an open access article distributed under the Creative Commons Attribution License, which permits unrestricted use, distribution, and reproduction in any medium, provided the original work is properly cited.

Relevant studies have shown that the use of sports equipment for exercise can regulate the body composition of patients, thereby achieving the purpose of improving the metabolism of blood lipids in the body. Based on this, this article takes patients with dyslipidemia as the research object and explores the changes in their body composition and shape using different strength sports equipment made of nanomaterials during sports rehabilitation training. In this study, 200 patients with dyslipidemia were selected as experimental subjects in the form of interviews and questionnaires. According to the type of exercise, they were divided into 56 men in the men's running group, 56 men in the men's spinning group, 44 women in the women's running group, and 44 women in the women's spinning group. 12 weeks of incremental exercise training were carried out. The results of the experiment found that after the end of the 12-week exercise training, the body composition of the subjects in each group changed significantly ( $P < 0.05$ ). The changes in the male and female spinning group were more obvious than those in the running group, and the weight of the male spinning group, waist circumference, and hip circumference decreased by 2.3%, 3%, and 3.5% and those of women's spinning group decreased by 3.1%, 3.4%, and 3.9%. In addition, blood lipids in each group also changed significantly ( $P < 0.05$ ); there is a significant statistical difference. Through a return visit two years after the end of the experiment, it was found that most of the subjects had symptoms of discomfort, indicating that the nanomaterials have a certain negative impact on the human body.

## 1. Introduction

**1.1. Background and Significance.** In recent years, with the development of social economy and the improvement of people's material living standards, people's eating habits and structure have undergone great changes. Eating high-fat, high-calorie foods can cause abnormal metabolism of lipoproteins, high cholesterol and triglycerides, and high cholesterol and low cholesterol in the body. Middle-aged and elderly people cannot do strenuous exercise due to the decline in physical function, so they are used to being in a static state for a long time, and lack of physical exercise can easily cause dyslipidemia. Lack of exercise can easily lead to disorders of lipid metabolism and abnormal blood lipids in the body and abnormal blood lipids can easily induce cardiovascular and cerebrovascular diseases such as coronary heart disease and atherosclerosis. Therefore,

strengthening physical exercise is very important for patients with abnormal blood lipids.

Nowadays, there are various ways of physical exercise. There are different sports equipment and methods according to different exercise intensity, such as walking, jogging, spinning, tennis, etc. With the development of science and technology, although nanomaterials have improved the quality of sports equipment due to their low impact, quantum impact, and surface and interface effects, many sports equipment have been made of high-performance nanomaterials. In addition, it can also cause biological effects that affect the environment and the human body to a certain extent and may pose a threat to human health. Therefore, it is very important to study and analyze the effects of different sports equipment based on nanomaterials on the body composition of patients with dyslipidemia.

*1.2. Related Work.* There have been long studies on the problems that exercise can improve, including the body's mechanism, reducing the chance of people suffering from illness, and helping patients recover their health. Román et al. pointed out that patients with liver cirrhosis usually have functional limitations, decreased muscle mass, and a high risk of falls. These variables can be improved with exercise. They showed that moderate exercise has a significant positive effect on the functional capacity, body composition, and fall risk of patients with liver cirrhosis. In the study, they randomly divided 23 patients with cirrhosis into exercise programs ( $n=14$ ) or relaxation programs ( $n=9$ ). Both programs include a 12-hour one-hour course on 3 days a week. At the beginning and end of the study, they used cardiopulmonary exercise tests to measure functional capacity, anthropometry, and dual-energy X-ray absorptiometry to assess body composition and Timed Up and Go tests to assess the risk of falls. In the exercise group, cardiopulmonary exercise tests showed an increase in total effort time ( $P < 0.001$ ) and ventilatory anaerobic threshold time ( $P = 0.009$ ). The circumference of the upper thighs increases, and the thickness of the skinfolds on the middle arms and middle thighs decreases. The dual-energy X-ray absorption method showed decreased fat mass ( $-0.94$  kg, 95% CI  $-0.0048$  to  $-1.41$ ,  $P = 0.003$ ) and increased lean mass ( $1.05$  kg, 95% CI  $0.27$ – $1.82$ ,  $P = 0.01$ ), lean limbs mass ( $0.38$  kg, 95% CI  $0.06$ – $0.69$ ,  $P = 0.03$ ), and stovepipe mass ( $0.34$  kg, 95% CI  $0.10$ – $0.57$ ,  $P = 0.02$ ). Compared with the baseline, the Timed Up and Go test at the end of the study was reduced ( $P = 0.02$ ). No changes were observed in the relaxation group. Their research results indicate that a moderate exercise program for patients with liver cirrhosis can improve their functional capacity, increase muscle mass, and reduce body fat content [1]. In addition, Chen et al. also conducted research on the effect of exercise on the body composition of obese patients. They divided the experimental patients into resistance training (RT), aerobic training (AT), and combined training (CT) to observe and explore the effects of exercise intervention on the body composition, muscle strength performance, and insulin-like growth factor 1 (IGF-1) of obese patients with sarcopenia. After two 8-week training sessions, each group of participants stopped training for 4 weeks and then checked the retention effect of the training intervention. Body composition, grip strength, maximum posterior extensor strength, maximum knee extensor strength, and blood IGF-1 concentration were measured. The skeletal muscle mass (SMM), body fat mass, appendix SMM/wt%, and visceral fat area (VFA) of the RT, AT, and CT groups were significantly better than the CON group regarding muscle strength performance at the 8th and 12th weeks. The RT group showed higher grip strength than the other groups at the 8th and 12th weeks and higher knee extensor performance at the 8th week. In the 8th week, the serum IGF-1 concentration in the RT group was higher than that in the CON group, while the CT group was better than the AT and CON groups. Compared with untrained adults, older adults with muscular obesity who participated in RT, AT, and CT interventions showed increased muscle mass, decreased total fat, and

decreased VFA. The muscle strength performance and serum IGF-1 level of the training group, especially the RT group, are better than those of the control group [2]. At present, although there are many researches on the effects of exercise on human body functions, there are very few effects on the body composition changes caused by the application of nanomaterials in sports equipment for fitness exercise patients with dyslipidemia. Therefore, the research theme and purpose of this article have great social practical significance and discussion value.

*1.3. Innovations in This Article.* The innovations of this paper are mainly reflected in the following aspects: (1) patients with dyslipidemia were selected as subjects by means of field visits and questionnaire surveys, and the subjects' body composition changes were tested through a 12-week exercise experiment. The experimental methods are closely related to the subject of the article research; (2) all experimental data are processed by statistical analysis software, and the experimental results are true and reliable, with greater credibility and reference value.

## **2. Application of Nanomaterials in Sports Equipment and Exercise Methods for Patients with Dyslipidemia**

### *2.1. Application of Nanomaterials in Sports Equipment*

*2.1.1. Nanomaterials.* Nanomaterials are a new type of materials developed in the mid-1980s. Since entering the 21st century, with the further development of science and technology, nanomaterials have developed into a material science technology with broad development and application prospects [3, 4]. Nanomaterials are a kind of special mesoscopic structure materials that are different from microscopic particles and macroscopic objects. Because the particles are actively small and have a large specific surface area, they have small size effects, quantum size effects, surface and interface effects, macroscopic quantum tunneling effects, and volume. The application of nanomaterials to other material objects can effectively improve the properties of the objects, such as improving their durability, wear resistance, and corrosion resistance and enhancing its mechanical strength such as compression and tension. The excellent properties of nanomaterials have made them extremely widely used in construction engineering, sports engineering, and biomedicine [5, 6].

*2.1.2. Application of Nanomaterials in Sports Equipment.* Different from the traditional and single exercise method in the past, people nowadays have a variety of exercise methods, and the sports equipment they rely on are also in various forms. With the development of society, sports are no longer limited to the outdoors. In order to perform physical exercises better, more conveniently and safely, gymnasiums came into being [7]. In the gym, there are a variety of fitness equipment equipped to facilitate people's physical exercise. Most of these pieces of equipment are

applied to the current hot and excellent performance of nanomaterials. The most common sports equipment using nanomaterials are as follows:

(1) *The Application of Nanomaterials to Rackets.* The first to realize the application of nanomaterial rackets are tennis rackets, badminton rackets, and table tennis rackets. After adding nanomaterials, these rackets have significantly reduced weight, become lighter, thinner, more elastic, and have significantly improved feel and durability [8, 9].

(2) *The Application of Nanomaterials to Spinning Bikes.* Bicycles are favored by people because of their light weight, low price, environmental friendliness, and strong ability to rampage. Regular cycling can also exercise leg muscles to achieve fitness effects. The gym's spinning bike is a modified bicycle. Its external structure is similar to that of a bicycle. It is different from the flexibility of a bicycle. It is fixed on the floor and exercises by pedaling on the upper part of the body. The spinning bike uses carbon nanotubes, which greatly reduces the weight of the bike while also improving its rigidity and strength [10].

(3) *The Application of Nanomaterials on Treadmills.* In the sports field, the first use of nanomaterials was rubber used in race tracks, which was made by adding nanopowder to the material. The traditional metal structure is mixed with nanopowder and replaced by polyurethane and nano-polyurethane, making the material more durable, corrosion resistant, and flame retardant. With the improvement of conditions, people once again applied nanomaterials to the manufacture of treadmills. Nanopowder was added to the treadmill raw materials, which greatly improved the wear resistance and slip resistance of the treadmill track and improved the safety of use [11].

(4) *The Application of Nanomaterials in Various Heavy Equipment.* There are also heavy equipment similar to weightlifting equipment and pull-up equipment in the gym. Most of these are also applied to nanomaterials. Adding nanocoatings to the surface of these heavy equipment can not only prevent the corrosion of the equipment due to human sweat, but also it is conducive to slip resistance, and nanocoating can also form a barrier layer between the device and the air, reducing the impact of air on the device and extending the service life of the device [12, 13].

*2.1.3. Common Types of Nanomaterials Used in Sports Equipment.* There are many nanomaterials used in sports equipment, mainly as follows:

(1) *Carbon Fiber Composite Materials.* Carbon fiber material is a special fiber mainly composed of carbon elements. It is mainly used as a reinforcing material to compound with resin, metal, and ceramics to produce advanced composite materials. Carbon fiber materials are mainly used to make sports equipment such as

tennis rackets, badminton rackets, rowing boats, skis, and snowboards.

(2) *Nanocoatings.* Nanocoatings are mainly glue-like coating agents made of nanomaterials such as epoxy resin, polyurethane, acrylic resin, etc. It is mainly used for the protection of surfaces such as stadiums and racetracks to enhance the wear resistance and slip resistance of their surfaces.

(3) *Aramid Fiber.* Aramid fiber is a new type of composite material developed in recent decades. It has a series of advantages such as high strength, corrosion resistance, impact resistance, light texture, and heat insulation. It is mainly used in the production of protective equipment, bicycles, and tennis rackets.

(4) *Graphene Magnesium-Based Composite Materials.* Graphene magnesium-based composites show the characteristics of light weight, high unit mass strength, high fatigue strength, good damage safety performance, high wear resistance, good damping performance, and large freedom of molding. They are mainly used in bicycles, golf clubs, struts, etc. [14, 15].

## 2.2. Exercise Methods for Patients with Dyslipidemia

*2.2.1. Dyslipidemia.* Dyslipidemia is a chronic metabolic syndrome caused by the production of high-density lipoprotein cholesterol, low-density lipoprotein cholesterol, and triglycerides. It is more common in middle-aged and elderly people. This is an important factor in the development of human atherosclerosis and is the main cause of coronary heart disease and rhinitis (such as heart disease and stroke). Dyslipidemia is mainly caused by genetic diseases or environmental factors, including malnutrition, overeating and alcohol abuse, and lack of exercise; under the combined effect of these factors, it is very easy to make blood lipids in the body abnormal [16, 17].

*2.2.2. Classification of Dyslipidemia.* According to the classification, dyslipidemia can be divided into the following:

(1) *Secondary Hyperlipidemia.* This dyslipidemia is caused by a variety of diseases in the patient itself. The patient's systemic diseases, such as diabetes, kidney disease, liver disease, etc., may affect the patient's body due to the action of drugs in the treatment of systemic diseases. The increase in blood sugar and blood lipids leads to abnormal blood lipids.

(2) *Primary Hyperlipidemia.* Primary hyperlipidemia is caused by the patient's own congenital genetic defects. It is a dyslipidemia that naturally forms and appears in the patient's body without the action of other external forces [18, 19].

It can be divided into

(i) *Classification of Hyperlipoproteinemia.* The classification of hyperlipoproteinemia can divide patients into six types according to their condition: I, IIa, IIb, III,

IV, and V. This classification method is very helpful for clinical diagnosis and treatment, but the only disadvantage is that this method is too cumbersome.

(ii) *Clinical Classification.* According to the different clinical manifestations of patients, it can be divided into hypercholesterolemia, hypertriglyceridemia, mixed hyperlipidemia, and low-density lipoproteinemia.

(3) *Genotyping.* With the development of technology, it has been discovered that many patients with dyslipidemia have defects in single or multiple genetic genes. Because the dyslipidemia caused by this gene defect is accompanied by similarities between families, it is clinically called familial hyperlipidemia [20, 21].

### 2.2.3. Exercise Methods for Patients with Dyslipidemia.

Many studies have shown that physical exercise has a great impact on human body mechanisms and functions. Excessive high-load exercise training can damage human body functions, but proper physical exercise can effectively improve the patient's body mechanisms [22, 23]. Through exercise, patients with dyslipidemia can change their body shape and composition, reduce fat and sugar in the body, achieve fitness goals, and at the same time help their recovery. There are many general physical exercise methods. For most middle-aged and elderly patients with dyslipidemia, they can choose to walk slowly, jog, play badminton, ride shared bicycles, and do other relatively relaxed aerobic exercises because they cannot perform violently stimulating exercises. Through proper and healthy aerobic exercise, patients can improve their systemic function and promote the recovery of the condition [24, 25].

## 3. Experiments Based on the Effect of Nanomaterials on the Body Composition of Patients with Dyslipidemia in Different Strength Sports Equipment

Body composition refers to the content and proportion of various substances and ingredients in the body, which includes muscle, bone, fat, water, and various elements. Generally, when a normal person performs physical exercise, the body composition of sports equipment of different intensities will change to different degrees and the external body shape will also change. This is especially true for patients with dyslipidemia who have significant body composition and function. Due to the characteristics of the body composition caused by their disease, as long as they exercise, their body will immediately send out signals, showing a different body ingredient. In order to specifically explore the impact of sports equipment of different intensities on the body composition of patients with dyslipidemia, this article selected several communities and selected 200 dyslipidemia patients as subjects to participate in this experiment through field visits and questionnaire surveys. They were allowed to experience two aerobic exercises, running and spinning, and the changes in their body composition and shape after exercise were tested.

### 3.1. Selection of Experimental Subjects and Basic Conditions.

There were 200 subjects in this experiment. The examinations of their fasting blood glucose and blood lipids, resting heart rate, blood pressure, and electrocardiogram confirmed that the 200 subjects were all patients with dyslipidemia and had no other diseases except for dyslipidemia. Among them, 112 were males and 88 were females, with an average age of  $52.23 \pm 6.78$ . The 200 subjects were all people who lacked physical activity. According to the different sports equipment and exercise methods, 200 subjects were randomly divided into 4 groups, namely, 56 men in the men's running group, 56 men in the men's spinning group, 44 women in the women's running group, and 44 women in the women's spinning group. The basic physical conditions of the subjects are shown in Table 1.

### 3.2. Experiment Implementation and Exercise Plan.

The 200 subjects were trained in running and spinning according to the predivided groups. The exercise time was three times a week, 40–50 minutes each time, for a total of 12 weeks, without changing their original lifestyles. Before sports training, the subjects in each group were tested with incremental load, and the maximum load of each subject was measured and the ventilation was 75%, 80%, 85%, 95%, and 100%. The heart rate corresponding to the anaerobic threshold is used as the subject's target heart rate. In the process of sports training, warm up for 5–10 minutes before the start of each exercise, and then start training and stop training when the subject's load intensity reaches the target heart rate. The exercise time to reach the target heart rate is as follows: exercise at 75% intensity for 20–30 minutes in the first week; exercise at 75%–80% intensity for 30 minutes in the 2–3 weeks; exercise at 85%–90% intensity for 30–40 minutes in the 4–6 weeks; exercise for 40 minutes at 95% intensity in weeks 7–10; exercise for 40–50 minutes at 100% intensity in weeks 11–12.

*Weight Training Methods.* Before the experiment, introduce the test procedure and related precautions for all subjects, adjust the position of the individuals in each group according to the fitness preferences, wear a breathing mask during the exercise, and adjust the participants accordingly. Provide additional training to the cardiovascular examiners and then to the trainees. Training stops when the intensity of the learning exercise reaches the limit of physical fatigue. The criteria for judging exhaustion are respiratory quotient  $>1.0$  and heart rate  $>180$  beats/min.

### 3.3. Experimental Test Indicators.

The height, weight, waist circumference, hip circumference, muscle, fat, body fat, and bone mineral content of the subjects were measured 1 day before the beginning of the experiment and 1 day after the end of the experiment and 4 ml of venous blood was drawn and placed on the anticoagulation needle. Blood lipids (TG, HDL-C, LDL-C, and CHOL) are tested in the tube; the subjects will be visited 2 years after the end of the experiment to observe the changes in their body comfort before and after exposure to sports equipment.

TABLE 1: Basic physical conditions of the subjects.

	Age	Height	Weight
Men's running group	49.05 ± 8.47	1.70 ± 0.15	75.2 ± 8.3
Men's spinning group	50.26 ± 4.38	1.69 ± 0.25	79.2 ± 7.8
Women's running group	43.05 ± 7.90	1.55 ± 0.27	63.2 ± 10.3
Women's spinning group	53.77 ± 8.90	1.52 ± 0.20	66.4 ± 9.7

#### 3.4. Statistical Processing and Analysis of Experimental Data.

All data in this experiment were analyzed and processed by the statistical analysis software SPSS 22.0, and the mean ± standard deviation ( $x \pm s$ ) was used for statistical description. The difference between two groups was tested by variance  $S$  test, and the difference between multiple groups was used. With  $t$  test,  $P < 0.05$  is considered to have a significant statistical difference and  $P < 0.01$  is considered to have an extremely significant statistical difference. The formulas involved are

$$\sigma = \sqrt{\frac{1}{n} \sum_{i=1}^n (x_i - \mu)^2},$$

$$s^2 = \frac{(M_1 - x_1)^2 + (M_2 - x_2)^2 + (M_3 - x_3)^2 + \dots + (M_n - x_n)^2}{n},$$

$$t = \frac{\overline{X_1} - \overline{X_2}}{\sqrt{(\sigma_{x_1}^2 + \sigma_{x_2}^2 - 2\gamma\sigma_{x_1}\sigma_{x_2})/(n-1)}} \quad (1)$$

## 4. Analysis of the Experimental Results Based on the Effect of Nanomaterials in Different Strength Sports Equipment on the Body Composition of Patients with Dyslipidemia

In the third section of the article, we selected 200 subjects with dyslipidemia symptoms to participate in the running and spinning training of this experiment by means of interviews and questionnaire surveys. In this section, we will conduct specific experimental results, analysis, and discussion.

**4.1. Changes in Body Mass Index and Waist and Hip Circumference of Patients with Dyslipidemia before and after Exercise.** During the experiment, we separately counted the height, weight, and hip and waist circumference of all subjects before and after 12 weeks of exercise training and calculated their body mass index ( $\text{BMI} = \text{kg}/\text{m}^2$ , namely, weight/height<sup>2</sup>) and waist-to-hip ratio (waist/hip circumference), as shown in Tables 2 and 3 and Figure 1.

It can be seen from Tables 2 and 3 that the body index and waist-to-hip circumference ratio of patients with dyslipidemia before and after exercise training changed significantly, and the body weight, waist circumference, and hip circumference of the subjects in each group decreased significantly ( $P < 0.05$ ). There are significant statistical differences; between these groups, the male group's weight increased by 3.3%, waist circumference increased by 3.0%,

and waist circumference was 3.5%, which is a noticeable change between the four groups. The changes in body weight, waist circumference, and hip circumference of the women who ran the circle were 3.1%, 3.4%, and 2.9% compared to the runner group. The changes in weight and waist and hip circumference of the women's spinning group were also more obvious than those of the running group, which were 3.1%, 3.4%, and 2.9%, respectively. Overall, the changes in the spinning group were more obvious than the running group. This shows that spinning training is more intense than running training, and it has a greater impact on the body shape of patients with dyslipidemia.

According to Figure 1, there was no significant change in the body index of subjects in each group before and after exercise ( $P > 0.05$ ), and there was no significant statistical difference, while the waist-to-hip ratio of each group changed significantly, with the male spinning group and the female spinning group is the most obvious, with extremely significant statistical differences ( $P < 0.01$ ). It is once again confirmed that spinning training with a larger exercise load has a greater impact on the body shape of patients with dyslipidemia.

**4.2. Changes in Body Composition of Patients with Dyslipidemia before and after Exercise.** The changes in body composition of the subjects before and after exercise are shown in Table 4 and Figure 2.

According to Table 1 and Figure 2, it can be seen that after 12 weeks of exercise, the body components of the subjects in each group have significantly changed compared with those before exercise. The bone mineral content of the subjects increased compared with that before exercise, but the changes were more significant. There is no statistical significance if  $P > 0.05$ ; the muscle content showed an increasing trend, and the change was significant, with extremely significant statistical difference ( $P < 0.01$ ); the fat content and body fat percentage both decreased significantly, with extremely significant statistical difference ( $P < 0.01$ ). At the same time, compared with the men's running group and the women's running group, the men's spinning group and the women's spinning group had more obvious changes in body components ( $P < 0.05$ ), and the increase in bone mineral and muscle content was more obvious, while the fat content and the percentage of physique decreased more significantly.

**4.3. Changes in Blood Lipids in Patients with Dyslipidemia before and after Exercise.** One day before the experiment and one day after the end of the experiment, we took the venous blood of all subjects for the detection of TG, HDL-C, LDL-C, and CHOL. Now the detection results of various blood lipids are plotted as shown in Figure 3.

It can be seen from Figure 3 that after the end of the 12-week exercise training, TG and CHOL in the men's running group decreased but there was no statistical difference ( $P < 0.01$ ); HDL-C increased significantly ( $P < 0.05$ ); LDL-C showed an upward trend but not significant ( $P > 0.05$ ); TG in the male spinning group has a

TABLE 2: Changes in body index of patients with dyslipidemia before and after exercise.

Group	Height (m <sup>2</sup> )		Weight (kg)		BMI (kg/m <sup>2</sup> )	
	Before exercise	After exercise	Before exercise	After exercise	Before exercise	After exercise
Men's running group	1.70 ± 0.15	1.70 ± 0.15	75.2 ± 8.3	72.4 ± 7.32	25.02 ± 3.18	24.88 ± 3.30
Men's spinning group	1.69 ± 0.25	1.69 ± 0.25	79.2 ± 7.8	75.4 ± 8.14	25.75 ± 3.45	25.53 ± 3.43
Women's running group	1.55 ± 0.27	1.55 ± 0.27	63.2 ± 10.3	59.4 ± 6.42	24.37 ± 4.86	24.19 ± 4.25
Women's spinning group	1.52 ± 0.20	1.52 ± 0.20	66.4 ± 9.7	62.12 ± 5.31	24.28 ± 3.64	24.07 ± 3.16

TABLE 3: Changes in waist-to-hip ratio in patients with dyslipidemia before and after exercise.

Group	Waist circumference (cm)		Hip circumference (cm)		Waist-to-hip ratio	
	Before exercise	After exercise	Before exercise	After exercise	Before exercise	After exercise
Men's running group	86.56 ± 9.45	83.74 ± 9.25	97.23 ± 8.55	94.39 ± 7.51	0.83 ± 0.46	0.83 ± 0.14
Men's spinning group	88.73 ± 10.43	84.33 ± 10.71	97.52 ± 5.81	93.22 ± 5.41	0.88 ± 0.14	0.86 ± 0.09
Women's running group	84.76 ± 11.27	81.24 ± 9.17	99.45 ± 4.31	96.44 ± 4.13	0.89 ± 0.04	0.88 ± 0.06
Women's spinning group	85.14 ± 7.29	81.27 ± 7.36	98.24 ± 7.70	94.17 ± 5.24	0.86 ± 0.09	0.84 ± 0.07

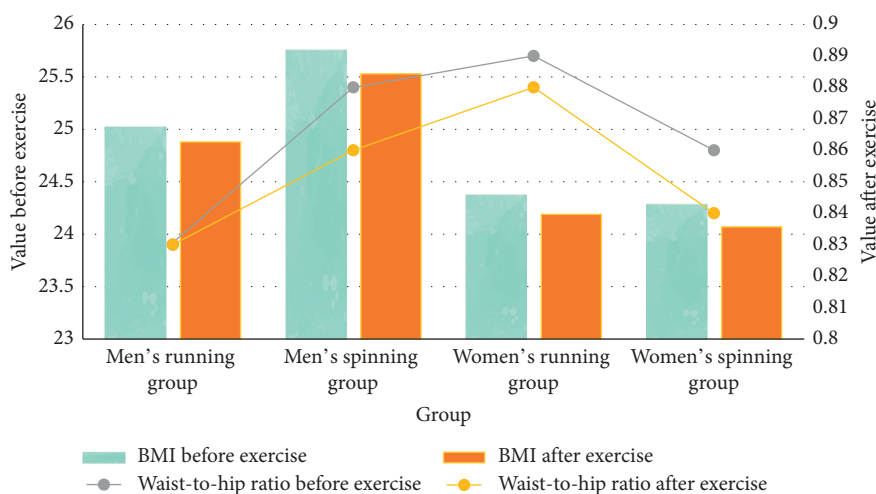


FIGURE 1: Comparison of BMI and waist-to-hip ratio of patients with dyslipidemia before and after exercise.

TABLE 4: Changes in body composition of patients with dyslipidemia before and after exercise.

Group	Bone mineral content (kg)		Muscle weight (kg)		Fat weight (kg)		Body fat percentage (%)	
	Before exercise	After exercise	Before exercise	After exercise	Before exercise	After exercise	Before exercise	After exercise
Men's running group	2.95 ± 3.72	3.55 ± 4.32	40.55 ± 9.70	45.24 ± 9.03	22.23 ± 4.75	18.01 ± 7.21	33.12 ± 5.40	30.46 ± 5.14
Men's spinning group	3.05 ± 3.14	3.94 ± 3.42	42.43 ± 6.45	48.33 ± 5.71	23.72 ± 5.41	17.73 ± 4.34	34.48 ± 6.14	29.56 ± 5.34
Women's running group	2.94 ± 3.71	3.65 ± 5.74	38.46 ± 6.27	43.24 ± 6.17	21.47 ± 4.01	17.53 ± 4.13	32.15 ± 5.43	29.36 ± 5.12
Women's spinning group	2.95 ± 3.92	3.98 ± 3.06	39.24 ± 7.38	45.02 ± 7.24	21.74 ± 6.81	16.86 ± 6.34	31.46 ± 4.76	26.55 ± 4.17

downward trend but not obvious ( $P > 0.05$ ); and HDL-C is significantly increased ( $P < 0.05$ ). TG and CHOL in the female running group have a downward trend ( $P > 0.05$ ), HDL-C increased significantly ( $P < 0.05$ ), and LDL-C decreased significantly ( $P < 0.05$ ). TG and CHOL in the female spinning group had a downward trend ( $P > 0.05$ ),

HDL-C increased significantly ( $P < 0.01$ ), and LDL-C decreased significantly ( $P < 0.05$ ). In short, there are significant statistical differences in blood lipids between the women's running group and the spinning group ( $P < 0.05$ ) and the men's running group and the spinning group have significant differences in TG, HDL-C, and

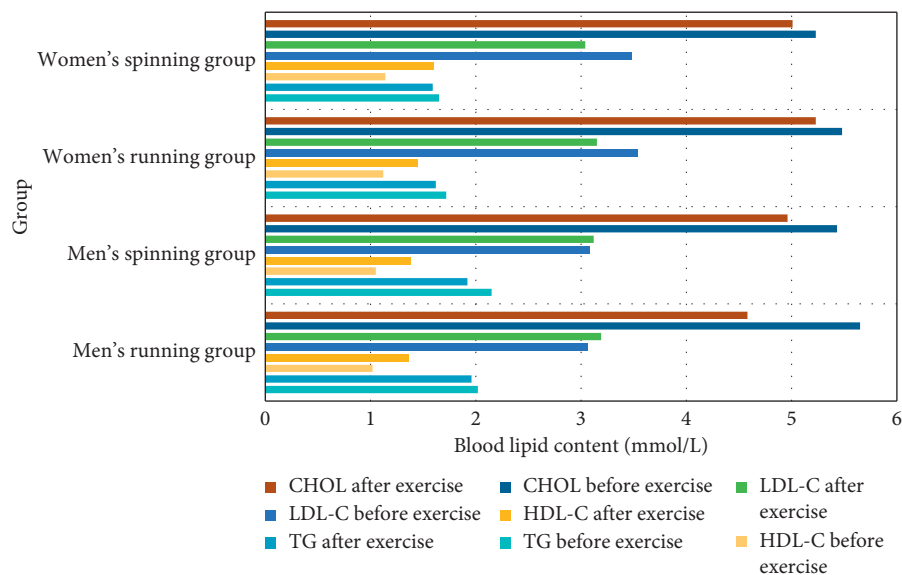


FIGURE 2: Changes in body composition of patients with dyslipidemia before and after exercise.

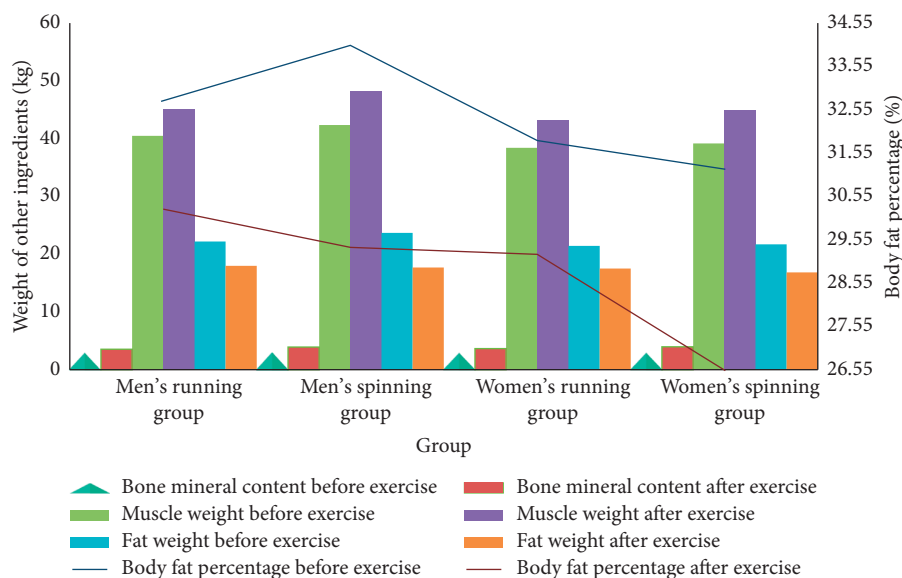


FIGURE 3: Changes in blood lipids in patients with dyslipidemia before and after exercise.

CHOL. This shows that exercise training has a greater impact on the changes in blood lipids in patients with dyslipidemia, and the changes in the spinning group are more obvious than those in the running group, indicating that the overall effect of spinning on blood lipids is greater than running.

**4.4. Changes in Body Comfort of Patients with Dyslipidemia before and after Exercise.** Research has found that nano-materials have some very special properties, which make it possible for them to have a certain negative impact on the environment and organisms due to biological effects, thereby affecting human health. In order to explore whether the 12-week exercise training caused the exercise bike and treadmill to have an impact on the physical comfort of the

subjects, two years after the end of the experiment, we conducted a return visit to all the subjects again and investigated them within 2 years. Due to the fact that some subjects have moved out of the original community or other factors during the period, we finally got 145 valid data. Through the investigation, it was found that the physical characteristics of the subjects after the end of the experiment were generally as follows: uncomfortable throat, frequent coughing; lung lesions, mild pneumonia symptoms; no obvious symptoms, but occasional physical discomfort; and nothing variety. The specific statistical results are shown in Figure 4.

It can be seen from Figure 4 that most of the 145 subjects who returned to the interview indicated that their physical comfort has changed after the exercise training. 69 indicated

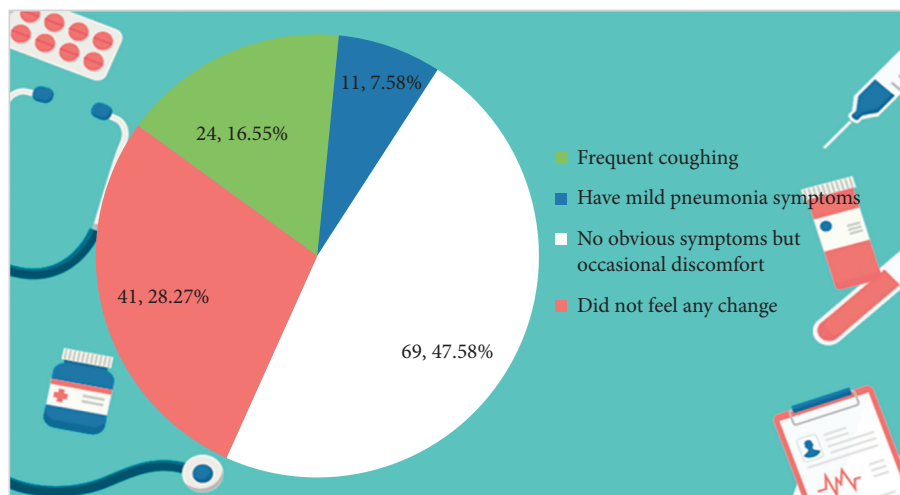


FIGURE 4: Changes in body comfort of patients with dyslipidemia before and after exercise.

that although the body had no obvious symptoms, they often experienced physical discomfort, accounting for 47.58%; 24 people said they had frequent coughing, accounting for 16.55%; 11 people said they had mild pneumonia symptoms during the period, accounting for 7.58%; and the remaining 41 people said they had not felt any changes in their body, accounting for 28.27%. Nearly 70% of the subjects indicated that their bodies had adverse reactions after the end of the experiment. This shows that sports equipment made of nanomaterials can cause some harm to the human body to a certain extent. The cause of the disease is explained in this article: fitness during exercise, nanoparticles in sports equipment may enter the human body through human breathing and skin contact and accumulate and transfer to the body to produce biological effects. In the long run, it will be harmful to human cells, lungs, liver, kidney, and brain tissue influences.

To sum up, for patients with dyslipidemia, exercise can change their body composition and shape, help them effectively promote the metabolism of blood lipids in the body, and thus benefit their recovery. But nowadays, many sports and fitness equipment are added with nanomaterials, which are easy to have an adverse effect on the human body. Patients with dyslipidemia suffer from diseases and their immunity is reduced, so they are more vulnerable to injury. Therefore, this article believes that patients with dyslipidemia can take outdoor exercises to achieve the purpose of exercise, such as elderly exercises, Tai Chi, square dancing, or slow walking and jogging.

## 5. Conclusions

Since the reform and opening up, Chinese economy has developed rapidly and the people's living standards have improved significantly. This has been accompanied by changes in the dietary structure and eating habits of the residents. The days of eating good food only during the Chinese New Year are gone. However, long-term rich and greasy eating habits have disrupted the balance of

lipoproteins in many people, abnormally elevated blood lipid levels in the body, and various diseases caused by abnormal blood lipids also pose a major threat to human health. With the acceleration of aging, the prevalence of dyslipidemia among middle-aged and elderly people is getting higher and higher.

Studies have shown that exercise can change the shape of the body and is aimed at effectively stimulating blood lipid metabolism in the body. For middle-aged people and older with dyslipidemia, moderate exercise can help get rid of the dyslipidemia. In today's society, people often use sports equipment to achieve better sports results. As technology advances, more sports devices are converted into nanoparticles to optimize performance. Nanotechnology is a form of high technology with special properties that can biologically affect the molecular structure of sports equipment, possibly adversely affecting the environment and human body.

This study found through experiments that both spinning and running training for a period of time can change the body composition of patients with dyslipidemia, improve their blood lipid content, reduce body fat percentage, and increase muscle content; at the same time, the effect of spinning exercise on changes in body composition was most obvious. However, in the course of the experiment, we also found that the addition of nanomaterials to sports equipment caused a negative impact on the body of patients with dyslipidemia. Some subjects experienced frequent coughing, and mild pneumonia. Two years after the experiment, the body felt unwell and other symptoms. Therefore, this study suggests that middle-aged and elderly patients with dyslipidemia should choose outdoor exercise as the main exercise method. Exercise methods such as elderly exercises, Tai Chi, slow walking, and jogging are all good choices.

## Data Availability

No data were used to support this study.

## Conflicts of Interest

The authors declare that there are no conflicts of interest regarding the publication of this paper.

## References

- [1] E. Román, C. García-Galcerán, T. Torrades et al., "Effects of an exercise programme on functional capacity, body composition and risk of falls in patients with cirrhosis: a randomized clinical trial," *PLoS One*, vol. 11, no. 3, Article ID e0151652, 2016.
- [2] H.-T. Chen, Y.-C. Chung, Y.-J. Chen, S.-Y. Ho, and H.-J. Wu, "Effects of different types of exercise on body composition, muscle strength and IGF-1 in the elderly with sarcopenic obesity," *Journal of the American Geriatrics Society*, vol. 65, no. 4, pp. 827–832, 2017.
- [3] X. Guo, "Application of bio-engineering plastics in sports equipment," *Plastics Industry*, vol. 44, no. 9, pp. 100–102, 2016.
- [4] G. Zhang, "Research on the application of carbon fiber reinforced plastics in sports equipment," *Plastics Industry*, vol. 47, no. 6, pp. 166–169, 2019.
- [5] U. Geissler, S. Thomas, M. Schneider-Ramelow, B. Mukhopadhyay, and K.-D. Lang, "Aluminum-scandium: a material for semiconductor packaging," *Journal of Electronic Materials*, vol. 45, no. 10, pp. 5456–5467, 2016.
- [6] C. H. Lee, B. Tiwari, D. Zhang, and Y. K. Yap, "Water purification: oil-water separation by nanotechnology and environmental concerns," *Environmental Science: Nano*, vol. 4, no. 3, pp. 514–525, 2017.
- [7] J. D. Benck, T. R. Hellstern, J. Kibsgaard, P. Chakthranont, and T. F. Jaramillo, "Catalyzing the hydrogen evolution reaction (her) with molybdenum sulfide nanomaterials," *ACS Catalysis*, vol. 4, no. 11, pp. 3957–3971, 2016.
- [8] A. Akbarzadeh, M. Mohammadhosseini, A. J. N. Abadi et al., "Nano-materials toxin contamination in laboratories and potential harmful effects of their products: a review," *Toxin Reviews*, vol. 35, no. 3-4, pp. 1–7, 2016.
- [9] J. H. Shin and Y. Lim, "Brand globalization and brand equity promotion of sporting goods with nanotechnology," *International Journal of Applied Engineering Research*, vol. 11, no. 18, pp. 9488–9490, 2016.
- [10] F. Piccinno, R. Hischier, A. Saba, D. Mitrano, S. Seeger, and C. Som, "Multi-perspective application selection: a method to identify sustainable applications for new materials using the example of cellulose nanofiber reinforced composites," *Journal of Cleaner Production*, vol. 112, no. 1, pp. 1199–1210, 2016.
- [11] Y. Shi and B. Zhang, "Correction: recent advances in transition metal phosphide nanomaterials: synthesis and applications in hydrogen evolution reaction," *Chemical Society Reviews*, vol. 45, no. 6, p. 1781, 2016.
- [12] L. Ren, P. Lu, M. Wu et al., "Application progress of nanocellulose in gas barrier packaging materials," *Packaging Engineering*, vol. 40, no. 7, pp. 51–59, 2019.
- [13] X. Wang, X. Liu, and C. Li, "The effect of preoperative body composition and nutritional status measurements on clinical outcomes for patients with gastrointestinal cancer," *Parenteral and Enteral Nutrition*, vol. 24, no. 6, pp. 377–380, 2017.
- [14] C. D. Liao, J. Y. Tsauo, L. F. Lin et al., "Effects of elastic resistance exercise on body composition and physical capacity in older women with sarcopenic obesity: a consort-compliant prospective randomized controlled trial," *Medicine*, vol. 96, no. 23, Article ID e7115, 2017.
- [15] S. Kristin, H. J. Herrmann, S. Raphaela et al., "Effects of whole-body electromyostimulation combined with individualized nutritional support on body composition in patients with advanced cancer: a controlled pilot trial," *BMC Cancer*, vol. 18, no. 1, p. 886, 2018.
- [16] J. P. Lomenick, M. S. Buchowski, and A. H. Shoemaker, "A 52-week pilot study of the effects of exenatide on body weight in patients with hypothalamic obesity," *Obesity*, vol. 24, no. 6, pp. 1222–1225, 2016.
- [17] Y. Chen, Y. Wang, C. Jiang, X. Ziong, and Z. Liu, "Effect of enteral and parenteral nutrition on body composition and disease activity in patients with severe crohn's disease," *Chinese Journal of Gastroenterology*, vol. 22, no. 11, pp. 662–665, 2017.
- [18] M. J. Chapman, R. P. Narayanan, A. Cross, R. Moots, J. Wilding, and N. Goodson, "SAT0209 observational study on the effects of il-6 inhibitor therapy on myostatin in patients with rheumatoid arthritis," *Annals of the Rheumatic Diseases*, vol. 76, no. 2, p. 852, 2017.
- [19] N. Konijn, L. V. Tuyl, B. Dijkstra, M. Van Der Schueren, and W. Lems, "FRI0542 bioelectrical impedance analysis is not a valid method for the assessment of body composition in patients with rheumatoid arthritis," *Annals of the Rheumatic Diseases*, vol. 75, no. 2, 2016.
- [20] Y. Zhou, P. Höglund, and N. Clyne, "Comparison of dexa and bioimpedance for body composition measurements in non-dialysis patients with CKD," *Journal of Renal Nutrition*, vol. 29, no. 1, pp. 33–38, 2019.
- [21] K. Bhattacharya, S. P. Mukherjee, A. Gallud et al., "Biological interactions of carbon-based nanomaterials: from coronation to degradation," *Nanomedicine: Nanotechnology, Biology and Medicine*, vol. 12, no. 2, pp. 333–351, 2016.
- [22] T. Aoyama, Y. Maezawa, T. Yoshikawa et al., "Comparison of weight and body composition after gastrectomy between elderly and non-elderly patients with gastric cancer," *In Vivo*, vol. 33, no. 1, pp. 221–227, 2019.
- [23] H. Irisawa and T. Mizushima, "Correlation of body composition and nutritional status with functional recovery in stroke rehabilitation patients," *Nutrients*, vol. 12, no. 7, p. 1923, 2020.
- [24] M. Braga, "Impact of body composition on outcome in GI cancer patients (see CD-ROM for details)," *Journal of Cancer Metabolism and Nutrition*, vol. 6, no. 2, p. 199, 2019.
- [25] N. C. Salvoza, D. C. Klinzing, J. Gopez-Cervantes, and M. O. Baclig, "Association of circulating serum miR-34a and miR-122 with dyslipidemia among patients with non-alcoholic fatty liver disease," *PLoS One*, vol. 11, no. 4, Article ID e0153497, 2016.

## Research Article

# Prevention and Control Technology for Harmful Toxic Gas Intrusion in High-Fire-Hazard-Risk Areas of Close-Distance Coal Seams

Wei Wang <sup>1,2,3</sup> and Yuntao Liang<sup>2,3</sup>

<sup>1</sup>Graduate School of China Coal Research Institute, Beijing 100013, China

<sup>2</sup>State Key Laboratory of Coal Mine Safety Technology, Fushun 113122, China

<sup>3</sup>CCTEG Shenyang Research Institute, Fushun 113122, China

Correspondence should be addressed to Wei Wang; wangwei@syccri.com

Received 14 August 2020; Revised 14 September 2020; Accepted 10 October 2020; Published 29 October 2020

Academic Editor: Tifeng Jiao

Copyright © 2020 Wei Wang and Yuntao Liang. This is an open access article distributed under the Creative Commons Attribution License, which permits unrestricted use, distribution, and reproduction in any medium, provided the original work is properly cited.

Fire hazard-risk area in small coal pits can be found in the southern part of the Shigetai Coal Mine, a close-distance coal seam mining sector in the Shendong mining area, which is susceptible to the risk of harmful toxic gas intrusion, seriously threatening the safety of mining around the working surface. Aiming at this problem, a numerical model representing the mining activity on the close-distance coal seams was established to simulate the movement pattern of overlying strata and the development process of fractures based on the horizontal stress “normalization” technology. Also, the principal air-leak passageways were detected with the SF<sub>6</sub> tracer analysis. On this basis, the influencing pattern of harmful toxic gas intruding into the working surface can be comprehensively analyzed, providing a basis for effectively preventing and controlling gas intrusion disasters. The research findings show that, after a lower coal seam has been mined, the caving zone ranges from 73 m to 94 m in height, and the fractured zone tends to develop all the way to the surface. Furthermore, shear fractures are the major passageways for air leakage, and the occurrence of gas intrusion disasters is basically taking place at the same time frame as the occurrence of roof weighting. Meanwhile, the harmful toxic gas intrudes the working surface through the fractures on the security coal pillars and shear fractures on the overlying strata. To prevent intrusion disasters from occurring, the applications of inorganic foaming and curing materials for filling were studied in combination with the actual engineering conditions. The construction grounds in sections where the fire hazard-risk area in small coal pits have not been stripped were drilled, and filling materials were poured into the goaf to create an isolation belt. As can be observed from the applied areas, constructing isolation belts to block the major air-leak passageways can effectively prevent the harmful toxic gases from intruding into the working surface, ensuring the safety of mining on the working surface.

## 1. Introduction

In recent years, the distribution of coal resource production capacity in China is gradually converging towards the advantaged regions, where the coal resource is naturally abundant, and the market competitiveness is high. As a result, the locus of production and development focus has also been shifting westward [1]. Close-distance coal seam mining on shallow burial depth is a common place in western China. For instance, there are 9 primary minable

seams in the Shendong Mine, which lies about 70 m below the average surface. To be specific, the distance separating upper coal seam 12# on the upper group and coal seam 52# on the lower group is merely 170 m [2]. The coating layer is primarily made of quaternary thick alluvium and Cretaceous-Jurassic bedrock. With the completion of the exploitation of the primary mineable coal seams in the upper group, the mining activities in many of the mining sectors in the Shendong Mine are now being successively shifted into the mining sectors of the primary mineable coal seams in the

lower group [3, 4]. The resulting coexistence of surface air leakage, interlayer air leakage, and air leakage in this layer has greatly increased the probability of spontaneous combustion by the residual coal in the goafs. A large number of small unwarranted pits can be found around parts of the mines in the western coal region; some are adjacent to or overlapping with larger mine fields, while others have seen overexploitation beyond their predetermined boundaries. The mining of small pits have also been largely disordered, causing the locations of interconnected small pit goafs to be erratically scattered. Furthermore, huge amounts of residual coals can still be found in the goafs, resulting in poor air circulation and oxidative spontaneous combustion. Signs of fire hazards have appeared in some of the small pits, while high-fire-hazard-risk areas have formed in others. As the mining continues in large mines, surface fractures become increasingly apparent, increasing the probability for small pits with low fire-hazard risks to develop into high-fire-hazard-risk areas [5, 6]. Due to the high content of harmful toxic gases inside the small pits, the concealed locations of fire source, and the continued development of fracture in the coal seam strata, the highly concentrated harmful toxic gases in the small pits may pose severe threat to the mining activities conducted in the surrounding coal seams, bringing huge challenges to the fire-hazard-prevention staff in the mine pits [7, 8].

The formation of air-leak passageways from fracture development is a necessary precondition for the intrusion of harmful gases from the high-fire-hazard-risk areas into the working surface. Concerning the study of fracture development pattern, Miao [9] believes that the evolution of fractures on overburden rock strata is dependent upon structural ruptures and motion. On this basis, Miao proposed a quantitative description method for fracture distribution in overburden rock strata, including the dynamic distribution of longitudinal fractures and the dynamic evolution of abscission crevices, as well as the distribution pattern of the "O" ring. Chen and Zhu [10] pointed out that the formation mechanism of mining ground fissures formed by deep mining and high-intensity mining in ecologically fragile mining areas in the western China may be different from those resulted from traditional mining methods. Pan et al. [11] proposed a computation method for aggregate mining thickness applicable in close-distance mining of double-layered thick coal seams, as well as the formula for calculating the development of fracture zones associated with fully mechanized caving mining, ultimately revealing the air leakage mechanism along the ground surface, upper mining area, and lower mining area. Zeng et al. [12] determined the spatial range of different fracture areas in the coal fire control body and the calculation method for its air permeability according to the movement pattern of overlying rock strata amid the mining of coal seams. Fan et al. [13] analyzed the dynamic evolution characteristics of overlying rock strata movement as well as the expansion and distribution of fractures along the horizontal and vertical directions resulting from shallow burial depth long-coal-seam-wall mining. Ma et al. [14] indicated that fractures can be formed on rock masses in a coalfield's high-fire-hazard-

risk zone through thermal rupturing, which in turn provide passageways for air and pyrolysis gases, promoting the development of high-fire-hazard-risk areas, causing the overlying rock mass to collapse due to breakage or weight loss, eventually forming a complete coupling process involving thermal rupturing, air flow, solidification, and then breaking down. When it comes to searching the air-leak passageways, the energy level measurement and tracer technique was combined to jointly detect the air leakage state [15–17].

When the effects of harmful toxic gases in the high-fire-hazard-risk area become apparent, the open-area pressure equalization technology is generally adopted for prevention and control [18–20]. Nevertheless, before adopting the pressure equalization technology to create air flow, every technical parameter related to the air flow creation through the passageways nearby the high-fire-hazard-risk area needs to be well grasped. These parameters include the distribution of wind pressure, air flux magnitude, air leakage magnitude, the wind resistance in each passageway, and the network structure of the air flow passageways. In other words, high levels of technical and management expertise by the mine owner are required since once the pressure-regulating fan stops working, secondary disasters will readily occur. And no fan with automatic pressure adjustment is presently available. Besides, an automatic pressure-regulating fan has yet to exist, which means that it is currently impossible to reactively adapt the "pressure equalization" process based on the values of all other parameters, i.e., the current pressure-regulation method is in itself a considerably "rash" approach. In general, the equal-pressure air circulation is replaced with a positive-pressure air circulation, which makes it even more difficult to conduct an early warning for spontaneous combustion in the mine goafs. Moreover, this may also cause fresh air to enter the adjacent goafs or the high-fire-hazard-risk area, the first of which may lead to spontaneous combustion, whereas the second may result in the expansion of the combustion range. Hence, the Coal Production Technology and Equipment Policy Orientation, jointly issued by four ministries, including the National Development and Reform Commission, specifies the open-area pressure equalization technology as a restricted application technology and stipulates the prohibition of carrying out pressure equalization in working surfaces with high gas content [21].

In this paper, the development pattern of fractures in the overlying strata formed by close-distance coal seam mining was numerically simulated based on the horizontal stress "normalization" technique. Meanwhile, the air-leak passageways and the corresponding leakage scope were tested using the SF<sub>6</sub> tracer gas analysis, thereby not only providing a theoretic basis for harmful toxic gas intrusion disasters in the fire-hazard-risk area in small coal pits but also guiding the prevention and control of gas intrusion disasters. By drilling a hole through the construction surface, inorganic foaming and curing filling materials can be poured into the mine goaf to block the principal air-leak passageways. When these are conducted in conjunction with removal projects for the fire-hazard-risk area in a small coal pit, the occurrence of

harmful toxic gas intrusion disasters in the process of close-distance coal seam mining can be effectively prevented and controlled, while the safety of mining activities on the working surfaces can also be simultaneously ensured.

## 2. Project Overview

The primary coal seam 31# in the Shigetai Coal Mine of Shendong mining area has a burial depth that ranges from 109 m to 132 m, with a coal seam thickness of 3.9 m and a dip angle that ranges from 1° to 3°, belonging to Class I spontaneous combustion coal seam. There were coal seam 22#, coal seam 12#, and upper coal seam 12# on the overlying strata of coal seam 31#, of which coal seam 22# has been completely exploited and now has a coal seam thickness of 4.8 m, while coal seam 12# and upper coal seam 12# have not been mined. The distance between coal seam 31# and coal seam 22# is about 38.2 m, and the distance between coal seam 22# and coal seam 12# is about 31.2 m; hence, they can be categorized as a close-distance coal seam group. Their structure is shown in Figure 1.

There are 24 small pits around the Shigetai Coal Mine, all of which are mainly distributed in the first and second panels. Most of the small pits have been closed down by 2011. The surrounding small pits are adjacent to or overlapping with larger coal mine fields. Severe occurrences of illegal mining are prevalent in the small pit, some of which have even been mined over their predetermined boundaries into the territories of the larger mine shafts. While the methods of mining selected are unclear, the signs of room-and-pillar-type mining are the most predominantly found, and the locations of the small pit passageways are unknown [22]. Due to the large numbers of disorderly mined small pits, the locations of small pit goafs are erratically scattered, most of which are interpenetrated. Huge amounts of residual coals can also be found in the goafs, where the ventilation is poor, making it easy for oxidative spontaneous combustion to happen. The environment where surface fissures and collapses are connected to abandon wellheads and passageways, forming cyclic exchanges between the underground high-temperature air flow and surface low-temperature air flow after contacting with the surface atmosphere, provides the oxygen supply required for the development of the fire-hazard-risk area in small coal pits. If it is not blocked timely, it may lead to the spread of coal fires and ignition of the surrounding coal seams, ultimately causing the massive aerial formation of fire-hazard-risk area in small coal pits.

High-concentration gases resulting from the fire could be found in primary coal seam 12# and coal seam 22# of the 7 small pits to the south of the third panel of the Shigetai Coal Mine. Its CO and C<sub>2</sub>H<sub>4</sub> volume fractions reach as high as 0.8129% and 0.0125%, respectively, indicating that the fire-hazard-risk area in small coal pits have been formed. 20 m to 30 m security coal pillars between the small pits and large mine fields are retained, but cross-boundary mining can also be found in small pits such as the Tangjiangqu mMine, Qianqu Mine, Yemaowan Mine, and Tangjiangqu 2nd Mine. Moreover, both the cross-boundary positions and the degrees

are unknown. Security coal pillars are easily deformed and broken under the action of long-term underground pressure, forming a system of interconnecting air-leak passageways between the small pit and the goaf of larger mines.

Multiple technical means, such as blocking the wellheads in the small pit, nitrogen injection, and partial stripping have been carried out successively to deal with the fire-hazard-risk area in small coal pit. However, the high-fire-hazard-risk area has not been effectively treated. When the 31201 working surface of the Shigetai Coal Mine was 75 m away from the cutting hole position, the CO volume fraction of the return air corner increased abruptly from 0.0021% to 0.0128% and remained at 0.01% to 0.0188%. The CO volume fraction of the goaf increased from 0.006% to 0.02% and remained at 0.0134% to 0.0244%. Moreover, the CO volume fraction of the overlying coal seam 22# goaf increased from 0.01% to 0.062% and remained at 0.05% to 0.112%. As the CO volume fractions have been abruptly increased at each monitoring point with a noncontinuous growth trend, and no other fire gases such as C<sub>2</sub>H<sub>4</sub> and C<sub>2</sub>H<sub>2</sub> were detected, the possibility of spontaneous combustion in the goaf was ruled out. This was deemed as the result of harmful toxic gases in the small pit flowing to a variety of monitoring points through fractures under the action of negative ventilation pressure.

## 3. Pattern of Fracture Development

*3.1. Selection of Macroparameters.* In a previous study [23], an empirical equation for macroscopic parameters of the material was established with PFC<sup>2D</sup>. A histogram with three drilling holes was formulated in line with the second panel of coal seam 31# in the Shigetai Coal Mine, as shown in Figure 2.

*3.2. Model Establishment.* According to the histogram of the Shigetai Coal Mine geological synthesis in Figure 3, the model shown in Figure 3 was established using the central symmetry model using FLAC 2D 5.0, with the length and height set to 160 m and 135 m, respectively.

The measured ground stress in the Shigetai Coal Mine is shown in Table 1.

Due to the unique industrial and mining conditions in the Shendong mining area, it is difficult to analyze the roof damage evolution process and collapse failure mechanism of the Shendong mining area using the traditional mining area theory. Based on this, by referring to the horizontal stress “normalization technology” established by Jan (2016) [24], normalization was conducted on the horizontal stress in line with the elastic property of the overlying strata as follows:

$$\sigma_{NL} = \frac{E_N}{E_M[(\sigma_{ML} - \sigma_V)\nu/(1 - \nu)]} + \frac{\sigma_V\nu}{(1 - \nu)}, \quad (1)$$

where  $\sigma_{NL}$  is the normalised horizontal stress, in MPa;  $\sigma_{ML}$  is the horizontal stress of the measurement layer, in MPa;  $\sigma_V$  is the vertical stress of the measurement layer, in MPa;  $E_N$  is the normalised Young's modulus, in MPa;  $E_M$  is Young's modulus of the measurement layer, in MPa; and  $\nu$  is Poisson's ratio.

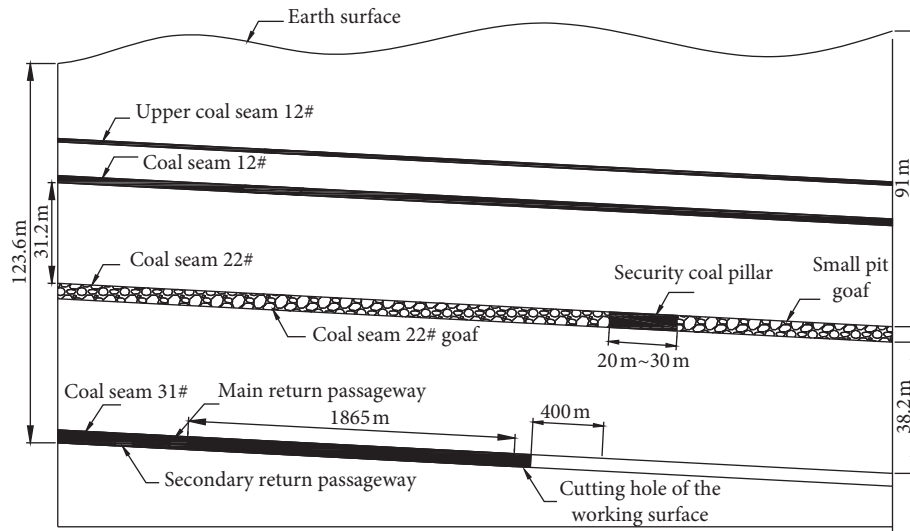


FIGURE 1: Relationship between coal seam 31# and the overlying coal seam.

Seam no	Lithology	Seam thickness (m)	Burial depth (m)	Columnnar	Poisson's ratio	Elastic modulus	Tesnsile strength (MPa)	Cohesion (MPa)	Internal friction angle (°)
27	Aeolian sand	5.14	5.14						
26	Sandy mudstone	19.15	24.29		0.17	7.4	1.6	7.6	38.8
25	Medium sandstone	9.62	33.91		0.18	15.4	2.58	4.35	35.3
24	Coal seam 11#	0.6	34.51		0.27	6.9	1.33	2.42	42.6
23	Sandy mudstone	0.4	34.91		0.17	7.4	1.6	7.6	38.8
22	Fine sandstone	7.38	42.29		0.14	17.4	3.06	5.77	38.8
21	Siltstone	0.3	42.59		0.23	9.7	4.66	11.05	36
20	Upper coal seam 12#	1.52	44.11		0.27	6.9	1.33	2.42	42.6
19	Fine sandstone	2.1	46.21		0.14	17.4	3.06	5.77	38.8
18	Siltstone	7.43	53.64		0.23	9.7	4.66	11.05	36
17	Sandy mudstone	1.59	55.23		0.17	7.4	1.6	7.6	38.8
16	Coal seam 12#	2.26	57.49		0.27	6.9	1.33	2.42	42.6
15	Sandy mudstone	0.9	58.39		0.17	7.4	1.6	7.6	38.8
14	Siltstone	4.92	63.31		0.23	9.7	4.66	11.05	36
13	Fine sandstone	7.49	70.8		0.14	17.4	3.06	5.77	38.8
12	Medium sandstone	2.2	73		0.18	15.4	2.58	4.35	35.3
11	Siltstone	4.04	77.04		0.23	9.7	4.66	11.05	36
10	Medium sandstone	2.8	79.84		0.18	15.4	2.58	4.35	35.3
9	Upper coal seam 22#	3.71	83.55		0.27	6.9	1.33	2.42	42.6
8	Mudstone	1.43	84.98		0.15	7.2	1.36	6.32	39.4
7	Siltstone	15.43	100.41		0.23	9.7	4.66	11.05	36
6	Fine sandstone	6.94	107.35		0.14	17.4	3.06	5.77	38.8
5	Siltstone	5.33	112.68		0.23	9.7	4.66	11.05	36
4	Fine sandstone	6.48	119.16		0.14	17.4	3.06	5.77	38.8
3	Siltstone	1.05	120.21		0.23	9.7	4.66	11.05	36
2	Upper coal seam 31#	3.8	124.01		0.27	6.9	1.33	2.42	42.6
1	Siltstone	2.8	126.81		0.23	9.7	4.66	11.05	36

FIGURE 2: Macrophysical and mechanical properties of the coal seam and strata.

The top of the model was the surface, which was set as a free boundary, while the bottom was set as a fixed constrained boundary. A bonded face was set between the fracture zone and the caving zone inside the model, and a structural surface was set between the fractured zone and the caving zone. The cutting hole and its overlying strata were set as the vertical structural surface. Moreover, horizontal loads

were applied horizontally in the model based on the measured stress and the calculated equivalent stress.

**3.3. Result Analysis.** When the working surface of coal seam 31# in the Shigetai Coal Mine has been mined to a position 92 m from the cutting hole, the displacement vector and

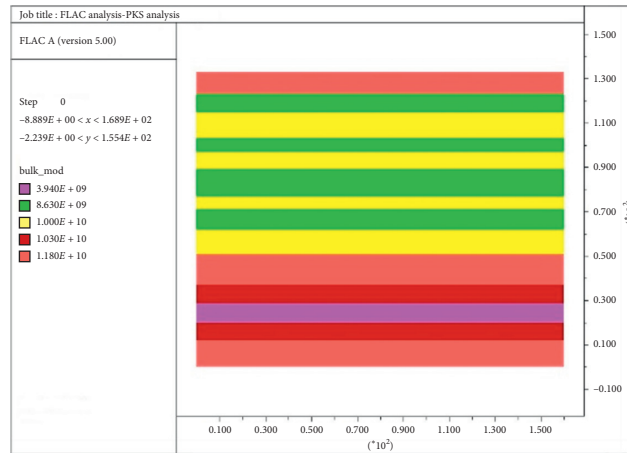


FIGURE 3: Numerical simulation model.

TABLE 1: Actual measured ground stress.

Measured location	Stress category	Principal stress value (MPa)	Azimuth (°)	Dip angle (°)
31201 air-return laneway	Maximum principal stress $\sigma_1$	6.57	264.7	2.9
	Intermediate principal stress $\sigma_2$	5.76	37.0	85.7
	Minimum principal stress $\sigma_3$	5.15	174.5	3.1

plastic deformation of the overburden strata can be shown in Figure 4. The distance and strength analysis results of the first roof weighting and periodic weighting are shown in Figure 5. The process of fracture development in the overlying rock layer is shown in Figure 6.

The immediate roof was caved immediately after the mining of the working surface. The caving zone ranges from 73 m to 94 m in height, and the fractured zone developed all the way to the surface. Subsequent roof weighting occurred thrice at the weighting interval of about 10 m after the roof weighting position reached 67 m away from the cutting hole position. The maximum strength was obtained in the first weighting. Apparent stratification could be witnessed in the early stage of fracture formation. Gradually, shear fractures were formed around the coal pillar with the development of the working surface, whereas stratified fractures away from the working surface were compacted. Consequently, shear fractures have transformed into the major air-leak passageways.

According to [25], the coalfield high-fire-hazard-risk area comprises three basic types (structural fractures, mining collapse fractures, and combustion fractures) and five composite types. These fractures connected oxygen with underground coal seams or the residual coal in goafs, forming a primary passageway consisting of air-leaked oxygen supply, heat dissipation, smoke exhaust, and venting circulation. Meanwhile, a point  $\rightarrow$  line  $\rightarrow$  area expansion evolution of the coalfield fire also took place. Although the 20 m to 30 m security coal pillars are retained between the fire-hazard-risk area in small coal pit and the Shigetai Coal Mine, they still have the abovementioned fractures, and some of which have suffered from the cross-boundary mining. Harmful toxic gases in the fire-hazard-risk area in

small coal pits inevitably came into contact with the overlying goaf of coal seam 31#. Harmful toxic gases then permeate into the working surface through fractures on the security coal pillars and shear fractures of coal seam 31#'s overlying strata under the joint effect of negative air circulation and atmospheric pressure. The first weighting of the working surface occurred 67 m away from the cutting hole. CO gas anomaly was detected at a 75 m mark along the progression of the working surface. The consistent time frames proved the validity of the model.

#### 4. The Search for Air-Leak Passageways

SF<sub>6</sub> tracer gas analysis was employed to determine the interconnections and influencing range of the fire-hazard-risk area in small coal pit and the working surface, so as to verify the presence of air-leak passageways.

*4.1. Determination of Air-Leaking Source.* Concealed combustion sources in parts of the small pits in the south of the Shigetai Mine Coal were detected using the instantaneous (differential) radon measurement method [26]. Collected gases were tested directly with the alpha particle detector in the RAD7 professional electronic radon meter. Meanwhile, radon measurement data were also processed, as shown in Figure 7.

The temperature anomaly area was about 5000 m<sup>2</sup> and was located to the east of the former Qianqiu coal mine office area, belonging to the joint airway overlying area #24 of the 31206 main and auxiliary transport passageway in the Shigetai Coal Mine. The location was selected as the air-leak source or the area releasing SF<sub>6</sub>.

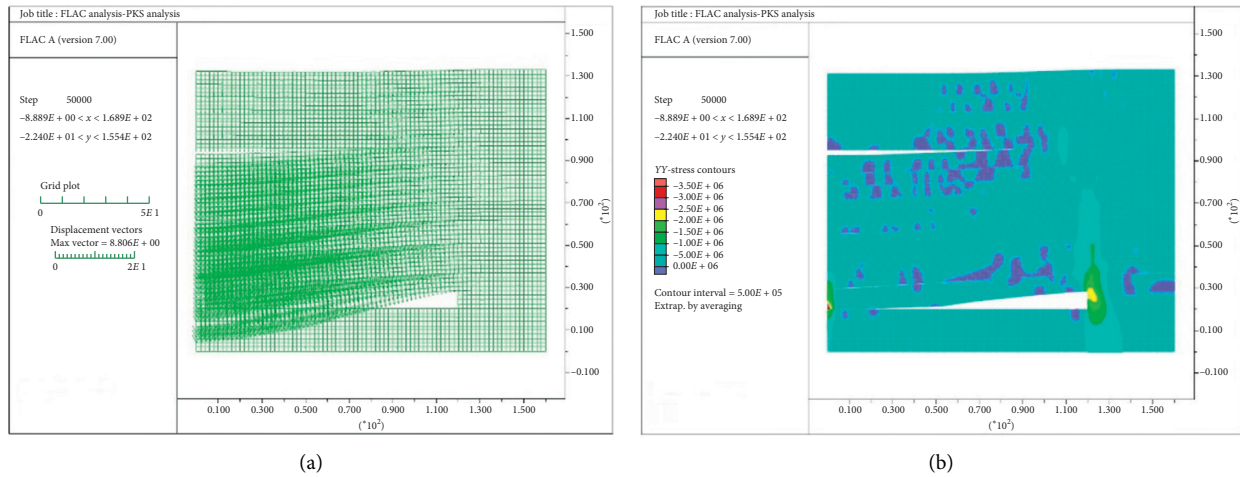


FIGURE 4: (a) Displacement vector and (b) plastic deformation of overlying strata.

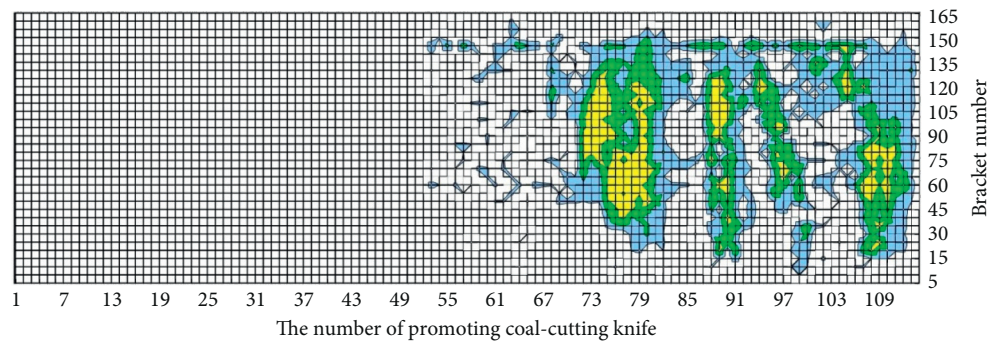


FIGURE 5: The distance and strength of first and periodic roof weighting.

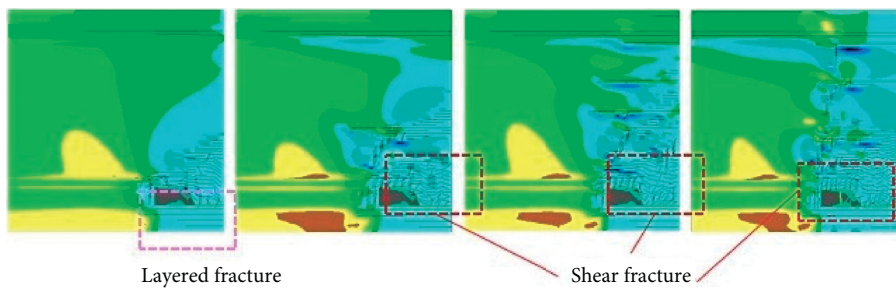


FIGURE 6: Fracture development in the overlying strata.

**4.2. Determination of Air Leakage.** SF<sub>6</sub> gas with 99.99% concentration was released all in once at the air-leak source using instantaneous release with the release rate of 2 L/min and the continuous release time of 2 hours. The 31201 return air corner, 31201 return air roadway joint roadway 26# closed observation hole, 31201 auxiliary transport roadway joint airway 34# closed observation hole, and 31202 cutting hole 2# and 5# drawing off water holes in the shunting chamber (detecting the goaf of overlying coal mine 22#) were selected as receiving locations. Gas samples were collected every 10 min to 20 min at the underground

reception site, while the testing time was decided according to the specific situation. The release time of air-leaking SF<sub>6</sub> was 12:00 at the air-leakage measurement. The underground detection lasted for 3 hours. Collected gas samples were analyzed with a gas chromatograph to determine whether the sample contained SF<sub>6</sub> gas. The test results are shown in Table 2.

According to the measurement results, air-leak passageways can be found among the fire-hazard-risk areas in a small coal pit, coal seam 22# goaf and coal seam 31# goaf. The air-leaking route stretched from the fire-hazard-risk area in

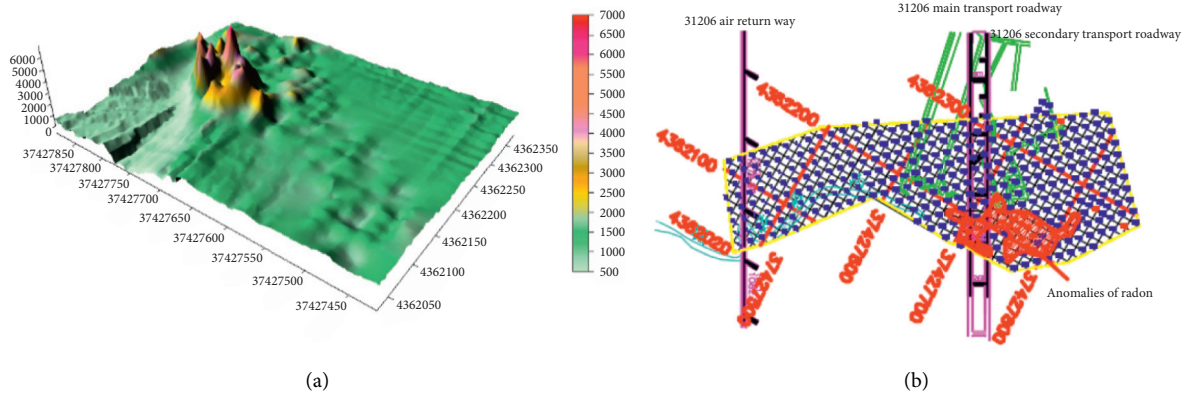


FIGURE 7: Temperature anomaly. (a) Radon surface concentration. (b) Anomalies of radon.

TABLE 2: SF<sub>6</sub> gas sample analysis results.

Sampling location	Sampling time	Volume content ( $\times 10^{-6}$ )
31202 cutting hole 2# drawing off water hole	12:30	1.2129
	12:50	1.1048
31202 cutting hole 5# drawing off water hole	12:20	1.0376
	12:40	1.3867
31201 return air roadway joint roadway 26# closed observation hole	12:50	2.8301
	13:00	1.6324
31201 auxiliary transport roadway joint airway 34# closed observation hole	12:55	1.2351
	13:10	1.0235
31201 return air corner	13:15	1.0630
	13:35	0.9562
31201 return air flow	13:40	0.1056
	14:00	0.0987

the small coal pit to the goafs of coal seam 22# and coal seam 31#, as shown in Figure 8.

## 5. Partitioning the High-Fire-Hazard-Risk Area with Inorganic Curing Materials

By analyzing the development pattern of fractures in the overlying strata on the working surface, it can be seen that fractures generated after the cessation of the working surface provide passageways for the intrusion of harmful toxic gases, which will severely threaten the safe mining of the working surface. The local government has led a local stripping fire extinguishing project for the small pit in the south of the Shigetai Coal Mine since October 2014, which is composed of Liushipan open-air stripping and Tangjiangqu 2nd Mine open-pit stripping. Specifically, the Liushipan Comprehensive Treatment Project Team stripped the Liushipan Coal Mine, Beidaqu Mine, and Shenfu Tanyaoqu Mine in the south of the Tangjiangqu ditch for fire distinguishing. And the Tangjiangqu 2nd Mine Comprehensive Management Project Team stripped the Tangjiangqu 2nd Mine in the northeast of the Tangjiangqu ditch for fire distinguishing. But the Yemaowan Mine, Tangjiangqu Mine, and Qianqu Mine in the north of the Tangjiangqu ditch (near the second panel of 31# coal seam) were not included in the stripping treatment. A technique of filling inorganic curing materials

into the drilling holes of the construction surface for fire isolation has been proposed against the area without stripping.

**5.1. Inorganic Foaming and Curing Materials.** Materials used for fire isolation should effectively block air-leak passageways with a high expansion ratio and certain strength. Based on this, cementing materials dominated by aluminosilicate were selected as main raw materials in conjunction with the accelerator and composite reinforcing agent for improving the setting speed and initial setting strength. Furthermore, the composite foaming agent was employed to increase its expansion ratio, satisfying the requirements of filling and isolating high-fire-hazard-risk areas [27].

52.5 sulfoaluminate cement was selected as main material of the cementing material. Besides, Ca(OH)<sub>2</sub> exciter and accelerator must be added due to insufficient active alkali ions. The excitation of Ca(OH)<sub>2</sub> on the activity of cementing materials provided not only (OH)<sup>-</sup> that breaks the bond of Si-O and Al-O but also Ca<sup>2+</sup> required for hydrating the cementing material to form a hard cementing material.

The reinforcing agent was mainly composed of sulfate, and Aft, or ettringite generated by SO<sub>4</sub><sup>2-</sup>, and Al<sub>2</sub>O<sub>3</sub> dissolved in the liquid phase under the action of Ca<sup>2+</sup> was the

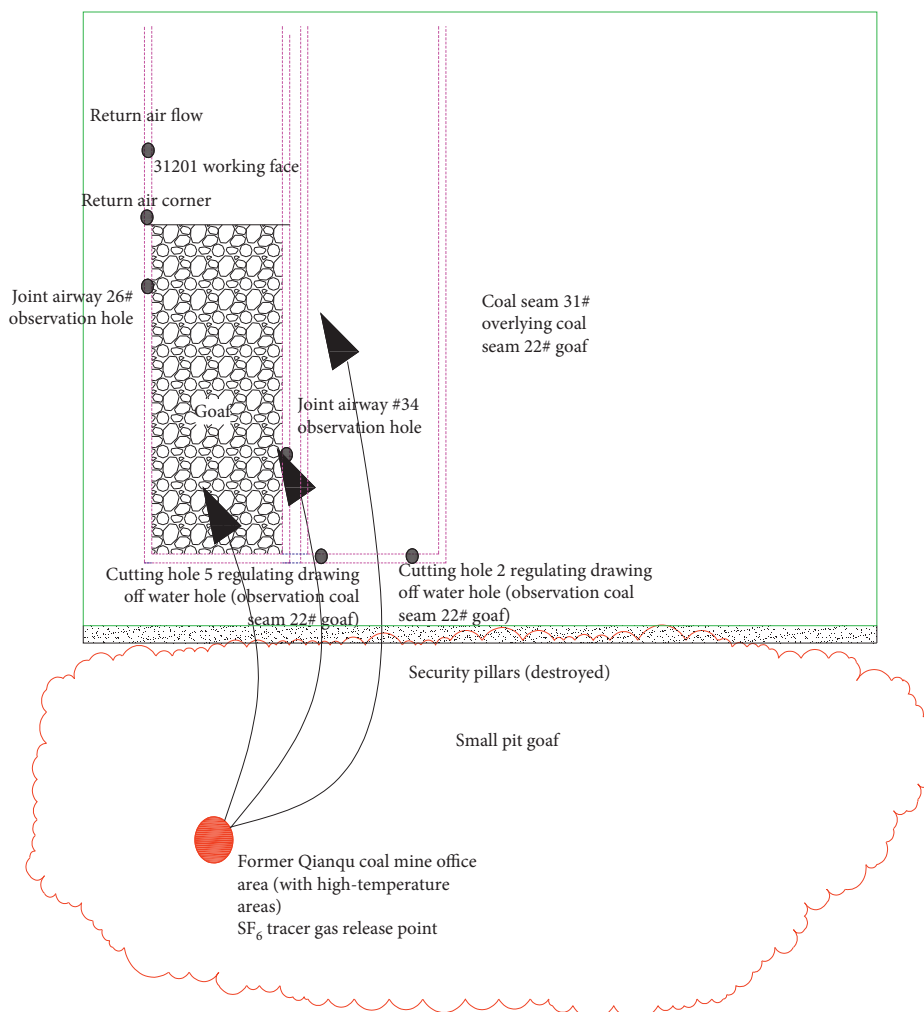


FIGURE 8: Detection of air-leaking route.

excitation of activity of the cementing material.  $\text{Na}_2\text{SO}_4$  that is more soluble in water was selected as sulfate, which can form highly dispersed  $\text{CaSO}_4$  upon the reaction with  $\text{Ca}(\text{OH})_2$ , enhancing the alkalinity of the material. Tests proved that scum could be caused when the added amount of  $\text{Na}_2\text{SO}_4$  exceeded 3%, and microcracks could be detected inside the test block, leading to the decline in strength in the later period [28]. 2% of  $\text{Na}_2\text{SO}_4$  was added in the material.

High-efficiency quick-setting agent was selected as the initial and final setting regulator of the material, so that the initial and final setting time and compressive strength of the material could be more stable. After adding different amounts of quick-setting agent, the setting time of the cured material can be adjusted from 2 minutes to 6 hours. Besides, primary liquid could maintain a high strength after foaming. 3% of accelerator was added in the material.

A variety of surfactants and foam stabilizing agents were selected and mixed as the foaming agent stock can produce foaming agent mixtures upon the mixture of water at a certain ratio. And fine foams can be formed upon mixing with the compressed air.

With cementing materials as the base materials, reinforcing agent, water-reducing agent, and quick-setting agent were added in proportion to form a powdery curing material, forming slurry liquid with the mixture of a small amount of water. Meanwhile, foams were obtained using the foaming agent. The slurry liquid was mixed with foams to form the foaming liquid and deliver to the designated site through pumps. Inorganic curing filling materials were obtained. Basic properties of the material are shown in Table 3.

The pore structure of the inorganic cured material was observed at a magnification of 60 times under an optical microscope, as shown in Figure 9.

TABLE 3: Test results of properties of inorganic cured materials.

Density ( $\text{kg/m}^3$ )	Compressive strength (MPa)	Air tightness ( $\text{m}^3/(\text{m}^2/\text{min})$ )
250	1.8	$0.85 \times 10^{-6}$

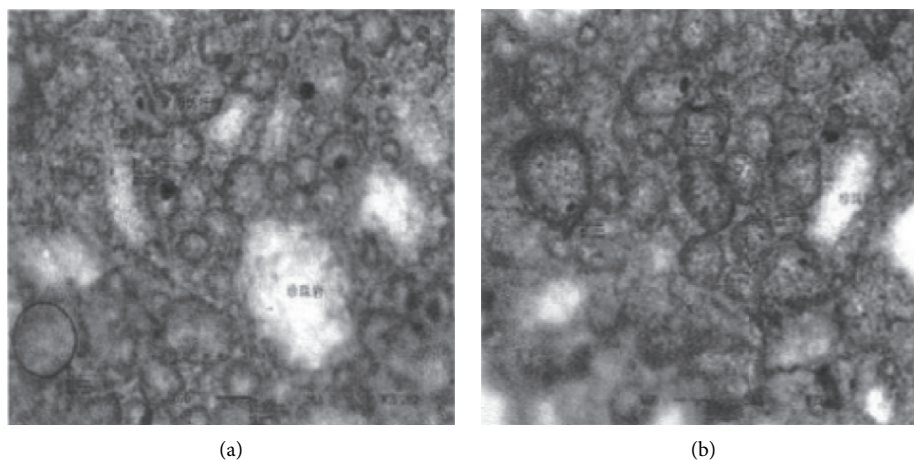


FIGURE 9: Material hole structure.

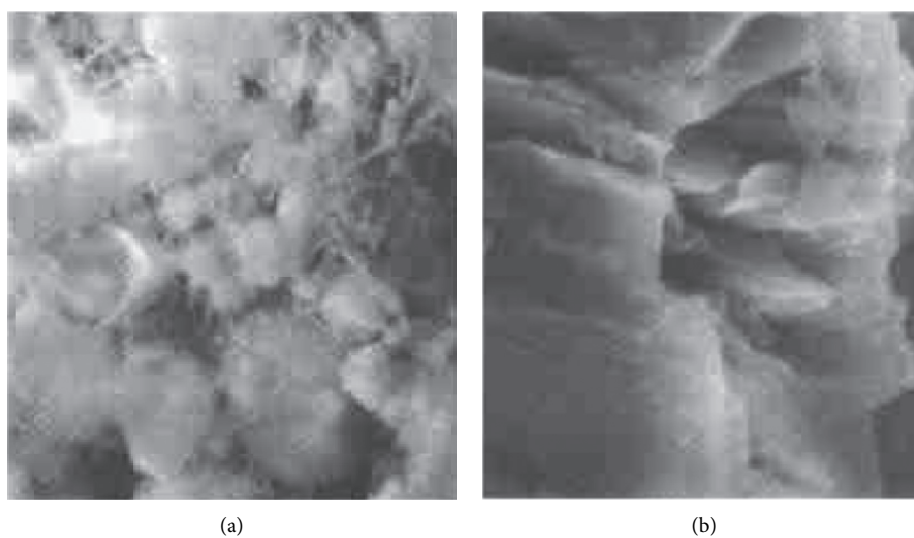


FIGURE 10: Material SEM photo. (a) Curing period: 3 days. (b) Curing period 28 days.

Pores inside the material are evenly distributed at the pore diameter below 1 mm. Most of which are closed circular holes, exerting a good effect of blocking air leakage.

Internal structures of inorganic curing materials in different curing periods were observed with the scanning electron microscope. SEM photos are shown in Figure 10.

During material molding, a large amount of ettringite crystals were formed and connected into pieces or even covered the whole test sample with the extended curing time. In this way, the compressive strength of the material was increased.

*5.2. Surface Drilling Design.* Regarding the area that is not stripping in the small pit, 22# coal goaf construction surface was drilled along the security coal pillars between the small pit and the 22# coal goaf. The final position of the drilling hole was located at 3 m in the north of the security coal pillar. Inorganic curing filling materials were poured through the surface drilling hole to build an isolation zone, so as to remove the influence of harmful toxic gas in the small pit on the safe stopping of the 31# coal second panel.

The first ground drilling hole (GL1) was arranged at 30 m away from the 220403 working surface along the roadway,



FIGURE 11: Construction of the isolation zone.

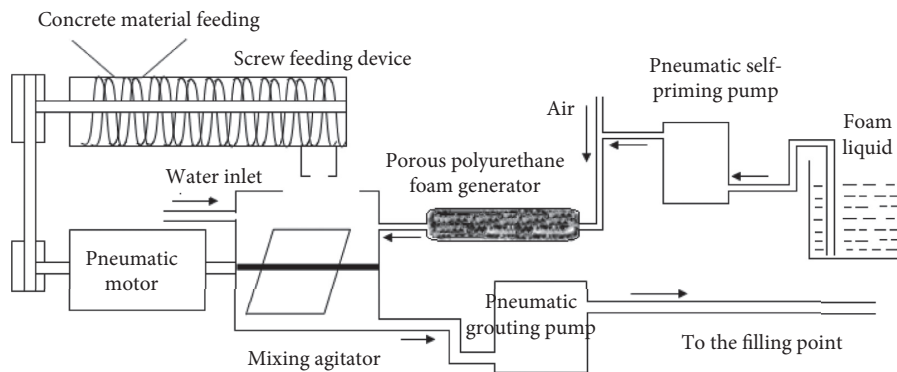


FIGURE 12: Filling and pouring process of inorganic foaming and curing.

and one ground drilling hole was constructed every 50 m along the direction of the security coal pillar. The entire isolation zone is covered from 220403 goaf to 220502 goaf, covering 31# coal seam 31201, 31202, and 31203 working surfaces. With 1100 m in total, a total of 25 grouting holes were designed, as shown in Figure 11.

**5.3. Pouring Technique and Plugging Capacity.** The compressed air was used as power to pour inorganic solidified filling materials with the pneumatic equipment. Inorganic curing filler materials were added to the feed port, and water was added to the mixer driven by the pneumatic air motor. The ratio of water volume and inorganic curing filler is 1 : 1 to 1 : 2. Besides, the foaming agent and water are mixed as foaming liquid at 1 : 30, which forms foams upon the contact of the pneumatic self-priming pump and the compressed air. And fine foams were generated through the porous polyurethane foam generator. After that, fine foams and inorganic curing fillers were transported to drilling holes in the ground, forming foaming fillers in the goaf. Ultimately, an isolation zone was constructed, as shown in Figure 12.

When the isolation zone was constructed, the SF<sub>6</sub> tracer gas analysis technology was utilized once more to detect air

leakage. The SF<sub>6</sub> release location remained the above-mentioned temperature anomaly area, and the receiving location was the return air corner of the working surface of 31# coal second panel, 31# coal goaf, and overlying 22# coal goaf. No SF<sub>6</sub> gas was detected from the collected gas samples, indicating that the 22# coal goaf was well isolated from the small pit goaf.

Under the combined effect of the stripping and isolation of the fire-hazard-risk area in a small coal pit, the remaining working surfaces (31202 to 31205 working surfaces) of the 31# coal 2nd panel of the Shigetai Coal Mine have not been affected by the harmful toxic gas in the fire-hazard-risk area in a small coal pit during the mining process, safeguarding the safe cessation of the working surface.

## 6. Conclusions

- (1) The movement rule of overlying strata and the development process of fissures are simulated numerically based on the horizontal stress "normalisation" technology. The immediate roof is caved immediately after the underlying coal seam is mined. The caving zone ranged from 73 m to 94 m in height, and the fractured zone is developed through

the surface. Apparent stratification can be witnessed in the early stage of formation. Gradually, shear fractures are formed, whereas stratified fractures are compacted. As a result, shear fractures become major air-leak passageways. The roof weighting position is 67 m away from the cutting hole position, which is nearly consistent with the time node of gas intrusion into the working surface in the fire zone.

- (2) SF<sub>6</sub> tracer gas analysis technology is used to further verify and judge the air leakage channel and the affected range. Air-leak passageways and their influencing ranges were verified with the SF<sub>6</sub> tracer analysis. The fire-hazard-risk area in small coal pit detected by the radon measurement technique is regarded as the release point. Meanwhile, the return air corner of the working surface, return air flow, goaf, and overlying coal seam goaf are considered as receiving points. SF<sub>6</sub> gases are received in all receiving points. Based on the analysis of the movement pattern of the overlying strata, harmful toxic gases can penetrate into the working surface through fractures on the security coal pillars and shear fractures of the overlying strata on the working surface under the joint effect of negative air circulation and atmospheric pressure.
- (3) An inorganic foaming and curing filling material that can effectively block the air-leak passageway and construct the isolation zone is introduced. The construction ground is drilled in the area, and inorganic foaming and curing filling materials are poured to the mine goaf for constructing an isolation belt to block principal air-leak passageways, which can effectively prevent the harmful toxic gas from intruding into the working surface, and safeguard the safe mining on the working surface.

## Data Availability

The data used to support the findings of this study are available from the corresponding author upon request.

## Conflicts of Interest

The authors declare that they have no conflicts of interest.

## Acknowledgments

The authors gratefully acknowledge the financial support from the National Key Research and Development Program (2018YFC0807900, topic 6), the CCTEG Science and Technology Innovation Fund (Grant no. 2018-2-MS016 and 2018MS015), and the Plan of Social Development and Industrialization Guidance Plan in Liaoning Province (2019JH8/10300099).

## References

- [1] Y. G. He, *China Coal Outlook 2019*, pp. 16–20, China Coal Industry Publishing House, Beijing, China, 2019.
- [2] J. R. Wang and G. W. Zhai, *Modern Coal Production Technology*, pp. 3–32, China Coal Industry Publishing House, Beijing, China, 2012.
- [3] W. Wang, “Discussion on spontaneous fire prevention and control in Shendong coal mining area,” *Safety in Coal Mines*, vol. 47, no. 1, pp. 167–169, 2016.
- [4] M. G. Yu, F. Teng, T. X. Chu, J. K. Chao, and P. Li, “Simulation study on the evolution of the overlying strata fracture development and air-leaking passage under repeated mining of shallow buried coal seams,” *Journal of Henan Polytechnic University (Natural Science)*, vol. 37, no. 1, pp. 1–7, 2018.
- [5] J. Deng, B. Li, K. Wang, and C. P. Wang, “Research status and outlook on prevention and control technology of coal fire disaster in China,” *Coal Science and Technology*, vol. 44, no. 10, pp. 1–7, 2016.
- [6] Z.-Y. Song, H.-Q. Zhu, B. Tan, H.-Y. Wang, and X.-F. Qin, “Numerical study on effects of air leakages from abandoned galleries on hill-side coal fires,” *Fire Safety Journal*, vol. 69, pp. 99–110, 2014.
- [7] Y. I. Xu, L. Y. Wang, T. X. Chu, and M. G. Yu, “Research progress on coal-fire diffusion and fracture development of coal rocks in coal-fire areas,” *Journal of Henan Polytechnic University (Natural Science)*, vol. 32, no. 6, pp. 668–672, 2013.
- [8] T. X. Chu and M. G. Yu, S. H. Q. Yang and H. L. Jia, “Air leaking induced by well-developed coal fractures and prevention of spontaneous combustion in goaf,” *Journal of Mining and Safety Engineering*, vol. 27, no. 1, pp. 87–93, 2010.
- [9] X. X. Miao, “Review of research on mechanical behaviors of mining rock mass and its related engineering technological innovation progress,” *Chinese Journal of Rock Mechanics and Engineering*, vol. 29, no. 10, pp. 1988–1998, 2010.
- [10] C. H. Chen and Q. Zhu, “Research advances in formation mechanism of ground crack due to coal mining subsidence in China,” *Journal of China Coal Society*, vol. 43, no. 3, p. 810823, 2018.
- [11] R. K. Pan, S. H. G. Cao, Y. Li, and G. D. Li, “Development of overburden fractures for shallow double thick seams mining,” *Journal of China Coal Society*, vol. 43, no. 8, pp. 2261–2268, 2018.
- [12] Q. Zeng, D. M. Wang, and Z. H. Y. Cai, “The distribution of fissures/cracks and its permeability with coal fire zones,” *Journal of China Coal Society*, vol. 35, no. 10, pp. 1670–1673, 2010.
- [13] G. W. Fan, D. S. H. Zhang, and L. Q. Ma, “Overburden movement and fracture distribution induced by longwall mining of the shallow coal seam in the Shendong coalfield,” *Journal of China University of Mining and Technology*, vol. 40, no. 2, pp. 196–201, 2011.
- [14] L. Ma, G. Liu, Y. Xiao, J. H. Lu, and Y. J. He, “Research on multi-field coupling process of coalfield fire area development and evolution,” *Science and Technology Review*, vol. 34, no. 2, pp. 190–194, 2016.
- [15] H. Y. Wang, C. H. Feng, L. Geng, B. Yu, X. L. Cui, and M. Z. H. Chen, “Study on air leakage in underground coal fire based on energy level and tracer test,” *Journal of Safety Science and Technology*, vol. 10, no. 1, pp. 118–123, 2014.
- [16] W. Jiang, “SF<sub>6</sub> tracking technology and energy level detecting combined to detect and measure ventilation leakage in complicated goaf,” *Coal Science and Technology*, vol. 31, no. 8, pp. 9–11, 2003.
- [17] B. M. Shi and X. L. Cheng, “Using potential energy measurement and tracing technique to detect air leakage in complicated gob,” *Mining Safety and Environmental Protection*, vol. 29, no. 2, pp. 14–17, 2002.

- [18] G. Wang, R. Wang, M. M. Wu, L. Xin, X. H. Zhou, and C. H. W. Liu, "Prevention and control technology of harmful gas intrusion in close-up coal seam under fire area," *Journal of China Coal Society*, vol. 42, no. 7, pp. 1765–1775, 2017.
- [19] Z. H. Y. Zheng, C. Sang, H. F. Yao, H. J. Wu, and C. H. F. Xu, Y. Q. Liu, "Study of voltage sharing fire preventing and extinguishing under fire area mining in shallow," *Coal Mining Technology*, vol. 23, no. 1, pp. 73–77, 2018.
- [20] J. G. Hao, W. Lu, and J. Xu, "Research on fire prevention technology of coal mining face in shallow depth seam under large air leakage firing zone," *Coal Science and Technology*, vol. 42, no. 3, pp. 53–56, 2014.
- [21] National development and reform commission, *Coal Production Technology and Equipment Policy Guidance*, pp. 138–146, China Coal Industry Publishing House, Beijing, China, 2014.
- [22] W. B. Zhu, J. L. Xu, L. Chen, Z. H. Li, and W. Liu, "Mechanism of disaster induced by in room-and-pillar mining dynamic instability of coal pillar group of shallow and close coal seams," *Journal of China Coal Society*, vol. 44, no. 2, pp. 358–366, 2019.
- [23] T. Wang, W. Zhou, J. Chen, X. Xiao, Y. Li, and X. Zhao, "Simulation of hydraulic fracturing using particle flow method and application in a coal mine," *International Journal of Coal Geology*, vol. 121, pp. 1–13, 2014.
- [24] N. Jan, W. J. Gale, and M. W. Fabjanczyk, "Methods of interpreting ground stress based of underground stress measurements and numerical modelling," in *Proceedings of the 2006, Coal Operators' Conference*, Wollongong, Australia, July 2006.
- [25] D. Y. Cao, X. J. Fan, C. H. Wu, and G. L. Wang, "Study on the fractures related with coalfield fire area in Wuda coalfield, Inner Mongolia," *Journal of China Coal Society*, vol. 34, no. 8, pp. 1009–1014, 2009.
- [26] Z. H. Liu and W. Wang, "Application of instantaneous measurement of radon in the detection of hidden fire sources in small coal pits," *Safety in Coal Mines*, vol. 48, no. 7, pp. 148–150, 2017.
- [27] X. Yi, F. R. Kang, J. Deng, Q. Xiang, and L. Ma, "Research and application on inorganic solidified foam filling material for mine," *Journal of Safety Science and Technology*, vol. 13, no. 10, pp. 136–142, 2017.
- [28] W. Z. H. Guo, Y. F. Jin, and H. T. Li, "Effects of additives properties of high Volume fly ash slurry," *Coal Technology*, vol. 33, no. 11, pp. 7–10, 2014.

## Research Article

# Industry Development of Derivative Functionalized Gold Nanomaterials and Their Application in Chemiluminescence Bioanalysis: Based on the Industrial Practice of China's Central Yunnan Urban Agglomeration

Tengfei Ma<sup>1</sup> and Hao Wu<sup>2</sup> 

<sup>1</sup>Faculty of Management and Economics, Kunming University of Science and Technology, Kunming 650093, Yunnan, China

<sup>2</sup>Faculty of Materials Science and Engineering, Kunming University of Science and Technology, Kunming 650093, Yunnan, China

Correspondence should be addressed to Hao Wu; luck@stu.kust.edu.cn

Received 22 July 2020; Revised 27 August 2020; Accepted 28 September 2020; Published 23 October 2020

Academic Editor: Tifeng Jiao

Copyright © 2020 Tengfei Ma and Hao Wu. This is an open access article distributed under the Creative Commons Attribution License, which permits unrestricted use, distribution, and reproduction in any medium, provided the original work is properly cited.

Electrochemiluminescence biosensor is an analytical method combining electrochemiluminescence technology with biosensor. Using nanomaterials as electrochemical luminescence sensor platform can not only immobilize a large number of biomolecules but also improve the performance of the sensor to realize the supersensitive detection of biomacromolecules. Although these methods have high sensitivity for bioanalysis, there are still some shortcomings which limit the practical application. Therefore, this paper discusses the development of functional gold nanomaterials industry and its application in chemiluminescence bioanalysis. In this paper, two methods of synthesizing luminescent functional gold nanomaterials at room temperature were studied by using chemiluminescent reagents as reducing agent and protective agent. Based on luminescent functionalized gold nanoparticles, immunoassay and DNA bioanalysis probes were constructed, and their applications in chemiluminescence and electrochemiluminescence bioanalysis were discussed. Finally, the simulation results show that the relative deviation between the experimental results and the existing clinical methods is less than 17%. The sensor has good stability and selectivity and can be used for the determination of CEA in human serum. The gold nanomaterials synthesized by further research have excellent chemiluminescence activity and can be used to label biomolecules and prepare biological probes. This article aims to explore the application of chemical methods in the transformation of new industries, to achieve breakthroughs in new products in industrial innovation, and to achieve the cross-fusion of management science and engineering disciplines and chemical disciplines. The industrial development of derivative functionalized gold nanomaterials has broad application prospects in biological analysis.

## 1. Introduction

Electrochemiluminescence (ECL) is a kind of chemiluminescence phenomenon caused by the electrochemical method. Some special substances are produced on the electrode surface by applying a certain voltage or a certain current. These special substances or other coexisting components in the system form high-energy excited states through electron transfer, and the excited states transits back to the ground state. As a new material, gold nanomaterials can serve the development of emerging industries. When

developing emerging industries, Yunnan Province, China, focuses on eight key industries and actively builds three world-class brands. In this process, the development of gold nanomaterials industry is very important. Good bonding point: in recent years, the conversion of new and old kinetic energy in Yunnan Province has accelerated. Eight key industries such as biomedicine and general health, as well as the development of green energy, green food, and healthy living destinations “three cards” have become a new driving force for Yunnan’s economic development. In the work of the modern industrial system oriented to 2035, it is crucial to

understand the specific properties of gold nanomaterials and their application in chemiluminescence bioanalysis.

Electroluminescence (ECL) is generally based on a three electrode system, which is connected by wires, respectively. The ECL signal changes on the working electrode surface are detected by photomultiplier tube or charge coupled element, so as to realize quantitative or qualitative analysis [1, 2]. Amine-rich nitrogen-doped carbon nanoparticles have been successfully used as coreactants in the electrochemiluminescence process. Carrara identified the primary or tertiary amino groups on NCNDs as coreaction sites for Ru (bpy) 32+ ECL, indicating that they are powerful substitutes for tripropylamine. Carrara also reported the synthesis and electrochemiluminescence behavior of NCNDs covalently bonded with Ru (bpy) 32+. NCNDs in the hybrid are not only ECL-labeled carriers but also coreactants for ECL production. The results show that the ECL emission of the hybrid product is higher than that of the single component combination, indicating that the self enhanced ECL of ruthenium complex is due to the intramolecular electron transfer process [3, 4]. Liu constructed a label-free electrochemiluminescence sensor for the detection of acetylcholinesterase using gold nanoparticles functionalized g-c3n4 nanocomposite as light-emitting carrier. Liu et al. used au-g-c3n4-nh and thiol-modified ache-specific aptamer-modified glassy carbon electrode to prepare the sensor. In the presence of acetylcholinesterase, acetylcholinesterase can hydrolyze the substrate acetylcholine to produce acetic acid, which reacts with triethylamine, leading to the consumption of CO reactant. The ECL response of the sensor was linear with the concentration of ache in the range of 0.1 pg/ml~10 ng/ml, and the detection limit was 42.3 FG/ml. This novel ECL sensing strategy provides a highly sensitive and selective method for ache detection and is expected to have potential application prospects in clinical diagnosis and biomedical technology [5, 6]. Zhang proposed a small molecule dye Alexa flow 488 as the donor and electrochemiluminescence resonance energy transfer strategy. Zinc Cadmium selenium quantum dots were used as acceptors to construct a DNA nanomachine-based regenerative biosensor for ultrahigh sensitivity cancer cell detection without any enzyme. Zhang et al.'s research shows that it can be used for on-site environmental analysis and monitoring, thus providing a new modular platform for the construction of functional DNA nanomachines, which can be used for the ultrahigh sensitivity analysis of promising biomarkers and toxic metals [7, 8]. Zhang et al. studied the electrochemiluminescence (CL) behavior of mesoporous tetraporphyrin in strong and stable emission aqueous solution and determined the nanomolar concentration of copper ion. Zhang et al. proposed two possible reaction mechanisms to understand the mechanism of ECL formation in TSP/K2S2O8 system. Zhang et al. proposed and successfully applied it to the electrochemiluminescence analysis of tap water samples. Zhang et al. predicted that TSP would be a new type of ECL luminescent material [9, 10]. A new type of double stabilizer-capped CdSe quantum dots with unique electrochemiluminescence properties was prepared by Jie, and it was used for the first

time to detect thrombin with high sensitivity by the target-triggered multiple amplification method. Ji et al.'s research shows that this flexible biosensor system has good performance in the detection of human serum and has a wider application prospect than other systems based on ECL reagent [10, 11].

With the rapid development of nanomaterials, self-luminescent nanomaterials such as quantum dots and metal nanoclusters have attracted extensive attention and have been widely used in the construction of biosensors [12, 13]. The sensitivity, selectivity, and stability of ECL biosensor can be effectively improved by using the special properties of functionalized nanomaterials [14, 15]. Silica nanoparticles with unique morphology can be used as an effective template to prepare silicon metal hybrid nanomaterials, which has a wide range of applications in many fields. Mesoporous silica nanoparticles with high-specific surface area and abundant pores can be used to synthesize mesoporous silica core metal shell nanostructures with catalytic activity centers. Wongyun et al. have successfully synthesized DFNS/AU hybrid nanomaterials using high-specific surface area dendritic fiber nanosilicon as template. Gold nanoparticles were initially synthesized on the surface of DFNS by selective reduction of gold ions after surface modification. Wongyun et al. used the seed-mediated growth method to grow Au nanoparticles on the DFNS/Au sites to generate DFNS core Au nanoparticles shell hybrid and DFNS core Au layer shell hybrid. Wongyun et al. compared the catalytic activity of DFNS/Au nanoparticles and DFNS/Au layers in the reduction of 4-nitrophenol [16, 17]. Ushakov studied the effect of pore structure on the height of electron barrier in Au-Al<sub>2</sub>O<sub>3</sub> structure. Ushakov studied the pore structure of two types of anodic alumina: through-pass and pass. The results show that the deposited Au films produce electron barriers with different heights at the metal insulator interface, which depends on the shape of the hole profile. Linear optical spectroscopy showed that the barrier height with through-hole structure was increased by 2.0 eV [18, 19]. It is difficult to preserve the properties of gold nanoparticles in the form of solution and dry powder for a long time. Fernández Lodeiro et al. synthesized gold nanoparticles using organic tellurium derivatives as reducing agents and stabilizers. Fernández Lodeiro et al.'s research shows that the organic tellurium shell can be easily removed by the resuspension of nanoparticles in environmentally friendly solvents, so that the gold core can be used for subsequent applications [20, 21]. Liu prepared gold nanomaterials with different morphologies by the wet chemical reduction method and characterized by transmission electron microscope and ultraviolet visible spectrophotometer. TEM results show that Au nanomaterials with different morphologies, such as spherical, rod-shaped, cubic, and triangular, have been prepared. The UV absorption spectra of au-24-23 are given. Some nanomaterials can be used as coreaction reagents to effectively enhance the luminescence of the ECL system [22].

Guang discussed the development trend of intelligent robots and put forward some thoughts and suggestions on the development of intelligent robots in China. The main technologies of intelligent robots at home and abroad are

summarized, and the relevant theories, methods, and technical guidance of intelligent robot technology and industrial development are provided. The design and synthesis of photocatalysts for efficient degradation of organic pollutants in China are considered to be a promising way for environmental protection and governance. The photodegradation efficiency of the optimized BiVO<sub>4</sub>/NIS/Au ternary composite for tetracycline is 4.25 times higher than that of pure BiVO<sub>4</sub>. Through capture experiments and liquid chromatography-mass spectrometry (LC-MS) analysis, Zhang et al. proposed a possible degradation mechanism and pathway [23, 24]. Simin et al. proposed a layer by the layer self-assembly method. The nanostructures composed of hydrophobic CdSe/CdZnS and hydrophilic CdTe and Au nanoparticles were formed on the slide by a layer of functional silica. In contrast, when the glass layer thickens, a bright PL appears. LBL self-assembled glass film has good stability and transparency and has broad application prospects in biochemical, photoelectric, clinical diagnosis, and other fields [25]. Ruirui can spontaneously form injectable and self-healing collagen—gold hybrid hydrogels via electrostatic self assembly and subsequent biomineralization. Cuihong proposed a two-step method for the synthesis of perovskite quantum dots and large-size nanoparticles (LNPS). The growth of QDs and LNPS involves two possible pathways, namely, the rapid intercalation reaction process and the dissolution recrystallization process. On the basis of a comprehensive understanding of its formation mechanism, Cuihong partially realized the transformation from LNPS to quantum dots by properly adding surfactants, which is expected to pave the way for the development of pure production of perovskite quantum dots [26].

In order to improve the sensitivity and biocompatibility of ECL biosensor, a new type of low toxicity self-luminescent nanomaterial was introduced as ECL reagent and functional nanomaterial was used as carrier of biomolecule and luminescent reagent. Combined with the immunosandwich analysis method and target induced shear, ECL biosensor with good stability, high sensitivity, and low toxicity was constructed. The construction of sensors, enhancement of electroluminescence signal, exploration of electroluminescence mechanism, and detection performance of biosensors are discussed. Compared with other chemiluminescence immunoassay methods with gold nanoparticles, the labeling process is simple, fast, and cheap. In principle, the sensor can be used to detect other biomolecules based on antigen and antibody.

## 2. Derivative Functionalized Gold Nanomaterials and Chemiluminescence Bioanalysis

*2.1. Derivative Functionalized Gold Nanomaterials.* Nanomaterials are new materials with at least one-dimensional size between 1–100 nm in three-dimensional space. Because of its various characteristics, it has unique electrical and optical properties and catalytic activity. Nanomaterials with large specific surface area can support a large number of antibodies or luminescent reagents, the conductive

nanomaterials can promote the electron transfer in the reaction process, and the good catalytic nanomaterials can promote the ECL reaction and speed up the reaction rate. These nanomaterials can enhance the stability of the sensor or improve its sensitivity. Nanomaterials have the characteristics of large specific surface area, good biocompatibility, and easy to modify and assemble. Therefore, nanomaterials can be used as carriers to improve the immobilization efficiency of luminescent reagents or biomolecules, so as to improve the sensitivity of sensors.

Conductive polymer/metal nanocomposites, combined with the dual advantages of organic materials and inorganic materials, have composite properties that other materials do not have. Using macromolecular acids and polymers as dopants, aniline was polymerized with p-aminothiophenol functionalized gold colloid in the aqueous system. Due to the high conductivity of Au and the strong interfacial effect between the two phases, the electrochemical properties of the materials are obviously enhanced. The composite materials with various morphologies can be obtained by in situ polymerization. The conductive polymer monomer and metal oxide were added into the dispersion, then the oxidant was added to initiate polymerization, and the composite was obtained after purification. In the process of synthesis, the change of each parameter may change the final morphology of nanocomposites. Transition metal oxides are one of the inorganic nanomaterials. Transition metals represent a series of metal elements in the D region of the periodic table, which have an unfilled valence layer of d orbitals and are easy to form metal complexes. In addition to gold and silver, most transition metals exist in the earth's crust in the form of sulfides or oxides. Transition metal oxide is the compound obtained by the combination of oxygen atom and transition metal. Its nanostructure has the characteristics of common nanomaterials. Due to its good biocompatibility, polyvinyl alcohol is considered as a kind of bionic material with excellent performance and is widely used in medical treatment. In theory, the preparation of polymer is made by monomer polymerization, but "aterials. Due is easy to produce isomerization to acetaldehyde, so it is not easy to prepare polyvinyl alcohol according to the theory. They can only be prepared by alcoholysis or hydrolysis of polyvinyl acetate. The PVA prepared by alcoholysis method not only has high purity but also has good performance.

In a broad sense, biomaterials refer to the applied materials or materials that can contact with organisms through a series of biological processes; in a narrow sense, biomaterials refer to a kind of natural or synthetic special functional materials that can contact with the physiological environment of organisms, have strong biocompatibility, and can diagnose, replace, and repair their cells, tissues, and organs, or enhance their functions. So, biomaterials are also called biomedical materials. Bionic design is not only required to be similar to biological objects in structure but also to achieve certain similarity in function. The fracture property of shell is much stronger than that of ceramic. It is found that the main reason is the strength and toughness of nacre in the three-

layer structure. The arrangement of aragonite crystal and organic matrix in nacre layer alternately makes it form multilayer toughened structure with alternating soft and hard layers. Organic matrix is easy to induce the deflection of vertical cracks in the outer layer, thus preventing the crack growth. This is the key to the high fracture toughness of nacre. The water droplets on the surface of lotus leaf will automatically gather and take away the dust on the surface. This superhydrophobic property has been widely used in self-cleaning, antipollution, and antiadhesion. Botanists have studied thousands of leaves. The superhydrophobicity is mainly determined by the micromorphology and surface energy of the surface. There are many papillary microconvex bodies on the surface of lotus leaf. The gap of micron scale is filled with air, and the outer area of milky convex surface is covered by many nanorods with low surface energy. This is the reason why water can not soak lotus leaves. Zheng Zhenrong et al. prepared PVDF films with nano-/micron bilayer structure by deposition method, which reached a contact angle of  $157^\circ$  and increased the surface hydrophobicity.

**2.2. Chemiluminescence.** In other spectral quantitative methods, not only external light source is needed but also the factors that affect the signal-to-noise ratio, which are not necessary for chemiluminescence analysis. Since each chemiluminescence process includes the process of chemiluminescence reaction, the rate of chemical reaction, the yield of material that can be excited as luminescent body, and the luminous efficiency of the luminescent body itself have a crucial impact on the intensity of chemiluminescence. The chemiluminescence detection method is based on the luminous intensity of a certain time to detect the object. The  $I_{CL}$  at a given time  $t$  can be expressed by the following equation:

$$I_{CL}(t) = \varphi_{CL} \frac{dc(t)}{dt} = \varphi_{EX} \varphi_{EM} \frac{dc(t)}{dt}, \quad (1)$$

where  $dc(t)/dt$  represents the chemiluminescence reaction rate at a specific time,  $\varphi_{CL}$  represents the quantum yield of chemiluminescence, and  $\varphi_{EX}$  and  $\varphi_{EM}$  represent the excited state quantum yield and luminescence quantum yield, respectively.  $\varphi_{CL}$  can be regarded as a constant in the chemiluminescence reaction, but factors such as pH, ionic strength, temperature, and components contained in the solution have an important influence on the determination of chemiluminescence, which also leads to any quantum factor in the chemical reaction and can interfere with the intensity of chemiluminescence. Therefore, the concentration of a substance in a chemical reaction system can be determined by measuring the intensity of chemiluminescence under certain reaction conditions. That is, the quantitative analysis of chemiluminescence can be applied by the formula shown in (1) in a first-level or quasi-first-level chemical reaction. In the actual chemical reaction, when only the concentration of the substance M changes, the concentration of M can be measured by the signal value of chemiluminescence through the following formula:

$$I_{CL} = \int I_{CL}(t) dt = \int \varphi_{CL} \left[ \frac{dC_A(t)}{dt} \right] dt = \varphi_{CL} C_A. \quad (2)$$

The chemiluminescence analysis method can be used to determine the substances that can enhance or inhibit the chemiluminescence reaction, the reactants in the chemiluminescence reaction system or the substances produced in the reaction, and some substances that can produce coupling effect in the chemiluminescence reaction.

Some compounds with oxidation or fluorescence properties and aromatic oxalates are the main components in the chemiluminescence reaction system of oxalate peroxide. The effect of compounds with fluorescence properties in this system is to improve the stability and weak luminescence of the luminescent system of oxalate peroxide and oxidant, and the fluorescence spectrum of the fluorescent material itself is consistent with that in the chemiluminescence system. The energy transfer luminescence system is the most efficient chemiluminescence system at present. Different from luminol and other chemiluminescent systems, oxalate peroxides are characterized by energy transfer. The main applications of oxalate chemiluminescence system include that the chemiluminescence emitted by the system is not only high intensity but also the emission wavelength can be controlled within a certain range, so the development of multimode light sources has been industrialized; oxalate ester luminescent system has been widely recognized in chemiluminescence analysis. For the determination of hydrogen peroxide, enzyme reactants, and fluorescent substances, it is a typical analytical application.

**2.3. Chemiluminescence Catalyst and Biosensor.** Metal nanoparticles are widely used in the field of analytical sensing due to their unique structure and excellent physical and chemical properties. Among them, gold, silver, and platinum nanoparticles are the most common catalysts in chemiluminescence analysis. Generally, gold is considered to be an inert metal material. However, the properties of gold nanoparticles are quite different and show good catalytic activity. Therefore, gold has become the first nanomaterial for chemiluminescence analysis. In addition to the luminol hydrogen peroxide chemiluminescence system, gold nanoparticles can also catalyze luminol the  $\text{NaIO}_4$  system and luminol  $\text{AgNO}_3$  system. Compared with gold nanoparticles, silver nanoparticles have stronger catalytic activity for the luminol hydrogen peroxide system. It can be used for the selective determination of cysteine because of its adsorption on Ag nanoparticles and competitive consumption of active intermediates. Platinum nanoparticles and alloys also have good catalytic activity for luminol hydrogen peroxide.

As a member of the family of carbon nanomaterials, carbon dots mainly refer to photoluminescence carbon nanoparticles less than 10 nm, which have the characteristics of surface modification or functionalization and can be rapidly synthesized and functionalized. As a catalyst, carbon dots effectively catalyze the decomposition of dissolved oxygen to produce superoxide radicals, which accelerates the

electron transfer rate between dissolved oxygen and luminol, resulting in enhanced chemiluminescence. The good catalytic activity of carbon point is closely related to its surface state and particle size. MOFs have a large number of unsaturated metal sites, showing good catalytic activity, and can be used for quantitative detection of a variety of analytical substances. MIL-53 (FE) has good chemiluminescence activity, which can catalyze luminol hydrogen peroxide system to produce enhanced chemiluminescence, which can be used for the determination of glucose in human serum. In addition, MOFs with large specific surface area can also be used as a support for stabilizing and dispersing the catalyst, so as to improve the catalytic activity. The dispersion of MOFs used in luminol chemiluminescence system is poor in water, and more MOFs with good chemiluminescence activity can be explored for use in chemiluminescence system. Therefore, it is of great significance to improve the dispersion and catalytic activity of MOFs in water by surface modification. Although most MOFs contain metal ions (Fe, Ni, and CO) as catalytic sites, their catalytic activity can be further enhanced by carbonization. The carbon material prepared by MOFs as sacrificial template has a large specific surface area, which can expose more active sites. At the same time, the doping of heteroatoms into the carbon matrix can improve the catalytic activity. Therefore, it is of great significance to prepare catalysts with higher catalytic activity for the luminol chemiluminescence system based on the existing MOFs.

ECL immunosensor is a biosensor composed of antigen, antibody, and other immune recognition elements. It combines the high sensitivity of the ECL analysis method and the high specificity of immune recognition. ECL reagent can be immobilized on the electrode surface, labeled on the capture antibody, or directly placed in the detection base solution. Then, based on the antigen antibody specific immune reaction, the ECL reagent forms an immune complex, which causes the change of ECL signal to realize the sensitive detection of target antigen. ECL direct immunization mode is to immobilize the antibody on the electrode surface directly. When the target antigen of different concentration appears, the antigen and antibody will have different degrees of immune reaction and then lead to different intensities of ECL response. Generally, with the increase of the concentration of target antigen, the formation of immune complex will hinder the electron transfer in the process of ECL, and the detected ECL signal will decrease, so as to realize the quantitative detection of target antigen. Electrochemiluminescence (ECL) DNA sensor is generally used to label ECL reagent directly or indirectly to form DNA probe at the end of double-stranded DNA. The probe can hybridize with target DNA strand through base complementary pairing. The change of ECL during hybridization can be detected to infer the concentration of target DNA.

### 3. Experiment Materials and Methods

**3.1. Experimental Materials.** 1 g  $\text{HAuCl}_4 \cdot 4\text{H}_2\text{O}$  was dissolved in 412 mL three times distilled water to make a 0.2% (w/w) stock solution, stored at 4°C protected from

light. Experimental materials include N-(4-aminobutyl)-N-ethylisoluminol, 1-ethyl-(3-dimethylaminopropyl) carbodiimide hydrochloride, N-hydroxysuccinimide and 1,3-propanedithiol, immunoglobulin G, goat anti-Human IgG, and bovine serum albumin. 5.6 mg ABEI was dissolved in 10 mL of 0.1 mol/L phosphate buffer to prepare a 2 mmol/L ABEI stock solution and stored at 4°C in the dark. The purity of all reagents is analytically pure, and the experimental water is Milli-Q ultrapure water.

#### 3.2. Preparation of Gold Electrode Modified by Nanogold.

After the glassware used in the experiment was soaked with aqua regia, it was washed with ultrapure water and air-dried. The bare gold electrode was first polished with fine sandpaper and suede, washed with ethanol and ultrapure water, and then dried with filter paper. The electrode was then electrochemically cleaned in sulfuric acid solution until the redox peak of the gold electrode was reproduced. The electrode was put into 0.1 mol/L pH7.0 and phosphate buffer solution was contained with a concentration of  $1 \times 10^{-3}$  mol/L  $[\text{Fe}(\text{CN})_6]^{3-}$  and  $[\text{Fe}(\text{CN})_6]^{4-}$  for cyclic voltammetry. Until the redox peak with a peak potential difference of less than 100 mV appears, the electrode can be modified after washing with ultrapure water. The electrode is put into a 2 mmol/L 1,3-propanedithiol solution at room temperature for 20 hours and taken out. In order to remove the physically adsorbed 1,3-propanedithiol molecules, it should be repeatedly washed with ethanol and ultrapure water. On the electrode surface, a 1,3-propanedithiol self-assembled modified electrode was obtained. At 4°C, the thiol-modified electrode was immersed in a 16 nm gold sol for 10 hours and then washed with ultrapure water to obtain a nanogold-modified electrode for the next experiment. 100 mL of 0.3 mmol/L  $\text{HAuCl}_4$  solution was heated to boiling. Under vigorous stirring, 5.0 mL of 1% (w/v) citrate solution was added quickly. After the mixture was heated to reflux for 30 minutes, the heating was stopped and stirring was continued for 15 minutes. After the synthetic sol was naturally cooled to room temperature, the cellulose particles with a pore size of 0.22  $\mu\text{m}$  were used to filter and remove the large particles in the sol and stored at 4°C in the dark.

## 4. Development of Derivative Functionalized Gold Nanomaterial Industry and Its Application in Chemiluminescence Bioanalysis

**4.1. Application of Electrochemiluminescence Immunosensor in Real Human Serum Samples.** The recovery results of IgG in human serum samples determined by ECL immunosensor are shown in Table 1.

The results showed that the recovery was between 89.6% and 117.8%. Therefore, the sensor constructed in this work can be applied to the detection of IgG in human serum samples. The comparative analysis of ECL immunosensor and other immunoassay methods for the determination of IgG is shown in Figure 1.

Before detection, the sample should be diluted to the appropriate concentration, that is, the detection range of the

TABLE 1: Recovery of IgG in human serum by electrochemiluminescence immunosensor.

Background content (ng/ml)	Added concentration (ng/ml)	Detected concentration (mean $\pm$ SD, $n = 5$ ) (ng/ml)	Recovery ratio (%)
9.81	10	17.49 $\pm$ 0.84	89.9
9.81	15	24.57 $\pm$ 0.69	115.7
9.81	25	36.48 $\pm$ 0.68	119.4
9.81	40	45.77 $\pm$ 1.37	113.6
9.81	60	67.69 $\pm$ 2.47	116.4

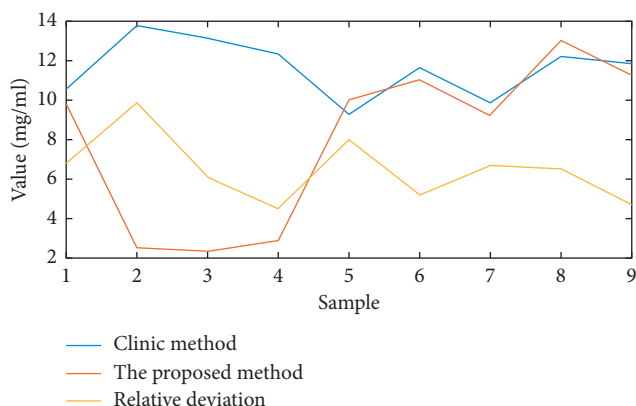


FIGURE 1: Comparison of electrochemiluminescence immunosensor with other immunoassay methods for the determination of IgG.

sensor. Compared with the existing clinical methods, the relative deviation of the two methods is less than 17%. In the electrochemical way of two-step pulse, the immunosensor showed excellent electrochemiluminescence signal response in 0.01 mol/L salt buffer containing 2 mmol/L hydrogen peroxide. The detection concentration range of human IgG was 10~150 ng/m. The detection of IgG by the sensor was three orders of magnitude higher than other double antibody sandwich immunoassay methods based on the modified electrode as carrier. Although the sensitivity of this method is lower than that of homogeneous immunoassay, the presence of interferents in serum samples will have a great impact on luminescence in homogeneous immunoassay due to the influence of matrix. Therefore, it needs to be improved in practice.

4.2. *ECL Assay of Thrombin by ECL Aptamer Sensor.* The performance comparison between ECL aptamer sensor and other sensors is shown in Table 2.

Compared with other sensors, the proposed ECL sensor has lower detection limit and larger detection range, which indicates that the ECL sensor has higher sensitivity. The performance comparison and analysis between ECL aptamer sensor and other sensors is shown in Figure 2.

The reason for the low detection limit of the sensor is that AuNP has the effect similar to the electron channel, which can accelerate the electron transfer ability and increase the load of DNA and qgds; qgds has high ECL strength and good conductivity, which can realize ECL signal amplification; pica/fgns nanocomposites have the dual advantages of fgns and pica, providing larger specific surface area. It promoted the immobilization of bioactive molecules. The combination

of the three can not only accelerate the electron conduction rate but also enhance the specific surface area of the electrode, which can effectively improve the detection effect of the sensor. The sensor has a wide linear range of 0.001–15 nm and a low detection limit of 0.06 pm. At the same time, the sensor shows good stability, selectivity, and reproducibility, which can be used to detect thrombin in real human serum samples. The sensor not only provides a simple method to detect thrombin but also expands the application range of pica/fgns nanocomposites in biological detection. This ECL strategy based on conductive polyindole derivatives also has potential application value in clinical diagnosis of other bioproteins.

4.3. *Analysis of ECL Properties of Metal Ion Bifunctional Gold Nanoparticles.* The  $I_{ECL}$ -E curve obtained by cyclic voltammetry of  $Co^{2+}$ /DTDTPA/ABEI-GNPs under air saturation condition is shown in Figure 3.

There is an obvious ECL peak in  $Co^{2+}$ /DTDTPA/ABEI-GNPs at positive potential, while ABEI-GNPs hardly shows any luminescence. When pH is 12.4,  $Co^{2+}$ /DTDTPA/ABEI-GNPs have a strong ECL peak at positive potential, while ABEI-GNPs have weak luminescence under this condition. The results show that the ECL intensity of  $Co^{2+}$ /DTDTPA/ABEI-GNPs is at least two orders of magnitude higher than ABEI-GNPs under neutral or alkaline conditions. Two ECL peaks, ECL-1 and ECL-2 at -0.89v and 0.74v, were observed under cyclic voltammetry. These two peaks were related to the formation of OOH- and ABEI- by electrooxidation of dissolved oxygen as well as the formation of many intermediate products. The results showed that BF-GNPs had good ECL properties under neutral and

TABLE 2: Performance comparison between ECL aptamer and other sensors.

Material science	Test method	Detection range (nM)	Detection limit (pM)
Ru(bpy) <sub>3</sub> <sup>2+</sup>	ECL	0.02–12	6.8
CD/AuNF	ECL	0.6–43	82
Fc-GNs	ECL	0.7–27	213
Eu-MWCNTs	ECL	0.003–5.2	0.24
Tris(bpyRu)- $\beta$ -CD	ECL	0.002–10.4	0.14
PTC-Tb	ECL	0.006–10.7	1.73
GQDs/PICA/FGNs	ECL	0.001–10.5	0.06

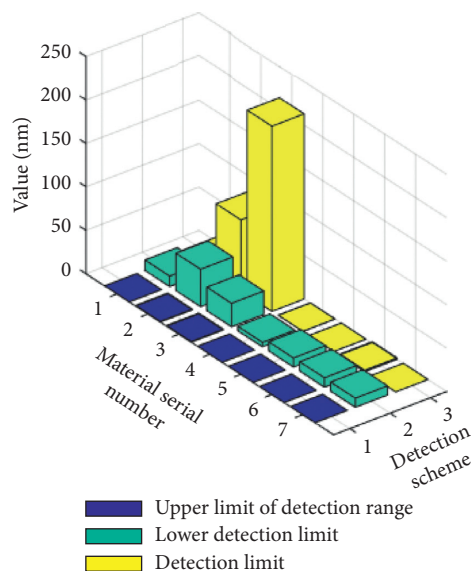
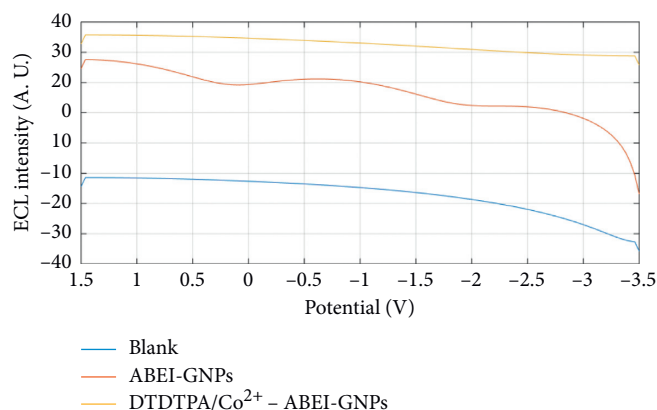


FIGURE 2: Comparative analysis of the performance of the experimentally constructed ECL aptamer sensor and other sensors.

FIGURE 3: The  $I_{\text{ECL}}$ -E curves of  $\text{Co}^{2+}$ /DTDTPA/ABEI-GNPs obtained by cyclic voltammetry under air saturation.

alkaline conditions, and the detection of bioactive substances under physiological conditions had important application potential.

**4.4. Analysis of Chemiluminescence Mechanism.** In the presence of catalyst, the chemiluminescence intensity of luminol reaction with hydrogen peroxide was significantly

enhanced. The effect of different free radical scavengers on CL of luminol- $\text{H}_2\text{O}_2$ -MOF-235/ $\beta$ -CD system is shown in Figure 4.

The chemiluminescence intensity was strongly inhibited by ascorbic acid and thiourea, indicating that a large amount of  $\text{OH}^\bullet$  was produced in the reaction. At the same time, p-benzoquinone is usually used to detect  $\text{O}_2^{\bullet-}$ . The results showed that p-benzoquinone inhibited the

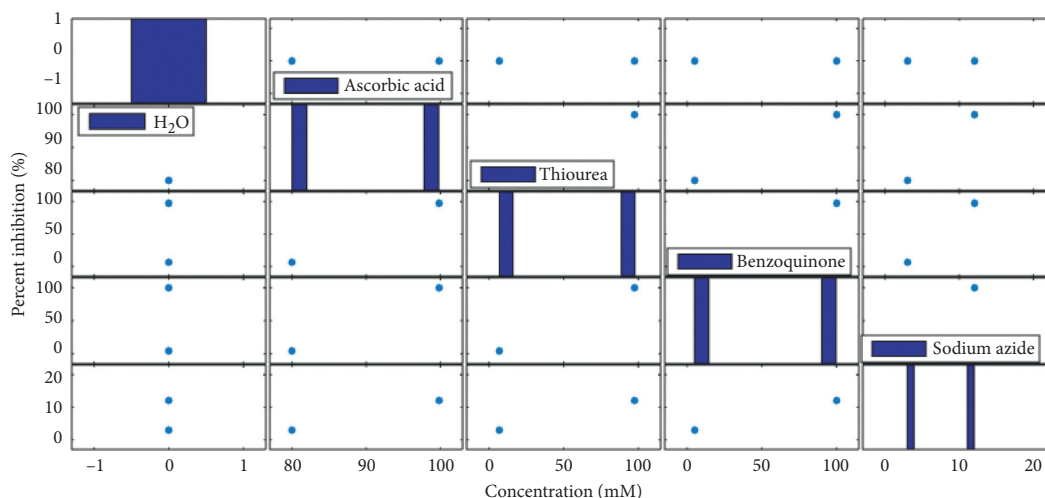


FIGURE 4: Effect of different free-radical scavengers on CL of the luminol-h<sub>2</sub>O<sub>2</sub>-mof-235/ $\beta$ -CD system.

chemiluminescence reaction of luminol-h<sub>2</sub>O<sub>2</sub>-mof-235/ $\beta$ -CD system, and superoxide anion radical participated in the chemiluminescence reaction. In addition, sodium azide is an effective scavenger for singlet oxygen. The addition of 3 mM sodium azide inhibited the chemiluminescence signal by 14%, indicating that singlet oxygen played a secondary role in the process. Compared with mof-235 alone, mof-235/ $\beta$ -CD exhibited higher catalytic activity due to the synergistic effect between  $\beta$ -CD and mof-235. The gold nanomaterials synthesized by further research have excellent chemiluminescence activity and can be used to label biomolecules and prepare biological probes. The industrial development of derivative functionalized gold nanomaterials has broad application prospects in biological analysis.

## 5. Conclusions

This paper adopts the strategy of functionalizing MOF-235 with  $\beta$ -CD, and the obtained MOF-235/ $\beta$ -CD complex has been proved to be an effective catalyst in the hydrogen peroxide-Luminol CL system. In view of the advantages of functionalized MOF and chemiluminescence, it is believed that the success of this work will facilitate the future development of CL catalysts through MOF functionalization.

In this paper, the study of the effects of luminescent reagents found that luminol and isoluminol dual-functionalized nanophosphors have strong ECL emission without coreactive reagents. In addition, Co<sup>2+</sup>/DTDTPA/ABEI-GNPs have strong and stable ECL signals under double-order pulse conditions, indicating that the material has potential for analysis.

The electroluminescence functionalized gold nanoparticles with special morphology were synthesized by the seed-induced growth method using isoluminol as reducing agent in aqueous phase at room temperature. Compared with other gold nanomaterials, this gold nanomaterial not only has special morphology and special properties but also can be used in biochip connection, nanoelectronic devices,

etc. and also has chemiluminescence activity and good biocompatibility. According to the morphology and properties of this material and its application in electrochemiluminescence biosensor platforms, gold nanomaterials, as a new type of material, can be used as a breakthrough in the development of new industries in Yunnan Province, China, to realize the differentiated development and application of nanomaterials. It provides new ideas for the construction of a modern industrial system in the central Yunnan urban agglomeration in Yunnan Province, China. This is the application of chemical methods to industrial development, which can provide targeted and efficient path suggestions for the development of emerging industries. It can be used in immune analysis and nucleic acid analysis and has broad application prospects. The application of chemical methods in emerging industries has direct and practical significance. As the kingdom of non-ferrous metals, gold nanomaterials have a good development prospect in the central Yunnan urban agglomeration. They can become an important part of the local modern industrial system. The entry point of nanomaterials analysis requires innovation. This article finds that the application of gold nanomaterials in chemiluminescence bioanalysis has huge industrial development prospects, so the development possibilities of related industries are explored from the perspective of chemical analysis to realize management science and engineering disciplines and chemistry interdisciplinary integration.

## Data Availability

The data used to support the findings of this study are included within the article. There is no other data to support this research.

## Conflicts of Interest

The authors declare that there are no conflicts of interest regarding the study.

## References

- [1] L. Wu, Y. Zhang, Y. Wang et al., "A paper-based electrochemiluminescence electrode as an aptamer-based cytosensor using PtNi@carbon dots as nanolabels for detection of cancer cells and for in-situ screening of anticancer drugs," *Microchimica Acta*, vol. 183, no. 6, pp. 1873–1880, 2016.
- [2] J. M. Sosenko, L. Yu, J. P. Krischer et al., "The use of electrochemiluminescence assays to predict autoantibody and glycemic progression toward type 1 diabetes in individuals with single autoantibodies," *Diabetes Technology & Therapeutics*, vol. 19, no. 3, pp. 183–187, 2017.
- [3] S. Carrara, F. Arcudi, M. Prato, and L. De Cola, "Amine-rich nitrogen-doped carbon nanodots as a platform for self-enhancing electrochemiluminescence," *Angewandte Chemie International Edition*, vol. 56, no. 17, pp. 4757–4761, 2017.
- [4] H. Chen, H. Zhang, and R. Yuan, S. Chen, "Novel double-potential electrochemiluminescence ratiometric strategy in enzyme-based inhibition biosensing for sensitive detection of organophosphorus pesticides," *Analytical Chemistry*, vol. 89, no. 5, pp. 2823–2829, 2017.
- [5] Q. Liu, Y.-J. Peng, J.-C. Xu et al., "Label-free electrochemiluminescence aptasensor for highly sensitive detection of acetylcholinesterase based on Au-Nanoparticle-Functionalized g-C<sub>3</sub>N<sub>4</sub> nanohybrid," *Chemelectrochem*, vol. 4, no. 7, pp. 1768–1774, 2017.
- [6] Z. Li, Y. Zhou, L. Peng, D. Yan, and M. Wei, "A switchable electrochromism and electrochemiluminescence bifunctional sensor based on the electro-triggered isomerization of spiropyran/layered double hydroxides," *Chemical Communications*, vol. 53, no. 63, pp. 8862–8865, 2017.
- [7] P. Zhang, Z. Li, H. Wang, Y. Zhuo, R. Yuan, and Y. Chai, "DNA nanomachine-based regenerated sensing platform: a novel electrochemiluminescence resonance energy transfer strategy for ultra-high sensitive detection of microRNA from cancer cells," *Nanoscale*, vol. 9, no. 6, pp. 2310–2316, 2017.
- [8] S. Li, C. Liu, B. Han, and J. Luo, G. Yin, "An electrochemiluminescence aptasensor switch for aldcarb recognition via ruthenium complex-modified dendrimers on multiwalled carbon nanotubes," *Microchimica Acta*, vol. 184, no. 6, pp. 1669–1675, 2017.
- [9] J. Zhang, S. Devaramani, D. Shan, and X. Lu, "Electrochemiluminescence behavior of meso-tetra(4-sulfonatophenyl)porphyrin in aqueous medium: its application for highly selective sensing of nanomolar Cu<sup>2+</sup>," *Analytical and Bioanalytical Chemistry*, vol. 408, no. 25, pp. 7155–7163, 2016.
- [10] K. Shao, B. Wang, S. Ye et al., "Signal-amplified near-infrared ratiometric electrochemiluminescence aptasensor based on multiple quenching and enhancement effect of graphene/gold nanorods/G-quadruplex," *Analytical Chemistry*, vol. 88, no. 16, pp. 8179–8187, 2016.
- [11] G. Jie, K. Chen, X. Wang, and Z. Lu, "Dual-stabilizer-capped CdSe quantum dots for "Off-On" electrochemiluminescence biosensing of thrombin by target-triggered multiple amplification," *RSC Advances*, vol. 6, no. 3, pp. 2065–2071, 2016.
- [12] M. L. D. O. Pereira, D. Grasseschi, and H. E. Toma, "Photocatalytic activity of reduced graphene oxide-gold nanoparticle nanomaterials: interaction with asphaltene and conversion of a model compound," *Energy & Fuels*, vol. 32, no. 3, pp. 2673–2680, 2018.
- [13] Q. H. Quach and J. C. Y. Kah, "Non-specific adsorption of complement proteins affects complement activation pathways of gold nanomaterials," *Nanotoxicology*, vol. 11, no. 3, pp. 382–394, 2017.
- [14] M. Alrahili, R. Peroor, V. Savchuk, K. McNear, and A. Pinchuk, "Morphology dependence in photothermal heating of gold nanomaterials with near-infrared laser," *The Journal of Physical Chemistry C*, vol. 124, no. 8, pp. 4755–4763, 2020.
- [15] A. K. Alanazi, A. Mezni, N. B. Saber et al., "Aquatic ecotoxicity effects of gold/titania based nanomaterials," *Journal of Biomaterials and Tissue Engineering*, vol. 9, no. 2, pp. 262–267, 2019.
- [16] B. Wongyun, J. Soeun, N. M. Tran, and H. Yo, "Synthesis and application of dendritic fibrous nanosilica/gold hybrid nanomaterials," *ChemistryOpen*, vol. 7, no. 5, pp. 349–355, 2018.
- [17] S. Chakraborty, R. C. Rocha, A. Desireddy et al., "Gold nanocluster formation using morpholino oligomer as template and assembly agent within hybrid bio-nanomaterials," *RSC Advances*, vol. 6, no. 93, pp. 90624–90630, 2016.
- [18] N. M. Ushakov, M. Y. Vasil'kov, and V. R. Shaturnuy, "Influence of the pore structure on the electron barrier height of metal-ceramic nanomaterials based on gold-anodic aluminum oxide," *Semiconductors*, vol. 52, no. 16, pp. 2078–2080, 2018.
- [19] Y. Shi and B. Zhang, "Correction: recent advances in transition metal phosphide nanomaterials: synthesis and applications in hydrogen evolution reaction," *Chemical Society Reviews*, vol. 45, no. 6, p. 1781, 2016.
- [20] J. Fernández-Lodeiro, B. Rodríguez-González, H. M. Santos et al., "Unraveling the organotellurium chemistry applied to the synthesis of gold nanomaterials," *Acs Omega*, vol. 1, no. 6, pp. 1314–1325, 2016.
- [21] T. Y. Sun, N.A. Bornhöf, K. Hungerbühler, and B. Nowack, "Dynamic probabilistic modeling of environmental emissions of engineered nanomaterials," *Environmental Science & Technology*, vol. 50, no. 9, pp. 4701–4711, 2016.
- [22] S. Choi, H. Lee, R. Ghaffari, T. Hyeon, and D.-H. Kim, "Recent advances in flexible and stretchable bio-electronic devices integrated with nanomaterials," *Advanced Materials*, vol. 28, no. 22, pp. 4203–4218, 2016.
- [23] G. C. Zhang, J. Zhong, M. Xu et al., "Ternary BiVO<sub>4</sub>/NiS/Au nanocomposites with efficient charge separations for enhanced visible light photocatalytic performance," *Chemical Engineering Journal*, vol. 375, Article ID 122093, 2019.
- [24] M. Feng, J. Gu, G. C. Zhang et al., "Homogeneous nickel bicarbonate nanocrystals as electrode materials for high-performance asymmetric supercapacitors," *Journal of Solid State Chemistry*, vol. 282, Article ID 121084, 2020.
- [25] L. Simin, L. Meng, L. Debaio, Y. Yang, P. Yang et al., "Self-assembly of Au nanoparticles and quantum dots by functional sol-gel silica layers," *Journal of Nanoscience and Nanotechnology*, vol. 18, no. 1, pp. 288–295, 2018.
- [26] C. Jin, M. Feng, J. Zhong et al., "Insights into mechanism of size-controlled synthesis of CH<sub>3</sub>NH<sub>3</sub>PbBr<sub>3</sub> perovskite quantum dots and large nanoparticles with tunable optical properties," *Organic Electronics*, vol. 82, Article ID 105712, 2020.

## Research Article

# Muscle Injury in Bodybuilding Based on Mesoporous Multifunctional Nanomaterials for Sports Rehabilitation Training

Changjun Zhao 

Department of Physical Education, Guangxi University of Chinese Medicine, Nanning 530200, Guangxi, China

Correspondence should be addressed to Changjun Zhao; zhaochangjun78@163.com

Received 10 August 2020; Revised 18 September 2020; Accepted 21 September 2020; Published 23 October 2020

Academic Editor: Tifeng Jiao

Copyright © 2020 Changjun Zhao. This is an open access article distributed under the Creative Commons Attribution License, which permits unrestricted use, distribution, and reproduction in any medium, provided the original work is properly cited.

As an important means of treating diseases, chemical-based drugs have always guaranteed people's health and longevity. However, due to the nature of some drugs, their use in the medical field is limited. This study mainly discusses the treatment of muscle damage based on sports rehabilitation training mesoporous multifunctional nanomaterials in bodybuilding. The biological characteristics of the targeted control of mesoporous multifunctional nanomaterials for target drugs were studied by analyzing the regeneration of skeletal muscles of mice after gastrocnemius strain under computer control. The electrostatic interactions modified by the consensus binding between AS1411 and Dimer-PPTcDA on the surface of mesoporous silicon are used to block the pores, and the release of objective molecules depends on the concentration of the drug in the tendon cells and the time of action. In this system, AS1411 has both the characteristics of the target substance and the active site of the targeted stimulus response in the cell. After FAM is labeled AS1411, the fluorescence of FAM can be used to monitor the release of the drug in real time, so as to directly release the drug to the lesion, maintain local effectiveness, and greatly improve the biological activity of the drug. In addition, in the safety analysis of mesoporous multifunctional nanomaterials on cells, if the concentration of nanoparticles is 90  $\mu\text{g}/\text{mL}$ , the cell survival rate is almost 100%. The results show that the mesoporous multifunctional nanomaterials have low cytotoxicity and cell activity is not affected. The smaller the particle size of mesoporous silicon, the easier it is to invade the focus cells. In addition, confocal microscopy imaging has also effectively demonstrated the targeting effect of mesoporous multifunctional nanomaterials on cells.

## 1. Introduction

In recent years, great progress has been made in the application of nanotechnology and its biomedical or chemical sensing fields. Due to the special advantages of inorganic nanoparticles, many functional nanomaterials have gradually expanded from traditional organic-based nanomaterials to hybrid nanocomposite materials.

As a porous material, the mesoporous multifunctional nanomaterials have extremely high loading efficiency for drugs due to their large and uniform pore size, and the mesoporous multifunctional nanomaterials have wide applications in many fields. The nature of its catalytic drugs will make it highly valuable in medicine.

Molecular imaging is not only widely used as an important detection technology for cancer diagnosis in the field

of medical imaging, but also as a treatment method for cancer in recent years. Yanyan believes that multifunctional carbon-based nanomaterials (MCBNs) with unparalleled optical, electronic, and thermal properties have attracted more and more interest and show the greatest hope in the field of biomolecular imaging and therapy. Therefore, carbon-based nanomaterials have a large number of potential applications in the field of biomedicine, such as bioimaging, drug delivery, and tumor treatment [1]. His research only stayed at the theoretical level and did not use experimental exploration. Sustainable and cost-effective energy production has become the key to meeting current energy needs. Paul believes that a cheap, scalable, efficient, and reliable catalyst must be developed. Carbon-based heteroatom-doped 3D and mesoporous electrodes are very promising as catalysts for electrochemical energy conversion and storage.

Various carbon allotropes doped with various heteroatoms can be used to mass-produce electrode materials cost-effectively. 3D porous carbon electrodes have many advantages, such as 3D conductive paths for efficient electron transport and porous channels that promote electrolyte diffusion. However, synthesizing and functionalizing isotropic 3D carbon structures are challenging. He summarized various synthetic processes of 3D porous carbon materials to understand their physical and chemical properties [2]. His research did not give a specific process for storing energy by doping carbon-based heteroatoms. Carbon-based nanomaterials have been developed for photothermal cancer treatment, but it is still a huge challenge to manufacture their multifunctional counterparts with simple methods, good biocompatibility and dispersion, and efficient cancer therapeutic methods. Li et al. have developed an alternative multifunctional nanopatform based on carbon silica nanocapsules, which have gold nanoparticles (Au @ CSN) in the cavity for cancer treatment. The encapsulated chemical doxorubicin can be released from Au @ CSN with mesoporous and hollow structure in the manner of near-infrared light and pH stimulation, which is beneficial to spatio-temporal treatment to reduce off-target toxicity. Nanocapsules with efficient photothermal conversion and excellent biocompatibility have achieved synergy between photothermal and chemotherapy [3]. Exercise under hypoxic conditions represents additional stress associated with normoxia. Santos believes that hypoxia can induce inflammation of oxidative stress, which may increase after exercise. In addition, vitamin E supplementation may reduce oxidative stress and inflammation caused by hypoxia during exercise. He evaluated the effect of vitamin E supplementation (250 mg) on inflammatory parameters and cell damage after simulated hypoxia exercise at an altitude of 4200 m. Nine volunteers were supplemented with vitamin E 1 hour before exercise and performed three 60-minute exercises (maximum oxygen uptake 70%) under normoxia, hypoxia, and hypoxia for a week. Blood was collected before exercise, after exercise, and 1 hour after exercise to measure inflammation parameters and cell damage [4]. His research only judged the effect of oxygen content on body health and did not analyze the exercise time in detail.

In this study, the targeted characteristics of mesoporous multifunctional nanomaterials were used to treat the injured parts in the bodybuilding process in a timely manner, which improved the activity of the drugs and quickly recovered the injured parts.

## 2. Mesoporous Multifunctional Nanomaterials

*2.1. Advantages of Mesoporous Multifunctional Nanomaterials.* The particle size of mesoporous multifunctional nanomaterials and ribose proteins, natural carriers, etc., and the structure of the hydrophilic polymer shell of ordinary long-circulating nanoparticles are difficult to be rejected by cells [5]. The PEG surface of the mesoporous multifunctional nanomaterials and the hydrophilic chain of PEO make it have good flexibility and can pass through the space with sufficient plasma density. Its

conformation is formed to prevent the aggregation of particles. Therefore, stable mesoporous multifunctional nanomaterials will spend a lot of time on cycling. The CMC of polymers is usually low (approximately 5–10 MOL), so the entire nanosystem has very high thermodynamic stability. The activity of mesoporous multifunctional nanomaterials is shown as follows:

$$V\% = \frac{[A]_{\text{sample}} - [A]_{\text{blank}}}{[A]_{\text{positive control}} - [A]_{\text{blank}}} \times 100\%. \quad (1)$$

where  $[A]_{\text{sample}}$  is the sample quality,  $[A]_{\text{blank}}$  is the quality of the blank control, and  $[A]_{\text{positive control}}$  is the corresponding positive control. In addition, mesoporous multifunctional nanomaterials are mainly used for intravenous injection. The thermodynamic (depolymerization potential energy) and kinetic (depolymerization rate) stability of polymer micelles after intravenous injection and vascular dilution must also be considered. The mesoporous multifunctional nanomaterials must be stable enough to avoid sudden drug release and must exist in the form of nanoparticles for a relatively long time to ensure that their concentration in the target area is sufficiently high [6]. The critical mesoporous multifunctional nanomaterial concentration indicates that when the monomer concentration is lower than this value, the nanoparticles begin to decompress, but due to the dynamic stability, the decompression speed of the nanomaterial particles is determined. However, many binary block copolymerized nanoparticles have excellent kinetic stability and will slowly dissociate the monomer after large-scale dilution. Therefore, the polymer nanoparticles will be diluted below the monomer CMC after intravenous injection, but due to their kinetic stability, they are suitable for drug delivery. This is also the biggest difference between high-resolution mesoporous multifunctional nanomaterials and ordinary small-molecule surfactants [7, 8].

*2.2. Nanodrug Carrier.* For the present, mesoporous multifunctional nanomaterials have many advantages, such as proper improvement of drug dynamics and biological distribution, improvement of biodiversity, and reduction of side effects. However, the method of further achieving the localization and release of drugs at the injured site is still a compelling research topic. Localized medications have high specificity for the injured site, which can reduce the dosage to a certain extent, but will be limited by the injury. Systemic administration is still the preferred method of administration for most types of muscle damage. Therefore, the discovery of drug or gene release strategies at the site of muscle injury is the focus of nanomaterial development. Compared with previous drug preparations, nanodrug carriers have many advantages [9].

- (1) Optimized drug delivery path: nanodrug carrier strengthens the drug delivery mode, multilayer carrier structure, and surface hydrophilic layer, to avoid the immune elimination of nanodrug carrier after entering the body, achieve long-term drug circulation, and shorten the drug delivery time.

- (2) Controlled release: the advantage of the size of the nanomaterials carrying the drug is that it can slowly release the drug at the targeted site through the intercellular space and through the blood-brain gate. In terms of corresponding drug treatment, targeted ligands are transplanted to the surface and bind to receptors in different tissues to achieve targeted control and drug release [10].
- (3) Reduce toxicity: encapsulating drugs in a closed environment through nanodrug carriers can improve the stability of the drugs to the external environment, prevent the drugs from decomposing before reaching the lesion, and reduce the systemic drug concentration. Controlled release can also maintain a stable drug concentration in the blood and reduce drug toxicity and side effects [11].
- (4) Improving absorption: nanodrug carriers are mostly carried to cells through the terminal nervous system, which can improve the transparency of the cell membrane and the compatibility of the compound during transportation, increase the absorption rate of the drug, and make the absorption efficiency of the drug larger. At this time, statistics on drug absorption and drug loading are required [12]:

$$EE\% = \frac{C_{\text{sample}} \times V}{M_{\text{drug}}} \times 100\% + C_{\text{sample}} \times V_{\text{min}}, \quad (2)$$

$$DL\% = \frac{C_{\text{sample}} \times V}{(C_{\text{sample}} \times V + M_{\text{micelle}})} \times 100\%. \quad (3)$$

where  $C_{\text{sample}}$  is the DOX concentration measured with drug-loaded nanoparticles, the unit is  $\mu\text{g/mL}$ , and  $EE\%$  represents the osmotic pressure value of nanoparticles. After analysis, the volume of a certain volume is  $V$ .  $M_{\text{micelle}}$  is the total dosage and the unit is  $\mu\text{g}$ .  $DL$  is the component, and the corresponding unit is  $\text{g}$ .

Ultraviolet spectrophotometry and high-speed liquid tomography are the two most commonly used methods for drug analysis in vitro. The biggest advantage of high-speed liquid tomography is that it can separate and detect multicomponent samples online [13, 14]. However, because the components need to be separated before detection during the detection process, the analysis time of HPLC is long, the device requirements are high, and the analysis cost is high, avoiding environmental problems caused by the use of mobile phases. The advantages of UV spectrophotometry include high-speed analysis and high sensitivity. However, in multicomponent sample analysis, other components may hinder the measurement of existing components, so there are restrictions. The absorbance of each sample is measured using an ultraviolet-visible spectrophotometer. The release curve of DOX is the vertical axis with the release rate and the horizontal axis with the time. The calculation formula of the corresponding release rate  $Er$  is as follows:

$$Er = \frac{V_{\varepsilon} \sum_{i=1}^{i-1} C_{i-1} + V_0 C_i}{m_{\text{drug}}}, \quad i \geq 1. \quad (4)$$

where  $V_{\varepsilon}$  is the amount of replacement of the buffer storage solution,  $V_0$  is the volume of the solution in the remote sink tube and the corresponding drug concentration in the solution released during the replacement sampling is  $C_i$  ( $\text{mg/mL}$ ); the amount of drug in the micelle that delivers the drug for release is  $m_{\text{drug}}$   $\text{mg}$ .

### 2.3. Modification of Mesoporous Multifunctional Nanomaterials

**2.3.1. Plasticity Characteristics.** After plasticization, the tensile strength and bending elastic modulus of nanomaterials will increase. In recent years, plasticizers used include polyethylene glycerin, alanine ester, and glucose monosaccharide. These plasticizers have good biocompatibility. People perform experimental evaluation of physical properties and improve thermal analysis of nanomaterials, such as studying the specific functions of various plasticizers such as compression elasticity, elastic modulus, and glass transition temperature. According to many investigations, mesoporous multifunctional nanomaterials are relatively general plasticizers. Adding 5% of polyethylene glycerol to nanomaterials will greatly improve the physical properties of the material, and the glass transition temperature will drop from fifty degrees to ten degrees [15].

**2.3.2. Denaturation of Copolymer.** With the development of polylactic acid, the demand for higher compressive strength and hydrophilicity of polylactic acid has been studied; clinical medicine needs multiple lactic acid carriers to meet the needs of drug controlled release systems to control the decomposition rate of various drugs. Polylactic acid is a part of monomers synthesized by recondensation or ring-opening polymerization in a specific ratio, the characteristics of mesoporous multifunctional nanomaterials will be improved, and some new monomers can be obtained. Due to the fusion of poly (lactic acid) molecular structure, usually polyethylene (lactic acid) is copolymerized with mesoporous multifunctional nanomaterials [16].

**2.4. Effect of Mesoporous Multifunctional Nanomaterials on Drug Release.** Mesoporous multifunctional nanomaterials can also release drugs when the structure changes. Structural changes are the most important properties of nanogels. The stimulus response of nanogels will affect their structural changes with temperature changes, causing their particle size to change almost. When the mesoporous multifunctional nanomaterials are stimulated and swelled in the environment, the amount of swollen drug will be released from the gel, or the nanogel will be stimulated and contracted in the environment. As the nanogel shrinks, the loaded drug

molecules will accumulate and dissociate. The molecules will accumulate and dissociate. Different parts of the body have different pH values. The normal physiological environment of the human body is about 7.5, the pH of the tumor tissue is about 6, and the internal terminal system of the tumor cell has three to four different pH adaptation values. Therefore, the nanogel can be used as a control for tumor treatment according to the sensitivity of reduction to pH use at release point. As a polymer of core-N, N-lysine, and N-isopropanol acrylamide, the loaded DOX mesoporous multifunctional nanomaterial (NLSC-NG) created the acidity of the pH value of the nanogel of the reactive shell surroundings. According to the corresponding structure, if the drug kills the cells, the part of the structure that does not expand will retain the contraction function and can improve the transparency of infected cells and solid tumors. Due to the huge difference in GSH content between tumor cells and normal cells, reduced mesoporous multifunctional nanomaterials can also be prepared by adjusting the receptive controlled release point of drugs [17, 18].

**2.5. Skeletal Muscle Injury.** Muscle injuries mostly occur in daily sports and sports, especially in professional athletes engaged in bodybuilding. Not only muscle injuries but also the incidence of disease is very high, the initial lack of function and structure, damage, muscle atrophy, restraint shrinking, pain, followed. Training and competition will also be affected. Now, the diagnosis of muscle damage mainly depends on the clinical symptoms, so the image examination is usually only a rough guess at the specific injury site and the injury site. The scope of ultrasound is widely used in the diagnosis of muscle injury, but the recovery and prognosis evaluation have not been widely used afterwards. The contrast ultrasound used for muscle injury is very few, but there is a small amount of muscle ultrasound repair process. However, there is a small amount of application of contrast ultrasound evaluation in the repair process of muscle damage [19].

Physiological skeletal muscle injuries can be divided into trimming injuries (fractures of tendon fibers and muscle-associated tissues) and muscle fiber injuries. In daily life, muscle pressure, muscle mass, nutritional status, training style, and balance of muscle strength all affect the occurrence of muscle damage. After the skeletal muscle injury and repair process begins, it can be divided into the following two stages [20, 21]:

- (1) Injury stage: muscle injury due to various reasons, local hematoma formation, rupture of myofibrillar membrane, cell mass calcium overflow, increased calcium ion concentration in tissue fluid, activation of calcium-dependent protease and obstruction of mitochondrial respiratory function, and necrotic sites continuous damage. If the tissue is inflamed, macrophages will gather at the injury site and devour the diseased tissue [22].
- (2) Repair stage: after muscle damage, the relevant stimulation signals are released, cell growth factors

are secreted, and skeletal muscle satellite cells in the resting phase near the injury site are activated. The activated satellite cells transfer to the injury site and begin to proliferate. Some of them are the differentiation of muscle cells to form muscle tubes, which eventually merge with muscle fibers that have not been damaged before to form new lines. The proliferating satellite cells differentiate into fibroblasts, invade the extracellular space of tendon fibers, secrete extracellular matrix, form a tissue framework, and restore the connection between tendon fibers and bound tissues. At the same time, the new muscle tissue angiogenesis occurs. In this process, the damaged part is too large, and excessive proliferation of fibroblasts will produce a lot of tight coagulated tissue, hinder muscle regeneration, and form permanent muscle necrosis. Therefore, after muscle injury, in order to avoid muscle tension, it is necessary to reduce activity and affect the repair of muscle injury.

**2.6. Sports Rehabilitation Training.** Reasonable aerobic exercise will improve the physical condition. For patients with cardiopulmonary system, with proper diet, cardiovascular function will be normal, body fat rate will decrease, and blood fat content will decrease. Improved blood pressure and insulin sensitivity can be achieved with the goal of improving the prognosis of coronary artery disease. During exercise, the blood volume of the heart increases, the pressure of the heart increases, the blood pressure during the left ventricular dilatation increases, the subendocardial blood flow increases, the heart rate and blood pressure decrease, and the myocardial oxygen consumption decreases, thereby improving myocardial ischemia to achieve goodness purpose. On the other hand, resistance training will improve the basal metabolic rate, increase muscle mass, and reduce the proportion of body fat. After training, muscle strength and endurance will improve, and patients return to daily life, which is also helpful for work. By stretching joints and ligaments, flexible training can expand the movement area of the joints and prevent injuries to the extensive movement areas of the joints during exercise.

### 3. Muscle Injury Treatment Experiment

**3.1. Experimental Reagents.** The experimental reagents and names used in the experiment are shown in Table 1. The aseptic operation was strictly observed during surgery. Mice were anesthetized with cyclophospholipids (100 mg/kg). After the rats were successfully anesthetized, the parameter changes on both sides of the muscles they contacted were measured. After disinfection, 10% ethanol solution was used to collect the sterilized muscle cells for use.

**3.2. Experimental Materials.** The selected mice are all male mice, with a body weight ranging from  $30 \pm 2$  g, and reared for 3-4 weeks. Water and food were provided for 4 weeks, and the temperature was kept at  $25\text{--}30^\circ\text{C}$  under natural light.

TABLE 1: Experimental reagents and names used in the experiment.

Number	Reagent name	Manufacturer
1	0.5% saline	Celestial creature
2	10% chloral hydrate	Chenxin Pharmaceutical Company
3	Hematoxylin staining solution	Qingdao Yulong Company
4	SuperECL Plus luminous liquid	Beijing Biotechnology Company

The mice were observed for a week before the experiment. The experiment was started after getting used to the environment.

**3.3. Experimental Modeling.** After abdominal anesthesia with 3% pentbalbiteru sodium (0.3 ml/kg), the skin was prepared for incision on both lower limbs. After disinfecting with alcohol and iodine, the mouse was laid on a sterile operating table. A longitudinal incision was made at the distal end of the gastrocnemius muscle (about 4 cm in length), taking care to separate the distal gastrocnemius tendon. The data connection instrument was used for parameter determination and was fixed at one end of the universal material tester. The distal tendon of the lower leg was held with vascular forceps and the tension sensor of the universal material testing machine was connected. Under the control of the computer, the gastrocnemius muscle is stretched at a speed of 4 cm/min, and the stretching load curve is recorded at the same time. When the curve ball reaches the highest point, the power was turned off immediately, so that the muscles are in a relaxed state. The vascular forceps and towel forceps were disinfected, and the fascia and skin were sterilized layer by layer after disinfecting the wound.

**3.4. Experimental Grouping.** 140 adult SD rats were selected and randomly divided into 7 groups. The rats are grouped as follows:

- (1) Blank control group (group A,  $n = 20$ ): regular feeding without intervention.
- (2) Immediate group (group B,  $n = 20$ ): a sample was taken immediately and checked according to the rat's acute gastrocnemius animal model
- (3) The first week's group (group C,  $n = 20$ ): according to the animal model, the test was conducted after one week of feeding.
- (4) Natural cure group (group D,  $n = 20$ ): the animal model of the acute system of the gastrocnemius of rats is caused by a normal diet without exercise intervention and natural cure. According to different sampling time, the samples are divided into 4 different control groups.
- (5) Drug treatment group (group E,  $n = 20$ ): an animal model of acute gastrocnemius strain of mice was made, and dynamic stimulation was performed during the recovery period. According to different sampling times, they are divided into 4 groups.
- (6) The medicament group using mesoporous multifunctional nanomaterials as a carrier (group F,  $n = 20$ ): the animal model of the acute system of the gastrocnemius of rats is caused by the stimulation of eccentric exercise during the recovery period. According to different sampling times, they are divided into group a, group b, group c, and group d.
- (7) Combination group (exercise method plus mesoporous multifunctional nanomaterial drug carrier) (group G,  $n = 20$ ): induced acute gastrocnemius muscle distortion in mice, and increased central body and centrifugal stimulation during the recovery period. According to different sampling time, the samples are divided into M group, N group, P group, and Q group.

**3.5. Drug Release Control.** At 37°C, 120 mL of phosphate-buffered saline (PBS) solution was added to the beaker, and then a dialysis bag ( $M_n = 14000$ ) containing 5 mL of the same buffer solution and 10 mg of drug-loaded micelles was submerged. The drug release behavior was studied under different conditions (pH or reducing agent). In a prescribed time gradient, the release solution was replaced with PBS solution, and the drug release rate was measured using a drug measuring instrument.

**3.6. Determination of Encapsulation Rate and Drug Loading.** The encapsulation efficiency of liposomes in this study was determined by the centrifugal membrane filtration method. An appropriate amount of collected muscle cell solution was taken and centrifuged at 500 r/min for 15 min. The resulting supernatant was filtered with a 0.22  $\mu\text{m}$  filter. An appropriate amount of filtrate was diluted with methanol, and the drug content in the filtrate was measured by HPLC to obtain the amount of drug encapsulated in the liposome; the original solution of muscle cells was taken to break the emulsion with quantitative methanol, and the total dose was determined by HPLC.

**3.7. Determination of Drug Load.** During the experiment, the centrifugal membrane filtration method was used to derive the drug encapsulation rate. Take an appropriate amount of muscle cell solution and centrifuge at 500 r/min for 5 minutes. Use 0.11  $\mu\text{m}$  membrane to filter the resulting clean. Dilute the stock solution containing muscle cells and record the drug content. The original muscle cell solution was emulsified with quantitative methanol, and the total dosage was determined by HPLC.

3.8. *Statistical Analysis.* Prism 5.0 was used for the analysis of the original dispersing solution, Dunnett's test was used for comparison between each group and control group, and *T*-test was used for comparison between each group. This difference was considered statistically significant at  $p < 0.05$ .

#### 4. Analysis of Muscle Injury Treatment

4.1. *Muscle Injury Treatment Results.* Muscle healing in different groups is shown in Figure 1. Blood samples were collected from the drug treatment group, mesoporous multifunctional nanomaterials as the carrier, and the combination group at different time gradients. Serum was separated to detect CK concentration, and the average CK content of the three groups of mice was determined. After 24 hours of cell transplantation injury self-healing group and treatment group, serum CK levels increased significantly. After 3 days, the CK group decreased, and the cell transplantation in the combined group was reduced compared with the drug treatment group. After 5 days, the cell transplantation in both groups decreased and the CK level decreased, and the cells with muscle damage decreased further. After 7 days, the CK content of the two groups decreased steadily. The cell damage self-recovery group was always lower than the cell damage cell content of the CK treatment group, and the muscle tissue of the mice had near-normal adrenaline kinase. The increase of CK content indicates that the muscle tissue has been damaged, but the transplantation of muscle satellite cells has greatly reduced the CK content. The damage of the muscle tissue has not continued to expand and has been effectively repaired. The content of CK is stable and tends to be close to the normal value. This indicates that the damage of the mouse's muscle tissue has been improved. The results of MCF-7 cell uptake indicate that intracellular drug uptake increases over time. However, the absorption of free DOX at a given time is much lower than the absorption of nanoparticles incorporating a drug. Quantitative cell uptake results for 24 hours. The intake rates of MCF-7 for CSO-SA/DOX and CSO-FBA-SA/DOX nanoparticles were the same ( $p > 0.1$ ) and free DOX ( $p < 0.05$ ). This is caused by the strong affinity of the mesoporous multifunctional nanomaterial hydrophobic aliphatic chain membrane and the effective invasion of cells during the active drug transport through the nanoparticles.

In this study, an LC-MS/MS analysis method for the determination of TID-101 in rat plasma was established. After methodological investigation, this method is fast, sensitive, and specific and can meet the needs of pharmacokinetic research. The drug concentration at different times is shown in Table 2. TID-101 showed a good linear relationship between 100 and 3000 ml ( $r^2 = 0.9996$ ), the sample recovery rate was in the range of 83%–86% (all RSD  $< 15\%$ ), and the matrix effect was in the range of 89.62%–91.92%. Within RSD  $< 15\%$ , it meets the requirements of biological samples. The intraday and interday precision (RSD) are less than 15%, the stability of the sample during storage and analysis is good, and the relative error RE is reasonable. The pH responsiveness of mesoporous multifunctional nanomaterials is determined by the measurement of the change of

the average hydrodynamic diameter at different pH values. The ATRP method is used to design functional polymer drug carriers and their controlled release behavior. When the pH is maintained at 3–4, the mesoporous multifunctional nanomaterials maintain a low Dh; when the pH increases to 5–6, Dn shows a linear growth trend; when the pH is higher than 6, Dh increases significantly. The reason is attributed to the pH responsiveness of the PAA block. This phenomenon not only reveals the pH-responsive characteristics of mesoporous multifunctional nanomaterials, but also shows its potential as a smart drug carrier.

4.2. *Targeted Therapy Analysis of Mesoporous Multifunctional Nanomaterials.* The drug release image obtained after the mesoporous multifunctional nanomaterial-loaded drug released in PBS buffer at pH = 7.5 for 15 days is shown in Figure 2. It can be seen from the figure that the drug release process can be divided into two stages of rapid release and stable and slow release. The release amount of TNT samples in the rapid release stage was about 88.7%, which lasted 5 hours, and the release amount of TNTs-P25 samples at this stage was about 79%. The proportion of the drug release amount in the rapid release stage after modification of P25 decreased. At this stage, the drug IBU attached to the mesoporous multifunctional nanomaterial is released. After 5 h, it is the slow release phase of the drug, which releases ibuprofen adsorbed inside and deep in the nanotubes and lasts longer. Comparing the release curve of the unmodified P25 sample, it can be seen that the P25 sample was modified by hydrothermal treatment. During the slow release stage, the amount of drug released increased significantly, which may be because the specific surface area and the roughness of the wall of the mesoporous multifunctional nanotube array after P25 modification were greatly increased, which was more conducive to the adsorption of drugs and the inside of the tube and the wall. The release of the drug has a delayed effect, and the total drug release has increased by 33%, which further shows that the modified mesoporous multifunctional nanomaterials are more conducive to the adsorption of the drug, which is consistent with the results of the previous analysis.

The release behavior of CLB and DOX from the mesoporous multifunctional nanomicelle combined drug delivery system under different conditions is shown in Figure 3. When GSH is not added, both CLB and DOX are slowly released, and the cumulative release of CLB is less than 6% within 200 minutes, basically not released, and the release of DOX is relatively fast, nearly 18%; when 3SH of GSH is added, the release rate increased slightly, reaching 9% and 23%, respectively. When 10.0 mol MGSH was added, the release of DOX increased rapidly, reaching a maximum release rate of 86.5% at 50 min, CLB was also released quickly at 30–90 min, and the maximum cumulative release rate was 85.6%. The results show that the constructed mesoporous multifunctional nanomicelle combined drug delivery method has obvious reduction sensitivity. Doxorubicin enters the core of the carrier through physical embedding and is first released relative to the CLB integrated into the

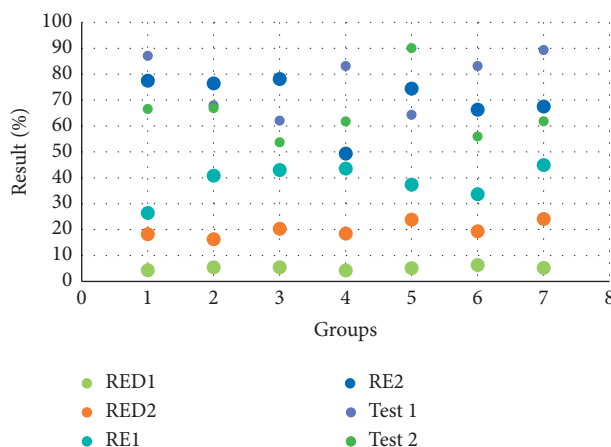


FIGURE 1: Muscle healing in different groups.

TABLE 2: Drug concentration at different times.

Test drug	Concentration	Daytime			Within days		
		Determination of concentration	RED	RE	Determination of concentration	RSD	RE
TID-101	40	$35 \pm 2$	6.2%	-3.9%	$37 \pm 2$	5.8%	-4.2%
	400	$320 \pm 50$	2.6%	-4.8%	$330 \pm 50$	2.3%	-5.1%
	4000	$3200 \pm 100$	2.7%	-6.6%	$3200 \pm 200$	2.5%	-8.0%

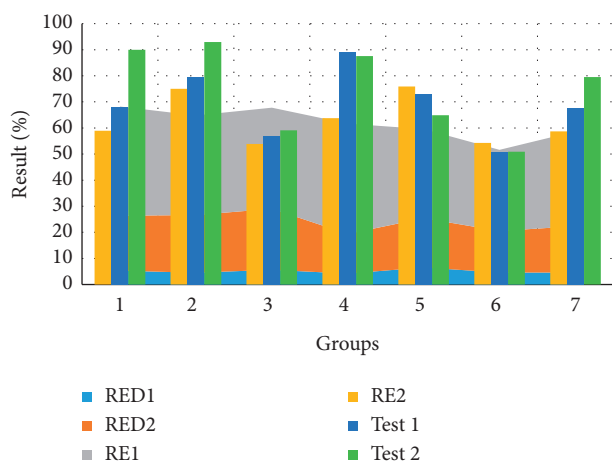


FIGURE 2: Drug release images obtained by mesoporous multifunctional nanomaterials loaded with drugs.

carrier through chemical bonds. At the same time, the release rate of the two under physiological conditions is very low, and the drug delivery system shows good stability. When reaching the injured muscle, both are released quickly under reducing stimulation. The mesoporous multifunctional nanomicelle lyophilized powder was configured into 1 mg/mL, 2 mg/mL, and 5 mg/mL solutions with water, and all samples were placed in a constant temperature steam bath shaker (25°C) and shaken at a constant speed for 10 h and then statically placed for 3 h (room temperature), and the particle size of the drug-loaded micelles was measured by a dynamic laser light scattering instrument. The average

particle size was 11.2 nm, 15.4 nm, and 13.5 nm, respectively. The values of polydispersity index (PDI) are 0.4, 0.3, and 0.5 in order. Because TAT polypeptide can effectively bind to the nuclear transporter on the nuclear membrane, drugs mainly modify the TAT polypeptide on the surface of mesoporous silicon by covalent bond modification to achieve the nuclear fusion effect. The results show that the smaller the particle size of mesoporous silicon, the easier it is to enter the cell nucleus, and the confocal microscopy imaging effectively proves the targeting effect of mesoporous multifunctional nanomaterials on the cell nucleus.

**4.3. Safety Analysis of Mesoporous Multifunctional Nanomaterials on Cells.** The survival rate of cells under the environment of mesoporous multifunctional nanomaterials is shown in Figure 4. As a carrier material for drug delivery, mesoporous multifunctional nanomaterials have good biocompatibility and will not destroy the normal structure of cells. Cytotoxicity tests are commonly used to evaluate the safety of mesoporous multifunctional nanomaterial carriers on cells. Therefore, in the nanoparticle transport and absorption experiments, different concentrations of 100  $\mu\text{g}/\text{mL}$  nanoparticles were used. The cell safety of mesoporous multifunctional nanomaterials and pSLN particles with different modification ratios was investigated by using the tetrazolium blue colorimetric method (MTT assay). MTT method is used for cytotoxicity detection. Exogenous pigments are produced in the mitochondria of living cells under the reduction of succinate dehydrogenase to produce water-insoluble purple crystalline methylamine, which is positively correlated with the number of cells. Formazan can be

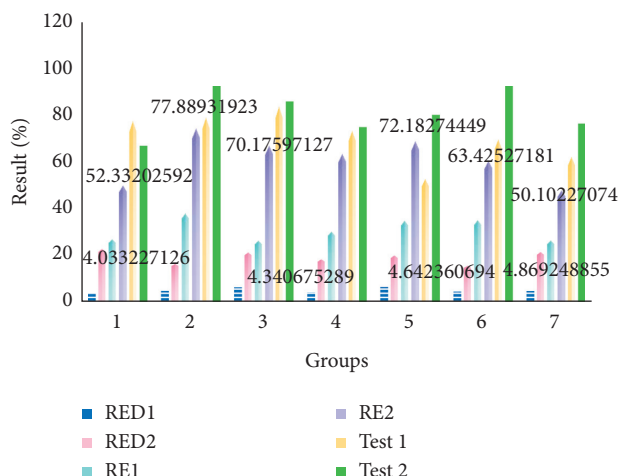


FIGURE 3: Simultaneous release behavior of CLB and DOX from the mesoporous multifunctional nanomicelle combined drug delivery system under different conditions.

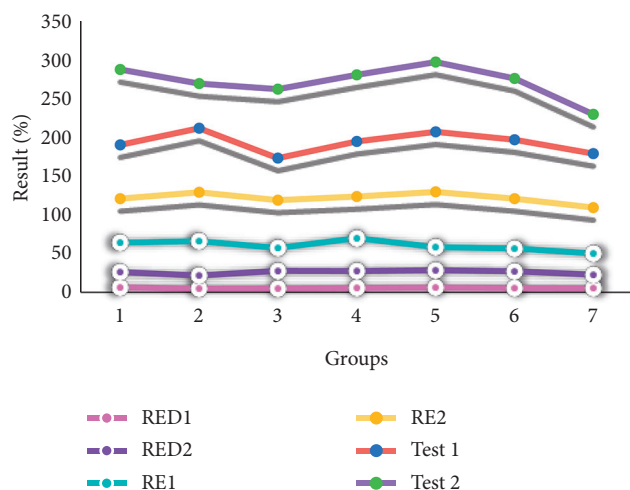


FIGURE 4: Cell survival rate in the environment of mesoporous multifunctional nanomaterials.

dissolved in DMSO, and the photometric value of cell transport studies of lipid-absorbing nanocarriers and PEG-modified lipid nanocarriers can be measured by enzyme-linked immunoassay at a wavelength of 570 nm, which can indirectly reflect cell growth and proliferation activity. By the MTT method, the half lethal amount of SLN and pSLN muscle cells can be measured about 300  $\mu\text{g}/\text{ml}$ . In addition, as the modification ratio of mesoporous multifunctional nanomaterials increases, the cytotoxicity of the carrier decreases. The results show that the mesoporous multifunctional nanomaterials have low cytotoxicity. When the nanoparticle concentration is 90  $\mu\text{g}/\text{ml}$ , the cell survival rate is close to 100%, and the cell activity is not affected.

In addition, when the sustained drug release time exceeds 72 h, some drugs are still released, which shows that the mesoporous multifunctional nanomaterials can significantly prolong the circulation time of the drug, reduce the

probability of the drug being degraded in the body fluid circulation and reduce the toxicity caused by the high concentration of drug and side effects, and improve drug efficacy. Comparing the drug release of  $\beta$ -HPC/GFT at two pH values, the release rate is faster than the neutral pH 7.4 under the condition of low pH 5.0, which shows that the drug release depends on pH, and this pH-dependent release behavior is beneficial to drug release in the lysosome and muscle damaging environment. Therefore, we can imagine that the cationic polymer engulfed into the cell through the cell released the drug in the acidic lysosome of the cell, and due to the “proton sponge efficiency” of the mesoporous multifunctional nanomaterials, the lysosomal membrane was broken, and thus, the drug was released into the cytoplasm to play a role.

**4.4. Rehabilitation Intervention of Sports Training on Muscle Injury.** Sports training refers to various buffering actions that the human body gradually changes from a tense action state to a relatively quiet state. The quality of relaxation activities is directly related to the improvement of sports and fitness levels in the process of physical health. After exercise, relax activities, eliminate fatigue, adjust internal organs, and bring good effects to mental relaxation. Although relaxing and organizing activities have a very important role and significance in improving sports ability, in actual teaching and training, they often do not attract enough attention and are usually only optional. Psychological factors are an indirect factor to avoid or reduce sports injuries. If sports injuries occur during bodybuilding training, there must be corresponding psychological fear and psychological fatigue. If they cannot be eliminated in time, it will have a negative impact on the recovery of sports injuries. Therefore, the rational use of the organic combination of muscle relaxation and psychological relaxation can better promote the elimination of physical fatigue.

## 5. Conclusions

This study explored the drug loading function of nanocapsules. First, it shows high loading capacity and efficiency. Secondly, under different pH and reducing agent conditions, the release behavior shows a great difference, and the content of the drug also changes dynamically with pH, proving the existence of pH and reduction reactivity.

At present, mesoporous multifunctional nanomaterials have many advantages, such as proper improvement of drug dynamics and biological distribution, improvement of biodiversity, and reduction of side effects. However, the method of further achieving the localization and release of drugs at muscle injury sites is still a compelling research topic. The specificity of local drug damage is high, and the dosage can be reduced to a certain extent, but it will be limited by the damage category. Systemic administration is still the preferred method of administration for most types of muscle damage. Therefore, targeted therapy at the site of muscle injury is the focus.

The nanodrug carrier encapsulates the drug in a closed environment, which can improve the stability of the drug to the external environment, prevent the drug from decomposing before reaching the lesion, and reduce the systemic drug concentration. Controlled release can also maintain a stable drug concentration in the blood and reduce drug toxicity and side effects. Cytotoxicity indicates that it is very safe for cells. Mesoporous multifunctional nanomaterials will become the focus of medical development.

## Data Availability

The data used to support the findings of the study are available from the corresponding author upon request.

## Conflicts of Interest

The authors declare that they have no conflicts of interest.

## References

- [1] Z. Yanyan, W. Minghao, W. Mingjie et al., "Multifunctional carbon-based nanomaterials: applications in biomolecular imaging and therapy," *Acs Omega*, vol. 3, no. 8, pp. 9126–9145, 2018.
- [2] R. Paul, F. Du, L. Dai et al., "3D heteroatom-doped carbon nanomaterials as multifunctional metal-free catalysts for integrated energy devices," *Advanced Materials*, vol. 31, no. 13, Article ID 1805598, 2019.
- [3] L. Li, C. Chen, H. Liu et al., "Cancer therapy: multifunctional carbon-silica nanocapsules with gold core for synergistic photothermal and chemo-cancer therapy under the guidance of bimodal imaging (advanced functional materials 24/2016)," *Advanced Functional Materials*, vol. 26, no. 24, pp. 4252–4261, 2016.
- [4] S. A. Santos, E. T. Silva, A. V. Caris et al., "Vitamin E supplementation inhibits muscle damage and inflammation after moderate exercise in hypoxia," *Journal of Human Nutrition and Dietetics*, vol. 29, no. 4, pp. 516–522, 2016.
- [5] L. Zhang, T. Liu, and Y. Chen, "Magnetic conducting polymer/mesoporous SiO<sub>2</sub> yolk/shell nanomaterials: multifunctional nanocarriers for controlled release of doxorubicin," *Rsc Advances*, vol. 6, no. 11, pp. 8572–8579, 2016.
- [6] M. Marisa and S. Miriam, "Multifunctional nanomaterials: design, synthesis and application properties," *Molecules*, vol. 22, no. 2, p. 243, 2017.
- [7] W. Gong, Z. Hu, and Y. Liang, "Graphene-based multifunctional nanomaterials in cancer detection and therapeutics," *Journal of Nanoence & Nanotechnology*, vol. 18, no. 8, pp. 5155–5750, 2018.
- [8] L. Qiu, Z. He, and D. Li, "Multifunctional cellular materials based on 2D nanomaterials: prospects and challenges," *Advanced Materials*, vol. 30, no. 4, Article ID 1704850, 2018.
- [9] G. Yang, H. Gong, T. Liu et al., "Mesoporous silica-coated WS<sub>2</sub>@Fe<sub>3</sub>O<sub>4</sub> nanosheets as a multifunctional theranostic nanocarrier for combination therapy of cancer," *Nanomedicine Nanotechnology Biology & Medicine*, vol. 12, no. 2, p. 523, 2016.
- [10] Z. Libo, J. Ying, L. Yubin et al., "Mesoporous carbon nanospheres as a multifunctional carrier for cancer theranostics," *Theranostics*, vol. 8, no. 3, pp. 663–675, 2018.
- [11] D. Wang, N. B. Saleh, W. Sun et al., "Next-generation multifunctional carbon-metal nanohybrids for energy and environmental applications," *Environmental Ence and Technology*, vol. 53, no. 13, pp. 7265–7287, 2019.
- [12] A. A. Oun, S. Shankar, and J. W. Rhim, "Multifunctional nanocellulose/metal and metal oxide nanoparticle hybrid nanomaterials," *C R C Critical Reviews in Food Technology*, vol. 60, no. 3, pp. 435–460, 2020.
- [13] T. Wiewelhove, J. Fernandez-Fernandez, C. Raeder et al., "Acute responses and muscle damage in different high-intensity interval running protocols," *The Journal of Sports Medicine and Physical Fitness*, vol. 56, no. 5, pp. 606–615, 2016.
- [14] C. K. Deli, I. G. Fatouros, V. Paschalis et al., "A comparison of exercise-induced muscle damage following maximal eccentric contractions in men and boys," *Pediatric Exercise Science*, vol. 29, no. 3, p. 316, 2017.
- [15] O. Eisuke and T. Yosuke, "Eicosahexanoic acid (EPA) and docosahexanoic acid (DHA) in muscle damage and function," *Nutrients*, vol. 10, no. 5, p. 552, 2018.
- [16] De Anta-Díaz, Belén, J. Serralta-Gomis, A. Lizaur-Utrilla et al., "No differences between direct anterior and lateral approach for primary total hip arthroplasty related to muscle damage or functional outcome," *International Orthopaedics*, vol. 40, no. 10, pp. 2025–2030, 2016.
- [17] n P. AbiÁ, J. Del Coso, and J. J. Salinero, "Muscle damage produced during a simulated badminton match in competitive male players," *Research in Sports Medicine*, vol. 24, no. 1, pp. 104–117, 2016.
- [18] J. Del Coso, M. Valero, J. José Salinero et al., "ACTN3 genotype influences exercise-induced muscle damage during a marathon competition," *European Journal of Applied Physiology*, vol. 117, no. 3, pp. 409–416, 2017.
- [19] M. A. Brown, E. J. Stevenson, and G. Howatson, "Whey protein hydrolysate supplementation accelerates recovery from exercise-induced muscle damage in females," *Applied Physiology, Nutrition, and Metabolism*, vol. 43, no. 4, p. 324, 2018.
- [20] F. Damas, K. Nosaka, C. Libardi et al., "Susceptibility to exercise-induced muscle damage: a cluster Analysis with a large sample," *International Journal of Sports Medicine*, vol. 37, no. 08, pp. 633–640, 2016.
- [21] E. D. Withee, K. M. Tippens, R. Dehen et al., "Effects of methylsulfonylmethane (MSM) on exercise-induced oxidative stress, muscle damage, and pain following a half-marathon: a double-blind, randomized, placebo-controlled trial," *Journal of the International Society of Sports Nutrition*, vol. 14, no. 1, p. 24, 2017.
- [22] M. Malakoutian, J. Street, H. J. Wilke et al., "Role of muscle damage on loading at the level adjacent to a lumbar spine fusion: a biomechanical analysis," *European Spine Journal*, vol. 25, no. 9, pp. 2929–2937, 2016.

## Research Article

# Carbon Nanomaterials in the Treatment of Infectious Bone Defects and Wound Scars after Wushu Fractures

Shenghui Wei,<sup>1</sup> Lei Zou ,<sup>2</sup> Xu Hu,<sup>3</sup> and Qiuming Li<sup>4</sup>

<sup>1</sup>College Chongqing Normal University School of Physical Education and Health Sciences, Chongqing 401331, China

<sup>2</sup>Wuhan Engineering Institute, Wuhan 430080, Hubei, China

<sup>3</sup>Department of Military Basic Training and Force Management of Army Medical University, Chongqing 400038, China

<sup>4</sup>Panlong Primary School, Jiulongpo District, Chongqing 400051, China

Correspondence should be addressed to Lei Zou; [zoulei456@163.com](mailto:zoulei456@163.com)

Received 10 August 2020; Revised 18 September 2020; Accepted 25 September 2020; Published 22 October 2020

Academic Editor: Tifeng Jiao

Copyright © 2020 Shenghui Wei et al. This is an open access article distributed under the Creative Commons Attribution License, which permits unrestricted use, distribution, and reproduction in any medium, provided the original work is properly cited.

Although modern antibiotics and surgical technology have made great progress, when using carbon nanomaterials to treat bone marrow-induced inflammation after martial arts fractures, how to simultaneously repair bone defects and control wound infections is the current focus of orthopedics research. This paper uses electrospinning technology to develop a carbon nanomaterial based on PLA, HA-g-PLA, and vancomycin. The surface morphology, biocompatibility, drug release, and osteogenesis of carbon nanomaterials are studied, selecting animal models to verify its effect in the treatment of osteomyelitis with bone defects and provide new ideas and new methods for the treatment of bone defects complicated by osteomyelitis infection. In this paper, carbon nanofibers containing doxycycline, a small molecule protease inhibitor, were prepared by simple blending. Encapsulation of carbon nanofibers can control the slow release of doxycycline and improve the effect of doxycycline in treating chronic wounds. This article uses two methods to prepare different types of osteomyelitis models and compare them. After injecting saline or bacterial solution, the two groups were sealed with bone wax and the incision was closed; the blank group did not do any treatment. Within 30 days after surgery, the appearance of the left hind limb wound and general signs of infection were closely monitored, body temperature was measured, and blood was collected from the ear veins of experimental animals to analyze the changes in C-reactive protein (CRP) and procalcitonin levels (PCT); X-ray, CT imaging, and histological observation were performed on 14 and 28 days. Studies have shown that when the drug loading of doxycycline increases from 10% to 15%, this is related to the change in properties of the polylactic acid fiber membrane from hydrophobic to hydrophilic caused by the increase in doxycycline drug loading.

## 1. Introduction

In recent years, with the development of social transportation, industry and construction, traffic accidents, and industrial accidents have increased, and the severity and complexity of physical injuries have become higher and higher. It is reported that after martial arts training, osteomyelitis is more likely to develop. This type of injury has large wounds and heavy pollution, coupled with improper early first aid techniques, improper application of internal fixation techniques, etc., which can easily lead to delayed fracture healing and bone and soft tissue infections and gradually develop into chronic osteomyelitis, skin defects,

and sinus formation. Osteomyelitis persists, bone necrosis leaks out, or after repeated surgical debridement, necrotic bone removal, and other reasons, martial arts personnel have bone defects and short limbs. Infective bone defects cannot be cured for a long time, and patients have to bear multiple pressures such as disease pain and economic and mental pressure. This is one of the most complex, tricky, and challenging problems in the orthopedics field.

In the study of foreign researchers in the treatment of infectious bone deficiency after fracture, Soichi randomly divided the rabbits into groups A, B, and C. Group A used TBC and BC to repair bone defects, Group B used TBC combined with BC and bBMP to repair, and Group C used

TBC combined with BC, bBMP, and AB to repair. The conclusion shows that TBC is a good carrier for AB and bBMP. The carbon nanocomposite material can slowly release AB and bBMP at its implantation site [1]. Park retrospectively analyzed the bacteriological characteristics of 32 patients with postoperative chronic infection of femoral shaft fractures and the difficulty and treatment strategies of postoperative femoral shaft fractures. All patients underwent debridement, drainage, internal fixation, and bone extension. Results of 32 cases of infection were confirmed by bacteriological examination before operation, including 20 cases of *Staphylococcus aureus* [2]. Papadia used induction membrane technology to treat 36 patients with infectious bone defects in 37 cases of bone disease, 28 males and 8 females, with an average age of 36 years (range 20–68 years). In the first stage, after removing the internal fixator (for patients with internal fixation), debridement of the infected and necrotic bone tissue and surrounding soft tissues was completed, and the bone defect was repaired [3].

In related domestic research, Guo has developed a new type of antibacterial bone graft substitute that can repair bone defects and inhibit related infections at the same time. This bone composite is prepared by introducing vancomycin (VCM) into nano-hydroxyapatite/collagen/calcium sulfate hemihydrate (nHAC/CSH). The results showed that the VCM/nHAC/CSH composite material performed well in terms of antibacterial ability and bone regeneration. This new type of bone graft substitute should be very promising in the treatment of bone defect-related infections in bone surgery [4]. In order to study how carbon nanomaterials affect infected bone defects, a 3 mm diameter skull defect infected by methicillin-resistant *Staphylococcus aureus* (MRSA) was created in adult female Sprague Dawley rats. Micro-CT analysis showed that the newly formed bone volume fraction (BV/TV) in the defect treated with gelatin/silver significantly increased [5].

In this paper, carbon nanofibers containing both protein and protease inhibitor were prepared. The synergistic effect of protein and protease inhibitor can improve the therapeutic effect of carbon nanofibers on chronic wounds. The preloaded protein chitosan nanoparticles were dispersed into a solution of doxycycline and polylactic acid in hexafluoroisopropanol, electrospinning was performed, and the preloaded particles and doxycycline in the carbon nanofibers were simultaneously embedded inside the fiber. The preloaded particles and doxycycline were uniformly distributed inside the fiber; the protein was continuously released for more than four weeks without burst release, and doxycycline was continuously released for more than two weeks; nanofibers have good cytocompatibility and support cell adhesion and spreading; when carbon nanofibers prepared by this method that simultaneously delivered epidermal growth factor and doxycycline were used for the treatment of back wounds in diabetic rats, they can obtain better treatment than nanofibers that only contain a single drug effect.

## 2. Carbon Nanomaterials in the Treatment of Infectious Bone Defects and Wound Scars after Wushu Fractures

### 2.1. VAN/PLGA Microsphere $\beta$ -TCP Composite Carbon Nanoscaffold for the Treatment of Infectious Bone Defect after Martial Arts Fracture

**2.1.1. Construction of VAN/PLGA Microsphere  $\beta$ -TCP Composite Carbon Nanoscaffold.** 10 ml of chitosan solution was prepared with a concentration of 2% with 1% glacial acetic acid solution. A dropper was used to soak the material slowly and evenly. It was placed in a 37°C oven to dry. This operation was repeated 3 times to make the triphosphate blank stent coated with a layer of positively charged chitosan; the chitosan-coated scaffold was put into a centrifuge tube, and the negatively charged VAN/PLGA sustained-release microspheres were dropped in distilled water suspension at the same time and gently shaken, and slightly shake and mix for 10 minutes. The balls were uniformly adsorbed and filled in the pores of the scaffold and centrifuged at 10 rpm for 5 minutes, and the material was taken out and freeze-dried; then the scaffold loaded with microspheres was soaked in the chitosan solution, and after it is completely soaked and saturated, it was taken out and freeze-dried [6, 7].

**2.1.2. Determination of Porosity of Blank Scaffold, TCS, and EACS.** The porosity of the scaffold refers to the percentage of the pore volume of the scaffold in the apparent total volume of the scaffold. The blank sample can be calculated according to the actual parameters of 3D printing. The apparent volume of the blank sample is  $V_0 = 6 \text{ m} \times 6 \text{ m} \times 5 \text{ m}$ , and the material is absolutely dense. The volume of the blank scaffold is  $V_1$ , and the volume of composite carbon nanoscaffold is  $V_2$  [1, 8]. The absolute compact volume of the stent was measured by the pycnometer method. Under the environment of 30°C, the pycnometer was filled with absolute ethanol and the sample was weighed as  $W_1$ . The composite carbon nanoscaffold sample with mass  $W_0$  was immersed in the pycnometer filled with absolute ethanol, and vacuum was applied to make the bubbles disappear completely and make anhydrous ethanol fill the pores of the sample, and the sample was weighed as  $W_2$  after being filled with absolute ethanol. The sample was taken out and weighed again as  $W_3$ , and the experimental data were recorded. The blank scaffold and composite carbon nanoscaffold samples were repeated three times each, and the porosity of the composite sample ( $n$ ) was calculated according to the following formula ( $n = \rho / (1 + \rho)$ ).  $\rho$  is the density of absolute ethanol at 30°C ( $\rho = 0.78 \text{ g/cm}^3$ ).

**2.1.3. Determination of Sustained Release of Drugs in TCS and EACS.** 3 TCS and EACS of equal quality were randomly

taken and put in a 10 ml test tube, 1 ml dichloromethane was added to fully dissolve the microspheres in the composite carbon nanoscaffold, and 4 ml PBS solution was added to the test tube and centrifuged to take the supernatant. The absorbance at 260 nm was measured in a spectrometer, and the average value was repeated 3 times, and the mass of VAN contained in the composite carbon nanoscaffold was calculated using the standard curve [9, 10]. Then, 3 TCS and EACS of equal quality were randomly taken, respectively, and 50 ml PBS (pH 7.4) solution was added, sealed, and placed in a constant temperature plate shaker at 37°C, and shaken at a constant speed, and 0.5 ml was taken out at 1 d, 2 d, 3 d, 6 d, 12 d, and 24 d. The solution was stored for testing and replaced with 0.5 ml PBS. After the sample was centrifuged, the supernatant was taken, and the absorbance at 260 nm was detected by an ultraviolet spectrophotometer. The drug concentration was calculated using the standard curve, and the average value was used to calculate the cumulative drug release and sustained release rate.

*2.2. Carbon Nanomaterials Treat Wounds Caused by Martial Arts Fractures.* Nanofibers will be ejected from a place on the Taylor cone where the electrostatic force of the liquid is greater than the surface tension. When the fiber passes through the air after being ejected, the solvent evaporates quickly and deposits on the receiver [11, 12]. Although the research of electrospinning technology has been going on for a hundred years, the use of this cheap manufacturing process of nano- or microfiber is still attracting attention. At present, many natural and synthetic polymers can be made into nanofibers by electrospinning.

*2.2.1. Tissue Engineering.* Electrospun polyester carbon nanofibers have the characteristics of extremely high porosity, large specific surface area, and interconnected pores. These characteristics make it mimic the extracellular matrix to a certain extent and provide the necessary environment for cell proliferation and differentiation. In addition, the morphology and mechanical properties of the fiber can be controlled by adjusting the system parameters (such as the molecular weight of polyester and solution properties) and process parameters (such as flow rate, voltage, and distance between needle and receiver) in the electrospinning process. The morphology and mechanical properties of the fiber can be controlled by adjusting the system parameters (such as the molecular weight of polyester and solution properties) and process parameters (such as flow rate, voltage, and distance between the needle and the receiver) in the electrospinning process to meet biological requirements, i.e., engineering needs [13, 14]. Currently, electrospun polyester carbon nanofibers have been reported to be used to construct tissue engineering scaffolds such as cartilage, skin, bone, nerves, and blood vessels.

*2.2.2. Drug Delivery.* Electrospun polyester carbon nanofibers for drug delivery have the characteristics of high drug loading, good biocompatibility, and degradability. At the

same time, the size and degradation rate of nanofibers can be controlled by changing the parameters in the electrospinning process, thereby adjusting the drug release rate in the body.

*2.2.3. Wound Healing.* Electrospun polyester carbon nanofibers also have unique advantages as trauma dressings. The pore size of the electrospun polyester carbon nanofiber membrane is usually in the nanometer level, while the size of the bacteria is in the micron level, which can resist the invasion of external bacteria into the wound, thereby preventing wound infection and promoting wound healing [15, 16]. At the same time, because the electrospun polyester carbon nanofiber membrane has a higher porosity and a larger specific surface area, as a wound dressing, on the one hand, it can ensure the penetration of water and gas on the wound surface, so as to keep the wound surface moist. The proliferation and differentiation provide nutrients; on the other hand, it can quickly absorb the tissue fluid secreted by the wound, which is conducive to the coagulation of blood, keeps the surface of the wound clean, and promotes the repair of the wound. From the perspective of the patient, electrospun polyester carbon nanofibers as a trauma dressing can reduce the formation of scar tissue and the frequency of dressing changes, thereby reducing the mental and physical pressure of the patient [17, 18].

In view of the advantages of polyester nanofibers in drug delivery and wound healing, many drugs are encapsulated in the fibers to construct bioactive wound dressings for the treatment of chronic wounds. These drugs include growth factors, antibiotics, and vitamins.

### *2.3. Surgical Methods*

*2.3.1. Debridement and Soft Tissue Treatment.* The patient was placed in a supine position, disinfected, and draped after general anesthesia intubation. During the operation, the sinus, infected tissue, and soft tissue defect surrounding necrotic fascia and inflammatory tissue were removed from the wound to ooze blood. Infected bone, dead bone, and hardened bone were removed. For those who have undergone internal fixation, the internal fixation material needs to be removed completely, and the inflammatory granulation tissue under the steel plate and in the medullary cavity should be scraped off to open the closed medullary cavity [19, 20]. The two fractured ends of the bone defect were repaired with an electric saw, resulting in "spot hemorrhage" on the surface of the cortical bone, and the bone was pale red. Try to protect the periosteum around the fracture. Part of the scar tissue and bone fragments were sent for examination and bacterial culture during the operation. The surgical wound was continuously flushed with hydrogen peroxide solution and 0.9% sodium chloride solution, soaked in the diluted iodophor solution for 10 minutes, and flushed again with 0.9% sodium chloride solution. Under normal circumstances, after debridement, the wound can be sutured to cover the broken end of the bone. The wound does not need to be sutured forcibly. Open dressing can be

given to avoid skin necrosis due to excessive skin tension [21, 22]. If the wound is combined with exposed tendons, combined with skin flap transfer to repair the wound, the choice of the flap can be based on the situation. Adjacent fasciocutaneous flap, cutaneous nerve nutrient vessel flap, or free skin flap can be used.

**2.3.2. Osteotomy.** Before the osteotomy, the iodophor gauze covering the wound bread should be tied up to protect the surgical field, the gloves were changed, and the osteotomy area was disinfected again to prevent contamination of the osteotomy site. The location of the osteotomy is determined according to the location of the bone defect and the length of the bone segment. Generally, the distal femur and the proximal metaphysis were selected, away from the lesion, and the location with good blood supply and healthy skin was selected. A small incision was used at the metaphyseal osteotomy during the operation to protect the periosteum. The 2.5 m Kirschner wire was used for low-energy osteotomy under a special minimally invasive osteotomy sleeve [23, 24]. During the operation, a C-arm X-ray machine can be used to assist the fluoroscopy positioning of the osteotomy site. After the osteotomy was completed, the severed end was appropriately pressurized to help stop bleeding and promote the rapid formation of callus. The timing of osteotomy was determined by the degree of wound infection. If the infection is mild, an external fixation frame, metaphyseal osteotomy, open wound dressing, and iodophor gauze fill the wound cavity. This method was used in 12 patients in this group. If the infection is serious, debridement of the wound was completed in the first stage, an external fixator is fixed, and osteotomy was performed 3 to 6 weeks after infection control. The 5 cases in this group were severely infected and were treated in two phases.

**2.3.3. Postoperative Treatment.** The sensation, movement of the affected limb, and blood supply at the end of the toe after the operation were closely observed. The affected limb was elevated to reduce swelling. According to the results of bacterial culture, sensitive antibiotics were routinely applied for 4 weeks, the dressing was changed according to the wound condition 2 to 3 days after the operation, pay attention to aseptic operation, the dressing was changed every day or every other day, and the wound was filled with iodophor gauze. Patients were encouraged to do leg-lift training and exercise for muscle isometric contraction. The active and passive activities of adjacent joints were strengthened, the muscles of the lower limbs were trained, and further contractures of the hip and knee joints were avoided. After 5 days after operation, they can walk with crutches and part of the weight-bearing to give stress stimulation to the new bone. Antibiotics are routinely used after surgery. In order to keep the needle track clean, the needle track needs to be cleaned with saline and disinfected with alcohol every day. Strengthening needle tract care can effectively prevent needle tract infections.

The osteotomy began to be extended 7 to 10 days, and the stretch was extended at 1 m/d, 0.25 mm each time, in 2 to 4

times. During the bone removal process, the frontal and lateral X-rays of the affected limb shall be taken every 2 weeks to observe the prolongation and extension of the osteotomy, whether there is axial offset, etc., and the changes in the length of the affected limb were observed, and the bone lengthening speed and lower limb force line in time were adjusted. If the bone growth at the osteotomy site is poor, the transportation should be stopped in time or retracted by 2 cm, and the callus should be observed for 1 to 2 weeks to continue the transportation. In the process of stretch extension, if skin stretch pain occurs, oral analgesics can be used to relieve it. If the relief is not obvious or if the pain symptoms worsen, the speed of stretch should be appropriately slowed down. During the follow-up, the healing of the femur of the affected limb, the sensation, movement, and function of the affected limb were observed. Follow up on time after the operation and reasonably guide them to perform functional exercises, get out of bed as soon as possible under the guidance of the rehabilitation doctor, and gradually move from partial weight-bearing activities to full-weight exercises. When the affected limb is stretched to align with the fractured end of the bone defect and is the same length as the contralateral limb, the extension or bone movement is stopped. Axial compression is applied once every 2 weeks, and the contact surface stress is stimulated by 1 mm each time to promote bone fracture.

According to the reexamination of X-rays, the new bone mineralization is complete and the bone defect ends completely reach the clinical healing standard, and the external fixation needle and connecting rod can be removed in stages. Strenuous exercise should be avoided within half a year after the external fixator is removed to avoid refracture of the affected limb. If there are lines of force, abnormal alignment, and nonunion of the fractured ends of the bone defect, it is necessary to adjust the line of force and alignment of the femur, and the fractured end was fixed with bone grafting and compression to promote its healing. Great attention should be paid to postoperative follow-up, to strengthen postoperative management and communication with the affected limb and to establish patient confidence in treatment.

### **3. Experimental Study of Carbon Nanomaterials for Treating Infectious Bone Defects and Wound Scars after Martial Arts Fractures**

#### *3.1. Preoperative Preparation and Postoperative Treatment*

**3.1.1. Preoperative Preparation.** After admission, the patient's sinus wounds dressings should be changed immediately. When dressings were changed, secretions were taken from the depths of the wounds, and bacterial culture and drug sensitivity experiments were performed. While selecting sensitive antibiotics, the overall condition of patients with infectious nonunion is evaluated. Most patients with infectious nonunion have been in bed for a long time and have undergone multiple operations. Some patients have repeated infections and have poor general conditions. It

can improve the heart and lung function, enhance the patient's endurance for surgery, and improve related muscle strength, joint function, and osteoporosis. Determine whether the patient has systemic diseases such as diabetes and anemia. At the same time, it is necessary to evaluate the local soft tissue condition of the injured limb, the location and type of fracture, the size of the bone defect, the wound condition around the bone defect, and the condition of the original fixation.

**3.1.2. Postoperative Treatment.** Strict aseptic operation should be maintained during dressing change after surgery to prevent reinfection of the wound. Antibiotics were applied once before surgery and for 2 days after surgery. Depending on the exudation of the wound, the wound is usually opened 2 days after the operation, the dressing is changed, and then the dressing is changed every other day. When the dressing is changed, part of the exudate and blood clot on the wound surface is removed. If the granulation tissue formation is slow, scraping can be used. Scrape the spoon gently until the wound oozes blood, apply gentamicin mixed with saline keep the moist environment covering the wound, and the outer layer shall be bandaged with sterile gauze. After the wound granulation tissue is fresh, the wound can be sealed by flap transfer or free skin grafting.

**3.2. Double Drug Loading of Electrospun Carbon Nanofibers.** The method of encapsulating protein and protease inhibitor mentioned in this article simultaneously encapsulates two drugs. First, a hexafluoroisopropanol solution of polylactic acid was prepared (concentration of 2 wt.%). Then, a certain amount of preloaded protein chitosan nanoparticles and doxycycline were mixed with the above polylactic acid solution so that the mass content of the preloaded particles was 9.1 wt.% and the drug loading amount of doxycycline between 10 and 15%, the mixture was stirred for 1 to 3 hours to make the preloaded particles and doxycycline uniformly dispersed in the solution. Next, the mixture was transferred into a 1 mL glass syringe connected to a 12-gauge stainless steel needle and spun at 15 kV. An aluminum plate with a diameter of 10 cm was used to receive nanofibers at a distance of 15 cm from the needle.

**3.3. Porosity, Mechanical Properties, Drug Sustained Release Determination, and Data Collection of TCS and EACS.** The blank sample volume is  $6\text{ m} \times 6\text{ m} \times 5\text{ m}$ , trabecular =  $40\text{ }\mu\text{m}$ , aperture =  $50\text{ }\mu\text{m}$ . After measurement, the actual porosity of the blank stent is  $48 \pm 1.2\%$ ; the porosity of TCS is  $25.46 \pm 2.45\%$ ; the porosity of EACS is  $21.9 \pm 0.79\%$ .

The maximum bearing capacity of TCS material measured by universal material mechanics is  $215.9\text{ N} \pm 12.4\text{ N}$ ; the maximum bearing capacity of EACS material is  $21.5\text{ N} \pm 9.7\text{ N}$ . According to the formula:  $1\text{ Pa} = 1\text{ N}/\text{square meter}$ , the support area of the stent material is  $36\text{ m}^2$  and the conversion strength is about

6 MPa (much higher than the minimum compressive strength of cancellous bone 2 MPa).

In vitro drug release experiments were performed on TCS and EACS. In order to simulate the release of composite stents in vivo to the maximum, we conducted drug release experiments in PBS solution at  $37^\circ\text{C}$ . The figure shows the VAN/PLGA microspheres, TCS, and EACS. The figure shows the release of VAN in VAN/PLGA microspheres, TCS, and EACS. The first 3 d VAN microspheres and TCS both had burst releases to varying degrees. However, in EACS, the burst release of chitosan coating was significantly reduced. After 3 d, the drug release of each group was slow and stable, and the drug release rate at 24 d was about 70%.

**3.4. Immunohistochemical Detection of BMP-2 and VEGF Expression.** Using the SP (streptavidin-peroxidase) method, that is, the streptavidin-peroxidase linkage method, the nucleus and/or the cytoplasm of light brown particles, brown particles, and yellow brown particles, the expression is a positive expression, and no particles are attached, or only a chip or yellow staining is regarded as a negative expression. The expression is a positive expression, and no particles are attached, or only a chip or yellow stain is regarded as a negative expression. In this experiment, an Olympus optical microscope was used to take pictures and for observation. First, the bone tissue expression site was located through a 40x low-power lens, and then the absorbance value of the specific expression site was determined at 400x. The microscopic imaging system uses 8 Olympus CCDP73 to collect immunohistochemical pictures of bone tissue. 10 400x fields of view were randomly selected for each slice and Image Pro 6.0 software was used to calculate the average absorbance value and read the positive expression rate.

## 4. Experimental Research and Analysis of Carbon Nanomaterials in the Treatment of Infected Bone Defects and Wound Scars after Martial Arts Fractures

**4.1. TCS and EACS Load BMSCs Culture.** BMSCs were seeded on blank scaffolds, TCS, and EACS and cultured for 7 days. Observed by scanning electron microscope, it was found that the three scaffolds all had cell proliferation, and the outer surface was covered with long flat cells. The CCK8 experimental analysis showed that BMSCs on these three scaffolds increased with the extension of the culture time, and these three scaffolds were all conducive to cell replication. The experiment is shown in Figure 1.

As shown in Figure 1, the number of cells in the blank scaffold was less on the 1 d, and the difference between the blank scaffold and the composite scaffold was statistically significant ( $P < 0.05$ ), and the number of cells on the blank scaffold was slightly more than that on the 3rd, 5th, and 7th days. Compared with TCS and EACS, blank stents on the 3rd and 5th days of TCS and EACS had statistically significant differences ( $P < 0.05$ ). The growth trend of TCS and EACS groups was roughly the same, and the comparison was not statistically significant ( $P > 0.05$ ).

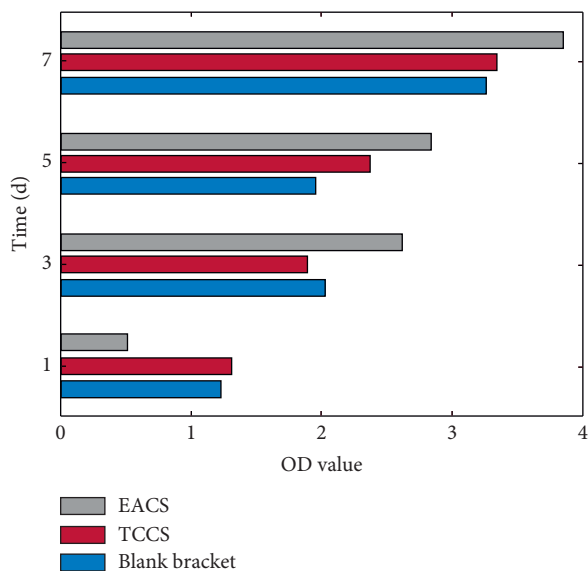


FIGURE 1: Proliferation of BMSCs on blank stents, TCS, and EACS.

**4.2. Analysis of Postoperative Improvement.** During the follow-up period, there was no refracture of new bone and no secondary hip dislocation. 7 cases of needle tract infections were given oral antibiotics, active dressing changes, and needle eye debridement and suture, and the infection was cured. Three cases showed axial deviation during bone lengthening, which was gradually corrected after adjustment by external fixator. 9 patients with skin traction pain were given oral analgesics to slow down the traction speed and improve the effect, as shown in Table 1.

According to the Paley fracture healing scoring standard, the excellent and good rate was 82.4%. At the last follow-up, the scores of all dimensions of the SF-36 scale were significantly higher than those before the operation ( $P < 0.05$ ), the difference was statistically significant, and the patient's physical and mental health levels were comprehensively improved. Through functional exercises after surgery, the knee joint extension and flexion function were improved compared to before surgery, and normal walking was not affected. All patients were very satisfied with the treatment results.

**4.3. VEGF Test Results.** By comparing the VEGF expression levels of the four groups at 1 week, 2 weeks, and 4 weeks after surgery, at each time point between group A and group B, and group C and group D, there was no significant difference in VEGF expression ( $P > 0.5$ ). Histogram of VEGF expression at 1, 2, and 4 weeks after surgery is shown in Figure 2.

The difference between the expression levels of the groups A and B and the expression levels of the groups C and D is statistically significant. The expression level of VEGF in each group at the three time points was statistically significant ( $P < 0.5$ ), and the expression level of VEGF in the four groups was the highest in the second week.

TABLE 1: Comparison of SF-36 scale scores of 19 patients with femoral infectious bone defect before operation and last follow-up.

Project	SF-36 scale score ( $X \pm S$ , points)		$t$ value	$P$ value
	Preoperative	Postoperative		
Physiological function	$45.37 \pm 3.56$	$68.36 \pm 4.29$	13.28	$<0.05$
Body pain	$36.39 \pm 12.37$	$58.13 \pm 13.56$	12.39	$<0.05$
Mental health	$42.38 \pm 5.38$	$58.38 \pm 5.32$	15.34	$<0.05$

**4.4. Results of Fracture Healing and Functional Recovery.** Patients in the microparticle group were followed up regularly for 3 to 48 months after surgery, with an average follow-up of 24 months. VSD was placed in 25 patients for granulation culture after surgery. The average survival time of granulation was 9.5 days. The bone graft is covered by granulation tissue for an average of 7 weeks after the microgranular bone graft. Flap transfer or simple skin grafting surgery was used to fill the wound. The fractures of all patients healed with an average healing time of 6 months (3–8 months). After an average of 7 months (4–12 months) after surgery, no bone abnormalities were found, and the external fixator was removed. Bone healing and functional recovery are good. Comparison of bone healing between the two groups is shown in Figure 3.

Patients in the traditional granule group were followed up regularly for 9 months to 26 months after surgery, with an average follow-up of 19 months. Twenty-seven patients were also implanted with ordinary granular bone after the granulation survived. The bone has been covered by granulation tissue for an average of 9 weeks after bone grafting. Fill the wound with further bone grafting. One patient reinfectd after operation and healed completely after retreatment. The two groups of patients recovered well after the operation and were discharged. According to the Ilizarov method, the fracture healing and functional recovery of the two groups reached satisfactory results. There was no significant difference and no statistical significance ( $P > 0.05$ ).

**4.5. Release Behavior of Two Drugs.** Figure 4 shows the release behavior of doxycycline from dual drug nanofibers with a drug loading of 10% and 15%. Nanofibers containing only doxycycline served as a control. It can be seen that when the drug loading amount of doxycycline is 10%, after two weeks of culture, the carbon nanofibers containing only doxycycline released 24% of the total doxycycline, while the dual drug nanofibers released 5% of doxycycline. The experiment is shown in Figure 4 when the drug loading of doxycycline is 15%.

After two weeks of culture, the carbon nanofibers containing only doxycycline released 34% of the total doxycycline, while the dual drug nanofibers released 62% of the doxycycline, and the latter had obvious burst. Simultaneous protein encapsulation speeds up the release of doxycycline, which may be because the chitosan particles used for protein preencapsulation are more hydrophilic than

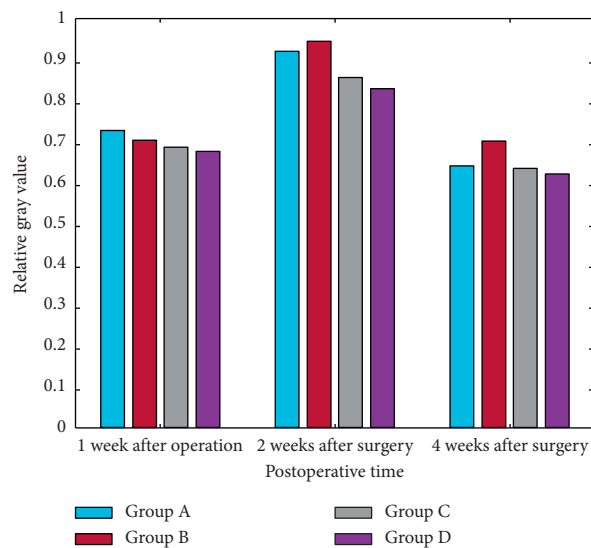


FIGURE 2: Histogram of VEGF expression at 1, 2, and 4 weeks after surgery.

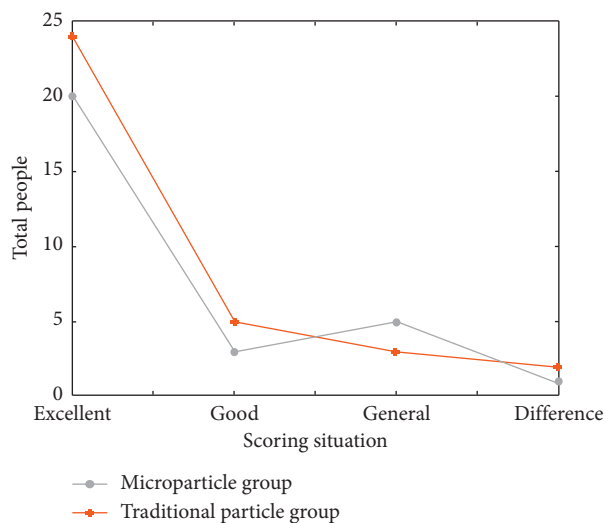


FIGURE 3: Comparison of bone healing between the two groups.

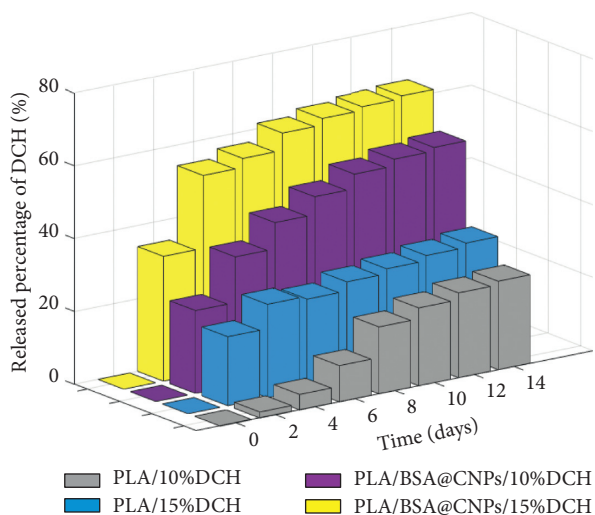


FIGURE 4: Release behavior of doxycycline.

polylactic acid, which is more conducive to the diffusion of doxycycline chitosan. When the drug loading of doxycycline increases from 10% to 15%, its release rate from the dual drug nanofibers increases. This should be related to the increase in doxycycline drug loading that causes the nanofiber membrane to change from hydrophobic. It is related to changes in hydrophilic properties. Water molecules enter the hydrophilic fibers more easily, allowing the doxycycline inside to diffuse out faster.

## 5. Conclusions

Autologous microgranular bone has the characteristics of strong osteogenesis and release of more cytokines. It has been used in clinical treatment of infectious bone defects and nonunion to achieve good results. Autogenous microgranular bone grafting has greater advantages than traditional granular bone grafting in the treatment of infectious

bone defects and nonunion. Therefore, autologous micro-particle bone grafting can improve the efficiency of treating infectious bone defects and is a more active and effective method.

In this paper, a reasonably designed particle pre-encapsulation method is used to realize the encapsulation and controlled release of protein by carbon nanofibers while maintaining protein activity. The nanofiber has a smooth surface and uniform size. The preloaded particles are evenly distributed in the nanofibers. The protein retains its biological activity and can be continuously released from the nanofibers for more than four weeks without obvious burst release. Nanofibers have good cell compatibility and can support cell adhesion, spreading, and proliferation. When the carbon nanofibers coated with epidermal growth factor prepared by this method are used for the treatment of back wounds of diabetic rats, they obtain better therapeutic effects than blank nanofibers.

Excluding hyperplastic scars and contaminated or poorly healed granulation tissue, eliminating dead space, draining pus and blood, and improving local blood circulation have become one of the important principles for the treatment of infectious bone defects such as chronic osteomyelitis. It is generally believed in clinical practice that any dead space with dead bones, or sinus formation, discharge of pus, or sufficient new bone formation to form a package, should be treated with surgical intervention to achieve clinical healing conditions. Lesion debridement is the basis and effective method for the treatment of infectious bone defects. During debridement, the suspiciously infected tissue should also be completely removed until healthy and bleeding bone is exposed. For the treatment of infectious bone defects, thorough surgical debridement, adequate drainage, and avoiding the formation of dead spaces have become the consensus of many scholars. Among them, the control of infection is still considered to be the most critical link to successfully cure infectious bone defects.

## Data Availability

The data that support the findings of this study are available from the corresponding author upon reasonable request.

## Conflicts of Interest

The authors declare that they have no conflicts of interest.

## Acknowledgments

This study was supported by the 2017 National Social Science Foundation Project "A Study of Bashu Body Graphs" (no. 17BTY013) and Youth Project of Science and Technology Research Program of Chongqing Education Commission of China (no. KJQN202000509).

## References

[1] H. Soichi, M. Akihiko, O. Kotaro et al., "Treatment of mandibular fracture-associated infectious pseudarthrosis

- accompanied by osteomyelitis in a peritoneal dialysis patient," *Journal of UOEH*, vol. 40, no. 2, pp. 209–215, 2018.
- [2] J. Park and W. Y. Chung, "Osteochondral allograft reconstruction of talar body fracture with a large bone defect," *Archives of Orthopaedic and Trauma Surgery*, vol. 136, no. 1, pp. 35–40, 2015.
- [3] D. Papadia, A. Musetti, and E. Dematte, "An injectable bone substitute eluting antibiotic in the treatment of traumatic bone defects and its prophylactic effect," *Georgian Mathematical Journal*, vol. 97-B, no. 16, pp. 161–186, 2015.
- [4] Z. M. Guo, T. C. Shangguan, M. Zhang et al., "Prevention and treatment of the related complications of tibial fractures bone defect by bone transport," *Zhongguo Gu Shang = China Journal of Orthopaedics and Traumatology*, vol. 29, no. 8, pp. 756–760, 2016.
- [5] L. Zhong, X. Hong, Z. Zhang et al., "Staged treatment of infectious long bone defect in lower extremity," *Zhongguo Xiu Fu Chong Jian Wai Ke Za Zhi*, vol. 28, no. 10, pp. 1212–1216, 2014.
- [6] C. Zongjie and W. Zhan-You, "Additional steel plate and bone graft in the treatment of bone nonunion after intramedullary nail fixation for femoral fractures," *Chinese and Foreign Medical Research*, vol. 64, no. 6, pp. 433–437, 2015.
- [7] Y. Yang, X. Niu, Q. Zhang et al., "Efficacy of bioactive glass and allogenic bone in repair of bone defect after benign bone tumor curettage," *Chinese Journal of Reparative & Reconstructive Surgery*, vol. 30, no. 6, pp. 675–679, 2016.
- [8] M. J. Rose, P. C. Cevallos, L. Gellis, and L. Bergersen, "Late-term development of an atrial defect and thrombus formation after device fracture following successful transcatheter closure of an atrial septal defect with a STARFlex device," *Cardiology in the Young*, vol. 27, no. 5, pp. 975–977, 2017.
- [9] W. Bin, J. Song, L. U. Aidong et al., "Bone transportation by ring type external fixator combined with locked intramedullary nail for tibial non-infectious defect," *Chinese Journal of Reparative & Reconstructive Surgery*, vol. 29, no. 11, pp. 1348–1352, 2015.
- [10] A. M. H. Raphael, A. V. Roberto, R. Alejandro et al., "Management of craniocerebral gunshot injuries: a review," *Korean Journal of Neurotrauma*, vol. 11, no. 2, pp. 35–43, 2015.
- [11] W. Yicun, J. Hui, D. Zhantao et al., "Comparison of monolateral external fixation and internal fixation for skeletal stabilisation in the management of small tibial bone defects following successful treatment of chronic osteomyelitis," *BioMed Research International*, vol. 2017, Article ID 6250635, 8 pages, 2017.
- [12] K. Naito, Y. Sugiyama, H. Obata, A. Mogami, O. Obayashi, and K. Kaneko, "Screw fixation and autogenous bone graft for an irreducible distal ulna fracture associated with distal radius fracture," *The Journal of Hand Surgery Asian-Pacific Volume*, vol. 22, no. 2, p. 236, 2017.
- [13] M. L. Kaneko, C. J. A. Van Bergen, L. Blankevoort et al., "Computed tomography analysis of osteochondral defects of the talus after arthroscopic debridement and microfracture," *Knee Surgery, Sports Traumatology, Arthroscopy*, vol. 24, no. 4, pp. 1286–1292, 2016.
- [14] D. Lin, D. Luo, K. Lian, W. Zhai, and Z. Ding, "Reconstruction of traumatic bone defect with in situ implantation of dropped traumatic segmental bone fragments," *Orthopedics*, vol. 39, no. 1, pp. e14–e18, 2016.
- [15] N. M. Haines, W. D. Lack, R. B. Seymour, and M. J. Bosse, "Defining the lower limit of a "critical bone defect" in open

- diaphyseal tibia fractures,” *Journal of Orthopaedic Trauma*, vol. 30, no. 5, pp. e158–e163, 2016.
- [16] H. Wang, W. Jiang, X. Wei, Y. Rui, and Z. Sun, “Ulnus formation for forearm fracture with segmental radial defect,” *International Journal of Clinical & Experimental Medicine*, vol. 8, no. 10, pp. 17835–17838, 2015.
- [17] F. J. M. Verstraete, B. Arzi, D. J. Huey, D. D. Cissell, and K. A. Athanasiou, “Regenerating mandibular bone using rhBMP-2: part 2-treatment of chronic, defect non-union fractures,” *Veterinary Surgery*, vol. 44, no. 4, pp. 410–416, 2015.
- [18] J. Silva, C. F. Mourão, H. Rocha Junior, L. F. Magacho da Silva, G. Moraes, and N. Homs, “Treatment of frontal bone fracture sequelae through inversion of the bone fragment,” *Revista Do Colegio Brasiro De Cirurgioes*, vol. 43, no. 6, pp. 472–475, 2016.
- [19] H. Qu, W. Guo, R. Yang et al., “Reconstruction of segmental bone defect of long bones after tumor resection by devitalized tumor-bearing bone,” *World Journal of Surgical Oncology*, vol. 13, no. 1, p. 282, 2015.
- [20] Y. Yang, X. C. Ramirez, X. Wang et al., “Impact of carbon nanotube defects on fracture mechanisms in ceramic nanocomposites,” *Carbon*, vol. 115, pp. 402–408, 2017.
- [21] Z. Guo, L. Shi, S. Tian, W. Chen, and B. Lin, “Effectiveness of limbs shortening and re-lengthening in treatment of tibial infectious bone defect and chronic osteomyelitis,” *Zhongguo Xiu Fu Chong Jian Wai Ke Za Zhi = Zhongguo Xiufu Chongjian Waike Zazhi = Chinese Journal of Reparative and Reconstructive Surgery*, vol. 31, no. 8, pp. 941–945, 2017.
- [22] H. Chen, X. Ji, M. Hao, Q. Zhang, and P. Tang, “A three-stage procedure using bone transportation for the treatment of sternoclavicular infectious arthritis,” *Journal of Orthopaedic Surgery & Research*, vol. 11, no. 1, p. 152, 2016.
- [23] U. S. Gill, A. Zissimopoulos, S. Al-Shamma et al., “Assessment of bone mineral density in tenofovir-treated patients with chronic hepatitis B: can the fracture risk assessment tool identify those at greatest risk?” *Journal of Infectious Diseases*, vol. 211, no. 3, pp. 374–382, 2015.
- [24] L. Burke, C. Yazhou, L. Peijuan et al., “Effect of unilateral producible external fixation apparatus on treating open tibia fracture(Gustilo III B/C) with bone defect,” *Lingnan Modern Clinics in Surgery*, vol. 49, no. 4, pp. 200–212, 2015.

## Research Article

# Planning Research on Application of Nanomaterial Technology in Disaster Prevention and Reconstruction

Jun Shao,<sup>1</sup> Huihui Yan ,<sup>2</sup> and Haosheng Xu<sup>3</sup>

<sup>1</sup>School of Urban Construction, Wuhan University of Science and Technology, Wuhan, Hubei 430081, China

<sup>2</sup>Wuhan Planning and Design Institute, Wuhan, Hubei 430074, China

<sup>3</sup>Electronic Circuit Division, GCI Science & Technology Co. Ltd., Guangzhou, Guangdong 510220, China

Correspondence should be addressed to Huihui Yan; shaojun@wust.edu.cn

Received 14 August 2020; Revised 17 September 2020; Accepted 28 September 2020; Published 20 October 2020

Academic Editor: Tifeng Jiao

Copyright © 2020 Jun Shao et al. This is an open access article distributed under the Creative Commons Attribution License, which permits unrestricted use, distribution, and reproduction in any medium, provided the original work is properly cited.

An earthquake causes a huge loss of life and property. After an earthquake, many buildings are seriously damaged or collapsed. On the one hand, it is necessary to make full use of nanomaterials technology to improve seismic strength during reconstruction; on the other hand, scientific planning is needed to reduce pollution, carbon emissions, and energy consumption. This paper mainly studies the application of nanomaterial technology in disaster prevention and reconstruction. Through a series of planning safeguard measures, the overall seismic performance of the city is improved in order to provide theoretical guidance and technical support for disaster prevention and reconstruction. This paper mainly introduces the stress analysis of frame joints after earthquake and the planning of urban disaster prevention and reconstruction. In addition to the different types of concrete materials (ordinary concrete, nano silica fiber concrete, PVA fiber concrete), the fixed amount of water, superplasticizer, reinforcement, sand, and gravel, the concrete strength grade is C30. Then, three kinds of concrete frame joints are tested under low cycle cyclic loading to compare the seismic performance of the three kinds of concrete. The experimental results show that the fuzzy evaluation of urban disaster prevention and reconstruction planning has been carried out for 6 communities in this city. Among them, 4 communities are qualified and 2 communities are unqualified. Therefore, it is necessary to focus on seismic reinforcement or carry out urban planning research again. Compared with ordinary concrete, the bearing capacity and ductility coefficient of nano silica fiber concrete and PVA fiber concrete are increased by 37.8% and 15.6%, respectively. It is proved that the seismic performance of nano silica fiber reinforced concrete is far better than that of ordinary concrete.

## 1. Introduction

In recent years, Wenchuan earthquake, Yushu earthquake, and other frequent earthquake disasters have accelerated the seismic planning-related research [1–3]. Building is the main constituent element of city. It is an important way to minimize the collapse and damage of buildings during earthquakes [4]. Due to the serious damage of earthquake, especially the damage of high-rise buildings, the structure in earthquake area should have enough ductility to ensure that the frame structure has sufficient seismic capacity. Reinforced concrete frame structure has been widely used in multistorey buildings for its many advantages. However, due to the large number of stories, the phenomenon of “thick

column with less reinforcement” often appears in the lower column, which not only takes up the indoor space, but also increases the weight of the building, which is particularly unfavorable to earthquake resistance. The beam column joints of frame structure bear the shear and bending moment of frame column and frame beam at the same time, which is prone to shear failure. As the transfer hinge of frame structure, beam column joint is the key part of the whole structure. In order to improve the energy dissipation capacity and seismic performance of frame structures, the seismic fortification requirements of “strong joints and weak members” are proposed in seismic codes at home and abroad. Generally, in the actual project, more stirrups are arranged in the core area of the joint to meet the

requirements of “strong joint.” However, more shear reinforcement will cause reinforcement crowding in the joint, which will increase the construction difficulty and project cost. At the same time, the reinforcement of beam column joint is crowded, which is easy to make the concrete pouring vibration not dense, and the joint is easy to crack, so that the water and oxygen in the air contact with the reinforcement in the component through the crack, which makes the reinforcement rust, reduces the strength of the reinforcement, and shortens the service life of the steel bar. In addition, the tensile performance of concrete is far lower than its compressive strength performance, and its damage is often characterized by brittleness. The brittleness failure and cracking performance of concrete cannot be brought into full play, which reduces the durability of the structure, shortens the service life of the concrete structure, increases the maintenance cost of the concrete structure, and limits the use of concrete in the structure. Therefore, improving the strength and ductility of columns, especially low-rise columns, has become one of the main measures to improve the seismic performance of multistorey buildings.

Field investigation and related scientific research show that beam column joints without lateral limit and poor details cannot resist medium and large earthquake events. In order to improve the seismic performance of existing RC beam column joints, Vecchio et al. proposed a new strength bearing capacity model to explain the strength increase provided by FRP system in seismic reinforcement of low-detail angle joints. Through the analysis of a large number of experimental data, the accuracy of the model is verified [5]. Del Vecchio et al. discuss the numerical seismic evaluation of reinforced concrete structural systems designed without appropriate seismic details of gusset plates and the benefits of local FRP reinforcement. Del Vecchio et al. proposed a new finite element analysis method to consider the nonlinear behavior of joints and fiber reinforced polymer (FRP) reinforcement. Several case studies are selected to verify the model. On the component level, the model predictions were compared with recent test results on full-scale beam to column joints with or without FRP reinforcement [6]. The Del Vecchio study evaluates the effectiveness of a new seismic strengthening method for reinforced concrete beam column joints and establishes a shear strength model of the strengthened joints. Under the action of reversed cyclic load, the four joints without transverse reinforcement were poured and tested. The first joint is used as the control specimen, and the other three joints are bonded around the column with concrete cover in the joint area, which is changed from square section to circular section, and then wrapped with different proportions of CFRP. Based on the concept of average plane stress, the shear strength model of joints was established and evaluated by the collected database. Among them, 32 joints were strengthened with conventional FRP and 3 nodes were strengthened with new methods [7]. Verderame et al. carried out an experimental study on the full-scale external unreinforced reinforced concrete beam column joints of four typical unqualified reinforced concrete frame structures. Verderame et al. observed different

failure modes, i.e., the failure of joints with or without beam yielding, analyzed the local response of gusset plates, and evaluated different joint deformation mechanisms and their contributions to deformation capacity and energy dissipation capacity [8]. In this paper, the mechanical behavior of beam column joints strengthened under cyclic loading is studied experimentally. The test scheme includes eight external beam column joint components, which are tested in two stages: one is the failure stage, the second stage is the repair stage. Beam column joints are designed for gravity loads only. There is no transverse reinforcement of beam column joint, and there is no special stirrup in the critical zone of beam column. These nonseismic design (NS) joints were damaged to varying degrees in the first stage of the test. In the second stage, damaged joints were strengthened with carbon fiber reinforced polymer (c-frp) sheets [9].

In addition to the different types of concrete materials (ordinary concrete, nano silica fiber concrete, and PVA fiber concrete), the fixed amount of water, superplasticizer, reinforcement, sand and gravel, and the concrete strength grade is C30. Then, the low cycle repeated load test is carried out on the sample frame joints. In this paper, the bearing capacity, ductility, energy dissipation capacity, and stiffness degradation of ordinary concrete, PVA fiber concrete, and nano silica fiber concrete frame joints are compared and analyzed. It is proved that the seismic performance of nano silica fiber reinforced concrete is far better than that of ordinary concrete.

The application of nanomaterials technology is essential in postdisaster reconstruction. On the one hand, the application of nanomaterials can effectively improve the seismic level of buildings and ensure the safety of people's lives and property. On the other hand, the application of nanomaterials technology can improve the level of building science and technology and reduce pollutant emissions and energy consumption, which is one of the important contents of scientific reconstruction.

## 2. Seismic Resistance of Nanomaterials and Reinforced Concrete Nodes

*2.1. Planning Research on Urban Disaster Prevention and Reconstruction.* The idea of urban planning first appeared in the West and then spread to China, which provided a strong support for China's urban planning. From the background of the formation of the theory, we can see that before World War II, Western developed countries had relatively concentrated capital, urban industrial development was abnormal, population density was large, land use was very tight, and people's living space was facing more and more problems. After World War II, these problems became more prominent. Environmental pollution, deterioration of living conditions, and shortage of urban land make these countries aware of the crisis and put forward urban planning theory to solve these problems. Urban planning is the rational allocation of urban land and space, which aims to coordinate the urban environment, allocate land reasonably, and promote social prosperity and development.

In many urban planning theories, urban planning considers the impact of various disasters on the city, which is the best performance. Obviously, there will be a reasonable green space layout in various plannings. The distribution form of urban green space is closely related to urban planning, which determines the layout of the city. Urban green space should meet the requirements of disaster prevention and mitigation according to the distribution of the city. Urban planning theory will inevitably affect the disaster prevention and mitigation function of urban green space.

*2.1.1. Urban Disaster Prevention and Reconstruction Planning.* Disaster prevention and reconstruction should conform to and coordinate with the requirements of urban master plan and comprehensive disaster prevention plan [10]. In addition, the supporting facilities for disaster prevention and reconstruction of Greenland station are relatively complete, which is a very important shelter for nearby residents, and can be used as the command center for disaster prevention and reconstruction in case of disaster. Therefore, the urban green space disaster prevention and reconstruction planning should become the content that cannot be ignored in the overall urban planning and disaster prevention planning.

Urban green space system is the basis of urban disaster prevention and reconstruction planning, which is a special planning under the green space system. Disaster prevention and risk avoidance planning should be combined with urban green space system planning to form a reasonable disaster prevention and risk avoidance system. Due to the limited area of urban green space, stadiums, parking lots, and schools in the city can be used as disaster relief and disaster prevention and reconstruction green space. Therefore, when making urban disaster prevention and reconstruction planning, other open space and public facilities in the city should be comprehensively considered for unified planning. Moreover, the diversity of disasters should also be considered comprehensively. People oriented means putting people's life and needs in the first place. In terms of urban disaster prevention and reconstruction, the capacity of green space for disaster prevention and reconstruction must meet the number of asylum seekers, and each person has a reasonable disaster avoidance area. Green space should be evenly distributed around people's lives, so that people can escape quickly and effectively when disasters occur.

*2.1.2. Disaster Prevention of Collapse.* Slope reinforcement is an effective way to prevent the development of slope weathering. The retaining wall is constructed on the high and steep slope with poor stability, which is used to cover with cement mortar. This method can effectively reduce the weathering of the slope and improve the stability of the slope. Leakage plugging, water blocking, and roof support pointed out that joints are also an effective method to control landslides and are mainly used for highway slope treatment where there is a danger of collapse. Occlusion and interception are used to deal with large-scale collapse and control small-scale collapse, respectively [11].

*2.1.3. Disaster Prevention of Ground Collapse.* According to the inducing factors and formation mechanism of surface subsidence, active prevention and control measures should be taken for the areas that have not yet collapsed, and the areas that have collapsed should be renovated to slow down or prevent the further development of surface subsidence. The specific disaster prevention measures are as follows:

- (1) We should pay attention to patrol and real-time monitoring. Engineers and relevant personnel shall conduct inspection and real-time monitoring, record the occurrence of collapse truthfully, and report to relevant departments in time.
- (2) The collapse area and goaf should be sealed and tamped in combination with the actual collapse area. At the same time, the backfill volume shall be measured, and the safety management department and geodetic survey center shall strictly check the backfill volume. In case of repeated landslides, the backfill shall be repeated.
- (3) When karst collapse occurs on the ground, it is necessary to prevent pedestrians, vehicles, livestock, and other animals from entering the collapse area according to the size of the collapse, so as to prevent further casualties and property losses. It is necessary to strengthen targeted safety publicity and education and enhance people's awareness of disaster prevention, and on this basis, the collapse pit should be treated.

*2.1.4. Evaluation of Seismic Performance of Buildings.* Evaluation of seismic performance of buildings is an important part of seismic disaster prevention planning. At present, many scholars have put forward many methods to evaluate the seismic capacity of individual buildings and group buildings [12–15]. The evaluation results are basically expressed by vulnerability matrix or earthquake damage index.

*2.2. Stress Analysis of Joints.* In the seismic design of strong earthquakes, frame joints are important components that affect the nonlinear response of frame structures. In the reinforced concrete frame structure, the beam reinforcement and the column reinforcement converge at the joint, and the joint composition is relatively complex. Because the frame joint is an internal force transfer center, including pressure, shear force, and bending moment, the stress state of the joint is also complex. The joint is the joint of beam and column, and it is the key part of frame structure. It bears bending moment, shear force, and axial force from beam end and column end. Under the repeated action of earthquake, the node often becomes one of the vulnerable parts of earthquake. Through the stress analysis of the joint, the following conclusions are drawn.

Under the action of horizontal load, the deformation of the joints around the beam column is the bending moment of the tie beam in the same direction. The pressure of the bending moment on the concrete at the beam end is related

to the tensile strength of the reinforcement. Therefore, for the longitudinal reinforcement of the same beam, under the action of pressure and tension, they are on both sides of the node, respectively. Therefore, under the action of horizontal load, the horizontal shear force is greater than that of the joint under vertical load shear force. Therefore, under the synergistic action of vertical pressure and horizontal shear stress, the core area of frame joints will bear large diagonal tension. At the same time, due to the weak tensile strength of concrete, the concrete at the joint will produce inclined cracks, which leads to shear failure of concrete in the core area.

When the load of the joint is vertical, the shear force of the beam to column joint is smaller than that of the beam end column joint. Under the action of the bending moment in the opposite direction of the beam column joint beam, the bending moment of the left and right sides of the beam is relatively small after the offset of the two ends. At the same time, due to the vertical load acting on the ends of the beams at both ends, the column is under the dominant action of the vertical internal force, resulting in the beam column eccentric compression in the center of small or compression state. Because the upper reinforcement of the beam end on both sides of the column is long and the stress direction is different, the transverse shear force in the core area of the joint and the shear force at the end of the column are relatively small. As only one side of the beam end column is connected to the beam end, the negative bending moment of the beam end is transmitted to the column end through the node, which makes the column end bear a large bending moment. Therefore, in order to transfer the moment at the column end, the core area of the joint needs to bear a large shear force [16].

In recent decades, the emergence of high-rise reinforced concrete frame structure makes the seismic work of high-rise buildings more and more important. When the earthquake disaster occurs, the collapse of the whole frame structure is often due to the first failure of the joints, which makes the maintenance work more difficult. Therefore, the safety and reliability of the node is the guarantee of the normal operation of the whole structure. In seismic design, the strength and ductility of beam column members should be guaranteed, and the strength and ductility of joint area should be improved. The theory of load transfer mechanism and joint failure characteristics needs to be improved, and the corresponding reasonable joint design method should also be put on the agenda [17].

**2.3. Nanotube Model Solution.** In order to evaluate the elastic modulus of the nanocomposites obtained by solving the model of doped ZrO<sub>2</sub> nanotubes, the H-T theory was used for the first time to calculate the elastic modulus of the doped ZrO<sub>2</sub> nanotube model. The model is based on the self-consistent method of classical theoretical methods and takes into account the influence of the length diameter ratio and filling ratio of ZrO<sub>2</sub> nanotubes on the mechanical properties of random reinforced phase reinforced composites [18]:

$$\frac{E_C}{E_m} = \frac{3}{8}E_1 + E_2. \quad (1)$$

In the formula,  $E_C/E_m$  is the ratio of elastic modulus of composite material to elastic modulus of matrix material:

$$E_1 = \frac{1 + 2\eta_1 V_Z (l/d)}{1 - \eta_1 V_Z}, \quad (2)$$

$$E_2 = \frac{1 + 2\eta_T V_Z}{1 - \eta_T V_Z}.$$

$V_Z$  is the filling ratio of ZrO<sub>2</sub> nanotubes in the matrix material, and  $l/d$  is the length diameter ratio of ZrO<sub>2</sub> nanotubes, which is the filling ratio in the whole RVE model:

$$\eta_L = \frac{E_Z/E_m - 1}{E_Z/E_m + 2(l/d)}, \quad (3)$$

$$\eta_T = \frac{E_Z/E_m - 1}{E_Z/E_m + 2}.$$

It can be seen from the above formula that the method can only calculate the elastic modulus of the composite, but cannot observe the stress distribution between the ZrO<sub>2</sub> nanotube and the matrix material. Therefore, many researchers have improved the method from the aspect of aspect ratio, material geometric parameters, and loading direction.

## 2.4. Nanoparticles

**2.4.1. Nano Ultrafine Calcium Carbonate.** The particle size of ultrafine calcium carbonate is in the range of 1~100 nm. It is mainly used in rubber, plastics, coatings, and other industries, and the most mature industry is the plastic industry. It is mainly used for PVC plastic sol and high-grade plastic products for automobile inner sealing. It can improve the rheological property of plastic masterbatch and improve its formability. At the same time, as a plastic filler, it has the function of strengthening and toughening; it can improve the bending modulus and bending strength of the plastic, improve the thermal deformation temperature and dimensional stability of the plastic, and make the plastic have thermal hysteresis. In addition, in the coating industry, it can greatly improve the thixotropy of the system, significantly improve the washability, adhesion, stain resistance, surface finish, and strength of the coating, and has good anti-settlement effect [19].

The main production methods of calcium carbonate are physical method and chemical method. The physical method is that the raw ore is directly crushed into calcium carbonate powder by mechanical processing. The products prepared by this method usually have large particle size and wide distribution and are generally used as fillers for medium- and low-end products. Chemical method is a method to obtain calcium carbonate by controlling reaction conditions and chemical reactions between substances. Calcium carbonate produced by chemical method has small particle size, narrow distribution, and controllable crystal shape. Its performance

is obviously better than that of calcium carbonate prepared by physical method [20].

At present, most enterprises use carbonization method to produce nano calcium carbonate. According to the different carbonization methods, it can be divided into continuous spray carbonization and intermittent bubbling carbonization.

Continuous spray carbonization is the principle of putting the lime milk pressure atomizer on the top of the carbonization tower and atomizing it uniformly into small droplets. Carbon dioxide gas is ejected from the bottom of the tower. The contact between them is carbonized. This method usually uses two or three carbonization towers in series with multiple process stages. The solution obtained from the first carbonization tower enters into the second carbonization tower for carbonization reaction, and the solution obtained from the second carbonization tower continues to enter the third carbonization tower for carbonization reaction until the finished nano calcium carbonate is obtained [21]. This method is a continuous carbonization process with high production capacity and easy control of product quality. However, the equipment investment is large and the practical application is less.

Intermittent bubbling carbonization is the most commonly used carbonization method with mature technology, moderate equipment investment, and simple operation. A certain concentration of lime milk is pumped into the carbonization tower, and a certain concentration of kiln gas is introduced from the bottom of the tower for bubbling and carbonization. In order to make the reaction fast, the gas distributor is usually installed in the carbonization tower at the bottom, and the agitator and baffle plate are installed in the carbonization tower, which can improve the quality and heat transfer effect of the system, make the kiln gas more evenly enter the lime milk, and improve the reaction speed.

**2.4.2. Nano Silica.** Nano silica is a kind of fine powder, nontoxic, white, and amorphous. The particle size is small, and the surface contains hydroxyl group, which is easy to aggregate. Nano silica has large internal surface area, good chemical stability, light weight, good dispersion, and no combustion. Nano silica has good compatibility with other materials and can be used as other nano materials. Due to its small proportion, it is easy to fly in the air, which brings great inconvenience to transportation and storage. Nano silica has a large number of highly active silicon hydroxyl groups, which can react with most of the modifiers. It can improve the physical and chemical properties of silica surface, improve the processing performance, and optimize the performance of nano silica.

At present, the common preparation methods of nano silica are physical method and chemical method. As the name implies, the physical method is to crush the silicon aggregate into silica particles through physical methods [22]. Chemistry is the preparation of nano silica by chemical reaction, mainly including microemulsion method, sol-gel method, and high gravity method.

**(1) Preparation of Nano Silica by the High Gravity Method.** The overweight method is to put the filtered sodium silicate solution into a high gravity reactor according to a certain concentration, heat it to the specified temperature, add flocculant and surfactant, turn on the liquid material circulation pump, rotate the packed bed, and let carbon dioxide pass through after the temperature is stable. When the pH value is stable, stop carbon dioxide emission. Add acid to adjust pH value, keep temperature aging; finally through washing, filtering, drying, grinding, and screening, produce silica particles.

**(2) Preparation of Nano Silica by the Microemulsion Method.** Among these processes, controlling the synthesis of uniform nanoparticles has great attraction. The microemulsion was prepared by using octanol/TritonX-100/water/cyclohexane as raw material and nanoparticles were hydrolyzed by tetraethyl orthosilicate.

**(3) Sol-Gel Method.** The size of SiO<sub>2</sub> nanoparticles prepared by sol-gel method is different from the influence of ammonia concentration of the reactants, the type of silicates, the type of alcohols, the catalyst, and the temperature. By controlling these conditions, nano silica with different particle size and structure can be obtained [23].

### 3. Seismic Behavior Test of Concrete Frame Joints

**3.1. Experimental Materials.** Materials needed in the experiment are ordinary portland cement, sand, first-class sand ash, high-efficiency polycarboxylate water reducer, steel bar, PVA fiber, and nano silica.

When pouring concrete, it should start from the node core area and adopt the method of mechanical vibration. After pouring, it is placed on the vibration table for vibration.

The experimental samples are divided into three 200 × 200 × 400 mm concrete prisms and three 200 mm × 200 mm × 300 mm concrete cubes.

**3.2. Experimental Design.** According to the seismic code, the frame joints should be designed as “strong column and weak beam.” In order to ensure that the plastic hinge appears at the beam end first, the bearing capacity of the column end must be greater than that of the beam end. With the development of modern seismic theory, deformation capacity, stiffness degradation, ductility, and energy dissipation capacity have replaced the traditional strength indicators and become the indexes to measure the seismic performance.

Because the stress state near the bending point is the same as the actual stress state, the beam column joints in the middle story of plane frame are selected as the research object. Except for the different types of concrete materials, the other sample sizes and reinforcement are the same, and the concrete strength grade is C30.

Some scholars have shown that concrete with PVA fiber will show obvious strain hardening characteristics, and its

tensile strength, toughness, and shear strength will be greatly improved. In order to study the influence of concrete on the seismic performance of joints, low cycle cyclic loading tests were carried out on frame joints of ordinary concrete, nano silica fiber reinforced concrete, and PVA fiber reinforced concrete. For simple identification, ordinary concrete, PVA fiber concrete, and nano silica fiber concrete are marked as N1, N2, and N3, respectively.

#### 4. Analysis of Seismic Performance of Concrete Frame Joints

*4.1. Fuzzy Evaluation of Urban Disaster Prevention and Reconstruction Planning.* The values of urban building density, population density, ratio, earthquake suitability, earthquake resistance capacity of land and buildings, and temporary evacuation conditions are calculated, and the corresponding membership functions are generated [24]. The membership degrees are normalized. The membership degrees of qualified, basically qualified, and unqualified are 0.3598, 0.4896, and 0.0589.

The fuzzy evaluation of disaster prevention and reconstruction planning is calculated in six communities in the city.

It can be seen from Figure 1 that the building density and seismic capacity of the six communities selected in this paper are 0.658, 1.123, 0.913, 0.895, 0.935, 0.785, and 0.165, 0.569, 0.459, 0.789, 0.685, and 0.158, respectively. The six index values of the six communities selected in this paper are substituted into the corresponding membership function, and the corresponding membership degrees of the six communities can be calculated as 0.0369, 0.5123, 0.5638, 0.5469, 0.5879, and 0.0468. Other communities 1 and 6 are not qualified, so they need to be included in the key seismic reinforcement or carry out urban planning research again. In the remaining four communities, although qualified, we still need to pay attention to the building density and population density and other issues. We need to reduce the building density and population density. Otherwise, there will be an earthquake, which is not conducive to the earthquake evacuation and disaster relief.

*4.2. Bearing Capacity and Deformation Capacity of Frame Joints.* The bearing capacity of a member is one of the important bases to measure its seismic performance. The load reflected includes the cracking load when the core area of the frame joint is cracked and the yield load of the longitudinal reinforcement when it is in tension. When the beam end reaches the maximum bearing capacity, the ultimate load and ultimate load of the member are reduced by 15%. The bearing capacity, deformation capacity, and ductility coefficient of frame joints of ordinary concrete, PVA fiber concrete, and nano silica fiber concrete are shown in Tables 1 and 2.

Usually, in the process of reciprocating loading, due to the Bauschinger effect, the value obtained by each loading is different. In order to eliminate this error, the positive and negative data of the left end beam and the right end beam are

averaged. It can be seen from Figure 2 that the values of nano silica fiber concrete in cracking, yield, limit, and failure under load pressure are much higher than those of ordinary concrete. The value of PVA fiber concrete is slightly worse than that of nano silica fiber concrete, but it is also higher than that of ordinary concrete. It can also be seen from Figure 3 that the displacement and ductility coefficient of nano silica fiber concrete are much higher than those of ordinary concrete.

It can be seen from Figures 2 and 3 that fiber reinforced concrete can significantly improve the bearing capacity, deformation capacity and ductility of samples. In particular, nano silica fiber reinforced concrete can significantly improve the deformation capacity and ductility of joints.

*4.3. Stiffness Degradation of Frame Joints.* In the low cycle reciprocating test, the stiffness decreases with the cyclic loading of load and displacement. The slope of the straight line between the peak point and the origin of each cycle is defined as the equivalent stiffness, which is used to characterize the stiffness of the member. In order to eliminate the influence of different batches of materials and the asymmetry of equivalent stiffness calculation caused by pre- and postloading, stiffness residual rate is used to represent the stiffness degradation of components. The stiffness residual rate formula is as follows:

$$\omega = \frac{X_y}{X_0} \quad (4)$$

In the formula,  $\omega$  is the residual stiffness,  $X_y$  is the equivalent stiffness under operating conditions, and  $X_0$  is the equivalent stiffness of the first cycle.

The equivalent stiffness residual rates of samples N1, N2, and N3 are shown in Figure 4.

One part of the energy is dissipated by the elastic deformation of the structure, and the other part is dissipated by the inelastic deformation of the structure. It can be seen from Figure 4 that the equivalent viscous damping coefficient of the member increases with the increase of displacement after the drop ( $n-2$ ) and slow growth in the loading stage and after  $n$  ( $n-3$ ), and the growth rate of the member after reaching the yield stage is obviously accelerated and then presents the trend of slow decrease or slow increase. The main reason is that in the stage of elastic energy dissipation, the internal damage factors such as fracture development speed and internal friction of materials develop continuously, but the development speed is slow, and the equivalent viscous damping coefficient increases slowly. After the member reaches the yield stage, the concrete cracks develop rapidly, the deformation of reinforcement and internal friction of materials increase, and the formation of plastic hinge increases the rotational energy dissipation capacity of the member. When the member reaches the limit state, the crack continues to develop into concrete falling off, and the residual deformation of the component increases significantly, resulting in the slow change of equivalent viscous damping coefficient at this stage.

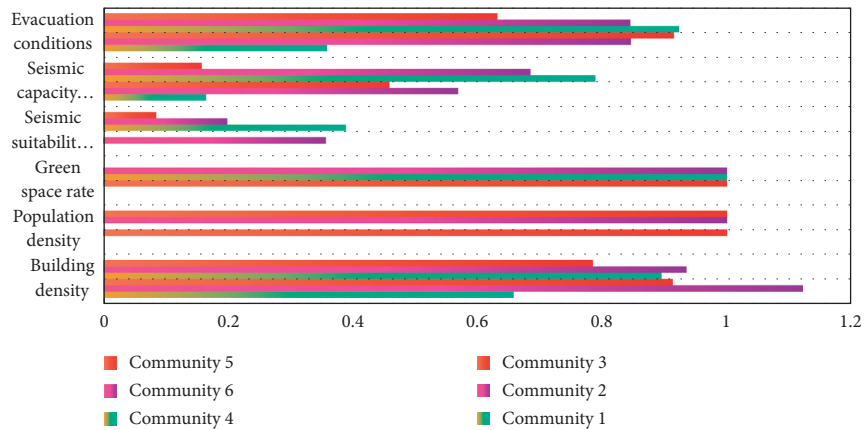


FIGURE 1: The value of six evaluation indexes in six communities.

TABLE 1: Bearing capacity of frame joints.

Experiment number		Load (kN)			
		Crack	Yield	Limit	Destruction
N1	Average value	48.69	85.65	108.35	75.65
N2	Average value	55.49	94.56	131.65	77.89
N3	Average value	76.89	95.67	145.37	79.56

TABLE 2: Displacement and ductility coefficient of frame joints.

Experiment number		Displacement (mm)				$u$
		Crack	Yield	Limit	Destruction	
N1	Average value	12.15	32.56	84.65	103.35	3.34
N2	Average value	17.35	31.65	73.56	152.42	3.65
N3	Average value	16.35	32.56	58.56	152.89	4.56

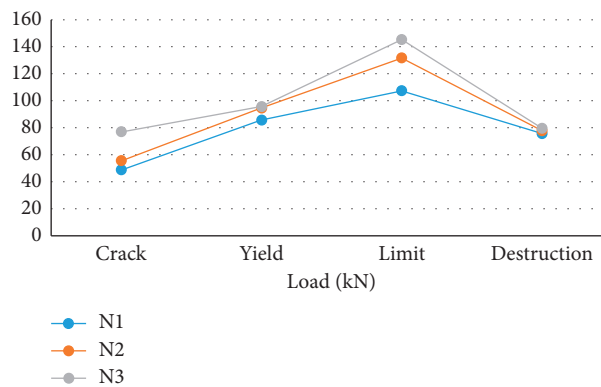


FIGURE 2: Bearing capacity of frame joints.

It can be seen from Figure 4 that the initial stiffness degradation values of the three groups of samples are the same. Compared with N1 sample, the displacement span of N2 and N3 samples is larger and the curve is more gentle, which indicates that the stiffness degradation of fiber reinforced concrete structure is gentle when it enters into the ductility stage, which is conducive to the structural seismic resistance. The curvature of sample N3 is small at the later

stage of loading, and the stiffness degradation is slow, which indicates that nano silica fiber reinforced concrete can improve the stiffness degradation performance of joints.

## 5. Discussion

With the development of materials science, nanoparticles have large specific surface area, small particle size, high

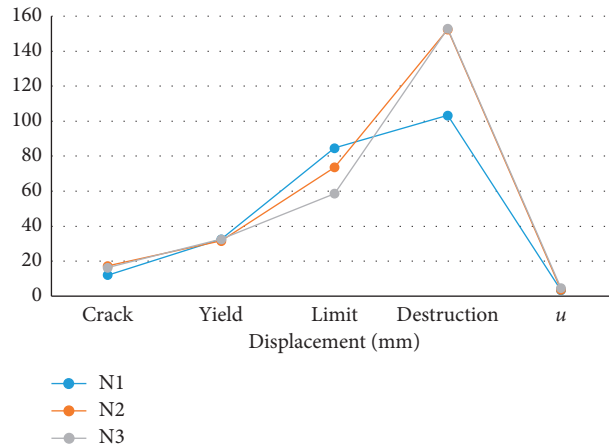


FIGURE 3: Displacement and ductility coefficient of frame joints.

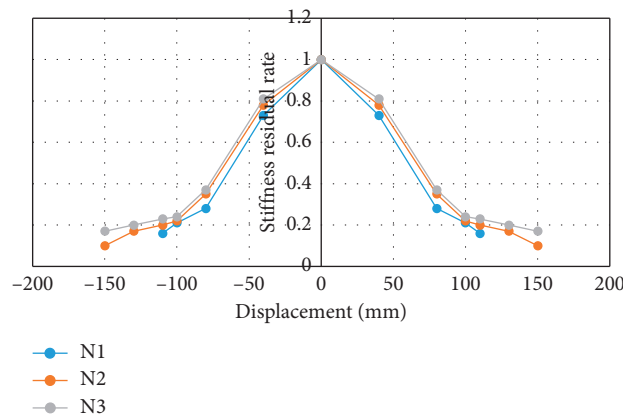


FIGURE 4: Node stiffness residual rate degradation curve.

surface energy, and unique nano effect. Adding nanoparticles to concrete can effectively improve the tensile strength of concrete and inhibit the early plastic cracking and crack propagation, so as to improve the crack resistance and durability of concrete.

In this paper, the bearing capacity, ductility capacity, energy dissipation capacity, and stiffness degradation of frame joints of ordinary concrete, PVA fiber concrete, and nano silica fiber concrete are compared and analyzed. The experimental results show that the frame joints with nano silica fiber concrete have good bearing capacity and ductility index. Compared with ordinary concrete, the bearing capacity and ductility coefficient of nano silica fiber concrete and PVA fiber concrete are increased by 37.8% and 15.6%, respectively. Compared with ordinary concrete frame joints, the energy dissipation capacity of nano silica fiber reinforced concrete and PVA fiber reinforced concrete frame joints is much higher. In particular, nano silica fiber reinforced concrete joints have excellent equivalent viscosity coefficient and energy dissipation capacity. Therefore, the seismic performance of nano silica fiber reinforced concrete frame joints is far superior to that of ordinary concrete frame joints.

Due to the error of the experimental method, the complex stress of the frame joints, and the limitations of the cast concrete samples, the experimental results may be affected. In this paper, only two kinds of materials, nano silica fiber concrete and PVA fiber concrete, are considered. The next step should be to consider whether there is better fiber concrete to improve the seismic performance of frame joints.

The application of nanomaterials technology requires a series of planning safeguards. The next step should be to scientifically formulate the seismic performance standards of buildings in seismic disaster prevention planning, encourage the adoption of new materials and new technologies, and improve the overall seismic level of cities. At the same time, the application standards of supervision and control of seismic technology in postdisaster reconstruction should be studied according to the design code, seismic fortification standard, project schedule, and quality requirements.

### Data Availability

The data in this article are available from the corresponding author upon request.

## Disclosure

The authors confirm that the content of the manuscript has not been published or submitted for publication elsewhere.

## Conflicts of Interest

The authors declare that there are no conflicts of interest regarding the publication of this paper.

## Authors' Contributions

All the authors have read and approved to submit the manuscript.

## Acknowledgments

This work was supported by the Young Scientific and Technological Backbone Cultivation Project of Wuhan University of Science and Technology (no. 2017xz021) and Innovation and Entrepreneurship Training Program for College Students in Hubei Province in 2019 (no. S201910488014).

## References

- [1] P. He, S. M. Nie, T. Wang, and C. C. Mao, "Study on urban seismic disaster prevention planning based on assessment and analysis of disaster-bearing capacity," *Journal of Catastrophology*, vol. 33, no. 4, pp. 141–148, 2018.
- [2] X. Z. Lu and X. Zeng, "Challenges in building resilient earthquake cities," *City and Disaster Reduction*, no. 4, pp. 29–34, 2017.
- [3] D. H. Ma, "Development prospect of urban seismic disaster prevention planning," *Standardization of Engineering Construction*, no. 6, pp. 15–16, 2019.
- [4] D. L. Zhong and Q. M. Feng, "Investigation on building destruction based on seismic coefficient," *Earthquake Engineering and Engineering Vibration*, vol. 24, no. 5, pp. 46–51, 2015.
- [5] C. D. Vecchio, M. D. Ludovico, A. Prota, and G. Manfredi, "Analytical model and design approach for FRP strengthening of non-conforming RC corner beam-column joints," *Engineering Structures*, vol. 87, pp. 8–20, 2015.
- [6] C. Del Vecchio, M. Di Ludovico, A. Prota, and G. Manfredi, "Modelling beam-column joints and FRP strengthening in the seismic performance assessment of RC existing frames," *Composite Structures*, vol. 142, pp. 107–116, 2016.
- [7] W. Kassem, "Strut-and-tie modelling for the analysis and design of RC beam-column joints," *Materials and Structures*, vol. 49, no. 8, pp. 3459–3476, 2016.
- [8] G. M. Verderame, M. T. De Risi, and P. Ricci, "Experimental investigation of exterior unreinforced beam-column joints with plain and deformed bars," *Journal of Earthquake Engineering*, vol. 22, no. 3–5, pp. 404–434, 2016.
- [9] E. Z. Beydokhty and H. Shariatmadar, "Behavior of damaged exterior RC beam-column joints strengthened by CFRP composites," *Latin American Journal of Solids and Structures*, vol. 13, no. 5, pp. 881–897, 2016.
- [10] J. L. Xi, X. Q. Peng, and L. G. Wang, "Preliminary study on urban civil air defense and seismic disaster prevention," *Modern Urban Research*, vol. 24, no. 5, pp. 33–37, 2009.
- [11] M. T. Gong, Q. Wei, and P. L. Feng, "Investigation on the damages of Sichuan removable cultural relics and its buildings in Wenchuan earthquake," *Sciences of Conservation and Archaeology*, vol. 28, no. 4, pp. 40–47, 2016.
- [12] Q. B. Zhao, Y. Shi, Q. Y. Zou, and C. Wang, "Design of evaluation model for seismic damage degree based on BIM building," *China Earthquake Engineering Journal*, vol. 41, no. 1, pp. 227–232, 2019.
- [13] H. Shi, "Estimation model of invulnerability of buildings under strong shock based on complex networks," *China Earthquake Engineering Journal*, vol. 39, no. 6, pp. 1024–1028, 2017.
- [14] X. S. Fan and S. W. Li, "Application of seismic performance evaluation of urban building groups in seismic disaster prevention planning," *Earthquake Resistant Engineering and Retrofitting*, vol. 39, no. S1, pp. 63–68, 2017.
- [15] X. Y. Pu and J. Zeng, "Study on seismic disaster prevention in urban residential area planning," *Architectural Journal*, no. 1, pp. 83–85, 2009.
- [16] P. Alaei and B. Li, "High-strength concrete exterior beam-column joints with high-yield strength steel reinforcements," *Engineering Structures*, vol. 145, no. 7, pp. 305–321, 2017.
- [17] W. Wang, H. Chan, and H. Shao, "Seismic performance of beam-column joints with SMA tendons strengthened by steel angles," *Journal of Constructional Steel Research*, vol. 109, pp. 61–71, 2015.
- [18] S. Yan, K. Li, Y. Zhang et al., "Experimental research on mechanical behavior of beam-column joints in reinforced concrete frame with weakened flanges," *Shenyang Jianzhu Daxue Xuebao (Ziran Kexue Ban)/Journal of Shenyang Jianzhu University (Natural Science)*, vol. 31, no. 2, pp. 219–227, 2015.
- [19] A. Rezvani-Boroujeni, M. Javanbakht, M. Karimi, and C. Shahrjerdi, "Immobilization of thiol-functionalized nanosilica on the surface of poly(ether sulfone) membranes for the removal of heavy-metal ions from industrial wastewater samples," *Industrial & Engineering Chemistry Research*, vol. 54, no. 1, pp. 502–513, 2015.
- [20] H. A. Heydary, E. Karamian, E. Poorazizi, A. Khandan, and J. Heydaripour, "A novel nano-fiber of Iranian gum tragacanth-polyvinyl alcohol/nanoclay composite for wound healing applications," *Procedia Materials Science*, vol. 11, pp. 176–182, 2015.
- [21] M. Cao, C. Wang, R. Xia et al., "Preparation and performance of the modified high-strength/high-modulus polyvinyl alcohol fiber/polyurethane grouting materials," *Construction and Building Materials*, vol. 168, pp. 482–489, 2018.
- [22] M. Nili and A. Ehsani, "Investigating the effect of the cement paste and transition zone on strength development of concrete containing nanosilica and silica fume," *Materials & Design*, vol. 75, pp. 174–183, 2015.
- [23] H. Zhou, T. J. F. Luchini, A. K. Agarwal et al., "Development of monetite-nanosilica bone cement: a preliminary study," *Journal of Biomedical Materials Research B Applied Biomaterials*, vol. 102, no. 8, pp. 1620–1626, 2015.
- [24] L. Zhang and J. Gao, "Attaining standard fuzzy evaluation of planning on seismic resistance and disaster prevention for urban residential areas," *World Earthquake Engineering*, vol. 24, no. 2, pp. 78–84, 2018.

## Research Article

# Spectrochemical Technology in Nanomaterial Preparation and Art Appraisal Technology Research

**Xiao Tang** 

*Department of Oil Painting, Hubei Institute of Fine Arts, Wuhan 430205, Hubei, China*

Correspondence should be addressed to Xiao Tang; [tangxiao@hifa.edu.cn](mailto:tangxiao@hifa.edu.cn)

Received 7 August 2020; Revised 4 September 2020; Accepted 20 September 2020; Published 15 October 2020

Academic Editor: Tifeng Jiao

Copyright © 2020 Xiao Tang. This is an open access article distributed under the Creative Commons Attribution License, which permits unrestricted use, distribution, and reproduction in any medium, provided the original work is properly cited.

With the rapid development of science and technology in micro/nanofield, it is urgent to carry out the research on new technology of micro/nanomechanics test and multiscale-related experimental mechanical analysis method. There is still a lot of work to be done in the basic theory and analysis method of micro-Raman spectroscopy as a new microscale mechanical test method applied to the experimental research of material mechanics. Based on the above background, the purpose of this paper is the application of spectrochemical technology in the preparation of nanomaterials and art identification technology. In this paper, different morphologies of SiO<sub>2</sub> nanomaterials, such as crystalline nanoparticles, amorphous nanowires, nanospheres, and nanonets, were prepared by a simple hot steaming method in the presence of argon. The samples were characterized by Raman spectroscopy. In addition, this paper also carried out art identification work, using spectral technology to detect some paintings and calligraphy. The experimental results show that the Raman spectra of these paintings and calligraphy papers are in the visible region because their fluorescence is too strong, and almost all the peaks are submerged. In the near-infrared region (1064 nm), their peaks are also very weak, but they can be distinguished by fluorescence and scanning electron microscopy.

## 1. Introduction

The rapid development of micro-nanotechnology brings new challenges to machine experiments. Small-scale, large-scale effect, multiscene combination effect, and nonclassical force become the factors to be considered, which is difficult to apply to many macroscopic high-type mechanical experiment methods. On the contrary, in the fine structure of materials, the study of macromechanical properties requires a variety of experimental tests and analysis. Therefore, it is very important to study the new testing technology and multifunctional correlation analysis method of micro/nanomachinery. Raman spectroscopy is a new micro-experimental mechanical testing technology developed recently. The basis of physical measurement is Raman spawning, which reflects the vibration energy information of material lattice, and the basic principle is determined deformation. The deformation rate is related to the fine mesh deformation, which can induce the change in Raman characteristic peak frequency, and the deformation (or

stress) can be measured by sensing the change in Raman spectrum. This technology has the characteristics of non-contact, destruction, and high-spatial decomposition and can measure the inherent stress and external stress. It is a potential test method in the field of micromechanics characterization.

Template synthesis is an important kind of nanofabrication methods. Quintana reviewed the recent progress in the preparation of nanomaterials by nanoporous membrane extrusion, namely, “nonsacrificial template synthesis.” Firstly, the types of nanoporous membranes in extrusion applications were introduced. Secondly, four common extrusion strategies of nanoporous membrane were studied: vesicle extrusion, membrane emulsification, precipitation extrusion, and biofilm extrusion. This paper discusses the principle and historical background of each specific technology, lists prominent examples, and evaluates their positive and negative characteristics. Finally, the research status and development prospect of nanoporous membrane extrusion methods are discussed. Abdel Salam

studied the structure function relationship of new nanomaterials and its effect on the properties of concrete. In addition, Abdel Salam also discussed the mechanism of using new nanomaterials to improve the durability of concrete. Finally, the application of this material in practical engineering is briefly introduced. Gonciarz reported the preparation of nanosized cobalt disulfide by a simple liquid-phase method with thiophenol as the end-capped agent in the cationic surfactant cetyltrimethylammonium bromide (CTAB) micelles. The product was characterized by spectrum, electron microscope, and magnetic moment measurement [1]. Duan first synthesized a novel multifunctional nanomaterial by combining superparamagnetism of nanoiron oxide with fluorescence properties of morin- $\text{Al}_3^+$  complex. First, the iron oxide nanoparticles are coated with silica to isolate them from the complex and the surrounding environment.  $\text{NH}_2\text{O}$ , which provides active aluminum atoms, was deposited on the silica shell. Finally, morin reacted with active aluminum atom to prepare the final multifunctional nanomaterial [2].

Calligraphy and painting identification is the basic history of calligraphy and painting research. The empirical means of traditional calligraphy and painting identification rely on intuition, which is very uncertain and easy to make. And because of ancient calligraphy and painting, even though we can collect samples for measurement, its specificity and accuracy are still difficult to determine time. Therefore, Bajju emphasizes that we should treat calligraphy and painting identification correctly and reasonably and recognize the uncertainty and uncertainty limitation of calligraphy and painting identification, and we should effectively use the research results of evaluation as methodology, not just pay attention to its conclusion, which is of great significance to the study of calligraphy and painting history [3]. By reviewing the development of Xu Bangda's research on traditional Chinese calligraphy and painting identification, Callery fully affirmed Xu Bangda's basic contribution to traditional Chinese painting and calligraphy identification and summarized Xu Bangda's methodology: artistic style comparison, style research, and demonstration and visual inspection and text combination research. Finally, the relationship between calligraphy and painting identification and art history is analyzed [4]. Throughout their masterpieces, there are many outstanding Chinese painters. The imitation, forgery, and ghost creation of ancient Chinese painting and calligraphy have brought many troubles and confusion to the appreciation and research of ancient Chinese painting and calligraphy. On the basis of certain theories and practices of calligraphy and painting identification, Chooto and Manaboot summed up eight basic methods for identification of ancient Chinese calligraphy and painting [5].

Based on the Raman measurement experiment, the microscale mechanical behavior of materials was studied from the response of material lattice structure to load. Combined with the experimental results of other scales, the multiscale mechanical properties and micromechanism of carbon nanotube fiber and film materials were systematically analyzed.

## 2. Nanomaterial Preparation and Art Appraisal

### 2.1. Spectral Pretreatment Method

**2.1.1. Smoothing.** Smoothing is usually used to avoid the influence of random noise on the spectrum, so it can make the sudden change in signal smoother and improve the signal to noise equipment, but spectral distortion may occur [5, 6]. Generally, three compressor methods are used, namely, semiaverage method, moving average compressor method, and SG line compressor method. The semiaverage method is to divide the spectral data equally, using the central average of each segment instead of the original value of the equal segment [7]. The more data points in each class, the more serious the spectral distortion. To improve the averaging method, the fans of different cars overlap. The SG integration method is also called polynomial compressor method because of the same processing and signal distortion, so it is not necessary to grasp and maintain the peak and minimum positions of spectrum [8, 9].

The basic principle of SG smoothing is the polynomial *D* "multiplication" of the measured points and the left and right sides of the measurement points. The fitting value of the center point is obtained from the measured point after 20 points, and the new value can be obtained by using 13 new polynomials in the new window. In the window, the data of equidistant points  $n = 2m + 1$  are matched with *k*-degree polynomial:

$$x_j^i = a_0 + a_1j + a_2j^2 + \dots + a_kj^k, \quad (1)$$

$$j = -m, -m + 1, \dots, m - 1, m; i = 1, \dots, n.$$

Formula (1) displays the position of data points in the overall measurement vector, and *j* displays the position of data points on the left and right of the window. SG smoothing can adjust the window size and polynomial series number to get the desired smoothing effect. If the window width is too large, it will distort and the noise will not be eliminated if it is too small, so the appropriate window width is chosen [10, 11].

**2.1.2. Derivative.** The derivative algorithm can clear the outline of pectin and amplify the noise signal by eliminating the standard drift and change caused by the background color and other factors [12]. Spectrum's Judo generally adopts the SG interactive induction method and direct differentiation method. Direct precipitation method has large parameters in the spectral derivation of rare wavelength sampling points, but the SG interactive derivation method has no such problem in the spectral derivation of rare wavelength sampling points. The direct precipitation method is more suitable for high-resolution multiwavelength sampling. Since the spectra of bright spots are derived, different methods are directly used in this paper [13, 14]. If the first derivative of the spectrum is obtained, the conversion error will be eliminated. By obtaining the second derivative spectrum, the rotation error of the spectrum can be eliminated. The derivation formula is as follows.

The formula of the first derivative (FD) of direct difference is as follows:

$$y' = \frac{y_{(i+1)} - y_i}{\Delta\lambda}. \quad (2)$$

The formula of the second derivative (SD) is as follows:

$$y'' = \frac{y_{(i+1)} - 2y_i + y_{(i-1)}}{\Delta\lambda^2}. \quad (3)$$

Among them,  $y$  is the absorbance and  $\Delta\lambda$  is the wavelength interval.

**2.1.3. Light Scattering Correction.** The spectral difference caused by scattering is greater than that caused by the internal components of the sample itself. The scattering degree is related to the wavelength, particle size, and refractive index of the sample, which mainly shows the conversion, rotation, quadratic, and high curve of the standard line. Scattering correction can effectively eliminate or reduce low light-level problems, reduce noise, and improve signal to noise. The commonly used methods are multivariable scattering correction and standard normal transformation [15].

The multideformation scattering correction can modify the various spectra due to scattering and obtain ideal spectra. The average spectrum of the set to be modified is the ideal spectrum. Each spectrum has an ideal spectrum and linear relationship, so the calculation based on the inclination of the line can be obtained by linear regression [16]. By the mathematical method, the scattering signal of the sample spectrum is separated from the internal component information of the sample, and the random variation is eliminated as much as possible. The calibration process is as follows:

- (1) Calculate the average spectrum of the set to be corrected:

$$\bar{A} = \sum_{i=1}^n \frac{A_i}{n}. \quad (4)$$

- (2) The regression coefficient  $M_i$  and the regression constant  $B_i$  of each spectrum were obtained by linear regression:

$$A_i = m_i \bar{A} + b_i. \quad (5)$$

- (3) After subtracting the regression constant from each original spectrum and dividing it by the regression coefficient, the multiple scattering correction is performed for the spectrum:

$$A_{i(\text{MSC})} = \frac{(A_i - b_i)}{m_i}. \quad (6)$$

Formally,  $A$  represents the  $n \times p$  spectrum matrix to be modified,  $n$  is the number of samples, and  $p$  is the wavelength fraction of the spectrum.  $A_i$  represents the spectrum of the second sample of  $i$ . The size of the interactive  $m_j$  can reflect the inherent reflection effect of the sample, and the size of the slope reflects the uniformity of the sample. Adjusting the size of  $m_i$  and  $b_i$  can minimize the scattering signal of the spectrum [17, 18].

SNV (standard norm variate) assumes that the absorbance value of each wavelength point in each spectrum satisfies a specific distribution (such as a regular distribution). According to the difference of the family, each spectrum will be modified [19]. First, the mean value  $\bar{X}_i$  and standard deviation of the sample spectrum is calculated to be corrected as  $q$ , and then, the mean value is subtracted from the sample spectrum to be corrected and divided by the standard deviation even if the original spectrum standard is normalized. It is calculated as follows:

$$X_{i(\text{snv})} = \frac{X_i - \bar{X}_i}{\sigma_i}, \quad (7)$$

where  $X_i$  represents the spectrum of the  $i$ -th sample.

**2.2. Qualitative Analysis Methods.** By comparing the spectra of known samples and unknown samples for qualitative analysis, due to the large overlap of absorption peaks in the broadband, it is difficult to judge the similarity with the naked eye, so a pattern recognition method is required. The pattern recognition method is to form a multidimensional space through the spectral information of the sample or the extracted characteristic data. Similar substances exist in similar positions in the space [20, 21]. Therefore, the unknown range of the sample can be investigated based on this. At this time, there is no need to know the characteristic information of the sample. The spectral characteristics of the sample are analyzed. Commonly used pattern recognition methods include partial least squares, discriminative analysis, random forest, and extreme learning instruments [22].

**2.2.1. Random Forest.** Random Forest (RF) algorithm is a classification machine that contains multiple random decision trees that are essentially unrelated. The output result is the most output category of all christmas trees, and its generalization performance is excellent. The decision tree and the number of node division variables  $m$  in RF are two important parameters. In this article, the number of decision trees is optimized, and the number of node division variables is the basic value. The detailed process of the specific algorithm is as follows:

- (1)  $N$  crystal trees  $C_1, C_2, \dots, N$  training suits  $S_1$  and  $S_2$ , corresponding to  $CN$ ; in order to randomly generate SN, the start band method is used.
- (2) Before selecting the attribute in each internal node, the segmentation attribute of the node is the  $m$  attribute selected arbitrarily in the  $M$  sample attributes, and the node is divided into the best segmentation method among the  $m$  attributes (the value of  $m$

generally does not change during the process, which is 0 and an integer between  $M$ ).

- (3) Each tree grows worthless, and each crystalline tree is used to distinguish the predicted sample  $X$ , and the corresponding categories  $C_2(X)$ ,  $C_2(X)$ , and  $CN(X)$  are obtained.
- (4) According to the principle followed by a few people, the category with the most output categories in all decision trees is regarded as the category of the prediction sample  $X$ .
- (5) The principle of starting the trap method sampling includes  $n$  different samples  $(x_1, x_2, \dots, x_n)$  in the set  $S$ . Each time the sample is changed, the number of extractions is assumed to be  $n$ . Second, after combining the extracted samples into the new set  $S^*$ , the probability that a specific sample  $x_i$  ( $i = 1, 2, \dots, n$ ) is not included in  $S^*$  is as follows:

$$p = \left(1 - \frac{1}{n}\right)^n. \quad (8)$$

When  $n \rightarrow \infty$ , there are

$$\lim_{n \rightarrow \infty} = \lim_{n \rightarrow \infty} \left(1 - \frac{1}{n}\right)^n = e^{-1} \approx 0.368. \quad (9)$$

From the perspective of the total number of samples, the new set  $S^*$  and the original set  $S$  are both  $n$ , but due to the replacement of samples, the new set  $S^*$  may contain the same samples repeatedly configured.

**2.2.2. Extreme Learning Machine.** Extreme Learning Machine (ELM) solves the shortcomings of slow training speed, complex parameter selection, and the easiest to cross the local neural network. It provides fast learning speed, more powerful generalization functions, and fewer adjustments, few advantages of media variables. ELM will randomly generate the connection weight value of the input layer and the hidden layer and the critical value of the hidden layer Nurem, so there is no need to adjust. The number of hidden stacked neurons and their activation functions (only nonlinear, nondiscriminatory, and discontinuous functions) and the only optimal solution  $\beta$  can be obtained. The detailed process of the specific algorithm is as follows:

- (1) Set the number of hidden layer neurons and automatically generate the connection weight  $w$  between the input layer and the hidden layer and the hidden layer neuron value  $b$ .
- (2) Set the activation function of the hidden layer neuron and calculate the output matrix  $H$  of the hidden layer.
- (3) Calculate the weight of the output layer  
 $\hat{\beta}: \hat{\beta} = H + T'$ .

### 2.3. Physical Preparation Methods of Nanomaterials

**2.3.1. Mechanical Law.** Mechanical methods include mechanical ball, mechanical crushing, and high gravity technology. Mechanical ball method does not need external heat supply. Through ball sealing, due to the surface reaction between materials, large particles can be changed into small particles to obtain nanomaterials. Mechanical comminution adopts many methods, such as mechanical comminution of superfine micropowder and electric spark explosion, to directly crush raw materials into ultrafine powder, which is especially suitable for manufacturing ultrafine powder of finished products. High gravity technology is the high-speed rotation of high-gravity rotation layer. Centrifugal acceleration hundreds of times the acceleration of gravity greatly improves the material transmission and fine mixing between each other to produce nanomaterials.

**2.3.2. Gas Phase Method.** Meteorological methods include the evaporation condensation method, solution evaporation method, and plastic deformation method. Evaporation and condensation methods are to gasify raw materials or form plasma and to achieve a supersaturation state by resisting heating, high-frequency induction, plasma, laser, electron beam, and arc induction in vacuum or inactive gas and gas media. In order to form high-purity nanomaterials, the condensation solution evaporation method in the media is to make the solvent into small bells and then quickly evaporate them to minimize the separation of components. It can be treated by spray drying, spray pyrolysis, or freeze drying. Severe plastic deformation is a function of quasistatic pressure. In this case, the size of the material is slightly adjusted to nanolevel after plastic deformation.

**2.3.3. Magnetron Sputtering and Plasma.** Stamping technology uses high-energy particles to exchange energy or motion. Atoms or molecules on the surface of the target material fly to the surface of the target material and adhere to the substrate to form nanomaterials. The formation of the compound is not easy to change. At present, spring technology has been greatly developed, which generally uses carbide, DC magnetic field, high-frequency magnetic field, ion beam pusher, and electron tetranuclear tube resonance-assisted reactive magnetic field. The plasma method uses DC discharge in inactive or reactive atmosphere to ionize the gas and produce high-temperature plasma. The steam is cooled to form ultrafine particles by combining and evaporating the raw material solution. High ionic temperature can produce refractory metals or compounds with high purity. In an inactive atmosphere, almost all metal nanomaterials can be produced by the plasma method.

### 2.4. Chemical Preparation of Nanomaterials

**2.4.1. Sol-Gel Method.** The chemical engineering of gelation is to disperse raw materials in solvents and then generate active simulators through hydrolysis and decomposition.

**2.4.2. Ionic Liquid Method.** As a special organic solvent, ionic liquids have inherent physical and chemical properties such as high viscosity, high ionic conductivity, high thermal stability, low toxicity, excellent fluidity, and wide liquid temperature range. At a higher temperature, ionic liquid is still of low volatility, which is difficult to cause environmental pollution. It is a kind of green solvent, and ionic liquid is a good medium to synthesize different nanostructures.

**2.4.3. Solvothermal Method.** Solvothermal method is an effective method to realize controllable synthesis and manufacture of nanomaterials by heating the reaction system composed of various solvents in a closed reactor (such as automatic clay), so as to form an effective method in high-temperature and high-pressure environment.

**2.4.4. Microemulsion Method.** Nanoparticle microemulsion manufacturing is a newly developed research area with the advantages of being close to small particle size and monodisperse system.

### 3. Nanomaterial Preparation and Art Appraisal Test Design

**3.1. Experimental Materials and Testing Instruments.** *S* powder (purity 99.99%) and nanopowder (purity 99.99%) were used as raw materials. The sample collection substrate is an *n*-type monocrystalline silicon wafer (111) ground on one side. The substrate was washed with acetone and water. In the experiment, as a shielding gas, high-purity Ar gas is needed.

The surface morphology of samples on silicon wafers was detected and analyzed by injection electron microscopy (SEM, *s*-4800) equipped with energy spectrum X-ray (EDX). The structure of the sample was measured and analyzed by X-ray system (CRD, Rigaku Ultima IV, Cu-K $\alpha$  radiation). The Raman spectrum of the sample was detected and analyzed by LabRAM HR of 532 nm laser line. The luminescence (PL) spectrum was obtained by the detection of 325 nm He-Cd laser at room temperature.

**3.2. SiO<sub>2</sub> Nanocrystals and Amorphous Nanowires.** The growth of nanostructures is carried out in a traditional horizontal quartz tube. In the experiment, Si nanopowder and *s* powder (purity 99.99%) were mixed uniformly in the ratio of 1:1, and the quartz tube was placed in the high-temperature region of horizontal tube. The *n*-type Si (111) sheet is located 10–20 cm from the reaction source, and the Si sheet is relatively low in commercial use. The impurity gas of penicillin is removed as much as possible through the protective gas Ar for 20 minutes before the temperature rises. After that, it was heated to 1000°C in 2 hours at the rate of 20 ml/min under a certain flow of Ar. After the reaction, the flow of Ar stopped. At the end of the experiment, the samples were taken out, and white sponge and other substances were found on the surface of silica gel.

**3.3. Art Identification Experiment.** German Bruker Fourier-transform near-infrared Raman spectrometer, Japanese LSM-6390 scanning electron microscope, and German Bruker infrared absorption instrument were used as experimental instruments. By comparing the Raman spectra of the pigments studied with those of various monochromatic pigments, the formation and content of the studied pigments can be roughly obtained according to the position and intensity of the Raman peaks. The reflectance of various monochromatic pigments should be considered when comparing the Raman spectra of pigments with those of various monochromatic pigments.

### 4. Analysis of Nanomaterial Preparation and Art Appraisal Test Results

**4.1. Preparation and Analysis of Nanomaterials.** The experimental results show that a large number of nanowires and nanocrystals appear at 950°C due to the uneven growth. The diameter of the line is between 100 and 400 nm, and the length is 0.8–3  $\mu$ m. The grain size is about 200–460 nm. The EDX spectra show that the nanowires and nanocrystals are composed of Si and O elements. The ratio of silicon to oxygen is close to 1:2, and a small amount of extraoxygen may come from the test environment of EDX technology. The morphology of nanowires is grown at 950°C, 960°C, and 970°C, respectively. It is obvious that the diameter of nanowires increases and the length decreases with the increase in growth temperature. Nanoparticles are distributed on the surface of the whole Si substrate, and their sizes are between 100 nm and 380 nm. The three peaks at 21.5°C, 23.9°C, and 26.7°C positions can be indexed as crystalline SiO<sub>2</sub>, which matches the diffraction pattern of rhombic SiO<sub>2</sub> (PDF no. 03-0419). The structure of such “rhombic SiO<sub>2</sub>” nanocrystals is commonly referred to as  $\alpha$ -quartz. In addition to the crystalline phase, there is a wide peak of SiO<sub>2</sub> between 12.3°C and 32.1°C.

The Raman spectra of SiO<sub>2</sub> nanowires and nanoparticles are shown in Figure 1.

There is a unique peak at 521 cm<sup>-1</sup>, corresponding to the Si substrate. It has been reported that the signal of Si band in amorphous Si, Si nanocrystals, or Si nanowires is generally in the range of 480–510.5 cm<sup>-1</sup>. However, there is no peak in this range, which indicates that the product is likely to be oxidized.

The EDX spectrum of nanowires with large area is shown in Figure 2.

The test found that the content ratio of Si to O is close to 1:2. The silicon-oxygen 1:2 ratio will be affected by the silicon substrate, leading to inaccurate thoughts about the silicon-oxygen content ratio. But through the Raman test and through the above TEM results, except for the SiO<sub>2</sub> amorphous nanowires, the nanoparticles are essentially polycrystalline. The XRD results show that the synthesized crystal is a rhombohedral structure of SiO<sub>2</sub>. Therefore, it can be reasonably concluded that the products grown on Si substrates are SiO<sub>2</sub> amorphous nanowires and nanocrystals. Amorphous/nanocrystalline Si nanoparticles do not appear in the product.

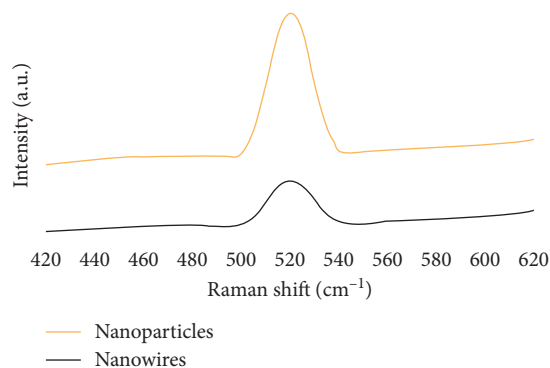


FIGURE 1: Raman spectrum of synthesized  $\text{SiO}_2$  nanowires and nanoparticles.

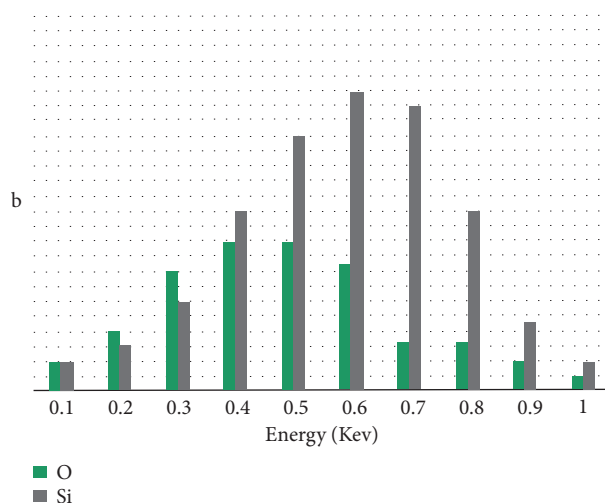


FIGURE 2: EDX spectrum of the synthesized nanowire.

S powder reacts with Si wafers at a lower temperature (about  $900^\circ\text{C}$ ) to form silicon sulfide ( $\text{SiS}$ ). When the temperature rises above  $1000^\circ\text{C}$ , Si nanowires are precipitated from  $\text{SiS}$  and grow into nanowires in a certain direction.  $\text{SiS}$  is located at the tip of the Si nanowire. It can be said that  $\text{SiS}$ , as a nucleation center, plays an important role in assisting the growth process. In our experimental study, Si powder and S powder were thermally evaporated at a lower temperature under argon flow to prepare  $\text{SiO}_2$  ANW and NC. The Si/O content ratio at different positions of the nanowires was measured by EDX. Since a Si substrate is used, the Si content is usually relatively high. From the test in the figure, it is found that the O content at the top of the nanowire is slightly higher than the middle position. According to the SEM results, the length of the nanowires increases as the growth temperature decreases. This may indicate that the nanowires are growing in the radial direction. Similar to the previous report the nucleation center is located at the tip of the nanowire. The particle generation and oxidation during the reaction is accompanied by an increase in O. Therefore, the high oxygen content on the top of the nanowire corresponds to the top growth mechanism of the nanowire.

#### 4.2. Art Appraisal Analysis under Spectroscopic Technology.

The ten papers in the experiment were all manufactured in different places or by different manufacturers. During the experiment, visible Raman (wavelength is 514 nm) is first used to detect these samples. But most of the samples have too strong fluorescence, and some samples are very weak even with peaks. Therefore, the ultraviolet-visible Raman spectrometer was used to do the laser fluorescence of these samples, and the excitation wavelength was 514 nm. The fluorescence peaks are analyzed of the first five samples, as shown in Figure 3.

It is obvious from Figure 3 that the fluorescence peaks of the samples are not the same. Sample 1 and sample 4 both have a fluorescence peak at 630 nm, but sample 1 has a small shoulder at 673 nm. The fluorescence peaks of sample 2 and sample 4 are at 608 nm and 646 nm, respectively. The most special sample is No. 3, which has three very obvious fluorescence peaks, namely, 630 nm, 669 nm, and 760 nm. Their corresponding peak positions are shown in Table 1.

The fluorescence spectra of samples 6–10 are shown in Figure 4.

The fluorescence peaks of sample 6 and sample 7 are the same, the fluorescence peak of sample 9 at 640 nm is at

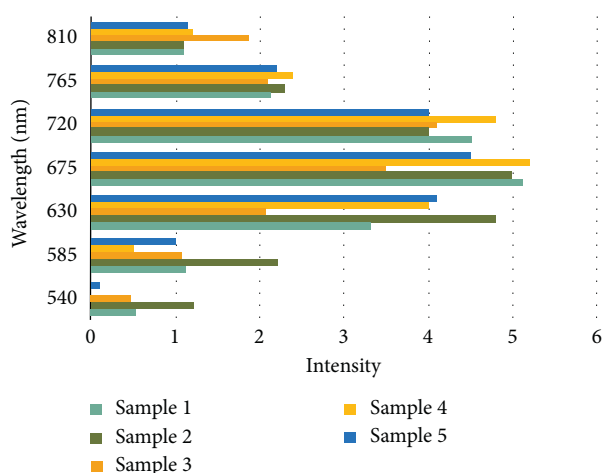


FIGURE 3: Laser fluorescence of samples 1–5 paper.

TABLE 1: Mahalanobis distance from inkpad on different carriers to its actual category.

Sample	Mahalanobis distance		
1	0.90	0.97	0.83
2	1.01	1.00	0.79
3	1.13	0.77	1.12
4	0.47	0.39	0.45
5	0.41	0.59	0.29

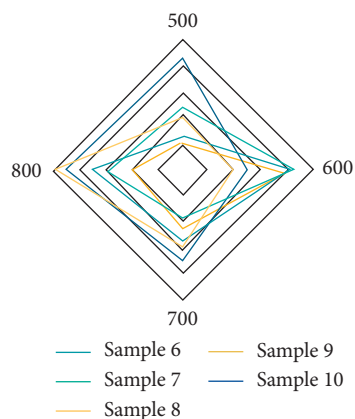


FIGURE 4: Laser fluorescence of samples 6–10.

623 nm, and there is a shoulder peak around 650. The peak of sample no. 8 is at 650 nm. The fluorescence peaks of sample no. 10 are 589 nm, 623 nm, and 671 nm, respectively.

By observing the scanning electron micrograph of the rice paper, we can analyze the general ratio of leather and grass in the paper from the surface structure of the rice paper or the number of long and short fibers in them and further use this method to identify the type of rice paper. By observing the scanning electron micrograph of rice paper, we can roughly distinguish the differences in the manufacturing

process of different manufacturers from the size and structure of the fiber. This also provides a way to identify different origins or manufacturers of rice paper.

## 5. Conclusions

Spectroscopy technology is widely used in the fields of medicine, cultural heritage, gemstone identification, and forensic medicine. Through the destruction analysis and research of cultural relic samples, the identification, dating, restoration, and preservation of cultural relics can be made safer and more trustworthy. Analysis and research can understand the different points contained in gems in different places and provide scientific basis for identifying and evaluating gems. The use of spectroscopy technology can achieve recognition accuracy and avoid damage to calligraphy and images. Therefore, with the development of modern technology, spectroscopic technology will become a necessary means of identification.

In this study, thermal evaporation was used to produce nano-SiO<sub>2</sub> materials with different shapes and structures. The basic structure, photoelectric properties, and manufacturing process of the surface were studied and analyzed. Through experiments, it is found that the structure and morphology of the samples obtained at different adhesion temperatures and increased pressures are different, and the diameter and length of the samples are affected by the growth temperature. In addition, the optical properties of nano-SiO<sub>2</sub> with different morphologies and structures are also very different. In these two aspects, in order to change the size 3 gap, the size or the band gap of other materials can be changed to improve the complexity and function of the nanostructure. Therefore, the research on other forms of nano-SiO<sub>2</sub> will help to develop its characteristics, which will greatly help the better application of electronic equipment and new materials.

In this study, rice paper from different manufacturers was selected. Due to its strong fluorescence, it is not only difficult to form a visible Raman spectrum, but the near-infrared signal is also weak. In this case, in order to perform laser fluorescence, the wavelength of 514 nm is used here, and finally, good experimental results are obtained. The rice paper of other manufacturers is made of other raw materials or the same kind of raw materials, but the ratio is different, and the final fluorescence spectrum is also different, which can distinguish the paper made by other manufacturers and provide a method for the identification of calligraphy and painting in the future.

## Data Availability

The data in this article are actually available.

## Disclosure

We confirm that the content of the manuscript has not been published or submitted for publication elsewhere.

## Conflicts of Interest

The author declares that there are no conflicts of interest in our paper.

## Acknowledgments

This work was supported by the Hubei Institute of Fine Arts.

## References

- [1] A. Gonciarz, M. Żuber, and J. Zwodziak, "Front cover: spectrochemical properties and solvatochromism of tetradentate schiff base complex with nickel: calculations and experiments (ChemistryOpen 9/2018)," *ChemistryOpen*, vol. 7, no. 9, p. 669, 2018.
- [2] P. Duan, B. Liu, C. L. M. Morais et al., "4-Nonylphenol effects on rat testis and sertoli cells determined by spectrochemical techniques coupled with chemometric analysis," *Chemosphere*, vol. 218, pp. 64–75, 2018.
- [3] G. D. Bajju, G. Devi, and A. S. Ashu, "Spectrochemical and biological evaluation of axially substituted zirconium (IV) meso-tetra (4-methoxyphenyl)porphyrins," *Russian Journal of Inorganic Chemistry*, vol. 64, no. 6, pp. 734–741, 2019.
- [4] E. L. Callery, C. L. M. Morais, M. Paraskevas et al., "New approach to investigate common variable immunodeficiency patients using spectrochemical analysis of blood," *Scientific Reports*, vol. 9, no. 1, p. 7239, 2019.
- [5] P. Chooto and S. Manaboot, "Electrochemical, spectrochemical and quantum chemical studies on dimedone as corrosion inhibitor for copper in acetonitrile," *Journal of Scientific Research and Reports*, vol. 15, no. 2, pp. 1–13, 2017.
- [6] A. S. Zakuskin, A. M. Popov, N. B. Zorov, and T. A. Labutin, "Confinement of laser plasma by shock waves for increasing signal intensity in spectrochemical determination of trace elements in ores," *Technical Physics Letters*, vol. 44, no. 1, pp. 73–76, 2018.
- [7] K. Li, C. F. Ma, Y. Ling, M. Li, Q. Gao, and W. J. Luo, "Acid/base bifunctional carbonaceous nanomaterial with large surface area: preparation, characterization, and adsorption properties for cationic and anionic compounds," *Materials Chemistry and Physics*, vol. 162, no. 8, pp. 149–161, 2015.
- [8] J. Kamalakkannan, V. L. Chandraboss, B. Karthikeyan, and S. Senthilvelan, "Preparation and characterization of TiInVO6-nanomaterial using precipitation method and its multi applications," *Journal of Materials Science: Materials in Electronics*, vol. 27, no. 3, pp. 2488–2503, 2016.
- [9] M. Hasanzadeh, S. A. Nahar, N. Shadjou, and A. Mokhtarzadeh, "Immobilization of proline dehydrogenase on functionalized silica mesoporous nanomaterial towards preparation of a novel thermostable enzyme biosensor," *Journal of Nanoscience and Nanotechnology*, vol. 18, no. 11, pp. 7786–7796, 2018.
- [10] S. Akai, N. K. Kumagai, Y. Sasaki et al., "Development of automatic TEM/SEM specimen preparation instrument for nanomaterial dispersed in liquid," *Microscopy and Microanalysis*, vol. 25, no. S2, pp. 774–775, 2019.
- [11] Q. Kikuchi, Y. Wang, J. Xiao, C. Chen, and H. Fan, "Preparation and characterization of magnetic nanomaterial and its application for removal of polycyclic aromatic hydrocarbons," *Journal of Hazardous Materials*, vol. 371, pp. 323–331, 2019.
- [12] A. Lisowska-Oleksiak, B. Wicikowska, A. Nowak et al., "Preparation and characterization of nanomaterial consisting of silica aerogel & carbon tested as an electrode in non-aqueous media containing lithium salt," *International Journal of Electrochemical Ence*, vol. 11, no. 3, pp. 1997–2007, 2016.
- [13] Y. B. Tao, C. H. Lin, and Y. L. He, "Preparation and thermal properties characterization of carbonate salt/carbon nanomaterial composite phase change material," *Energy Conversion and Management*, vol. 97, pp. 103–110, 2015.
- [14] A. Dash and R. Chakravarty, "Nanomaterial-based adsorbent: promises, opportunities, and challenges to develop column chromatography radionuclide generators for nuclear medicine," *Separation & Purification Reviews*, vol. 46, no. 2, pp. 91–107, 2016.
- [15] H. Gao, "The value and a preliminary study of the integration of traditional Chinese painting and calligraphy & modern and contemporary art in primary school art teaching," *International Education Studies*, vol. 12, no. 6, p. 75, 2019.
- [16] V. Y. Davydov, A. N. Smirnov, I. N. Goncharuk et al., "Raman spectroscopy as a tool for characterization of strained hexagonal GaN/AlxGa1-xN superlattices," *Physica Status Solidi*, vol. 234, no. 3, pp. 975–979, 2015.
- [17] P. Crow, J. S. Uff, J. A. Farmer et al., "The use of Raman spectroscopy to identify and characterize transitional cell carcinoma in vitro," *BJU International*, vol. 93, no. 9, pp. 1232–1236, 2015.
- [18] A. Akemi Ooka and R. L. Garrell, "Surface-enhanced Raman spectroscopy of DOPA-containing peptides related to adhesive protein of marine mussel, *Mytilus edulis*," *Biopolymers*, vol. 57, no. 2, pp. 92–102, 2015.
- [19] G. H. Smudde and P. C. Stair, "The oxidation of Mo (100) studied by XPS and surface Raman spectroscopy: the onset of MoO<sub>2</sub> formation and the formation of surface polymolybdate," *Surface Science*, vol. 317, no. 1-2, pp. 65–72, 2016.
- [20] F. Collard, B. Gilbert, G. Eppe, K. Das, and E. Parmentier, "Detection of anthropogenic particles in fish stomachs: an isolation method adapted to identification by Raman spectroscopy," *Archives of Environmental Contamination and Toxicology*, vol. 69, no. 3, pp. 331–339, 2015.
- [21] N. Q. Liem, D. X. Thanh, V. X. Quang et al., "Detection of lattice match between ZnSxSe1-x epilayers and GaAs substrates by polarisation Raman spectroscopy," *Physica Status Solidi*, vol. 229, no. 1, pp. 47–51, 2015.
- [22] S. A. Overman and G. J. Thomas, "Structural studies of viruses by Raman spectroscopy. Novel vibrational assignments for proteins from Raman spectra of viruses," *Journal of Raman Spectroscopy*, vol. 29, no. 1, pp. 23–29, 2015.

## Research Article

# Nanometer Montmorillonite Modified Fly Ash Ecological Slope Protection Material and Its Preparation and Application

Guochong Lou <sup>1,2</sup>, Qinghui Zhong,<sup>3</sup> and Jianguo Xie<sup>3</sup>

<sup>1</sup>School of Civil Engineering, Shijiazhuang Tiedao University, Shijiazhuang 050043, Hebei, China

<sup>2</sup>Key Laboratory Jointly Established by Ministry of Road and Railway Engineering, Shijiazhuang Tiedao University, Shijiazhuang 050043, Hebei, China

<sup>3</sup>Shanghai Teyan Information Technology Consulting Research Institute, Shanghai 201499, China

Correspondence should be addressed to Guochong Lou; [loug@stdu.edu.cn](mailto:loug@stdu.edu.cn)

Received 7 August 2020; Revised 17 September 2020; Accepted 27 September 2020; Published 14 October 2020

Academic Editor: Tifeng Jiao

Copyright © 2020 Guochong Lou et al. This is an open access article distributed under the Creative Commons Attribution License, which permits unrestricted use, distribution, and reproduction in any medium, provided the original work is properly cited.

In order to scientifically and reasonably evaluate and select the quality and effect of ecological slope protection construction project and the structural form of ecological slope protection, this paper mainly studies nanomontmorillonite modified fly ash ecological slope protection material and its preparation method and related applications. The nanomontmorillonite modified fly ash ecological slope protection material and its application in this paper are based on nanomontmorillonite modified fly ash as the basic carrier, and the pore structure is used to plant grass for slope protection to achieve the purpose of ecological slope protection. Firstly, the nanomontmorillonite modified fly ash ecological slope protection material was prepared through the selection of raw materials, the mix ratio design, and the reasonable selection of the preparation process, and the range analysis method was used to optimize the mix ratio of nanomontmorillonite modified fly ash. By reasonable selection of alkali-reducing measures, selection of slope protection vegetation, preparation of planting substrates, and research on phytobiology, through experimental analysis, we obtained nanomontmorillonite modified fly ash with high strength and good water permeability and alkalinity in the pores to meet the requirements of plant growth ecological slope protection materials. Finally, through engineering practice, we explored the construction method of nanomontmorillonite modified fly ash ecological slope protection material and obtained good ecological slope protection benefits. The experimental data show that, for dispersive soil, when the degree of compaction is 80%, the compressive modulus of the soil is 3.46 MPa; when the degree of compaction is 86%, the compressive modulus of the soil becomes 4.51 MPa, an increase of 46.57%. The experimental results show that the nanomontmorillonite modified fly ash ecological slope protection material can help the soil become more compact.

## 1. Introduction

The slope protection construction project is an important part of the urban reconstruction project, and the ecological slope protection technology has been widely used in recent years. Nanomontmorillonite is an aluminosilicate mineral. It has a multilayer porous three-dimensional structure, a large specific surface area, and a large cation exchange capacity. It has the unique advantage of assisting in ecological slope protection. Nanomontmorillonite modified fly ash ecological slope protection material is used for modification, and the nanolayer structure of montmorillonite is not damaged after modification. Ecological slope protection is an

engineering protection measure that uses natural or artificial materials to construct a stable ecological slope. It not only satisfies the basic function of slope protection, but also effectively integrates the urban landscape, culture, and ecology. The slope protection ecosystem plays an important role in increasing biodiversity and has gradually become an ecologically ideal slope protection technology with broad prospects.

This study summarizes the main factors of the water purification effect of ecological slope protection materials through experiments and can play a specific guiding role in the selection of slope protection materials in ecological slope protection projects [1]. The study of ecological slope

protection materials aims to realize the harmonious coexistence of human activities and nature. The inevitable requirement for the coordinated development of economic development and environmental protection is to repair the ecological problems caused by traditional slope protection, and the relationship between engineering construction and environmental damage. In addition, the research of ecological slope protection materials has contributed to the promotion and improvement of ecological slope protection technology suitable for China's national conditions and engineering practices [2].

At present, the research related to nanomontmorillonite modified fly ash is getting more and more in-depth. Alongi and Carosio conducted a research on a completely inorganic intumescent flame-retardant nanocoating composed of nanomontmorillonite nanosheets embedded in an ammonium polyphosphate matrix. The coating deposited from the diluted water-based suspension/solution through multistep adsorption uniformly covers each cotton fiber with an average thickness of less than 50 nm, and the addition amount is up to 5%. When the paint addition amount reached 5%, no fire was observed in the 35 kW/m<sup>2</sup> heat flux cone calorimetry test. However, the research data is not accurate enough [3]. In their research, Hong et al. synthesized subnanometer zero-valent copper (ZVC) using montmorillonite minerals as templates. The discrete distribution of surface charges on montmorillonite can effectively separate the formed ZVC particles and inhibit their aggregation. ZVC templated with montmorillonite (ZVCMMT) has excellent reactivity, and more than 90% of atrazine (15 μM) can be degraded within a few minutes. The hydroxyl group is confirmed to be a reactive substance, which is generated by ZVC activating oxygen. It also shows that the degradation process strongly depends on the hydration state of the synthesized ZVCMMT. Compared with freshly prepared ZVCMMT, freeze-dried ZVCMMT exhibits higher reactivity, which can be explained by the higher residual adsorption on the surface of freeze-dried ZVCMMT [4]. Xie et al. prepared nanomontmorillonite (MMT) plastic polymer electrolyte membrane by solution casting method. The organophilic modification of nanomontmorillonite is used as a channel for lithium ion transfer. By electrochemical impedance spectroscopy, the membrane composed of nano-OMMT electrolyte has a higher ionic conductivity of  $1.67 \times 10^{-4} \text{ S cm}^{-1}$  and a transference number of 0.67. SEM is used to determine the morphology of the electrolyte cross section. Fourier transform infrared spectroscopy studies explain the reason why lithium ion nano-OMMT channels are beneficial. The LiO-Si interaction between lithium ions and OMMT nanoparticles provides guiding transmission of lithium ions, thereby promoting the transfer fluidity of lithium ions in the plastic polymer electrolyte [5]. He et al. used ammonium polyphosphate-montmorillonite nanocompound to retard epoxy resin and compared it with the physical mixture of ammonium polyphosphate and montmorillonite. The thermal decomposition of epoxy resin composites was studied by thermogravimetric analysis. Through limited oxygen index measurement, UL-94 test, and cone calorimeter test, the flame retardancy of epoxy

resin composites was studied. Ammonium polyphosphate-montmorillonite nanocompounds show better flame retardancy (limiting oxygen index, UL-94, ignition time, peak heat release rate, etc.) than ammonium polyphosphate + montmorillonite mixture. The morphology of epoxy resin composite material was studied by scanning electron microscope. The rapid and effective formation of the carbon layer should be the main reason why the ammonium polyphosphate-montmorillonite nanocompound has better flame retardancy than the ammonium polyphosphate + montmorillonite mixture [6].

The main innovations of this paper include the following aspects: (1) This paper studies the engineering properties and modification mechanism of fly ash modified dispersive soil. Fly ash can effectively improve the dispersion characteristics of dispersive soils. Its mechanism of action is mainly through ion exchange and hardening reaction, reducing the dispersibility and compressibility of the soil, and improving the strength and impermeability of the soil. (2) The research in this paper found that PHBH can be used as a new type of environmentally friendly packaging material to prepare a polymer matrix for packaging films with a wide range of uses. Nanomontmorillonite has a natural nanoscale silicate layer, high aspect ratio, and interaction between polymer chains, which can improve the crystallization, mechanical properties, and barrier properties of PHBH.

## 2. Nanomontmorillonite Modified Fly Ash Ecological Slope Protection Material

*2.1. Modification Method of Fly Ash.* The porous structure of fly ash and its huge specific surface area provide a favorable foundation for the development and research of fly ash utilization, and it has received extensive attention from international researchers [7, 8]. However, due to insufficient physical and chemical properties of fly ash, its effect and scope of application are limited. In order to improve the added value and utilization rate of fly ash, modification methods of fly ash have been gradually developed. The commonly used correction methods are mainly divided into two categories: physical methods and chemical methods [9].

*2.1.1. Mechanical Mechanics Method.* The mechanical grinding method is a physical method. This method is mainly used for the further processing of fly ash, using mechanical methods such as crushing and crushing to refine the particle size and make it uniformly dispersed [10, 11]. The mechanical treatment method is used to destroy and separate part of the vitreous structure inside the fly ash, reduce the viscosity effect, expose the active materials of the fly ball such as Al<sub>2</sub>O<sub>3</sub> and 2SiO<sub>2</sub>, increase the specific surface area, and improve the surface activity and physical properties of the fly ash, characteristics, adsorption performance, etc. According to the method of mechanical and physical changes of fly ash, the changes in the structure and characteristics of fly ash are limited, so there is little increase in activity [12, 13].

**2.1.2. High Temperature Treatment Method.** Under appropriate high temperature conditions, the moisture in the fly ash volatilizes and opens several closed pores at the same time to increase the porosity of the fly ash and increase the activity of the fly ash. However, the specific structure of fly ash will be destroyed even at high temperatures, and the specific characteristics of fly ash will also change [14]. Therefore, the high temperature treatment of fly ash has certain restrictions, and the temperature must be properly controlled.

**2.1.3. Acid-Base Modification Method.** Acid-base modification methods include acid modification method and alkali modification method. These two treatment methods are similar. The fly ash is put into an acid solution or an alkali solution, and the reaction is carried out under a certain time and reaction conditions. After washing and filtering processes, the changed fly ash is formed. Both acid solution and alkali solution will destroy the surface structure of fly ash, increase the porosity, and further decompose the active material of fly ash to expose it, thereby increasing the surface activity of fly ash [15, 16].

**2.1.4. Surface Modification Method.** The surface modification method of fly ash is usually caused by the interaction of modifier and fly ash particles. The mechanism of action of this method is divided into physical action and chemical action. The former is mainly composed of intermolecular forces, including deep coating and adsorption on the surface. The latter is mainly changed by chemical reaction or chemical adsorption [17]. Surface modification methods such as surface modification, transplantation, and polymerization have better modification effects on fly ash and are one of the commonly used methods in fly ash modification technology.

**2.2. Structure and Properties of Nanomontmorillonite.** Nano-MMT (nanomontmorillonite) is a low-priced, abundant clay mineral. Clay minerals are widely distributed in nature, especially on weathered crust and sedimentary rocks [18, 19]. Clay is a kind of hydrophilic silicate mineral with a layered structure. Its particles are very fine, and the particle size is generally less than  $2\ \mu\text{m}$ . Clay contains bentonite, kaolin, illite, ATPARIGHT, chlorite, etc. depending on the nature and origin.

Nanomontmorillonite is the main component of bentonite minerals. In addition to the main components of nanomontmorillonite, bentonite also contains a small amount of other clay minerals such as long quartz and mica crystal chips. Nanomontmorillonite has a fine layered structure showing various colors such as white, gray, light yellow, light red, purple, and black, and its color varies according to the origin and the inorganic and organic substances contained. The main chemical composition of nanomontmorillonite is  $\text{Al}_2\text{O}_3$ ,  $\text{SiO}_2\cdot\text{H}_2\text{O}$ , and the theoretical percentage content of each composition is  $\text{SiO}_2$ : 62.7%,  $\text{Al}_2\text{O}_3$ : 26.3%,  $\text{H}_2\text{O}$ : 8% [20]. However, in fact, the composition of nanomontmorillonite is very complex, and its chemical composition varies greatly depending on the origin

and characteristics. The molecular formula of the theoretical structure of nanomontmorillonite is usually considered as  $\text{Na}_x\text{Al}_2[\text{Si}_4\text{O}_{10}(\text{OH})_2\text{nH}_2\text{O}]$ . This is a multilayer network structure composed of two layers of silicon-oxygen tetrahedron and an aluminum-oxygen octahedral layer sandwiched between each layer. The thickness is about 1 nm, the tetrahedron and the octahedron are connected by a common oxygen atom, and the length and width are both submicron. The multilayer network structure not only increases the specific surface area of montmorillonite to  $700\ \text{m}^2/\text{g}$  and sometimes to  $800\ \text{m}^2/\text{g}$ , but also provides excellent barrier properties. There are multiple cations such as  $\text{Li}^+$ ,  $\text{Na}^+$ ,  $\text{Mg}^{2+}$ ,  $\text{Ca}^{2+}$ , and  $\text{Fe}^{2+}$  between the nano-MMT layers, and each layer has electronegativity, so the same amount of cations is adsorbed between the layers. Generally, the cation exchange content of nano-MMT is  $100 \pm 50\ \text{m mol}/100\ \text{g}$ . This is mainly due to the isomorphic replacement of nano-MMT crystals [21, 22]. The  $\text{Si}^{4+}$  of the silicon-oxygen tetrahedron can be replaced by the high-valent cation  $\text{Al}^{3+}$ , and the  $\text{Al}^{3+}$  of the aluminum-oxygen octahedron can be replaced by the low-valent cations  $\text{Li}^+$ ,  $\text{Na}^+$ ,  $\text{Mg}^{2+}$ ,  $\text{Ca}^{2+}$ ,  $\text{Fe}^{2+}$ , etc. Through this homomorphic replacement, negative charges will be generated between the crystalline layer structures. These negative charges must absorb cations of equal charge to maintain the balance of charges between layers. According to these effects, nano-MMT has the ability to adsorb cations and polar organics [23].

**2.3. Adsorption Isotherms.** The adsorption isotherm refers to the relationship curve between the concentration of solute molecules in the two phases when the adsorption process of solute molecules at the two-phase interface reaches equilibrium at a certain temperature. Through static experiments, the adsorption data of shale on ceramsite sites of nitrogen and phosphorus, zeolite, quartz sand, and volcanic rocks have been obtained [24, 25]. Next, using Freundlich and Langmuir's adsorption isotherm models, the adsorption process is analyzed and explained, and the adsorption capacity of nitrogen and phosphorus is compared and analyzed. In order to achieve slope protection and water purification effects, a matrix material suitable for slope protection is chosen.

### 2.3.1. Freundlich Adsorption Isotherm

$$q = kc^{(1/n)}. \quad (1)$$

In the formula,  $k$  and  $n$  are constants;  $q$  represents the adsorption amount of the substrate at equilibrium,  $\text{mg}/\text{g}$ ; and  $c$  represents the concentration of the substrate in the solution at adsorption equilibrium,  $\text{mg}/\text{L}$ . By taking the logarithms on both sides of (1), the following formula can be obtained:

$$\lg q = \frac{1}{n} \lg c + \lg k. \quad (2)$$

Using  $\lg q$  and  $\lg c$  as a linear regression graph, a straight line can be obtained. The slope of the straight line is  $1/n$  and

the intercept is  $\lg k$ . From this, the constants  $n$  and  $k$  can be obtained, and then the Freundlich adsorption equation can be derived.

### 2.3.2. Langmuir Adsorption Isotherm

$$q = \frac{k_1 c}{1 + k_2 c}, \quad (3)$$

$$k_1 = q_m * k_2. \quad (4)$$

In the formula,  $q$  represents the maximum equilibrium adsorption capacity, mg/g; and  $k_1, k_2$  are constants. Formula (5) can be obtained by taking the reciprocal of both sides of formula (3).

$$\frac{1}{q} = \frac{1}{k_1} * \frac{1}{c} * \frac{1}{q_m}. \quad (5)$$

Plot  $1/c$  and  $1/q$ , and get a straight line after linear regression. The slope of the straight line is  $1/k_1$  and the intercept is  $1/q_m$ . From this,  $q_m, k_1$ , and  $k_2$  can be calculated, and the Langmuir adsorption isotherm equation can be obtained.

### 2.4. Mechanism of Ecological Slope Protection

- (1) The mechanism structure diagram of ecological gradient protection plants is shown in Figure 1.
- (2) Analyze the mechanism of ecological slope protection from the formula; the mechanical formula of slope stability is

$$k = \frac{Q}{F}. \quad (6)$$

Among them,  $k$  is the slope stability coefficient;  $Q$  is the anti-sliding force of the soil (rock) body of the slope,  $N$ ; and  $F$  is the sliding force of the side slope, and  $N$  passes through the slope after the vegetation protection project to produce the anti-sliding force of the vegetation engineering slope. The stability mechanics formula is

$$K = \left( \frac{(Q + Q_z)}{F} \right). \quad (7)$$

Among them,  $Q_z$  is the anti-sliding force of vegetation engineering,  $N$ . It can be seen from the above formula that the increased slope stability coefficient after vegetation slope protection is

$$K_s = \frac{Q_z}{F}. \quad (8)$$

- (3) Comparative analysis of traditional slope protection and ecological slope protection is carried out.

The traditional form of slope protection only pays attention to the stability of the slope protection structure and other engineering protection performances, and it does not consider the ecological performance of slope protection in terms of ecology, environment, and landscape [26, 27]. The slope protection, slope structure, and the stability of other engineering protection performances for protecting ecology have also been noted. The discovery of traditional artificial materials and technologies pays attention to improving traditional slope protection methods. At the same time, the ecological environment and biological requirements are more important in the design and construction process. The advantage of the traditional slope protection is its high civil protection ability, but its investment is relatively large and it is not important for environmental protection. In addition, it is very difficult to meet the specific requirements of the sustainable development strategy. The appearance is not beautiful enough, and if there is no vitality, it will be too dull. Slope protection is fully in line with the development trend of protecting the ecological environment, can effectively protect the surrounding environment, and has a high decorative value. Therefore, ecological slope protection is an improvement based on the expansion of the basic functions of slope protection. With the deepening of ecological and environmental protection concepts such as sponge cities and ecological towns, traditional slope protection needs to be converted into ecological slope protection technology. Ecological slope protection is a new stage in the development of slope protection engineering.

## 3. Preparation of Nanomontmorillonite Modified Fly Ash Ecological Slope Protection Material

**3.1. Preparation Materials.** Materials used in preparation are nanomontmorillonite, modified fly ash, matrix fly ash, MMT/SBS composite modified fly ash, PHBH, in which HH content is 11% and molecular weight is  $6 * 10^5$ , 3-amino-propyl triethoxy silicon, alkane (KH550), absolute ethanol, 95% ethanol, chloroform, and dichloromethane.

**3.2. Experimental Equipment.** Experimental equipment includes electric heating constant temperature blast drying oven, vacuum drying oven, rotary evaporator, electronic balance, magnetic stirrer, high precision digital display constant temperature heating table, constant temperature water bath, condenser tube 250 ml, pipette gun 0.1~2.5  $\mu$ l, laboratory ultrapure water heater, scanning electron microscope, thermogravimetric analyzer, X-ray diffractometer, upright hot stage microscope, Fourier transform infrared spectrum analyzer, universal testing machine, air permeability tester, water vapor transmission rate tester, and high-shearing dispersion emulsifier.

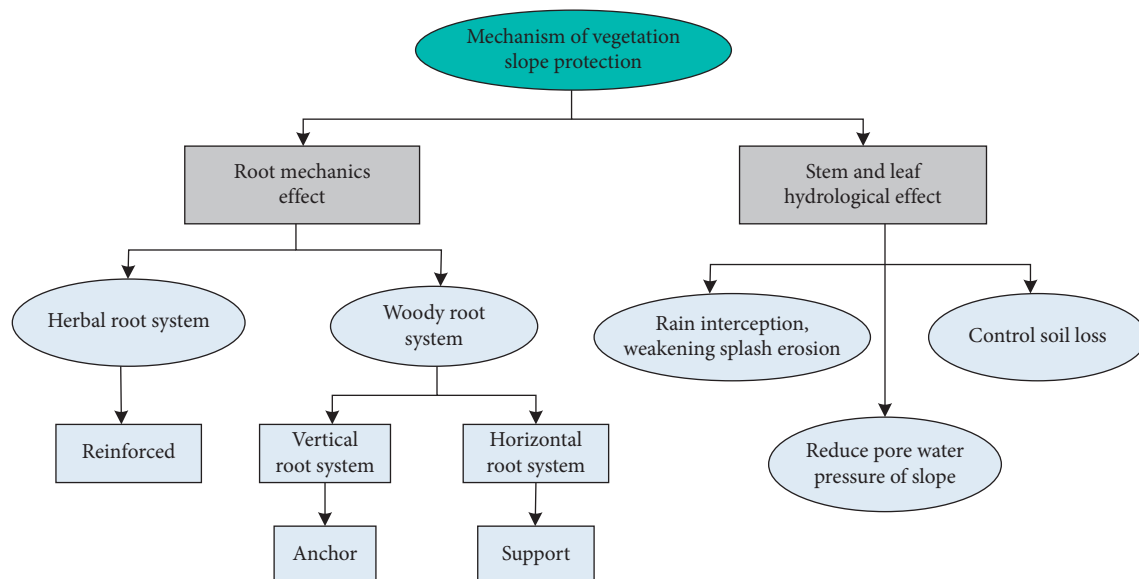


FIGURE 1: The mechanism structure diagram of ecological gradient protection of plants.

3.3. *Data Processing.* We used Microsoft Excel 2010 for data processing and graphing and SPSS 17.0 (Duncan test) for significant difference analysis.

3.4. *Preparation Steps of Nanomontmorillonite Modified Fly Ash Ecological Slope Protection Material.* The test method for preparing nanomontmorillonite modified fly ash adopts the melt blending method, including MMT modified fly ash and MMT/SBS composite modified fly ash. Heat the fly ash base ash to 160 degrees to make it in a molten state, with weigh of 800 g, and mix the weighed montmorillonite (8 g, 24 g, 40 g) with 800 g fly ash base ash in a mixer; the mixing process takes about 10 min. Subsequently, the high-shear dispersing emulsifier produced by our company was used to prepare MMT modified fly ash with three contents of 1%, 3%, and 5%. The shear speed is 5000 rad/min, the shear time is 1 h, and the shear temperature is 170°C. When preparing the modified fly ash of MMT/SBS composite material, the finished SBS modified fly ash is first heated to 170 degrees to make it in a molten state. Pay attention to mixing the fly ash evenly to reduce the influence of fly ash segregation. Weigh 800 g of SBS modified fly ash, and, after stirring evenly, mix the weighed montmorillonite (8 g, 24 g, 40 g) and 800 g of SBS modified fly ash using a mixer. The mixing process takes about 10 minutes, and then the high-shear dispersing emulsifier produced by our company is used to prepare MMT/SBS composite modified fly ash with three contents of 1%, 3%, and 5%. The preparation conditions are also a shear rate of 5000 rad/min, a shear time of 1 h, and a shear temperature of 170°C, which are consistent with the preparation conditions of MMT modified fly ash. The

modification of two types of fly ash by MMT modifier can be compared.

#### 4. Application Analysis of Nanomontmorillonite Modified Fly Ash Ecological Slope Protection Material

4.1. *Photocatalytic Performance of Nanomontmorillonite Modified Fly Ash Material under Visible Light.* In order to further explore the photocatalytic performance of the composite material, the degradation rate curve of methylene blue under visible light conditions is shown in Figure 2. It can be seen from Figure 2 that, under visible light, as the light time increases, the pollutants in the solution are gradually degraded. In the dark reaction stage, similar to the phenomenon mentioned earlier, the nanomontmorillonite modified fly ash adsorbs pollutants to the surface due to a large specific surface area, resulting in a decrease in absorbance.

Compared with nanomaterials, nanomontmorillonite materials have higher photocatalytic efficiency, which can reach about 92% within 160 min. In the process of sample preparation, the nanomontmorillonite material is mixed with nanomaterial elements to reduce the forbidden bandwidth, so that, under visible light, electrons in the valence band can still jump across the energy barrier to the conduction band, thereby exhibiting photocatalysis performance. Under visible light, the degradation rate of nanomontmorillonite modified fly ash with the same quality is lower than that of nanomontmorillonite material, which is only about 75% within 160 minutes. The possible reason is that the amount of nanomontmorillonite modified fly ash is

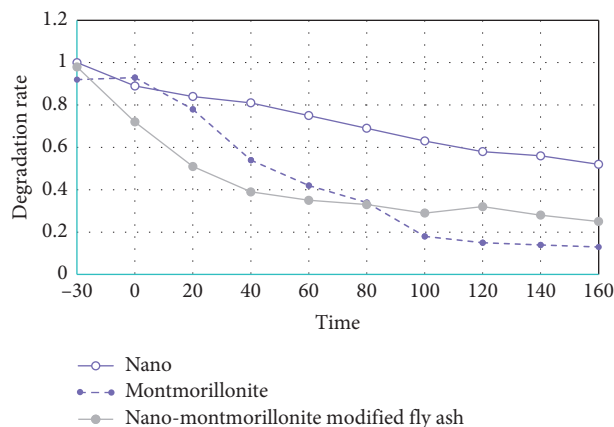


FIGURE 2: Degradation rate curve of methylene blue for composite materials under visible light.

less, resulting in the inability to provide enough active sites during the degradation process. Therefore, the mass of the composite nanomontmorillonite modified fly ash in the experiment was increased from 20 mg to 40 mg, so that the photocatalytic effects of different quality catalysts can be compared. The comparison results are shown in Figure 3. When the quality of nanomontmorillonite modified fly ash is doubled, its degradation rate of pollutants increases from 75% to about 93% within 160 minutes. This is due to the increase in the quality of the catalyst, which provides more supplies. The photocatalytic performance of the active sites of the reaction is significantly improved.

In the preparation process of the composite material, its loading rate is only 23.6%, which greatly saves the amount of photocatalyst and makes it possible to use high-value fly ash.

#### 4.2. Effect of Compaction on Soil Compression Characteristics.

Tables 1 and 2 present the test results of compressibility and compressibility of modified fly ash soil with different compaction degrees. Figures 4 and 5 show the relationship curves of the compressibility, compression modulus, and compaction degree of the modified soil with fly ash at different dosages at 0 d curing age.

It can be seen from Table 1 and Figure 4 that as the degree of compaction increases, the compressibility of the fly ash modified soil gradually decreases. For dispersibility, when the degree of compaction is 80%, the compressibility of the soil is  $0.63 \text{ MPa}^{-1}$ , and when the degree of compaction is 82%, the compressibility of the soil is reduced to  $0.45 \text{ MPa}^{-1}$ , which is reduced by 1%; when the degree of compaction is 84%, the compressibility of the soil decreases by 15.78%; when the degree of compaction is 86%, the compressibility of the soil is  $0.36 \text{ MPa}^{-1}$ . It can be seen that the compressibility of dispersive soils gradually decreases with increasing compaction. It can be seen in Table 1 and Figure 4 that when the dosage of fly ash is 2%, 4%, 6%, 8%, and 10%, the compressibility of the modified soil has a relatively similar change rule.

It can be seen from Table 2 and Figure 5 that the compressibility of the modified soil with different fly ash dosages is basically the same as the degree of compaction.

The performance is as follows: under the same dosage of fly ash, with the increase of compaction degree, the compression modulus of the modified soil gradually increases, and the soil compressibility decreases. For dispersive soil, when the degree of compaction is 80%, the compressive modulus of the soil is 3.46 MPa; when the degree of compaction is 82%, the compressive modulus of the fly ash modified soil increases by 12.98%; when the degree of compaction is 84%, the compressive modulus of the soil increases to 3.80 MPa; when the degree of compaction is 86%, the compressive modulus of the soil becomes 4.51 MPa, an increase of 46.57%. It can be seen that as the degree of compaction increases, the compressive modulus of dispersive soil gradually increases. It can be seen from Table 2 and Figure 5 that when the dosage of fly ash is 2%, 4%, 6%, 8%, and 10%, the compressive modulus of the modified soil has a relatively similar change rule. Compression modulus reflects the ability of soil to resist deformation. Modified soil will produce different soil structures under different compaction degrees, which leads to the difference in soil deformation characteristics. At the same dosage, the greater the degree of compaction of the soil, the lower the internal porosity of the soil, and the lower the compressibility of the soil.

4.3. Thermal Decomposition Performance Analysis. The dispersion effect and intercalation effect of nanomontmorillonite in PHBH have a certain influence on thermal stability. The processing conditions and the nanomontmorillonite-polymer interaction are two important factors that affect intercalation and dispersion. Silane coupling agent KH550 not only has aminopropyl group combined with polymer, the silanol formed after hydrolysis can also react with hydroxyl on the surface of nanomontmorillonite to form hydrogen bond and condense into Si-OM (M stands for inorganic surface of powder particles) covalent bond. Therefore, the addition of the silane coupling agent helps to enhance the dispersion effect and intercalation effect of the nanomontmorillonite, thereby improving the thermal stability of the nanocomposite. The thermogravimetric analysis of PHBH/MMT and PHBH/MMT/KH550 shows that compared with PHBH/MMT

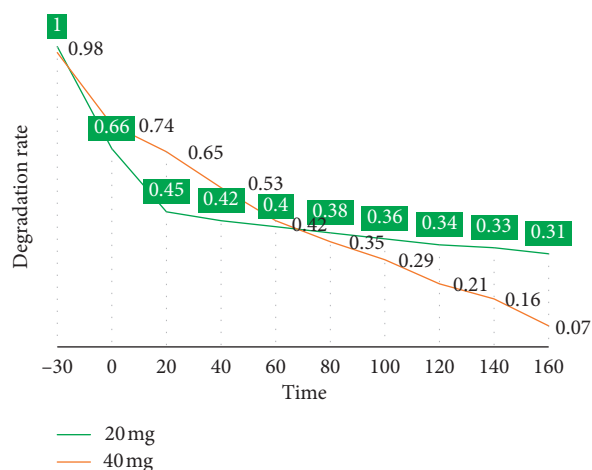


FIGURE 3: Degradation rate curve of methylene blue with different qualities of nanomontmorillonite modified fly ash under visible light.

TABLE 1: Compression coefficient ( $\text{MPa}^{-1}$ ) of modified fly ash soil with different compaction degrees.

Compactness (%)	Fly ash content (%)					
	0	2	4	6	8	10
80	0.76	0.63	0.59	0.43	0.39	0.34
82	0.69	0.65	0.46	0.57	0.45	0.32
84	0.57	0.47	0.42	0.39	0.26	0.23
86	0.48	0.37	0.32	0.28	0.20	0.18

TABLE 2: Compressive modulus of fly ash modified soil with different compaction degrees (MPa).

Compactness (%)	Fly ash content (%)					
	0	2	4	6	8	10
80	3.26	3.52	3.681	4.37	5.61	7.88
82	3.37	3.63	4.24	4.71	5.22	7.39
84	3.6	4.5	4.92	5.63	6.88	8.92
86	4.51	4.62	4.86	6.53	7.88	9.96

nanocomposite, after adding silane coupling agent KH550, the thermal decomposition temperature of PHBHMMT/KH550 nanocomposite increases, and the thermal stability improved. Table 3 shows the thermal weight loss data of PHBH/MMT/KH550 nanocomposites with different proportions of KH550.

According to data analysis, when the KH550 addition amount is 5 wt%,  $T_5$  is the largest, and if the addition amount of KH550 continues to increase,  $T_5$  decreases. According to the Hoffman elimination reaction and the nucleophilic attack reaction of the ammonium counterion, the surface modifier can promote the thermal decomposition of PHAs family polymers. Therefore, when the addition amount of KH550 exceeds a certain value, it will instead promote the thermal decomposition of PHAS. After adding the coupling agent to the PHBH/1 wt% MMT nanocomposite, the  $T_{10}$ ,

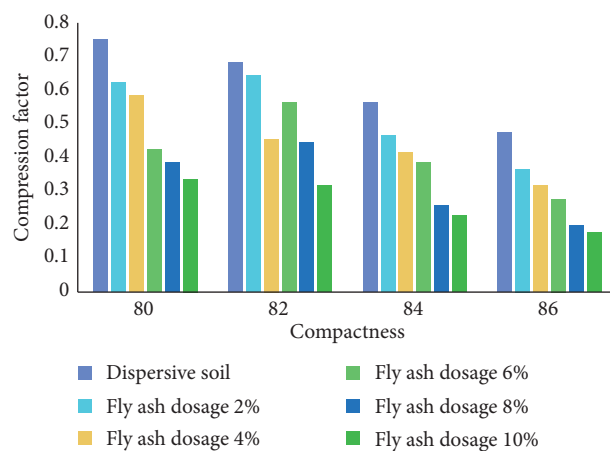


FIGURE 4: The relationship between compression factor and compaction.

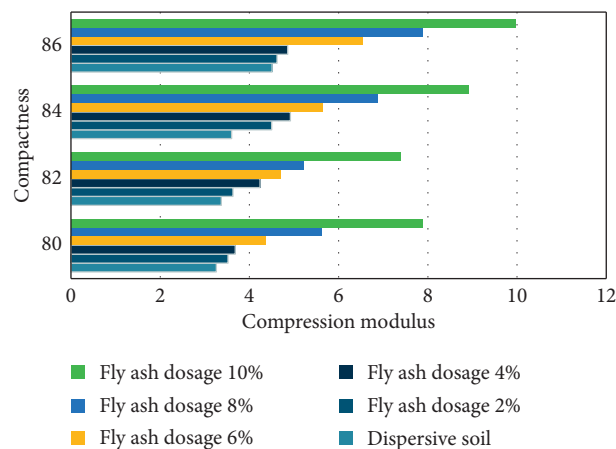


FIGURE 5: The relationship between compression modulus and compaction.

$T_{30}$ , and  $T_{50}$  of the PHBH/MMT/KH550 nanocomposite are significantly higher than those of the nanocomposite without the modifier. This is because of the coupling agent. After KH550 is added to PHBHMMT nanocomposites containing a small amount of MMT, the barrier effect of MMT plays a major role, and KH550 makes PHBH and nanomontmorillonite form a cross-linked structure, which limits the movement of the polymer backbone and effectively improves the thermal stability of the cross-linked hybrid composite PHBH/MMT/KH550. When the amount of KH550 added is 1 wt%, 3 wt%, 5 wt%, 7 wt%, the residual carbon content of PHBHMMT/KH550 at 700 degrees is higher than that of PHBH/MMT. Among them, PHBH/MMT/3 wt% KH550 nanocomposite membrane has the highest carbon residual content. It can be considered that the addition of KH550 makes PHBH and nanomontmorillonite form a cross-linked structure, and the presence of inorganic nanomontmorillonite improves the thermal stability of the hybrid composite membrane. When the addition of KH550

TABLE 3: Thermal weight loss data of PHBH/MMT/KH550 nanocomposites with different proportions of KH550.

Sample	$T_5$	$T_{10}$	$T_{30}$	$T_{50}$	$T_{max}$	Char yield (%)
PHBH/1 wt% MMT	233.43	238.52	247.94	253.52	252.97	23.81
PHBH/1 wt% MMT/1% KH550	235.16	244.16	256.24	273.47	260.6	32.57
PHBH/1 wt% MMT/3% KH550	232.94	250.1	262.43	272.75	264.13	50.8
PHBH/1 wt% MMT/5% KH550	243.26	269.66	259.88	266.63	263.85	29.74
PHBH/1 wt% MMT/7% KH550	228.72	237.38	250.46	253.95	235.1	31.31
PHBH/1 wt% MMT/9% KH550	218.82	244.64	256.89	271.71	265.14	16.75

is 9 wt%, the carbon residue of PHBH/MMT/KH550 is lower than that of PHBH/MMT. This may be because the decomposition of KH550 accelerates the thermal decomposition of PHBH and reduces the carbon residue.

## 5. Conclusions

According to the types of materials used in slope protection, this paper systematically investigates and summarizes various structural forms of traditional slope protection and ecological slope protection. The difference and connection between the two are detected in terms of structural form, constituent materials, main functions, and construction technology. Detailed comparative analysis was conducted with a summary analysis of general weighting calculation methods and comprehensive evaluation methods, and range analysis was used to determine weights. The combination of comprehensive evaluation index method and gray correlation method overcomes the past comprehensive evaluation model to a certain extent. According to the subjectivity and discreteness of the judgment matrix, the resolution and sensitivity are improved, and the evaluation results are more scientific, reasonable, and reliable.

Nanomontmorillonite modified fly ash ecological slope protection material is a comprehensive material integrating rock engineering, fluid mechanics, biology, soil and water conservation, fertilizer science, silicate chemistry, horticulture, automation chemistry, environmental ecology, and other disciplines. Technology is a complex system engineering. The formation of nanomontmorillonite modified fly ash ecological slope protection material does not rely on vibration tamping, but on continuous impact compaction of the mixture in the process of high-speed injection, which has high bonding strength. The electron microscope scanning of the microstructure shows that the ecological material has a porous structure similar to that of soil, including a large number of noncapillary pores and capillary pores. According to the mercury intrusion test, the content of small pores in the ecological material particles is very high, and the total porosity is about three times that of ordinary cement, which makes the material have the characteristics of strong water retention and good air permeability.

Based on the analysis of various components of the nanomontmorillonite modified fly ash ecological slope protection material, the prepared nanomontmorillonite/hyperbranched nanocomposite material is the first tape distribution. Two seedlings are prepared for extension, and the extension rate is studied. The characteristics of different biaxially stretched membranes are based on inorganic

modification, organic modification, and double-cation organic compound modification, which are introduced into anionic surface. The active agent accepts cation-anion composite modification, which improves the adsorption capacity of the original modified montmorillonite. In the absence of biaxial stretching, the tensile strength and breaking point extension of the composite film added with organic nanomontmorillonite are significantly higher than those of the pure hyperbranched unextended film. The extended film stretches as the growth rate increases. The strength is gradually increasing, and the breaking point growth continues to decrease. According to mechanical properties, when the extension ratio of the 2-axis stretched film reaches 3 \* 3, the properties of the water barrier and oxygen barrier of the nanomontmorillonite modified fly ash ecological slope protection material have reached the most suitable value.

## Data Availability

The data used to support the findings of this study are included within the article.

## Conflicts of Interest

The authors declare that they have no conflicts of interest regarding the publication of this paper.

## Acknowledgments

This work was supported by Key R & D Projects of Hebei Province (Grant no. 19274207D).

## References

- [1] G.-J. Kim, D. Kim, K.-J. Lee et al., "Effect of nano-montmorillonite on osteoblast differentiation, mineral density, and osteoclast differentiation in bone formation," *Nanomaterials*, vol. 10, no. 2, p. 230, 2020.
- [2] K. Zheng, T. Chen, J. Zhang et al., "Nano-montmorillonite regulated crystallization of hierarchical strontium carbonate in a microbial mineralization system," *Materials*, vol. 12, no. 9, p. 1392, 2019.
- [3] J. Alongi and F. Carosio, "All-inorganic intumescent nanocoating containing montmorillonite nanoplatelets in ammonium polyphosphate matrix capable of preventing cotton ignition," *Polymers*, vol. 8, no. 12, p. 430, 2016.
- [4] R. Hong, Z. Guo, J. Gao, and C. Gu, "Rapid degradation of atrazine by hydroxyl radical induced from montmorillonite templated subnano-sized zero-valent copper," *Chemosphere*, vol. 180, pp. 335–342, 2017.

- [5] M. Xie, L. Li, K. Yuan, Y. Ma, and B. Liu, "Preparation and performance evaluation of organophilic nano-montmorillonite conducting polymer electrolyte for all-solid-state lithium ion batteries," *Journal of Materials Science*, vol. 30, no. 3, pp. 2030–2036, 2019.
- [6] X. He, W. Zhang, D. Yi, and R. Yang, "Flame retardancy of ammonium polyphosphate–montmorillonite nano compounds on epoxy resin," *Journal of Fire Sciences*, vol. 34, no. 3, pp. 212–225, 2016.
- [7] Z. Ren, Y. Zhu, Q. Wu et al., "Enhanced storage stability of different polymer modified asphalt binders through nano-montmorillonite modification," *Nanomaterials*, vol. 10, no. 4, p. 641, 2020.
- [8] G. Xu, B. Xue, L. Wei, J. Yu, Z. Yang, and S. Qin, "Effect of multistage stretching extrusion on morphology and property of organic nano montmorillonite/high density polyethylene composites," *Fuhe Cailiao Xuebao/Acta Materiae Compositae Sinica*, vol. 35, no. 7, pp. 1822–1831, 2018.
- [9] M. Chi, K. Tao, Q. Chen, H. Liu, P. Gao, and Z. Gao, "Dielectric properties of nano-montmorillonite modified insulation pressboard," *Gaodiyanya Jishu/High Voltage Engineering*, vol. 43, no. 9, pp. 2842–2848, 2017.
- [10] Y. Li, W. Zhu, T. Chen et al., "Synergistic metallogenesis of simulated radionuclide strontium by carbonate-mineralization bacteria/nano-montmorillonite," *Journal of Radio-analytical and Nuclear Chemistry*, vol. 314, no. 1, pp. 333–341, 2017.
- [11] Z. Li, J. Gong, S. Du et al., "Nano-montmorillonite modified foamed paste with a high volume fly ash binder," *RSC Advances*, vol. 7, no. 16, pp. 9803–9812, 2017.
- [12] M. H. Sheikh-Mohseni, S. Sedaghat, P. Derakhshi, and A. Safekordi, "Electrochemical activity of Ni-montmorillonite/Vulcan XC-72R carbon black nano-catalyst for the oxidation of methanol in acidic medium," *Journal of Nanostructure in Chemistry*, vol. 9, no. 3, pp. 217–224, 2019.
- [13] H. Azimi and M. Hayati-Ashtiani, "Morphological and structural characterization of nano-structured montmorillonite for separation process applications," *Desalination and Water Treatment*, vol. 110, pp. 129–138, 2018.
- [14] F. Li, W. Wu, R. Li, and Z. Fu, "Adsorption of phosphate by acid-modified fly ash and palygorskite in aqueous solution: experimental and modeling," *Applied Clay Science*, vol. 132–133, pp. 343–352, 2016.
- [15] S. Wang, Y. Zhang, Y. Gu et al., "Using modified fly ash for mercury emissions control for coal-fired power plant applications in China," *Fuel*, vol. 181, pp. 1230–1237, 2016.
- [16] J. Yang, Y. Zhao, J. Zhang, and C. Zheng, "Removal of elemental mercury from flue gas by recyclable  $\text{CuCl}_2$  modified magnetospheres catalyst from fly ash. Part 2: identification of involved reaction mechanism," *Fuel*, vol. 167, pp. 366–374, 2016.
- [17] C. An, S. Yang, G. Huang, S. Zhao, P. Zhang, and Y. Yao, "Removal of sulfonated humic acid from aqueous phase by modified coal fly ash waste: equilibrium and kinetic adsorption studies," *Fuel*, vol. 165, pp. 264–271, 2016.
- [18] A. Ghazy, M. T. Bassuoni, and A. Shalaby, "Nano-modified fly ash concrete: a repair option for concrete pavements," *ACI Materials Journal*, vol. 113, no. 2, pp. 231–242, 2016.
- [19] Y. Xiang, L. Wang, and Y. Jiao, "Ultrasound strengthened biodiesel production from waste cooking oil using modified coal fly ash as catalyst," *Journal of Environmental Chemical Engineering*, vol. 4, no. 1, pp. 818–824, 2016.
- [20] C. Li, H. Zhu, M. Wu, K. Wu, and Z. Jiang, "Pozzolanic reaction of fly ash modified by fluidized bed reactor-vapor deposition," *Cement & Concrete Research*, vol. 92, pp. 98–109, 2017.
- [21] Y. Gu, Y. Zhang, J. Lin et al., "Homogeneous mercury oxidation with bromine species released from HBr-modified fly ash," *Fuel*, vol. 169, pp. 58–67, 2016.
- [22] A. M. Rashad and A. S. Ouda, "An investigation on alkali-activated fly ash pastes modified with quartz powder subjected to elevated temperatures," *Construction & Building Materials*, vol. 122, pp. 417–425, 2016.
- [23] V. Masindi, W. Gitari, and H. Tutu, "Adsorption of As, B, Cr, Mo and Se from coal fly ash leachate by  $\text{Fe}^3$  modified bentonite clay," *Journal of Water Reuse & Desalination*, vol. 6, no. 3, pp. 382–391, 2016.
- [24] A. Ebelegi, S. S. Angaye, A. Nimibofa, and W. Donbebe, "Removal of Congo red from aqueous solutions using fly ash modified with hydrochloric acid," *Current Journal of Applied Science and Technology*, vol. 20, no. 4, pp. 1–7, 2017.
- [25] A. K. Nikolaidis and D. S. Achilias, "Thermal degradation kinetics and viscoelastic behavior of poly(methyl methacrylate)/organomodified montmorillonite nanocomposites prepared via in situ bulk radical polymerization," *Polymers*, vol. 10, no. 5, p. 491, 2018.
- [26] A. Hassani, A. Khataee, S. Karaca, and M. Fathinia, "Degradation of mixture of three pharmaceuticals by photocatalytic ozonation in the presence of  $\text{TiO}_2$ /montmorillonite nanocomposite: simultaneous determination and intermediates identification," *Journal of Environmental Chemical Engineering*, vol. 5, no. 2, pp. 1964–1976, 2017.
- [27] X. Zhou and Q. Huang, "Quantitative evaluation on oil diffusion mechanisms in nano-organic-montmorillonite modified castor oil based polyurethane foam for oil/water separation," *Polymers for Advanced Technologies*, vol. 31, no. 6, pp. 1231–1244, 2020.

## Research Article

# The Analysis of the Transformation Mechanism of cBN Crystals with the First-Principle Calculation

Lichao Cai <sup>1</sup>, Bin Xu <sup>1,2</sup>, Meizhe Lv,<sup>2</sup> and Xiaohong Fan<sup>2</sup>

<sup>1</sup>School of Materials Science and Engineering, Shandong University, Jinan 250101, China

<sup>2</sup>School of Materials Science and Engineering, Shandong Jianzhu University, Jinan 250101, China

Correspondence should be addressed to Bin Xu; xubin@sdjzu.edu.cn

Received 11 July 2020; Accepted 24 September 2020; Published 14 October 2020

Academic Editor: Tifeng Jiao

Copyright © 2020 Lichao Cai et al. This is an open access article distributed under the Creative Commons Attribution License, which permits unrestricted use, distribution, and reproduction in any medium, provided the original work is properly cited.

To clarify the synthesis mechanism of cubic boron nitride (cBN) with catalysts at high temperature and high pressure, we calculate the surface energy of the main phases in the Li-N-B synthesis system using the first-principle method. Based on the density functional theory, the surface energy of low-index surfaces of cBN, hexagonal boron nitride (hBN), and lithium boron nitride ( $\text{Li}_3\text{BN}_2$ ) at the cBN synthetic temperature of 1700 K and synthetic pressure of 5.0 GPa is calculated. The surface energy of the main low-index surfaces of cBN is  $\sigma(111) > \sigma(001) > \sigma(110)$ , that of hBN is  $\sigma(10\bar{1}0) > \sigma(11\bar{2}0) > \sigma(0001)$ , and that of  $\text{Li}_3\text{BN}_2$  is  $\sigma(100) > \sigma(110) > \sigma(001)$ . The energy orders of the main low-index surfaces were well contrary to the corresponding orders of the valence electron density of the low-index surfaces of cBN, hBN, and  $\text{Li}_3\text{BN}_2$ , which were calculated by the empirical electron theory (EET) of solids and molecules. The result shows that the calculation results in this paper are well consistent with the previous results of the EET theory and support for the results of the “direct transformation of hBN to cBN under the catalysis of  $\text{Li}_3\text{BN}_2$ ” obtained by the EET theory.

## 1. Introduction

Cubic boron nitride (cBN) single crystals have a high hardness value, high melting point, high thermal conductivity, wide energy gap, and low dielectric constant, which make them highly attractive as promising materials [1–4]. At present, cBN single crystals are synthesized using hexagonal boron nitride (hBN) as raw materials and lithium nitride ( $\text{Li}_3\text{N}$ ) as catalysts by the static high-temperature and high-pressure (HPHT) catalytic method [5–7]. However, the present cBN single crystals still cannot meet the demand for advanced product development. The clear transformation mechanism of cBN crystals is significant to determine the quality of cBN crystals at HPHT. The research on the material surface and material catalysis mainly adopts the methods of characterization and theoretical research.

In our previous experimental study, the main phases are hBN, cBN, and  $\text{Li}_3\text{BN}_2$  in the interface layers [8]. The empirical electron theory (EET) of solids and molecules has been successfully applied to the analysis of phase diagrams, phase transformation, and natural properties [9–11]. In the previous study, the transformation possibilities from hBN to cBN and from  $\text{Li}_3\text{BN}_2$  to cBN were discussed with the valence electron structure [9]. However, the first-principle calculations based on the density functional theory became the most successful method and were applied widely in material calculations [12, 13]. The most stable surface of cBN crystals has been reported in detail using the CASTEP code [14, 15]. Meanwhile, the analysis about properties of (110) surfaces of cBN crystals has been discussed systematically [16]. The characters and properties of (111) and (100) of cBN crystals have also few reports in the previous studies [17, 18].

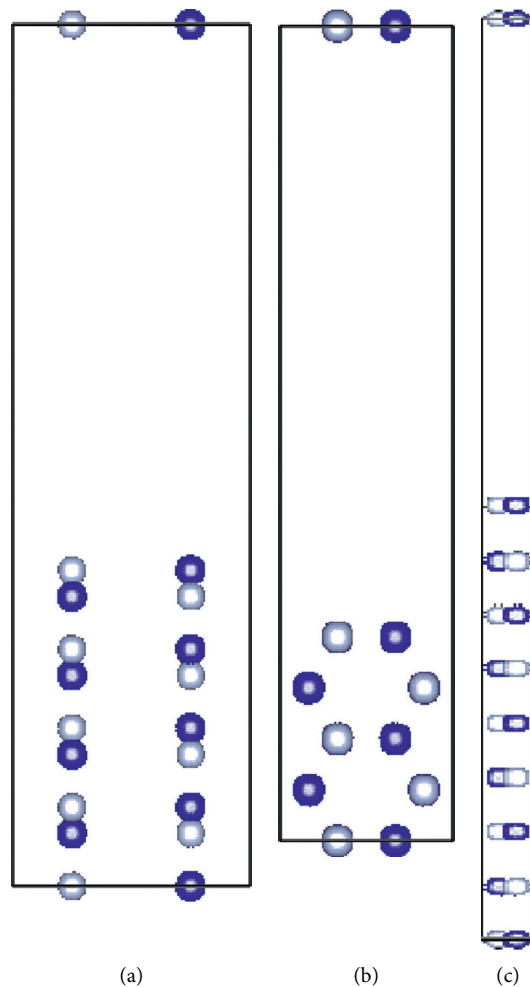


FIGURE 1: Schematic view of supercells for hBN along the  $\langle 001 \rangle$  axis: (a)  $(10\bar{1}0)$  slab with 9 layers, (b)  $(11\bar{2}0)$  slab with 5 layers, and (c)  $(0001)$  slab with 9 layers. The gray and blue spheres represent B and N atoms, respectively.

However, the information of surfaces for hBN and  $\text{Li}_3\text{BN}_2$  phases is barely referred in the previous studies. Thus, it is undoubtedly necessary to analyze the surface stability of three phases systematically, which helps understand the transformation mechanism of cBN crystals.

## 2. Materials and Methods

All calculations in the study were performed in the framework of the density functional theory using the VASP code (Vienna ab initio simulation program). The surface energies of lower-index surface planes on the three main phases, hBN, cBN, and  $\text{Li}_3\text{BN}_2$ , were calculated systematically [8]. An energy cutoff of 550 eV for the plane-wave basis was sufficient to obtain converged structural properties. Brillouin zone sampling was set with the  $9 \times 9 \times 1$   $k$ -point Monkhorst Pack grid meshes for all surfaces and with  $9 \times 9 \times 3$ ,  $9 \times 9 \times 9$ , and  $9 \times 9 \times 8$   $k$ -points for hBN, cBN, and  $\text{Li}_3\text{BN}_2$  bulks, respectively. For Perdew–Burke–Ernzerhof (PBE) calculations, the lattice constants used were as follows:  $a = 2.505 \text{ \AA}$  and  $c = 6.601 \text{ \AA}$  for hBN,  $a = 3.615 \text{ \AA}$  for cBN, and  $a = 4.643 \text{ \AA}$  and  $c = 5.259 \text{ \AA}$  for  $\text{Li}_3\text{BN}_2$  [14, 15].

Symmetrically repeated slabs were adopted to avoid artificial charge transfer. After the convergence test, the slabs for cBN (100), (110), and (111) were created by 9, 9, and 13 layers, respectively; the slabs for hBN (0001),  $(10\bar{1}0)$ , and  $(11\bar{2}0)$  were created by 9, 9, and 5 layers, respectively; and the slabs for  $\text{Li}_3\text{BN}_2$  (001), (100), and (110) were created by 9, 15, and 11 layers, respectively. The models for hBN, cBN, and  $\text{Li}_3\text{BN}_2$  with different layers are shown in Figure 1–3, respectively. A vacuum region of  $15 \text{ \AA}$  for cBN,  $\text{Li}_3\text{BN}_2$ , and  $(10\bar{1}0)$  and  $(11\bar{2}0)$  of hBN and  $30 \text{ \AA}$  for (0001) of hBN is adopted to prevent interactions between periodic images along the surface normal direction.

After structural relaxation, the surface energies ( $\sigma$ ) [16, 17] of cBN, hBN, and  $\text{Li}_3\text{BN}_2$  crystals were calculated as follows:

$$\sigma = \frac{(E_{\text{slab}} - E_{\text{bulk}})}{2A}, \quad (1)$$

where  $A$  is the area of the surface unit cell,  $E_{\text{slab}}$  is the total energy of the slab after relaxation, and  $E_{\text{bulk}}$  is the total energy of the crystals after relaxation. The main lower-index surfaces (100), (001), and (110) of  $\text{Li}_3\text{BN}_2$  are polar with

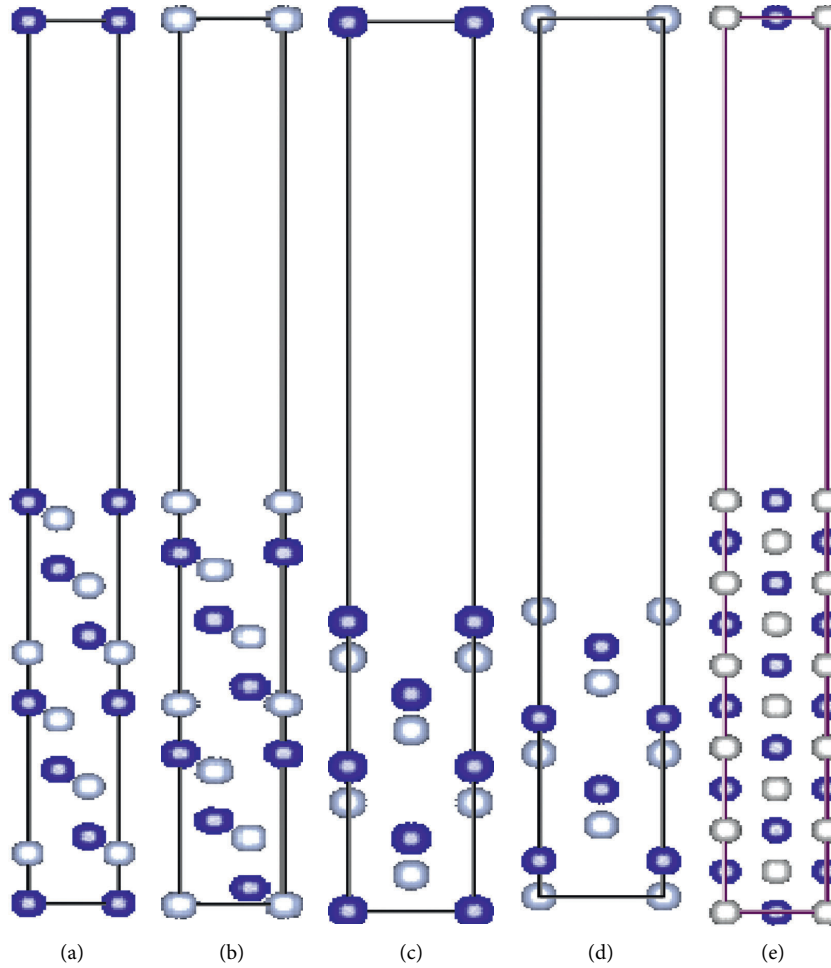


FIGURE 2: Schematic view of supercells for cBN along the  $\langle 001 \rangle$  axis: (a) (111)-B slab with 13 layers, (b) (111)-N slab with 13 layers, (c) (100)-B slab with 9 layers, (d) (100)-N slab with 9 layers, and (e) (110) slab with 11 layers. The gray and blue spheres represent B and N atoms, respectively.

different types of B-, Li-, and N-terminated surfaces; however, their calculated surface energies were almost the same. Thus, the  $\text{Li}_3\text{BN}_2$  surface energies of (100), (001), and (110) are defined by their average of the sum of all B-, Li-, and N-terminated surfaces, respectively. Five cBN schematic views for cBN single crystals can be obtained because of the polar surfaces of cBN (100) and (111), as shown in Figure 2, i.e., including (110), B- and N-terminated (100), and B- and N-terminated (111) surfaces. These surface energies ( $\sigma$ ) [19, 20] of cBN single crystals can be calculated as follows:

$$\sigma = \frac{1}{2A} [E_{\text{slab}} - N_{\text{B}}\mu^{\text{bulk}} + (N_{\text{B}} - N_{\text{N}})\mu_{\text{N}}^{\text{slab}}], \quad (2)$$

where  $N_{\text{B}}$  and  $N_{\text{N}}$  are the number of B and N atoms in the surface slab, respectively;  $\mu^{\text{bulk}}$  is the total energy of an atom in a bulk crystal at  $T = 0$  K, and  $\mu_{\text{N}}^{\text{slab}}$  is the chemical potential of nitrogen.

### 3. Results

Figure 4 shows the surface energies of different cBN single-crystal models as a function of the N chemical potential in its

allowed range. The calculated (110) surface energy was  $0.175 \text{ eV}/\text{\AA}^2$  in this work, which is in good agreement with the calculation results in [14–16]. Figure 4 shows that all lower surface energies of cBN single crystals are well consistent with those reported in previous theoretical studies [15]. The accuracy of the calculated cBN surface energy results ensures the validity of the calculation method used in the present study. For further analysis, the surface energies of cBN (111) and (100) are defined by the average surface energy of their B-terminated and N-terminated surfaces. Therefore, the main lower-index surface energies of cBN, hBN, and  $\text{Li}_3\text{BN}_2$  at the cBN synthetic temperature of 1700 K and synthetic pressure of 5.0 GPa are obtained by the first-principle method.

The main average surface energies of the lower-index surfaces (100), (111), and (110) at 1700 K and 5.0 GPa for cBN are  $0.475 \text{ eV}/\text{\AA}^2$ ,  $0.436 \text{ eV}/\text{\AA}^2$ , and  $0.25 \text{ eV}/\text{\AA}^2$ , respectively. Thus, the order of the average lower-index surface energy of cBN at 1700 K and 5.0 GPa is  $\sigma(100) > \sigma(111) > \sigma(110)$ . According to the previous EET study [9], valence electron density of surface (110) is greater than that of surfaces (111) and (100) at 1700 K and 5.0 GPa, so surface (110) of cBN is the most stable under this condition.

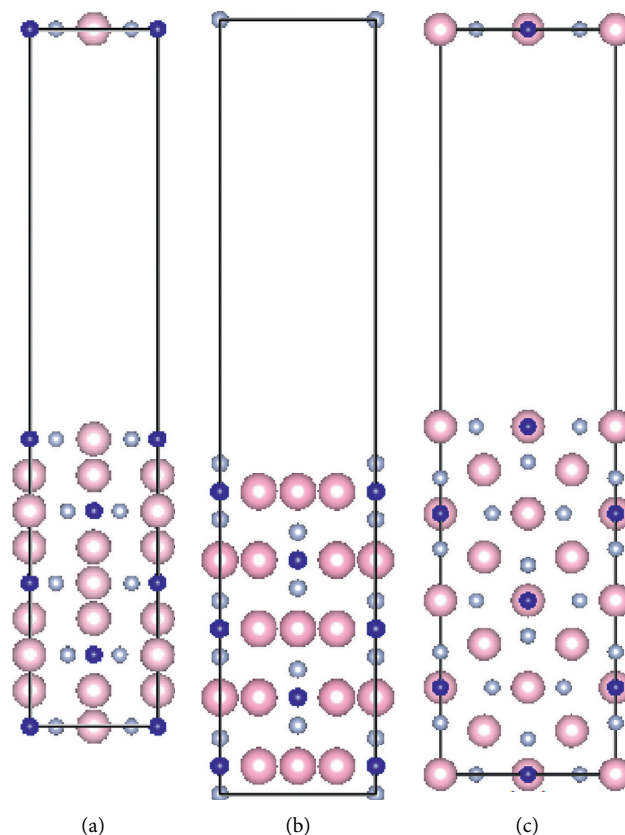


FIGURE 3: Schematic view of supercells for  $\text{Li}_3\text{BN}_2$  along the  $\langle 001 \rangle$  axis: (a) (001) slab with 9 layers, (b) (100) slab with 15 layers, and (c) (110) slab with 11 layers. The gray and blue spheres represent B and N atoms, respectively, and the big pink spheres represent Li atoms.

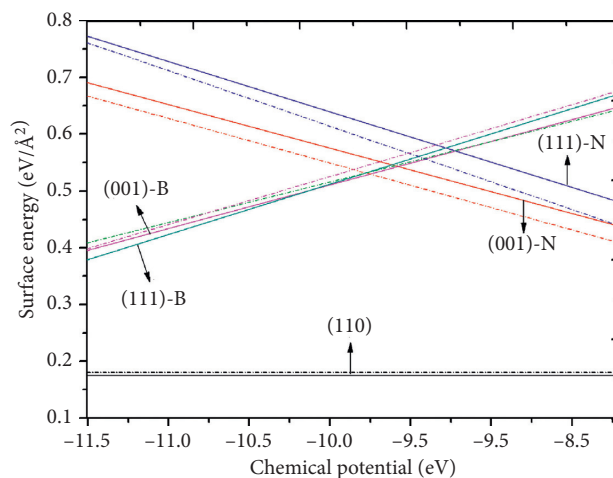


FIGURE 4: Surface energies of the three low-index cBN single-crystal surfaces as a function of the N chemical potential. The dashed line represents the theoretically calculated results obtained in [12].

Furthermore, the order of the valence electron density of cBN is  $\rho(110) > \rho(111) > \rho(100)$  [6], which is completely contrary to the corresponding order of the surface energy of cBN. The higher the valence electron density, the smaller the surface energy and the more stable the surface. This means that the result of the cBN surface energy calculated by the first-principle theory well verifies the conclusion of the

valence electron density calculated by the EET theory [9]. The surface energies of the main lower-index surfaces  $(10\bar{1}0)$ ,  $(11\bar{2}0)$ , and  $(0001)$  at 1700 K and 5.0 GPa for hBN are  $0.44 \text{ eV}/\text{\AA}^2$ ,  $0.22 \text{ eV}/\text{\AA}^2$ , and  $0.02 \text{ eV}/\text{\AA}^2$ , respectively. It can be found that the order of the surface energy of hBN is as follows:  $\sigma(10\bar{1}0) > \sigma(11\bar{2}0) > \sigma(0001)$ . The main lower-index surfaces (100), (110), and (001) at 1700 K and 5.0 GPa

for  $\text{Li}_3\text{BN}_2$  are  $0.82 \text{ eV}/\text{\AA}^2$ ,  $0.33 \text{ eV}/\text{\AA}^2$ , and  $0.25 \text{ eV}/\text{\AA}^2$ , respectively. Thus, the order of the surface energy of  $\text{Li}_3\text{BN}_2$  is  $\sigma(100) > \sigma(110) > \sigma(001)$ . Meanwhile, the order of the valence electron density of hBN and  $\text{Li}_3\text{BN}_2$  at 1700 K and 5.0 GPa is  $\rho(0001) > \rho(11\bar{2}0) > \rho(10\bar{1}0)$  and  $\rho(001) > \rho(110) > \rho(100)$ , respectively [9]. It could be concluded that the order of surface energies of hBN and  $\text{Li}_3\text{BN}_2$  is also completely contrary to the corresponding order of the valence electron density of hBN and  $\text{Li}_3\text{BN}_2$ . Thus, the surface energies of hBN and  $\text{Li}_3\text{BN}_2$  with the first-principle theory are well consistent with those results of the valence electron density by the EET theory. It could be concluded that the consistency between the first-principle theory for the surface energy and the EET theory for the valence electron density further confirms the credibility of the calculation results.

#### 4. Discussion

Previous studies proved that the transformation possibilities from hBN to cBN are more than those from  $\text{Li}_3\text{BN}_2$  to cBN at the cBN synthetic temperature of 1700 K and synthetic pressure of 5.0 GPa, and  $\text{Li}_3\text{BN}_2$  could be the real catalyst in the synthesis process of cBN crystals [9, 21–23]. The surface energy of the catalyst could directly influence the nucleation rate. Among all values of the surface energy obtained so far, the surface energy of the (100) surface of  $\text{Li}_3\text{BN}_2$  is the highest, i.e.,  $0.82 \text{ eV}/\text{\AA}^2$ , which is much greater than the other surface energies reported in this work. Thus, the nucleation of cBN crystals can easily occur around the (100) surface of  $\text{Li}_3\text{BN}_2$ ; therefore, the catalyst material  $\text{Li}_3\text{BN}_2$  using the (100) surface as the exposed surfaces could be used as substrates to induce effectively the growth of cBN single crystals.

#### 5. Conclusions

The order of the main lower-index surface energies of cBN is  $\sigma(100) > \sigma(111) > \sigma(110)$ ; the order of the main lower-index surface energies of hBN is  $\sigma(10\bar{1}0) > \sigma(11\bar{2}0) > \sigma(0001)$ ; and the order of the main lower-index surface energies of  $\text{Li}_3\text{BN}_2$  is  $\sigma(100) > \sigma(110) > \sigma(001)$ . The orders of the surface energy of cBN, hBN, and  $\text{Li}_3\text{BN}_2$  are all completely contrary to their corresponding orders of the valence electron density. Hence, the surface energies with the first-principle theory are well consistent with those results of the valence electron density by the EET. Comparing all surface energies in three phases (hBN, cBN, and  $\text{Li}_3\text{BN}_2$ ), the (100) surface of  $\text{Li}_3\text{BN}_2$  has the highest surface energy; therefore, it can be used as the substrate to induce effectively the growth of cBN crystals.

#### Data Availability

The data used to support the findings of this study are included within the article.

#### Conflicts of Interest

The authors declare no conflicts of interest.

#### Authors' Contributions

Lichao Cai contributed to data curation and wrote the original draft; Bin Xu was involved in funding acquisition and supervised the study; Meizhe Lv and Xiaohong Fan investigated the study; Xiaohong Fan contributed to methodology; and Meizhe Lv contributed to writing, reviewing, and editing.

#### Acknowledgments

This work was financially supported by the National Natural Science Foundation of China (Grant no. 51272139).

#### References

- [1] W. Ding, B. Linke, Y. Zhu et al., "Review on monolayer CBN superabrasive wheels for grinding metallic materials," *Chinese Journal of Aeronautics*, vol. 30, no. 1, pp. 109–134, 2017.
- [2] X. W. Zhang, "Doping and electrical properties of cubic boron nitride thin films: a critical review," *Thin Solid Films*, vol. 544, pp. 2–12, 2013.
- [3] R. Mohammad and Ş. Katircioğlu, "The structural and electronic properties of BAs and BP compounds and  $\text{BPxAs}_{1-x}$  alloys," *Journal of Alloys and Compounds*, vol. 485, no. 1–2, pp. 687–694, 2009.
- [4] X. L. Yuan, J. Niitsuma, T. Sekiguchi, M. Takase, and T. Taniguchi, "Characterization of p-n junction formed at the boundary of facets in cubic-BN using scanning electron microscope," *Diamond and Related Materials*, vol. 14, no. 11–12, pp. 1955–1959, 2005.
- [5] S. Nakano, H. Ikawa, and O. Fukunaga, "Synthesis of cubic boron nitride using  $\text{Li}_3\text{BN}_2$ ,  $\text{Sr}_3\text{B}_2\text{N}_4$  and  $\text{Ca}_3\text{B}_2\text{N}_4$  as solvent-catalysts," *Diamond and Related Materials*, vol. 3, no. 1–2, pp. 75–82, 1994.
- [6] O. Fukunaga and S. Takeuchi, "Growth mechanism of cubic BN using  $\text{Li}_3\text{BN}_2$  solvent under high pressure," *International Journal of Refractory Metals and Hard Materials*, vol. 55, pp. 54–57, 2016.
- [7] Y. Du, Z. Su, D. Yang et al., "Synthesis of black cBN single crystal in hBN-Li<sub>3</sub>N-B system," *Materials Letters*, vol. 61, no. 16, pp. 3409–3412, 2007.
- [8] S. Li, X. F. Guo, B. Xu, and H. Wang, "Fracture morphology and XRD layered characterization of cBN cake," *Journal of Synthetic Crystals*, vol. 41, no. 1, pp. 15–19, 2012.
- [9] M.-Z. Lv, B. Xu, L.-C. Cai, F. Jia, and X.-D. Yuan, "Analysis of transition mechanism of cubic boron nitride single crystals under high pressure-high temperature with valence electron structure calculation," *Chinese Physics Letters*, vol. 36, no. 1, Article ID 013101, 2019.
- [10] C. Lin, G. Yin, Y. Zhao, and J. Wang, "Analysis of the effect of alloy elements on allotropic transformation in titanium alloys with the use of cohesive energy," *Computational Materials Science*, vol. 111, pp. 41–46, 2016.
- [11] C. Lin, G. Yin, A. Zhang, Y. Zhao, and Q. Li, "Simple models to account for the formation and decomposition of athermal  $\omega$  phase in titanium alloys," *Scripta Materialia*, vol. 117, pp. 28–31, 2016.
- [12] H. Liu, Q. Li, L. Zhu, and Y. Ma, "Superhard and superconductive polymorphs of diamond-like BC<sub>3</sub>," *Physics Letters A*, vol. 375, no. 3, pp. 771–774, 2011.

- [13] S. N. Shirodkar and E. Kaxiras, "Li Intercalation at graphene/hexagonal boron nitride interfaces," *Physical Review B*, vol. 93, no. 24, 2016.
- [14] H. Ruuska and K. Larsson, "Surface reactivities of (111), (100), and (110) planes of c-BN: a quantum mechanical approach," *Diamond and Related Materials*, vol. 16, no. 1, pp. 118–123, 2007.
- [15] N. Wang, L. Dong, M. S. Li, and D. J. Li, "Comparison and stability of the low-index surfaces of c-BN by first-principles," *Vacuum*, vol. 104, pp. 92–96, 2014.
- [16] N. Ooi and J. B. Adams, "Ab initio studies of the cubic boron nitride (110) surface," *Surface Science*, vol. 574, no. 2-3, pp. 269–286, 2005.
- [17] F. Hui, P. Vajha, Y. Ji et al., "Variability of graphene devices fabricated using graphene inks: atomic force microscope tips," *Surface and Coatings Technology*, vol. 320, pp. 391–395, 2017.
- [18] B. Xu, M. Lv, X. Fan, W. Zhang, Y. Xu, and T. Zhai, "Lattice parameters of hexagonal and cubic boron nitrides at high temperature and high pressure," *Integrated Ferroelectrics*, vol. 162, no. 1, pp. 85–93, 2015.
- [19] H. Yamane, S. Kikkawa, and M. Koizumi, "High- and low-temperature phases of lithium boron nitride,  $\text{Li}_3\text{BN}_2$ : preparation, phase relation, crystal structure, and ionic conductivity," *Journal of Solid State Chemistry*, vol. 71, no. 1, 11 pages, 1987.
- [20] T. D. Beaudet, J. R. Smith, and J. W. Adams, "Surface energy and relaxation in boron carbide (10 $\bar{1}$ 1) from first principles," *Solid State Communications*, vol. 219, no. C, pp. 43–47, 2015.
- [21] M. Lv, B. Xu, L. Cai, X. Guo, and X. Yuan, "Auger electron spectroscopy analysis for growth interface of cubic boron nitride single crystals synthesized under high pressure and high temperature," *Applied Surface Science*, vol. 439, pp. 780–783, 2018.
- [22] X. Guo, B. Xu, W. Zhang, Z. Cai, and Z. Wen, "XPS analysis for cubic boron nitride crystal synthesized under high pressure and high temperature using  $\text{Li}_3\text{N}$  as catalysis," *Applied Surface Science*, vol. 321, pp. 94–97, 2014.
- [23] M. Lv, B. Xu, X. Guo, L. Cai, and X. Yuan, "Electron energy loss spectroscopy analysis for cubic boron nitride single crystals transition mechanism in  $\text{Li}_3\text{N}$ -BN system," *Materials Letters*, vol. 242, pp. 75–78, 2019.

## Research Article

# Plane Animation Simulation of the Interaction between Carbon Nanomaterials and Cell Lysosomes

Wen Liu , Feng Qiu, and Xi Zeng

*School of Art & Design, Wuhan Institute of Technology, Wuhan 430205, Hubei, China*

Correspondence should be addressed to Wen Liu; 09091401@wit.edu.cn

Received 4 August 2020; Revised 4 September 2020; Accepted 21 September 2020; Published 7 October 2020

Academic Editor: Tifeng Jiao

Copyright © 2020 Wen Liu et al. This is an open access article distributed under the Creative Commons Attribution License, which permits unrestricted use, distribution, and reproduction in any medium, provided the original work is properly cited.

With the continuous development of cell dynamics, Raman scattering has become more and more common in the application of cell imaging and dynamic changes in chemical substances. This research mainly discusses the plane animation simulation process of the interaction between carbon nanomaterials and cell lysosomes. Twenty parallel HeLa cells were seeded on 40 mm imaging scaffolds. The 15% bovine placental serum cell culture cells are placed in a thermostat for 12 hours at a CO<sub>2</sub> concentration of 6%. After washing 4 times, 20 μL of the dual control system is added to the confocal dish, and cycle optimization culture is performed at 2, 4, 6, and 8 hours. It is incubated for 10 hours, 20 hours, and 30 hours (35°C, 6% CO<sub>2</sub>). Next, the HeLa cells were taken out and seeded on three 30 mm confocal cell culture dishes. CCl<sub>4</sub> is added to the initial confocal Petri dish. After heating for 30 minutes, the nanoparticle system is added to the two confocal Petri dishes and circulated within an appropriate time. After washing with PBS, the SERS signal in the cells was imaged with a laser confocal Raman microscope, and the excitation channels were GFP 475 and Cy3 channels. LysoTrackerRed (2p μM) was used for local experiments of cell isotope. Deoxygen (2p μM) was used to induce cell death, and the pH changes in lysosomes in cells were imaged in real time with a confocal microscope. Two distinct peaks in the Raman spectrum were observed at 1246 cm<sup>-1</sup> and 1543 cm<sup>-1</sup>. The research results show that the carbon nanomaterial synthesized by a simple method at room temperature has high stability and is suitable for analysis and detection of imaging with cells as the target.

## 1. Introduction

Lysosome damage may cause various diseases and is an important cause of tuberculosis, joint rheumatism, and other diseases. For the cause of silicosis, silica in the air is swallowed by phagocytic cells inside the body, and after fusion with lysosomes, silica can hydrogenate hydroxyl groups and membrane phospholipids or proteins in cell lysosomes. It will cause the internal environment of the cell to be disordered, the cell itself will be destroyed, the indigestible silica is released, and then, other neighboring cells will be destroyed. This repeated cycle is connected with cell damage and continuous repair and then further causes muscle fibrosis.

In the past, nonviral vectors contained a variety of inorganic nanomaterials. At present, gene carriers combining inorganic nanomaterials and cationic polymers have the size

effect, the multifunctional properties of inorganic nanomaterials, and the strong gene loading capacity of cationic polymers. Based on this principle, in combination with cationic polymers, various nucleic acids can be effectively loaded so that carbon nanomaterials can better integrate into cell lysosomes without damaging the structure of cells. Therefore, studying the dynamic changes in carbon nanomaterials in cell lysosomes is more conducive for timely diagnosis of diseases.

The unique properties of carbon-based nanomaterials have aroused people's great interest, thereby promoting the development of large-scale industrial production methods. Zaytseva believes that, regardless of the application field, it is related to the increasing trend of the application of carbon nanomaterials to the environment, and it is still difficult to predict the biological impact in the environment. He researched different types of

carbon-based nanomaterials, major production technologies, and important trends in agricultural and environmental applications. His research process is too simple and not specific enough [1]. Geng proposed a study to improve the morphology, separation performance, and mechanical properties of the membrane. The PVDF/MWCNT/GO hybrid membrane was successfully prepared by using polyvinylidene fluoride (PVDF) as the polymer as the nanofiller, the combination of the mixed matrix and the solution coagulation bath. The morphology and structure of MWCNT and GO were characterized, and the influence of the addition of carbon nanomaterials on the morphology, separation performance, and mechanical properties of the film was studied. His research process lacks data [2]. Smart fabrics and interactive textiles have aroused great interest as an emerging material due to their multifunctional functions. Lee manufactured a highly durable wireless flexible strain sensor based on commercial textiles through the integration of functional hybrid carbon nanomaterials and piezoresistive materials. Specifically, a solution-processable spray-assisted coating method capable of forming a uniform coating on a large area fabric is adopted. Due to their different deflection behaviors, textile-based strain sensors show highly stable and instant response in various bending curvatures and structural characteristics of ZnO nanowires. The accuracy of the wireless flexible strain sensor he studied is not enough [3]. Carbon nanomaterials (CNMs), such as carbon nanofibers (CNFs), multiwalled carbon nanotubes (MWCNTs), and carbon nanorods (CNRs) have various industrial and commercial applications. Angoth believes that exposure to these CNMs has also greatly increased. His research evaluated the extrapulmonary toxicity induced by these CNMs. After 1 day, 1 week, 1 month, and 3 months after exposure, the characteristics of CNM were tested by dripping into the rat trachea, by using serum biochemical parameters (such as alanine aminotransferase (ALT) and creatinine) and diagnostic assays kit to assess extrapulmonary toxicity. His research process lacks actual control [4]. Carbon nanomaterials (CNMs), including carbon nanotubes (CNTs) and their derivatives, have a variety of technical and biomedical applications. Woodman believes that the potential toxicity of CNM to cells and tissues has become an important emerging issue in nanotechnology. To evaluate the toxicity of carbon nanotubes and fullereneol  $C_{60}(OH)_{24}$ , he used the budding yeast *Saccharomyces cerevisiae*, one of the simplest eukaryotes that shares the basic knowledge of eukaryotic cell biology. In order to study the underlying mechanism behind the growth defects induced by CNMs, he performed RNA-Seq-dependent transcription analysis and constructed a global gene expression profile of fullereneol  $C_{60}(OH)_{24}$  and CNT-treated cells. His research process is too complicated [5].

This research mainly introduces the basic principles of the molecular dynamic method, establishes related models of carbon nanomaterials and cell lysosomes, and conducts preliminary simulations without external force control. A

simple model (cell lysosome model) was established based on the characteristics of biofilms, and a pure single-walled carbon nanotube (carbon nanomaterial) was established. At the same time, a simulated environment model (water and saline model) was established. Based on the advantages of molecular dynamics and the characteristics of the model, corresponding simulation conditions are set. The effects of various spatial positions, various liquid environments (water environment and normal saline), and the size of carbon nanomaterials during the simulation are studied. These factors only have a slight influence on the interaction between carbon nanomaterials and cell lysosomes, but they did not cause direct contact between carbon nanomaterials and cell lysosomes.

## 2. Nanomaterials

*2.1. Cell Lysosomes.* Lysosomes have very important functions in cells. It can digest large particulate matter such as food and pathogenic bacteria into small molecules and can eliminate indigestible matter. The soluble enzymes of some aging cell organs and biological macromolecules can be transferred into the body, which is an important mechanism of body cell defense and self-replication. Therefore, lysosomes play a great role in the decomposition and digestion of cells.

Except for some cells such as red blood cells, most animal cells have lymphoid tissues, such as lysosomes, which play an important role in immune response, killing of harmful cells, and immune regulation. Cell lysosomes can kill pathogenic organisms such as bacteria, fungi, parasites, viruses, and aging cell organs that invade cells and play a very important role in the body's nonspecific immunity. Cell lysosomes can also digest microorganisms recognized by antibodies. However, cell lysosomes are also target cells that are often susceptible to H5N1 avian influenza virus. If the function of cell lysosomes to phagocytic cells is destroyed, it may prevent the H5N1 avian influenza virus from being excreted in the body and then further infects the patient with H5N1 avian influenza [6, 7].

*2.2. Mechanical Behavior of Nanomaterials and Cell Membrane Coupling.* The interaction between nanomaterials and cell membranes is accompanied by many complex biochemical processes. In recent years, researchers have gradually realized that external factors play an important role in the process of nanomaterials interacting with cell membranes, such as the human body's diet, internal circulation, and targeted transportation. These external factors include the following [8]:

- (1) The size, shape, deformation stiffness, surface microstructure, and porosity of nanomaterials.
- (2) The bending stiffness, surface tension, and initial structure of the cell membrane.
- (3) The bonding of nanomaterials and cell membranes.

At different temperatures, nanomaterials exhibit different stress conditions:

$$X(t - T_1) = (\tau_1 V_{C1} + \tau_2 V_{C2}) - \left( \tau_1 V_{C1} e^{-(t-T_1/\tau_1)} + \tau_2 V_{C2} e^{-(t-T_2/\tau_2)} \right), \quad (1)$$

where  $V_{C1}$  is the volume of nanomaterials and  $\tau$  is the stress coefficient. Studies have shown that the deformable properties of nanomaterials have a great impact on the function of the immune system because cell lysosomes cannot swallow very soft targets. From the perspective of external factors, the interaction between nanomaterials and cell membranes includes the combination between the deformation of the cell membrane and the deformation of nanomaterials and the combination between the movement of biomolecules that drive encapsulation and encapsulation and many other chemical processes. The research on the combination of nanomaterial cell membranes and chemical behaviors aims to provide an understanding of the final form and related phenomena of nanomaterials through systematic and multiscale research [9].

The nanoparticles used have the same size and shape. In addition to disposing different ligands on the surface, they also cover the monolayer of ligands with the same hydrophobicity and durability ratio. Using a confocal microscope, the cell intake rate and intracellular distribution of fluorescently labeled nanoparticles in live mouse cells were measured. It was found that nanoparticles with alternating hydrophobic and hydrophilic ligands on the surface can penetrate the cell membrane without signs of cell membrane damage [10, 11]. On the contrary, with the same hydrophobicity/hydrophilicity ratio, nanoparticles with hydrophobic and hydrophilic ligands randomly distributed on the surface will greatly reduce the possibility of penetrating the cell membrane. The terminal neurotic effect of the cell is blocked. It can be seen that the nanoparticles with rhombohedral ligands can directly invade the cell membrane, but the nanoparticles with random surface ligands cannot pass. Therefore, the distribution of ligands on the surface of nanoparticles plays a controlling role in the interaction between cells and nanoparticles [12].

**2.3. Medical Application Research of Fullerene Nanomaterials.** Many clinical and medical studies have reported the biological value of carbon nanomaterials, and its uses include DNA light splicing, enzyme blocking, tumor treatment, drug carriers, and antibacterial and cytoprotective effects [13, 14]. Carbon nanomaterial fibers have been proven to be a promising technology for in situ structural health monitoring of polymer composites. Self-inductive composites can be achieved through a variety of integrated strategies, including carbon nanotube- (CNT-) coated fiber (CNTF), graphene oxide- (RGO-) coated fiber (RGOF), and carbon fiber (CF) [15]. RGOF has the highest track gauge sensitivity, with clear two-level performance from linear to nonlinear, and CNTF always shows a well-organized signal before the final fracture [16].

Due to the small size of carbon nanoparticles, they can reach lesions that cannot be reached by traditional drugs through the body. The superior hydrophobic part can help

other substances passing through the cell membrane and can be used as a drug delivery carrier. For example, EPO is usually taken intravenously, but due to its sensitivity to intestinal enzymes, its activity will drop rapidly. When EPO is adsorbed by carbon nanomaterials, pharmacokinetic studies have shown that the biological activity of EPO is increased by 4 times [17, 18]. Generally speaking, a nonlinear inhibition model is used to analyze the relationship between drug concentration and the effect of the target site in the body:

$$E = E_{\max} - (E_{\max} - E_{\min}) \times \frac{C_{\text{eff}}^s}{EC_{50}^s + C_{\text{eff}}}. \quad (2)$$

Among them,  $E$  is the drug concentration in the blood and  $C_{\text{eff}}^s$  is the drug concentration in the abdominal cavity [19].

On the one hand, carbon nanomaterials and their polypeptide derivatives because of the hydrophobic surface of the carbon nanomaterials exhibit antibacterial activity, are easy to penetrate into the cell membrane, and can destroy the lipids of the cell membrane. On the other hand, carbon nanomaterials can make pathogenic microorganisms inactive by hindering energy metabolism. It has been found that carbon nanomaterials and their derivatives can change the composition of HIV protease and hinder the activity of the enzyme, thereby achieving antiviral function. Coordination number refers to the calculation of the nearest atom number near the molecule, which can represent the distribution density around the atom to a certain extent [20]:

$$g(r) = \frac{dN}{4\pi r^2 \rho dr} + \int \rho g(r) 4\pi r^2 dr + \rho dr. \quad (3)$$

Among them,  $r$  is the central radius of the atom and  $N$  is the number of atoms.

**2.4. Raman Imaging.** Raman spectroscopy is the basis of Raman spectroscopy imaging technology. It is the Raman scattering generated when light irradiates the material. The scattering types are mainly divided into two types: Rayleigh scattering and Raman scattering. Among the two types of scattering, Raman scattering becomes unstable because the material of a specific molecule is stimulated by light when it changes from the ground state to the unstable excited state [21]. The frequency components  $f$  of the measured data of the dual-spectrum study have a phase combination relationship between  $fz$  and  $f + f$ . In other words, they determine the second-order nonlinear relationship of the signal:

$$TP(f_1, f_2) = X_j(f_1) \cdot X_j(f_2) \cdot X_j(f_1 + f_2). \quad (4)$$

In the formula,  $X_j$  is the power spectrum.

Due to its high sensitivity, it can detect multiple targets at the same time, and the advantages of surface Raman enhancement such as fluorescence attenuation and light fading of the nonfluorescent probe are used in the design of a sensing system that detects multiple direct and indirect targets. The detection method is to directly combine the

target object with the Raman base, which causes the change in the Raman characteristic peak [22, 23]. Indirect detection refers to the interaction between the target molecule and the modified Raman matrix, but the Raman characteristic peak of the molecule has changed. Now, surface Raman enhancement is widely used in environmental testing of heavy carbons, polycyclic aromatic hydrocarbons, food additives, antibiotics, and residual pesticides, as well as biomedical testing [24].

### 3. Plane Animation Simulation Experiment

**3.1. Obtaining and Processing the Initial Structure.** Delete all unwanted compound molecules, leaving only the protein structure. The two models of carbon nanomaterial derivatives were established by Gaussview5.0 software, but the key length and key angle of this model may not be appropriate, so Gaussian09 software must be used to optimize its structure. HF/6-31G (d) was used to optimize the carbon nanomaterial derivative molecules, and the appropriate initial composition was obtained. The experimental equipment is shown in Table 1.

**3.2. Sample Processing.** Plasma provided by volunteers is used in the laboratory. At the beginning of the experiment, 50 mL of blood was collected and made into erythrocyte hemolysis products. It is placed in a solution of 11% sodium chloride (NaCl); then, the centrifuge tube is shaken well, diluted, and centrifuged for 15 minutes, and the blood sample is collected. Repeatedly, 50 ml of ionized water is used three times. Under the action of osmotic pressure, the red blood cells rupture; the free hydroxy iron erythrocyte elements of the cells are freed and then centrifuged to remove the bottom of the tube membrane such as the sediment; and it is hemolyzed and stored in a sterilization tube at 4°C. Before testing, the solution was diluted 50 times for analysis and testing of hemolytic products. In order to verify the feasibility of the established method, 10 blood samples were collected and centrifuged at 4000 rpm for 40 minutes with an ultrafiltration tube (with a molecular weight of 4 KDa). 5 mL of centrifugal fluid is diluted with PBS buffer (pH = 7) into 15 mL and stored in a refrigerator at 5°C. In the process of glucose measurement, first 2 mL glucose standard solution (or blood sample) and 2 mL glucuronidase (1 mg/mL) are taken and then centrifuged in 10 mL PBS buffer solution for 20 minutes for chemiluminescence detection.

**3.3. Molecular Docking and Molecular Dynamic Simulation.** Before the docking process, the first receptor protein and ligand were processed using AutoDockTools in the next docking process. Using AutoDockVina software, two optimized carbon nanomaterial ligands were connected to the active center of PTP1B, and a reasonable initial complex structure was obtained. The receptor binding site is represented by a cube box, the center of the box is near the active center and the second binding site, and then, the box covers the residues of the entire active area. In the open and closed

configuration, the three-dimensional grid points in the box are  $30 \times 30 \times 30$  and  $20 \times 20 \times 20$ , respectively, and the interval between the grid points is set to 0.4 Å. The Monte Carlo method was used to retrieve the stereo conformation, and the energy scores of different docking stereo conformations were obtained. Finally, in the first 10 best conformations, considering the energy rating and the rationality of the conformation, the first complex that is most suitable for simulation is selected.

**3.4. Simulation of the Direct Penetration of Carbon Nanoparticles through the Film.** In this study, carbon nanoparticles with a surface charge of 75% were initially selected. Through partial simulation, the free energy of the system is calculated by the umbrella sampling technique sampling method and weighted histogram analysis to obtain the average force potential (PMF) curve of the system and analyze the interaction between carbon nanoparticles and cell membranes. With carbon nanoparticles on the membrane (outside the cell), the free energy of the system decreases as the distance between the centers of gravity decreases. Therefore, carbon nanoparticles have a tendency to move from the outer membrane to the inner membrane, and the energy of the system is kept to a minimum. If carbon nanoparticles are placed under the membrane (inside the cell), the free energy of the system will increase as the distance between the centers of gravity decreases. That is, when carbon nanoparticles move into cells, an energy barrier is required. Therefore, if other substances in the cell are not involved in the uptake of carbon nanoparticles, the carbon nanoparticles will not enter the cytoplasm but stays inside the membrane. The attraction between the carbon nanoparticles and the bilayer membrane is mainly due to the electrostatic interaction between the cationic terminal of the ligand and the anion on the membrane. In addition, when the carbon nanoparticles are located on the lower side of the film, the generation value of the minimum energy point is the largest. This indicates that 75% of the surface-charged carbon nanoparticles penetrate the original plasma membrane and are embedded in it.

**3.5. Confocal Inverted Raman Imaging.** Twenty parallel HeLa cells were seeded on 20 40 mm imaging scaffolds. The 15% bovine placental serum cell culture cells are placed in a thermostat for 12 hours at a CO<sub>2</sub> concentration of 6%. After washing 4 times, 20 μL of the dual control system is added to the confocal dish, and cycle optimization culture is performed at 2, 4, 6, and 8 hours. Continue to incubate under the conditions of 10 hours, 20 hours, and 30 hours (35°C, 6% CO<sub>2</sub>). Next, HeLa cells were taken out and seeded on three 30 mm confocal cell culture dishes. CCl<sub>4</sub> is added to the initial confocal dish. After heating for 30 minutes, the nanoparticle system is added to the two confocal dishes and circulated within an appropriate time. After washing with PBS, the SERS signal in the cells was imaged with a laser confocal inverted Raman microscope. The excitation channels were GFP 475 and Cy3 channels. LysoTrackerRed (2p μM) was used for local experiments of cell isotope.

TABLE 1: Experimental equipment.

Serial number	Equipment	Factory
1	Fourier transform infrared spectrometer	Japan
2	UV-visible spectrophotometer	USA
3	JEM-2100 transmission electron microscope	Ray Magnetic Company
4	Potential analyzer	American microphone
5	X-ray diffractometer	Beijing Saiduo Company

Deoxygen ( $2\text{p}\mu\text{M}$ ) was used to induce cell death, and the pH changes in lysosomes in cells were imaged in real time with a confocal microscope.

**3.6. Transmission Electron Microscope Test.** The microstructure characteristics of the filled phase change material were studied, and the sample was tested by a transmission electron microscope (transmission electron microscope, TEM), model JEM-2100F. The suspension was prepared by mixing the sample in an ethanol solution after 15 seconds in ultrasonic waves, and the suspension was dropped into the porous copper mesh as a test sample.

#### 4. Raman Imaging Analysis

**4.1. In Vivo pH Imaging Analysis of Lysosome.** In this study, a confocal microscope was used to observe the colocalization of ECDs and LysoTracker to investigate its distribution in cells. The results showed that ECDs showed bright green fluorescence in A549 cells or HEp-2 cells, and LysoTracker showed red fluorescence, and they coincided well. In order to further verify the lysosomal targeting performance of ECDs, ECDs were incubated for 12 h, 24 h, or even 48 h, and the fluorescence of ECDs and LysoTracker coincided to a large extent. The above experimental results show that ECDs can selectively target living cell lysosomes for a long time. In general, the prepared ECDs have high quantum yield (relative quantum yields 15%, average value of three experiments), and excitation does not change with emission, good photobleaching resistance, good salt resistance, good oxidation resistance, and low toxicity. It has good biocompatibility and can indicate pH changes. Common interfering substances in cells do not interfere with pH response. At the same time, it has lysosomal targeting properties, so ECDs can be used to monitor the pH of lysosomes in the process of living cell apoptosis. The ECDs were incubated in A549 cells for 12 hours, and the fluorescence intensity changes in normal cells and apoptotic cells (with the addition of dexamethasone, an agent for inducing apoptosis) were observed with a fluorescent confocal microscope during 80 minutes. The table shows that the fluorescence intensity of normal cells is slightly reduced, while for apoptotic cells, the fluorescence of ECDs is significantly weakened due to the sudden increase in acidity. It is proved that the prepared emerald green fluorescent carbon dots can monitor the pH changes in the lysosome in real time. The analysis and detection method established in this experiment can successfully realize the determination of hemoglobin in normal human red blood cells, using the standard addition method

(standard concentrations of hemoglobin are 1, 5, and  $10\mu\text{M}$ , respectively). Through the investigation of the recovery rate, the reproducibility and accuracy of the evaluation method are shown in Table 2. The recovery rate of normal red blood cell samples randomly checked is in the range of 98.1% to 107.7%. At the same time, the relative standard deviation (RSD) of each normal human red blood cell sample is lower than 2.3%, indicating that the reproducibility and accuracy of this method are indeed very good. In short, the experiment proves that the established analytical detection method can successfully realize the highly selective detection of heme in normal human red blood cells.

**4.2. Investigation and Analysis of Probe Dual Control Capability.** The configuration changes in the system are composed of carbon nanoparticles with 75% positive charge on the surface and the film at different time periods, reflecting the dynamic process of carbon nanoparticles with a certain proportion of positive charge on the surface passing through the film. First, when the carbon nanoparticles are located on the outside of the membrane, they move rapidly towards the outer membrane, and the lipid molecules below also rapidly bulge upwards (0 ns–1.2 ns). Then, it is continued to move downward, penetrating the outer film (1.2 ns–20 ns) at a speed lower than the initial speed. After that, it is embedded in the middle part of the membrane and gradually penetrates the inner membrane (20 ns–30 ns). Finally, it reaches the inner surface of the membrane and causes the inner membrane lipid molecules surrounding it to bulge, and the partial body is exposed to the intracellular environment (after 30 ns). The Raman spectra of the probes in different control systems are shown in Figure 1. Obviously, the high speed at which the carbon nanoparticles approach the cell membrane in the first stage is the result of the rapid decrease in the free energy of the system due to the combined action of Coulomb force and van der Waals force. Then, the nanoparticles are partially embedded in the outer film. At this time, the negative charge in the outer film reduces the rate of free energy decline, resulting in a lower speed in the second stage. In the third stage, the strong electrostatic interaction between the cation at the end of the ligand and the anion in the inner membrane promotes its continued movement into the cell. In the final stage, the interaction between the carbon nanoparticles and the film reaches an equilibrium state, which corresponds to the stable configuration obtained by the average force curve analysis. At this time, the free energy of the simulated system is the smallest. The synthesized probes were added to the buffer solution with pH = 7.3 without ATP, pH = 7.3 with  $10\mu\text{M}$

TABLE 2: Reproducibility and accuracy of the evaluation method.

Samples	Added hematin ( $\mu\text{M}$ )	Found ( $\mu\text{M}$ )	Recovery (%)	RSD (%)
<i>Human blood sample 1</i>				
1	1.0	$1.061 \pm 0.05$	$106.0 \pm 0.8$	1.7
2	5.0	$4.96 \pm 0.13$	$99.2 \pm 0.6$	1.3
3	10.0	$10.10 \pm 0.56$	$101.04 \pm 0.5$	0.9
<i>Human blood sample 2</i>				
4	1.0	$1.07 \pm 0.08$	$107.0 \pm 0.6$	1.1
5	5.0	$5.21 \pm 0.21$	$104.2 \pm 0.3$	0.5
6	10.0	$10.21 \pm 0.43$	$102.1 \pm 1.1$	2.3

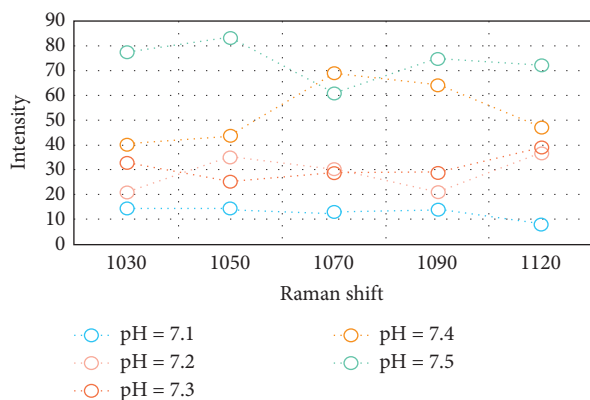


FIGURE 1: Raman spectra of probes in different control systems.

MATP, pH=3.5 without ATP, and pH=3.5 with  $10\mu\text{M}$  MATP. After reacting for 5 minutes,  $10\mu\text{L}$  of the solution was dropped on the surface of the silicon wafer to form small droplets, and the SERS signal was collected under laser irradiation. It can be seen from the Raman spectrum that, in a neutral environment, the Raman signal is very weak regardless of the presence of ATP. Under acidic conditions, there will be some background signals when there is no ATP. It may be that some connected DNAs do not form a double in the acidic chain, and the configuration of i-motif changes and generates a certain Raman signal, but it can be used as a background. Under acidic conditions, when there is ATP, the Raman signal is significantly enhanced. The chain double-control structure and the double-control system in which nanoparticles aggregate to form Raman hot spots can improve ATP in the lysosome.

#### 4.3. Surface Charge Density of Carbon Nanoparticles.

Carbon nanoparticles with 20%, 40%, 60%, 80%, and 100% positive charges on the surface were constructed to study the effects of carbon nanoparticles with different surface charge densities on their interaction with cell membranes. Figure 2 shows the results after 100 ns of interaction between carbon nanoparticles with different charged ratios and real cell membrane models. Obviously, carbon nanoparticles with 0% charge on the surface have no driving force to move towards the membrane due to their neutral and hydrophobic properties, and they are not close to the cell membrane. For charged carbon nanoparticles, as the proportion of surface charge increases, the degree of penetration of carbon nanoparticles through the film has been deepened; when the

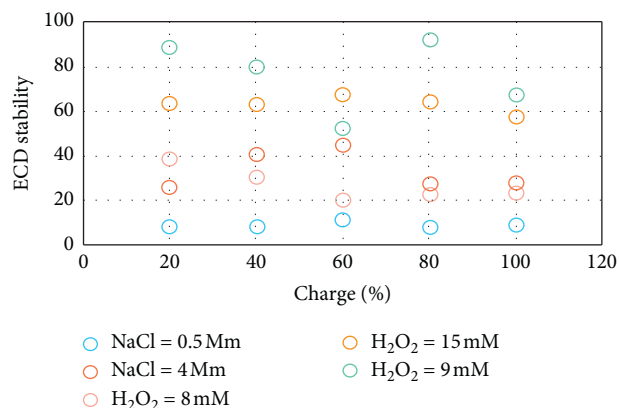


FIGURE 2: Results of 100 ns interaction between carbon nanoparticles with different charge ratios and the real cell membrane model ECDs stability.

proportion of surface charge is less than 60%, the carbon nanoparticles are only embedded in the middle of the film. Because when the limited electric field force pulls the carbon nanoparticles to the hydrophobic region of the lipid molecules, the hydrophobicity of the carbon nanoparticles and the van der Waals force between them and the membrane hinder them from continuing to penetrate the membrane. For carbon nanoparticles with 80% positive charge on the surface, they penetrate the cell membrane and cause the inner membrane around them to form a bump. It is continued to increase the charged ratio (100%). After the carbon nanoparticle penetrates the membrane, it is almost completely wrapped by lipid molecules, forming a structure similar to a vesicle. This phenomenon is caused by the excess between the end of the ligand and the inner membrane, showing strong electrostatic attraction. This paper also studied the cytotoxicity of carbon nanoparticles during ingestion. First, the average root variance of the cell membrane is calculated relative to its initial structure after the carbon nanoparticles penetrate the membrane. Its value can reflect the degree of structural change in the membrane. The larger the value, the more obvious the membrane change. It can be seen that, as the surface charge ratio increases, the overall trend of the mean root variance value is also increasing; that is to say, the surface charge ratio of carbon nanoparticles has a great influence on the integrity of the cell membrane. With ECDs' salt resistance and antioxidant capacity, no matter when the concentration of sodium chloride is 0.5–4 Mm or the concentration of hydrogen

peroxide is 8–15 mM, the fluorescence intensity of ECDs has not changed significantly, indicating the carbon dot. It has good salt resistance and antioxidant capacity. In short, ECDs synthesized by a simple method at room temperature have good stability and are very suitable for analysis and detection and cell-targeted imaging.

Then, the total leakage of water molecules in the process of penetrating the membrane is calculated, that is, the number of water molecules that enter the cytoplasm from the outside of the cell membrane. From the above simulation, it can be found that the carbon nanoparticles will cause a certain degree of damage to the cell membrane structure during the process of penetrating the membrane, so the solvent outside the membrane can easily enter the inside of the membrane. Figure 3 shows the variation in the leakage of water molecules with the charge. And because human cells are a relatively independent and balanced system, any substances outside the balance flowing into the cell may cause the acid-base balance inside and outside the cell to be broken, leading to functional damage and even cell death, so the amount of water leakage is measured: The cytotoxicity of carbon nanoparticles is a more direct aspect. It can be seen in Figure 3 that as the proportion of charged electricity increases, the amount of water leakage first increases and then gradually decreases after approximately 60% reaches the maximum value. This overall trend is consistent with the value of the centroid distance between the carbon nanoparticles and the film when it is finally stable and also proves the correctness of the calculation of the water leakage program in this study. Based on the above analysis of the cytotoxicity of carbon nanoparticles with different charged ratios, it can be seen that when the charged ratios are 20% and 60%, the damage to the membrane is the smallest and the largest. However, in the case of 20% charged ratios, due to a small electrostatic attraction, the carbon nanoparticles did not pass through the cell membrane. In addition, considering the release process of carbon nanoparticles after penetration, carbon nanoparticles with about 80% of the surface will be the best choice for drug delivery due to their lower cytotoxicity and higher penetration efficiency.

**4.4. Analysis of Carbon Spots in Lysosomes.** Subsequently, the carbon dots synthesized by a simple method in this article were characterized. The carbon dots are quasispherical with uniform particle size distribution. 100 particles are randomly counted, and the average particle diameter of the carbon dots is 11.8 nm. The lattice distribution of carbon dots is obvious, and the lattice parameters are 0.21 nm and 0.31 nm, respectively, which correspond to the 100 planes 188 in the graphene plane and the 002 plane between the graphene planes. The prepared carbon dots have an obvious ultraviolet absorption peak at 282 nm, which is attributed to the  $\pi$ - $\pi$  electronic transition of  $C_{-}C/C=C$ . At the same time, the carbon dots show the property that emission depends on excitation, and its maximum excitation wavelength is 350 nm and the maximum emission wavelength at 460 nm; under the excitation of 365 nm ultraviolet light, it shows bright blue fluorescence. In addition, we also investigated

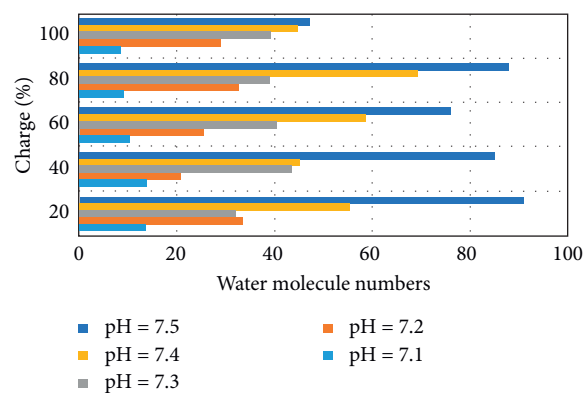


FIGURE 3: The number of leaked water molecules varies with charge.

the cytotoxicity of carbon dots. Even if the concentration of carbon dots is as high as 0.01 mg/mL, human laryngeal carcinoma epithelial cells (HEp-2 cells) still have a survival rate of more than 85%, indicating that the prepared carbon dots have good biocompatibility, and carbon dots are mostly distributed in the cytoplasm, almost not entering the nucleus, which is consistent with the carbon dots reported in most literature. The carbon dots corresponding to different covalent bonds are shown in Figure 4. The results are as follows: X-ray electron spectroscopy (XPS) shows that the carbon dots are mainly composed of carbon, oxygen, and nitrogen. The peaks corresponding to the XPS spectrum are as follows: 284.8 eV, 399.3 eV, and 533.1 eV, and the element content is 71.05%, 25.2%, and 3.75%; these elements just correspond to the elements in the raw materials. After analyzing the high-resolution XPS, the carbon dots have the following bonds: C-C, C-N, C=O, C-OH, and C-N-C. In order to further analyze the distribution of the surface functional groups of the carbon dots, the carbon dots were analyzed by FTIR, and the infrared absorption peak of  $3448\text{ cm}^{-1}$  corresponds to the stretching vibration peak of NH/OH, and the peak of  $2920/2854\text{ cm}^{-1}$  corresponds to the stretching vibration peak of the CH bond, while the infrared absorption peaks of  $1641$  and  $1083\text{ cm}^{-1}$  correspond to the stretching vibration of C=O and CO. Together with the results of FTIR, it proved that the surface of carbon dots has abundant functional groups such as amino, carboxyl, and hydroxyl groups, which makes the carbon dots have good water solubility. Finally, the Raman spectroscopy analysis of the synthesized carbon dots shows that there are two obvious peaks in the Raman spectra, located at  $1246\text{ cm}^{-1}$  and  $1543\text{ cm}^{-1}$ . The former belongs to the D-band peak of  $sp$  carbon, and the latter belongs to the G-band peak of  $sp^2$  carbon, which is consistent with the previous HRTEM results, which proves that the carbon dots have both  $sp^2$  and  $sp^3$  hybrid carbons. In summary, the above results show that, by selecting simple and easily available raw materials, a one-step solvothermal method has synthesized excellent carbon dots with excellent properties, abundant water-soluble functional groups, and good biocompatibility, which can be used for analysis, detection, and cell imaging. Due to the mild reaction conditions, the abundant amino functional

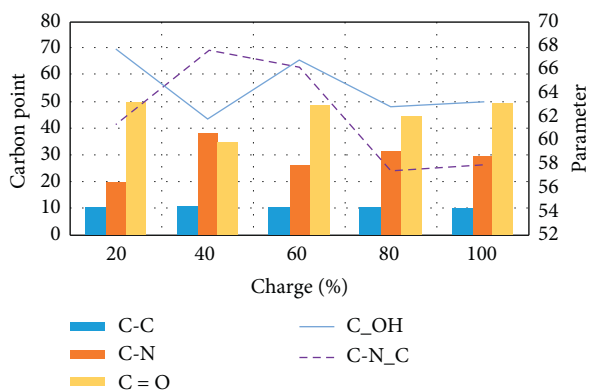


FIGURE 4: Carbon dots corresponding to different covalent bonds.

groups in the raw materials still remain in the ECDs, and the abundant amino, carboxyl, and hydroxyl functional groups on the surface of the ECDs endow ECDs with good water solubility, which is the carbon point as a pH response probe and intracellular solution. Enzyme targeting probes provide the possibility.

## 5. Conclusion

According to research, nanoparticles not only damage animal tissues and organs but also may show toxicity to various degrees from cells to protein genetic factors. The toxicity mechanism of nanoparticles has not yet been determined. C60 can cause the generation of reactive oxygen species (ROS), which may cause damage to cell membranes and cytotoxicity. Therefore, if nanomaterials are widely used, evaluating their safety is an urgent issue. It is necessary to conduct detailed research on the role and toxicity mechanism of nanometers to improve the biological safety of carbon nanomaterials.

In recent years, as a single-layer two-dimensional carbon nanomaterial, carbon nanomaterials have made great progress in the field of biomedicine. Due to their unique physical and chemical properties such as excellent biocompatibility and changeability, they have made greater progress. It can also participate in drug transport and photothermal effects in organisms. In this paper, a functional oxide nanomaterial is designed and synthesized, and its characteristics are changed to have a larger specific surface area, aromatic molecule loading capacity, conjugation, and a compound that can interact with hydrogen bonds and apply it to the treatment of chemical photothermal reaction and gene transfer. The results show that the synthesized carbon nanomaterials have great potential applications in the field of biomedicine.

Now, carbon nanotubes are widely used, and they are being used more and more in the field of biology. In the research direction of carbon nanotubes, or in the research direction of biological toxicity, whether they function as drugs or gene carriers must first be confirmed and then whether the specific mechanism of carbon nanotubes is a common problem. Carbon nanotubes enter the cell body, so the interaction between carbon nanotubes and biofilms is a

study of carbon nanotubes in the biomedical field. The hydrophilic and hydrophobic carbon nanomaterials prepared in this study show excellent application prospects in biological imaging or biomarker research. Hydrophobic carbon nanomaterials easily enter cells, accumulate in cells, and emit bright red fluorescence. Therefore, this research provides a new method for the preparation and development of carbon nanomaterials for the study of biological imaging.

## Data Availability

The data used to support the findings of this study are available from the corresponding author upon request.

## Conflicts of Interest

The authors declare that they have no conflicts of interest.

## Acknowledgments

This work was supported by the Youth Project Fund for Humanities and Social Sciences Research of Hubei Education Department (17Q080).

## References

- [1] O. Zaytseva and G. Neumann, "Carbon nanomaterials: production, impact on plant development, agricultural and environmental applications," *Chemical & Biological Technologies in Agriculture*, vol. 3, no. 1, p. 17, 2016.
- [2] H. Z. Geng, C. X. Xu, W. Y. Wang et al., "Preparation and performance of carbon nanomaterials/polyvinylidene fluoride hybrid membrane," *Journal of Tianjin Polytechnic University*, vol. 37, no. 4, pp. 1-6, 2018.
- [3] T. Lee, W. Lee, .S.-W. Kim, J. J. Kim, and B.-S. Kim, "Flexible textile strain wireless sensor functionalized with hybrid carbon nanomaterials supported ZnO nanowires with controlled aspect ratio," *Advanced Functional Materials*, vol. 26, no. 34, pp. 6206-6214, 2016.
- [4] B. Angoth, N. R. H. Lingabathula, and N. R. Yellu, "Assessment of extrapulmonary toxicity induced by carbon nanomaterials following intra-tracheal instillation in rats," *Asian Journal of Pharmaceutical and Clinical Research*, vol. 10, no. 5, p. 82, 2017.
- [5] S. Woodman, H. Short, A. K. Linan et al., "Carbon nanomaterials alter global gene expression profiles," *Journal of Nanoscience and Nanotechnology*, vol. 16, no. 5, pp. 5207-5217, 2016.
- [6] G. Wang, Y. Wang, P. Zhang et al., "Structure dependent properties of carbon nanomaterials enabled fiber sensors for in situ monitoring of composites," *Composite Structures*, vol. 195, pp. 36-44, 2018.
- [7] A. N. Li, Y. V. Plekhanova, S. E. Tarasov et al., "Effect of some carbon nanomaterials on ethanol oxidation by gluconobacter oxydans bacterial cells," *Applied Biochemistry and Microbiology*, vol. 53, no. 1, pp. 123-129, 2017.
- [8] M. Zhou, H. L. Wang, and S. Guo, "Towards high-efficiency nanoelectrocatalysts for oxygen reduction through engineering advanced carbon nanomaterials," *Chemical Society Reviews*, vol. 47, no. 16, pp. 1273-1307, 2016.
- [9] L. Cui, X. Y. Zhang, and G. Wei, "Computational study on thermal conductivity of defective carbon nanomaterials:

- carbon nanotubes versus graphene nanoribbons,” *Journal of Materials Science*, vol. 53, no. 6, pp. 4242–4251, 2018.
- [10] S. Araby, R. A. Qiu, R. Wang, Z. Zhao, C.-H. Wang, and J. Ma, “Aerogels based on carbon nanomaterials,” *Journal of Materials Science*, vol. 51, no. 20, pp. 9157–9189, 2016.
- [11] W. J. Ma, J. Lim, and S. O. Kim, “Nitrogen dopants in carbon nanomaterials: defects or a new opportunity?” *Small Methods*, vol. 1, no. 1-2, p. 1600014, 2017.
- [12] J. Majewska and B. Michalkiewicz, “Preparation of carbon nanomaterials over Ni/ZSM-5 catalyst using simplex method algorithm,” *Acta Physica Polonica A*, vol. 129, no. 1, pp. 153–157, 2016.
- [13] A. Hajian, S. B. Lindström, T. Pettersson, M. M. Hamed, and L. Wågberg, “Understanding the dispersive action of nanocellulose for carbon nanomaterials,” *Nano Letters*, vol. 17, no. 3, p. 1439, 2017.
- [14] D. A. Wågberg, M. I. Tulepov, S. Tursynbek et al., “Processing of the bottomhole zones of oil wells with use of the carbon nanomaterials,” *Rasayan Journal of Chemistry*, vol. 10, no. 2, pp. 344–348, 2017.
- [15] E. X. Ding, H. Z. Geng, J. Wang et al., “Hierarchical chrysanthemum-flower-like carbon nanomaterials grown by chemical vapor deposition,” *Nanotechnology*, vol. 27, no. 8, Article ID 085602, 2016.
- [16] K. Ozdemir, “Experimental investigation of trihalomethanes removal in chlorinated drinking water sources with carbon nanomaterials,” *Fresenius Environmental Bulletin*, vol. 25, no. 12, pp. 6202–6214, 2016.
- [17] P. Choudhury, S. D. Mandal, and P. K. Das, “Hydrophobic end-modulated amino-acid-based neutral hydrogelators: structure-specific inclusion of carbon nanomaterials,” *Chemistry—A European Journal*, vol. 22, no. 15, pp. 5160–5172, 2016.
- [18] D. Veclani, A. M. Tolazzi, and A. Melchior, “Molecular interpretation of pharmaceuticals’ adsorption on carbon nanomaterials: theory meets experiments,” *Processes*, vol. 8, no. 6, p. 642, 2020.
- [19] S. Liu, C. Ma, M.-G. Ma, and J.-F. Li, “Recent advances in carbon nanomaterials derived from biomass,” *Science of Advanced Materials*, vol. 11, no. 1, pp. 5–17, 2019.
- [20] S. Eissa, M. Almusharraf, and M. Zourob, “A comparison of the performance of voltammetric aptasensors for glycated haemoglobin on different carbon nanomaterials-modified screen printed electrodes,” *Materials Science and Engineering: C*, vol. 101, pp. 423–430, 2019.
- [21] M. Du, Y. Gao, H. Su, and H. Fang, “Carbon nanomaterials enhanced cement-based composites: advances and challenges,” *Nanotechnology Reviews*, vol. 9, no. 1, pp. 115–135, 2020.
- [22] Y. Jiang, X. L. Zhang, and T. Zhang, “Improving the performance of UV-curable coatings with carbon nanomaterials,” *Express Polymer Letters*, vol. 12, no. 7, pp. 628–639, 2018.
- [23] M. R. Taha and J. M. A. Alsharif, “Performance of soil stabilized with carbon nanomaterials,” *Chemical Engineering Transactions*, vol. 63, no. 2018, pp. 757–762, 2018.
- [24] F. Yu, B. Z. Chen, B. Wang, Z. Jin, S. Ma, and X. Liu, “The role of lysosome in cell death regulation,” *Tumor Biology*, vol. 37, no. 2, pp. 1427–1436, 2016.

## Research Article

# Comprehensive Evaluation of the Accelerated Aging Law of NEPE Propellants

Yulong Liang, Mi Zhang, Hui Ren , and Qingjie Jiao

State Key Laboratory of Explosion Science and Technology, Beijing Institute of Technology, Beijing 100081, China

Correspondence should be addressed to Hui Ren; renhui@bit.edu.cn

Received 3 August 2020; Revised 1 September 2020; Accepted 22 September 2020; Published 5 October 2020

Academic Editor: Tifeng Jiao

Copyright © 2020 Yulong Liang et al. This is an open access article distributed under the Creative Commons Attribution License, which permits unrestricted use, distribution, and reproduction in any medium, provided the original work is properly cited.

In order to study the accelerated aging law of nitrate ester plasticized polyether (NEPE) propellants, the mechanical properties, weight loss, adhesive network structure fracture, and stability of NEPE propellants during storage were analyzed. The results show that the maximum tensile strength  $\sigma_m$  shows good change law with the increase of storage time, and the failure of NEPE propellants is mainly strength failure. The content of the stabilizer decreased with the increase of storage time. With the prolongation of storage time, the weight loss ratio increases gradually with good regularity. The decomposition of the components in the propellant leads to the degradation of the polyethylene glycol (PEG) network structure. The thermal decomposition of the nitrate plasticizer in NEPE propellants will occur, and the products will cause the adhesive network structure to decompose and break the chain, leading to the destruction of the matrix structure. The thermal decomposition of the propellant has temperature-increasing rate dependency.

## 1. Introduction

Solid rocket engines are important defense products, and the health status has a critical impact on weapon reliability. To a large extent, the storage life of solid rocket engines depends on the storage properties of solid propellants, including physical and chemical properties, internal ballistic performance, and structural integrity [1]. However, the solid propellant is an unstable material that will cause physical and chemical aging during long-term storage [2]. Physical aging refers to changes in the physical properties of solid propellants during the storage periods, such as moisture absorption, dehumidification between the oxidant and the binder interface, solvent vitalization, debonding between the propellant and the liner, cracks and voids caused by stress or strain, and other changes in physical properties. Chemical aging refers to the change in properties of solid propellants caused by chemical changes during processing, storage, and use, such as thermal decomposition, hydrolysis, degradation, decomposition of oxidants, oxidative crosslinking, and degradation of adhesives. The chemical changes caused by

the interaction of various components of the propellant or reaction with the air are irreversible, and the rate of change varies with different storage conditions. Therefore, the study of the solid propellant aging mechanism is the basis of its storage life assessment and an important issue in the life prediction of solid rocket engines [3–5].

NEPE combines the advantages of the double-base propellant and composite propellant. It is a new type of propellant with excellent energy performance and mechanical properties at present and represents the development direction of high-energy solid propellants [6–8]. However, in the storage process, this type of propellant is prone to complex aging phenomena, causing engine failure and leading to safety risks and economic losses [9–11]. Therefore, it is necessary to carry out an in-depth analysis of the aging performance characteristics of NEPE propellants to provide a theoretical basis for the next step in finding effective antiaging measures. In the article, we analyze the storage performance of NEPE solid propellants, explore the accelerated aging rules of NEPE propellants, and study their health detection technology.

## 2. Materials and Characterization

The NEPE propellant used in the experiment adopts the general PEG/N100 system, and the propellant uses mixed nitrate (a mixture of NG and BTTN) as a plasticizer. First, propellant slurry is cast into a certain size of the propellant sample, and then a certain shape and size of the sample are prepared. Propellant mechanical property test specimens are prepared according to type B specimens in GJB770B-2005 method 413.1, "maximum tensile strength, breaking strength, maximum elongation, and breaking elongation unidirectional tension method," and the accelerated storage test specimens are a 120 mm × 120 mm × 10 mm sheet sample. Propellant adhesive test pieces were prepared in proportion with PEG, N100, and mixed nitrate.

The DU288 oil bath oven of Shanghai Experimental Instrument Factory Co., Ltd., was used to carry out the accelerated storage test, and the oven temperature uniformity was  $\leq 2^\circ\text{C}$ . The Instron 5567 tensile machine made in the United States was used to test the maximum tensile strength  $\sigma_m$  and maximum elongation  $\varepsilon_m$  of the propellant in different aging processes at  $25^\circ\text{C}$ . The test method follows GJB770B-2005 method 413.1, and the stretching rate is 100 mm/min. The thermoelectric company Nicolet 6700 Fourier-transform infrared spectrometer was used to analyze the functional group changes during the storage of the adhesive system. The DSC204F1 differential thermal scanning calorimeter of the German NETZSH company was used to analyze the thermal decomposition performance of the sample, and the heating rate was  $5^\circ\text{C}/\text{min}$ ,  $10^\circ\text{C}/\text{min}$ ,  $15^\circ\text{C}/\text{min}$ , and  $20^\circ\text{C}/\text{min}$ . The Mettler Toledo XP404S weighing balance was used to test the weightlessness of samples during the aging process. The FGD2-B-NO<sub>x</sub> nitrogen oxide analyzer was used to test the NO<sub>x</sub> gas released from the sample, and the FGD2-B-CO2 carbon dioxide detector was used to test CO2 gas.

## 3. Results and Discussion

**3.1. Mechanical Properties of the NEPE Propellant during Accelerated Storage.** NEPE propellant accelerates aging at  $55^\circ\text{C}$ ,  $60^\circ\text{C}$ ,  $65^\circ\text{C}$ , and  $70^\circ\text{C}$ , and the changes in the maximum tensile strength  $\sigma_m$  and the maximum elongation  $\varepsilon_m$  with the aging time during accelerated storage are tracked and measured, which are shown in Figure 1. Figure 2 shows the change of the stabilizer content in the propellant with aging time.

As shown in Figure 1, in the process of thermally accelerated aging at different temperatures, the maximum tensile strength value fluctuates within a small range in the initial stage of aging and decreases rapidly in the later stage. And as the aging temperature increased, the time for the maximum tensile strength value to decrease shortened. Figure 2 shows that stabilizers are continuously consumed as the aging time increases. Comparing the maximum tensile strength and the stabilizer content change chart, it can be seen that the maximum tensile strength fluctuates within a small range before the stabilizer is completely consumed, but the maximum tensile strength begins to reduce rapidly after

the stabilizer is consumed. It is speculated that the change law of the maximum tensile strength is related to the stabilizer content in the propellant. The initial stage is that the stabilizer is consumed by the nitrate decomposition products. In this stage, the stabilizer continuously reacts with nitrogen oxides decomposed by nitrate to form a nitroso product, which inhibits the decomposition of nitrate. When the stabilizer is consumed, nitrate decomposition products act on nitrate for the autocatalytic reaction, and the mechanical properties decrease rapidly.

At the initial stage, there is an obvious rising process of  $\varepsilon_m$ , which is mainly caused by the physical tensile action of constant strain. The reason may be that the polymer chain of the NEPE propellant binder matrix is degraded, and the chain scission effect is strengthened under the action of constant strain, which improves the elongation of the propellant. Under the action of constant strain, the polymer chains are unfolded from the collapsed state, the chains are oriented and rearranged, and the molecular chains are oriented more in the direction of the force, which increases the elongation of the propellant to a certain extent. In the later stage of aging, the influence of aging of the adhesive matrix and the dehumidification of the interface between the adhesive matrix and the solid filler is gradually significant. With the occurrence of the dehumidification phenomenon, the physical or chemical adsorption force between the dispersed phase and the continuous phase decreases, which weakens the stress transmission in the entire system and causes the maximum elongation of the propellant to decrease.

Based on the changes in the maximum tensile strength and the maximum elongation of NEPE propellants, it is shown that the failure of NEPE propellants is mainly strength failure.

Figure 3 is the state diagram of the NEPE propellant after accelerated storage. It indicated that the matrix structure became soft and bulging, and pores were present during the later accelerated storage period of the NEPE propellant. The appearance of pores indicates the emergence of gas inside the propellant. The polymer chain of the propellant will undergo a chain scission reaction. Under the condition of accelerated aging, the chemical reaction rate of chain scission will increase and be accompanied by gas precipitation. Then, the pores of the propellant matrix will appear.

**3.2. Weight Loss in the Process of Accelerated Storage.** The thermal weight loss during accelerated storage of the NEPE propellant and hydroxyl-terminated polybutadiene (HTPB) propellant is compared, which is shown in Figure 4.

NEPE propellant is aged by storing at  $70^\circ\text{C}$ , and its weight loss rate gradually increased with the extension of storage time and reached about 10% when stored for 140 days (3360 h), which has not yet reached the limit. It indicates that the NEPE propellant will undergo a significant decomposition reaction when stored at  $70^\circ\text{C}$ , but for the HTPB propellant, the value of weight loss is almost constant. For the thermal parameters for the NEPE propellant, the regularity between weight loss rate and storage time is great,

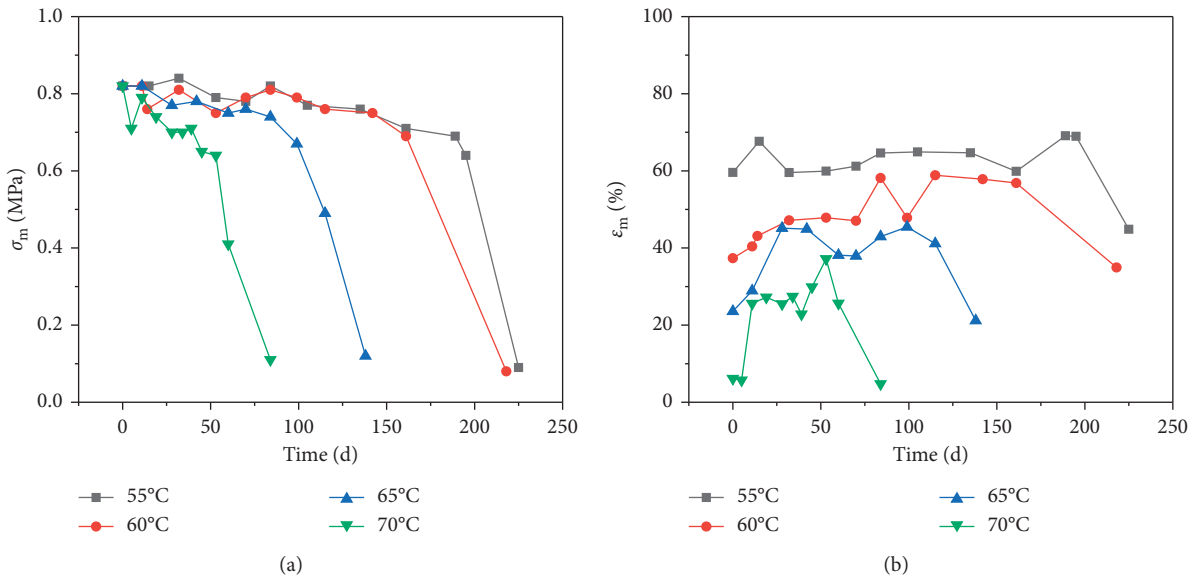


FIGURE 1: The change rule of  $\sigma_m$  and  $\epsilon_m$  of NEPE at different storage temperatures.

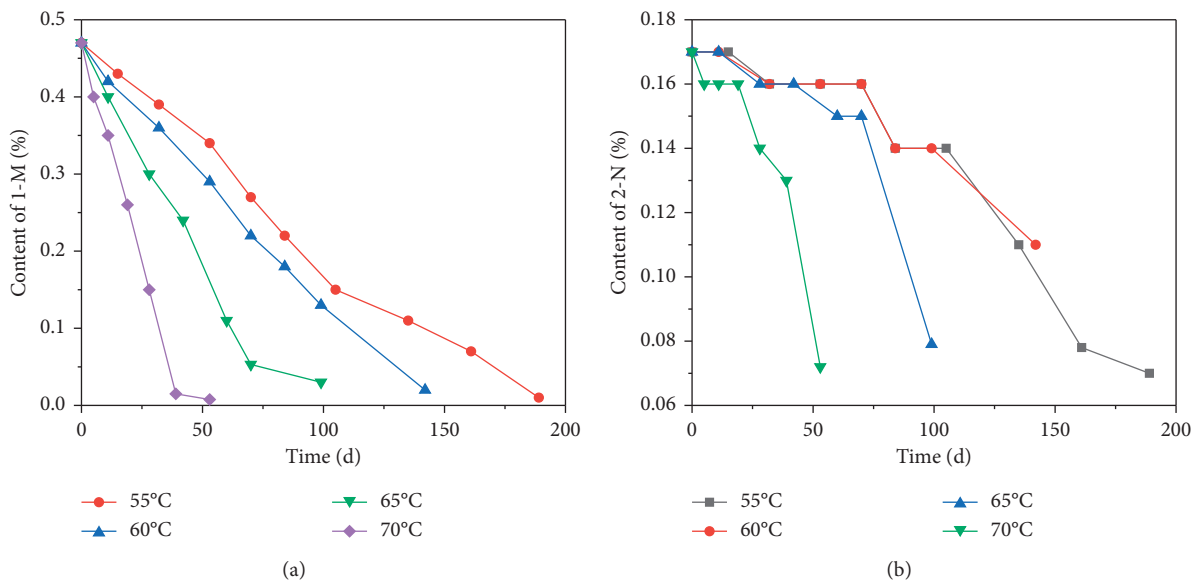


FIGURE 2: The content of the stabilizer at different storage temperatures.



FIGURE 3: The state diagram of NEPE after accelerated storage.

and the detection of the weight loss rate is easy to implement. Therefore, the weight loss rate can be used as a health monitoring index for similar propellants.

**3.3. Adhesive Network Structure Fracture Test.** Two groups of NEPE propellant adhesive samples were selected for the 80°C storage test. One group is PEG adhesive films. The other group is composed of PEG adhesive films and NEPE propellants. Figure 5 shows the PEG adhesive film before and after storage. Figure 6 exhibits the state of storage of the NEPE propellant with the PEG adhesive network structure before and after storage.

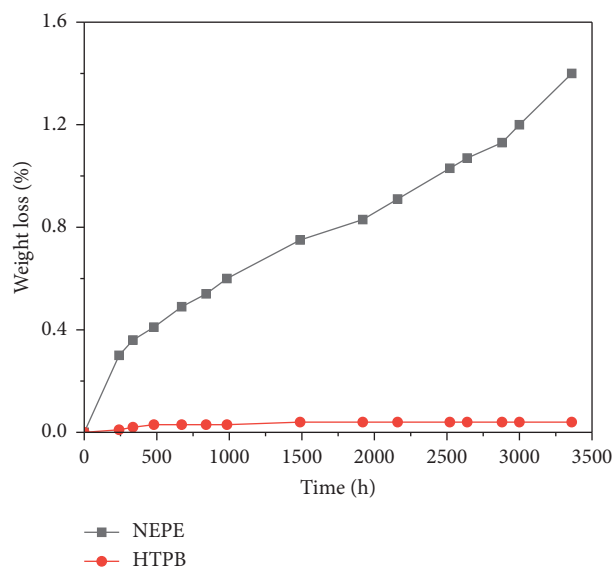


FIGURE 4: Comparison of the thermal weight loss of the NEPE propellant and hydroxyl-terminated polybutadiene propellant during accelerated storage at 70°C.



FIGURE 5: The images of the PEG adhesive film before (a) and after (b) storage.

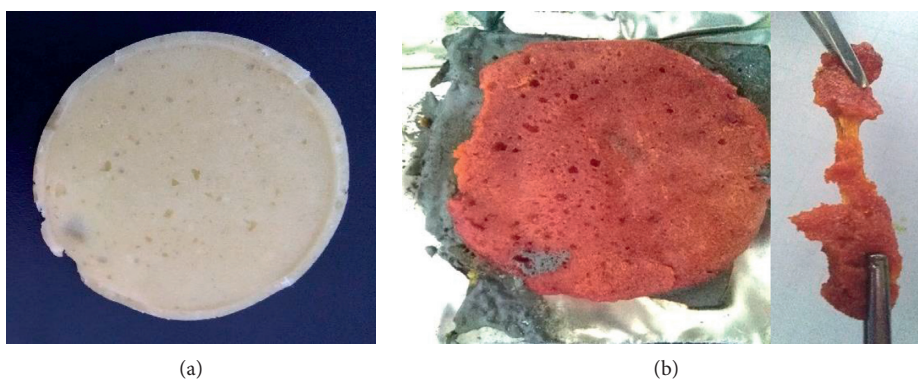


FIGURE 6: The images of storage of the NEPE propellant with the PEG adhesive network structure: before (a) and after (b).

TABLE 1: Gas release during accelerated aging of the NEPE propellant.

Time of storage (d)	50°C		Time of storage (d)	60°C		Time of storage (d)	70°C	
	Gas release			Gas release			Gas release	
	NO <sub>x</sub> (ppm)	CO <sub>2</sub> (%)		NO <sub>x</sub> (ppm)	CO <sub>2</sub> (%)		NO <sub>x</sub> (ppm)	CO <sub>2</sub> (%)
23	1.4	0.9	20	1.3	1.7	17	7.8	3.6
53	2.8	1.0	34	1.5	2.4	25	5.7	4.9
105	3.9	0.9	48	26	5.9	42	280	25.9
124	23	2.3	72	346	7.6	48	842	32
158	89	5.6	136	1508	15.7	52	1216	43
206	212	7.8	183	3860	23.7	62	5000	51

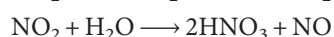
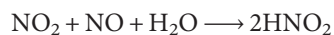
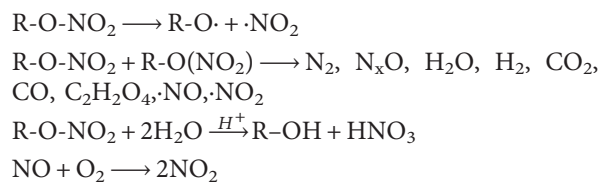
It can be seen from Figure 5 that matrix color turns yellow, and the structure has not changed after the single film is stored thermally. Figure 6 shows that the film and propellant are stored together for thermal storage, the PEG adhesive undergoes a significant degradation reaction, and the adhesive network structure is damaged. After degradation, the adhesive loses its original mechanical strength. The results indicate that the decomposition of components in the propellant leads to the degradation of the PEG network structure during the thermal storage of the NEPE propellant.

**3.4. Changes of NEPE Propellant Aging and Degradation Release Gas.** In the NEPE propellant accelerated storage experiment, the amount of gas in the sealed bag is regularly detected, and the result is shown in Table 1. Figure 7 exhibits the variation of NO<sub>x</sub> and CO<sub>2</sub> release with storage time at different temperatures.

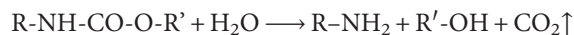
As shown in Figure 7, the gas release rate of the propellant is faster with a higher temperature. At 70°C, NO<sub>x</sub> and CO<sub>2</sub> released by the NEPE propellant increased exponentially and began to soften after around 60 days. The content is the maximum value to maintain the structural integrity of the propellant. At 60°C, the NEPE propellant did not soften after more than 180 days of storage. At this time, the amount of NO<sub>x</sub> released was 3860 ppm, and the amount of CO<sub>2</sub> released was 23.7%. The amount of gas released by the NEPE propellant slowly increased with the extension of storage time at 50°C. The NO<sub>x</sub> gas detected at 206 days was 212 ppm, and the amount of CO<sub>2</sub> was 7.8%.

**3.5. The Degradation Reaction of the NEPE Propellant.** NEPE propellant decomposition mainly includes nitrate decomposition and polyurethane decomposition. Combined with the above experiments, the decomposition reaction process of the NEPE propellant during accelerated storage can be speculated.

The nitrate decomposition reaction process is shown as follows:



The polyurethane adhesive of the NEPE propellant contains the ether group and urethane group and can react under the action of water:



The degradation of the NEPE propellant during storage is caused by the decomposition of nitrate. H<sub>2</sub>O and NO<sub>x</sub> radicals are generated during the decomposition of nitrate, and the free radicals promote the continued decomposition of nitrate. H<sub>2</sub>O is the main factor that promotes the decomposition of adhesive polyurethane, which leads to the chain breakage of the adhesive polymer and the damaged matrix structure of the propellant. When the decomposition reaction cannot be inhibited by the stabilizer, the decomposition reaction will continue to decompose to a certain degree, the polymer chain in the adhesive network structure is generally broken, and the propellant is transformed from a softened state into pulp. Figure 8 is the sketch of structural failure caused by aging and decomposition of the NEPE propellant.

The thermal decomposition of the nitrate plasticizer in NEPE will cause the decomposition of the adhesive network structure to cause chain breakage, resulting in damage to the matrix structure. It can be known from the decomposition process of propellants that NO<sub>x</sub> is mainly produced by the decomposition of nitrate, and CO<sub>2</sub> is produced by the decomposition of nitrate and binder. Therefore, NO<sub>x</sub> is used as a characteristic gas for the health characterization of propellants.

**3.6. Thermal Decomposition of NEPE Propellants.** TGA/DSC was used to characterize the thermal behavior of NEPE propellants at different heating rates. The results are shown in Figure 9. It demonstrates that the thermal decomposition of the propellant depends on the temperature-raising rate. As the heating rate increases, the temperature of the first decomposition peak increased, and the second decomposition peak showed almost inconspicuous change. The first decomposition peak of the propellant on DSC is a severe exothermic peak, which is the decomposition of some plasticizers (such as NG and BTTN) with HMX participation. The TG curve shows that the weight loss rates under different heating rates are about 16%, 23%, 28%, and 32% in

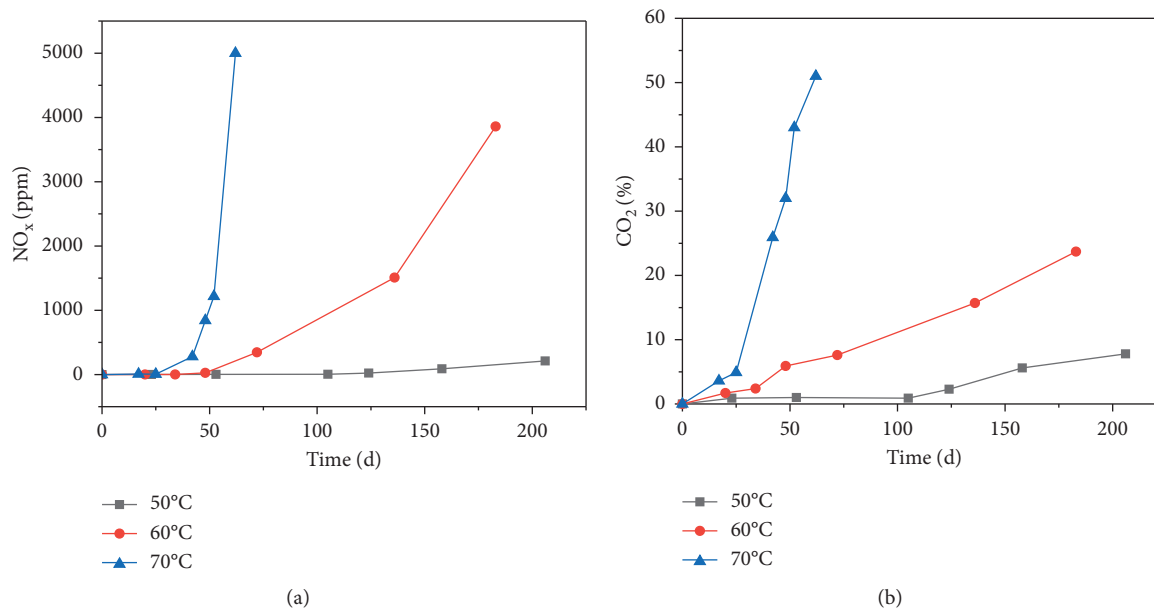


FIGURE 7: Variation of NO<sub>x</sub> and CO<sub>2</sub> release with storage time at different temperatures.



FIGURE 8: The sketch of structural failure caused by aging and decomposition of NEPE.

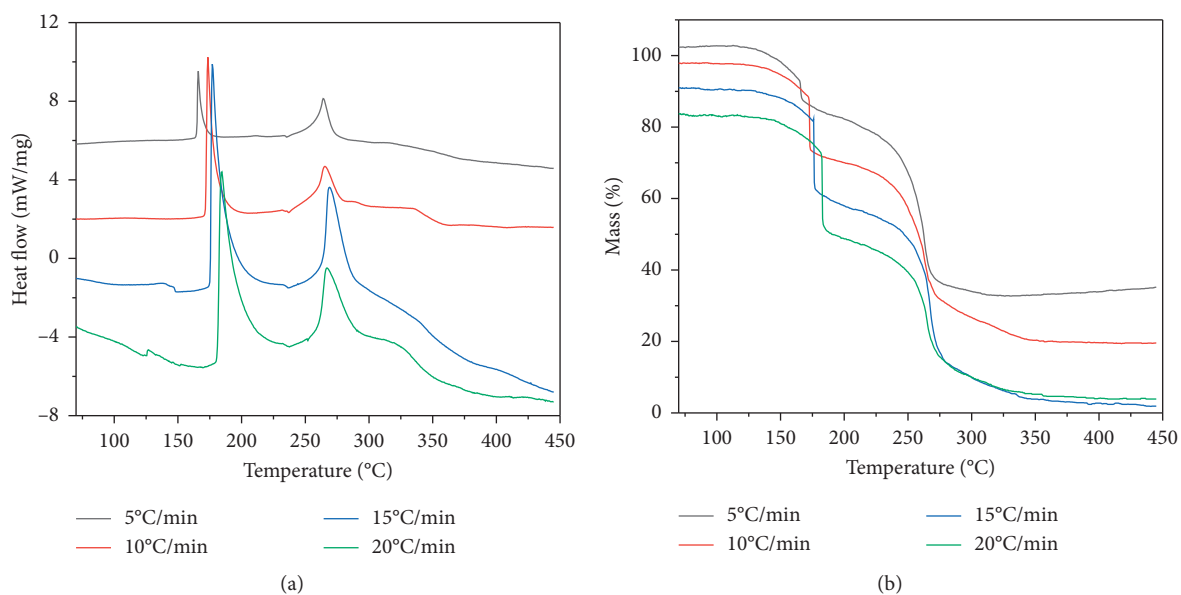


FIGURE 9: DSC and TG curves of NEPE at different heating rates

the first stage of decomposition. This illustrates that the thermal decomposition of mixed nitrate is affected by the heating rate. The endothermic peak at 237.9°C is the crystal transformation peak of AP. The second exothermic peak is mainly the decomposition of the binder, and the weight loss rates under different heating rates are about 42%. Therefore, the decomposition of the binder and heating rate are irrelevant.

#### 4. Conclusion

In this work, the mechanical properties, changes in the components, weight loss, adhesive network structure fracture test, degradation reaction, and thermal decomposition of NEPE were researched in the process of accelerated storage. At different storage temperatures, as the storage time prolongs, the maximum tensile strength, maximum elongation, stabilizer content, mixed nitrate content, weight loss rate, and other parameters all show great variation rules, which can be used as propellant storage health monitoring indicators. The decomposition of the components in the propellant leads to the degradation of the PEG network structure. The thermal decomposition of the nitrate plasticizer in NEPE propellants will cause the decomposition of the adhesive network structure, which leads to chain breakage, resulting in damage to the matrix structure. The degradation of the NEPE propellant is caused by the decomposition of nitrate, and  $\text{NO}_x$  is mainly produced by the decomposition of nitrate.  $\text{NO}_x$  can be used as a characteristic gas for the health characterization of the propellant.

#### Data Availability

The data used to support the findings of this study are included within the article.

#### Conflicts of Interest

The authors declare that they have no conflicts of interest.

#### References

- [1] Y. Xing and K. Dong, "Development and prospect of research on life prediction of solid rocket motors," *Journal of Solid Rocket Technology*, vol. 24, no. 3, pp. 30–33, 2001.
- [2] K. M. Ide, S.-Y. Ho, and D. R. G. Williams, "Fracture behaviour of accelerated aged solid rocket propellants," *Journal of Materials Science*, vol. 34, no. 17, pp. 4209–4218, 1999.
- [3] H. Xie, W. Zhou, and X. Wu, "Research progress on life prediction methods of solid rocket motors," *Journal of Solid Rocket Technology*, vol. 42, no. 3, pp. 377–395, 2019.
- [4] D. Zhou, X. Liu, and P. Zhang, "Study on probability storage life prediction of solid rocket motor grain under constant strain," *Journal of Propulsion Technology*, vol. 40, no. 9, pp. 2121–2129, 2019.
- [5] X. Xu, Y. Ding, and T. Li, "Research progress of storage life estimation technology of solid rocket motor propellant," *Journal of Ordnance Equipment Engineering*, vol. 40, no. 04, pp. 137–140, 2019.
- [6] Y. M. Milekhin, A. A. Koptelov, N. I. Shishov, I. A. Koptelov, and A. A. Rogozina, "Evaporation of plasticizer from NEPE type propellant," *Russian Journal of Applied Chemistry*, vol. 91, no. 5, pp. 802–812, 2018.
- [7] W. Xie, Z. Yu, Z. Wei et al., "Sensitivity and stability improvements of NEPE propellants by inclusion of FOX-7," *Propellants Explosives Pyrotechnics*, vol. 43, no. 3, 2018.
- [8] Y. Sun, H. Ren, and Q. Jiao, "Comparison of thermal behaviors and decomposition kinetics of NEPE propellant before and after storage," *Journal of Thermal Analysis and Calorimetry*, vol. 131, no. 4, pp. 1–11, 2017.
- [9] H. Zhang, S. Peng, A. Pang et al., "Coupling aging behaviors and mechanism between mechanical properties and chemical stability of NEPE propellant," *Journal of Propulsion Technology*, vol. 28, no. 3, pp. 327–332, 2007.
- [10] K. Dong, L. Pei, and L. Kong, "Aging performance of NEPE propellant under constant strain," *Journal of Solid Rocket Technology*, vol. 42, no. 3, pp. 403–408, 2019.
- [11] A. Jing, L. Ding, and Y. Liang, "Aging performance of NEPE propellant under temperature and pressure loading," *Chinese Journal of Explosives & Propellants*, vol. 42, no. 4, pp. 375–379, 2019.

## Research Article

# Aggregation of Nanochemical Microcrystals in Urine Promotes the Formation of Urinary Calculi

Yanting Lou <sup>1</sup>, Wei He,<sup>1</sup> and Zhengyao Song<sup>2</sup>

<sup>1</sup>Department of Urology, Chaohu Hospital Affiliated to Anhui Medical University, Chaohu 238000, Anhui, China

<sup>2</sup>Department of Urology, First Affiliated Hospital of Anhui Medical University, Hefei 230022, Anhui, China

Correspondence should be addressed to Yanting Lou; [huliangliang@ahmu.edu.cn](mailto:huliangliang@ahmu.edu.cn)

Received 6 August 2020; Revised 9 September 2020; Accepted 16 September 2020; Published 5 October 2020

Academic Editor: Tifeng Jiao

Copyright © 2020 Yanting Lou et al. This is an open access article distributed under the Creative Commons Attribution License, which permits unrestricted use, distribution, and reproduction in any medium, provided the original work is properly cited.

With the increasing incidence and recurrence rate of urinary calculi, urinary calculi have become a serious health risk, and the research on urinary calculi has become the focus of public attention. At present, the research results on the formation mechanism of urinary calculi are not ideal, and there is no unified conclusion. In order to further study the influencing factors of the formation of urinary calculi and provide new ideas for the prevention and clinical treatment of urinary calculi, the influence of agglomeration of nanochemical microcrystals in urine on urinary calculi was studied in this paper. In this study, fresh morning urine was collected from 10 urological stone patients and 10 healthy controls without urological stone in the urology department of a hospital. After processing the experimental specimens, we first use flame atomic absorption spectrometry and alcian blue colorimetric method to detect the content of  $\text{Ca}^{2+}$  and citrate in the urine and then use the nanoparticle size analyzer to detect the microcrystals in the urine. Diameter, distribution, degree of aggregation and potential, and finally HRTEM observation to observe the morphology, chemical composition, and element composition of the nanocrystals. The results showed that the content of  $\text{Ca}^{2+}$  and lemon hydrochloric acid in the urine of the experimental group was lower than that of the control group. The particle size of the nanocrystals increased with the increase in the pore size of the membrane. The average particle size of the experimental group increased gradually from  $163 \pm 31$  nm to  $3219 \pm 863$  nm, while the average particle size of the control group increased from  $183 \pm 65$  nm to  $997 \pm 522$  nm. The mean value of the potential decreased with the increase in the pore size of the filter membrane. The change amplitude of the experimental group was 6.57 mV, while the change amplitude of the control group was only 1.75 mV. In the composition of nanocrystals, element O accounts for the most, accounting for 42.54% of all elements. This indicates that the aggregation of nanocrystals in urine will lead to the rapid increase in the size of nanocrystals, which will eventually lead to the formation of stones.

## 1. Introduction

**1.1. Background Significance.** With the improvement of people's living standard, the economic income and diet structure have changed. The increase in protein and fat intake leads to the gradual decline of people's body function, and the incidence and recurrence rate of urinary calculi gradually increase, becoming one of the common diseases of urology worldwide [1]. Patients with urinary calculi will have severe pain, hematuria, urinary tract infection, renal injury, and other symptoms, which will bring a great impact on the normal life of patients [2]. At present, the research results on the formation mechanism of this disease are few and not

conclusive. Therefore, further research on the formation factors of urinary calculi is of great significance for the prevention and treatment of urinary calculi.

**1.2. Related Work.** Urinary calculi, as a disease with a high incidence and recurrence rate, have become the focus of medical research, and many researchers at home and abroad have investigated it. Habashy et al. studied whether the component analysis of urinary calculi determined by DECT scanning would lead to changes in patient management, performed DECT-KUB examination on all patients with renal colic symptoms who did not receive DECT

scanning, and reviewed the DECT data of all patients from September 2013 to July 2015 [3]. Their data, though extensive, are laborious to work with. Turk et al. summarise the latest recommendations of the Urological Guidelines Group of the European Urological Association for the interventional treatment of ureters and kidney stones [4]. Sewell et al. introduced the evidence-based guidelines from diagnosis to conservative surgical treatment and prevention of urinary calculi [5]. Both of their studies are limited to theoretical analysis and do not carry out corresponding experiments. Gkentzis A analyzed the pathogenesis and treatment of urolithiasis combined with inflammatory bowel disease (IBD) and the relevant literature after bariatric surgery. PubMed was used for systematic literature retrieval and other references to evaluate the correlation between IBD bariatric surgery and renal calculi in children and adults [6]. Some of the references they analyzed were old enough to be of little significance for the present situation.

*1.3. Innovative Points in This Paper.* In order to study the relationship between the agglomeration of nano-chemical microcrystals in urine and the formation of urinary calculi, and to provide new ideas for the prevention and treatment of urinary calculi, this study was conducted on fresh morning urine from urinary calculi patients and healthy controls in the urology department of a hospital. For collection and processing, the experimental group ( $n = 10$ ) is the urine of patients with urinary calculi, and the control group ( $n = 10$ ) is the urine of the healthy control group. By detecting the contents of citrate and  $\text{Ca}^{2+}$  in urine, the particle size, distribution, aggregation degree, and  $\xi$  potential of the nanocrystals, as well as the morphology, chemical composition, and elemental composition of the nanocrystals, the conclusion was finally reached that the agglomeration of the nanocrystals in urine promoted the increase in the particle size of the nanocrystals, which eventually led to the formation of stones.

## 2. Nanocrystallite Agglomeration and Urinary Calculi

### 2.1. Urological Stone Formation

*2.1.1. Formation Mechanism of Urinary Calculi.* The supersaturated crystallization theory believes that the stone-forming components in the urine are saturated enough and precipitated to form crystal nuclei, which grow into small particles with higher free energy through solute transport and surface action. After agglomeration under some physical and chemical forces, they are collected in the collecting tube or stay in the urinary tract, and may continue to grow and accumulate, eventually forming urinary stones [7]. Among them, supersaturation is the chemical driving force for the formation of urinary calculi because it is a necessary condition for the formation of crystal nucleus. The retention of crystals is another important cause of stone formation. When crystals remain in the urinary tract, they will grow and

accumulate, leading to stones. However, in fact, the crystal components in the urine of normal people are often in a supersaturated state, but not everyone can form urinary stones, because the supersaturated crystal theory ignores the organic molecules and other molecules in the urine and only focuses on the role of inorganic salts.

According to the Randall plaque theory, calculi originated from the calcium salt deposition at the renal papillary area, and Randall plaque originated from the basement membrane of the fine segment of Henle's capillary, and gradually developed from the stroma to the urinary epithelium. When plaque broke through the urinary epithelium and was exposed to urine, it became the origin of urinary calculi [8, 9]. Moreover, the collagen bundles between the renal papilla and the basement membrane can promote the adsorption and deposition of inorganic salts. The Randall plaque theory cannot fully explain the formation of urinary calculi, but it is of great significance for the study of the formation of urinary calculi.

The theory of inhibitor deficiency holds that there is a certain amount of substances in urine that can inhibit crystallization nucleation or growth aggregation, which can inhibit the formation of urinary calculi, and the lack of such substances may lead to calculi. Many substances have been found to inhibit the formation of stones, such as citric acid, renocalcin, ribonucleic acid, Tamm-Horsfall protein, and glucan [10]. They can be combined with crystal growth points, block crystallization nucleation, growth, and aggregation and can also be combined with some stone components in urine to form chelates to reduce saturation. At present, potassium citrate and orthophosphate and other drugs have been used clinically to treat or prevent urinary calculi [11].

The stroma theory believes that stroma is an activator to promote the formation of urinary calculi. It can combine with apatite to form small particles, which can induce the nucleation of calculi components in the supersaturated urine and provide a template for calculi growth. Acidic mucosaccharides, carbohydrates, and proteins are the main components of the matrix, and the weight of the matrix can account for about 5% in stones [12].

*2.1.2. Etiology of Urinary Calculi.* Obesity is an important factor affecting urinary calculi. Obese people consume more energy and have a lower PH value in urine, thus reducing the excretion of citric acid and increasing the excretion of oxalic acid [13]. In addition, the unbalanced diet of obese people will make them consume too much meat and fat food and lack dietary fiber, which is more likely to lead to the formation of urinary stones.

Diabetes can increase the risk of urinary stones. Compared with the general population, diabetic patients have a lower pH value of urine and a higher solubility of urinary calcium. Glucose and uric acid in urine will play a competitive role in reabsorption [14]. The increased excretion of oxalate and uric acid leads to the formation of calculi, which is also the reason why diabetic patients are prone to oxalate calculi and urate calculi.

Hyperlipidemia was positively associated with the formation and recurrence of urinary calculi. High lipid and protein diets promote the increase in lipid in renal tubules, weaken the function of sodium-hydrogen ion exchangers, and acidify urine, leading to the formation of calculi. Moreover, hyperlipidemia will cause inflammation. When inflammatory mediators gather in the kidney, renal mucosa will be easily damaged, creating conditions for the formation of stones.

Abnormal metabolism is closely related to the formation of urinary calculi, including abnormal oxalic acid metabolism, abnormal purine metabolism, abnormal citrate metabolism, abnormal cystinuria, and abnormal calcium metabolism, which will increase the risk of urinary calculi.

*2.1.3. Diagnosis and Treatment of Urinary Calculi.* In addition to clinical diagnosis and laboratory examination, the final diagnosis of urinary calculi requires imaging examination. The main examination methods include ultrasound, X-ray, CT, and intravenous urography (IVU). Among them, the most widely used examination means are ultrasound image and X-ray plain film. Most of the stones with a particle size greater than 0.2 cm can be found by ultrasound image, and whether the urinary tract at the proximal end of the stones is dilated can be observed [15]. X-ray plain film can visually observe the size, location, number, and shape of calculi, but there are some limitations in the examination of uric acid calculi, with low sensitivity. After IVU was injected intravenously with contrast agent, the development of contrast agent in the urinary tract was used for dynamic X-ray radiograph observation, which could not only observe the stones but also understand the relevant conditions of the kidney. CT can find small stones, is easy to operate quickly, and has good sensitivity and specificity.

The treatment of urinary calculi is divided into two categories: conservative treatment and surgical treatment.

Conservative treatment uses drugs for stone expulsion, which must meet the following requirements: diameter less than 6 mm or so, smooth surface, local residence time less than two weeks, and no obvious obstruction in the lower ureter [16]. Although some minimally invasive stone therapies can be effective in treating small and small stones, these techniques are risky and expensive. Patients without infection can choose to observe and wait appropriately and take oral medication to control pain, but this is closely related to pain tolerance and uncertainty and the potential risk of renal dysfunction. When using drugs to remove stones, attention should be paid to maintain adequate amount of water and appropriate activities every day, which can help to remove stones. At present, the commonly used drugs for the treatment of urolithiasis include nonsteroidal anti-inflammatory drugs, opioid analgesics, calcium ion blockers, and spasmolytic drugs.

Surgical treatment included extracorporeal shock wave therapy, ureteroscopic lithotripsy, percutaneous nephrolithotripsy, open surgery, and laparoscopic surgery. Extracorporeal shock wave therapy uses the high-energy shock wave generated by the lithotripter to break the calculi in the

body. However, in order to avoid the damage to the kidney caused by the shock wave, the frequency of each operation shock wave is not more than 5 times, and the interval of each operation is at least half a month. Ureteroscopic lithotripsy was performed to treat retrograde calculus through ureteroscopy or ureteral soft view, and calculus was shattered with holmium laser. Percutaneous nephrolithotripsy uses puncture technology to reveal the establishment of percutaneous renal channels and uses pneumatic trajectory and ultrasound to break stones. However, the selection of puncture sites is not easy and often leads to complications such as bleeding and infection. Open surgery mainly involves the lithotomy of kidney, ureter, and bladder, and its application has been significantly reduced.

## *2.2. Growth Agglomeration Theory of Chemical Nanocrystals*

*2.2.1. Crystal Growth Theory.* Crystal growth is not the combination of small particles but the result of crystal interface movement. The velocity of interfacial movement is related to the concentration difference between the surface layer and the inner layer, the curvature of the interfacial layer, and the temperature of the system. The higher the temperature is, the smaller the curvature radius is, and the faster the crystal interface moves to the center of curvature. Whether the pores move with or against the crystal interface is related to the curvature of the crystal interface and the diameter, number, diffusion rate, and gas pressure of the pores [17]. Another reason for limiting crystal growth is the presence of a small amount of liquid at the grain boundary. Due to a small amount of liquid phase, two new solid-liquid interfaces are formed at the grain boundary. The advancing force of interface movement decreases, and the diffusion distance becomes longer. Therefore, a small amount of liquid phase may inhibit crystal growth.

According to the traditional crystallization theory, there is a nearly static layer on the side near the solid, which is similar to the effect of a liquid film. This layer of liquid film can increase the solute diffusion resistance, and the size of the resistance is related to the thickness of the liquid film, temperature, and other factors.

The crystal interface has the effect of interfacial energy, and the grains will form a 3D array. If the surface tension of the crystal interface is the same, the grains will show a regular hexagon [18]. If the second kind of inclusions at the crystalline interface cannot be thought of as liquid phase at the sintering temperature, they will love the movement of the crystalline interface.

*2.2.2. Surface Dynamics of Nanocrystalline Growth.* The main reason for the growth of nanocrystals is the presence of the mixture film, which consists of solvent and water. In the process of growing nanocrystals, liquid film exists in the solid-gas system, while in the general process of crystal growth, liquid film exists in the solid-liquid system [19]. Due to the presence of solvents in the liquid film, the concentration difference on both sides of the solid and liquid film will occur, which is the main driving force for the growth of

nanocrystals. When the temperature increases, the thickness of liquid film increases and the viscosity decreases, and the growth of nanocrystals will be accelerated.

On the basis of diffusion theory, the formula for calculating the surface chemical kinetics of microcrystalline growth is shown:

$$D = \frac{M\delta N(Q_1 - Q_2)}{\eta}, \quad (1)$$

where  $M$  is the specific surface area,  $\delta$  is the thickness of the liquid film,  $N$  is the temperature,  $Q_1$  and  $Q_2$  are the concentrations of the liquid film on both sides of the gas phase and the liquid phase, respectively, and  $\eta$  is the viscosity of the liquid film.

At constant temperature and constant pressure, a certain volume of crystal forms an equilibrium shape, at which time the crystal surface energy is minimum. The equilibrium morphology is determined by the normal growth rate of each crystal, and the normal growth rate is proportional to the specific surface freedom. If the specific surface of the mirror changes freely, the equilibrium form will also change accordingly.

**2.2.3. Nanocrystalline Agglomeration Mechanism.** The kinetic reason for agglomeration is that, under a certain environment, crystal particles are affected by gravity and the interaction force. However, when the interaction force is greater than gravity, the particles are constrained by gravity to a lower degree, resulting in the occurrence of microcrystal agglomeration [20]. The main interactions between microcrystalline particles include van der Waals force and Coulomb force.

The criterion of microcrystalline agglomeration is the ratio of the force causing agglomeration to gravity, and its expression formula is shown:

$$P = \frac{D}{mg}, \quad (2)$$

where  $D$  is the sum of all forces causing agglomeration of microcrystals and  $mg$  is the gravity.

In addition to the influence of force, the morphology of microcrystal also affects the agglomeration of microcrystals to a certain extent. The morphology of microcrystalline is closely related to the surface energy, and the stable morphology of microcrystalline must have the minimum surface energy. Therefore, the growth of microcrystalline agglomerations, the decrease in specific surface area, and the tendency of particle surface energy to the minimum are all spontaneous thermodynamic processes. The basic way to solve micrite accumulation is to reduce the surface free energy of each crystal surface.

**2.3. Methods of Urine Detection.** Urine detection includes the detection of physical properties, chemical composition, and microparticles, and the detection of microparticles in urine is required in the detection of urinary calculi. The detection methods of microparticle spatial distribution in urine

include flow cytometry, microimage morphological analysis, and spatial dynamic coordinate tracking detection.

**2.3.1. Flow Cytometry.** Flow cytometry first requires fluorescent pigment staining of the tested specimens, and then, it is put into the sample tube to make it enter the flow chamber under the action of gas pressure. The flow chamber is full of hydrosheath, which can restrain the cells into a single row and form a cell column when it is ejected from the nozzle [21]. The fluorescence of the cells can be detected by the instrument to obtain relevant information. Through the calculation and analysis of the information, the size, length, volume, and chromatin length of the cells can be determined. Finally, according to the morphological characteristics of the cells, the scattering diagram and related reports of urine microparticles can be formed.

Flow cytometry is generally used in blood testing. The optical system in the device can provide fluorescence, light scattering, light absorption, and other signals, while the computer system can provide signal acquisition, storage, display, and analysis services, which can be used for rapid and automatic detection and statistical analysis of various indicators [22].

However, this method cannot detect all the microscopic particles, and when the urine samples contain luciferin or larger particulate pollutants, the reliability will be reduced and the diversion tube will be blocked. If the concentration of urine sample is too high, it will affect the results of the next sample, and this test cannot obtain a complete microscopic image of urine nor can it correct the results. The detection does not have traceability nor can it completely avoid the situation of less inspection and even wrong inspection.

**2.3.2. Morphological Analysis of Microscopic Images.** Morphological analysis of microscopic image obtains digital image of microscopic particles of urine by imaging equipment, and the results are obtained after processing and analyzing the digital image. The urine microparticle image detection method is an intuitive observation method. Before the image is obtained in the imaging system, the samples can be centrifuged at a certain speed and time, and the samples separated by centrifugation can be transferred to the cargo platform of the electron microscope [23]. Based on the microscopic particle images obtained by the imaging system, the next operation is carried out.

With the development of the automatic urine microparticle analysis system, the image-based urine microparticle analysis device has gradually developed from single functions such as image acquisition, patient information management, and examination report generation to automatic sampling collection and automatic focusing, image processing, particle recognition, counting, and reporting functions are integrated multifunctional detection and analysis system.

Morphological analysis of microscopic images has the advantages of traceability, visualization, meeting the gold standard of microscopy, drawing lessons from doctors'

experience, and reporting particle openness, but it is an important technology that needs to improve detection methods and technical means [24], for example, effective detection methods, high-quality image acquisition methods, subsequent image processing, segmentation, pattern recognition, algorithm effectiveness, and accuracy.

At present, most of the equipment detection system and detection item report are based on the statistical principle and normal distribution principle. Compared with the blood test, the urine test has certain specificity because of its complex granules and short specimen time.

**2.3.3. Spatial Dynamic Coordinate Tracking Detection Method.** At present, the general detection method requires the natural sedimentation of urine. All the urine microscopic particles are deposited at the bottom of the counting tank within a limited time. The microscopic particles in the detection tank can be photographed by the mobile platform and then analyzed [25]. This method is simple and convenient, but it has its drawbacks. For example, the settlement effect is not ideal, and all the microscopic particles cannot be guaranteed to settle to the bottom; the settlement time is long, and the sufficient settlement cannot be achieved within a short time and cannot avoid missing or less inspection.

Therefore, the spatial dynamic coordinate tracking and monitoring method of surface settlement or short-time settlement can be adopted. Therefore, the spatial dynamic coordinate tracking monitoring method of surface settlement or short-term settlement can be used for analysis. When the microscopic particles are not sufficiently settled, the focal plane needs to be focused on multiple levels from top to bottom, and the spatially distributed microscopic particles are decomposed into multilayer planes, and the visible area of the microscope is used for observation to ensure that the suspension can be detected. All the microscopic particles in the upper part of the detection tank can avoid missed and under-detected situations and improve the detection speed.

### 3. Experiments on Detection of Nanochemical Microcrystals in Urinary Calculi

#### 3.1. Research Objects and Materials

**3.1.1. Research Objects.** Ten patients with urinary calculi and ten healthy controls without urinary calculi in the urology department of a hospital were the subjects of this study. Patients with calculi were in the experimental group ( $n = 10$ ), and healthy controls were in the control group ( $n = 10$ ). Their fresh morning urine was collected as experimental specimens. Among them, there were 12 males and 8 females, ranging from 30 to 60 years old. Among them, the largest number was 41–50-year-old, followed by 51–60-year-old, and the least number was under 40-year-old. After the test,  $P > 0.05$  was found, and there was no difference in age distribution between the patients and the control group of different genders, as shown in Table 1.

TABLE 1: General information of experimental subjects.

Age range	Man	Woman	Total
30–40	3	1	4
41–50	6	3	9
51–60	3	4	7
Total	12	8	20

Note.  $X^2 = 0.581$ ;  $P = 0.613$ .

**3.1.2. Reagents and Instruments.** Conventional chemical reagents were analytically pure, and all glassware was cleaned with secondary distilled water.

The instruments include XL-30 environmental scanning electron microscope, Zetasizer Nano-ZS nanometer, X-ray powder diffraction, and KQ3200 DE ultrasonic instrument.

**3.2. Collection and Treatment of Urine.** Fasting morning urine was collected from 10 patients with urinary calculi and 10 healthy controls. In order to avoid the influence of tissue fragments and other macromolecular particles in urine on the detection results, 40 ml urine samples were collected from the control group and the experimental group, and 20 ml ethanol was added. After stirring for 3 min, the urine samples were placed for 30 min to remove the proteins. Stir in 15 ml of secondary distilled water dilution, with 0.23, 0.5, 1.5, 3.5, and 10 reserve  $\mu\text{m}$  aperture of organic membrane filtration.

**3.3. Determination of Citrate and  $\text{Ca}^{2+}$  in Urine.** The content of  $\text{Ca}^{2+}$  in the urine of 10 stone patients and 10 healthy controls was determined by flame atomic absorption spectrometry. The instrument radiates light with  $\text{Ca}^{2+}$  element characteristic spectral line from the light source, which is absorbed by  $\text{Ca}^{2+}$  ground state atoms in the urine sample when passing through the vapor, and the content of  $\text{Ca}^{2+}$  in the urine sample is determined by the degree to which the radiation characteristic spectral line light is weakened.

The citrate content in urine was determined by Alcian blue colorimetry in 10 patients with calculi and 10 healthy controls. Two sets of spare urine samples were placed in test tubes with borax solution with a concentration of 6% and a pH of 0.025 mol/LpH of 9.0 as electrode buffer. The voltage was adjusted to 100 V, the current was about 3 mA, the electrophoresis lasted for 4.5 hours, and the staining was performed after the electrophoresis. The polyacrylamide gel was fixed in the base solution for 1 hour, oxidized in the oxidation solution for 1.5 hours, reduced for 0.5 hours, soaked in Alcian blue staining solution for more than 2 hours, and finally placed in the base solution until the background was colorless, and then, the citrate content could be detected.

#### 3.4. Nanocrystalline Detection

**3.4.1. Nanometer Detection.** After the two groups of filtered urine were treated with ultrasonic instrument for 5 min,

the possible agglomeration of urine microcrystals was destroyed and detected by nanometer size analyzer, respectively. The particle size, distribution, aggregation degree, and potential of urine microcrystals could be obtained. The detection time immediately after ultrasound was recorded as 0 h, and the detection time was once every 1 hour, and the detection time was consecutively 3 times.

**3.4.2. HRTEM Observation of Urine Microcrystals.** After ultrasonic treatment for 3 min, the spare urine was dropped on the surface of the copper mesh. After vacuum drying, it was tested for 2 days to observe the morphology, chemical composition, and element composition of the nanocrystals.

## 4. Discussion on Relationship between Agglomeration of Nanochemical Microcrystals and Urinary Calculi

**4.1. Levels of  $\text{Ca}^{2+}$  and Citrate in Urine.** Urine  $\text{Ca}^{2+}$  and citrate concentrations were measured in 10 stone patients and 10 healthy controls, and the results are shown in Table 2.

As shown in Table 2, the content of  $\text{Ca}^{2+}$  and citrate in urine of patients with calculus in the experimental group was significantly different from that of healthy controls ( $P < 0.05$ ). The amount of  $\text{Ca}^{2+}$  in the urine of the experimental group was lower than that of the control group, but the error value was large. The content of lemon hydrochloric acid in the urine of the control group was higher than that of the experimental group.

### 4.2. Nanocrystalline Detection

**4.2.1. Particle Size Comparison.** The urine samples of the control group and the experimental group were filtered by organic membranes with different pore sizes of 0.23, 0.5, 1.5, 3.5, and 10  $\mu\text{m}$ , and then tested with a nanoparticle size analyzer. The average particle size of the nanocrystals in the urine is as follows.

As shown in Figure 1, as the pore size of the organic film keeps increasing, the average particle size of the two groups of urine nanocrystals also keeps increasing. The average diameter of urine nanocrystals in 10 patients with calculi gradually increased from  $163 \pm 31$  nm to  $3219 \pm 863$  nm. In healthy controls, the mean diameter of urine nanocrystal increased from  $183 \pm 65$  nm to  $997 \pm 522$  nm. This indicates that although the particle size of the nanocrystalline increases with the increase in the pore size of the organic film, it is smaller than the corresponding pore size. In addition, the particle size of the nanocrystals in the control group was larger than that in the experimental group at the beginning, but with the increase in pore size, the particle size of the control group was significantly smaller than that of the experimental group.

**4.2.2. Distribution and Agglomeration.** The distribution and aggregation degree of urine nanocrystals in the experimental group and the control group could be obtained after

TABLE 2: Contents of  $\text{Ca}^{2+}$  and citrate in urine of the two groups.

Group	$\text{Ca}^{2+}/(\text{mmol} \cdot \text{L}^{-1})$	Citrate/ $(\text{mg} \cdot \text{L}^{-1})$
Experimental group	$2.14 \pm 0.83$	$152 \pm 77.5$
Control group	$2.59 \pm 0.21$	$226 \pm 113.6$
$P$	$<0.05$	$<0.05$

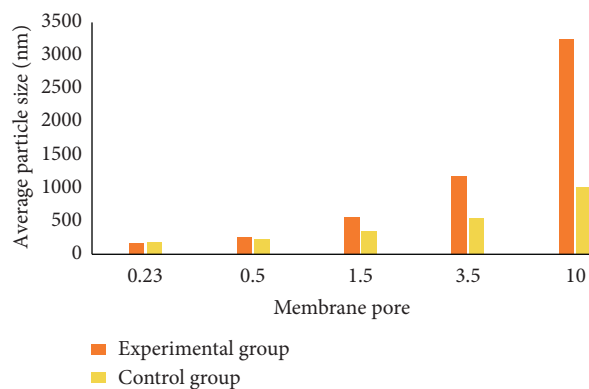


FIGURE 1: Mean particle size changes in urine nanocrystals filtered by organic membranes with different pore sizes.

continuous urine nanoparticle detection. Since there was little change in the control group, the aggregation state of the experimental group was only transformed into a schematic diagram for convenient observation, as shown below.

As shown in Figure 2, there was a small amount of aggregation after ultrasound, almost in a dispersed state. After 1 hour of placement, there was a slight phenomenon of aggregation, but it was mainly composed of a small number of nanocrystals less than 120 nm, with a relatively loose structure. After 2 hours, the degree of aggregation increased significantly, and a larger volume of aggregation was formed. Therefore, it can be proved that the formation of aggregates is the main reason for the rapid increase in the size of nanocrystals. The growth and aggregation of nanocrystals will eventually lead to the formation of stones.

**4.2.3.  $\xi$  Potential Difference.** The  $\xi$  potential reflects the electrostatic repulsion between the nanocrystals, and the greater the absolute value of  $\xi$  potential corresponds to the greater electrostatic repulsion, which also means that the agglomeration of nanocrystals becomes more difficult.  $\xi$  potential in urine is closely related to the ionic concentration of charge and opposite charge on the surface of urine microcrystalline. The urine of the experimental group and the control group was detected by nanometer, and the changes in  $\xi$  potential under organic membrane filtration with different pore sizes were recorded. The specific situation was as follows.

As shown in Figure 3, with the continuous increase in the pore size of the organic film, the average value of  $\xi$  potential decreases continuously. The mean value of  $\xi$  potential in the experimental group decreased from  $-2.62 \pm 0.52$  to  $-9.19 \pm 2.03$ , and the mean value of  $\xi$  potential in the control

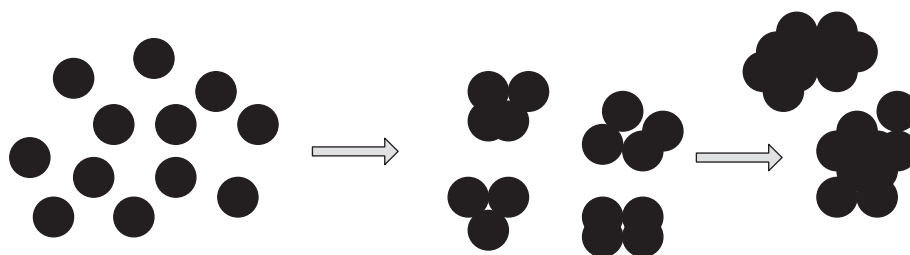


FIGURE 2: Changes of urine microcrystalline aggregates in the experimental group.

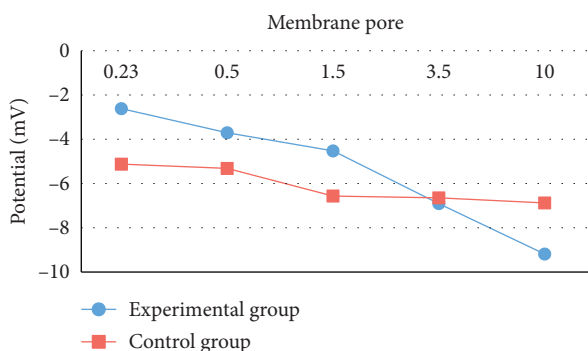


FIGURE 3: Changes in urine microcrystal  $\xi$  potential in the two groups.

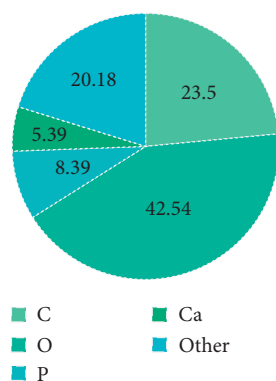


FIGURE 4: Element composition of urine nanocrystalline in a representative patient.

group decreased from  $-5.13 \pm 0.93$  to  $-6.88 \pm 1.1$ . It was obvious that there was a significant difference in the range of change between the two groups. The range of change in the experimental group was 6.57 mV, while that in the control group was only 1.75 mv.

**4.3. Chemical Element Composition of Nanocrystalline.** HRTEM was used to observe the urine nanocrystals of the two groups of patients, and the chemical elements in the urine nanocrystals of representative stone patients in the experimental group could be detected, mainly four elements C, O, P, and Ca. The proportions of these elements are as follows.

As shown in Figure 4, the chemical components and their proportions were accurately detected in the urine nanocrystalline of the patient with the stone. Other elements are temporarily ignored. Among the four main elements C,

O, P, and Ca, O element is the most, accounting for 42.54%. The next most important element is element C, accounting for 23.5%. P element and Ca element are second, accounting for 8.39% and 5.39%, respectively.

## 5. Conclusions

Urinary calculi are common multiple diseases of the urinary system, which can cause urinary tract infection and even lead to renal necrosis in severe cases. At present, the formation mechanism of urinary calculi mainly includes Randall spot theory, saturated crystal theory, inhibitor deficiency theory, and matrix theory. In fact, the formation of urinary calculi is very complex, and there is no unified conclusion on its specific pathogenesis.

The presence of nanochemical microcrystals in urine is closely related to the formation of urinary calculi. Nanocrystals in urine from patients with urinary calculi and healthy controls differed in size, distribution,  $\xi$  potential, and composition. The size of urine nanochemical microcrystals in patients with calculi was larger than that in healthy controls, and the degree of aggregation was also higher; urinary calculi were more likely to form.

Due to the limited time and knowledge, the urine detection in this study was not comprehensive enough, and there was no difference in the morphology and light intensity autocorrelation function of urine nanocrystals between stone patients and healthy controls. The above deficiencies will be improved in the next experiment in order to provide more reliable experimental data for the clinical treatment of urinary calculi.

## Data Availability

No data are available.

## Disclosure

Yanting Lou and Wei He are the co-first authors.

## Conflicts of Interest

The authors declare that there are no conflicts regarding this submission.

## References

- [1] K. Taguchi, D. S. T. Yasui, and T. ChiHoppe, "Genetic risk factors for idiopathic urolithiasis: a systematic review of the

- literature and causal network analysis,” *European Urology Focus*, vol. 3, no. 1, pp. 72–81, 2017.
- [2] B. H. Hancock, J. A. Warren, C. Marguet et al., “Concurrent laparoscopic hernia repair and cystoscopic laser cystolitholaxapy for urinary bladder calculus contained within a direct inguinal hernia,” *The American Surgeon*, vol. 83, no. 9, pp. e406–e408, 2017.
- [3] D. Habashy, W. R. Xia, and L. L. RidleyChan, “Impact of dual energy characterization of urinary calculus on management,” *Journal of Medical Imaging and Radiation Oncology*, vol. 60, no. 5, pp. 624–631, 2016.
- [4] C. Türk, A. Petřík, K. Sarica et al., “EAU guidelines on interventional treatment for urolithiasis,” *European Urology*, vol. 69, no. 3, pp. 475–482, 2016.
- [5] J. Sewell, D. J. Katz, O. Shoshany et al., “Urolithiasis—ten things every general practitioner should know,” *Australian Family Physician*, vol. 46, no. 9, pp. 648–652, 2017.
- [6] A. Gkentzis, J. M. Kimuli, and C. S. O. BiyaniTraxer, “Urolithiasis in inflammatory bowel disease and bariatric surgery,” *World Journal of Nephrology*, vol. 5, no. 6, pp. 538–546, 2016.
- [7] M. B. Carnahan, P. Hoang, and M. Yang, “Demonstration of 99mTc-MDP uptake in a mobile urinary bladder calculus on SPECT/CT,” *Clinical Nuclear Medicine*, vol. 45, no. 1, pp. 60–62, 2020.
- [8] D. Biswas and A. Saifuddin, “Death of non-descriptive male calf due to urolithiasis followed by rupture of urinary bladder,” *Bangladesh Journal of Veterinary Medicine*, vol. 13, no. 2, p. 63, 2016.
- [9] C. Türk, A. Petřík, K. Sarica et al., “EAU guidelines on diagnosis and conservative management of urolithiasis,” *European Urology*, vol. 69, no. 4, 2016.
- [10] H. Taskinlar, D. D. Yigit, and A. Nayci, “Unusual complication of a urinary stone in a child: spontaneous rupture of the renal pelvis with the migration of calculus into the retroperitoneum,” *Türk Üroloji Dergisi/Turkish Journal of Urology*, vol. 42, no. 1, p. 48, 2016.
- [11] J. W. Bartges, “Feline calcium oxalate urolithiasis,” *Journal of Feline Medicine and Surgery*, vol. 18, no. 9, pp. 712–722, 2016.
- [12] G. Bailey, C. L. Vaughan, and A. Krambeck, “Perinatal outcomes with tamsulosin therapy for symptomatic urolithiasis,” *Journal of Urology*, vol. 195, no. 1, pp. 99–103, 2016.
- [13] M. Bultitude, K. D. Smith, and K. Thomas, “Contemporary management of stone disease: the new EAU urolithiasis guidelines for 2015,” *European Urology*, vol. 69, no. 3, pp. 483–484, 2016.
- [14] Y. Yang, Y. Y. Deng, and Y. Wang, “Major geogenic factors controlling geographical clustering of urolithiasis in China,” *Science of The Total Environment*, vol. 571, pp. 1164–1171, 2016.
- [15] R. K. Muthusamy and S. S. Mehta, “Eosinophilic pyeloureteritis mimicking urinary calculus: a rare cause of ureteric obstruction in an adult[J],” *Open Journal of Clinical and Medical Case Reports*, vol. 2, no. 22, pp. 1–5, 2016.
- [16] B. K. Somani, G. Giusti, Y. Sun et al., “Complications associated with ureterorenoscopy (URS) related to treatment of urolithiasis: the clinical research office of endourological society URS global study,” *World Journal of Urology*, vol. 35, no. 4, pp. 1–7, 2016.
- [17] E. M. Huseynov, “Investigation of the agglomeration and amorphous transformation effects of neutron irradiation on the nanocrystalline silicon carbide (3C-SiC) using TEM and SEM methods,” *Physica B: Condensed Matter*, vol. 510, pp. 99–103, 2017.
- [18] Y. Cao, L. Luo, Q. Guo et al., “Synthesis and agglomeration control of nanocrystalline iowaite,” *Cailiao Kexue Yu Gongyi/Material Ence and Technology*, vol. 26, no. 2, pp. 27–33, 2018.
- [19] E. Magiorkinis, A. Diamantis, and L. Pantanowitz, “The fascinating story of urine examination: from uroscopy to the era of microscopy and beyond,” *Diagnostic Cytopathology*, vol. 43, no. 12, pp. 1020–1036, 2016.
- [20] C. Cavanaugh and M. A. Perazella, “Urine sediment examination in the diagnosis and management of kidney disease: core curriculum 2019,” *American Journal of Kidney Diseases*, vol. 73, no. 2, pp. 258–272, 2019.
- [21] P. X. Yu, Q. Zhao, Z. M. Meng et al., “Rhabditis axei found in urine routine examination: a case report,” *Chinese Journal of Schistosomiasis Control*, vol. 31, no. 5, pp. 565–566, 2019.
- [22] L. Yixiong, T. Zhihong, Y. Meng et al., “Object detection based on deep learning for urine sediment examination,” *Bio-cybernetics and Biomedical Engineering*, vol. 38, no. 3, pp. 661–670, 2018.
- [23] R. Prevel, A. M. Kostine, and M. Souayed, “Dark urine, hypotension and blood smear examination,” *Intensive Care Medicine*, vol. 45, no. 7, pp. 1015–1016, 2019.
- [24] K. Dantey, L. Pantanowitz, J. Xing, J. Cuda, R. Nestler, and S. E. Monaco, “Cell block preparation in urine cytology: examination of utility and workflow in an academic practice,” *Journal of the American Society of Cytopathology*, vol. 8, no. 2, pp. 61–68, 2019.
- [25] L. Jin and C. Cuiling, “Countermeasures and effects of quality control before routine examination and analysis of clinical urine,” *Journal of Clinical Laboratory (Electronic Edition)*, vol. 8, no. 1, pp. 72–73, 2019.

## Research Article

# Effect of Football on Fatigue of Patients with Breast Cancer Treated with Nano-Chemotherapy

Yu Zhang , Haonan Niu, and Zhiwei Peng

Hunan Normal University, Changsha 410006, Hunan, China

Correspondence should be addressed to Yu Zhang; zhangyu1978@hunnu.edu.cn

Received 7 August 2020; Revised 9 September 2020; Accepted 16 September 2020; Published 5 October 2020

Academic Editor: Tifeng Jiao

Copyright © 2020 Yu Zhang et al. This is an open access article distributed under the Creative Commons Attribution License, which permits unrestricted use, distribution, and reproduction in any medium, provided the original work is properly cited.

Cancer-related fatigue is one of the most common and uncontrollable subjective and persistent fatigue feelings in patients after breast cancer surgery, which seriously affects the rehabilitation effect and quality of life of patients. The purpose of this study was to investigate the effect of football intervention on cancer-related fatigue and quality of life in patients with breast cancer after nano-chemotherapy. The objective of this study is to explore the exercise program that can make patients actively carry out rehabilitation exercise and achieve good rehabilitation effect, so as to provide a theoretical and empirical basis for the study of cancer fatigue and quality of life of patients after breast cancer surgery. In this study, a quasi-experimental study method was used to conveniently select 60 breast cancer outpatients with tumor-related fatigue symptoms in a tertiary hospital in Liaoning Province. According to the convenience group, they were divided into a control group and an intervention group, 30 cases in each group. The control group received routine hospital nursing, while the intervention group received football intervention for 6 months on the basis of routine hospital nursing. The intervention measures include explaining the related knowledge of cancer-related fatigue, helping patients develop football projects, guiding patients to record football sports diaries, checking patients' football sports diary records at the beginning of each chemotherapy cycle, and discussing football sports feelings with patients. After six months of intervention, the researchers assessed cancer-related fatigue symptoms and quality of life. Football can improve the fatigue, physiological, psychological, and psychological states of breast cancer patients after nano-chemotherapy; reduce fatigue, anxiety, and depression; improve sleep; and ultimately improve the quality of life.

## 1. Introduction

Breast cancer [1] is gradually becoming the first malignant tumor threatening women's health. The incidence rate of breast cancer worldwide is 15% of all cancers, accounting for 37% of all cancer in women, accounting for 23% of all cancer deaths in women. Globally, the higher the geographic dimension, the higher the incidence rate; the high incidence areas are North America and Northern Europe; the central region is Israel, South America, and southern Europe; the low incidence areas are Asia and Africa. The incidence rate of incidence of white women in the United States is high. About 1 of the 8-9 people may have breast cancer, and the incidence rate is about 13.7%. The incidence rate of Asian women is 4–7%.

In order to explore the effect of this intervention method, football exercise intervention was carried out for 6 months for breast cancer outpatients with cancer-related fatigue [2]

symptoms. According to the principle of randomized controlled grouping, the patients were divided into an intervention group and a control group. Cancer-related fatigue scale (CFS), quality of life scale (WHOQOL-BREF), Pittsburgh Sleep Scale [3] (PSQI), and anxiety and depression scale [4] (SAS, SDS) were used for investigation and evaluation. Cancer-related fatigue, quality of life, sleep quality, anxiety, and depression of the two groups were regularly analyzed.

Football intervention can effectively reduce the fatigue degree of patients with breast cancer, and the rehabilitation effect is better than the traditional rehabilitation exercise after breast cancer surgery. Football intervention can improve the sleep quality of patients, reduce the anxiety and depression of patients, have good exercise compliance, and effectively improve the quality of life of patients with rehabilitation, and the effect is better than the control group of

traditional rehabilitation exercise. Exercise is a safe and feasible intervention method, which can effectively prevent the deterioration of cancer-related fatigue symptoms of patients with nano-chemical chemotherapy technology, but the effect of quality of life needs further research.

In this paper, the cancer-related fatigue status and its influencing factors of patients with breast cancer treated by nano-chemical chemotherapy [5] after breast cancer surgery were discussed. Only when we have a certain understanding of the factors can we design a reasonable experiment. Because of the various causes of cancer-related fatigue, we mainly discuss it by common factors. Using the design of a clinical randomized controlled trial, 60 patients were selected as volunteers in a hospital in Liaoning Province, and they were divided into two groups, one for the intervention group and the other for the control group. Finally, we concluded that football can reduce the fatigue, anxiety, and depression of patients with breast cancer after nano-chemical chemotherapy technology, improve the sleep of patients, and ultimately improve the quality of life of patients.

## 2. Cancer-Related Fatigue and Its Influencing Factors in Patients with Breast Cancer after Chemotherapy

*2.1. Cancer-Related Fatigue in Breast Cancer Patients Undergoing Chemotherapy.* Tumor-related fatigue is the most common and destructive clinical symptom in breast cancer patients undergoing chemotherapy. Relevant studies have shown that the incidence of cancer-related fatigue in breast cancer patients with chemotherapy is as high as 97%. In this study, breast cancer patients with chemotherapy have more serious physical fatigue, and emotional fatigue and cognitive fatigue are less. In this study, cancer-related fatigue is divided into two categories: peripheral fatigue [6] and central fatigue [7].

Peripheral fatigue includes somatic fatigue [8]. Peripheral fatigue is related to the activation of the vagal afferent nerve and changes in muscle metabolism. The tumor and tumor treatment can stimulate the peripheral nerve to release neuroactive substances and activate the vagal afferent nerve, which can inhibit the activity of skeletal muscle. As a result, the reduction of skeletal muscle activity leads to body fatigue and body fatigue.

Central fatigue, including emotional fatigue and cognitive fatigue, is mainly related to the imbalance of various nerve bundles and substances in the brain. In this study, physical fatigue is more serious than emotional fatigue and cognitive fatigue which may be due to changes in muscle metabolism, resulting in abnormal sarcoplasmic endoplasmic reticulum function [9], which increases intracellular calcium levels and decreases mitochondrial adenosine triphosphate [10] (ATP) synthesis. In addition, some patients may suffer from anemia and insufficient nutrition intake, which leads to the reduction of ATP synthesis nutrients and the change of ATP metabolism in muscle cells [11].

The influence of cancer-related fatigue on the physiological dimensions of breast cancer patients after chemotherapy is as follows: easy to fatigue, want to lie down and

rest, the body becoming heavy, feeling tired, emotional irritability, and not knowing how to deal with fatigue. The effects of chemotherapy on the emotional dimension of breast cancer patients include lack of vitality, loss of interest in many things, and inability to concentrate and motivate themselves to do things. The effect of chemotherapy on the cognitive dimension of breast cancer patients is that patients become careless, more likely to say wrong words, become very forgetful, and have a slow reaction.

*2.2. Common Factors of Cancer-Related Fatigue in Patients with Breast Cancer after Chemotherapy.* In this study, we learned from the literature that the demographic data of cancer-related fatigue in breast cancer chemotherapy patients include different numbers of children, different personality types, and different degrees of housework and appetite. The results show that the more the children, the higher the score of fatigue; the more the patient is extroverted, the less the fatigue symptoms; the more the housework, the heavier the degree of fatigue; the better the appetite, the lighter the degree of fatigue. The reason is the fact that during hospitalization, children take turns to take care of patients in the hospital except for work. As mothers, they feel sorry for their children when they see them working hard every day. On the contrary, they are more worried about their health. They have an increased degree of distraction, heart weakness, and physical insufficiency. At the same time, for patients in the process of cancer treatment, the use of chemotherapy drug tolerance is different; there are some side effects; at this time, physiological and psychological states have a certain impact. Personality is to take an optimistic and positive attitude toward extroverted patients, believe in their own ability, actively collect and understand the relevant knowledge of breast cancer treatment, seek help from others, and correctly understand and actively deal with the disease, so it has a positive impact on psychology and is full of confidence in cancer treatment. Introverted patients do not like to communicate with others. They are quiet and conservative in their lives. They do not want to reveal their ideas to others. They are reluctant to talk to others when they are faced with problems related to the disease. They tend to focus on themselves and their own events. They closed themselves and did not seek help from others and society. This is consistent with many studies. When patients return to their families, they habitually return to their previous roles in life, taking care of their families and doing housework. However, their physical condition and mood have been greatly different from those before the disease, and the degree of fatigue has also increased. Multivariate analysis showed that the frequency of housework had a significant impact on cancer-related fatigue. The higher the frequency of housework, the more serious the degree of fatigue. In the process of chemotherapy, the most common side effect of chemotherapy is a gastrointestinal reaction, which can lead to loss of appetite, nausea, and vomiting and reduce energy intake. In the process of treatment, some patients' pain and insomnia exacerbated the body's energy consumption. When the body's energy supply is not enough to maintain

the body's energy consumption, fatigue symptoms will appear in the body. Therefore, in the process of talking with cancer patients, clinical medical staff should pay more attention to observe the emotions of patients and find the root causes of such emotions, so as to better communicate with patients and their families and achieve good adjuvant treatment effect [12].

**2.3. Relationship between Anxiety, Depression, and Cancer-Related Fatigue.** The results showed that out of 60 cases of breast cancer chemotherapy patients, 83% have an anxiety state, and 77% have a depression positive rate. The reason for this result may be that the secondary sexual characteristics of women after breast cancer surgery have changed, affecting the family and social life of patients. Patients who have body image defects and who are unable to adapt to the role changes will produce a sense of inferiority and helplessness and will have increased depression. For women, it is more likely to cause depression than traditional mastectomy. Due to the different chemotherapy time and drug concentration, breast cancer patients are often accompanied by some adverse reactions, which limit the activity of patients and affect their life. Because some patients do not know the condition very well, but for various reasons, they are not willing to communicate with the medical staff, but at the same time, they want to know about the treatment-related information, inner contradictions, and anxiety. At present, chemotherapy drugs and some auxiliary drugs for breast cancer are expensive, and patients often need multiple courses of treatment, which will increase the economic burden of families. At this time, the increase in medical expenses makes some patients unable to afford, and anxiety and depression appear.

**2.4. Relationship between Sleep Status and Cancer-Related Fatigue.** The results showed that according to the cut-off value of sleep disorder of no less than 6 points, 60% of the subjects had sleep disorders. Insomnia is the most common sleep disorder in chemotherapy patients. Studies have shown that the incidence of insomnia in cancer patients during hospitalization is 67%. The possible reasons for this result are patients' ignorance of cancer-related knowledge, and fear and anxiety about cancer itself will affect their sleep state. In the process of chemotherapy for breast cancer patients, the discomfort caused by chemotherapy and the worry about the prognosis of the disease will make the sleep quality of patients worse. There is a real psychological gap in the life of breast cancer patients before and after their illness. The patients worried about high medical costs, the breakdown of family relations, future work, not adapting to the hospital ward environment, dependence on sleeping pills, or withdrawal symptoms.

### 3. Research Object and Operation Process

**3.1. Research Design.** First of all, we need to determine the purpose of the study and the content to be studied, reasonably select the research object for the experiment according to the random selection method, and then test the blood sample of the research object. Then, a reasonable

football program was developed; the subjects were trained for 6 months while the control group did not need any relevant training; only the conventional nursing mode was used. During the research process, we will test and record the indicators of patients in the intervention group and the control group for many times, and the test results were compared within and outside the group. Finally, the data were collected and sorted out to determine that the ability of patients with breast cancer treated by nano-chemotherapy after breast cancer surgery to resist fatigue was more significant due to the participation of football.

**3.2. Research Object and Inclusion Criteria.** The subjects of this study were breast cancer patients with fatigue undergoing chemotherapy in the breast surgery department of a hospital in Liaoning Province from March 2018 to 2018. They were aged from 30 to 45 years old; the total score of the cancer fatigue scale, i.e., fatigue, was used; patients who had the conditions to practice football at home voluntarily joined the study after the informed consent form was signed by patients and their families.

Inclusion Criteria:

- (1) Female patients who were with breast cancer confirmed by clinical pathology and who underwent a modified radical mastectomy, clinical stage II, pathological type of invasive ductal carcinoma, and chemotherapy regimen of TC (docetaxel, cyclophosphamide) were included
- (2) 24 hours after chemotherapy, the way of aerobic exercise was walking
- (3) No metastasis was found
- (4) Age was 30–55 years old
- (5) If the total score of the cancer fatigue scale is greater than 0, there is fatigue
- (6) After informed consent and signed informed consent, they voluntarily joined the study

Exclusion Criteria:

- (7) Patients with cancer or other body diseases such as cardiovascular disease, diabetes, hypertension, etc., were excluded
- (8) Patients who were diagnosed with breast cancer without chemotherapy or preoperative chemotherapy or only radiotherapy and chemoradiotherapy, targeted therapy, and other comprehensive treatment were excluded and if metastases were found
- (9) Patients who had past or present mental illness or disturbance of consciousness were also excluded
- (10) Regular exercise habits were observed after the operation (moderate-intensity aerobic exercise >3 times a week, exercise time >90 minutes)

### 3.3. Ethical Principles

- (1) Informed consent [13]: on the one hand, it explains the purpose and significance of the research to the

data acquisition unit and obtains its consent and permission; on the other hand, it introduces the research purpose, content, process, and the possible benefits of participating in the research. According to the principle of voluntariness, this study is only an observational study, and the results are only used for the analysis of the experiment, not involving the interests of the subjects. At the same time, all subjects were required to sign the informed consent form entitled “the effect of aerobic exercise at different times on cancer-induced fatigue of breast cancer patients undergoing chemotherapy”

- (2) Privacy and confidentiality: to protect the privacy of patients and inform the included subjects that the data will be strictly confidential and only used for this study
- (3) Fairness: after the end of the study, if the results show that the effect of football intervention is good, we will contact the patients in the control group, inform them of the research results, and recommend to help the patients in the control group to carry out rehabilitation training

*3.4. Assessment Tools and Contents.* This paper takes the form of a questionnaire for evaluation and statistics:

- (1) General information: the questionnaire was used to investigate age, education, education level, occupation, economic income, medical payment method, operation method, chemotherapy scheme, regular exercise habit after the operation, etc. The general information of this study is gender, residence, religious belief, nationality, marital status, fertility, family per capita monthly income, family relationship, personality type, housework, appetite, payment method, etc. Characteristics of clinical diseases: clinical stage, pathological type, operation type, chemotherapy scheme, complications, chemotherapy cycle, anemia, nausea and vomiting, pain, dry mouth, bitter mouth or oral ulcer, and other side effects.
- (2) Cancer-related fatigue: the revised fatigue scale (RPFS) was used to measure the fatigue. The scale was mainly composed of 22 items in four parts, and the behavioral severity, emotional aspect, sensory aspect, and cognitive emotion of fatigue were tested, respectively. The scale is widely used at home and abroad and has good reliability and validity. In this study, the expert validity (CVI) of the scale is 0.87; the higher the score of the scale, the more serious the fatigue. Experts believe that the scale score less than or equal to 3 represents mild fatigue, that between 3 and 6 represents moderate fatigue, and that higher than 6 represents severe fatigue.
- (3) Quality of life [14]: using a cancer treatment function evaluation system, breast cancer patient-specific scale measurement was used. There were five parts in the scale, including physical status (6 items), social and family status (6 items), personal emotional status (6 items), physical function status (6 items), and breast cancer-specific module (6 items). The 30 items of FACT-B are all classified into five levels: none (0), some (1), some (2), equivalent (3), and extraordinary (4). The higher the total score of the final statistical scale, the better the quality of life of patients. FACT-B has been proved to be a breast cancer patient-specific scale with good reliability and validity. This is also confirmed in the preliminary experiment of this study.
- (4) Anxiety and depression questionnaire: the scale is a general hospital anxiety and depression scale and is a common tool for the evaluation and management of emotional disorders in general hospitals. The hospital anxiety and depression scale (has) includes 14 items, which are composed of anxiety and depression. Two subscales, including seven items, are used to evaluate anxiety and depression, and the other seven items are used to evaluate the state. The scores of the two subscales are from 0 to 21 points, and the lowest score is 0. According to the criteria of the author's evaluation, the key differences of anxiety and depression subscale were asymptomatic 0–7, suspected anxiety and depression 8–10, and certain anxiety and depression 11–21. In addition, the two subscales were set with 8 points; that is, the patients suspected or confirmed anxiety and depression were positive for anxiety and depression. The reliability and validity of the hospital anxiety and depression scale were tested for the first time in China. The results showed that the Cronbach coefficient of the internal consistency of the anxiety scale was 0.92, and that of the depression scale was 0.84.
- (5) Sleep status table: in this study, insomnia was evaluated. Sleep was the main content of the Athens Insomnia Scale. The subjective feeling of sleep and sleep state were evaluated. It includes eight items: induction of sleep within a month, waking up at night, getting up in the morning, total sleep time, sleep quality, mental state, physical function, and daytime sleepiness. Moreover, each item was scored by Likert 4 points (0–3 points), and the total score of each item was accumulated. The critical points were as follows: the total score of no sleep disorder was no more than 3 points, the total score of possible sleep disorder was between 4 and 5 points, and the total score of sleep disorder was more than 6 points. The Chinese version of the scale has good reliability and validity with a Cronbach coefficient of 0.825.

*3.5. Football Intervention Methods.* According to the specific situation of each patient (different time and different recovery levels after the operation), the action of football practice was guided. Accompanied by professional football teachers, researchers, and chief doctors, according to the specific physical conditions of breast cancer patients, the rehabilitation football sport plan suitable for patients with

breast cancer after nano-chemotherapy technology in the initial, middle, and late stages is formulated, and the football sport teaching frequency is coordinated. The subjects and their families were trained on how to measure heart rate during exercise and the degree of mastery was investigated. Since the chemotherapy regimen is TC, the patient can be discharged without discomfort on the second or third day after chemotherapy, so the family members of patients are encouraged to accompany and supervise them to complete walking exercise after discharge. Patients were informed that they should stop the exercise immediately in case of nausea, vomiting, and irregular heart rate during exercise.

- (1) Centralized intervention: during the period of nano-chemotherapy after breast cancer surgery, the patients were accompanied by the chief physician and professional teachers of the breast department. Football practice was conducted three times a week, once every 2 days, for 1-2 hours each time. Until the end of the study, rehabilitation football CD was presented when discharged from the hospital.
- (2) Decentralized intervention: during the intermission of chemotherapy, the patients should practice football by themselves according to the football education video at home, preferably accompanied by family members, three times a week, once every 2 days, 1 to 2 hours each time, until the patient's next chemotherapy admission. The patients were asked to record the frequency of football practice in the register. The researchers regularly followed up the patients by telephone and video to monitor the exercises.

## 4. Results and Discussion

**4.1. Questionnaire for General Information of Patients.** As shown in Table 1, we have made a simple table from the patient's living conditions, marital status, education, and patient's appetite, which can intuitively see the basic situation of the volunteers participating in the study. There was no significant difference between the two groups.

**4.2. Effect of Football Intervention on Cancer-Related Fatigue.** We analyzed the data based on the interval time of each chemotherapy. The objective is to explore the effect of football intervention on the fatigue of patients with chemotherapy. The results showed that after the intervention, the scores of total fatigue, physical fatigue, emotional fatigue, and cognitive fatigue in the intervention group were lower than those in the control group.

As shown in Figure 1, sample 1 represents the first sampling, sample 2 represents the second sampling, sample 3 represents the third sampling, and sample 4 represents the fourth sampling. The four-sample comparison shows that the score of physical fatigue has a significant decline, while the emotional fatigue and cognitive fatigue are obvious enough, but the data score still has a decline.

TABLE 1: Questionnaire of general information of patients.

Project	Experience group	Control group	<i>P</i>
Place of residence			0.789
Countryside	13	15	
Town	17	15	
Marital status			0.996
Married/ Cohabitation	27	28	
Divorced/ Unmarried	3	2	
Appetite			0.968
Very good	4	4	
Good	5	7	
Commonly	11	9	
Poor	4	5	
Very poor	6	5	
Degree of education			0.798
Primary school	3	4	
Junior middle school	6	8	
High school/College	14	11	
University or above	7	7	

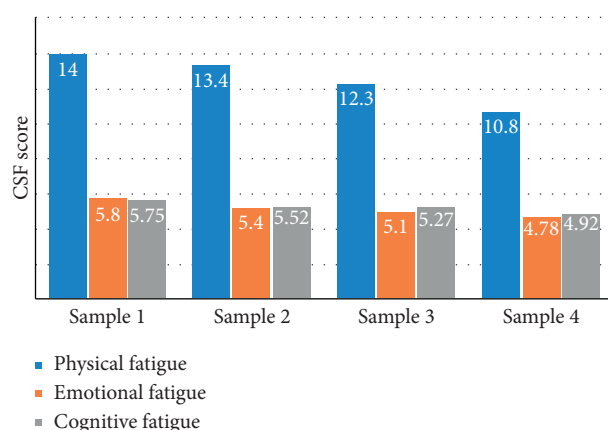


FIGURE 1: Changes of CFS score in the intervention group after football intervention.

**4.3. Influence of Football Intervention on the Quality of Life.** After the intervention, the quality of life scores of the intervention group and the control group at the third, sixth, and ninth chemotherapies are shown in Table 2.

As shown in Table 2, the results showed that after the intervention, in addition to the score of functional status, the scores of the overall quality of life, physiological status, family status, emotional status, and breast cancer additional attention of the intervention group were generally higher than those of the control group at each time point. The score of the functional status of the intervention group was lower than that of the control group at the third chemotherapy and higher than that of the control group at the sixth chemotherapy.

After the intervention, the scores of the quality of life between the two groups were compared.

As shown in Figure 2, in the comparison of the scores of the quality of life between the two groups after the

TABLE 2: Quality of life scores of the intervention group and control group in the third, sixth, and ninth chemotherapies.

Project	Experience group			Control group		
	The third chemotherapy	The sixth chemotherapy	The ninth chemotherapy	The third chemotherapy	The sixth chemotherapy	The ninth chemotherapy
Physiological status	15.1	15.8	17.5	16.3	14	13.6
Family status	20.23	20.05	20.0	19.5	19.2	18.9
Emotional state	15.80	15.81	16.89	15.34	14.58	15.34
Functional status	12.24	12.31	14.13	13.27	12.85	13.81
Additional attention to breast cancer	22.59	23.74	25.12	21.54	20.69	20.64
Overall quality of life	85.96	87.71	93.64	85.95	81.32	82.29

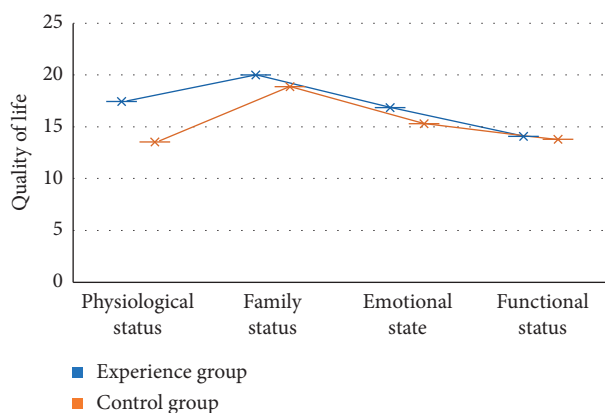


FIGURE 2: Comparison of quality of life scores between the two groups after the intervention.

intervention, we selected the data of the 9th chemotherapy to compare and analyze the patients in the intervention group and the control group, respectively, from the physiological status, family status, emotional status, and functional status. As shown in the figure, we can more intuitively see that the quality of life in the intervention group is significantly better than that in the control group.

**4.4. Effect of Football Intervention on Sleep Quality.** As shown in Figure 3, sample 1 represents the second chemotherapy, sample 2 represents the fourth chemotherapy, sample 3 represents the sixth chemotherapy, sample 4 represents the eighth chemotherapy, and sample 5 represents the tenth chemotherapy. Through the sleep quality records of the ten chemotherapy time cycles, the sleep quality of patients after the intervention is getting better and better, especially during the second to the fourth chemotherapy where it has an obvious effect. During this period, the sleep quality was improved rapidly, and it entered a stable state after the sixth chemotherapy. Therefore, adherence to football training can improve the quality of sleep and also can let patients have a full rest to achieve the effect of antifatigue.

**4.5. Influence of Football Intervention on Anxiety and Depression.** As shown in Figure 4, sample 1 represents the first chemotherapy, sample 2 represents the second chemotherapy, and sample 3 represents the third chemotherapy. For the influence of football intervention on the anxiety

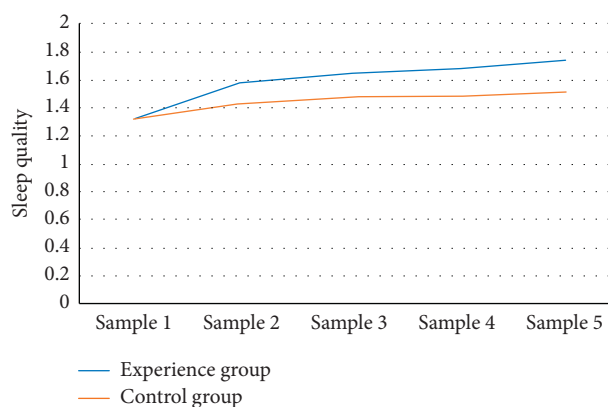


FIGURE 3: Effect of football intervention on sleep quality.

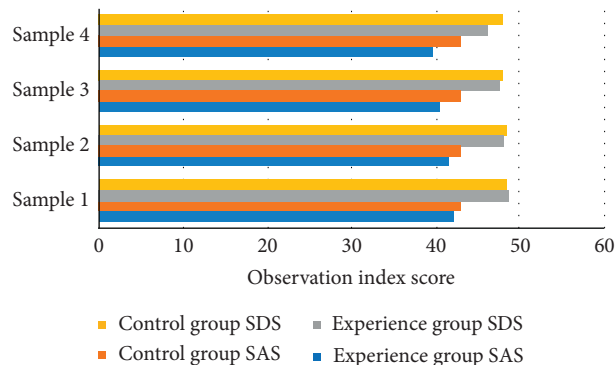


FIGURE 4: Score of anxiety and depression of football intervention.

and depression of chemotherapy patients, we compared the data of the intervention group and the control group, respectively. It can be seen that whether it is depression or anxiety, the score of the intervention group is lower than that of the control group. It can be concluded that football can significantly improve the anxiety and depression of patients with breast cancer after nano-chemotherapy.

## 5. Conclusion

Breast cancer is one of the main malignant tumors endangering women's health. Since the end of the century, the incidence of breast cancer has been in the first place in the world, and it is increasing at an annual rate. There are about

ten thousand women suffering from breast cancer every year in the world, and ten thousand women die of breast cancer. Cancer-related fatigue is the most common and very difficult to control the subjective and continuous fatigue feeling of patients after breast cancer surgery, which seriously affects the rehabilitation effect and quality of life of patients. This study explored the effect of football intervention on cancer-related fatigue, quality of life, sleep, anxiety, depression, and other conditions of breast cancer patients, in order to explore a better exercise program that can make patients actively carry out rehabilitation exercise and have good rehabilitation effect and provide theoretical basis and empirical basis for the research on cancer-related fatigue and quality of life of patients after breast cancer surgery. In this paper, we use the sublease intervention comparative experiment. We divided the volunteers into two groups: the intervention group and the control group. The control group was given routine treatment and nursing in the breast department, while the intervention group was given football practice from the first chemotherapy on the basis of routine treatment and nursing, and the patients were required to record their sports. With the participation of professional football teachers, doctors, and nurses, different guidance was given according to the different conditions of each patient. The patients were admitted to the hospital from the first chemotherapy. The intervention time of each patient was about 6 months. After the observation and comparison of the intervention group and the control group, we concluded that football can reduce physical fatigue, emotional fatigue, and cognitive fatigue in different degrees; compared with the control group, it greatly improves the physiological status, family status, emotional status, and functional status. Football training can improve the quality of sleep, improve the anxiety and depression of patients, and also can let patients have a full rest to achieve the effect of resist fatigue. Therefore, football can be used as a clinical intervention method to deal with breast cancer disease and disease treatment-related side effects, but collective intervention is very important, which helps to improve the compliance of patients. Therefore, clinical workers can observe the long-term effect of football on breast cancer patients.

### Data Availability

No data were used to support this study.

### Conflicts of Interest

The authors declare that there are no conflicts of interest regarding this submission.

### Acknowledgments

This work was supported by 2018 Hunan Provincial Department of Education General Project Fund (Project no. 18C044), the Teaching Research Project of , and Philosophy

and Social Science Fund of Hunan Province (No. 19YBA124).

### References

- [1] J. D. Shull, K. L. Dennison, A. C. Chack, and A. Trentham-Dietz, "Rat models of  $17\beta$ -estradiol-induced mammary cancer reveal novel insights into breast cancer etiology and prevention," *Physiological Genomics*, vol. 50, no. 3, pp. 215–234, 2018.
- [2] T. W. Hoenemeyer, T. J. Kaptchuk, T. S. Mehta, and K. R. Fontaine, "Open-label placebo treatment for cancer-related fatigue: a randomized-controlled clinical trial," *Scientific Reports*, vol. 8, no. 1, p. 2784, 2018.
- [3] Z. Veqar and M. E. Hussain, "Psychometric analysis of Epworth sleepiness scale and its correlation with Pittsburgh sleep quality index in poor sleepers among Indian University students," *International Journal of Adolescent Medicine and Health*, vol. 31, no. 2, pp. 30–36, 2018.
- [4] K. Cosansu, C. M. Ureyen, and S. Yilmaz, "Effect of novel oral anticoagulants on hospital anxiety and depression scale scores," *Herz*, vol. 44, no. 8, pp. 743–749, 2019.
- [5] M. Babincová, H. Vrbovska, P. Sourivong, P. Babinec, and Š Durd e, "Application of albumin-embedded magnetic nanoheaters for release of etoposide in integrated chemotherapy and hyperthermia of u87-mg glioma cells," *Anticancer Research*, vol. 38, no. 5, pp. 2683–2690, 2018.
- [6] F. L. Camati, O. ., F. G. Assunção, L. S. Kely, B. Daniel, B. Romulo, and L. S. A. Eduardo, "Caffeine increases both total work performed above critical power and peripheral fatigue during a 4-km cycling time trial," *Journal of Applied Physiology*, vol. 124, no. 6, pp. 1491–1501, 2018.
- [7] C. Audrey, R. Raquel, B. Andrea et al., "Effects of glutamine and alanine supplementation on central fatigue markers in rats submitted to resistance training," *Nutrients*, vol. 10, no. 2, p. 119, 2018.
- [8] D. N. Jarvis and R. E. Abergel, "What do we know about how acute physical fatigue affects movement in dancers?: a systematic review of the literature," *Medical Problems of Performing Artists*, vol. 34, no. 3, pp. 161–168, 2019.
- [9] V. Zsolnay, M. Fill, and D. Gillespie, "Sarcoplasmic reticulum  $Ca^{2+}$  release uses a cascading network of intra-SR and channel countercurrents," *Biophysical Journal*, vol. 114, no. 2, pp. 462–473, 2018.
- [10] S. Ling and L. Hui, "Evaluation of the complexity of indoor air in hospital wards based on PM2.5, real-time PCR, adenosine triphosphate bioluminescence assay, microbial culture and mass spectrometry," *BMC Infectious Diseases*, vol. 19, no. 1, p. 646, 2019.
- [11] L. Kai, W. Yong, Z. Anji, L. Baixue, and J. Li, "Mir-379 inhibits cell proliferation, invasion, and migration of vascular smooth muscle cells by targeting insulin-like factor-1," *Yons Medical Journal*, vol. 58, no. 1, pp. 234–240, 2017.
- [12] P. F. Parvin and F. Parvin, "Aromatase inhibitors as adjuvant therapy in postmenopausal women with early-stage hormone receptor positive breast cancer," *Current Opinion in Obstetrics and Gynecology*, vol. 30, no. 1, pp. 51–54, 2018.
- [13] J. D. Rendtorff, "Update of european bioethics: basic ethical principles in european bioethics and biolaw," *Bioethics Update*, vol. 1, no. 2, pp. 113–129, 2015.
- [14] M.-H. Shen, L.-P. Chen, T.-F. Ho et al., "Validation of the taiwan Chinese version of the EORTC QLQ-CR29 to assess quality of life in colorectal cancer patients," *BMC Cancer*, vol. 18, no. 1, p. 353, 2018.

## Research Article

# Simulation of the Conductive Process of Nano ZnO Varistors Based on Animation Plane Form

Xin Liu 

College of Art and Design, Lanzhou Jiaotong University, Lanzhou 730070, Gansu, China

Correspondence should be addressed to Xin Liu; [yunbogao@mail.lzjtu.cn](mailto:yunbogao@mail.lzjtu.cn)

Received 11 July 2020; Revised 21 August 2020; Accepted 15 September 2020; Published 30 September 2020

Academic Editor: Tifeng Jiao

Copyright © 2020 Xin Liu. This is an open access article distributed under the Creative Commons Attribution License, which permits unrestricted use, distribution, and reproduction in any medium, provided the original work is properly cited.

Among many nano materials and chemical materials, zinc oxide nanomaterials have attracted researchers' interest because of their high efficiency, low cost, easy preparation, and variable morphology. The purpose of this study is to explore the fabrication and conductive process of nano ZnO varistors under the simulation of an animation plane form. In this study, the chemical vapor deposition method was used to prepare nano ZnO. Then, ZnO nanomaterials were mixed with deionized water to form a suspension. Under the action of a micromechanical stirrer, impurities were removed by heat treatment, and then different amount of water was added to obtain a nano ZnO electrode. The conductive process and electrochemical properties of the nano ZnO electrode were investigated and analyzed. The results show that the pressure ratio of the varistor increases obviously after adding nano ZnO. In the range of 0–30%, the pressure ratio of the ZnO varistor increases with the increase in nano ZnO content. When  $w$  (nano ZnO) is 30%, the voltage ratio reaches 1.149 and the oxidation peak current ratio of LD decreases by 6%. Therefore, it is concluded that the electrode of nano ZnO varistor valve sheets maintains good stability for a LD conductivity detection process. It also plays an important role in electrochemical research.

## 1. Introduction

In the rapid development of chemical materials, pressure-sensitive zinc oxide valves are important equipment of zinc oxide thermometers. The properties of nano ZnO varistors mainly depend on the microstructure, material composition, and the function of raw materials. It represents a semiconductor valve plate with nonlinear bolt current intensity and is sensitive to electromotive force change. If the voltage is lower than the specified threshold voltage, the resistance value will rise and the current will hardly flow. However, if this threshold voltage exceeds (rheostat voltage), the resistance will change strongly and the current will immediately increase. Therefore, it is necessary to study the effect of ZnO particle size on the electrical properties of pressure-sensing valve discs.

Nano ZnO has many unique properties of nano materials, such as electrical conductivity, piezoelectricity, gas sensitivity, antibacterial, UV absorption, and scattering. Due to the advantages of nano ZnO, such as light, electricity,

magnetism, and sensitivity, it is used in gas sensors, thrusters, semiconductor materials, piezoelectric materials, antibacterial materials, UV shielding materials, thrusters, efficient catalysts, magnetic materials, thin film materials, and conductive materials.

According to the previous solid-state reaction method, Yang prepared ZnO-based varistor ceramics by immobilizing  $\text{La}_2\text{O}_3$  and doping  $\text{Y}_2\text{O}_3$  differently. He used X-ray diffraction (XRD), scanning electron microscopy (SEM), and direct current tests to study the phase composition, microstructure, and electrical properties of the materials. XRD and SEM analyses showed the  $\text{Y}_2\text{O}_3$  phase,  $\gamma$  phase, and La phase distributed in the grain boundary of ZnO particles. He also calculated that the average particle size of the primary stage was between 3.80 and 4.17  $\mu\text{m}$ . The ceramics doped with 0.1 mol%  $\text{La}_2\text{O}_3$  and 0.5 mol%  $\text{Y}_2\text{O}_3$  exhibited high comprehensive electrical properties and a destructive electric field strength of 1055 v/mm, a nonlinear coefficient of 65.5, and a leakage current of 0.6  $\mu\text{A}$  at 1100°C for

2 hours. Doping  $\text{La}_2\text{O}_3$  and  $\text{Y}_2\text{O}_3$  together with nano ZnO powder is a promising method to prepare pressure-sensitive ceramics with excellent electrical properties. His method is inflammable in the preparation process, the success rate is not high, and the operation is inconvenient [1]. Nano ZnO powder containing nano  $\text{KNO}_3$  eutectic was synthesized by Liu instead of organic additives. The samples were characterized by XRD, transmission electron microscopy, inductively coupled plasma atomic emission spectrometry, X-ray fluorescence, electron differential system, and scanning electron microscopy. In the presence of  $\text{NaNO}_3$ - $\text{KNO}_3$  eutectic, spherical doped nano ZnO powder with a particle size of 20–37 nm can be obtained simply. His solvent mediated  $\text{NaNO}_3$ - $\text{KNO}_3$  eutectic contributed to the formation of uniformly dispersed doped ZnO nanocrystals. At  $1100^\circ\text{C}$  for 2 hours, the density of the ZnO varistor sintered in air is  $5.43\text{ g/cm}^3$ , which is equivalent to 96.9% of the theoretical density. The insulation breakdown voltage is  $5893\text{ v/cm}$ , and the nonlinear coefficient is 26.6. The addition of molten salt can prevent the varistor from agglomerating and improve the electrical properties of varistors. The coffee maker made by his method is easy to be damaged and has low reliability [2]. Tsukamoto studied the transient electric field and current density distribution in and around the metal oxide varistor with a diameter of 42 mm and a thickness of 36 mm using the finite difference time domain (FDTD) method. The current injected into the varistor is  $4\text{ }\mu\text{s}$  lightning pulse current with a peak value of 100 kA and a rise time of  $4\text{ }\mu\text{s}$ . The battery has nonlinear resistance electric field characteristics in X, Y, and Z directions. This is based on the measured nonlinear voltage current characteristics. In his FDTD analysis, in the case of lightning current with a rise time of  $4\text{ }\mu\text{s}$ , the skin effect of 42 mm-diameter varistors is not obvious. When the nonlinear characteristics of ZnO elements and other elements do not change, the distribution of electric field and current density is greatly affected, which will lead to the deterioration and failure of varistors. His method is only suitable for research, but not for large-scale production, and has greater limitations [3].

In this study, the crystal structure and characteristics of ZnO are introduced firstly, and then the material, application, and mechanism of nano ZnO pressure-sensing valve discs are explained. This study illustrates the symptoms of planar animation. The preparation methods of six kinds of nano ZnO were summarized in detail. In this study, the calculation of electrochemical performance of nano ZnO pressure-sensing valve discs includes a resistance equation and nonlinear coefficient  $\alpha$ . In this study, the construction of a ZnO nano/ITO electrode, the analysis of the reproducibility and stability of the electrode, the analysis of the influence on the holding time of the electrical performance of ZnO varistor valves, and the experiment on the flattening of nano ZnO valves were carried out. Finally, the conclusion of this study is obtained by analyzing the conductive process and the composition of nano ZnO conductive materials.

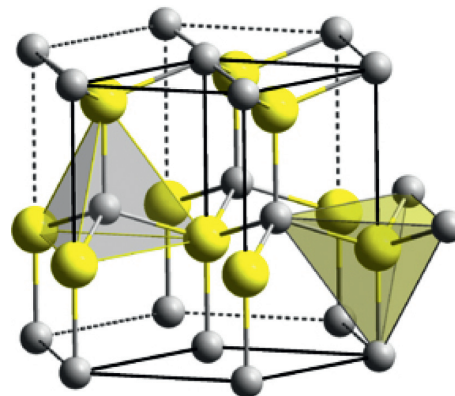


FIGURE 1: Atomic structure of nano ZnO.

## 2. Zinc Oxide Pressure-Sensitive Valve Piece and Animation Plane Form

**2.1. Crystal Structure and Properties of ZnO.** Electrical conductivity is one of the important properties of ZnO. At room temperature, the resistivity of ZnO may reach below  $0.068\text{ }\Omega\text{ cm}$ . The conductivity of ZnO is closely related to its crystal structure [4]. The lattice structure of ZnO is representative of the wurtzite structure. The lattice constants are  $a = 0.3325\text{ nm}$ ,  $c = 0.521\text{ nm}$ , and  $c/a = 1.6$ . In the crystal structure, oxygen ions are arranged in hexagonal close packing, and similarly, zinc ions are also arranged in hexagonal close packing. Zinc ions form a Zn-04 coordination tetrahedron around the oxygen ion tetrahedron, and vice versa. In order to produce polar symmetry along the hexagonal axis, the zinc oxide of wurtzite is a polar structure. At the same time, this polarity brings some unique characteristics to ZnO, such as high conductivity. Figure 1 shows the atomic structure of nano ZnO [5, 6].

Nano ZnO is a white hexagonal crystal or powder, odorless, nontoxic, and delicate. A new type of high-performance micro inorganic material with a particle size of 1–100 nm was prepared. It is also known as zinc oxide. The relative density is  $5.606\text{ g/cm}^3$ , the refractive index is 2.008–2.009, and the melting point is  $1975^\circ\text{C}$ . It is soluble in acid, sodium hydroxide, and ammonium chloride and insoluble in water, ethanol, and ammonia. It is an amphoteric oxide, which absorbs carbon dioxide and water from the air to form zinc carbonate. It turns yellow when heated and white after cooling. It does not allow ultraviolet light to penetrate and will not turn black when exposed to hydrogen sulfide [7, 8].

**2.2. Application of Nano ZnO Varistors.** It is used as a voltage regulator in TV receiver, CRT application equipment, lighting equipment, particle accelerator, and TV monitoring [9].

It is used as an overvoltage protection component in CNC lathe, automobile engine, loader, starter, copier, and telephone.

It is used as an overvoltage protection device in generator magnetization protection equipment and track system flash protection equipment [10].

### 2.3. Mechanism of ZnO Varistors

**2.3.1. Conductive Mechanism.** The band gap of ZnO is about 3.2 eV. At 27°C, the composite stoichiometric nano ZnO valve plate must have insulation, but due to the existence of inherent defects, it becomes an extra energy space area where the cycle is disturbed. The existence of these extra energy spaces will lead to the formation of aggressive zinc atoms. The activation energy of the attacking zinc atoms is low, most of which are ionized at 27°C. This is one of the reasons for the conductivity of ZnO conductive ceramics at room temperature. If there are no impurity ions, these conductive electrons mainly come from the ionization of interstitial zinc atoms, which presents the atomic electron conduction characteristics of nano ZnO. When metal oxide impurities are introduced into zinc oxide, these metal ions act as donors or acceptors (which is different from the type of zinc oxide that forms solid solution and metal ions) and the conductivity of zinc oxide is greatly different [11, 12].

**2.3.2. Aging Mechanism.** The annual power change of varistor zinc oxide valve discs is mainly due to the increase of leakage, the decrease of no-load voltage, and the absolute condition of voltage current function after long DC voltage or large impulse current [13]. The main reason is the potential energy distortion caused by the falling of electrons, the change of dipole direction, oxygen dissociation, and ion diffusion. Among them, for example, the degradation caused by the first two conditions is the result of subsequent experiments. The degradation phenomenon and mechanism of ZnO pressure-sensitive valve discs are described negatively. The aging due to DC and AC is caused by the deformation of astigmatism-bound barriers. Other theories suggest that the aging due to DC and AC is caused by changes in Scottish barriers. According to their methodology, the important reasons for aging caused by DC and AC are ion transfer and diffusion, which may be related to oxygen and invasive zinc ions [14].

**2.4. Forms of Planarization.** “Plane” refers to surfing without ups and downs, where two connecting lines are on the same plane. In the field of art and design, “planarization” has two sides. On the other hand, “planarization” refers to the material plane of art and design works and the limitation of objective conditions. In other words, the material of the work is medium sized. Designers or artists use a variety of methods to create and express art in space [15, 16]. On the other hand, “plane” refers to the plane visual effect that artists and designers make, not in the form of formal language but in combination with the configuration of image modeling elements. In order to convey the mood of the subjects, the flat performance was divided into the following three categories.

**2.4.1. Imagery Expression.** In order to obtain a pure planarization effect and abstract the abstract meaning of concrete and objective things, we refine and simplify the visual elements of traditional modeling, such as normal

transformation, spatial distance method, and light and shadow change, to create creators in the art process. Because of the integration of aesthetic feelings and objective things, it will bring a peaceful impression to the audience’s psychological level [17].

**2.4.2. Abstract Expression.** In the process of artistic creation, the creators give up the concept of traditional modeling, combine the basic elements such as pure point, line, surface, and color into unreasonable expression, and use bright morphological symbols to explain the spiritual connotation and realize the plane characteristics—very powerful visual effects.

**2.4.3. Graphic Expression.** In the process of artistic creation, the creator transforms various forms of expression space and three-dimensional space into plane graphics and color blocks for layout and combination, such as digital, traditional, and so on. The collage combination method can create simple, bright, and unique style of image effects [18].

### 2.5. Preparation Method of Nano Zinc Oxide

**2.5.1. Chemical Vapor Deposition (CVD).** Metal compound materials vaporize at a high temperature and then change the particles in the gas phase to obtain the required nano materials. The characteristics of this method are strong controllability and single product. The most important thing is that the quality of the extracted materials is very good, which can be used to observe and test the properties of materials [19].

**2.5.2. Hydrothermal Method.** In this method, the reagents are distributed into the solution according to a certain proportion at a high temperature and high pressure in a closed container and cooled at room temperature; the crystalline precipitate obtained from the reaction is cleaned and finally dried to obtain the required nano products. The hydrothermal process has the following advantages: simple equipment, simple operation, high uniformity, and high performance. The disadvantage is that the reaction time is long, the experimental process cannot be directly monitored, and the product cannot be controlled.

**2.5.3. Carbothermal Reduction Reaction Deposition Method.** In this way, the mixed material of ZnO and valve plate materials is heated in a special environment to cause a reduction reaction. The zinc vapor is used as a catalyst to oxidize it into liquid state and then oxidized to solid form to create a solid rosette. In addition, according to the pre-treatment of the experimental substrate, ZnO nanomaterials can be prepared by this process without catalysts [20, 21].

**2.5.4. Laser Pulse Deposition.** The mechanism of this process is that under the laser irradiation, the target becomes water vapor. The steam is very hot and dense. In the case of

transporting the gas, it condenses into nanostructures under the influence of liquid catalyst nanoparticles. Continuous growth in different environments and its growth diameter are limited by catalyst nanoclusters [22].

**2.5.5. Sol-Gel Method and Microemulsion Method.** These two processes are similar to the hydrothermal process, that is to say, transparent colloidal solution is formed after liquid-phase reaction and nanoparticles are prepared by different treatment processes. Each of these two methods has its own advantages and disadvantages. The nanoparticles prepared by sol-gel method have high uniformity and high-purity particles, but they must undergo long time combustion and synthesis. The monodisperse interface of nanoparticles prepared by the microemulsion method is good [23].

**2.5.6. Direct Precipitation Method.** The principle of this method is to use soluble salt solution  $\text{NH}_3\text{-H}_2\text{O}$  and other substances under certain conditions. After a chemical reaction is formed and precipitated, the extra anions are washed away by precipitation, and finally, the precipitate is heated to obtain zinc oxide.

## 2.6. Calculation of the Conductivity of Nano ZnO Varistors

**2.6.1. Resistance Equation.** In the same measuring circuit, Scotty's contact voltage current ratio remains unchanged regardless of the length of ZnO nanoribbons associated with the circuit [24, 25]. The total resistance of the circuit includes the contact resistance and the resistance of nano ZnO chemical bond, so the total energy is as follows:

$$V = V_{\text{contact}} + V_{\text{belt}} = (R_{\text{contact}} + R_{\text{belt}})I. \quad (1)$$

$V$  represents the applied voltage, and  $I$  is the corresponding current in the circuit. The electric density  $J_s$  for overcoming the barrier of hot electron emission is as follows:

$$J_s = -\frac{4\pi q m^* k^2 T^2}{h^3} \exp\left(-\frac{2\phi_B}{kT}\right) \exp\left(\left(\frac{qV}{kT}\right) - 1\right). \quad (2)$$

The current equation of hot electron emission theory is as follows:

$$\begin{aligned} J_s &= J_0 \exp\left(\left(\frac{qV}{kT}\right) - 1\right), \\ J_0 &= A^* T^2 \exp\left(-\frac{q\phi_B}{kT}\right), \\ A^* &= -\frac{4\pi q m^* k^2}{h^3}, \end{aligned} \quad (3)$$

where  $A^*$  is the Richardson constant,  $\phi_B$  is the Schottky barrier height,  $h$  is the Planck constant,  $T$  is the temperature,  $K$  is the Boltzmann constant,  $q$  is the electron charge, and  $V$  is the applied voltage. The Schottky contact voltage and resistance can be calculated by the following formula:

$$P_c = \lim_{V \rightarrow 0} \left( \frac{dV_{\text{contact}}}{dJ} \right) = \frac{KT}{qJ_s}, \quad (4)$$

$$R_{\text{contact}} = \frac{P_c}{A} = \lim_{V \rightarrow 0} \frac{KT}{qJ_s A},$$

where  $J$  is the current density of the circuit,  $A$  is the Scotty contact surface, and  $V$  is the applied voltage.

Since the limit value of  $P_c$  is used, the resistance value of Scotty contact resistance can be obtained. The resistance of nanoribbons connected to the circuit is obtained by subtracting a certain amount of random combined contact resistance from all resistors. The resistance is variable, and the magnitude of the change depends on the degree of oxidation in the zinc nanoribbon measurement circuit. The timing of the visit has changed. By adjusting the resistance point ( $R_b$ ) and length ( $d$ ) of a single ZnO nanobelt, the curve of the index can be expressed by the formula of coefficient ( $a_1 = 0568$ ,  $a_2 = 03577$ ):

$$R_b = a_1 \exp(a_2 d). \quad (5)$$

The experimental formula is expanded, and the change of crystal resistance of nano ZnO materials is combined into a formula:

$$R_b = \frac{0.9625d}{1 - 0.0565d} \quad (6)$$

It can be seen from the formula that the resistance characteristics of nano ZnO do not conform to the classical Ohm's law. This shows that the resistance of the material varies linearly with the length.

**2.6.2. Nonlinear Coefficient  $\alpha$ .**  $\alpha$  is an important parameter to explain the variable characteristics of nano ZnO. Generally, the larger the  $\alpha$  value is, the better the pressure sensitivity is. The formula is through a static resistance  $R_j$  to the dynamic resistance  $R_d$ :

$$\alpha = \frac{R_j}{R_d} = \left( \frac{U/I}{dU/dI} \right) = \frac{U}{I} \cdot \frac{dI}{dU}, \quad (7)$$

$$\frac{dI}{I} = \alpha \frac{dU}{U}.$$

After integration, we can get

$$\begin{aligned} \ln I &= \alpha (\ln U - \ln K), \\ I &= \left( \frac{U}{R} \right)^\alpha. \end{aligned} \quad (8)$$

$U$  is the applied voltage,  $I$  is the flow rate, and  $K$  is the material coefficient. By measuring the voltage  $U_a$  and  $U_b$  and the corresponding  $I_a$  and  $I_b$  on the varistor, the nonlinear coefficient  $\alpha$  can be obtained:

$$\alpha = \frac{\lg I_a - \lg I_b}{\lg U_a - \lg U_b} = \lg \left( \frac{I_a/I_b}{(U_a/U_b)^\alpha} \right). \quad (9)$$

### 3. Conducting Process Experiment of Nano ZnO Valves in a Plane Form

#### 3.1. Experimental Equipment

- (1) Measuring instruments: analytical balance and ordinary balance.
- (2) Powder mixing unit: QM-ISP04 planetary drilling rig.
- (3) Drying/heat treatment equipment: electric constant temperature drying oven and KXX-12-16A resistance furnace.
- (4) Test device: MY-3 KV propeller tester.
- (5) Microstructure analysis device: JSM-59000LV scanning electron microscope, X-650 scanning electron microscope, X'pertPro X-ray diffractometer, and V4150 electron spectrometer.

#### 3.2. Chemical Composition Design of Experimental Materials

**3.2.1. Raw Materials of Zinc Oxide.** This is the main raw material accounting for more than 90% of all raw materials. In addition to using high-purity raw materials as much as possible, the qualified standards for the composition, shape, particle size, processing temperature, and bulk density of zinc oxide raw materials must be formulated. Zinc oxide powder was purchased for this study.

**3.2.2. Additives.** There are many kinds of additives (5–8) and are of a small amount (less than 5 mol in total), which are the basis of excellent electrical performance of zinc oxide pressure-sensing valve discs.

**3.2.3. Composition and Formula of Experimental Materials.** Table 1 shows the composition and formula of experimental materials.

**3.3. Test for Performance and Structure.** The varistor voltage  $U_{1\text{mA}}$ , voltage ratio  $U_{1\text{mA}}/U_{0.1\text{mA}}$ , and leakage current  $I_0$  of each sample were measured using a MYZ-3 varistor automatic tester. The measured electrical performance parameters were compared and analyzed. A JEOL JSM-5900I scanning electron microscope was used to analyze the microstructure of the sample, analyze the microscopic image of the sample, and calculate the particle size distribution.

**3.4. Construction of ZnO Nano/ITO Electrodes.** The nano ZnO bubbles are fused with ionic water to form a mixture, which is stirred at a uniform speed under the function of the instrument to disperse the mixture evenly. Then zinc oxide was evenly distributed on the surface of ITO by spray equipment, and ITO was removed after cooling the heating plate.

The specific electrode design process is as follows:

- (1) The suspension was obtained by placing a 0.02 g ZnO nano electrode in 20 mL ionic water.

- (2) Place six pieces of clean ITO on the heating plate under the spraying device and seal both sides of ITO glass with a transparent tape. The reason is that nano ZnO will not cover the whole ITO surface, and the content of nano ZnO will increase during the electrochemical test.
- (3) After the heating plate is heated to 100°C, the distance between the spray gun and the spray gun is connected to 15 cm. Spray air provides spray power, inserts zinc oxide into the center of the container, and sprays the spray suspension in a mist form. After the ITO is cooled, heat treatment at 450°C for one hour to remove impurities, and drop solutions with different contents to obtain nano zinc oxide materials/ ITO electrode are performed.

### 4. Analysis of the Conductive Process of Nano ZnO Valve Plates in the Planar Form

**4.1. Detection and Analysis of Electrode Repeatability and Stability.** The repeatability of DPV was measured by using a 40  $\mu\text{M}$  LD on a graphene/ZnO nanoflower-modified electrode array. A total of 15 repeatability experiments were carried out with an interval of 10 minutes. The results show that the relative standard deviation (RSD) is 2.1%. The repeatability and stability of graphene/ZnO nanomaterials/ITO electrodes are shown in Figure 2.

From Figure 2, it can be concluded that graphene/ZnO nanoflowers/ITO electrodes have good repeatability in the detection of LD. All electrochemical tests were performed in 0.01 M PBS solution. In order to prove the stability of the graphene/ZnO nanoflower electrode, we placed the graphene/ZnO nanoflower-modified electrode for one week and then continued to test the DPV of 20  $\mu\text{M}$  LD every two days for two weeks. The results showed that the oxidation peak current of LD decreased by 6% compared with the initial value, so the graphene/ZnO nanoflower-modified electrode had good stability for LD detection.

**4.2. Effect of Holding Time on Electrical Properties of ZnO Varistors.** The sintering temperature is 1150. Table 2 shows the electrical properties of the samples with different holding time.

The sintering temperature is 1150. The variation of the electrical properties of the ZnO varistor valve piece with 1 mA varistor potential gradient and pressure ratio ( $U_{1\text{mA}}/U_{0.1\text{mA}}$ ) with insulation pairs is shown. Figure 3 shows the effect of holding time on the voltage gradient and voltage ratio of ZnO varistors.

It can be seen from Figure 3 that in the time range of 2–4 hours, with the extension of holding time, the varistor potential gradient of the zinc oxide varistor valve plate decreases, and the pressure-sensitive potential gradient of the zinc oxide pressure-sensitive valve piece after holding for 4 hours is almost double that of holding for 2 hours. In the time range of 2–2.5 hours, the pressure ratio of the zinc oxide pressure-sensitive valve decreases with the extension of holding time. In the time range of 2.5–4 hours, with the

TABLE 1: Material composition.

Number	Component%						
	Bi <sub>2</sub> O <sub>3</sub>	Sb <sub>2</sub> O <sub>3</sub>	Cr <sub>2</sub> O <sub>3</sub>	Co <sub>2</sub> O <sub>3</sub>	MnO <sub>2</sub>	ZnO	Nd <sub>2</sub> O <sub>3</sub> /CeO <sub>2</sub> /La <sub>2</sub> O <sub>3</sub>
1#	0.7	1.0	0.5	0.8	0.5	Allowance	0
2#	0.7	1.0	0.5	0.8	0.5	Allowance	0.02
3#	0.7	1.0	0.5	0.8	0.5	Allowance	0.04
4#	0.7	1.0	0.5	0.8	0.5	Allowance	0.06
5#	0.7	1.0	0.5	0.8	0.5	Allowance	0.08
6#	0.7	1.0	0.5	0.8	0.5	Allowance	0.1

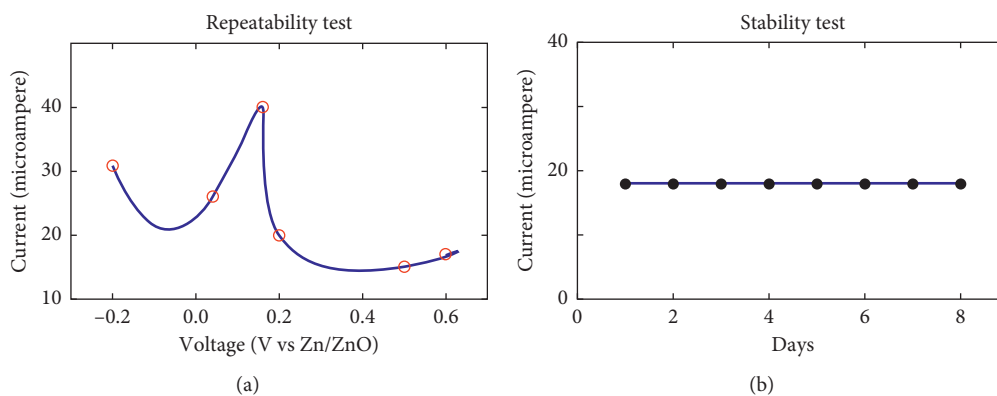


FIGURE 2: Repeatability and stability of graphene/ZnO nanomaterials/ITO electrodes.

TABLE 2: Conductivity of samples with different holding time.

Holding time (hours)	1 mA varistor gradient (V/mm)	$U_{1\text{ mA}}/U_{0.1\text{ mA}}$
2	446.27	1.224
2.5	375.96	1.089
3	332.16	1.157
3.5	309.45	1.201
4	262.87	1.297

further extension of holding time, the pressure ratio of the zinc oxide pressure-sensitive valve plate shows an increasing trend and the pressure ratio of 2.5 hours is the smallest. Considering the main electrical performance indexes of pressure-sensitive valves (high pressure-sensitive potential gradient and low pressure ratio), when the holding time is 2.5 hours, the voltage gradient is higher and the pressure ratio is minimum. Therefore, 2.5 hours is the best holding time.

In the process of preparation, temperature is the main stage. The components of this stage of material will undergo sufficient physical and chemical changes, so as to obtain compact sintered body without raw or over burning. Prolonged holding time can make the reaction between additives and between additives and zinc oxide complete, and the homogeneity of each phase is good, which is conducive to the recrystallization of the liquid phase and can promote the grain growth, so the varistor potential gradient decreases. In addition, with the increase in holding time, the grain distribution is more uniform and the ceramic structure is more compact, so the nonlinear coefficient increases and the pressure ratio decreases. However, if the holding time is too

long, the volatilization of Bi<sub>2</sub>O<sub>3</sub> in raw materials will be intensified, which will affect the quality of grain boundary layers. As a result, porosity increases, bulk density decreases, resistivity decreases, and nonlinear coefficient and other electrical properties deteriorate.

When nano ZnO is added into the varistor, the varistor voltage increases significantly. In the range of 0 to 30%, with the increase of nano ZnO, the influence voltage of pressure-sensitive ZnO varistors increases. When  $w$  (nano ZnO) is 30%, the varistor voltage is about 547.54 V/mm, which is about 54% higher than that of ordinary ZnO varistors without nano ZnO (about 354.42 V/mm). When nano ZnO is added into the varistor, the pressure ratio is increased significantly. In the range of 0–30%, the pressure ratio of ZnO varistors increases with the increase of nano ZnO content. When  $w$  is 30%, the maximum pressure ratio is 1.149. In the range of 0% to 10%, the leakage current of ZnO varistors decreases with the increase of nano ZnO content and increases with the increase of nano ZnO content in the range of 10%–30%. When  $w$  (nano ZnO) is 10%, the minimum leakage current is 0.6  $\mu$ A.

**4.3. Analysis of the Conducting Process of the Planarized Nano ZnO Valve Piece.** A 3D image of the ZnO nanobelt obtained through a scanning microscope shows that it is 30 microns wide and 1.5 microns thick and the surface of the sample is very smooth. The physical contact between the surface of ZnO nanoribbons and the platinum-plated conductive probe was established using atomic force microscope (AFM) contact mode. Thus, a closed circuit was formed to measure the current voltage curve. One of the

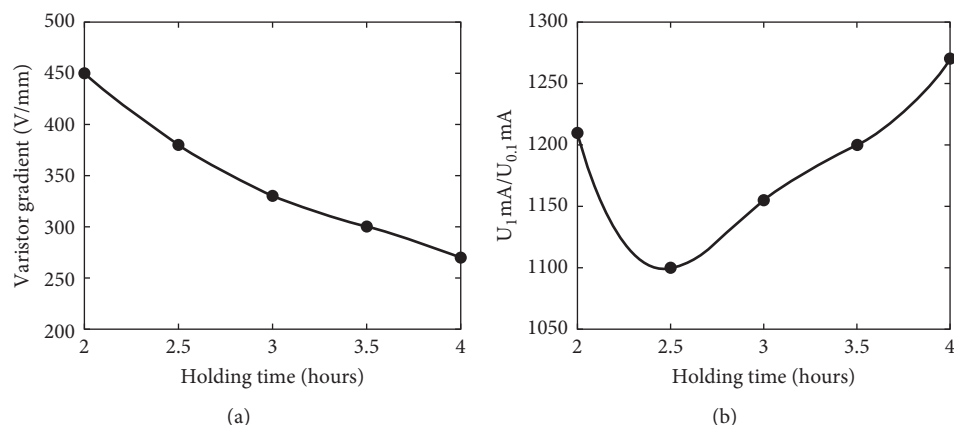


FIGURE 3: Effect of holding time on voltage gradient and voltage ratio of ZnO varistors.

characteristics of AFM is that it can select the contact position with ZnO nanobelts, so that a constant force can be maintained in the measurement to reduce the system error. When one end of the circuit is grounded, the voltage applied to the ZnO nanoribbon is negative. The type of thermoelectric elements is defined, the temperature is set at room temperature, and the isotropic and anisotropic characteristics of zinc oxide are simulated using software. Figure 4 shows the planar form of the conducting process of nano ZnO valve sheets.

It can be seen from Figure 4 that the surface atomic mobility of nano ZnO particles is high. In the sintering process, the nano ZnO particles wrapped on the micro ZnO particles first transfer the atoms to the vacancies on the surface lattice of the micron particles, which reduces the surface activity of the micro particles, weakens the vacancy diffusion and mass transfer between the micro ZnO particles, and hinders the grain boundary migration. The grain size decreases. On the one hand, the varistor voltage and other electrical properties of varistor valves are related to the number of grain boundaries between electrodes, and on the other hand, the number of some large grains in series. Therefore, the size and distribution of grains in varistor valve sheets are important grain microstructure parameters, which directly affect the electrical properties of varistor valves.

#### 4.4. Composition Analysis of Nano ZnO Conductive Materials.

TEM and XRD spectra of conductive ZnO powder heat treated at 500°C for 1.5 h in  $\text{H}_2$  atmosphere were studied. The distribution of ZnO particles is spherical, the particle size is relatively uniform, and the particle size is between 30 nm and 40 nm. There is a certain degree of agglomeration between the particles, which is consistent with the SEM observation. It can be seen from the XRD spectra that the sample is a single hexagonal system. When the spectrum is locally enlarged, the diffraction peaks of doping  $\text{m}^{3+}$  can be found at the places of  $2\theta$  59.3470 and 65.2390, but the intensity is very weak, which indicates that the dissolution amount of  $\text{ZnAl}_2\text{O}_4$  is very small. The average particle size calculated from the half peak width of the formula is about

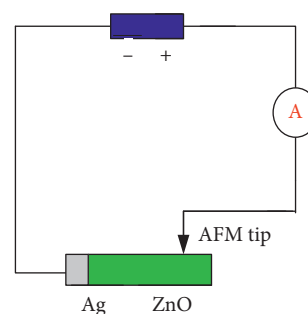


FIGURE 4: Planar form of conducting process of nano ZnO valve sheet.

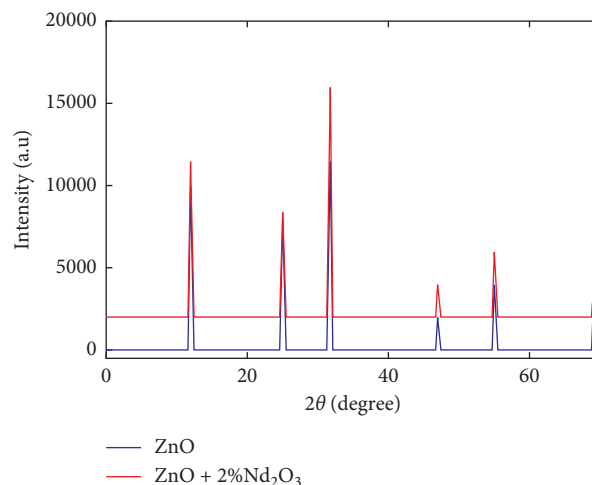


FIGURE 5: XRD spectrum of conductive ZnO powder.

36 nm, which is also roughly consistent with the observation of TEM photos, indicating that each particle is basically composed of single crystal. As shown in Figure 5 is the XRD spectrum of conductive zinc oxide powder.

It can be seen from Figure 5 that the peak value of ZnO reaches 1400, and the peak value increases again to 1600 after adding  $\text{Nd}_2\text{O}_3$ . The bet value of conductive zinc oxide powder is

24.4 m<sup>2</sup>/g, which is basically consistent with the results observed by TEM and calculated by half peak width of XRD. The results of XPS analysis showed that there was an obvious Zn<sub>2p</sub> peak at 1021.0eV and an obvious Al<sub>2s</sub> peak at 118.6eV, which indicated that the zinc oxide sample did contain AL. The results of XPS analysis showed that the Zn and can in the samples appeared in bivalent and trivalent forms respectively from the peak pattern of local amplification of XPS spectra, and there was no other valence state of these two elements.

## 5. Conclusion

When nano ZnO is added to the valve disc with high sensitivity, the voltage of the varistor will increase greatly. In the range of up to 30 wt%, the varistor voltage of the ZnO pressure-sensitive valve disc increases greatly with the increase in nano ZnO content. When adding 0–30% nano ZnO into the induction valve, the pressure ratio increases with the increase in nano ZnO content; within 10%, with the increase in nano ZnO dosage, the leakage current of the varistor zinc oxide valve plate decreases; in the range of 10% to 30%, with the increase in nano ZnO content, the leakage current increases; because nano ZnO is added to the pressure valve plate, ZnO particle size is reduced.

When the sintering temperature is 1150°C, the pressure gradient of the varistor ZnO valve disc is larger and the pressure ratio is the smallest. The best sintering temperature is 50°C. When the constant temperature state is 2.5 hours, the induced voltage potential of the material is the highest and the voltage ratio is the smallest, so two 2.5 hours is the best constant temperature state. The potential radius of the varistor zinc oxide valve plate increases sharply and the leakage current decreases with the addition of diluted upper oxide Nd<sub>2</sub>O<sub>3</sub> CeO<sub>2</sub> La<sub>2</sub>O<sub>3</sub>. In principle, the pressure ratio does not change but slightly decreases.

In this study, an experimental device was installed to measure the voltammetric characteristics of ZnO nanobelts. The results show that there is a specific ratio between the resistance of the chemical bond and the material length and nonlinearity. The change in the conductivity of ZnO nanomaterials was analyzed by a finite element method. Under isotropic conditions, the current density distribution of nano ZnO varistors is very uniform. Under the anisotropic condition, the current density is mostly distributed on the surface of nano ZnO varistors. Nano zinc/ITO electrodes have good electrochemical performance. The sensitivity of the electrode to LD is 0.32 μA/μm in the range of 1–60 μM. At the same time, graphene/ZnO nanoflowers/ITO electrodes also have excellent selectivity, stability, and reproducibility for LD.

## Data Availability

No data were used in the study.

## Conflicts of Interest

The authors declare that they have no conflicts of interest.

## Acknowledgments

This work was supported by the 2018 Gansu Provincial Science and Technology Plan Project “Research and Creation of Western Type Film and Television Brands in the Context of the Belt and Road Initiative,” project number: 18CX1ZA011, and the 2017 Lanzhou Jiaotong University School-Level Youth Project “Building a Multi-Ethnic Dunhuang Silk Road under the Belt and Road” Strategy Featured Film and Television Brands, project number: 2017023.

## References

- [1] S. Yang and D. Zhu, “Effect of co-doping Y<sub>2</sub>O<sub>3</sub>-La<sub>2</sub>O<sub>3</sub> on microstructure and electrical properties of ZnO-based varistor ceramics prepared from nanosize ZnO powder,” *Journal of Materials Science: Materials in Electronics*, vol. 29, no. 4, pp. 3104–3109, 2018.
- [2] T.-T. Liu, M.-H. Wang, H.-P. Zhang, and Y.-Z. Zhao, “Molten salt synthesis of doped nanocrystalline ZnO powders and applications in varistor ceramics,” *Journal of Materials Science: Materials in Electronics*, vol. 27, no. 4, pp. 3704–3709, 2016.
- [3] N. Tsukamoto, Y. S. Imato, and M. Ishii, “FDTD analysis of lightning impulse current distribution inside of ZnO varistor element,” *IEEE Transactions on Power and Energy*, vol. 136, no. 11, pp. 839–845, 2016.
- [4] S.-K. Choi, S.-M. Kang, J.-B. Lee et al., “Surge energy capability of ZnO-based varistors according to the Sb<sub>2</sub>O<sub>3</sub> and Bi<sub>2</sub>O<sub>3</sub>,” *Journal of Nanoscience and Nanotechnology*, vol. 16, no. 12, pp. 12702–12707, 2016.
- [5] N. Tsukamoto, T. Y. Tokita, and H. Okinaka, “Effects of aluminum doping on the electrical performance of ZnO varistor elements,” *Journal of the Japan Society of Powder and Powder Metallurgy*, vol. 64, no. 4, pp. 139–144, 2017.
- [6] Z.-Y. Zhao, M.-H. Wang, and H.-P. Zhang, “Microstructure and varistor properties of V-doped ZnO nanoparticles prepared by co-precipitation method,” *Journal of Materials Science: Materials in Electronics*, vol. 27, no. 2, pp. 1777–1782, 2016.
- [7] J. Liu, X. M. Wang, and Y. Chen, “Dispersion of ZnO nanocrystals using ammonium polycarboxylate (AMP) for the fabrication of ZnO-based ceramics,” *Journal of Electronic Materials*, vol. 49, no. 5, pp. 3216–3224, 2020.
- [8] R. Yang, M.-H. X. Qu, and M. H. Wang, “Sol-gel synthesis of Ba-doped ZnO nanoparticles and its use in varistor ceramics,” *Micro & Nano Letters*, vol. 13, no. 10, pp. 1506–1509, 2018.
- [9] F. Kharchouche and S. Belkhiat, “Effect of spark plasma sintering on microstructure and electrical properties of ZnO-based varistors,” *Journal of Materials Science: Materials in Electronics*, vol. 29, no. 19, pp. 16238–16247, 2018.
- [10] W.-J. Sun, J.-R. Liu, D.-C. Yao, Y. Chen, and M.-H. Wang, “Synthesis of carbon-coated ZnO composite and varistor properties study,” *Journal of Electronic Materials*, vol. 46, no. 3, pp. 1908–1913, 2017.
- [11] M. A. Kurbanov, S. M. Ahadzade, I. S. Ramazanov, Z. A. Dadashov, and I. A. Faradzhzade, “Varistor effect in highly heterogeneous polymer-ZnO systems,” *Semiconductors*, vol. 51, no. 7, pp. 953–958, 2017.
- [12] Y.-H. Kim, “The effect of Sb<sub>2</sub>O<sub>3</sub> Additive on the electrical properties of ZnO varistor,” *The Transactions of The Korean*

- Institute of Electrical Engineers*, vol. 65, no. 10, pp. 1697–1701, 2016.
- [13] S. H. Lee, C. K. Sohn, A. Djafar et al., “Ceramic Processing Research Electrical properties and microstructure of ZnO varistor with high surge protective characteristics,” *Journal of Ceramic Processing Research*, vol. 20, no. 2, pp. 164–168, 2019.
- [14] W.-J. Sun, R. Yang, M.-H Wang, and H.-P. Zhang, “Microstructure and varistor properties of Pr-Co co-doped ZnO ceramics obtained by sol-gel method,” *Journal of Materials Science: Materials in Electronics*, vol. 28, no. 14, pp. 10166–10172, 2017.
- [15] K. Zhang, E. S. Lee, I. M. Lee et al., “Photo-conductive detection of continuous THz waves via manipulated ultrafast process in nanostructures,” *Applied Physics Letters*, vol. 112, no. 3, Article ID 031102, 2018.
- [16] C. Wang, K. M. Zhang, H. X. WangGong, B. Guan, and Y. Zhang, “Intrinsically stretchable and conductive textile by a scalable process for elastic wearable electronics,” *ACS Applied Materials & Interfaces*, vol. 9, no. 15, pp. 13331–13338, 2017.
- [17] N. Yin, P. K. Jain, P. Tandon et al., “Additive manufacturing of flexible electrically conductive polymer composites via CNC-assisted fused layer modeling process,” *Journal of the Brazilian Society of Mechanical Encees & Engineering*, vol. 40, no. 4, p. 175, 2018.
- [18] Y.-Y. Feng, S.-J. Chen, and Y.-L. Tu, “Development of a vibration-based electromagnetic energy harvester by a conductive direct-write process,” *Energies*, vol. 10, no. 3, p. 337, 2017.
- [19] K. He, C. P. Xie, B. Y. LiWang, M. Z. Rong, and M. Q. Zhang, “A facile and scalable process to synthesize flexible lithium ion conductive glass-ceramic fibers,” *RSC Advances*, vol. 9, no. 8, pp. 4157–4161, 2019.
- [20] F. Han, D. C. Venet, D. D. ChaussyCurtill, J. E. Broquin, and N. Reverdy-Bruas, “Fabrication of 3D conductive circuits: print quality evaluation of a direct ink writing process,” *RSC Advances*, vol. 8, no. 46, pp. 26036–26046, 2018.
- [21] M. Vuong, D. Wu, Y. Liu et al., “Injection-compression-compression process for preparation of high-performance conductive polymeric composites,” *Applied Composite Materials*, vol. 26, no. 1, pp. 1–12, 2019.
- [22] H. Dong, Y. X. Li, and L. S. ZhaoGuo, “A novel preparation method of electrically conductive adhesives by powder spraying process,” *Materials*, vol. 12, no. 17, p. 2793, 2019.
- [23] K. Khoshelham, “Closed-form solutions for estimating a rigid motion from plane correspondences extracted from point clouds,” *ISPRS Journal of Photogrammetry and Remote Sensing*, vol. 114, pp. 78–91, 2016.
- [24] H. Sofie, K. Bart, and P. Z. Revesz, “Affine-invariant triangulation of spatio-temporal data with an application to image retrieval,” *ISPRS International Journal of Geo-Information*, vol. 6, no. 4, p. 100, 2017.
- [25] A. C. Polycarpou and M. A. Christou, “Closed-form expressions for the on-Axis scattered fields by a subwavelength circular aperture in an infinite conducting plane,” *IEEE Transactions on Antennas and Propagation*, vol. 65, no. 2, pp. 978–982, 2017.

## Research Article

# Magnetic Nanomaterials in Chinese Medicine Chemical Composition Analysis and Drug Metabolism and Its Industry Prospect and Development Path Research

Tengfei Ma<sup>1</sup> and Peng Liu <sup>2</sup>

<sup>1</sup>Faculty of Management and Economics, Kunming University of Science and Technology, Kunming 650093, Yunnan, China

<sup>2</sup>Faculty of Materials Science and Engineering, Kunming University of Science and Technology, Kunming 650093, Yunnan, China

Correspondence should be addressed to Peng Liu; [better@stu.kust.edu.cn](mailto:better@stu.kust.edu.cn)

Received 13 July 2020; Revised 24 August 2020; Accepted 19 September 2020; Published 30 September 2020

Academic Editor: Tifeng Jiao

Copyright © 2020 Tengfei Ma and Peng Liu. This is an open access article distributed under the Creative Commons Attribution License, which permits unrestricted use, distribution, and reproduction in any medium, provided the original work is properly cited.

The paramagnetism and superparamagnetism of magnetic nanomaterials are very important for in vivo applications. The magnetic particles with paramagnetism or superparamagnetism can redistribute the magnetic particles after the magnetic field is withdrawn, which is widely used for the separation and purification of biomolecules. At the same time, superparamagnetic particles can also be used as MRI imaging contrast agent. Compared with Western medicine, traditional Chinese medicine is different from Western medicine in that it is originated from nature and has thousands of years of clinical efficacy. Therefore, we hope to elaborate the complex mechanism of traditional Chinese medicine through some modern technical means: through the establishment of relevant quality control system, Chinese medicine will be recognized and popularized in the international field. Therefore, this paper discusses the application of magnetic nanomaterials in the chemical composition analysis and drug metabolism of traditional Chinese medicine and its industrial prospect and development path. Firstly, the advantages of magnetic nanomaterials and the shortcomings of chemical composition analysis technology of traditional Chinese medicine are analyzed theoretically. Then, through the experimental simulation, the results show that, under the optimal conditions, the magnetic nanomaterials can be used to analyze the chemical composition of traditional Chinese medicine. The peak current and concentration of THP showed a good linear relationship in the range of  $5.2 \times 10^{-8} \sim 2.1 \times 10^{-5}$  mol/L, and the detection limit was  $1.9 \times 10^{-7}$  mol/L. Moreover, it showed effective results in repeatability, stability, and interference tests. Therefore, magnetic nanomaterials play an important role in the chemical composition analysis and drug metabolism of traditional Chinese medicine as well as its industrial prospect and development path.

## 1. Introduction

The magnetic core of magnetic nanomaterials is mainly composed of iron, cobalt, and other magnetic metals and their oxides.  $\text{Fe}_3\text{O}_4$  is the first choice of magnetic nuclear materials because of its simple preparation process, easy modification, and biocompatibility. However, in the process of sample extraction, ferromagnetic oxide magnetic nanomaterials will have residual magnetism and agglomeration, which will reduce the extraction effect. Therefore, in order to prevent this phenomenon, carbon materials, silicon-based materials, and other polymer materials are often used to modify the surface of magnetic particles. This paper takes the

analysis and application of nanomaterials and the development of related industries as the research premise to study the actual effects produced in the actual application process, so as to provide specific path support for the industrial transformation and upgrading of the central Yunnan urban agglomeration in Yunnan Province, China. Prior to this, the study of the specific characteristics of materials has become particularly important. After clarifying the characteristics of materials, combining regional industrial policies and actual industrial development can better serve the construction of a modern industrial system in Yunnan Province, China. This article regards the interdisciplinary research of management science and engineering disciplines and chemistry

disciplines as an emerging discipline research direction, which is beneficial to the sustainable development of many disciplines.

Magnetic nanomaterials are different from conventional nanomaterials and magnetic materials. They refer to a kind of materials that are related to the characteristic physical length of magnetism which is just in the nanometer scale [1, 2]. In addition to the small size effect, surface effect, and quantum size effect of nanomaterials, it also has magnetic separation, biological compatibility, superparamagnetism, and catalytic-like activity [3, 4]. The analysis of particle morphology and structure is one of the important factors to characterize a material, powder or substance. In the scientific environment, there are several different methods to study the properties of materials, such as scanning electron microscopy, X-ray diffraction, energy-dispersive spectroscopy, and atomic force microscopy. From submicron to submicron particle, size is the final classification. Pantolimon synthesized a magnetic powder made of magnetite by coprecipitation method and analyzed it by XRD, SEM, and AFM to determine the particle/agglomeration size of the powder [5, 6]. Teremova studied the precipitation of iron and related heavy metals in industrial wastewater and model solution using ferritization and aerobic bacterial culture. Magnetic deposits that can be extracted by magnetic separation can be produced by precipitation of iron at  $p$  (8–10) and 60–80°C for 15–30 minutes by magnetic separation. In the model solution, the  $\text{Fe}^{3+}$  precipitation with bacterial temperature of 26–34°C resulted in the formation of iron hydroxide nanoparticles doped with related metals. The radius of the synthesized particles is 1–5 nm. The trihydrate iron nanoparticles are superparamagnetic in both undoped and doped groups. Teremova studied the dispersion structure, magnetic properties, and other properties of biological nanosol by atomic force microscope, small-angle X-ray scattering, X-ray diffraction, electron magnetic resonance, and Müssbauer and X-ray photoelectron spectroscopy [7, 8]. In the study of Li, nanosized zero-valent iron nanoparticles were coated with silica and polydopamine by two-step method. The coated nanoparticles are used as adsorbents to remove two common PAHs from aqueous system. The results show that the adsorption process is most suitable for Freundlich model and shows the characteristics of exothermic physical adsorption process. Due to their superparamagnetic properties and stability, these adsorbents can be easily collected, recycled, and reused [9, 10]. A variety of magnetic metal nanomaterials have been successfully prepared by using  $\text{CaH}_2$  at very low temperature. Due to its strong ability of solid reducing agent, it has attracted extensive attention in the field of solid chemistry in recent years. The advantage of using  $\text{CaH}_2$  instead of  $\text{H}_2$  as reducing agent is that the reaction temperature can be reduced by several hundred degrees centigrade. The rapid decrease of reaction temperature makes the structure of nanomaterials controlled accurately, and new functionalization technologies are developed. Yamamoto briefly summarized the

recent research results:  $\text{SiO}_2$ -coated  $\alpha$ -Fe nanoparticles, biocompatible  $\alpha$ -Fe nanoparticles, and carbon allotrope-coated  $\alpha$ -Fe and Ni nanoparticles [4, 11].

Drug metabolism is the main process of drug efficacy and toxicity in vivo. Develop a cheap, convenient, and rapid in vitro drug metabolism system to improve early and accurate prediction of the in vivo metabolic process, pharmacokinetics, and toxicity of candidate drugs [13, 14]. It is important for the development and design of new drugs, administration methods and dosages, and clinical drug testing [15, 16]. High-resolution mass spectrometry (HRMS) has become a powerful tool for the study of chemical constituents of traditional Chinese medicine. However, due to the complexity and content difference of traditional Chinese medicine compound components, it is difficult to distinguish chromatographic peaks clearly in data collection or analysis, which increases the difficulty of identification. Wang proposed a comprehensive identification strategy based on high-performance liquid chromatography linear ion trap mass spectrometry (HPLC-LIMS-MS) to identify the components of traditional Chinese medicine from high-dose herbs to formula milk powder with equivalent dose. At the same time, the constituents in Xiangsha Liujunzijaian granules were identified by mass spectrometry data, chromatographic behavior, reference standards, and previous reports. The results showed that the method can effectively and reliably identify the components of Xiangsha liujunjunjunjia decoction granules and reveal the material basis of its curative effect. This strategy provides a research idea for the characterization of multicomponent in traditional Chinese medicine prescriptions [16, 17]. Chengqi decoction is a group of famous traditional Chinese medicine preparations. It is used to treat the symptoms caused by “internal heat,” such as abdominal distension pain, difficulty in defecation, fever, and other clinical symptoms. Wen separation and identification of chemical constituents in Chinese herbal pieces were carried out by high-performance liquid chromatography electrospray ionization mass spectrometry and UPLC-TOF-MS. The results showed that 90 compounds were detected in CQS extract, including 7 anthraquinones, 39 flavonoids, 18 glycosides, 11 stilbene glycosides, 9 organic acids, 5 coumarins, and 1 lignan. Wen’s research results provide a scientific basis for clinical application of CQ similar formula, and HPLC-MS can be used for systematic identification of main components in traditional Chinese medicine formula [18, 19]. CKD affects a large proportion of the world’s population, and the prevalence of CKD is increasing. At present, the standard practice is to adjust the dosage of drugs that exclude renal function when renal function declines, so as to prevent adverse drug reactions. CYPs are responsible for the metabolism of many clinical drugs. Genetics, patient factors, and drug interactions can affect CYP metabolism, resulting in changes in pharmacokinetics and drug response. There is a lot of evidence that CKD can affect the activity of many CYP isomers by circulating uremic toxins directly and/or by reducing CYP gene

expression. There is evidence that renal transplantation can reverse the decrease of CYP metabolism in patients with end-stage renal disease and can be temporarily recovered by hemodialysis. Sugihara reviewed the effect of CKD on CYP metabolism and discussed the influence of CYP metabolic phenotype on the development of renal injury [17, 20]. Human precise liver section is an *in vitro* model for acute toxicity study. However, the rapid decline of metabolic enzyme activity limits its application in the study of long-term exposure to exogenous substances. The aim of Starokozhko is to extend the activity and function of hPCLS to 5 days. Starokozhko's research shows that hPCLS cultured in Cellartis® medium is a valuable human *in vitro* model, which can be used for toxicological and pharmacological studies requiring long-term exogenous exposure [21, 22]. Nanobiosensor technology is also one of the many analysis methods. The unique performance of nanomaterials in various aspects is combined with the biosensor technology, which significantly improves the analytical performance of biosensors and also provides rich materials for the analysis of chemical components of traditional Chinese medicine and the research of drug metabolism [23].

Lei, a new type of CS/RGO-based composite hydrogel, was prepared by using natural polymer materials, chitosan and graphene oxide as raw materials, and glutaraldehyde as crosslinking agent. In addition, CS/GA/RGO/Pd composite hydrogels were prepared by loading palladium nanoparticles. The morphology and microstructure of the prepared hydrogel were characterized by means of SEM, TEM, XRD, TG, and BET. The catalytic performance of CS/GA/RGO/Pd composite hydrogel was analyzed. The results showed that CS/GA/RGO/Pd composite hydrogel had good catalytic degradation performance for *p*-nitrophenol and *o*-nitroaniline. Using simple electrospinning and hydrothermal methods, new MoS<sub>2</sub> nanosheets were prepared on SrTiO<sub>3</sub> nanofibers and 2D, and heterojunction NFs were synthesized by SrTiO<sub>3</sub> and MoS<sub>2</sub>. It is necessary for Ran to study the functionalization of two-dimensional materials for the development of self-assembled nanomaterials. Ran prepared composite films based on black phosphorus and dye by Langmuir–Blodgett technique. Kaikai prepared self-assembled MXene gold nanoparticles and reported the size-adjustable nanocomposites. Kaikai prepared nanocomposites by self-reduction of MXene in HAuCl<sub>4</sub> solution at room temperature.

In this paper, by comparing with pure CNTs, the electrocatalytic activity of NCNTs on several biological small molecules was studied, and the catalytic mechanism of magnetic nanomaterials was preliminarily discussed. Based on the excellent electrocatalytic performance of NCNTs, current H<sub>2</sub>O<sub>2</sub> sensors and NO sensors were constructed. Glucose biosensors and choline sensors were successfully constructed by detecting the H<sub>2</sub>O<sub>2</sub> produced by glucose oxidase/glucose or choline oxidase/choline in the enzymatic reaction process, both of which have good detection performance. In addition, this paper initially tried a relatively mild surface functionalization method of NCNTs with the help of the special structure of pyrene molecules. This method does not destroy the original electronic structure of

the material and can well maintain the biological activity of the immobilized enzyme. The construction of CYP2C9 *in vitro* metabolic system has potential application prospects.

## 2. Magnetic Nanomaterials and Traditional Chinese Medicine

**2.1. Magnetite Nanoparticle.** Magnetic iron oxide nanoparticles are particles smaller than 1 μm, including paramagnetic nanoparticles and superparamagnetic nanoparticles. Paramagnetism refers to the preparation of magnetic nanoparticles subject to Curie–Weiss law with the change of magnetic susceptibility with temperature and the magnetic properties of the applied substances in the biological elutriation of drug targets. On the atomic scale, the magnetic moment is heated. The effect of the disturbance is that, in the absence of an external magnetic field, these magnetic moments are randomly distributed, so that the substance does not show magnetism. When a magnetic field is applied, this magnetic moment obtains a phenomenon that there are more statistical components in the direction of the external magnetic field. Under the normal magnetic field and temperature, the energy of the magnetic moment in the external field is much smaller than the thermal disturbance energy, so the susceptibility of the paramagnetic substance is close to zero, and the value is very small, only 10<sup>-2</sup>~10<sup>-5</sup>. In a certain external magnetic field, because the thermal motion of the molecule affects the arrangement of the magnetic moments, the magnetic properties of the substance decrease with increasing temperature. The relationship between the magnetic susceptibility of paramagnetic substances and temperature is subject to Curie–Weiss law; namely,

$$X\sigma = \frac{C}{T - \theta} \quad (1)$$

Here, *C* is called the Curie constant.  $\theta$  is a constant for a certain substance, and it can be greater than, equal to, or less than zero. When  $\theta = 0$ ,  $X\sigma = C/T$  is called Curie's law. Ferromagnetic metals are paramagnetic above the distance point; antiferromagnetic metals are paramagnetic above the Neel point. Superparamagnetism refers to a kind of magnetism that is different from the original substance itself but appears similar to paramagnetism after micronizing ferromagnetic or ferrimagnetic substance. If the ferromagnetic or ferrimagnetic material is broken into very fine single-domain particles, or the very fine single-domain particles are precipitated in the non-ferromagnetic alloy matrix, when the particles are small to a certain degree, compared with the bulk ferromagnetic material, they show different properties. Suppose the magnetization of the particle is *M<sub>s</sub>* and the volume is *v*. The magnetic anisotropy constant is positive. Since the magnetic moment of each particle  $\mu = M_s v$ , as a whole, the magnetic moment of each particle plays the same role as the magnetic moment of each atom in a paramagnetic substance. There is a magnetic behavior of the aggregate composed of such particles and common paramagnetic substances are similar, so it is called superparamagnetic.

The difference between super-quality and normal paramagnetism is that it is in a normal paramagnetic substance. The magnetic moment of each atom is about several Bohr magnetons and in a superparamagnetic substance, the magnetic moment of each particle is about  $10^4$  Bohr magnetons, so it can be magnetized to saturation in the usual magnetic field, superparamagnetic. An important feature is that there is no hysteresis. That is,  $B_r$  and  $H_c$  are both zero.

The particle size of  $Fe_3O_4$  magnetic particles is generally about 1–300 nm, and different particle sizes have slightly different properties. When the particle size of the magnetic particles is less than a certain critical value, it becomes a single-domain particle assembly, and the magnetic moment changes irregularly. At this time, a superparamagnetic phenomenon occurs.  $Fe_3O_4$  magnetic particles have been reported to be biocompatible, and based on their unique physical and magnetic properties,  $Fe_3O_4$  magnetic particles have been widely used in the medical field. Therefore,  $Fe_3O_4$  magnetic particles are expected to become one of the most promising materials in the medical field.

*2.2. Chinese Medicine Chemical Composition.* The components of traditional Chinese Medicine analyzed by the current-type electrochemical sensor need to have active groups which can produce redox. According to the structural formula analysis of the components, it can be found that most of them have active groups and have the potential to be determined by electrochemistry. The quality of traditional Chinese medicine is affected by many uncontrollable factors: in the process of cultivation and storage, in order to prevent and control diseases and insect pests, pesticides will be sprayed on Chinese medicinal materials, and the growth process will also be affected by the soil quality of the growing environment; illegal traders will add contraband in order to increase profits and sulfur fumigation in order to make the color of traditional Chinese medicine bright and lustrous.

The separation and purification of traditional Chinese medicine has been developed for a long time. There are many separation methods commonly used in industry, and different methods are selected for different compounds. High-speed countercurrent chromatography (HSCCC) is a new type of liquid–liquid partition chromatography technology. It is characterized by the separation of separated substances in two liquid phases, which overcomes the sample defects brought by traditional solid-phase carriers, and provides a new way for the separation and preparation of traditional Chinese medicine components and the analysis and identification of traditional Chinese medicine. The basic principle of high-performance liquid chromatography (HPLC) is based on the different partition coefficients of different substances in the chromatographic column, so as to achieve the separation effect. This method has many advantages, which is suitable for the separation and purification of multicomponent complex mixture. 80% of the compounds can be used. However, the chromatograph is expensive, and

the column is consumable, easy to pollute, and high in application cost. Macroporous resin has macroporous network structure, which has the characteristics of large specific surface area and high adsorption efficiency. There is no exchange group on the surface, which belongs to physical adsorption. There are two main separation mechanisms: adsorption and molecular sieve. The main advantages of macroporous resin are low application cost, and the resin can be used repeatedly; large sample size, suitable for the treatment of large quantities of samples, and has a high enrichment effect; macroporous resin can also remove nonpolar and polar impurities such as chlorophyll and sugar in traditional Chinese medicine; according to the polarity of solvent elution, the target compounds can also be separated by polarity.

Alkaloids are a kind of basic organic compounds containing nitrogen, which are similar to alkali. Most of them have complex ring structure. Nitrogen is contained in the ring and has significant biological activity. Flavonoid compounds generally refer to a series of compounds formed by connecting two benzene rings (A- and B-ring) with phenolic hydroxyl group through the central three carbon atoms, and the basic mother nucleus is 2-phenylchromone. Flavonoids are often linked with active functional groups. It is possible for the electrochemical determination of flavonoids; terpenoids refer to hydrocarbons and their oxygen-containing derivatives whose molecular formula is multiple of isoprene units in nature, and the unsaturated bond in terpenoids structural formula provides the possibility for electrochemical detection; sugars are an important class of organic compounds widely distributed in nature. It plays an important role in the process of life activities and is the main source of energy for all living bodies to maintain life activities. Glycosides, also known as glycosides, are compounds formed by the end group carbon atoms of sugars or sugar derivatives connected with another class of non-sugar substances.

*2.3. Application of Magnetic Nanomaterials Combined with Electrochemical Sensors in the Analysis of Traditional Chinese Medicine.* A large number of synthetic drugs play an undeniable role in the field of medicine, but their use is often accompanied by side effects that are difficult to predict. From the structure analysis, most of them have electrochemical active groups. In principle, all the active components of traditional Chinese medicine containing these electrochemical active groups can be studied by a suitable electrochemical technology, so as to realize quantitative analysis and infer the relevant mechanism. At present, carbon materials are the most widely studied and used materials. From the macro perspective, there are three kinds of allotropic carbon, namely, graphite, diamond, and amorphous carbon. Graphene is a single-layer  $sp^2$  hybrid two-dimensional crystal with hexagonal honeycomb. Graphene is composed of single-layer carbon atoms, which is a new type of carbon nanomaterials. The thickness of single-layer graphene is only 0.34 nm, and the theoretical surface area can reach  $2600\text{ m}^2/\text{g}$ , and it has

outstanding thermal conductivity and mechanical properties. In addition, the  $sp^2$  structure of graphene makes it have high electron mobility and a series of excellent physical and chemical properties, such as good quantum tunneling effect. Graphene oxide has a  $SP2$  plane structure without reduction and contains a large number of oxygen-containing groups. These active groups were used to open the ring of graphene, and the modified group was grafted onto the surface of graphene in the form of covalent bond, so as to realize the covalent functional modification of graphene. Covalent functionalization can not only improve the dispersion of graphene in solvent, but also prepare a series of novel graphene hybrid materials for various fields, which broaden the application range of graphene. In addition to covalent functionalization of graphene,  $\pi$ - $\pi$  bond, ionic bond, and hydrogen bond can also be used for noncovalent functionalization of graphene. The noncovalent functionalized modification will not destroy the  $n$ -electronic structure of graphene, and the original characteristics of graphene can be maintained by using the principle of physical adsorption or polymer coating on graphene surface. Carbon nanotubes (CNTs) are hollow nanotubes composed of single- or multilayer graphite-like planes composed of six membered rings. Each carbon atom of carbon nanotubes is bonded to three carbon atoms by  $sp^2$  hybridization. Because carbon nanotubes are round tubes made of single- or multilayer flake graphite, carbon nanotubes inherit the excellent physical and chemical properties of graphite and have many unique properties.

### 3. Experiment Materials and Methods

**3.1. Experimental Materials.** Eliminate residues 1–290 from the NOS oxygenase region to obtain D290nNOSoxy, with a molecular weight of about 49kDa. Phosphate buffer solution is prepared by mixing  $Na_2HPO_4 \cdot 12H_2O$  and  $NaH_2PO_4 \cdot 2H_2O$  solutions. Other reagents are analytically pure, and all solutions are prepared with double distilled water.

**3.2. Connection of Magnetic Nanoparticles and Traditional Chinese Medicine.** Add 150 mg of the prepared polymer-containing magnetic particles to 2 ml of ethylenediamine buffer to mix, then add 40 mg of carbodiimide, react at room temperature for 3 hours, dialyze 4 times with 1000 ml of 1000MCW0 dialysis bag to remove excess ethylenediamine and salt, and freeze-dry to obtain magnetic particles crosslinked with high-molecular-weight polymer and active group  $NH_2$ . Use EDC as the linking agent to prepare 20 mg of surface-crosslinked magnetic particles, in 1 ml of the connection buffer, prepare 2 mg of salvianolic acid B in the connection buffer, prepare 10 mg/ml EDC connection buffer, react at room temperature for 3 hours, and dialyze with 1000MCW0. The bag was dialyzed 5 times with 1000 ml of 0.85% NaCl aqueous dialysis solution and lyophilized. Take a small amount of lyophilized sample and salvianolic acid B for infrared detection.

## 4. Application of Magnetic Nanomaterials in Chemical Composition Analysis and Drug Metabolism of Traditional Chinese Medicine

**4.1. Determination and Analysis of THP by DPV.** The comparison results of the electrochemical method and other THP determination methods are shown in Table 1.

Compared with other methods, the electrochemical method was chosen because of its wider linear range, lower LOD, and easier sample processing. As the two electrochemical measurement methods of THP, SWV only preliminary studies the electrochemical characteristics of THP. The method used in this paper has made an in-depth discussion on the optimal conditions of THP and deduced its electrochemical mechanism. In the measurement of actual samples, the method adopted in this paper has shown satisfactory results. The differential pulse voltammograms of NiNPs/SGS/GCE at different concentrations of 0.5–20.0  $\mu M$  THP are shown in Figure 1.

Under optimized conditions, the DPV of NiNPs/SGS/GCE at different concentrations of  $5.0 \times 10^{-7}$ – $2.0 \times 10^{-5}$  mol/L-THP,  $I_{pa}$  has a linear relationship with the concentration:  $I_{pa} (\mu A) = 0.263c + 0.555 (\mu M, r = 0.9988)$ . The LOD of THP of this modified electrode was  $1.9 \times 10^{-7}$  mol/L. By comparing bare GCE, SGS/GCE, and NiNPs/GCE, NiNPs/SGS/GCE further increased the oxidation peak current of THP and promoted the electrochemical reaction of THP on the modified electrode. The optimal conditions of THP were optimized by using CV and DPV, such as pH, modification amount, resting time of electrochemical deposition, and scanning rate. Under the best conditions, the peak current of the modified electrode to THP and the concentration showed a good linear relationship in the range of  $5.2 \times 10^{-8}$ – $2.1 \times 10^{-5}$  mol/L, and the detection limit reached  $1.9 \times 10^{-7}$  mol/L, and in repeatability, stability, and interference tests, the results are satisfactory.

**4.2. Sample Recovery Analysis.** Prepare three groups of high-, medium-, and low-concentration drug model sample solutions, each group was tested in parallel for 5 times to calculate and analyze it. The results of the determination of the recovery rate of drug solutions with different concentrations are shown in Table 2.

According to the results in the table, the sample recovery rate of the drug models of each concentration is between 98.7% and 101.7%, and the relative standard deviation is between 2.18% and 3.36%. The UV-vis spectra of MP-1, MP-2, and MP-3 after adsorption of the drug model rutin and anacardiol are shown in Figure 2.

The analysis of the UV test results shows that the MP-1, MP-2, and MP-3 prepared have a certain amount of adsorption effect on the drug model, but the adsorption amount of each magnetic particle to the drug model is different, which is mainly caused by the magnetic property. The adsorption principle between particles and drug model molecules is different. MP-1 has a certain adsorption effect on drug model molecules. The main adsorption is physical adsorption. Second, there is a little  $Fe^{3+}$  on the surface of MP-1.  $Fe^{3+}$  can form a complex with catechol structure compounds through metal

TABLE 1: Comparison of electrochemical method with other THP determination methods.

Test method	The measuring object	Concentration range ( $\mu\text{M}$ )	LOD ( $\mu\text{M}$ )
LC-MS/MS	L-THP	$2.84 \times 10^{-4}$ –2.84	$2.84 \times 10^{-4}$
LC-ESI-MS	THP	$2.84 \times 10^{-3}$ –1.43	$2.81 \times 10^{-3}$
UPLC-FLD	L-THP and cocaine	$7.05 \times 10^{-3}$ –0.72	$7.05 \times 10^{-3}$
LC-QTQF/MS	(+)-THP and (-)-THP	$1.45 \times 10^{-2}$ –70.5	$1.45 \times 10^{-2}$
(CNTS/GCE) by SWV	THP	0.9–50.3	0.4
(NiNPs/SGS/GCE) by DPV	THP	0.51–20.3	0.19

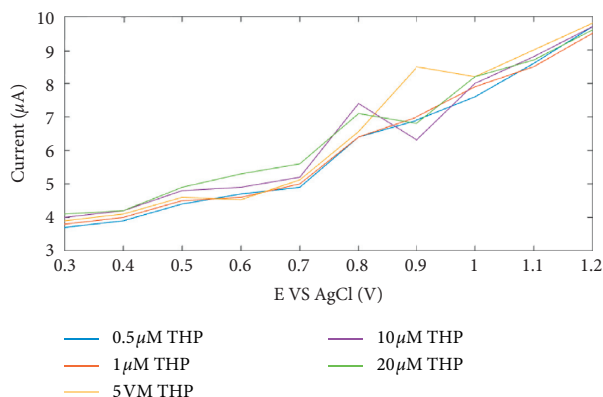
FIGURE 1: Differential pulse voltammetry of NiNPs/SGS/GCE at different concentrations of 0.5–20.0  $\mu\text{M}$  THP.

TABLE 2: Determination results of recovery rate of drug solution with different concentrations.

Sample	Added (mg/L)	Found (mg/L)	Recovery (%)	RSD (%)
Rutin	6.37	6.58	101.8	2.17
Rutin	15.16	14.92	98.8	3.17
Rutin	19.51	19.34	99.13	2.05
9.76	9.78	9.98	102.3	2.49
Rhoifolin	17.46	17.69	101.7	2.34
Rhoifolin	30.45	29.98	98.7	3.41

through metals. The site forms a complex and is adsorbed. The adsorption capacity of MP-3 to drug model molecules is much greater than that of MP-1 and MP-2 to drug model molecules. In addition to appealing the two adsorption effects, the most important adsorption is the effect caused by the boric acid modified on the surface of MP-3. Using the specific recognition effect of boric acid, the cyclic lactone structure is formed by the reversible covalent bond with the drug model molecule, so that the drug model is adsorbed and separated from the solution.

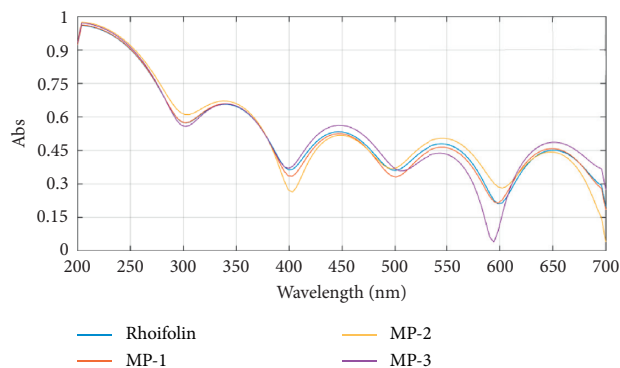


FIGURE 2: The UV-vis spectra of MP-1, MP-2, and MP-3 after adsorption of the drug model rutin and anacardin.

coordination. Compound MP-2, which has a certain adsorption effect on drug model molecules, adsorbs more on drug model molecules than MP-1, because it has rich  $\text{Fe}^{3+}$  on the surface of it, which can be matched with drug model molecules

4.3. Analysis of Magnetic Nanomaterials in Chinese Medicine Chemical Composition Analysis and Drug Metabolism and Its Industry Prospects and Development Path. The synthesis process of magnetic nanocomposites can be characterized by UV-vis absorption spectrum. The UV-vis absorption spectrum of centrifugal supernatant and PBA/G is shown in Figure 3.

After continuous washing/centrifugation cycles, the absorption peak of free PBA in the supernatant gradually weakened. After three washings, the absorption peak almost disappeared completely, indicating that free PBA molecules have been completely removed from PBA/G and PBA/NCNTs. At this time, the UV-vis spectra of PBA/G and PBA/NCNTs solutions still have obvious PBA absorption peaks. This shows that this method can successfully assemble PBA molecules on the surface of graphene and NCNTs. The carbon nanomaterials dispersed in the solution will reduce the light transmittance of the solution and increase the background. The modification of PBA molecules on NCNTs also reduced the redox peak on NCNTs/GC electrode. It can be seen that magnetic nanomaterials have practical value in the analysis of traditional Chinese medicine chemical

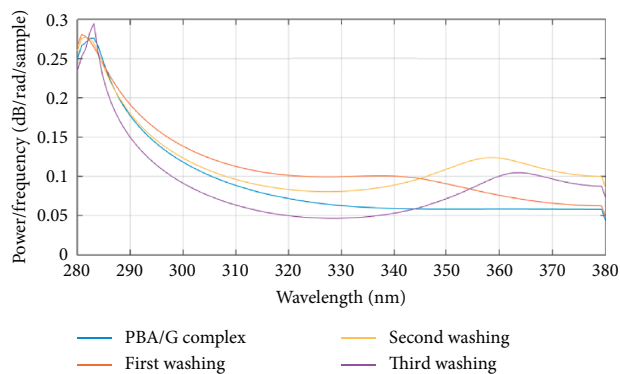


FIGURE 3: UV-vis absorption spectra of centrifuged supernatant and PBA/g.

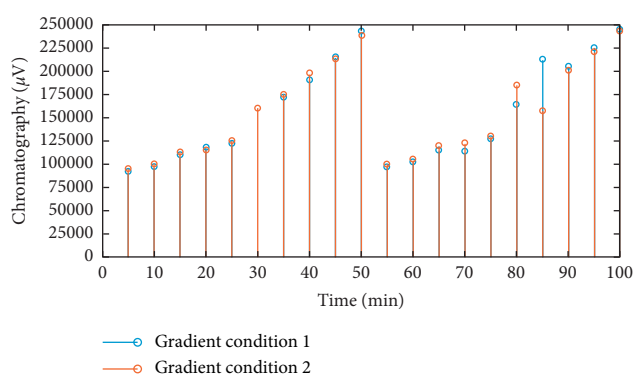


FIGURE 4: Comparison of chromatograms under two gradient conditions.

composition and drug metabolism, and magnetic nanomaterials have important research value for the industrial prospect and development path of traditional Chinese medicine chemical composition analysis.

**4.4. Optimization Analysis of Separation and Analysis Conditions of *Scutellaria baicalensis*.** The comparison results of the two gradient conditions chromatograms are shown in Figure 4.

It can be seen that the chromatogram analysis time of the gradient condition 1 is short, saving the use of mobile phase, and the separation effect is equivalent to the gradient condition 2, so the gradient condition 1 is selected as the *Scutellaria* chromatogram analysis condition. The molecular structure of baicalin contains orthophenolic hydroxyl- and carboxyl-like structures, baicalein molecular structure contains orthophenolic hydroxyl groups, and baicalin contains orthophenolic hydroxyl- and carboxyl-like structures, which can specifically adsorb to magnetic nanoparticles. However, baicalein only has metaphenolic hydroxyl groups and cannot specifically adsorb to magnetic nanoparticles. The volume ratio of *Scutellaria baicalensis* extract and magnetic nanoparticles is set to 5:1. The main components of *Scutellaria baicalensis* can be absorbed completely, saving the use of raw materials to the greatest extent, and the components in the desorption supernatant

contain hydroxyl and carboxyl groups. The specific adsorption capacity of phenolic hydroxyl and carboxyl groups was verified.

## 5. Conclusions

In this paper, the magnetic nanoparticles are used as the adsorption carrier, and the Chinese herbal medicine is the research object. The selective adsorption of alkylphenols, flavonoids, and cyclotriterpenoids was investigated. Through the analysis of the standard map and characterization results, we obtained the fact that magnetic nanoparticles have specific adsorption for orthophenolic hydroxyl and carboxyl groups and can desorb the target substance under the action of eluent to achieve the purpose of separation and purification. In this paper, new nanorod-like polymers are used as templates to synthesize magnetic nanoparticles. The polymer has abundant carboxyl groups, which provides a template for the synthesis of magnetic particles. After the synthesis is completed, the surface of the magnetic particles contains excess free carboxyl groups and the branched structure of the polymer, which can prevent the aggregation of particles. Suspension stability plays an important role in the suspension. This article combines the screening of the target of active ingredients of traditional Chinese medicine and the technology of phage display library to study the mechanism of active ingredients of traditional Chinese medicine on the molecular level and attempts to further study the mechanism of active ingredients of traditional Chinese medicine. In this paper, the preparation technology of nano new magnetic materials is organically integrated into medical technology, which provides a good research basis for the combination of magnetic nano medical technology. Aiming at the application of this material in chemiluminescence bioanalysis, combined with the current status of the industry in the central Yunnan city group, it is of great significance to the development prospects of the material industry. On the basis of the early industrial economic development research, combined with the practice of constructing a modern industrial system in Yunnan Province, China, it is found that the nanomaterial industry is a good breakthrough in the process of industrial transformation and upgrading of the central Yunnan urban agglomeration. It also provides a research basis for the analysis of magnetic nanomaterials in the analysis of chemical composition of traditional Chinese medicine and drug metabolism and its industrial prospect and development path. This article discusses the possibility of the integration of materials' chemistry and industrial development from the perspective of chemistry. In the author's research on the industrial development of the central Yunnan urban agglomeration in Yunnan Province, China, we will further study the interdisciplinary research of management science and engineering and chemistry.

## Data Availability

The data used to support the findings of this study are included within the article.

## Conflicts of Interest

The authors declare that there are no conflicts of interest regarding the publication of this paper.

## References

- [1] X. Chen and L. Zhang, "A review on micromixers actuated with magnetic nanomaterials," *Microchimica Acta*, vol. 184, no. 1, 11 pages, 2017.
- [2] A. H. Qi, A. Z. Li, A. H. Zheng, and Q. Jia, "Facile preparation of hydrophilic glutathione modified magnetic nanomaterials for specific enrichment of glycopeptides," *Chinese Chemical Letters*, vol. 30, no. 12, pp. 2181–2185, 2019.
- [3] D. Zhao, J. Li, and M. Wang, "Iron-based magnetic nanomaterials and their environmental applications," *Critical Reviews in Environmental Science and Technology*, vol. 46, no. 8, pp. 783–826, 2016.
- [4] H. Yamamoto, L. Seinberg, and H. Kageyama, "Low temperature synthesis of magnetic metal nanomaterials by using calcium hydride," *Journal of the Japan Society of Powder and Powder Metallurgy*, vol. 64, no. 4, pp. 147–154, 2017.
- [5] M. C. Pantilimon, C. I. Dragan, C. Gradinaru et al., "Morphological analysis of magnetic nanomaterials through comparative methods," *UPB Scientific Bulletin, Series B: Chemistry and Materials Science*, vol. 80, no. 3, pp. 175–182, 2018.
- [6] C. Song, L. ü Yi, and R. Wu, "Application prospect of nanomaterials mediated magnetic technology in the diagnosis and treatment of surgical diseases," *Chinese Science Bulletin*, vol. 65, no. 13, pp. 1251–1263, 2020.
- [7] M. I. Teremova, E. A. Petrakovskaya, A. S. Romanchenko et al., "Ferritization of industrial waste water and microbial synthesis of iron-based magnetic nanomaterials from sediments," *Environmental Progress & Sustainable Energy*, vol. 35, no. 5, pp. 1407–1414, 2016.
- [8] H. Fu, J. Hu, H. Y. Zhang et al., "Preparation of the magnetic mesoporous silica nanomaterials with formic acid solution as the medium and its adsorption properties," *Journal of East China University of Ence & Technology*, vol. 43, no. 2, pp. 207–212, 2017.
- [9] M. Lei, Q. Zhou, and Y. Liu, "Recyclable nanoscale zero-valent iron-based magnetic polydopamine coated nanomaterials for the adsorption and removal of phenanthrene and anthracene," *Science and Technology of Advanced Materials*, vol. 18, no. 1, pp. 3–16, 2017.
- [10] C. R. Laili and S. Hamdan, "Heating behaviour of iron oxide nanomaterials via magnetic nanoparticle hyperthermia," *Asian Journal of Chemistry*, vol. 28, no. 12, pp. 2675–2679, 2016.
- [11] D. J. Yue, Y. Jin, and D. J. Sellmyer, "Effect of boron addition on magnetic-domain structure of rapidly quenched Zr<sub>2</sub>Co<sub>11</sub>-Based nanomaterials," *MRS Advances*, vol. 1, no. 34, pp. 2379–2385, 2016.
- [12] R. Olsson, P. Aadal Nielsen, and F. Ek, "An ex vivo model for evaluating blood-brain barrier permeability, efflux, and drug metabolism," *ACS Chemical Neuroscience*, vol. 7, no. 5, pp. 668–680, 2016.
- [13] K. K. Filipiski, M. A. Pacanowski, and A. N. Freedman, "Dosing recommendations for pharmacogenetic interactions related to drug metabolism," *Pharmacogenetics and Genomics*, vol. 26, no. 7, pp. 334–339, 2016.
- [14] M. A. López-García, I. A. FERIA-Romero, H. Serrano et al., "Influence of genetic variants of CYP2D6, CYP2C9, CYP2C19 and CYP3A4 on antiepileptic drug metabolism in pediatric patients with refractory epilepsy," *Pharmacological Reports*, vol. 69, no. 3, pp. 504–511, 2017.
- [15] A. A. Oyagbemi, D. Bester, J. Esterhuysen et al., "Evaluating the role of drug metabolism and reactive intermediates in trazodone-induced cytotoxicity toward freshly-isolated rat hepatocytes," *Drug Research*, vol. 66, no. 11, pp. 592–596, 2016.
- [16] X. Tang, Q. Zhang, and Z. Lu, "Identification of chemical constituents in traditional Chinese medicine formula using HPLC coupled with linear ion trap-orbitrap MS from high doses of medicinal materials to equivalent doses of formula: study on Xiang-Sha-Liu-Jun-Zi-Jia-Jian granules," *Journal of Separation Science*, vol. 39, no. 9, pp. 1619–1627, 2016.
- [17] Y. Sugihara, K. I. Watanabe, and A. Végvári, "Novel insights in drug metabolism by MS imaging," *Bioanalysis*, vol. 8, no. 6, pp. 575–588, 2016.
- [18] X. Fan, K. Luo, and S. Xiao, "Qualitative analysis of chemical constituents in traditional chinese medicine analogous formula cheng-Qi decoctions by liquid chromatography-mass spectrometry," *Biomedical Chromatography*, vol. 30, no. 3, pp. 301–311, 2016.
- [19] C. Swart and C. Dandara, "MicroRNA mediated changes in drug metabolism and target gene expression by efavirenz and rifampicin in vitro: clinical implications," *OMICS: A Journal of Integrative Biology*, vol. 23, no. 10, pp. 496–507, 2019.
- [20] M. A. Ladda and K. B. Goralski, "The effects of CKD on cytochrome P450-mediated drug metabolism," *Advances in Chronic Kidney Disease*, vol. 23, no. 2, pp. 67–75, 2016.
- [21] D.-C. Hao and P.-g. Xiao, "Impact of drug metabolism/pharmacokinetics and their relevance upon traditional medicine-based cardiovascular drug research," *Current Drug Metabolism*, vol. 20, no. 7, pp. 556–574, 2019.
- [22] G. M. M. Groothuis, S. Vatakuti, and B. H. Schievink, "Maintenance of drug metabolism and transport functions in human precision-cut liver slices during prolonged incubation for 5 days," *Archives of Toxicology*, vol. 91, no. 5, pp. 2079–2092, 2016.
- [23] K. Thiengsusuk, K. Boonprasert, and K. Na-Bangchang, "A systematic review of drug metabolism studies of plants with anticancer properties: approaches applied and limitations," *European Journal of Drug Metabolism and Pharmacokinetics*, vol. 45, no. 2, pp. 173–225, 2020.

## Research Article

# Enzyme Producing Activity of Probiotics and Preparation of Compound Enzyme

Ruokun Yi,<sup>1</sup> Yanni Pan,<sup>1</sup> Xingyao Long,<sup>1</sup> Fang Tan <sup>2</sup> and Xin Zhao <sup>1</sup>

<sup>1</sup>Chongqing Collaborative Innovation Center for Functional Food, Chongqing Engineering Research Center of Functional Food, Chongqing Engineering Laboratory for Research and Development of Functional Food, Chongqing University of Education, Chongqing 400065, China

<sup>2</sup>Department of Public Health, Our Lady of Fatima University, Valenzuela 838, Philippines

Correspondence should be addressed to Fang Tan; [tanfang@foods.ac.cn](mailto:tanfang@foods.ac.cn) and Xin Zhao; [zhaoxin@cque.edu.cn](mailto:zhaoxin@cque.edu.cn)

Received 15 July 2020; Revised 15 August 2020; Accepted 8 September 2020; Published 30 September 2020

Academic Editor: Tifeng Jiao

Copyright © 2020 Ruokun Yi et al. This is an open access article distributed under the Creative Commons Attribution License, which permits unrestricted use, distribution, and reproduction in any medium, provided the original work is properly cited.

Probiotics are a group of active microorganisms, which benefit the host by colonizing and changing the composition of host flora. It is of great significance to promote the development of human gastrointestinal nutrition and health by regulating the host mucosal and systemic immune function or regulating the balance of intestinal flora. The purpose of this study is to analyze the production activity of the enzyme, evaluate its biological characteristics and safety as a preventive drug, and provide reference for the research of enzyme production and compound enzyme preparation by probiotics. In this study, four groups of probiotics were set up: *Clostridium butyricum* experimental group, *Lactobacillus plantarum* experimental group, drinking water control group, and *Bacillus licheniformis* experimental group. In addition, a variety of complex enzyme experiments were set up to study the influence on the digestive tract and single factor experiment. The results showed that probiotics and compound enzyme preparations could significantly promote the intestinal digestibility. Under the effect of probiotics, the weight of the chicken was almost 1 Jin heavier than that of the control group, and the average digestibility was increased by 4.3%. The effect of the enzyme on digestibility is stronger than that of probiotics, but the final effect tends to be stable.

## 1. Introduction

**1.1. Background and Significance.** With the increasing serious problems of antibiotic resistance and antibiotic residues, it has become a global research topic to develop green feed additive products which can replace antibiotics. Microbial agents can supplement, adapt, and maintain the balance of intestinal microorganisms, which can be used for disease prevention and treatment, promoting health, and enhancing productivity. In recent years, the mushroom technology in China has developed rapidly, and the large-scale industrial production has gradually developed. The quantity of residual substrate mushroom bran increased rapidly after harvest. The fungus bran was rich in mycelium and rich in nutrients. The rational utilization of edible fungus bran became an urgent problem in the edible fungus industry, and the production of probiotics from mushroom bran provided a solution.

**1.2. Related Work.** The role of probiotics in reducing gastrointestinal inflammation and preventing colorectal cancer has been widely confirmed. However, the immunomodulatory effect of probiotics on the growth of extraintestinal tumors and its mechanism are still unclear. Here, Li used a mouse model and genome sequencing to study the efficacy of probiotic feeding in controlling liver cancer and the potential mechanism of inhibiting tumor progression. Prohep is a new probiotic mixture, which can significantly slow down the growth of tumor and reduce the tumor volume and weight by 40% compared with the control group. From the point of view of mechanism, the levels of IL-17 cytokines and their main producer Th17 cells decreased sharply, which played a key role in tumor reduction after probiotics feeding. Cell staining showed that the main reason for the decrease of

Th17 cells in the probiotics treatment group was the lower migration frequency of Th17 cells in intestinal and peripheral blood [1].

In order to study the probiotic colonies, Tanaka established an optimized fluorescence in situ hybridization (FISH) method to detect and count the host borne probiotics in abalone intestines. The samples were fixed with 4% paraformaldehyde and hybridized with TAMRA-labeled probe (RPT probe) at 40°C for 3 hours. Strain Ab1 is obviously different from other control bacteria (*Enterococcus*, *Lactobacillus*). The fluorescence signal of RPT positive bacteria can be easily distinguished from any detectable background noise. RPT positive bacteria were detected in both probiotics and control abalone, but the number of RPT positive bacteria in abalone with probiotics was two orders of magnitude higher than that of the control. In addition, the average number of RPT positive bacteria in the intestinal attachment zone (abalone supplemented by probiotics) was two orders of magnitude higher than that in the free living area. A single colony from each group was identified by the biochemical method (id32c system) and molecular biological method (sequencing of D1/D2 domain of 26srDNA and its 1-5.8-its2rdna region). Both methods can identify candida. The cytotoxicity, adhesion, surface properties, hemolytic activity, and survival rate of famata strain Y5 in simulated gastrointestinal environment were studied [2].

To isolate probiotics from pig intestines, Balasingham collected 63 isolates (24 caeca, 24 colonic mucosal scraps, and 15 rectal swabs) from Yorkshire pigs. The isolate was inoculated in Man Rogosa Sharpe broth at 37°C and 5% CO<sub>2</sub> for 48 hours, and morphological identification was performed. The colony with gram positive bacilli was selected for further physiological and biochemical identification test. Each selected isolate was tested twice and three times with the standard protocol. The probiotic characteristics among the identified species were determined through a number of tests related to pH tolerance, bile tolerance, and antimicrobial activity. Morphological identification showed that only 23 strains of gram positive bacilli were detected. Physiological tests on these 23 strains further showed that four of them did not show any growth under all the studied conditions. The remaining 19 strains were detected by biochemical methods [3].

**1.3. Innovation.** Using the method of single factor experiment, this paper studies the  $\beta$ -amylase, acid protease, and neutral protease which have good effect in industry at present, and their functions in reducing sugar content and digestibility of digestive tract, etc., and roughly determines the best kind and dosage of enzymes. Then, response surface methodology was used to optimize the selected enzymes and develop a new composite enzyme.

## 2. Function of Probiotics and Enzymes

**2.1. Compound Enzyme Preparation.** Compound enzyme preparation is one or more preparations of a single enzyme as the main body being mixed or fermented with other single

enzyme preparation to form one or more microorganisms [4]. There are many factors that affect the digestibility of specific nutrients. They are not only related to animal species, age, and normal period but also related to food composition and processing technology. According to the digestion characteristics and feed composition of different livestock and poultry, specific enzyme preparation can be prepared for different animals and poultry. Different kinds of food may also form different specific enzymes [5]. The use of specific complex enzyme preparation can degrade a variety of food substrates (a variety of antinutrients and a variety of nutrients), and different kinds of enzymes also have synergistic effect, which can maximize the nutritional value of food [6].

At present, the enzyme feed preparations commonly used in livestock and poultry production can be divided into the following categories according to their functional characteristics: (1) compound feed enzymes mainly composed of protein and amylase, which are mainly used to supplement the deficiency of congenital enzymes. (2) Compound feed enzyme mainly composed of  $\beta$ -glucanase and xylanase. This enzyme preparation is mainly used in the feed with grains as the main raw material, such as barley, oats, wheat, and rye, in order to neutralize the antinutritional effect of NSP. (3) Cellulose and pectinase are the main enzymes in compound food. This enzyme is mainly produced by trichoderma, aspergillus, and penicillium. Its main function is to destroy the plant cell wall, release nutrients to the cells, easily contact with digestive enzymes, eliminate antinutritional ingredients in the diet, and reduce the viscosity of gastrointestinal contents and promote digestion and absorption of animals. (4) Feed enzyme is composed of cellulose, protease, amylase, glucoamylase, glucanase, and pectinase. This compound enzyme preparation combines the common characteristics of these enzyme systems and has good nutritional effect [7, 8].

**2.2. Probiotics.** From the beginning of human civilization, fermented milk may have become the first food containing active microorganisms. The concept of probiotics comes from Latin, meaning life. It is produced by organic substances, and the substances can stimulate the development of another substance [9]. Later, after continuous exploration by experts and researchers, it was defined as a kind of sustainable substance, which can be properly added, harmless to animals, and can ensure the health of animals [10]. As probiotics, they must meet the following conditions: (1) they must be able to survive in the intestinal transport. (2) They must be able to adhere to the animal surface, the mucous membrane and its colonization in the gut. (3) In the process of survival, they must resist the external environment. (4) They must be safe and harmless to animals. (5) It turns out to be good for animals. (6) Taxonomic identification was carried out in genera, species, and strains. Conclusions of the current requirements are *Bifidobacterium*, *Bacillus*, and yeast [11, 12].

**2.3. Research Methods of Enzyme Producing Activity of Probiotics.** At present, researchers have carried out a large number of in vitro and in vivo experiments to confirm that

probiotics have a high antioxidant effect [13]. The antioxidant effects of probiotics are as follows: reactive oxygen species and free root scanning, metal chelating ions, oxygen reduction control system in preventive agents, activation of antioxidant system, reduction of metabolic capacity after absorption by the body, and lipid lowering effect [14]. At present, the research on antioxidant activity of disease prevention drugs mainly focuses on the scanning ability of free roots and the detection of antioxidant enzyme activity. Among them, the most extensive research involves the activity of antioxidant enzymes derived from probiotics. For example, peroxide disulfide (SOD) can eliminate free roots in the body, while aniline peroxide can produce water [15]. Catalase (CAT) is a porphyrin-binding enzyme containing iron. Its main function is to participate in the active metabolism of oxygen and scavenge hydrogen peroxide produced in the process of metabolism. The main enzyme systems in vivo are SOD, CAT, and glutathione peroxidase [16, 17].

In addition to producing antioxidant-related enzymes, probiotics also have other enzyme-related functions. Probiotics can reduce cholesterol, which is directly related to the production of bile salt hydrolase. Bile salt hydrolase can combine with the cholate solution to reduce serum cholesterol [18]. A strain of *Lactobacillus casei* can produce cholesterol hydrolase, and its cholesterol degrading ability can reach 35.74%. *Lactobacillus plantarum* contains bile salt lyase gene and produces bile salt hydrolase. In addition, studies have shown that some prebiotics, such as *Lactobacillus reuteri* and *Bacillus*, can produce amylase [19, 20]. In addition, prophylactic drugs may also produce enzymes related to lactose reduction, among which  $\alpha$ -lactosidase can hydrolyze nonreducing lactose glycosidase compounds related to bonds, and  $\beta$ -lactosidase can catalyze the decomposition of lactose into one molecule of glucose and one molecule of lactose to achieve the result of lactose cleavage.

*Lactobacillus fermentans* can produce  $\alpha$ -lactose, and its maximum enzyme activity is 21.38 u/ml. *Lactobacillus fermentans* and *Bifidobacterium longum* can produce  $\alpha$ -lactose, and the enzyme activity can reach 22.41 u/ml. Many studies have shown that *Lactobacillus bulgaricus* can produce  $\beta$ -lactose. Finally, a high-yield  $\beta$ -lactose strain was obtained from Yunnan Tempe samples, which was identified as *Lactobacillus brevis* [21]. In conclusion, probiotics can produce antioxidant-related enzymes during development and reproduction. Among them, there are many researches on SOD, and the activity of SOD produced by different preventive drugs is significantly different. In addition to producing enzymes related to antioxidants, probiotics may also produce other enzymes related to normal function [22].

**2.4. Function of Feed Enzyme.** The cell wall of wheat food is rich in protein, lipids, and polysaccharides without starch. These substances are linked to various chemical bonds, such as peptide bonds. The digestive enzymes in the digestive tract of monogastric animals cannot decompose polysaccharides without starch. Protein and starch in cells are released from cells by preparing nonstarch polysaccharide enzymes, which

destroy the structure of the plant cell wall and participate in the normal metabolism of the body. Cellulose can significantly improve the digestibility of cell wall components, increase the dissolution rate of minerals, improve the production efficiency of chicken, and improve the utilization rate of nutrients [23].

Many metabolites in feed cannot be hydrolyzed by endogenous enzymes. These metabolites have antinutritional effects on animals and prevent the digestion and utilization of nutrients such as protein, fat, and starch. For feeds that have antinutritional effects on animals, such as nonstarch polysaccharides, phytic acid, phytosanitary hemolysin, and protease inhibitors [24], enzyme preparations can partially or completely eliminate the antinutritional effects of antinutrients and improve feed utilization. Adding the nonstarch polysaccharide enzyme and protein and planting enzyme preparation in the diet can significantly improve the utilization rate of nutrients and improve livestock and poultry production efficiency, reduce environmental pollution, and improve economic benefits [25].

### 3. Experimental Design and Analysis

**3.1. Preparation of Materials.** There were four groups of probiotics, including CG in the drinking water control group, KJT of *Lactobacillus plantarum*, DSSJ of *Clostridium butyricum*, and DB of *Bacillus licheniformis*. Lactating chickens come from a farm in Zhejiang Province, and their feed is provided by a vegetable market in Zhejiang Province.

Before the experiment, the chickens were starved for eight hours. When slaughtering, they need to be put on a board, their heads are cut off and killed, and then they are dissected quickly, the gastrointestinal tract is removed, and the whole digestive system separates the two parts of the intestine in the stomach with scissors. The tissue samples were cut with scissors, and part of the connective tissue was removed and washed with cold saline water to remove the remaining contents. Filter paper is used to absorb the water on the surface, and 5 times the volume of cold brine solution is weighed and added. After homogenization, it is used and centrifuged at the speed of 1200 R/min on the ultralow temperature high-speed freezing centrifuge. After the supernatant was taken, it was the original enzyme solution, which was frozen and stored at 30°C. The frozen samples should be avoided to prevent from affecting the enzyme activity.

**3.2. In Vitro Digestion Experiment.** First, the weighing dish was dried in an oven at 530°C to the weight of the solid and it was weighed. About 2 g of the feed sample was weighed, it was put in the weighing dish and dried for 3 hours, it was transferred to the dryer to cool for half an hour, and it was weighed, it was put in the oven for 45 minutes, and it was moved to the dryer to cool for 20 minutes. Drying was repeated until the weight remains unchanged. The mass lost during drying is the weight of water. The dried feed sample was put into a 100 ml conical flask, 10 ml of homogeneous raw stomach enzyme solution was added, and then 10 ml PBS adjustable solution was added. The pH was adjusted to about 3 with HCl, and then 2 ml of 60 u/ml penicillin was

added, once every hour. After adding the rubber cover, the rubber cover was placed in a 25°C constant temperature shaker for 60 times/min and shaken for 2 hours. In the second stage, the conical flask from the shaking table was taken out, sodium hydroxide solution was added, the pH of the system was adjusted to about 6.5, and then 20 ml of intestinal homogenate enzyme solution, 15 ml of PBS adjustable solution, and finally 2 ml of 60 u/ml streptomycin were added, once every two hours. After the rubber cap was added, it was placed in a thermostatic stirrer at 25°C for 60 times/min for 8 hours. In the third stage, 1 ml of 35% trichloroacetic acid was added to the cone, and the enzyme reaction was stopped for 20 minutes. Then, the residue was washed with ethanol and acetone, respectively, with quantitative filter paper of known quality, and the residue was collected and dried and weighed.

**3.3. Test Index.** Preparation of the reducing sugar curve: 3 ml acetic acid and sodium acetate control solution were absorbed, 2 ml Idns reagent was added and heated in boiling water for 8 minutes, cooled with tap water at room temperature and added 20 ml distilled water to make a typical blank sample. Glucose standard solution with concentrations of 0.3–0.5 mg/ml was prepared by diluting glucose solutions of 1, 2, 3, 4, and 5 ml pipettes to 50 ml with sodium acetate and acetic acid, respectively. 100 ml each of the above standard glucose solutions in the above concentration sequence (two parallel) into the calibration tube were put, and then 1 ml acetic acid, sodium acetate, and 4 ml Idns reagent were added. Electromagnetic oscillation for 3S and heating in boiling water for 5 minutes were done. After that, the samples were cooled with tap water at room temperature; distilled water was added to 30 ml volume, and the OD absorption value was determined at 380 nm. The standard curve was drawn ( $y = ax + b$ ).

After enzymolysis, the sample was filtered into an 80 ml volumetric flask under vacuum. 1 ml of the solid volume filter was taken and 3 ml of acetic acid was added. Sodium acetate adjustable solution and reagent 4 ml LDNS is mixed and boiled in boiling water for 10 minutes. Then, it was diluted to 30 ml with distilled water. After mixing, the color was compared with 380 nm. The content of reducing sugar was calculated. The blank control group was added with 1 ml water, 3 ml acetic acid, and 4 ml sodium acetate-regulating solution. The net yield of reducing sugar = the amount of reducing sugar produced in the enzyme solution – the amount of reducing sugar produced in the blank solution. The compound enzyme after enzymatic hydrolysis of the feed sample is measured. Measurement method: the residue was filtered and digested under vacuum, and finally it was dried to constant weight with nitrogen-free filter paper of known weight in an oven at 100°C, and then the energy value of the residue was weighed and measured.

**3.4. Experimental Theory.** When analyzing and studying the relationship between experimental data, the relationship between any two variables is called correlation. The correlation among test data includes linear correlation,

exponential correlation, and arithmetic correlation. Among them, linear association is the simplest and the most studied one. Other different associations can also be transformed into linear association through specific transformation. The reliability of the results of this study is based on the statistical analysis method of correlation analysis. The experiments of four probiotics and a variety of enzymes on chickens were carried out, and the relationship between them was discussed. In this paper, Pearson correlation factor is calculated by linear correlation analysis. The Pearson correlation factor is used to measure whether all data points belong to a straight line, that is, the description of the correlation between two variables. The calculation formula is as follows:

$$r = \frac{N \sum x_i y_i - \sum x_i \sum y_i}{\sqrt{N \sum x_i^2 - (\sum x_i)^2} \sqrt{N \sum y_i^2 - (\sum y_i)^2}} \quad (1)$$

The Pearson correlation coefficient is between –1 and 1. When the correlation coefficient approaches –1 to 1, the stronger the correlation is, the weaker the correlation will be. Results belonging to 0.8–1 means extremely strong correlation; results belonging to 0.6–0.8 indicate strong correlation; results belonging to 0.4–0.6 indicate moderate correlation; results belonging to 0.2–0.4 indicate weak correlation; and results belonging to 0–0.2 indicate extremely weak correlation or no correlation.

## 4. Influence of Probiotics and Compound Enzyme

**4.1. Test Results of Chicken Growth Performance.** Four experimental groups were set up: control group CG with drinking water, KJT with *Lactobacillus plantarum*, DSSJ with *Clostridium butyricum*, and DB with *Bacillus licheniformis*, and each experimental group was tested three times to ensure the accuracy of the experiment. The experimental data are shown in Table 1.

For these experimental objects, the weight of these chickens was detected at 5 days, 10 days, and 15 days respectively, and the weight of these chickens in the corresponding time period was recorded, so as to analyze the influence of different weights produced by different probiotics, as shown in Figure 1.

In the figure, we can clearly see the weight change of the chicken. In these 15 days, the weight gain of the experimental group of *Clostridium butyricum* was the most obvious, and the weight was as high as 1.16 Jin, and in 5 days, 10 days, and 15 days of these three periods are the heaviest weight, with the average daily gain of 0.39 Jin. The results of the *Lactobacillus plantarum* experimental group and *Clostridium butyricum* experimental group had no significant difference, which were within 0.1 Jin, and had great effect on weight, with an average weight gain of 0.3 Jin. The weight gains of the control group with only drinking water were 1.38, 1.47, and 1.63 Jin, respectively, which were the least weight gain group, and the difference between the two groups was significant. The weight gains of *Bacillus licheniformis* experimental group were 1.5, 1.81, and 2.42 Jin,

TABLE 1: Test results of growth performance.

Experiment	Group	Repeat	Treating
1	CG	3	Drinking water
2	KJT	3	Drinking water + 0.3% <i>Lactobacillus plantarum</i>
3	DSSJ	3	Drinking water + 0.3% <i>Clostridium butyricum</i>
4	DB	3	Drinking water + 0.3% <i>Bacillus licheniformis</i>

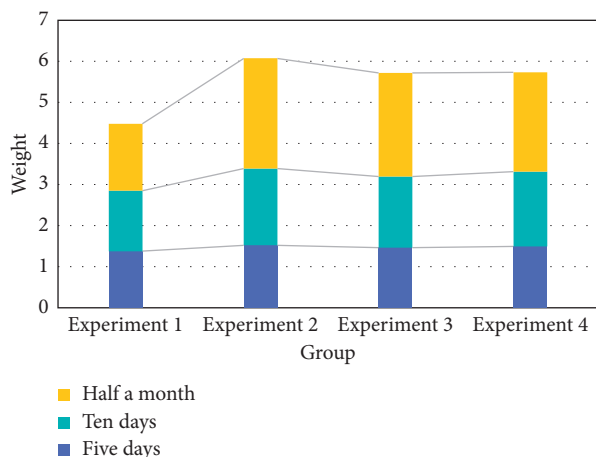


FIGURE 1: Weight change pattern.

respectively. Although the effect of probiotics was not obvious in the other two groups, it still had great advantages compared with the control group.

**4.2. Apparent Digestibility of Compound Enzyme Preparation in the Terminal Ileum and Total Digestive Tract (%).** The compound enzyme, which is mainly composed of cellulose and pectinase, may destroy the plant cell wall, release nutrients in the cells, easily contact with digestive enzymes, and eliminate antinutrients in diet, so as to reduce food viscosity and gastrointestinal contents and promote animal digestion and absorption. If the rate of gastric emptying slows down and the amount of digestive juice discharged per unit time decreases, the digestion of nutrients is limited, as shown in Figure 2.

As can be seen from the figure, most of the available nutrients in the food have been released before they enter the animal body. On the other hand, the decrease of the geometric mean size of food may also increase the intestinal digestibility. In four groups of experiments, the ileum terminal, dry matter, crude protein, and organic compounds were detected. Under the condition of drinking water, the digestibility of these four substances were 67.8%, 72.3%, 54.1%, and 70.4%, respectively. In the third group, the digestibility was the highest, 78.3%, 80.2%, 63.8%, and 79.1%, respectively. The excellent digestive system also led to the heaviest weight of this chicken. Secondly, the digestive capacity of the second group was catalyzed by *Lactobacillus plantarum*, and the last group was *Bacillus licheniformis*. From the data in the figure, we can not only see the influence of the four probiotics on the digestibility but also find the digestibility performance of the four probiotics in the terminal ileum and the whole digestive tract. The digestibility of

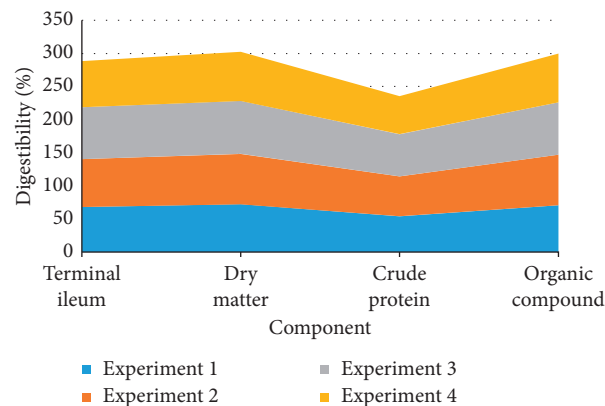


FIGURE 2: Apparent digestibility.

the dry matter and organic compounds is the best, with the digestibility of above 70%, while the crude protein is the worst, with the digestibility of about 50%–60%.

**4.3. Effect of  $\beta$ -Amylase on the Digestive Tract.** After saccharification experiment with  $\beta$ -amylase, the content of reducing sugar was measured every 1 hour, the relationship between the reduction of sugar in the intestinal tract and the change of time and the relationship between the content of reducing sugar and the amount of  $\beta$ -amylase, as shown in Figure 3.

With the passage of time, the content of reducing sugar in the intestinal tract increased significantly in the process of 1–3 hours, indicating that  $\beta$ -amylase has a certain catalytic effect on the degradation of starch in the process of reducing sugar, and the content of reducing sugar slightly increased on both sides of 3–4 h, but not obviously. This may be related to the total amount of residues in the intestine. With the increase of saccharification time, the content of reducing sugar increased slightly, indicating that saccharification was basically mature. Assuming that the amount of  $\beta$ -amylase increases, the sugar rate of the sample will increase, thus increasing the content of reducing sugar in the solution. In the initial stage of the saccharification process, the  $\beta$ -amylase must maintain sufficient activity under certain conditions, while the initial stage of saccharification cannot provide proper temperature and pH environment for  $\beta$ -amylase two hours before the beginning of saccharification, so the content of reducing sugar in the reaction solution has little change. As the reaction time goes on, when the reaction time is long enough to 3 hours, the reducing sugar content in the reaction solution will increase rapidly, especially, when the enzyme concentration in the reaction solution increases, the rate at which the sugar content decreases also increases.

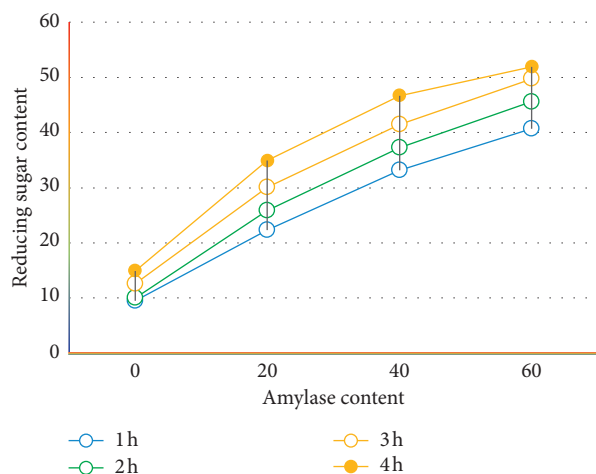


FIGURE 3: Change of reducing sugar content.

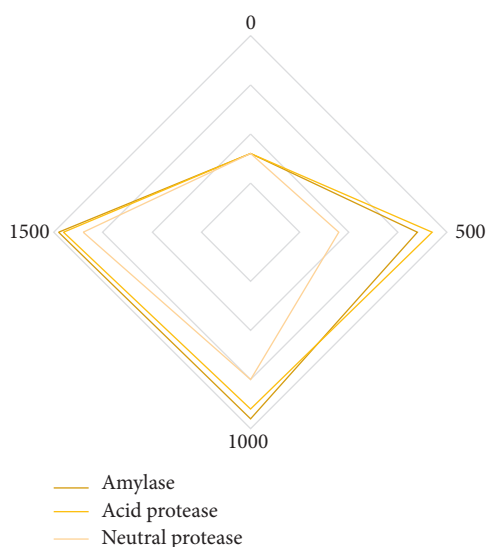


FIGURE 4: Single factor experiment.

When the concentration of  $\beta$ -amylase in the reaction solution is 30 U/g, the yield of reducing sugar reaches the maximum value, so the optimal addition amount of  $\beta$ -amylase is 30–40 u/g.

**4.4. Single Factor Experiment.** In the single factor experiment, amylase, acid protease, and neutral protease should be added into the conical flask, respectively, and the enzyme contents are 500, 1000, and 1500 (U/g). Then, the experimental results obtained from the three groups of data are detected, respectively. The *in vitro* digestibility is affected by different enzyme types and different contents, as shown in Figure 4.

From the data in the figure, it can be seen that the feed digestibility of the enzyme group is higher than that of the control group. The general trend of adding enzyme preparation is rapidly increased and then tend to be gentle, but on the whole, it is gradually increasing. The digestibility of amylase increased from 16% to 39% with the increase of the

enzyme content. The digestibility of acid protease increased from 16% to 38%. The digestibility of neutral protease at 1500 (U/g) was 34%. If the enzyme was added later, the digestibility would increase. The enzyme activity will be seriously affected by temperature, too low or too high will make the enzyme lose activity; when the temperature is most appropriate, the enzyme activity is the highest, the impact on digestibility is the best, and the ability to promote digestion is the strongest.

## 5. Conclusions

The intestinal tract of chicks is aseptic at birth. After birth, with the environmental contact of lactation and delivery clinic, foreign bacteria gradually enter into the intestine. After attachment and colonization, the intestinal flora is created to maintain its own intestinal microecological balance. Therefore, *Lactobacillus* and other beneficial bacteria are used to complete infant breast-feeding so that the beneficial bacteria occupy the effective position of the intestinal tract earlier, which has an absolute advantage in quantity and action intensity, effectively inhibit the attachment of other pathogenic bacteria to the site, and effectively prevent the generation and invasion of harmful bacteria. Compound probiotics is an important antibacterial compound. Lactic acid production can reduce the intestinal pH value and inhibit the growth of pathogenic bacteria such as *Escherichia coli* and *Salmonella*. By consuming oxygen, *Bacillus* creates an environment conducive to the growth of anaerobes (such as lactic acid bacteria and *Bifidobacteria*) or anaerobic bacteria and prevents the reproduction of *Escherichia coli* and *Salmonella*, and maintains the balance of intestinal flora to prevent the occurrence of diseases. The bacteria and lactic acid bacteria in the compound preparation can produce rich digestive enzymes, organic acids, and vitamins.

Enzyme preparation is a kind of safe, reliable, and pollution-free green feed additive. It has the ability of biocatalysis reaction, which can improve the production efficiency of livestock and poultry, reduce environmental pollution, and save animal feed resources. Enzyme preparation can improve the utilization rate of feed and raw materials by decomposing the antinutritional agents in feed and affect the digestion and metabolism of animals. The flora found in the digestive tract is considered a new nutrient because it is closely related to the health of host diseases, metabolism, and regulation of the immune system. They allow the host to increase the absorption of nutrients and affect energy intake. Studies have shown that there are many factors affecting the distribution and stability of intestinal microflora, such as the changes of environment, seasons, and the role of food additives, so that the intestinal microorganisms affect the development of animals to a certain extent. As a kind of food additive, probiotics play a beneficial role in the intestinal flora. The addition of probiotics can help the host control harmful bacteria and have beneficial effects on intestinal flora. In addition, probiotics can also regulate the immune system to fight against various diseases to produce resistance to diseases.

The evaluation methods of the enzyme nutritional value of compound feed mainly include the in vivo method and in vitro method. The in vivo method is an animal feeding test and metabolism test, also known as the biological method. This is a logical and scientific test method, but it costs a lot of manpower and time. It is seriously affected by external factors (climate, environment, human function, etc.) and it is not easy to evaluate a large amount of feed or food in a short time. The in vitro method was used to simulate the digestive system of monogastric animals to evaluate the nutritional value of food. The method is rapid, simple, labor-saving, and time-saving. In this experiment, the effects of probiotics and complex enzymes on the chicken digestive tract were studied by using this technology. The net yield of reducing sugar and the total energy of the digestive tract residue were taken as indexes. The results showed that the compound enzyme preparation and probiotics played an important role in the growth and development of the chicken.

### Data Availability

No data were used to support this study.

### Conflicts of Interest

The authors declare no conflicts of interest.

### Authors' Contributions

Ruokun Yi performed the majority of the experiments and wrote the manuscript. Yanni Pan and Xingyao Long contributed to the data analysis. Xin Zhao and Fang Tan designed and supervised the study and checked the final manuscript.

### Acknowledgments

This research was funded by the Children's Research Institute of National Center for Schooling Development Programme and Chongqing University of Education (CSDP19FS01103), the Science and Technology Research Program of Chongqing Municipal Education Commission (KJZD-K201901601), and Research Project of Chongqing University of Education (KY2015TBZC), China.

### References

- [1] J. Li, N. Sung, Y. Ni, G. Panagiotou, and H. El-Nezami, "Probiotics modulated gut microbiota suppresses hepatocellular carcinoma growth in mice," *Proceedings of the National Academy of Sciences*, vol. 113, no. 9, pp. E1306–E1315, 2016.
- [2] R. Tanaka, M. Aoki, T. Miyazaki, H. Mitsuya, M. Ootsubo, and P. Bossier, "In situ enumeration and localization of the probiotic *Pediococcus* sp. strain Ab1 in the gut of abalone *Haliotis gigantea*," *Fisheries Science*, vol. 82, no. 3, pp. 481–489, 2016.
- [3] K. Balasingham, L. Radhakrishnan, C. Valli, and D. Balasuramanyam, "Probiotic characterization of lactic acid bacteria isolated from swine intestine," *Veterinary World*, vol. 10, no. 7, pp. 825–829, 2017.
- [4] L. Jacobs, "Probiotics, prebiotics, and synbiotics," *Journal of Pediatric Surgical Nursing*, vol. 6, no. 3, pp. 53–55, 2017.
- [5] R. R. Watson and V. R. Preedy, "Probiotics, prebiotics, and synbiotics," *Journal of Food Ence & Technology*, vol. 52, no. 12, pp. 7577–7587, 2015.
- [6] M. Panduru, N. M. Panduru, C. M. Sălăvăstru, and G.-S. Tiplica, "Probiotics and primary prevention of atopic dermatitis: a meta-analysis of randomized controlled studies," *Journal of the European Academy of Dermatology and Venereology*, vol. 29, no. 2, pp. 232–242, 2015.
- [7] C. A. Cuello-Garcia, J. L. Brożek, A. R. Fiocchi et al., "Probiotics for the prevention of allergy: a systematic review and meta-analysis of randomized controlled trials," *Journal of Allergy and Clinical Immunology*, vol. 136, no. 4, pp. 952–961, 2015.
- [8] K. Chau, S. E. Lau, S. Greenberg, P. Yazdani-Brojeni, S. Jacobson, and G. Koren, "Probiotics for infantile colic: a randomized, double-blind, placebo-controlled trial investigating *Lactobacillus reuteri* DSM 17938," *The Journal of Pediatrics*, vol. 166, no. 1, pp. 74–78, 2015.
- [9] P. D. Cani and M. Van Hul, "Novel opportunities for next-generation probiotics targeting metabolic syndrome," *Current Opinion in Biotechnology*, vol. 32, no. 32, pp. 21–27, 2015.
- [10] C. Hicks, S. Moore, and A. Andrade, "Probiotics for the prevention of antibiotic-associated diarrhea," *Explore the Journal of Ence & Healing*, vol. 12, no. 6, pp. 463–466, 2016.
- [11] P. Markowiak and K. Śliżewska, "Effects of probiotics, prebiotics, and synbiotics on human health," *Nutrients*, vol. 9, no. 9, pp. 1–12, 2017.
- [12] P. A. Bron, M. Kleerebezem, P. D. Cani et al., "Can probiotics modulate human disease by impacting intestinal barrier function?" *British Journal of Nutrition*, vol. 117, no. 1, pp. 93–107, 2017.
- [13] S. Cruchet, A. R. Furnes, J. Palacios, E. Hebel et al., "The use of probiotics in pediatric gastroenterology: a review of the literature and recommendations by Latin-American experts," *Pediatric Drugs*, vol. 17, no. 3, pp. 199–216, 2015.
- [14] J. Plaza-Díaz, F. Ruiz-Ojeda, L. Vilchez-Padial, and A. Gil, "Evidence of the anti-inflammatory effects of probiotics and synbiotics in intestinal chronic diseases," *Nutrients*, vol. 9, no. 6, p. 555, 2017.
- [15] M. Sáez-Lara, C. Robles-Sanchez, F. Ruiz-Ojeda, J. Plaza-Díaz, and A. Gil, "Effects of probiotics and synbiotics on obesity, insulin resistance syndrome, type 2 diabetes and non-alcoholic fatty liver disease: a review of human clinical trials," *International Journal of Molecular Sciences*, vol. 17, no. 6, p. 928, 2016.
- [16] S. Park and J.-H. Bae, "Probiotics for weight loss: a systematic review and meta-analysis," *Nutrition Research*, vol. 35, no. 7, pp. 566–575, 2015.
- [17] A. G. Cid, M. C. Goldner, M. Daz, and G. Ellenrieder, "The effect of endozym  $\beta$ -split, a commercial enzyme preparation used for aroma release, on tannat wine glycosides[J]," *South African Journal for Enology & Viticulture*, vol. 33, no. 1, pp. 51–57, 2016.
- [18] L. T. Piemolini-Barreto, R. V. Antônio, and S. Echeverrigaray, "Comparison of a pectinolytic extract of *Kluyveromyces marxianus* and a commercial enzyme preparation in the production of Ives (*Vitis labrusca*) grape juice," *World Journal of Microbiology and Biotechnology*, vol. 31, no. 5, pp. 755–762, 2015.

- [19] K. R. Kishore, "Targeting glucocerebrosidase: reduced enzymatic activity and Parkinson's disease," *Movement Disorders*, vol. 30, no. 12, p. 1620, 2015.
- [20] K. Ziervogel, S. B. Joye, and C. Arnosti, "Microbial enzymatic activity and secondary production in sediments affected by the sedimentation pulse following the Deepwater Horizon oil spill," *Deep Sea Research Part II: Topical Studies in Oceanography*, vol. 129, pp. 241–248, 2016.
- [21] M. S. Islam and D. J. Moore, "Mechanisms of LRRK2-dependent neurodegeneration: role of enzymatic activity and protein aggregation," *Biochemical Society Transactions*, vol. 45, no. 1, pp. 163–172, 2017.
- [22] J. F. Siebel, A. Adamska-Venkatesh, S. Rumpel, and K. Weber, E. Reijerse and W. Lubitz, Hybrid [FeFe]-Hydrogenases with modified active sites show remarkable residual enzymatic activity," *Biochemistry*, vol. 54, no. 7, pp. 1474–1483, 2015.
- [23] A. Piotrowska-Długosz and P. Charzynski, "The impact of the soil sealing degree on microbial biomass, enzymatic activity, and physicochemical properties in the Ekranic Technosols of Toruń (Poland)," *Journal of Soils & Sediments*, vol. 15, no. 1, pp. 47–59, 2015.
- [24] D. Zou, Y. Huang, X. Zhao et al., "A novel New Delhi metallo- $\beta$ -lactamase variant, NDM-14, isolated in a Chinese hospital possesses increased enzymatic activity against carbapenems," *Antimicrobial Agents and Chemotherapy*, vol. 59, no. 4, pp. 2450–2453, 2015.
- [25] F. I. Ndwiga, "Enzymatic activity, and secondary metabolites of fungal isolates from lake sonachi in Kenya," *International Journal of Imaging Systems & Technology*, vol. 21, no. 2, pp. 211–222, 2017.

## Research Article

# Sunlight-Driven Synthesis of Silver Nanoparticles Using Pomelo Peel Extract and Antibacterial Testing

Vinh Tien Nguyen 

Faculty of Chemical and Food Technology, Ho Chi Minh City University of Technology and Education, 01 Vo Van Ngan Street, Thu Duc District, Ho Chi Minh City, Vietnam

Correspondence should be addressed to Vinh Tien Nguyen; [tiennv@hcmute.edu.vn](mailto:tiennv@hcmute.edu.vn)

Received 4 June 2020; Revised 21 July 2020; Accepted 21 August 2020; Published 23 September 2020

Guest Editor: Tifeng Jiao

Copyright © 2020 Vinh Tien Nguyen. This is an open access article distributed under the Creative Commons Attribution License, which permits unrestricted use, distribution, and reproduction in any medium, provided the original work is properly cited.

A green approach, including using phytochemicals in pomelo peel extract (PPE) and direct sunlight, was used to synthesize silver nanoparticles (AgNPs). PPE was prepared by treating pomelo peel with a citric acid solution at 85°C for 2 h. PPE was then mixed with AgNO<sub>3</sub> and exposed to sunlight to induce the formation of AgNPs. Time-dependent UV-vis spectra of the reaction mixture demonstrated that AgNPs are formed under sunlight irradiation faster than under heating at 90°C. Characterization techniques, including X-ray diffraction, transmission electron microscopy, and scanning electron microscopy, confirmed the formation of AgNPs with sizes of 20–30 nm. AgNPs synthesized in PPE were more stable toward electrolyte-induced aggregation than those synthesized using the conventional NaBH<sub>4</sub>/citrate method. The AgNPs synthesized in PPE showed antibacterial activities comparable to those of AgNO<sub>3</sub> at the same silver concentration against four pathogenic bacterial strains. The obtained PPE containing AgNPs, pectin, and other phytochemicals can be utilized further to produce antibacterial and antioxidant films in food packaging and medical applications.

## 1. Introduction

Nowadays, it is well known that silver nanoparticles (AgNPs) are highly toxic to a wide range of microorganisms, including bacteria, fungi, and viruses [1, 2]. AgNPs can be synthesized using a physical, chemical, or biological approach. The latter is considered green for using renewable sources of chemicals to reduce silver ions into metallic Ag and cap the AgNPs to maintain their sizes in the nanoscale. The most common source of these renewable chemicals is phytoextracts from different parts of plants. Some examples of aqueous extracts that were utilized to produce AgNPs are those of *Polyalthia longifolia* leaves [3], *Carica papaya* fruit [4], *Embllica officinalis* fruit [5], *Citrus limon* juice [6], *Rosa rugosa* leaves [7], *Jatropha curcas* seeds [8], *Capsicum annuum* L. leaves [9], and *Murraya koenigii* leaves [10].

Beside the use of renewable sources of chemicals, another way to make the process of AgNPs production greener is to use energy-efficient techniques, such as microwave, ultrasound, and light irradiations [11]. An interesting

technique for the light irradiation approach is to use solar energy from direct sunlight to assist the formation of AgNPs. This technique was successfully applied to produce AgNPs in the presence of plant extracts, including *Allium sativum* cloves [12], *Ocimum sanctum* Linn leaves [13], spinach fraction containing ferredoxin and ferredoxin-NADP<sup>+</sup> reductase [14], *Polyalthia longifolia* leaves [3], *Zingiber officinale* rhizome [15], *Pleurotus citrinopileatus* [16], and *Piper longum* catkins [17]. In some cases, sunlight irradiation can induce AgNPs formation without using any intrinsically reducing agents [18, 19].

Pomelo (*Citrus maxima* Merr.) in the citrus family is cultivated mainly in some Asian countries. Pomelo fruit is consumed fresh or as juice, while its peel is discarded as biological waste. However, pomelo peel, which weighs up to 30% of the total fruit, is considered a good source of valuable phytochemical compounds, such as flavonoids, essential oils, cellulose, and pectin [20, 21]. The flavonoids in pomelo peel extract can reduce silver ions into metallic Ag particles, and pectin can cap the formed AgNPs to protect them from

further growth in size. To the best of our knowledge, only few studies used pomelo juice or pomelo peel extract to synthesize AgNPs, and none of these studies utilized sunlight to assist the formation of AgNPs [22–24]. Therefore, we studied the formation of AgNPs in PPE upon exposure to direct sunlight and characterize the synthesized AgNPs, including their stability against electrolyte-induced agglomeration and antibacterial activity against four bacterial strains. The obtained PPE containing AgNPs, pectin, and other phytochemicals can be utilized further to produce antibacterial and antioxidant films in food packaging or medical applications.

## 2. Materials and Methods

**2.1. Materials and Reagents.** Pomelo peels were collected from a local market (Ho Chi Minh City, Vietnam). Trisodium citrate was purchased from Xilong Scientific Co., Ltd. (China), silver nitrate from Fisher Scientific (USA), sodium hydroxide and sodium borohydride from Sigma-Aldrich (US), trisodium citrate (TSC) from Prolabo Chemicals (France), and ethanol from Chemsol (Vietnam). All the reagents were of at least 99% pure and used without further purification.

**2.2. Preparation of Pomelo Peel Extract (PPE).** The green outer skin of pomelo peel was removed, and the white inner layer (with high pectin content) was sliced, cut into small pieces, and sun-dried for 3 days. These dried pieces were then ground into a powder and stored at 4°C. The procedure for pectin extraction was adapted from a previous study [25]. For each extraction batch, 2 g of the dried peel powder was mixed thoroughly with 80 mL of deionized water containing 0.91 g of citric acid. The mixture was heated to 85°C and kept for 120 min with continuous stirring (550 rpm). Afterward, the mixture was filtered and centrifuged for 15 min at 14000 rpm to remove the peel particles. The pale yellow supernatant was used immediately for AgNPs synthesis or stored at 4°C.

To evaluate the pectin content in PPE, the extract was mixed with 95% ethanol (ethanol:extract of 2:1 v/v), stirred for 10 min, and then left for 1 h. The precipitated pectin gel was filtered, washed 3 times with 95% ethanol, and finally dried at 70°C for 8 h.

**2.3. Sunlight-Induced Synthesis of AgNPs in PPE.** Predetermined volumes of deionized water, PPE, 0.1 M AgNO<sub>3</sub> solution, and 0.1 M NaOH solution (to adjust pH) were mixed thoroughly and then put under sunlight for 30 min. UV-vis spectrum of the reaction mixture was recorded from 380 to 800 nm at 400 nm/min every 5 min using a UV-Vis-NIR-V670 spectrophotometer (JASCO, Japan). In the following text, PPE containing the synthesized AgNPs is denoted as AgNPs/PPE while the PPE containing AgNO<sub>3</sub> before sunlight irradiation as AgNO<sub>3</sub>/PPE.

**2.4. Test of Stability against Electrolyte-Induced Agglomeration.** The aggregation stability of the AgNPs/PPE was compared with a control AgNPs solution synthesized by

drop-wise adding 2 mL of 4 mM NaBH<sub>4</sub> into 30 mL of a solution containing 25 mM trisodium citrate and 0.13 mM AgNO<sub>3</sub> under stirring [26].

The stability test was carried out by mixing 9 mL of each AgNPs solution with 1 mL of 1 M NaCl [27]. The agglomeration of AgNPs was monitored by regularly recording the absorbance of the mixture for 5 h.

**2.5. Characterization of AgNPs.** Sizes and shapes of the AgNPs/PPE were evaluated using images recorded by a JEM-1400 transmission electron microscope (JEOL, USA).

To obtain the AgNPs solid for X-ray diffraction measurements, the AgNPs/PPE were coagulated using 0.1 M ZnSO<sub>4</sub>, centrifuged at 10 000 rpm, washed three times with deionized water, and dried at 70°C. The diffraction was measured at 2 theta angles scanned from 35° to 80°.

**2.6. Antibacterial Assay for AgNPs/PPE.** The Kirby–Bauer disk diffusion method was used to evaluate the antimicrobial activity of AgNPs/PPE on three Gram-positive (*Staphylococcus aureus*, *Streptococcus pyogenes*, and *Bacillus subtilis*) and one Gram-negative strain (*Salmonella typhi*). Each bacterial strain was cultured in Luria–Bertani (LB) nutrient medium at 37°C for 12 h. Each bacterial suspension was diluted with sterile LB medium to an absorbance of 0.45–0.50 at 625 nm. The bacterial suspension (100 µL) was spread on the dried surface of LB agar in Petri dishes. Each of the following solutions (20 µL) was dropped onto a piece of sterilized filter paper: 0.8 mM kanamycin (positive control), PPE (negative control), 0.8 mM AgNO<sub>3</sub>, and 0.8 mM AgNPs/PPE. The pieces of filter paper loaded with the solutions were put on the surface of the Petri dish with bacteria. After 24-hour incubation at 37°C, the diameters of inhibition zones were measured using a Vernier caliper and considered as an indication of antibacterial activity.

The antibacterial test was replicated three times for each bacterial strain. The difference in diameters of the inhibition zones were evaluated using the *t*-test.

## 3. Results and Discussion

**3.1. Pectin Content in PPE.** In this study, pectin was extracted from pomelo peel using citric acid treatment at pH 3.5 and temperature 85°C for 120 min. The extract and the obtained pectin were slightly yellow in color. From 2.00 g of pomelo peel, 0.23 g of crude pectin was obtained (11.5% yield from pomelo peel). Compared to other studies, this result was lower due to higher pH and lower temperature of extraction [25]. When using mineral acids such as HCl or HNO<sub>3</sub>, the percentages of extracted pectin were approximately 3 times higher than ours [21]. However, citric acid was chosen because of its greenness and its ability to cap AgNPs in the further synthetic step.

**3.2. Sunlight-Driven Formation of AgNPs/PPE.** UV-vis spectroscopy is a simple yet useful technique to characterize colloids of metallic nanoparticles. It is known that AgNPs

induce a surface plasmon resonance (SPR) at approximately 410 nm. A lower value of the wavelength at maximum ( $\lambda_{\max}$ ) indicates a lower average size of AgNPs, and a higher value of absorbance at  $\lambda_{\max}$  indicates a higher concentration of AgNPs [6]. Figure 1 shows the UV-vis spectra and the appearance (inset) of PPE and AgNO<sub>3</sub>/PPE after 30 min treated with high temperatures and under sunlight. PPE and AgNO<sub>3</sub>/PPE had the same pale yellow color, possibly due to the caramelization of neutral sugars in PPE during the extraction step. Heating the AgNO<sub>3</sub>/PPE mixture to 90°C only increased the yellow color intensity and the absorbance, but no new peak appeared. These results indicate that in PPE, which is acidic due to the presence of remaining citric acid, the reduction reaction of silver ions was slow even at 90°C. This is in agreement with other studies, which reported that the reduction reaction of silver ions by conventional heating is preferred at higher pH [28, 29].

Under sunlight irradiation, the reaction mixture quickly changed from pale yellow to orange-red in less than one minute and gradually turned to deep brown-red for over 3 h. This color change was associated with the development of a peak at 400–434 nm in the UV-vis spectrum (Figure 2), indicating the formation of AgNPs [28, 30–32].

The influence of electromagnetic irradiation on the formation of AgNPs has been known in several studies [17, 33–35]. A detailed mechanism was proposed for the action of UV light on the formation of AgNPs in the presence of methoxy polyethylene glycol and silver ions [36, 37]. However, it should be noted that in many studies, including ours, the reagents were contained in plastic tubes or glass vials that do not transmit UV part of the sunlight [15, 17]. Therefore, the blue light, which has lower energy than UV light but higher than other regions in the visible spectrum, may play a major role in reducing Ag<sup>+</sup> ions into metallic Ag [16, 38]. A possible mechanism for the reduction of Ag<sup>+</sup> ions is that the blue light induced tautomerization of the flavonoids in PPE from the enol to the keto form that can release reactive hydrogen atoms responsible for the reduction of Ag<sup>+</sup> ions [17].

The TEM image (Figure 3(a)) shows that the AgNPs synthesized in PPE were close to spheres with a size range of  $13 \pm 6$  nm (mean  $\pm$  SD,  $n = 29$ ). These low sizes of AgNPs are comparable with those prepared by strong reducing agents such as NaBH<sub>4</sub> and N<sub>2</sub>H<sub>4</sub> [39, 40]. The SEM image (Figure 3(b)) shows aggregates of AgNPs, which are possibly formed during the sample preparation step for SEM recording. However, one can find in Figure 3(b) that these aggregates are built from AgNPs of approximately 20–30 nm.

The XRD pattern of the synthesized AgNPs/PPE shows four characteristic peaks (Figure 4). These peaks are well matched with those of bulk silver in the face-centered cubic (fcc) structure (JCPDS file No. 04-0783). This result confirmed the ability of PPE to reduce Ag<sup>+</sup> ions to metallic silver under sunlight.

**3.3. Influence of the Reactant Concentrations on the Formation of AgNPs.** Figure 5 shows that increasing the concentration

of Ag<sup>+</sup> ions from 0.4 to 0.8 mM resulted in the same  $\lambda_{\max}$  but higher absorbance, indicating the formation of more AgNPs with almost the same size distribution. However, further increase of Ag<sup>+</sup> ions to 7.4 and 16.7 mM shifted  $\lambda_{\max}$  to the red region and decreased the maximum absorbance, indicating the formation of larger AgNPs [6]. These different characteristics of AgNPs produced under different concentrations of Ag<sup>+</sup> ions can be explained by the limited amount of reducing and protecting agents in the PPE. When Ag<sup>+</sup> ion concentration was low, the present reducing and capping agents can effectively reduce Ag<sup>+</sup> ions and protect AgNPs from agglomeration. When the concentration of Ag<sup>+</sup> ions was too high, the limited pectin could not protect all the AgNPs produced, which resulted in their agglomeration into larger and less particles [28, 32]. This result implies that a careful choice of Ag<sup>+</sup> concentration is required to synthesize AgNPs with low sizes.

#### 3.4. Influence of PPE Amount on the Formation of AgNPs.

In our study, PPE played the role of a capping agent that protects AgNPs from agglomeration. Therefore, its amount used in the reaction mixture must be an essential factor in controlling the amount and size of the produced AgNPs. Figure 6 shows that PPE volumes lower than 0.25 mL did not change the color of the reaction mixture, associating with no peak around 430 nm. This was possibly due to the low reaction rates at low concentrations of reducing agents from PPE. The inset table in Figure 6 shows that increasing the PPE volumes higher than 0.5 mL resulted in higher maximum absorbance at lower values of  $\lambda_{\max}$ , indicating the formation of more AgNPs with lower sizes.

**3.5. Stability Test of AgNPs.** To evaluate the effectiveness of using PPE pectin as a protecting agent for AgNPs, we compared the stability of AgNPs/PPE with that of AgNPs commonly synthesized using NaBH<sub>4</sub> as the reducing agent and trisodium citrate as the protecting agent (Figure 7).

In this test, 0.1 M NaCl was used as a coagulating agent to accelerate the agglomeration of AgNPs [27]. After 120 min of NaCl addition, AgNPs protected by citrate ions were significantly agglomerated, as expressed by the reduction in the peak absorbance. At the same time, AgNPs/PPE showed a slight reduction in the peak absorbance, indicating a superior protective effect of pectin against agglomeration of nanoparticles. This is due to the electrosterically stabilizing effect of pectin molecules. They surround the surface of AgNPs to form a polymeric capping layer with negative charges of carboxylate groups. This negative surface charge induces repulsions between AgNPs when they approach each other, thus reducing the chance of their collisions (electrostatic stabilization). Moreover, the polymeric surrounding layer further reduces the chance of their agglomeration upon collisions (steric stabilization). In other studies, polymers (polyvinylpyrrolidone and branched polyethyleneimine) also showed a stabilizing effect better than citrate anions for AgNPs in solutions containing monovalent and divalent coagulants [27, 41].

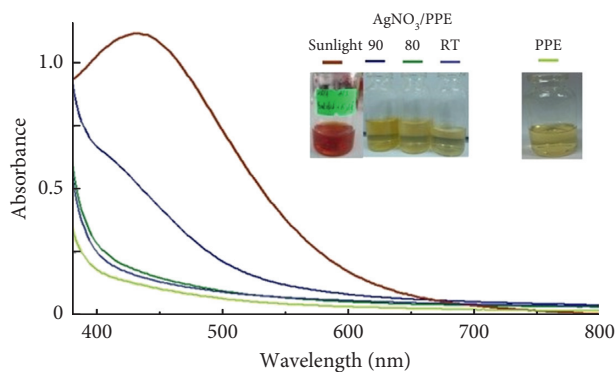


FIGURE 1: UV-vis spectra and appearance of PPE and  $\text{AgNO}_3/\text{PPE}$  after 30 min under different reaction conditions: at room temperature (RT),  $80^\circ\text{C}$ ,  $90^\circ\text{C}$ , and under sunlight.

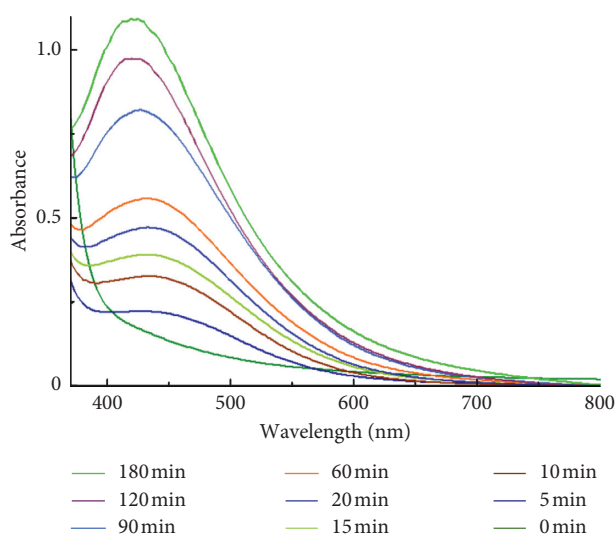


FIGURE 2: Time-dependent UV-vis spectra of  $\text{AgNO}_3/\text{PPE}$  under sunlight irradiation.

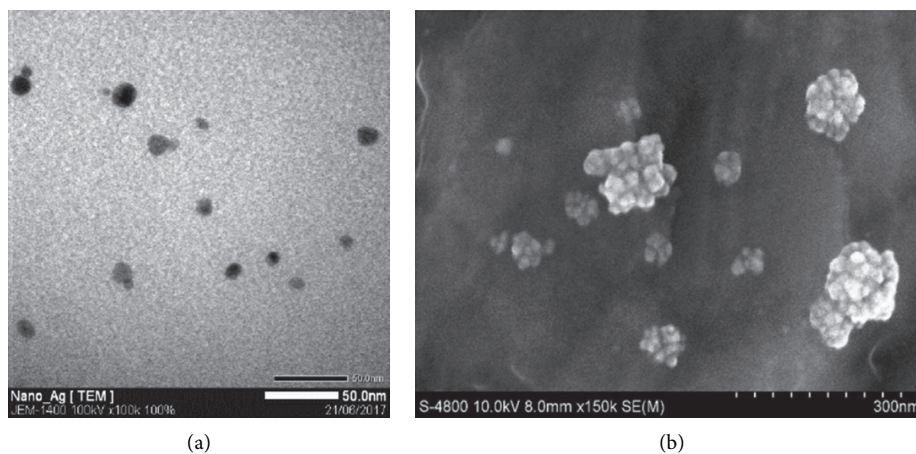


FIGURE 3: (a) TEM image of  $\text{AgNPs}/\text{PPE}$  and (b) SEM image of  $\text{AgNPs}$  clusters after precipitated together with pectin from PPE.

3.6. *Antibacterial Activity of  $\text{AgNPs}/\text{PPE}$ .* Based on the diameters of the inhibition zones in the antibacterial tests (Figure 8 and Table 1), the order of antibacterial strengths

( $p < 0.05$ ) was kanamycin  $>$   $\text{AgNPs} = \text{AgNO}_3 >$  PPE. PPE itself possessed antibacterial effects, possibly due to the presence of citric acid and/or phytochemicals from pomelo

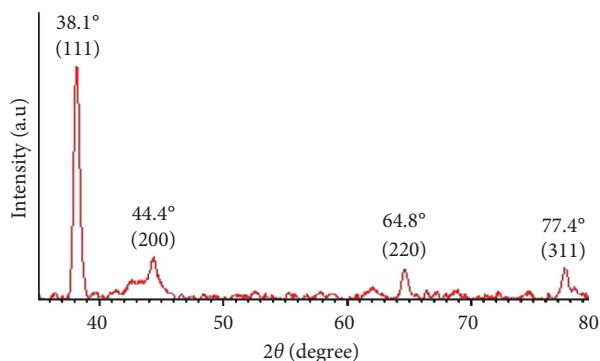
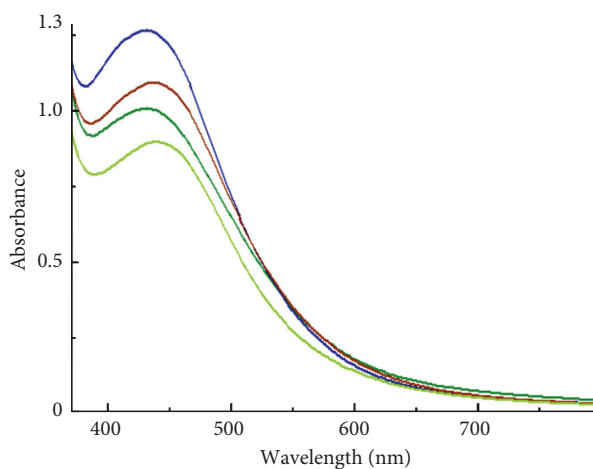


FIGURE 4: XRD pattern of the AgNPs-pectin powder.



AgNO <sub>3</sub> (mM)	λ <sub>max</sub> (nm)	A <sub>max</sub>
0.4	432	1.00
0.8	432	1.26
7.4	438	1.09
16.7	440	0.89

FIGURE 5: UV-vis spectra of AgNO<sub>3</sub>/PPE with different Ag<sup>+</sup> concentrations after 30 min of sunlight irradiation. Inset table: maximum absorbance (A<sub>max</sub>) and λ<sub>max</sub> of these mixtures.

peel. The higher antibacterial effect of AgNPs/PPE compared to that of PPE indicates that AgNPs in the PPE possesses intrinsic antibacterial activity.

There have been extensive studies on possible antibacterial mechanisms of AgNPs, which revealed that the main mechanism involves the release of Ag<sup>+</sup> ions from metallic silver [42]. These ions have very high affinities for phosphates, amines, and especially thiols, with which they form a quasi-covalent Ag-S bond (binding energy of approximately 65 kcal/mol) [43]. Moreover, silver ions can bridge several thiol groups, forming an irreversible aggregation of the thiol-bearing biological molecules [44]. Therefore, unlike antibiotics that target specific components of the bacterial life cycle, silver ions attack readily any biological molecules

(DNA, membrane-bound peptides, intracellular peptides, or cofactors) bearing target groups [45].

The results above demonstrate that the antibacterial effects of AgNPs/PPE were not different from those of AgNO<sub>3</sub> at the same 0.8 mM silver concentration. This seems contradictory common sense that silver ions from AgNO<sub>3</sub> should have a higher mobility, and hence a higher antibacterial effect than silver ions released from solid AgNPs. We suggest that the enhanced antibacterial effect of AgNPs/PPE was due to the presence of citric acid in PPE. Citric acid can release (1) H<sup>+</sup> ions, which increase the redox potential of dissolved oxygen E(O<sub>2</sub>, H<sup>+</sup>/H<sub>2</sub>O), and (2) citrate ions, which chelate silver ions and thus reduce the redox potential E(Ag<sup>+</sup>/Ag). These two combined effects of citric acid could

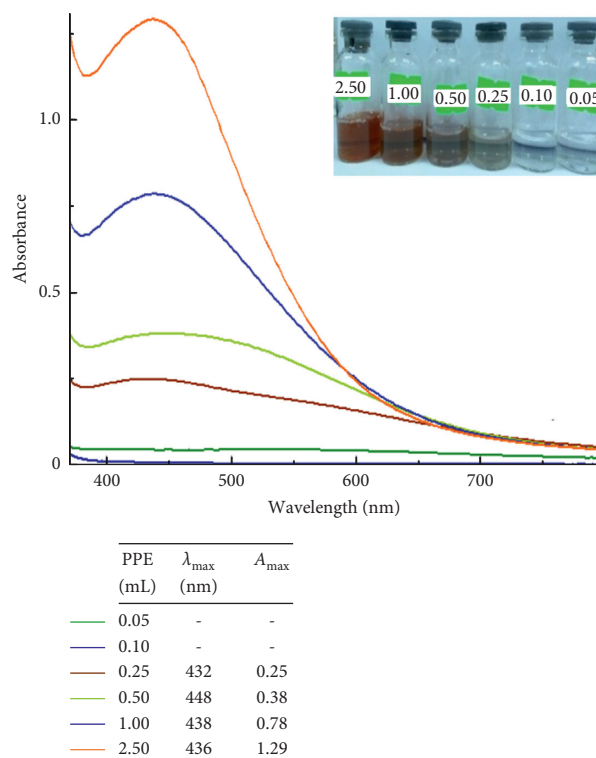


FIGURE 6: Higher amounts of PPE yielded more AgNPs. Inset table: maximum absorbance ( $A_{\max}$ ) and  $\lambda_{\max}$  of the reaction mixtures.

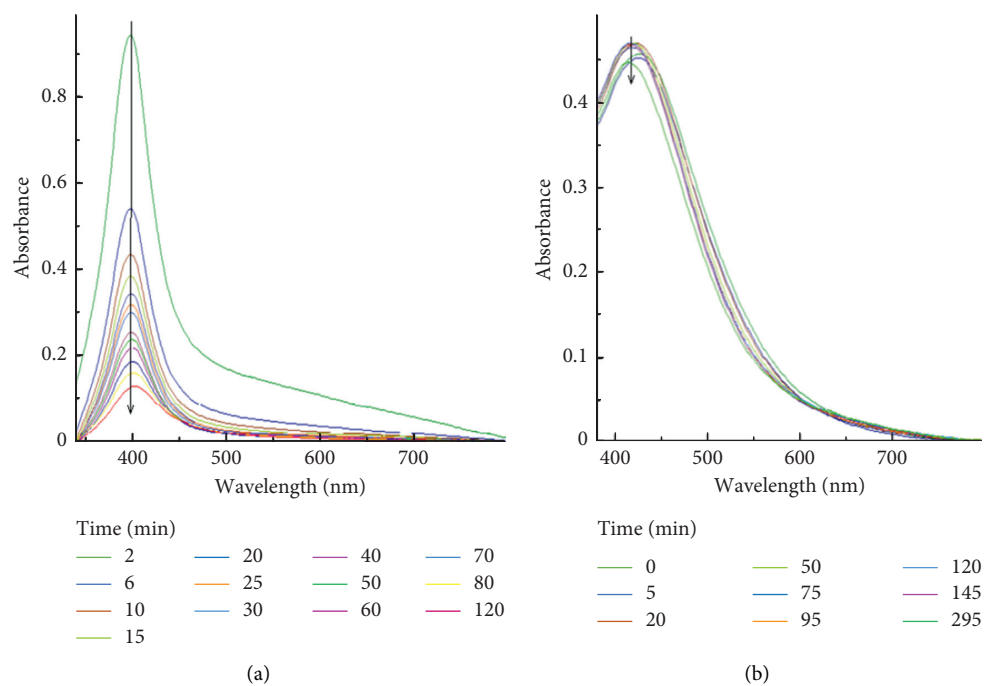


FIGURE 7: Time-dependent UV-vis spectra of AgNPs solution in the presence of 0.1 M NaCl. (a) AgNPs prepared using  $\text{NaBH}_4$  and trisodium citrate; (b) AgNPs/PPE.

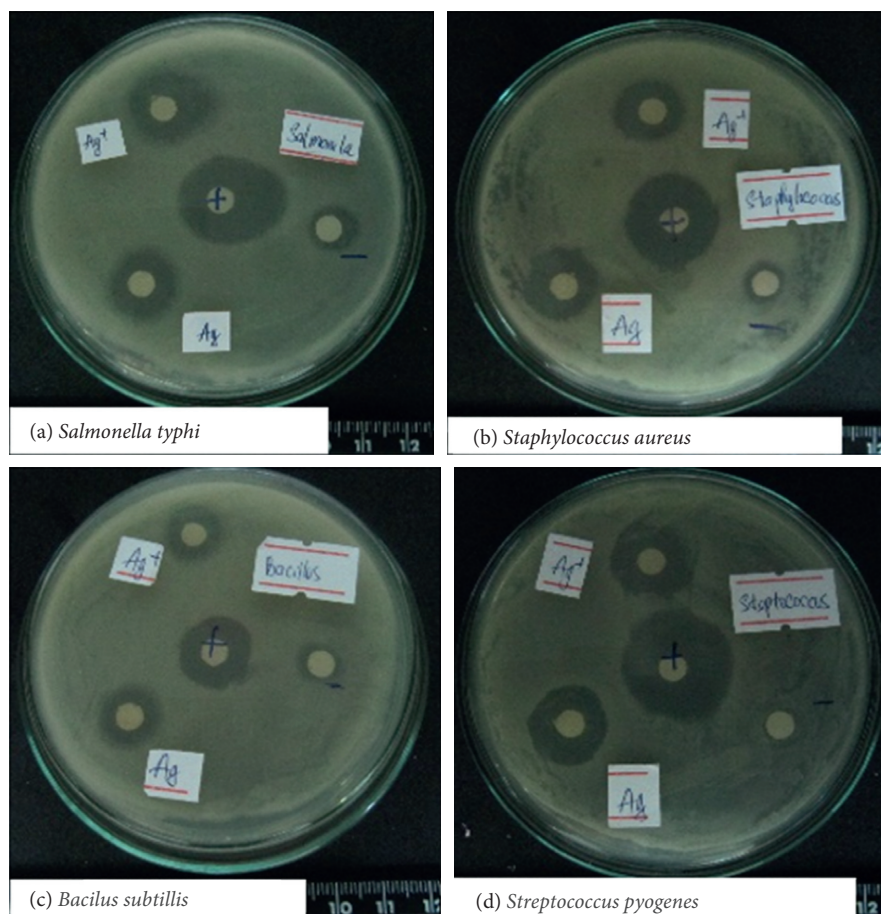


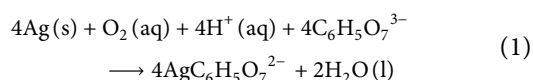
FIGURE 8: Antibacterial activity of AgNPs in comparison with  $\text{AgNO}_3$ , kanamycin (+), and PPE (-).

TABLE 1: Diameters of inhibition zones (mm) in the antibacterial tests of AgNPs/PPE, PPE, kanamycin, and  $\text{AgNO}_3$  against four bacterial strains.

Bacteria	Kanamycin (+)	PPE (-)	$\text{AgNO}_3$	AgNPs/PPE
<i>Salmonella typhi</i>	$17.5 \pm 1.5^a$	$10.4 \pm 0.2^c$	$13.0 \pm 1.9^b$	$13.9 \pm 0.2^b$
<i>Staphylococcus aureus</i>	$17.4 \pm 1.2^a$	$8.9 \pm 0.1^c$	$12.4 \pm 1.9^b$	$11.6 \pm 1.1^b$
<i>Bacillus subtilis</i>	$13.8 \pm 1.5^a$	$8.5 \pm 0.2^c$	$11.5 \pm 0.7^b$	$11.5 \pm 0.5^b$
<i>Streptococcus pyogenes</i>	$17.7 \pm 4.2^a$	$8.3 \pm 0.1^c$	$10.8 \pm 0.8^b$	$11.2 \pm 1.5^b$

The results are expressed as mean  $\pm$  SD ( $n=3$ ). The means in a row with different letters <sup>a</sup>, <sup>b</sup> or <sup>c</sup> are significantly different ( $p < 0.05$ ).

enhance the oxidative dissolution of AgNPs into Ag (I) according to the following overall reaction:



For AgNPs and  $\text{AgNO}_3$ , the inhibition zone against the Gram-negative *S. typhi* was significantly larger than the other three Gram-positive strains ( $p < 0.05$ ). This higher resistance of Gram-positive strains is consistent with other studies and can be explained by the thick peptidoglycan cell walls that resist the penetration of silver ions into the bacterial cell [15, 46].

## 4. Conclusions

In this study, we proved that direct sunlight facilitates the formation of AgNPs in acidic pomelo peel extract (PPE). The flavonoids in PPE are supposed to be the reducing agents for silver ions and pectin as the capping agent for AgNPs. The AgNPs synthesized in PPE demonstrated enhanced stability against agglomeration due to the protective effect of pectin. AgNPs/PPE showed antibacterial effects comparable to those of  $\text{AgNO}_3$ , possibly due to the presence of citric acid and other components in PPE. The obtained PPE containing AgNPs, pectin, and phytochemicals from pomelo peels can be utilized further to produce antibacterial and antioxidant films in food packaging and medical applications.

## Data Availability

The data used to support the findings of this study are available from the corresponding author upon request.

## Conflicts of Interest

The author declares that there are no conflicts of interest regarding the publication of this paper.

## Acknowledgments

The author gratefully thanks Mr. Minh Thang Nguyen Canh for helpful advices and Ho Chi Minh City University of Technology and Education for financial and facility support in completing this research.

## References

- [1] H. H. Lara, E. N. Garza-Treviño, L. Ixtepan-Turrent, and D. K. Singh, "Silver nanoparticles are broad-spectrum bactericidal and virucidal compounds," *Journal of Nanobiotechnology*, vol. 9, no. 1, p. 30, 2011.
- [2] K. S. Siddiqi, A. Husen, and R. A. Rao, "A review on biosynthesis of silver nanoparticles and their biocidal properties," *Journal of Nanobiotechnology*, vol. 16, no. 1, p. 14, 2018.
- [3] V. Kumar, D. Bano, S. Mohan, D. K. Singh, and S. H. Hasan, "Sunlight-induced green synthesis of silver nanoparticles using aqueous leaf extract of *Polyalthia longifolia* and its antioxidant activity," *Materials Letters*, vol. 181, pp. 371–377, 2016.
- [4] M. Firdaus, S. Andriana, W. Alwi, E. Swistoro, A. Ruyani, and A. Sundaryono, "Green synthesis of silver nanoparticles using *Carica papaya* fruit extract under sunlight irradiation and their colorimetric detection of mercury ions," *Journal of Physics: Conference Series*, vol. 817, p. 012029, 2017.
- [5] P. S. Hien, T. Kokila, and D. Geetha, "Plant mediated green synthesis and antibacterial activity of silver nanoparticles using *Emblica officinalis* fruit extract," *Spectrochimica Acta Part A: Molecular and Biomolecular Spectroscopy*, vol. 142, pp. 339–343, 2015.
- [6] T. C. Prathna, N. Chandrasekaran, A. M. Raichur, and A. Mukherjee, "Biomimetic synthesis of silver nanoparticles by *Citrus limon* (lemon) aqueous extract and theoretical prediction of particle size," *Colloids and Surfaces B: Biointerfaces*, vol. 82, no. 1, pp. 152–159, 2011.
- [7] S. P. Dubey, M. Lahtinen, and M. Sillanpää, "Green synthesis and characterizations of silver and gold nanoparticles using leaf extract of *Rosa rugosa*," *Colloids and Surfaces A: Physicochemical and Engineering Aspects*, vol. 364, no. 1–3, pp. 34–41, 2010.
- [8] H. Bar, D. K. Bhui, G. P. Sahoo, P. Sarkar, S. Pyne, and A. Misra, "Green synthesis of silver nanoparticles using seed extract of *Jatropha curcas*," *Colloids and Surfaces A: Physicochemical and Engineering Aspects*, vol. 348, no. 1–3, pp. 212–216, 2009.
- [9] S. Li, Y. Shen, A. Xie et al., "Green synthesis of silver nanoparticles using *Capsicum annuum* L. extract," *Green Chemistry*, vol. 9, no. 8, pp. 852–858, 2007.
- [10] A. Suganya, K. Murugan, K. Kovendan, P. Mahesh Kumar, and J.-S. Hwang, "Green synthesis of silver nanoparticles using *Murraya koenigii* leaf extract against *Anopheles stephensi* and *Aedes aegypti*," *Parasitology Research*, vol. 112, no. 4, pp. 1385–1397, 2013.
- [11] M. Mohammadlou, H. Maghsoudi, and H. Jafarizadeh-Mal-miri, "A review on green silver nanoparticles based on plants: synthesis, potential applications and eco-friendly approach," *International Food Research Journal*, vol. 23, no. 2, 2016.
- [12] L. Rastogi and J. Arunachalam, "Sunlight based irradiation strategy for rapid green synthesis of highly stable silver nanoparticles using aqueous garlic (*Allium sativum*) extract and their antibacterial potential," *Materials Chemistry and Physics*, vol. 129, no. 1-2, pp. 558–563, 2011.
- [13] G. Gopal, S. Sarkar, R. Ghosh et al., "Sunlight-induced rapid and efficient biogenic synthesis of silver nanoparticles using aqueous leaf extract of *Ocimum sanctum* Linn. with enhanced antibacterial activity," *Organic and Medicinal Chemistry Letters*, vol. 4, no. 1, p. 18, 2014.
- [14] K. B. A. Ahmed, R. Senthilnathan, S. Megarajan, and V. Anbazhagan, "Sunlight mediated synthesis of silver nanoparticles using redox phytoprotein and their application in catalysis and colorimetric mercury sensing," *Journal of Photochemistry and Photobiology B: Biology*, vol. 151, pp. 39–45, 2015.
- [15] S. Mathew, A. Prakash, and E. K. Radhakrishnan, "Sunlight mediated rapid synthesis of small size range silver nanoparticles using *Zingiber officinale* rhizome extract and its antibacterial activity analysis," *Inorganic and Nano-Metal Chemistry*, vol. 48, no. 2, pp. 139–145, 2018.
- [16] A. K. Bhardwaj, A. Shukla, S. Maurya et al., "Direct sunlight enabled photo-biochemical synthesis of silver nanoparticles and their bactericidal efficacy: photon energy as key for size and distribution control," *Journal of Photochemistry and Photobiology B: Biology*, vol. 188, pp. 42–49, 2018.
- [17] M. Jayapriya, D. Dhanasekaran, M. Arulmozhi, E. Nandhakumar, N. Senthilkumar, and K. Sureshkumar, "Green synthesis of silver nanoparticles using *Piper longum* catkin extract irradiated by sunlight: antibacterial and catalytic activity," *Research on Chemical Intermediates*, vol. 45, no. 6, pp. 3617–3631, 2019.
- [18] M. Annadhasan, V. R. SankarBabu, R. Naresh, K. Umamaheswari, and N. Rajendiran, "A sunlight-induced rapid synthesis of silver nanoparticles using sodium salt of N-cholyl amino acids and its antimicrobial applications," *Colloids and Surfaces B: Biointerfaces*, vol. 96, pp. 14–21, 2012.
- [19] G. A. Bhaduri, R. Little, R. B. Khomane et al., "Green synthesis of silver nanoparticles using sunlight," *Journal of Photochemistry and Photobiology A: Chemistry*, vol. 258, pp. 1–9, 2013.
- [20] R. Huang, M. Cao, H. Guo, W. Qi, R. Su, and Z. He, "Enhanced ethanol production from pomelo peel waste by integrated hydrothermal treatment, multienzyme formulation, and fed-batch operation," *Journal of Agricultural and Food Chemistry*, vol. 62, no. 20, pp. 4643–4651, 2014.
- [21] P. Methacanon, J. Krongsin, and C. Gamonpilas, "Pomelo (*Citrus maxima*) pectin: effects of extraction parameters and its properties," *Food Hydrocolloids*, vol. 35, pp. 383–391, 2014.
- [22] K. A. Ali, R. Yao, W. Wu et al., "Biosynthesis of silver nanoparticle from pomelo (*Citrus maxima*) and their antibacterial activity against *acidovorax oryzae* RS-2," *Materials Research Express*, vol. 7, no. 1, p. 015097, 2020.
- [23] N. S. Jalani, W. Michell, W. E. Lin, S. Z. Hanani, U. Hashim, and R. Abdullah, "Biosynthesis of silver nanoparticles using citrus grandis peel extract," *Malaysian Journal of Analytical Sciences*, vol. 22, no. 4, pp. 676–683, 2018.

- [24] D. Sarvamangala, K. Kondala, U. Murthy, B. N. Rao, G. Sharma, and R. Satyanarayana, "Biogenic synthesis of AGNP's using Pomelo fruit—characterization and antimicrobial activity against Gram +Ve and Gram -Ve bacteria," *International Journal of Pharmaceutical Sciences Review and Research*, vol. 19, no. 2, pp. 30–35, 2013.
- [25] S. Q. Liew, G. C. Ngoh, R. Yusoff, and W. H. Teoh, "Acid and deep eutectic solvent (DES) extraction of pectin from pomelo (*Citrus grandis* (L.) Osbeck) peels," *Biocatalysis and Agricultural Biotechnology*, vol. 13, pp. 1–11, 2018.
- [26] K. Mavani and M. Shah, "Synthesis of silver nanoparticles by using sodium borohydride as a reducing agent," *International Journal of Engineering Research & Technology*, vol. 2, no. 3, pp. 1–5, 2013.
- [27] K. A. Huynh and K. L. Chen, "Aggregation kinetics of citrate and polyvinylpyrrolidone coated silver nanoparticles in monovalent and divalent electrolyte solutions," *Environmental Science & Technology*, vol. 45, no. 13, pp. 5564–5571, 2011.
- [28] N. V. Ivanova, N. N. Trofimova, L. A. Eskova, and V. A. Babkin, "The study of the reaction of Pectin-Ag (0) nanocomposites formation," *International Journal of Carbohydrate Chemistry*, vol. 2012, Article ID 459410, 9 pages, 2012.
- [29] M. Vanaja, G. Gnanajobitha, K. Paulkumar, S. Rajeshkumar, C. Malarkodi, and G. Annadurai, "Phytosynthesis of silver nanoparticles by *Cissus quadrangularis*: influence of physicochemical factors," *Journal of Nanostructure in Chemistry*, vol. 3, no. 1, p. 17, 2013.
- [30] X. Jiang, C. Chen, W. Chen, and A. Yu, "Role of citric acid in the formation of silver nanoplates through a synergistic reduction approach," *Langmuir*, vol. 26, no. 6, pp. 4400–4408, 2009.
- [31] G. A. Kahrilas, L. M. Wally, S. J. Fredrick, M. Hiskey, A. L. Prieto, and J. E. Owens, "Microwave-assisted green synthesis of silver nanoparticles using orange peel extract," *ACS Sustainable Chemistry & Engineering*, vol. 2, no. 3, pp. 367–376, 2014.
- [32] M. K. Zahran, H. B. Ahmed, and M. H. El-Rafie, "Facile size-regulated synthesis of silver nanoparticles using pectin," *Carbohydrate Polymers*, vol. 111, pp. 971–978, 2014.
- [33] M. Bernabò, A. Pucci, F. Galembeck, C. A. d. P. Leite, and G. Ruggeri, "Thermal- and sun-promoted generation of silver nanoparticles embedded into poly(vinyl alcohol) films," *Macromolecular Materials and Engineering*, vol. 294, no. 4, pp. 256–264, 2009.
- [34] A. N. Krklješ, M. T. Marinović-Cincović, Z. M. Kacarevic-Popovic, and J. M. Nedeljković, "Radiolytic synthesis and characterization of Ag-PVA nanocomposites," *European Polymer Journal*, vol. 43, no. 6, pp. 2171–2176, 2007.
- [35] D. V. Phu, V. T. K. Lang, N. T. Kim Lan et al., "Synthesis and antimicrobial effects of colloidal silver nanoparticles in chitosan by  $\gamma$ -irradiation," *Journal of Experimental Nanoscience*, vol. 5, no. 2, pp. 169–179, 2010.
- [36] K. Mallick, M. J. Witcomb, and M. S. Scurrall, "Polymer stabilized silver nanoparticles: a photochemical synthesis route," *Journal of Materials Science*, vol. 39, no. 14, pp. 4459–4463, 2004.
- [37] K. Mallick, M. Witcomb, and M. Scurrall, "Silver nanoparticle catalysed redox reaction: an electron relay effect," *Materials Chemistry and Physics*, vol. 97, no. 2-3, pp. 283–287, 2006.
- [38] N. Yang, X.-F. Wei, and W.-H. Li, "Sunlight irradiation induced green synthesis of silver nanoparticles using peach gum polysaccharide and colorimetric sensing of  $H_2O_2$ ," *Materials Letters*, vol. 154, pp. 21–24, 2015.
- [39] S. Agnihotri, S. Mukherji, and S. Mukherji, "Size-controlled silver nanoparticles synthesized over the range 5-100 nm using the same protocol and their antibacterial efficacy," *RSC Advances*, vol. 4, no. 8, pp. 3974–3983, 2014.
- [40] Z. Khan, S. A. Al-Thabaiti, E. H. El-Mossalamy, and A. Y. Obaid, "Studies on the kinetics of growth of silver nanoparticles in different surfactant solutions," *Colloids and Surfaces B: Biointerfaces*, vol. 73, no. 2, pp. 284–288, 2009.
- [41] A. M. El Badawy, K. G. Scheckel, M. Suidan, and T. Tolaymat, "The impact of stabilization mechanism on the aggregation kinetics of silver nanoparticles," *Science of the Total Environment*, vol. 429, pp. 325–331, 2012.
- [42] Z.-m. Xiu, Q.-b. Zhang, H. L. Puppala, V. L. Colvin, and P. J. J. Alvarez, "Negligible particle-specific antibacterial activity of silver nanoparticles," *Nano Letters*, vol. 12, no. 8, pp. 4271–4275, 2012.
- [43] B. M. Barngrover and C. M. Aikens, "Incremental binding energies of gold(I) and silver(I) thiolate clusters," *The Journal of Physical Chemistry A*, vol. 115, no. 42, pp. 11818–11823, 2011.
- [44] A. N. Milanese, S. D. Gillmor, J. D. Beers, K. M. Beardmore, R. W. Cutts, and B. I. Swanson, "Characterization of chain molecular assemblies in long-chain, layered silver thiolates: a joint infrared spectroscopy and X-ray diffraction study," *The Journal of Physical Chemistry B*, vol. 103, no. 15, pp. 2850–2861, 1999.
- [45] B. Le Ouay and F. Stellacci, "Antibacterial activity of silver nanoparticles: a surface science insight," *Nano Today*, vol. 10, no. 3, pp. 339–354, 2015.
- [46] P. Pallavicini, C. R. Arciola, F. Bertoglio et al., "Silver nanoparticles synthesized and coated with pectin: an ideal compromise for anti-bacterial and anti-biofilm action combined with wound-healing properties," *Journal of Colloid and Interface Science*, vol. 498, pp. 271–281, 2017.

## Research Article

# Microstructure and Corrosion Behavior of Laser-Cladding CeO<sub>2</sub>-Doped Ni-Based Composite Coatings on TC4

Fangxia Ye <sup>1,2,3</sup>, Wenxuan Shao,<sup>3</sup> Xuchao Ye,<sup>4</sup> Mingxia Liu,<sup>1,3</sup> Yanxiang Xie,<sup>1,2,3</sup> Peiying Bian,<sup>1,2,3</sup> Xiaoyan Wang,<sup>1,2,3</sup> Ling Liu,<sup>1,3</sup> and Hong Wu<sup>5</sup>

<sup>1</sup>The Key Laboratory for Surface Engineering and Remanufacturing of Shaanxi Province, Xi'an University, Xi'an 710065, China

<sup>2</sup>Xi'an Key Laboratory on Intelligent Additive Manufacturing Technologies, Xi'an University, Xi'an 710065, China

<sup>3</sup>School of Mechanical and Material Engineering, Xi'an University, Xi'an 710065, China

<sup>4</sup>Xinjiang Petroleum Engineering Construction Supervision Co., Ltd., Xin Jiang, Kelamayi 834000, China

<sup>5</sup>School of Electrical and Mechanical Engineering, Xi'an University of Architecture and Technology, Xi'an 710055, China

Correspondence should be addressed to Fangxia Ye; 407510325@qq.com

Received 9 June 2020; Accepted 29 June 2020; Published 22 September 2020

Guest Editor: Tifeng Jiao

Copyright © 2020 Fangxia Ye et al. This is an open access article distributed under the Creative Commons Attribution License, which permits unrestricted use, distribution, and reproduction in any medium, provided the original work is properly cited.

Laser-cladding CeO<sub>2</sub>-doped Ni-based composite coatings were prepared on the surface of a titanium alloy, and the effects of CeO<sub>2</sub> addition on the microstructure, microhardness, and corrosion resistance of the prepared coatings were studied. The results showed that TiC, NiTi, Ni<sub>3</sub>Ti, and Ti<sub>2</sub>Ni phases were formed on the prepared coatings. Moreover, the addition of CeO<sub>2</sub> in laser-cladding coatings effectively refined the microstructure and reduced the number of cracks generated in the laser-cladding process. When the amount of CeO<sub>2</sub> was 2%, the number of cracks in the laser-cladding coating was significantly reduced compared with that of 0%. When the content of CeO<sub>2</sub> was 2% or 3%, the microhardness of laser-cladding coatings reached the maximum value. At the same time, it was found that the appropriate addition of CeO<sub>2</sub> was helpful to improve the corrosion resistance of the laser-cladding coating. However, excessive CeO<sub>2</sub> addition could reduce the corrosion resistance of the laser-cladding coating.

## 1. Introduction

Titanium alloys are widely adopted for aerospace, defense, automobile, medical, and other applications due to their low density, high specific strength, good corrosion resistance, and fatigue resistance. Nevertheless, titanium alloys have many limitations, which include a high friction coefficient, weak erosion-corrosion, poor machinability, and relatively poor ability to resist high-temperature oxidation [1, 2]. The limitations have negatively affected the safety and reliability of Ti alloy components and limited their applications. Titanium and its alloys can be corroded in certain environments, especially in environments containing chloride ions. In such environments where the concentration of chloride ion is high, the corrosion attacks will be severe and thus the alloys are corroded. Ti-6Al-4V (TC4) alloy is generally resistant to corrosion, but it can also be rapidly corroded in

corrosive environments where the protective oxide layer is destroyed. On the other hand, titanium has a great tendency to react with oxygen. Therefore, it is of importance to protect titanium alloys from corrosion attacks by forming a stable and continuous surface layer.

Different protection approaches such as plasma nitriding [3, 4], physical vapor deposition (PVD) [5–7], chemical vapor deposition (CVD) [8, 9], and plasma spraying process [10, 11] have been applied on Ti-6Al-4V for improving the corrosion resistance. Among these approaches, laser cladding is considered as a promising and effective method because of its large coating thickness, improved compact structure, and excellent performance [12–17]. Also, thanks to the high hardness, good wear resistance, and high-temperature oxidation resistance, Ni-based self-fluxing alloys are widely used in surface-strengthening technologies, such as laser cladding and thermal spraying. As such, this strategy

is often employed not only in academic research but also in industry practice. For instance, it is well known that the laser cladding of Ni-based alloys on the surface of steels can greatly improve the surface properties of the substrate materials. Other representative works are cited in the following. Li et al. [18] fabricated Ni-based composite coatings added with  $\text{La}_2\text{O}_3$  on carbon steel through laser cladding. Liu et al. [19–21] examined the microstructure and tribological properties of laser-clad Ni-based high-temperature, self-lubricating, and wear-resistant composite coatings. Zhang et al. [22] prepared a Ni60 alloy-cladding layer added with rare earth  $\text{CeO}_2$  on the surface of 6063 Al alloys through laser cladding, and they achieved outstanding results. Farahmand et al. [16] investigated the effects of synthesizing a nano-WC powder and rare earth element (RE) on the quality of Ni-WC coatings. Furthermore, they studied the evolution of the molten pool in laser cladding assisted with induction heating and found that the addition of nano-WC particles and  $\text{La}_2\text{O}_3$  enhanced the coating homogeneity, microstructure refinement, and coating microhardness correspondingly.

This study aims to investigate the effects of  $\text{CeO}_2$  amount on the microstructure, microhardness, and corrosion behavior of  $\text{CeO}_2$  doped Ni-based composite coatings which are laser clad on the surface of TC4 alloy in NaCl solutions. In particular, we are interested in knowing if there is an optimal amount of  $\text{CeO}_2$  addition in the composite coating. For this purpose, various  $\text{CeO}_2$  additions were designed, laser-cladding experiments were carried out, and the obtained coatings were thoroughly evaluated.

## 2. Experimental Details

The substrate material of this experiment is the TC4 titanium alloy sheet. The chemical composition of TC4 titanium alloy is shown in Table 1. The substrates were prepared from a large TC4 titanium alloy sheet, which was cut to  $100\text{ mm} \times 100\text{ mm} \times 10\text{ mm}$  by a wire electrical discharge machining (EDM) system. The Ni25 alloy powder and  $\text{CeO}_2$  powder with different mass ratios were weighed by a balance. By using a QM3SP04L planetary ball-milling machine, the two powders were mixed and milled to ensure uniformity. The typical physical properties of  $\text{CeO}_2$  and the chemical composition of Ni25 are shown in Tables 2 and 3.

Before laser cladding, the surfaces of TC4 substrate plates were cleaned by sandpapers, washed with alcohol, and then dried. An LDM2000 fiber laser processing system was employed for laser cladding, which consists of a 2000W fiber laser system, a powder feeder, and a 3-axis CNC mechanism. Argon gas was used as a protective gas for the cladding operation. The laser-cladding process parameters are listed in Table 4. After cladding, the samples were cut into rectangular specimens of dimensions of  $10\text{ mm} \times 10\text{ mm} \times 3\text{ mm}$  with the wire EDM system.

The longitudinal section of the specimen was used for characterization. After being well polished with diamond paste and etched with an  $\text{HF}:\text{NH}_4\text{OH}:\text{H}_2\text{O} = 2:5:43$  solution, the microstructure of the specimen was examined using a scanning electron microscopy (Nova Nano SEM 450)

equipped with energy-dispersive X-ray spectroscopy (EDS) unit. The X-ray diffraction (XRD) data were recorded using a PW 1730 X-ray diffractometer (Philips, The Netherlands) with monochromated  $\text{Cu K}\alpha$  radiation at 40 kV and 40 mA in the  $2\theta$  range of  $10^\circ$ – $90^\circ$ . Microhardness of the specimen was measured by using an HDX-1000 digital microhardness tester (Taiming Test Co., China), which consists of a square-based pyramidal diamond indenter with a  $136^\circ$  angle between two opposite faces. The static load applied was 50 g and the dwell time of loading was 15 sec. An average value of microhardness was taken from at least five different measurements. Immersion corrosion analysis was carried out using a CS310H electrochemical workstation. The 3.5% NaCl solution was chosen as the immersion medium and its pH was maintained at 6.5.

The corrosion resistance of the laser-cladding coatings was tested using an electrochemical work station. At the beginning of the experiment, the surface of each sample was polished with sandpapers and then wrapped with copper wire of 1 mm in diameter. The other exposed areas of the sample were sealed with 703 silicone rubber, and only a cylindrical surface of  $\Phi 6\text{ mm}$  was left on the surface of the sample. The sample was the working electrode, the saturated Mercury electrode was used as the reference electrode, the metal platinum sheet was used as the auxiliary electrode, and the reference electrode and the research electrode were connected by a salt bridge. A sodium chloride solution with a mass fraction of 3.5% was used as a reaction solution. The dynamic potential scan was performed at a scanning speed of 1 mV/s, and the scanning range was  $-1\text{ V}$  to  $+1.5\text{ V}$ .

## 3. Results and Discussion

Figure 1 shows the X-ray diffraction spectrum of laser-cladding coatings with different  $\text{CeO}_2$  contents. The XRD result indicates that TiC, NiTi,  $\text{Ni}_3\text{Ti}$ , and  $\text{Ti}_2\text{Ni}$  exist in the laser-cladding coatings. It can be observed that the higher content of  $\text{CeO}_2$  leads to the stronger the  $\text{Ti}_2\text{Ni}$  diffraction peaks. However, the types of other phases are not changed.

Figure 2 presents the macromorphology of coatings with different  $\text{CeO}_2$  contents. It can be seen that there are no visible defects, such as lack of fusion and porosity, in the laser-cladding coatings. The number of cracks in the laser-cladding coatings varies with the rare earth  $\text{CeO}_2$  content. When the content of  $\text{CeO}_2$  is less than 2%, it can effectively reduce the crack generation of the laser-cladding coatings. When the content of  $\text{CeO}_2$  is more than 2%, the number of cracks begins to increase again. As such, the proper amount of rare earth  $\text{CeO}_2$  can effectively inhibit the laser-cladding cracks, and the excessive amount of rare earth  $\text{CeO}_2$  can increase the number of laser-cladding cracks. The reason can be illustrated as follows. The addition of rare earth elements in the laser-cladding process can effectively refine the structure and increase the grain boundary. The crack propagation in the laser-cladding coatings is hindered and further reduces the harmful effect on the substances. All these lead to the improvement of strength and toughness of the laser-cladding coatings.

TABLE 1: The chemical composition of TC4 titanium alloy (wt.%).

Elements	Al	V	Fe	C	N	H	O	Ti
Wt.%	5.5 ~ 6.8	3.5 ~ 4.5	≤0.3	≤0.1	≤0.05	≤0.01	≤0.02	Balance

TABLE 2: The physical performance of CeO<sub>2</sub>.

Melting point (°C)	Specific gravity (g·cm <sup>-2</sup> )	Color	Heat of formation (kJ·mol <sup>-1</sup> )	Free energy (kJ·mol <sup>-1</sup> )	Enthalpy change (kJ·mol <sup>-1</sup> )	Purity (%)
1965	7.13	Yellow and white	-2596.65	-1025.35	62.34	99.99

TABLE 3: The chemical composition of Ni25 (wt.%).

	C	B	Si	Cr	Fe	Ni	HRC
Ni25	≤0.2	1.0~2.0	2.0~3.5	5.0~10.0	≤4	Balance	20~30

TABLE 4: Specimen numbers and corresponding laser-cladding process parameters and CeO<sub>2</sub> contents.

Specimen number	S0	S1	S2	S3	S4	S5	S6
Laser power (kW)	1	1	1	1	1	1	1
Laser scanning rate (mm·min <sup>-1</sup> )	600	600	600	600	600	600	600
Powder feeding rate (g·min <sup>-1</sup> )	8	8	8	8	8	8	8
Argon gas velocity (L·min <sup>-1</sup> )	15	15	15	15	15	15	15
Spot diameter (mm)	3	3	3	3	3	3	3
CeO <sub>2</sub> (wt.%)	0	1	2	3	4	5	6

Figure 3 shows the SEM photographs of the laser-cladding coatings for different CeO<sub>2</sub> contents. As it can be seen from Figure 3(a), the dendritic structures of the Ni25 cladding layers are coarse, and many grain segregations, accompanied by a large number of pores, can be observed in the local area, whereas the Ni25-cladding layers added with rare earth oxides exhibit compact dendritic structures, and the grains are refined. This finding agrees with the existing related studies [23, 24]. This phenomenon can be attributed to the improved liquidity of the molten pool as a result of the addition of rare earth oxides, which is beneficial for gas discharge from the molten pool. Consequently, the pores and cracks in the cladding layers are eliminated. Nevertheless, the degree of rare earth refinement is not unlimited. When the content of rare earth CeO<sub>2</sub> is more than 2%, the microstructure of the laser-cladding coatings becomes coarser. In particular, the size of dendrite in the laser-cladding coatings increases significantly. Thus, it can be seen that there is an optimum value for the content of the rare earth in the process of refining the microstructure of the laser-cladding coatings. It can be illustrated as follows. Firstly, when the rare earth element is segregated in the grain boundary due to its adsorptivity, it can block the growth of the grain and reduce the grain boundary. At the same time, the driving force of the grain growth is reduced and the microstructure is refined [25]. Secondly, according to the analysis of physical and chemical aspects, the contradiction exists in the solid-liquid system after the formation of the crystal nucleus. In the temperature below the freezing point,

the formation of the crystal nucleus will bring about a free enthalpy reduction of the system which is the driving force of the nucleation. Moreover, the generated crystal nuclei are small and the degree of dispersion is high, which causes an increase in free enthalpy and resists the nucleation. It can be seen that the free enthalpy of the new grain boundaries plays an important role in the formation and development of crystal nuclei. With the increase of nucleation radius  $r$ , the free enthalpy  $\Delta G$  of the whole solid-liquid system undergoes a process of rising first and then decreasing. Therefore, there exists a maximum value, which is the critical nucleation work. At this time, the nucleation radius of the whole solid-liquid system should be the critical radius  $r_k$ , and  $r_k$  equation is calculated as  $r_k = 2\sigma/\Delta G$ , in which  $\sigma$  is the surface tension on solid-liquid interface and  $\Delta g$  is the free volume change of unit volume.

Because of the strong electronegativity and active chemical properties of Ce atom, it is easy to fill the surface defects of alloy phase in liquid metal, so that the surface tension on the interface between the two phases is low. Based on  $r_k$  equation, it is understandable that the critical radius of the nucleus reduces after the reduction of surface tension, and the number of effective nucleation increases. As a result, the refinement of the microstructure can be achieved.

Figure 4 illustrates the point spectrum analysis of the cross section of sample S2, and it can be seen that the main elements in the coating are C, Ti, and Ni, and the atomic ratio of C and Ti is close to 1 : 1. Furthermore, the results of line scanning analysis from the substrate to the coating of sample S2 are shown in Figure 5. It can be seen that there are mainly Ti, Ni, C, and other elements in the coating. The Ni elements are mainly distributed in the coating layer, the Ti elements are distributed in the coating and the matrix, and the content in the substrate is higher. Other elements are distributed uniformly in the coating and the substrate, which indicates that the rare earth CeO<sub>2</sub> is diffused into the substrate, and a metallurgical bond is developed between the coating and the substrate.

Figure 6 shows the microhardness distribution curves of laser-cladding coatings with various CeO<sub>2</sub> contents. It can be seen that the curves follow a similar trend in which the microhardness is higher in the cladding layer and much lower in the substrate. More importantly, the hardness of cladding coatings appears to be different with various additions of CeO<sub>2</sub>. When the addition of CeO<sub>2</sub> is at 0% and 1%, the maximum microhardness of cladding coatings is below 750HV<sub>0.05</sub>. When the amount of the rare earth CeO<sub>2</sub> is 2%

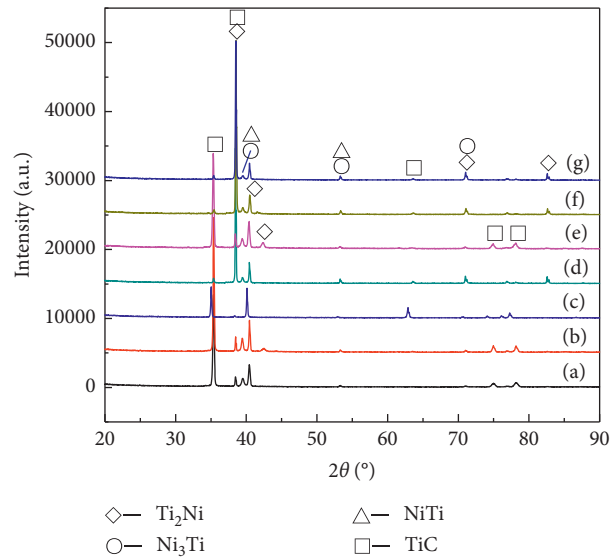


FIGURE 1: X-ray diffraction spectrum of laser-cladding coatings with different  $\text{CeO}_2$  contents: (a) 0%, (b) 1%, (c) 2%, (d) 3%, (e) 4%, (f) 5%, and (g) 6%.

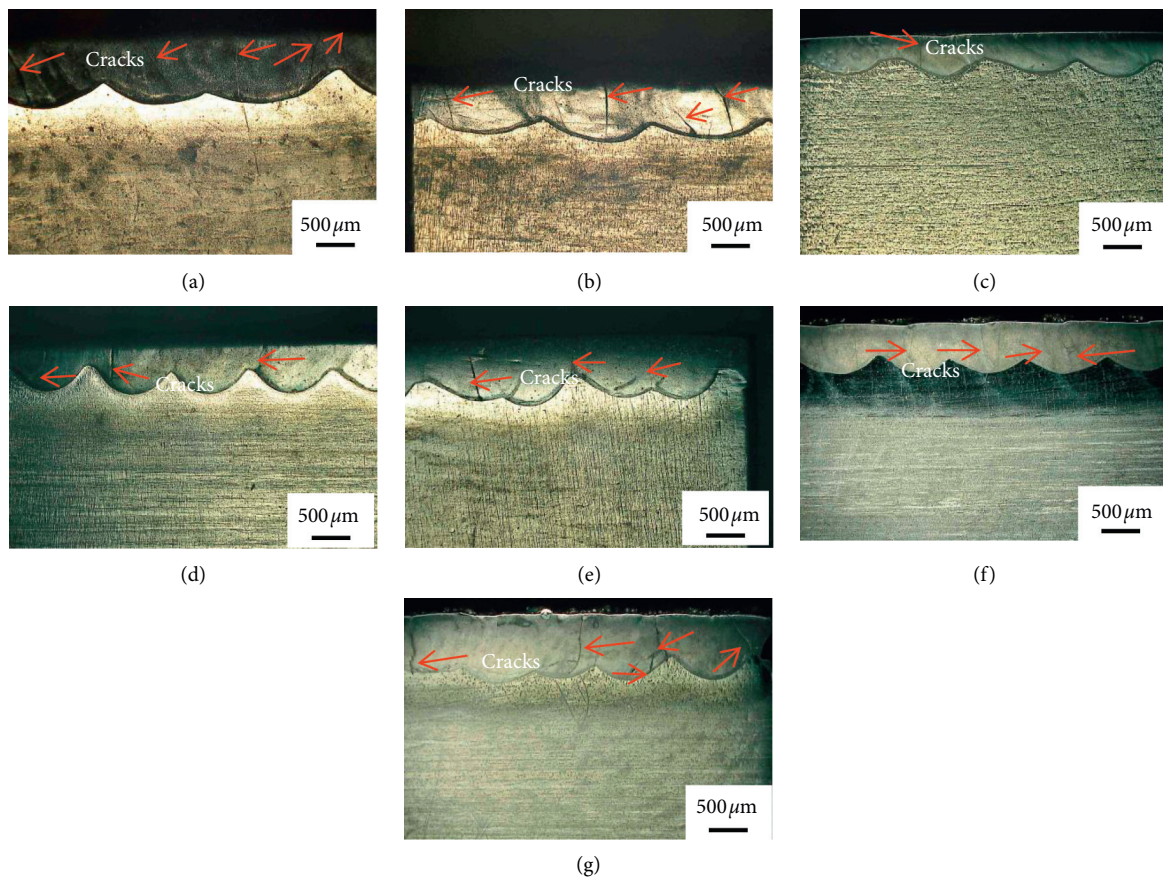


FIGURE 2: The macromorphology of the coatings with different  $\text{CeO}_2$  contents: (a) 0%, (b) 1%, (c) 2%, (d) 3%, (e) 4%, (f) 5%, and (g) 6%.

and 3%, the maximum microhardness of cladding coatings exceeds  $900\text{HV}_{0.05}$ . The microhardness increase is expected in that the microstructure of the cladding layer is refined by the addition of rare earth elements. The rare earth oxide is

dissolved in the solid solution and acts as a solid solution strengthening agent. The laser-cladding process is a non-equilibrium process, and it is possible to obtain the supersaturated solid solution of the rare earth element. The

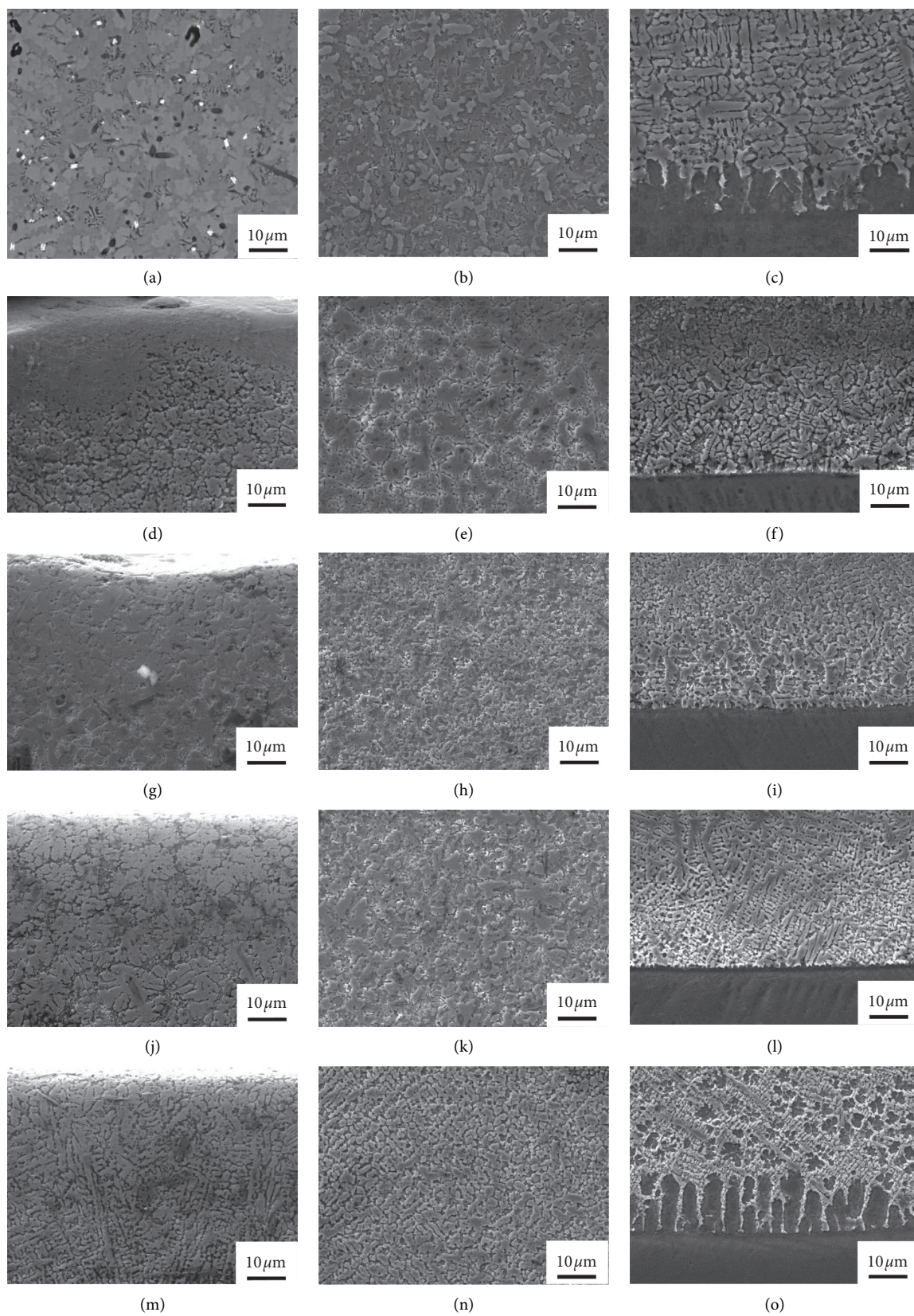


FIGURE 3: Continued.

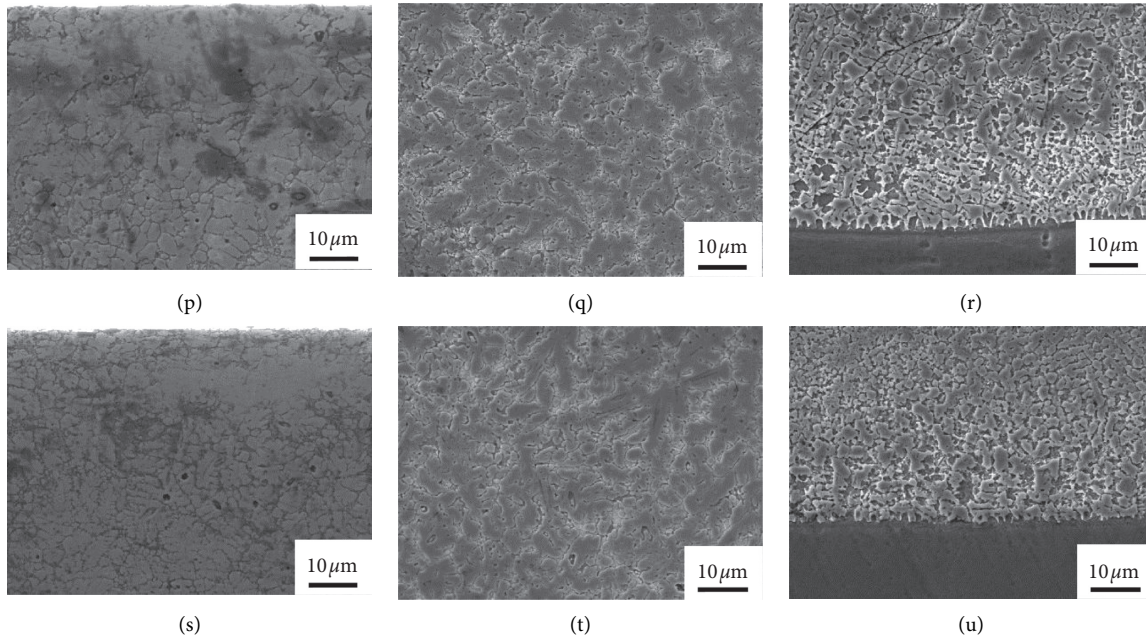
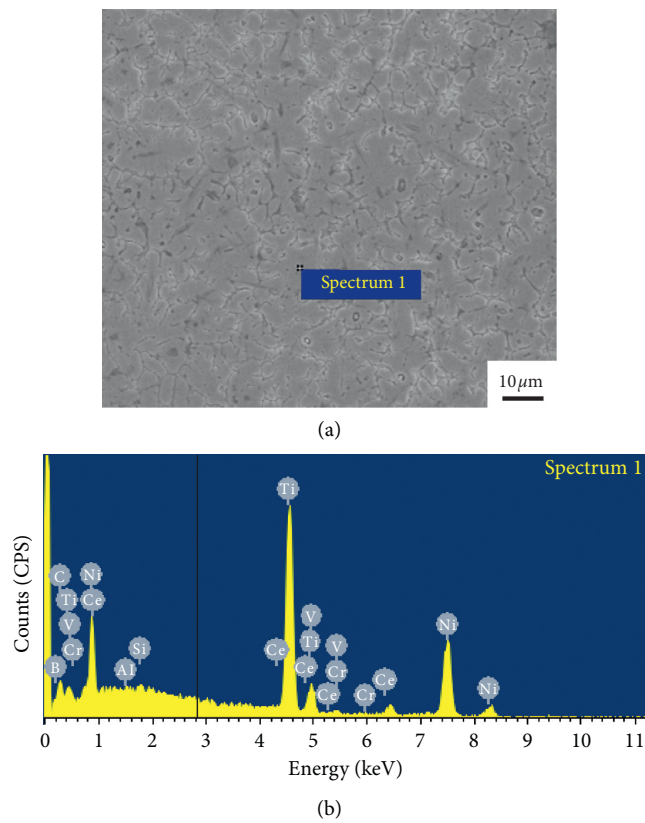


FIGURE 3: The SEM photographs of the laser-cladding coatings for different  $\text{CeO}_2$  contents: (a–c) 0%, (d–f) 1%, (g–i) 2%, (j–l) 3%, (m–o) 4%, (p–r) 5%, and (s–u) 6%. (a, d, g, j, m, p, and s) The surface portion of coatings. (b, e, h, k, n, q, and t) The middle portion of coatings. (c, f, i, l, o, r, and u) The surface portion of coatings.



Elements	BK	CK	Al K	Si K	Ti K	V K	Cr K	Ni K	Ce L	Total
Wt. %	2.12	10.17	0.21	1.13	27.95	0.15	1.17	56.33	0.77	100.00
At. %	7.36	31.77	0.29	1.50	21.90	0.11	0.85	36.01	0.21	100.0

(c)

FIGURE 4: The point spectrum analysis of the cross section of sample S2: (a) the cross section of the S2 coating, (b) elements distribution of coating, and (c) the atomic ratio of elements.

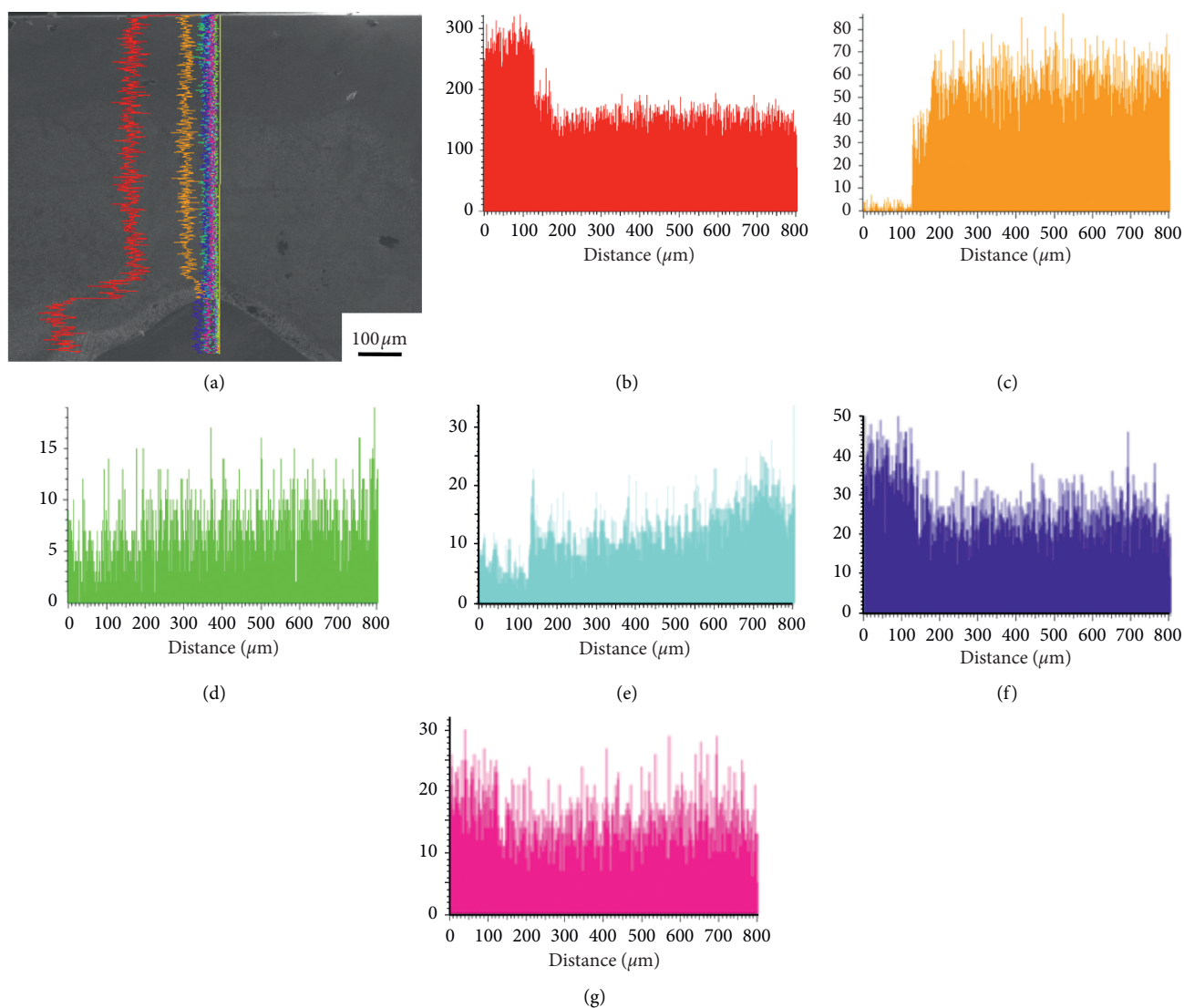


FIGURE 5: The results of line scanning analysis from the substrate to the coating of sample S2: (a) line scan image; (b) Ti element, (c) Ni element, (d) B element, (e) C element, (f) V element, and (g) Ce element.

formation of the solid solution will produce strong lattice distortion, resulting in significant solid solution strengthening. Nevertheless, with the further increase of  $\text{CeO}_2$  content, the microhardness of the cladding layer gradually decreases because the excessive addition of rare earth oxides is easy to form internal inclusions with other components, which in turn decreases the density and the microhardness of the laser-cladding coating.

It can be seen from the above analysis that the amount of rare earth  $\text{CeO}_2$  addition influences the phase composition, microstructure, density of cracks, and microhardness of the cladding coating. It is thus intuitive that the rare earth  $\text{CeO}_2$  addition may have an effect on the corrosion resistance of the laser-cladding coating. The corrosion resistance of the laser-cladding coating with different contents of  $\text{CeO}_2$  is obtained by an electrochemical work station.

Figure 7 shows the potentiodynamic polarization curves of samples added with different  $\text{CeO}_2$  contents in 3.5% NaCl

solution. For each sample, the test result consists of a cathode polarization curve and an anode polarization curve. The cathode polarization curves remain unchanged in the experiment, which means that none of all the cathode polarization processes are changed. With the increase of voltage, the anodizing starts to occur. It can be seen from the diagram that the self-corrosion potential of the sample with  $\text{CeO}_2$  content of 2% is  $-0.15$  V, which is much higher than that ( $-0.30$  V) of the sample with rare earth content of 0%.

It shows that the addition of the proper amount of rare earth can improve the corrosion resistance of the laser-cladding coating. However, with the  $\text{CeO}_2$  content higher than 3%, the corrosion potential decreases again. In particular, the corrosion potential of the coating decreases from  $-0.2$  V (with 3%  $\text{CeO}_2$ ) to  $-0.45$  V (with 6%  $\text{CeO}_2$ ). This is because the grains in the coating will be refined obviously when the amount of  $\text{CeO}_2$  is moderate. With the increase of the number of crystals, the segregation of components can

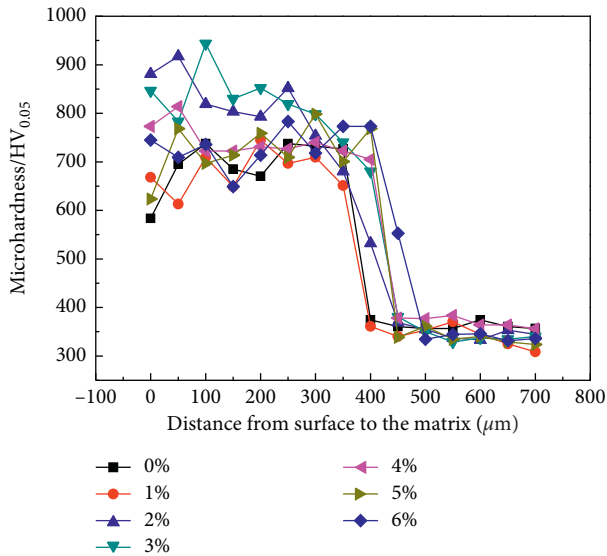


FIGURE 6: The microhardness distribution curves of laser-cladding coatings with various  $\text{CeO}_2$  contents.

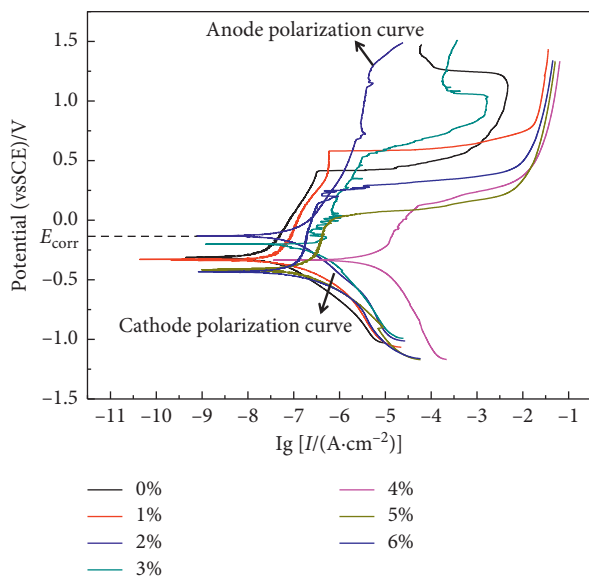


FIGURE 7: The potentiodynamic polarization curves of samples added with different  $\text{CeO}_2$  contents in 3.5% NaCl solution.

be improved and the grain boundary can be prolonged, so the impurity density and the corrosion tendency at the grain boundary are reduced.

Figure 8 shows the Nyquist plot of the laser-cladding coating with different  $\text{CeO}_2$  contents in a 3.5% NaCl solution. It can be seen that the diameter of the capacitive reactance circle in the Nyquist diagram is small, indicating that the laser-cladding coating is excellent in corrosion resistance in the high-frequency region. The Nyquist image is equivalent to a straight line at this time, indicating that the cladding layer is equivalent to an insulating layer with a large capacitance value and a small resistance value, which can effectively protect the titanium alloy substrate from corrosion. Moreover, the linear slope of 2%  $\text{CeO}_2$  content is the

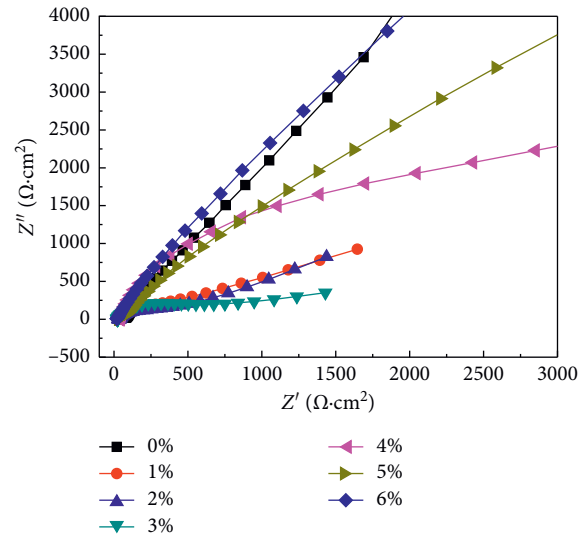


FIGURE 8: Nyquist plot of the laser-cladding coating with different  $\text{CeO}_2$  contents in 3.5% NaCl solution.

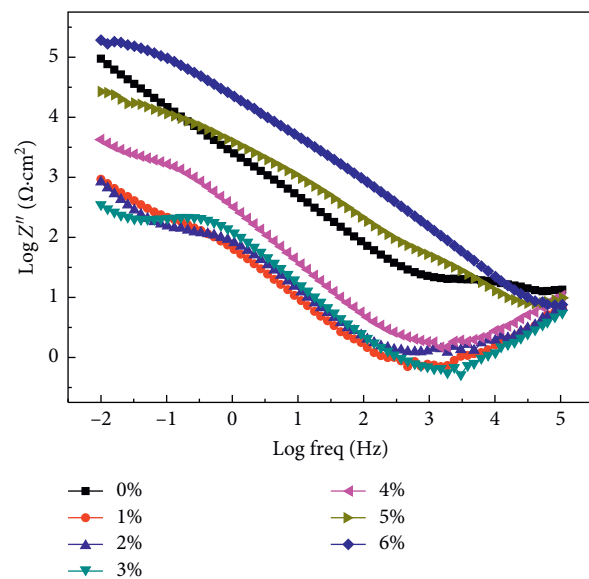


FIGURE 9: Bode plot of the laser-cladding coatings with different  $\text{CeO}_2$  contents in 3.5% NaCl solution.

largest, indicating that the corrosion resistance of the laser-cladding coating is the best when the rare earth content is 2%.

Figure 9 shows the bode plot of the laser-cladding coatings with different  $\text{CeO}_2$  contents in a 3.5% NaCl solution. It can be seen that the high-frequency impedance increases with the increase of  $\text{CeO}_2$  content, while the low-frequency impedance firstly increases and then decreases with the increase of  $\text{CeO}_2$  content. The reduction of the low-frequency impedance means the decrease of the solution resistance, and the increase of the high-frequency impedance indicates that the grains in the coatings will be refined when the amount of  $\text{CeO}_2$  is at a proper level.

#### 4. Conclusions

In conclusion, this study shows that doping the Ni-alloy coatings with CeO<sub>2</sub> could change the microstructure and properties of the Ni-alloy coatings. The XRD result indicates that TiC, NiTi, Ni<sub>3</sub>Ti, and Ti<sub>2</sub>Ni phases exist in the laser-cladding coatings. The phase composition of the coatings does not change with the increase of CeO<sub>2</sub> content up to 6%. The microstructure of the sample with CeO<sub>2</sub> content of 2% is significantly refined, because the Ce atom reduces the critical radius of the crystal nucleus and the number of effective nucleus increases. When the rare earth addition exceeds the critical value, grain refinement effect starts to deteriorate, and the grains become coarser. The addition of CeO<sub>2</sub> can increase the microhardness of the coating. With 2% CeO<sub>2</sub>, the maximum microhardness of the coating reaches over 900 HV<sub>0.05</sub>, while that of coating with 0% CeO<sub>2</sub> is below 750HV<sub>0.05</sub>. The addition of the proper amount of rare earth can significantly improve the corrosion resistance of the laser-cladding coating. This is because the grains in the coatings will be refined when the amount of CeO<sub>2</sub> is at a proper level.

#### Data Availability

The data used to support the findings of this study are included within the supplementary information files.

#### Conflicts of Interest

The authors declare that they have no conflicts of interest.

#### Acknowledgments

The authors (Ye, Shao, Xie, Bian, Wang, Liu, and Wu) are grateful for financial support from the Shaanxi Provincial Natural Science Foundation Project (2019JQ-891 and 2020JQ-889), Xi'an Science and Technology Plan Project (2020KJWL01), the Science Foundation of Shaanxi Provincial Department of Education (20JS133), the National Innovation and Entrepreneurship Training Program for College Students (DC2020022), the Special Research Project of Shaanxi Provincial Department of Education (19JK0739), the research team of advanced surface engineering and equipment life extension of Xi'an University (XAWL-KYTD013) the General Projects in the Industrial Field of Shaanxi Provincial Science and Technology Department (2020GY-193), and the Science Foundation of Shaanxi Provincial Department of Education (15JS054).

#### References

- [1] M. Nabhani, R. Shoja Razavi, and M. Barekat, "Corrosion study of laser clad Ti-6Al-4V alloy in different corrosive environments," *Engineering Failure Analysis*, vol. 97, pp. 234–241, 2019.
- [2] D. Nam, J. Do, and S. Lee, "Microstructure and corrosion behaviour of laser-cladding Al-Ni-TiC-CeO<sub>2</sub> composite coatings on S355 offshore steel," *Journal of Alloys and Compounds*, vol. 770, pp. 771–783, 2019.
- [3] O. Unal, E. Maleki, and R. Varol, "Effect of severe shot peening and ultra-low temperature plasma nitriding on Ti-6Al-4V alloy," *Vacuum*, vol. 150, pp. 69–78, 2018.
- [4] T. T. Peng, X. B. Zhao, Y. Chen, L. Tang, K. X. Wei, and J. Hu, "Improvement of stamping performance of H13 steel by compound-layer free plasma nitriding," *Surface Engineering*, vol. 36, no. 5, pp. 492–497, 2019.
- [5] C. Song, M. Liu, Z.-Q. Deng, S.-P. Niu, C.-M. Deng, and H.-L. Liao, "A novel method for in-situ synthesized TiN coatings by plasma spray-physical vapor deposition," *Materials Letters*, vol. 217, pp. 127–130, 2018.
- [6] E. Marin, R. Offoiach, A. Lanzutti, M. Regis, S. Fusi, and L. Fedrizzi, "Hybrid diffusive/PVD treatments to improve the tribological resistance of Ti-6Al-4V," *Bio-medical Materials and Engineering*, vol. 24, no. 1, pp. 581–592, 2014.
- [7] V. V. Sáenz, M. G. Barandika, G. U. Ruizde et al., "Characterization of Ti-C-N coatings deposited on Ti6Al4V for biomedical applications," *Journal of Inorganic Biochemistry*, vol. 117, pp. 359–366, 2012.
- [8] A. Reina, X. Jia, J. Ho et al., "Large area, few-layer graphene films on arbitrary substrates by chemical vapor deposition," *Nano Letters*, vol. 9, no. 1, pp. 30–35, 2009.
- [9] S. Chaitoglou and E. Bertran, "Effect of temperature on graphene grown by chemical vapor deposition," *Journal of Materials Science*, vol. 52, no. 13, pp. 8348–8356, 2017.
- [10] K. A. Khor, Y. W. Gu, C. H. Quek, and P. Cheang, "Plasma spraying of functionally graded hydroxyapatite/Ti-6Al-4V coatings," *Surface & Coatings Technology*, vol. 168, no. 2-3, pp. 195–201, 2003.
- [11] T. Valente and C. Bartuli, "A plasma spray process for the manufacture of long-fiber reinforced Ti-6Al-4V composite monotapes," *Journal of Thermal Spray Technology*, vol. 3, no. 1, pp. 63–68, 1994.
- [12] Y.-F. Liu, Y.-L. Zhou, Q. Zhang, F. Pu, R.-H. Li, and S.-Z. Yang, "Microstructure and dry sliding wear behavior of plasma transferred arc clad Ti5Si3 reinforced intermetallic composite coatings," *Journal of Alloys and Compounds*, vol. 591, no. 13, pp. 251–258, 2014.
- [13] X. Nie, W. He, S. Zang, X. Wang, and J. Zhao, "Effect study and application to improve high cycle fatigue resistance of TC11 titanium alloy by laser shock peening with multiple impacts," *Surface and Coatings Technology*, vol. 253, pp. 68–75, 2014.
- [14] F. Weng, H. Yu, C. Chen et al., "Effect of process parameters on the microstructure evolution and wear property of the laser cladding coatings on Ti-6Al-4V alloy," *Journal of Alloys and Compounds*, vol. 692, pp. 989–996, 2017.
- [15] C. Tan, H. Zhu, T. Kuang, J. Shi, H. Liu, and Z. Liu, "Laser cladding Al-based amorphous-nanocrystalline composite coatings on AZ80 magnesium alloy under water cooling condition," *Journal of Alloys and Compounds*, vol. 690, pp. 108–115, 2017.
- [16] P. Farahmand, S. Liu, Z. Zhang, and R. Kovacevic, "Laser cladding assisted by induction heating of Ni-WC composite enhanced by nano-WC and La<sub>2</sub>O<sub>3</sub>," *Ceramics International*, vol. 40, no. 10, pp. 15421–15438, 2014.
- [17] M. Z. Mehrizi, M. Shamanian, A. Saidi, R. Shoja-Razavi, and R. Beigi, "Evaluation of oxidation behavior of laser clad CoWSi-WSi<sub>2</sub> coating on pure Ni substrate at different temperatures," *Ceramics International*, vol. 41, no. 8, pp. 9715–9721, 2015.
- [18] M. Li, B. Han, Y. Wang, and K. Pu, "Effects of La<sub>2</sub>O<sub>3</sub> on the microstructure and property of laser cladding Ni-based ceramic coating," *Optik*, vol. 130, pp. 1032–1037, 2017.

- [19] X.-B. Liu, X.-J. Meng, H.-Q. Liu et al., "Development and characterization of laser clad high temperature self-lubricating wear resistant composite coatings on Ti-6Al-4V alloy," *Materials & Design*, vol. 55, pp. 404–409, 2014.
- [20] X.-B. Liu, H.-Q. Liu, X.-J. Meng et al., "Effects of aging treatment on microstructure and tribological properties of nickel-based high-temperature self-lubrication wear resistant composite coatings by laser cladding," *Materials Chemistry and Physics*, vol. 143, no. 2, pp. 616–621, 2014.
- [21] X.-B. Liu, C. Zheng, Y.-F. Liu et al., "A comparative study of laser cladding high temperature wear-resistant composite coating with the addition of self-lubricating WS<sub>2</sub> and WS<sub>2</sub>/(Ni-P) encapsulation," *Journal of Materials Processing Technology*, vol. 213, no. 1, pp. 51–58, 2013.
- [22] G. Zhang, C. Wang, and Y. Gao, "Mechanism of rare earth CeO<sub>2</sub> on the Ni-based laser cladding layer of 6063 Al surface," *Rare Metal Materials and Engineering*, vol. 45, no. 4, pp. 1002–1006, 2016.
- [23] C. Wang, Y. Gao, R. Wang, D. Wei, M. Cai, and Y. Fu, "Microstructure of laser-clad Ni60 cladding layers added with different amounts of rare-earth oxides on 6063 Al alloys," *Journal of Alloys and Compounds*, vol. 740, pp. 1099–1107, 2018.
- [24] X. He, R. G. Song, and D. J. Kong, "Microstructure and corrosion behaviour of laser-cladding Al-Ni-TiC-CeO<sub>2</sub> composite coatings on S355 offshore steel," *Journal of Alloys and Compounds*, vol. 770, pp. 771–783, 2019.
- [25] S. G. Chen, X. M. Zhang, Q. C. Zheng, and R. F. Li, "Effect of CeO<sub>2</sub> on microstructure and properties of Ni60 alloy coating by laser cladding," *Laser Technology*, vol. 41, pp. 904–908, 2017.

## Research Article

# Application and Effect of the Gymnastic Exercise Mode during Chemotherapy for Breast Cancer Patients

**Feifei Xie** 

*Department of Humanities and Social Sciences, Zhejiang Industry Polytechnic College, Shaoxing 312000, Zhejiang, China*

Correspondence should be addressed to Feifei Xie; 20010013@zjipc.edu.cn

Received 7 August 2020; Revised 2 September 2020; Accepted 11 September 2020; Published 21 September 2020

Academic Editor: Tifeng Jiao

Copyright © 2020 Feifei Xie. This is an open access article distributed under the Creative Commons Attribution License, which permits unrestricted use, distribution, and reproduction in any medium, provided the original work is properly cited.

Breast cancer is one of the most common malignant tumors in women, which seriously threatens the health of women. With the improvement of living standards, the incidence rate of breast cancer is also rising. In the past ten years, the incidence rate of breast cancer in China's major cities has increased by 37%, far higher than that in Europe and America. At present, chemotherapy and radiotherapy are the main treatment methods for breast cancer, but many patients will have cancer-related fatigue after surgery. Some studies believe that appropriate sports can improve cancer-related fatigue, but there is no specific research in this area. In view of this problem, this paper puts forward a rehabilitation training method based on gymnastics for breast cancer surgery. This paper is divided into three parts. The first part is the basic theory and core concept of breast cancer and cancer-related fatigue. Through the in-depth study of the theory, this paper believes that breast cancer patients paying attention to rehabilitation training can effectively improve cancer-related fatigue and affect the final therapeutic effect. The second part is the rehabilitation training program based on the way of gymnastics. The corresponding experimental model is established by using real cases as samples. In order to ensure the quality of the experiment, this paper gives the treatment plan in detail and establishes a unified evaluation system. In the third part of this paper, the relevant experiments and results analysis are given, and through data analysis, this paper believes that gymnastics can effectively help breast cancer patients with postoperative rehabilitation and continuous recovery of the upper limb function and improve cancer-related fatigue and other issues.

## 1. Introduction

Breast cancer is one of the most common malignant tumors in women. According to statistics, more than 1.32 million women suffer from breast cancer every year, and 560000 women die of breast cancer. The incidence rate of breast cancer is the highest in developed countries in North America, Western Europe, and Northern Europe and the lowest in Africa. The incidence rate of breast cancer is increasing all over the world. The incidence rate of breast cancer is increasing at 6% to 25% in high incidence areas and low incidence areas. With the improvement of living standards in Asian countries, the incidence rate of breast cancer in Asian women is significantly higher than that in Europe and America and has become one of the most popular areas of breast cancer incidence rate in Asia. China's incidence rate of breast cancer has increased by 41% in the

past ten years. City cancer experts have shown that breast cancer has become the leading cause of cancer in some cities, especially in Shanghai, Beijing, and coastal areas. It is the highest incidence area of breast cancer in China, and the highest in Shanghai.

At present, the treatment of breast cancer mainly adopts the comprehensive treatment mode of surgery combined with radiotherapy, chemotherapy, endocrine therapy, immunobiological therapy, and various supportive therapies. Among them, chemotherapy has become an important treatment for breast cancer. With the deepening of the understanding of cancer and the continuous breakthrough of treatment technology, new chemotherapy methods are constantly added in cancer chemotherapy. The basic purpose of chemotherapy is to reduce the local lesions, surrounding tissue infiltration and lymph node metastasis, improve the surgical resection rate or increase the curative effect of

radiotherapy, eliminate micrometastasis, or delay the process of tumor metastasis. With the improvement of diagnosis and comprehensive treatment technology, the survival time of breast cancer patients has been prolonged. According to recent estimates, in the United States, 99% of breast cancer patients without metastatic disease and 85% of patients with local metastasis survive for more than five years. Chinese scholars followed up breast cancer patients diagnosed in a cancer hospital from 1975 to 2000. They found that the 3-year survival rate of breast cancer was 83.2% in the 1980s and 84.9% in the 1990s.

In different stages of treatment, cancer patients need to receive different intensity and methods of chemotherapy and radiation therapy, which can kill tumor cells and normal tissue cells and lead to different degrees of toxicity and side effects, complications and even be life-threatening. Severe side effects include gastrointestinal reactions such as nausea and vomiting, bone marrow suppression, leukocyte predominance, decreased hemoglobin, and neurotoxicity. It is characterized by numbness and pain of limbs, as well as other liver and kidney damage and cardiac toxicity. Some scholars have found that many chemotherapeutic drugs, such as platinum, tubulin inhibitors, borosamine, and sallydol, are widely used in the treatment of solid tumors and hematological malignancies. Many chemotherapy drugs, such as platinum, microtubulin inhibitors, boromine, and thalidol, have neurotoxicity, causing a series of nerve disorders in peripheral nerve or autonomic nerve injury, known as peripheral neuropathy caused by chemotherapy. There are also views that breast cancer surgery, radiotherapy, and chemotherapy patients in pain and tension for a long period of time affect the patient's physical and mental health and can make the patient appear weak and have other symptoms, such as very low mood, the whole body decline, drowsiness, fatigue, and interest decline, such as in cancer, because it is tiring. The best way to improve cancer-related fatigue is exercise therapy, such as core strength training and lower limb strength training, and postoperative rehabilitation exercise training research on breast cancer is less. At present, there is a unified guidance in this field, and a solution based on gymnastics in chemotherapy for breast cancer patients is proposed.

First of all, the core theory of breast cancer and cancer-related fatigue was deeply studied, and it was concluded that breast cancer chemotherapy had a certain impact on women's body structure, including physiological and psychological effects. It is for this reason that many women are emotional and physically tired after surgery. At present, the treatment of breast cancer has been relatively complete and greatly improved the survival rate of patients, but little attention has been paid to the postoperative rehabilitation training, which is also one of the important problems to be solved in this field. The rehabilitation training method based on gymnastics is specially customized according to the postoperative needs of breast cancer patients. It can strengthen the training of upper limb muscle strength and reduce the training burden of patients. This paper presents a rehabilitation method for breast cancer patients based on

gymnastics and establishes the corresponding experimental model. The experimental samples in this paper are all from real cases, after screening, and they are divided into an intervention group and control group. The intervention group uses gymnastics training for exercise intervention, while the control group uses individual free training. At the end of the article, through a number of comparative experiments including upper limb dysfunction and uncertainty of disease, through the analysis of experimental data, it is believed that the gymnastics training method in this paper can help patients recover upper limb function quickly after chemotherapy and improve their mental health. This experiment has achieved a better effect and further verified that gymnastics can play a positive role in the postoperative rehabilitation of breast cancer patients [1-3].

## 2. Basic Theories and Core Concepts of Breast Cancer

*2.1. Epidemiology of Breast Cancer.* Breast cancer is a serious threat to women's health in the world. It is also one of the common malignant tumors of women. There are about 1.32 million women suffering from breast cancer every year in the world, and 560000 women die of breast cancer. On average, one woman is diagnosed with breast cancer every 25 seconds and one woman loses her life every 80 seconds. In Canada and other European and American countries, breast cancer is the leading cause of female cancer. One in seven women has breast cancer, which is one of the main causes of female death. Our country originally belonged to a low incidence rate of breast cancer. But, in the recent years, with the development of social economy and the improvement of people's living standard, the incidence rate of breast cancer has also been increasing. In China, in Beijing, Guangzhou, Shanghai, and Shenzhen, the incidence rate of breast cancer has ranked the city's leading place in women's malignant tumors, rising from 16/10 million in 1995 to 56/10 million in 2005. Compared with foreign countries, the incidence rate of breast cancer in Europe and the United States is 1/10, although China is still at a low level, but the growth rate is too fast. It is still growing at 3% to 4% per year, and its growth rate is faster than that of Europe and America. In addition, the incidence rate of breast cancer is obviously in younger people in the recent years, especially for the patients aged 22~33 years. There is another 42~50 years of age after the peak. This is 10 years ago as a whole in the western countries with a peak age of 40~50 years than the female breast cancer. The incidence rate is high, but most of them are elderly women. The incidence of female diseases in China is positive. Especially for the society and families, their morbidity is disastrous. The incidence rate of breast cancer in China still has some outstanding characteristics. The city is higher than in the rural areas, and the knowledge level of the developed areas is higher than that of the less developed areas, the income level is lower than that of the less developed ones, and the income is higher than the lower income [4, 5].

## 2.2. History and the Current Status of Breast Cancer Treatment.

The treatment of breast cancer mostly adopts comprehensive treatment methods, including surgical treatment, radiotherapy, chemotherapy, biological therapy, and endocrine therapy. In the past 20 years, with the deepening understanding of the pathogenesis and biological characteristics of breast cancer and the improvement of early diagnosis and adjuvant treatment technology, systematic comprehensive treatment of breast cancer has been paid attention to and developed. In developed countries, breast conserving surgery for early breast cancer has been recognized and gradually replaced radical or modified radical mastectomy. The literature shows that the curative effect of radiotherapy and chemotherapy for breast cancer with breast augmentation stage I and stage II is not lower than that of radical breast cancer.

At the end of the 19th century, radical mastectomy was established based on anatomy. This method mainly focused on the prevention and treatment of local lymphatic spread of tumor cells. However, a large number of clinical data show that radical mastectomy has poor efficacy. In the 1920s, the reason why radical mastectomy was not designed based on radical mastectomy was that radical mastectomy failed. However, the clinical results showed that the curative effect of expansion radical operation was not better than that of radical operation. Soon, we found that the thoracic fascia can prevent the invasion of cancer cells. The modified radical operation of thoracic fascia with preservation of pectoralis major muscle can not only preserve the main function of the upper limb and good appearance of the chest but also achieve the effect of radical operation. It was not until 1980s that people proposed that distant metastasis of breast cancer preceded lymph node metastasis and that breast cancer was not a local cancer, but a systemic disease. Studies have shown that the metastasis of breast cancer cells is disorderly jumping, rather than from near to far, which provides a theoretical basis for the comprehensive treatment of breast cancer, reducing the scope of surgery and breast conserving surgery. A large number of clinical studies in developed countries have shown that breast conserving surgery combined with radiotherapy is as effective as mastectomy. In the recent years, efforts have been made to develop new treatment strategies to reduce tumor-related symptoms, maintain the quality of life of patients, and maximize the survival rate of breast cancer patients. Rehabilitation training has been widely used in clinical practice because of its advantages in relieving fatigue symptoms, enhancing the physiological function of patients, and regulating the psychology of patients. The general trend of surgical treatment for breast cancer is that the scope of surgery tends to be reasonable and multidisciplinary and systematic treatment should be emphasized [6–8].

**2.3. Concept of CRF.** Fatigue is a kind of clinical symptom that is difficult to define. In a broad sense, fatigue is a subjective feeling of weakness and lack of passion. Many physiological and psychological diseases have fatigue manifestations. Fatigue is one of the common feelings of

normal people. Although it is often associated with systemic objective consumption, its self-evaluation can only be reported by the patient subjectively and cannot be directly tested by the observer, so it is difficult to conduct clinical research. Cancer-induced fatigue (CRF) is one of the most important symptoms of cancer patients. It is a common symptom of cancer patients and cancer patients. It may be caused by cancer itself, or it may be the result of cancer treatment, such as chemotherapy, radiotherapy, and biological therapy.

Fatigue is defined as a subjective, unpleasant symptom, ranging from fatigue to a feeling of exhaustion, as well as systemic conditions that may interfere with a person's daily life. The United States Cancer Network (NCCN) defines CRF as a persistent and universal subjective fatigue feeling, which is related to cancer itself and cancer treatment that affects physiological function. This definition highlights the characteristics of CRF in order to distinguish it from the fatigue experienced by healthy people, which can be recovered by adequate rest and sleep. CRF is a subjective perception of unusual systemic fatigue, related to cancer and cancer treatment, affected by the physiological cycle, the duration and intensity are different, and its remission is disproportionate or unrelated to the individual's behavior and effort. For cancer patients, cancer-related fatigue often becomes chronic, leading to unpleasant feelings. Cancer patients describe fatigue as, lack of vitality, inability to concentrate, weakness, lethargy, and depression. In view of the importance of CRF, the 10th edition of the international classification of diseases (ICD) lists CRF as an independent diagnosis and describes CRF as nonspecific fatigue, weakness, systemic decay, and drowsiness. At present, cancer-related fatigue is usually described as a series of subjective feelings caused by chronic stress and pain caused by cancer and its related treatment, such as weakness, activity intolerance, inattention, and decreased motivation or interest. It seriously affects patients' work, study, entertainment, housework, and family life and seriously affects patients' self-care ability and quality of life [9–11].

**2.4. Intervention Effect of Exercise on CRF.** For a long time, the cytotoxicity of cancer and cancer treatment, coupled with physical consumption, is easy to lead to fatigue, resulting in increased physical consumption in daily activities. Over the years, doctors have often advised cancer patients to rest and reduce activity, based on their experience, because cancer and related treatments can lead to reduced levels of physical activity, while exercise can cause symptoms such as fatigue, dyspnea, and tachycardia. Avoidance can reduce discomfort; however, in order to avoid the opposite effect of exercise recommendations, reducing activity leads to muscle loss and decreased cardiopulmonary function, which only increases fatigue and other side effects, which may explain the function of feeling tired and physically damaged after treatment. In the recent years, scientific evidence has changed the relationship between exercise, rest, and fatigue. It seems counterintuitive that learning exercise can relieve fatigue during or after

treatment. But, muscle and blood volume have adaptive changes, increased lung ventilation and perfusion, enhanced heart reserve, and highly concentrated muscle oxidase, so exercise can relieve fatigue by normalizing body function.

Exercise training, even moderate exercise, can make the heart and lung produce more adaptive response, increase cardiac output, reduce heart rate, reduce fatigue, and reduce the need for physical strength. Another hypothesis is that exercise training can accelerate circulation, reduce some cytotoxins or other substances, and reduce the fatigue response. In a study on the relationship between exercise training, fatigue, and quality of life in patients with breast cancer chemotherapy, some scholars found that 7 weeks of family aerobic exercise can improve the quality of life by reducing fatigue. In addition, exercise can also improve mood, improve immunity, reduce vomiting and other side effects, reduce depression, improve sleep, improve disease adaptability and self-efficacy, and ultimately improve the quality of life. Therefore, exercise directly or indirectly reduces the degree of fatigue and improves the quality of life [12, 13].

### 3. Rehabilitation of Breast Cancer Patients after Operation Based on Gymnastics

**3.1. Research Object and Grouping.** The subjects were women with breast cancer who were admitted to the General Service Department of a hospital from May 2019 to October 2019. Among the 120 patients who met the inclusion criteria, 10 of them did not receive chemotherapy during the operation or dropped out of chemotherapy, and did not fall off because of death or serious complications. A total of 110 patients completed the experiment, with an average age of  $47.36 \pm 8.26$  years. One hundred and ten people were divided into two groups, with 55 people in each group.

**3.2. Inclusion and Exclusion Criteria.** Inclusion criteria:

- (1) The patient was 18–70 years old. The condition was stable after chemotherapy. The first cycle of chemotherapy had ended, and the second cycle of chemotherapy was in the outpatient department.
- (2) There is no regular exercise habit after breast cancer surgery. In this study, regular moderate intensity gymnastics should be no more than four times a week, no more than 80 minutes each.
- (3) There are no serious health problems, and the body is suitable for 7 weeks of gymnastics intervention.
- (4) The revised Piper Fatigue Scale showed cancer-related fatigue symptoms.
- (5) Those who voluntarily participated in the study and completed the informed consent form.

Exclusion criteria:

- (1) The main health problems that may affect exercise intervention include coronary heart disease, acute and chronic respiratory diseases, severe hypertension, diabetes, thyroid disease, tuberculosis, anemia,

breast cancer, malignant tumor, severe liver and kidney dysfunction, diseases affecting bone and joint movement, and mental disorders

- (2) Distant metastasis or recurrence occurred
- (3) Regular exercise habits after breast cancer surgery; in this study, regular moderate intensity gymnastics exercise more than four times a week, lasting more than 80 minutes

**3.3. Materials and Instruments.** In this experiment, 23 kinds of materials and instruments including different dyes were used. The specific name, model, and manufacturer are shown in Table 1.

**3.4. Peripheral Blood Sample Collection.** After the patient signed the informed consent, 10 ml of superficial venous blood was collected by using an EDTA anticoagulant vacuum container before the first chemotherapy. After the completion of the first chemotherapy, the pollution of 3 ml blood was extracted and discarded for the first time to eliminate the skin epithelial tissue. After the blood was collected, it was immediately reversed and gently mixed to avoid coagulation. According to the Iset standard test procedure, CTC was detected within 1.5 hours. When ctcbiopsy is used within 1.5 hours, the biopsy should be placed at 5°C and the blood samples should be kept for no more than 24 hours. The blood samples to be transported should be placed vertically in the specimen transport box with low temperature (5°C–10°C) to prevent reversion and violent shaking.

**3.5. Chemotherapeutic Drugs and Drug Regimen**

- (1) Xiaoyangping injection: the component of this product is rattan, and the auxiliary material is polysorbic acid vinegar.
- (2) Chemotherapy drug: docetaxel 65 mg/m<sup>2</sup>; adriamycin 45 mg/m<sup>2</sup>.
- (3) Chemotherapy group and combination group: chemotherapy group, chemotherapy regimen: docetaxel 63 mg/m<sup>2</sup>; adriamycin 45 mg/m<sup>2</sup>. On the first day, 23 repetitions and 7 cycles were performed. The combination group was given xiaoxinping injection on the basis of chemotherapy, once a day, intravenous administration of 8% glucose injection 280 ml + 60 ml xiaoxinping injection, starting from the first day of chemotherapy, and xiaoxinping injection was given intravenously for 15 consecutive days.

**3.6. Observation Index**

- (1) Clinical symptoms: nausea and vomiting, alopecia, diarrhea, and other side effects of chemotherapy
- (2) Laboratory indicators: bone marrow suppression and liver function damage
- (3) ECG changes

TABLE 1: List of experimental materials and instruments.

Peripheral blood 5 ml in patients with breast cancer	Blood samples	On-site
	Reagent	
0.9% normal saline		Self-control
Neutral balsam		Zhuhai Besso
Medical alcohol		Domestic
Superclean sealed tablets		Zhuhai Besso
Deionized water (DI)		Self-control
Diff staining solution		Zhuhai Besso
Polyoxymethylene solution (PFA)		EMS
PBS buffer		Domestic
	Consumables	
Cell filter		Wuhan Youzhiyou company
EDTA vacuum blood collection 2 ml/6 ml		BD company
Slide		Shitai
Cover glass		Shitai
Gun head 200 $\mu$ L/1000 $\mu$ L		Axygen
Pasteurella		NEST
Centrifuge tube 15 ml		Nunc
	Instrument	
Membrane 8 $\mu$ M		Wuhan Youzhiyou company
CTC biopsy detection equipment D-100		Wuhan Youzhiyou company
Membrane remover		Wuhan Youzhiyou company
Drying box		Shanghai Yiheng
Single channel pipette 200 $\mu$ L/1000 $\mu$ L		Thermo
Microscope Olympus BX41		Olympus
Tweezers		Domestic

3.7. *Immunohistochemical Assay.* The biopsies were fixed with 8% formaldehyde solution for 24 hours, and 8  $\mu$ m thick serial sections were taken for histochemical staining. Ki67 was nuclear stained and yellow: 12 visual fields were randomly observed under 450 X-ray microscopes. According to the proportion of positive cells in all the cells, they were divided as positive cells  $\leq 15\%$  were negative and positive cells  $>15\%$  were positive. Over 25% of the positive cells were highly expressed, and  $<25\%$  were of low expression.

3.8. *Rehabilitation Medical Gymnastics Training.* There are three stages of medical gymnastics training.

The first stage: the patients take the lying position or sitting position, and the nurses guide the patients to exercise the muscle groups of the upper limbs and neck on the operation side, including fist and palm practice, shaking the palm root, hand rubbing, ten rotation, neck flexion, back extension, and body wrapping at the same time, combined with auxiliary massage, through relaxing muscle movement, accelerating lymph and blood return, preventing edema of the affected limb, and alleviating discomfort of the neck, shoulder, and back three to four times a week for 7 weeks.

The second stage: with active and auxiliary movement, the healthy side of the upper limb assists the operating side and shoulder muscles to contract the muscle movement of the upper arm. Through the strength of the neck and body, the fibrous tissue of the patients with axillary scar at the bottom of the collapse is gradually reduced, the shaving situation is alleviated, the shoulder joint activity is gradually

improved, and the recovery of the upper limb function of the shoulder joint is slowly promoted three to four times a week for 7 weeks.

The third stage: at-home or outdoor exercise, using cycle and resistance training, muscle groups alternate movement, local and overall combination. Through its forward bending, expansion, abduction, adduction, encirclement, and other full range of motion, the upper arm shoulder joint can strengthen the strength of its shoulder joint-related deltoid muscle, shoulder sub-spleen muscle, supraspinatus muscle, infraspinatus muscle, and other muscle tissue strength, such as dim biceps brachii, obscure triceps brachii, and intercostal muscle three to four times a week for 7 weeks.

The visual analogue scale (VAS), range of motion (ROM) (including flexion, extension and extension), and Barthel index of activities of daily living (ADL) scale were measured and recorded [14, 15].

3.9. *Evaluation of Clinical Efficacy.* RECIST (1.1), revised in 2008, was used by the European Organization for Research and Treatment of Cancer (EORTC), the National Cancer Institute (NCI), and the National Cancer Institute of Canada to assess tumor size and the efficacy of neoadjuvant chemotherapy for breast cancer.

- (1) Complete remission (CR): all target lesions disappeared and no new lesions appeared
- (2) Partial response (PR): total reduction of baseline maximum diameter of all target lesions  $\geq 35\%$

- (3) No change (SD): the sum of the longest baseline diameters of all target lesions decreased, PR remained unchanged, and PD remained unchanged
- (4) Progression (PD): the total maximum diameter of all target lesions increased by more than 25% or new lesions appeared

**3.10. Evaluation of the Pathological Effect.** In this study, the Fisher score and pathological features of chemotherapy breast cancer edited by the Ministry of Health were used to describe and classify the diagnosis and treatment of breast cancer. After the chemotherapy, the pathological properties of the tumor were degenerative. The cell death was mostly in the piece, interstitial fibrous tissue hyperplasia, and the granulation tissue was infiltrated into the foam cells, lymphocytes, and plasma cells around the nests and nests.

The pathological remission rate was divided into three grades.

- (1) Grade I pathological changes (PSD): mild tissue reaction, effective but not sensitive to chemotherapy, and less than one-third of the sections are in the reaction area, infiltrating more cancer components, showing the remaining life of cancer cells and high lymph node metastasis rate
- (2) Grade II pathological remission (PPR): mild tissue reaction, mild sensitivity to chemotherapy, chemotherapy is about 1/2 of the response, and the lymph node metastasis of invasive cancer can be seen
- (3) Grade III pathological complete remission chemotherapy response (PCR): severe tissue reaction, the effect of chemotherapy, the patient is very sensitive to chemotherapy, and the composition of intraductal cancer tissue section, see infiltration, lymph node and metastasis rate is very low

**3.11. Statistical Treatment.** SPSS13.0 statistical software was used for analysis. All the measurement data were expressed as mean  $\pm$  SD. The indexes of cardiac function before and after chemotherapy were paired/tested. The correlation between the two variables was analyzed by person correlation analysis. Bland Altman analysis was used to determine the consistency boundary between intraobserver and interobserver repeatability.

## 4. Experimental Results and Analysis

**4.1. Shoulder Score.** At baseline, the scores of the two groups did not conform to the normal distribution, the median and quartile were used to describe, the Mann-Whitney test was used for the control group, and the Wilcoxon test was used for internal comparison because the difference in shoulder score was not normal distribution.

It can be seen from the analysis results in Figure 1 that the shoulder joint score of the two groups at 24 weeks was significantly different from the baseline ( $P < 0.05$ ). The experiment shows that the timely rehabilitation training of

gymnastics for breast cancer patients after chemotherapy cannot substantially affect the shoulder joint of patients.

**4.2. Patients with Upper Limb Dysfunction.** The DASH scores of the two groups at baseline and 24 hours were in accordance with normal distribution. An independent sample *t*-test was used for comparison between groups, and a paired *t*-test was used for comparison between the two groups before and after intervention.

According to the analysis results in Figure 2, there was no statistically significant difference between the two groups in the baseline and control group ( $P > 0.05$ ), but there was a statistically significant difference between the two groups. The DASH score between the two groups at 24 weeks and before and after the intervention group ( $P < 0.05$ ) was determined. The experimental data show that the intervention group through gymnastics rehabilitation training has obvious rehabilitation signs on upper limb function after chemotherapy, which is significantly faster than the control group without gymnastics rehabilitation training. The experimental results further proved that effective gymnastics training for breast cancer patients after chemotherapy is conducive to functional recovery and brings positive effect to the treatment effect.

**4.3. Comparative Analysis of Disease Uncertainty and Coping Style.** In order to evaluate the effect of intervention, the uncertainty of disease and coping style of subjects after intervention were adjusted.

According to the analysis chart in Figure 3, after the intervention, there were statistically significant differences in the overall disease uncertainty, uncertainty dimension, complexity dimension, lack of dimension between information, and unpredictability between the intervention group and the control group ( $P < 0.05$ ), and the score of the intervention group was lower than that of the control group. As a response, the difference in the total reaction score and avoidance response score between the intervention group and the control group was statistically significant ( $P < 0.05$ ). The total score and face response score of the intervention group were higher than those of the control group, while the score of avoidable treatment was lower than that of the control group. The difference in the production response score between the two groups was not statistically significant ( $P > 0.05$ ).

**4.4. Comparative Analysis of Disease Uncertainty and Coping Style.** According to the analysis results in Figure 4, the overall disease uncertainty, uncertainty dimension, complexity dimension, information loss dimension, and unpredictability score of the intervention group before and after intervention were statistically significant ( $P < 0.05$ ), and the scores after intervention were lower than those before intervention. In the aspect of coping, the total coping score and coping score of the intervention group before and after the intervention also had statistical difference ( $P < 0.05$ ), and the score after intervention was higher than that before

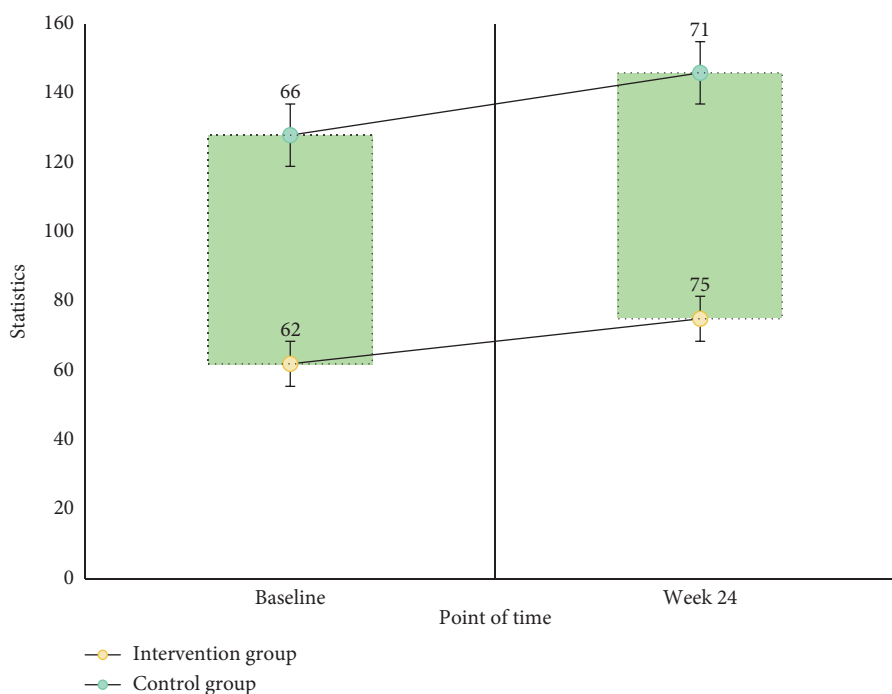


FIGURE 1: Analysis of the shoulder joint score in two groups.

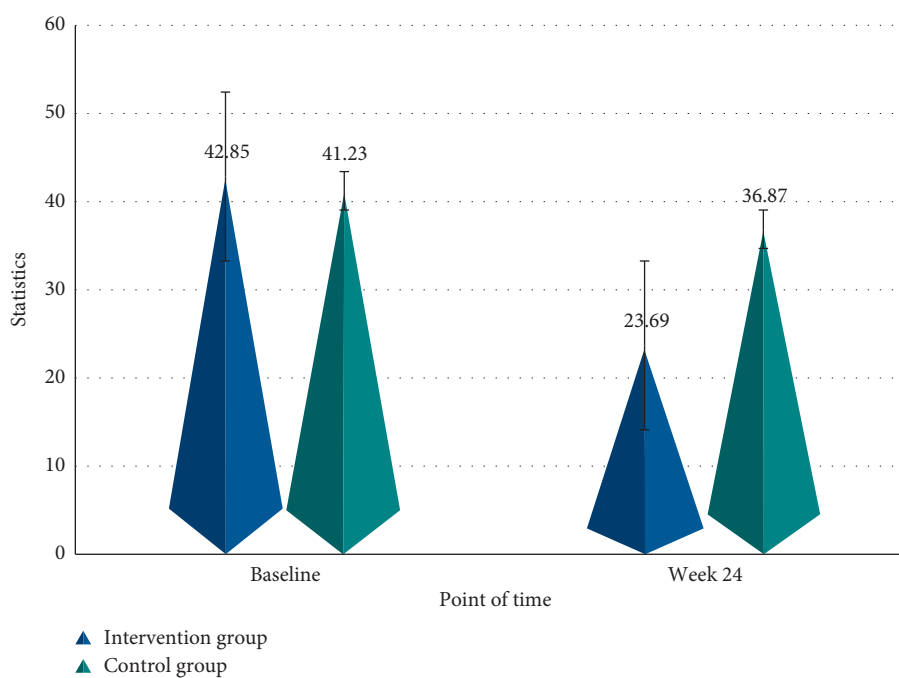


FIGURE 2: Comparative analysis of upper limb dysfunction between the two groups.

intervention, and there was no significant difference in other indexes of the intervention group before and after the intervention ( $P > 0.05$ ). In the control group, there were statistically significant differences in the scores of overall disease uncertainty, uncertainty dimension, and information loss dimension before and after the intervention

( $P < 0.05$ ). In the aspect of coping, the score of the control group before and after the intervention was statistically significant ( $P < 0.05$ ), and the score after intervention was higher than that before intervention, and there was no significant difference in other indicators of the control group before and after the intervention ( $P > 0.05$ ).

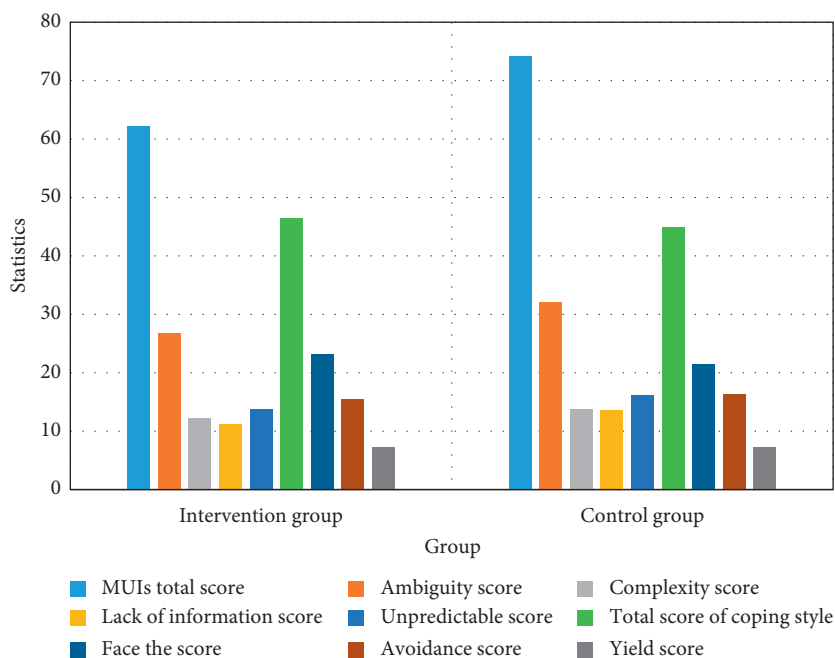


FIGURE 3: Comparison and analysis of uncertainty of disease and coping style between the two groups after intervention.

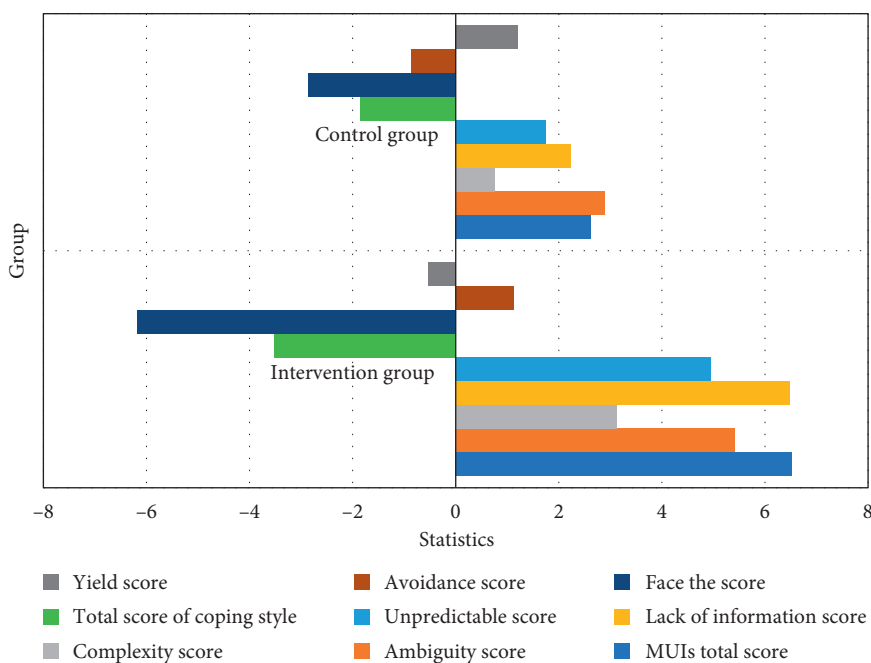


FIGURE 4: Self-comparison and analysis of uncertainty and coping style of patients in two groups before and after intervention.

## 5. Conclusions

The prevalence of breast cancer in China is increasing year by year, which seriously threatens the life and health of women. At present, the pathogenesis of breast cancer is not clear, and genetic factors, environmental factors, behavior habits, and so on will induce breast cancer. At present, chemotherapy and radiotherapy are the main treatment for breast cancer, but no matter which treatment, it will bring

serious harm to patients. Although the cure rate of breast cancer has been improved in the recent years, cancer-related fatigue, which is common after operation, is also worthy of attention. Cancer-related fatigue has a serious harm to breast cancer patients. Improving cancer-related fatigue has a positive effect on the treatment of breast cancer. In this paper, through the establishment of gymnastics exercise for breast cancer patients after intervention, we set up a unified evaluation mechanism. The patients were divided into two

groups: one group was the exercise intervention group, and the other group was the control group. Through a number of comparative experiments including shoulder joint, upper limb dysfunction, and the patient's emotional score, this paper analyzes the experimental data and believes that the current chemotherapy can effectively prevent the spread of cancer cells and improve the cure rate of breast cancer, but the existing postoperative rehabilitation therapy is too backward. The gymnastics rehabilitation therapy in this paper can significantly improve the physical functions of patients after strengthening upper limb training and make the patients' emotions become more positive and sunnier, which is helpful for the postoperative rehabilitation of patients.

### Data Availability

The data used to support the findings of this study can be obtained from the corresponding author upon request.

### Conflicts of Interest

The authors declare that they have no conflicts of interest.

### References

- [1] P. De Andrés, S. Cáceres, M. Clemente, M. Pérez-Alenza, J. Illera, and L. Peña, "Profile of steroid receptors and increased aromatase immunoreexpression in canine inflammatory mammary cancer as a potential therapeutic target," *Reproduction in Domestic Animals*, vol. 51, no. 2, pp. 269–275, 2016.
- [2] A. Msaki, A. Pastò, M. Curtarello et al., "A hypoxic signature marks tumors formed by disseminated tumor cells in the balb-neut mammary cancer model," *Oncotarget*, vol. 7, no. 22, pp. 33081–33095, 2016.
- [3] R. Rostoker, S. Ben-Shmuel, R. Rashed, Z. Shen Orr, and D. Leroith, "Cd24 cell surface expression in mvt1 mammary cancer cells serves as a biomarker for sensitivity to anti-igf1r therapy," *Breast Cancer Research*, vol. 18, no. 1, pp. 1–12, 2016.
- [4] J. D. Shull, K. L. Dennison, A. C. Chack, and A. Trentham-Dietz, "Rat models of 17 $\beta$ -estradiol-induced mammary cancer reveal novel insights into breast cancer etiology and prevention," *Physiological Genomics*, vol. 50, no. 3, pp. 215–234, 2018.
- [5] W. Nie, T. Yu, Y. Sang, and X. Gao, "Tumor-promoting effect of il-23 in mammary cancer mediated by infiltration of m2 macrophages and neutrophils in tumor microenvironment," *Biochemical and Biophysical Research Communications*, vol. 482, no. 4, pp. 1400–1406, 2017.
- [6] J. Cao, M. Huang, Y. Jing et al., "Effect of acupuncture on the expression of er,pr in breast cancer rats induced by dmbs," *Shanghai Journal of Acupuncture and Moxibustion*, vol. 35, no. 3, pp. 344–348, 2016.
- [7] Y. Jing, M. T. Bejarano, J. Zaias, and J. R. Merchan, "In vivo anti-metastatic effects of upar retargeted measles virus in syngeneic and xenograft models of mammary cancer," *Breast Cancer Research and Treatment*, vol. 149, no. 1, pp. 99–108, 2015.
- [8] P. Owens, M. W. Pickup, S. V. Novitskiy et al., "Inhibition of bmp signaling suppresses metastasis in mammary cancer," *Oncogene*, vol. 34, no. 19, pp. 2437–2449, 2015.
- [9] E. Ream, G. Gargaro, A. Barsevick, and A. Richardson, "Management of cancer-related fatigue during chemotherapy through telephone motivational interviewing: modeling and randomized exploratory trial," *Patient Education and Counseling*, vol. 98, no. 2, pp. 199–206, 2015.
- [10] N. Stob, M. J. Müller, S. K pferling, J. D. Schulzke, and K. Norman, "Low recent protein intake predicts cancer-related fatigue and increased mortality in patients with advanced tumor disease undergoing chemotherapy," *Nutrition & Cancer*, vol. 67, no. 5, pp. 818–824, 2015.
- [11] X. Wang and J. You, "Clinical study of Yiqi Jianpi Recipe in treating lung cancer patients with fatigue associated with chemotherapy," *Chinese Journal of Integrated Traditional Chinese and Western Medicine*, vol. 35, no. 9, pp. 1069–1073, 2015.
- [12] Q. Huang, Z. Yan, and X. Wu, "The effect of concurrent radiotherapy and chemotherapy on cancer-related fatigue and psychological care needs of patients with advanced lung cancer," *China Medical Science*, no. 1, pp. 117–120, 2016.
- [13] D. M. Norden, R. Devine, S. Bicer et al., "Fluoxetine prevents the development of depressive-like behavior in a mouse model of cancer related fatigue," *Physiology & Behavior*, vol. 140, no. 3, pp. 230–235, 2015.
- [14] A. H. Deyneko, "Formation of culture motor activity of pupils of 5-6 classes by means of basic gymnastics," *Pedagogics, Psychology, Medical-Biological Problems of Physical Training and Sports*, vol. 19, no. 1, pp. 24–28, 2015.
- [15] R. Tanioka, H. Sugimoto, Y. Yasuhara et al., "Characteristics of transactive relationship phenomena among older adults, care workers as intermediaries, and the pepper robot with care prevention gymnastics exercises," *The Journal of Medical Investigation*, vol. 66, no. 1.2, pp. 46–49, 2019.

## Research Article

# Preparation and Photocatalytic Performances of WO<sub>3</sub>/TiO<sub>2</sub> Composite Nanofibers

Xiuping Han <sup>1,2</sup>, Binghua Yao <sup>1</sup>, Keying Li,<sup>1</sup> Wenjing Zhu,<sup>2</sup> and Xuyuan Zhang<sup>3</sup>

<sup>1</sup>*Xi'an University of Technology, Xi'an 710048, China*

<sup>2</sup>*School of Science, Hainan University, Haikou 570228, China*

<sup>3</sup>*Hainan Vocational University of Science and Technology, Haikou 571126, China*

Correspondence should be addressed to Binghua Yao; [bhyao@xaut.edu.cn](mailto:bhyao@xaut.edu.cn)

Received 3 July 2020; Accepted 23 July 2020; Published 30 August 2020

Guest Editor: Tifeng Jiao

Copyright © 2020 Xiuping Han et al. This is an open access article distributed under the Creative Commons Attribution License, which permits unrestricted use, distribution, and reproduction in any medium, provided the original work is properly cited.

The use of sunlight for photocatalytic oxidation is an ideal strategy, but it is limited by factors such as insufficient light absorption intensity of the photocatalyst and easy recombination of photogenerated electron holes. TiO<sub>2</sub> is favored by researchers as an environment-friendly catalyst. In this paper, TiO<sub>2</sub> is combined with WO<sub>3</sub> to obtain a nanofiber with excellent catalytic performance under sunlight. The WO<sub>3</sub>/TiO<sub>2</sub> composite nanofibers were synthesized by using the electrospinning method. The X-ray diffraction (XRD) analysis indicated that WO<sub>3</sub> was successfully integrated onto the surface of TiO<sub>2</sub>. The photodegradation performance and photocurrent analysis of the prepared nanofibers showed that the addition of WO<sub>3</sub> really improved the photocatalytic performance of TiO<sub>2</sub> nanofibers, methylene blue (MB) degradation rate increased from 72% to 96%, and 5% was the optimal composite mole percentage of W to Ti. The scanning electron microscopy (SEM), X-ray photoelectron spectroscopy (XPS), UV-Vis diffuse reflectance spectra (UV-Vis DRS), and Brunauer-Emmett-Teller (BET) analysis further characterized the properties of 5% WO<sub>3</sub>/TiO<sub>2</sub> nanofibers. The H<sub>2</sub> generation rate of 5% WO<sub>3</sub>/TiO<sub>2</sub> nanofibers was 107.15 μmol·g<sup>-1</sup>·h<sup>-1</sup>, in comparison with that of TiO<sub>2</sub> nanofibers (73.21 μmol·g<sup>-1</sup>·h<sup>-1</sup>) under the same condition. The 5% WO<sub>3</sub>/TiO<sub>2</sub> produced ·OH under illumination, which played an important role in the MB degradation. Also, the enhanced photocatalytic mechanism was also proposed based on the detailed analysis of the band gap and the active species trapping experiment. The results indicated that the effective separation of Z-scheme photogenerated electron-hole pairs and transfer system constructed between TiO<sub>2</sub> and WO<sub>3</sub> endowed the excellent photocatalytic activity of 5% WO<sub>3</sub>/TiO<sub>2</sub> nanofibers.

## 1. Introduction

Photocatalytic oxidation is a green, environmentally friendly, inexpensive, and efficient wastewater treatment technology. The efficient degradation of toxic and hazardous substances in wastewater is the goal that researchers have always sought and has achieved very good results. For example, Jiao and coworkers have prepared a series of environmentally friendly composite hydrogel photocatalysts, which can efficiently degrade the toxic and harmful substances nitrophenol and nitroaniline that are difficult to degrade in wastewater [1–3].

The core of photocatalytic oxidation technology is photocatalyst. Since Fujishima reported that TiO<sub>2</sub> would

decompose water under ultraviolet light irradiation in 1972 [4], TiO<sub>2</sub> has attracted considerable attention in photocatalysis because of its superior photocatalytic activity, good chemical stability, nontoxicity, low cost, and no secondary pollution [5]. However, several disadvantages of TiO<sub>2</sub> photocatalyst severely blocked its practical application such as the limited visible light response, low specific surface area, and high recombination efficiency of charge carriers, which lead to the fact that the photocatalytic activity of TiO<sub>2</sub> was relatively unsatisfactory [6]. Numerous efforts such as morphology designing [7], noble metal [8, 9], or nonmetal doping [10], ion doping [11, 12], composite material forming [13, 14], and heterojunction fabricating [15] had been devoted to improving its photocatalytic performance. Among

the abovementioned methods, heterojunction fabricating had been considered as an efficient strategy for broadening spectrum response range and effectively improving the separation efficiency of photogenerated charge carriers. For instance, Li and coworkers [16] fabricated  $\text{TiO}_2/\text{MoS}_2$  nanoheterojunctions by electrospinning and hydrothermal method and demonstrated that as-prepared samples exhibited super photocatalytic hydrogen evolution activity of  $171.24 \mu\text{mol}\cdot\text{g}^{-1}\cdot\text{L}^{-1}$ . Chen et al. [17] also reported that coupling  $\text{LaNiO}_3$  with  $\text{TiO}_2$  would remarkably enhance the photocatalytic activity of  $\text{TiO}_2$  and explained that the heterojunction formed between them played an important role in improving the photocatalytic performance. Recently,  $\text{TiO}_2\text{-C}_3\text{N}_4$  [18],  $\text{CdS}/\text{TiO}_2$  [19],  $\text{TiO}_2/\text{NiO}$  [20], and  $\text{TiO}_2/\text{Cu}_2\text{O}$  [21] had been reported and shown enhanced photocatalytic performance for organic pollutant degradation and  $\text{H}_2$  evaluation.

$\text{WO}_3$  as an n-type semiconductor with an energy band gap of 2.7 eV has also been considered as an efficient candidate for the formation of heterojunction with other photocatalysts due to its excellent physiochemical stability and strong visible light response [22, 23]. Thus, fabricating  $\text{WO}_3$  with  $\text{TiO}_2$  to form heterojunction might be an effective strategy to enhance the photocatalytic performance of  $\text{TiO}_2$ . For example, Pan et al. prepared  $\text{WO}_3$ -coated  $\text{TiO}_2$  catalysts via alcoholthermal synthesis; thus, the  $\text{WO}_3$ -coated  $\text{TiO}_2$  heterostructure exhibited excellent photocatalytic performance compared with anatase  $\text{TiO}_2$  [24]. Hunge et al. synthesized  $\text{WO}_3/\text{TiO}_2$  thin films by the two-step spray pyrolysis method, and because a junction is formed between the  $\text{WO}_3$  and  $\text{TiO}_2$ , their photoelectrocatalytic activity was enhanced [25]. Khan et al. fabricated hybrid  $\text{TiO}_2/\text{WO}_3$  samples, and  $\text{TiO}_2$  and  $\text{WO}_3$  act in synergy effectively separated holes and electrons and improved photocatalytic performance [26].

The photocatalytic performance of the catalyst was closely related to its micromorphology and porous structure. The fibrous photocatalyst had a large specific surface area and more exposed active sites, which ensured its higher adsorption capacity and better photocatalytic activity [27]. Moreover, the special fibrous structure was beneficial to transfer photogenerated electrons and holes from the bulk phase to the catalyst surface and inhibited the recombination of electron-hole pairs. Therefore, fibrous photocatalysts could generate higher photocatalytic performance in comparison with traditional materials [28, 29]. Hu et al. synthesized  $\text{TiO}_2/\text{WO}_3$  nanofibers by electrospinning technique and clarified that the heterojunction formed after the addition of  $\text{WO}_3$  in  $\text{TiO}_2$  fibers increased  $\text{H}_2$  production rate [30]. Gao et al. prepared  $\text{TiO}_2/\text{WO}_3$  nanofibers where the hydrogen production rate is  $27.73 \mu\text{mol}/\text{h}$  and clarified the formation of band bending and artificial Z-scheme when there is a  $\text{WO}_3$  contact with  $\text{TiO}_2$  [31]. Soares and Alves synthesized  $\text{TiO}_2/\text{WO}_3$  fibers by electrospinning which increased the photocatalytic performance due to the addition of  $\text{H}_2\text{WO}_4$  and degraded 51% of the dye in 135 min [32].

In this work, the fibers  $\text{TiO}_2$  and  $\text{WO}_3/\text{TiO}_2$  fibers were successfully synthesized through a one-step electrospinning process and were characterized by using XRD, SEM, XPS,

UV-Vis DRS, and BET techniques. The photocatalytic performance and stability of as-prepared samples were estimated by photocatalytic degradation of MB and hydrogen evolution under UV-Vis light irradiation. Finally, the possible enhanced photocatalytic mechanism of  $\text{WO}_3/\text{TiO}_2$  heterojunction nanofibers was proposed.

## 2. Experimental

**2.1. Synthesis by Electrospinning.** The nanofibers of  $\text{TiO}_2$  were obtained from the precursor solution made by mixing 2.50 g of tetrabutyl titanate, 9.0 mL of glacial acetic acid, 1.10 g of polyvinylpyrrolidone (PVP), and 10 mL of ethanol solution containing N,N-dimethylformamide ( $v:v=1:1$ ) as the solvent. The  $\text{WO}_3/\text{TiO}_2$  precursor solution was prepared by mixing the abovementioned reactants plus different amounts of  $(\text{NH}_4)_2\text{WO}_4$ . These solutions were continuous stirring for 12 h and then transferred into an electrospinning device. The electrospinning parameters were optimized such as flow rate for solution 2.7 mL/h, an applied voltage of 14 kV, and the tip to collector distance of 11 cm. The samples collected on aluminum-foil collectors were designated as precursors.

Finally, the precursors prepared were heated up to  $520^\circ\text{C}$  at a heating rate of  $1^\circ\text{C}/\text{min}$  for four hours in a tube furnace, and the nanofibers of  $\text{TiO}_2$  and  $\text{WO}_3/\text{TiO}_2$  were obtained. We prepared a set of  $\text{WO}_3/\text{TiO}_2$  nanofibers by varying  $(\text{NH}_4)_2\text{WO}_4$  molar percent at 1%, 5%, and 10% where all other parameters remained unchanged.

**2.2. Characterization of As-Prepared Samples.** XRD patterns of samples were collected in the range of  $10\text{--}80^\circ$  using a 6100 X-ray diffract meter with  $\text{Cu K}\alpha$  radiation. The morphologies of photocatalysts were characterized by VTGA3 SBH scanning electron microscopy. XPS analysis was performed using a K-alpha photoelectron spectroscope. UV-Vis DRS of photocatalysts were analyzed by UV-2102, UV-Vis spectrophotometers with  $\text{BaSO}_4$  as the internal reflectance standard. The BET surface area of samples was carried out using the JK-BK122W apparatus. The photocurrent was measured using a CHI-660b electrochemical analyzer.

### 2.3. Evaluation of Photocatalytic Activity

**2.3.1. Photocatalytical Degradation of MB.** The photocatalytic performance was estimated by the degradation of MB and was performed. In a typical process, 50 mg of as-prepared samples was dispersed in 50 mL  $20 \text{mg}\cdot\text{L}^{-1}$  MB and stirred in the dark for 30 min before irradiation to reach the adsorption/desorption equilibrium. Then, the solution was illuminated with a 250 W Xenon lamp. 5 mL of the sample was collected sequentially at every 20 min and then centrifuged, and the supernatant dye solution was analyzed by TU-1901 spectrophotometer at 664 nm. The degradation efficiency was calculated according to the equation of  $D\% = (A_0 - A_t)/A_0 \times 100\%$ .  $A_0$  and  $A_t$  were the were the absorbance of MB at an initial time and time  $t$ , respectively.

**2.3.2. Photocatalytic Hydrogen Evolution.** The photocatalytic hydrogen evolution experiments were carried out by a DS-GHX-V system with a 100 W Mercury lamp as the light source. In short, 30 mg of as-prepared photocatalysts was added to a sealed 100 mL quartz tube containing a mixture of 60 mL of  $0.25 \text{ mol}\cdot\text{L}^{-1} \text{ Na}_2\text{S}$  and  $0.35 \text{ mol}\cdot\text{L}^{-1} \text{ Na}_2\text{SO}_3$  aqueous solution as a sacrificial agent. Before irradiation, the reaction solution was purged with  $\text{N}_2$  for 30 min to exhaust the air in the quartz tube. The quartz tube was kept in a circulating cooling water system to maintain the temperature at  $25^\circ\text{C}$  and stirred continuously to make an even dispersed solution. A Thermo Trace 1300 gas chromatograph equipped was adopted to determine the amount of hydrogen production on an 80/100 PORAPAK N molecule column. The temperature of the thermal conductivity detector, column box, and filament was assigned at 200,  $150^\circ\text{C}$ , and  $300^\circ\text{C}$ , respectively, and the gas flow rate is  $10 \text{ mL}/\text{min}$  in the constant pressure mode. The holding pressure is  $60.0 \text{ kPa}$  and the ion mode is in negative ion mode. After preheating the gas chromatography,  $300 \mu\text{L}$  of air for zero adjustments was injected. After each irradiation for one hour,  $300 \mu\text{L}$  of gas was taken out to analyze the quantity of hydrogen according to the peak areas with the retention time around  $0.625\text{--}0.630 \text{ min}$  through the external standard method.

### 3. Results and Discussion

**3.1. XRD Analysis.** XRD was employed to investigate the crystal phase structures of the samples as shown in Figure 1, and the characteristic peaks of pure  $\text{TiO}_2$  corresponding to both anatase and rutile were observed. The peaks at  $2\theta$  of  $25.3^\circ$ ,  $37.9^\circ$ ,  $48.2^\circ$ , and  $62.7^\circ$  were indexed to (101), (004), (200), and (204) planes of anatase  $\text{TiO}_2$  (PDF NO. 21-1272), and those at  $2\theta$  of  $27.4^\circ$ ,  $36.1^\circ$ ,  $41.2^\circ$ , and  $54.3^\circ$  corresponded to (110), (101), (111), and (211) planes of rutile  $\text{TiO}_2$  (PDF NO. 21-1276), respectively [33]. For  $\text{WO}_3/\text{TiO}_2$  nanofibers, the diffraction peaks of were similar to those of  $\text{TiO}_2$  nanofibers and the peak intensities gradually decreased with the increase of  $\text{WO}_3$  content and characteristic peaks corresponding to rutile phase diminished in 10%  $\text{WO}_3/\text{TiO}_2$  samples, indicating that the introduction of  $\text{WO}_3$  into  $\text{TiO}_2$  affected the crystal structure of  $\text{TiO}_2$ . In addition, no diffraction peaks related to  $\text{WO}_3$  were detected which might be due to its high dispersion or low content [34].

**3.2. Photocatalytic Degradation Performance.** The photocatalytic performance of  $\text{TiO}_2$  and  $\text{WO}_3/\text{TiO}_2$  nanofibers was assessed by degrading MB under Xenon lamp illumination. The experimental results are displayed in Figure 2(a). Apparently, as shown in Figure 2(a), 5%  $\text{WO}_3/\text{TiO}_2$  exhibited the highest photocatalytic activity with the elimination rate of 96.2% for MB within 150 min, in comparison with that of  $\text{TiO}_2$  nanofibers (72.0%), 1%  $\text{WO}_3/\text{TiO}_2$  (91.5%) nanofibers, and 10%  $\text{WO}_3/\text{TiO}_2$  nanofibers (79.0%) under the same condition. This result indicates that the content of  $\text{WO}_3$  in  $\text{WO}_3/\text{TiO}_2$  composites had a significant effect on the degradation efficiency of MB. The reasons could be attributed to

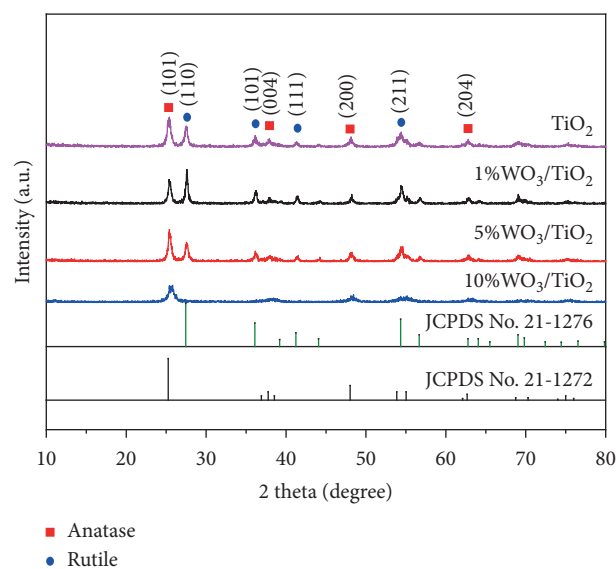


FIGURE 1: XRD patterns of  $\text{TiO}_2$  and  $\text{WO}_3/\text{TiO}_2$  nanofibers.

the following: the lower the amount of  $\text{WO}_3$  is, the less the electron transfer center can be formed, leading to the low photocatalytic activity; on the contrary, too much amount of  $\text{WO}_3$  might change the electron transfer centers to the electron-hole recombination centers; in addition, the  $\text{W}^{6+}$  could scramble electrons from  $\text{TiO}_2$ ; all of these lead to the low photocatalytic activity. In terms of the charge layer thickness, excessive doping of  $\text{WO}_3$  can make the depth of incident light less than the surface charge layer thickness, decreased potential difference, and reduced the electron-hole migration force. Thus, the recombination of photogenerated electrons and holes becomes more easily. Moreover, the larger specific surface area of 5%  $\text{WO}_3/\text{TiO}_2$  nanofibers could supply more magnificent active sites, resulting in the promoted photocatalytic performance.

The photocatalytic activity of 5%  $\text{WO}_3/\text{TiO}_2$  nanofibers is shown in Figure 2(b). With the photocatalytic degradation, the absorption peak at  $664 \text{ nm}$  blueshifts and turns broadened at the same time, which may be caused by the gradual deethylation of MB [35]. The strong chromophore and conjugated structure of MB were destroyed during degradation [36]. Those characteristic peaks disappeared after 150 min irradiation, indicating that the aromatic rings and the conjugated  $\pi$  bond in the MB molecules were completely broken [34]. Obviously, 5%  $\text{WO}_3/\text{TiO}_2$  nanofibers could degrade MB completely under illumination.

The significant stability of the photocatalyst was very substantial for its practical applications. To confirm the stability of 5%  $\text{WO}_3/\text{TiO}_2$  nanofibers, recycling degradation tests were conducted by successive batches degradation of MB as shown in Figure 3. It was clear that at the end of the 5<sup>th</sup> cycle, 5%  $\text{WO}_3/\text{TiO}_2$  nanofibers could still degrade 93% MB within 140 min (shown in Figure 3(a)) under Xenon lamp illumination, indicating the high stability of 5%  $\text{WO}_3/\text{TiO}_2$  nanofibers. The crystal structure of used 5%  $\text{WO}_3/\text{TiO}_2$  nanofibers was also determined to be stable as shown in Figure 3(b). In summary, 5%  $\text{WO}_3/\text{TiO}_2$  nanofibers showed

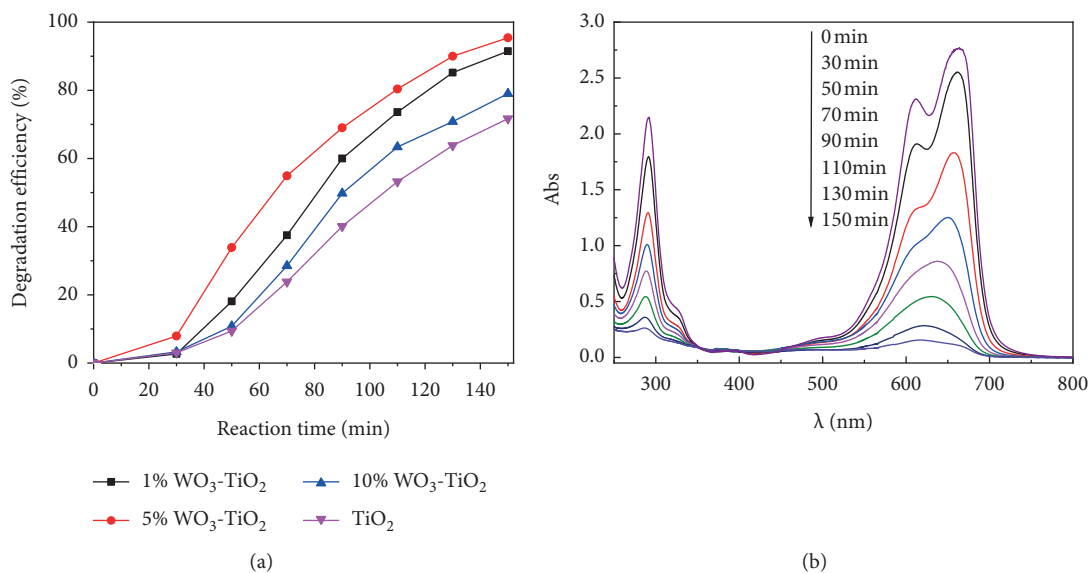


FIGURE 2: (a) Decomposition of MB by TiO<sub>2</sub> and WO<sub>3</sub>/TiO<sub>2</sub> nanofibers; (b) UV-Vis absorption spectra of MB during the photodegradation process by 5% WO<sub>3</sub>/TiO<sub>2</sub> nanofibers.

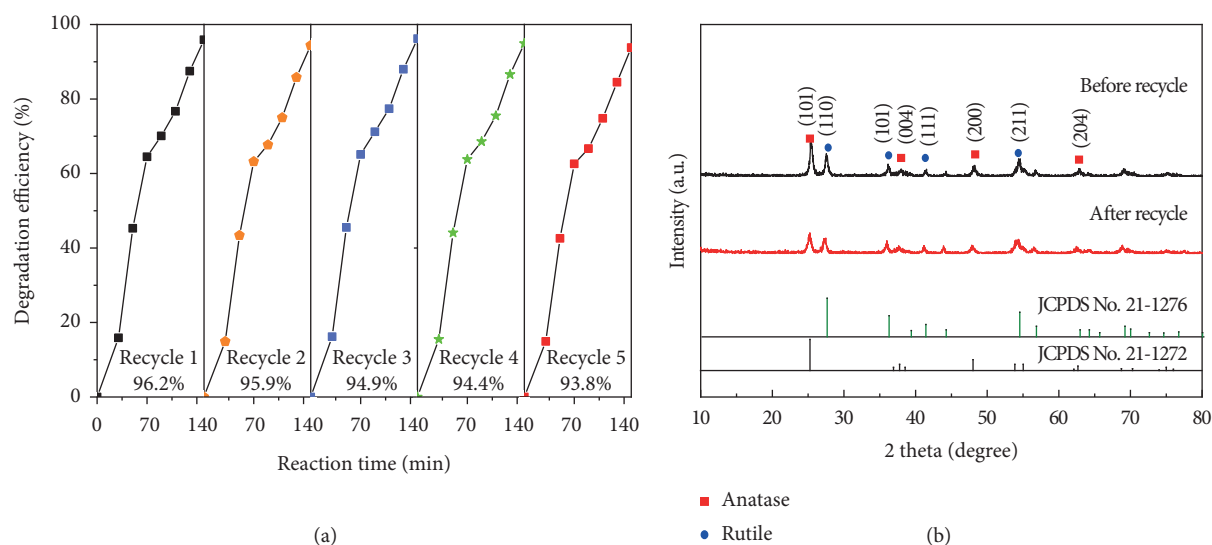


FIGURE 3: (a) Photodegradation performance within five cycles for 5% WO<sub>3</sub>/TiO<sub>2</sub> nanofibers; (b) XRD patterns of 5% WO<sub>3</sub>/TiO<sub>2</sub> nanofibers before and after photocatalysis.

high photocatalytic activity and stability in the catalytic process.

**3.3. Photocurrent Analysis.** The photocurrent test is one of the important means to characterize the response intensity of carriers to illumination and the difficulty of carrier separation. A common method for detecting photocurrent is to use a photocatalyst as a working electrode and a saturated calomel electrode as a reference electrode. When light is irradiated, due to the photoelectric effect, the movement of

the electrons emitted by the electrode will form a photocurrent. The intensity of the generated photocurrent is closely related to the nature of the photocatalyst, and the intensity of the photocurrent is directly proportional to the separation efficiency of photogenerated carriers.

The TiO<sub>2</sub> and WO<sub>3</sub>/TiO<sub>2</sub> nanofibers were coated on the glass plate as the working electrode (coating amount is 3 mg), and the working electrode was irradiated by the 125 W Mercury lamp every 10 s, and the cycle was repeated. The results are shown in Figure 4. It can be seen from Figure 4 that the photocurrent response intensity of WO<sub>3</sub>/

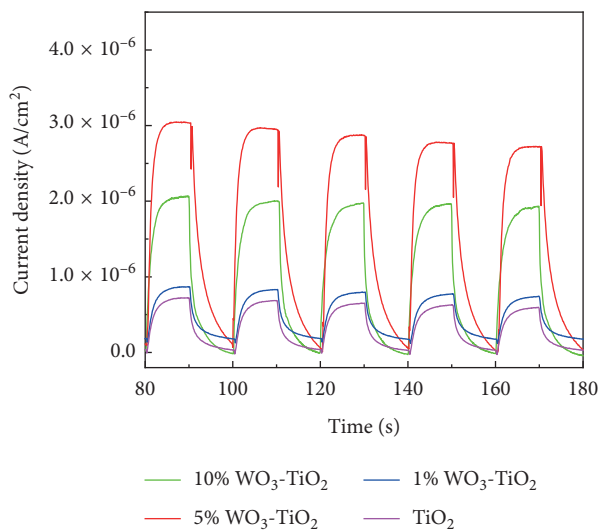


FIGURE 4: Photocurrent response curves of  $\text{TiO}_2$  and  $\text{WO}_3/\text{TiO}_2$  nanofibers.

$\text{TiO}_2$  nanofibers is higher than that of  $\text{TiO}_2$  nanofibers ( $0.7 \times 10^{-6} \text{ A/cm}^2$ ), which indicates that the doping of  $\text{WO}_3$  improves the separation efficiency of photogenerated carriers. 5%  $\text{WO}_3/\text{TiO}_2$  nanofibers have the highest photocurrent response intensity, reaching  $3.0 \times 10^{-6} \text{ A/cm}^2$ , indicating that the light-induced electron-hole pairs are effectively separated in the 5%  $\text{WO}_3/\text{TiO}_2$  nanofiber system, and the recombination trend is lower.

Based on the above analysis results, we believe that 5%  $\text{WO}_3/\text{TiO}_2$  nanofibers are the best composite percentage samples, and their comprehensive performance is the best. Therefore, 5%  $\text{WO}_3/\text{TiO}_2$  nanofibers were further characterized and their hydrogen production performance was studied.

**3.4. SEM and EDS Analysis.** The SEM images of  $\text{TiO}_2$  and 5%  $\text{WO}_3/\text{TiO}_2$  nanofibers are displayed in Figure 5. From Figures 5(a) and 5(c), it was clear that the  $\text{TiO}_2$  precursor and 5%  $\text{WO}_3/\text{TiO}_2$  precursor were composed of smooth fibers with about 200 nm in diameter and 20–30  $\mu\text{m}$  in length. After calcination, these smooth fibers fractured to short fibers with several hundred nanometers in length and the surface became rough as shown in Figures 5(b) and 5(d), which might be resulting from the oxidative decomposition of precursor fibers. As we all know, a rough surface possessed a larger surface area and is conducive to the adsorption reaction, which is helpful to improve the photocatalytic activity [37].

To further identify the chemical composition of both  $\text{TiO}_2$  nanofibers and 5%  $\text{WO}_3/\text{TiO}_2$  nanofibers, EDS analysis was conducted, and the results are illustrated in Figure 6. As expected,  $\text{TiO}_2$  nanofibers were composed of Ti, O elements as shown in Figure 6(a). Three Ti, O, and W elements were detected in 5%  $\text{WO}_3/\text{TiO}_2$  nanofibers as shown in Figure 6(b), implying the successful incorporation of  $\text{WO}_3$  into  $\text{TiO}_2$  nanofibers. Table 1 shows the element contents of

$\text{TiO}_2$  and 5%  $\text{WO}_3/\text{TiO}_2$  samples, which were basically consistent with the raw material ratio in the precursor.

**3.5. XPS Analysis.** The surface chemical status and elemental composition of the as-prepared 5%  $\text{WO}_3/\text{TiO}_2$  nanofibers were analyzed by XPS. Figure 7(a) demonstrates the survey XPS spectra of sample, which indicated that 5%  $\text{WO}_3/\text{TiO}_2$  nanofibers consisted of Ti, W, and O elements, in consistent with EDS results (Figure 6(b)). As indicated in Figure 7(b), the typical peak at 285.49 eV could be ascribed to the carbon contamination in the XPS measurements [38] or organic residues from raw material PVP while calcination [23]. Figure 7(c) displays the high-resolution XPS spectra of O1s with the binding energy at 530.69 eV, which could be attributed to O atom in Ti-O bond and W-O; they share the orbital O1s [26, 39]. The binding energies of Ti  $2p_{3/2}$  and Ti  $2p_{1/2}$  at 459.3 and 464.8 eV in Figure 7(d) confirmed the existence of  $\text{Ti}^{4+}$  in 5%  $\text{WO}_3/\text{TiO}_2$  [40]. The peaks centered at 37.52 and 35.78 eV in Figure 7(e) were attributed to W  $4f_{5/2}$  and W  $4f_{7/2}$ , which fitted well with the characteristic peaks of  $\text{W}^{6+}$  [30].

**3.6. UV-Vis DRS Analysis.** The optical absorption property of  $\text{TiO}_2$  and 5%  $\text{WO}_3/\text{TiO}_2$  nanofibers was characterized by UV-Vis diffuse reflectance technique. Figure 8(a) indicated that the light absorption ability of 5%  $\text{WO}_3/\text{TiO}_2$  nanofibers was slightly enhanced compared with  $\text{TiO}_2$  nanofibers. The band gaps of  $\text{TiO}_2$  and 5%  $\text{WO}_3/\text{TiO}_2$  nanofibers were evaluated according to the equation [41]  $(\alpha h\nu)^2 = A(h\nu - E_g)$ , where  $A$  is a constant,  $h$  is Planck's constant,  $\nu$  is the photon frequency,  $\alpha$  is the absorption coefficient (replaced with absorbance in the calculation), and  $E_g$  is the band gap energy. Figure 8(b) displays the plots of  $(\alpha h\nu)^2$  versus  $(h\nu)$  and the band gap energy of  $\text{TiO}_2$  and 5%  $\text{WO}_3/\text{TiO}_2$  nanofibers was estimated to be 3.23 eV and 3.16 eV, respectively, by extrapolating the linear portion of the graphs to energy axis.

**3.7. BET Analysis.**  $\text{N}_2$  adsorption-desorption measurements were conducted to characterize the specific surface areas and pore size distributions of  $\text{TiO}_2$  and 5%  $\text{WO}_3/\text{TiO}_2$  nanofibers. According to the International Union of Pure and Applied Chemistry (IUPAC) classification, the  $\text{N}_2$  adsorption-desorption isotherms of both  $\text{TiO}_2$  and 5%  $\text{WO}_3/\text{TiO}_2$  nanofibers in Figure 9(a) all corresponded to type IV with the obvious H3-type hysteresis loops, indicating the existence of large mesopores. Figure 9(b) shows the Barret-Joyner-Halenda (BJH) pore size distribution curves of  $\text{TiO}_2$  and 5%  $\text{WO}_3/\text{TiO}_2$  nanofibers. The pore size of  $\text{TiO}_2$  and 5%  $\text{WO}_3/\text{TiO}_2$  nanofibers was mainly distributed in the range of 2–10 nm, further confirming the existence of mesopores. In addition, the BET specific surface areas and detailed BJH pore size of  $\text{TiO}_2$  and 5%  $\text{WO}_3/\text{TiO}_2$  nanofibers are listed in Table 2. The 5%  $\text{WO}_3/\text{TiO}_2$  nanofibers had a larger surface area ( $51.457 \text{ m}^2/\text{g}$ ) than that of  $\text{TiO}_2$  ( $45.067 \text{ m}^2/\text{g}$ ), implying that the coupling of  $\text{WO}_3$  with  $\text{TiO}_2$  boosts the specific surface areas and provided abundant active sites for

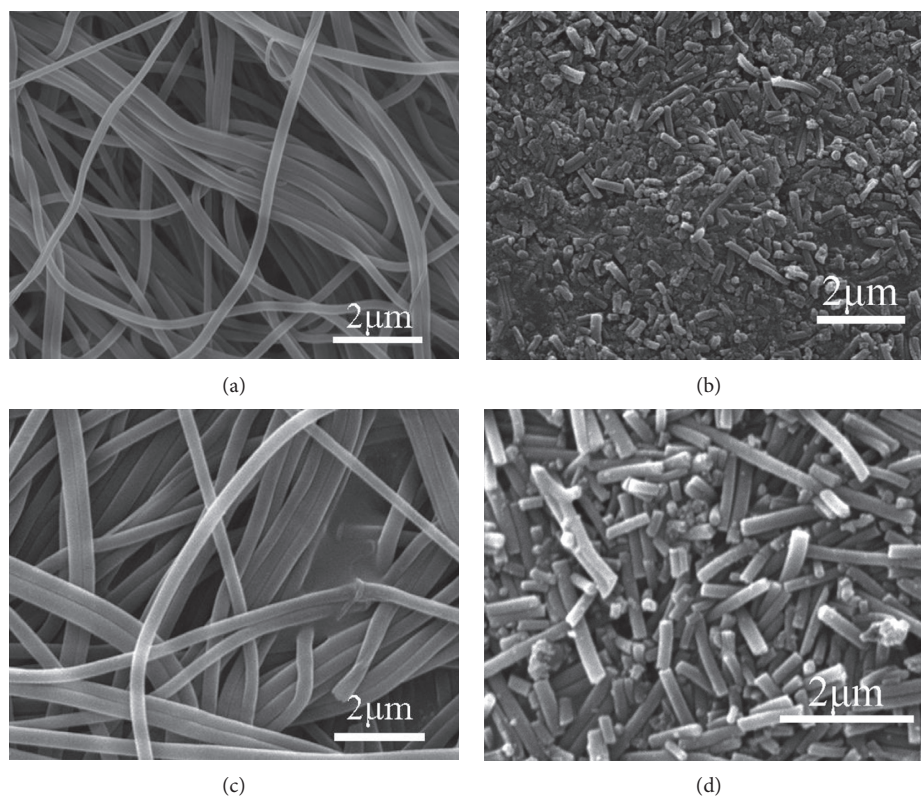


FIGURE 5: SEM patterns of TiO<sub>2</sub> precursor (a), TiO<sub>2</sub> nanofibers (b), 5% WO<sub>3</sub>/TiO<sub>2</sub> precursor (c), and 5% WO<sub>3</sub>/TiO<sub>2</sub> nanofibers (d).

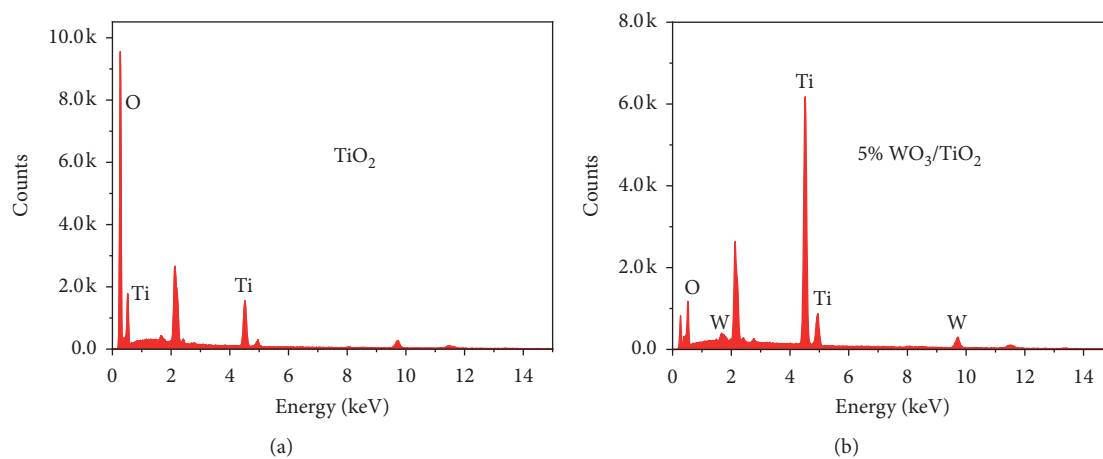


FIGURE 6: EDS of TiO<sub>2</sub> (a) and 5% WO<sub>3</sub>/TiO<sub>2</sub> (b) nanofibers.

TABLE 1: Elemental composition and content of TiO<sub>2</sub> and 5% WO<sub>3</sub>/TiO<sub>2</sub> nanofibers.

Sample	Element	Weight percentage	Atomic percentage
TiO <sub>2</sub>	O	39.89	66.02
	Ti	60.11	32.89
5% WO <sub>3</sub> /TiO <sub>2</sub>	O	37.21	67.18
	Ti	51.87	31.17
	W	10.52	1.64

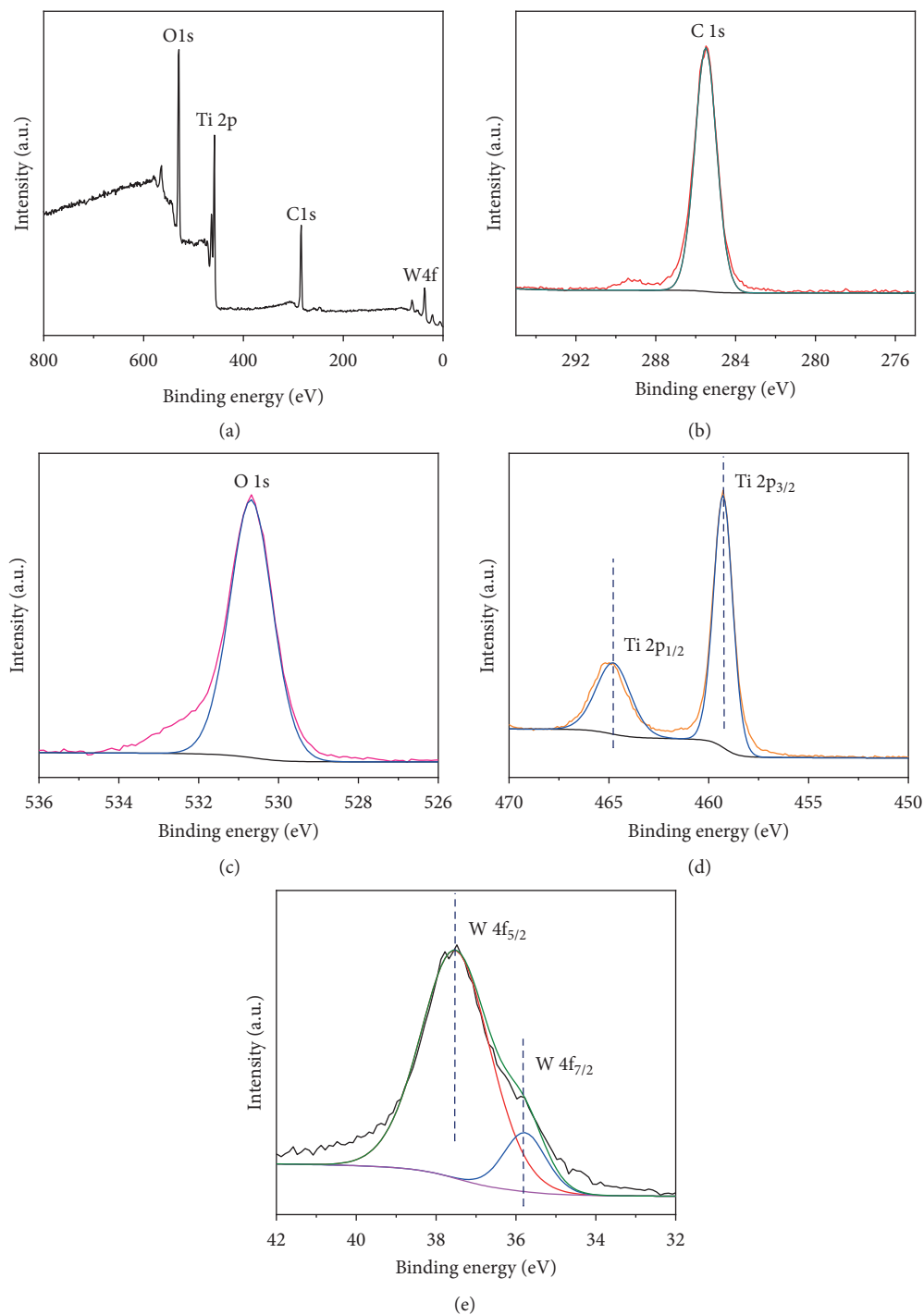


FIGURE 7: XPS spectra of 5%  $\text{WO}_3/\text{TiO}_2$  nanofibers. (a) Survey spectra, (b) C 1s, (c) O 1s, (d) Ti 2p, and (e) W 4f.

adsorption and surface reactions, which could be attributed to their rough surface as shown in Figure 5(d).

**3.8. Photocatalytic Hydrogen Production Performance.** Hydrogen production performance of 5%  $\text{WO}_3/\text{TiO}_2$  nanofibers by water splitting was evaluated under 100 W Mercury lamp irradiation. The  $\text{Na}_2\text{S}$  solution and  $\text{Na}_2\text{SO}_3$  solution were added to splitting water to capture

photogenerated holes and accelerate the outward migration of photogenerated electrons, which is conducive to  $\text{H}_2$  generation. Figure 10(a) shows the photocatalytic  $\text{H}_2$  evolution capabilities of  $\text{WO}_3$ ,  $\text{TiO}_2$ , and 5%  $\text{WO}_3/\text{TiO}_2$  nanofibers. It was obvious that  $\text{WO}_3$  exhibits no  $\text{H}_2$  generation activity, perhaps due to the higher positive CB potential (0.79 eV) [42] than  $\text{H}^+/\text{H}_2\text{O}$  (-0.33 eV), while  $\text{TiO}_2$  nanofibers display a relatively low photocatalytic  $\text{H}_2$  production activity with  $73.32 \mu\text{mol}\cdot\text{g}^{-1}\cdot\text{h}^{-1}$ , due to the rapid

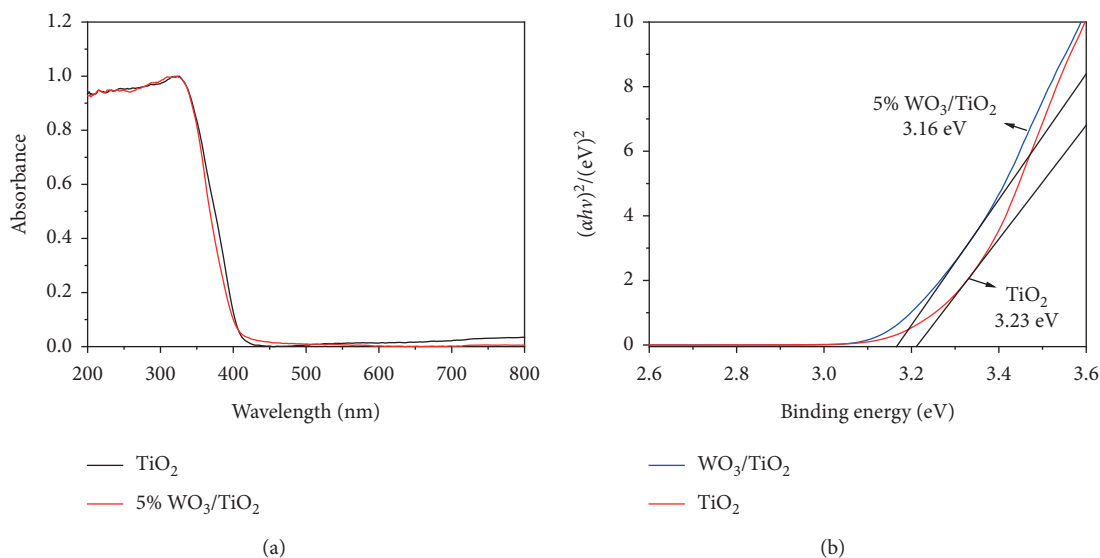


FIGURE 8: UV-Vis DRS spectra of  $\text{TiO}_2$  and 5%  $\text{WO}_3/\text{TiO}_2$  nanofibers.

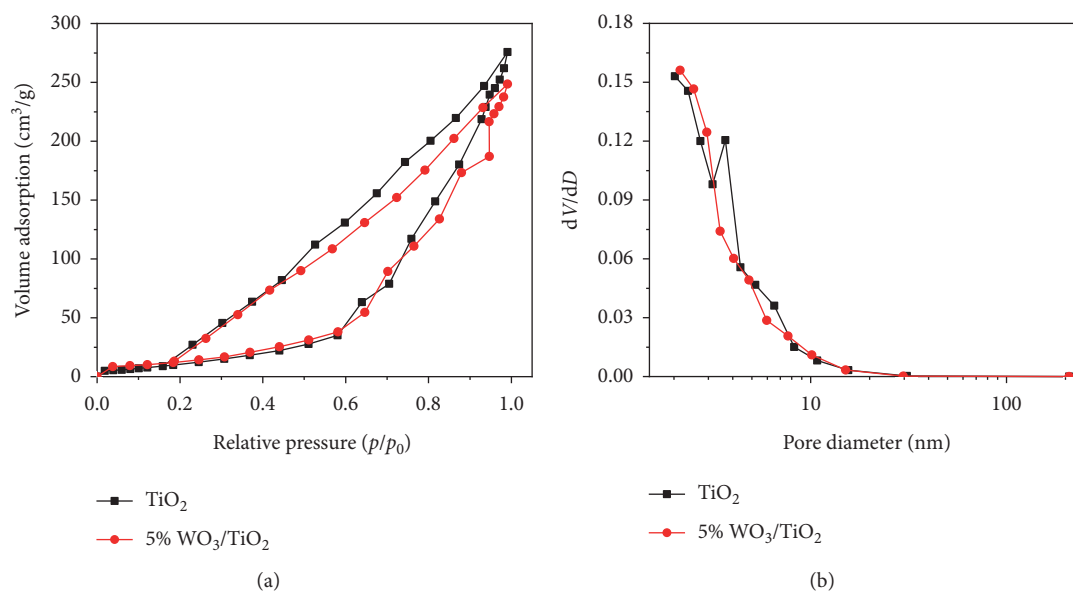


FIGURE 9:  $\text{N}_2$  adsorption and desorption isotherms (a) and the BJH pore size distribution of  $\text{TiO}_2$  and 5%  $\text{WO}_3/\text{TiO}_2$  nanofibers (b).

TABLE 2: Specific surface area, average pore size, and pore volume of  $\text{TiO}_2$  and 5%  $\text{WO}_3/\text{TiO}_2$  nanofibers.

Sample	$S_{\text{BET}}$ ( $\text{m}^2/\text{g}$ )	APS (nm)	PV ( $\text{cm}^3/\text{g}$ )
$\text{TiO}_2$	45.067	4.678	0.635
5% $\text{WO}_3/\text{TiO}_2$	51.457	4.737	0.563

$S_{\text{BET}}$ : specific surface area; APS: average pore size; PV: pore volume.

recombination of electrons in CB and holes in VB. For the 5%  $\text{WO}_3/\text{TiO}_2$  nanofibers, the  $\text{H}_2$  yield rate was  $107.15 \mu\text{mol}\cdot\text{g}^{-1}\cdot\text{h}^{-1}$  which was approximately 1.5 times that of  $\text{TiO}_2$  nanofibers. This result can be attributed to the formation of  $\text{WO}_3/\text{TiO}_2$  Z-scheme heterostructure, which can effectively separate useful electrons and holes, and the

relatively useless electrons and holes are compounded nearby. In other words, the photoinduced electrons were injected onto the CB of  $\text{TiO}_2$ , while the holes were migrated onto the VB of  $\text{WO}_3$ . Thus the recombination of photo-generated charge carriers was effectively inhibited. As a result, the reduction of  $\text{H}^+$  to  $\text{H}_2$  could easily be achieved on 5%

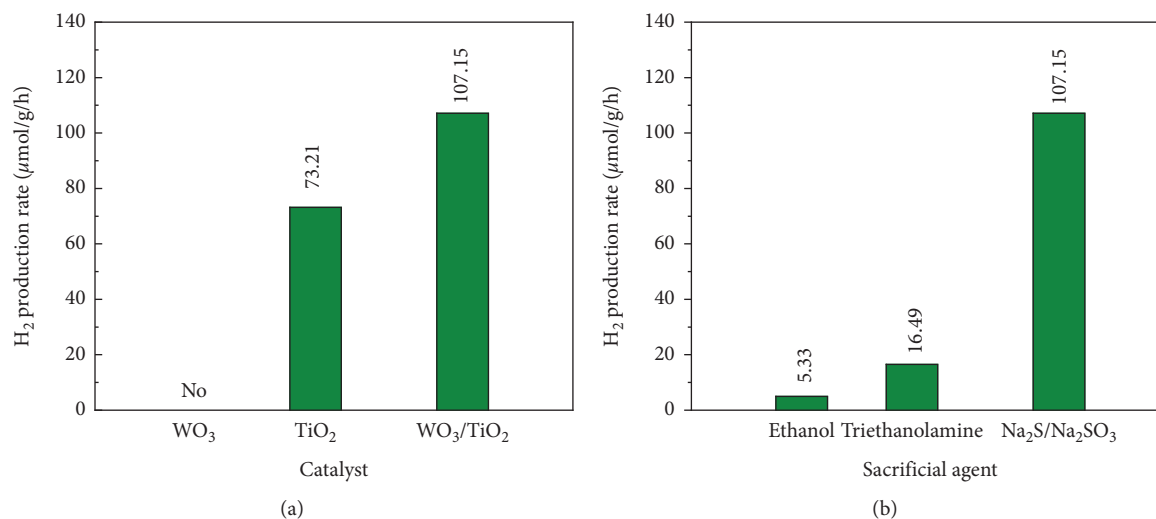


FIGURE 10: (a) H<sub>2</sub> production rate over WO<sub>3</sub>, TiO<sub>2</sub>, and 5% WO<sub>3</sub>/TiO<sub>2</sub> nanofibers. (b) H<sub>2</sub> production rate from different sacrificial agents over 5% WO<sub>3</sub>/TiO<sub>2</sub> nanofibers.

WO<sub>3</sub>/TiO<sub>2</sub> nanofibers system by electrons, while the holes were reacted with S<sup>2-</sup> and SO<sub>3</sub><sup>2-</sup>.

Some photocatalytic materials can only oxidize (electron acceptor) or reduce (electron donor) water to generate oxygen or hydrogen with the participation of sacrificial agents (including electron acceptor and electron donor). Therefore, sacrificial agents are widely used to verify the photocatalytic properties of the materials. The selection of the sacrificial agent has a great influence on hydrogen production. In this experiment, Na<sub>2</sub>S/Na<sub>2</sub>SO<sub>3</sub>, triethanolamine, and ethanol were selected as electron donors, which are combined with photogenerated holes to promote hydrogen production and prevent photocorrosion. From Figure 10(b), it was apparent that the mixture of Na<sub>2</sub>S/Na<sub>2</sub>SO<sub>3</sub> was the best sacrificial agents for hydrogen evolution over 5% WO<sub>3</sub>/TiO<sub>2</sub> photocatalyst.

Therefore, the reason why 5% WO<sub>3</sub>/TiO<sub>2</sub> nanofibers have high hydrogen production activity may be that, on the one hand, the structure of the catalyst is Z-scheme heterojunction, which reduces the recombination probability of photogenerated electrons and holes; on the other hand, the addition of Na<sub>2</sub>S and Na<sub>2</sub>SO<sub>3</sub> hole trapping agents further inhibits the recombination of photogenerated electrons and holes.

**3.9. Photocatalytic Mechanism Analysis.** The band edge positions of 5% WO<sub>3</sub>/TiO<sub>2</sub> nanofibers were theoretically calculated by the following empirical equation [43]:

$$\begin{aligned} E_{\text{CB}} &= E_{\text{VB}} - E_g, \\ E_{\text{VB}} &= X - E_e + 0.5E_g, \end{aligned} \quad (1)$$

where  $X$  is the electronegativity of the semiconductor ( $X_{\text{TiO}_2} = 5.81$  eV and  $X_{\text{WO}_3} = 6.59$  eV [44]),  $E_e$  is the energy of free electrons on the hydrogen scale ( $\approx 4.5$  eV), and  $E_g$  is the band gap energy of the semiconductor ( $E_{g\text{TiO}_2} = 3.23$  eV and

$E_{g\text{WO}_3} = 2.6$  eV). According to this empirical expression, the calculated CB ( $E_{\text{CB}}$ ) and VB ( $E_{\text{VB}}$ ) edge positions for WO<sub>3</sub> and TiO<sub>2</sub> are displayed in Figure 11(a). The CB potential of WO<sub>3</sub> (+0.79 eV) is more negative than the VB of TiO<sub>2</sub> (-0.31 eV) but more positive than the CB of TiO<sub>2</sub> (+2.93 eV); therefore, a Z-scheme charges transportation system is formed between WO<sub>3</sub> and TiO<sub>2</sub>. The photoinduced electrons on the CB of TiO<sub>2</sub> can efficiently inject onto the CB of WO<sub>3</sub> and the holes on VB of WO<sub>3</sub> can transfer onto the VB of TiO<sub>2</sub>. As a result, the highly effective separation and migration system are generated for boosting the photocatalytic performance of 5% WO<sub>3</sub>/TiO<sub>2</sub> composite nanofibers.

To further elucidate the photocatalytic mechanism and identify the main reactive species in the MB degradation process, the active species trapping experiment was conducted. The detailed free radical capture experiment processes were similar to the photocatalytic activity experiments. The reactive free species in MB photocatalytic process over 5% WO<sub>3</sub>/TiO<sub>2</sub> nanofibers were identified by using isopropanol (IPA), benzoquinone (BQ), sodium ethylenediaminetetraacetic acid (Na<sub>2</sub>EDTA), and potassium bromate (KBrO<sub>3</sub>) as scavengers of ·OH, ·O<sub>2</sub><sup>-</sup>, h<sup>+</sup>, and e<sup>-</sup>, respectively. As indicated in Figure 11(b), with the addition of IPA, BQ, and Na<sub>2</sub>EDTA, the degradation efficiency of MB declined to 60.3%, 42.3%, and 60.5%, indicating that H<sub>2</sub>O and/or OH<sup>-</sup> trap h<sup>+</sup> and turn into ·OH in the system. The addition of BQ did not show a significant impact on the photocatalytic activity, indicating that no ·O<sub>2</sub><sup>-</sup> radicals involved in the process. The comparison results confirmed that ·OH, h<sup>+</sup>, and e<sup>-</sup> are the dominant reactive radicals in the MB photodegradation process. ·OH with strong oxidation ability (the standard redox potential is +2.8 eV) can oxidize most organic dyes. Due to the formation of Z-scheme heterojunction, the photogenerated electrons and holes were transferred onto the CB of TiO<sub>2</sub> and VB of WO<sub>3</sub>, respectively. As the CB level of TiO<sub>2</sub> (-0.31 eV) is close to the potential value of ·O<sub>2</sub><sup>-</sup>/O<sub>2</sub> (-0.33 eV) [45], ·O<sub>2</sub><sup>-</sup> could not be

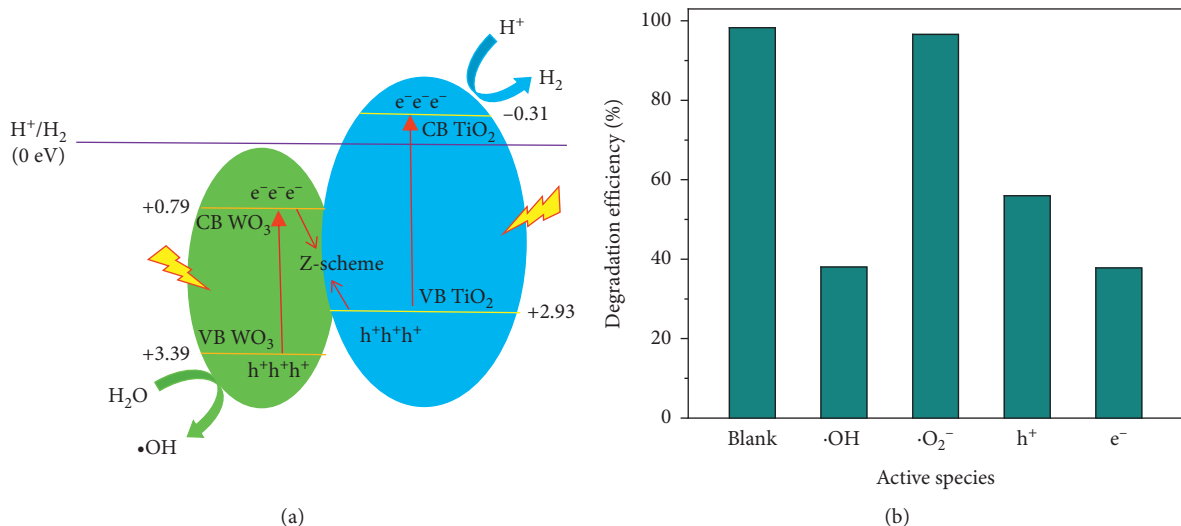


FIGURE 11: (a) Z-scheme charge transfer and surface redox reactions for 5% WO<sub>3</sub>/TiO<sub>2</sub> nanofibers. (b) Catalytic degradation of MB over 5% WO<sub>3</sub>/TiO<sub>2</sub> nanofibers with different quenchers.

formed on TiO<sub>2</sub>. Since holes are accumulated on VB of WO<sub>3</sub> with more positive potential (+3.39 eV) than the redox potential of ·OH/OH<sup>-</sup> (+2.27 eV) [45], therefore, large amounts of ·OH are generated in 5% WO<sub>3</sub>/TiO<sub>2</sub> composite nanofibers.

The highest photocurrent response intensity of 5% WO<sub>3</sub>/TiO<sub>2</sub> nanofibers further confirmed that intimate contact between TiO<sub>2</sub> and WO<sub>3</sub> could efficiently separate the photogenerated charge carriers and accelerate efficient charge transfer [34, 46].

#### 4. Conclusions

In this paper, highly efficient WO<sub>3</sub>/TiO<sub>2</sub> nanofibers were prepared by the electrospinning method. The mole percentage of W and Ti in the composite fibers has an important influence on their performance. The optimized 5% WO<sub>3</sub>/TiO<sub>2</sub> nanofibers exhibited tremendous enhanced photocatalytic degradation capability for MB solution with a 96.2% removal rate under the Xenon lamp irradiation. In addition, under the irradiation of Mercury lamp, the photocatalytic H<sub>2</sub> production rate over 5% WO<sub>3</sub>/TiO<sub>2</sub> nanofibers is 107.15 μmol·g<sup>-1</sup>·h<sup>-1</sup>, which is about 1.5 times of TiO<sub>2</sub> nanofibers. The enhanced activity may be due to the formation of Z-scheme heterojunction, which is conducive to the effective separation and transfer of photoinduced carriers. It could be seen from the experimental results of free radical trapping that ·OH was the main oxidant for MB degradation. Our work provides a useful reference for the preparation of other TiO<sub>2</sub> based photocatalysts towards both solar energy conversion and wastewater recovery.

#### Data Availability

All the data generated or analyzed during this study are included within the article.

#### Conflicts of Interest

The authors declare that there are no conflicts of interest regarding the publication of this paper.

#### Acknowledgments

This work was supported by the National Natural Science Foundation of China (21767008), Research initiation fund of Hainan University (KYQD(ZR)1993), and Hainan Natural Science Foundation (218QN187).

#### References

- [1] T. Jiao, H. Zhao, J. Zhou et al., "Self-assembly reduced graphene oxide nanosheet hydrogel fabrication by anchorage of chitosan/silver and its potential efficient application toward dye degradation for wastewater treatments," *ACS Sustainable Chemistry & Engineering*, vol. 3, no. 12, pp. 3130–3139, 2015.
- [2] L. Ge, M. Zhang, R. Wang et al., "Fabrication of CS/GA/RGO/Pd composite hydrogels for highly efficient catalytic reduction of organic pollutants," *RSC Advances*, vol. 10, no. 26, pp. 15091–15097, 2020.
- [3] Y. Feng, J. Yin, S. Liu, Y. Wang, B. Li, and T. Jiao, "Facile synthesis of Ag/Pd nanoparticle-loaded poly(ethylene imine) composite hydrogels with highly efficient catalytic reduction of 4-nitrophenol," *ACS Omega*, vol. 5, no. 7, pp. 3725–3733, 2020.
- [4] A. Fujishima and K. Honda, "Electrochemical photolysis of water at a semiconductor electrode," *Nature*, vol. 238, no. 5358, pp. 37–38, 1972.
- [5] Z. Xing, J. Zhang, J. Cui et al., "Recent advances in floating TiO<sub>2</sub>-based photocatalysts for environmental application," *Applied Catalysis B: Environmental*, vol. 225, pp. 452–467, 2018.
- [6] L. Wu, S. Shi, Q. Li, X. Zhang, and X. Cui, "TiO<sub>2</sub> nanoparticles modified with 2D MoSe<sub>2</sub> for enhanced photocatalytic activity on hydrogen evolution," *International Journal of Hydrogen Energy*, vol. 44, no. 2, pp. 720–728, 2019.

- [7] A. Hajjaji, S. Jemai, A. Rebhi et al., "Enhancement of photocatalytic and photoelectrochemical properties of TiO<sub>2</sub> nanotubes sensitized by SILAR-deposited PbS nanoparticles," *Journal of Materiomics*, vol. 6, no. 1, pp. 62–69, 2020.
- [8] J. Liu, S. Zou, L. Lu, H. Zhao, L. Xiao, and J. Fan, "Room temperature selective oxidation of benzyl alcohol under base-free aqueous conditions on Pt/TiO<sub>2</sub>," *Catalysis Communications*, vol. 99, pp. 6–9, 2017.
- [9] A. J. Jafari, M. Kermani, A. Hosseini-Bandegharai et al., "Synthesis and characterization of Ag/TiO<sub>2</sub>/composite aerogel for enhanced adsorption and photo-catalytic degradation of toluene from the gas phase," *Chemical Engineering Research and Design*, vol. 150, pp. 1–13, 2019.
- [10] S. Suphankij, W. Mekprasart, and W. Pecharapa, "Photocatalytic of N-doped TiO<sub>2</sub> nanofibers prepared by electrospinning," *Energy Procedia*, vol. 34, pp. 751–756, 2013.
- [11] C. O. Amor, K. Kais elghniji, C. Virlan, A. Pui, and E. Elaloui, "Effect of dysprosium ion (Dy<sub>3+</sub>) doping on morphological, crystal growth and optical properties of TiO<sub>2</sub> particles and thin films," *Physica B: Condensed Matter*, vol. 560, pp. 67–74, 2019.
- [12] Y. Xu, R. Ahmed, D. Klein et al., "Improving photo-oxidation activity of water by introducing Ti<sub>3+</sub> in self-ordered TiO<sub>2</sub> nanotube arrays treated with Ar/NH<sub>3</sub>," *Journal of Power Sources*, vol. 414, pp. 242–249, 2019.
- [13] D. Sánchez-Rodríguez, M. G. Méndez Medrano, H. Remita, and V. Escobar-Barrios, "Photocatalytic properties of BiOCl-TiO<sub>2</sub> composites for phenol photodegradation," *Journal of Environmental Chemical Engineering*, vol. 6, no. 2, pp. 1601–1612, 2018.
- [14] K. Li, T. Jiao, R. Xing et al., "Fabrication of tunable hierarchical MXene@AuNPs nanocomposites constructed by self-reduction reactions with enhanced catalytic performances," *Science China Materials*, vol. 61, no. 5, pp. 728–736, 2018.
- [15] X. Xing, H. Zhu, M. Zhang, L. Xiao, Q. Li, and J. Yang, "Effect of heterojunctions and phase-junctions on visible-light photocatalytic hydrogen evolution in BCN-TiO<sub>2</sub> photocatalysts," *Chemical Physics Letters*, vol. 727, pp. 11–18, 2019.
- [16] Y. Li, P. Zhang, D. Wan, C. Xue, J. Zhao, and G. Shao, "Direct evidence of 2D/1D heterojunction enhancement on photocatalytic activity through assembling MoS<sub>2</sub> nanosheets onto super-long TiO<sub>2</sub> nanofibers," *Applied Surface Science*, vol. 504, pp. 144361–144370, 2020.
- [17] C. Chen, J. Zhou, J. Geng et al., "Perovskite LaNiO<sub>3</sub>/TiO<sub>2</sub> step-scheme heterojunction with enhanced photocatalytic activity," *Applied Surface Science*, vol. 503, pp. 144287–144295, 2020.
- [18] K. V. Özdokur, B. Bozkurt Çırak, Ç. Eden, M. Ahmad Boda, and Ç. Çırak, "Facile synthesis and enhanced photo-electrocatalytic performance of TiO<sub>2</sub> nanotube/g-C<sub>3</sub>N<sub>4</sub> composite catalyst by a novel synthesis approach," *Optik*, vol. 206, p. 164262, 2020.
- [19] S. Y. Janbandhu, A. Joshi, S. R. Munishwar, and R. S. Gedam, "CdS/TiO<sub>2</sub> heterojunction in glass matrix: synthesis, characterization, and application as an improved photocatalyst," *Applied Surface Science*, vol. 497, pp. 143758–143768, 2019.
- [20] J. Chen, M. Wang, J. Han, and R. Guo, "TiO<sub>2</sub> nanosheet/NiO nanorod hierarchical nanostructures: p-n heterojunctions towards efficient photocatalysis," *Journal of Colloid and Interface Science*, vol. 562, pp. 313–321, 2020.
- [21] Z. Guo, J. Wei, B. Zhang, M. Ruan, and Z. Liu, "Construction and photoelectrocatalytic performance of TiO<sub>2</sub>/BiVO<sub>4</sub> heterojunction modified with cobalt phosphate," *Journal of Alloys and Compounds*, vol. 821, pp. 153225–153234, 2020.
- [22] J. Jia, C. Jiang, X. Zhang et al., "Urea-modified carbon quantum dots as electron mediator decorated g-C<sub>3</sub>N<sub>4</sub>/WO<sub>3</sub> with enhanced visible-light photocatalytic activity and mechanism insight," *Applied Surface Science*, vol. 495, pp. 143524–142534, 2019.
- [23] M. Parthibavarman, M. Karthik, and S. Prabhakaran, "Facile and one step synthesis of WO<sub>3</sub> nanorods and nanosheets as an efficient photocatalyst and humidity sensing material," *Vacuum*, vol. 155, pp. 224–232, 2018.
- [24] K. M. Pan, K. N. Shan, S. Z. Wei et al., "Two-step alcohol-thermal synthesis and characterization of enhanced visible-light-active WO<sub>3</sub>-coated TiO<sub>2</sub> heterostructure," *Ceramics International*, vol. 46, no. 2, pp. 2101–2109, 2020.
- [25] Y. M. Hunge, A. A. Yadav, M. A. Mahadik et al., "Degradation of organic dyes using spray deposited nanocrystalline stratified WO<sub>3</sub>/TiO<sub>2</sub> photoelectrodes under sunlight illumination," *Optical Materials*, vol. 76, pp. 260–270, 2018.
- [26] H. Khan, M. G. Rigamonti, G. S. Patience, and D. C. Boffito, "Spray dried TiO<sub>2</sub>/WO<sub>3</sub> heterostructure for photocatalytic applications with residual activity in the dark," *Applied Catalysis B: Environmental*, vol. 226, pp. 311–323, 2018.
- [27] L. Zhang, J. Yin, K. Wei et al., "Fabrication of hierarchical SrTiO<sub>3</sub>@MoS<sub>2</sub> heterostructure nanofibers as efficient and low-cost electrocatalysts for hydrogen-evolution reactions," *Nanotechnology*, vol. 31, no. 20, p. 205604, 2020.
- [28] B. Su, K. Wang, N. Dong et al., "Biomorphic synthesis of long ZnO hollow fibers with porous walls," *Journal of Materials Processing Technology*, vol. 209, no. 8, pp. 4088–4092, 2009.
- [29] Y. J. Li, T. P. Cao, C. L. Shao, and L. M. Wei, "Preparation and photocatalytic properties of ZnO/PAN submicron composite fibers," *Chinese Journal of Inorganic Chemistry*, vol. 27, no. 7, pp. 1348–1352, 2011.
- [30] J. Hu, L. Wang, P. Zhang, C. Liang, and G. Shao, "Construction of solid-state Z-scheme carbon-modified TiO<sub>2</sub>/WO<sub>3</sub> nanofibers with enhanced photocatalytic hydrogen production," *Journal of Power Sources*, vol. 328, pp. 28–36, 2016.
- [31] H. Gao, P. Zhang, J. Zhao, Y. Zhang, J. Hu, and G. Shao, "Plasmon enhancement on photocatalytic hydrogen production over the Z-scheme photosynthetic heterojunction system," *Applied Catalysis B: Environmental*, vol. 210, pp. 297–305, 2017.
- [32] L. Soares and A. Alves, "Photocatalytic properties of TiO<sub>2</sub> and TiO<sub>2</sub>/WO<sub>3</sub> films applied as semiconductors in heterogeneous photocatalysis," *Materials Letters*, vol. 211, pp. 339–342, 2018.
- [33] C. Byrne, L. Moran, D. Hermosilla et al., "Effect of Cu doping on the anatase-to-rutile phase transition in TiO<sub>2</sub> photocatalysts: theory and experiments," *Applied Catalysis B: Environmental*, vol. 246, pp. 266–276, 2019.
- [34] Z. Ma, L. Deng, G. Fan, and Y. He, "Hydrothermal synthesis of p-C<sub>3</sub>N<sub>4</sub>/f-BiOBr composites with highly efficient degradation of methylene blue and tetracycline," *Spectrochimica Acta Part A: Molecular and Biomolecular Spectroscopy*, vol. 214, pp. 103–110, 2019.
- [35] C. Peng, B.-H. Yao, W. Zhang, J.-F. Niu, and J. Zhao, "Synthesis of CuAPTPP-TDI-TiO<sub>2</sub> conjugated microspheres and its photocatalytic activity," *Chinese Journal of Chemical Physics*, vol. 27, no. 2, pp. 200–208, 2014.
- [36] Z. S. Sun, Y. X. Chen, Q. Ke, Y. Yang, and J. Yuan, "Photocatalytic degradation of a cationic azo dye by TiO<sub>2</sub>/bentonite nanocomposite," *Journal of Photochemistry and Photobiology A: Chemistry*, vol. 149, no. 1-3, pp. 169–174, 2002.
- [37] L. Zhang, Q. Zhang, H. Xie et al., "Electrospun titania nanofibers segregated by graphene oxide for improved visible

- light photocatalysis," *Applied Catalysis B: Environmental*, vol. 201, pp. 470–478, 2017.
- [38] J. F. Moulder, W. F. Stickle, P. E. Sobol, K. D. Bomben, and J. Chastain, *Handbook of X-Ray Photoelectron Spectroscopy*, Perkin-Elmer Corporation, Waltham, MA, USA, 1992.
- [39] U. Diebold, "TiO<sub>2</sub> by XPS," *Surface Science Spectra*, vol. 4, no. 3, pp. 227–231, 1998.
- [40] O. Akhavan, "Lasting antibacterial activities of Ag-TiO<sub>2</sub>/Ag/a-TiO<sub>2</sub> nanocomposite thin film photocatalysts under solar light irradiation," *Journal of Colloid and Interface Science*, vol. 336, no. 1, pp. 117–124, 2009.
- [41] J. Singh, S. Sharma, S. Sharma, and R. C. Singh, "Effect of tungsten doping on structural and optical properties of rutile TiO<sub>2</sub> and band gap narrowing," *Optik*, vol. 182, pp. 538–547, 2019.
- [42] D. Tsukamoto, M. Ikeda, Y. Shiraishi et al., "Selective photocatalytic oxidation of alcohols to aldehydes in water by TiO<sub>2</sub> partially coated with WO<sub>3</sub>," *Chemistry-A European Journal*, vol. 17, no. 35, pp. 9816–9824, 2011.
- [43] S. Shenawi-Khalil, V. Uvarov, Y. Kraitsman, E. Menes, I. Popov, and Y. Sasson, "A new family of BiO(Cl<sub>x</sub>Br<sub>1-x</sub>) visible light sensitive photocatalysts," *Catalysis Communications*, vol. 12, no. 12, pp. 1136–1141, 2011.
- [44] M. R. S. Joice, T. M. David, and P. Wilson, "WO<sub>3</sub> nanorods supported on mesoporous TiO<sub>2</sub> nanotubes as one-dimensional nanocomposites for rapid degradation of methylene blue under visible light irradiation," *The Journal of Physical Chemistry C*, vol. 123, no. 45, pp. 27448–27464, 2019.
- [45] X. Zeng, Z. Wang, G. Wang et al., "Highly dispersed TiO<sub>2</sub> nanocrystals and WO<sub>3</sub> nanorods on reduced graphene oxide: Z-scheme photocatalysis system for accelerated photocatalytic water disinfection," *Applied Catalysis B: Environmental*, vol. 218, pp. 163–173, 2017.
- [46] Z. Ma, L. Hu, X. Li, L. Deng, G. Fan, and Y. He, "A novel nano-sized MoS<sub>2</sub> decorated Bi<sub>2</sub>O<sub>3</sub> heterojunction with enhanced photocatalytic performance for methylene blue and tetracycline degradation," *Ceramics International*, vol. 45, no. 13, pp. 15824–15833, 2019.

## Research Article

# Analysis of Cubic Boron Nitride Single Crystal Defects Growth under High Temperature and High Pressure

Lichao Cai,<sup>1</sup> Bin Xu,<sup>2</sup> Meizhe Lv ,<sup>1</sup> Feng Jia,<sup>2</sup> and Xingdong Yuan<sup>2</sup>

<sup>1</sup>School of Materials Science and Engineering, Shandong University, Jinan 250101, China

<sup>2</sup>School of Materials Science and Engineering, Shandong Jianzhu University, Jinan 250101, China

Correspondence should be addressed to Meizhe Lv; lvmeizhe19@sdjzu.edu.cn

Received 11 July 2020; Accepted 3 August 2020; Published 24 August 2020

Guest Editor: Tifeng Jiao

Copyright © 2020 Lichao Cai et al. This is an open access article distributed under the Creative Commons Attribution License, which permits unrestricted use, distribution, and reproduction in any medium, provided the original work is properly cited.

Cubic boron nitride (cBN) single crystals are synthesized under high temperature and high pressure in the Li-based system. The growth defects on hexagonal and triangular (111) surfaces of cBN single crystals after rapid cooling are discussed systemically for the first time using the atomic force microscope. Some impurity particles, triangle cone hole defects, lamellar-fault structures, and big steps are obvious on the surfaces of cBN single crystals. The formation mechanism of these defects is analyzed briefly at the synthetic process of cBN single crystals, and the growth mechanism of cBN single crystals transform from the two-dimensional growth to dislocation growth mechanism under high temperature and high pressure.

## 1. Introduction

Cubic boron nitride (cBN) single crystals have a high hardness, high melting point, high thermal conductivity, wide energy gap, and low dielectric constant, which make them highly promising materials [1–4]. At present, cBN single crystals are synthesized using hexagonal boron nitride (hBN) as the source material and lithium nitride ( $\text{Li}_3\text{N}$ ) as the catalyst by the static high temperature and high pressure (HPHT) catalytic method [5–7]. The further development of electronic and optical applications need large cBN single crystals with high quality, while the size of present cBN single crystals cannot meet the demand for the study of advanced functional products [8, 9]. In a previous experimental study, the cBN nucleation was discussed, which indicates that cBN crystal nuclei are formed directly by the transition of hBN [10]. The growth process of cBN single crystals determines their quality after cBN nucleation under HPHT. The growth defects could affect the crystal quality; thus, the importance of growth defects in cBN single crystals

growth should be clearly recognized [11]. It is almost impossible to study in situ the growth process of cBN single crystals under HPHT; however, much information about cBN growth under HPHT is preserved on the cBN crystal surfaces and the interface layer of cBN single crystals at room temperature and ambient pressure when the synthetic cell assembly was cooled rapidly. The morphology of crystals surfaces and the constituent of the interface layer are closely associated with the cBN single crystals growth under HPHT, and it may be of great significance to explain the growth mechanism of cBN single crystals.

At present, the study of crystal growth at nanometer scale has attracted much interest, and some new growth theories have been established with the help of the AFM [11]. The surface topography of synthetic cBN single crystals was reported [4, 10, 12]; however, thus far, there is almost no report on the analysis of cBN single crystal surfaces by atomic force microscopy (AFM). The factors that affect the formation of defects on (111) surfaces of cBN single crystals and the growth mechanism of cBN single crystals are

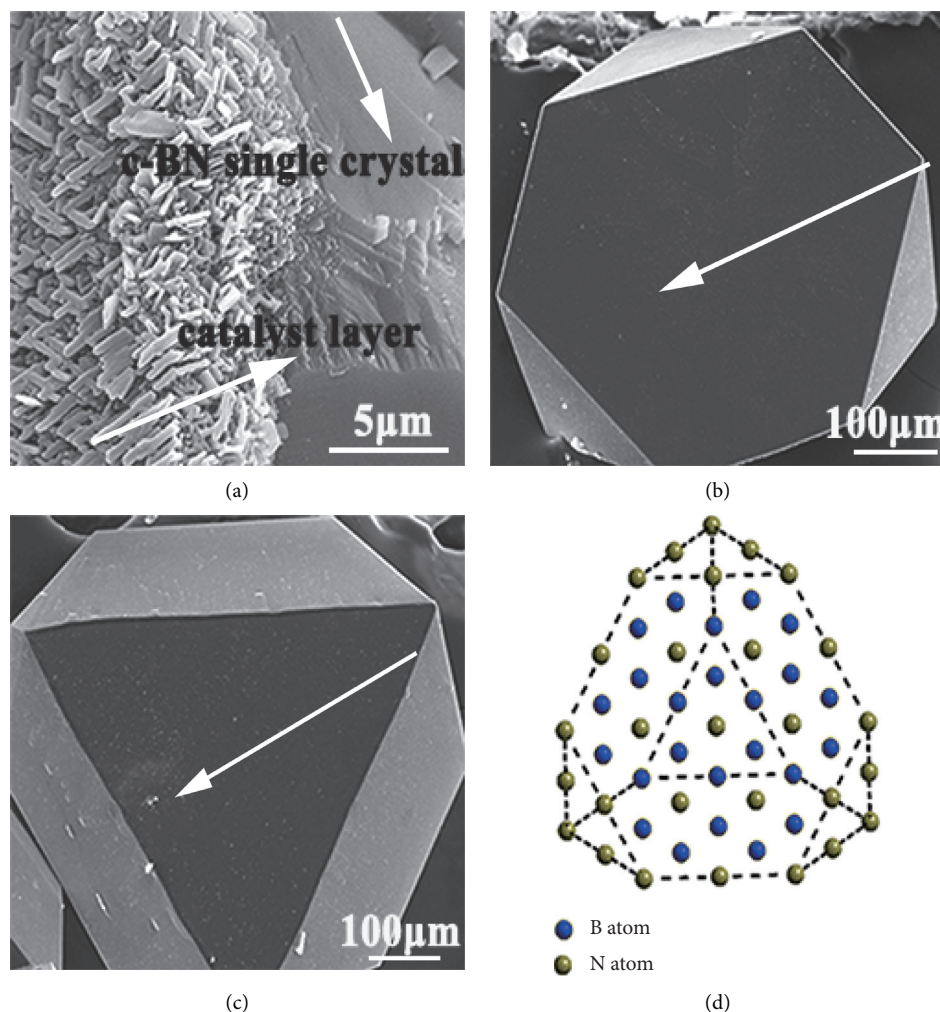


FIGURE 1: (a) SEM images of cBN single crystals surrounded by the powders in the interface layer. (b, c) cBN with hexagonal and triangular (111) surfaces. (d) Plane projection drawing of a cBN single crystal.

discussed on the basis of the AFM observations. The present study provides a better understanding of cBN single crystals growth mechanism under HPHT.

## 2. Materials and Methods

cBN single crystals were synthesized from high purity hBN (>98%) with  $\text{Li}_3\text{N}$  as catalyst, and the weight ratio of the two was 9:1 by the static HPHT catalyst method. HPHT experiments were performed using the cubic anvil apparatus HTDS-034 mm. In these experiments, the synthetic pressure, temperature, and time were 4.5 GPa, 1700 K, and 10 min, respectively. After rapid cooling, the synthesized cBN bulk was removed from the cubic anvil and prepared for further examination. As shown in Figure 1(a), the cBN single crystal was surrounded by powders. The samples were cleaned, and then, the images of cBN single crystals were taken using a JSM-6380 LA-type scanning electron microscope (SEM). The morphology of HPHT as-grown crystal surfaces was obtained using a Bruker Multimode 3D AFM in contact mode under ambient atmosphere and room temperature.

The powders around the HPHT as-grown cBN single crystals were carefully collected under the view of an optic microscope. A JEOLJEM-2010F-type high resolution transmission electron microscope (HRTEM) was used to examine their phases in powders with an operating voltage of 200 kV.

## 3. Results and Discussion

Since the facets are in direct contact with the molten catalyst under HPHT in the cBN crystal growth process, the surface morphology provides much information to analyze the crystal growth. Figures 1(b) and 1(c) shows the SEM images of cBN single crystals with triangular and hexagonal facets (111) and their plane projection drawing. The sizes of cBN single crystals are about 0.5 mm. The synthesized cBN single crystals have truncated tetrahedron structures, which are composed of four coordination  $\text{B-N}_4$  or  $\text{N-B}_4$  growth units. There exist solid structures in short or medium range order in the molten catalyst when cBN single crystals are synthesized under HPHT [10, 12]; thus, much information about the molten catalyst can be remained in the powders

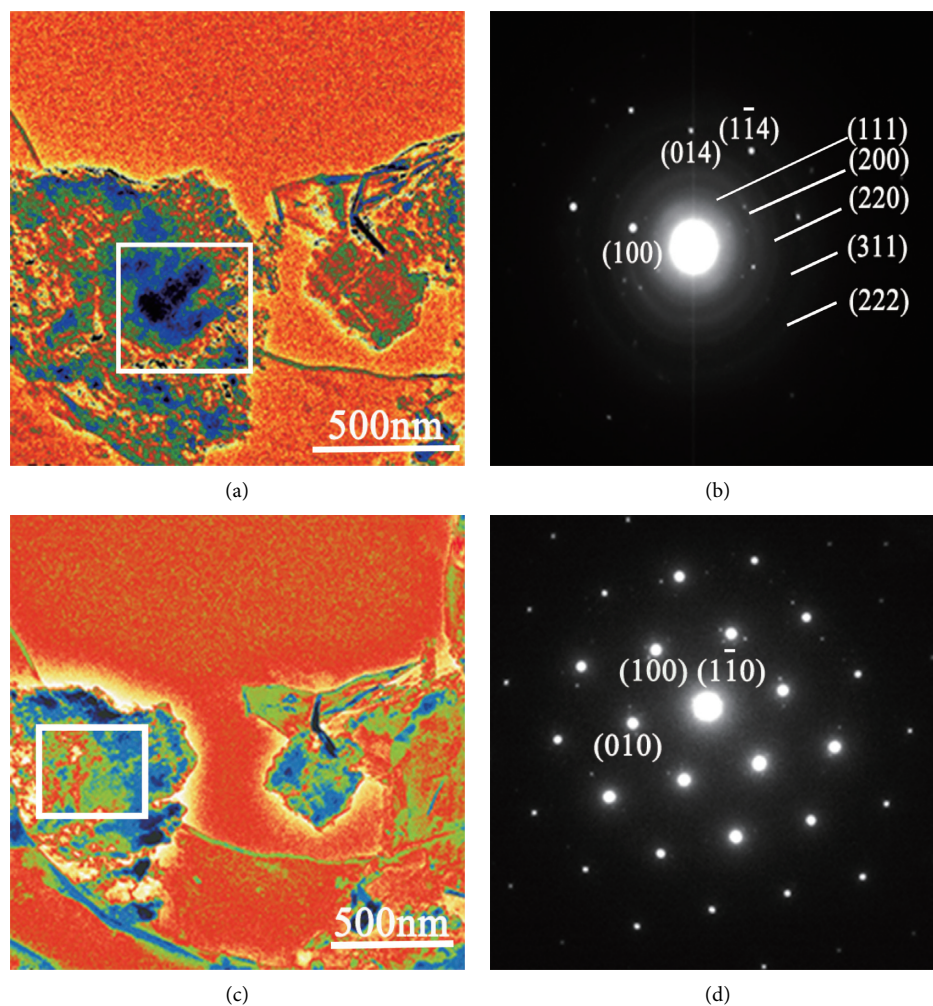


FIGURE 2: (a) The morphology of powders surrounded cBN single crystals. (b) The corresponding SAD pattern in the white grid of (a). (c) The morphology at same position as (a) after irradiated by HRTEM. (d) The corresponding SAD pattern in the white grid of (c).

surrounded by cBN single crystals at ambient condition after the cell assembly is cooled rapidly.

The powders in the interface layer (in Figure 1(a)) were collected, and their compositions were determined with HRTEM. Figures 2(b) and 2(d) show the SAD patterns of powders surrounded cBN single crystals in Figures 2(a) and 2(c), respectively. The corresponding SAD pattern in Figure 2(b) indicates that the white powders in Figure 2(a) are cBN and hBN, from which cBN can be identified by (111), (200), (220), (311), and (222) diffraction ring, while hBN can be identified by (100), (014), and (11 4) diffraction pattern. This means many microcubic grains are formed under HPHT in the growth process of cBN crystals. However, the corresponding SAD pattern in Figure 2(d) indicates that the white powders in Figure 2(c) are all hBN, from which hBN can be identified by (100), (010), and (11 0) diffraction pattern. Figures 2(a) and 2(c) are the morphologies of the same zone of the same powders before and after electron beam irradiation. It is obvious that the black material in Figure 2(a) disappears.

This means the bunching electron beam by HRTEM induces the occurrence of the reaction from cBN to hBN.

From Figure 2(b), it can be inferred that it is a good corresponding relation between (200) of cBN and (100) of hBN crystal planes. The cBN growth process suggests that when hBN transform into micro-cBN grain under HPHT, various micro-cBN grains are delivered to the growing single crystal surfaces, and the collision or coalescence of micro-cBN grains in the molten catalyst induces the growth of cBN single crystals under HPHT. Meanwhile, it is possible that the recrystallization of hBN exists in HPHT experiments. This suggests are consistent with the previous experimental results that cBN with higher quality is synthesized under 4.5 GPa and 1800 K [13]. In our earlier work,  $\text{Li}_3\text{BN}_2$  are found in the interface by meaning of XRD, and it is the real catalyst [10, 12]. The crystal surface energy can directly affect the nucleation and growth of the crystal.  $\text{Li}_3\text{BN}_2$  has higher surface energy [14]; thus, the  $\text{Li}_3\text{BN}_2$  phase can restrain the crystals' nucleation at the initial stage of the reaction and then promote the maximum growth of the nucleus under high temperature and low pressure.

Figure 3 shows different growth defects on the surfaces of cBN single crystals. Although cBN crystal surfaces were cleaned, some microscopic particles were still covered on the

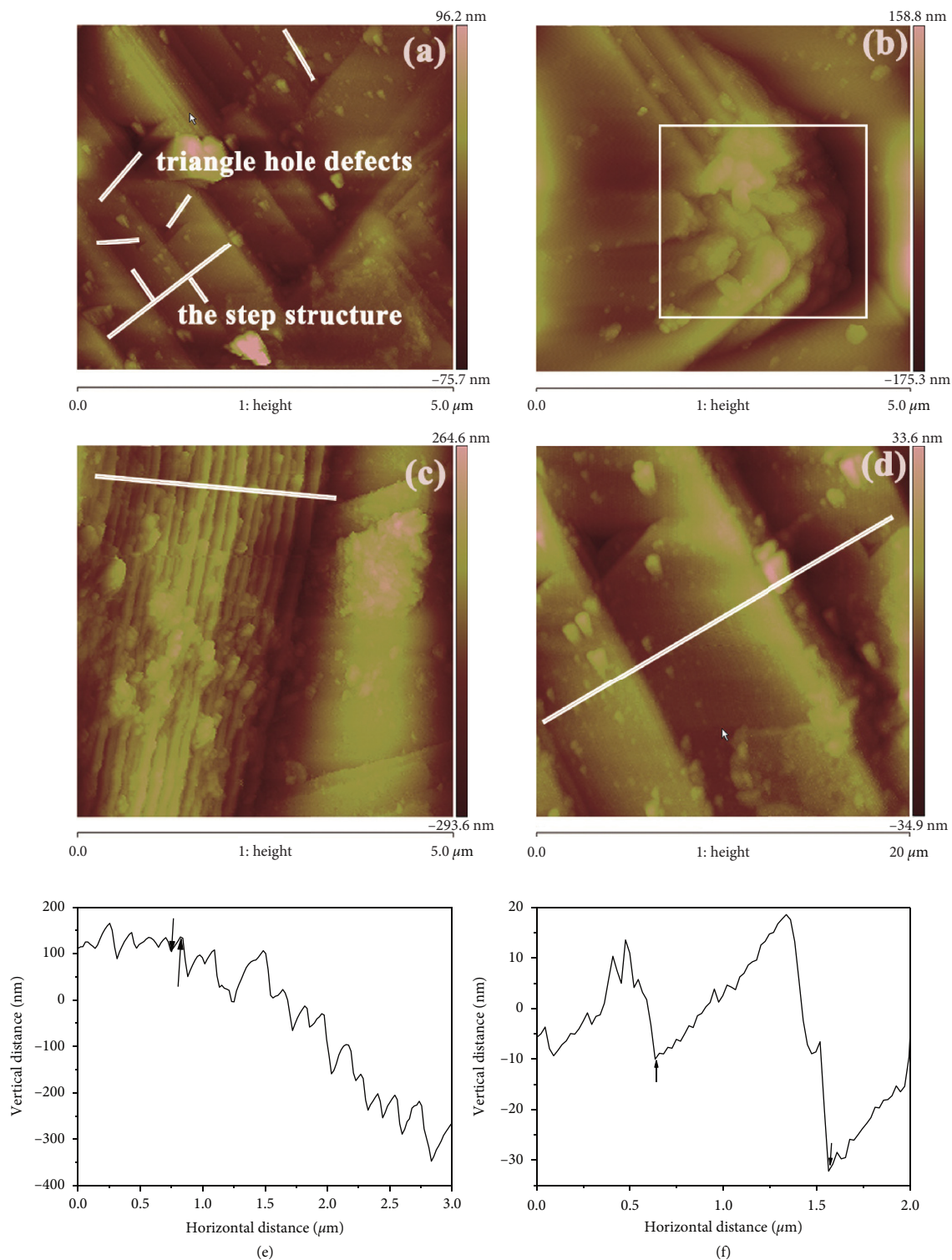


FIGURE 3: (a) Microparticles on (111) facets, (b) the lamellar-fault structure on (111) facets, and (c) the big step structures and triangle-hole defects on (111) facets. (d) The amplification image of area A in (c), (e), and (f) section analyses suggest the height of two steps shown by arrows in (b) and (c), respectively.

single crystal surfaces, as shown in Figure 3(a). Microscopic particles were probably derived from impurities adhering on the crystal surfaces or remaining powders surrounding cBN single crystals. Meanwhile, triangular hole defects, lamellar-fault structures, and big step structures are found in

Figure 3(a). Figures 3(c) and 3(d) show the 2D AFM images of lamellar-fault structures and big step structures on cBN crystal (111) facets in an area of  $5\ \mu\text{m} \times 5\ \mu\text{m}$ , respectively. From section analysis in Figure 3(e), it was found that the height of a lamellar demonstrated by an arrow in Figure 3(c)

is about 27 nm, and the height of the lamellar-fault structures has relatively homogeneous distribution. The height of a big step in Figure 3(d) is about 28 nm, which is basically the same as the height of the lamellar-fault structures. Compared to the height of lamellar-fault structures in Figure 3(c), the big step structures in Figure 3(d) have a heterogeneous distribution. The lamellar-fault structures derive from two-dimensional crystal nuclei.

The impurity in raw materials and the residual gas in working cells could produce a certain amount of impurities in the synthesis process of cBN crystals. The impurities adsorbed on the growing crystal surface prompt the lamellar-fault structures to form a big step under HPHT [10, 11]. When the parallel steps were disturbed during the HPHT step growth process, the growth steps merged locally, as shown in Figure 3(b). The big steps on single crystal surfaces probably derive from dislocations. Because of the presence of some twisting defects and steps, the surface energy barrier of nucleation decreases; furthermore, cubic BN crystal nuclei have a higher possibility to grow around the twisting defects and big steps. The nucleation and growth mechanism transform the two-dimensional growth to dislocation growth mechanism.

The direction of all triangle-hole defects on (111) facets are pretty consistent relative to the edge of cBN single crystals, as shown in Figure 3(d). The reasons for the formation of triangle-hole defects are probably inclusions, vacancies, or dislocations. For (111)-B facets of cBN single crystals, B atoms have an  $sp^3$  empty orbit that can be stable; thus, (111)-B facets should be smooth surfaces. For (111)-N facets of cBN single crystals, N atoms have an  $sp^3$  hybridization orbit with a lone pair electron. Thus, it can easily bind with other atoms and form inclusions inside the cBN single crystals. The triangle-hole defects can be produced on the (111)-N facets of cBN single crystals when those inclusions cleaned out the surfaces of cBN single crystals effectively. When inclusions can exist in cBN single crystals under HPHT, some big vacancy loops were produced to relieve the internal stress of cBN single crystals [15]. The triangle-hole defects probably are the etch pits of edge dislocations exist on the surfaces of cBN single crystals when cBN single crystals were cleaned using the alkaline solutions.

#### 4. Conclusion

The growth defects on (111) surface of cBN single crystals after rapid cooling are discussed for the first time by AFM technique. Some impurity particles, triangle-hole defects, lamellar-fault structures, and big steps were found on single crystal surfaces. A possible formation mechanism of several types of defects is revealed briefly. The analysis provides a better understanding for the growth mechanism of cBN single crystals under HPHT. The growth mechanism of cBN single crystals transforms the two-dimensional growth to dislocation growth mechanism under HPHT.

#### Data Availability

The data used to support the findings of this study are included within the article.

#### Conflicts of Interest

The authors declare no conflicts of interest.

#### Authors' Contributions

Lichao Cai conceptualized the study. Feng Jia and Xing-Dong Yuan formally analyzed the manuscript. Lichao Cai was responsible for investigation. Bin Xu and Meizhe Lv were responsible for methodology. Bin Xu supervised the work. Lichao Cai wrote the original draft. Bin Xu and Meizhe Lv wrote, reviewed, and edited the manuscript.

#### Acknowledgments

This study was funded by the Natural Science Foundation of China (grant no. 51272139).

#### References

- [1] W. Ding, B. Linke, Y. Zhu et al., "Review on monolayer CBN superabrasive wheels for grinding metallic materials," *Chinese Journal of Aeronautics*, vol. 30, no. 1, pp. 109–134, 2017.
- [2] X. W. Zhang, "Doping and electrical properties of cubic boron nitride thin films: a critical review," *Thin Solid Films*, vol. 544, pp. 2–12, 2013.
- [3] R. Mohammad and Ş. Katircioğlu, "The structural and electronic properties of BN and BP compounds and  $BN_xP_{1-x}$  alloys," *Journal of Alloys and Compounds*, vol. 478, no. 1–2, pp. 531–537, 2009.
- [4] X. L. Yuan, J. Niitsuma, T. Sekiguchi, M. Takase, and T. Taniguchi, "Characterization of p-n junction formed at the boundary of facets in cubic-BN using scanning electron microscope," *Diamond and Related Materials*, vol. 14, no. 11–12, pp. 1955–1959, 2005.
- [5] S. Nakano, H. Ikawa, and O. Fukunaga, "Synthesis of cubic boron nitride using  $Li_3BN_2$ ,  $Sr_3B_2N_4$  and  $Ca_3B_2N_4$  as solvent-catalysts," *Diamond and Related Materials*, vol. 3, no. 1–2, pp. 75–82, 1994.
- [6] O. Fukunaga and S. Takeuchi, "Growth mechanism of cubic BN using  $Li_3BN_2$  solvent under high pressure," *International Journal of Refractory Metals and Hard Materials*, vol. 55, pp. 54–57, 2016.
- [7] Y. Du, Z. Su, D. Yang et al., "Synthesis of black cBN single crystal in hBN-Li<sub>3</sub>N-B system," *Materials Letters*, vol. 61, no. 16, pp. 3409–3412, 2007.
- [8] T. Taniguchi and S. Yamaoka, "Spontaneous nucleation of cubic boron nitride single crystal by temperature gradient method under high pressure," *Journal of Crystal Growth*, vol. 222, no. 3, pp. 549–557, 2001.
- [9] T. Taniguchi and K. Watanabe, "Synthesis of high-purity boron nitride single crystals under high pressure by using B-BN solvent," *Journal of Crystal Growth*, vol. 303, no. 2, pp. 525–529, 2007.
- [10] M. Lv, B. Xu, L. Cai, X. Guo, and X. Yuan, "Auger electron spectroscopy analysis for growth interface of cubic boron nitride single crystals synthesized under high pressure and high temperature," *Applied Surface Science*, vol. 439, pp. 780–783, 2018.
- [11] L.-W. Yin, M.-S. Li, Z.-G. Gong, B. Xu, Y.-J. Song, and Z.-Y. Hao, "Analysis of nanometer inclusions in high pressure synthesized diamond single crystals," *Chemical Physics Letters*, vol. 355, no. 5–6, pp. 490–496, 2002.

- [12] X. Guo, B. Xu, W. Zhang, Z. Cai, and Z. Wen, "XPS analysis for cubic boron nitride crystal synthesized under high pressure and high temperature using  $\text{Li}_3\text{N}$  as catalysis," *Applied Surface Science*, vol. 321, pp. 94–97, 2014.
- [13] Z. X. Wen, B. Xu, L. C. Cai, Y. C. Cai, Z. Wen, and M. Z. Lv, "Influence of particle size of  $\text{Li}_3\text{N}$  catalyst on synthetic effect of cubic boron nitride single crystal," *Journal of Synthetic Crystals*, vol. 43, pp. 285–288, 2014.
- [14] H. Yamane, S. Kikkawa, and M. Koizumi, "High-and low-temperature phases of lithium boron nitride,  $\text{Li}_3\text{BN}_2$ : preparation, phase relation, crystal structure, and ionic conductivity," *Journal of Solid State Chemistry*, vol. 71, no. 1, pp. 1–11, 1987.
- [15] L.-W. Yin, M.-S. Li, F.-Z. Li, D.-S. Sun, and Z.-Y. Hao, "Defect formation in diamond single crystals grown from the Fe-Ni-C system at high temperature and high pressure," *Materials Research Bulletin*, vol. 36, no. 13-14, pp. 2283–2288, 2001.

## Research Article

# Efficient Optimization of *Gluconobacter oxydans* Based on Protein Scaffold-Trimeric CutA to Enhance the Chemical Structure Stability of Enzymes for the Direct Production of 2-Keto-L-gulonic Acid

Lili Gao <sup>1</sup>, Yuefeng Liu,<sup>2</sup> Xiaoyu Zhang,<sup>1</sup> and Hongsheng Zhang<sup>1</sup>

<sup>1</sup>Hebei Key Laboratory of Applied Chemistry,  
Heavy Metal Deep-Remediation in Water and Resource Reuse Key Lab of Hebei Province,  
School of Environmental and Chemical Engineering, Yanshan University, Qinhuangdao 066004, China

<sup>2</sup>Qinhuangdao Vocational and Technical College, Qinhuangdao 066100, China

Correspondence should be addressed to Lili Gao; gllqhd@163.com

Received 7 June 2020; Accepted 10 July 2020; Published 4 August 2020

Academic Editor: Peizhi Guo

Copyright © 2020 Lili Gao et al. This is an open access article distributed under the Creative Commons Attribution License, which permits unrestricted use, distribution, and reproduction in any medium, provided the original work is properly cited.

2-Keto-L-gulonic acid (2-KLG), the direct precursor of vitamin C, is produced by a two-step fermentation route from D-sorbitol in industry. However, this route is a complicated mix-culture system which involves three bacteria. Thus, replacement of the conventional two-step fermentation process with a one-step process could be revolutionary in vitamin C industry. The one-step fermentation of 2-keto-L-gulonic acid (2-KLG) has been achieved in our previous study; 32.4 g/L of 2-KLG production was obtained by the one-step strain *G. oxydans*/pGUC-*tufB-sdh*-GGGGS-*sndh* after 168 h. In this study, L-sorbose dehydrogenase (SDH) and L-sorbose dehydrogenase (SNDH) were expressed in *G. oxydans* after the codon optimization. Furthermore, the trimeric protein CutA was used to improve the chemical structure stability of SDH and SNDH. The recombinant strain *G. oxydans*/pGUC-*tufB-SH3-sdh*-GGGGS-*sndh-tufB-SH3<sub>lig</sub>*-(GGGGS)<sub>2</sub>-*cutA* produced 40.3 g/L of 2-KLG after 168 h. In addition, the expression levels of the cofactor PQQ were enhanced to further improve 2-KLG production. With the stepwise metabolic engineering of *G. oxydans*, the final 2-KLG production was improved to 42.6 g/L. The efficient one-step production of 2-KLG was achieved, and the final one-step industrial-scale production of 2-KLG is drawing near.

## 1. Introduction

Vitamin C (L-ascorbic acid, L-AA) is widely used in pharmaceutical, food, beverages, cosmetics, and feed industries [1]. The most successful route for industrial production of vitamin C is the classical two-step fermentation process. The fermentation process contains one-step conversion from D-sorbitol to L-sorbose by *Gluconobacter oxydans*, followed by another step of converting L-sorbose to 2-keto-gulonic acid (2-KLG), the precursor of vitamin C, by a mixed culture system of *Ketogulonicigenium vulgare* and *Bacillus megaterium*. *K. vulgare* is difficult to culture alone and it possesses a rather low production capacity of 2-KLG. The accompany bacterium *B. megaterium* does not produce

2-KLG, but it can promote the growth and 2-KLG production of *K. vulgare* [2]. Over the years, researchers have attempted to improve fermentation processes in many ways; tremendous advances have been achieved in microbial production of vitamin C [2–5]. However, the culture broth from the “first step” by *G. oxydans* containing L-sorbose needs to be transferred to another bioreactor, added with other culture media, and sterilized for the second time. The addition process involves three microorganisms which significantly increases the cost of both raw materials and energy requirement [6]. Besides, the mix-culture system makes the process optimization difficult.

In consideration of problems presented above in the two-step fermentation process, using D-glucose or

D-sorbitol as a carbon source for the production of 2-KLG in one-step fermentation process would be more cost-effective and it will be a revolutionary advancement in the vitamin C industry. Although the strain which can catalyze D-glucose or D-sorbitol to 2-KLG efficiently by single strain fermentation has not been found, advances in biochemistry and recombinant DNA technology, together with the genomic revolution, have promoted the construction of the direct microbial processes to 2-KLG via genetic engineering [1, 7]. In the earlier study, membrane-bound sorbose dehydrogenase and cytosolic sorbose dehydrogenase were cloned from *G. oxydans* T-100 and expressed in *G. oxydans* G624, which is able to accumulate L-sorbose. The recombinant strain produced 88 g/L of 2-KLG from D-sorbitol [8]. However, there was no research about one-step fermentation over the last decade, and the results obtained in our previous study showed that the expression of SDH and SNDH genes in *G. oxydans* could only result in a yield of 2-KLG of no more than 5 g/L [9].

*G. oxydans* is an industrially important bacterium for its ability to oxidize sugars and sugar alcohols at high levels. Many compounds such as acetic acid, D-gluconic acid, L-sorbose, and dihydroxyacetone have been produced successfully with *G. oxydans* [10–14]. In industrial 2-KLG synthesis, *G. oxydans* was initially found to be used in the Reichstein process for the oxidation of D-sorbitol to L-sorbose, which is a species of choice for the construction of genetically engineered strain that equipped the crucial dehydrogenases required for the conversion of D-sorbitol to 2-KLG [15]. *G. oxydans* WSH-003, in this study, is an L-sorbose-accumulating strain of industrial interest due to its powerful ability to oxidize D-sorbitol into L-sorbose with a high quantitative yield of over 98% on an industrial scale. *G. oxydans* WSH-003 was mutated by different methods from a wild-type strain for at least 90 times to improve the production of L-sorbose and the tolerance to saccharides and alditols. Finally, the industrial strain possessed both high L-sorbose productivity and extreme tolerance to saccharides and alditols [16]. In addition, in our previous study, it was identified that even 100 g/L of 2-KLG did not obviously affect the cell growth of *G. oxydans* WSH-003 and no obvious degradation of 2-KLG could be detected when *G. oxydans* WSH-003 was grown with 2-KLG [9].

Following the development of next-generation sequencing technology, the three bacteria involved in the classical two-step fermentation process for L-AA production have all been sequenced in my original laboratory. The gene clusters encoding D-sorbitol dehydrogenase and responsible for the synthesis of the cofactor pyrroloquinoline quinone (PQQ) were identified from the genome sequence of *G. oxydans* WSH-003 [16]. Meanwhile, in *K. vulgare* WSH-001, five L-sorbose dehydrogenases (SDHs) and two L-sorbose dehydrogenases (SNDHs) were confirmed by expression of the DNA in *Escherichia coli*, which were a group of PQQ-dependent dehydrogenases for the catalysis of L-sorbose to L-sorbose and further to 2-KLG [17]. In our previous study, five SDH genes and two SNDH genes were overexpressed in *G. oxydans* with different combinations, and by a series of biological engineering, the 2-KLG production

increased to 32.4 g/L. In this study, the cross-linker protein CutA was used as a protein scaffold to improve the chemical structure stability of SDH and SNDH, which was the first time for the application of CutA in metabolic engineering. The recombinant strain pGUC-*tufB*-SH3-*sdh*-GGGGS-*sndh*-*tufB*-SH3<sub>lig</sub>-(GGGGS)<sub>2</sub>-*cutA* produced 40.3 g/L of 2-KLG after 168 h, and the production was improved efficiently. Furthermore, the expression levels of the cofactor PQQ were enhanced to further improve 2-KLG production. With the stepwise metabolic engineering of *G. oxydans*, the final 2-KLG production was improved to 42.6 g/L, which was 5.7% higher than that by pGUC-*tufB*-SH3-*sdh*-GGGGS-*sndh*-*tufB*-SH3<sub>lig</sub>-(GGGGS)<sub>2</sub>-*cutA*.

## 2. Materials and Methods

**2.1. Strains and Plasmids.** *K. vulgare* WSH-001 and *G. oxydans* WSH-003 were provided by Jiangsu Jiangshan Pharmaceutical Co., Ltd. *Escherichia coli* JM109 (Novagen, Darmstadt, Germany) was used as the host for plasmid construction. The pMD19-T vector was used for gene cloning (TakaRa, Dalian, China). All plasmids used in this study are provided in Table 1. PrimeSTAR HS DNA polymerase, restriction endonucleases, DNA gel extraction kit, and PCR reagents were purchased from TakaRa (Dalian, China). FastPure DNA kit and SanPrep Column Plasmid Mini-Preps Kit were purchased from Sangon (Shanghai, China). DNA Sanger sequencing was performed by Sangon (Shanghai, China).

**2.2. Culture Conditions.** *G. oxydans* strains were cultivated in a broth (15% D-sorbitol, 1.5% corn steep liquor, and 2% CaCO<sub>3</sub>) at 30°C for 168 h. *G. oxydans* transformants were cultivated in medium containing 75 µg/mL ampicillin. *E. coli* strains were cultivated in the Luria-Bertani (LB, Oxoid) medium. 100 µg/mL of ampicillin was added to the LB medium to screening transformants with plasmids.

**2.3. Codon Optimization of SDH and SNDH.** The codons of the *sdh*-*sndh* gene (the two genes were fused with GGGGS linker peptide) were optimized based on the codon preference of *G. oxydans* using a codon algorithm with the GeMS software [18]. The codon-optimized gene was synthesized by Genewiz (Nanjing, China).

**2.4. Expression of Trimeric Protein CutA in *G. oxydans* WSH-003.** CutA is a small trimeric protein from *Pyrococcus horikoshii* (GenBank Accession number: BAA30089.1) [19]. In order to verify whether the expression of *cutA* could take effect in *G. oxydans*, *cutA* was optimized as stated above and was synthesized by Genewiz. The fragment of the codon-optimized *cutA* was digested and inserted into the *KpnI*/*Bam*HI site of pGUC (the shuttle vector of *E. coli*-*G. oxydans* that constructed in our previous study). Then, the promoter of elongation factor TU (*tufB*) [20] was inserted into the *SacI*/*KpnI* site of pGUC-*cutA*, resulting in pGUC-*tufB*-*cutA*,

TABLE 1: Plasmids used in this study.

Plasmids	Relevant characteristics	Sources
pGUC	Ampr <i>E. coli</i> - <i>G. oxydans</i> shuttle vector	This study
pGUC- <i>tufB</i> - <i>sdh</i> -GGGGS- <i>sndh</i>	pGUC containing <i>tufB</i> - <i>sdh</i> -GGGGS- <i>sndh</i>	This study
pGUC- <i>tufB</i> - <i>cutA</i>	pGUC containing <i>tufB</i> - <i>cutA</i>	This study
pGUC- <i>tufB</i> - <i>SH3</i> - <i>sdh</i> -GGGGS- <i>sndh</i> - <i>tufB</i> - <i>SH3</i> <sub>lig</sub> - (GGGGS) <sub>2</sub> - <i>cutA</i>	pGUC containing <i>tufB</i> - <i>SH3</i> - <i>sdh</i> -GGGGS- <i>sndh</i> - <i>tufB</i> - <i>SH3</i> <sub>lig</sub> - (GGGGS) <sub>2</sub> - <i>cutA</i>	This study
pGUC- <i>tufB</i> - <i>SH3</i> - <i>sdh</i> -GGGGS- <i>sndh</i> - <i>tufB</i> - <i>SH3</i> <sub>lig</sub> - (GGGGS) <sub>2</sub> - <i>cutA</i> - <i>tufB</i> - <i>pqq</i> ABCDE	pGUC containing <i>tufB</i> - <i>SH3</i> - <i>sdh</i> -GGGGS- <i>sndh</i> - <i>tufB</i> - <i>SH3</i> <sub>lig</sub> - (GGGGS) <sub>2</sub> - <i>cutA</i> - <i>tufB</i> - <i>pqq</i> ABCDE	This study

and was transformed into *G. oxydans* WSH-003 by electroporation [21].

**2.5. Fusion Expression of SDH and SNDH with CutA.** For the ligation of SDH-GGGGS-SNDH with CutA, adaptor protein (*SH3*) and its ligand (*SH3*<sub>lig</sub>) were used as the docking protein and docking station peptide, respectively [22–24]. Both *SH3* and *SH3*<sub>lig</sub>-(GGGGS)<sub>2</sub>-*cutA* were optimized as stated above and were synthesized by Genewiz. The *SH3* was fused with codon-optimized *sdh*-GGGGS-*sndh*, resulting in *SH3*-*sdh*-GGGGS-*sndh*. The *SH3*<sub>lig</sub>-(GGGGS)<sub>2</sub>-*cutA* was fused with the promoter *tufB*, resulting in *tufB*-*SH3*<sub>lig</sub>-(GGGGS)<sub>2</sub>-*cutA*. The obtained *SH3*-*sdh*-GGGGS-*sndh* and *tufB*-*SH3*<sub>lig</sub>-(GGGGS)<sub>2</sub>-*cutA* were further digested and inserted into the *Kpn*I/*Bam*HI and *Bam*HI/*Xba*I site of pGUC-*tufB*, respectively, resulting in pGUC-*tufB*-*SH3*-*sdh*-GGGGS-*sndh*-*tufB*-*SH3*<sub>lig</sub>-(GGGGS)<sub>2</sub>-*cutA*, and were transformed into *G. oxydans* WSH-003 by electroporation [21]. The time courses of sorbitol oxidation by the recombinant strains were performed, every 12 h to take a sample, and were analyzed by HPLC. The mean value out of three independent experiments was calculated.

**2.6. Overexpression of the Cofactor PQQ in *G. oxydans* WSH-003.** *pqq*ABCDE was amplified using *G. oxydans* WSH-003 genomic DNA with the primers (Table 2). Because of the lack of restriction enzyme site, the promoter *tufB* was fused with *pqq*ABCDE, which was digested and inserted into the *Xba*I/*Pst*I site of pGUC, resulting in pGUC-*tufB*-*SH3*-*sdh*-GGGGS-*sndh*-*tufB*-*SH3*<sub>lig</sub>-(GGGGS)<sub>2</sub>-*cutA*-*pqq*ABCDE. The construct was transformed into *G. oxydans* WSH-003 by electroporation [21].

**2.7. Analysis Procedures.** The optical density of the culture broth was measured using a Biospec-1601 spectrophotometer (Shimadzu, Kyoto, Japan) at 600 nm after an appropriate dilution. D-sorbitol, 2-KLG, and intermediate metabolites in the fermentation broth were determined by HPLC, using an Aminex HPX-87H column (Bio-Rad, Richmond, CA) at 35°C with a flow rate of 0.6 mL/min and 5 mmol/L H<sub>2</sub>SO<sub>4</sub> as the eluent [25–27]. The concentration of PQQ in the culture supernatants was measured using LC-MS-IT-TOF under the conditions reported by Noji et al. [28].

### 3. Results and Discussion

**3.1. Overexpression of SDH and SNDH in *G. oxydans* WSH-003 after Codon Optimization.** *G. oxydans* WSH-003 is an industrial strain with high L-sorbose productivity and extreme tolerance to saccharides and alditols. The metabolic pathway of D-sorbitol in the recombinant *G. oxydans* strains is shown in Figure 1. In our previous study, five SDHs (KVVU\_pmdA\_0245, KVVU\_2142, KVVU\_2159, KVVU\_1366, and KVVU\_0203) and two SNDHs (KVVU\_0095 and KVVU\_pmdB\_0115) in *K. vulgare* WSH-001 were identified [17], which were introduced into *G. oxydans* WSH-003 in different combinations to construct the one-step strain. After a series of biological engineering, the production of 2-KLG was up to 32.4 g/L after 168 h of fermentation by *G. oxydans*/pGUC-*tufB*-*k0203*-GGGGS-*k0095* (*G. oxydans*/pGUC-*tufB*-*sdh*-GGGGS-*sndh*) [9].

Codon optimization is a key technique to achieve the efficient expression of heterologous proteins. Codon preference optimization strategy is the most commonly used codon optimization strategy at present, which mainly replaces the donor codon with the synonymous codon with the highest frequency in the host genome and uses the most abundant codon in the host to encode the amino acids in the optimized sequence [29]. In this study, codon preference optimization was conducted to further enhance the efficiency of expression of SDH and SNDH in *G. oxydans*. The *sdh*-GGGGS-*sndh* shares 82% similarity with its parental nucleotide sequence while maintaining the identical amino acid sequence. After 168 h of fermentation, the 2-KLG production reached 33.2 g/L. It was not significant for the enhancement of 2-KLG production by codon optimization, which may be due to the complex and varied factors, such as posttranslational folding and metabolic level, and thus, the expression of SDH and SNDH remains low [30].

**3.2. Expression of Trimeric Protein CutA in *G. oxydans* WSH-003.** CutA is a small trimeric protein from *P. horikoshii*, which is used as the cross-linker protein [19]. It has an extremely high denaturation temperature of nearly 150°C [31]. Furthermore, CutA retains its trimeric quaternary structure in a solution containing as much as 5 M GuHCl [32]. It was reported that the remarkably increased number of ion pairs in the monomeric structure contributes to the stabilization of the trimeric structure and plays an important

TABLE 2: Primers used in this study.

Primer	Sequences of primers (5'-3')*	Restriction enzyme
<i>tufB</i> -F1	<b>CGAGCTCGTACGATGGTAAGAAATCCACTG</b>	<i>SacI</i>
<i>tufB</i> -R1	<b>CGGGGTACCGTCTTTCTCCAAAACCCC</b>	<i>KpnI</i>
<i>SH3</i> -F	<b>CGGGGTACCGCCGAGTATGTGCGCGCCCT</b>	<i>KpnI</i>
<i>SH3</i> -R	GGGTCGTGAGCTTCATGTACTTCTCCACGTACGGCACCG	—
<i>sdh</i> -GGGGS- <i>sndh</i> -F	GTACGTGGAGAAGTACATGAAGCTCACGACCCTGCTGC	—
<i>sdh</i> -GGGGS- <i>sndh</i> -R	<b>CGCGGATCCTCACGCCGCGGAAATCCGC</b>	<i>BamHI</i>
<i>tufB</i> -F2	<b>CGCGGATCCGTACGATGGTAAGAAATCCACTG</b>	<i>BamHI</i>
<i>tufB</i> -R2	GCAGGGCCGGCGGCGGCGTCTTTCTCCAAAACCCCCT	—
<i>SH3<sub>lig</sub></i> -(GGGGS) <sub>2</sub> - <i>cutA</i> -F	AGCGGGGTTTTGGAGAAAGACGCCGCCGCCGCCCTGC	—
<i>SH3<sub>lig</sub></i> -(GGGGS) <sub>2</sub> - <i>cutA</i> -R	<b>CTAGTCTAGATCACTTCTTCGTCTCCTCGATCAGC</b>	<i>XbaI</i>
<i>tufB</i> -F3	<b>CTAGTCTAGATGCAGATCCGGTGGCCATGTTC</b>	<i>XbaI</i>
<i>tufB</i> -R3	TTCGGCGTGTTCCAAGCCATCGTCTTTCTCCAAAACCCCCT	—
<i>pqq</i> ABCDE-F	CGGGGTTTTGGAGAAAGACGATGGCTTGAACACGCCG	—
<i>pqq</i> ABCDE-R	<b>AAAACTGCAGTTACATTCTTCGGTAAACAAAAGT</b>	<i>PstI</i>

\*Restriction sites used for cloning are in bold and are underlined.

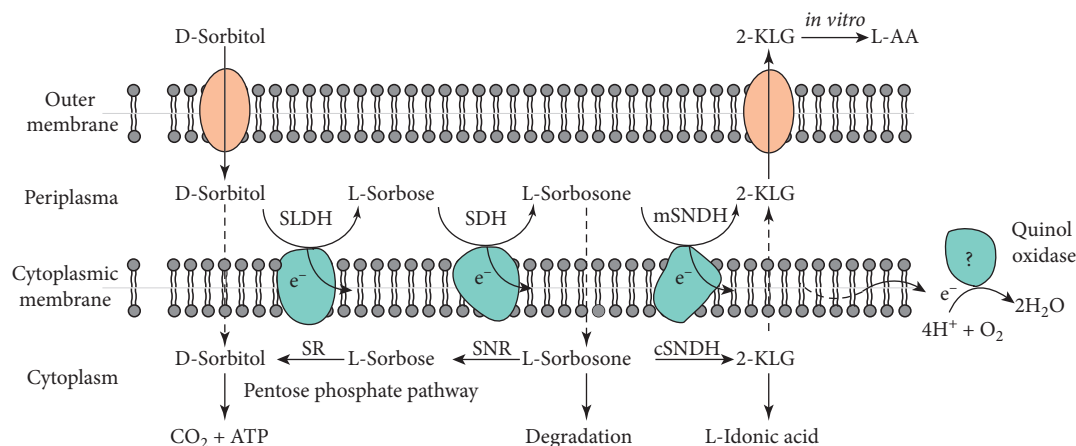


FIGURE 1: The metabolic pathway of D-sorbitol in the recombinant *G. oxydans* strains. SLDH, D-sorbitol dehydrogenase; SDH, L-sorbose dehydrogenase; SNDH, L-sorbose dehydrogenase; mSNDH, membrane-bound SNDH; cSNDH, cytosolic SNDH; SR, L-sorbose reductase; SNR, L-sorbose reductase.

role in enhancing the denaturation temperature up to 150°C [31].

Overexpression of CutA in *G. oxydans* WSH-003 was conducted to verify whether it would influence the growth of the strain. After the codon optimization of *cutA*, *G. oxydans* strain harboring pGUC-*tufB*-*cutA* was constructed. The growth curve of *G. oxydans*/pGUC-*tufB*-*cutA* and the wild strain was determined (Figure 2). The results showed that the growth was consistent with each other at 30°C, and *G. oxydans*/pGUC-*tufB*-*cutA* grew faster at 37°C and 42°C than the wild strain. After 12 h of fermentation, the OD<sub>600</sub> of *G. oxydans*/pGUC-*tufB*-*cutA* and the wild strain at 37°C was 6.74 and 5.99, respectively, and at 42°C was 5.31 and 4.1, respectively. However, the growth of *G. oxydans*/pGUC-*tufB*-*cutA* and the wild strain was both inhibited at 45°C. It was found that the expression of the cross-linker protein CutA improved the heat resistance of the strain.

### 3.3. Overexpression of SDH and SNDH in *G. oxydans* WSH-003 Based on CutA.

Ramirez et al. developed a novel self-

assembling protein hydrogel with cross-linked protein CutA and formed a highly cross-linked protein network. The building blocks initiate an intein trans-splicing reaction that yields a hydrogel that is highly stable over a wide range of pH (6–10) and temperature (4–50°C) [22]. Inspired by this study, the stability of SDH and SNDH may be improved by generating a longer protein chain with the cross-linker CutA, and the catalytic efficiency of the enzymes may be increased further.

The trimeric protein CutA from *P. horikoshii* was able to be used as the protein scaffold, which may improve the stability of SDH and SNDH in *G. oxydans*. The adaptor protein SH3 and its ligand SH3<sub>lig</sub> were used as docking protein and docking station peptide, respectively. They possess high affinity for each other because of their relatively small size (56 and 11 amino acids, respectively) (Figure 3). After SH3 and SH3<sub>lig</sub>-(GGGGS)<sub>2</sub>-*cutA* were optimized and synthesized, they were fused or ligated with the promoter *tufB* and codon-optimized *sdh*-GGGGS-*sndh*, and a recombinant plasmid pGUC-*tufB*-SH3-*sdh*-GGGGS-*sndh*-*tufB*-SH3<sub>lig</sub>-(GGGGS)<sub>2</sub>-*cutA* was constructed and was

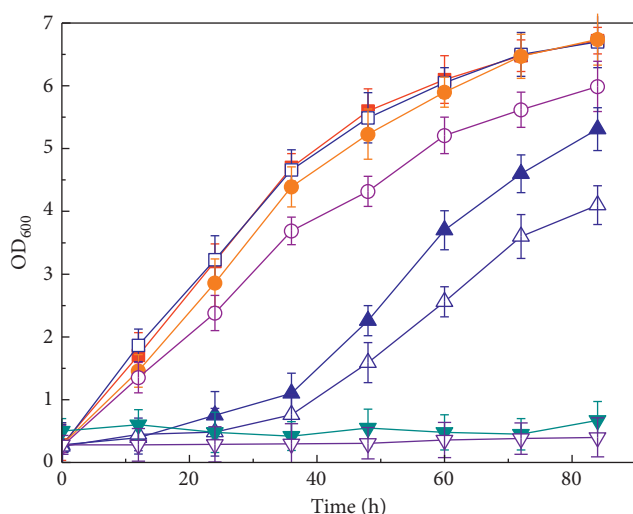


FIGURE 2: The effect on temperature tolerance of *G. oxydans* after the expression of CutA. The symbols ■, ●, ▲, and ▼ represent the growth curve of *G. oxydans*/pGUC-*tufB*-*cutA* at 30°C, 37°C, 42°C, and 45°C, respectively. The symbols □, ○, △, and ▽ represent the growth curve of *G. oxydans*/pGUC at 30°C, 37°C, 42°C, and 45°C, respectively. Error bars represent the standard deviation of three biological replicates.

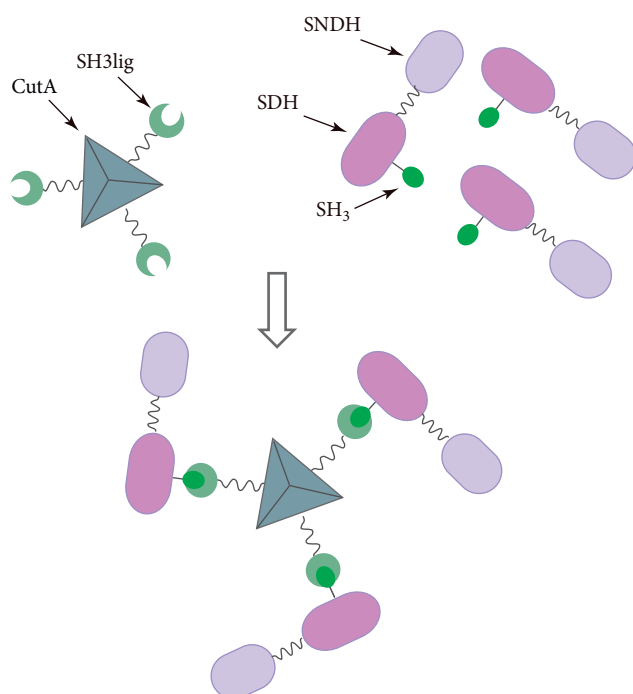


FIGURE 3: The scheme of protein expression based on the trimeric protein CutA. A longer protein chain with the trimeric CutA was generated under the use of the adaptor protein SH3 and its ligand SH3<sub>lig</sub> as docking protein and docking station peptide, respectively.

transferred into *G. oxydans* WSH-003. Comparison of optical densities at 600 nm ( $OD_{600}$ ) and product formation in the recombinant strains is shown in Figure 4. *G. oxydans*/pGUC-*tufB*-*SH3*-*sdh*-GGGGS-*sndh*-*tufB*-*SH3*<sub>lig</sub>-(GGGGS)<sub>2</sub>-*cutA* grew basically consistent with *G. oxydans*/pGUC-*tufB*-

*sdh*-GGGGS-*sndh*, and the 2-KLG production by the *G. oxydans* strain harboring pGUC-*tufB*-*SH3*-*sdh*-GGGGS-*sndh*-*tufB*-*SH3*<sub>lig</sub>-(GGGGS)<sub>2</sub>-*cutA* was 40.3 g/L after 168 h of fermentation, which was 24.4% higher than that obtained by *G. oxydans*/pGUC-*tufB*-*sdh*-GGGGS-*sndh*, indicating that application of the cross-linker protein CutA efficiently increased the yield of 2-KLG.

**3.4. Fermentation of Engineering *G. oxydans* at Different Temperatures.** In the above study, it has been proved that the expression of CutA makes the strain more tolerable to temperature. Therefore, in order to investigate the fermentation performance at different temperatures, the recombinant strain *G. oxydans*/pGUC-*tufB*-*SH3*-*sdh*-GGGGS-*sndh*-*tufB*-*SH3*<sub>lig</sub>-(GGGGS)<sub>2</sub>-*cutA* was fermented at 30°C, 35°C, and 37°C, respectively. The recombinant strain *G. oxydans*/pGUC-*tufB*-*sdh*-GGGGS-*sndh* was used as control. The  $OD_{600}$  and the production of 2-KLG at different temperatures are summarized in Figure 5. The results showed that the growth of *G. oxydans*/pGUC-*tufB*-*SH3*-*sdh*-GGGGS-*sndh*-*tufB*-*SH3*<sub>lig</sub>-(GGGGS)<sub>2</sub>-*cutA* was nearly consistent with each other at these three temperatures, and it grew better at 35°C and 37°C than the control strain. The production of 2-KLG of *G. oxydans*/pGUC-*tufB*-*SH3*-*sdh*-GGGGS-*sndh*-*tufB*-*SH3*<sub>lig</sub>-(GGGGS)<sub>2</sub>-*cutA* was higher than the control at different temperatures. Furthermore, the specific activity of SDH and SNDH in the recombinant and the control strain at different temperatures is summarized in Figure 6. The results showed that the specific activity of SDH and SNDH was also higher than that of the control at different temperatures, which revealed that the stability and catalytic efficiency of the dehydrogenases may be improved after the expression of CutA. However, both strains of *G. oxydans*/pGUC-*tufB*-*SH3*-*sdh*-GGGGS-*sndh*-*tufB*-*SH3*<sub>lig</sub>-(GGGGS)<sub>2</sub>-*cutA* and the control produced less 2-KLG at 35°C and 37°C than at 30°C. This may be caused by that the enzyme activities were affected at higher temperatures.

**3.5. Overexpression of *pqqABCDE* to Improve the 2-KLG Production.** It has been confirmed that *G. oxydans* WSH-003 possesses a complete PQQ synthesis and regeneration system. However, the biosynthesis of 2-KLG is an oxidative process, and a large amount of the reduced cofactors, such as PQQH<sub>2</sub>, should be rapidly regenerated for the following oxidation process. This means that the introduction of the extra PQQ-dependent dehydrogenases could lead to cofactor imbalances in metabolic pathways and significantly increase the burden for the global metabolic networks, thereby affecting 2-KLG production [33]. Cofactor engineering is often adopted to compensate the imbalance of cofactors to improve product synthesis [34]. In our previous study, SDH and SNDH from *K. vulgare* WSH-001 and SLDH from *G. oxydans* WSH-003 were all identified as PQQ-dependent dehydrogenases, and it was noted that increasing PQQ level could further improve the production of 2-KLG [9]. In this study, pGUC-*tufB*-*SH3*-*sdh*-GGGGS-*sndh*-*tufB*-*SH3*<sub>lig</sub>-(GGGGS)<sub>2</sub>-*cutA*-*tufB*-*pqqABCDE* was constructed. The production of 2-KLG by *G. oxydans* strain harboring

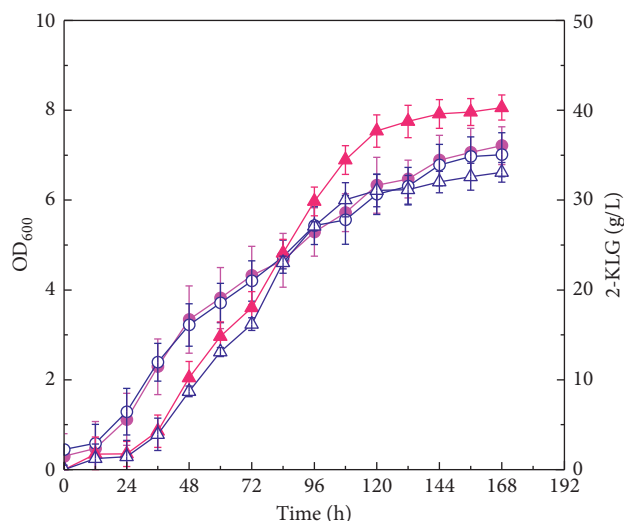


FIGURE 4: Time course of fermentation by CutA-based engineered strain. The symbols ▲ and △ represent the concentration of 2-KLG produced by *G. oxydans*/pGUC-*tufB-SH3-sdh-GGGGS-sndh-tufB-SH3<sub>lig</sub>-(GGGGS)<sub>2</sub>-cutA* and *G. oxydans*/pGUC-*tufB-sdh-GGGGS-sndh*, respectively. The symbols ● and ○ represent OD<sub>600</sub> of *G. oxydans*/pGUC-*tufB-SH3-sdh-GGGGS-sndh-tufB-SH3<sub>lig</sub>-(GGGGS)<sub>2</sub>-cutA* and *G. oxydans*/pGUC-*tufB-sdh-GGGGS-sndh*, respectively. Error bars represent the standard deviation of three biological replicates.

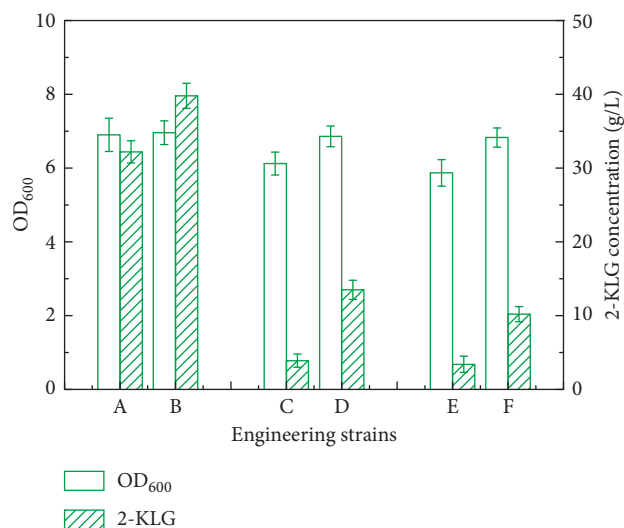


FIGURE 5: Production of 2-KLG by CutA-based engineered strain and the control strain at different temperatures. A, C, and E are OD<sub>600</sub> and 2-KLG production of *G. oxydans*/pGUC-*tufB-sdh-GGGGS-sndh* at 30°C, 35°C, and 37°C, respectively. B, D, and F are OD<sub>600</sub> and 2-KLG production of *G. oxydans*/pGUC-*tufB-SH3-sdh-GGGGS-sndh-tufB-SH3<sub>lig</sub>-(GGGGS)<sub>2</sub>-cutA* at 30°C, 35°C, and 37°C, respectively. Error bars represent the standard deviation of three biological replicates.

pGUC-*tufB-SH3-sdh-GGGGS-sndh-tufB-SH3<sub>lig</sub>-(GGGGS)<sub>2</sub>-cutA-tufB-pqqABCDE* after 168 h of fermentation is summarized in Figure 7. Overexpression of *pqqABCDE* gene clusters enhanced PQQ production by 262.5% compared with

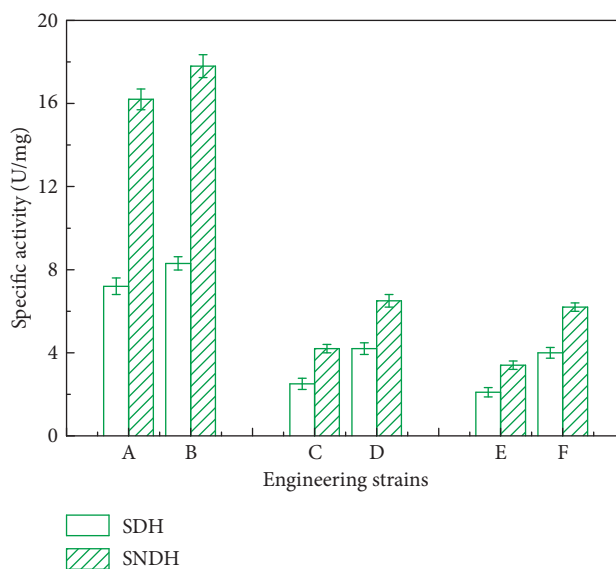


FIGURE 6: The specific activities of SDH and SNDH in the CutA-based engineered strain and the control strain at different temperatures. A, C, and E are SDH and SNDH specific activities of *G. oxydans*/pGUC-*tufB-sdh-GGGGS-sndh* at 30°C, 35°C, and 37°C, respectively. B, D, and F are SDH and SNDH specific activities of *G. oxydans*/pGUC-*tufB-SH3-sdh-GGGGS-sndh-tufB-SH3<sub>lig</sub>-(GGGGS)<sub>2</sub>-cutA* at 30°C, 35°C, and 37°C, respectively. Error bars represent the standard deviation of three biological replicates.

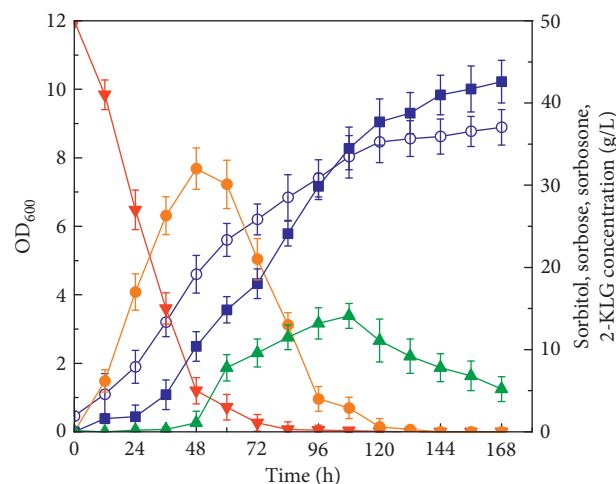


FIGURE 7: Time course of oxidative fermentation of D-sorbitol by the PQQ biosynthesis enhanced engineered strains. The symbols ▼, ●, ▲, and ■ represent the concentration of D-sorbitol, L-sorbose, L-sorbose, and 2-KLG produced by *G. oxydans*/pGUC-*tufB-SH3-sdh-GGGGS-sndh-tufB-SH3<sub>lig</sub>-(GGGGS)<sub>2</sub>-cutA-tufB-pqqABCDE*, respectively. The symbol ○ represents OD<sub>600</sub> of *G. oxydans*/pGUC-*tufB-SH3-sdh-GGGGS-sndh-tufB-SH3<sub>lig</sub>-(GGGGS)<sub>2</sub>-cutA-tufB-pqqABCDE*, respectively. Error bars represent the standard deviation of three biological replicates.

the wild-type strain. Furthermore, overexpression of PQQ biosynthesis genes significantly enhanced cell growth, and the likely reason for this is that PQQ is also a signaling molecule in signal transduction pathways that affect bacterial growth by

neutralizing reactive species [35, 36]. The 2-KLG production by *G. oxydans*/pGUC-*tufB*-*SH3*-*sdh*-GGGGS-*sndh*-*tufB*-*SH3*<sub>lig</sub>-(GGGGS)<sub>2</sub>-*cutA*-*tufB*-*pqq*ABCDE reached 42.6 g/L, which was 5.7% higher than that by *G. oxydans*/pGUC-*tufB*-*SH3*-*sdh*-GGGGS-*sndh*-*tufB*-*SH3*<sub>lig</sub>-(GGGGS)<sub>2</sub>-*cutA*. Unfortunately, the overexpression of *pqq*ABCDE did not increase the yield significantly, but the fermentation cycle could be shortened.

In the past several decades, tremendous advances have been achieved in VC production by the classical two-step fermentation process. However, the further decreasing of VC price is significantly restricted because of many problems such as the two times of sterilization and mix-culture fermentation. Therefore, much more attention has been focused on the development of one-step fermentation route, but it is to be regretted that the progress is not ideal. In this study, the production of 2-KLG reached 42.6 g/L with the stepwise metabolic engineering of *G. oxydans*. Nowadays, with the development of biological technology, many new metabolic engineering methods were developed. The comprehensive optimization of metabolic engineering strategies and fermentation optimization should further facilitate the research process for VC production by one-step fermentation route.

#### 4. Conclusions

In summary, SDH and SNDH were expressed in *G. oxydans* after the codon optimization. Furthermore, the trimeric protein CutA was used to improve the chemical structure stability of SDH and SNDH. The recombinant strain *G. oxydans*/pGUC-*tufB*-*SH3*-*sdh*-GGGGS-*sndh*-*tufB*-*SH3*<sub>lig</sub>-(GGGGS)<sub>2</sub>-*cutA* produced 40.3 g/L of 2-KLG after 168 h. In addition, the expression levels of the cofactor PQQ were enhanced to further improve 2-KLG production. With the stepwise metabolic engineering of *G. oxydans*, the final 2-KLG production was improved to 42.6 g/L. Efficient one-step production of 2-KLG was achieved.

#### Data Availability

The data used to support the findings of this study are included within the article.

#### Conflicts of Interest

The authors declare that there are no conflicts of interest regarding the publication of this paper.

#### Acknowledgments

This work was supported by grants from the Natural Science Foundation of Hebei Province (no. C2018203374).

#### References

- [1] P. Wang, W. Zeng, S. Xu, G. Du, J. Zhou, and J. Chen, "Current challenges facing one-step production of L-ascorbic acid," *Biotechnology Advances*, vol. 36, no. 7, pp. 1882–1899, 2018.
- [2] Mandlaa, Z. Sun, R. Wang et al., "Enhanced 2-keto-L-gulonic acid production by applying L-sorbose-tolerant helper strain in the co-culture system," *AMB Express*, vol. 8, pp. 1–7, 2018.
- [3] Y. Zou, M. Hu, Y. Lv et al., "Enhancement of 2-keto-gulonic acid yield by serial subcultivation of co-cultures of *Bacillus cereus* and *Ketogulonigenium vulgare*," *Bioresource Technology*, vol. 132, pp. 370–373, 2012.
- [4] C.-H. Pan, E.-X. Wang, N. Jia et al., "Reconstruction of amino acid biosynthetic pathways increases the productivity of 2-keto-L-gulonic acid in *Ketogulonigenium vulgare*-*Bacillus endophyticus* consortium via genes screening," *Journal of Industrial Microbiology & Biotechnology*, vol. 44, no. 7, pp. 1031–1040, 2017.
- [5] C. Wang, Y. Li, Z. Gao et al., "Establishing an innovative carbohydrate metabolic pathway for efficient production of 2-keto-L-gulonic acid in *Ketogulonigenium robustum* initiated by intronic promoters," *Microbial Cell Factories*, vol. 17, pp. 81–94, 2018.
- [6] Y. Zhu, J. Liu, G. Du, J. Zhou, and J. Chen, "Spore stability of *Bacillus megaterium* enhance *Ketogulonigenium vulgare* propagation and 2-keto-L-gulonic acid biosynthesis," *Bioresource Technology*, vol. 107, pp. 399–404, 2012.
- [7] R. D. Hancock and R. Viola, "Biotechnological approaches for L-ascorbic acid production," *Trends in Biotechnology*, vol. 20, no. 7, pp. 299–305, 2002.
- [8] Y. Saito, Y. Ishii, H. Hayashi et al., "Cloning of genes coding for L-sorbose and L-sorbose dehydrogenases from *Gluconobacter oxydans* and microbial production of 2-keto-L-gulonate, a precursor of L-ascorbic acid, in a recombinant *G. oxydans* strain," *Applied Environmental Microbiology*, vol. 63, no. 2, pp. 454–460, 1997.
- [9] L. Gao, Y. Hu, J. Liu, G. Du, J. Zhou, and J. Chen, "Stepwise metabolic engineering of *Gluconobacter oxydans* WSH-003 for the direct production of 2-keto-L-gulonic acid from D-sorbitol," *Metabolic Engineering*, vol. 24, pp. 30–37, 2014.
- [10] M.-H. Li, J. Wu, X. Liu, J.-P. Lin, D.-Z. Wei, and H. Chen, "Enhanced production of dihydroxyacetone from glycerol by overexpression of glycerol dehydrogenase in an alcohol dehydrogenase-deficient mutant of *Gluconobacter oxydans*," *Bioresource Technology*, vol. 101, no. 21, pp. 8294–8299, 2010.
- [11] X. Lin, S. Liu, G. Xie, J. Chen, P. Li, and J. Chen, "Enhancement of 1,3-dihydroxyacetone production from *Gluconobacter oxydans* by combined mutagenesis," *Journal of Microbiology and Biotechnology*, vol. 26, no. 11, pp. 1908–1917, 2016.
- [12] X. Hua, G. Du, and Y. Xu, "Cost-practical of glycolic acid bioproduction by immobilized whole-cell catalysis accompanied with compressed oxygen supplied to enhance mass transfer," *Bioresource Technology*, vol. 283, pp. 326–331, 2019.
- [13] X. Ke, Y. Pan-Hong, Z.-C. Hu, L. Chen, X.-Q. Sun, and Y.-G. Zheng, "Synergistic improvement of PQQ-dependent D-sorbitol dehydrogenase activity from *Gluconobacter oxydans* for the biosynthesis of miglitol precursor 6-(N-hydroxyethyl)-amino-6-deoxy- $\alpha$ -L-sorbofuranose," *Journal of Biotechnology*, vol. 300, pp. 55–62, 2019.
- [14] S. Morena, M. G. Acedos, V. E. Santos, and F. García-Ochoa, "Dihydroxyacetone production from glycerol using *Gluconobacter oxydans*: study of medium composition and operational conditions in shaken flasks," *Biotechnology Progress*, vol. 35, pp. 2803–2811, 2019.
- [15] U. Deppenmeier, M. Hoffmeister, and C. Prust, "Biochemistry and biotechnological applications of *Gluconobacter* strains,"

- Applied Microbiology and Biotechnology*, vol. 60, no. 3, pp. 233–242, 2002.
- [16] L. Gao, J. Zhou, J. Liu, G. Du, and J. Chen, “Draft genome sequence of *Gluconobacter oxydans* WSH-003, a strain that is extremely tolerant of saccharides and alditols,” *Journal of Bacteriology*, vol. 194, no. 16, pp. 4455–4456, 2012.
- [17] L. Gao, G. Du, J. Zhou, J. Chen, and J. Liu, “Characterization of a group of pyrroloquinoline quinone-dependent dehydrogenases that are involved in the conversion of L-sorbose to 2-keto-L-gulonic acid in *Ketogulonicigenium vulgare* WSH-001,” *Biotechnology Progress*, vol. 29, no. 6, pp. 1398–1404, 2013.
- [18] S. Jayaraj, R. Reid, and D. V. Santi, “GeMS: an advanced software package for designing synthetic genes,” *Nucleic Acids Research*, vol. 33, no. 9, pp. 3011–3016, 2005.
- [19] M. Sawano, H. Yamamoto, K. Ogasahara et al., “Thermodynamic basis for the stabilities of three CutA1s from *Pyrococcus horikoshii*, *thermus thermophilus*, and *Oryza sativa*, with unusually high denaturation temperatures,” *Biochemistry*, vol. 47, no. 2, pp. 721–730, 2008.
- [20] Y. Hu, H. Wan, J. Li, and J. Zhou, “Enhanced production of L-sorbose in an industrial *Gluconobacter oxydans* strain by identification of a strong promoter based on proteomics analysis,” *Journal of Industrial Microbiology & Biotechnology*, vol. 42, no. 7, pp. 1039–1047, 2015.
- [21] L. Zhang, J. Lin, Y. Ma, D. Wei, and M. Sun, “Construction of a novel shuttle vector for use in *Gluconobacter oxydans*,” *Molecular Biotechnology*, vol. 46, no. 3, pp. 227–233, 2010.
- [22] M. Ramirez, D. Guan, V. Ugaz, and Z. Chen, “Intein-triggered artificial protein hydrogels that support the immobilization of bioactive proteins,” *Journal of the American Chemical Society*, vol. 135, no. 14, pp. 5290–5293, 2013.
- [23] L. Ge, M. Zhang, R. Wang et al., “Fabrication of CS/GA/RGO/Pd composite hydrogels for highly efficient catalytic reduction of organic pollutants,” *RSC Advances*, vol. 10, no. 26, pp. 15091–15097, 2020.
- [24] Y. Feng, J. Yin, S. Liu, Y. Wang, B. Li, and T. Jiao, “Facile synthesis of Ag/Pd nanoparticle-loaded poly(ethylene imine) composite hydrogels with highly efficient catalytic reduction of 4-nitrophenol,” *ACS Omega*, vol. 5, no. 7, pp. 3725–3733, 2020.
- [25] J. Zhang, J. Liu, Z. Shi, L. Liu, and J. Chen, “Manipulation of *B. megaterium* growth for efficient 2-KLG production by *K. vulgare*,” *Process Biochemistry*, vol. 45, no. 4, pp. 602–606, 2010.
- [26] R. Wang, X. Yan, B. Ge et al., “Facile preparation of self-assembled black phosphorus-dye composite films for chemical gas sensors and surface-enhanced Raman scattering performances,” *ACS Sustainable Chemistry & Engineering*, vol. 8, no. 11, pp. 4521–4536, 2020.
- [27] L. Zhang, J. Yin, K. Wei et al., “Fabrication of hierarchical SrTiO<sub>3</sub>@MoS<sub>2</sub> heterostructure nanofibers as efficient and low-cost electrocatalysts for hydrogen-evolution reactions,” *Nanotechnology*, vol. 31, no. 20, pp. 205604–205615, 2020.
- [28] N. Noji, T. Nakamura, N. Kitahata et al., “Simple and sensitive method for pyrroloquinoline quinone (PQQ) analysis in various foods using liquid chromatography/electrospray-ionization tandem mass spectrometry,” *Journal of Agricultural and Food Chemistry*, vol. 55, no. 18, pp. 7258–7263, 2007.
- [29] S. Tan, Y. Chen, Y. Gao et al., “ $\beta$ -Galactosidase gene codon optimization results in post-transcriptional enhancement of expression,” *Gene*, vol. 748, 2020.
- [30] T. E. F. Quax, N. J. Claassens, D. Söll, and J. van der Oost, “Codon bias as a means to fine-tune gene expression,” *Molecular Cell*, vol. 59, no. 2, pp. 149–161, 2015.
- [31] T. Tanaka, M. Sawano, K. Ogasahara et al., “Hyper-thermostability of CutA1 protein, with a denaturation temperature of nearly 150°C,” *FEBS Letters*, vol. 580, no. 17, pp. 4224–4230, 2006.
- [32] Y. Tanaka, K. Tsumoto, T. Nakanishi et al., “Structural implications for heavy metal-induced reversible assembly and aggregation of a protein: the case of *Pyrococcus horikoshii* CutA1,” *FEBS Letters*, vol. 556, no. 1–3, pp. 167–174, 2004.
- [33] A. M. Sánchez, G. N. Bennett, and K.-Y. San, “Effect of different levels of NADH availability on metabolic fluxes of *Escherichia coli* chemostat cultures in defined medium,” *Journal of Biotechnology*, vol. 117, no. 4, pp. 395–405, 2005.
- [34] Y. Wang, K.-Y. San, and G. N. Bennett, “Cofactor engineering for advancing chemical biotechnology,” *Current Opinion in Biotechnology*, vol. 24, no. 6, pp. 994–999, 2013.
- [35] O. Choi, J. Kim, J.-G. Kim et al., “Pyrroloquinoline quinone is a plant growth promotion factor produced by *Pseudomonas fluorescens* B16,” *Plant Physiology*, vol. 146, no. 2, pp. 657–668, 2008.
- [36] M. Shrivastava, Y. S. Rajpurohit, H. S. Misra, and S. F. D’Souza, “Survival of phosphate-solubilizing bacteria against DNA damaging agents,” *Canadian Journal of Microbiology*, vol. 56, no. 10, pp. 822–830, 2010.

## Research Article

# Microstructure and Texture Evolution of Aluminum in the Al-Nb/Ti/Ni Composite Fabricated by the ARB Process

Nan Ye  and Xueping Ren 

School of Materials Science and Engineering, University of Science and Technology Beijing, Beijing 100083, China

Correspondence should be addressed to Xueping Ren; rxp33@ustb.edu.cn

Received 5 June 2020; Revised 1 July 2020; Accepted 7 July 2020; Published 27 July 2020

Guest Editor: Tifeng Jiao

Copyright © 2020 Nan Ye and Xueping Ren. This is an open access article distributed under the Creative Commons Attribution License, which permits unrestricted use, distribution, and reproduction in any medium, provided the original work is properly cited.

The Al-Nb/Ti/Ni composite was fabricated from pure Al, Ni, Ti, and Nb sheets by the ARB technology. The microstructure evolution was observed by scanning electron microscopy, x-ray diffraction, and transmission electron microscopy. The evolution was evaluated by the electron backscattered diffraction (EBSD) technique. A couple of results we obtained showed that the microstructure of Al changed from equiaxed grains to a lamellar structure, and the grain size in the ND decreased gradually. Finally, the average grain size in the ND was  $0.31\ \mu\text{m}$ . Additionally, the fraction of HAGBs increased after the third pass, resulting from the dynamic recovery and the shear bands. The texture evolution was tested by electron backscattered diffraction. After the fourth pass, the Al exhibited a combination texture of rolling texture and shear texture. The rolling texture components were composed of Copper{112}<111>, Dillamore{4 4 11}<11 11 8>, S{123}<634>, and Brass{011}<211>, and the shear texture components were Rotated Cube {001}<110> and {111}//ND. The microhardness of Ni, Ti, Nb, and Al was improved in the ARB process and finally reached 226.4, 246.3, 187.2, and 44.2 HV, respectively.

## 1. Introduction

Metal matrix composites (MMC) combine the advantages of each component and makes up for the shortcomings, which has excellent comprehensive properties that cannot be matched by a single metal or alloy so that it becomes a focus in materials science today. Metal matrix composites are prepared by the bonding technology to achieve metallurgical bonding between two or more metals with different characteristics. [1–5].

At present, the major methods of producing metal composites are casting, powder metallurgy, spray deposition, etc. However, most of these technologies require expensive equipment and complex processes, limiting their industrial application [6–10]. The accumulative roll bonding (ARB) technology is a kind of severe plastic deformation (SPD) process which can fabricate bulk composites continuously and has a good potential for industrialization. Compared with other SPD processes, ARB technology, it can

produce not only ultrafine grained metals but also metal matrix composites.

Aluminum is generally used as a matrix for metal matrix composites due to its lightweight and good formability. Recently, a number of researchers have reported the Al-matrix composite produced by the ARB process, such as Al-Ti [11], Al-Cu [12], Al-Ni [13, 14], Al-Mg [15–17], Al-Mg-Ti [18], Al-Ti-Nb [19], Al-Cu-Ni [20], Al-Cu-Sn [21], and Al-Cu-Zn [22]. However, the research about multimetal composites fabricated by the ARB process is insufficient. Titanium aluminum alloys are widely used in the automobile and aviation industries due to its low density-high strength, excellent corrosion resistance, and high-temperature performance. Adding nickel to the titanium aluminum alloy can improve its corrosion resistance, and adding niobium can enhance its high-temperature performance [19, 23]. Therefore, the Al-Nb/Ti/Ni composite will have excellent comprehensive properties. Metal sheets are arranged in a symmetrical form in order to ensure the stability of the

composites. Aluminum sheets located on the surface and in the middle can improve the feasibility of the ARB process. Therefore, the metal sheets were stacked in the order of Al/Ni/Ti/Al/Nb/Al/Ti/Ni/Al.

Texture analysis is a very critical means to explore the grain oriental of metals during plastic deformation so that we can more clearly understand the changes in the microstructure of the material. Existing researches have focused on the texture evolution of single metals or alloys [24–31] prepared by the ARB technology. However, the investigation on the texture of multimetal composites is insufficient.

In previous studies, we have prepared Ni-Ti-Al-Cu composites and investigated their microstructure evolution and mechanical properties. We will pay more attention to the texture evolution of the Al-Nb/Ti/Ni composite in this work. The EBSD technology was used to investigate the texture evolution of the Al-Nb/Ti/Ni composite.

## 2. Experimental Procedures

The chemical compositions and dimensions of raw sheets (pure aluminum, nickel, titanium, and niobium) are depicted in Table 1.

Al, Ni, Ti, and Nb sheets with a thickness of 0.2 mm were annealed, respectively, at 623 K, 1073 K, 1073 K, and 1473 K, for 30 minutes. The surface of the metals needed to be polished with a steel brush due to the oxides formed during the annealing process and then degreased in alcohol and acetone. Four aluminum sheets, two nickel sheets, two titanium sheets, and one niobium sheet were stacked (as depicted in Figure 1). The stacked sheets were fastened by steel wires at the four corners to keep stability.

The rolling process was conducted on a two-high mill with a 50% reduction at room temperature. The diameter of the roller was 350 mm, and the rolling speed was 10 rpm. The bonded samples were cut into two, degreased, and brushed. The samples were stacked and continued to roll with a target of 50% reduction. The experiment procedure was repeated for four times without lubrication. The Al-Nb/Ti/Ni composite was fabricated successfully after four passes accumulative roll bonding process. The Von Mises equivalent strains for each pass of the ARB process are 0.8, 1.6, 2.4, and 3.2, respectively. The complete accumulative roll bonding process is illustrated in Figure 1.

Microstructure evolution of the Al-Nb/Ti/Ni composite was observed by scanning electron microscopy (SEM, JSM-7001F) and transmission electron microscopy (TEM, JEM2010, 200 kV). The texture evolution of the Al layer in the ARB process was analyzed using an electron back-scattered diffraction (EBSD) technique, and the EBSD test was conducted at a scanning electron microscopy (SEM, JSM-7001F) equipped with a TSL-OIM EBSD analysis system. The EBSD measurements were performed at a voltage of 20 kV, a tilt angle of 70°, a magnification of 2500, and a scan step size of 0.06 microns. The EBSD samples were electropolished in an ethanol and perchloric acid (5 vol.%) solution at 20 V for 20~30 s. The microhardnesses (HV) of

TABLE 1: Chemical composition and dimensions of the used sheets.

	Chemical composition (wt%)	Dimension (mm × mm × mm)
Al	0.05Cu, 0.25Si, 0.35Fe, 0.03Mg, Al bal	100 × 50 × 0.2
Ni	0.01Fe, 0.01 Si, 0.03Mn, Ni bal	100 × 50 × 0.2
Ti	0.4Si, 0.4Fe, 0.04Zn, Ti bal	100 × 50 × 0.2
Nb	0.03Mn, 0.01 Fe, 0.01Si, Nb bal	100 × 50 × 0.2

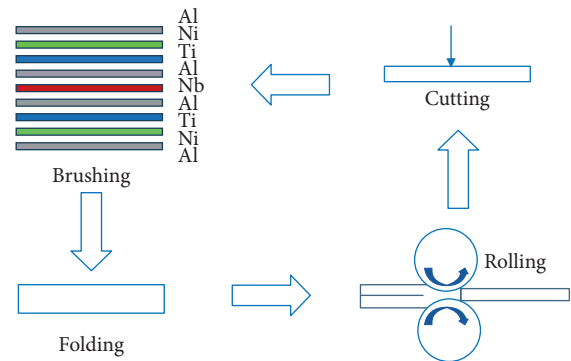


FIGURE 1: Schematic illustration of the accumulative roll bonding process.

the composites were measured by a hardness tester at a load of 50 g for 10 s.

## 3. Result and Discussion

**3.1. Microstructures.** Figure 2 is the SEM image of the Al-Nb/Ti/Ni composite on the RD-ND plane. The microstructural evolution of various layers of the Al-Nb/Ti/Ni composite after the different passes (1, 2, 3, and 4) is demonstrated in Figure 2. A good bonding between individual layers could be observed in Figure 2(a). The size of nickel, titanium, and niobium decreased with the further deformation, and the thickness of the niobium fragments was visibly smaller than that of Ni and Ti due to the smaller deformation resistance. In Figure 2(d), Nb fragments with extremely small size could be observed.

In the first pass, the composite material also exhibited a layered structure with the locally uneven deformation. Obvious neckings and fractures appeared in Ti, Ni, and Nb layers when the ARB pass increased. A couple of investigations [18, 19] reported similar results. The plastic instability occurred because of the different mechanical properties of individual layers, and then neckings eventually breaking were visible in the hard phase. Since the metals Ni, Ti, and Nb are hard phases relative to the matrix Al, then the Ti, Ni, and Nb layers necked and fractured with the further deformation. In the fourth pass, the metal fragments (nickel, titanium, and niobium) were homogeneously distributed in the multimetal composite.

Another reason for the formation of metal fragments was that the reinforcements (nickel, titanium, and niobium) were cut by the shear band during the plastic deformation process, and finally, the metal fragments are

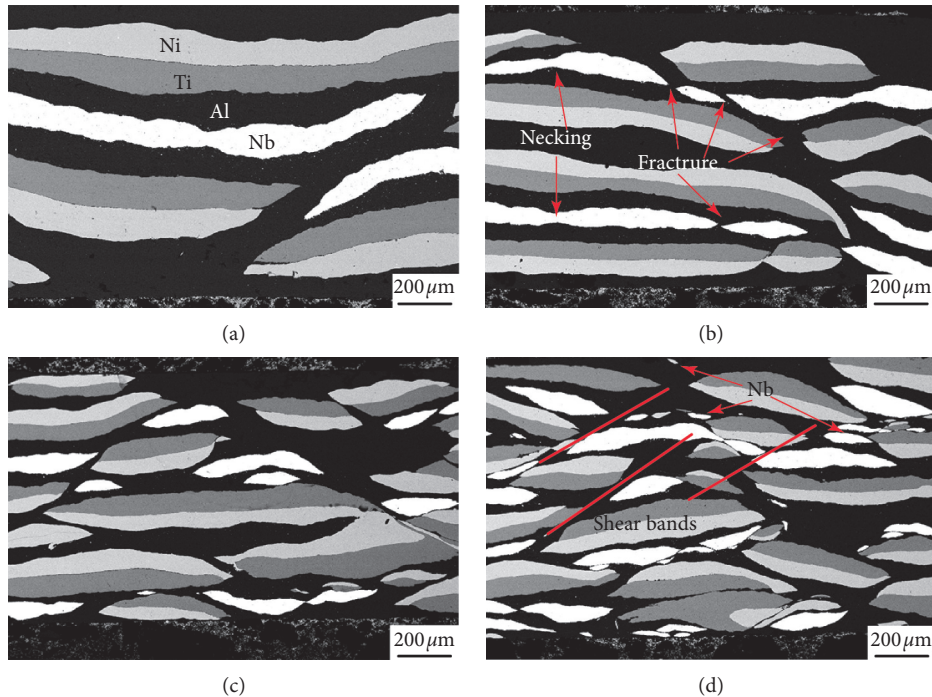


FIGURE 2: SEM micrographs on the RD-ND plane of the Al-Nb/Ti/Ni composites: (a) 1st pass, (b) 2nd pass, (c) 3rd pass, and (d) 4th pass.

formed. In Figure 2(d), we could observe that there were shear bands in the matrix. The shear bands were at an angle to the RD and the angle was generally about  $30^{\circ}$ – $45^{\circ}$ . Because of the different mechanical properties of the four metals, a shear band was generated with the effect of shear forces [18]. At last, the reinforcements (Ni, Ti, and Nb) were further broken and distributed homogeneously due to the effect of shear bands.

Interfacial bonding is a key issue of composites. The improvement of interface strength is beneficial to mechanical properties. Intermetallic compounds will be generated in different metal interfaces. In composites, brittle intermetallic compounds formed at the interface seriously affect the overall performance. A large amount of heat is released during the severe plastic deformation, which will lead to the formation of brittle intermetallic compounds. The XRD tests were conducted to check if there was a new phase. The results showed that there were only peaks of the raw metals in the XRD pattern, and no new intermetallics were observed (as shown in Figure 3.)

The orientation maps on the RD-ND plane after the 1st, 2nd, 3rd, and 4th pass are illustrated in Figure 4. Since the severe plastic deformation of the ARB process, an electro-polishing treatment should be conducted on the surface of samples before the EBSD test. The EBSD data is collected by an OIM software. In Figure 4, The correspondence between the colors and the orientations is shown in the triangle. Al grains were initially compressed, gradually elongated, and finally formed a lamellar structure. According to Alizadeh [32, 33], typical dislocation cells were generated in the initial stage. With the increasing ARB pass, a lamellar structure forms. The grain size in the ND was decreased gradually.

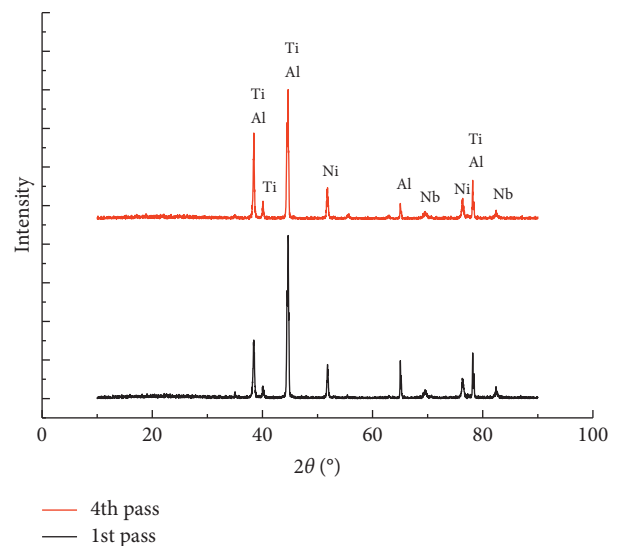


FIGURE 3: The XRD pattern of the Al-Nb/Ti/Ni composite.

The grain size in the ND of Al can be calculated, and results are demonstrated in Figure 5. The range of size distribution was smaller and nearer to Y-axis, indicating that the grain size in the ND decreased. Based on the data in Figure 5, the average grain size is calculated, and the results are shown in Figure 6. The average grain size in the ND decreased significantly. After the fourth pass, the average grain size in the ND was  $0.31 \mu\text{m}$ . Such a result suggests that rolling deformation plays a critical role in the grain size change in the ND.

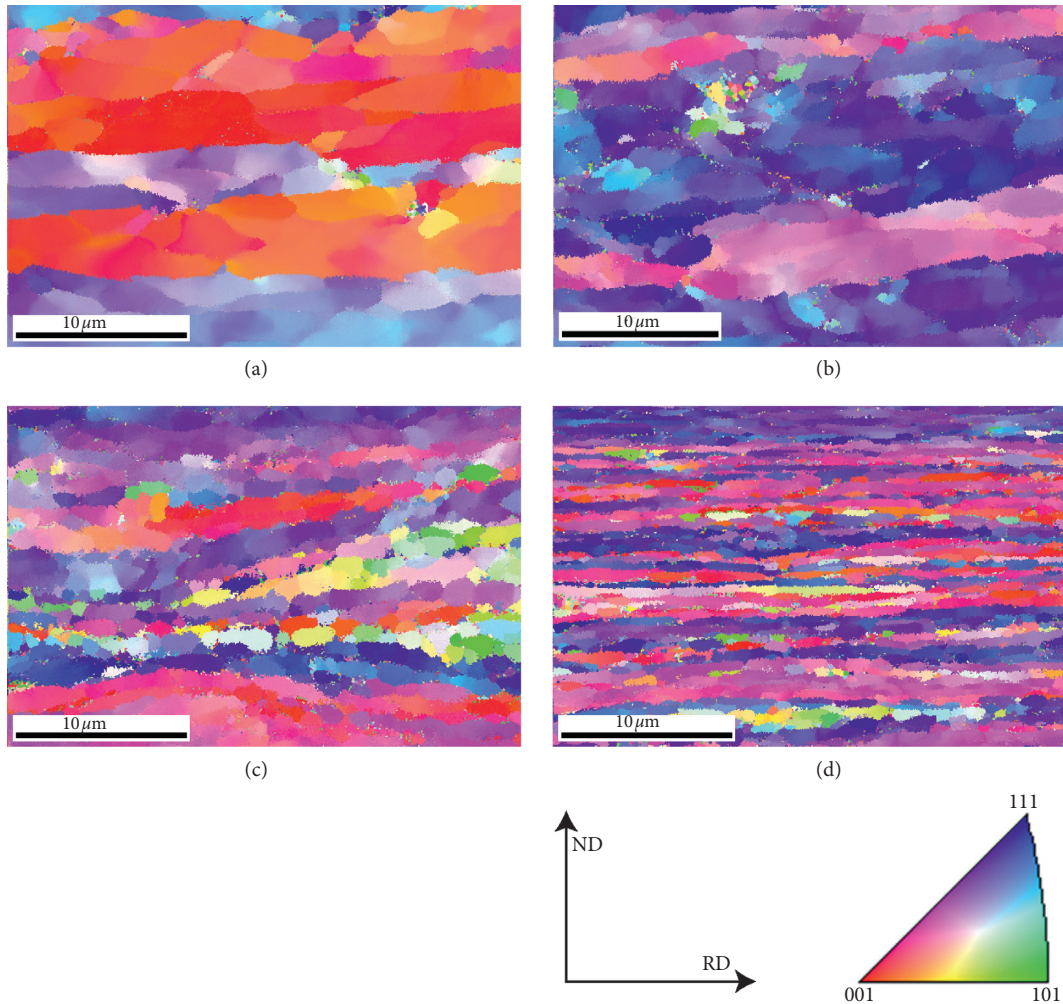


FIGURE 4: The orientation maps of aluminum in the Al-Nb/Ti/Ni composites: (a) the first pass, (b) the second pass, (c) the third pass, and (d) the fourth pass.

Interestingly, we can find that the rate of grain size reduction in the ND is slower gradually in Figure 6. The reasons for this result may be more complicated and related to various factors, such as properties and status of metals. One of the most important reasons is the increase in metal strength and deformation resistance in severe plastic deformation. Due to the effects of work hardening and fine grain strengthening, it is becoming more and more difficult for metals to deform. Consequently, the rate of grain size reduction decreases.

The bright-field TEM micrographs and corresponding selected area diffraction (SAD) patterns on the rolling direction (RD) normal direction (ND) plane are shown in Figure 7. The microstructure of Al observed in Figure 7 was consistent with that in Figure 4. Moreover, the average grain size calculated in Figure 6 was also confirmed in Figure 7. Obviously, the microstructure of the annealed Al sheets was changed from equiaxed grains to a lamellar structure during the ARB process. Grains had not been wholly elongated along the rolling direction after the first pass (as shown in Figure 7(a)). Dislocation tangles and dislocation cells are formed in the metal. By increasing ARB passes, Al grains

were gradually elongated along the RD, and then the elongated grains were subdivided into smaller grains by boundaries [32–35].

In Figure 7(a), a great number of dislocations were visible. After the second pass, the dislocation density was increased and the grains became finer. The dislocation density was significantly reduced in Figure 7(c), and there were a large number of clear grains with a low density of dislocations (indicated by arrows) among other grains with high dislocation density [36, 37]. Deformation heat during the ARB process provided energy for the dynamic recovery of aluminum. The temperature of aluminum rose, and then the dynamic recovery occurred in the ARB process. The dynamic recovery easily occurred in metals with high stack fault energy (SFE), such as aluminum and aluminum alloys.

Figure 8 depicts the misorientation angle distributions after different ARB passes. The fraction of HAGBs after the 1st, 2nd, 3rd, and 4th pass was 0.407, 0.34, 0.515, and 0.646, respectively. In the initial stage, the structure of Al changed from a recrystallized structure to a lamellar structure, and high-angle grain boundaries were reduced due to the rolling deformation. In the cold-rolling process, the dislocation

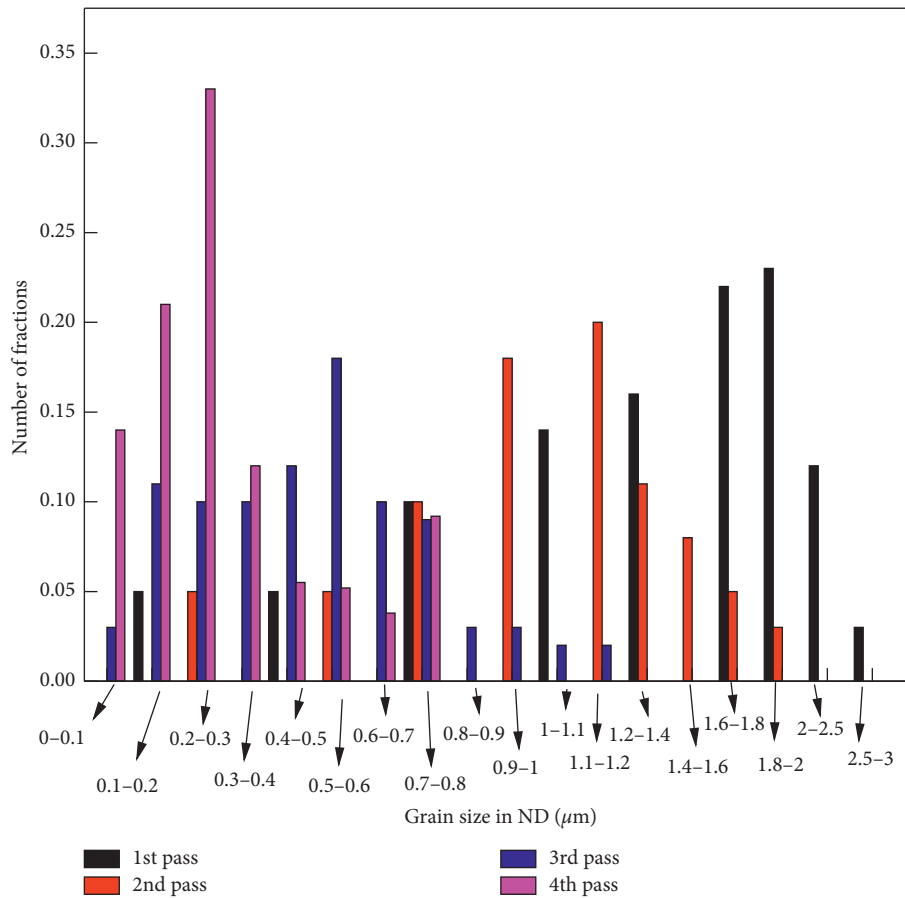


FIGURE 5: Distribution of Al grain size in the ND in the Al-Nb/Ti/Ni composites.

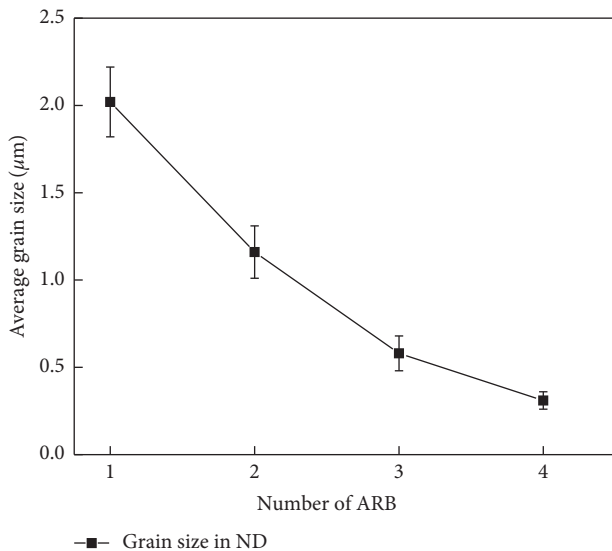


FIGURE 6: Dependence of Al grain size in the ND on the number of the ARB pass.

density accumulates and the internal distortion energy increases, which causes the initially clear grains to be divided into substructures by a large number of entangled dislocations. These substructures are small-angle grain

boundaries resulting in the decrease of HAGBs. After the third pass, the occurrence of dynamic recovery led to an increase in HAGB fraction. At the same time, the elongated grains could be divided by the local shear bands, forming the equiaxed grains, and more HAGBs are generated [19, 24]. Several investigations [38–40] reported that the grain refinement could form high-angle grain boundaries.

**3.2. Texture Evolution.** Figure 9 shows the orientation distribution function (ODF) of Al in the Al-Nb/Ti/Ni composite. The  $\varphi_2 = 45^\circ, 65^\circ, 90^\circ$  sections are illustrated in the figure. For face-centered cubic (FCC) metals, these sections can contain all the relevant texture components [19, 26, 41]. Figures 9(a)–9(d) show the ODF diagrams of the aluminum after the first, second, third, and fourth pass, respectively, and Figure 9(e) shows the ideal texture composition of Al.

The texture distribution on the RD-ND plane was complex because of the repetition of the rolling process. The texture components obtained in the 1st pass can be characterized as the strong cube  $\{001\}\langle 100 \rangle$  and weak  $S\{123\}\langle 634 \rangle$ . The Al layer had a strong recrystallization texture due to a full annealing treatment before rolling, and then a small amount of recrystallization texture changed to the rolling texture after the first pass. The recrystallization texture disappeared and completely transformed into the

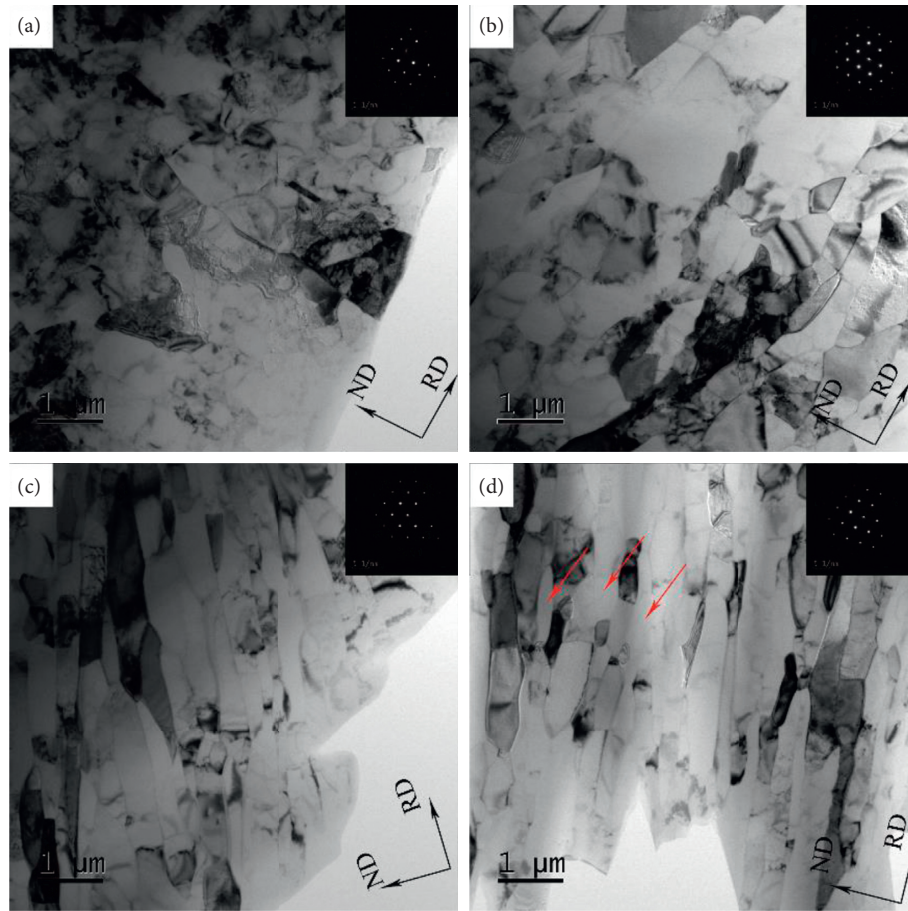


FIGURE 7: TEM micrographs on the RD-ND plane of Al in the Al-Nb/Ti/Ni composites: (a) 1st pass, (b) 2d pass, (c) 3rd pass, and (d) 4th pass.

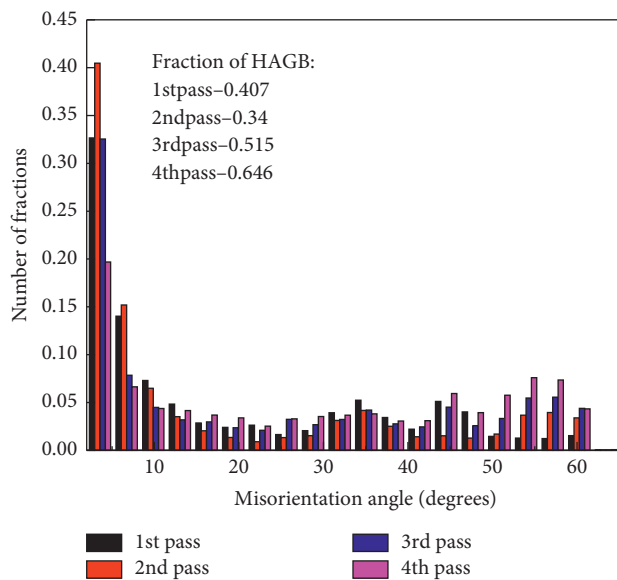


FIGURE 8: Distributions of misorientation angles of the aluminum in the Al-Nb/Ti/Ni composite.

rolling texture and the shear texture in the third pass. The rolling texture components were composed of Copper  $\{112\} \langle 111 \rangle$ , Dillamore  $\{4\ 4\ 11\} \langle 11\ 11\ 8 \rangle$ , S  $\{123\} \langle 634 \rangle$ , and Brass

$\{011\} \langle 211 \rangle$ , and the shear texture components were Rotated Cube  $\{001\} \langle 110 \rangle$  and  $\{111\} // ND$  (Figures 9(c) and 9(d)).

This result was different from the texture components in the aluminum ARB process. Pirgazi and Kim [26, 27] reported that the main textural components were the Copper  $\{112\} \langle 111 \rangle$  and Dillamore  $\{4\ 4\ 11\} \langle 11\ 11\ 8 \rangle$  components in aluminum alloys ARB process, and no obvious shear texture component was observed. The formation of shear texture component was related to two main factors [19, 26]. One was the generating of shear bands in the composite. The other was the shear deformation caused by great friction between the sample and the roller. Due to the repetition of the rolling, cutting, and stacking of the ARB, the surface of samples moved to the center in the next pass. Therefore, the shear texture also appeared in the center.

For the cold-rolling process of aluminum or aluminum alloys [24–31], the main rolling texture components were  $\beta$ -fiber and  $\tau$ -fiber. Generally, the intensity of  $\beta$ -fiber and  $\tau$ -fiber increased with the increasing amount of cold-rolling deformation. Pirgazi et al. [27] reported that the intensity of  $\beta$ -fiber and  $\tau$ -fiber increased significantly in the deformation. Kim et al. [26] also observed similar results of the intensity of  $\tau$ -fiber after four passes of the ARB process.

However, no obvious increase in rolling texture intensity could be seen in the Al-Nb/Ti/Ni composite (Figure 9). The

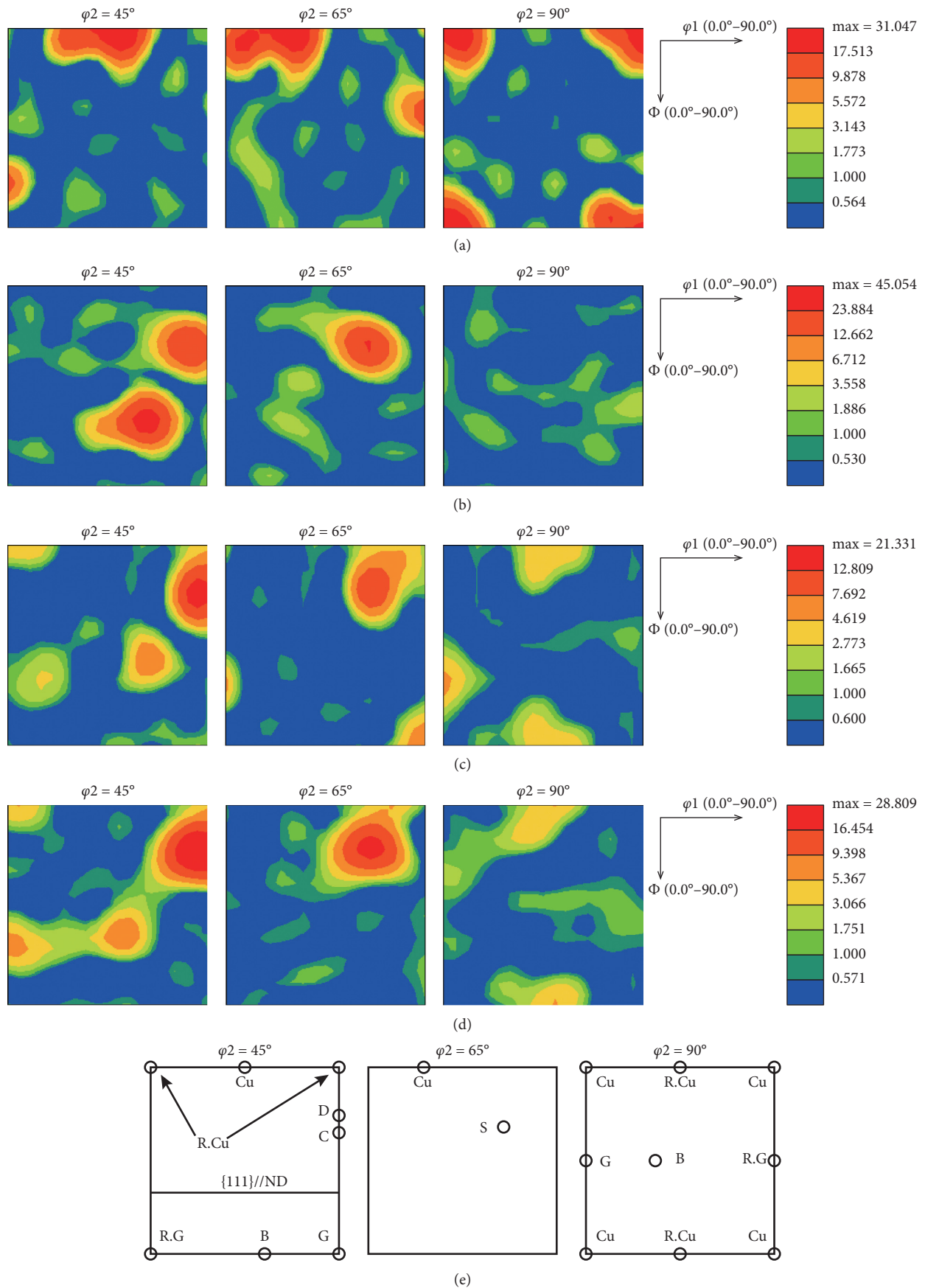


FIGURE 9: The ODFs of Al in the Al-Nb/Ti/Ni composites: (a) 1st pass, (b) 2nd pass, (c) 3rd pass, (d) 4th pass, and (e) an ideal texture components of Al. Cu: cube; D: dillamore; C: copper; B: brass; G: goss; R.G: rotated goss; R.Cu: rotated cube; S: S.

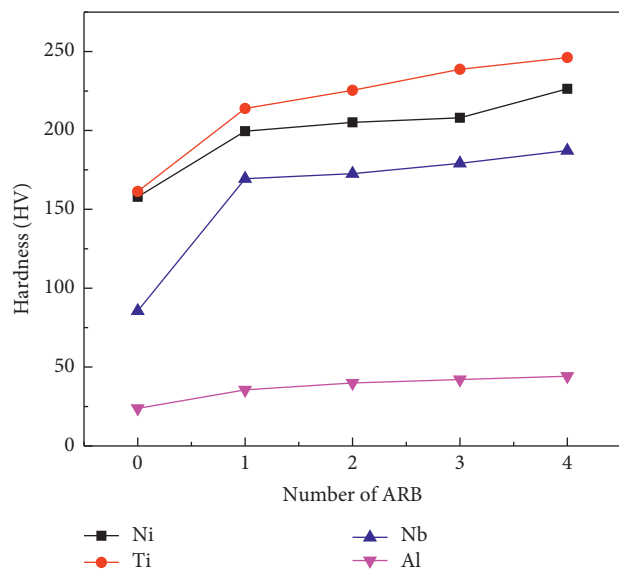


FIGURE 10: Variation of microhardness after different passes.

reason why the rolling texture intensity is not significantly improved is the effect of the shear bands. Qu et al. [19] found that shear bands led to not only a  $15^\circ$  deviation of rolling texture from the RD but also a decreasing intensity of rolling texture in aluminum. Chang et al. [15] reported that the shear bands reduced the intensity of rolling texture and  $t$  changed the texture orientation in the Mg/Al composite. Li et al. [42] observed a similar phenomenon in the Mg/Al composite. Furthermore, Toroghinejad et al. [24] showed that the intensity decrease of major texture components could be explained by the continuous recrystallization. Therefore, the dynamic recovery in this ARB process might influence the intensity of rolling texture components.

Figure 10 shows the microhardness variations of the Al-Nb/Ti/Ni composite. The microhardness of nickel, titanium, niobium, and aluminum was enhanced significantly from 157.9, 161.3, 85.6, and 23.8 HV to 199.5, 213.9, 169.4, and 35.6 HV, respectively. The rapid increase of microhardness after the first pass was due to the hardening. In the subsequent deformation, the microhardness change was mainly determined by the fine grain strengthening. Due to the dynamic recovery of Al, its microhardness growth rate was less than the other three. Finally, the microhardness of Ni, Ti, Nb, and Al reached 226.4, 246.3, 187.2, and 44.2 HV.

One of the reasons for the increasing hardness in the composite may be the different thermal conductivities between the four metals [18, 43]. Generally, the temperature of the sample increases due to plastic deformation and the friction between the roller and the sample. Finally, due to the different cooling rates of the four metals, regions with severe thermal stress are generated. According to the thermal expansion coefficients (CTE) of each layer (Ni, Ti, Nb, and Al are 13, 8.6, 7.1, and  $23 \mu\text{m}/\text{mK}$ , respectively), dislocations occur at the interface during deformation, thereby improving the microhardness of the composite.

In addition, we can observe that the microhardness growth rate of Al is the slowest in Figure 10. It is majorly due to the dynamic recovery in the deformation process, which has a softening effect. At the same time, pure aluminum as a relatively soft metal is difficult to reach a high level of microhardness. Furthermore, niobium has the fastest hardness growth among the other three metals. It is not difficult to find out the reasons through the analysis of the microstructure of composites (Figure 2). The size of Nb fragments is significantly smaller than that of nickel and titanium, indicating that niobium obtains greater deformation during the ARB process. Therefore, the microhardness of niobium gets a larger increment due to the effect of strain accumulation. In general, the changes in the mechanical properties of the individual metals in the composites are still determined by their own characteristics.

#### 4. Conclusions

In summary, the multimetal composite was successfully fabricated by the ARB technology. The following conclusions were obtained.

- (1) Nickel, titanium, and niobium fragments were homogeneously distributed in the multimetal composite, and the average size of Nb fragments was smaller than the other two. In the fourth pass, Nb fragments with extremely small size were distributed in the Al matrix. Additionally, Neckings and fractures appeared in the reinforcements (Ni, Ti, and Nb). There was no new intermetallic compound generated in the rolling at room temperature.
- (2) In the ARB process, the microstructure of Al changed from equiaxed grains to a lamellar structure, and the grain size in the ND decreased gradually. Finally, the average grain size in the ND was  $0.31 \mu\text{m}$ .
- (3) After the third pass, the dynamic recovery occurred in the Al matrix, resulting in an increase of the HGAB fraction and the decrease of the dislocation density. Additionally, the increasing fraction of HGABs was also contributed by shear bands.
- (4) After the fourth pass, the Al exhibited a combination texture of rolling texture and shear texture. The rolling texture components were composed of Copper $\{112\}\langle 111 \rangle$ , Dillamore $\{4\ 4\ 11\}\langle 11\ 11\ 8 \rangle$ , S $\{123\}\langle 634 \rangle$ , and Brass $\{011\}\langle 211 \rangle$ , and the shear texture components were Rotated Cube  $\{001\}\langle 110 \rangle$  and  $\{111\}/\text{ND}$ .
- (5) The microhardness of Ni, Ti, Nb, and Al was improved in the ARB process and finally reached 226.4, 246.3, 187.2, and 44.2 HV, respectively.

#### Data Availability

The experimental data used to support the findings of this study are included in the article. The other data are available from the corresponding author upon request.

## Conflicts of Interest

The authors declare that they have no conflicts of interest.

## References

- [1] S. V. Prasad and R. Asthana, "Aluminum metal-matrix composites for automotive applications: tribological considerations," *Tribology Letters*, vol. 17, no. 3, pp. 445–453, 2004.
- [2] J. W. Kaczmar and K. Pietrzak, "The production and application of metal matrix composite materials," *Journal of Materials Processing Technology*, vol. 106, no. 1–3, pp. 58–67, 2000.
- [3] W. D. Jeffrey, "Ancient and modern laminated composites—from the great pyramid of gizeh to Y2K," *Materials Characterization*, vol. 45, no. 4-5, pp. 289–313, 2000.
- [4] S. Ozden, R. Ekici, and F. Nair, "Investigation of impact behaviour of aluminium based SiC particle reinforced metal-matrix composites," *Composites Part A: Applied Science and Manufacturing*, vol. 38, no. 2, pp. 484–494, 2007.
- [5] Y. P. Li, G. P. Zhang, W. Wang, J. Tan, and S. J. Zhu, "On interface strengthening ability in metallic multilayers," *Scripta Materialia*, vol. 57, no. 2, pp. 117–120, 2007.
- [6] Y. Saito, N. Tsuji, H. Utsunomiya, T. Sakai, and R. G. Hong, "Ultra-fine grained bulk aluminum produced by accumulative roll-bonding (ARB) process," *Scripta Materialia*, vol. 39, no. 9, pp. 1221–1227, 1998.
- [7] R. Z. Valiev, R. K. Islamgaliev, and I. V. Alexandrov, "Bulk nanostructured materials from severe plastic deformation," *Progress in Materials Science*, vol. 45, no. 2, pp. 103–189, 2000.
- [8] V. M. Segal, "Equal channel angular extrusion: from macromechanics to structure formation," *Materials Science and Engineering A*, vol. 271, no. 1-2, pp. 322–333, 1999.
- [9] G. Sakai, Z. Horita, and T. G. Langdon, "Grain refinement and superplasticity in an aluminum alloy processed by high-pressure torsion," *Materials Science and Engineering A*, vol. 393, no. 1-2, pp. 344–351, 2005.
- [10] N. Tsuji, Y. Ito, Y. Saito, and Y. Minamino, "Strength and ductility of ultrafine grained aluminum and iron produced by ARB and annealing," *Scripta Materialia*, vol. 47, no. 12, pp. 893–899, 2002.
- [11] D. Yang, P. Cizek, P. Hodgson, and C. E. Wen, "Ultrafine equiaxed-grain Ti/Al composite produced by accumulative roll bonding," *Scripta Materialia*, vol. 62, no. 5, pp. 321–324, 2010.
- [12] M. Eizadjou, A. Kazemitalachi, H. Daneshmanesh, H. Shakurshahabi, and K. Janghorban, "Investigation of structure and mechanical properties of multi-layered Al/Cu composite produced by accumulative roll bonding (ARB) process," *Composites Science And Technology*, vol. 68, no. 9, pp. 2003–2009, 2008.
- [13] A. Mozaffari, M. Hoseini, and H. D. Manesh, "Al/Ni metal intermetallic composite produced by accumulative roll bonding and reaction annealing," *Journal of Alloys and Compounds*, vol. 509, no. 41, pp. 9938–9945, 2011.
- [14] A. Mozaffari, H. Danesh Manesh, and K. Janghorban, "Evaluation of mechanical properties and structure of multilayered Al/Ni composites produced by accumulative roll bonding (ARB) process," *Journal of Alloys and Compounds*, vol. 489, no. 1, pp. 103–109, 2010.
- [15] H. Chang, M. Y. Zheng, W. M. Gan, K. Wu, E. Maawad, and H. G. Brokmeier, "Texture evolution of the Mg/Al laminated composite fabricated by the accumulative roll bonding," *Scripta Materialia*, vol. 61, no. 7, pp. 717–720, 2009.
- [16] K. Wu, H. Chang, E. Maawad, W. M. Gan, H. G. Brokmeier, and M. Y. Zheng, "Microstructure and mechanical properties of the Mg/Al laminated composite fabricated by accumulative roll bonding (ARB)," *Materials Science and Engineering A*, vol. 527, no. 13-14, pp. 3073–3078, 2010.
- [17] H. Chang, M. Y. Zheng, C. Xu, G. D. Fan, H. G. Brokmeier, and K. Wu, "Microstructure and mechanical properties of the Mg/Al multilayer fabricated by accumulative roll bonding (ARB) at ambient temperature," *Materials Science and Engineering A*, vol. 543, no. 1, pp. 249–256, 2013.
- [18] P. D. Motevalli and B. Eghbali, "Microstructure and mechanical properties of Tri-metal Al/Ti/Mg laminated composite processed by accumulative roll bonding," *Materials Science and Engineering: A*, vol. 628, no. 25, pp. 135–142, 2015.
- [19] P. Qu, L. Zhou, and V. L. Acoff, "Deformation textures of aluminum in a multilayered Ti/Al/Nb composite severely deformed by accumulative roll bonding," *Materials Characterization*, vol. 107, pp. 367–375, 2015.
- [20] A. Shabani, M. R. Toroghinejad, and A. Shafyei, "Fabrication of Al/Ni/Cu composite by accumulative roll bonding and electroplating processes and investigation of its microstructure and mechanical properties," *Materials Science and Engineering: A*, vol. 558, pp. 386–393, 2012.
- [21] M. M. Mahdavian, H. Khatami-Hamedani, and H. R. Abedi, "Macrostructure evolution and mechanical properties of accumulative roll bonded Al/Cu/Sn multilayer composite," *Journal of Alloys and Compounds*, vol. 703, pp. 605–613, 2017.
- [22] M. M. Mahdavian, L. Ghalandari, and M. Reihanian, "Accumulative roll bonding of multilayered Cu/Zn/Al: an evaluation of microstructure and mechanical properties," *Materials Science and Engineering: A*, vol. 579, pp. 99–107, 2013.
- [23] N. Ye, X. Ren, and J. Liang, "Microstructure and mechanical properties of the Ni/Ti/Nb multilayer composite manufactured by accumulative pack-roll bonding," *Metals*, vol. 10, no. 3, p. 354, 2020.
- [24] M. R. Toroghinejad, F. Ashrafzadeh, R. Jamaati, M. Hoseini, and J. A. Szpunar, "Textural evolution of nanostructured AA5083 produced by ARB," *Materials Science and Engineering A*, vol. 556, pp. 351–357, 2012.
- [25] M.-y. Zhan, W.-w. Zhang, and D.-t. Zhang, "Production of Mg-Al-Zn magnesium alloy sheets with ultrafine-grain microstructure by accumulative roll-bonding," *Transactions of Nonferrous Metals Society of China*, vol. 21, no. 5, pp. 991–997, 2011.
- [26] H. W. Kim, S. B. Kang, N. Tsuji, and Y. M. Amino, "Deformation textures of AA8011 aluminum alloy sheets severely deformed by accumulative roll bonding," *Metallurgical and Materials Transactions A*, vol. 36, no. 11, pp. 3151–3163, 2005.
- [27] H. Pirgazi, A. Akbarzadeh, R. Petrov, J. Sidor, and L. Kestens, "Texture evolution of AA3003 aluminum alloy sheet produced by accumulative roll bonding," *Materials Science and Engineering A*, vol. 492, no. 1-2, pp. 110–117, 2008.
- [28] M. R. T. Roohollahjamaati, M. Hoseini, and J. A. Szpunar, "Texture development in Al/Al<sub>2</sub>O<sub>3</sub> MMCs produced by anodizing and ARB processes," *Materials Science and Engineering A*, vol. 528, no. 10-11, pp. 3573–3580, 2011.
- [29] Y. N. Wang and J. C. Huang, "Texture analysis in hexagonal materials," *Materials Chemistry and Physics*, vol. 81, no. 1, pp. 11–26, 2003.
- [30] S. G. Chowdhury, A. Dutta, B. Ravikumar, and A. Kumar, "Textural evolution during accumulative roll bonding of an Al-Li alloy," *Materials Science and Engineering A*, vol. 428, no. 1-2, pp. 351–357, 2006.

- [31] M. Raei, M. R. Toroghinejad, R. Jamaati, and J. A. Szpunar, "Effect of ARB process on textural evolution of AA1100 aluminum alloy," *Materials Science and Engineering: A*, vol. 527, no. 26, pp. 7068–7073, 2010.
- [32] M. Alizadeh and E. Salahinejad, "Processing of ultrafine-grained aluminum by cross accumulative roll-bonding," *Materials Science and Engineering: A*, vol. 595, pp. 131–134, 2014.
- [33] S. H. Lee, Y. Saito, T. Sakai et al., "Microstructures and mechanical properties of 6061 aluminum alloy processed by accumulative roll-bonding," *Materials Science and Engineering A*, vol. 325, no. 1-2, pp. 228–235, 2002.
- [34] M. Alizadeh and E. Salahinejad, "A comparative study on metal-matrix composites fabricated by conventional and cross accumulative roll-bonding processes," *Journal of Alloys and Compounds*, vol. 620, pp. 180–184, 2015.
- [35] A. H. Yaghtin, E. Salahinejad, and A. Khosravifard, "Processing of nanostructured metallic matrix composites by a modified accumulative roll bonding method with structural and mechanical considerations," *International Journal of Minerals, Metallurgy, and Materials*, vol. 19, no. 10, pp. 951–956, 2012.
- [36] M. Hosseini, N. Pardis, H. D. Manesh, M. Abbasi, and D. Kim, "Structural characteristics of Cu/Ti bimetal composite produced by accumulative roll-bonding (ARB)," *Materials and Design*, vol. 113, pp. 128–136, 2016.
- [37] K. Edalati and Z. Horita, "High-pressure torsion of pure metals: influence of atomic bond parameters and stacking fault energy on grain size and correlation with hardness," *Acta Materialia*, vol. 59, no. 17, pp. 6831–6836, 2011.
- [38] X. Huang, N. Tsuji, N. Hansen, and Y. Minamino, "Microstructural evolution during accumulative roll-bonding of commercial purity aluminum," *Materials Science and Engineering A*, vol. 340, no. 1-2, pp. 265–271, 2003.
- [39] N. Tsuji, T. Toyoda, Y. Minamino et al., "Microstructural change of ultrafine-grained aluminum during high-speed plastic deformation," *Materials Science and Engineering A*, vol. 350, no. 1-2, pp. 108–116, 2003.
- [40] X. Huang, N. Tsuji, N. Hansen, and Y. Minamino, "Microtexture of lamellar structures in Al heavily deformed by accumulative roll-bonding (ARB)," *Materials Science Forum*, vol. 408–412, pp. 715–720, 2002.
- [41] P. Qu, L. Zhou, H. Xu, and V. L. Acoff, "Microtexture development of niobium in a multilayered Ti/Al/Nb composite produced by accumulative roll bonding," *Metallurgical and Materials Transactions A*, vol. 45, no. 13, pp. 6217–6230, 2014.
- [42] M. Li, X. Liu, Y. Liu, M. Zheng, C. Wang, and D. Chen, "Texture evolution and mechanical properties of Mg/Al multilayered composite sheets processed by accumulative roll bonding," *Acta Metallurgica Sinica*, vol. 52, no. 4, pp. 463–472, 2016.
- [43] R. N. Dehsorkhi, F. Qods, and M. Tajally, "Investigation on microstructure and mechanical properties of Al-Zn composite during accumulative roll bonding (ARB) process," *Materials Science and Engineering: A*, vol. 530, pp. 63–72, 2011.

## Research Article

# Facile Fabrication of SrTiO<sub>3</sub>@MoS<sub>2</sub> Composite Nanofibers for Excellent Photodetector Application

Jinghong Li,<sup>1</sup> Lun Zhang,<sup>1</sup> Di Wang,<sup>2</sup> Ran Wang,<sup>1</sup> Xiujuan Liu,<sup>3</sup> and Jingxin Zhou <sup>1</sup>

<sup>1</sup>Hebei Key Laboratory of Applied Chemistry,

Heavy Metal Deep-Remediation in Water and Resource Reuse Key Lab of Hebei Province,

School of Environmental and Chemical Engineering, Yanshan University, Qinhuangdao 066004, China

<sup>2</sup>School of Materials Science and Engineering, Shijiazhuang Tiedao University, Shijiazhuang 050043, China

<sup>3</sup>The First Hospital of Qinhuangdao City, Qinhuangdao 066000, China

Correspondence should be addressed to Jingxin Zhou; [zhoujingxin@ysu.edu.cn](mailto:zhoujingxin@ysu.edu.cn)

Received 31 May 2020; Accepted 29 June 2020; Published 23 July 2020

Academic Editor: Peizhi Guo

Copyright © 2020 Jinghong Li et al. This is an open access article distributed under the Creative Commons Attribution License, which permits unrestricted use, distribution, and reproduction in any medium, provided the original work is properly cited.

Molybdenum disulfide (MoS<sub>2</sub>), as a kind of transition metal dichalcogenide, has been widely studied for its excellent compatibility with most of inorganic nanomaterials. Nevertheless, its microscale and agglomeration limit the performance severely. Therefore, the special structure of V-MoS<sub>2</sub> has drawn a lot of interest, which can not only reduce the size of MoS<sub>2</sub> nanosheets but also improve the valence electron structure of the materials. In this work, SrTiO<sub>3</sub>@MoS<sub>2</sub> composite nanofibers were synthesized by the simple electrospinning and hydrothermal method, and it was applied as a novel material for photodetector. SEM, TEM, EDX, XRD, I-T curves, and EIS analysis were used to study the structure and properties of the prepared SrTiO<sub>3</sub>@MoS<sub>2</sub> composite nanofibers. Simulating under sunlight at a potential of 1.23 V, the prepared composite materials exhibited a superior photoelectric performance of photocurrent density of 21.4 μA and a resistance of 2.3 Ω. These results indicate that the composite of SrTiO<sub>3</sub> nanofiber adhered with V-MoS<sub>2</sub> has a stable composite structure, good electrical conductivity, and photoelectric sensitivity and is a suitable material for photodetectors. This work provides new ideas for the preparation of self-assembled materials and their application in photodetectors.

## 1. Introduction

As we all know, water pollution, greenhouse effect, and fumes are hazardous to human beings, but few people notice that potential light pollution is also threatening our health [1–4]. Light is everywhere in our life; in fact, proper sunlight is useful for our health. However, excessive light may damage our eyesight, affect our emotions, and even induce cancer [5]. The light pollution mainly originated from assimilation lighting and massive use of architectural glass, particularly in the developed region. To solve this problem, photodetector has been widely studied as optoelectronic devices [6–8].

As a member of semiconductors, transition metal dichalcogenides (TMDCs) have shown perfect properties of its special band structure, fairly physical character, and

superconductive performance [9, 10]. Within all kinds of materials of TMDCs, molybdenum disulfide (MoS<sub>2</sub>) has attracted more and more attention due to its special structure, excellent compatibility with abundant nanoscale materials, and attractive price [11]. Therefore, MoS<sub>2</sub> has been used in many fields such as nano-electronic devices and optoelectronics. However, the performance of MoS<sub>2</sub> was limited by the lamellae stacking and the lack of active sites [12]. Recently, vertical MoS<sub>2</sub> (V-MoS<sub>2</sub>) has been reported frequently in the field of photoelectricity [13]. The photoelectric performance of MoS<sub>2</sub> nanosheets has been improved by building a V-MoS<sub>2</sub> structure at the nanoscale and changing MoS<sub>2</sub> from a multilayer structure to a single-layer structure. Moreover, high-quality V-MoS<sub>2</sub> structure has a stable reproducible optoelectronic performance and is easy to fabricate. In addition, V-MoS<sub>2</sub> with a single-layer

structure can form Mo-O bonds, which can further improve the sensitivity of the photodetector [14–16]. However, many efforts have been made to construct the V-MoS<sub>2</sub> structure, but most of them are still unsatisfactory for their poor performance and instability.

In this work, porous SrTiO<sub>3</sub> nanofibers embedded with MoS<sub>2</sub> nanosheets were constructed through electrospinning and hydrothermal method, which showed a V-MoS<sub>2</sub> structure [17–20]. The porous nanofibers can provide a stable substrate for delamination of MoS<sub>2</sub> to form a vertical monolayer structure. The prepared MoS<sub>2</sub>-based material exhibited a sensitive optoelectronic performance through current density curves and Nyquist EIS plots characterization [21–23].

## 2. Materials and Methods

**2.1. Materials.** PVP (molecular weight = 1 300 000), thioacetamide (C<sub>2</sub>H<sub>5</sub>NS), tetrabutyl titanate (TBOT; C<sub>16</sub>H<sub>36</sub>O<sub>4</sub>Ti), acetic acid (C<sub>2</sub>H<sub>4</sub>O<sub>2</sub>), 2-methoxyethanol (C<sub>3</sub>H<sub>8</sub>O<sub>2</sub>), strontium acetate (C<sub>4</sub>H<sub>6</sub>O<sub>4</sub>Sr), sodium molybdate (Na<sub>2</sub>MoH<sub>4</sub>O<sub>6</sub>), thioacetamide (C<sub>2</sub>H<sub>5</sub>NS), Pluronic F127, and hexadecyl trimethylammonium bromide (CTAB) were purchased from Aladdin Reagent Co, Ltd. All chemical reagents were of analytical grade (AR) and used without any further purification. The ultrapure water used throughout the experiments was extracted from a Milli-Q Millipore All Filter system (Millipore Co, Bedford, MA, USA).

**2.2. Synthesis of Porous SrTiO<sub>3</sub> Nanofibers.** In brief, tetrabutyl titanate (TBOT) and strontium acetate were dissolved in 10 mL acetic acid at a mass ratio of 1.6:1. The mixture was vigorously stirred for 15 min until the solution transformed to transparent, and it was named solution A. Then, PVP, Pluronic F127, and CTAB were put into 6 mL 2-methoxyethanol at a mass ratio of 1:0.5:0.7 with vigorous stirring for 15 min, which has been deeply explored in previous work to ensure the proper ratio of these reagents [17]. When the mixture became transparent viscous liquid, solution A was dropped to the liquid slowly and stirred overnight. Next, the mixture was put into syringe and applied a 15 kV electric voltage at the distance of 20 cm. The ejected rate was set 0.5 ml h<sup>-1</sup> to obtain the nanofiber membrane. Then, the prepared membrane was under pyroprocessing at 700°C for 3 h at a ramp rate of 2°C min<sup>-1</sup> to obtain the porous SrTiO<sub>3</sub> nanofibers.

**2.3. Synthesis of SrTiO<sub>3</sub>@MoS<sub>2</sub> 2D Structure.** Typically, C<sub>2</sub>H<sub>5</sub>NS and Na<sub>2</sub>MoO<sub>4</sub>·2H<sub>2</sub>O with a mass ratio of 3:5 were dissolved in 15 mL ultrapure water. Then, 150 mg porous SrTiO<sub>3</sub> nanofibers were put into the solution. The mixed solution was then shifted to a 50 mL hydrothermal reactor and heated at 220°C for 24 h. Ultimately, the SrTiO<sub>3</sub>@MoS<sub>2</sub> 2D structure was obtained through filtration separation and vacuum drying [24].

**2.4. Photo(electro)chemical Measurements.** 8 mg SrTiO<sub>3</sub>@MoS<sub>2</sub> sample and 1 mg acetylene black were transferred to a

25 mL beaker with 10 mL absolute alcohol, and then, 10 μL PTFE was dropped into the mixture with vigorous stirring. The mixed solution was ultrasonic treated for about 30 min and shaken well at last 2 min. After that, the beaker was put into a vacuum drying oven to evaporate the alcohol for 3 h and then transferred the sediment to the nickel foam. Finally, put the nickel foam into a vacuum oven at 100°C overnight and obtain the working electrodes. The photo (electro) chemical test was performed using a CHI660 electrochemical workstation with a standard three-electrode system with a graphene rod, an Ag/AgCl electrode, and nickel foam, respectively. All the measurements were tested in 1 M KOH aqueous solution under simulated solar light, which was provided by a 300 W Xe lamp. The change in the current density curve with time was tested at a potential of 1.23 V under light on/off condition [25]. The electrochemical impedance spectroscopy (EIS) tests were measured in a frequency range from 100 kHz to 0.1 Hz with an amplitude of 5 mV at η = -0.24 V [26–30].

**2.5. Characterizations.** X-ray diffraction (XRD) analyses of the as-prepared samples were investigated with an X-ray diffractometer (SmartLab, Rigaku, Akishima, Japan). The morphologies of prepared samples were obtained by using transmission electron microscopy (TEM) (HT7700, Hitachi High Technologies Corporation, Ibaraki, Japan) and field-emission scanning electron microscopy (SEM, S-4800II, Hitachi, Japan). Elemental map results were investigated with an Oxford Link-ISIS X-ray EDXS microanalyzer at 200 kV with SEM. All the ultrapure water used in the experiment was purified in a Milli-Q Millipore All Filter system (Millipore Co, Bedford, MA, USA).

## 3. Results and Discussion

**3.1. Characterization of SrTiO<sub>3</sub>@MoS<sub>2</sub>.** The morphologies of as-prepared materials were obtained by transmission electron microscopy (TEM) and scanning electron microscopy (SEM). Figure 1(a) shows the SEM image of electrospun nanofibers before calcined, which mainly consisted of PVP, F127, and other ions. The diameter of nanofibers is approximately 1–3 μm and evenly distributed with a network structure. Figure 1(b) shows the image of nanofibers after being calcined at 700°C, and the surface of fibers becomes rough and shows many pores. It can be clearly observed that the diameter of fiber reduced to about 300 nm with 10–20 nm aperture gap uniform distributes on the surface. This special morphology is mainly caused by the synergistic effect of F127 and CTAB, which has been studied systematically in the earlier works. This special structure can greatly increase the surface area of SrTiO<sub>3</sub> NFs and provide suitable sites for loading MoS<sub>2</sub> [31–36]. In addition, the pores in the nanofibers can magnify the contact area between electrodes and electrolytes and optimize the structure of valence electron transmission. Figure 1(c) exhibits the result of SrTiO<sub>3</sub>@MoS<sub>2</sub> composite nanofibers. It can be found that the triangular MoS<sub>2</sub> nanosheets firmly embed in the aperture gap of SrTiO<sub>3</sub> nanofibers to form a V-MoS<sub>2</sub> structure. TEM is carried out to further

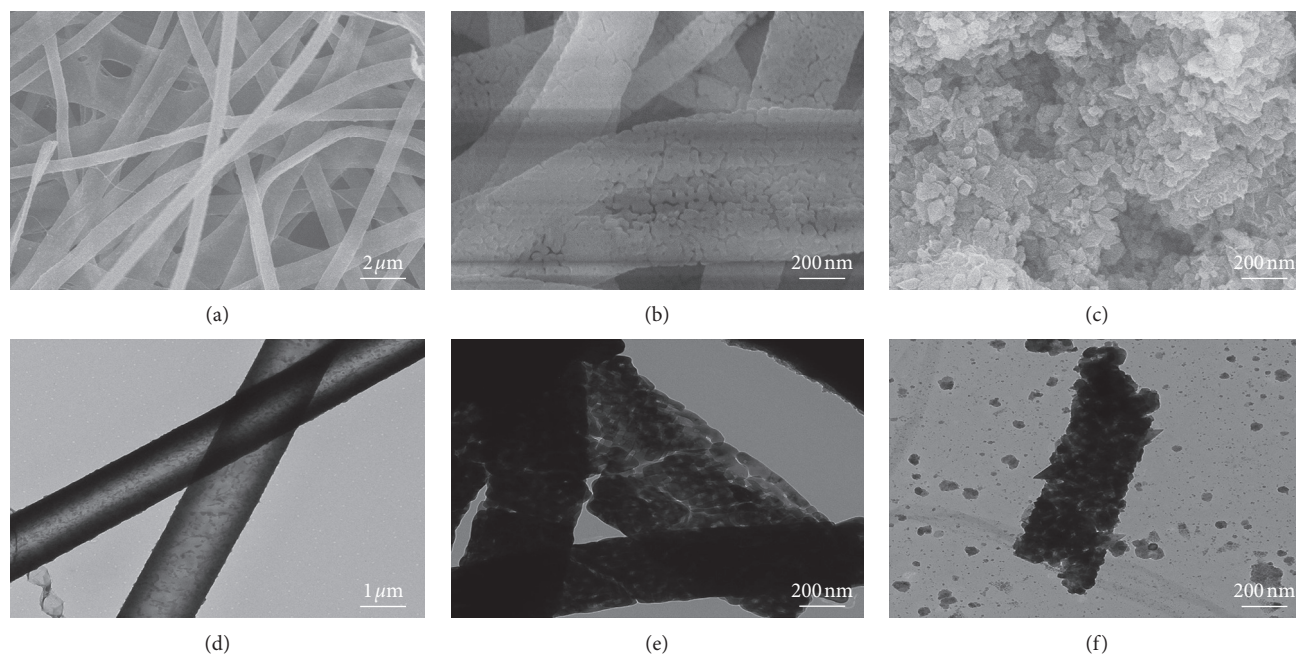


FIGURE 1: SEM images of (a) nanofibers before calcination, (b) porous SrTiO<sub>3</sub> NFs, and (c) SrTiO<sub>3</sub>@MoS<sub>2</sub> composite nanofibers. TEM images of (d) nanofibers before calcination, (e) porous SrTiO<sub>3</sub> NFs, and (f) SrTiO<sub>3</sub>@MoS<sub>2</sub> composite nanofibers.

explore the structure of MoS<sub>2</sub> on SrTiO<sub>3</sub>@MoS<sub>2</sub> hybrids, as shown in Figures 1(d)–1(f). From Figure 1(d), the diameter of as-spun nanofibers is about 200 nm, which corresponds to the SEM images. As shown in Figure 1(e), it can be observed that the calcined nanofibers are highly porous due to the different electron penetrability of various positions [37–46]. Figure 1(f) shows the composite nanofibers of SrTiO<sub>3</sub>@MoS<sub>2</sub>, and it can be clearly seen that the MoS<sub>2</sub> nanosheets and porous nanofibers combine tightly. Furthermore, the sample was under ultrasonic treatment for about 15 min before TEM operation, and the MoS<sub>2</sub> nanosheets were still adhered in the nanofibers. This phenomenon can convincingly demonstrate the stability of SrTiO<sub>3</sub>@MoS<sub>2</sub> composite nanomaterials. The mesoporous structure in NFs provided an excellent adhesion environment to form the V-MoS<sub>2</sub> structure [47].

The elemental map is one of the most commonly used techniques to observe the morphology of elements distribution. The SEM mapping of bare SrTiO<sub>3</sub> nanofibers and SrTiO<sub>3</sub>@MoS<sub>2</sub> hybrids is shown in Figure 2. Figures 2(a)–2(d) illustrate that the elemental map of SrTiO<sub>3</sub> nanofibers includes Ti, Sr, and O elements. The distribution of elements matches well with the shape of nanofibers, which indicate that the porous SrTiO<sub>3</sub> nanofibers have been successfully prepared. Figures 2(e)–2(j) show the presence of Ti, Sr, O, Mo, and S elements on the surface of SrTiO<sub>3</sub>@MoS<sub>2</sub> hybrids, proving that the MoS<sub>2</sub> nanosheets have been successfully adhere to the nanofibers.

The crystallographic structure of the prepared materials is shown in Figure 3, illustrated by the XRD profiles. The porous SrTiO<sub>3</sub> nanofibers and pure MoS<sub>2</sub> are precisely indexed to the JCPDS 35-0734 and JCPDS 37-1492, respectively. For 2D SrTiO<sub>3</sub>@MoS<sub>2</sub> composite nanofibers, the XRD peaks of SrTiO<sub>3</sub> appeared at 23°, 32°, 40°, 47°, 52°, 58°, 68°, and 77° can be assigned to the (100), (110), (111), (200), (210), (211), (220), and (310) planes, respectively. Nevertheless, the peaks of

MoS<sub>2</sub> are very weak or deviated in the composite XRD patterns. The V-MoS<sub>2</sub> delaminated in the porous nanofibers may be due to the crystalline form changed. Interestingly, we can see some hetero peaks in the composite XRD patterns, and we discovered that the hetero peaks can fit well with the elemental sulfur. Thus, we inferred that not all the thioacetamide transferred to the MoS<sub>2</sub>, a small amount of thioacetamide transferred to elemental S and adhered to the nanofibers, and causes some hetero peaks.

In order to illustrate the high photoelectric conversion capacity of the SrTiO<sub>3</sub>@MoS<sub>2</sub> composite nanofibers, the mechanism illustration is shown in Figure 4. Under simulate sunlight illumination, the porous SrTiO<sub>3</sub> nanofibers produce photogenerated electrons, and the holes were left in the nanofibers. For the pure SrTiO<sub>3</sub>, the electrons and holes will recombine quickly and decrease the photoelectric performance immensely. However, after composing the V-MoS<sub>2</sub>, the conduction band position of SrTiO<sub>3</sub> is much higher than MoS<sub>2</sub>. The photogenerated electrons will transfer to MoS<sub>2</sub> and restrain the recombine of electrons and holes, which make the electrons more mobile and promote the photoelectric performance. Therefore, the V-MoS<sub>2</sub> structure can enlarge the surface area of materials and increase the active sites. In addition, the particular structure can retard the recombination of electrons and holes and then enhance the prolong of photoelectrons.

**3.2. Optoelectronic Performance Test.** Photocurrents and the electrochemical impedance spectroscopy (EIS) were used to explore the photoelectric conversion sensitivity and electronic transmission rate of the as-prepared samples. Figure 5(a) shows the I-T curves tested in the condition of the on-off cycle simulated sunlight for the pure SrTiO<sub>3</sub> nanofibers and SrTiO<sub>3</sub>@MoS<sub>2</sub> heterostructure. The result of

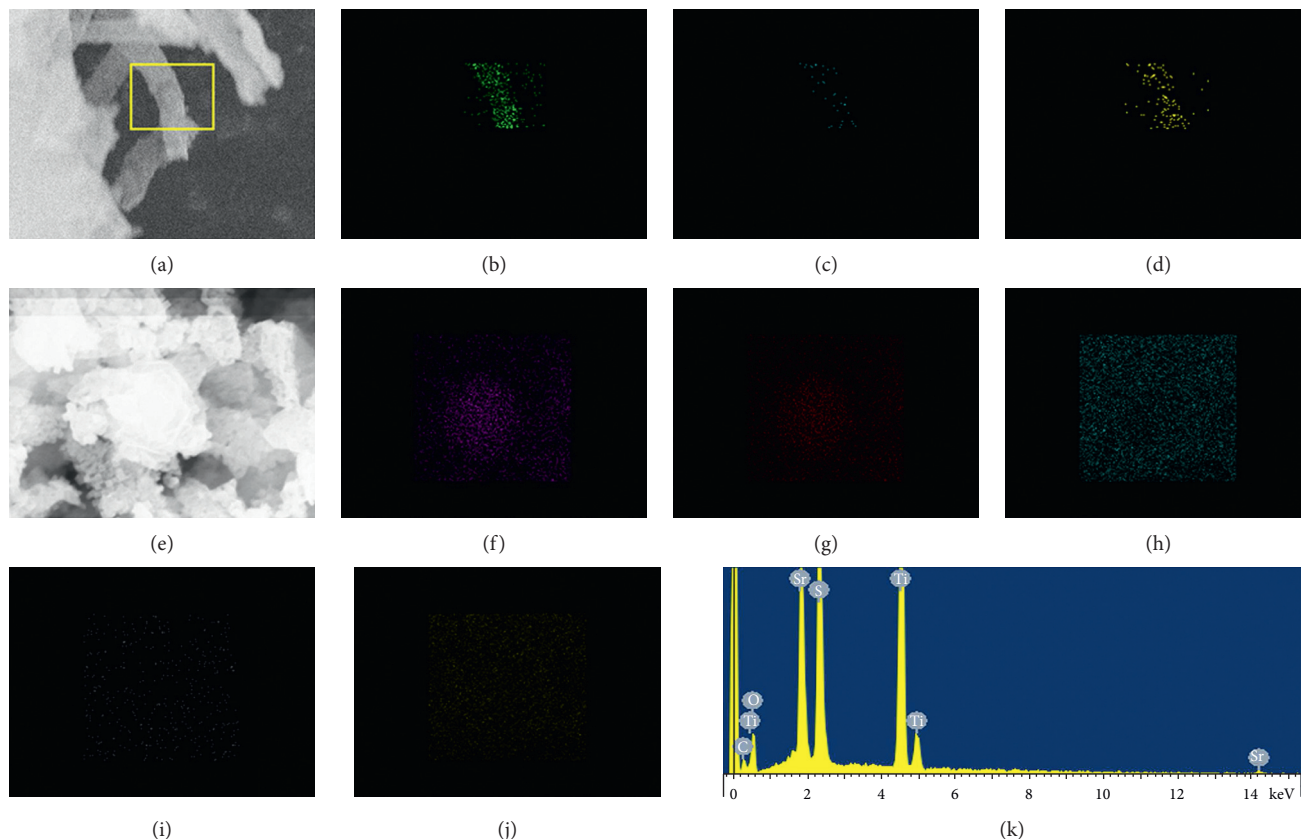


FIGURE 2: SEM image of (a) porous SrTiO<sub>3</sub> nanofibers with (b–d) Ti/S/Sr elemental mapping and SEM image of (e) SrTiO<sub>3</sub>@MoS<sub>2</sub> composite nanofibers with (f–j) Mo/S/Ti/S/Sr/O elemental mapping and (k) EDX images of SrTiO<sub>3</sub>@MoS<sub>2</sub> composite nanofibers.

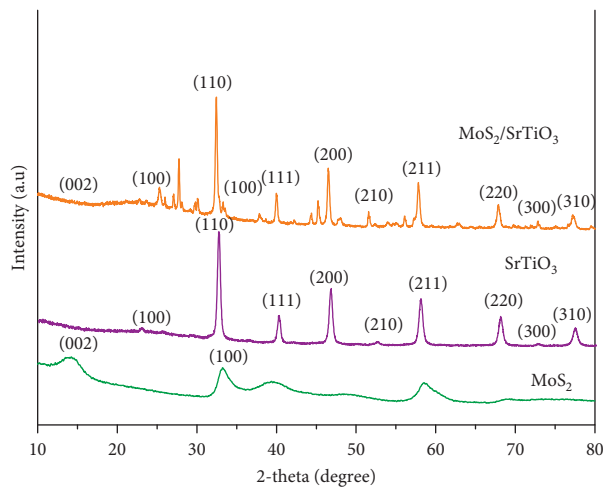


FIGURE 3: XRD patterns of pure MoS<sub>2</sub> nanosheets, porous SrTiO<sub>3</sub> nanofibers, and SrTiO<sub>3</sub>@MoS<sub>2</sub> composite nanofibers.

SrTiO<sub>3</sub>@MoS<sub>2</sub> indicates the photocurrent density is 21.4  $\mu$ A, which is nearly twice higher than the pure SrTiO<sub>3</sub> nanofibers (10.1  $\mu$ A). These results can prove that the adhering of MoS<sub>2</sub> improves the conductivity of materials and promotes the electron transfer rate. In addition, the V-MoS<sub>2</sub> nanosheets can increase the surface area of nanofibers and improve the photosensitivity and the separation of photo-induced carriers. It is also worth noting that photocurrent curves show a

regular rectangle shape, indicating the stability of composite materials. The EIS results in Figure 5(b) were applied to confirm the conductivity of the prepared composite. Moreover, the Rct of SrTiO<sub>3</sub>@MoS<sub>2</sub> is lower than that of porous SrTiO<sub>3</sub> nanofibers, indicating that the V-MoS<sub>2</sub> on the nanofibers can accelerate the interfacial transfer and separation of charge carriers and then improve the optoelectronic performance. The use of MoS<sub>2</sub> to improve the

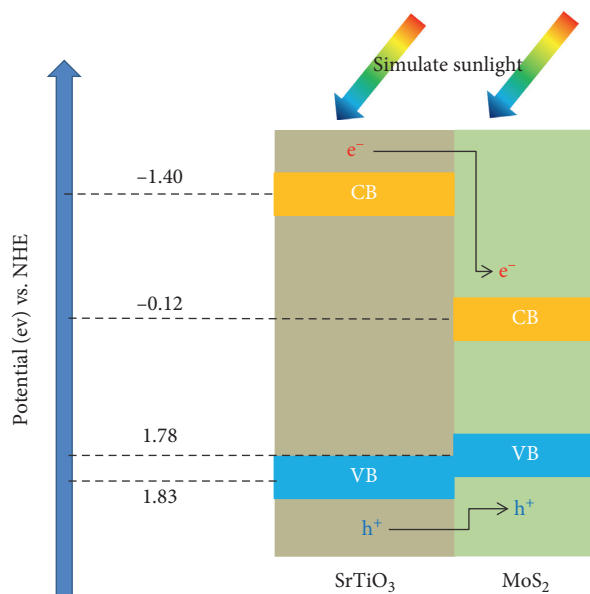


FIGURE 4: Schematic diagram of the photoelectric conversion mechanism of SrTiO<sub>3</sub>@MoS<sub>2</sub> composite nanofibers.

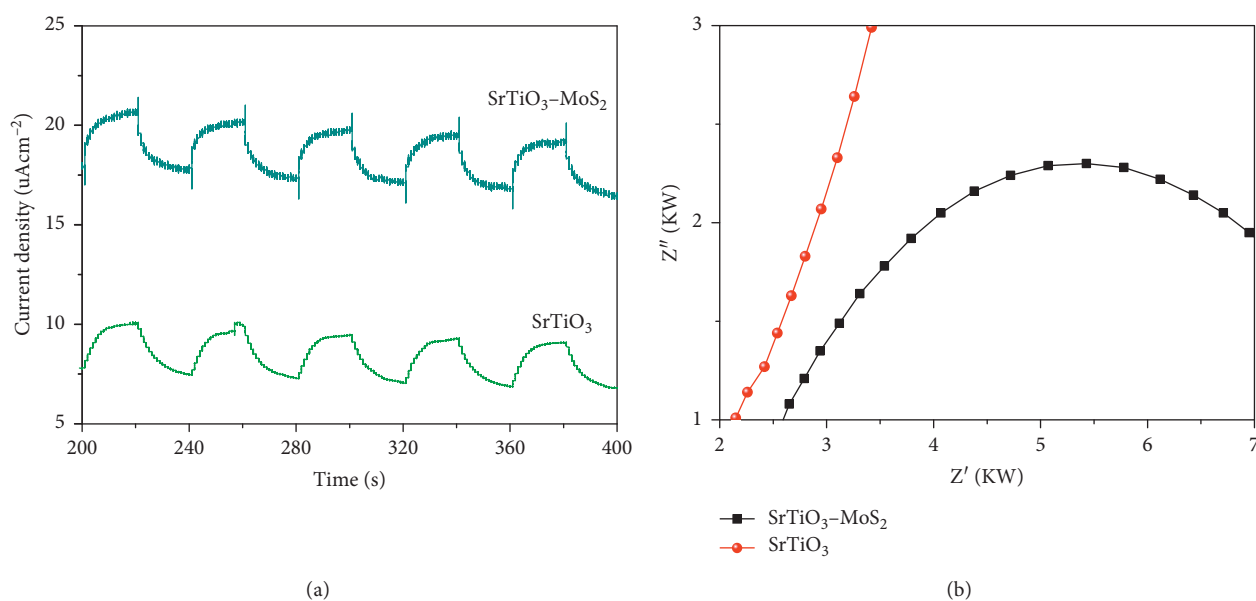


FIGURE 5: (a) The current density curves as a function of the time for SrTiO<sub>3</sub> and SrTiO<sub>3</sub>@MoS<sub>2</sub> at 1.23 V in 1 M KOH electrolyte; (b) Nyquist plots of samples at -0.24 V versus RHE measured from EIS in the frequency range from 100 kHz to 0.1 Hz.

performance of materials can be included in two reasons: first, the MoS<sub>2</sub> improves the electronic orbital structure of the SrTiO<sub>3</sub> and prolongs the life of photoelectrons. Then, constructing the structure of V-MoS<sub>2</sub> enlarges the surface area of materials, which means a larger contact area between electrodes and electrolytes.

#### 4. Conclusions

In summary, new SrTiO<sub>3</sub>@MoS<sub>2</sub> composite materials were successfully synthesized. The structure and morphologies of the prepared composite were studied by SEM, TEM, EDX, XRD, I-T curves, and EIS analysis. The large surface area of

the obtained SrTiO<sub>3</sub> NFs can provide suitable sites for loading MoS<sub>2</sub>. Under simulate sunlight at a potential of 1.23 V, the prepared composite materials exhibited a superior photoelectric performance of photocurrent density of 21.4  $\mu$ A and a resistance of 2.3  $\Omega$ . This study provides new clues for the preparation of MoS<sub>2</sub>-based composite materials and is widely used in the field of photodetector.

#### Data Availability

The experimental data used to support the findings of this study are included in the manuscript. The other data are available from the corresponding author upon request.

## Conflicts of Interest

The authors declare that there are no conflicts of interest.

## Acknowledgments

The authors greatly appreciate the financial supports of National Natural Science Foundation of China (no. 21872119), Qinhuangdao Science and Technology Support Project (no. 201602A112), Science and Technology Support Project of Department of Health of Hebei Province (no. 20171246), and Project of Human Resources and Social Security Department of Hebei Province (no. A2017002075).

## References

- [1] S. Shi, Z. Sun, and Y. H. Hu, "Synthesis, stabilization and applications of 2-dimensional 1T metallic MoS<sub>2</sub>," *Journal of Materials Chemistry A*, vol. 6, no. 47, pp. 23932–23977, 2018.
- [2] J. Kou, Y. Liu, Y. Zhu, and J. Zhai, "Progress in piezotronics of transition-metal dichalcogenides," *Journal of Physics D: Applied Physics*, vol. 51, no. 49, p. 493002, 2018.
- [3] Y. Fang, Y. Ge, C. Wang, and H. Zhang, "Mid-infrared photonics using 2D materials: status and challenges," *Laser and Photonics Reviews*, vol. 14, no. 1, Article ID 1900098, 2020.
- [4] R. Hany, M. Cremona, and K. Strassel, "Recent advances with optical upconverters made from all-organic and hybrid materials," *Science and Technology of Advanced Materials*, vol. 20, no. 1, pp. 497–510, 2019.
- [5] B. Rahmati, I. Hajzadeh, R. Karimzadeh, and S. M. Mohseni, "Facile, scalable and transfer free vertical-MoS<sub>2</sub> nanostructures grown on Au/SiO<sub>2</sub> patterned electrode for photodetector application," *Applied Surface Science*, vol. 455, pp. 876–882, 2018.
- [6] S. Ni, F. Guo, D. Wang et al., "Optimal Sr-Doped Free TiO<sub>2</sub>@SrTiO<sub>3</sub> heterostructured nanowire arrays for high-efficiency self-powered photoelectrochemical UV photodetector applications," *Crystals*, vol. 9, no. 3, p. 134, 2018.
- [7] X. Lu, P. Jiang, and X. Bao, "Phonon-enhanced photo-thermoelectric effect in SrTiO<sub>3</sub> ultra-broadband photodetector," *Nature Communications*, vol. 10, no. 1, p. 138, 2019.
- [8] W. Yang, Y. Zhang, Y. Zhang, W. Deng, and X. Fang, "Transparent Schottky photodiode based on AgNi NWs/SrTiO<sub>3</sub> contact with an ultrafast photoresponse to short-wavelength blue light and UV-shielding effect," *Advanced Functional Materials*, vol. 29, no. 46, Article ID 1905923, 2019.
- [9] X. Cui, Y. Wang, G. Jiang et al., "A photonic crystal-based CdS-Au-WO<sub>3</sub> heterostructure for efficient visible-light photocatalytic hydrogen and oxygen evolution," *RSC Advances*, vol. 4, no. 30, pp. 15689–15694, 2014.
- [10] S. Zhou, Y. Liu, J. Li et al., "Facile in situ synthesis of graphitic carbon nitride (g-C<sub>3</sub>N<sub>4</sub>)-N-TiO<sub>2</sub> heterojunction as an efficient photocatalyst for the selective photoreduction of CO<sub>2</sub> to CO," *Applied Catalysis B: Environmental*, vol. 159, pp. 20–29, 2014.
- [11] X. Cui, Y. Wang, G. Jiang et al., "The encapsulation of CdS in carbon nanotubes for stable and efficient photocatalysis," *Journal of Materials Chemistry*, vol. 2, no. 48, pp. 20939–20946, 2014.
- [12] X. Cui, G. Jiang, M. Zhu et al., "TiO<sub>2</sub>/CdS composite hollow spheres with controlled synthesis of platinum on the internal wall for the efficient hydrogen evolution," *International Journal of Hydrogen Energy*, vol. 38, no. 22, pp. 9065–9073, 2013.
- [13] J. Xiong, J. Li, J. Shi et al., "Metallic 1T-MoS<sub>2</sub> nanosheets in-situ entrenched on N, P, S-codoped hierarchical carbon microflower as an efficient and robust electro-catalyst for hydrogen evolution," *Applied Catalysis B: Environmental*, vol. 243, pp. 614–620, 2019.
- [14] J. Liu, L. Zhang, N. Li, Q. Tian, J. Zhou, and Y. Sun, "Synthesis of MoS<sub>2</sub>/SrTiO<sub>3</sub> composite materials for enhanced photocatalytic activity under UV irradiation," *Journal of Materials Chemistry A*, vol. 3, no. 2, pp. 706–712, 2015.
- [15] L. Wang, X. Liu, J. Luo et al., "Self-optimization of the active site of molybdenum disulfide by an irreversible phase transition during photocatalytic hydrogen evolution," *Angewandte Chemie International Edition*, vol. 56, no. 26, pp. 7610–7614, 2017.
- [16] H. Zhou, Y. Liu, L. Zhang, H. Li, H. Liu, and W. Li, "Transition metal-doped amorphous molybdenum sulfide/graphene ternary cocatalysts for excellent photocatalytic hydrogen evolution: synergistic effect of transition metal and graphene," *Journal of Colloid and Interface Science*, vol. 533, no. 3, pp. 287–296, 2019.
- [17] Y. Fu, X. Chen, X. Mou, Z. Ren, X. Li, and G. Han, "A dual-color luminescent localized drug delivery system with ratiometric-monitored doxorubicin release functionalities," *ACS Biomaterials Science & Engineering*, vol. 2, no. 4, pp. 652–661, 2016.
- [18] H. Bai, Z. Liu, and D. D. Sun, "Facile fabrication of TiO<sub>2</sub>/SrTiO<sub>3</sub> composite nanofibers by electrospinning for high efficient H<sub>2</sub> generation," *Journal of the American Ceramic Society*, vol. 96, no. 3, pp. 942–949, 2013.
- [19] Z. Cao, C. Wang, and J. Chen, "Synthesis and photocatalytic property of p-n junction YMnO<sub>3</sub>/SrTiO<sub>3</sub> composites," *Materials Research Express*, vol. 5, no. 11, Article ID 115512, 2018.
- [20] D. Hou, X. Hu, W. Ho, P. Hu, and Y. Huang, "Facile fabrication of porous Cr-doped SrTiO<sub>3</sub> nanotubes by electrospinning and their enhanced visible-light-driven photocatalytic properties," *Journal of Materials Chemistry A*, vol. 3, no. 7, pp. 3935–3943, 2015.
- [21] C. Grandclément, A. Piram, M.-E. Petit et al., "Biological removal and fate assessment of diclofenac using *Bacillus subtilis* and *Brevibacillus laterosporus* strains and ecotoxicological effects of diclofenac and 4'-Hydroxy-diclofenac," *Journal of Chemistry*, vol. 2020, Article ID 9789420, 12 pages, 2020.
- [22] J. Zhao, P. Zhang, J. Fan, J. Hu, and G. Shao, "Constructing 2D layered MoS<sub>2</sub> nanosheets-modified Z-scheme TiO<sub>2</sub>/WO<sub>3</sub> nanofibers ternary nanojunction with enhanced photocatalytic activity," *Applied Surface Science*, vol. 430, pp. 466–474, 2018.
- [23] H. Hou, F. Gao, L. Wang et al., "Superior thoroughly mesoporous ternary hybrid photocatalysts of TiO<sub>2</sub>/WO<sub>3</sub>/g-C<sub>3</sub>N<sub>4</sub> nanofibers for visible-light-driven hydrogen evolution," *Journal of Materials Chemistry A*, vol. 4, no. 17, pp. 6276–6281, 2016.
- [24] L. Zhang, J. Yin, K. Wei et al., "Fabrication of hierarchical SrTiO<sub>3</sub>@MoS<sub>2</sub> heterostructure nanofibers as efficient and low-cost electrocatalysts for hydrogen-evolution reactions," *Nanotechnology*, vol. 31, no. 20, Article ID 205604, 2020.
- [25] X. Yue, S. Yi, R. Wang, Z. Zhang, and S. Qiu, "Well-controlled SrTiO<sub>3</sub>@Mo<sub>2</sub>C core-shell nanofiber photocatalyst: boosted photo-generated charge carriers transportation and enhanced catalytic performance for water reduction," *Nano Energy*, vol. 47, pp. 463–473, 2018.
- [26] Y. Li, N. Luo, Z. Tian et al., "H<sub>2</sub>O<sub>2</sub>-free photo-Fenton degradation of organic pollutants on thermally exfoliated

- g-C<sub>3</sub>N<sub>4</sub>,” *Colloids and Surfaces A: Physicochemical and Engineering Aspects*, vol. 586, Article ID 124190, 2020.
- [27] M. Yang, R. Liu, H. Chen, H. Li, and P. Guo, “Synthesis of self-assembled nickel cobaltite microspheres and their electrocapacitive behavior in aqueous electrolytes,” *Colloids and Surfaces A: Physicochemical and Engineering Aspects*, vol. 587, Article ID 124329, 2020.
- [28] J. Sun, M. Yang, Y. Gong, H. Li, and P. Guo, “Synthesis of Pd<sub>3</sub>Pb colloidal nanocrystal assembly and their electrocatalytic activity toward ethanol oxidation,” *Colloids and Surfaces A: Physicochemical and Engineering Aspects*, vol. 586, Article ID 124224, 2020.
- [29] X. Yang, Z. Tian, Y. Chen, H. Huang, and J. Hu, “One-pot calcination preparation of graphene/g-C<sub>3</sub>N<sub>4</sub>-Co photocatalysts with enhanced visible light photocatalytic activity,” *International Journal of Hydrogen Energy*, vol. 45, no. 23, pp. 12889–12902, 2020.
- [30] L. Ge, M. Zhang, R. Wang et al., “Fabrication of CS/GA/RGO/Pd composite hydrogels for highly efficient catalytic reduction of organic pollutants,” *RSC Advances*, vol. 10, no. 26, pp. 15091–15097, 2020.
- [31] J. Yin, F. Zhan, T. Jiao et al., “Facile preparation of self-assembled MXene@Au@CdS nanocomposite with enhanced photocatalytic hydrogen production activity,” *Science China Materials*, vol. 63, 2020.
- [32] J. Yin, Q. Liu, J. Zhou et al., “Self-assembled functional components-doped conductive polypyrrole composite hydrogels with enhanced electrochemical performances,” *RSC Advances*, vol. 10, no. 18, pp. 10546–10551, 2020.
- [33] R. Wang, X. Yan, B. Ge et al., “Facile preparation of self-assembled black phosphorus-dye composite films for chemical gas sensors and surface-enhanced Raman scattering performances,” *ACS Sustainable Chemistry & Engineering*, vol. 8, no. 11, pp. 4521–4536, 2020.
- [34] K. Ma, R. Wang, Y. Rao, W. Zhao, S. Liu, and T. Jiao, “Langmuir-Blodgett films of two chiral perylene bisimide-based molecules: aggregation and supramolecular chirality,” *Colloids and Surfaces A: Physicochemical and Engineering Aspects*, vol. 591, Article ID 124563, 2020.
- [35] Y. Feng, J. Yin, S. Liu, Y. Wang, B. Li, and T. Jiao, “Facile synthesis of Ag/Pd nanoparticle-loaded poly(ethylene imine) composite hydrogels with highly efficient catalytic reduction of 4-nitrophenol,” *ACS Omega*, vol. 5, no. 7, pp. 3725–3733, 2020.
- [36] Y. He, R. Wang, C. Sun et al., “Facile synthesis of self-assembled NiFe layered double hydroxide-based azobenzene composite films with photoisomerization and chemical gas sensor performances,” *ACS Omega*, vol. 5, no. 7, pp. 3689–3698, 2020.
- [37] J. Song, C. Yuan, T. Jiao et al., “Multifunctional antimicrobial biometallohydrogels based on amino acid coordinated self-assembly,” *Small*, vol. 16, no. 8, Article ID 1907309, 2020.
- [38] C. Cai, R. Wang, S. Liu et al., “Synthesis of self-assembled phytic acid-mxene nanocomposites via a facile hydrothermal approach with elevated dye adsorption capacities,” *Colloids and Surfaces A: Physicochemical and Engineering Aspects*, vol. 589, Article ID 124468, 2020.
- [39] Y. Xu, R. Wang, Y. Zheng et al., “Facile preparation of self-assembled Ni/Co phosphates composite spheres with highly efficient her electrocatalytic performances,” *Applied Surface Science*, vol. 509, Article ID 145383, 2020.
- [40] R. Geng, J. Yin, J. Zhou et al., “In situ construction of Ag/TiO<sub>2</sub>/g-C<sub>3</sub>N<sub>4</sub> heterojunction nanocomposite based on hierarchical co-assembly with sustainable hydrogen evolution,” *Nanomaterials*, vol. 10, no. 1, p. 1, 2020.
- [41] F. Zhan, J. Yin, J. Zhou et al., “Facile preparation and highly efficient catalytic performances of Pd-Cu bimetallic catalyst synthesized via Seed-mediated method,” *Nanomaterials*, vol. 10, no. 1, p. 6, 2020.
- [42] Y. Feng, R. Wang, J. Yin et al., “Facile synthesis of Cu<sub>2</sub>O nanoparticle-loaded carbon nanotubes composite catalysts for reduction of 4-Nitrophenol,” *Current Nanoscience*, vol. 16, no. 4, pp. 611–618, 2020.
- [43] J. Zhao, J. Yin, J. Zhong et al., “Facile preparation of a self-assembled Artemia cyst shell-TiO<sub>2</sub>-MoS<sub>2</sub> porous composite structure with highly efficient catalytic reduction of nitro compounds for wastewater treatment,” *Nanotechnology*, vol. 31, no. 8, p. 85603, 2020.
- [44] Y. Meng, J. Yin, T. Jiao et al., “Self-assembled copper/cobalt-containing polypyrrole hydrogels for highly efficient ORR electrocatalysts,” *Journal of Molecular Liquids*, vol. 298, Article ID 112010, 2020.
- [45] J. Yin, F. Zhan, T. Jiao et al., “Highly efficient catalytic performances of nitro compounds via hierarchical PdNPs-loaded MXene/polymer nanocomposites synthesized through electrospinning strategy for wastewater treatment,” *Chinese Chemical Letters*, vol. 31, no. 4, pp. 992–995, 2020.
- [46] K. Ma, R. Wang, T. Jiao et al., “Preparation and aggregate state regulation of co-assembly graphene oxide-porphyrin composite Langmuir films via surface-modified graphene oxide sheets,” *Colloids and Surfaces A: Physicochemical and Engineering Aspects*, vol. 584, Article ID 124023, 2020.
- [47] X. Xu, Y. Liu, W. Fu et al., “Poly(N-isopropylacrylamide)-based thermoresponsive composite hydrogels for biomedical applications,” *Polymers*, vol. 12, no. 3, p. 580, 2020.